ANALYTICAL CHEMISTRY
JULY 1, 1995

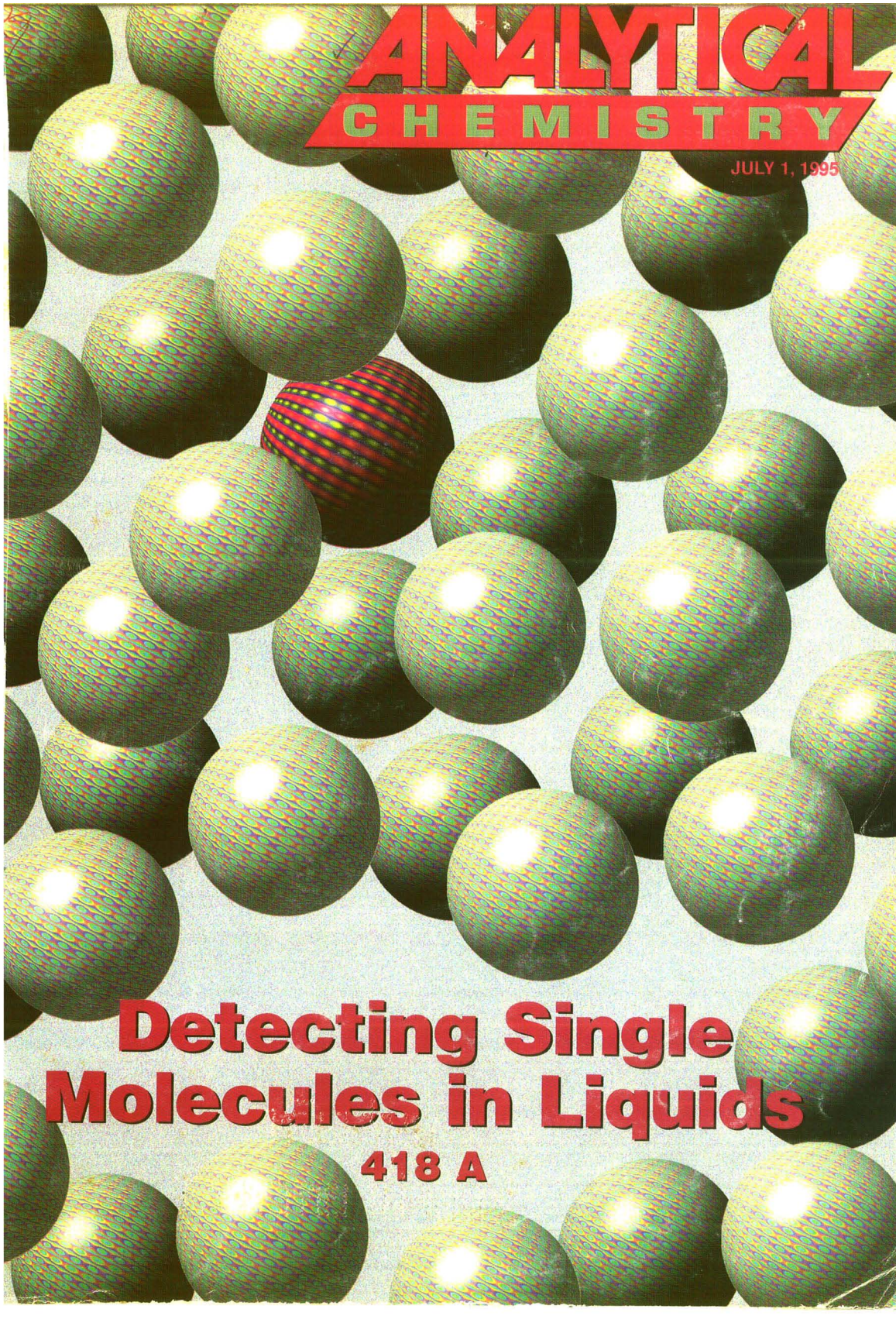

Detecting Single Molecules in Liquids

418 A

METROHM RAISES MOISTURE ANALYSIS TO A NEW LEVEL.

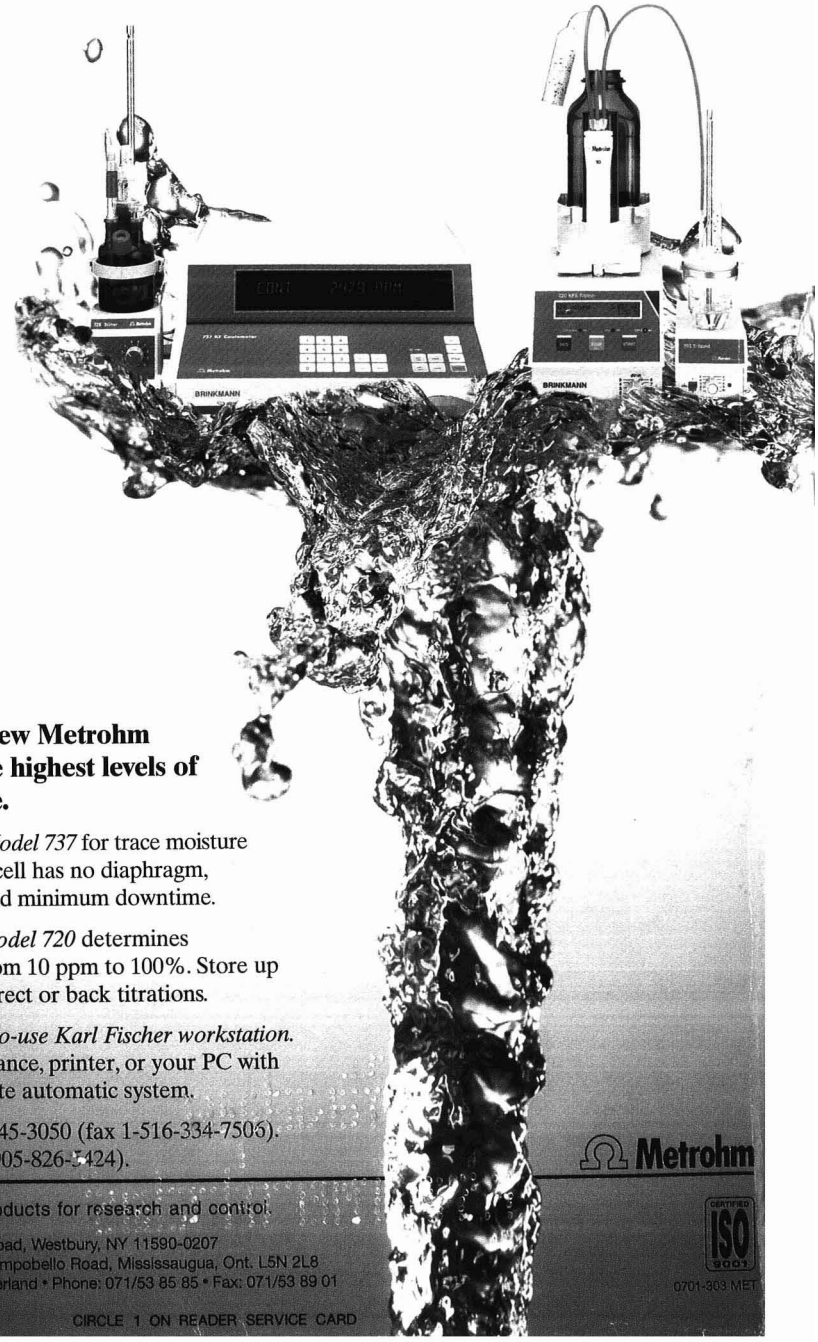

Brinkmann brings you two new Metrohm Karl Fischer Titrators for the highest levels of quality data and convenience.

NEW Coulometric Karl Fischer Model 737 for trace moisture analysis as low as 1 ppm. Titration cell has no diaphragm, allowing quick and easy cleaning and minimum downtime.

NEW Volumetric Karl Fischer Model 720 determines moisture quickly and accurately from 10 ppm to 100%. Store up to 60 titration methods. Perform direct or back titrations.

NOW have an economical, easy-to-use Karl Fischer workstation. Connect either instrument to a balance, printer, or your PC with *ready-to-use software* for an accurate automatic system.

For a demonstration, call 1-800-645-3050 (fax 1-516-334-7506). In Canada, call 800-263-8715 (fax 905-826-3424).

Metrohm

BRINKMANN Quality products for research and control

Brinkmann Instruments, Inc., One Cantiague Road, Westbury, NY 11590-0207
Brinkmann Instruments (Canada) Ltd., 6670 Campobello Road, Mississaugua, Ont. L5N 2L8
Outside U.S. and Canada: Metrohm Ltd., Switzerland • Phone: 071/53 85 85 • Fax: 071/53 89 01

CERTIFIED ISO 9001

0701-303 MET

CIRCLE 1 ON READER SERVICE CARD

New

Whatman GD/X and ZC Syringe Filters go to great depths to double your efficiency

Increase flow rates with the combined prefiltration technology of graded-density glass microfibers and a variety of membrane filters in a single device

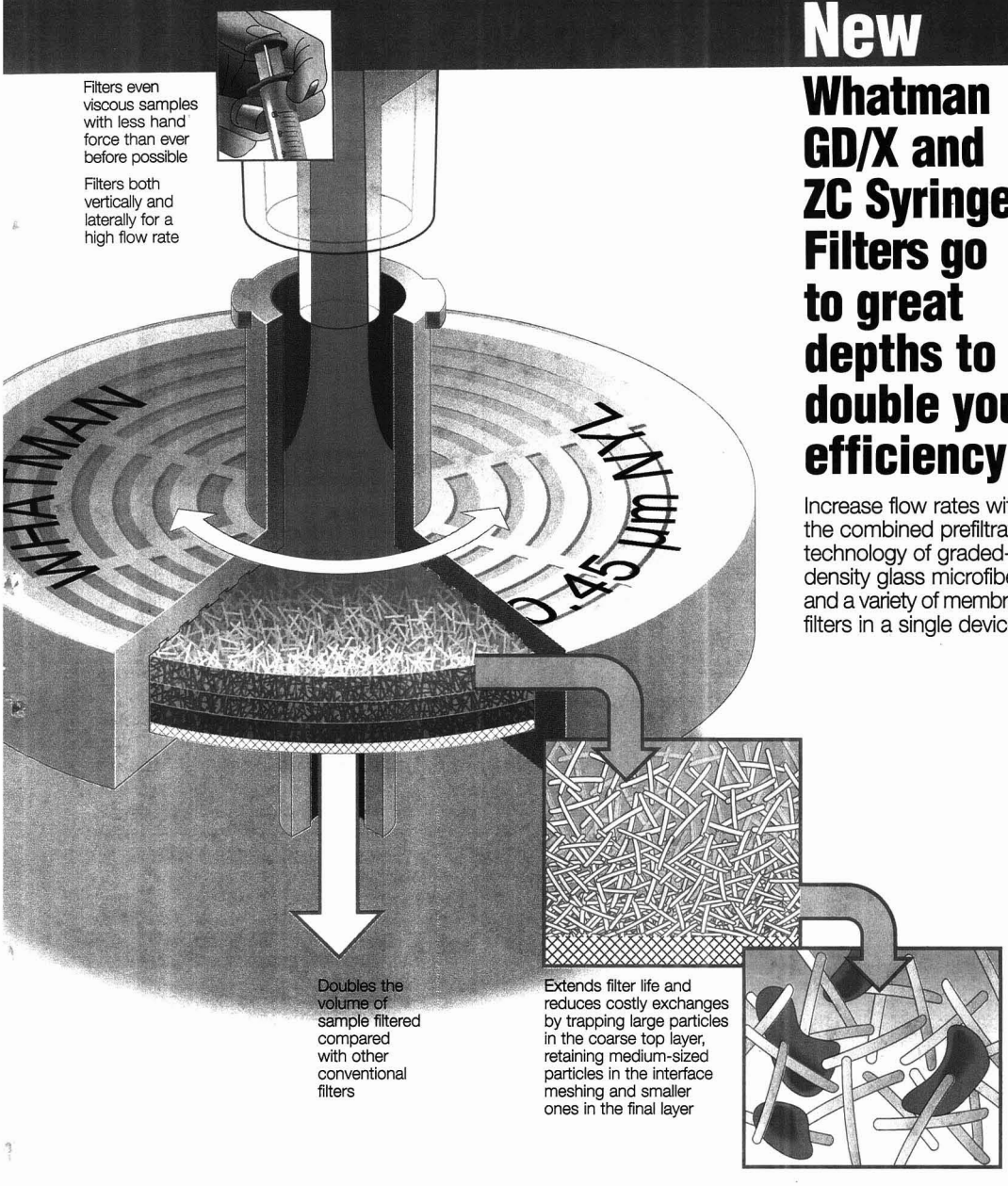

Double your filtration efficiency today. Whatman provides innovative solutions to even your most difficult applications. For a test sample of new GD/X or ZC Syringe Filters with graded-density glass microfiber prefilters, or for applications assistance, call **1-800-922-0361**.

CIRCLE 7 ON READER SERVICE CARD

Whatman

Whatman Inc., 6 Just Road, Fairfield, New Jersey 07004
Telephone: 201-882-9277 Fax: 201-882-5134

Whatman (word and device) and Whatman (word only) are trademarks of Whatman International Ltd.

746-11-500

Contents

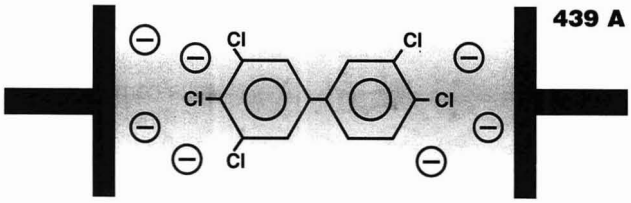

439 A

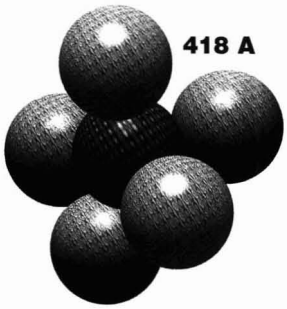

418 A

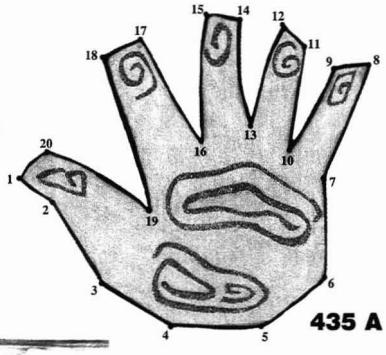

435 A

428 A

REPORT

418 A
ON THE COVER. Detecting single molecules in liquids
The ability to make highly sensitive and selective measurements could lead to enormous breakthroughs in DNA analysis, groundwater monitoring, fluorescence immunoassay, chemical separations, and fundamental studies of physical and chemical phenomena. J. Michael Ramsey, William B. Whitten, and Michael D. Barnes of Oak Ridge National Laboratory discuss the trade-offs between sample throughput and sensitivity in single-molecule fluorescence detection and provide examples of different detection schemes.

A/C INTERFACE

428 A
Electronic lab notebooks
Electronic notebooks can improve the discovery process, turning ideas into products in a shorter time. Raymond E. Dessy of Virginia Polytechnic Institute and State University examines the need to change our concept of a scientific notebook and what work habits must be altered to gain the benefits associated with shared electronic lab notebooks.

ANALYTICAL CHEMISTRY

JULY 1, 1995

ANCHAM
67(13) 393 A–450 A/1913–2314 (1995)
ISSN 0003-2700

Registered in U.S. Patent and Trademark Office
©Copyright 1995 by the American Chemical Society

DEPARTMENTS

397 A
In AC Research

409 A
Editorial

***Analytical Chemistry*'s measurement cop.** A conversation between our measurement cop, an eminent chemist, and an elected official raises the issues of legislation and risk assessment.

411 A
Analytical Currents

416 A
News

Immunoassay methods into the hands of users. • BAS purchases Technicol. • Division of Analytical Chemistry awards to go to Kuwana, Morris, Winefordner, and Zare. • For Your Information.

424 A
Software

The ultimate solution for technical graphics? *Origin*, a full-featured graphics program aimed at the scientific market, is reviewed by John C. Marshall of St. Olaf College. • Software released.

426 A
Books

Method development in CE. Howard Drossman of Colorado College reviews *Capillary Electrophoresis of Small Molecules and Ions.* • **Principles of laser spectroscopy.** *Applied Laser Spectroscopy: Techniques, Instrumentation, and Applications* is reviewed by John C. Wright of the University of Wisconsin. • Books received.

434 A
Meetings

Conferences.

435 A
Focus

Vanished into thin air: The search for children's fingerprints. Researchers at Oak Ridge National Laboratory find that the chemical profile of a fingerprint residue may "fingerprint" age and health.

439 A
Product Review

Electron capture detection for GC. Applications for ECDs continue to appear as needs for routine GC detection change. We review the basic theory involved and compare the features of representative instruments.

444 A
New Products

A benchtop sector GC/MS, a dual-view ICP-AES, and a digital electron energy analyzer are featured. • Instrumentation. • Literature. • Catalogs.

448 A
Information Express

1C
AC Research Contents

1913–2313
AC Research

2314
Author Index

Analytical Chemistry (ISSN 0003-2700) is published semimonthly by the American Chemical Society, 1155 Sixteenth St., N.W., Washington, DC 20036. Second-class postage paid at Washington, DC, and additional mailing offices. Postmaster: Send address changes to *Analytical Chemistry*, Member & Subscriber Services, P.O. Box 3337, Columbus, OH 43210.

Canadian GST Reg. No. R127571347.

ห้องสมุดกลาง [illegible] บริการ
27 ก.ค. 2538

At last! The piece that helps you solve the health and safety puzzle for everyone working with chemicals

NEW!
A sharp bimonthly focus on chemical health & safety

This new bimonthly magazine combines magazine-style articles with news reports, case studies, accident updates, and peer-reviewed research papers.

Current, unbiased information for working with chemicals in the lab and on the job

Chemical Health & Safety (CHAS) connects you with practitioners who know the issues and are finding the solutions. You'll share in new tools, technical and regulatory information, plus effective new practices for chemical handling, storage, use, and disposal.

It's powerful new help for anticipating — and resolving — the tough challenges related to chemical exposure.

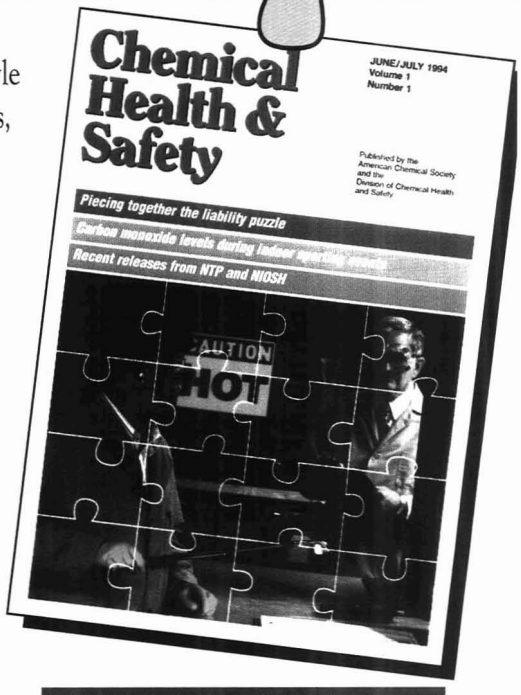

Experts take you beyond the regulations to real-world solutions

Winner of the 1984 Division of Chemical Health and Safety award, Founding Editor **Warren Kingsley** comes to ***Chemical Health & Safety*** from J.T. Baker, Inc. where he was Manager of Safety Training. Associate Editor **Eileen Segal** is a well-known consultant in chemical health and safety. Along with a distinguished board of editors, these experts deliver the information you need...in time to make a difference.

Copublished by the American Chemical Society and the Division of Chemical Health and Safety

1995 Subscription Rates (bimonthly, 6 issues)

	U.S.	Canada & Mexico	Europe (Air Service)	All Other Countries (Air Service)
ACS Members	$ 25	$ 30	$ 34	$ 36
CHAS Division Members	$ 15	$ 20	$ 24	$ 26
CHAS Division Affiliates	$ 25	$ 30	$ 34	$ 36
Nonmembers (Individuals)	$ 55	$ 55	$ 59	$ 61
Nonmembers (Institutions)	$ 250	$ 255	$ 259	$ 261

Start your subscription today!

Call 1–800–333–9511

(Outside the U.S. call 614–447–3776.
Fax 614–447–3671)

Or mail your order to: **American Chemical Society**, Publications Marketing, 1155 Sixteenth Street, N.W., Washington, D.C. 20036

Brief introductions to the research articles appearing in the July 1 issue and tentatively scheduled to appear in the July 15 issue

Accelerated Articles

A new matrix for DNA sequencing

Although cross-linked polyacrylamide gel matrices provide higher resolution for sequencing large DNA fragments, the gel's instability, irreproducibility, and fragile nature make the matrix unsuitable for large-scale sequencing. Edward S. Yeung and Eliza N. Fung of Iowa State University describe using non-crossed-linked poly(ethylene oxide) in two size ranges as a sieving matrix. The PEO provides identical separation performance for small DNA fragments, better performance for large DNA fragments, increased separation speed, and lower viscosity. ("High-Speed DNA Sequencing by Using Mixed Poly(ethylene oxide) Solutions in Uncoated Capillary Columns"; AC950217P; p. 1913)

Preparing gold disk nanoelectrodes

Although disk electrodes with microscopic dimensions are being investigated for numerous new applications, they can be difficult to make. Charles R. Martin and Vinod P. Menon of Colorado State University use an electroless deposition method to fill the pores of nanoporous filtration membranes with gold and to fabricate ensembles of gold nanodisk electrodes with diameters as small as 10 nm. The electrochemical response characteristics of these nanoelectrodes are in agreement with theoretical predictions, and the detection limits for electroactive species are as much as 3 orders of magnitude less than those at large-diameter gold disk electrodes. ("Fabrication and Evaluation of Nanoelectrode Ensembles"; AC941215A; p. 1920)

Attenuating metal oxide ions in ICPMS

Although atomic ions (M^+) are the major species obtained under normal ICPMS atomization conditions, other ions such as MO^+, ArM^+, ArO^+, and Ar_2^+ hamper the determination of several important elements. R. S. Houk and colleagues at Iowa State University/Ames Laboratory describe a graphite injector that provides a simple way to extract M^+ ions from a region of the plasma that is physically separated from the zone inhabited by MO^+ ions. They demonstrate that signal ratios for MO^+/M^+ can be reduced to 0.01%–0.05% and that analyte sensitivity can be improved by factors of 1.5 to 15. ("Attenuation of Metal Oxide Ions in Inductively Coupled Plasma Mass Spectrometry with a Graphite Torch Injector"; AC950121V; p. 1929)

Sol–gel RNase mop

Ribonucleases (RNases) secreted from the hands of a researcher can easily contaminate solutions for nucleic acid analyses and can lower the yield of RNA during sample preparation. Frank V. Bright and colleagues at the State University of New York at Buffalo describe the sol–gel fabrication and use of RNase-binding silica particles doped with an encapsulated RNase inhibitor. The particles can be used as an affinity column packing to remove RNases from solutions and can be regenerated with NaCl. ("Removal of Ribonucleases from Solution Using an Inhibitor-Based Sol–Gel-Derived Biogel"; AC950230+; p. 1935)

A herbicide-detecting biosensor

One way to detect herbicides in the environment is to measure the inhibition of photosynthetic electron transport (PET) activity in cells. Elizabeth A. H. Hall and Monika Preuss of the University of Cambridge (U.K.) demonstrate a diamindurene-mediated PET biosensor using the cyanobacterial *Synechoccus sp.* to measure atrazine and diuron. Diuron exhibits a first-order binding rate constant that is ~ 7 times that of atrazine under the same light-and-dark cycle. ("Mediated Herbicide Inhibition in a PET Biosensor"; AC950147M; p. 1940)

High-resolution MALDI TOFMS

Although TOF mass spectrometers are inexpensive to construct and simple to operate, they exhibit low mass resolving power for the detection of ions generated by MALDI. Liang Li and Randy M. Whittal of the University of Alberta (Canada) use a time-lag focusing method to improve the resolution of MALDI TOFMS to the range of 3000–6000 fhm. Isotopically resolved mass spectra are observed for peptides with masses up to 3000 Da. ("High-Resolution Matrix-Assisted Laser Desorption/Ionization in a Linear Time-of-Flight Mass Spectrometer"; AC950339H; p. 1950)

QCM sensor for biotin

Measuring the binding of small molecules (MW ≤ 500) by QCM is difficult because the change in frequency can be too small for the apparatus to detect. Masuo Aizawa and colleagues at the Tokyo Institute of Technology (Japan) report on an on-line FIA QCM sensor for measuring biotin (MW 244), based on the complexation between avidin and immobilized desthiobiotin. The measurement ranges are 0.05–100 μg/mL (stop-flow mode) and 0.2–10,000 μg/mL (continuous-flow mode). ("Quartz Crystal Microbalance Bioaffinity Sensor for Biotin"; AC9500388; p. 2212)

Statistically correlating cell growth with surface chemistry ♦

The interaction of anchorage-dependent cells with synthetic polymer substrates is of interest in biotechnology, biofouling, and the design of biomaterials. Buddy D. Ratner and colleagues at the University of Washington use partial least-squares (PLS)

♦ Denotes articles that are tentatively scheduled for the July 15 issue

regression and secondary ion MS to investigate the relationship between bovine arterial endothelial cells grown on plasma-deposited films and the surface properties of those films. Their results suggest that the molecular structure of the surface is more relevant in describing cell growth than is the elemental composition. ("Relationship between Surface Chemistry and Endothelial Cell Growth: Partial Least-Squares Regression of the Static Secondary Ion Mass Spectra of Oxygen-Containing Plasma Deposited Films"; AC941241Q)

Drying and aging biogels ♦

A better understanding of the long- and short-term interactions between biorecognition elements and the sol–gel matrix encapsulating them is needed if biosensors based on these materials are to be developed. Frank V. Bright and colleagues at the State University of New York at Buffalo investigate the effects of biogel aging and drying on acrylodan-labeled bovine and human serum albumin entrapped in a tetramethylorthosilane-derived biogel composite. Time-resolved anisotropy experiments show that the acrylodan residue and the protein can undergo nanosecond motion within the biogel. ("Dynamics of Acrylodan-Labeled Bovine and Human Serum Albumin Entrapped in a Sol–Gel-Derived Biogel"; AC941197E)

Estimating the SAW response to vapors

Surface acoustic wave (SAW) devices can be coated with vapor-sorbent polymers to create dedicated vapor sensors for particular applications. Jay W. Grate and colleagues at Pacific Northwest Laboratory and the University College–London (U.K.) demonstrate the use of a linear solvation energy relationship to model acoustic-wave vapor sensor responses. The method is used to guide selection of appropriate polymer coatings for optimal detection of specified vapors at given threshold concentrations. ("Method for Estimating Polymer-Coated Acoustic Wave Vapor Sensor Responses"; AC950058+; p. 2162)

Phenolic antioxidants in food

Determining phenolic antioxidants, such as BHA and BHT, in food involves extracting the food with organic solvents and concentrating the extracts. J. M. Pingarrón and colleagues at Complutense University of Madrid (Spain) use cylindrical carbon fiber microelectrodes to directly measure BHA and BHT in acetonitrile. A detection limit of ~ 70 μg/L of BHA or BHT is achieved and two well-defined oxidation peaks are obtained with a difference between peak potentials of ~ 300 mV, allowing simultaneous determination of both compounds. ("Analytical Applications of Cylindrical Carbon Fiber Microelectrodes. Simultaneous Voltammetric Determination of Phenolic Antioxidants in Food"; AC941139T; p. 2195)

Correlating surface blistering with electrolyte anion intercalation

Highly oriented pyrolytic graphite (HOPG) is often used in studies of carbon oxidation because of its well-defined structure with large crystallites and atomically flat, low defect-density basal plan surfaces. Royce W. Murray and colleagues at the University of North Carolina use cyclic voltammetry, atomic force microscopy, optical microscopy, and in situ atomic force microscopy/electrochemistry to investigate the relationship of blister formation on HOPG surfaces with the intercalation properties of the electrolyte anion solution in which the electrode is submerged. The results support a model in which blister formation reflects electrolyte anion intercalation followed by subsurface gas evolution. ("Incipient Electrochemical Oxidation of Highly Oriented Pyrolytic Graphite: Correlation between Surface Blistering and Electrolyte Anion Intercalation"; AC950066Q; p. 2201)

Structure and function of biosensor polymer membranes

Overoxidized polypyrrole membranes, which are formed directly on amperometric peroxidase-type biosensors via electrolysis, improve the selectivity and sensitivity of the biosensors through their size exclusion, ion exchange, and hydrophobic interaction properties. P. G. Zambonin and co-workers at the Università degli Studi (Italy) investigate the correlation between permselectivity and chemical structure of these membrane coatings using X-ray photoelectron spectroscopy. They observe C=O and COH functional groups as well as a transformation from positively charged nitrogens to imine groups on overoxidized membranes. ("Correlation between Permselectivity and Chemical Structure of Overoxidized Polypyrrole Membranes Used in Electroproduced Enzyme Biosensors"; AC940649K; p. 2207)

Linear calibration curve for sulfate determination

The potentiometric determination of sulfate can involve tedious procedures and suffers from unpredictable uncertainties that result from nonlinear or semilinear calibration plots. Hsuan-Jung Huang of the National Sun Yat-Sen University (Taiwan) and Tzyh-Chyang Tang of the Chia-Nan Junior College of Pharmacy (Taiwan) derive equations describing the explicit linear relationships between the measured potential of the lead ion-selective electrode and the sulfate concentration in sample solutions. By using the linear calibration curve, the researchers improve the sensitivity of a flow injection method for sulfate determination and the reliability of the results. ("Flow Injection Analysis of Sulfate with a Potentiometry-Based Linear Calibration Graph"; AC941155Q; p. 2299)

Screen-printed enzyme pastes

Sensors used for one-shot measurements, such as blood analysis, manufactured by ink jet and screen printing processes are not durable enough to be used in process and flow injection systems. Ingrid Rohm and colleagues at GBF-Gesellschaft für Biotechnologische Forschung mbH (Germany) combine screen printing with UV polymerization to create enzyme layers on amperometric thick-film electrodes that can withstand insertion in wall-jet cells of flow injection systems. They find that these sensors are more stable but less sensitive than sensors based on glutardialdehyde cross-linked glucose oxidase. ("UV-Polymerizable Screen-Printed Enzyme Pastes"; AC951115M; p. 2304)

$\Delta R/R$ by QCM ♦

The theoretical basis for understanding reflectance spectroscopy in the UV–vis range, particularly for adsorbed layers only one atom or molecule thick, has not yet been fully developed, primarily because the formation of the adsorbate/substrate in-

♦ Denotes articles that are tentatively scheduled for the July 15 issue

terface causes changes in the properties of the two phases. Daniel A. Scherson and colleagues at Case Western Reserve University describe a QCM that provides in situ electrochemical, $\Delta R/R$, and microgravimetric data from metal film electrodes sputtered on the surface of optically polished quartz crystals. Changes in weight and relative reflectivity associated with the adsorption of ions can be correlated without the uncertainties caused by preparation of the electrode surface. ("Simultaneous Normalized Optical Reflectivity and Microgravimetric Measurements at Electrode/Electrolyte Interfaces: The Adsorption of Bromide on Gold in Aqueous Media"; AC941082A)

Understanding the interaction between NMP–TCNQ and GOx ♦

That organic conducting salt electrodes can accept electrons from biological molecules is well known, but the debate involving the mechanism of current generation continues. E.A.H. Hall and C. C. Jung at the Institute of Biotechnology (U.K.) investigate the biocatalytic properties of *N*-methylphenazinium tetracyano-*p*-quinodimethane (NMP–TCNQ) as a prototype system in connection with the enzyme glucose oxidase using impedance spectroscopy. They propose a model involving $TCNQ^0$ as the mediating species to account for the observed experimental data. ("Impedance Analysis of NMP–TCNQ at Glucose Oxidase Interfaces"; AC941071H)

Stop-and-go electron transfer ♦

Achieving direct electron transfer between electrodes and proteins is of interest because of the applications to biosensors, chemical synthesis, and fundamental studies. James F. Rusling and colleagues at the University of Connecticut determine that electron transfer to myoglobin is facilitated when electrodes are coated with surfactant and is blocked when electrodes are coated with unpurified myoglobin. Their results indicate that surfactant adsorbed at the electrode–film interface appears to inhibit adsorption of macromolecules from myoglobin, which could block electron transfer between myoglobin and electrodes. ("Electron Transfer from Electrodes to Myoglobin: Facilitated in Surfactant Films and Blocked by Adsorbed Biomacromolecules"; AC950106Q)

Building a better UME ♦

The use of ultramicroelectrodes (UMEs) in electroanalytical investigations has dramatically increased over the past 15 years, primarily because of the benefits that result from the small physical dimensions of the electrodes. Jon R. Kirchhoff and coworkers at the University of Toledo construct carbon fiber disk UMEs with well-defined geometries by chemical vapor deposition techniques and study the effect of precursor concentration and type, gas flow rates, and temperature on the UMEs as well as on their electrochemical responses. They report that the deposition of hard and inert ceramic materials imparts durability to the fragile carbon fibers and that use of an epoxy sealant at the electrode tip is not required. ("Chemical Vapor Deposition Fabrication and Characterization of Silica-Coated Carbon Fiber Ultramicroelectrodes"; AC9411886)

Improving selectivity for Na^+ in solvent polymeric membrane electrodes ♦

The attachment of a geminal–propyl group to the polyether ring carbon that bears an oxygen-containing side arm markedly increases the selectivity for Na^+ relative to larger cations. Richard A. Bartsch and colleagues at Texas Tech University examine the influence of structural variation in 21 alkyl *sym*-R-dibenzo-16-crown-5-oxyacetates on the selectivity for Na^+ in solvent polymeric membrane electrodes. They observe very high Na^+/Li^+ selectivities ($10^{3.8}$–$10^{3.9}$) for eight of the lariat ether ester ionophores studied. ("Sodium Ion-Selective Electrodes Based on Dibenzo-16-crown-5 Compounds with Pendent Ester Groups"; AC950187Q)

MALDI in mid-air

MALDI is usually conducted by mixing a sample with a matrix compound, coating a probe surface with it, and using a laser to desorb and ionize the sample for MS analysis. Mikhail A. Khodorkovski and colleagues of LEPTA-Petersburg Ltd. (Russia) develop a variation in which laser desorption of a mixture of analyte and matrix material creates neutral clusters for injection into a supersonic jet and analysis by TOFMS. The clusters are dissociated by selective two-photon ionization at a wavelength that affects only the matrix compound, followed by intercluster proton or cation transfer to the analyte. ("Matrix-Assisted Laser Desorption Ionization of Neutral Clusters Composed of Matrix and Analyte Molecules"; AC940855S; p. 1963)

Understanding aerosol MALDI

Aerosol MALDI helps overcome some of the problems inherent in introducing liquid samples into the spectrometer. To better understand the parameters that affect the ionization process, David H. Russell and colleagues at Texas A&M University examine analyte concentration and matrix-to-analyte ratio to determine what role they play in analyte ion yield. They use bradykinin, gramicidin S, bovine insulin, and myoglobin as analytes, and α-cyano-4-hydroxycinnamic acid and 4-nitroaniline as matrices and find that the optimum matrix-to-analyte molar ratio is 10–100:1 and that relative sensitivities are a result of the chemical properties of the analytes. ("Aerosol Matrix-Assisted Laser Desorption Ionization: Effects of Analyte Concentration and Matrix-to-Analyte Ratio"; AC9409344; p. 1981)

A crown for gold

Activated carbon is under investigation as an alternative to zinc powder as a precipitant for solubilized gold, but the speciation of the adsorbed gold on carbon has not been well characterized. G. S. Groenewold and co-workers at the Idaho National Engineering Laboratory and the University of Idaho describe a static SIMS method for detecting gold and gold cyanide complexes on carbon precipitant. The carbon surface is doped with a crown ether to promote the release of $Au(CN)_2^-$. ("Static SIMS Detection of Gold and Gold Cyanide Complexes on Carbon Using Crown Ether Enhancement"; AC950053C; p. 1987)

Measuring $^2H/^1H$

Continuous-flow isotope ratio MS has simplified the measurement of many light-element stable isotopes, except hydrogen. Simon J. Prosser of Europa Scientific Ltd. (U.K.) and Charles M. Scrimgeour of the Scottish Crop Research Institute describe a method using a modified isotope ratio mass spectrometer that allows measurement of $^2H/^1H$ in H_2 by removing the interference caused by the $^4He^+$ carrier peak. Samples of H_2 with

♦ Denotes articles that are tentatively scheduled for the July 15 issue

$^2H/^1H$ at the natural abundance level can be analyzed in < 2 min with precision of ± 1.5‰. ("High-Precision Determination of $^2H/^1H$ in H_2 and H_2O by Continuous-Flow Isotope Ratio Mass Spectrometry"; AC950166W; p. 1992)

Enhancing mass resolution in MALDI

A MALDI TOF mass spectrometer design that combines the advantages of pulsed ion extraction and high ion-source accelerating potentials offers significant advantages over conventional designs. Robert S. Brown and John J. Lennon of Utah State University describe the technical design and performance of a high-voltage (0–3 kV) pulsed extraction system capable of being biased up to 30 kV that is coupled to an otherwise conventional linear TOF mass spectrometer. They study the effect of pulse voltage, bias voltage, delay time, and analyte m/z on the obtainable mass resolution of MALDI-generated ions and determine the optimal experimental parameters. ("Mass Resolution Improvement by Incorporation of Pulsed Ion Extraction in a Matrix-Assisted Laser Desorption/Ionization Linear Time-of-Flight Mass Spectrometer"; AC950086S; p. 1998)

Electrospray LC/MS of carotenoids

Although HPLC is generally regarded as the method of choice for the separation, identification, and quantification of carotenoids, the complex mixtures of structurally closely related carotenoids often found in biological tissues present a formidable analytical challenge. Richard B. van Breemen of the University of Illinois–Chicago presents a method in which the LC effluent passes through a photodiode array absorbance detector and into the electrospray LC/MS interface without splitting. The detection limits for lutein and β-carotene are between 1 and 2 pmol each. ("Electrospray Liquid Chromatography–Mass Spectrometry of Carotenoids"; AC9411987; p. 2004)

Characterizing chiral drugs by CE/ion spray MS

Characterization of chiral drugs is important because many have only one active enantiomer; the other is either inactive or, in some cases, potentially harmful. Jack D. Henion and colleagues at Cornell University describe a combination of CE and ion spray MS to analyze three chiral drug mixtures and a spiked urine sample using cyclodextrin-based electrolyte solutions. They report that the selectivity provided by MS gives unequivocal support needed to verify chiral composition of enantiomeric mixtures and that, although SIM/CE/MS is sufficient to selectively detect terbutaline in urine, the additional specificity provided by CE/MS/MS should be useful in the determination and characterization of chiral drugs in biological samples and pharmaceutical formulations. ("Chiral Separation and Detection of Terbutaline and Ephedrine by Capillary Electrophoresis Coupled with Ion Spray Mass Spectrometry"; AC9502099; p. 2054)

Carius tube digestion for Re–Os analysis

To optimize Re and Os data on geologically old samples, full equilibration of the Re and Os in the spike and sample during isotope dilution is essential. Steven B. Shirey of the Carnegie Institute of Washington and Richard J. Walker of the University of Maryland adapt a Carius tube digestion procedure to replace other commonly used techniques. After comparing conventional Teflon vessel and Carius tube digestions for diverse geological samples, they report that the Carius tube digestion liberates more Os from most matrices and is a more robust method for reproducibly measuring a sample's isotopic composition. ("Carius Tube Digestion for Low-Blank Rhenium–Osmium Analysis"; AC950102L; p. 2136)

CID and MALDI

Collision-induced dissociation (CID) enhances the structural information available from MS by increasing fragmentation of molecular and fragment ions through energetic collisions with an inert gas. Robert J. Cotter and Vladimir M. Doroshenko of the Johns Hopkins University School of Medicine use a modified ion trap detector to obtain high-performance CID mass spectra of peptide ions formed by matrix-assisted laser desorption/ionization. Their results indicate that the CID mass spectra of protonated and sodium-cationized peptides are often characterized by a series of rearrangement ions that can be used to determine amino acid sequences. "High-Performance Collision-Induced Dissociation of Peptide Ions Formed by Matrix-Assisted Laser Desorption/Ionization in a Quadrupole Ion Trap Mass Spectrometer"; AC950030Y; p. 2180)

Characterizing IRM GC/MS ♦

Despite the popularity of on-line combustion to facilitate precise determinations of the isotopic compositions of GC effluents, termed isotope ratio monitoring (IRM) GC/MS, few reports about the construction and operation of IRM GC/MS systems have appeared. J. M. Hayes and colleagues of Indiana University describe the combustion interface, recommend optimal operating conditions, and describe the analytical performance and limitations of IRM GC/MS for analyses of individual compounds over a range of sample sizes. From the data obtained, they conclude that the technique combines the speed, convenience, and sensitivity of GC/MS with the precision of conventional isotopic analyses. ("Performance and Optimization of a Combustion Interface for Isotope Ratio Monitoring Gas Chromatography/Mass Spectrometry"; AC941205R)

Laser ablation ICPMS for rock analysis ♦

Because of its wide dynamic range and elemental sensitivity, laser ablation ICPMS seems destined to play a major role in the analysis of geological materials, often cited as among the most difficult materials to characterize because of their wide composition range and complex mineralogy. Frederick E. Lichte of the U.S. Geological Survey has developed a new method of analyzing rocks and soils based on a lithium borate fusion and laser ablation ICPMS using the free-running mode of a Nd:YAG laser. Limits of detection are 0.01 μg/g for many trace elements, and accuracy approaches 5% for all 49 elements that can be quantified. ("Determination of Elemental Content of Rocks by Laser Ablation Inductively Coupled Mass Spectrometry"; AC941164A)

LC/MS of pesticides

As environmental testing regulations become more stringent, more structural confirmation is required for pesticides found in drinking water and other matrices. GC/MS methods don't provide this kind of detailed information for all regulated pesticides, but electrospray ionization (ESI) has made it possible to couple LC with MS. Antonio Di Corcia and co-workers at the Università "La Sapien-

♦ Denotes articles that are tentatively scheduled for the July 15 issue

za" (Italy) describe a protocol for extracting acidic pesticides from water using graphitized carbon black for subsequent determination on a benchtop LC/pneumatically assisted ESI mass spectrometric analyzer. ("Determination of Acidic Pesticides in Water by a Benchtop Electrospray Liquid Chromatography Mass Spectrometer"; AC9411637; p. 1968)

Detergent extraction from sludge

Nonylphenol ethoxylates (NPEs) are nonionic surfactants used in household detergents and printing processes that can degrade in the environment to 4-nonylphenol (4-NP), a lipophilic pollutant that has estrogen-like effects in fish and may also be linked with human fertility problems and cancer. Hing-Biu Lee and Thomas E. Peart of the National Water Research Institute (Canada) determine 4-NP in sewage treatment plant effluents and sludge samples using supercritical CO_2 extraction with online acetylation followed by silica gel sample cleanup and capillary GC/MS in the selected ion monitoring mode. ("Determination of 4-Nonylphenol in Effluent and Sludge from Sewage Treatment Plants"; AC941149U; p. 1976)

Keeping the sample isolated

The sample injection procedure for a capillary isoelectric focusing imaging detector requires that bubbles not be introduced and that the sample not mix with the electrolytes in the reservoirs. Janusz Pawliszyn and Jiaqi Wu of the University of Waterloo (Canada) demonstrate a capillary cartridge made with sections of dialysis hollow fibers to isolate the sample from the electrolytes and allow continuous injection into the capillary. When used with the detector, sample analysis time is only 4 min. ("A Capillary Cartridge with an On-line Desalting Device That Allows Fast Sampling for Capillary Isoelectric Focusing"; AC950163J; p. 2010)

CE/DIN-ICPMS

The development of highly sensitive and selective detectors for CE is one of the most important and challenging prerequisites for the growth of CE. Viorica Lopez-Avila and colleagues at the Midwest Research Institute, CETAC Technologies, and the U.S. Environmental Protection Agency couple CE on line with direct-injection nebulization ICPMS for elemental speciation. Preliminary results indicate that the system can be used to determine metal species at the part-per-trillion to part-per-billion level. ("Capillary Electrophoresis Coupled On-Line with Inductively Coupled Plasma Mass Spectrometry for Elemental Speciation"; AC941072+; p. 2020)

Harnessing electroosmotic flow for routine CEC

Electroosmotic flow can be a serious problem for CE but is sometimes used as the pump that drives separations in capillary electrochromatography (CEC), a method that can be used to separate neutral aromatic compounds that are unresolvable in CE. Richard N. Zare and co-workers at Stanford University and Sandia National Laboratories describe the fabrication of packed capillary columns for CEC and demonstrate the use of CEC with laser-induced fluorescence detection for the determination of 16 polycyclic aromatic hydrocarbons. They obtain separation efficiencies of up to 400,000 theoretical plates/m for analytes in the femtomole to attomole range. ("Capillary Electrochromatography: Analysis of Polycyclic Aromatic Hydrocarbons"; AC9500038; p. 2026)

Solid-phase trapping mechanisms

One of the requirements for a successful SFE procedure is that the analytes be quantitatively trapped. Using results from the SFE of digitalis glycosides, L. T. Taylor and W. N. Moore of Virginia Polytechnic Institute and State University discuss how the method used to introduce a modifier can affect the solid-phase trapping of the analytes and the various mechanisms that can result in analyte loss. They discuss extraction and trapping conditions that favor each mechanism, tandem trapping, and recommendations for successful trapping when using modifiers. ("Solid Phase Trapping Mechanisms Involved in the Supercritical Fluid Extraction of Digitalis Glycosides with Modified Carbon Dioxide"; AC9501598; p. 2030)

A dual-CD variant of MECC

Although CE is an exceptionally efficient technique, it is limited by its inability to separate neutral species. Michael J. Sepaniak and colleagues at the University of Tennessee describe a dual-cyclodextrin phase variant of micellar electrokinetic capillary chromatography in which separation is based on differential distribution between a neutral primary CD phase and a charged secondary CD phase rather than solute charge. Efficiency, selectivity, and system retention are evaluated on the basis of the separation of polyaromatic hydrocarbons. ("Evaluation of a Dual-Cyclodextrin Phase Variant of Capillary Electrokinetic Chromatography for Separations of Nonionizable Species"; AC9501147; p. 2037)

CEC with charged polyacrylamide

CEC often uses HPLC packings in a capillary column for separations driven by electroosmotic flow. Chuzo Fujimoto of the Hamamatsu University School of Medicine (Japan) uses charged polyacrylamide gels instead of the usual silica packing for CEC. The composition of the gel packing is evaluated for its effect on column performance and insights into separation mechanisms are discussed. ("Charged Polyacrylamide Gels for Capillary Electrochromatographic Separations of Uncharged, Low Molecular Weight Compounds"; AC9500803; p. 2050)

From glass to quartz

The substrates used for miniaturized chemical analysis instrumentation have, until now, been made of glass. To demonstrate the superior optical properties of substrates made from quartz, Stephen C. Jacobson and colleagues at Oak Ridge National Laboratory describe the electrophoretic separation and UV laser-induced fluorescence detection of complexed metal ions. Detection limits in the part-per-billion range for zinc, cadmium, and aluminum are reported. ("Fused Quartz Substrates for Microchip Electrophoresis"; AC9412037; p. 2059)

SFE of pesticides from soil

Supercritical CO_2 is frequently used for SFE of low-polarity compounds from environmental samples. John R. Dean and coworkers at the University of Northumbria at Newcastle (U.K.) examine the role of pressure, temperature, extraction time, and percentage of added methanol modifier on SFE of 16 PAHs from soil using supercritical CO_2. They compare the performance and recovery for an optimized extraction protocol with those for Soxhlet extraction and microwave-assisted extraction. ("Experimental Design Approach for the Extraction of Polycyclic Aromatic Hydrocarbons from Soil Using Supercritical Carbon Dioxide"; AC950144+; p. 2064)

Positively charged, not neutral

The electrokinetic separation behavior of hydrophobic drugs is not yet fully understood, and most CE studies of these substances have focused primarily on electrically neutral solutes. Wolfgang Thormann and colleagues at the University of Bern (Switzerland) examine the electrokinetic separation behavior of positively charged hydrophobic drugs using plain aqueous buffers, binary media with organic solvents, and systems with surfactants at concentrations between 0.0005 and 75 mM or other buffer additives. They find that CZE in binary systems with organic solvents at a buffer pH near or lower than the solute's pK_a or at low pH in the presence of an electrically neutral complexing agent are effective. ("Separation of Hydrophobic, Positively Chargeable Substances by Capillary Electrophoresis"; AC950020X; p. 2070)

Modeling chromatographic retention of mixtures

Although a variety of methods have been developed over the past decade to enhance the information obtained from a multicomponent chromatogram, these methods provide no information about individual peaks or peak homogeneity. Attila Felinger of the University of Veszprém (Hungary) studies the effect of superposition when the sample being analyzed is a mixture of a structured series of compounds and reports that even a mixture of samples that give strictly deterministic chromatograms individually turns disordered. He proposes a model that includes a second-order property, the variance–time curve, to recognize superposition and applies it to two distinctly different multicomponent chromatograms. ("Superposition of Chromatographic Retention Patterns"; AC9411379; p. 2078)

Improving efficiency and selectivity of antibiotic-based CE enantioseparations

Vancomycin, an oligophenolic glycopeptide macrocyclic antibiotic, exhibits exceptional enantioselectivity for many chiral compounds. Daniel W. Armstrong and Kimber L. Rundlett of the University of Missouri–Rolla demonstrate that adding SDS micelles to vancomycin solutions has a beneficial effect on the efficiency, analysis time, and resolution of enantiomers. Because previously postulated model systems and treatments are not applicable in this case, they also derive an equation to calculate the binding constants of the solutes for the antibiotic–SDS mixed micelles. ("Effect of Micelles and Mixed Micelles on Efficiency and Selectivity of Antibiotic-Based Capillary Electrophoretic Enantioseparations"; AC950091W; p. 2088)

Improving microwave extraction of organic pollutants

Microwave-assisted extraction has been proposed as an alternative to traditional Soxhlet/Soxtec and sonication extraction procedures because of the potential for preventing or minimizing pollution in analytical laboratories, improving target analyte recoveries, and reducing sample preparation costs. Viorica Lopez-Avila and colleagues at Midwest Research Institute and the U.S. Environmental Protection Agency present recovery data for microwave-assisted extraction of 187 compounds and 4 Aroclors listed in EPA Methods 8250, 8081, and 8141A. Their results indicate that most of these compounds can be recovered in good yields from spiked topsoil. ("Extraction of Organic Pollutants from Solid Samples Using Microwave Energy"; AC9410732; p. 2096)

Stability of slurry-packed microcolumns

Most LC column packing protocols are based on slurry packing. According to Johannes P. C. Vissers and co-workers of Eindhoven University of Technology (The Netherlands), the solvents used for slurry suspensions and coagulation properties of the packing material are more critical for fused-silica capillary column stability than they are for larger columns in conventional HPLC. The researchers evaluate the factors leading to colloidal instability in packed capillary columns by performing sedimentation and ζ-potential experiments and derive expressions for the theoretical sedimentation rates of noncoagulated particle suspensions. ("Colloid Chemical Aspects of Slurry Packing Techniques in Microcolumn Liquid Chromatography"; AC941187D; p. 2103)

Two-dimensional conductometric detection

Although suppressed conductometric detection has been successfully used for ion chromatography, it suffers from poor sensitivity and nonlinear calibration behavior for very weak acid anions. Purnendu K. Dasgupta and Anna Sjögren of Texas Tech University describe two-dimensional suppressed conductometric detection. They use NaOH as the eluent and as an electrical suppressor so the first detector will respond to strong acid anions. The eluite is then transported through a microscale electrodialytic NaOH generator to the second detector, which records a decrease in the NaOH background, responding to very weak acid anions. ("Two-Dimensional Conductometric Detection in Ion Chromatography. Analyte Identification, Quantitation of Very Weak Acid Anions, and Universal Calibration"; AC950026M; p. 2110)

Solute partitioning into IAMs

One of the most promising applications of immobilized artificial membrane (IAM) surfaces is their ability to predict drug permeability through membranes and drug absorption in tissues and animals. To gain a better understanding of the solute retention mechanism involved, Charles Pidgeon and Shaowei Ong of Purdue University prepare three IAM-bonded phases by immobilizing either single-chain or double-chain phosphatidylcholine (PC) ligands. They report that solute affinity for the single-chain IAMPC columns is threefold lower than on the double-chain IAMPC column, suggesting that solute retention on IAMs is dominated by a solute partitioning mechanism. ("Thermodynamics of Solute Partitioning into Immobilized Artificial Membranes"; AC9411942; p. 2119)

Modeling *n*-alkylsilica sorbents

Critical to the development of physically relevant molecular retention models is knowledge about the interactive structure of the immobilized ligands. Milton T. W. Hearn and co-workers at Monash University (Australia) construct a molecular model of several *n*-alkylsilica sorbents and subject it to a detailed molecular dynamics simulation. Results of the conformational analysis indicate that the simulated structures for the *n*-alkylsilica surface reproduce the behavior of the *n*-alkyl ligands chemically immobilized onto the silica in a manner that is qualitatively consistent with published spectroscopic data and chromatographic measurements. ("Influence of the Chain Length and Surface Density on the Conformation and Mobility of *n*-Alkyl Ligands Chemically Immobilized onto a Silica Surface"; AC940925V; p. 2145)

♦ Denotes articles that are tentatively scheduled for the July 15 issue

CE/LIF analysis of reducing sugars

The analysis of carbohydrates is limited by their lack of outstanding structural features, and methods of detection are limited because most sugars do not contain chromophoric moieties. Fu-Tai A. Chen and colleagues at Beckman Instruments describe the analysis of reducing sugars and fructose by CE/LIF using 9-aminopyrene-1,4,6-trisulfonate (APTS) as a derivatizing reagent. By using a 488-nm argon ion laser for excitation and a narrow band filter at 520 nm for fluorescence emission, the researchers selectively detect APTS-derivatized sugars while drastically suppressing the signal of excess APTS reagent. ("Characterization of 9-Aminopyrene-1,4,6-trisulfonate-Derivatized Sugars by Capillary Electrophoresis with Laser-Induced Fluorescence Detection"; AC9410833; p. 2239)

Investigating injection artifacts

Efficient separation in CE can involve optimizing the injection process as well as the separation itself. Andras Guttman and Herbert E. Schwartz of Beckman Instruments and Palomar Analytical Services describe two injection-related problems that can affect precision and accuracy as well as separation performance. The first occurs with consecutive injection from the same low-volume sample, and the second is related to the physical shape of the gel-filled capillary. Simple solutions are proposed for both problems. ("Artifacts Related to Sample Introduction in Capillary Gel Electrophoresis Affecting Separation Performance and Quantitation"; AC941206J; p. 2279)

Manipulating sample fractions on a CE chip

Although stopped-flow techniques and electrical grounding of the capillary before the outlet orifice allow collection of fractions separated by CE, interrupting the separation potential leads to considerable dilution of the collected sample zones, and manufacturing on-column frits or grounding tees with sufficiently small dead volumes is difficult. Carlo S. Effenhauser and colleagues at Ciba Ltd. adopt an approach to fraction collection that is based on the use of microfabricated planar devices. By switching the applied potentials to a channel system etched into a glass plate, they selectively isolate both single sample zones and groups of zones from unwanted sample components in a few minutes. ("Manipulation of Sample Fractions on a Capillary Electrophoresis Chip"; AC9500693; p. 2284)

SFE of soybean oil

Helium is often used to pressurize CO_2 cylinders for SFE, but it may cause solubility problems for some analytes. Jerry W. King and colleagues at the U.S. Department of Agriculture compare the solubilities of soybean oil in neat supercritical CO_2 and in supercritical CO_2 with entrained helium and find that the solubilities dropped when the CO_2/He source was used. They attribute the drop to small amounts of dissolved He in the supercritical fluid. ("Effect of Supercritical Carbon Dioxide Pressurized with Helium on Solute Solubility during Supercritical Fluid Extraction"; AC950158F; p. 2288)

Cold storage for HPLC of reactive compounds

HPLC is often used to determine impurities in pharmaceuticals, but some extraneous chromatographic zones in a drug profile may represent on-column degradation of the starting compound rather than impurities. Nelu Grinberg and co-workers at Merck Research Laboratories monitor the cyclization of mesylate, an active ester, to a cyclic ether during normal-phase HPLC. They use proton NMR to determine the contents of HPLC fractions collected under a variety of solvent and temperature conditions and conclude that lowering the running temperature for HPLC to –30° C eliminates the unwanted reaction. ("Kinetic Analysis and Subambient Temperature Chromatography of an Active Ester"; AC941134W; p. 2292)

Low-pressure mineral digestion

Microwave acid digestion of mineral and inorganic samples is rapid but requires stringent temperature and pressure regulation to avoid safety problems. Instruments designed to provide good temperature control for this method are often expensive; for samples that do not require short digestion cycles, conventional heating is easier to control and can be used for large-batch digestions. M. Ravey and co-workers at IMI Institute for Research and Development (Israel) describe a vessel design for low-pressure acid digestion of mineral samples with conventional heating. ("A Vessel for Low-Pressure Acid Dissolutions of Mineral and Inorganic Samples"; AC950015T; p. 2296)

Water in supercritical separations ♦

Because water is often an important component in SFE and other separations, water solubility data are needed when implementing a new process. John L. Fulton and colleagues at Pacific Northwest Laboratory report that using near-IR spectroscopy to obtain these data is ideal because the technique requires a long-pathlength optical cell commonly found in high-pressure laboratories. Water absorbs strongly in the near-IR region, and solvent bands do not interfere with water bands. Their method is used to obtain water solubility in carbon dioxide and refrigerants at temperatures of 40–110 °C and pressures of 10–344.8 bar. ("Water Solubility Measurements in Supercritical Fluids and High-Pressure Liquids Using Near-Infrared Spectroscopy"; AC941232H)

Analysis of technical DDT ♦

Detailed analyses of technical DDT are required to study the biological and environmental fate of this important pesticide. Hans-Rudolph Buser and Markus D. Müller of the Swiss Federal Research Station use achiral and chiral high-resolution GC/EIMS to investigate the composition of technical DDT and chiral HPLC to resolve 2,4′-DDT and 2,4-DDD, two important chiral components of technical DDT. The researchers suggest that these methods should also be applicable to the analysis of environmental and biological samples. ("Isomer-Selective and Enantiomer-Selective Determination of DDT and Related Compounds Using Chiral High-Resolution Gas Chromatography/Mass Spectrometry and Chiral High-Performance Liquid Chromatography"; AC950073E)

Protein-binding chiral discrimination ♦

Ovomucoid-based bonded-phase columns offer long-term stability and have been used to resolve acidic, basic, and neutral enantiomers in bulk drugs and formulations, but researchers' understanding of the enantioselective recognition mechanism is limited. Thomas C. Pinkerton and colleagues at the Upjohn Company, Mukogawa Women's University (Japan), and the University of Wisconsin prepare HPLC columns with single domains, a combination of two domains, and whole turkey ovomucoid and test the columns for chiral recognition by their abil-

ity to resolve enantiomers among a wide range of racemates. They identify a chiral binding site on the third domain of turkey ovomucoid and characterize it by chromatography, NMR, and molecular modeling. ("Protein Binding Chiral Discrimination of HPLC Stationary Phases Made with Whole, Fragmented, and Third Domain Turkey Ovomucoid"; AC941222G)

Aqueous Al(III) speciation ♦

Procedures for determining aluminum species are limited by recurring problems: detection limits too high for use with natural waters, the operational definition of aluminum species, and problematic application to real samples. Stephen E. Cabaniss and Susan H. Sutheimer of Kent State University describe a gradient cation exchange HPLC method that separates aquo and hydrolyzed aluminum species from organic and inorganic aluminum complexes at submicromolar levels. They demonstrate complete detection of organic and inorganic monomeric species of aluminum with quantitation independent of the pH and the ionic strength of the sample. ("Aqueous Al(III) Speciation by High-Performance Cation Exchange Chromatography with Fluorescence Detection of the Aluminum–Lumogallion Complex"; AC9500949)

Determining the effect of counterions ♦

Micellar electrokinetic chromatography is most commonly performed using sodium dodecyl sulfate micelles. Joe P. Foley and Eric S. Ahuja of Villanova University investigate the effects of using lithium and potassium rather than sodium as the micelle counterion on efficiency, retention, resolution, elution range, and selectivity. The effect of using acetonitrile as an organic modifier with each micellar system is also studied. ("Influence of Dodecyl Sulfate Counterion on Efficiency, Selectivity, Retention, Elution Range, and Resolution in Micellar Electrokinetic Chromatography"; AC950388U)

Immunosorbents for herbicide enrichment ♦

The increasing demand for multiresidue analyses has led to the development of new methods for extracting and concentrating traces of pesticides from aqueous samples. M-C. Hennion and colleagues at the École Supérieure de Physique et de Chimie Industrielles de la Ville de Paris (France), École Nationale Supérieure de Chimie de Paris (France), and CID-CSIC (Spain) develop immunosorbents for the selective solid-phase extraction of phenylurea and triazine herbicides from environmental waters. Isoproturon can be detected in surface waters at the 0.1 μg/L level with no cleanup. ("Preparation and Evaluation of Immunosorbents for Selective Trace Enrichment of Phenylurea and Triazine Herbicides in Environmental Waters"; AC941240Y)

Ion exchange of oligonucleotides on zirconia ♦

Ion-exchange chromatography is often used to separate low molecular weight inorganic and organic anions as well as biomolecules such as ribonucleotides, oligonucleotides, amino acids, and proteins. Peter W. Carr and Clayton McNeff of the University of Minnesota use porous, quaternized polyethyleneimine-coated zirconia particles to separate nucleosides, nucleotides, oligonucleotides, and oligodeoxynucleotides. The method can separate oligonucleotides and oligodeoxynucleotides differing in length by a single nucleotide unit as well as RNAs of the same length but differing by only one deoxynucleotide. ("High-Performance Anion-Exchange Chromatography of Oligonucleotides and Oligodeoxynucleotides on Quaternized Polyethylenimine-Coated Zirconia"; AC941192H)

Characterizing perfluorocarbon oligomers

A recent report indicates that oligomeric byproducts generated in the commercial synthesis of perfluorotetradecahydrophenanthrene are excellent atmospheric pressure solvents for PTFE, a discovery that may make new characterization and processing of this polymer possible. William H. Tuminello and colleagues at DuPont and Rhône-Poulenc Chemicals characterize a complex mixture of oligomeric perfluorocarbons to identify PTFE sufficiently for government certification, to strengthen any patents referring to the oligomer, to formulate a basis for manufacturing specifications, and to gain a better understanding for additional research efforts. They use NMR, ESCA, and TOF SIMS as the primary tools for analysis, as well as IR and UV–vis spectrometry, elemental analysis, and GC/MS. ("Characterization of a Perfluorotetradecahydrophenanthrene Oligomer"; AC940923A; p. 1955)

Gasoline characterization by GC/FT-IR

Clean fuel legislation has created a need for regulatory determination of oxygenates and aromatic hydrocarbons in reformulated gasolines. John W. Diehl and colleagues of Mobil Research and Development evaluate GC/FT-IR spectroscopy for the quantitation of 25 aromatic hydrocarbons in gasolines and compare their results with those obtained by the EPA GC/MS method. The GC/FT-IR method can quantitate oxygenates simultaneously with the aromatic compounds. ("Determination of Aromatic Hydrocarbons in Gasolines by Gas Chromatography/Fourier Transform Infrared Spectroscopy"; AC950072M; p. 2015)

Renewable gas-sampling interface

As a gas stream flows across a liquid droplet, the soluble constituents in the gas diffuse to and dissolve in the liquid drop, making the droplet a potential sampling interface for such soluble constituents. Purnendu K. Dasgupta and Shaorong Liu of Texas Tech University address the design, characteristics, and deployment of a droplet-based gas analysis system. By coupling the sampling interface with a sequential analysis system, they demonstrate its applicability for measurement of part-per-billion levels of gaseous NH_3. ("Liquid Droplet. A Renewable Gas Sampling Interface"; AC950046O; p. 2042)

Determining oxide content

One reason that plating steel with tantalum is difficult is the presence of oxides in the molten fluoride solution used in the process. N. J. Bjerrum and colleagues at the Technical University of Denmark use IR and Raman vibrational spectroscopy to measure the oxide content of a series of quenched alkali metal fluoride melts that contain a fixed amount of tantalum and varying amounts of oxide. They can determine the oxide content of a melt to within ± 0.1 mol% from the intensity ratio of two vibrations. ("Use of Vibrational Spectroscopy To Determine Oxide Content of Alkali Metal Fluoride–Tantalum Melts"; AC9410272; p. 2129)

♦ Denotes articles that are tentatively scheduled for the July 15 issue

Biomimetic sensors based on molecularly imprinted polymers

Traditional biosensors are based on a recognition element of biological origin, but for some potential applications no biocomponent is available. Klaus Mosbach and colleagues at the University of Lund (Sweden) describe the use of a molecularly imprinted polymer as a recognition element for fiber-optic detection of an amino acid derivative with a fluorescent labeling group. Although the response time is relatively long (4 h), the authors postulate that it should be possible to drastically reduce this time by using either smaller particles or smaller membranes. ("Introducing Biomimetic Sensors Based on Molecularly Imprinted Polymers as Recognition Elements"; AC941190X; p. 2142)

Modeling complex systems using neural networks

Artificial neural networks are increasingly being used to model complex multivariate systems. Jure Zupan and colleagues at the National Institute of Chemistry (Slovenia), CINKARNA (Slovenia), and the University of Ljubljana (Slovenia) evaluate two different neural network strategies for building a model for the quantitative prediction of "total color difference" of paint based on spectroscopic measurement of eight complex oxide concentrations. The models produced using both error backpropagation and counterpropagation are compared with the multivariate linear regression model. ("Modeling of Property Prediction from Multicomponent Analytical Data Using Different Neural Networks"; AC941026+; p. 2154)

Dealing with interferences in multivariate predictions

A serious problem can occur when a multivariate model is used for compositional analysis of an unknown mixture that contains an unexpected constituent not modeled in the calibration phase. Marco M. A. Ruyken and colleagues at Solvay Duphar B.V. (The Netherlands) and the University of Amsterdam (The Netherlands) describe how spectral residuals resulting from a multivariate prediction can be used to detect and identify unknown interfering compounds. These methods are demonstrated using a relatively simple principal component regression calibration model to predict the concentrations of organic vapors and gases in ambient air with FT-IR spectroscopy. ("On-Line Detection and Identification of Interferences in Multivariate Predictions of Organic Gases Using FT-IR Spectroscopy"; AC9409905; p. 2170)

^{13}C NMR of coals

Although direct polarization is less difficult to perform than cross-polarization, questions arise over its quantitative reliability, particularly because the three ^{13}C NMR intensity standards most commonly used for coal analyses produce some overlap with the peaks of a typical coal spectrum. Gary E. Maciel and Antoni Jurkiewicz of Colorado State University use an intensity standard with a peak at 217 ppm, which does not overlap with the coal spectrum, to compare results from direct- and cross-polarization experiments, both with magic angle spinning, on a series of eight Argonne Premium coals. They observe a relationship between the number of unpaired electron spins and the fraction of ^{13}C spins detected. ("^{13}C NMR Spin–Lattice Relaxation Properties and Quantitative Analytical Methodology of ^{13}C NMR Spectroscopy for Coals"; AC950239B; p. 2188)

Generating cadmium atoms at room temperature

Recent work has shown that some types of volatile cadmium species can be produced by reduction of Cd^{2+} with sodium borohydride in an aqueous solution of vesicles of didodecyldimethylammonium bromide. A. Sanz-Medel and colleagues at the University of Oviedo (Spain) use absorption measurements to investigate the transport mechanism of the volatile cadmium species to the atomizer and the nature of those species reaching the measurement cell. Their results indicate that room-temperature atomic absorption of the resonance radiation of cadmium by the volatile species formed takes place in the quartz absorption cell. ("Generation of Cadmium Atoms at Room Temperature Using Vesicles and Its Application to Cadmium Determination by Cold Vapor Atomic Spectrometry"; AC941227D; p. 2216)

Chemiluminescent chemical sensors

Because it is free from Raman and Rayleigh scattering, chemiluminescence detection can provide excellent sensitivity over a wide dynamic range using simple instrumentation. Greg E. Collins and Susan L. Rose-Pehrsson of the Naval Research Laboratory describe chemiluminescent chemical sensors for O_2 and NO_2 based on immobilization of luminol within a hydrogel or polymeric sorbent coating positioned in front of a photomultiplier tube. Selectivity is achieved by careful selection of the polymer type, pH, and metal catalyst incorporated into the film. ("Chemiluminescent Chemical Sensors for Oxygen and Nitrogen Dioxide"; AC950065Y; p. 2224)

Fluorescence optosensing of low molecular weight alcohols

The chromatographic and spectroscopic methods generally used to quantify methanol, ethanol, and isopropyl alcohol in processes such as fermentation and distillation of spirits and the blending of fuels are time consuming and suffer from interferences. Guillermo Orellana and colleagues at Complutense University (Spain) develop a fiber-optic fluorescent sensor using the dyes 5-(4-aminophenyl)-2-(2-pyrazinyl)-1,3-oxazole and 5-(4-aminophenyl)-2-(2-pyrazinyl)-1,3-thiazole as indicators. They test gasoline samples and find typical response times for methanol of 2–4 min with a relative standard deviation of 1.5–3%. ("Reversible Fiber-Optic Fluorosensing of Lower Alcohols"; AC941242I; p. 2231)

Reworking the optical arrangements for LEAFS

Electrothermal atomizer laser-excited atomic fluorescence spectroscopy (ETA-LEAFS) can be used to achieve femtogram detection limits and a broad linear dynamic range. Graphite tube atomizers suffer less from diffusion losses and vapor-phase interferences than open graphite atomizers do, but the tube atomizer geometry may require a different optical arrangement for fluorescence collection than has been used with flames, plasmas, and open graphite electrothermal atomizers. Robert G. Michel and colleagues of the University of Connecticut compare a 90° off-axis ellipsoidal mirror with plane mirror systems that contain lenses for performance in front-surface illustration. ("Spatial Discrimination against Background with Different Optical Systems for Collection of Fluorescence in Laser-Excited Atomic Fluorescence Spectrometry with a Graphite Tube Electrothermal Atomizer"; AC941074U; p. 2246)

♦ Denotes articles that are tentatively scheduled for the July 15 issue

Detecting ^{14}N and ^{35}Cl in cocaine

Widespread use of nuclear quadrupole resonance (NQR) in analysis has been limited, but superconducting quantum interferometric device (SQUID) techniques to determine unknown NQR frequencies for pulsed NQR detection may make NQR analysis viable for a greater variety of substances. James P. Yesinowski and colleagues at the Naval Research Laboratory, the University of California, and Lawrence Berkeley Laboratory report results for ^{14}N NQR signals in samples of cocaine free-base and cocaine hydrochloride as well as ^{35}Cl NQR and high-filed stepped-frequency ^{35}NMR results for cocaine hydrochloride. They also discuss issues related to searching for unknown resonances, identifying NQR transitions, determining impurity effects, measuring parameters that influence detection sensitivity, and using different pulse schemes to improve sensitivity. ("Detection of ^{14}N and ^{35}Cl in Cocaine Base and Hydrochloride Using NQR, NMR, and SQUID Techniques"; AC941121I; p. 2256)

A linear CO_2 sensor

One problem with the two types of sensors currently used to measure CO_2 is that the calibration curves are not theoretically linear. Garry A. Rechnitz and Xiaoying He of the University of Hawaii use the ratio of fluorescence intensities in the absence and presence of CO_2 as the response function for a fiber-optic sensor. They demonstrate that a linear range in the response curve can be obtained and that the response curve is independent of instabilities in the light-source intensity and small variations in the concentration of the indicator that result from photobleaching. ("Linear Response Function for Fluorescence-Based Fiber-Optic CO_2 Sensors"; AC950188I; p. 2264)

Performing quantitative analysis with FT-IR interferograms

Analysis of data from nonlaboratory FT-IR applications is often complicated by lack of a representative background or reference spectrum for use in conventional processing of ratioed spectra. This can produce artifacts in the computed ratioed spectrum that severely complicate subsequent data analysis. Gary W. Small and Mutua J. Mattu of Ohio University demonstrate the feasibility of performing quantitative analysis with short segments of bandpass-filtered FT-IR interferograms. They report that this interferogram-based analysis performs analogously to a conventional spectral-based analysis, is computationally more efficient than spectral analysis, and is compatible with a completely automated implementation. ("Quantitative Analysis of Bandpass-Filtered Fourier Transform Infrared Interferograms"; AC941186L; p. 2269)

Long-lived radioluminescence-based UV photometer

Common UV photometers use lamps with a lifetime of 3–12 months, which is too short for process control applications because the lamp is left on all day. Günter Rinke and Christian Hartig of Forschungszentrum Karlsruhe (Germany) describe a UV photometer that uses a luminous crystal irradiated by a radioactive element as its source. The lifetime of the source is 10 years, and the minimum detectable absorbance is 1.2×10^{-5} AU. The photometer is suitable for process control applications, explosive environments, and HPLC. ("UV Photometer Based on Radioluminescence with Applications in HPLC and Process Control"; AC940982O; p. 2308)

Selecting a shorter list of variables with Procrustes rotation ♦

Determining if all the variables initially considered in an experiment should be included in subsequent samplings would result in a better understanding of the system under study and improve laboratory productivity. J. M. Andrade and colleagues at the Universidade da Coruña (Spain) and Chalmers University of Technology (Sweden) demonstrate how Procrustes rotation can be used to select the minimum number of original variables important for describing an urban soil system and for statistically comparing samples taken in different seasons. Initially 12 variables (9 metals, humidity, pH, and loss on ignition) are studied, and the authors determine that in the future only 2 or 3 will need to be monitored, assuming that the present pollution sources do not change significantly. ("Procrustes Rotation as a Way To Compare Different Sampling Seasons in Soils"; AC950057H)

Phospholipids as organized media in spectroluminescence analysis ♦

Organized media are increasingly being used in luminescence analysis because sequestration of the analyte can often improve discrimination and detection limits. Sharon L. Neal and Michele M. Villegas of the University of California–Riverside investigate the utility of phospholipid vesicles as organized media in spectroluminescence analysis by comparing the membrane properties of pure dimyristoyl phosphatidylcholine, dimyristoyl phosphatidylserine, and dimyristoyl phosphatidylglycerol (DMPG) with those of pyrene. Their results indicate that although significant improvements in dynamic range would be possible using DMPG, improvement in detection limits would be moderate compared with those observed in bile salts, cyclodextrins, or surface aggregates. ("Phospholipid Vesicles as Organized Media in Spectroluminescence Analysis"; AC941092B)

Getting the same response on different instruments ♦

In spectroscopy, problems such as instrument bandwidth and stray light can cause a calibration that works on one instrument not to work on another. Bruce Kowalski and colleagues at the University of Washington present background correction improvements for direct standardization (DS) and piecewise DS, two methods that have shown the greatest potential in overcoming this instrument-to-instrument problem. The DS and background-corrected DS methods are compared using a simulated data set, and the piecewise DS and background-corrected piecewise DS methods are compared using an experimental data set. ("Additive Background Correction in Multivariate Instrument Standardization"; AC941253B)

Detecting TNT in water ♦

Poor storage facilities for explosives and contamination of water and soil with byproducts of explosives manufacturing have created a general health hazard. Frances S. Ligler and colleagues at the Naval Research Laboratory describe an evanescent wave fiber-optic biosensor that uses a competitive immunoassay for the detection of TNT in water. Detection sensitivities of 10 ng/mL TNT (~ 8 ppb) in buffer are achieved, and tests on river, harbor, and bilge water samples spiked with TNT show results similar to those obtained with laboratory (buffer matrix) samples. ("Detection of TNT in Water Using an Evanescent Wave Fiber-Optic Biosensor"; AC941221O)

♦ Denotes articles that are tentatively scheduled for the July 15 issue

PUT THE POWER OF MS/MS INTO YOUR LAB.

Our GCQ™ Tandem breakthrough should overcome any reason you may have for not considering MS/MS. First, it's now much more affordable. Second, it automatically optimizes the system for fast, reproducible data. Third, this kind of analytical power and productivity have never been available in so small a benchtop package. And it's easy to use, thanks to our Windows™ NT-based data and control software.

Now you can confidently go far beyond basic GC/MS with GCQ Tandem.

Find out how far you can extend your analytical powers by circling the reader response number.

Finnigan MAT

ISO 9001 REGISTERED COMPANY

THE MASS SPECTROMETRY COMPANY

Australia Tel. (02) 646 2211 • France Tel. (0169) 41 98 00 • Germany Tel. (0421) 54 930 • Italy Tel. (02) 66011742 • Japan Tel. (03) 3372 3001 • Netherlands Tel. (08385) 27266 • People's Republic of China Tel. (01) 835 0281 • Sweden Tel. (08) 6800101 • United Kingdom Tel. (0442) 233555 • U.S.A. Tel. (408) 433-4800

Copyright 1995 by Finnigan Corporation, a subsidiary of Thermo Instrument Systems Inc., a Thermo Electron Company. All rights reserved.

CIRCLE 6 ON READER SERVICE CARD

ANALYTICAL CHEMISTRY

EDITOR: **ROYCE W. MURRAY**
University of North Carolina

ASSOCIATE EDITORS: **Catherine C. Fenselau,** University of Maryland Baltimore County, **William S. Hancock,** Hewlett Packard, **James W. Jorgenson,** University of North Carolina, **Robert A. Osteryoung,** North Carolina State University, **Edward S. Yeung,** Iowa State University/Ames Laboratory

Editorial Headquarters, research section
Department of Chemistry
Venable and Kenan Laboratories
University of North Carolina
Chapel Hill, NC 27599-3290
Phone: 919-962-2541
Fax: 919-962-2542
E-mail: Murray@uncvx1.oit.unc.edu

Editorial Headquarters, A-page section
1155 Sixteenth St., N.W.
Washington, DC 20036
Phone: 202-872-4570
Fax: 202-872-4574
E-mail: acx96@acs.org

Managing Editor: Mary Warner

Senior Editor: Louise Voress

Associate Editor: Felicia Wach

Editorial Assistant: Deborah Noble

Contributing Editor: Marcia Vogel

Head, Graphics and Production: Leroy L. Corcoran

Division Art Director: Alan Kahan

Art Director: Michele Telschow

Manager, Copy Editing: Elizabeth Wood

Production Editor: Eric Sorensen

Electronic Composition: Wanda R. Gordon

Journals Dept., Columbus, Ohio

Editorial Office Manager: Mary E. Scanlan

Journals Editing Manager: Kathleen E. Duffy

Associate Editor: Lorraine Gibb

Assistant Editor: Stephanie L. Mallon

Advisory Board: Phyllis Brown, Karl Cammann, Brian Chait, Bruce Chase, Joseph Glajch, Joseph G. Gordon, David M. Haaland, Kiyokatsu Jinno, Peter Kissinger, Gary E. Maciel, Linda B. McGown, Scott McLuckey, Milos V. Novotny, Jeanne Pemberton, J. Michael Ramsey, James A. Yergey *Ex Officio:* Henry Blount, III

A-page Advisory Panel: Frank V. Bright, Therese M. Cotton, Royce C. Engstrom, Curtis Marcott, Mary Ellen P. McNally, Jonathan V. Sweedler, Thomas Tiernan, Vicki Wysocki, Robert D. Voyksner

Publications Division

Director: Robert H. Marks

Director, Special Publishing Operations: Anthony Durniak

Director, Journal Publishing Operations: Charles R. Bertsch

Head, Publications Marketing: David Schulbaum

Copyright permission: Reprographic copying beyond that permitted by Section 107 or 108 of the U.S. Copyright Act is allowed, provided that the fee of $9.00 per article copy is paid directly to the Copyright Clearance Center (CCC), 222 Rosewood Dr., Danvers, MA 01923, USA. A CCC code printed at the bottom of the first page of an article indicates that ACS owns copyright or has permission to collect the copying fee for that article. A record of that code should accompany payment. Direct reprint permission requests to ACS Copyright Office, Publications Division, 1155 Sixteenth St., N.W., Washington, DC 20036.

Registered names and trademarks, etc., used in this publication, even without specific indication thereof, are not to be considered unprotected by law.

1995 subscription rates include air delivery outside the U.S., Canada, and Mexico. Canadian subscriptions are subject to 7% GST.

	Members	Nonmembers (personal)	Nonmembers (institutional)
U.S.	$ 40	$ 85	$ 570
Canada and Mexico	77	122	607
Europe	123	168	653
Other countries	148	193	678

Members may share/donate their personal subscriptions with/to libraries and the like but only after 5 years from publication.

Nonmember rates in Japan: Rates above do not apply to nonmember subscribers in Japan, who must enter subscription orders with Maruzen Company Ltd., 3–10. Nihonbashi 2-chome, Chuo-ku, Tokyo 103, Japan. Tel: (03) 272-7211.

For multi-year and other rates, call toll free 800-227-5558 in the U.S. and Canada; in the Washington, DC, metropolitan area and outside the U.S., call 202-872-4363; fax 202-872-4615.
Single issues, current year, $24.00 except review issue, $50.00, and LabGuide, $50.00; **back issues and volumes and microform editions** available by single volume or back issue collection. For information or to order, call the number listed for subscription orders; or write the Microform & Back Issues Office at the Washington address.

Subscription orders by phone may be charged to VISA, MasterCard, or American Express. Call toll free 800-333-9511 in the continental U.S.; in the Washington, DC, metropolitan area and outside the continental U.S., call 202-872-8065. Mail orders for new and renewal subscriptions should be sent with payment to American Chemical Society, Department L-0011, Columbus, OH 43268-0011.
Changes of address must include both old and new addresses with ZIP code and a recent mailing label. Send all address changes to the ACS Columbus address. Please allow 6 weeks for change to become effective. **Claims for missing issues** will not be allowed if loss was due to failure of notice of change of address to be received in the time specified; if claim is dated (a) North America—more than 90 days beyond issue date, (b) all other foreign—more than 180 days beyond issue date. Hard copy claims are handled at the ACS Columbus address.

Instructions for authors of AC Research and guidelines for the Instrumentation, Report, Analytical Approach, and A/C Interface features are published in the Jan. 1 issue, p. 229. Please consult these instructions prior to submitting a manuscript for consideration for publication.

Manuscripts for publication in AC Research (4 copies of text and illustrative material) should be submitted to the Editor at the University of North Carolina address. Please include a signed copyright status form; a copy of this document appears on p. 235 of the Jan. 1 issue. Manuscripts for publication in the A-page section should be submitted to the Washington editorial staff.

Supporting information is noted in the table of contents with a ■. It is available as photocopy ($12.00 for up to 3 pages and $1.50 per page for additional pages, plus $2.00 for foreign postage) or as 24X microfiche ($10.00, plus $1.00 for foreign postage). Canadian residents should add 7% GST. See supplementary material notice at end of journal article for number of pages. Orders *must* specify either photocopy or microfiche and give complete title of article, names of authors, journal, issue date, and page numbers. Prepayment is required and prices are subject to change. Order from Microforms & Back Issues Office at the ACS Washington address.

The American Chemical Society and its editors assume no responsibility for the statements and opinions advanced by contributors. Views expressed in the editorials are those of the editors and do not necessarily represent the official position of the American Chemical Society.

Journals Department, American Chemical Society, 2540 Olentangy River Road, P.O. Box 3330, Columbus, OH 43210 (614-447-3600, Ext. 3171; TELEX 6842086; Fax 614-447-3745)

Member & Subscriber Services: American Chemical Society, P.O. Box 3337, Columbus, OH 43210 (614-447-3776; 800-333-9511)

ACS membership information: Lorraine Bowlin (202-872-4567)

Advertising Management: Centcom, Ltd., 1599 Post Rd. East, P.O. Box 231, Westport, CT 06881 (203-256-8211; fax 203-256-8175)

Analytical Chemistry's Measurement Cop

Hello. I'm your local Measurement Cop, now patrolling *Analytical Chemistry*. I set standards, settle disagreements, and arbitrate interesting discussions. My unlimited accuracy and precision are great qualifications for this job. Some have even said I have the wisdom of Solomon, Abraham Lincoln, and Charlie Reilley. Well, here comes a visitor walking across the page. Good day! How is your investigation?

Eminent Chemist: Good day, my friend. The research is going great. Success is just around the corner and over the next grant hill. I'm trying to achieve the quantitative determination of a single molecule.

Measurement Cop: How accurate will your determination be? It sounds like a binary problem.

Eminent Chemist: We should think about that. Look, here comes an Elected Official.

Elected Official: Hello, Voter. I've been very busy. After lowering taxes and slashing my budget, I'm going to provide everyone who voted for me with all the services they could want.

Eminent Chemist: I have colleagues who've talked about the principles of that. They called it a perpetual motion machine, I think.

Elected Official: I'll have my office get one of those. But I have a new project now, to keep all you folks who voted for me safe. I'm working on a bill to outlaw toxic chemicals. You remember that I campaigned with a toxic plank in my platform. I'm looking for some help with the wording of my bill.

Eminent Chemist: You've come to the right place. I'm working on determination of single molecules—you know, the chaste unmarried kind.

Elected Official: That's perfect! I think the law should say that our citizens' food and water and air and homes and cars and offices must contain no detectable amounts of toxic chemicals. If you can determine single molecules, can the rules read, for example, that a bunch of broccoli must contain less than one toxic single molecule?

Measurement Cop: Well, you might want to think about how many would be allowed in a half bunch—that may be a problem. But let me ask you: Which molecules are toxic ones?

Elected Official: Well, that should be obvious, shouldn't it? Anything that could make you sick.

Eminent Chemist: Well, a little beer will make me happy, but a lot will make me sick. My colleague down the hall gets sick on just a taste, so us Voters are not all alike, and there is a lot that's not known, including toxic molecules. That is, how much would make you sick or not isn't necessarily a linear question. Also, the water pipes in my house are made from a very toxic chemical, but once the pipes are made, they and the water in them are quite safe. So what will I use for water pipes if you don't let manufacturers use that toxic chemical?

Elected Official: But I want a law that will make this important public issue very simple. Isn't it best just to make a law that if you measurement scientists can detect a toxic chemical, it's too much to have around?

Eminent Chemist: Hum, I think I've just learned about another challenge in detecting single molecules. I'd better get back to the lab.

Elected Official: Well, I'm sorely disappointed. I didn't know making rules about chemicals would be complicated.

Measurement Cop: Well, it's true that there is a great deal of diversity among chemicals. You should ask Eminent Chemist to come talk to your staff. I'll try to get him out of the lab more often. And I'm afraid he hasn't told you even half the problems you Elected Officials face. Let me give you some directions to the journal on the next aisle over. I think its name is *Risk Assessment*.

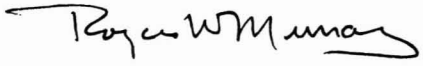

WHY STRUGGLE ALONE?

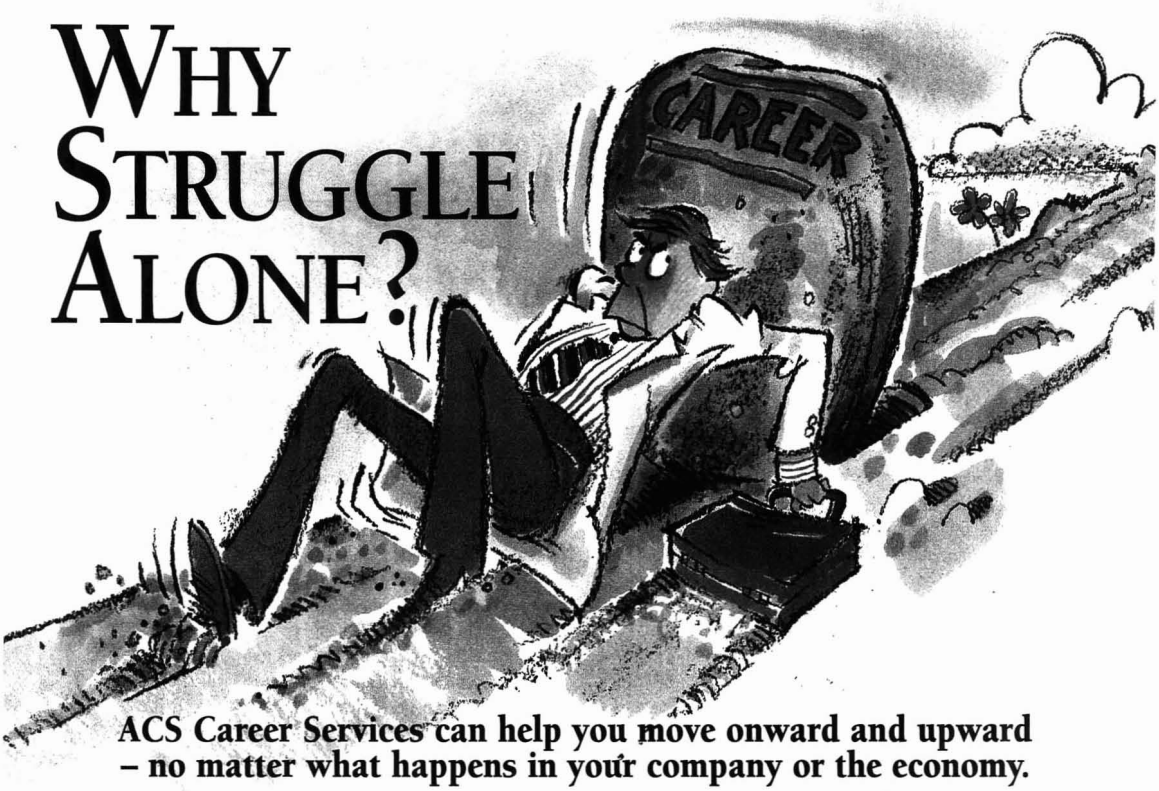

ACS Career Services can help you move onward and upward – no matter what happens in your company or the economy.

There are two kinds of people in the chemical industry and its related fields. Those who are aware of what it takes to remain marketable in the changing work environment. And those who are unsure.

At the Career Services Department of the American Chemical Society, we can help you manage your career on an ongoing, year-round basis, whether you're an undergraduate looking for your first job or a mid-career chemist searching for a new position. Our complete services include:

- **Workshops and presentations.** Part of the program at our national and regional meetings, these services include one-on-one assistance in fine-tuning job search and transitioning skills. Also available onsite at your local section, place of employment, or college/university, upon request.
- **Videos.** Can't make a meeting? Here's the next best way to acquire the career skills you need. These videos are an extension of our workshops and presentations.
- **Publications.** A wealth of literature based on research and interviews with employers and chemical industry professionals. Includes in-depth analyses of the current employment and economic status of professionals in your field.
- **Career assistance.** Personal guidance with résumé preparation, job searches, interview strategies, and employment issues. You'll talk with members who are experienced chemists in their fields.
- **Employment services.** The ACS Professional Data Bank is where top employers turn for job-seekers year-round; so do companies looking for consultants and volunteers. Our Employment Clearing Houses give you the opportunity to interview on-site with employers looking to hire now!

You'd expect to pay handsomely for such valuable advice and personal assistance, but ACS Career Services are offered at minimal or no cost to members. Indeed, most services are free – reason enough to join ACS, if you're not already among our over 150,000 members.

Whether you simply want to enhance your career or you're ready to make a major career change, call ACS Career Services today.

Because your career shouldn't be an uphill battle.

Call 1-800-227-5558 and give reference to code 301.

ACS Career Services

ACS Career Services can help you create the career you've always wanted.

Synopses of significant analytical articles from other publications

Screening Pap smears with near-IR

The Papanicolaou (Pap) smear is a commonly used cervical cancer screening technique. Pap smears are traditionally evaluated visually, which can lead to both false negatives and false positives. Chris W. Brown and colleagues at the University of Rhode Island have developed a rapid method for analyzing Pap smears with near-IR spectroscopy.

The researchers obtained near-IR spectra from Pap smears collected from 50 female patients, including 30 with normal cells, 9 with atypical cells, and 11 with cervical cancer. They found that ordinary near-IR spectra show minor differences among the normal, atypical, and abnormal Pap smears, whereas second-derivative spectra show more obvious differences. Principal component analysis of the second-derivative spectra can be used to classify the normal and abnormal Pap smears, but cannot completely separate the normal and atypical Pap smears. The authors note that because the available samples were limited, resulting in a small data set for classification by PCA and discriminant analysis, further studies with a larger data set are necessary to establish a diagnostic method for cervical cancer. (*Appl. Spectrosc.* **1995**, *49*, 432–36)

Taking advantage of antibody cross-reactions

Cross-reactions between an antibody and nontarget analytes can spell disaster for clinical assays that are intended to be specific, but in cases where an immunoassay is designed to screen for a general class of analytes, cross-reactivity is actually desirable. However, few accurate methods exist to quantitate the contributions of individual analytes to the overall signal in these cases. Bruce D. Hammock and colleagues at the University of California–Davis developed a mathematical model for simultaneous quantitation of four cross-reacting atrazine herbicides in a multiantibody immunoassay designed for atrazine determination in drinking water.

Both mono- and polyclonal antibodies were used in the immunoassay to provide a variable degree of cross-reactivity for individual atrazine analogues. The cross-reactivity profiles for each of the analytes with the array of antibodies were used to characterize the four herbicide analogues. Individual analyte concentrations were estimated from these profiles and from the assay signals by using a mathematical model that was an extension of the empirical four-parameter log–logistic fit. The four analytes could be quantitated simultaneously at concentrations in the low to sub-part-per-billion range. (*Anal. Chim. Acta* **1995**, *304*, 339–52)

Large peptide sequences by MS/MS

Tandem MS has been used successfully for amino acid sequencing of peptides smaller than ~ 3500 Da, but for larger peptides, FAB and similar single-charge ionization methods for precursor ions yield incomplete fragmentation of the peptide backbone. Electrospray ionization (ESI) produces abundant multiply-protonated intact peptide precursor ions, which appear to fragment more easily than singly-charged ions with a given CAD energy. Ron Orlando and V. S. Kumar Kolli of the University of Georgia used ESI with high-energy CAD in a four-sector mass spectrometer to achieve complete fragmentation of several peptides in the MW range of 4000–5000 Da.

The high mass resolution of the sector instrument permitted the researchers to assign charge states to the fragment ions by identifying their isotopic spacing. MS1 had a resolution of ~ 500 and MS2 had a resolution of ~ 3600 for most of the experiments. CAD was performed in the third field-free region using helium as the collision gas. The use of ESI in this study reduced the amount of sample required for tuning and mass spectral acquisition as compared with FAB methods from 10–100 nmol down to 500 pmol of peptide. The authors concluded that ESIMS/MS using a four-sector mass spectrometer simplified the peptide sequencing process considerably as compared with Edman degradation and extended the mass range of sequenceable peptides for MS methods. (*J. Am. Soc. Mass Spectrom.* **1995**, *6*, 234–41)

Determining two-electron reaction currents

In the stepwise oxidation or reduction of a molecule, the removal or addition of the first electron typically occurs more readily (with lower potential) than that of the second and subsequent electrons. Dennis H. Evans and Zhou Rongfeng have determined that the common assumption that the current of a two-electron reaction is always twice that of a one-electron reaction can lead to significant errors when removal of the second electron is more difficult than that of the first electron.

The researchers used chronoamperometric digital simulation, normal pulse voltammetry, and cyclic voltammetry to determine that in such cases, the comproportionation reaction between the final product and the original reactant to give two molecules of the one-electron intermediate is favored and can occur in the diffusion–reaction layer. Thus, when the diffusion coefficients of the three species are different, the current observed at potentials at which the two-electron reaction occurs will not necessarily be twice that seen at potentials at which the one-electron reaction occurs. (*J. Electroanal. Chem.* **1995**, *385*, 201–7)

Mediated electron transfer across Nafion interfaces

Nafion perfluorosulfonated ionomer coatings for electrodes that contain Ru(II) cationic complexes undergo electron transfer with anionic oxidants in solution. One possible application for these coated electrodes might be electrocatalysis. However, the mediator couples in the coatings frequently display non-ideal Nernstian behavior that could be interpreted as mediator–molecule interactions in the coating or as the result of a Gaussian distribution of formal potentials from individual redox couples within the coating. Fred Anson and Eyal Sabatani of the California Institute of Technology developed a mathematical model based on this Gaussian distribution to examine the kinetics of electron-transfer cross-reactions

at interfaces between mediator coatings and reactants in solution.

Expanding on preliminary work using a small number of mediator–substrate combinations with high rate constants, the authors applied their model to cross-reactions between Ru(II) complexes in the Nafion coatings and Fe(III) or Ru(III) complexed with chelators in solution and with several iron-substituted heteropolytungstate complexes. The heteropolytungstate complexes were size excluded from the coating, and reactions for them occurred exclusively at the coating–solution interface. The model was compared with Marcus theory to show that the linear correlation between the rate constants and the driving forces of the electron transfer cross-reactions was not affected when one reactant exhibited a distribution of formal potentials instead of a single value. (*J. Electroanal. Chem.* **1995**, *386*, 111–19)

What's going on at the interface?

The development of in situ spectroscopic and spatial microscopic methods provides information at the atomic and molecular levels for ordered metal–solution interfaces that is comparable to that available for metal–ultrahigh vacuum (UHV) systems. This situation has encouraged the examination of electrode–adsorbate systems that offer direct comparisons with metal–UHV analogues. Michael J. Weaver and colleagues at Purdue University used UHV experiments to examine the IR spectral and surface potential properties of Pt(111) dosed with carbon monoxide, water, and potassium with the goal of understanding the various electrostatic and other environmental factors that influence the structure and bonding of carbon monoxide and water at these electrochemical interfaces.

They chose this UHV-based ternary coadsorption system in light of the availability of in situ IR reflection–absorption spectroscopy data for the electrode–solution interface at negative electronic charges, thereby enabling the validity of the UHV electrochemical modeling approach to be assessed. Variations in the metal–UHV surface potential attending alterations in the interfacial composition were evaluated with a Kelvin probe. In addition to providing insights into surface solvation, the measurements provided the required link to the in situ electrode potential scale. (*J. Phys. Chem.* **1995**, *99*, 7677–88)

Estimating molecular weights of polymers using MALDI

Although MALDI-TOFMS was originally developed to help elucidate protein structure, its use to perform direct identification of mass-resolved synthetic polymer chains, including intact oligomers within a molecular weight distribution, measure molecular weight and molecular weight distributions, and simultaneously determine end groups in polymer samples has been the goal of polymer scientists. Because several practical problems can be encountered when polymer molecular weights are determined from their MALDI-TOF spectra, Giorgio Montaudo and colleagues at the Università di Catania and the Consiglio Nazionale delle Richerche (Italy) studied the accuracy of molecular weight estimates obtained from linear-mode spectra of samples of poly(methyl methacrylate), poly(styrene), poly(ethylene glycol), and several condensation polymers.

They found that the molecular weight estimates obtained from MALDI-TOF measurements agree with those obtained from conventional techniques such as gel permeation chromatography only in the case of polymer samples with narrow molecular weight distributions (M_w/M_n= 1.01–1.05). When the polydispersity index approached 1.10, the difference in molecular weight of poly(methyl methacrylate) samples measured by GPC and MALDI increased to about 20%, and at higher dispersions, the MALDI spectra failed to provide reliable molecular weight values. The researchers concluded that great caution must be exercised when one attempts to estimate molecular weights and molecular weight distributions of polymers using MALDI-TOFMS. (*Rapid Commun. Mass Spectrom.* **1995**, *9*, 453–60)

Charged derivatives for CID MS/MS of peptides

For several years researchers have recognized that fixed-charge derivatives can be used to direct the fragmentation pattern of high-energy collision-induced dissociation (CID) tandem mass spectra. Placing a fixed charge at a terminus of a peptide simplifies the pattern of fragment ions produced in CID. Trimethylammoniumacetyl, dimethyloctylammoniumacetyl, and triphenylphosphoniumethyl derivatives have all been used for this purpose, but to date no comparison of charged derivatives for CID to determine which has the best mass spectrometric characteristics has been published. Klaus Biemann and Joseph Zaia of the Massachusetts Institute of Technology have studied these derivatives, as well as some new N-terminal derivatives.

To evaluate the derivatives, the researchers used criteria that included ease of synthesis and purification of the derivatized peptide as well as the effects of the derivative on the peptide sequence fragment ion yield and ionization efficiency. All reactions were carried out on relatively large samples (50 nmol) to produce measurable amounts of each derivative and to avoid the possibility that low chemical yield might be mistaken for low ionization efficiency. They concluded that for general use, the trimethylammoniumacetyl derivative is the most practical; the dimethyloctylammoniumacetyl derivative is best suited for use with hydrophilic peptides. (*J. Am. Soc. Mass Spectrom.* **1995**, *6*, 428–36)

Particle beam MS in pesticide monitoring

MS detection is increasingly important for LC determination of pesticides in environmental analyses because it can provide the unambiguous structural confirmation required by new environmental regulations. Although particle beam MS is not inherently sensitive enough for the new pesticide tolerance thresholds being set by European regulatory bodies, it allows both positive and negative ion formation by EI and CI and can be coupled on line with a diode array detector. R. M. Marcé and co-workers at Universitat Rovira i Virgili (Spain), the University of Ljubljana (Slovenia), and the Free University (The Netherlands) used on-line SPE to enrich trace polar pesticides for RPLC with UV diode array and particle beam MS detection.

Coupling the diode array detector to the particle beam interface appeared to cause no additional peak broadening and allowed the acquisition of UV and MS data from a single injection. Detection limits for the method were in the range of nanograms per liter to micrograms per liter. The researchers found that matrix effects in real water samples enhanced the response to pesticides for MS over the predicted response from Milli-Q water samples, which suggests that quantification must be carried out using standard additions rather than calibration standards made up in Milli-Q water. (*J. Chromatogr. A* **1995**, *696*, 63–74)

Phosphorus-selective MS detection

Phosphorus-containing compounds play important roles in biochemistry, medicine, and environmental applications, but there are few detection methods sensitive and selective enough over a wide linear dynamic range for trace determinations in biological samples. Fred Abramson and Hengchang Song of George Washington University have developed a chemical reaction interface that converts phosphorus to PF_5 for selective MS detection of GC eluates.

The microwave-powered helium plasma interface was installed in a GC oven between the column and the MSD inlet. SF_6 reaction gas was added for the initial experiments to show proof of concept but was subject to significant sulfur species interferences when the dissociated atoms recombined. The researchers then tried the more expensive NF_3 and were able to detect PF_4^+ selectively over a 10^3 linear dynamic range to 10 pg/s concentrations. The method could also be used to determine hydrogen isotopes, chlorine, and sulfur simultaneously. The researchers used the method in a therapeutic drug monitoring application to determine cyclophosphamide and its metabolite in patient blood plasma. (*J. Am. Soc. Mass Spectrom.* **1995**, *6*, 421–27)

Imaging the chromatographic process

Although LC is one of the most commonly used separation methods, the structure of the column packing and its relationship to column performance are still generally unknown. Georges Guiochon and colleagues at the Universität Tübingen (Germany) have used NMR to image the migration and separation of gadolinium chelate bands.

Using the NMR imaging techniques developed for medical diagnostics, the researchers observed chromatographic bands of gadolinium compounds in shades of gray that become lighter with increasing gadolinium concentration. The results showed the existence of unexpectedly wide distributions of the local mobile phase velocity and the local HETP in an efficient chromatographic column. They also documented formation and resorption of fissured and/or compact zones in the column where the external porosity appeared lower or higher than average. The authors' results confirm that the local separations achieved are often much better than the apparent separations recorded with a bulk detector, and that considerable improvement in resolution would be obtained if bulk detectors were replaced by local detectors. (*J. Chromatogr. A* **1995**, *696*, 1–18)

Automated drug screening and confirmation by CE

As the use and abuse of drugs continues throughout the world, the need for more rapid, cost-effective, and accurate analytical techniques is increasing. Urine drug testing is widely used, and current methods for drug screening and confirmation are based on spectrophotometry, immunoassays, and chromatography. Each of these techniques, however, has disadvantages as well as advantages. In an effort to devise a scheme for automated drugs-of-abuse screening and confirmation, Wolfgang Thorman and Lone Steinmann of the University of Bern (Switzerland) developed a general approach using capillary electrophoretic techniques with on-column polychrome UV absorption detection.

The researchers found that urine pretreatment with a two-step solid-phase extraction using copolymeric sorbents provided extracts that allow screening and confirmation of commonly abused drugs. Using the same aliquot of urine, they determined barbiturates, selected benzodiazepines or their metabolites, and methaqualone in the first eluate by micellar electrokinetic chromatography (MECC), and opioids, cocaine, benzoylecgonine, selected benzodiazepines or their metabolites, diphenhydramine, and amphetamines in the second eluate by the same technique. Methadone and its metabolite, compounds found in the second eluate, were determined by CZE. Based on the results obtained, they proposed a capillary analyzer featuring automated sample cleanup, multiple capillaries for simultaneous analysis of the fractions in one or several buffers, and computer-aided peak identification. (*J. Cap. Elec.* **1995**, *2*, 81–88)

Opening the elution window

Separating uncharged compounds by micellar electrokinetic capillary chromatography (MECC) is based on differences in partitioning between the mobile phase and the micellar phase. The distribution between these phases is expressed by the retention factor, and the elution window is the time interval within which the compounds will be detected. Assuming that the selectivity is determined by the surfactant system, resolution is determined primarily by the retention factors and elution windows of the uncharged compounds. To better understand the effects of different experimental conditions on retention factors and elution windows, P.G.H.M. Muijselaar and colleagues at the Eindhoven University of Technology (The Netherlands) varied the applied field strength, buffer pH, ionic strength, capillary surface modifications, alkyl chain length of the surfactant, and other conditions in an MECC separation.

They found that the elution window can be increased by decreasing the pH of the electrolyte system, although retention factors remained fairly constant, and that using coated capillaries was not helpful. They also found that adding an organic modifier to the background electrolyte resulted in an increase in the elution window and a decrease in the retention factors. (*J. Chromatogr. A* **1995**, *696*, 273–84)

Using less solvent

In the sample preparation part of EPA Method 608 (a gas chromatographic method for the determination of organochlorine pesticides and PCBs in wastewater), a 1-L sample of water is extracted with 200 mL dichloromethane. The dichloromethane is released into the environment by evaporation when it is solvent switched with hexane. Because Method 608 is one of the most widely used EPA methods, it is estimated that $\sim 10^5$ kg of dichloromethane are released into the atmosphere every year from this method alone, and one of EPA's goals for this decade is to reduce the amount of solvents used in this and other methods. Ronald Hites and Voon S. Ong of Indiana University have developed a low-solvent GC-electron capture detector/MS method to replace Method 608.

The sample is passed through octadecylsilica extraction disks that are then extracted with supercritical carbon dioxide into a vial of hexane. Analyte recoveries are at least 80% and solvent consumption is reduced by 90%. By using a GC/MS analysis, quantitation and identification are accomplished in one analytical run, rather than the two runs on two separate columns called for in the GC-only analysis of Method 608. The procedure also reduces background interference problems resulting from solvent impurities. (*Environ. Sci. Technol.* **1995**, *29*, 1259–66)

Detecting dyes with diode laser/fiber-optic Raman

Fiber-optic probe technology provides fast and easy remote sampling in many environmental applications, such as inside storage tanks and wells. Combined with diode laser Raman spectroscopy, such fiber-optic probes are extremely useful in characterizing Superfund sites after closure. M. Bonner Denton and colleagues at the University of Arizona and the U.S. EPA have developed a compact diode laser/fiber-optic Raman spectrometer for quantitating four environmentally important dyes (trypan blue, acid black 1, acid blue 40, and basic blue 7).

The system uses diode laser excitation at 782 nm, fiber-optic probe technology, an imaging spectrometer, and a state-of-the-art CCD camera. Detection sensitivities range from 0.2 ppm for acid black 1 to 25 ppm for basic blue 7. The authors note that these sensitivities were achieved with normal Raman, without the problems associated with resonance Raman or surface-enhanced Raman. With additional development of the fiber-optic probe technology and more powerful diode lasers, they believe that detection limits can be further improved. (*Appl. Spectrosc.* **1995**, *49*, 508–12)

Paleodental studies with FT-Raman spectroscopy

The investigation of the growth and development of dental remains has assumed importance for the taxonomic classification of species in recent years. The techniques used for analysis must be nondestructive because chemical pretreatment, mechanical sectioning, and physical preparation of archaeological specimens are generally not permitted. H.G.M. Edwards and colleagues at the University of Bradford (U.K.) have extended their FT-Raman spectroscopic characterizations of proteins at a molecular level and their conformational order in human and animal keratotic biopolymers to protein and hydroxyapatite vibrational structure in human teeth.

They obtained spectra from the enamel surfaces of samples ranging from modern times to prehistoric: a child's deciduous exfoliated tooth, Romano–British teeth from a burial site (~ 2000 years old) and fossilized animal teeth (~ 1 million–70 million years old). The features in the spectrum of the child's tooth were assigned to hydroxyapatite and protein, and a comparison of that spectrum with those obtained from the older teeth indicated that the organic protein component disappeared with interment. Spectroscopic features resulting from the inorganic phosphatic matrix, on the other hand, were found to be common to all modern and ancient samples. The researchers also reported that the presence of impurities leached from surrounding soil or rock did not degrade the quality of the observed FT-Raman spectra. (*Biospectroscopy* **1995**, *1*, 29–36)

How much chlorine?

The ability to measure chlorine is important because of its toxicity and its routine use in the chemical industry and for the sterilization of water. Measuring chlorine in water is made difficult by interferences from the combined forms of chlorine and other disinfectants. Satyajit Kar and Mark A. Arnold of the University of Iowa have developed a fiber-optic probe for measuring free chlorine in aqueous solution.

The probe is based on fluorescence quenching by chloride ions and a redox reaction by chlorine of the indicator dye *N*-(6-methoxyquinolyl)acetoethyl ester (MQAE). The aqueous dye solution is trapped in a microporous gas-permeable membrane in front of a fiber-optic assembly. The chlorine and chloride ions diminished the fluorescence of the MQAE, measured as a function of time through the fiber-optic assembly. Although the magnitude of total fluorescence decay was independent of the chlorine concentration, the initial rate of decrease in fluorescence intensity was linearly proportional to the chlorine concentration over the range 8.4–418 μM. Once the probe has been exposed to chlorine, the dye solution must be replaced, but the probe displayed excellent reproducibility, had an RSD of 1%, and could also be used to measure aqueous hypochlorous acid. (*Talanta* **1995**, *42*, 663–70)

Exerting influence on CDs

When β-cyclodextrins (CDs) form complexes with pyrene, a barrel-like configuration results, which allows the interaction of smaller organic modifiers such as amines with the open primary ends of the CDs. Although amines are fluorescence quenchers, it has been observed that the emission of β-CD–pyrene is enhanced as a function of concentration of either *tert*-butylamine or *n*-propylamine because the fluorescence of pyrene is not quenched. Isiah M. Warner and colleagues at Louisiana State University studied the influence of triethanolamine (TEA) on the complexation of β-CD and pyrene using steady-state fluorescence measurements.

The stoichiometry and association constant of the β-CD–pyrene complex in the presence of TEA were evaluated by following the changes in the fluorescence intensity of pyrene at 382 nm as a function of β-CD concentration. Although collisional quenching of pyrene by TEA is indicated by Stern–Volmer plots, a decrease in quenching was observed in the presence of β-CD, indicating effective protection of the included pyrene molecules against quenching from TEA. A decrease in the apparent formation constant of β-CD–pyrene also occurred in the presence of TEA because of increased bulk solvent hydrophobicity and competitive equilibrium between the pyrene and TEA for the β-CD cavity. (*Appl. Spectrosc.* **1995**, *49*, 520–25)

Real-time mid-IR imaging

The availability of high-sensitivity multichannel imaging detectors has made the collection of chemical images more accessible to chemists and spectroscopists. Although IR spectroscopy provides intrinsically higher sensitivity than conventional Raman spectroscopic methods, diffraction considerations limit the spatial resolution to ~ 10 μm at 500 cm^{-1}. E. Neil Lewis and Ira W. Levin of the National Institutes of Health have developed a mid-IR spectroscopic imaging instrument designed around an InSb multichannel focal-plane array detector and a variable-bandpass dielectric filter.

The system can be configured for either macroscopic or microscopic applications and can obtain high-fidelity, chemically specific images in real time. Spectral images are collected by focusing the broadband IR radiation from a globar with an off-axis ellipsoid through a small spot in the tunable filter. The filter is then rotated to the desired wavenumber and the light is collected by a Cassegrainian optic that acts as the microscope condenser. The image then is focused onto the InSb focal-plane array with a second Cassegrainian optic that serves as the microscope objective. Continuous tuning is provided in the IR region from 4000–2320 cm^{-1} with spectral resolutions of ~ 35–18 cm^{-1} at the extremes of the range. The researchers have used the microscope to image polystyrene microspheres, lipids and an amino acid embedded in KBr disks, and a tissue sample from a coronal slice of a monkey cerebellum. (*Appl. Spectrosc.* **1995**, 49, 672–78)

New Elements.

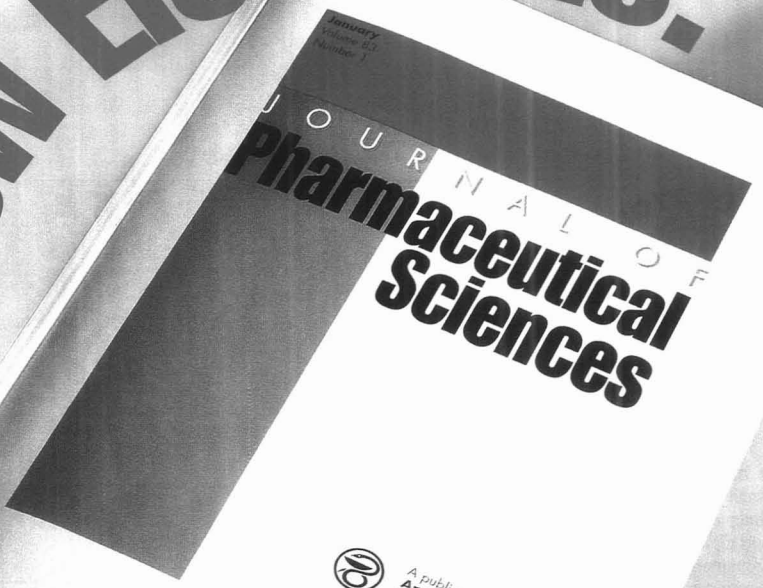

A Stronger Bond.

The American Chemical Society and The American Pharmaceutical Association Working Together As Co-Publishers

APhA and ACS are working to provide unprecedented exposure of pharmaceutical sciences to the broader scientific community. The *Journal of Pharmaceutical Sciences* is now expanding its coverage of:

- Chemical processing of pharmaceuticals
- Chemical stability of drugs
- Pharmacokinetics
- Biopharmaceutics
- Pro-drug development
- Metabolic disposition of bioactive agents
- Dosage form design
- Protein-peptide chemistry
- Biotechnology and much more.

Special Low Member Price!

Editor Dr. William I. Higuchi has brought a new focus to the *Journal of Pharmaceutical Sciences*. It's been expanded to better serve chemists and scientists in pharmaceutical science research, technology and targeted drug delivery. Dr. Higuchi is Distinguished Professor and Chair, Department of Pharmaceutics and Pharmaceutical Chemistry at the University of Utah.

Best of all, the *Journal* is available at a low member price–just $30 a year! Members: $30/year, Individual nonmembers: $85/year, Institutions: $310/year (U.S. rates).

Call toll-free, 1-800-333-9511 and subscribe today! Outside the U.S. call 614-447-3776. Fax to 614-447-3671.

APhA Members order through APhA. To order directly, call 1-800-237-APhA or FAX to 202-638-3783.

Money-Back Guarantee: ACS offers a prompt, pro-rata refund policy covering all unmailed issues.

Editor
William I. Higuchi
Department of Pharmaceutics and Pharmaceutical Chemistry University of Utah

Associate Editors
David J. W. Grant
University of Minnesota
Ho-Leung Fung
State University of New York at Buffalo
Bradley D. Anderson
University of Utah
C. Russell Middaugh
Merck and Co.

Editorial Advisory Board
Gordon L. Amidon, Gregory E. Amidon, Bruce J. Aungst, Meir Bialer, Ronald T. Borchardt, David W. A. Bourne, Robert L. Bronaugh, Stephen R. Byrn, John F. Carpenter, Jens T. Carstensen, Win Loung Chiou, Jeffrey L. Cleland, Kenneth A. Connors, Michael G. Cordingley, Daan J. A. Crommelin, William J. Curatolo, Meindert Danhof, William E. Evans, David Fitzgerald, Jeffrey L. Fox, Detlef Groeger, Iris H. Hall, James N. Herron, William J. Jusko, Gerald B. Kasting, Kristine Knutson, William J. Lambert, Robert S. Langer, Abraham M. Lenhoff, Thomas M. Ludden, Michael Mayersohn, Andrew T. McPhail, Kamal K. Midha, Marilyn E. Morris, Tsuneji Nagai, Michael S. Roberts, Nair Rodriguez-Hornedo, Robert A. Ronfeld, Malcom Rowland, Gautam Sanyal, Jean-Michel Schermann, Miklos Simonyi, John T. Slattery, Valentino J. Stella, Raj G. Suryanarayanan, Felix Theeuwes, John A. Thomson, Daniel L. Weiner, Dominic J. Wells, Peter York, George Zografi

AMERICAN CHEMICAL SOCIETY
1155 Sixteenth Street, NW Washington, DC 20036

AMERICAN PHARMACEUTICAL ASSOCIATION
2215 Constitution Avenue, NW Washington, DC 20037
APhA

Into the hands of users

Immunochemistry has evolved from a clinical technique used only in the laboratory for specific applications to a maturing environmental technique that can run the gamut from a field screening procedure to a very sensitive laboratory assay. Jeanette Van Emon and her colleagues at the EPA's Office of Research and Development have been at the forefront of developing immunochemical techniques that are cost effective and provide reliable data in a timely fashion to measure environmental contamination, cleanup efficacy, and potential exposure levels.

Van Emon's interest in immunoassay methods stems from a lecture she attended in graduate school. "Bruce Hammock of the University of California–Davis championed the technique back in the 1980s. Very few researchers were using immunoassays to solve environmental analytical problems. I liked the combination of biology and chemistry, and I could apply my interest in methods development as well." Of her role at EPA, Van Emon says, "Our job is to get the method or test kit into the hands of those who need it. We evaluate kits that are already commercially available, create our own field-portable methods, and also evaluate methods from academic labs. In the case of test kits, the user may not be a trained analyst. For example, farmers, field crews, and emergency response teams need straightforward and accurate methods."

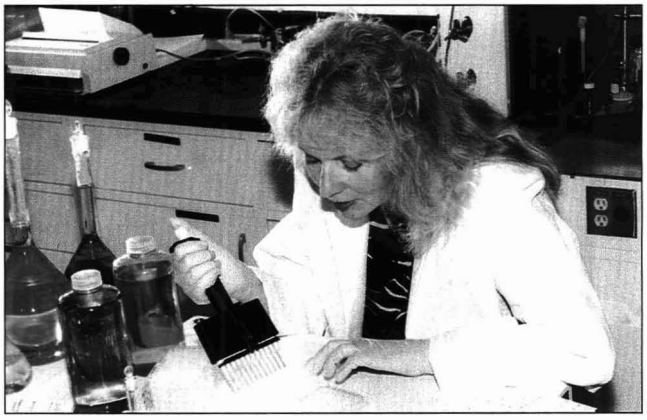

EPA

Van Emon performing one of the steps in a microplate immunoassay.

Van Emon's research projects address the needs of the various EPA offices as well as those of other federal and state agencies. For example, EPA's Office of Pesticides Programs needs rapid and simple field methods to measure "dislodgeable" pesticide residues from crops to quickly determine worker exposure in near real time. Dislodgeables are those residues that, just after application of the pesticide, an individual might be exposed to by brushing against the plants on a walk through the fields or that can be easily washed off by the first rain after the application. Knowing the amount of dislodgeable residues is also necessary to determine if the application was successful, to decide when it is safe for workers to enter the fields, and to ascertain if the pesticide drifted to neighboring areas. Dislodgeable residues are measured by literally hole-punching the leaves, lightly extracting the punches with a surfactant and water, and performing the immunoassay on the extract.

Another of her projects is coupling supercritical fluid extraction (SFE) to enzyme-linked immunosorbent assay (ELISA) to evaluate pesticides in foods. This project supports the National Human Exposure Assessment Survey being conducted by EPA and other agencies. "SFE is very compatible with ELISA," says Van Emon. "Fats and food colorings, and the nature of multicomponent samples consisting of a variety of dietary items, are what make foods in this study a difficult matrix. Samples are crudely separated into either 'beverage' [milk, juice, ice cream, and other frozen items that could melt] or solid [meat, vegetable, pasta]. You need a powerful extraction technique for the ELISA that is quick, widely applicable, and cost effective."

Although most of her work seems to be "client generated," Van Emon does have her hand in the future of immunochemical methods. One project is the modification of recently patented clinical immunosensors (antibodies imbedded in conducting polymers wrapped around an electrode) for environmental applications. In the clinical setting, these biosensors have been used to take blood-based measurements, and Van Emon envisions their being used in waste streams and effluents for compliance monitoring and pollution prevention.

BAS purchases Technicol

In an effort to expand its pharmaceutical and neuroscience customer base, Bioanalytical Systems (BAS; West Lafayette, IN) has purchased Technicol (Stockport, U.K.). Explaining the purchase, BAS president Peter Kissinger said, "Our focus is on the pharmaceutical industry and biomedical research, especially neuroscience and drug metabolism. The U.K. has a strong position in these areas and it has become clear that we have to have a direct presence there. [The newly named] BAS Technicol will ultimately become the European distribution and service center for our company, serving customers and distributors throughout the EC."

BAS Technicol will offer products for chromatography, electrochemistry, and in vivo sampling using microdialysis and ultrafiltration. Speaking about the change in ownership, company manager Denise Wallworth said, "The initial aim is to expand our activities in chiral, preparative, and process chromatography while broadening our range of analytical columns and accessories. At the same time, we will continue actively developing the market for BAS's range of products. With 15 years of experience in the market, we believe that joining forces in this way will provide a strong new base for BAS in the U.K."

Division of Analytical Chemistry award recipients

Theodore Kuwana, Michael D. Morris, James D. Winefordner, and Richard N. Zare are this year's winners of the ACS Division of Analytical Chemistry awards, which will be presented at special symposia at the fall ACS national meeting in Chicago.

Theodore Kuwana, professor of chemistry at the University of Kansas, will receive the Award in Electrochemistry, sponsored by EG&G Princeton Applied Research. Kuwana is best known for his work in electroanalytical methods for biomolecules, carbon microelectrodes, photoelectrochemistry, electroluminescence, and developing electrochemical detectors for LC. For almost a decade, Kuwana has been involved in a summer program that allows college teachers to conduct research in bioanalytical chemistry.

Michael D. Morris, professor of chemistry at the University of Michigan, will receive the Award in Spectrochemical Analysis, sponsored by Perkin-Elmer Corp. Morris is best known for his work in biological applications of Raman and laser spectroscopy. His research interests also include capillary and gel electrophoresis of biomolecules and DNA analysis.

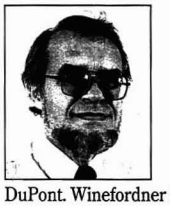

James D. Winefordner, professor of chemistry at the University of Florida, will receive the Award for Excellence in Teaching, cosponsored by the Division of Analytical Chemistry and DuPont. Winefordner is best known for his work in atomic and molecular spectroscopy and for developing detection methods based on luminescence, absorption, and emission, including GC and LC detectors and spectroscopic instrumentation.

Richard N. Zare, professor of chemistry at Stanford University, will receive the Award in Chemical Instrumentation, sponsored by the Dow Chemical Company Foundation. Zare is best known for his work on improving and developing detectors. His research interests include molecular photodissociation, fluorescence and chemiluminescence, and applying lasers to chemical problems.

FOR YOUR INFORMATION

Pigliucci quits Perkin Elmer

Riccardo Pigliucci, president and chief operating officer at Perkin Elmer, has resigned after 29 years with the company. His resignation follows a March announcement that the company would consider outside candidates in its search for a successor to Gaynor Kelley, chairman and CEO, who is retiring next year. Kelley has assumed Pigliucci's responsibilities until a successor is found.

Gasoline SRMs

To help gasoline producers meet EPA guidelines for oxygenates in gasoline, NIST has produced a series of standard reference materials (SRMs 2286–2293) containing ethanol, *tert*-amyl-methyl ether, ethyl-*tert*-butyl ether, and methyl-*tert*-butyl ether. Each standard contains two ampules of gasoline with a certified concentration of one of the oxygenates and a third ampule of gasoline with no oxygenate. For more information, contact NIST SRM Program, Rm. 204, Bldg. 202, Gaithersburg, MD 20899-0001 (301-975-6776; fax 301-975-3730).

New methods

AOAC International has adopted six LC methods to be published in the second supplement to the *16th Edition of Official Methods of Analysis of AOAC International*: dithianon in technical products and formulations (995.01), cyfluthrin in pesticides (995.02), extracted capsaicinoids and capsicums (995.03), tetracycline residues in milk (995.04), vitamin D in infant formulas and enteral products (995.05), and D-malic acid in apple juice (995.06). For more information, contact AOAC International (703-522-3032).

Detecting Single Molecules in Liquids

The ability to identify single molecules can reduce sample size requirements for a variety of applications

An important challenge facing analytical chemists today is the efficient detection and identification of single molecules. The ability to make such highly sensitive and selective measurements could lead to enormous breakthroughs in DNA analysis, groundwater monitoring, fluorescence immunoassay, chemical separations, and fundamental studies of physical and chemical phenomena at the single-molecule level. For example, given single-molecule sensitivity, analyte quantitation can be performed in a discrete or "digital" manner, thus greatly reducing initial mass requirements for some of these applications.

Over the past few years, several fluorescence-based techniques have evolved with sufficient sensitivity to detect single molecules. The best known of these are the methods developed by Moerner (*1, 2*) and Orrit (*3, 4*), in which single molecules of impurities in cryogenic solids are probed using narrowband dye lasers in the far wings of an inhomogeneously broadened transition. Recently, several groups have reported detection of single molecules on room-temperature surfaces using near-field microscopy techniques (*5–7*) that, in addition to being highly sensitive, reveal interesting information on dipole orientation and surface dynamics.

Of greatest interest to analytical chemists are techniques for single-molecule detection in liquids. These techniques, based on time-gated detection in a flowing stream, were pioneered by Keller (*8–10*) and Mathies (*11, 12*). Recent improvements in Keller's technique include near-IR excitation (*13*) and avalanche-photodiode detection (*14*). Using fluorescence correlation techniques, researchers have demonstrated single-molecule detection by illuminating a very small volume (~ 1 fL) in a drop of solution suspended below the objective of a confocal microscope (*15*). In a similar setup, confocal fluorescence microscopy was recently used to detect single molecules directly (*16*). A technique developed in our laboratory uses either levitated or falling-droplet streams of micrometer-sized droplets (*17–19*).

There are advantages and disadvantages associated with each technique. The principal trade-off is sample throughput versus S/N. The technique of choice for a particular application would of course depend on the priorities of the experiment. In this Report, we discuss the nature of this trade-off by considering the intrinsic sensitivity limitations involved in single-molecule fluorescence detection in liquids and give some examples of different detection schemes.

Sensitivity limitations

Several factors limit sensitivity in fluorescence detection of single molecules and limit the fraction of molecules in the sam-

Michael D. Barnes
William B. Whitten
J. Michael Ramsey
Oak Ridge National Laboratory

0003-2700/95/0367-418A/$09.00/0
© 1995 American Chemical Society

ple that can actually be detected (molecular detection efficiency). The fluorescence process begins with absorption of a photon, which drives the molecule from the ground electronic state S_0 to the first excited electronic singlet state S_1 (Figure 1). The rate constant for absorption k_{abs} is the product of the absorption cross section σ (cm^2) and the laser photon flux F ($cm^{-2}\ s^{-1}$). Absorption rates are usually limited only by the laser intensity. Following dissipation of a small fraction of the absorbed laser energy in a fast ($< 10^{-14}$ s) nonradiative relaxation step, emission of a fluorescence photon occurs in a few nanoseconds for most ionic dyes. The molecule has now returned to the ground electronic state and is prepared for another absorption–emission cycle. At saturation excitation intensities, the absorption–emission cycle time is limited by the fluorescence lifetime of the molecule so that, for high quantum efficiency dyes, millions of fluorescence photons per second may be emitted.

An advantage of ionic dyes for single-molecule detection is that fluorescence quantum efficiencies are near unity. However, for some combinations of dye and solvent, singlet–triplet intersystem crossing rates k_{nr} (to T_1) can be significant, resulting in a substantial reduction in fluorescence count rates. Absorption cross sections for most dyes ($\sim 10^{-16}\ cm^2$) are typically many orders of magnitude larger than other inelastic light-scattering processes such as Raman scattering.

The temporal and spectral properties of fluorescence are also advantageous to single-molecule detection. Fluorescence emission is typically red shifted significantly with respect to the excitation frequency and is generally a much slower process, occurring in nano- to microseconds, than Rayleigh or Raman scattering, which occurs on a femtosecond scale. These properties facilitate separation of the signal from background in both the time and frequency domains.

There are several important limitations on the magnitude of the signal that can be obtained from a single molecule. The fluorescence count rate, defined approximately by the absorption–emission cycle time, is limited at saturation by the finite fluorescence lifetime $1/A_{spont}$. In addition to limitations imposed by the finite fluorescence lifetime, dyes also have a finite photochemical lifetime that limits the average number of absorption–emission cycles the molecule may undergo before photochemical destruction or "bleaching" takes place.

Photobleaching competes with spontaneous emission such that the total number of fluorescence photons emitted per molecule is proportional to the spontaneous emission rate divided by the photobleaching rate (*20*). Thus, even in an experiment in which the laser–analyte interaction time is essentially infinite, there will be a finite number of fluorescence events.

The photochemical lifetime can be expressed as the product of the excitation rate k_{abs} and the photobleaching quantum yield Φ, which is the probability of photobleaching per excitation cycle. The photobleaching quantum yield is a function of

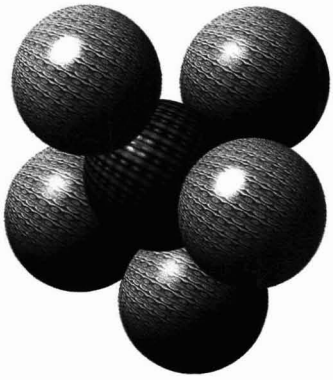

both dye and solvent (*21*) with typical values ranging from $\sim 10^{-5}$ to 10^{-7}. The average number of absorption–emission cycles that the molecule may undergo before photobleaching occurs is $1/\Phi$, or about 10^6. In the saturation limit ($k_{abs} \sim 10^8$/s), the photochemical lifetime is on the order of 10 ms.

What matters most, however, is not the signal but the S/N and the magnitude of the background signal. Source noise (from Rayleigh and Raman scattering from the solvent and fluorescence from impurities in the solvent) in these types of experiments usually dominates the background. Fluorescence from impurities can often be minimized by using ultrapure solvents, but preparation and handling of extremely dilute solutions is still not a trivial problem. For example, dilute solutions of dye can undergo photodegradation in room light, or dye molecules can stick to container walls.

The contribution of Rayleigh and Raman scattering can also be significant because of the finite out-of-band rejection of bandpass filters typically used in single-molecule detection experiments. Because the magnitude of the background signal scales with the probe volume, minimizing the illuminated volume is critical. As a rule of thumb, solvent scattering places an upper limit on the probe volume ($\sim$ 10 pL).

Because photon counting is universally used for single-molecule detection experiments, it is important to maximize the photon detection efficiency. Fluorescence emission is isotropic in space; typically only 10–20% is collected by the detection optics. Combined with finite filter transmission of $\leq$ 50% and detector quantum efficiency of 10–50%, typical photon detection efficiencies range from $\sim$ 0.5 to 5%. Combining the photon detection efficiency with the finite single-molecule signal (resulting from photobleaching) yields a maximum of a few thousand detectable fluorescence photons.

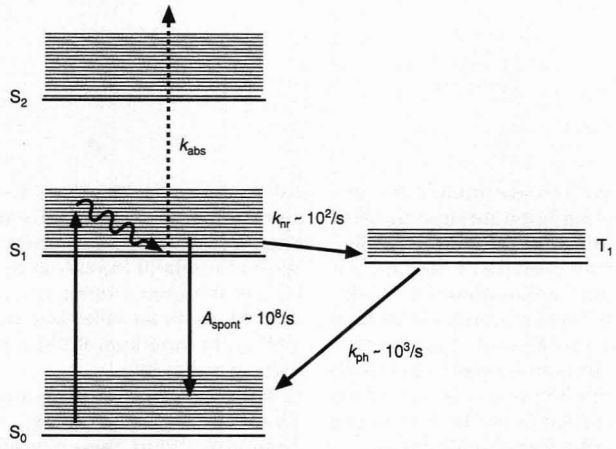

Figure 1. Energy-level schematic typical of most solvated ionic dyes.

The dashed line k_{abs} represents excited-state absorption and may be important at high intensities. After fast intramolecular relaxation, the molecule may spontaneously radiate A_{spont} or undergo intersystem crossing k_{nr}.

Detection criteria

Detection of a single molecule is usually defined by a threshold criterion similar to the operation of a discriminator circuit that outputs a logic pulse when the amplitude of an (analog) input signal exceeds some predefined threshold level. In a typical experiment, the threshold level is usually ~3 times the standard deviation in the nonfluorescent background signal. For Poisson-distributed (shot-noise limited) background signals, detection is achieved when the fluorescence signal generated from the molecule of interest exceeds ~ 3 times the square root of the mean background signal. Unfortunately, most of the "proof" that a single molecule has been detected in liquids is based on S/N, supported by small probabilities of more than one molecule occupying the probe volume in a given measurement interval. The relatively small number of fluorescence photons emitted from molecules in liquids has precluded definitive tests, such as photon antibunching, observed in cryogenic solids (*22*).

Although the selection of a threshold value is arbitrary, this setting strongly influences molecular detection efficiencies and concentration detection limits. Figure 2 shows typical signal and background photocount probability distributions for single-chromophore molecules such as rhodamine 6G (R6G) with a threshold set at an arbitrary position. The probability of spurious detection resulting from statistical fluctuations in the background (a false positive) is represented by the dark green area. Likewise, the probability that a true single-molecule event is ignored (a false negative) is represented by the light green area.

Choosing a high threshold value of 5 or 6 σ_b ensures a vanishingly small probability of spurious detection; however, it also implies that a large fraction of molecules will not be detected because the signal failed to exceed the threshold. Conversely, lowering the threshold value increases the fraction of detectable molecules with a concomitant increase in the probability of error. Thus, the molecular detection efficiency, or the probability that the signal amplitude generated from a single molecule will exceed the threshold, is related to amplitude probability distributions for the background and signal and the extent of overlap between them.

Molecular detection efficiency

The overlap between signal and background photocount distributions affects the probability of molecular detection. Because the signal and background photocount distributions are characterized by the average number of signal counts <s> and the noise σ_b, respectively, molecular detection efficiencies can be quantified for specified values of the average S/N or $\langle s \rangle / \sigma_b$. Figure 3 shows the dependence of molecular detection probability on average S/N for single-chromophore molecules such as R6G. The threshold for each value of $\langle s \rangle / \sigma_b$ is chosen to minimize the total error probability (false positive + false negative). Because the photocount probability distribution for single-chromophore molecules is a decaying exponential, overlap with the background distribution decreases slowly with increasing S/N such that the unit molecular detection efficiency is only an asymptotic limit. Even with an average S/N of 50, the molecular detection efficiency is only about 95%. The average S/N therefore provides an upper bound with respect to error probability. Other experimental factors such as laser intensity inhomogeneity or molecular diffusion could cause molecular detection efficiencies to be much lower than those given by the average S/N.

Molecular detection probabilities are influenced by the shape of the signal photocount distribution as well as the average S/N. The photocount statistics associated with fluorescence from a single molecule are highly dependent on the number of independent chromophores (*23*). Figure 4 shows background and signal photo-

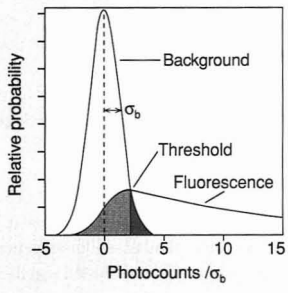

Figure 2. Fluorescence and background photocount probability distributions for R6G.

Detection threshold is indicated by the vertical line. The false-positive error probability is represented by the dark green area, and the false-negative error probability is represented by the light green area (which corresponds to the fraction of molecules undetected).

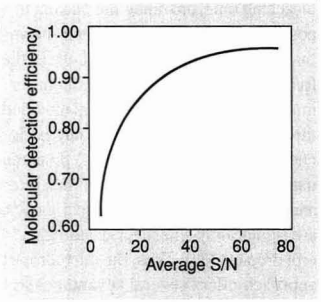

Figure 3. Molecular detection efficiencies for single-chromophore molecules as a function of average S/N.

The threshold for each point is chosen to minimize the total error (false positive + false negative) probability.

count distributions (complete photobleaching) for molecules with 1, 2, and 34 independent chromophores, all with the same average S/N. However, the difference in overlap among the three different signals and background distributions implies very different molecular detection probabilities.

For example, β-phycoerythrin, a large molecule with 34 independent chromophores, has a detection probability approaching unity for a very modest average S/N of 10 whereas the detection probability for R6G is only 0.77 for the same average S/N. The signal photocount distribution also depends on the fraction of molecules that undergo photobleaching (*24*). In other words, when the laser–analyte interaction time is much less than the average photochemical lifetime, only a fraction of the molecules will undergo photobleaching. However, incomplete photobleaching predominantly affects the part of the distribution that does not overlap with the background and therefore does not significantly influence molecular detection probabilities.

How many?

How accurately can a distinction be made among zero, one, two, or more molecules? Just as molecular detection efficiencies are highly dependent on photocount statistics, so is the ability to clearly determine the number of molecules in a given probe volume. As demonstrated by Ng (*18*), the distribution of signal bursts from molecules of β-phycoerythrin shows well-defined peaks corresponding to one, two, and three molecules. In the case of single-chromophore molecules, the similarity between the photocount distributions precludes a clear determination of the number of molecules from the fluorescence burst amplitude. However, if the laser–analyte interaction time is long enough to measure the photobleaching kinetics, it is possible to distinguish between one or more molecules based on the time dependence of the fluorescence count rate versus time (*19*).

Often the laser–analyte interaction time is much less than the average photobleaching time and the fluorescence signal is limited by the transit time of the molecule through the detection volume. In these cases, usually only the burst amplitude is measured, which makes the distinction between one or two single-chromophore molecules more obscure. The fraction of total signal bursts expected from two molecules is the Poisson probability of having two molecules in the probe volume divided by the probability of there being one molecule in the probe volume—there can be a significant fraction of two-molecule bursts even if the probability of there being two molecules present is very small. Complications such as excitation intensity inhomogeneity, molecular diffusion, and other processes can also obscure the distinction between one or two molecules.

Some examples

The experimental techniques that have evolved for single-molecule detection in liquids share several common characteristics—they all illuminate and/or image a small volume to minimize background scattering from the solvent, use high-numerical aperture objectives to maximize light collection efficiency, and use some means, such as tight spatial and optical filtering, to further reduce background signals. Aspects of four of these techniques are examined here.

Time-gated detection. This technique, developed by Keller (*9*), is based on the fact that the time scales for fluorescence and Raman and Rayleigh scattering differ by several orders of magnitude. Fluorescence lifetimes in the visible region of the spectrum are usually on the order of a few nanoseconds, and Rayleigh and Raman scattered light from the solvent occurs essentially instantaneously. Thus, background radiation and fluorescence are separated in time as well as in frequency. The arrival time distribution for Rayleigh and Raman scattering is mapped by the detector response function (typically Gaussian-like with full-width half-maximum of about 500–750 ps), and the temporal profile for fluorescence is a decaying exponential (with a typical time constant of $\tau \sim 3.5$ ns) convoluted with the instrument response function. Thus, by choosing a suitable counting window in time, the number of background counts can be reduced by rejecting photocathode events that occur outside the defined window.

Time-correlated photon counting instrumentation is used in this technique. An analog voltage pulse with an amplitude proportional to the arrival time is generated for each photocathode event. Pulse-height discrimination can then be used to accept or reject the pulse, thereby reducing the background signal. The major advantage of this technique is speed and high sample throughput. Used with a simple flow cell or flow cytometry apparatus, single molecules can be detected with laser–analyte interaction times on the

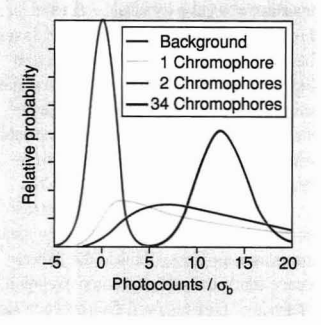

Figure 4. Fluorescence and background photocount probability distributions for molecules containing 1, 2, and 34 independent chromophores.

The overlap with the background distribution is much different for the three types of molecules even though the average S/N is the same. Molecular detection efficiencies are much higher for multiple-chromophore molecules than for single-chromophore molecules that have the same average S/N.

order of a few milliseconds with photon burst amplitudes of ~ 10–20 counts.

However, there are some disadvantages. In a simple flow cell without hydrodynamic focusing, only ~ 0.01% of the analyte molecules are actually interrogated in the probe volume (*13*). There are also significant detector dead-time limitations imposed on the single-molecule fluorescence count rate because of the finite processing time of time-to-amplitude converters (TAC) used in these experiments. Typical TAC dead times are about 5 μs, which effectively limits input count rates to < 100 kHz.

Some of these problems have been addressed (*14*) by inserting a small-bore capillary (~ 0.3 μm diameter) into a sheath flow cuvette just above a focused laser beam. This configuration significantly reduced diffusive losses for sulforhodamine 101 as evidenced by the molecular detection efficiency of 80%, which is close to the theoretical limit based on an average S/N of ~ 10. S/N ratios were also improved by using a subnanosecond anticoincidence gate as a temporal prefilter in front of the TAC to reduce the amount of time spent processing background events.

Fluorescence correlation spectroscopy and confocal microscopy. Confocal fluorescence microscopy techniques (*14*) are well suited for single-molecule detection. The high-numerical aperture objective (typically > 1) used for both fluorescence collection and laser beam focusing allows for very efficient light collection and an extremely small illumination volume of ~ 1 fL, which results in small background signals and saturation intensities (for R6G) that can be reached with average powers < 1 mW.

In fluorescence correlation spectroscopy (*25, 26*), a confocal microscope measures average fluctuations in the fluorescence signal using digital autocorrelation analysis of time-resolved fluorescence signals (*27*). The benefit of this type of approach is that the autocorrelation function carries information on diffusion constants that can be related to the size of the analyte (i.e., distinguish a small polypeptide from a large protein or DNA fragment). Zare (*16*) recently showed that single-molecule detection can also be accomplished directly using confocal fluorescence microscopy without autocorrelation analysis. S/N ratios of ~ 10 against a shot-noise limited background of ~ 6 counts were obtained for R6G and fluorescein in a 1-ms integration period.

From the standpoint of ultradilute solution analysis, perhaps the biggest limitation of confocal fluorescence microscopy is the extremely small imaging volume. In a typical experimental configuration, a drop of solution is placed on a microscope slide and the number of photon bursts per unit time is controlled by diffusion of the analyte into and out of the illumination region. If a molecule does not undergo photobleaching, it can return several times to the laser beam, producing more than one photon burst. Thus, the number of photon bursts may exceed the actual number of individual molecules interrogated. Furthermore, because of the small probe dimensions, confocal microscopy is not well suited for applications involving flowing sample streams, such as CE, where the capillary dimension perpendicular to the flow direction is typically > 10 μm, allowing a large fraction of analyte molecules to pass undetected.

The microdroplet approach offers several advantages in terms of the total single-molecule signal level.

Microdroplets. The microdroplet approach to single-molecule detection in liquids is unique in several respects. First, the 1-pL probe volume is defined by the droplet instead of by the laser beam, which means that, assuming negligible vapor pressure, analyte molecules are confined to the probe region without diffusive losses, every molecule present can be interrogated, and the molecular detection efficiency is limited only by the average S/N. Second, by levitating droplets in an electrodynamic trap (*28*), the laser–analyte interaction time can be made much larger than the average photobleaching time, providing the maximum possible signal. Third, it has been shown that the radiative properties, both in the frequency and time domains, of atoms or molecules may be significantly modified through cavity quantum electrodynamic effects in microdroplets (*29, 31*). In particular, both the spontaneous emission rate and integrated fluorescence yield for R6G are significantly enhanced in 4-μm glycerol droplets (*31*). Thus, the microdroplet approach offers several advantages in terms of the total single-molecule signal level.

In earlier work (*19*), single R6G molecules were detected in levitated glycerol microdroplets with S/N ratios of 10–40 and the integrated fluorescence signals ranged from ~ 150 to 2200 photons using continuous wave (cw) laser excitation and ordinary photomultiplier tube detection. The distribution of signals agreed well with theoretical predictions. Much of the sensitivity associated with the levitated droplet technique, however, is obtained at the expense of speed. The time required for levitation, fluorescence measurement, and size determination is typically several minutes, making the approach impractical for applications that demand high throughput. In particular, analysis of ultradilute solutions using digital molecular detection techniques (*18*) requires ~ 10^4–10^6 measurements. A high-speed version of microdroplet fluorometry is therefore highly desirable.

To improve the throughput capacity of microdroplet fluorescence, we have developed instrumentation for single-molecule detection in a stream of free-falling droplets. Droplets fall through the extended cavity of a high-power Ar^+ laser, leaving the tip of the droplet generator at ~ 1 m/s. Because of this high speed, a large beam width to maximize laser–analyte interaction time and extremely high average power to maximize the fluorescence count rate are required. Average cw powers of ~ 20 kW and a beam width of ~ 1.5 mm are required to saturate the $S_0 \rightarrow S_1$ transition for R6G.

Typically, the average intracavity power for an Ar^+ laser generating 8 W at 514.5 nm is only about 150 W. We added a custom high reflector with a transmission of 5×10^{-5}, resulting in a maximum cw power of ~ 10 kW. Without forming a

waist inside the cavity, we can generate intensities at the droplet of ~ 300–500 kW/cm^2. An advantage of high-intensity cw excitation is that fluorescence count rates are limited only by the fluorescence lifetime of the analyte. In addition, the intensity distribution within the droplet generated by standing-wave excitation becomes much more uniform than the internal intensity distribution associated with traveling-wave excitation. In the current configuration, we have determined a detection limit for R6G of ~ 10 molecules. Improvements currently being made will allow us to reach the single-molecule detection level with rates of 5–10 kHz.

Down the road

The past several years have seen great advances in both instrumentation and methodology for single-molecule detection in liquids. Application of these techniques is now moving into areas such as DNA fragment sizing (*34*) and CE (*35*). Future research will most likely concentrate on increasing speed and sensitivity to provide efficient discrimination among different types of molecules and to lower concentration detection limits below the femtomolar level.

This research was sponsored by the U.S. Department of Energy, Office of Basic Energy Sciences and Office of Research and Development with Martin Marietta Energy Systems.

References

(1) Moerner, W. E. *Science* **1994**, *265*, 46.
(2) Moerner, W. E.; Kadar, L. *Anal. Chem.* **1989**, *61*, 1217 A.
(3) Orrit, M.; Bernard, J. *Phys. Rev. Lett.* **1990**, *65*, 2716.
(4) Orrit, M.; Bernard, J.; Personov, R. *J. Phys. Chem.* **1993**, *97*, 10256.
(5) Betzig, E.; Chichester, R. J. *Science* **1993**, *262*, 1422.
(6) Xie, X. S.; Dunn, R. C. *Science* **1994**, *265*, 361.
(7) Ambrose, W. P.; Goodwin, P. M.; Martin, J. C.; Keller, R. A. *Phys. Rev. Lett.* **1994**, *72*, 160.
(8) Nguyen, D. C.; Keller, R. A. *Anal. Chem.* **1987**, *59*, 2158.
(9) Shera, E. B.; Seitzinger, N. K.; Davis, L. M.; Keller, R. A.; Soper, S. A. *Chem. Phys. Lett.* **1990**, *174*, 553.
(10) Wilkerson, C. W.; Goodwin, P. M.; Ambrose, W. P.; Martin, J. C.; Keller, R. A. *Appl. Phys. Lett.* **1993**, *62*, 2030.
(11) Peck, K.; Stryer, L.; Glazer, A. N.; Mathies, R. A. *Proc. Natl. Acad. Sci. USA* **1989**, *86*, 4087.
(12) Mathies, R. A.; Peck, K.; Stryer, L. *Anal. Chem.* **1990**, *62*, 1786.
(13) Soper, S. A.; Mattingly, Q. L.; Vegunta, P. *Anal. Chem.* **1993**, *65*, 740.
(14) Li, L. Q.; Davis, L. M. *Rev. Sci. Instrum.* **1993**, *64*, 1524.
(15) Eigen, M.; Rigler, R. *Proc. Natl. Acad. Sci. USA* **1994**, *91*, 5740.
(16) Nie, S.; Chiu, D. T.; Zare, R. N. *Science* **1994**, 266, 1018.
(17) Whitten, W. B.; Ramsey, J. M.; Arnold, S.; Bronk, B. V. *Anal. Chem.* **1991**, *63*, 1027.
(18) Ng, K. C.; Whitten, W. B.; Arnold, S.; Ramsey, J. M. *Anal. Chem.* **1992**, *64*, 2914.
(19) Barnes, M. D.; Ng, K. C.; Whitten, W. B.; Ramsey, J. M. *Anal. Chem.* **1993**, *65*, 2360.
(20) Hirschfeld, T. *Appl. Opt.* **1976**, *15*, 3135.
(21) Soper, S. A.; Nutter, H. L.; Keller, R. A.; Davis, L. M.; Shera, E. B. *Photochem. Photobiol.* **1993**, *57*, 972.
(22) Basché, T.; Moerner, W. E.; Orrit, M.; Talon, H. *Phys. Rev. Lett.* **1992**, *69*, 1516.
(23) Whitten, W. B.; Ramsey, J. M. *Appl. Spectrosc.* **1992**, *46*, 1587.
(24) Kollner, M. *Appl. Opt.* **1993**, *32*, 806.
(25) Magde, D.; Elson, E.; Webb, W. W. *Phys. Rev. Lett.* **1972**, *29*, 705.
(26) Schneider, M. B.; Webb, W. W. *Appl. Opt.* **1981**, *20*, 1382.
(27) Koppel, D. E. *Phys. Rev. A* **1974**, *10*, 1938.
(28) Arnold, S.; Folan, L. M. *Rev. Sci. Instrum.* **1986**, *57*, 2250.
(29) Barnes, M. D.; Whitten, W. B.; Arnold, S.; Ramsey, J. M. *J. Chem. Phys.* **1992**, *97*, 7842.
(30) Benner, R. E.; Barber, P. W.; Owen, J. F.; Chang, R. K. *Phys. Rev. Lett.* **1980**, *44*, 475.
(31) Barnes, M. D.; Whitten, W. B.; Ramsey, J. M. *J. Opt. Soc. Am. B* **1994**, *11*, 1297.
(32) Barnes, M. D.; Whitten, W. B.; Ramsey, J. M. *Chem. Phys. Lett.* **1994**, *227*, 628.
(33) Lin, H-B.; Eversole, J. D.; Merrit, C. D.; Campillo, A. J. *Phys. Rev. A* **1992**, *45*, 6756.
(34) Castro, A.; Fairfield, F. R.; Shera, E. B. *Anal. Chem.* **1993**, *65*, 849.
(35) Lee, Y-H.; Maus, R. G.; Smith, B. W.; Winefordner, J. D. *Anal. Chem.* **1994**, *66*, 4142.

Michael D. Barnes, staff scientist, conducts research on ultrasensitive fluorescence detection and photophysics of microparticles. William B. Whitten, senior staff scientist, focuses on applying microparticle techniques to chemical analysis. J. Michael Ramsey, group leader, conducts research on miniature chemical instrumentation, nonlinear spectroscopies, real-time microparticle characterization, and ultrasensitive laser-based detection techniques. Address correspondence to Ramsey at the Chemical and Analytical Sciences Division, Oak Ridge National Laboratory, P.O. Box 2008, Oak Ridge, TN 37831-6142.

We're revolutionizing the Art of Electrochemistry.

EG&G Princeton Applied Research is pleased to announce the new Model 283 Potentiostat/Galvanostat. The M283 is compatible with all of our present software. You can combine the unit with our impedance systems and take your research to frequencies of up to 5 MHz. Or, add a wave form generator and take your CVs to unheard of speeds. The new Model 283 has an impressive low current range of 20 picoamps* for your microelectrode research! For more information please contact us at 1-800-366-2741.

* Under computer control; call for complete specifications.

EG&G INSTRUMENTS
Princeton Applied Research
P.O. Box 2565 • Princeton, N.J. 08543 • (609) 530-1000 • FAX: (609) 883-7259 • TELEX: 843409
United Kingdom (44) 734-773003 • Canada 905-827-2400 • Netherlands (31) 034-0248777
Italy (39) 02-27003636 • Germany (49) 89-926920 • France (33) 01-69898920 • Japan (03) 638-1506

Circle 2 for Literature. Circle 3 for Sales Rep.

The Ultimate Solution for Technical Graphics?

Origin
Microcal Software
One Roundhouse Plaza
Northampton, MA 01060
800-969-7720; 413-586-2013; 413-585-0126 (fax); tch_microcal@delphi.com (e-mail)
Version 3.5; $495, commercial ($545 with 3D/Contour supplement); $396, academic ($436 with 3D/Contour supplement)

Origin, self-proclaimed as "The Ultimate Solution," is a full-featured graphics program aimed at the scientific market. As such, its obvious competitors include Jandel Scientific's *Sigma Plot* and Software Publishing Corporation's *Harvard Graphics*, as well as spreadsheets such as Microsoft's *Excel* and Novell's *Quattro Pro* that offer increasingly potent graphics capabilities.

Origin, which arrives in a nifty blue slipcase, installs quickly and easily under Windows. The package includes a reference manual; a manual describing Labtalk, the software's macro language; a tutorial manual; and a small pamphlet describing the 3D/Contour Supplement. A minor quibble is that two identical icons are produced if you install both *Origin* and the 3D/Contour Supplement: one labeled Origin 3.5 and the other labeled 3D + Contour 3.5. In fact, the second program includes all the features of the first plus some expanded ones. It is not clear why, in the contemporary market, Microcal considers the 3D capabilities an option.

Almost all the testing was done on either a 66-MHz 486 running Windows for Workgroups as a task under OS/2 3.0 (Warp) or a 60-MHz Pentium running Windows for Workgroups. Both machines had 16 MB RAM. On these computers, *Origin* loaded and performed crisply. The machine requirements of the program are extremely modest. The manual says it will run on "any computer on which Windows will operate properly," and installation requires only about 3 MB of disk space. It is refreshing to see this powerful program require such modest resources. During testing, the one call I made to Microcal for technical support was handled efficiently and courteously.

Documentation

The tutorial manual is the first and, for many users, the only manual supplied that will be used on a regular basis. Although it tends to be verbose, it is easy to follow, usually accurate, and presents examples that are appropriate in both level and scope for the average user of a technical plotting package. The 3D/Contour supplement is essentially an addition to the tutorial manual. The reference manual covers some general points about the philosophy of "layers" in *Origin*, how to resize plots, how to use the tools on the tool menu, and a bit about how to customize the user interface. The bulk of the user manual is devoted to detailing the commands on the menus and submenus. The Labtalk manual focuses on the scripting language that is the basis of *Origin*. With this full-featured, C-like language, the user can create very elaborate custom applications, but in my opinion, only experienced C programmers will have much success with Labtalk and few users will require its capabilities.

Ease of use and flexibility

Origin is easy to use after you adjust to some of its conventions. For example, column titles are reserved words. That is, *x*, *y*, error bars, and text are defined by the column titles. At first that seemed rather awkward, but actually in practice it turns out to be very useful. Simple plots can be created with a few mouse clicks. Adding more data and plots to previously defined graphs and preparing plots with error bars, operations that are difficult with

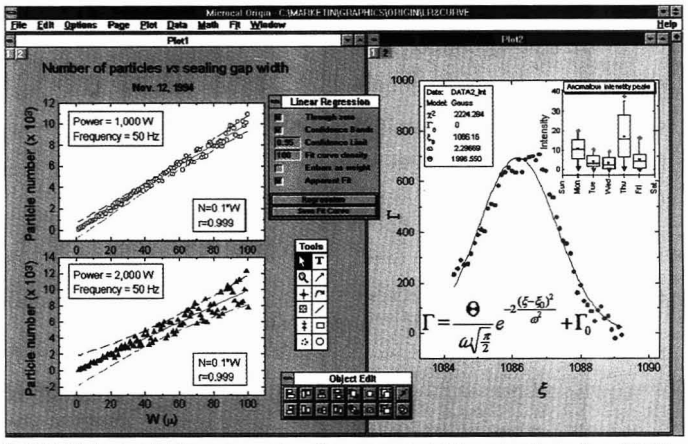

(Left) Origin*'s powerful linear regression offers convenient fitting using the toolbar. (Right) The interactive curve fitter allows users to fit data to built-in and user-defined functions with the Levenberg–Marquardt algorithm.*

some graphing programs, are simple with *Origin*. Customizing the features of a plot is convenient: Simply click on the feature of interest (e.g., a title, an axis, or a line) and a menu pops up. Anyone familiar with plotting programs should be able to produce attractive plots in a short time.

Unfortunately, there are several areas in which this program does not follow normal Windows conventions for handling screen objects, one of which is the resizing of plots. The more advanced features of the program such as curve fitting with user-defined functions and complex data manipulation are sometimes difficult and nonintuitive.

Mathematical power

Origin contains powerful facilities for transforming data and statistics and for curve fitting. Data can be fit to a function of the user's design or the user can select from an extensive list of common functions supplied. In reasonable (and some not so reasonable) cases, the iterative fitting process converged rapidly and correctly. Once entered, user-defined functions can be saved to become menu-selectable items in the program.

In addition, *Origin* supports a rich variety of mathematical and statistical functions and even includes the obligatory Fourier transform, although one might well ask whether many users actually do FFTs with their plotting programs and spreadsheets. One caveat here: Confidence intervals in *Origin* are not what many users will expect. The common Student's *t* calculation of confidence limits has been replaced by a differential treatment. Put another way, physicists and some physical chemists will be pleased and many of the rest of us will be caught completely by surprise. I believe that *Origin* is at least the equal of any plotting program available in terms of its rich array of mathematical capabilities.

Windows compatibility

Finally, any true Windows application should facilitate the exchange of data and graphics among other Windows applications. This was tested using *WordPerfect for Windows 6.1*, *Word for Windows 6.0*, and *Excel 5.0*.

Naturally, any veteran Windows user does not expect data transfer and dynamic data exchange links to work correctly in all cases, and *Origin* is no exception. Direct cutting and pasting was flawless. Linking data and graphics between *Origin* and both *Word* and *WordPerfect* as clients worked, but the automatic update failed. Although *Word* was able to update the link to *Origin* when asked, *WordPerfect* could not. *Origin* could update both clients when asked. As a client for a data link with *Excel*, *Origin* functioned flawlessly. All things considered, I found compatibility with Windows applications to be well within the expected norms.

Summary

If there are scientific and technical graphics in your future, would this software program be a wise purchase? The simple answer to this question is yes, although the more detailed answer is not quite so simple.

Origin is the most flexible scientific graphics program I ever have used. However, the user interface can be confusing and screen handling is sloppy. The program does not appear to have any fatal bugs, but it does have some. The good news is that most of the bugs are in the area of screen handling and, although they are annoying, they do not seem to be serious. In all tests, the desired graphs could be prepared and the printed plots were of professional quality.

If you want a powerful graphics program that offers the ultimate in flexibility and are willing to overlook minor flaws in screen handling, *Origin* is a very good choice. One thing is sure: If you can imagine it, *Origin* can plot it. Is *Origin* "The Ultimate Solution"? No, not yet, but stay tuned.

Reviewed by John C. Marshall, Department of Chemistry, St. Olaf College, Northfield, MN

SOFTWARE RELEASED

CARD

Westing Software Inc.
134 Redwood Ave.
Corte Madera, CA 94925
800-325-1862; 415-945-3877 (fax);
westing@aol.com (e-mail)
Version 4.0; $495

CARD (Computer Aided Research and Development), an advanced program for design of experiments, defines experiment goals, evaluates design options, generates structured analysis-ready data matrices, and organizes the most efficient testing procedure. It handles all types of variables as well as multiple constraints and features an online navigator to guide users to the correct experimental design for each application. Minimum system requirements include DOS 3.1, Windows 3.1, a 386 CPU, 4 MB RAM (8 MB recommended), 10 MB free hard disk space, a mouse or Windows-compatible pointing device, and a VGA monitor.

gNMR

Cherwell Scientific
744 San Antonio Rd., Ste. 27A
Palo Alto, CA 94303
415-852-0720; 415-852-0723 (fax);
csp@netcom.com (e-mail)
Version 1.0; $599

gNMR is a Macintosh program that simulates one-dimensional NMR spectra and performs iterative calculations to fit calculated spectra to experimental spectra. Users can choose between two basic fitting procedures: assignment iteration, which uses individual peak position as observed data, and full-lineshape iteration, which uses a generalized least-squares procedure to fit the entire calculated spectrum to the observed one. The software, which imports experimental spectra from a wide variety of sources, runs on all Macs and requires System 6.05 or higher, 1.5 MB RAM (4 MB recommended), and 4.5 MB free hard disk space.

Method Development in CE

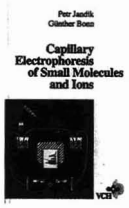

Capillary Electrophoresis of Small Molecules and Ions
Petr Jandik and Günther Bonn
VCH
220 E. 23rd St.
New York, NY 10010
1993, 298 pp., $65

From the title of this book, a reader might expect a comprehensive review of how to separate small molecules and ions. However, Jandik and Bonn's main goal is to provide readers with enough information to develop new CE instruments and methods. The authors achieve this goal in their very brief but informative historical account of development of CE and in the two following chapters on fundamentals and instrumentation for CE. The last two chapters, which focus almost exclusively on the authors' research on CE separations of small inorganic and organic ions and carbohydrates, provide the reader with several strategies for solving one type of separations problem. Although this approach is an effective way to introduce method development, it does not satisfy the needs of readers who want a comprehensive review of many different applications.

Methods for separation of biomolecules, such as isoelectric focusing or capillary gel electrophoresis, are mentioned briefly, but the authors make little attempt to discuss them. Instead, they compare and contrast counterelectroosmotic and coelectroosmotic flow separations. Such organization helps the novice understand the important differences between the two general CZE methods; the more advanced practitioner will probably discover connections between apparently unrelated methods.

The chapter on fundamentals of CE is comparable to those in other books already in print and is complete enough for a newcomer to the field. Though the authors are not encyclopedic in coverage of all CE methods, they treat detection, injection, and quantitation methods in more detail than do many similar-sized books on CE. Such complete coverage gives the experienced user some new insights about subtle points that are often ignored in other CE books. For instance, the authors discuss the relation between injection and detection efficiency and peak quantitation in great detail when evaluating the overall sensitivity of a given technique.

One great strength of this book is the readable length achieved by the authors'

The chapter on fundamentals of CE is complete enough for a newcomer to the field.

limited focus on small molecules and ions. Most references are from the period 1988–1992. The table of contents is not highly detailed, but the subject index seemed entirely appropriate. Though no author index is provided, references are provided at the end of each chapter rather than in a single bibliography. The diagrams in the book are all readable, but their quality is not always crisp.

I believe that this book will be useful for chemists of different experience with CE. Those unfamiliar with CE will be able to learn the fundamentals and read about simple applications that make the chemistry underlying a CE separation understandable. Those familiar with CE will undoubtedly learn something new in the exhaustive chapter on instrumentation and will gain a different perspective by thinking about CE on a level of organization that they may not be accustomed to. The authors have clearly written this book for separations chemists and analytical chemists, and not for biochemists; they have done an excellent job for this intended audience.

Reviewed by Howard Drossman, The Colorado College, Colorado Springs, CO

Principles of Laser Spectroscopy

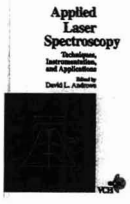

Applied Laser Spectroscopy: Techniques, Instrumentation, and Applications
David L. Andrews, Ed.
VCH
220 E. 23rd St.
New York, NY 10010
1993, 472 pp., $125

This book is a multiauthor work that covers most of the range of laser spectroscopy. It has two introductory chapters on fundamental principles and basic instrumentation, followed by eight chapters on different methods, including UV–vis absorption, high-resolution IR, fluorescence, Raman, nonlinear Raman, multiphoton, ultrafast, and mass spectroscopies. Most chapters are directed toward using laser methods for fundamental characterization in molecular spectroscopy, particularly gas-phase analysis. There is less emphasis on laser methods that are important to analytical and technological applications. In fact, important contribu-

tions from the analytical chemistry literature are ignored. The chapter by Michael Morris on Raman spectroscopy is a notable exception in that it not only covers important advances in Raman spectroscopy, but gives details on the subtler aspects of how well a method works and how it is actually used. These are insights that only an active practitioner can provide.

The book is directed toward an informed scientist with some understanding of spectroscopy. Although the authors are conscientious about writing clearly so that most readers will understand the material, the book is not meant to be a tutorial. Generally, important equations are stated without derivation or much insight into their origins. The introductory chapters are particularly careful to give the basic information required for a novice to get started in the field; the later chapters start with introductory material but rapidly progress deeply into different applications. The treatments, which are rigorous and cover an impressively wide range of topics, are written by authoritative specialists in each field.

The book contains abundant references to allow efficient entry into the literature. The most recent references, however, are to 1991, making the treatment of each field somewhat dated. Generally, the individual authors describe applications without providing a perspective on their usefulness. There are many examples of ideas that were interesting at the time they were developed, but have since found no significant applications. The book has a good subject index, but lacks an author index. There is also a handy index of laser spectroscopy acronyms.

The book contains a great deal of information about what has been accomplished in laser spectroscopy, and would be worthwhile in a reference collection. It is not a book that most analytical scientists would be interested in purchasing for themselves, because it is somewhat out of date and is geared largely toward a gas-phase molecular spectroscopy audience.

Reviewed by John C. Wright, University of Wisconsin, Madison

BOOKS RECEIVED

Selective Detectors Environmental, Industrial, and Biomedical Applications

Robert E. Sievers, Ed.
John Wiley & Sons
605 Third Ave.
New York, NY 10158
1995, 261 pp., $59.95

This book contains nine contributed chapters on the theory and practice of selective detectors. Chapter topics include sulfur-selective chemiluminescence, selective detection based on nitric oxide/ozone chemiluminescence, the oxygen-sensitive flame ionization detector, metal selectivity by ion mobility discrimination in an FID, element-selective gas chromatographic detection by atomic plasma emission spectroscopy, selective detection using plasma MS, and peroxyoxalate chemiluminescence.

Physical Electrochemistry

Israel Rubinstein, Ed.
Marcel Dekker
270 Madison Ave.
New York, NY 10016
1995, 608 pp., $150

This volume, part of the Monographs in Electroanalytical Chemistry and Electrochemistry series edited by Allen J. Bard, contains 12 contributed chapters devoted to "nontraditional" areas of electrochemistry, primarily interfacial electrochemistry. Chapter topics include heterogeneous electron transfer kinetics at metallic electrodes, digital simulations with the fast implicit finite difference algorithm, electrochemistry at ultramicroelectrodes, scanning electrochemical microscopy, electrochemical impedance spectroscopy, the electrochemical quartz crystal microbalance, in situ synchrotron techniques in electrochemistry, ellipsometry and spectroellipsometry applications in electrochemistry, analysis of surface layers on well-defined electrode surfaces, electrodeposition of II–VI semiconductors, and electronically conducting soluble polymers.

Carbohydrate Analysis High-Performance Liquid Chromatography and Capillary Electrophoresis

Ziad El Rassi, Ed.
Elsevier Science
655 Avenue of the Americas
New York, NY 10010
1995, 672 pp., $250

This book, volume 58 in the *Journal of Chromatography* series, contains contributed chapters on the use of LC and CE for determination of carbohydrates and glycoconjugates. Three major sections cover sample preparation, separation (capillary electrophoresis and reversed-phase, hydrophobic interaction, hydrophilic interaction, ion exchange, affinity, and size-exclusion chromatography), and detection (electrochemical, refractive index, mass spectrometric, light scattering, chiroptical, and absorption). Each chapter discusses the basic principles, advantages, limitations, and applications of the technique. A subject index is included.

Chemical Pretreatment of Nuclear Waste for Disposal

Wallace W. Schulz and E. Philip Horwitz
Plenum
233 Spring St.
New York, NY 10013
1994, 212 pp., $75

This book describes the sequence of separations processes used to partition nuclear wastes into a small volume of high-level waste for deep geologic disposal and a larger volume of low-level waste for disposal in a near-surface facility. Contributed chapter topics include waste minimization, separation processes being developed to pretreat the large volume of nuclear waste stored at U.S. DOE sites, waste pretreatment technologies, and microbiological and photochemical techniques for treating liquid waste. A brief subject index is included.

ELECTRONIC LAB NOTEBOOKS

A Shareable Resource

Every scientist creates a special form of diary: the scientific notebook. It is a log of the day-to-day experiments performed, as well as a partial interpretation of their results. These diaries are rarely published, and they are usually read only by colleagues who witness the results. Instead, reports containing parts of the log are distributed, and papers containing detailed interpretations of the reports are published. Although verbal disclosures of its contents are common, the notebook remains private.

All of these reports, papers, and oral presentations constitute communication. But, in an information sense, these forms of exchange are filtered, bandwidth limited, and subject to noise. The reports contain only a fraction of what is in the original log, and papers reflect a personal interpretive flavor. Oral presentations may be less connected to fact, are ephemeral, and can be affected by the fluency of the speaker and the attention of the listener. The original notebooks are often difficult to follow because of arcane notations or incompleteness. Even the flow of the research is difficult to track because many activities are usually intertwined. As a result, sharing our most personal scientific document is not straightforward.

There are many reasons to improve this process. From the corporate perspective, these include accelerating the development cycle by improved group communication, preserving scientific data and information, and supporting possible patent litigation. From a creative perspective, we often arrange face-to-face meetings to communicate results, concepts, and problems to individuals who have different acquisition rates, modes of thinking, and verbal communication habits. These meetings are vital, yet they are often inefficient.

Electronic notebooks can improve the discovery process, turning ideas into products in a shorter time

Most scientists use electronic services such as Dialog, CAS, and STN to search older literature. A smaller subset use individualized search profiling to electronically access current journals, but few use authorized access to collaborators' research notebooks. Why shouldn't our research notebooks become a shareable resource? Scientific electronic notebooks that offer many new, interesting features are now available (*1*). In this article we will examine the need to change our concept of a scientific notebook, how these notebooks can be used to improve the discovery process, and what work habits need to be altered to gain these benefits.

Raymond E. Dessy
Virginia Polytechnic Institute and State University

Electronic formats

Wouldn't it be desirable to have a way to share portions of our lab work with others electronically, and to permit controlled-access searching across many lab notebooks for scientific or legal purposes?

Object-oriented databases. A research notebook is a collection of various objects: written records of experimental design, drawings of apparatus and chemical structures, circuit schematics, images obtained from various photographic records, graphs of results, and tables of data. Clearly the paper notebook can be replaced by an object-oriented database (OODB) that could handle these various formats electronically. An OODB treats all elements as objects with associated characteristics. They are usually manipulated by the use of simple icons that represent them pictorially.

The power of OODBs, in contrast to more traditional hierarchical databases or relational databases, is that the characteristics of an object are easily inherited by newly spawned objects, opening up easy expansion to novice users. The concept also reduces the development costs of vendors and maintenance time of on-site programmers. Today, some commercial electronic lab notebook products use

0003-2700/95/0367-428A/$09.00/0
© 1995 American Chemical Society

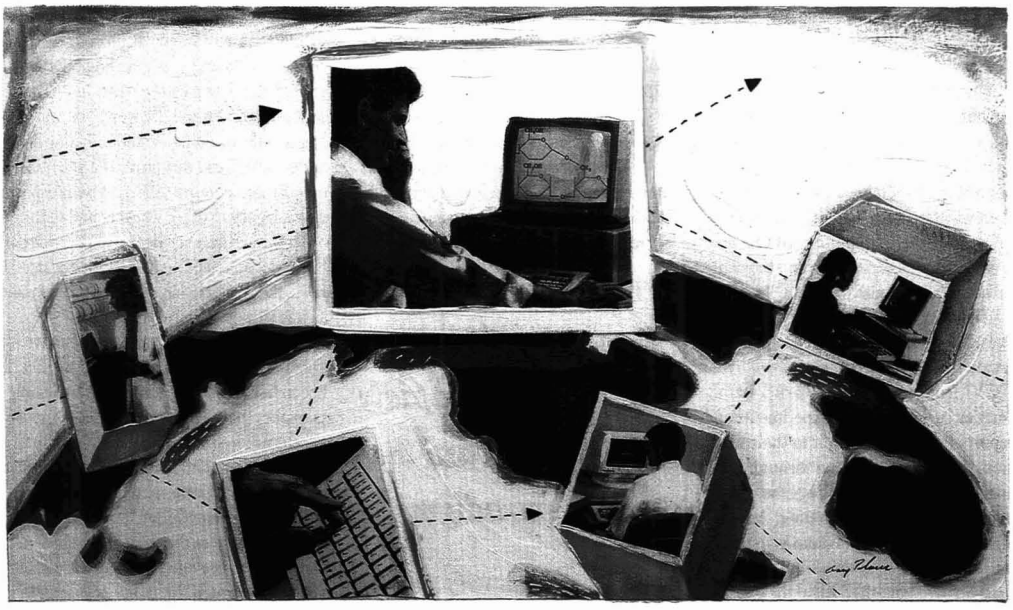

GARY PALMER

this approach, providing only a good graphic user interface (GUI) for an OODB to coordinate the presentation and juxtaposition of data objects created by other vendors' programs. Other commercial products have many specialized creation elements built in. Either approach permits the user to electronically navigate through a multidimensional space of data and information entered into the notebook.

Hyperspace navigation: the thread that binds. This developing technology offers an exciting prospect—a research record that is not limited to the linear chronological and physical format of paper-based notebooks. What follows is a simple extrapolation from existing products and technology. All of the concepts have been demonstrated, and many are operational in various environments. Let's look at the near future.

It is a simple matter to create multiple threaded views (MTVs) that logically link related elements into a virtual sub-notebook for improved continuity and clarity. For example, most scientists work on many problems in parallel. One must manually page through a paper notebook to follow the progress line. It is possible to write forward and backward page pointers (a linked list) within individual experiments in a paper notebook to aid the worker and other readers, but this is seldom done. After all, even a complete and up-to-date index is uncommon.

In electronic format, autoindexing among related experiments is simple. By using overlapping windows and icons, it is possible to establish linked lists that can then be stored as virtual sub-notebook objects. As just another object in the OODB, each can be viewed, searched, and manipulated. Separate projects are viewed as discrete, logically contiguous sequences of experiments, excluding unconnected work. The timeline can even be warped (while the original experimental time/date stamps are retained) to provide a smoother flow. This is most useful when later experiments reveal the explanation for earlier experiments. Automatic indexing on keywords and full-text searching are possible. This makes it easier to find results.

Existing software permits a user to file material with related items automatically and to use either keywords or a trial document as a search template. These approaches have been used as dynamic databases (dynabases) for both individual and group work (*2, 3*). Literature sources and experiments can now be easily merged.

Client/server sharing. Client/server versions of this type of software permit the author to share authorized portions of such a notebook with other individuals who can help in interpretation of the data or who might find the work valuable in solving their own problems. The material can be digested at the reader's own pace, and interactive queries can be handled electronically. If groups are involved, a virtual meeting can minimize the confrontations, dominant personalities, and different cognition rates associated with live gatherings. Most researchers do not expect large-group team efforts to be the new creative paradigm in science. However, the expectation is that the networking of notebook and other materials will facilitate small-group interactions. Successful examples of this approach in medical research and the clinical area already exist.

This approach encourages collaborative seeding of creativity. Colleagues can create their own personal threaded view (PTV) from a variety of workers and sources, selecting those experiments and reports that are important to their mission. They can then page through their own sequence to discern patterns, ideas, explanations, and anomalies. Another ideal use of this new medium is to facilitate transfer of responsibility from one team leader to another. All of the experimental data can be made available in an organized format. In a client/server configuration "your" pages continue to reside in your private notebook. They can only be used by "others" with proper access; "your" copy remains the accessible compound document, allowing updates and changes visible to your privileged colleagues.

Change

Such approaches will work effectively only if the new form of notebook is kept in a way that promotes understanding by other persons. This requires a consistent, logical, and complete presentation of all work. Carefully crafted abstracts are necessary, and an annotated dictionary of terms is essential. Some degree of standardization in format is required, and adherence to a common data format, such as the ADISS/AIM standard, would be helpful (*4*). However, the new electronic journal needs to be much more if it is to serve individual, group, and corporate needs in unique ways.

A journal model. In this vein, scientists can take lessons from the psychologist Ira Progoff, who has proposed a tool called "journaling" (*5*). This approach, which should not be confused with what a computer programmer calls journaling, asks that individuals commit to paper various logs of their activity to more fully understand what they are doing and why. Journaling involves a daily log that is akin to our scientist's paper notebook, as well as a period log that involves longer time spans, an intersection log that involves critical decision points as well as paths taken and not taken, and periodic time-expansion logs that re-examine the antecedents and potential consequences of actions taken and not taken. The reader of a Progoff journal is, of course, the author, along with others who are participating in what is called a "journal workshop." This approach has applicability to our lab work. Clear articulation of action, motivation, and result help clarify a person's effort.

Electronic lab notebooks are rapidly evolving toward the SEA paradigm.

Our own journal. First experiments are seldom clean, clear, or completely explicable. False starts are common and misinterpretations are rife. Points or intersections are reached at which one must decide future research directions. Paper notebooks seldom explain why decisions were made, and if they do, only the selected path is developed in detail. The paths not taken are not described. This makes it difficult to backtrack, particularly for other scientists taking up the work. Any feedback in the project's flow that connects prior work with current work is usually logged in the mind of the worker, not in the notebook. Long-term (period) analysis is usually lacking, and attempts to put milestones in place are uncommon. In fact, most paper notebooks are organizationally challenged. An electronic journal can help the user create a feedback log that explicitly shows connections and makes use of the other logs simple.

Scientific electronic accounts

Another type of electronic document would require somewhat more time to create, but its utility would compound exponentially. Because the word "notebook" seems confining and the word "journal" has specific meanings in the scientific literature, we will call this product a scientific electronic account (SEA). It would provide a legacy to other workers and to the organization. In a sense, the SEA creates a history of an experimental effort; it is useful as the work is being done and essential as it is viewed in retrospect.

The threaded views suggested above are interactive formats. With multimedia becoming common, there is good reason to expect that SEAs will eventually incorporate not just text and drawings, but moving images and visualization objects, as well as narrative and sound. We've never done these things in paper notebooks because of the restrictions of that medium. At least one commercial product has demonstrated the utility of narrative transmission in the highly litigious clinical environment. Intel demonstrated video-supported problem solving, coupled with CD-ROM database access and video conferencing, at the fall 1991 Comdex (*6*). Intel's Indeo video compression allows personal conferencing over ISDN lines and makes image storage possible (*7*). Kouzes and Schur have demonstrated scientific uses in their elegant development of the Collaboratory paradigm, a collaborating lab environment (*8*).

Acceptability. SEAs can be easily stored on optical drives, where data are recorded by laser ablative removal of material from the disk's surface, or by laser degradation of a polymer film beneath a reflective surface. Such recording does not have the impermanence of magnetic recording.

In addition, the data on such an optical disk are encrypted in various ways; usually an 8- to 14-bit run-length-limited (RLL)

binary code conversion is used, and the original logically adjacent bytes are physically separated (interleaved) on the disk. This process occurs in addition to the normal sector interleaving always used in recording to rotating media. The material entered is time and date stamped, and finally each block of data has a companion redundant section that is used for error detection and recovery, similar to the technique used in CD-ROMs. This redundant section involves generating a bit pattern from the original data file using a nonbinary polynomial cyclic redundancy check (CRC) algorithm. The approach is called Reed–Solomon code (*9*). It is one of many elements that make such recordings secure and acceptable. Because this point is often one of contention, let's examine how it all works.

Most readers have encountered the abbreviation CRC in their computer work. The CRC is usually a 16-bit section appended to magnetic disk files. Each byte, as written to disk, is also multiplied by a binary polynomial (a 16-term polynomial whose coefficients are 1 or 0). Simple logic operations generate a running sum as each succeeding datum in the file is sequentially processed. The least significant bytes of the final sum are called the CRC. If you read such a data file, calculate your own CRC on the fly, and then compare it with the redundant CRC stored on disk, a match indicates that the "read" has been successful. In practice this can detect (but not correct) burst errors of up to 16 bits.

Reed–Solomon approaches create a redundant record that can be more than 25% the size of the original data file. Imagine the original data file as a travel expense spreadsheet, with sums at the borders of each column and row and a check sum-of-sums at the bottom right (cross additions). Cross-interleaved Reed–Solomon (CIRC) encoding can both detect and correct singular and burst read errors, providing hard error rates far better than any magnetic disk in laboratory use. However, this complex encoding, encryption, and redundancy approach has great legal impact. Destruction of an existing record is impossible to hide. Falsifying an already written record is physically impossible (how do you alter a few 1-μm spots that have been destroyed?), and logically difficult (how do you fix the CIRC redundant code?). When one considers how simple it is to burn or shred paper records and how easy it is to alter a written number on a piece of paper, it is clear why many groups are quite sanguine concerning the legal admissibility of write-once-read-mostly (WORM) optical drive records (*10–13*). Although no court case has yet tested this analysis, it is just a matter of time before the precedent is set.

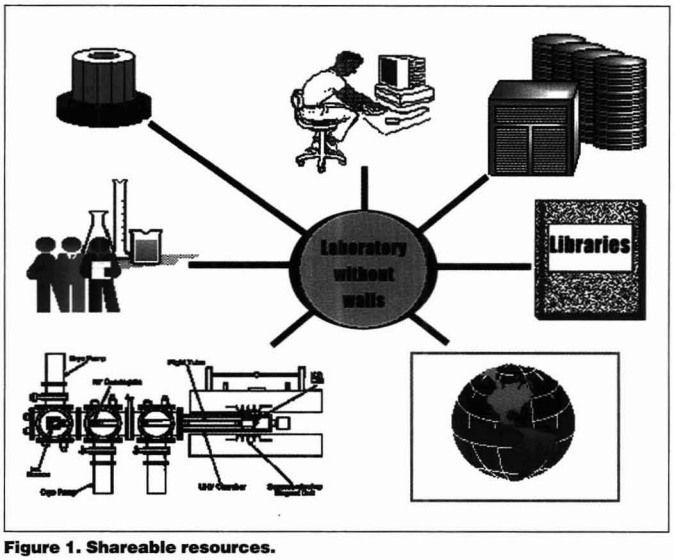

Figure 1. Shareable resources.

Electronic libraries, electronic lab notebooks, and other groupware products can facilitate creation of new ideas, quickly flesh them out from literature sources, help expedite group research, and turn the ideas into products in a shorter time. (Adapted with permission from Pacific Northwest Laboratory.)

One problem does remain—the lifetime or nature of the disk drive. As technology matures, new drive systems will develop, and eventually backward compatibility will cease. At that point, legally bonded disk rewriting services will emerge that can write legacy disks to new media and maintain acceptability.

Getting from here to there. Prophetic transmission scenarios that have been explored by Steve Schmidt of Parke Davis and our research group involve wireless (rf and IR) links from bench laptops or docking laptops, coupled with a server with a redundant array of inexpensive disks (RAID, magnetic) that serve as a high-speed cache buffer to the WORM drive archive. Time and date stamping is done at the server, providing further protection and certifiability. The RAID drives are hot swappable, assuring that any component failure does not result in loss of data.

Present and future

Management recognizes that shareable tools (groupware) like those described are a way to more effectively use the research it supports, shorten the product development cycle, and respond to regulatory and customer queries (Figure 1). But the bench scientist may view them with suspicion and question. They appear to invade personal space and private possessions, yet the accounts of our research should eventually be available to a broader audience, and in a corporate environment are company property.

Perhaps our concerns can be ameliorated by reviewing what a good SEA can give us as individuals: automatic indexing of experiments, full-text search and retrieval, multithread viewing, automatic report generation, parallel literature reference storage, seamless interaction with chemometrics software, image storage of relevant materials generated locally or absorbed over the Internet, voice-over narration of complex procedures supporting compressed video images, simplified network

communication with other workers for assistance and distribution, and manuscript preparation by electronic "cut-and-paste" operations. These capabilities alone justify the effort involved in re-engineering our work practices.

So far we have addressed the questions "should we?" and "can we?" What about "will we?" No implementation will succeed without strong support and input from the users, nor will it succeed without highly visible commitment from technically aware higher management. Getting these steps to occur concurrently, along with a dramatic change in work habits, different communication pathways, and altered management structures and styles, will be a formidable task. The shareable resource provides its own problems because of human nature. A professional's responsibility to colleagues and their ideas should be the same whether the communication is in verbal, written, or electronic form. Good computer records and proper access control can help curb, but not cure, abuses. We are the most formidable problem these new tools face.

Current electronic lab notebook products are just the first of a series of groupware products that will affect laboratory scientists. Project planning tools, conferencing tools, and decision-support tools will slowly drift from the business environment to the scientific lab. Many groupware products created for the business environment will take on new features such as image management and migrate into the lab (Figure 2). Scientific databases, particularly those with molecular CAD capabilities, will mature into real SEAs. The next few years will be critical. Logic and product quality do not always determine success in the marketplace. Lab workers need to take part in the development of these products, which are too important to be left to information scientists, marketing cleverness, or chance.

Questions to ask

How do you evaluate first-generation products? The current environment is similar to the LIMS market in the mid-1980s. Electronic lab notebooks are rapidly evolving toward the SEA paradigm because better software creation tools are available. Do you experiment now and start up the learning–adaptation curve or do you wait until a stable environment exists? This is a question you must answer, but there are some simple tests you can apply to today's products.

Remember that there is no substitute for hands-on experience. Market pressures have made the words "release version" apply to beta-level developments. Today's beta forms are usually alpha-level code. The short half-life of products has forced vendors to pre-announce products, deliver them too early, and rely on upgrades to fix problems.

Is the system configurable to your lab's needs? Each type of lab, and each lab within that subset, has a unique personality. That personality must change as it adapts to these powerful tools, but neither human nor lab personalities can change immediately.

Does the product import and export data with equal facility? Does it support the data structures (objects) commonly in use? Some products have word-processing capabilities that do not support subscripts and superscripts, a fatal flaw in a chemical environment. Is it easy to make literature sources part of the account?

Can equivalents of Post-it notes be used for attaching personal comments or for small-group exchanges? Is the equivalent of a whiteboard available for larger group communications? Are these notes made a permanent part of the record? Can they be hidden for those who want an uncluttered view of the original work?

In OODBs, the space requirements can grow at a phenomenal rate as new types of objects are added to the system. Be sure to try your activities on the software for "size."

Is journaling (transaction logging) supported? All activities at the server need to be recorded. Are audit trails maintained for Good Laboratory Practices (GLP) purposes? WORM optical disks do not and cannot remove old files or change updated records. They create entire new copies. But back-links to the original data or records must be maintained and be automatically accessible.

Graphic, tabular, and CAD objects can be embedded in other text objects. The anchoring in these compound documents should be "live," so that alteration of any object is automatically reflected in all other connected objects and that fact is visually flagged.

Is it possible to define trigger conditions that automatically cause the execution of predefined procedures? This per-

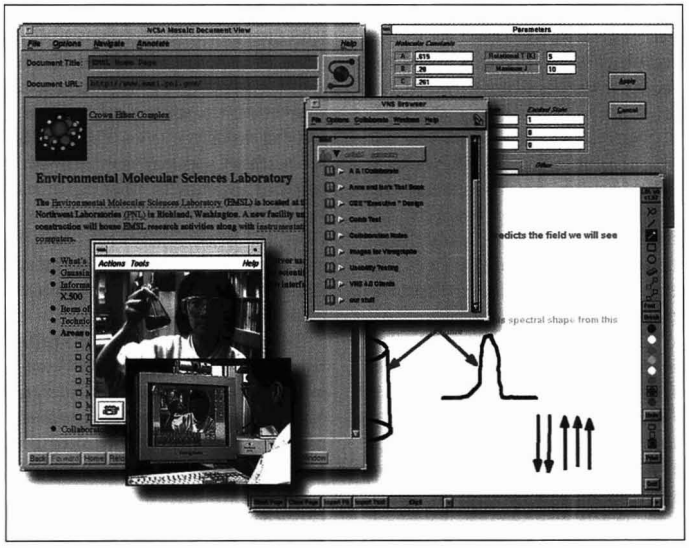

Figure 2. A new view of the lab.

A typical screen image of a collaboratory environment showing electronic lab notebooks, whiteboards, shared database views, electronic library browsing, and personal conferencing. (Adapted with permission from Pacific Northwest Laboratory.)

mits the user to define conditions (such as concentration, time, and conjunctions of observations) that will automatically create reports, flag the user's terminal, or create warning messages.

Optical scanning, both optical character recognition (OCR) and bitmapped, is important. New algorithms for lossless (2–3:1) and lossy (20:1) storage compression are powerful tools for conserving space. Many scientific textual applications can use bitonal compression. Standards are in a great state of flux and there are legal squabbles over several common storage and encryption methods.

Are access control schemes available that satisfy both corporate and user needs for privacy and security?

What user identification and verification methods are supported and needed? The responses to the FDA white paper circulated to industry asking its attitude toward such techniques for use in electronic submission of new drug applications (NDAs) ranged from ID/password, through "smart cards," to biometrics (signature or fingerprint). The current consensus is that any two of these will be acceptable to FDA.

Access control and simple identification procedures may not be enough. Further encryption may be an important security issue. This may involve encryption on disk and/or encryption for network communication. Asymmetric private key/public key approaches involve two keys, both of which are needed for clear text exchange (*14*). The transmitter encrypts the source with a private key. Authorized readers have a public decryption code that unscrambles the data stream. This is a "pretty secure" system, particularly if certificate objects and an authentication code are used.

Other approaches generate separate faster symmetric session keys in which the same key encrypts and decrypts (*15*). It might take 64 MIPS years (million instructions per second) to crack such a 40-bit cipher, one year on a 64 MIPS machine (full military grade is 128-bit ciphers; cipher length is random bit pattern used for encryption.) Some techniques involve multipartite keys, and the several parts can be separately escrowed for emergency recovery. Some paranoia exists in this arena.

All of these developments will stress existing networks, and distance and bandwidth will achieve paramount importance. Ethernet will evolve into Switched Ethernet, fiber-distributed data interface (FDDI), or asynchronous transfer mode (ATM) (*16*) to increase capability as users exchange larger and different types of records. Current copper-based Ethernet runs at 10–100 Mbit/s, but as the system load increases, user bandwidth drops precipitously. Although switching hubs can regain some of this, Ethernet is basically a contention protocol and is not deterministic. FDDI is a time-token protocol that is deterministic. (In contention protocols, users compete for the facility. In deterministic protocols, use is scheduled.) The packet lengths in Ethernet are variable and inherently long. Interactive work and wider area network applications work best with shorter lengths, called cells. ATM, which uses 53-byte cells, is a time-division multiplexed approach (one in which available time is sliced into sections and allocated to users). Eventually, gigabit/second nets will be needed.

Although scientists should rely on in-house communications and network groups, it is important to monitor their activities. Too often control of communications leads to control of power. Premature, delayed, or incorrect decisions can prove disastrous to the lab. One example is the explanation of why ATM cells are 53 bytes long. Europe originally wanted 16 (phone and voice); the U.S. 128 (computers). The final compromise was 48 (plus 5 header bytes), simultaneously too short and too long (*16*). Logic doesn't always win!

I thank Mary Woodward of Tripos, Kris Pettersen of Megalon, Esther Allen of MDL, and Steve Schultz of ForeFront Technologies, whose questions prompted much of the first articulation of these ideas. David Kilman of the Advanced Computing Laboratory at Los Alamos first brought the connection between scientific electronic notebooks and Progoff's work to my attention. I extend special thanks to research colleagues Ching-Wan Yip and Yue-Ling Wong, who opened their minds and personal databases to many queries regarding networking and ciphers and who performed the digital modifications of the figures. Richard Kouzes of Pacific Northwest Laboratory's Collaboratory Project (http://www.emsl.pnl.gov:2080) provided the original screen images. Kewal Likhyani of DuPont/Electronic Records Consortium and Steve Schmidt of Parke-Davis provided valuable references on legal aspects of electronic records.

References

(1) Borman, S. *Chem. Eng. News* **1994**, *72*(21), 10–20.
(2) Press, L. *J. Assoc. Comput. Mach.* **1992**, *35*, 26.
(3) Peat-Marwick group resource sharing project (ftp: pub/wais/doc/wais-corp.txt@think.com).
(4) Lysakowski, R. *J. Chromatogr. Sci.* **1994**, *32*, 236–42.
(5) Progoff, I. *At a Journal Workshop*; Jeremy Tarcher: Los Angeles, CA, 1992.
(6) "The Second Decade—Computer-Supported Collaboration"; Intel Video 241226-001; Literature DA03; 800-548-4725.
(7) *InfoWorld* **1994**, *16*, Nov. 14 issue, p. 65.
(8) Kouzes, R. *Nat. Sci.*, March 1995, pp. 190–97.
(9) Dessy, R. *Anal. Chem.* **1985**, *57*, 692 A–698 A.
(10) "Authentication of Electronic Records for Legal Defensibility"; Electronic Records Consortium, Oct. 1994. The document contains information on legal issues of weight versus admissibility, and relevance, reliability, and uniqueness (FDA criteria), as well as credibility and corroboration (PTO criteria). Contact Kewal Likhyani at DuPont Fibers, Chestnut Run Plaza, Laurel Run Building, Wilmington, DE 19880-0705 (302-999-3845; fax 302-999-2805) for more information.
(11) Perritt, H. H., Jr. "Electronic Records Management and Archives," *Univ. of Pittsburgh Law Review* **1992**, *53*(4), 998.
(12) "Guidelines for Admissibility of Records Produced by Information Technology Systems as Evidence," AIIM Technical Report, TR 31-19920.
(13) Barry, R. E. "Electronic Document Management and Records Management Systems: Toward a Methodology for Requirements Definition," In *OIS 93: Proceedings of the Document Management Conference*; Hendley, T., Ed.; Meckler Ltd: London, 1993.
(14) Simmons, G. J. *Commun. ACM* **1994**, *37*(11), 56.
(15) http://home.mcom.com/info/rsa.html; http://www.rsa.com/; http://home.mcom.com/home/manual_docs/index.html; http://home.mcom.com/info/security-overview.html; ftp://ftp.csn.net/mpj; and ftp://ftp.eff.org/pub/Net_info/Tools/Crypto.
(16) *Commun. ACM* **1995**, *38*(2).

Raymond E. Dessy, Emeritus Professor of Chemistry at VPI&SU, became interested in SEAs in 1987 when he wrote a prototype in Forth that he still uses for his research involving the design and study of microbiosensors. Address comments to him at the Department of Chemistry, VPI&SU, Blacksburg, VA 24061-0212.

This article is available in the Hot Articles section of the ACS Publications Division home page (http://pubs.acs.org).

Conferences

11th Annual Waste Testing & Quality Assurance Symposium
July 23–28. Washington, DC
Contact: Meetings Dept., 1155 16th St., N.W., Washington, DC 20036 (202-872-6286; fax 202-872-6128)

210th ACS National Meeting
Aug. 20–24. Chicago, IL
Contact: ACS, Meetings Dept., 1155 16th St., N.W., Washington, DC 20036 (202-872-6059; fax 202-872-6128)

109th AOAC International Annual Meeting and Exposition
Sept. 17–21. Nashville, TN
Contact: AOAC International, Meetings Dept., 2200 Wilson Blvd., Suite 400, Arlington, VA 22201-3301 (703-522-3032; fax 703-522-5468)

1995 Pacific Conference on Chemistry and Spectroscopy
Oct. 4–6. Fullerton, CA
Contact: Joe McGuire, The Pacific Conference, P.O. Box 5732, Pasadena, CA 91117-0732 (714-855-2510; fax 714-855-2515)

22nd Annual Conference of the Federation of Analytical Chemistry and Spectroscopy Societies
Oct. 15–20. Cincinnati, OH
Contact: Jo Ann Brown, FACSS, 201-B Broadway St., Frederick, MD 21701 (301-694-8122; fax 301-694-6860; e-mail: jbrownsas@aol.com) or Joseph Caruso, University of Cincinnati, College of Arts and Sciences, P.O. Box 210037, ML 37, Cincinnati, OH 45221-0037 (513-556-5858; fax 513-556-0142; e-mail: joseph.caruso@uc.edu.)

Anachem Symposium
Nov. 2. Dearborn, MI
Contact: Christine Evans, Dept. of Chemistry, University of Michigan, 4807 Chemistry Bldg., Ann Arbor, MI 48109-1055 (313-763-8012; e-mail: c.evans@chem.lsa.umich.edu)

Eastern Analytical Symposium and Exposition
Nov. 12–17. Somerset, NJ
Contact: EAS, P.O. Box 633, Montchanin, DE 19710-0633 (302-738-6218; fax 302-738-5275)

AACC's 47th National Meeting and Clinical Laboratory Exposition
July 16–20. Anaheim, CA
Contact: AACC, Meetings Dept., 2101 L St., N.W., Suite 202, Washington, DC 20037 (800-892-1400, 202-857-0717; fax 202-833-4576)

2nd Annual Symposium on Biomedical and Biopharmaceutical Applications of Capillary Electrophoresis
Aug. 10–11. East Rutherford, NJ
Contact: Joan Lantowski, ISC Technical Conferences, 30 Controls Dr., P.O. Box 559, Shelton, CT 06484 (203-926-9300; fax 203-926-9722)

15th International Symposium on HPLC of Proteins, Peptides, and Polynucleotides
Nov. 19–22. Boston, MA
Contact: Judy Heine, Dept. of Chemistry, Purdue University, West Lafayette, IN 47907 (317-494-1648; fax 317-494-0359)

3rd International Glycobiology Symposium
Nov. 29–Dec. 1. San Diego, CA
Contact: Paddy Batchelder, 7948 Foothill Knolls Dr., Pleasanton, CA 94588 (510-426-9601; fax 510-484-3024)

188th Meeting of The Electrochemical Society
Oct. 8–13. Chicago, IL
Contact: The Electrochemical Society, 10 South Main St., Pennington, NJ 08534-2896 (609-737-1902; fax 609-737-2743; e-mail: ecs@electrochem.org)

11th Asilomar Conference on Mass Spectrometry
Sept. 24–28. Pacific Grove, CA
Contact: American Society for Mass Spectrometry, 1201 Don Diego Ave., Santa Fe, NM 87501 (505-989-4517; fax 505-989-1073)

10th International Conference on Secondary Ion Mass Spectrometry and Related Techniques
Oct. 1–6. Münster, Germany
Contact: H. Fehmer, SIMS X Secretariat, Physikalisches Institut, Universitat Münster, Wilhelm-Klemm-Str. 10, 48149 Münster, Germany (49-251-833611; fax 49-251-833682)

8th Lake Louise Workshop on Tandem Mass Spectrometry
Nov. 29–Dec. 2. Alberta, Canada
Contact: Marg Northcott, Geological Survey of Canada, 3303 33rd St., N.W., Calgary, Alberta, Canada T2L 2A7 (403-292-7041; fax 403-292-5377)

5th International Symposium on Field-Flow Fractionation
July 10–12. Park City, UT
Contact: Julie Westwood, FFF Research Center, Dept. of Chemistry, University of Utah, Salt Lake City, UT 84112 (801-581-5419; fax 801-581-4353)

3rd European Symposium on Analytical Supercritical Chromatography and Extraction and the 6th International Symposium on Supercritical Chromatography and Extraction
Sept. 6–8. Uppsala, Sweden
Contact: Karin Markides, Dept. of Analytical Chemistry, Uppsala University, Box 531, S-751 21 Uppsala, Sweden (46-18-183691; fax 46-18-508542)

6th Annual Frederick Conference on Capillary Electrophoresis
Oct. 23–25. Frederick, MD
Contact: Margaret L. Fanning, PRI, NCI-FCRDC, P.O. Box B, Frederick, MD 21702-1201 (301-846-5865; fax 301-846-5866)

10th International Conference on FT Spectroscopy
Aug. 27–Sept. 1. Budapest, Hungary
Contact: János Mink, Dept. of Analytical Chemistry, University of Veszprém, P.O. Box 158, H-8201 Veszprém, Hungary (36-88-421869; fax 36-88-426016)

Good experiments can be done almost anywhere, even in the back seat of a police cruiser. This is how one police investigator and spare-time scientist made a startling discovery about children's fingerprints and brought it to Michelle Buchanan's MS laboratory at the Oak Ridge National Laboratory (ORNL; Oak Ridge, TN) for a closer look at the chemistry involved.

In July 1993, Art Bohanan, a criminologist with the Knoxville Police Department (TN), was working on the case of a three-year-old girl who'd been abducted and brutally murdered. The defendant, who had confessed early on, later recanted, which made finding the little girl's fingerprints in his car essential to the case. This was Bohanan's second child abduction case in less than a year, and what worried him was that in the first one, the child's fingerprints could not be detected where they should have been.

"The first kidnapping was in April 1993," he recalls, "and we didn't get the car for four days." He was certain the child had been inside the defendant's car; witnesses said they saw her being pulled into it. But when Bohanan and other crime scene investigators examined the inside of the car, the girl's fingerprints were nowhere to be found. "We couldn't find anything, and I started thinking that maybe the child's fingerprints just weren't lasting very long. After that, I promised myself I would do whatever I could to look for fingerprint evidence much earlier." When the car from the second abduction case was brought in only seven hours after the three-year-old was taken, Bohanan's team rushed to examine it within half an hour and was able to find the little girl's palm prints inside the back windows.

ORNL finds that the chemical profile of a fingerprint residue may "fingerprint" age and health

Apparently no one, not even experts at the Federal Bureau of Investigation (FBI), had ever considered the possibility of a difference between the fingerprints adults leave behind and the ones children produce. "That's not all that surprising," Bohanan says. "The FBI works mostly with adult criminals. Usually if they're involved in one of these child abduction cases they're analyzing fingerprints we send in to them, not collecting the evidence, so they don't get the kind of routine experience that we do investigating these crime scenes."

Still, the lack of any formal data on children's fingerprints bothered him. He realized he needed to test his idea and find out for certain why the children's fingerprints were undetectable in one case and present in the other. "The month after the murder I took every car we had in the pound, had children sit in them and touch the insides, waited 24 hours, and examined the cars for their fingerprints," he says. "We didn't find a thing." He then got 10 cases of new plastic and glass soda bottles donated by a local bottling com-

pany, cleaned them, and had adults touch half the bottles in each case and children touch the other half for a series of experiments he conducted over the next year. Half the cases he stored in his basement as controls; the others he left in the back of his police car. "The inside of a car is exactly the environment we were trying to investigate," he says.

Bohanan found that the adults' prints lasted at least several days, but the children's prints often vanished within 24 h. On average, he says, the adults' prints lasted four times longer than the children's. The fingerprints on the bottles in his car disappeared faster than the ones on the bottles in his basement, which was cooler. Time, temperature, and humidity all appeared to affect how long the fingerprints lasted on the nonporous surface of the bottles. "These were crude experiments," says Buchanan, "but he was able to show proof of principle."

Taking it to the lab

Given the typical constraints on police budgets and the limited sophistication of chemical analysis methods available to most police departments, Bohanan's back-seat experiments could have ended there. But the criminologist had met Al Trivelpiece, director of ORNL, during a tour of the Knoxville Police Department. Bohanan knew he needed more detailed information about the disappearing fingerprints if he ever wanted to convince a jury. Last August he talked with Trivelpiece about his frustration over the first abduction case, described his experiments, and asked if it was possible that the fingerprints left by young children just weren't durable at the high temperatures of an east Tennessee summer day. Trivelpiece promptly invited Bohanan to ORNL to consult with a roundtable of researchers from several laboratories about possible causes for what he'd observed.

At that first meeting, says Michelle Buchanan, "It sounded like the children's fingerprints were evaporating faster. Maybe they didn't have the longer lasting compounds that are in adult fingerprints. Suspecting chemical differences, we did literature searches on CAS, Medline, and other databases using every search strategy we could think of. There was nothing out there on kids' fingerprints and very little on fingerprints in general. We eventually decided that the fastest way to find out what was in them was to do GC/MS profiles and compare them, so my lab took on the project." Trivelpiece allocated Buchanan some internal funding, and two undergraduate students, Jennifer Fletcher of Auburn University and C. Scott Shultz of Transylvania University, have conducted the first experiments under the direction of Buchanan and her colleague Keiji Asano.

The students rounded up 50 subjects, half of them children from 4 to 12 years old, the other half adults from 17 years old to over 40. The subjects shook 2-mL glass vials of ordinary rubbing alcohol from a local pharmacy (isopropanol ~ 70% v/v with water) against their fingers for 1 min to collect fingerprint secretion samples. "We used rubbing alcohol instead of the kinds of pure solvents you'd usually extract with because of the potential toxicity problem," Buchanan explains. "First of all, we were collecting the secretions right off their skin, but there was also the risk that some of the younger kids might put their fingers in their mouths."

Extracting samples directly from the subjects' fingertips allows the collection of much more material than extracting individual latent fingerprints off glass or cellulose might, although it may also introduce compounds that would not ordinarily be found in a latent print left on a surface. "Fingerprint extracts contain hundreds of different compounds, so for the initial experiments, quantity has been a factor." Individual components in the sample extracts range from the low part-per-million level to high part-per-billion concentrations, enough to get good-quality mass spectra.

The extracted samples from individual children or adults were derivatized with a methylating reagent to enhance the determination of polar compounds such as amino acids, fatty acids, and other compounds known to make up much of the residue of a fingerprint. They were then separated and analyzed on a Finnigan MAT ITS 40 GC/ion trap MS system using both electron impact ionization and isobutane chemical ionization.

Oak Ridge National Laboratory

Art Bohanan demonstrates conventional black powder fingerprint dusting in Michelle Buchanan's lab. On screen is a reference chromatogram for cholesterol, one component of fingerprint residues in both adults and children.

That greasy kid stuff

Despite the relatively simple analytical treatment, differences between children's and adults' fingerprints showed up clearly in the total ion chromatograms (TICs). "You can lay the TICs down one by one and say 'this is an adult' or 'this is a child'," says Buchanan. Free fatty acids, which are fairly small and volatile, appear

to be the major component in children's fingerprints, whereas adult fingerprints, although they also contain some free fatty acids, contain larger concentrations of long-chain alkyl esters and other heavy, later eluting compounds.

The preliminary results indicate that fingerprint composition tends to change around puberty, Buchanan says. "The esters of the fatty acids are probably not coming from the finger itself—they're more typical of sebaceous secretions." Samples taken from the faces and freshly washed hands of adults indicate that the longer chain alkyl esters are probably transferred to the subjects' fingertips whenever they touch their faces.

Another important difference, says Buchanan, is that cholesterol is found at higher levels in the children's samples, whereas the adults' samples contain higher levels of cholesterol esters. "We see a big squalene peak in the fingerprints of both children and adults. Squalene is a precursor for cholesterol, hormones, and other compounds," she notes. There also appear to be subtle differences between male and female subjects, but those differences are not yet well characterized.

Then there are the odd findings. One adult's fingerprint extracts contained an as-yet unidentified compound that wasn't found in any of the other subjects' samples. Nicotine has been found in the extracts from smokers; another adult quit smoking two weeks before the experiment but was chewing nicotine gum. Nicotine appeared in his chromatograms, but Buchanan says she is unsure whether the nicotine was being secreted actively from his skin or was the result of contamination (e.g., from touching furniture or other objects with old traces of nicotine on them).

Toward a child fingerprint test

So far, the work done by Buchanan's students to identify volatile compounds has demonstrated why children's fingerprint residues don't last as long as adults'. After 24 h, there's a lot less material left in the fingerprints, and the compounds that do remain may not be very reactive with the conventional cyanoacrylate, ninhydrin, and amido black dyes used in police work. To develop a new test for children's fingerprints, Buchanan's lab must determine what's left in the residues when the free fatty acids and other volatile compounds evaporate.

Buchanan says that more specific experiments to identify signature compounds in the residues will have to include MS/MS structural analyses; derivatization and GC/MS protocols for nitrogen-containing compounds and basic compounds, which the group has not yet studied; and electrospray ionization MS for nonvolatile compounds that may be present in all fingerprints but aren't being detected by current visualization methods. Once target compounds are identified, she hopes to do matrix-assisted laser desorption/ionization MS studies of latent prints on glass, cellulose, and other supports, as well as volatility studies to get temperature-dependent spectrum profiles of the target compounds. If all goes well, some relatively nonvolatile signature compounds will be present and another lab at ORNL will try to develop a sensitive chemical visualization field kit for them.

A test for children's fingerprints must be able to show what's left when free fatty acids evaporate.

At the moment, the fingerprint project is being funded internally at ORNL, so research is being run on a small scale. Setting a timetable for future experiments, says Buchanan, will depend on whether her group can get additional support from the FBI, the Department of Justice, or other sources. Bohanan's discovery may have serious implications for numerous cases involving child victims as well as for child protection efforts such as the "Thumbs Up" National Fingerprint Program, operated through the University of Illinois (Chicago). Program director Diana Apa says the voluntary child fingerprint registry, which has worked with the FBI and provides database searches for identification of juvenile accident or crime victims, has grown steadily in the 12 years since she started it and is set for a significant expansion next year from the current ~ 15,000 a year through promotion in shopping malls.

Clinical applications

In addition to providing information on the compositional differences of fingerprints, Buchanan says the research her students are doing eventually might lead to skin tests for the clinical laboratory. If drugs such as the nicotine in the ex-smoker's fingerprint extract really are secreted in sweat or skin oils, she says, GC/MS profiling of skin secretions could be used to monitor physiological levels for therapeutic drug monitoring or clinical research. Biochemical indicators for some diseases may also be present on skin. "We do have reason to believe some compounds in skin secretions change with metabolic disorders," Buchanan says. One of the few relevant studies Buchanan found in her literature searches reported changes in the skin secretions of chronic alcoholics, who produced ethylester compounds instead of the normal long-chain alkyl esters.

Buchanan speculates that some "blue skies" health-related applications that might come out of her lab's research on fingerprint extracts could include assays for diabetes and other metabolic disorders or diseases. The key question would be whether the diseases affect the composition of the normal skin secretion compounds, the way alcoholism appears to, or produce unusual compounds that are specific enough for accurate diagnosis.

GC/MS might be used either as the clinical assay itself or as a way of pinpointing signature compounds for a disease so that a specific assay could be developed for them. Bohanan says that if it's possible, he would like to see a color indicator-based skin patch assay developed for drugs of abuse. "It would be a big help if all a police officer had to do was touch a suspect with a reactive pad and get a positive or negative for a drug." How possible some of these applications are will depend on how individual target compounds are distributed physiologically, what concentration of them can be detected in skin secretions, and whether ef-

Your Partner in Research...

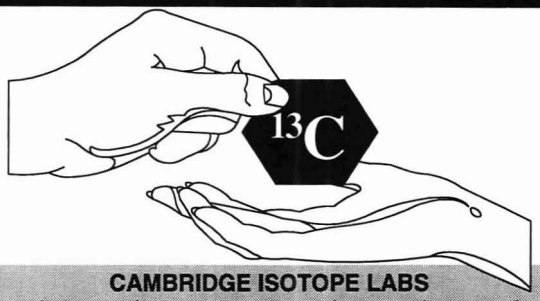

CAMBRIDGE ISOTOPE LABS
2nd Research Grant Program - $100,000 in Awards

In 1993, CIL provided $100,000 of stable isotope labeled compounds to 38 different groups for novel research in NMR, MRS, and Mass Spectrometry.

CIL recognizes that economic conditions continue to limit the scope and number of valuable research projects. In order to assist the research community in overcoming these economic constraints, CIL is pleased to announce the second Research Grant Program for stable isotopes.

CIL is seeking proposals from researchers who have ideas for new applications, analytical methods, or novel experiments which could expand the body of scientific knowledge in this area. We believe that this program represents the best in cooperative research between private industry and the scientific community.

CIL
CAMBRIDGE ISOTOPE LABORATORIES
50 Frontage Road, Andover, Massachusetts 01810
800-322-1174 or 508-749-8000 (USA) 508-749-2768 (Fax) 800-643-7239 (Canada)

Deadline for applications is August 15, 1995. Please call to apply.

CIRCLE 8 ON READER SERVICE CARD

Compound Your Knowledge

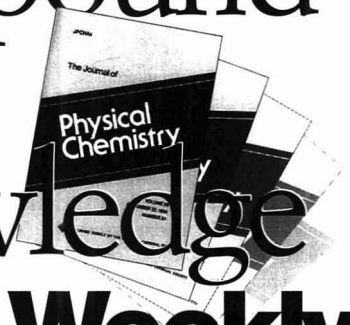

Weekly.

The *Journal of Physical Chemistry* provides weekly distribution of research on every topic that is in the forefront of research. Over 300 pages published very week.

Letters—for fast publication of new and urgent results
Articles—on original research, full-length studies, and new findings
Invited Papers and Selected Symposia Proceedings—appear throughout the year

—*All at very low annual subscription rates.*

Order today and have this valuable information at hand every week.

To order your one-year subscription today, call toll-free, 1-800-333-9511 (U.S. only). Outside the U.S. call 614-447-3776. Fax your order to 614-447-3671. ACS PUBLICATIONS

fective indicator-based assays can be developed for them.

Forging new ties

Progress on Bohanan's fingerprint problem has been encouraging enough that ORNL, which is better known for its core of energy and environmental research, is now setting up a forensic program. ORNL has lent its efforts to a few forensic investigations such as the neutron activation analysis (NAA) it performed four years ago on the exhumed remains of Zachary Taylor to determine whether the pre-Civil War president could have died of arsenic poisoning. Trivelpiece says that ORNL has forged closer ties with the forensic anthropology department at the University of Tennessee–Knoxville and local police departments to find practical forensic applications for ORNL's high-tech expertise and equipment. One project that's already in the works is to apply ORNL's supercomputer-based surface modeling programs to automated reconstruction of facial features from the skulls of unidentified corpses.

"Not all of these applications are really fundamental research," says Trivelpiece, "but they're also not routine testing; we can't get into the business of competing with commercial contract labs. Some of our projects might be to make simplified devices for blood testing at the site of an accident or crime or, for samples like those in the Zachary Taylor case, we have people asking if we could make a portable little ^{252}Cf source that they can carry to the crime scene for NAA."

Bohanan's second child abduction case went to court on May 1, and the jury returned a guilty verdict for first-degree murder on May 9. Bohanan says he believes the findings he made and continues to make from the back seat of his car (which now include comparisons of fingerprints on porous paper samples), and the chemical explanations furnished by Buchanan's lab, bolstered the prosecution's case. Beyond the individual case, however, his collaboration with ORNL has produced valuable information for forensic investigators and provided ORNL with a project of public importance, Buchanan says. "Being given a good problem is what prompts an analytical chemist." *Deborah Noble*

Electron Capture Detection for GC

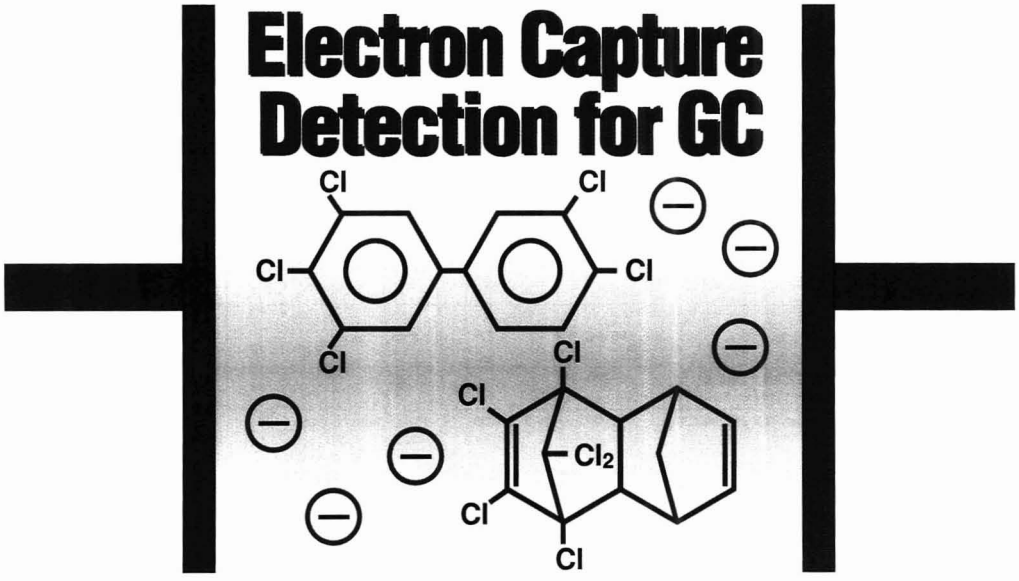
Cl
Cl
Cl

high voltage for a good signal when the voltage was on. These "constant frequency" ECDs, commercially available in the 1960s, had an improved dynamic range but still gave a nonlinear response.

"It didn't take very long to get the idea of using variable frequency," says Hill. Variable-frequency voltage pulsing, also commonly known as "constant current" mode, was introduced in the early 1970s. The pulse frequency is increased as needed to keep the current constant and is a linear function of the analyte concentration. Most commercial ECDs employ variable-frequency pulsing for linearization, but as electronics technology has continued to improve, a few companies have developed microprocessor-based

Table 1. Summary of representative products

Product	902B	ECD	ECD-80	Model 311
Company	Chrompack 1130 Highway 202 S. Raritan, NJ 08869 800-526-3687	Finnigan/Tremetrics 2215 Grand Avenue Pkwy. Austin, TX 78728 512-251-1555	Fisons Instruments 55 Cherry Hill Dr. Beverly, MA 01915 508-524-1000	HNU Systems 160 Charlemont St. Newton, MA 02161 800-724-5600
Detector price	$4055	$3390	$4000	$4295
Type	Integral	Integral or add-on for retrofit	Integral or add-on for retrofit	Integral in portable GC-ECD system
Compatible with other GC systems	No	No	No	No
Specifications				
Source	10 mCi ^{63}Ni	16 mCi ^{63}Ni	10 mCi ^{63}Ni	10 mCi ^{63}Ni
Voltage/pulse frequency range	3–24 kHz; ideal signal 6–10 kHz	0–200 kHz	0–500 kHz	2–500 kHz
Voltage/signal adjustment	4 detector attenuation ranges	Current range 0–0.9 nA	Pulse width control	Current range 0–10 nA
Temperature range (°C)	50–400	Ambient–350	Ambient–400, 10 °C increments	Ambient–350
Max. no. of detectors	2 with independent temperature control	2	2 ECDs or 1 ECD in series with other detector	2
Column interface	Direct connection for 0.125-in. column; adaptors available for 0.53-, 0.32-, and 0.25-mm columns	Accommodates packed or capillary columns with Swagelok adaptors	Metal-encased graphite ferrule attaches column to detector	Capillary column adaptors available
Data handling				
Output	Integrator; chart recorder; RS-232C interface	Integrator; data system; 0–1 V or 0–10 V recorder	Analog output 0–1 V or 0–10 V; PC; integrator; chart recorder	Printer/plotter; chart recorder 0–1 V or 0–10 V; RS-232C interface
Control	GC system controller	GC system microprocessor	Independent of GC system	GC system microprocessor
Analysis	4 sensitivity settings	Autozero, linearizer	Autozero	Autozero; programmable methods; 100-compound library
Performance				
Linear dynamic range	$2 \times 10^3 \pm 5\%$ (aldrin)	10^3 (N_2); 10^4 (Ar/CH_4)	10^4	$> 10^4$ (Ar/CH_4)
Detection limits				
Pesticides	< 5 fg/s aldrin	0.1 pg/s lindane	< 0.1 pg/s lindane	10–100 pptr
Organochlorines	INA	INA	INA	INA
Fluorinated cpds.	INA	INA	INA	1.8 ppb SF_6
Special features	INA	Large detector cell volume for high-concentration sample loads	External mount for quick interchange of detectors; ECD mounts on splitter for co-detection in GC/MS	300 µL cell volume
Reader Service Number	401	402	403	404

NA = Not applicable
INA = Information not available at press time

"linearizer" chips for their constant-frequency instruments.

Sources

Most commercial ECDs use 10–20 mCi ^{63}Ni, a β-emitter with a very long half-life, as the electron source. The radioisotope provides an even stream of thermal electrons for years, and if handled properly and left sealed inside its shielding poses little hazard. A few ECDs have been built with a source of ^{3}H infused in scandium metal; the higher flux of β particles is claimed to give greater detector sensitivity, but the source requires lower operating temperatures than the conventional ^{63}Ni sources so that the radioisotope doesn't leak out of the metal.

HP 6890	AutoSystem XL	ECD-17	PDECD	GC Star CX ECD
Hewlett Packard 2850 Centerville Rd. Wilmington, DE 19808 302-633-8000	Perkin Elmer 761 Main Ave. Norwalk, CT 06859 203-762-4000	Shimadzu Scientific Instruments 7102 Riverwood Dr. Columbia, MD 21046 410-381-1227	Valco Instruments P.O. Box 55603 Houston, TX 77255 713-688-9345	Varian Chromatography Systems 2700 Mitchell Dr. Walnut Creek, CA 94598 510-945-2400
$3820 with manual pneumatics control; $4145 with electronic pneumatics control	$3400	$3000	$4000 with all electronics and He purifier	$4000–$4500
Integral or add-on for retrofit	Integral or add-on	Integral or add-on	Nonradioactive constant-frequency add-on for commercial GCs	Integral or add-on
HP 5890	No	No	Yes	No
13.5 mCi ^{63}Ni	15 mCi ^{63}Ni	10 mCi ^{63}Ni	Pulsed dc discharge with He/CH_4 dopant	15 mCi ^{63}Ni
100–600 Hz baseline; 143 kHz	INA	INA	NA	1.6–500 kHz
Reference current for constant current signal processing adjustable for 0.5–5.0 nA	200- or 800-ms signal filtration	0.05–2.0 nA, adjustable	Autozero	Range selection
Ambient–400	100–450; 1 °C increments	Ambient–350; 1 °C increments	Ambient–400	Ambient–420; 1 °C increments
2	2 ECDs	3 with independent temperature control	NA	2 with independent control; can be operated in series
Accommodates capillary and packed columns	Direct connection for 0.125-in. column; adaptors for 0.25-in. column and 0.53-mm capillary column	Accommodates packed or capillary columns	Direct connection for capillary columns 0.05–0.53-mm i.d.; adaptor for packed columns	Accommodates packed or capillary columns
Computer or integrator for full range digital data; analog integrators and recorders for 0–1 mV, 0–1 V, and 0–10 V data	Recorder; integrator; RS-232C interface	0–±1 V or 0–±1 mV analog output, compatible with computer, integrator, or recorder	Recorder 0–1 mV or 0–1 V	0–1 mV recorder; 0–1 V integrator; 0–10 V computer
GC or workstation	GC system controller	GC keyboard or PC software	Stand-alone or integrated with GC system controller	GC system controller or workstation
Reference current can be automatically adjusted to stabilize detector output frequency	Noise filtration, signal scaling, background subtraction, detector attenuation	Autozero	Autozero; Wentworth equation microprocessor linearizer	Background subtraction; in-board data handling; autozero
> 10^4 (lindane)	10^4 ± 10%	> 10^4	> 10^4	10^4 (lindane)
< 0.04 pg/s lindane	50 fg/s lindane	0.1 pg/s lindane	< 50 fg/s lindane	< 20 fg/s lindane
INA	10 fg/s perchloroethylene	INA	35 fg/s CCl_4	INA
INA	INA	0.1 pg/s SF_6 (ppb range)	INA	< 100 ag/s
Digital programmable or conventional pneumatics control	Programmable or conventional pneumatics	Cell current is user selectable from 0.05–2.0 nA	Switch on detector changes source operation to He ionization or PID; 60-μL cell is tailored for capillary GC; compatible with field-portable GC units; can run on battery power	Sealed cell; specific or general radiation user licenses are provided
405	406	407	408	409

One concern for buyers who wish to retrofit their GC systems with an ECD or to buy a GC system with an integral ECD is that the use of a radioactive source, even though it's a well-sealed and shielded solid, may require the laboratory to get a radiation user's permit for it. Because of health, production, and licensing costs in areas where radiation use is stringently controlled, Hill says, "A lot of people have worked on electrical source generation for ECDs. The Japanese, among others, are adamant about getting a nonradioactive system." One approach has been photoelectron generation, which works, Hill says, but the lamp lifetime, intensity, and stability don't compare to the output stability of ^{63}Ni sources. "^{63}Ni is hard to beat for long-term use and you don't need extra electronics to generate the electron cloud," he says. The other approach has been to generate a corona and funnel the electrons into the detector. Although most of this work is still at the research stage, Valco (Houston, TX) has recently introduced a commercial nonradioactive ECD with a pulsed discharge source.

Running conditions

Unlike FIDs, which respond to the total amount of an analyte in a peak, ECDs respond to the concentration of the analyte in a carrier gas, so changing the flow rate will change the detector response. ECDs usually run at flow rates of ~ 30 mL/min and use high-purity N_2 or Ar/CH_4 carrier gas. The β particles emitted by the source produce free electrons with very high energy; the desired electron population is under no potential and has only thermal energy (thermal electrons). Nitrogen absorbs the excess energy fairly well, but argon does not, so when argon is used, CH_4 is added to the system at 5–10%. The added CH_4 also prevents argon from undergoing Penning ionization.

For capillary GC, which is increasingly in routine use, flow rates are only 3–4 mL/min, so the eluent must be augmented with a makeup gas. Hydrogen and helium are often used as GC carrier gases. Like argon, however, helium can undergo Penning ionization, so if it's used a small amount of CH_4 should be added to the makeup gas. Small-volume detector cells are desirable for capillary GC to prevent peak broadening.

Contamination is usually preventable, says Hill. Running the detector, which has its own heater, at sufficiently high temperatures to prevent condensation and leaving it on with a small flow of makeup gas overnight allows the detector to "bake out" most contaminants. It also prevents laboratory contaminants such as acetonitrile vapor and oxygen from getting into the detector and oxidizing the radioactive nickel foil.

Most ECDs are included as an integral part of a GC system, but some are available as add-ons or stand-alone instruments, and most include their own column interfaces. The critical parameter, says Hill, is the interface dead volume. Capillary columns can be inserted all the way to the detector so that no transfer lines are needed. "If you're interfacing the detector yourself," says Hill, "make sure the makeup gas sweeps the dead volume in the interface and that your transfer lines are heated—the best are made from coated glass that prevents eluent absorption. Also, electrically shielding the detector from external static lowers the noise." Oxygen traps placed upstream from the detector prevent oxidation of the nickel foil and reduce noise from O_2 electron capture.

ECDs continue to be valuable in routine environmental labs.

Detector response

Detector response to electron-capturing compounds is extremely variable, says Hill. "Everybody seems to think ECDs are quantitative, but you can't count on getting uniform response from different compounds." Because most chlorinated compounds dissociate to give individual chloride ions, the detector response depends in part on the number and location of the chlorines in the molecule; response may also depend on the recombination rate. Brominated and iodinated compounds are also detectable, as are nitroaromatics, but fluorine compounds do not produce a very strong signal in most ECDs. Calibration is a problem for GC-ECD, says Hill. "Every compound has a different response factor, so you need to use both external and internal standards for quantitation. ECD is useful for target compounds, but it can't really be used reliably to identify unknowns."

Applications

Apart from features to accommodate capillary GC and improvements in computer technology for control, few things have changed for ECD design in the past 10 years. However, applications continue to appear as needs for routine GC change and environmental regulatory policy shifts priorities.

An ECD is more selective than the nonselective FID, but it still responds to a wide variety of compounds, says Hill. He notes that Grimsrud and others have reported protocols for manipulating the relative response factors for desired compounds. Although the normal way to run an ECD is without any oxygen interference, some of these protocols call for the addition of oxygen or nitrous oxide to sensitize the detector for some compounds and decrease sensitivity for others.

Ray Clement notes that as mass spectrometers become more affordable, the increasing pressure from environmental regulations that require definitive identification of specific compounds may relegate ECDs to screening protocols. ECDs may find a niche, he says, in industrial process monitoring for chlorinated or nitroaromatic compounds where the stoichiometry of the analytes is known.

ECD and MS can be used simultaneously for GC detection by splitting the flow. Hill's group uses ECD as the inlet for ion mobility spectrometry, though they haven't figured out how to use the pulsed approach with it. GC-ECD/IMS allows them to characterize the positive ions produced for analytes such as insect pheromones and to detect negative molecular ions from nondissociative electron capture (e.g., trinitrotoluene).

Despite the advance of MS, Hill says, most MS systems are more prone to contamination and require more maintenance than ECDs. "I do see a major advance in electron capture applications for field analyses," he says. Portable GC-ECD, GC-ECD/IMS, and GC-ECD/MS may be the next developments for monitoring hazardous waste sites for CCl_4 and similar compounds or for rapid detection of explosives. In the meantime, ECDs will continue to be valuable in routine environmental labs, says Hill. "These labs need an FID as a first detector, but the second detector should be an ECD. Electrolytic conductivity detectors have higher specificity for chlorinated compounds and don't require a radiation user's license, but they have more parameters to deal with. An ECD just works." *Deborah Noble*

Just Released!

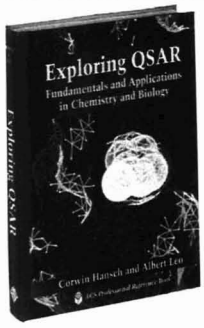

Exploring QSAR

This new two-volume set provides a thorough introduction to quantitative structure-activity relationships (QSAR).

In *Volume 1: Fundamentals and Applications in Chemistry and Biology* the authors show how structure-activity relationships should be considered as a whole in quantitative terms, starting with physical organic chemistry and including all types of biochemical and biological processes. They give a unified view with extensive cross-referencing and show the interrelatedness of SAR from the ionization of acetic acid to the action of hallucinogens in humans. Throughout the book, QSAR in biological processes are related to those in physical organic chemistry.

Volume 2: Hydrophobic, Electronic, and Steric Constants contains comprehensive tables of physicochemical parameters (substituent constants and octanol-water log P values) that are necessary for quantitative structure-activity relationships and qualitative SAR. These values were collected over 25 years by two of the most renowned researchers in the field.

***Volume 1* by Corwin Hansch and Albert Leo**

***Volume 2* by Albert Leo, Corwin Hansch, and David Hoekman**

ACS Professional Reference Book
880 pages (1995) Clothbound
ISBN 0-8412-2993-7
$99.95

ORDER FROM
American Chemical Society
Distribution Office Dept. 74
1155 Sixteenth Street, NW
Washington, DC 20036
Or CALL TOLL FREE
1-800-227-5558
(in Washington, DC 872-4363) and use your credit card!
FAX: 202-872-6067.
ACS Publications Catalog now available on internet:
gopher acsinfo.acs.org

ACS PUBLICATIONS
Essential Resources for the Chemical Sciences

American Chemical Society Presents

Gas Chromatography: Theory And Practice

Tuesday-Friday
August 29-September 1, 1995
Virginia Tech, Blacksburg, Virginia

An Intensive Four-Day Short Course Providing Hands-On Experience with State-of-the-Art Techniques and Equipment in Gas Chromatography

Want to learn more about GC? This dynamic course is designed for beginners in gas chromatography who want practical lab experience. Through lectures and hands-on laboratory sessions in this basic course, you'll learn to:

- solve tough separation problems
- install, optimize, and use both packed and capillary columns
- perform qualitative and quantitative analyses
- interpret and troubleshoot from chromatograms
- AND MUCH, MUCH MORE!

About the Instructor

Harold M. McNair, Professor of Chemistry, Virginia Tech, Blacksburg, Virginia, is one of the most highly praised instructors in the ACS Short Course program. Dr. McNair has had extensive industrial experience at EXXON Research and Engineering, F&M Division of Hewlett Packard Corporation, and Varian Aeograph. He is the recipient of the Virginia Tech Alumni Teaching Award, the COLACRO Medal in chromatography, and the EAS award in chromatography.

Register Today!

Because of the extensive lab work performed by participants, enrollment in this unique course is limited to 24.

For more information, mail in the coupon below or call the Continuing Education Short Course Office at (800) 227-5558 (TOLL FREE) or (202) 872-4508.

YES! Please send me information on the ACS Short Course, Gas Chromatography: Theory and Practice, to be held August 29-September 1, 1995, in Blacksburg, Virginia.

Name _____

Title _____

Organization _____

Address _____

City, State, Zip _____

Phone _____ FAX _____

Mail to: American Chemical Society, Dept. of Continuing Education, Meeting Code GCPC9508, 1155 Sixteenth Street, N.W., Washington, DC 20036

Benchtop sector GC/MS

The GCmate is a benchtop reverse-geometry double-focusing mass spectrometer designed to interface with a commercial gas chromatograph for accurate mass determination in pharmaceutical and environmental applications. Double-focusing mass spectrometers, which have an electrostatic sector and a magnetic sector, feature much higher mass resolution than quadrupole instruments, typically ~ 10,000, but most have very large magnets arranged with relatively long focal lengths and take up a great deal of floor space.

The GCmate ion optics include five quadrupole ion lenses to compress the ion beam and shorten the focal length, allowing a more compact configuration for the instrument. Three lenses in front of the magnet compress the beam height to send the beam through a very narrow magnet gap. The narrow gap makes it possible to maintain high magnetic density and mass dispersion using less power and a smaller

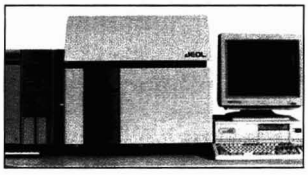

magnet. The magnet in the 180-kg benchtop instrument, with an acceleration voltage of 2.5 kV, provides maximum mass resolution of 5000 with scan rates of 0.07 s/decade.

The system has a mass range of 1–1000 Da and mass accuracy of 5 ppm RMS under high-resolution conditions and 0.1 Da at low resolution. It features a combination EI/CI ion source and a PMT-type detector for positive or negative ion detection as well as direct coupling for capillary columns and can be configured for use with a GC autosampler. A 486/DX 66 PC with Windows-based operating software is used for control. **JEOL** ■ **411**

INSTRUMENTATION

SPM

The Accurex scanning probe microscope features closed-loop scanner linearization, dual positioning optics with 90° and 45° viewing, a large-sample stage that accommodates samples up to 14 in. in diameter and 4 in. thick, and a kinematically mounted tilt-up head for tip and sample exchange. Windows-based control software allows image acquisition with 1000 × 1000 pixel resolution. The instrument can image in all SPM scan modes in air or liquid environments. **TopoMetrix** ■ **410**

FT-IR

The IR-Plan Advantage FT-IR microscope has on-axis, high numerical aperture cassegrain reflecting optics and performs transmittance and reflectance sampling at or below the diffraction limit. The substage condenser in the fixed-compensation optics automatically compensates for a 2-mm-thick window during transmission analyses. The instrument also features a rotatable full-field aperture, an integral 0.25-mm MCT detector, and a four-place nosepiece for optional objective accessories. **Spectra-Tech** ■ **412**

Thin-film analysis

Series 300 FT-IR thin-film process analyzer monitors film thickness, composition, and temperature simultaneously in real time. Combined thickness and composition measurements are made using FT-IR reflectance spectroscopy together with a parametric model for the wavelength-dependent complex dielectric function and a model for reflectance from a multilayer stack. Temperatures are measured by combining data from simultaneous reflectance and emission spectra from a sample surface. The analyzer monitors films 0.02–50 μm thick at temperatures of 50–3000 °C for doping density, the presence of impurities, and other composition parameters. **On-Line Technologies** ■ **413**

LITERATURE

HPLC and SFC

"Applications Compendium," Vol. 1, is a collection of sample chromatograms for HPLC and SFC. Applications areas for HPLC include peptides and nucleic acids, drugs, sugars and vitamins, surfactants and polymers, and environmental contaminants. The booklet presents 12 applications chromatograms for SFC, a column packings conversion table, a column selection guide, and a guide to HPLC filters and guard columns. **Keystone Scientific** ■ **414**

Process GC

Brochure describes simulated-distillation analyzers for process monitoring of boiling-point distributions in petroleum refineries. The instruments are based on the HP 6890 gas chromatograph with automated liquid injection and sampling and a workstation with simulated-distillation analysis software. **Hewlett Packard** ■ **415**

Nitrogen determination

"A Guide to Kjeldahl Nitrogen Determination Methods and Apparatus" explains procedures, techniques, and equipment for these methods. A history of the methods, a discussion of macro and micro Kjeldahl processes, and a glossary and bibliography are included. **Labconco** ■ **416**

For more information, please circle the appropriate numbers on one of our Reader Service Cards.

CATALOGS

HPLC

1995 catalog lists HPLC columns and accessories. Products include microbore, minibore, analytical, preparative, rapid analysis, and guard columns. Applications products include columns for biopolymers, EPA Method 300 anions, and basic drugs as well as for nonaqueous GPC, chiral HPLC, and CE. Accessories include SPE cartridges, column heaters, solvent handling systems, degassers, recyclers, fittings, filters, and biocompatible hardware. The catalog also lists software and training materials. **Phenomenex** ■ **417**

Atomic spectroscopy

1995/1996 atomic spectroscopy supplies catalog describes instruments and accessories for AAS, ICP-AES, and ICPMS. Products include spectrometers, a flow injection mercury determination system, burners and lamps for AAS, and supplies for discontinued AAS spectrometers. **Perkin Elmer** ■ **418**

HPLC

Catalog for HPLC lists microbore and semipreparative columns, guard columns, filtration products, vials, syringes, tubes, lamps, valves, fittings, solvents and reagents, optimization software, and accessories. **Phase Separations** ■ **419**

Dual-view ICP-AES

The Optima 3000 DV is an echelle polychromator ICP-AES system that provides both radial and axial plasma viewing. The axially oriented plasma operates with a shear gas to move the part of the plume in which most recombination interferences occur out of the viewing region. A computer-controlled mirror placed in the optical path permits radial viewing. The software included with the system allows selection of view type, vertical and horizontal adjustment of plasma viewing, and optimization of the viewing position.

Axial plasma viewing increases the method sensitivity ~ 10-fold for most elements as compared with radial viewing, but is subject to greater interferences at the higher end of the concentration range, so it does not extend the linear dynamic range on its own. Axial plasmas are also more prone to molecular interferences than radial plasmas, and because viewing is end-on, some overlap effects occur between easily ionizable species. The ability to sample a specimen both ways on the same instrument allows the determination of both high- and low-concentration species.

The spectrometer operates in the wavelength range of 167–782 nm and can determine 73 elements in < 1 min. It uses an *f*/6.7 echelle grating polychromator with two cross-dispersers, one with Schmidt correction for UV light and one for visible light. Resolution is 0.007 nm at 200 nm. A segmented array CCD views > 5000 emission lines simultaneously. The detector allows simultaneous signal and background measurement.

The system is controlled through dedicated multitasking software that performs automatic plasma ignition, calibration, data storage, and parameter optimization. It also features two modes of spectral interference correction. A reference table of > 50,000 analytical wavelengths is included. **Perkin Elmer** ■ **420**

Digital electron energy analyzer

Model EA 125 is a digitally controlled hemispherical electron energy analyzer for XPS and Auger electron spectroscopy. The digital electronics control the analyzer's pass energy and lens voltages for a broader range of settings and permit the pass energy to be varied continuously rather than in discrete steps.

The first stage of the electrostatic input lens can be operated in three magnification modes that control the sample area for analysis and the acceptance angle for photoelectrons. The selected magnification is constant throughout the energy range. The second stage is an energy zoom lens that operates over the retard ratio range of 0.2–200 and focuses the electrons to the input aperture of the analyzer.

Two multielement lenses are available: a variable-magnification lens for imaging to small spot sizes in XPS and a wide-angle lens for applications such as Auger electron spectroscopy that require maximum collection efficiency. These lenses can be switched by exchanging elements and reprogramming the controller. The analyzer mounts on a 6-in. flange and is designed for use in existing UHV systems. It can be configured with fixed or variable slits, multichannel detection, and controllers for high (up to 2000 V) or low (up to 300 V) energy levels. **Topac** ■ **421**

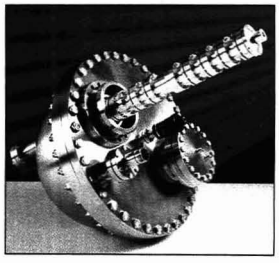

Come visit our new Home

(Page, that is)

URL: http://pubs.acs.org

The American Chemical Society Publications Division welcomes you to visit our new Home Page on the World Wide Web. Here you can find all kinds of useful information on ACS Publications including detailed descriptions of books and periodicals, new releases, product information, hot articles and more.

Continuously updated, our new Home Page brings you:

- **Hot Articles**
  A special section containing articles or news items of interest.
- **Advertised Product Information Network (PIN)**
  A new way to get more information on products and services advertised in ACS publications electronically.
- **Supporting Information (formerly known as Supplementary Material)**
  FREE to subscribers of Journal of the American Chemical Society and soon all other ACS journals.
- **Books and Journal Information**
  New releases, author information and the full catalog containing descriptions and tables of contents of ACS titles—including the backlist.

Plus, an easy "back" to the American Chemical Society Home Page (URL: http://www.acs.org) for full information on the Society and its activities.

Visit the ACS Publications Home Page. We're open 24 hours a day.

ACS III PUBLICATIONS
Essential Resources for the Chemical Sciences

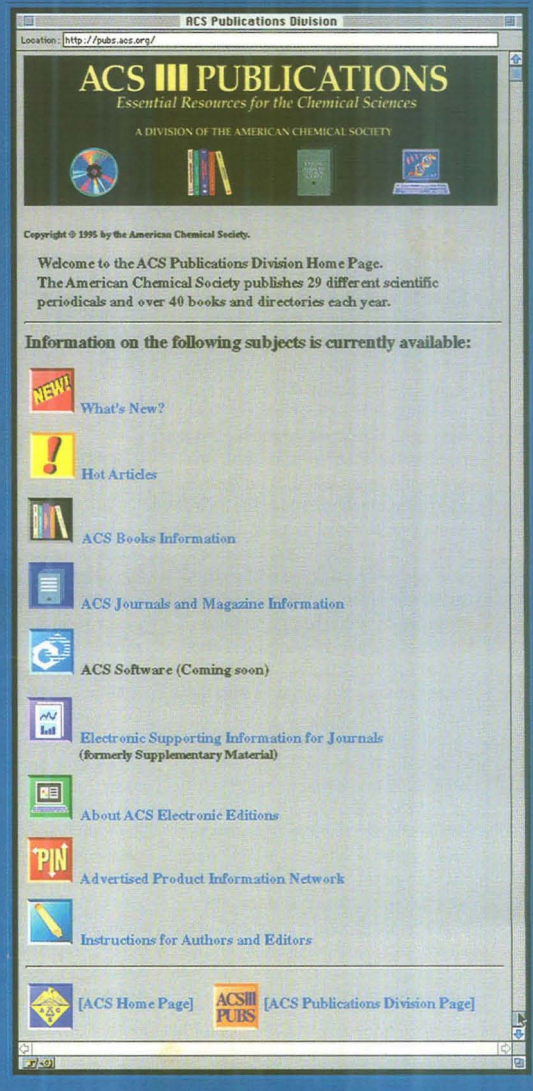

Laboratory Service Center

LABORATORY SERVICE CENTER

(Equipment, Materials, Services, Instruments for Leasing). Maximum space — 4 inches per advertisement. Column width, 2-3/16"; two column width, 4-9/16". Artwork accepted. No combination of directory rates with ROP advertising. Rates based on number of inches used within **12** months from first date of first insertion. Per inch: **1" — $200; 12" — $195; 24" — $190; 36" — $185; 48" — $180.**

ANALYTICAL CHEMISTRY
1599 Post Road East
P.O. Box 231
Westport, CT 06881
203-256-8211/FAX: 203-256-8175

1-Amino-2-Naphthol-4-Sulfonic Acid • Benzamide • 2-Bromoethylamine HBr
1-Bromonaphthalene • Chloranil • 2-Chloro-4-Nitrobenzoic Acid
p-Cyanobenzaldehyde • 4-Cyanophenol • 3, 3' -Diaminobenzidine TetraHCl
2, 6-Dibromopyridine • Diethyl Succinate • Digitonin • Dimedone
Dimethyl Chloroacetal • 3, 3-Dimethylglutaric Acid • Dipropyl Ketone
2,2' -Dipyridyl • EDTA & Salts • 8-Hydroxyquinoline Sulfate • INT
Levulinic Acid • p-Methylaminophenol Sulfate • Neocuproine & HCl
1, 10-Phenanthroline • Silver Diethyldithlocarbamate • Sodium Succinate

Write for our Products List of over 3,000 chemicals

Tel: 516-273-0900 • TOLL FREE: 800-645-5566 Telefax: 516-273-0858 • Telex: 497-4275

EASTERN CHEMICAL
ADMIRAL SPECIALTY PRODUCTS, INC.
P.O. Box 2500
DEPT. AC
SMITHTOWN, N.Y. 11787

FREE DATA, FAST

To quickly amass data on all of the products you need, consult the Lab Data Service Selection on our *Analytical Chemistry* reader reply card insert.

Index to Advertisers

CIRCLE INQUIRY NO.	ADVERTISERS	PAGE NO.
8	*Cambridge Isotope Laboratories	438A
2, 3	* EG&G Instruments/Princeton Applied Research	423A
6	Finnigan MAT, Inc. Communications West	407A
4	Hamilton Company	OBC
1	Metrohm Ltd. Ecknauer & Schoch Werbeagentur ASW	IFC
7	Whatman Inc.	393A

Directory section, page 447A.
**See ad in 1995 LabGuide Edition.*

Advertising Management for the American Chemical Society Publications

CENTCOM, LTD.
President
James A. Byrne
Executive Vice President
Benjamin W. Jones
Joseph P. Stenza, *Production Director*
Laurence J. Doyle, *Director of Marketing*

1599 Post Road East
P.O. Box 231
Westport, Connecticut 06881-0231
(Area Code 203) 256-8211
Fax No. 203-256-8175

DIRECTOR, ADVERTISING SALES, LABORATORY PRODUCTS
Bruce E. Poorman

ADVERTISING PRODUCTION MANAGER
Jane F. Gatenby

SALES REPRESENTATIVES

Philadelphia, PA. . . . CENTCOM, LTD., The Meadows, 485 Devon Park Drive, Suite 106, Wayne, PA 19087. Telephone: 610-964-8061, FAX: 610-964-8071

New York/New Jersey . . . Dean A. Baldwin, John F. Raftery, CENTCOM, LTD., Schoolhouse Plaza, 720 King Georges Post Road, Fords, NJ 08863. Telephone: 908-738-8200, FAX: 908-738-6128

Westport, CT./Boston, MA. . . . Dean A. Baldwin, Michael J. Pak, CENTCOM, LTD., 1599 Post Road East, P.O. Box 231, Westport, CT 06881-0231. Telephone: 203-256-8211, FAX: 203-256-8175

Cleveland, OH. . . . Bruce E. Poorman, Dean A. Baldwin, CENTCOM, LTD., 19035 Old Detroit Road, Suite 203. Rocky River, OH 44116. Telephone: 216-331-5151, FAX: 216-331-3432

Chicago, IL. . . . Michael J. Pak, CENTCOM, LTD., 540 Frontage Rd., Northfield, IL. 60093. Telephone: 708-441-6383, FAX: 708-441-6382

Houston, TX./Atlanta, GA. . . . Edward M. Black, CENTCOM, LTD., P.O. Box 820966, Houston, TX 77082-0966. Telephone: 713-493-1560, FAX: 713-493-6673

West Coast. . . .Bob LaPointe, CENTCOM, LTD., Suite 808, 2672 Bayshore Parkway, Mountain View, CA 94043-1010. Telephone: 415-969-4604, FAX: 415-969-2104

Denver, CO. . . .Bob LaPointe, CENTCOM, LTD., Suite 808, 2672 Bayshore Parkway, Mountain View, CA 94043-1010. Telephone: 415-969-4604, FAX: 415-969-2104

United Kingdom, Scandinavia and Europe (Except: Germany, Switzerland, Austria, France, Italy, Spain) . . . Malcolm Thiele, Technomedia Ltd., Wood Cottage, Shurlock Row, Reading RG10 OQE, Berkshire, England. Telephone: 1734-343-302, FAX: 1734-343-848

Germany, Switzerland, Austria . . . IMP InterMediaPartners, GmbH, Deutscher Ring 40, 42327 Wuppertall, Germany. Telephone: (0202) 711091, FAX: (0202) 712431

France . . . Gerard Lecoeur, Aidmedia, 31–33 Grand rue de Saint-Rambert, 69009 Lyon, France. Telephone: 78-64-20-37, FAX: 78-83-56-67

Italy, Spain . . . Tess Serranti, Serranti Communications, 43 Van Sant Road, New Hope, PA 18938. Telephone: 610-598-0668, FAX: 610-598-0670

Hong Kong. . .SEAVEX, LIMITED, 503 Wilson House, 19 Wyndham Street, Central, Hong Kong, Telephone: 868-2010, FAX: 810-1283

Japan. . . Shigeyuki Yasui, Intercommunications (Japan), Inc. 2F Ginza ElwaBldg. 8-18-7 Ginza, Chuo-ku, Tokyo 104, Japan. Telephone: (03) 5565-0861, FAX: (03) 5565-0860.

Korea. . .DooBee International Limited, Center Building (Byulgwan), 1-11 Jeong-dong, Choong-ku C.P.O. Box 4557, Seoul, Korea, Telephone: 822-776-2096, FAX: 822-755-9860

Singapore.. . .SEAVEX, LIMITED, 400 Orchard Road, #10-01 Orchard Towers, Singapore 0923, Telephone: 734-9790, FAX: 732-5129

Taiwan. . .Epoch Limited, 2F No. 3, Lane 52, Nanking East Road, Section 4, P.O. Box 1642, Taipei, Taiwan, R.O.C. Telephone: 577-5441, FAX: 578-4308

South America . . .Bruce E. Poorman, CENTCOM, LTD., 19035 Old Detroit Road, Suite 203, Rocky River, OH 44116. Telephone: 216-331-5151, FAX: 216-331-3432

ANALYTICAL CHEMISTRY Information Express

Get the product data you need fast...

By Phone: Use the reference list below, and contact the companies to fill an immediate need, or...
By Fax: Use the fax form on the opposite page to send a direct written request.

Company	Page	Issue	RSN	Data+	Phone	Fax	Contact
Applied Systems	386 A	6/1/95	406		410-224-8200	410-224-8205	Alan Rein
Astra Scientific International	324 A	5/1/95	401	●	510-426-6900	510-426-6990	John D. Jones
ATI Mattson	382 A	6/1/95	401	●	800-423-6641	608-831-2093	Dean Roberts
J. T. Baker	280 A	5/1/95	8	●	800-582-2537	908-859-9318	William Broad
Brooks Rand	328 A	5/1/95	414		206-632-6206	206-632-6017	Paul Danilchik
Bruker Instruments	383 A	6/1/95	404	●	508-667-9580	508-667-3954	Mark Chaykovsky
Calorimetry Sciences	324 A	5/1/95	402		801-375-8181	801-375-8282	Dennis Hunter
Cambridge Isotope Laboratories	438 A	7/1/95	8	●	617-938-0067	617-932-9721	Cheryl Savard
CDS Analytical	386 A	6/1/95	409	●	610-932-3636	610-932-4158	Vernon Bailey
Cetac Technologies	329 A	5/1/95	417	●	800-369-2822	402-733-5292	John J. Uhr
Chapman & Hall	371 A	6/1/95	15		212-780-6245	212-260-1730	D. Teahan
Chrompack	440 A	7/1/95	401	●	800-526-3687	908-722-8365	Judy Sparks
Comstock	385 A	6/1/95	2	●	615-483-7690	615-481-3884	John Talmadge
Dionex	386 A	6/1/95	408	●	800-346-6390	408-739-4398	Nancy Jensen
EG&G Instruments (Princeton)	423 A	7/1/95	2,3	●	609-530-1000	609-883-7259	Ruth Rearick
Finnigan MAT	407 A	7/1/95	6	●	408-433-4800	408-433-4823	Gary Spear
Finnegan/Tremetrics	440 A	7/1/95	402	●	512-251-1555	512-251-1597	Elaine Moody
Fisons Instruments	440 A	7/1/95	403	●	508-524-1000	508-524-1100	Cathy Schaub
Gilson	387 A	6/1/95	414	●	608-836-1551	608-831-4451	Paul Preidecker
Gow-Mac	328 A	5/1/95	410	●	610-954-9000	610-954-0599	Gail Smith
Hamamatsu	378 A	6/1/95	none	●	800-524-0504	908-231-1218	Robert Wisner
Hamilton	OBC	7/1/95	4	●	800-648-5950	702-856-7259	Robert Beavers
Hewlett-Packard	441 A	7/1/95	405	●	302-633-8000	302-633-8959	Dave Olsavsky
Hewlett-Packard	444 A	7/1/95	415	●	415-857-5603	415-857-8228	Doug Forsyth
HNU Systems	440 A	7/1/95	404	●	617-964-6690	617-558-0056	John Moore
Instrument Specialists	324 A	5/1/95	403		815-675-1550	815-675-1552	Robert Behme
Isco	367 A	6/1/95	6-9	●	402-464-0231	402-464-0318	Gary Bakken
Jeol USA	OBC	6/1/95	14	●	508-535-5900	508-536-2205	Brian Musselman
Jeol USA	444 A	7/1/95	411	●	508-535-5900	508-536-2205	Brian Musselman
JM Science	328 A	5/1/95	412	●	800-495-1678	716-774-8708	
Keystone Scientific	444 A	7/1/95	414	●	800-437-2999	814-353-2305	Mary DeArmitt
K&M Electronics	303 A	5/1/95	11		413-781-1350	413-737-0608	Rick Brighenti
KVB/Analect	383 A	6/1/95	403	●	714-206-4042	714-855-2535	Linda Marcus
Labconco	444 A	7/1/95	416	●	800-821-5525	816-353-0130	Ginny Pressly
Lab Connections	386 A	6/1/95	407	●	508-480-9777	508-481-9764	Megan O'Sullivan
McPherson	328 A	5/1/95	411	●	800-255-1055	508-263-1458	Christi Schoeffel
Metrohm	IFC	7/1/95	1	●	41-071-538-901	41-071-538-585	R. Steiner
Mettler-Toledo	386 A	6/1/95	410	●	800-638-8537	609-426-0121	Tom Basalik
Nicolet Instrument	383 A	6/1/95	405	●	800-356-8088	608-273-5046	Z. Stanek
On-Line Technologies	444 A	7/1/95	413		800-556-6584	203-528-0648	Sally Soloman
Particle Measuring Systems	328 A	5/1/95	408	●	303-443-7100	303-449-6870	Jerith L. Gronski
Perkin Elmer	OBC	6/15/95	none	●	203-761-2574	203-762-6000	Mary Cooke-Kager
Perkin Elmer	441 A, 445 A	7/1/95	406, 418, 420	●	203-761-2574	203-762-6000	Carol Blaszczynski
Phase Separations	445 A	7/1/95	419	●	44-01244-288500	44-01244-289500	Rebecca Andrews
Phenomenex	445 A	7/1/95	417	●	310-212-0555	310-328-7768	Tom Cleveland
Philips Electron Optics	387 A	6/1/95	413		31-40-7-88620	31-40-7-88256	
Photometrics	368 A	6/1/95	411	●	602-889-9933	602-573-1944	Michelle Downs
Prochrom	328 A	5/1/95	413		317-297-1667	317-297-5564	Augusto Olalde
Scott Specialty Gases	IFC	5/1/95	5		215-766-8861	215-766-0320	Donna M. Vito
Scinco America	329 A	5/1/95	419		602-888-5770	602-888-6776	Mark Johnston
Shimadzu	441 A	7/1/95	407	●	800-477-1227	410-381-1222	Mark Taylor
Spectra-Tech	444 A	7/1/95	412	●	203-926-8998	203-926-8909	Debbie Esposito
TA Instruments	325 A	5/1/95	407	●	302-427-4000	302-427-4001	Robert Hassel
Topac Scientific Instruments	445 A	7/1/95	421		617-740-8778	617-740-8779	Antoni Drybanski
TopoMetrix	444 A	7/1/95	410	●	408-982-9700	408-982-9751	Donna Bakale
Valco	441 A	7/1/95	408	●	713-688-9345	713-688-3948	Jack Frank
Varian Associates	441 A	7/1/95	409	●	510-945-2235	510-945-2335	Mark Caballero
Whatman	393 A	7/1/95	7	●	800-922-0361	201-472-6949	Sharman Pate

Data+ Column: A bullet indicates that additional product and company information is available in the 1995 *Analytical Chemistry* LabGuide Edition.
RSN: Reader Service Number

PRODUCT DATA SERVICE

VALID THROUGH NOVEMBER 1995

ANALYTICAL CHEMISTRY

JULY 1, 1995

Please circle the appropriate Reader Service Numbers to receive additional information.

Please help us determine your future laboratory buying trends. Which of the following products do you use, buy, specify, recommend or purchase? Circle all appropriate numbers on the attached reply card.

327 AA Spectroscopy
328 Analytical Services
329 Baths/Circulators
330 Biotechnology
331 Books/Periodicals
332 Centrifugation
333 Chemicals/Gases/Solvents
334 Computers/Software
335 Cooling/Freezing/Refrig.
336 Databases, Online
337 Densitometry
338 Detectors
339 Dryers/Evaporators
340 Electrochemistry
341 Elemental Analysis
342 Filtration
343 Flow Meters/Regulators
344 FT-IR Spectroscopy
345 Furnaces/Ovens
346 Gas Chromatography
347 General Lab Equipment
348 Heating/Temperature
349 Ion Chromatography
350 Lab Furniture/Hoods
351 Labware/Apparatus
352 Lasers/Fiber Optics
353 Liquid Chrom./HPLC
354 Mass Spectrometry
355 Microscopy
356 Capillary Electrophoresis
357 Mix/Stir/Blend/Grind
358 NMR Spectroscopy
359 Particle Size Analysis
360 Plasma Spectroscopy
361 pH/Ion Meters/Titrators
362 Pumping Monitoring
363 Recording/Integrating
364 Robotics/Automation
365 Sampling/Dispensing
366 Supercritical Fluid Chrom.
367 Spectrofluorometry
368 Stills/Purification
369 Surface Analysis
370 Thermal Analysis
371 Thin Layer Chrom.
372 UV-Vis Spectroscopy
373 Valves/Tubes/Fittings
374 Viscometry
375 Water/Moisture Analysis
376 Weighing/Balances
377 X-Ray Diffraction
378 X-Ray Spectroscopy

1	2	3	4	5	6	7	8	9	10	11	12	13	14	15	16	17
18	19	20	21	22	23	24	25	26	27	28	29	30	31	32	33	34
35	36	37	38	39	40	41	42	43	44	45	46	47	48	49	50	51
52	53	54	55	56	57	58	59	60	61	62	63	64	65	66	67	68
69	70	71	72	73	74	75	76	77	78	79	80	81	82	83	84	85
86	87	88	89	90	91	92	93	94	95	96	97	98	99	100	101	102
103	104	105	106	107	108	109	110	111	112	113	114	115	116	117	118	119
120	121	122	123	124	125	126	127	128	129	130	131	132	133	134	135	136
137	138	139	140	141	142	143	144	145	146	147	148	149	150	151	152	153
154	155	156	157	158	159	160	161	162	163	164	165	166	167	168	169	170
171	172	173	174	175	176	177	178	179	180	181	182	183	184	185	186	187
188	189	190	191	192	193	194	195	196	197	198	199	200	201	202	203	204

PRODUCT DATA SERVICE 327 328 329 330 331 332 333 334 335 336 337 338 339 340

341	342	343	344	345	346	347	348	349	350	351	352	353	354	355	356	357
358	359	360	361	362	363	364	365	366	367	368	369	370	371	372	373	374
375	376	377	378													

NEW PRODUCTS 401 402 403 405 406 407 408 409 410 411 412 413 414 415

416	417	418	419	420	421	422	423	424	425	426	427	428	429	430	431	432
433	434	435	436	437	438	439	440	441	442	443	444	445	446	447	448	449
450	451	452	453	454	455	456	457	458	459	460	461	462	463	464	465	466
467	468	469	470	471	472	473	474	475	476							

NAME (PLEASE PRINT)

TITLE

COMPANY

ADDRESS MAIL STOP

CITY STATE ZIP

TELEPHONE FAX

A. PRIMARY FIELD OF WORK

01 ☐ Energy
02 ☐ Environmental
03 ☐ Medical/Clinical
04 ☐ Drug/Toiletries
05 ☐ Forensic/Narcotic
06 ☐ Biotechnology
07 ☐ Metals
08 ☐ Pulp/Paper/Wood
09 ☐ Soaps/Cleaners
10 ☐ Paint/Coating/Inks
11 ☐ Electrical/Electronic
12 ☐ Instrument Dev./Design
13 ☐ Plastic/Polymer/Rubber
14 ☐ Agriculture/Food/Bev.
15 ☐ Inorganic Chemicals
16 ☐ Organic Chemicals

B. MY PRIMARY AREA OF EMPLOYMENT IS:

INDUSTRIAL
17 ☐ Research & Development
18 ☐ Quality/Process Control

MEDICAL/HOSPITAL
19 ☐ Research & Development
20 ☐ Clinical/Diagnostic

GOVERNMENT
21 ☐ Research & Development

COLLEGE/UNIVERSITY
22 ☐ Research & Development
23 ☐ Teaching

INDEPENDENT/CONSULTING
24 ☐ Research & Development
25 ☐ Analysis/Testing

C. INTENSITY OF PRODUCT NEED

26 ☐ Purchasing Immediately 27 ☐ Within 3-6 months 28 ☐ Within 6-12 months 29 ☐ Future project

D. Is this your personal copy of Analytical Chemistry?

☐ Yes ☐ No

ANALYTICAL CHEMISTRY FAX EXPRESS

FOR FASTEST SERVICE, USE THIS CARD TO FAX YOUR REQUEST DIRECTLY TO THE ADVERTISER.

PLEASE PHOTOCOPY THIS CARD FOR MULTIPLE USE.

TO: _____

FROM: _____

FAX: ( ) _____ DATE : _____

MY NEED IS:

☐ Immediate
☐ 6 - 12 Mos.
☐ 12 + Mos.

I WANT TO KNOW MORE, PLEASE...

☐ Send Literature
☐ Have a Salesman Call
☐ Send Name of Nearest Dealer
☐ Send Me a Price Quote

Description: _____

_____

Quantity: _____

I saw your... ☐ Advertisement ☐ Editorial Listing Regarding...

_____ on page _____ of the (date) _____ issue of AC

NAME:

TITLE:

COMPANY:

MAILSTOP:

STREET:

CITY: STATE: ZIP:

PHONE: FAX:

NO POSTAGE NECESSARY IF MAILED IN THE UNITED STATES

BUSINESS REPLY MAIL
FIRST CLASS MAIL PERMIT NO 307 PITTSFIELD MA

POSTAGE WILL BE PAID BY ADDRESSEE

ANALYTICAL CHEMISTRY

PO BOX 5511
PITTSFIELD MA 01203-9384

PRODUCT DATA SERVICE

Please help us determine your future laboratory buying trends. Which of the following products do you use, buy, specify, recommend or purchase? Circle all appropriate numbers on the attached reply card.

327 AA Spectroscopy
328 Analytical Services
329 Baths/Circulators
330 Biotechnology
331 Books/Periodicals
332 Centrifugation
333 Chemicals/Gases/Solvents
334 Computers/Software
335 Cooling/Freezing/Refrig.
336 Databases, Online
337 Densitometry
338 Detectors
339 Dryers/Evaporators
340 Electrochemistry
341 Elemental Analysis
342 Filtration
343 Flow Meters/Regulators
344 FT-IR Spectroscopy
345 Furnaces/Ovens
346 Gas Chromatography
347 General Lab Equipment
348 Heating/Temperature
349 Ion Chromatography
350 Lab Furniture/Hoods
351 Labware/Apparatus
352 Lasers/Fiber Optics
353 Liquid Chrom./HPLC
354 Mass Spectrometry
355 Microscopy
356 Capillary Electrophoresis
357 Mix/Stir/Blend/Grind
358 NMR Spectroscopy
359 Particle Size Analysis
360 Plasma Spectroscopy
361 pH/Ion Meters/Titrators
362 Pumping Monitoring
363 Recording/Integrating
364 Robotics/Automation
365 Sampling/Dispensing
366 Supercritical Fluid Chrom.
367 Spectrofluorometry
368 Stills/Purification
369 Surface Analysis
370 Thermal Analysis
371 Thin Layer Chrom.
372 UV-Vis Spectroscopy
373 Valves/Tubes/Fittings
374 Viscometry
375 Water/Moisture Analysis
376 Weighing/Balances
377 X-Ray Diffraction
378 X-Ray Spectroscopy

ANALYTICAL CHEMISTRY
FAX EXPRESS

FOR FASTEST SERVICE, USE THIS CARD TO FAX YOUR REQUEST DIRECTLY TO THE ADVERTISER.
PLEASE PHOTOCOPY THIS CARD FOR MULTIPLE USE.

TO: _____

FROM: _____

FAX: ( ) _____ DATE : _____

MY NEED IS:
- ☐ Immediate
- ☐ 6 - 12 Mos.
- ☐ 12 + Mos.

I WANT TO KNOW MORE, PLEASE...
- ☐ Send Literature
- ☐ Have a Salesman Call
- ☐ Send Name of Nearest Dealer
- ☐ Send Me a Price Quote

Description: _____

_____

Quantity: _____

I saw your... ☐ Advertisement ☐ Editorial Listing Regarding...
_____ on page _____ of the (date) _____ issue of AC

NAME:
TITLE:
COMPANY:
MAILSTOP:
STREET:
CITY: STATE: ZIP:
PHONE: FAX:

ANCHAM 67(13) 1913–2314 (1995)
ISSN 0003-2700

Registered in the U.S. Patent and Trademark Office

Copyright 1995 by the American Chemical Society

ANALYTICAL CHEMISTRY®

JULY 1, 1995
Volume 67, Number 13

ACCELERATED ARTICLES

*Eliza N. Fung and Edward S. Yeung** **1913** **High-Speed DNA Sequencing by Using Mixed Poly(ethylene oxide) Solutions in Uncoated Capillary Columns**

*Vinod P. Menon and Charles R. Martin** **1920** **Fabrication and Evaluation of Nanoelectrode Ensembles**

*P. Scott Clemons, Michael G. Minnich, and R. S. Houk** **1929** **Attenuation of Metal Oxide Ions in Inductively Coupled Plasma Mass Spectrometry with a Graphite Torch Injector**

Upvan Narang, M. H. Rahman, Jui H. Wang, Paras N. Prasad,* and Frank V. Bright** **1935** **Removal of Ribonucleases from Solution Using an Inhibitor-Based Sol–Gel-Derived Biogel**

*Monika Preuss and Elizabeth A. H. Hall** **1940** **Mediated Herbicide Inhibition in a Pet Biosensor**

*Randy M. Whittal and Liang Li** **1950** **High-Resolution Matrix-Assisted Laser Desorption/Ionization in a Linear Time-of-Flight Mass Spectrometer**

ARTICLES

William H. Tuminello, Ioannis V. Bletsos, Fredric Davidson, Frank J. Weigert, Nigel Simpson, and David Slinn* **1955** **Characterization of a Perfluorotetradecahydrophenanthrene Oligomer**

*Andrew N. Krutchinsky, Anatoli I. Dolguine, and Mikhail A. Khodorkovski** **1963** **Matrix-Assisted Laser Desorption Ionization of Neutral Clusters Composed of Matrix and Analyte Molecules**

Carlo Crescenzi, Antonio Di Corcia, Stefano Marchese, and Roberto Samperi* **1968** **Determination of Acidic Pesticides in Water by a Benchtop Electrospray Liquid Chromatography Mass Spectrometer**

Hing-Biu Lee and Thomas E. Peart* **1976** **Determination of 4-Nonylphenol in Effluent and Sludge from Sewage Treatment Plants**

*Michelle D. Beeson, Kermit K. Murray, and David H. Russell** **1981** **Aerosol Matrix-Assisted Laser Desorption Ionization: Effects of Analyte Concentration and Matrix-to-Analyte Ratio**

G. S. Groenewold, J. C. Ingram, A. D. Appelhans, J. E. Delmore, and B. Pesic*	**1987**	**Static SIMS Detection of Gold and Gold Cyanide Complexes on Carbon Using Crown Ether Enhancement**
Simon J. Prosser and Charles M. Scrimgeour*	**1992**	**High-Precision Determination of $^2H/^1H$ in H_2 and H_2O by Continuous-Flow Isotope Ratio Mass Spectrometry**
Robert S. Brown and John J. Lennon*	**1998**	**Mass Resolution Improvement by Incorporation of Pulsed Ion Extraction in a Matrix-Assisted Laser Desorption/Ionization Linear Time-of-Flight Mass Spectrometer**
Richard B. van Breemen	**2004**	**Electrospray Liquid Chromatography–Mass Spectrometry of Carotenoids**
*Jiaqi Wu and Janusz Pawliszyn**	**2010**	**A Capillary Cartridge with an On-line Desalting Device That Allows Fast Sampling for Capillary Isoelectric Focusing**
John W. Diehl, John W. Finkbeiner, and Frank P. DiSanzo*	**2015**	**Determination of Aromatic Hydrocarbons in Gasolines by Gas Chromatography/Fourier Transform Infrared Spectroscopy**
Yan Liu, Viorica Lopez-Avila, Jim J. Zhu, Daniel R. Wiederin, and Werner F. Beckert*	**2020**	**Capillary Electrophoresis Coupled On-Line with Inductively Coupled Plasma Mass Spectrometry for Elemental Speciation**
Chao Yan, Rajeev Dadoo, Hui Zhao, Richard N. Zare, and David J. Rakestraw*	**2026**	**Capillary Electrochromatography: Analysis of Polycyclic Aromatic Hydrocarbons**
*W. N. Moore and L. T. Taylor**	**2030**	**Solid Phase Trapping Mechanisms Involved in the Supercritical Fluid Extraction of Digitalis Glycosides with Modified Carbon Dioxide**
Michael J. Sepaniak, Christine L. Copper, Kylen W. Whitaker, and Vincent C. Anigbogu*	**2037**	**Evaluation of a Dual-Cyclodextrin Phase Variant of Capillary Electrokinetic Chromatography for Separations of Nonionizable Solutes**
*Shaorong Liu and Purnendu K. Dasgupta**	**2042**	**Liquid Droplet. A Renewable Gas Sampling Interface**
Chuzo Fujimoto	**2050**	**Charged Polyacrylamide Gels for Capillary Electrochromatographic Separations of Uncharged, Low Molecular Weight Compounds**
*Robin L. Sheppard, Xinchun Tong, Jianyi Cai, and Jack D. Henion**	**2054**	**Chiral Separation and Detection of Terbutaline and Ephedrine by Capillary Electrophoresis Coupled with Ion Spray Mass Spectrometry**
Stephen C. Jacobson, Alvin W. Moore, and J. Michael Ramsey*	**2059**	**Fused Quartz Substrates for Microchip Electrophoresis**
Ian J. Barnabas, John R. Dean, William R. Tomlinson, and Susan P. Owen*	**2064**	**Experimental Design Approach for the Extraction of Polycyclic Aromatic Hydrocarbons from Soil Using Supercritical Carbon Dioxide**
*Chao-Xuan Zhang, Franz von Heeren, and Wolfgang Thormann**	**2070**	**Separation of Hydrophobic, Positively Chargeable Substances by Capillary Electrophoresis**

Attila Felinger	**2078**	**Superposition of Chromatographic Retention Patterns**
*Kimber L. Rundlett and Daniel W. Armstrong**	**2088**	**Effect of Micelles and Mixed Micelles on Efficiency and Selectivity of Antibiotic-Based Capillary Electrophoretic Enantioseparations**
Viorica Lopez-Avila, Richard Young, Janet Benedicto, Pauline Ho, Robert Kim, and Werner F. Beckert*	**2096** ■	**Extraction of Organic Pollutants from Solid Samples Using Microwave Energy**
Johannes P. C. Vissers, Henk A. Claessens, Jozua Laven, and Carel A. Cramers*	**2103**	**Colloid Chemical Aspects of Slurry Packing Techniques in Microcolumn Liquid Chromatography**
*Anna Sjögren and Purnendu K. Dasgupta**	**2110**	**Two-Dimensional Conductometric Detection in Ion Chromatography. Analyte Identification, Quantitation of Very Weak Acid Anions, and Universal Calibration**
*Shaowei Ong and Charles Pidgeon**	**2119** ■	**Thermodynamics of Solute Partitioning into Immobilized Artificial Membranes**
N. J. Bjerrum, R. W. Berg, E. Christensen, D. H. Kerridge, and J. H. von Barner*	**2129**	**Use of Vibrational Spectroscopy To Determine Oxide Content of Alkali Metal Fluoride–Tantalum Melts**
Steven B. Shirey and Richard J. Walker*	**2136**	**Carius Tube Digestion for Low-Blank Rhenium–Osmium Analysis**
*Dario Kriz, Olof Ramström, Anders Svensson, and Klaus Mosbach**	**2142**	**Introducing Biomimetic Sensors Based on Molecularly Imprinted Polymers as Recognition Elements**
*Irene Yarovsky, Marie-Isabel Aguilar, and Milton T. W. Hearn**	**2145**	**Influence of the Chain Length and Surface Density on the Conformation and Mobility of *n*-Alkyl Ligands Chemically Immobilized onto a Silica Surface**
*Nineta Majcen, Karmen Rajer-Kanduč, Marjana Novič, and Jure Zupan**	**2154**	**Modeling of Property Prediction from Multicomponent Analytical Data Using Different Neural Networks**
Jay W. Grate, Samuel J. Patrash, and Michael H. Abraham**	**2162**	**Method for Estimating Polymer-Coated Acoustic Wave Vapor Sensor Responses**
Marco M. A. Ruyken, Joop A. Visser, and Age K. Smilde*	**2170**	**On-Line Detection and Identification of Interferences in Multivariate Predictions of Organic Gases Using FT-IR Spectroscopy**
*Vladimir M. Doroshenko and Robert J. Cotter**	**2180**	**High-Performance Collision-Induced Dissociation of Peptide Ions Formed by Matrix-Assisted Laser Desorption/Ionization in a Quadrupole Ion Trap Mass Spectrometer**
*Antoni Jurkiewicz and Gary E. Maciel**	**2188**	**^{13}C NMR Spin–Lattice Relaxation Properties and Quantitative Analytical Methodology of ^{13}C NMR Spectroscopy for Coals**
*M. L. Agüí, A. J. Reviejo, P. Yáñez-Sedeño, and J. M. Pingarrón**	**2195**	**Analytical Applications of Cylindrical Carbon Fiber Microelectrodes. Simultaneous Voltammetric Determination of Phenolic Antioxidants in Food**

*Kevin W. Hathcock, Jay C. Brumfield, Charles A. Goss, Eugene A. Irene, and Royce W. Murray**

2201 **Incipient Electrochemical Oxidation of Highly Oriented Pyrolytic Graphite: Correlation between Surface Blistering and Electrolyte Anion Intercalation**

*F. Palmisano, C. Malitesta, D. Centonze, and P. G. Zambonin**

2207 **Correlation between Permselectivity and Chemical Structure of Overoxidized Polypyrrole Membranes Used in Electroproduced Enzyme Biosensors**

*Már Másson, Kyusik Yun, Tetsuya Haruyama, Eiry Kobatake, and Masuo Aizawa**

2212 **Quartz Crystal Microbalance Bioaffinity Sensor for Biotin**

A. Sanz-Medel, M. C. Valdés-Hevia y Temprano, N. Bordel García, and M. R. Fernández de la Campa*

2216 **Generation of Cadmium Atoms at Room Temperature Using Vesicles and Its Application to Cadmium Determination by Cold Vapor Atomic Spectrometry**

Greg E. Collins and Susan L. Rose-Pehrsson*

2224 **Chemiluminescent Chemical Sensors for Oxygen and Nitrogen Dioxide**

Guillermo Orellana, Ana M. Gómez-Carneros, César de Dios, Ana A. García-Martínez, and María C. Moreno-Bondi**

2231 **Reversible Fiber-Optic Fluorosensing of Lower Alcohols**

*Ramon A. Evangelista, Ming-Sun Liu, and Fu-Tai A. Chen**

2239 **Characterization of 9-Aminopyrene-1,4,6-trisulfonate-Derivatized Sugars by Capillary Electrophoresis with Laser-Induced Fluorescence Detection**

*Alexander I. Yuzefovsky, Robert F. Lonardo, and Robert G. Michel**

2246 **Spatial Discrimination against Background with Different Optical Systems for Collection of Fluorescence in Laser-Excited Atomic Fluorescence Spectrometry with a Graphite Tube Electrothermal Atomizer**

James P. Yesinowski, Michael L. Buess, Allen N. Garroway, Marcia Ziegeweid, and Alexander Pines*

2256 **Detection of ^{14}N and ^{35}Cl in Cocaine Base and Hydrochloride Using NQR, NMR, and SQUID Techniques**

*Xiaoying He and Garry A. Rechnitz**

2264 **Linear Response Function for Fluorescence-Based Fiber-Optic CO_2 Sensors**

*Mutua J. Mattu and Gary W. Small**

2269 **Quantitative Analysis of Bandpass-Filtered Fourier Transform Infrared Interferograms**

TECHNICAL NOTES

András Guttman and Herbert E. Schwartz*

2279 **Artifacts Related to Sample Introduction in Capillary Gel Electrophoresis Affecting Separation Performance and Quantitation**

Carlo S. Effenhauser, Andreas Manz, and H. Michael Widmer*

2284 **Manipulation of Sample Fractions on a Capillary Electrophoresis Chip**

Jerry W. King, James H. Johnson, and Fred J. Eller*

2288 **Effect of Supercritical Carbon Dioxide Pressurized with Helium on Solute Solubility during Supercritical Fluid Extraction**

John O. Egekeze, Michael C. Danielski, Nelu Grinberg, George B. Smith, Daniel R. Sidler, Holly J. Perpall, Gary R. Bicker, and Patricia C. Tway* **2292** **Kinetic Analysis and Subambient Temperature Chromatography of an Active Ester**

M. Ravey, B. Farberman, I. Hendel, S. Epstein, and R. Shemer* **2296** **A Vessel for Low-Pressure Acid Dissolutions of Mineral and Inorganic Samples**

*Tzyh-Chyang Tang and Hsuan-Jung Huang** **2299** **Flow Injection Analysis of Sulfate with a Potentiometry-Based Linear Calibration Graph**

Ingrid Rohm, Wolfgang Künnecke, and Ursula Bilitewski* **2304** **UV-Polymerizable Screen-Printed Enzyme Pastes**

Günter Rinke and Christian Hartig* **2308** **UV Photometer Based on Radioluminescence with Applications in HPLC and Process Control**

■ Supporting information for this paper is available separately (consult the masthead page for ordering information); all supporting information except structure factor tables will also appear following the paper in the microfilm edition of this journal.

* In papers with more than one author, the asterisk indicates the name of the author to whom inquiries about the paper should be addressed.

Accelerated Articles

Anal. Chem. **1995,** *67,* 1913–1919

High-Speed DNA Sequencing by Using Mixed Poly(ethylene oxide) Solutions in Uncoated Capillary Columns

Eliza N. Fung and Edward S. Yeung*

Ames Laboratory—USDOE and Department of Chemistry, Iowa State University, Ames, Iowa 50011

We describe a new non-cross-linked polymer matrix and a new column treatment procedure for high-speed DNA sequencing by using capillary electrophoresis. A solution of commercially available poly(ethylene oxide) (PEO) in two size ranges is used as the sieving matrix under denaturing conditions. When compared to a commercial 6% *T* polyacrylamide solution, the mixed PEO matrix offers identical separation performance for the small DNA fragments, better performance for the large DNA fragments, increased separation speed, and a lower viscosity. To avoid degradation of the standard bonded coating on the capillary column over many runs, we evaluated the resolution of DNA fragments in the mixed PEO matrix in bare fused-silica capillaries. In a dry, fresh column, the performance is identical to that observed in coated (bonded) capillaries. To regenerate the favorable surface characteristics after each run, 0.1 N HCl was used to retitrate the surface silanol groups back to the fully protonated form. The sequencing runs in fact proceeded much faster, with bases 28–420 from the Sanger ladder eluting in a span of only 16 min. We observed little degradation of the performance over tens of sequencing runs.

Several research groups have shown that capillary gel electrophoresis (CGE) is an attractive alternative to slab gel electrophoresis (SGE) for DNA sequencing.[1-10] The medium used (cross-linked polyacrylamide), buffer composition, separation mechanism, sequencing chemistry, and tagging chemistry for CGE are all derived from proven SGE schemes. A 25-fold increase in the sequencing rate per capillary (per lane) has already been demonstrated. This is a direct consequence of the small internal diameter of the capillary tubes, typically around 50–75 μm, greatly reducing Joule heating associated with the electrical current. Gel distortions and temperature gradients that can affect resolution of the bands are thus virtually absent. More importantly, much higher electric fields can be applied to speed up the separation. For comparison, conventional SGE is limited to field strengths below 50 V/cm while CGE has been successfully used for sequencing up to 500 V/cm.[3] The unique aspect ratio of capillary gels (25–50 cm long) provides uniform field strengths, and the large surface-to-volume ratio favors efficient heat removal. These combine to produce much sharper bands than are possible in slab gels.

Early on, cross-linked polymers such as polyacrylamide[1-10] (PA) were used as gel matrices in CGE because of their known utility in slab gels for the separation of proteins and DNA. The separation performance is controlled by the pore structure of the gel matrices, which is based on the amount and characteristics

(1) Cohen, A. S.; Najarian, D. R.; Paulus, A.; Guttman, A.; Smith, J. A.; Karger, B. L. *Proc. Natl. Acad. Sci. U.S.A.* **1987,** *85,* 9660–9663.
(2) Drossman, H.; Luckey, J. A.; Kostichka, A. J.; D'Cunha, J.; Smith, L. M. *Anal. Chem.* **1990,** *62,* 900-903.
(3) Swerdlow, H.; Zhang, J. Z.; Chen, D. Y.; Harke, H. R.; Grey, R.; Wu, S.; Dovichi, N. J.; Fuller, C. *Anal. Chem.* **1991,** *63,* 2835–2841.
(4) Chen, D. Y.; Swerdlow, H. P.; Harke, H. R.; Zhang, J. Z.; Dovichi, N. J. *J. Chromatogr.* **1991,** *559,* 237–246.
(5) Baba, Y.; Tsuhako, M. *Trends Anal. Chem.* **1992,** *11,* 280–287.
(6) Luckey, J. A.; Drossman, H.; Kostichka, A. J.; Mead, D. A.; D'Cunha, J.; Norris, T. B.; Smith, L. M. *Nucleic Acids Res.* **1990,** *18,* 4417–4421.
(7) Luckey, J. A.; Smith, L. M. *Anal. Chem.* **1993,** *65,* 2841–2850.
(8) Baba, Y.; Matsuura, T.; Wakamoto, K.; Morita, Y.; Nishitsu, Y. *Anal. Chem.* **1992,** *64,* 1221–1225.
(9) Lu, H.; Arriaga, E.; Chen, D. Y.; Dovichi, N. J. *J. Chromatogr., A* **1994,** *680,* 497–501.
(10) Lu, H.; Arriaga, E.; Chen, D. Y.; Figeys, D.; Dovichi, N. J. *J. Chromatogr., A* **1994,** *680,* 503–510.

0003-2700/95/0367-1913$9.00/0 © 1995 American Chemical Society

of the monomer and cross-linking agents. However,[11] due to the instability over time, irreproducibility in the polymerization processes, and the fragile nature of the medium, cross-linked PAs in CE have not been reported to last for more than a few runs and are therefore not suitable for large-scale DNA sequencing, especially in multiplexed operation. The longevity issue also applies to ultrathin gels.[12-15] So, despite the distinct advantage of higher resolution for the large fragments in cross-linked PA, alternative sieving matrices are urgently needed.

Low to moderate viscosity entangled polymers have been used to overcome some of the above problems.[16-25] Unlike cross-linked gels, they are replaceable and more stable for use at higher temperatures and electric field strengths. Linear PA (0% *C*) has been used for the size separation of DNA or proteins by sieving.[16,17,26,27] In addition, methyl cellulose,[18,19] hydroxyalkyl cellulose,[20-22] poly(hydroxymethacrylate) and poly(ethylene glycol–methacrylate),[23] and poly(vinyl alcohol)[24,25] also have been employed for DNA separations.

Several important problems remain before entangled polymers can be routinely used for large-scale DNA sequencing. Despite the grand idea of replacing the sieving matrix after every run, implementation has been difficult. For example,[26] the pressure required to replace the PA matrix (6% *T*, 1 × TBE, 30% formamide, 3.5 M urea) in a 33-cm-long, 75-μm-i.d. capillary in 3 min is 84 atm (1.25×10^3 psi). Even more critical is that Pouiselle flow implies that the material near the capillary walls will require yet higher pressures or longer times to be cleaned out. The high pressure may preclude many simple, automated schemes for flushing out a large number of capillaries in an array.

The preparation of the linear PA polymer solutions is also difficult to control and to reproduce. Only a few laboratories have repeated success. The polymerization process depends critically on oxygen content,[28] temperature,[26] time for complete reaction, reagent purity, and contamination. While one day the Human Genome Project may drive commercial manufacturers to produce "standard" polymer mixtures, at the present time only a 10% *T* solution (700 000–1 000 000 M_n) and a solid (8 000 000 M_n) PA product is available.

A separate problem is the internal coating of the capillary tubes. Without exception, the fused-silica capillaries used in DNA sequencing by CE have all been pretreated with a bonded coating. These are mostly variations of a bonded polyacrylamide layer.[29] The reason is that electroosmotic flow (EOF) exists in bare fused-silica capillaries. In the worst case, it can expel the sieving matrix from the capillary. Even when EOF is slow, the fact that it is opposite to the migration direction of DNA fragments means long separation times. Since the net motion is dictated by ($\mu_{DNA} - \mu_{EOF}$), the corresponding difference in mobilities, the large fragments are affected much more severely than the small fragments. One therefore quickly loses the ability to read to large base numbers in the run. Unfortunately, the coating degrades with usage.[26] This is not surprising since PA, when used as the sieving medium, also breaks down with time on interaction with the typical buffers used for DNA sequencing.[11,30] There is definitely a need for better surface treatment procedures for the capillary columns to retain their integrity over many runs.

In this article, we report the performance of the separation of DNA fragments from the Sanger reaction in a mixed poly(ethylene oxide) polymer solution in capillary columns that do not have a bonded coating.[24,29]

EXPERIMENTAL SECTION

Laser-Excited Fluorescence Detection. The experimental setup is similar to that described before.[31] A high-voltage power supply (Glassman High Voltage, Whitehorse Station, NJ) was used to drive the electrophoresis. The entire electrophoresis and detection system was enclosed in a sheet-metal box with a HV interlock. A 1-mW He–Ne laser with 543.6-nm output from Melles Griot (Irvine, CA) was used for excitation. Two RG610 filters were used to block scattered light. The fluorescence signal was transferred directly through a 10-kΩ resistor to a 24-bit A/D interface at 4 Hz (Justice Innovation, Palo Alto, CA; Model DT2802) and stored in a computer (IBM, Boca Raton, FL; Model PC/AT 286).

Capillary and Reagents. Capillaries with 75-μm-i.d. and 365-μm o.d. were obtained from Polymicro Technologies (Phoenix, AZ). Coated capillaries were prepared by Hjertén's method.[29] All chemicals for preparing buffer solutions and for coating capillaries were purchased from ICN Biochemicals (Irvine, CA); acrylamide and formamide were from Sigma Chemical (St. Louis, MO); and poly(ethylene oxide) was obtained from Aldrich Chemical (Milwaukee, WI). Fuming hydrochloric acid was obtained from Fisher (Fairlawn, NJ). Polyacrylamide solution (10% v/v in water, 700 000–1 000 000 M_n) was obtained from Polysciences (Warrington, PA). PGEM/U DNA samples were obtained from Nucleic Acid Facilities (Iowa State University, Ames, IA).

Gel and Buffer Preparations. The buffer solution was prepared by dissolving 89 mM tris(hydroxymethyl)aminomethane (THAM), 89 mM boric acid, 2 mM ethylenediaminetetraacetic acid (EDTA), and 3.5 M urea in deionized water.

The sieving matrix was prepared by gradually adding 1.5 g of 8 000 000 M_n poly(ethylene oxide) (PEO) and 1.4 g of 600 000 M_n PEO in 100 mL of buffer solution at 50–60 °C. During the

(11) Swerdlow, H.; Dew-Jager, K. E.; Brady, K.; Gray, R.; Dovichi, N. J.; Gesteland, R. *Electrophoresis* **1992**, *13*, 475–483.
(12) Stegemann, J.; Schwager, C.; Erfle, H.; Hewitt, N.; Voss, H.; Zimmermann, J.; Ansorge, W. *Nucleic Acids Res.* **1991**, *19*, 675–676.
(13) Brumley, R. L.; Smith, L. M. *Nucleic Acids Res.* **1991**, *19*, 4121–4126.
(14) Kolner, D. E.; Mead, D. A.; Smith, L. M. *Biotechniques* **1992**, *13*, 338–339.
(15) Kostichka, A. J.; Marchbanks, M. L.; Brumley, R. L., Jr.; Drossman, H.; Smith, L. M. *Bio/Technology* **1992**, *10*, 78–81.
(16) (a) Heiger, D. N.; Cohen, A. S.; Karger, B. L. *J. Chromatogr.* **1990**, *516*, 33–48. (b) Cohen, A. S.; Najarian, D. R.; Karger, B. L. *J. Chromatogr.* **1990**, *516*, 49–60.
(17) Ganzler, K.; Greve, K. S.; Cohen, A. S.; Karger, B. L.; Guttman, A.; Cooke, N. C. *Anal. Chem.* **1992**, *64*, 2665–2671.
(18) Crehan, W. A. M.; Rasmussen, H. T.; Northrop, D. M. *J. Liq. Chromatogr.* **1992**, *15*, 1063–1080.
(19) Zhu, M.; Hansen, D. L.; Burd, S.; Gannon, F. *J. Chromatogr.* **1989**, *480*, 311–319.
(20) Nathakarnkitkool, S.; Oefner, P. J.; Bartsch, G.; Chin, M. A.; Bonn, G. K. *Electrophoresis* **1992**, *13*, 18–31.
(21) Ulfelder, K. J.; Schwartz, H. E.; Hall, J. M.; Sunzeri, F. *Anal. Biochem.* **1992**, *200*, 260–267.
(22) Grossman, P. D.; Soane, D. S. *J. Chromatogr.* **1991**, *559*, 257–266.
(23) Zewert, T.; Harrington, M. *Electrophoresis* **1993**, *13*, 817–824.
(24) Kleemiss, M. H.; Gilges, M.; Schomburg, G. *Electrophoresis* **1993**, *14*, 515–522.
(25) Chrambach, A.; Aldroubi, A. *Electrophoresis* **1993**, *14*, 18–22.
(26) Ruiz-Martinez, M. C.; Berka, J.; Belenkii, A.; Foret, F.; Miller, A. W.; Karger, B. L. *Anal. Chem.* **1993**, *65*, 2851–2858.
(27) Carson, S.; Cohen, A. S.; Belenkii, A.; Ruiz-Martinez, M. C.; Berka, J.; Karger, B. L. *Anal. Chem.* **1993**, *65*, 3219–3226.
(28) Chrambach, A.; Rodbard, D. *Science* **1971**, *172*, 440–450.
(29) Hjertén, S. *J. Chromatogr.* **1985**, *347*, 191–198.
(30) Starita-Geribaldi, M.; Houri, A.; Sudaka, P. *Electrophoresis* **1993**, *14*, 773–781.
(31) Chang, H.-T.; Yeung, E. S. *J. Chromatogr.*, in press.

addition of PEO, a magnetic stirring rod was used at a high setting to enhance the dissolution of the polymer powder. After the addition was complete, the solution was stirred for another 30 min. Then the solution was degassed in an ultrasonic bath for 30 min.

Capillary Wall Treatment. The bare capillary, typically 45-cm total length (35-cm effective length) was flushed with methanol for 10 min and then 0.1 N HCl for 2 h, filled with a low-viscosity polymer solution (e.g., 0.5% PEO), and then filled with the polymer matrix with a syringe. The capillary was then equilibrated at the running voltage (12 kV) for 10 min before sample injection. The DNA sample was denatured by heating in a denaturing solution (5:1 formamide–50 mM aqueous EDTA solution) at 95 °C for 2.5 min, and the injection was performed at 6 kV for 12 s. Between runs, the used polymer matrix was flushed out of the capillary with high pressure (400 psi, 3 min), rinsed with 0.1 N HCl for 15–30 min, and then filled with new polymer matrix.

Base Calling. The base calling was performed according to the method of Li and Yeung.[32] Briefly, this involves using the ratio of emission intensities recorded through two different optical filters. Independent confirmation was accomplished by comparison with data obtained on a commercial DNA sequencer (ABI).

RESULTS AND DISCUSSION

Novel Sieving Medium. In the earlier stages of our work, we used protocols that are in the literature[26,27] to prepare non-cross-linked PA solutions for DNA separations. Due to the inexperience of our personnel and the lack of direct training, e.g., in one of the leading CGE laboratories, we were not able to consistently produce sieving matrices suitable for DNA sequencing. We therefore explored the use of alternative matrices that may serve the same function.

To form a sieving medium, the concentration of polymers has to be higher than a certain value called the overlap threshold.[22] Polymer chains then interact with one another to form an entangled solution. In order to create a small mesh, one wants to use a polymer with short chains and vice versa. Poly(ethylene oxide) with a large range of molecular weights from 300 000 to 8 000 000 is available commercially. In addition, it is easy to prepare homogeneous solutions of these in typical electrophoretic buffers to provide highly reproducible separation matrices.[31] Initially, to evaluate the applicability of this alternative polymer matrix for DNA sequencing, we studied the separation performance by using the ds fragments of pBR 322 DNA/*Hae*III digest (intercalated with ethidium bromide and detected by fluorescence excited at 543 nm).[31] This sample provides a good range of fragment sizes in a simple electropherogram to allow quick comparisons. It should be noted that DNA fragments from standard Sanger reactions are denatured single-stranded and covalently tagged rather than double-stranded and intercalated with a fluorophore. One actually expects ss-DNA separations to be even more efficient because there will not be a distribution of conformations or fluorophore numbers per DNA fragment.

We found that the smaller fragments can be well separated in matrices prepared from individual polymers with M_n of 600 000–2 000 000. For DNA fragments from 80 to 400 base pairs, better resolution is achieved in matrices prepared from polymers with higher M_n. No single polymer size provided adequate efficiencies over the entire size range. Drawing from gradient elution in chromatography, we next tested mixtures of polymer sizes for the same separation.[31] In the mixed-polymer matrices, a polymer network with random pore sizes is formed. This provides optimum pore sizes for a large range of DNA fragments. The mixed-polymer matrix made from equal amounts of polymers (0.6%) with different molecular masses provided comparable resolution, while retaining a much lower viscosity, compared to all other matrices (made from single polymers) used in that study.[31] Further optimization of the ratio between the amounts of low-M_n and high-M_n materials in the mixed solutions should lead to even better separation performance.

We have successfully used these mixed polymers for actual DNA sequencing by CE. Here, we will provide a direct comparison between PEO and 6% *T* non-cross-linked PA. The test sample was the set of DNA (PGEM/U) fragment ladder prepared by the Iowa State University Nucleic Acid Facility using cycle sequencing and the standard dye-labeled terminators (ABI DyeDeoxy) and Taq polymerase. The sample preparation procedure was not altered in any way from that used to produce samples for the commercial DNA sequencing instrument (ABI). The injected sample is identical in concentration and composition to those suggested for loading into the commercial instrument. The test sample was independently analyzed (sequenced on the commercial instrument) and was found to be well-behaved. We have developed a matrix based on 1.4% PEO 600 000 M_n, 1.5% PEO 8 000 000 M_n, 1 × TBE (pH 8.2), and 3.5 M urea for DNAsequencing. Apparently, the intermediate M_n polymers[31] are not needed because the polymers at the two extremes of the size range can entangle in such a way to form the intermediate pore sizes as well. This binary matrix provides a performance very similar to the 0.7% multiple polymer matrix[31] but has even lower viscosity (1200 CP at room temperature) than the 0.7% mixture. While further optimization should be possible, all experiments below were performed in this particular matrix.

For comparison, commercial non-cross-linked PA (10% *T* solution, 700 000–1 000 000 M_n) was diluted to form a 6% *T*, 1 × TBE, 3.5 M urea matrix. This solution has a measured viscosity of 4900 CP at room temperature. This is in the general range of viscosities for home-prepared material,[26] although it is difficult to pin down the average molecular weights for each preparation. Otherwise identical conditions were used throughout. Excitation by a He–Ne laser at 543 nm and two RG610 long-pass filters select primarily the *C* and *T* fragments. The results are shown in Figures 1 and 2 for the regions of 24–108 and >420 bp, respectively. Presently, the resolution is insufficient for identifying the bases beyond 420 bp. In constructing Figures 1 and 2, the ordinate of each electropherogram was adjusted to roughly match each other and to emphasize the small peaks, as those would cause the most problems in base calling due to overlap and inadequate S/N. All peaks were in fact on scale; they were merely truncated in the figures to allow plotting one on top of another. The abscissa of each electropherogram has also been adjusted to plot the same base pair region in each case. However, the actual time scale for each is different and is listed in the captions.

Figure 1A,B shows that, for the small fragments, PEO provides a resolving power quite close to that of PA. PA is able to resolve certain partially overlapped peaks as well as shoulders next to large peaks in the first half of the plots. It should be noted that the run in Figure 1A does provide adequate resolution for base calling.[32] The major difference is separation speed. The PEO

(32) Li, Q.; Yeung, E. S., unpublished results.

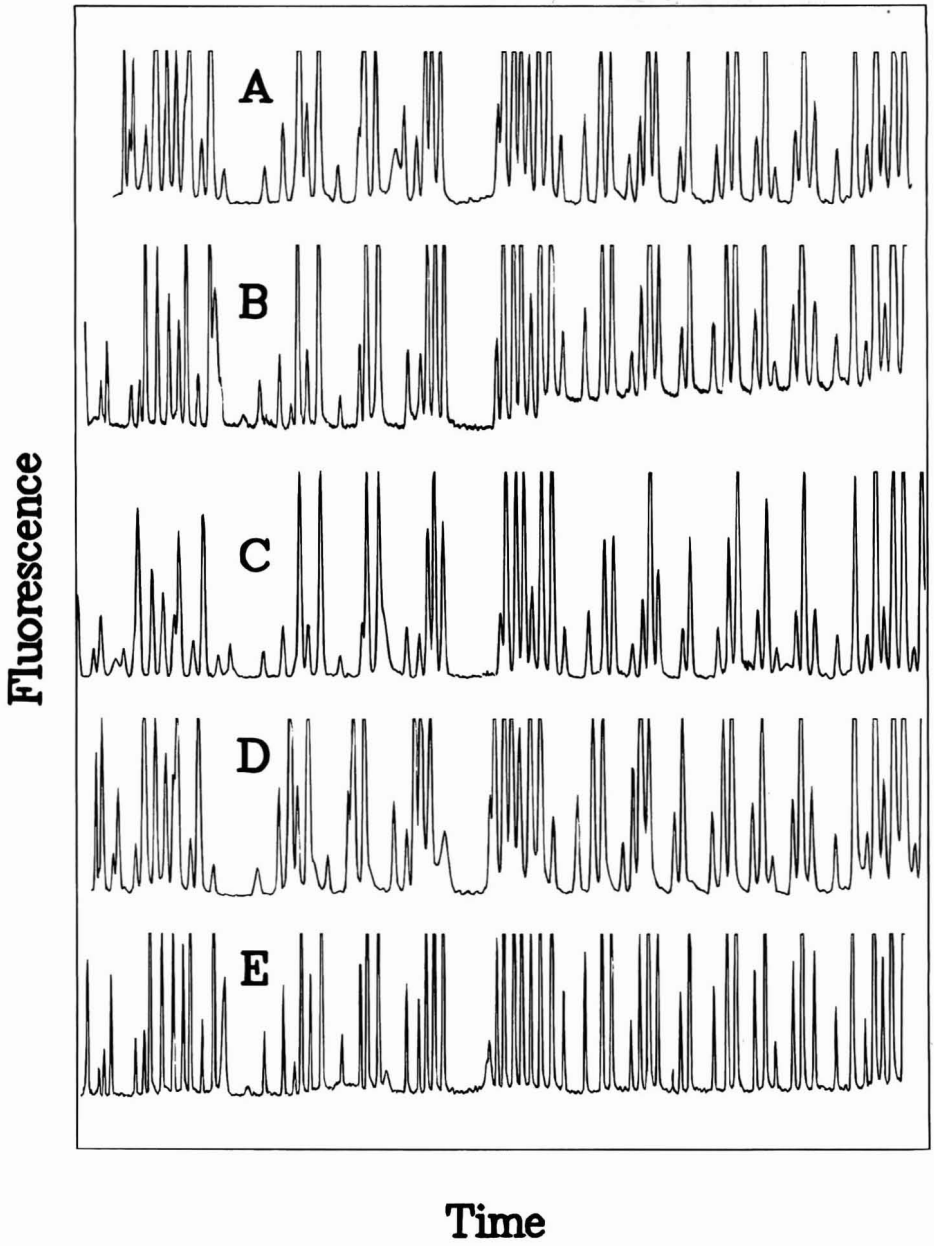

Figure 1. Separation of DNA fragments from Sanger reaction by CE from base 28 (leftmost peak) to base 108 (rightmost peak). The span of the abscissa is different in each case and is specified below: (A) PEO in coated capillary, 14–19 min; (B) PA in coated capillary, 37–55 min; (C) PEO in fresh bare capillary, 15–20.3 min; (D) PEO in HCl-reconditioned bare capillary, sixth run, 9.5–13 min; (E) PA in bare capillary, second run, 14.5–26.5 min.

plot (A) was from 14 to 19 min while the PA plot (B) was from 37 to 55 min. This is expected from the higher viscosity of the PA matrix. Very striking is the difference in separation for the large fragments, Figure 2A,B. The PEO matrix clearly provides better resolution and may even be extending the convergence limit to higher base numbers. This is important because the further one can call bases in a run the less front- and back-end work will be needed. Figure 2A,B again shows that separations run much faster in PEO than in PA. In the middle range (108–420 bp, data not shown), there is a one-to-one correspondence between the resolution of DNA fragments in PEO compared to that in PA, although some degradation is already evident in PA past 320 bp.

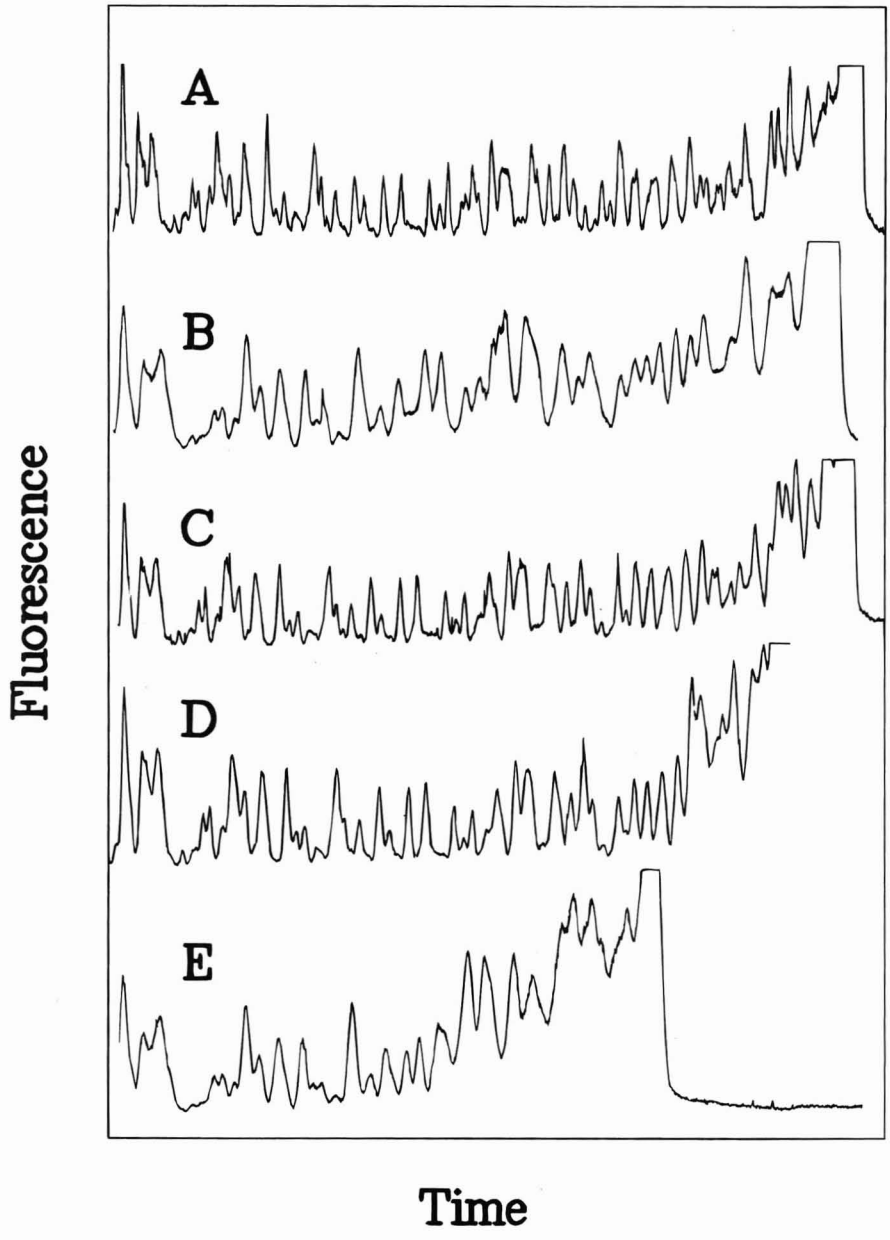

Figure 2. Separation of DNA fragments from Sanger reaction by CE from base 420 (leftmost peak) upwards. The span of the abscissa is different in each case and is specified: (A) PEO in coated capillary, 39–52 min; (B) PA in coated capillary, 111–129 min; (C) PEO in fresh bare capillary, 40–52 min; (D) PEO in HCl-reconditioned bare capillary, sixth run, 26–33 min; (E) PA in bare capillary, second run, 60–69.5 min.

It should be noted that our migration times for PA (Figures 1B and 2B) cannot be directly compared with the work of others because of differences in the way the PA matrix and the column coating was prepared. Comparisons among the times for the individual traces in Figures 1 and 2 are however valid.

There is a reasonable explanation for the differences in performance. Apparently, the maximum length of our PA polymer (up to 1 000 000 M_n) is not sufficient to form dynamic pore sizes large enough for the large DNA fragments. In fact, a PEO molecule of the same M_n should be longer than PA because of the specific atomic arrangement along the backbone. The same is true when PEO is compared with any other polymer that has been used for CE sieving. A related polymeric material is poly(ethylene glycol) (PEG). Structurally, PEG is almost identical to

PEO; only the starting monomer and the polymerization process are different. The latter is probably the main reason why commercial PEG preparations are not available out to the millions of daltons that PEO can be purchased at. Incidentally, any of the PEO polymers costs only around $10/g, and we are using 2–3% solutions in the 2-μL range per capillary.

Other workers[26,27,33] have demonstrated base calling in CE with 6% *T* PA out to >400 bp. Presumably, the home-prepared PA matrices have higher M_n components and thus include larger pore sizes in solution. The low catalyst concentration and long polymerization times at low temperatures[26] support this argument. In fact, it may well be true that a wide range of polymer lengths are (fortuitously) produced to allow non-cross-linked PA to separate a large range of DNA sizes with good efficiency. We tried to mix our PA solution with some 8 000 000 M_n PA from the same manufacturer. However, we were not able to obtain a homogeneous mixture for testing its performance.

Column Treatment Protocol. The problems with the protective coating on the internal wall of the capillary have been discussed above. Even though in principle one can replace the sieving medium after every run to allow repeated usage of the capillaries, the coating[29] gradually degrades.[11,26,30] We are not aware of any report where a capillary column has been used for tens of runs in DNA sequencing. One thought is to regenerate the coating[29] after several runs by repolymerization of PA in situ. Our experience is that the original performance cannot be restored in this manner. Another thought is to avoid the PA coating, which definitely will degrade in time.[11,30] We attempted to cap the silanol groups on the fused-silica wall by treating with [3-(methacryloxy)-propyl]trimethoxysilane (silanization) and use the capillaries without further polymerization with PA. The electroosmotic flow was indeed substantially reduced, as judged by the migration times of the primer peak and the high molecular weight convergence peak. However, the separation efficiency was compromised to the extent that calling bases beyond 200 bp was not possible.

Since the main purpose of coating the capillary column is to eliminate electroosmotic flow, we proceeded to evaluate alternative approaches toward this goal. In the zone electrophoretic separation of small molecules and even proteins, it is common to use a dynamic coating of a linear polymer such as PEG, hydroxymethyl cellulose, hydroxyethyl cellulose, methyl cellulose, or PEO. The electrophoretic buffer contains a dilute solution of these to continuously replenish the adsorbed polymer at the wall. This suggests that DNA sequencing can be performed on a bare fused-silica column. The sieving polymer will also dynamically coat and isolate the capillary walls. Even if there is some residual surface charge, the high viscosity of the polymer matrix will lead to further reduction of this undesirable counterflow during DNA separation.[34] We therefore started with commercial capillary columns and washed out the inside with methanol. Immediately afterward, the polymer matrix was introduced into the capillaries and a DNA sequencing run was started.

DNA separations in bare capillary columns are shown in Figures 1C and 2C for the PEO mixed-polymer matrix. There is practically no difference in the electropherograms with or without a coating on the capillary wall (comparing plots C with plots A). Even the actual migration times are almost identical. This is the first demonstration of DNA sequencing in CE without a bonded coating on the column wall. Unfortunately, while we can reproduce these results every time for a new capillary column, the resolution invariably started to degrade immediately (after one or two runs). The migration times became progressively longer and the largest fragment peaks became unrecognizable. Naturally, having to replace the capillary array[35] after every run is not a viable option for high-throughput DNA sequencing.

With the surprising results in Figures 1C and 2C, we attempted to regenerate the original column surface after a run by flushing with deionized water, methanol, buffer solution, 1 M NaOH, and combinations of these. In no case was the original performance restored. Finally, we realized that the symptoms associated with column degradation are those of increased electroosmotic flow in subsequent runs. For a dry, fresh column (fused-silica) surface, the silanol groups should be fully protonated. A methanol wash further minimizes any adsorbed moisture. So, initially the electroosmotic flow should be negligible. The viscous polymer matrix has the advantage of reducing the effects of any residual surface ζ potential[34] on bulk flow. However, since the separation matrix is at pH 8.2, it will eventually cause ionization of the silanol groups to increase the electroosmotic flow. The remedy is to flush the column in between runs with 0.1 N HCl, to retitrate the surface silanol groups back to their original protonated state.

The performance of a bare fused-silica CE column in separating DNA fragments after six cycles of PEO fill, DNA electrophoresis, pressure removal of PEO, and 0.1 N HCl reconditioning is shown in Figures 1D and 2D. There is no obvious difference in resolution between this electropherogram and those for coated column/PEO (Figures 1A and 2A) or for a fresh bare column/PEO (Figures 1C and 2C), except for a somewhat earlier onset of the convergence limit. This is in a region of >600 bp, where the resolution is not sufficient for calling bases and where the Taq polymerase reaction is not expected to be reliable anyway. These results are very recent; so far we have observed reproducible performance in separation efficiency over 30 runs in a 3-week period. There are slight random variations in migration times (±2% for different batches of matrix, different columns, different days), but no systematic change over time. This is to be expected since we relied on a manual flush–fill operation and have not yet defined the time and concentrations required to completely rejuvenate the column surface. Since no bonded coating is used, there is nothing to degrade and the column should in principle last indefinitely. This is the first demonstration of extended usage of a CE capillary for DNA sequencing.

A surprising result is that the migration times observed in the HCl-treated capillaries are much shorter than those found for any polymer matrix–surface preparation, either reported here or in the literature. One possible explanation is that the coating (bonded) on the capillaries and the fresh fused-silica surface both have residual electroosmotic flow to oppose DNA migration. The HCl treatment was able to eliminate electroosmotic flow entirely. Regardless of the mechanism, the bottom line is that bases 28–420 eluted within a time span of only 16 min for an average rate of 25 bp/min. This is faster by a factor of 3–5 compared to reported results using non-cross-linked PA in coated capillaries.

Finally, it is interesting to see how a non-cross-linked PA matrix performs in a bare fused-silica capillary. This is shown in Figures 1E and 2E. Resolution for the small fragments (Figure 1E) is

(33) Best, N.; Arriaga, E.; Chen, D. Y.; Dovichi, N. J. *Anal. Chem.* **1994**, *66*, 4063–4067.

(34) Lee, T. T.; Yeung, E. S. *Anal. Chem.* **1991**, *63*, 2842–2848.

(35) Ueno, K.; Yeung, E. S. *Anal. Chem.* **1994**, *66*, 1424–1431.

the best of all the systems studied here, but the resolution beyond 420 bp (Figure 2E) is the worst. This electropherogram is actually the second run on the bare column, indicating that degradation is slower than for the case of the PEO matrix on a bare column. There was still gradual degradation due to an increase in electroosmotic flow, as the first run started 0.5 min earlier and ended 10 min earlier. This is consistent with the fact that PA is a more viscous matrix, so it takes longer for the ions in the bulk medium to titrate the surface silanol groups to the same extent. Unfortunately, the same HCl-reconditioning procedure was not effective after a column was filled with PA. The implication is that we were not able to completely flush out this more viscous matrix to allow HCl to react with the surface effectively. Another possibility is that HCl causes rapid decomposition of PA[11,30] and contaminates the column surface.

System Integration. In anticipation of the need to flush out, recondition, and refill the capillary columns after each of many runs and the need to inject multiple samples separately into the array,[35] we have developed a pressure cell suitable for these operations. Note the pressure needed for this relatively low-viscosity sieving matrix is only 100–400 psi, depending on the time allowed for each operation. The cell shown in Figure 3 has been used for single-capillary operation in most of the experiments described above. For 100 capillaries in a bundle, the exit end can be gathered together to form a close-packed group of only 2 mm in diameter. This can go through the same fitting as shown in Figure 3 to implement the same recycling process.

It is worth noting that we have obtained results virtually identical to those in Figures 1A and 2A in runs derived from pressure injection of the DNA sample in the pressure cell (100 psi, 20 s). The high viscosity of the polymer matrix means that only a very narrow plug of sample was injected in a controlled manner. The electropherograms showed the same resolution as the electrokinetically injected runs in the traces in Figures 1 and 2. Actually one would expect that pressure injection will avoid the electroinjection bias[36] that discriminates against the larger DNA fragments. Evaluation of such an advantage will be performed in the next phase of this project. Finally, pressure injection avoids cross contamination of the sample from the electrodes and avoids the need to make electrical contacts with each sample vial in a large array entirely.

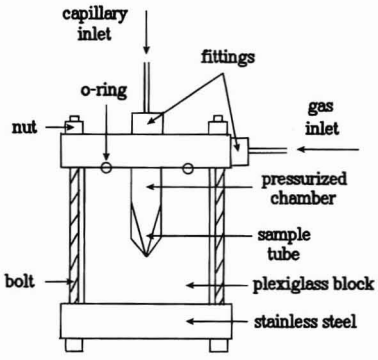

Figure 3. Pressure injection–flush cell for one capillary. About 100–500 psi can be used. Fittings are standard liquid chromatographic plumbing.

ACKNOWLEDGMENT

The Ames Laboratory is operated for the U.S. Department of Energy by Iowa State University under Contract W-7405-Eng-82. This work was supported by the Director of Energy Research, Office of Health and Environmental Research.

Received for review March 1, 1995. Accepted April 15, 1995.[⊗]

AC950217P

(36) Lee, T. T.; Yeung, E. S. *Anal. Chem.* **1992**, *64*, 1226–1231.

[⊗] Abstract published in *Advance ACS Abstracts*, May 15, 1995.

Anal. Chem. **1995,** *67,* 1920–1928

Fabrication and Evaluation of Nanoelectrode Ensembles

Vinod P. Menon and Charles R. Martin*

Department of Chemistry, Colorado State University, Fort Collins, Colorado 80523

An electroless deposition procedure for filling the pores in nanoporous filtration membranes with metal (gold) nanowires is described. This method allows us to routinely prepare ensembles of gold nanodisk electrodes in which the nanodisks have diameters as small as 10 nm. Results of electrochemical experiments at ensembles of 30- and 10-nm-diameter gold disk electrodes are described. The electrochemical response characteristics of these nanoelectrode ensembles are in agreement with predictions of the relevant electrochemical theories. Cyclic voltammetric detection limits for electroactive species at ensembles containing 10-nm-diameter gold disks can be as much 3 orders of magnitude lower than those at large-diameter gold disk electrodes.

Electrochemistry at electrodes with microscopic dimensions constitutes one of the most important frontiers in modern electrochemical science.[1] Such electrodes offer a myriad of opportunities including the possibility of doing electrochemistry in highly resistive media[2–4] and the possibility of investigating the kinetics of redox processes that are too fast to be studied at electrodes of conventional dimensions.[5–9] Numerous methods for preparing microscopic electrodes have been devised,[10] and it is now fairly easy to make electrodes with dimensions on the order of micrometers (e.g., a 5-μm-diameter metal disk).[8]

While White's group has developed a method for preparing band electrodes with nanoscopic bandwidths,[11] making nanoscopic disk-shaped electrodes (e.g., diameters less than 100 nm) has proven to be a much more elusive goal.[12–14] This is, however, an extremely important goal because theory predicts that such truly nanoscopic electrodes could be useful for studying the kinetics of ultrafast electron transfer reactions.[15] In addition, interesting and unusual electrochemical phenomena have been predicted to occur at such nanoscopic electrodes.[16] Diffusion to ensembles of nanoelectrodes is also quite interesting.[17] Hence, this is an area of science where theory is ahead of experimental practice due to the difficulties in preparing truly nanoscopic electrodes.

We have previously shown that the pores in microporous filtration membranes can be used as templates for the preparation of ensembles of microdisk electrodes.[18,19] The membranes employed contain cylindrical pores with uniform diameters. We electrochemically deposited metal microwires within these pores; the ends of these microwires (at one face of the membrane) defined the microscopic disk-shaped electrodes. Unfortunately, the smallest electrodes we could achieve using electrochemical deposition of metal within the pores of such membranes had diameters on the order of 200 nm.[18]

In this report we introduce a new electroless deposition procedure for filling the pores of such membranes with metal (gold) nanowires. This electroless deposition chemistry allows us to routinely prepare ensembles of gold nanodisk electrodes in which the nanodisks have diameters as small as 10 nm. We describe the results of electrochemical experiments at ensembles of 30- and 10-nm-diameter gold disk electrodes. We show via comparisons of experimental and simulated cyclic voltammograms, and through other experimental data, that the electrochemical response characteristics of these new nanoelectrode ensembles are in agreement with predictions of the relevant electrochemical theories. We also show that cyclic voltammetric detection limits for electroactive species[19] at ensembles containing 10-nm-diameter gold disks can be as much as 3 orders of magnitude lower than those at large-diameter (3.17 mm) gold disk electrodes.

EXPERIMENTAL SECTION

Materials. Anhydrous $SnCl_2$ (Aldrich), $AgNO_3$ (Spectrum), trifluoroacetic acid, Na_2SO_3, NH_4OH, formaldehyde, anhydrous methanol, and concentrated HNO_3 (Mallinckrodt) were used as received. Commercial gold electroless plating solution (Oromerse Part B, Technic Inc.) was diluted (40 times with water) prior to use. Milli Q 18-MΩ water was used for rinsing and for all solutions. $NaNO_3$ (Mallinckrodt) and $Ru(NH_3)_6Cl_3$ (Strem) were recrystallized prior to use. [(Trimethylamino)methyl]ferrocene ($TMAFc^+$) perchlorate was prepared by metathesis from the iodide salt[20] and recrystallized. The iodide salt was prepared from

(1) Montenegro, M. I., Queiros, M. A., Daschbach, J. L., Eds. *Microelectrodes: Theory and Applications;* NATO ASI Series 197, Series E: Applied Sciences; Kluwer: Dordrecht, The Netherlands, 1990.
(2) Drew, S. M.; Wightman, R. M. *J. Electroanal. Chem.* **1991,** *317,* 117–124.
(3) Bento, M. F.; Medeiros, M. J.; Montenegro, M. I.; Beriot, C.; Pletcher, D. *J. Electroanal. Chem.* **1993,** *345,* 273–286.
(4) Reference 1, Section 3, pp 177–189.
(5) Russell, A.; Repka, K.; Dibble, T.; Ghoroghchian, J.; Smith, J. J.; Fleischmann, M.; Pitt, C. H.; Pons, S. *Anal. Chem.* **1986,** *58,* 2961–2964.
(6) Bond, A. M.; Henderson, T. L. E.; Mann, D. R.; Thormann, W.; Zoski, C. G. *Anal. Chem.* **1988,** *60,* 1878–1882.
(7) Oyama, N.; Ohsaka, T.; Yamamoto, N.; Matsui, J.; Hatozaki, O. J. *Electroanal. Chem.* **1989,** *265,* 297–304.
(8) Karpinski, Z. J.; Osteryoung, R. A. *J. Electroanal. Chem.* **1993,** *349,* 285–297.
(9) Safford, L. K.; Weaver, M. J. *J. Electroanal. Chem.* **1992,** *331,* 857–876.
(10) Reference 1, Section 4, pp 189–227.
(11) Morris, R. B.; Franta, D. J.; White, H. S. *J. Phys. Chem.* **1987,** *91,* 3559–3564.
(12) Penner, R. M.; Heben, M. J.; Longin, T. L.; Lewis, N. S. *Science* **1990,** *250,* 1118–1121.
(13) Pendley, B. P.; Abruna, H. D. *Anal. Chem.* **1990,** *62,* 782–784.
(14) Sabatani, E.; Rubinstein, I. *J. Phys. Chem.* **1987,** *91,* 6663–6669.
(15) Bond, A. M.; Oldham, K. B.; Zoski, C. G. *Anal. Chim. Acta* **1989,** *216,* 177–230.
(16) Smith, C. P.; White, H. S. *Anal. Chem.* **1993,** *65,* 3343–3353.
(17) Sharifker, B. R. *J. Electroanal. Chem.* **1988,** *240,* 61–76.
(18) Penner, R. M.; Martin, C. R. *Anal. Chem.* **1987,** *59,* 2625–2630.
(19) Cheng, I. F.; Whiteley, L. D.; Martin, C. R. *Anal. Chem.* **1989,** *61,* 762–766.

0003-2700/95/0367-1920$9.00/0 © 1995 American Chemical Society

Table 1. Characteristics of the Membranes Used To Prepare the NEEs

pore diameter[a] (nm)	pore density (pores/cm^2)[a]	average center-to-center distance (nm)[b]	fractional pore area[c]	fractional electrode area[d]
30	6×10^8	200	0.0042	0.0045
10	6×10^8	200	0.00047	0.00094

[a] From Poretics Inc. product literature. [b] Calculated from eq 1 in ref 19. [c] Calculated from nominal pore size and density. [d] Obtained experimentally from double layer charging currents.

[(dimethylamino)methyl]ferrocene (Aldrich) according to the established procedure.[21] $K_4[Mo(CN)_8]$ was synthesized according to the established procedure and purified.[22]

"Track-etch" [23] polycarbonate membrane filters were obtained from Poretics. Filters with pore diameters of 10 and 30 nm were used to make the nanoelectrode ensembles (NEEs). The pore densities and average center-to-center distances between pores for these membranes are shown in Table 1. Multiplying the pore density (pores/cm^2) by the cross-sectional area of a single pore (cm^2/pore) provides a parameter called the fractional pore area[18,19,24,25] (Table 1). This is an important parameter because, assuming that each pore produces an active nanodisk electrode, the fractional pore area is equivalent to the fractional electrode area, which is the sum of the areas of the Au nanodisk elements in the NEE divided by the geometric area of the NEE. We have shown that the fractional electrode area can be determined experimentally from the double-layer charging currents obtained at the NEE.[18,19] Ideally, this experimental fractional electrode area and the fractional pore area should be equivalent (Table 1). Finally, these membranes have a "rough" and a "smooth" face.[19] The rough face has a dull (i.e., nonshiny) appearance.

Electrochemical and Other Measurements. Cyclic voltammetry was used to explore both the faradaic and the double-layer charging currents at the NEEs. Electrochemical measurements were made with a PAR Model 273 potentiostat in conjunction with a PAR Model 175 programmer and a Soltec Model VP6424S *X*–*Y* recorder or a Nicolet Model 310 digital storage oscilloscope. A 90% *iR* compensation was employed for all measurements.[18] All solutions were purged with nitrogen prior to use. Scanning electron micrographs were obtained on a Philips 505 microscope. Transmission electron micrographs were obtained on a JEOL 2000. Digital simulations were carried out using DIGISIM (BAS Inc.), a cyclic voltammetric simulations program, running on an Applied Computer Technology Model 486/66-520 E/S computer.

Electroless Deposition. Electroless metal deposition involves the use of a chemical reducing agent to plate a metal from solution onto a surface.[26] The advantage of the electroless method (relative to electrochemical plating) is that the surface to be coated need not be electronically conductive. The key requirement of an electroless deposition bath of this type is to arrange the chemistry such that the kinetics of homogeneous electron transfer from the reducing agent to the metal ion are slow. This is essential because otherwise the metal ion would simply be reduced in the bulk solution. A catalyst that accelerates the rate of metal ion reduction is then applied to the surface to be coated. In this way, metal ion is reduced only at the surface, and the surface becomes coated with the desired metal.

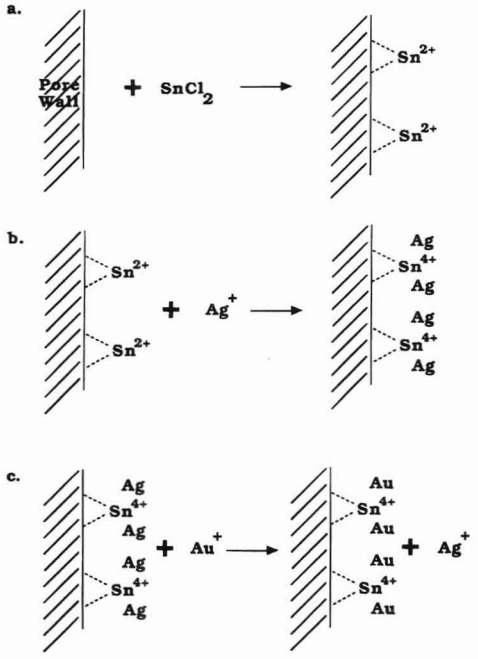

Figure 1. Schematic diagram of the electroless procedure used to deposit gold in the pores of the polycarbonate template membrane.

The electroless deposition chemistry used here is shown schematically in Figure 1. Prior art in the electroless deposition field[27] was very useful in developing this chemistry; however, we have made significant modifications in the prior art in order to make this process compatible with the membrane chemistry and with the objective of plating gold uniformly in nanoscopic pores. A "sensitizer" (Sn^{2+}) was first applied to the surfaces (pore walls plus faces) of the membrane. This was accomplished by simply immersing the membrane in a solution that was 0.026 M in $SnCl_2$ and 0.07 M in trifluoroacetic acid; the solvent was 50/50 methanol/water. The membrane was immersed in this solution for 3 min. The membrane was then rinsed with three 100-mL portions of methanol. Sn^{2+} adheres to the pore walls (Figure 1a) and membrane faces because the membrane is coated with a layer of poly(vinylpyrrolidone) (PVP) during production. This is done in order to render the membranes hydrophilic. PVP contains metal-ion-complexing amine and carbonyl groups. We believe that these groups act as "molecular anchors" [28] that bond the Sn^{2+} to the surfaces of the membrane (Figure 1a).

(20) Szentirmay, M. N.; Martin, C. R. *Anal. Chem.* **1984**, 56, 1898–1902.
(21) Lindsay, J. K.; Hauser, C. R. *J. Org. Chem.* **1957**, *22*, 355–358.
(22) Van de Poel, J.; Neuman, H. M. *Inorg. Synth.* **1968**, *11*, 53–56.
(23) Fleischer, R. L.; Price, P. B.; Walker, R. M. *Nuclear Tracks in Solids, Principles and Applications*; University of California Press: Berkeley, CA, 1975.
(24) Amatore, C.; Savéant, J. M.; Tessier, D. *J. Electroanal. Chem.* **1983**, *147*, 39–51.
(25) Gueshi, T.; Tokuda, K.; Matsuda, H. *J. Electroanal. Chem.* **1978**, *89*, 247–260.
(26) Mallory, G. O., Hajdu, J. B., Eds. *Electroless Plating: Fundamentals and Applications*; American Electroplaters and Surface Finishers Society: Orlando, FL, 1990; Chapter 1, pp 1–55.
(27) Reference 24, Chapter 17, pp 441–444.
(28) Brumlik, C. J.; Menon, V. P.; Martin, C. R. *J. Mater. Res.* **1994**, *9*, 1174–1183.

The Sn^{2+}-sensitized membrane was then activated by immersion in an aqueous solution of ammoniacal $AgNO_3$ (0.029 M)[29] for 2 min. This causes a redox reaction in which the surface-bound Sn(II) is oxidized to Sn(IV) and the Ag^+ is reduced to elemental Ag; some silver oxide is also obtained.[30] As a result, the pore walls and membrane faces become coated with discrete, nanoscopic Ag particles (Figure 1b). After Ag deposition, the membrane was rinsed in two 100-mL portions of methanol and then immersed in water. These processes of Sn(II) activation followed by reduction of Ag(I) to Ag(0) have been studied in detail on glass surfaces.[27]

The Ag-coated membrane was then immersed in a Au plating bath that was 7.9×10^{-3} M in $Na_3Au(SO_3)_2$ (the diluted form of the commercial plating solution), 0.127 M in Na_2SO_3, and 0.625 M in formaldehyde; the temperature of this bath was ~2 °C. The Ag particles are galvanically displaced by Au since gold is a more noble metal. As a result, the pore walls and faces become coated with Au particles (Figure 1c). These particles are excellent catalytic sites for the oxidation of formaldehyde and the concurrent reduction of Au(I) to Au(0). As a result, gold plating continues on the gold particles, with formaldehyde as the reducing agent. This reaction can be represented as follows:

$$2Au(I) + HCHO + 3OH^- \rightarrow HCOO^- + 2H_2O + 2Au \quad (1)$$

Au plating was continued for a period of 24 h, resulting in the deposition of Au nanowires (see below) into the pores. In addition, both faces of the membrane become coated with thin (~500 nm thick) Au films. We refer to this membrane that has Au films on both faces and Au nanowires running through the pores as the Au/Au-PC/Au membrane, where Au-PC stands for the Au-nanowire-containing polycarbonate. After plating, the Au/Au-PC/Au membrane was thoroughly rinsed with water and then immersed in 25% nitric acid for 12 h. This was done to dissolve any residual Sn or Ag that might be left in the membrane. The membrane was then rinsed thoroughly in water and air-dried.

NEE Fabrication. The NEE fabrication procedure is shown schematically in Figure 2. A 5-mm × 6-mm piece of the Au/Au-PC/Au membrane is first affixed to a 6-mm × 15-mm piece of adhesive aluminum foil tape (All-Foils Inc.) (Figure 2a). The Au/Au-PC/Au membrane is placed on the Al foil tape such that the Au film covering the rough face (see above) of the membrane is down (i.e., against the adhesive). A rectangular strip (6 mm × 40 mm) of a copper foil, with a conductive adhesive (3M Scotch brand electrical tape No. 1739-7), is then affixed to the upper Au-coated surface of the Au/Au-PC/Au membrane. (The adhesive is conductive because it contains Ni particles.) The copper foil is positioned such that it covers only about 1 mm of the 6-mm length of the Au/Au-PC/Au membrane (Figure 2b).

This Cu foil tape acts as a current collector and working electrode lead for the NEE. The upper Au surface layer from the portion of the Au/Au-PC/Au membrane not covered by the Cu foil tape is then removed by simply applying and then removing a strip of Scotch tape (3M Scotch brand Magic tape No. 810) (Figure 2c). Removal of the Au surface layer exposes the disk-shaped ends of the Au nanowires within the pores of the membrane (Figure 2c). These nanodisks will become the active electrode elements.

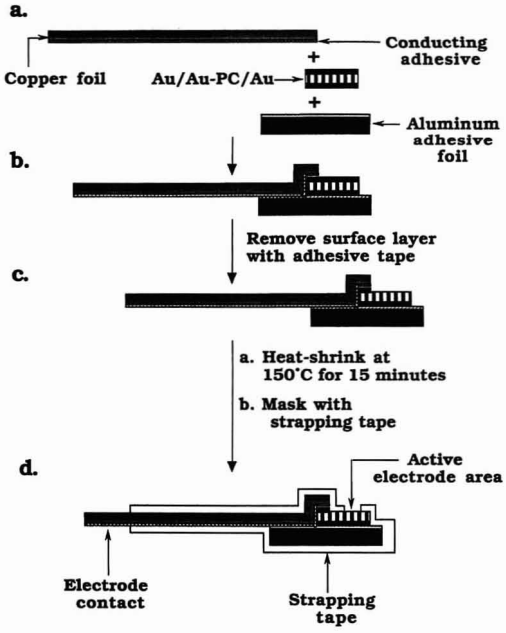

Figure 2. Schematic diagram of the fabrication of the nanoelectrode ensembles.

At this point, the NEE assembly is heat-treated at 150 °C for 15 min. As will be discussed in detail below, this produces a water-tight seal between the Au nanowires and the pore walls. Finally, strips of strapping tape (3M Scotch brand No. 898) are applied to the lower and upper surfaces of the assembly to insulate the Al and Cu foil tapes (Figure 2d). A 0.079-cm^2 hole is punched into the upper piece of tape prior to placement on the assembly. This hole defines the area of the NEE that is exposed to the solution. We refer to this area as the geometric area of the NEE. The active electrode area of the NEE is this geometric area multiplied by the fractional electrode area (Table 1).[18,19] The electrochemical response at the NEEs was compared to that of a "macroscopic" Au disk electrode that had an active area equivalent to the geometric area of the NEE, 0.079 cm^2. This gold macrodisk electrode was obtained from BAS Inc.

Optical Characterization of the NEEs. Nanometals have interesting and characteristic optical properties.[31,32] Optical absorption spectra of the Au nanowire-containing membranes were obtained by removing both of the Au surface layers from the Au/Au-PC/Au membranes. A piece of the resulting Au-PC membrane was then placed in the beam of a Hitachi U-3501 UV/visible/near-IR spectrophotometer, and a conventional transmittance spectrum of the membrane was obtained.[31,32]

RESULTS AND DISCUSSION

Au Deposition and NEE Fabrication. The key feature of the electroless deposition process is that Au deposition begins at

(29) Furness, R. W. *The practice of plating on plastics*; Robert Draper Ltd.: Surrey, U.K., 1968; Chapter 8, pp 41–42.
(30) McDermott, J. *Plating of Plastics with Metals*; Noyes Data Corp.: Park Ridge, NJ, 1974; p 181.
(31) Foss, C. A.; Hornyak, G. L.; Stockert, J. A.; Martin, C. R. *J. Phys. Chem.* **1992,** *96,* 7497–7499.
(32) Foss, C. A.; Hornyak, G. A.; Stockert, J. A.; Martin, C. R. *J. Phys. Chem.* **1994,** *98,* 2963–2971.

the pore wall. As a result, after brief deposition times, a hollow Au tubule is obtained within each pore.[33] These tubules can be imaged by taking transmission electron micrographs of microtomed sections of the tubule-containing membrane. An image of this type for a membrane that contained 50-nm-diameter pores is shown in Figure 3A. The Au tubules (black rings) appear elliptical (and ragged) due to distortion by the microtoming process.

Scanning electron microscopy can be used to image the surface of the membrane after removal of the Au surface layer. An image of this type for a membrane that contained 30-nm-diameter pores is shown in Figure 3B. Nearly circular Au disks with diameters of ~30 nm are observed at the surface. Ideally all of the pores should make an angle of 90° with the membrane surface. In fact, however, pores that vary by as much as ±34° from the surface normal are obtained. Since electrons are capable of penetrating through some finite thickness of the polycarbonate membrane, small portions of the Au nanowires in the angled tracks are visible in the electron micrograph. This is responsible for the streaks observed in the micrograph (Figure 3B). Counting the number of nanodisks observed in such images allows for an experimental evaluation of the pore density. We have found that the pore densities for these membranes are, within experimental error, identical to the values supplied by the manufacturer (Table 1).

Finally, dissolving away the polycarbonate template membrane in dichloromethane[18] (after removing both Au surface layers) allows us to view the Au nanowires that extend through the membrane thickness. Figure 3C shows a scanning electron micrograph of nanowires grown in a 50-nm-pore diameter membrane. As expected, these nanowires are ~6 μm in length (the thickness of the membrane).

As indicated in Figure 2, the NEEs were fabricated by applying the bottom surface of the Au/Au-PC/Au membrane to Al foil tape and then applying a Cu foil tape with a conductive adhesive to the upper surface of the membrane. The alternative would be to simply apply the Cu foil tape to the bottom of the Au/Au-PC/Au membrane and thus eliminate the need for the Al foil tape. The adhesive used for the Cu foil is conductive because it contains Ni particles. When this foil was applied directly to the bottom of the Au/Au-PC/Au membrane, the Ni particles often punctured the membrane. Applying the Al foil tape to the bottom of the Au/Au-PC/Au membrane, and then making electrical contact from the top with the Cu foil tape, prevents punctures in the region of the membrane that is exposed to the solution (Figure 2).

Optical Properties of the NEEs. Nanometals have interesting optical properties. For example, suspensions of nanoscopic Au particles can be pink, purple, or blue depending on the diameter of particles.[34] These colors arise from the plasmon resonance absorption of the nanometal particle, a phenomenon we have explored in some detail.[31,32] We have shown that membranes containing Au nanowires like those described here also show this plasmon resonance band, and as a result, such membranes can show a wide variety of colors.[31,32,35] This absorption in the visible region provides an interesting optical approach for characterizing the Au nanowire-containing membranes.

Figure 4 compares absorption spectra for membranes containing 10- and 30-nm-diameter Au nanowires. Note that the wavelength of maximum absorption intensity for the membrane

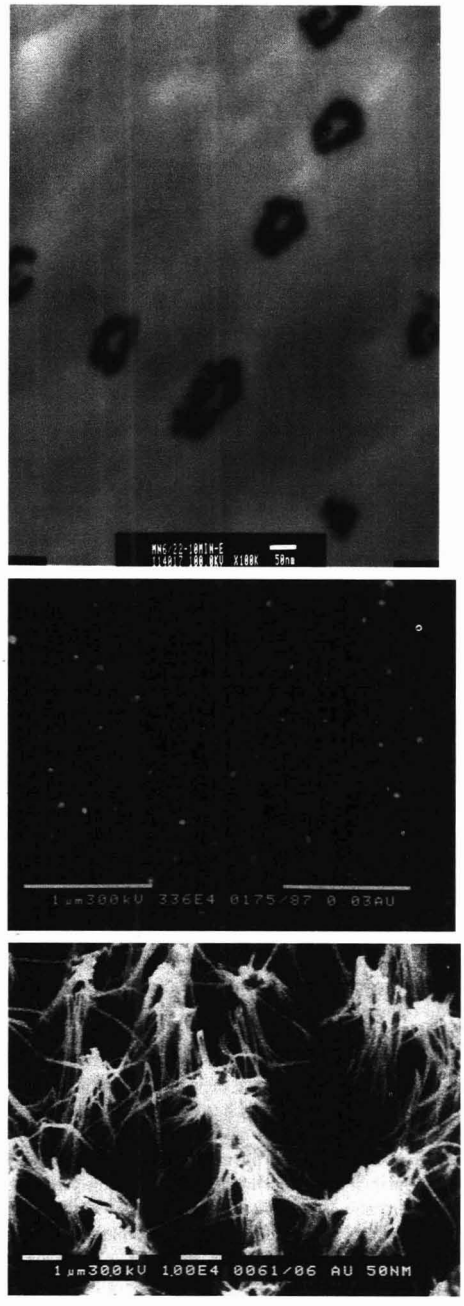

Figure 3. (A, top) Transmission electron micrograph of a microtomed section of a polycarbonate template membrane after deposition of Au tubules within the pores of the membrane. Pore diameter was 50 nm; plating time was 10 min. (B, middle) Scanning electron micrograph of surface of a 30NEE. (C, bottom) Scanning electron micrograph of Au nanowires (50 nm diameter) obtained after dissolving away the polycarbonate template membrane. In micrographs B and C, the sample was sputtered with a thin (<30 nm) layer of Au prior to imaging in order to eliminate surface charging.

(33) Nishizawa, M.; Menon, V. P.; Martin, C. R. *Science*, in press.
(34) Van de Hulst, H. C. *Light Scattering by Small Particles*; Dover Publications, Inc.: New York, 1981; p 397.
(35) Martin, C. R. *Science* **1994,** *266,* 1961–1966.

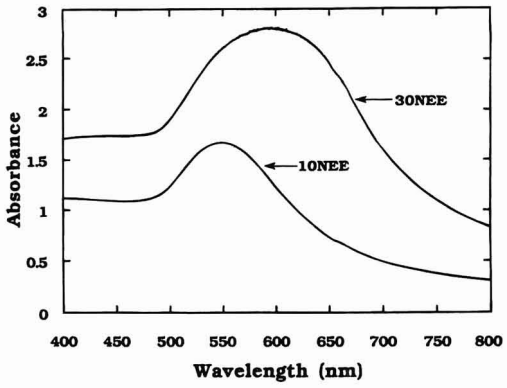

Figure 4. UV–vis spectra of a 30NEE and a 10NEE.

containing the 10-nm-diameter nanowires is blue-shifted relative to that for the membrane containing the 30-nm-diameter nanowires. This blue shift for the smaller diameter nanowires is in qualitative agreement with the predictions of effective medium theory.[31,32] As would be expected from the spectra shown in Figure 4, the membranes containing the 10-nm-diameter nanowires appear pink in color, whereas the membranes containing the 30-nm-diameter nanowires are purple. Because of these distinctive colors, it is easy to distinguish the 30-nm-disk diameter NEEs (30NEEs) from the 10-nm-disk diameter NEEs (10NEEs).

Double-Layer Charging Currents. A persistent problem with micro- and nanoelectrodes is the sealing of the conductive element to the insulating material that surrounds the element such that solution does not creep into this junction.[18,36] This solution creeping is undesirable because it causes the double-layer charging currents to be spuriously large.[18,36] Previous methods for improving the seal have included silanizing of the surrounding insulator[36] and impregnating the junction between the electrode and the insulating material with low molecular weight polyethylene.[18] However, neither of these methods has proven completely satisfactory. In this report we introduce a superior method for sealing the junction between the Au nanowires and the polycarbonate host membrane. This method exploits the heat-shrinkability of the template membrane.

The polycarbonate membranes are stretch-oriented during fabrication in order to improve their mechanical properties. If the membrane is subsequently heated above its glass transition temperature (~150 °C), the polymer chains relax to their unstretched conformation, and the membrane shrinks. This shrinking of the membrane around the Au nanowires in the pores causes the junction between the nanowire and the pore wall to be sealed. This is illustrated in Figure 5, which shows voltammograms for $TMAFc^+$ before (Figure 5A) and after (Figure 5B) the heat treatment procedure. Before heat treatment, the double-layer charging currents are pronounced. In contrast, after heat treatment, the charging currents are not discernible at the current sensitivity setting used.

We have used voltammetric measurements in the absence of the electroactive species to quantitatively evaluate this new heat-sealing procedure. The magnitude of the double-layer charging

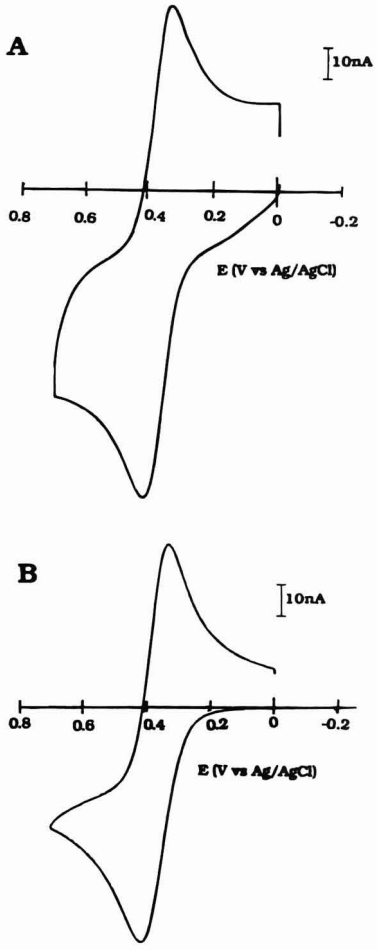

Figure 5. Cyclic voltammograms at 100 mV/s at a 10NEE in 5 μM aqueous $TMAFc^+$ and 1 mM $NaNO_3$ (A) before thermal treatment and (B) after thermal treatment of the NEE.

current can be obtained from these voltammograms,[18,19] and this allows for a determination of the fractional electrode area (Table 1). This experimental fractional electrode area can then be compared to the fractional pore area calculated from the known pore diameter and density of the membrane (Table 1). In order to use this method, the double-layer capacitance of the metal must be known.[18,19] The double-layer capacitance of Au was determined from measurements of charging currents at Au macrodisk electrodes of known area (Figure 6, curve a). A value of 21 μF cm^{-2} was obtained.

Figure 6 compares double-layer charging currents obtained at a 10NEE, a 30NEE, and a Au macrodisk electrode with an active area equal to the geometric areas of the NEEs. As would be expected, the charging currents at the NEEs are significantly lower than those at the macrodisk electrode. The fractional electrode areas obtained from the double-layer charging currents at the NEEs are shown in Table 1. The fractional electrode area for the 30NEE is, within experimental error, identical to the fractional pore area (Table 1). This indicates that all pores are

(36) Wehmeyer, K. R.; Wightman, R. M. *J. Electroanal. Chem.* **1985,** *196,* 417–421.

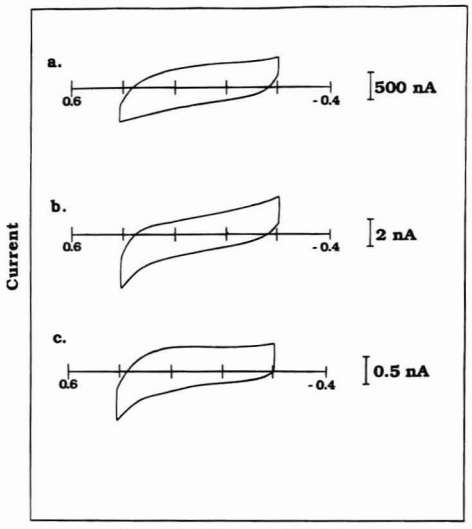

Figure 6. Background cyclic voltammograms in 50 mM sodium nitrate at 100 mV/s for (a) a gold macrodisk electrode, (b) a 30NEE, and (c) a 10NEE. The geometric area for all electrodes was 0.079 cm^2.

filled with Au and that the heat-shrinking procedure used to seal the 30-nm-diameter Au nanowires that run through the membrane is quite effective.

The fractional electrode area at the 10NEE is within a factor of 2 of the fractional pore area. This larger-than-expected fractional electrode area may result from a small amount of solution leakage around the 10-nm-diameter Au nanowires. The alternative possibility is that the pore density and/or pore size determined by electron microscopy is slightly off. This is a likely possibility because it is difficult to image 10-nm structures using scanning electron microscopy. Given the general observation that the sealing problem for a micro- or nanoelectrode becomes worse as the diameter of the electrode decreases,[18,36] the agreement between the fractional electrode areas and the fractional pore areas (Table 1) is satisfactory.

Faradaic Currents. The nature of the faradaic currents observed at a NEE depends on the distance between the electrode elements and the time scale (i.e., scan rate) of the experiment.[17-19,24] The NEEs used here are in the "total-overlap" [17-19,24] response regime. In this total overlap regime, the diffusion layers at the individual elements of the NEE have overlapped to produce a diffusion layer that is linear to the entire geometric area of the NEE.[17-19,24] As a result, conventional peaked-shaped voltammograms are obtained. Indeed, for the reversible case, the voltammogram at a NEE operating in this total overlap regime should be identical to the voltammogram obtained at a macrodisk electrode with active area equivalent to the geometric area of the NEE.[17-19,24]

Experimental and simulated cyclic voltammograms for a solution that was 5 μM in $TMAFc^+$ and 0.5 mM in supporting electrolyte (sodium nitrate) are shown in Figure 7. The experimental data were obtained at a 10NEE. In agreement with the above discussion, the experimental voltammograms are peak

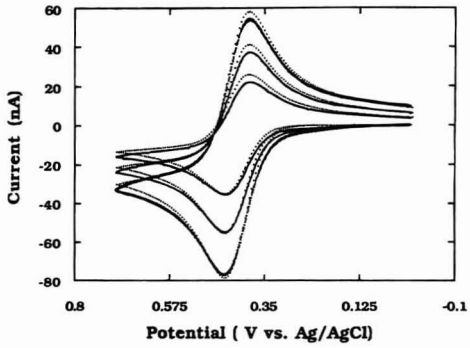

Figure 7. Simulated (···) and experimental (—) voltammograms at 100 mV/s at a 10NEE (0.079 cm^2 geometric area) in 5 M $TMAFc^+$ and 0.5 mM sodium nitrate. Simulation assumes the total overlap limiting case (i.e., a macroelectrode with area 0.079 cm^2).

shaped, and peak current increases with the square root of the scan rate. This latter point is proven by the agreement between the experimental and simulated voltammograms. The simulated data were obtained by assuming reversible electrochemistry at a macrodisk electrode with active area equivalent to the geometric area of the NEE. Other than an arbitrarily high value assumed for the standard heterogeneous rate constant, there are no adjustable parameters in these simulations. The quantitative agreement between the experimental and simulated voltammograms indicates that the reversible, total overlap limiting case is, indeed, operative at the NEE.

Three other comments are worth making regarding the data in Figure 7. First, the concentrations of both the electroactive species (5 μM) and the supporting electrolyte (0.5 mM) are low. Low concentrations were used because we have discovered an interesting effect of supporting electrolyte concentration on the electrochemistry observed at the NEEs: the reversibility of the voltammetric waves for all couples investigated to date ($TMAFc^{+/2+}$, $Ru(NH_3)_6^{3+/2+}$, and $Mo(CN)_8^{4-/3-}$) improves as the concentration of supporting electrolyte decreases (see below). This is why low concentrations of supporting electrolyte (and correspondingly low concentrations of electroactive species) were used here.

Second, it is possible that such low supporting electrolyte concentrations exacerbate problems of uncompensated solution resistance. At the concentration of electroactive species and the scan rates used here, the currents at the NEEs are low (e.g., <100 nA in Figure 7). As a result, uncompensated solution resistance distorts the voltammograms to a negligible extent, even at the millimolar supporting electrolyte concentrations used here. Indeed, voltammograms with and without application of 90% *iR* compensation are identical.

Third, the experimental voltammograms in Figure 7 have not been corrected for background currents. Nevertheless, the agreement between the experimental and simulated voltammograms (where only faradaic currents are simulated) is good. Background subtraction is not necessary at these scan rates, because the double-layer charging currents at the NEEs are orders of magnitude lower than those at a macroelectrode of equivalent geometric area (Figure 6). Because the faradaic currents at the NEE and the macroelectrode are, for the reversible case, identical (Figure 7), this diminution in the background currents also means the signal-to-background ratio[14,19] at the NEE is orders of

magnitude larger than that at the macroelectrode. This point will be explored further below. It is this enhancement in signal-to-background ratio that allows us to use such low concentrations of electroactive species.

So far we have discussed only the reversible case. The equivalence of the net faradaic current at the NEE and at a macroelectrode of the same geometric area (Figure 7) means that the flux at the individual elements of the NEE are many orders of magnitude larger than the flux at the macroelectrode. Indeed, the experimentally determined fractional electrode areas (Table 1) indicate that, for the reversible case, the flux at the elements of a 10NEE will be ~1000 times higher than that at the macroelectrode; the flux at the elements of the 30NEE will be ~250 times higher. The higher fluxes at the NEE elements mean that the NEEs will be more sensitive to the kinetics of electron transfer than would a macroelectrode.[14,15]

The simplest way to think about this situation is to consider that for any redox couple, the quasireversible case can be observed at a NEE at much lower scan rates than at a macroelectrode.[14] Indeed, because flux is related to the square root of scan rate, the 10^3-fold enhancement in flux at the 10NEE means that one would have to scan a macroelectrode at a scan rate 10^6 times higher in order to obtain the same kinetic information obtainable at the NEE. That is, if for a particular redox couple one observed quasireversible voltammetry at the 10NEE at scan rates above 1 V s^{-1}, one would have to scan at rates above 10^6 V s^{-1} to achieve the quasireversible case for this couple at a macroelectrode. This ability to obtain kinetic information at dramatically lower scan rates is an important advantage of a NEE.[14]

The $Ru(NH_3)_6^{3+/2+}$ voltammograms shown in Figure 8 illustrate this point. The standard heterogeneous rate constant for this couple has been measured by a number of groups;[12,14,37] values of 0.26,[12] 1.8,[14] and 76 cm s^{-1} [37] have been reported. Assuming, for the sake of illustration, a value of 1 cm s^{-1}, Nicholson's theory shows that quasireversible $Ru(NH_3)_6^{3+/2+}$ voltammograms will be obtained, at a macroelectrode, at scan rates above ~5 V s^{-1}.[38]

Figure 8A shows voltammograms at various scan rates for $Ru(NH_3)_6^{3+/2+}$ at a 30NEE. The peak separation (ΔE_{pk}) values are shown in Table 2. This couple shows reversible voltammetry ($\Delta E_{pk} \approx 59$ mV) at the lowest scan rates shown, but the voltammograms become quasireversible at scan rates above 0.01 V s^{-1} (Table 2). Therefore, as expected, the transition to quasireversible behavior is observed at dramatically lower scan rates at the 30NEE than would be observed at a macroelectrode. It is again important to emphasize that the increase in ΔE_{pk} observed in Table 2 is not due to uncompensated solution resistance.

Because the fractional electrode area at the 10NEE is lower than that at the 30NEE (Table 1), the transition to quasireversible behavior would be expected to occur at even lower scan rates at the 10NEE. Voltammograms for $Ru(NH_3)_6^{3+/2+}$ at a 10NEE are shown in Figure 8B. The corresponding ΔE_{pk} values are shown in Table 2. At the 10NEE, it is impossible to obtain the reversible case, even at a scan rate as low as 5 mV s^{-1} (Table 2). The effect of quasireversible electrochemistry is also clearly seen in the diminution of the voltammetric peak currents at the 10NEE (relative to the 30NEE). This diminution in peak current (relative to the reversible case) is characteristic of the quasireversible case

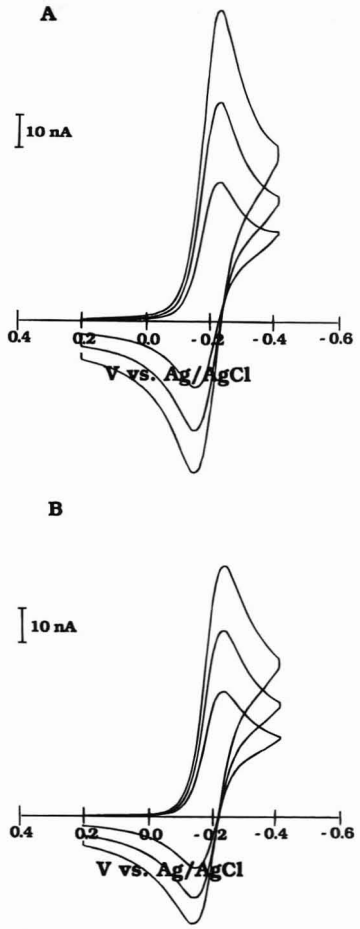

Figure 8. Cyclic voltammograms for 5 μM $Ru(NH_3)_6Cl_3$ and 10 mM pH 7 phosphate buffer as supporting electrolyte. (A) 30NEE; (B) 10NEE. Scan rates are 20, 50, and 100 mV/s.

Table 2. ΔE_{pk} Values as a Function of Scan Rate for $Ru(NH_3)_6^{3+}$ Cyclic Voltammograms at a 30NEE and a 10NEE

	ΔE_{pk} (mV)	
scan rate (mV/s)	30NEE	10NEE
5	60	72
10	62	76
20	65	80
50	70	90
100	75	100

at an ensemble of nanoelectrodes.[14,24]

We will have more to say about the kinetics of electron transfer reactions at NEEs in a forthcoming paper.[39] These preliminary studies indicate, however, that the response characteristics of the NEEs are in qualitative agreement with theoretical predictions.[14,24]

Electroanalytical Detection Limits at the NEEs. For the reversible case, the voltammetric detection limit for a redox

(37) Bilewicz, R.; Majda, M. *J. Am. Chem. Soc.* **1991,** *113,* 5464–5466.
(38) Nicholson, R. S. *Anal. Chem.* **1965,** *37,* 1351–1355.
(39) Menon, V. P.; Martin, C. R., manuscript in preparation.

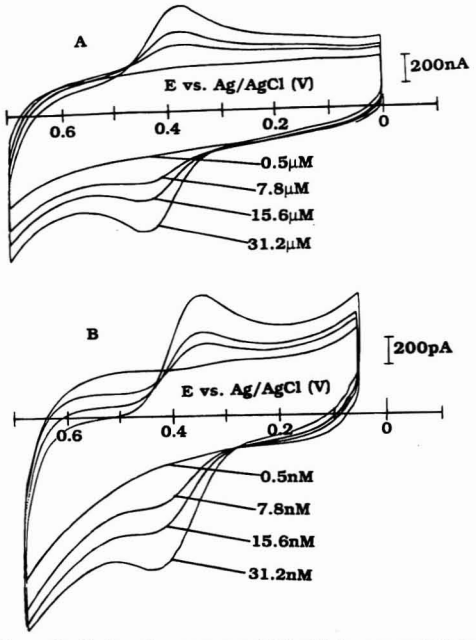

Figure 9. Cyclic voltammograms at 100 mV/s in aqueous $TMAFc^+$ at (A) a gold macrodisk electrode in 50 mM sodium nitrate and (B) a 10NEE in 1 mM sodium nitrate. $TMAFc^+$ concentrations are as indicated; electrode geometric areas in both cases are 0.079 cm^2.

species at a NEE should be the detection limit for the same species at the corresponding macroelectrode multiplied by the fractional electrode area (Table 1) of the NEE.[19] Because the fractional electrode area for the 10NEE is $\sim 10^{-3}$, this suggests that the voltammetric detection limit at a 10NEE should be 3 orders of magnitude lower than the detection limit obtained at a macroelectrode. Figure 9A shows voltammograms at a macroelectrode at various low concentrations of $TMAFc^+$. As would be expected, the faradaic signal ultimately vanishes into the background double-layer charging currents. Taking a total measured current that is twice the background charging current as the criterion for establishing the detection limit,[19] these voltammograms show that the detection limit for $TMAFc^+$ at the macroelectrode is $\sim 1.6\ \mu M$ (see Figure 10A).

Voltammograms for various low concentrations of $TMAFc^+$ at a 10NEE are shown in Figure 9B. While the voltammograms look nearly identical to those obtained at the macroelectrode, the concentrations are 3 orders of magnitude lower. Using the same criterion for the detection limit, we obtain a detection limit at the 10NEE that is 3 orders of magnitude lower (1.6 nM) than that at the macroelectrode. This is illustrated by the calibration curve shown in Figure 10B. It is gratifying that the experimentally observed enhancement in detection limit at the NEE is exactly as would be predicted from the fractional electrode area data in Table 1.

Cyclic voltammetry is generally considered to be a poor electroanalytical technique. This is because the high double-layer charging currents observed at a macroelectrode make the signal-to-background ratio low. The voltammograms in Figure 9B, and the corresponding calibration curve for the 10NEE in Figure 10B,

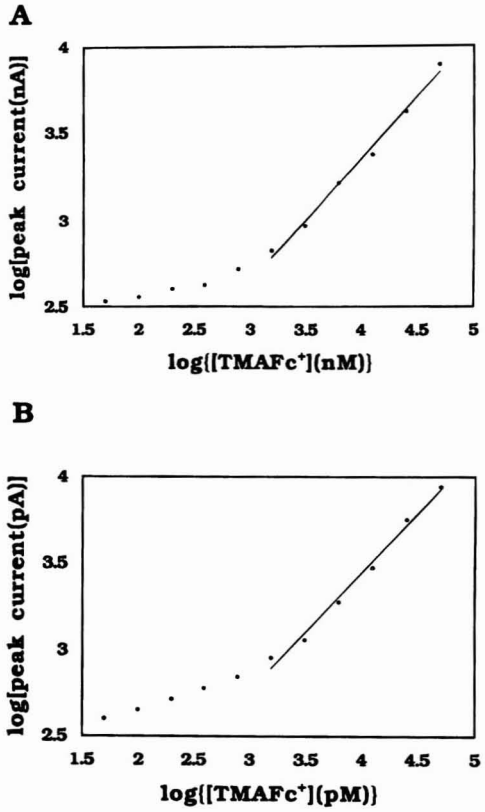

Figure 10. Plot of log(anodic peak current) from $TMAFc^+$ voltammograms vs log([$TMAFc^+$]). (A) Macrodisk electrode; (B) 10NEE. Conditions as in Figure 10.

clearly show that at the NEEs, cyclic voltammetry is a very powerful electroanalytical technique. There is, however, a caveat. Because the NEEs are more sensitive to electron transfer kinetics, the enhancement in detection limit that is, in principle, possible could be lost for couples with low values of the heterogeneous rate constant. This is because one effect of slow electron transfer kinetics at the NEE is to lower the measured faradaic currents (e.g., Figure 8).[14,24]

This sensitivity to slow electron transfer kinetics could, however, prove to be an advantage in sensor applications where a mediator, with fast electron transfer kinetics, is used to shuttle electrons to a redox enzyme.[40] Chemical species that are electroactive in the same potential region as the mediator can act as interferants at such sensors. If such an interfering electroactive species shows slow electron transfer kinetics, it might be possible to eliminate this interference at the NEE. This is because at the NEE, the redox wave for the kinetically slow interferant might be unobservable in the region where the kinetically fast mediator is electroactive. We are currently exploring this possibility.

Effect of Supporting Electrolyte. As indicated above, all of the experimental data reported thus far were obtained at low

(40) Ballarin, B.; Brumlik, C. J.; Lawson, D. R.; Liang, W.; Van Dyke, L. S.; Martin, C. R. *Anal. Chem.* **1992**, *64*, 2647–2651.

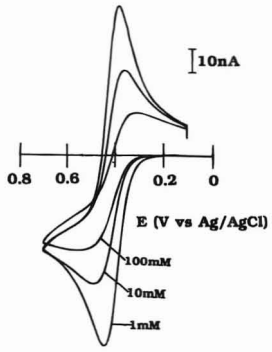

Figure 11. Cyclic voltammograms illustrating the effect of supporting electrolyte concentration at a 10NEE for 5 μM $TMAFc^+$ in aqueous $NaNO_3$ at the indicated concentrations of $NaNO_3$. Scan rate, 100 mV/s.

concentrations of both supporting electrolyte ($\approx$mM) and electroactive species ($\approx\mu$M). This was done because we have observed an interesting effect of supporting electrolyte concentration on the shape of the voltammetric waves observed at the NEEs. We have found that the reversibility of the voltammetric waves for all couples investigated to date ($TMAFc^{+/2+}$, $Ru(NH_3)_6^{3+/2+}$, and $Mo(CN)_8^{4-/3-}$) improves as the concentration of supporting electrolyte decreases. This effect is illustrated for $TMAFc^{+/2+}$ in Figure 11. Note that the peak currents decrease and the ΔE_{pk} values increase as the concentration of supporting electrolyte increases.

This effect has been observed in all of the supporting electrolytes we have investigated to date; these include $NaNO_3$, $NaClO_4$, Na_2SO_4, Et_4NBF_4, Et_4NClO_4, $Mg(NO_3)_2$, KNO_3, KPF_6, $ZnSO_4$, and pH = 7.0 phosphate buffer. Furthermore, this effect is reproducible and reversible. By "reversible" we mean that if the NEE is taken out of a solution with high supporting electrolyte concentration (e.g., 50 mM) and returned to a solution with low electrolyte concentration (e.g., 1 mM), the voltammetric wave immediately assumes the reversible appearance characteristic of the low electrolyte concentration solution (Figure 11). Furthermore, we have observed this effect for NEEs prepared from both polycarbonate and polyester membranes, and we have observed it for NEEs prepared from membranes with and without the PVP that is used to improve membrane wettability.

This supporting electrolyte effect will be discussed in detail in a forthcoming paper, which will focus on using these NEEs to obtain standard heterogeneous rate constant data for fast redox couples.[39]

CONCLUSIONS

We have described in this paper a new method for preparing electrodes with nanoscopic dimensions. We have used this method to prepare nanoelectrode ensembles with individual electrode element diameters as small as 10 nm. This method is simple, inexpensive, and highly reproducible. The reproducibility of this approach for preparing nanoelectrodes is illustrated by the fact that NEEs given to other groups yielded the same general electrochemical results as obtained in our laboratory.[41] These NEEs display cyclic voltammetric detection limits that are as much as 3 orders of magnitude lower than achievable at a conventional macroelectrode.

The electroless metal deposition procedure described here is general and can be extended to the deposition of a number of metals. It can also be modified to create interesting nanostructures such as metal nanotubules.[33] Indeed, the methods developed here are a part of a much larger research effort in this laboratory aimed at using the pores in such nanoporous membranes as a general approach for preparing nanomaterials.[35]

ACKNOWLEDGMENT

This work was supported by the Office of Naval Research. We acknowledge Ranjani V. Parthasarathy for help with scanning electron microscopy and Matsuhiko Nishizawa for help with transmission electron microscopy. We also acknowledge valuable discussions with Henry White and Steven Feldberg.

Received for review December 14, 1994. Accepted March 17, 1995.[⊗]

AC941215S

(41) White, H. S.; Bard, A. J.; Fan, F.-R. Personal communication, July, 1994.

[⊗] Abstract published in *Advance ACS Abstracts,* April 15, 1995.

Anal. Chem. **1995,** *67,* 1929–1934

Attenuation of Metal Oxide Ions in Inductively Coupled Plasma Mass Spectrometry with a Graphite Torch Injector

P. Scott Clemons, Michael G. Minnich, and R. S. Houk*

Ames Laboratory—U.S. Department of Energy, Department of Chemistry, Iowa State University, Ames, Iowa 50011

Desolvated solution aerosols are injected into the axial channel of an inductively coupled plasma through a graphite tube inserted directly into the plasma. This hot injector constricts the stream of analyte and prevents it from widening excessively as it travels through the plasma. Thus, the sampling orifice for the mass spectrometer can be positioned several millimeters downstream from the tip of the initial radiation zone without substantial loss of analyte ion signal. The signal ratio for LaO^+/La^+ can be reduced to 0.05% with conventional desolvation or 0.01% with cryogenic desolvation under operating conditions that yield maximum metal ion signal. These values are greatly superior to those obtained with conventional torch injectors. The graphite injector also improves sensitivity for atomic ions by factors of 1.5–15, with the best improvements seen for elements such as As and Zn that have high ionization energies. This modification to the plasma does not compromise other analytical figures of merit such as rinse-out time or the suitability of a single set of operating conditions for multielement analysis.

Inductively coupled plasma mass spectrometry (ICPMS) is a sensitive and selective method for trace multielement analysis. The ability of the ICP to efficiently atomize the sample is one dimension of the overall selectivity of the technique. Although atomic ions (M^+) are the major species seen under normal operating conditions, other ions such as MO^+, ArM^+, ArO^+, and Ar_2^+ hamper the determination of several important elements. Corrections based on isotope ratios can often be done for moderate cases of spectral interference,[1,2] but these procedures become suspect when the analyte signal is small relative to that for the interferent.

This paper focuses on a new method to remove most of the interference from MO^+ ions. A variety of such measures have been demonstrated for low-resolution instruments based on quadrupole mass analyzers. These schemes include mixed gas plasmas[3–8] and introduction of the sample in as dry a form as possible, i.e., by desolvation,[4,9,10] electrothermal vaporization,[11–14] or laser ablation.[1] A double-focusing mass spectrometer can separate MO^+ from M^+ ions at the same nominal m/z value. In general, reducing the slit widths to attain the resolution required (6000–15 000) also reduces the transmission by at least a factor of 10.[15,16] Measures that reduce the level of MO^+ ions in the plasma would be valuable for either low- or high-resolution experiments.

The fundamental reasons for the persistence of MO^+ ions have been discussed by several groups.[17–20] Suppose an aqueous solution is dispersed into droplets with a conventional nebulizer. The larger droplets, and much of the water vapor, are then removed by a cooled spray chamber. The spray chamber still transmits wet droplets in a range of sizes to the plasma. As these droplets leave the torch injector and traverse the plasma, they are first desolvated and then the solutes are progressively vaporized, atomized, and ionized. The axial positions where these processes take place overlap. The smaller droplets desolvate, vaporize, etc., relatively quickly, while the larger droplets persist much farther downstream.[21–25] Furthermore, the stream of droplets, and the resulting clouds of atoms and ions, spread out as they travel further downstream. In ICPMS, the sampler–skimmer combination transmits ions essentially from a small zone (of approximately the same diameter as the skimmer hole) that

(1) Jarvis, K. E.; Gray, A. L.; Houk, R. S. *Handbook of ICP-MS*; Blackie: London, 1992; Chapters 4.2 and 10.3.
(2) Date, A. R.; Cheung, Y. Y.; Stuart, M. E. *Spectrochim. Acta, Part B* **1987,** *42B,* 3–20.
(3) Lam, J. W. H.; Horlick, G. *Spectrochim. Acta, Part B* **1990,** *45B,* 1313–1326.
(4) Lam, J. W. H.; McLaren, J. W. *J. Anal. At. Spectrom.* **1990,** *5,* 419–424.
(5) Louie, H.; Soo, S. Y.-P. *J. Anal. At. Spectrom.* **1992,** *7,* 557–564.
(6) Evans, E. H.; Ebdon, L. *J. Anal. At. Spectrom.* **1990,** *5,* 425–430.
(7) Wang, J.; Evans, E. H.; Caruso, J. A. *J. Anal. At. Spectrom.* **1992,** *7,* 929–936.
(8) Laborda, F.; Baxter, M. J.; Crews, H. M.; Dennis, J. *J. Anal. At. Spectrom.* **1994,** *9,* 727–736.
(9) Alves, L. C.; Wiederin, D. R.; Houk, R. S. *Anal. Chem.* **1992,** *64,* 1164–1169.
(10) Alves, L. C.; Allen, L. A.; Houk, R. S. *Anal. Chem.* **1993,** *65,* 2468–2471.
(11) Gregoire, D. C. *J. Anal. At. Spectrom.* **1988,** *3,* 309–314.
(12) Shibata, N.; Fudagawa, N.; Kubota, N. *Spectrochim. Acta, Part B* **1992,** *47B,* 505–516; **1993,** *48B,* 1127–1137.
(13) Gregoire, D. C.; Sturgeon, R. E. *Spectrochim. Acta, Part B* **1993,** *48B,* 1347–1364.
(14) Ediger, R. D.; Beres, S. A. *Spectrochim. Acta, Part B* **1992,** *47B,* 907–922.
(15) Bradshaw, N.; Hall, E. F. H.; Sanderson, N. E. *J. Anal. At. Spectrom.* **1989,** *4,* 801–803.
(16) Morita, M.; Ito, H.; Uehiro, T.; Otsuka, K. *Anal. Sci.* **1989,** *5,* 609–610.
(17) Tanner, S. D. J. *Anal. At. Spectrom.* **1993,** *8,* 891–897.
(18) French, J. B.; Etkin, B.; Jong, R. *Anal. Chem.* **1994,** *66,* 685–691.
(19) Olesik, J. W.; Hobbs, S. E. *Anal. Chem.* **1994,** *66,* 3371–3378.
(20) Vanhaecke, F.; Dams, R.; Vandecasteele, C. *J. Anal. At. Spectrom.* **1993,** *8,* 433–438.
(21) Olesik, J. W.; Smith, J. J.; Williamsen, E. J. *Anal. Chem.* **1989,** *61,* 2002–2008.
(22) Olesik, J. W.; Fister, J. C., III *Spectrochim. Acta, Part B* **1991,** *46B,* 869–883.
(23) Cicerone, M. T.; Farnsworth, P. B. *Spectrochim. Acta, Part B* **1989,** *44B,* 897–907.
(24) Winge, R. K.; Crain, J. S.; Houk, R. S. *J. Anal. At. Spectrom.* **1991,** *6,* 601–604.
(25) Winge, R. K.; Chen, X.; Houk, R. S., in preparation.

0003-2700/95/0367-1929$9.00/0 © 1995 American Chemical Society

is just in front of the sampler.[26,27] Thus, the best sensitivity for M^+ ions generally occurs when the aerosol gas flow rate, plasma power, and sampling position are selected so that the sampler tip is just downstream from the end of the initial radiation zone (IRZ).[28–32] Metal oxide ions from the larger droplets and solid particles do not pass through the middle of the normal analytical zone (NAZ), which is probably the hottest part of the axial channel.[33–36] Thus, these metal oxide ions are extracted into the sampler before they are dissociated properly, so the spectrum consists of a mixture of M^+ and MO^+.

Much of the MO^+ ions can be dissociated into M^+ by retracting the plasma farther away from the sampler or by reducing the aerosol gas flow rate. These simple measures do attenuate the MO^+ interference, but at the expense of the M^+ signal.[28–32] The stream of analyte ions is now too wide at the sampler, so a larger fraction of the ions lies outside the narrow central region (~1 mm wide) transmitted through both the sampler and skimmer. At the gas kinetic temperatures prevalent in the axial channel of the ICP (~5000 K),[33,34] some MO^+ ions probably persist, particularly for refractory oxides like LaO^+ and UO^+, even if drastic measures are taken to reduce the density of O atoms in the plasma.[37]

Ideally, then, the MO^+ ions should be attenuated by (a) use of a nebulizer that produces either monodisperse droplets or polydisperse droplets without overly large ones, (b) preventing the cloud of analyte from expanding as it travels through the axial channel, so the sampler can be positioned in the middle of the NAZ rather than at the tip of the IRZ, and (c) removing solvent and other sources of oxygen. The first two of these measures are incorporated in the new monodisperse dried microparticulate injection device described by French et al.[18] and Olesik and Hobbs.[19] The present work describes a way to accomplish much the same objectives using a conventional nebulizer. Essentially, a desolvated polydisperse aerosol passes through a hot graphite tube inserted directly into the axial channel of the ICP (Figure 1). This approach resembles the direct solid introduction experiments with graphite cups described by several groups,[38–40] particularly those of Horlick, Salin, and Karanassios.[41–43] In most of these previous experiments, the injector is solid graphite, the sample is a solid rather than a solution aerosol, and there is no gas flow through the injection device. Gervais and Salin have described ICP emission experiments with a solution aerosol in a carrier gas passing through a heated injector (either graphite or alumina) inserted directly into the plasma. The main goal of their study was to improve the stability of the plasma with new sample introduction systems that were either erratic or loaded the plasma heavily.[44] To the best of our knowledge, this latter approach for injecting aerosols has not been described previously for ICPMS.

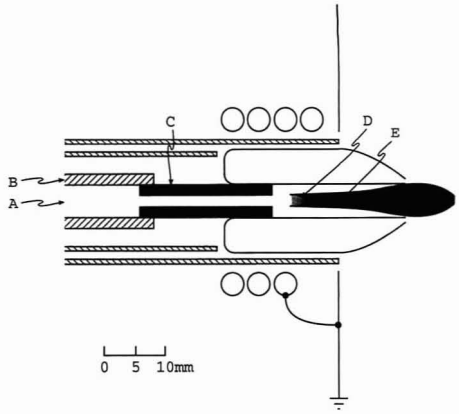

Figure 1. Diagram of ICP with graphite torch injector: A, desolvated aerosol from ultrasonic nebulizer; B, stainless steel support tube; C, graphite injector; D, initial radiation zone (IRZ); E, normal analytical zone (NAZ).[28] The sizes and positions of the IRZ and NAZ are shown to scale when a concentrated solution (~1000 mg L^{-1}) of yttrium is nebulized.

EXPERIMENTAL SECTION

Nebulizer and Torch Injector. Aqueous aerosols are produced with an ultrasonic nebulizer (Model U-5000, Cetac Technologies, Inc.) and desolvated by heating to 140 °C, followed by condensation at 0 °C.[45] The resulting dry particles, and residual water vapor, then pass through a Tygon transfer tube (8 mm i.d. × 1 m long) connected to the end of the stainless steel tube shown at the left side of Figure 1. This tube is held on center by a tapered piece of Teflon that fits into the taper joint at the base of the torch. A pyrolytic graphite tube (2 mm i.d. × 5 mm o.d. × 22 mm long) is press fit into the end of the stainless steel support. The tip of the graphite injector protrudes into the axial channel of the plasma by ~8 mm. The exposed end of the injector is even with the middle turn of the load coil. Longer injectors erode too rapidly. Before use, each tip is leached in 5% HCl for 8 h. Otherwise, a variety of metal impurity ions are observed.

In several experiments, the performance of the graphite injector shown in Figure 1 is compared to that of a conventional injector. In the latter case, the conventional injector is quartz with a tapered jet tip (1.5 mm i.d.) positioned even with the end of the intermediate tube.[46]

(26) Douglas, D. J.; French, J. B. *J. Anal. At. Spectrom.* **1988**, *3*, 743–747.
(27) Douglas, D. J. Fundamental Aspects of ICPMS. In *ICPs in Analytical Atomic Spectrometry*, 2nd ed.; Montaser, A., Golightly, D. W., Eds.; VCH: New York, 1992; Chapter 13.
(28) Koirtyohann, S. R.; Jones, J. S.; Yates, D. A. *Anal. Chem.* **1980**, *52*, 1965–1966.
(29) Horlick, G.; Tan, S. H.; Vaughan, M. A.; Rose, C. A. *Spectrochim. Acta, Part B* **1985**, *40B*, 1555–1572.
(30) Tan, S. H.; Horlick, G. *J. Anal. At. Spectrom.* **1987**, *2*, 745–763.
(31) Vaughan, M. A.; Horlick, G. *Appl. Spectrosc.* **1986**, *40*, 434–445.
(32) Horlick, G.; Shao, Y. ICP-MS for Elemental Analysis. In *ICPs in Analytical Atomic Spectrometry*, 2nd ed.; Montaser, A., Golightly D. W., Eds.; VCH: New York, 1992; Chapter 12.
(33) Hasegawa, T.; Umemoto, M.; Haraguchi, H.; Hsiech, C.; Montaser, A. In *ICPs in Analytical Atomic Spectrometry*, 2nd ed.; Montaser, A., Golightly, D. W., Eds., VCH: New York, 1992; Chapter 8.
(34) Hanselman, D. S.; Sesi, N. N.; Huang, M.; Hieftje, G. M. *Spectrochim. Acta, Part B* **1994**, *49B*, 495–526.
(35) Furuta, N.; Horlick, G. *Spectrochim. Acta, Part B* **1982**, *37B*, 53–64.
(36) Houk, R. S.; Olivares, J. A. *Spectrochim. Acta, Part B* **1984**, *39B*, 575–587.
(37) Nonose, N. S.; Matsuda, N.; Fudagawa, N.; Kubota, M. *Spectrochim. Acta, Part B* **1994**, *49B*, 955–974.
(38) Sommer, D.; Ohls, K. *Fresenius Z. Anal. Chem.* **1980**, *304*, 97–103.
(39) Zaray, G.; Broekaert, J. A. C.; Leis, F. *Spectrochim. Acta, Part B* **1988**, *43B*, 241–253.
(40) Kirkbright, G. F.; Li-Xing, Z. *Analyst* **1982**, *107*, 617–621.
(41) Salin, G. D.; Horlick, G. *Anal. Chem.* **1979**, *51*, 2284–2286.
(42) Karanassios, V. K.; Horlick, G.; Abdullah, M. *Spectrochim. Acta, Part B* **1990**, *45B*, 105–118.
(43) Boomer, D. W.; Powell, M.; Sing, R. L. A.; Salin, E. D. *Anal. Chem.* **1986**, *58*, 975–976.
(44) Gervais, L. S.; Salin, E. D. *J. Anal. At. Spectrom.* **1991**, *6*, 493–495.
(45) Bear, B. R.; Fassel, V. A. *Spectrochim. Acta, Part B* **1986**, *41*, 1089–1113.

Table 1. Standard Operating Conditions

solution uptake rate, mL min^{-1}	1.5
argon gas flow rates, L min^{-1}	
outer gas	16
auxiliary	0.9
aerosol gas	0.4–0.6
forward power, kW	1.5
reflected power, W	< 5
sampling position	5 mm from load coil on center; see Figure 2

[a] Selected on daily basis to maximize signal for La^+.

Cryogenic Desolvation. In some experiments, the aerosol is dried further by cryogenic desolvation, as described previously.[9,10] Essentially, the stream of solid particles from the condenser of the regular desolvator passes through a series of hot (140 °C) and cold (−80 °C) loops, which repeatedly dry the particles and freeze out the solvent vapor. The dry aerosol particles then go into the injector and ICP.

ICPMS Instrumentation. These experiments were performed with a homemade ICPMS device that has been described previously.[47,48] The offset ion lens was changed slightly in that a tapered metal cylinder was substituted for the cone (see Figure 2 of ref 47). This arrangement yielded slightly higher ion signals with the same background as that seen previously.[47,48]

Data were collected with a multichannel analyzer by either single-ion monitoring or scanning. For measurement of M^+ and MO^+ signals, a m/z window 20 D wide was scanned 100 times, using 4096 channels and a dwell time of 50 μs per channel. The mass analyzer was adjusted to provide unit mass resolution (5% valley) in the mass window monitored.

In general, operating conditions, particularly aerosol gas flow rate and ion lens voltages, were selected at the beginning of each day's experiments to maximize the signal for the analyte(s) of interest. Because different injectors were used on different days, these optimum conditions differed slightly from day to day. Typical operating conditions are cited in Table 1. Generally, the same power and sampling position were used from day to day, and the aerosol gas flow rate was optimized to provide maximum signal for La^+.

Solutions and Standards. Standard solutions of the elements of interest were prepared by diluting standard stock solutions (1000 mg L^{-1}, Plasma Chem) with 1% HCl to known concentrations, usually either 100 or 500 μg L^{-1}.

RESULTS AND DISCUSSION

General Observations. The plasma ignites readily with the injector in place using the normal ignition procedure with a Tesla coil. The injector emits orange light during operation, which indicates that its temperature is ~1800 K. The appearance of the plasma is shown in Figures 1 and 2. When a solution of yttrium is injected, the IRZ and NAZ[28] are roughly as depicted in Figure 1. In particular, the IRZ is very short, and the NAZ is visually longer and narrower than that seen with a conventional torch injector. A gap can clearly be seen between the analyte stream and the outer edge of the axial channel, i.e., the boundary between the axial channel and the induction region. When the sampling orifice is inserted at the usual sampling position (Figure 2), virtually all the analyte stream flows into the sampler, even though the sampler is several millimeters downstream from the tip of the IRZ. With a conventional injector, the analyte stream is much wider and fills the entire axial channel almost immediately after the IRZ.

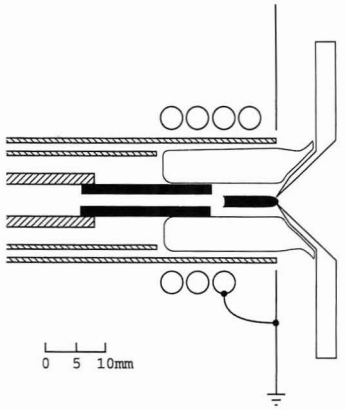

Figure 2. ICP with graphite injector from Figure 1 with sampling orifice of MS present at usual sampling position. Note that virtually all the analyte ions flow into the sampling orifice.

The injector erodes slowly during use and lasts 6–8 h. The erosion occurs primarily inside the downstream tip of the injector. The hole expands gradually at the tip from a cylindrical bore to a fluted end. A fresh injector is therefore used each day. The injector is replaced easily by simply reaching into the open end of the torch with a pair of tweezers (with the plasma off, of course).

Direct current voltages between −100 and +100 V can be applied to the stainless steel support tube without any noticeable change in the plasma or in the ion signal seen by the mass analyzer. Therefore, the injector is simply kept grounded.

The background spectrum is somewhat different from usual when the graphite injector is used. Carbon ions ($^{12}C^+$) are a major peak with the injector and are of comparable intensity to $^{16}O^+$, H_2O^+, and $^{40}Ar^+$. Also, CO^+ ($m/z = 28$) becomes more abundant than O_2^+ ($m/z = 32$) with the graphite injector. These and other carbon-containing ions are more abundant under conditions in which the injector erodes more rapidly. The erosion rate is, in turn, related to the type of graphite used; pyrolytic graphite erodes more slowly than spectroscopic grade graphite. The precise relation between erosion rate, the character of the background spectrum, and the abundance of MO^+ is presently under detailed study. Deposition of solid carbon on the sampler has not been a problem so far.

MO^+/M^+ Ratios with Desolvation at 0 °C. A plot of signal for La^+ and LaO^+ vs aerosol gas flow rate is shown in Figure 3. The best signal for La^+ is ~10^6 counts s^{-1} at an aerosol gas flow rate of ~0.6 L min^{-1}. At this value for aerosol gas flow rate, the LaO^+ signal is ~10^3 counts s^{-1}, so the ratio of signals for LaO^+/La^+ is ~0.1%. At 0.45 L min^{-1}, the La^+ signal falls off only slightly to 8×10^5 counts s^{-1}, whereas the LaO^+/La^+ signal ratio drops to 0.05%. This latter value is comparable to that achieved with conventional torch injectors for similar elements by drying the

(46) Scott, R. H.; Fassel, V. A.; Kniseley, R. N.; Nixon, D. E. *Anal. Chem.* **1974**, *46*, 75–80.
(47) Hu, K.; Clemons, P. S.; Houk, R. S. *J. Am. Soc. Mass Spectrom.* **1993**, *4*, 16–27.
(48) Hu, K.; Houk, R. S. *J. Am. Soc. Mass Spectrom.* **1993**, *4*, 28–37.

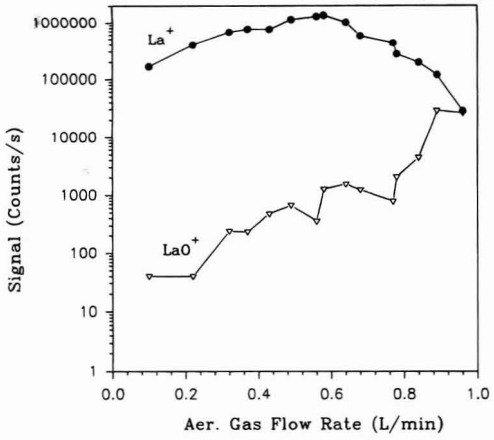

Figure 3. Plots of ion signal vs aerosol gas flow rate for La^+ and LaO^+ with graphite injector and conventional desolvation.

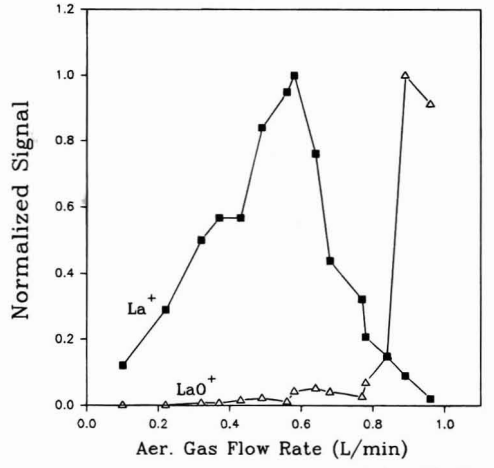

Figure 4. Plots of normalized ion signals for La^+ and LaO^+ vs aerosol gas flow rate, conventional desolvation.

plasma thoroughly by cryogenic desolvation,[9,10] membrane desolvation,[49] or electrothermal vaporization.[11–14]

This result can be shown more clearly by normalizing the signals for La^+ and LaO^+ to their maxima and plotting the results on a linear scale (Figure 4). Two separate peaks (commonly called "mountains" in ICPMS parlance) for La^+ and LaO^+ result. The peak of the mountain for La^+ lies at a much lower flow rate than that for LaO^+, by 0.3 L min^{-1}. Furthermore, the left edge of the mountain for LaO^+ is steep, and only a small amount of LaO^+ remains under the peak for La^+. With conventional torch injectors, the mountain top for M^+ lies much closer to that for MO^+, and the left edge of the MO^+ mountain has a much more gradual slope than that shown in Figure 4. Thus, a substantial amount of MO^+ remains under conditions that maximize M^+ signal, for the reasons described in the introduction.

At the "best" aerosol gas flow rate in Figures 3 and 4 (0.6 L min^{-1}), the relative positions of the IRZ and sampling orifice are

(49) Zhu, J. J.; Smith, F. G. Federation of Analytical Chemistry and Spectroscopy Societies Mtg., St. Louis, MO, October 1994; Paper 780.

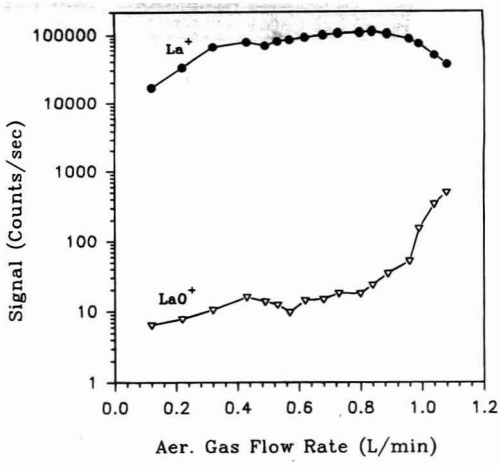

Figure 5. Ion signals vs aerosol gas flow rate with cryogenic desolvation.

those shown in Figure 2. With the graphite torch injector, the sampler can be 4–5 mm downstream from the tip of the IRZ without substantial loss of signal for M^+. In contrast, with conventional torch injectors, the maximum M^+ signal is generally obtained with the sampler only ~1 mm downstream from the tip of the IRZ, which complicates selection of operating conditions that maximize sensitivity for M^+ while also minimizing the abundance of MO^+.[30–32]

MO^+/M^+ Ratios with Cryogenic Desolvation. Figure 5 shows the dependence of La^+ and LaO^+ signals on aerosol gas flow rate with cryogenic desolvation and the graphite torch injector. Within the flow rate range from 0.4 to 0.8 L min^{-1}, the La^+ signal is a maximum while the LaO^+/La^+ signal ratio is only 0.01%–0.02%. This represents roughly a 5-fold improvement in LaO^+/La^+ over the oxide ratio obtained by either regular desolvation with the graphite torch injector or cryogenic desolvation with a conventional torch injector.[9,10]

Unfortunately, the La^+ signal is reduced by cryogenic desolvation with either the graphite injector or a conventional one.[9,10] With the graphite injector, adding H_2 gas at 2% of the aerosol gas flow boosts the M^+ signal by a factor of 2. This signal enhancement is slightly poorer than the factor of 3 seen previously.[10] Adding H_2 through the graphite torch injector also increases the oxide ratio for LaO^+/La^+ by a factor of 4, so use of H_2 has not proven advantageous so far.

Multielement Operating Conditions. Ideally, the signal from all analytes should be nearly optimum at a single set of operating conditions. The constriction of the analyte stream induced by the graphite injector could also induce substantial differences in the "best" plasma parameters for different elements, which was a problem for the long torches used in some early ICPMS devices[29] and in atomic fluorescence with the ICP.[50]

Ion signals for a variety of elements are shown as functions of aerosol gas flow rate in Figure 6. For all these elements, the M^+ signal is at or within 10% of its maximum value at a single setting for aerosol gas flow rate (0.45 L min^{-1}). This value is lower than

(50) Demers, D. R.; Montaser, A. In *ICPs in Analytical Atomic Spectrometry*, 2nd ed.; Montaser, A., Golightly, D. W., Eds.; VCH: New York, 1992; Chapter 11.

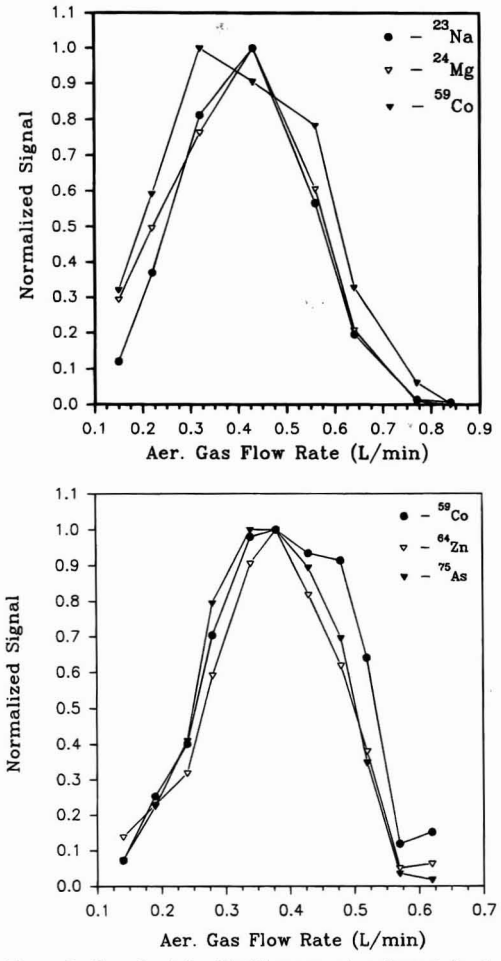

Figure 6. Normalized signal for M^+ vs aerosol gas flow rate for six common analyte elements, each at 100 μg L^{-1}.

the "best" value of 0.6 L min^{-1} from the previous figures because this experiment was done on a different day with a fresh injector. Each injector behaves slightly differently and requires a somewhat different aerosol gas flow rate to provide optimum M^+ signal and to minimize oxide ions.

Analogous results are seen if forward power and sampling position are varied. These operating conditions are all interrelated, as pointed out by Horlick and co-workers.[29-32] To a first approximation, an increase in power requires an increase in aerosol gas flow rate, positioning the sampler further upstream in the plasma, or both.

Sensitivity Improvements. For these experiments, sensitivity is defined as net ion signal per unit concentration. These values are compared in Table 2. The results for both the graphite injector and the conventional injector were obtained with the same power and sampling position. In each case, the aerosol gas flow rate was adjusted to maximize La^+ signal. Thus, the sensitivities provided by the two injectors are compared under conditions of best sensitivity for each. Also, each injector was operated under

Table 2. Relative Sensitivity for Various Elements with Conventional Injector and Graphite Injector

element	ionization energy, eV	sensitivity, counts s^{-1}/mg L^{-1} conv injector	graphite injector	sens ratio
^{56}Fe	7.87	2.28×10^5	3.42×10^5	1.5
^{59}Co	7.86	1.88×10^5	6.34×10^5	3.4
^{64}Zn	9.39	4.53×10^4	6.64×10^5	15
^{75}As	9.81	1.15×10^4	1.69×10^5	14.6
^{89}Y	6.38	1.00×10^6	5.28×10^6	5.3
^{98}Mo	7.10	2.05×10^5	1.16×10^6	5.7
^{103}Rh	7.46	6.62×10^5	4.02×10^6	6.0
^{165}Ho	6.02	4.42×10^6	7.98×10^6	1.8
^{208}Pb	7.42	9.32×10^5	1.52×10^6	1.6

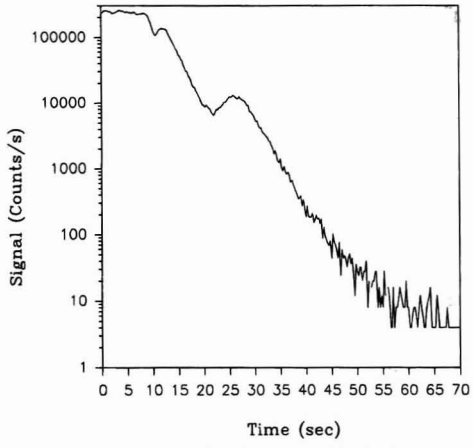

Figure 7. Rinse-out curve for Cd at 1 mg L^{-1}. The rinse solution reaches the transducer of the nebulizer at time ~5 s.

multielement conditions; conditions were not optimized separately for individual elements.

With the conventional injector, sensitivities are in the range 10^5–10^6 $counts^{-1}$/mg L^{-1}, as seen previously with this particular ICPMS device.[47,48] For every element, these values improve with the graphite injector. Sensitivities for Fe, Ho, and Pb improve by factors of 1.5–1.8. The graphite injector improves the sensitivity for other elements by larger factors ranging from 5 (for Y, Mo, and Rh) to 10–15 (for Zn and As).

These element-dependent sensitivity improvements can be explained as follows. The injector constricts the stream of analyte ions somewhat for all elements, as depicted in Figures 1 and 2. A larger fraction of the analyte ions stays on-axis within the zone of gas that passes through both the sampler and skimmer. Thus, sensitivity improves somewhat for all elements, even those like Fe and Y that are almost completely ionized in the normal ICP. Also, the graphite injector allows the sampling orifice to be positioned near the middle of the NAZ where the "temperature" for analytes is highest.[33-36] Of the various elements studied, this change in sampling position improves the degree of ionization most for elements like As and Zn, which are not efficiently ionized at the tip of the IRZ in a normal ICP. Thus, the sensitivity for As and Zn improves by larger factors than those seen for more easily ionized elements.

The sensitivity improvements seen in Table 2 are welcome even if their fundamental causes are not yet fully understood.

Because these improvements result from a change in the structure of the plasma, they should be useful with other ICPMS devices as well.

Rinse-Out Curves. Conceivably, injecting the sample aerosol through a hot graphite tube could induce additional memory problems and extend the time needed to change samples. A typical rinse-out curve is presented in Figure 7. The Cd solution is replaced with the blank solution at time zero. The blank reaches the transducer at time 10 s, after which the Cd^+ signal decays gradually. After an additional 30 s, the Cd^+ signal reaches 0.1% of its original level. After 55 s, the Cd^+ signal cannot be distinguished from the blank.

This rinse-out behavior (i.e., 30 s to attenuate the signal from the previous sample by 0.1%) is identical to that of the nebulizer alone. Similar curves are seen for a variety of other elements, including Zn and Co. For these elements, the graphite injector induces no additional memory. Naturally, severe memory effects occur for highly volatile elements such as B, Os, and Hg, as generally seen whenever the aerosol passes through a spray chamber.[45] We have not yet tested the graphite injector extensively with wet aerosols.

CONCLUSION

The graphite injector described in this paper provides a simple way to extract M^+ ions from a region of the plasma that is physically separated from the zone inhabited by the noxious MO^+ ions. Signal ratios for MO^+/M^+ can be reduced to 0.01%–0.05% by this means. Analyte sensitivity can be improved by factors of 1.5–15. The basic reasons for these improvements are being investigated further in our laboratory, as are other analytical characteristics such as matrix effects.

ACKNOWLEDGMENT

Ames Laboratory is operated for the U.S. Department of Energy by Iowa State University under Contract W-7405-Eng-82. This research was supported by the Office of Basic Energy Sciences. The graphite tubes were provided gratis by Union Carbide.

Received for review February 2, 1995. Accepted April 7, 1995.[⊗]

AC950121V

[⊗] Abstract published in *Advance ACS Abstracts,* June 1, 1995.

Removal of Ribonucleases from Solution Using an Inhibitor-Based Sol–Gel-Derived Biogel

Upvan Narang, M. H. Rahman, Jui H. Wang,* Paras N. Prasad,* and Frank V. Bright*

Department of Chemistry and Photonics Research Laboratory, Natural Sciences and Mathematics Complex, State University of New York at Buffalo, Buffalo, New York 14260-3000

Currently, there are no simple one-step methods available to remove ribonucleases (RNases) from solution; however, such is imperative for researchers working with ribonucleic acids (RNAs) because RNases can destroy RNA. We report a simple means to remove RNase from solution. The scheme is based on the encapsulation of a new RNase inhibitor, poly[2′-*O*-(2,4-dinitrophenyl)]poly(adenylic acid) (DNP-poly(A)), within porous tetramethoxysilane- (TMOS) or tetraethoxysilane- (TEOS) based sol–gel-derived silica particles that are used to form a small bioaffinity column. We investigate the activity, binding capacity, and stability of the hybrid DNP-poly(A)/sol–gel-derived bioaffinity material. Radioactivity and fluorometric assays are used to determine the response of the sol–gel entrapped DNP-poly(A) to a variety of RNases. The results clearly demonstrate that DNP-poly(A) entrapped within the sol–gel matrix is active and binds to all RNases tested. There is minimal (<6%) leaching of the DNP-poly(A) from the column. The DNP-poly(A)-doped sol–gel-derived particles do not require hydrated storage conditions. Biocolumn performance and stability are comparable for DNP-poly(A)-doped TMOS- and TEOS-derived materials. Sodium chloride can be used to regenerated the DNP-poly(A) column. The binding capacity of the biocolumn decreases over time; however, the binding capacity of a 2-month-old DNP-poly(A)-doped biocolumn is several orders of magnitude greater than the typical levels of RNase encountered in contaminated solutions.

Bioaffinity or bioselective chromatography is a common means to separate a target analyte specifically and selectively.[1–3] In order to prepare a bioaffinity column, one must immobilize a biorecognition element such as an enzyme or an antibody onto the solid-phase support material. To prepare such materials, it is common to simply physisorb or covalently bind the biorecognition element to some form of "inert" support.[4–6] Unfortunately, while these methods work, the final material is prone to leaching, the preparation can be tedious and time consuming, and there is often substantial reduction in the activity/affinity of the immobilized biospecies.[1,4–6]

It is well-known that ribonucleases (RNases) hydrolyze ribonucleic acids (RNAs)[7] and RNases are constantly secreted from humans. As a result, analysts must exercise extreme care to avoid solution contamination because even trace amounts of RNase can lead to lower yields in in vitro transcription reactions and degradation during RNA purification protocols.[7,8] Thus, during any RNA isolation procedure, it is imperative to have RNase-free working solutions.

Currently, there is no simple methodology available to remove RNases from solution. The two most common methods involve treating the contaminated solution with diethyl pyrocarbonate (DEPC)[9] or RNasin (Promega).[10] Both methods are prone to one or more drawbacks such as multistep reactions, tedious protocols, expensive inhibitors, and material/reagent toxicity, and most importantly, they do not "remove" all RNases.

Several reports have appeared on the preparation of affinity columns based on an inhibitor covalently attached to Sepharose or agarose beads to remove and/or purify RNases. For example, Brison and Chambon[11] prepared an agarose-5′(4′-aminophenyl)-uridine2′(3′) phosphate column to remove pancreatic RNase from a pancreatic DNase solution. Wilchek and Gorecki[12] coupled the inhibitor 5′-[(4-aminophenyl)phosphoryl]uridine-2′(3′)phosphate (APUP) to cyanogen bromide-activated Sepharose to purify RNase A. Wang and Moore[13] prepared an APUP-Sepharose column to generate RNase-free DNase solutions. Unfortunately, the aforementioned columns are specific for only one or two RNases.

We recently synthesized an RNase inhibitor, poly[2′-*O*-(2,4-dinitrophenyl)]poly(A) (DNP-poly(A)), which binds to a variety of RNases.[14] We also demonstrated that DNP-poly(A) bound to RNases A, B, S, T_1, T_2, and H (endo-RNases), 5′-exonuclease (phosphodiesterase I), and 5′-exonuclease (phosphodiesterase II) in solution and the binding constant exceeded 10^6 M^{-1}. Thus, if

(1) (1) *Chromatography; Part A: Fundamentals and Techniques*; Heftmann, E., Ed.; Elsevier: New York, 1992; pp A309–A338.
(2) Turkova, J. *Affinity Chromatography*; Elsevier: New York, 1978; Chapter 5, pp 51–87, and Chapter 9, pp 203–223.
(3) Weetall, H. H.; Filbert, A. M. *Methods Enzymol.* **1974**, *34*, 59–72.
(4) Madden, J. K.; Thorn, D. In *Affinity Chromatography and Related Techniques*; Gribnau, T. C. J., Visser, J., Nward, R. J. F., Eds.; Elsevier: Amsterdam, 1982; pp 113–129.
(5) Taylor, R. F. *Protein Immobilization: Fundamentals and Applications*; Marcel Dekker, Inc.: New York, 1991; Chapter 8, pp 263–303.
(6) Weetall, H. H. *Immobilized Enzymes, Antigens, Antibodies, and Peptides: Preparation and Characterization*; Marcell Dekker, Inc.: New York, 1975; Chapter 6, pp 246–292, and Chapter 8, pp 419–497.
(7) Deutscher, M. P. *Trends Biochem. Sci.* **1988**, *13*, 136–139.
(8) Kawn, J. D. *Biochemistry*; Neil Patterson Publishers: Raleigh, NC, 1989; Chapter 22, pp 665–701.
(9) Humm, D. G.; Humm, J. H.; Shoe, L. I. *Biochim. Biophys. Acta* **1971**, *246*, 458–463.
(10) Blackburn, P.; Wilson, G.; Moore, S. *J. Biol. Chem.* **1977**, *252*, 5904–5910.
(11) Brison, O.; Chambon, P. *Anal. Biochem.* **1976**, *75*, 402–409.
(12) Wilchek, M.; Gorecki, M. *Eur. J. Biochem.* **1969**, *11*, 491–494.
(13) Wang, D.; Moore, S. *J. Biol. Chem.* **1978**, *253*, 7216–7219.
(14) Rahman, M. H.; Narang, U.; Bright, F. V.; Wang, J. H., submitted for publication in *Anal. Biochem.*

0003-2700/95/0367-1935$9.00/0 © 1995 American Chemical Society

we could develop a simple DNP-poly(A) immobilization strategy, one could use DNP-poly(A) to remove RNases from contaminated solutions.

Sol–gel processing[15–23] has attracted considerable interest because it represents a simple means to immobilize organic and even bioactive species for applications ranging from nonlinear optics to platforms for chemical sensors.[15–23] In this paper we use the simplicity of sol–gel processing to immobilize DNP-poly(A) and develop an affinity column to remove RNases from contaminated solutions. Our work differs significantly from that of Osaka and coworkers,[24] which demonstrated selective chiral recognition using sol–gel-derived columns based on entrapped L-tartaric acid. We report on the preparation protocol, the effect of precursor structure, the affinity of the DNP-poly(A)/sol–gel composite material, long-term stability of the column, column binding capacity, and leaching of the DNP-poly(A). Our results show that the RNase binding capacity remains in the microgram range and is orders of magnitude greater than the RNase concentration seen in clinical working solutions.[25] We also demonstrate that a RNase-loaded column can be easily regenerated using 1 M NaCl.

EXPERIMENTAL SECTION

Materials. The following chemicals were used: tetraethoxysilane (TEOS), tetramethoxysilane (TMOS), bovine serum albumin (BSA), trichloroacetic acid (TCA), potassium salt of poly(adenylic acid) (5′) (poly(A); average MW $\sim 1 \times 10^5$), 1-fluoro-2,4-dinitrobenzene (FDNP), ribonucleases A, B, S, and T_1, and diethyl pyrocarbonate (DEPC) (Sigma); tris(hydroxymethyl)-aminomethane (TRIS buffer; American Biorganics, Inc.); HCl, K_2HPO_4, and $KH_2PO_4{\cdot}2H_2O$ (Fisher Scientific Co.); disposable syringes and scintillator counting cocktail (VWR Scientific); and [^{3}H]poly(adenylic acid) (Amershan Corp.). Poly[2′-*O*-(2,4-dinitrophenyl)]poly(A) (DNP-poly(A)) was synthesized in our laboratory as described elsewhere.[14,26] All other reagents were used as received without further purification and aqueous solutions were prepared in doubly distilled–deionized water unless otherwise noted. All the glassware was autoclaved prior to use.

Equipment. UV–visible absorbance data were acquired using a Gilford 250 UV-Vis spectrophotometer. All steady-state fluorescence measurements were made on a SLM-Aminco 48000 spectrofluorometer. Radioactivity measurements were recorded on a Wallac liquid scintillation counter (Model 1409).

(15) Brinker, C. J.; Scherer, G. W. *Sol–Gel Science*; Academic Press: New York, 1989.
(16) *Chemical Processing of Advanced Materials*; Hench, L. L., West, J. K., Eds.; Wiley: New York, 1992.
(17) Lev, O.; Tsionsky, M.; Rabinovich, L.; Glezer, V.; Sampath, S.; Pankratov, I.; Gun, J. *Anal. Chem.* **1995**, *67*, 22A–29A.
(18) Dave, B. C.; Dunn, B.; Valentine, J. S.; Zink, J. I. *Anal. Chem.* **1994**, *66*, 1121A–1127A.
(19) Ellerby, L. M.; Nishida, C. R.; Nishida, F.; Yamanaka, S. A.; Dunn, B.; Valentine, J. S.; Zink, J. I. *Science* **1992**, *255*, 1113–1115.
(20) Levy, D.; Gigozin, I.; Zamir, I.; Kuyavskaya, B. I.; Ottolenghi, M.; Avnir, D.; Lev, O. *Sep. Sci. Technol.* **1992**, *27*, 589–597.
(21) Shtelzer, S.; Rappoport, S.; Avnir, D.; Ottolenghi, M.; Braun, S. *Biotechnol. Appl. Biochem.* **1992**, *15*, 227–235.
(22) Wang, R.; Narang, U.; Prasad, P. N.; Bright, F. V. *Anal. Chem.* **1993**, *65*, 2671–2675.
(23) Narang, U.; Dunbar, R. A.; Bright, F. V.; Prasad, P. N. *Appl. Spectrosc.* **1993**, *47*, 1700–1703.
(24) Mizukami, F.; Izutsu, H.; Osaka, T. *Adv. Mater.* **1994**, *6*, 854–855.
(25) Roth, J. S. In *Methods in Cancer Research*; Busch, H., Ed.; Academic Press: New York, 1967; pp 153–252.
(26) Kang, I.; Wang, J. H. *J. Biol. Chem.* **1994**, *269*, 12024–12031.

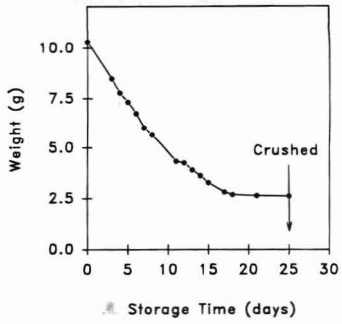

Figure 1. Change in weight of a DNP-poly(A)-doped TMOS-derived sol–gel as a function of storage time.

DNP-Poly[A]-Doped Sol–Gel Monolith Preparation. Two stock sol–gel solutions were prepared using TMOS and TEOS as the precursor materials. A stock sol–gel solution was prepared by mixing TMOS or TEOS, water, and HCl in the molar ratio 1:2:1.6×10^{-5}. After complete hydrolysis of the stock sol–gel solution (1 h for TMOS and 6 h for TEOS), 1.0 mL of phosphate buffer (pH 7.0; 0.01 M) was added to 4.0 mL of the stock sol–gel solution. Immediately after the phosphate buffer addition, 0.5 mL of stock DNP-poly(A) solution (130 μM; prepared in TRIS buffer) was added to the above mixture. The DNP-poly(A)-doped sol–gel solution was then stored under ambient conditions (room temperature and pressure) in a glass vial for aging and drying until constant weight was attained. The change in weight of a typical TMOS-derived DNP-poly(A)-doped sol–gel-derived monolith as a function of storage time is shown in Figure 1. These results show that at least 22 days is required for a DNP-poly(A)-doped TMOS-derived sol–gel monolith to attain constant weight. (Other processing schemes[15,16] could greatly reduce this time.) A similar profile was observed for a DNP-poly(A)-doped TEOS-derived sol–gel (data not shown). The dry, doped monoliths were light yellow. Blank, undoped monoliths were prepared following the above protocol using TRIS buffer instead of DNP-poly(A) solution.

Bioaffinity Column Preparation. Once the monoliths reached constant weight, they were crushed using a mortar and pestle and sieved. All DNP-poly(A)-doped sol–gel-derived particles were stored at 4 °C. The final DNP-poly(A)-doped particles were irregularly shaped and varied in size from 1 to 30 μm. Actual bioaffinity columns were fabricated by placing a circular piece of Whatman filter paper into the syringe barrel and loading a slurry containing 250 mg of the particles (doped or undoped) into a 1-mL syringe. The average column dead volume was 100 ± 5 μL (five TMOS and TEOS replicates). Gravity-induced flow rates through these column were generally very low ($\sim$50 μL/min), and we applied a modest argon head pressure to increase the flow rate to 400 ± 10 μL/min.

In the remainder of this paper, we refer to a DNP-poly(A)-doped sol–gel-derived bioaffinity column as a "doped column" and a sol–gel-derived column without DNP-poly(A), but otherwise prepared identically, as an "undoped column".

Radioactive Assay Method for RNase Determinations. The total volume of each reaction mixture was 100 μL, which consisted of 10 μL of TRIS buffer (0.1 M), 25 μL of the labeled [^{3}H]poly(A) (96 nM) prepared in TRIS buffer, and 25 μL of the

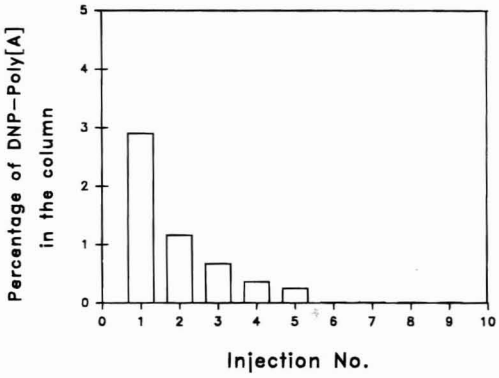

Figure 2. Percentage of the total, available DNP-poly(A) eluted from a doped column as a function of discrete 2-mL injections of DEPC-treated water.

solution eluting from the distal end of the column or 25 μL of a 0.8 μM RNase control solution. DEPC-treated water was added each time to make up the volume. After incubation at 37 °C for 1 h, the enzyme reaction was terminated by addition of 100 μL of BSA (10 mg/mL) and 600 μL of CTA (12%). Sample tubes containing the quenched reaction mixture were placed in crushed ice for 20 min and centrifuged at 13 000 rpm for an additional 20 min. A 600-μL aliquot from each sample tube was then mixed with 10 mL of the commercial scintillation cocktail and counted for 10 min. Blanks were run without the enzyme.

RESULTS AND DISCUSSION

Leaching Studies. The extinction coefficient of DNP-poly(A) at 259 nm is 1×10^6 M^{-1} cm^{-1}. This relatively high value results from the large number of adenosine groups ($\epsilon_{259} = 15\,400$ M^{-1} cm^{-1})[26] present in its structure. With our current spectrophotometer, the DNP-poly(A) detection limits are 2 nM. As a result, if all the DNP-poly(A) present within a doped column were to leach into a 2-mL volume, it would correspond to ~5 μM DNP-poly(A) solution (i.e., a concentration over 3 orders of magnitude above the detection limit). Thus, the absorbance of the column effluent at 259 nm is used to detect trace amounts of DNP-poly(A) leaching from the doped column.

In order to determine the fraction of total column-bound DNP-poly(A) that leaches from the column, we injected successively 2-mL volumes of DEPC-treated water and measured the absorbance at 259 nm. A calibration curve was constructed using known concentrations of DNP-poly(A). The percentage of the total column-bound DNP-poly(A) that leached from the doped column with each 2-mL injection is shown in Figure 2. These results show that a small fraction of DNP-poly(A) leaches from the column during the first few washings. However, after five washings, no detectable DNP-poly(A) was observed to leach from the doped column. We also note that the total amount of DNP-poly(A) that leaches from a doped column (10 columns were tested) was always less than 6% of the total amount of DNP-poly(A) present. The extent of DNP-poly(A) leaching from the doped columns is minimal compared to previous reports on dopant leaching from organically doped sol–gel-derived particles.[20] This most likely results because a DNP-poly(A) molecule is large (MW ~10^5); therefore, once it is entrapped within a sol–gel matrix, it is unlikely to meander through the connected pores and into the

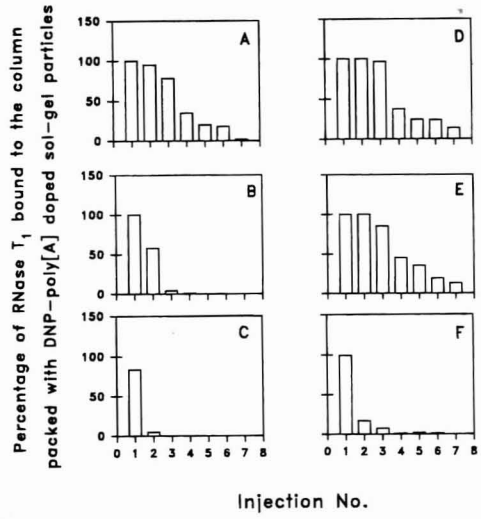

Figure 3. Effects of precursor material used for sol–gel processing and storage time on the RNase T_1 binding capacity of a DNP-poly(A)-doped column. Panels A–C represent the binding profiles for a TMOS-derived doped column prepared from particles stored at 4 °C for 28, 34, and 48 days, respectively. Panels D–F represent the binding profiles for a TEOS-derived doped column prepared from particles stored at 4 °C for 28, 33, and 50 days, respectively. Each injection corresponds to a 400-μL addition of 0.8 μM RNase T_1.

solution phase. Similar types of behavior have been observed for large enzymes or antibodies doped within sol–gel-derived materials.[21,22] We speculate that the DNP-poly(A) leaching that *is* observed results from loosely adsorbed DNP-poly(A) molecules desorbing from the surface of the sol–gel particles.

In all remaining studies, we washed the doped column with 10 successive 2-mL volumes of DEPC-treated water prior to use. No detectable DNP-poly(A) leaching was observed under these conditions.

RNase Removal. We tested DNP-poly(A) doped and undoped columns for binding to a variety of ribonucleases. In these particular experiments, we injected 400 μL of each ribonuclease solution (0.8 μM) and determined the percentage of the total injected amount of RNase that was bound by the column. The total binding of RNases T_1, A, B, and S to an undoped column was always less than 5%. In contrast, a DNP-poly(A)-doped column bound 100% of the RNases A, B, S, and T_1 injected onto the column. These results demonstrate that DNP-poly(A) remains active within the sol–gel-derived column, the sol–gel-entrapped DNP-poly(A) binds a variety of RNases, and at most 5% of the RNase binding is nonspecific.

TMOS and TEOS are the two most common precursor materials used to prepare silica-based sol–gel glasses.[15,16] The hydrolysis and condensation reactions for these alkoxides are somewhat different and result in a final material exhibiting different microporosities, pore volumes, and surface areas.[15,16] In order to compare the performance of TMOS- and TEOS-derived DNP-poly(A)-doped columns, we prepared a series of columns and studied their RNase binding capacity. For these and all subsequent studies, we used RNase T_1 alone as the model ribonuclease. Figure 3 summarizes the combined effects of the cumulative amount of RNase T_1 injected, storage time, and

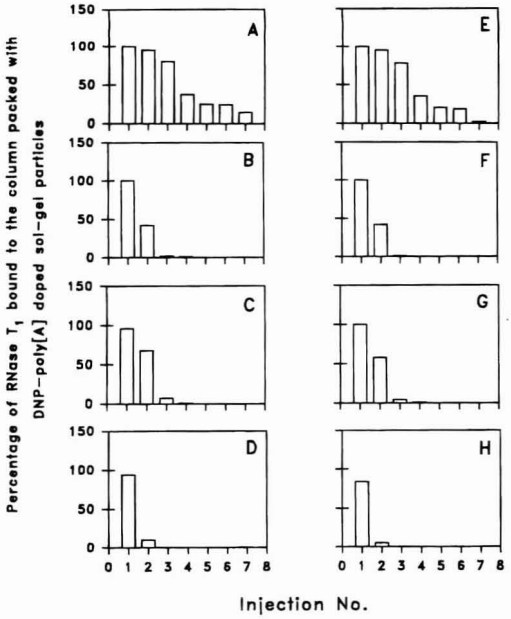

Figure 4. Effects of storage conditions and storage time on the RNase T_1 binding profile of a TMOS-derived DNP-poly(A)-doped column. Panels A–D represent the binding profiles for doped columns prepared from particles stored at 4 °C under dry conditions for 28, 34, 48, and 58 days, respectively. Panels E–H represent the binding profiles for doped columns prepared from particles stored at 4 °C under hydrated conditions for 28, 33, 40, and 50 days, respectively. Each fraction corresponds to a 400-μL addition of 0.8 μM RNase T_1.

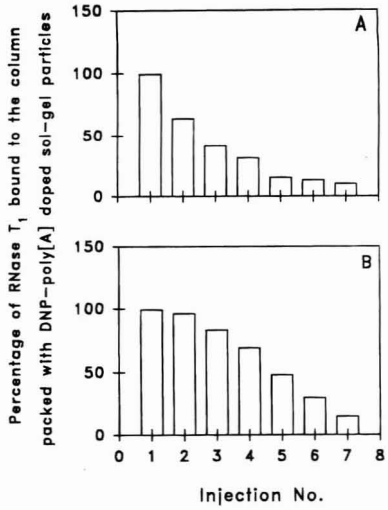

Figure 5. Percentage of RNase T_1 bound to a DNP-poly(A)-doped sol–gel-derived column upon injecting 400-μL aliquots of 0.8 μM RNase T_1: (A) radioactive assay; (B) fluorescence detection.

precursor type (TMOS, panels A–C; TEOS, panels D–F) on the DNP-poly(A)-doped columns. Each column was stored at 4 °C and each injection number represents an individual, discrete 400-μL injection of 0.8 μM RNase T_1 (3.52 μg) onto the column. The results demonstrate that (1) there is a decrease in the column binding capacity with storage time, (2) the column capacities for TMOS and TEOS-based doped columns are comparable, and (3) the total column capacity even after 2 months of storage exceeds several micrograms. The estimated level of RNases in clinical working solutions is in the nanogram (or lower) range;[25] therefore, our columns exhibit orders of magnitude greater capacity compared to RNase levels found in clinical working solutions.

Previous work from our laboratory demonstrated that hydration improved the stability of a sol–gel-entrapped antibody.[22] In order to investigate the effect of hydration on the DNP-poly(A)-doped sol–gel particles, we prepared a batch of DNP-poly(A)-doped TMOS-derived sol–gel particles. Half the batch was used to prepare a dry column. The remainder was used to form a column that remained hydrated in phosphate buffer. Both columns were stored at 4 °C. Doped columns (dry and hydrated) were studied as a function of storage time and tested for their binding capacity. Figure 4 summarizes the results of these experiments for dry (panels A–D) and hydrated conditions (panels E–H). The injection number again represents separate 400-μL injections of 0.8 μM RNase T_1 (3.52 μg) onto the column. Clearly, there is little if any change in the column binding capacity between dry or hydrated materials. There are generally two reasons for decreased response of a recognition element doped within a sol–gel matrix. The first involves a reduction in the recognition element activity/affinity due to denaturation or degradation. A second possibility arises from the extensive networking of the sol–gel material and shrinkage of the pores within a sol–gel matrix over time.[15–18,23] The decreased pore size reduces the accessibility of the target analyte to the recognition element resulting in an apparent decrease in the overall system response with time.[23] In the current system, the reduced binding capacity of the doped column over time most likely arises from a combination of both effects. It is beyond the scope of this study to deconvolute these factors.

To this point, we have used radioactive assay methods to quantify RNase binding. Unfortunately, this assay, despite its low detection limits (nM), is long and tedious, taking 3–4 h and a minimum of four separate steps. Fluorescence is potentially a more simple analytical approach with comparable detection limits. Further, many RNases possess fluorescent tryptophan residues. Thus, one can potentially use the intrinsic tryptophan fluorescence to quantify RNases. Figure 5 compares the percentage of RNase T_1 bound to a doped column upon injecting discrete 400-μL volumes of 0.8 μM RNase T_1, using radioactivity- (panel A) and fluorescence-based assays (panel B). These results clearly demonstrate that one can use fluorescence as effectively as the radioactivity-based assay for the detection of ribonucleases containing a fluorescent moiety without all the complexities associated with the radioactivity-based assays.

A very important aspect of any affinity-based column is its ability to be regenerated/reset. To investigate this issue, we loaded a column with RNase T_1 (Figure 6A). Sodium chloride is routinely used to reduce the binding of antigen–antibody complexes and has also been used to elute RNases bound to an affinity column.[1,13] We tested the suitability of NaCl to regenerate our columns by injecting five 0.5-mL volumes of 1 M NaCl through the RNase T_1-loaded DNP-poly(A)-doped column. Figure 6B illustrates the binding profile of the doped column *after* NaCl regeneration. Regeneration of a fully RNase T_1-loaded column

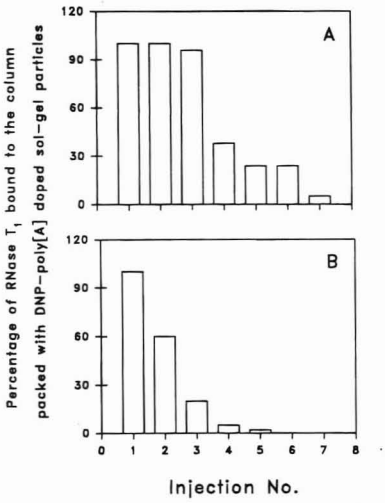

Figure 6. Sodium chloride regeneration of DNP-poly(A)-doped sol–gel-derived columns: (A) freshly prepared DNP-poly(A)-doped sol–gel-derived column on injecting 400-μL aliquots of 0.8 μM RNase T_1 solution; (B) same as (A) following regeneration by 1 M NaCl.

using up to 10 0.5-mL volumes of 1 M NaCl yielded similar profiles. Sodium chloride regeneration of a DNP-poly(A) column loaded with RNase A, B, or S was also similar (data not shown). These results demonstrate that (1) one can easily regenerate an RNase-loaded DNP-poly(A)-doped sol–gel-derived column using NaCl and (2) the binding capacity of the regenerated column is reduced upon regeneration. However, we again stress that the column capacity following regeneration is orders of magnitude greater than the level of RNase in normal contaminated samples.[25] We are currently investigating other regeneration protocols to maintain the column binding capacity.

CONCLUSIONS

We report on the preparation of a simple, low-cost sol–gel-derived bioaffinity column for the removal of a variety of RNases from solution using DNP-poly(A) as a molecular recognition element. In this particular work, we entrapped DNP-poly(A), an RNase inhibitor, within TMOS- or TEOS-derived sol–gels and formed particles that were packed into a 1-mL syringe. We demonstrated that DNP-poly(A) is active within the sol–gel matrix and binds to a variety of RNases. An undoped sol–gel-derived column exhibited <5% nonspecific binding to all the RNases tested. Overall, there is <6% leaching of DNP-poly(A) from the doped column. The binding capacities of TMOS- and TEOS-derived columns are comparable to one another. The binding capacities of doped columns, prepared with particles stored at 4 °C under dry and hydrated conditions are comparable. The doped columns could be regenerated using NaCl, but the regenerated column showed a reduced RNase binding capacity. However, despite this decrease, the RNase binding capacity for the columns exceeds the level of RNase in typical solutions by at least 1000-fold. These results also demonstrate the viability of preparing columns for separation techniques such as liquid, affinity, and bioaffinity chromatography based on sol–gel-derived materials.

Finally, Kang and Wang[26] recently demonstrated that DNP-poly[A], in aqueous solution, reversibly inhibits reverse transcriptase (RT) within the human immunodeficiency virus (HIV-RT). Therefore, in principle, a DNP-poly(A)-derived bioaffinity column can *potentially* be used to remove HIV from contaminated blood and plasma. This avenue is currently under investigation.

ACKNOWLEDGMENT

This work was supported in part by the National Science Foundation (CHE-9300694). The work at the Photonics Research Laboratory was supported in part by the National Science Foundation (DMR-9213907) and the Air Force Office of Scientific Research, Directorate of Chemistry and Materials Science, through Contract F49620-93-C-0017.

Received for review March 7, 1995. Accepted April 18, 1995.[⊗]

AC950230+

[⊗] Abstract published in *Advance ACS Abstracts,* May 15, 1995.

Anal. Chem. **1995,** *67,* 1940–1949

Mediated Herbicide Inhibition in a Pet Biosensor

Monika Preuss and Elizabeth A. H. Hall*

Institute of Biotechnology, University of Cambridge, Tennis Court Road, Cambridge, CB4 5HL U.K.

Many commonly employed herbicides are active on the photosynthetic electron transport chain. The main components of the reaction center of photosystem II (PSII) are the so-called D1 and D2 proteins, where herbicidal inhibition can occur. The inhibition can be monitored due to the mediated photocurrent, employing mediators that report on the reduction of the native plastoquinone, Q_B, at D1. This study employs diaminodurene to mediate the photocurrent in cells from the cyanobacteria *Synechoccus sp*. A comparison of the inhibition kinetics of atrazine and diuron is reported and the noncompetitive inhibitor, diuron, is shown to give an apparent first-order rate constant for binding that is ~7 times that of atrazine under the same light and dark cycle. Atrazine was shown to have a stronger binding affinity during the light regime than with the dark unexcited PSII state. In contrast with diuron, it also demonstrated evidence of interaction with PSI. In the case of atrazine, 50% inhibition of the photocurrent is predicted for 29 ppb herbicide, giving a theoretical minimum detection below 1 ppb. The stronger binding affinity with diuron would lead to a much lower level of detection under the same conditions. The action of the different inhibition kinetics, light and dark affinities, and interactions at PSI and PSII allow distinction to be made between the different herbicides, which could be extracted from the photocurrent in suitable light/dark cycles.

The detection and monitoring of herbicides at low levels is one of the prime ecological analytical targets. Even years after their application, many chemicals that have been applied in an agricultural environment are so stable that they remain in the soil and field waters.[1] At a more on-going and current level, the monitoring and control at or near the point of application, manufacture, or both can prevent accidental overapplication or early warning of spillage. In general, it is agreed that the most desirable method of detection should give a quick result, preferably at the site of sampling, such that remedial action can be taken immediately when necessary. The agreement is not quite so unanimous as to whether this "alarm" must be specific to just one molecule causing the pollution or whether detection of a family is preferred. In the former case, prior knowledge is required as to the precise expected nature of the pollutant, else the system will fail; on the other hand, in the latter case, the detector is more likely to provide the early warning signal but will not give information on the exact molecule involved.

One approach is to use the broad specificity of a first response to initiate a cascade of more specific analyses when a positive result occurs. The first response identifies the "group", and deconvolution of the measured signal may then give more precise information regarding the precise pollutant detected. In the case of herbicide detection, the compounds targeted may be so chemically dissimilar that their common analysis is unlikely, even by a group method. Nevertheless, progress can be made in this direction by focusing the method of detection on the transduction of their mode of action.

One of the actions of herbicides is on the photosynthetic electron transport (PET) chain. The PET includes two photosystems, photosystem I (PSI) and II (PSII). The reaction center of PSII mainly consists of the D protein (D1 and D2) and in an uninhibited system; the effect of a single photon can be measured on the water splitting complex located in PSII facing toward the lumen. However, electron transport through PSII involves two quinone molecules, Q_A and Q_B, and on the outer side of the membrane, facing toward the stroma, two quinone-type domains (Q_A and Q_B) are attached to the D protein. Q_A is considered to be the first stable electron acceptor molecule, which becomes reduced when the D protein becomes excited by light, and which remains bound with the D2 protein. On the other hand, Q_B is a plastoquinone, a mobile redox species, supplied from the plastoquinone pool, associated with the complex (Scheme 1). It is this domain which is susceptible to inhibition by atrazine and diuron. In its fully oxidized form, Q_B has a relatively low binding affinity for the hydrophobic pocket created by the D1 protein, but it is able to accept electrons from Q_A to become the tightly bound semiquinone Q_B^-.[2] In the absence of illumination, the Q_B site is fully occupied by the tightly bound semiquinone. During illumination, a second electron, transferred from Q_A to Q_B^-, reduces it to Q_B^{2-} and initiates charge compensation by H^+ transfer from the cytoplasm. The resulting Q_BH_2 has a low binding affinity for D1 and is released from the binding pocket. Normally, the Q_BH_2 would transfer its electrons to the cytochrome b_6–f, while the D1 binding site becomes occupied by another molecule from the plastoquinone pool. It is at this stage that the herbicide has the opportunity to enter the empty binding site and inhibit the electron transport. For an inhibitor acting in this way, the rate at which inhibition occurs will depend on the turnover of D1 giving the vacant binding site and thus should be related to the illumination cycle.

In the main, for PSII herbicides, the mode of action is in competition with the native plastoquinone for the binding site of Q_B at the D1 protein of the PSII complex.[3,4] Detection of this

(1) Charles, D. *New Sci.* **1991**, (2 March), 43.

(2) McPherson, P. H.; Schönfeld, M.; Paddock, M. L.; Okamura, M. Y.; Fehler, G. *Biochemistry* **1994**, *33*, 1181–1193.

(3) Oettmeier, W. In *The Photosystem: Structure, Function and Molecular Biology*; Elsevier Science Publishers: New York, 1992; pp 349–401.

(4) Pakrasi, H.; Vermaas, W. F. J. In *The Photosystem: Structure, Function and Molecular Biology*; Elsevier Science Publishers: New York, 1992; pp 231–245.

0003-2700/95/0367-1940$9.00/0 © 1995 American Chemical Society

Scheme 1. Photocycle at D1/D2 Reaction Center of PSII and Interaction of Mediator and Herbicides

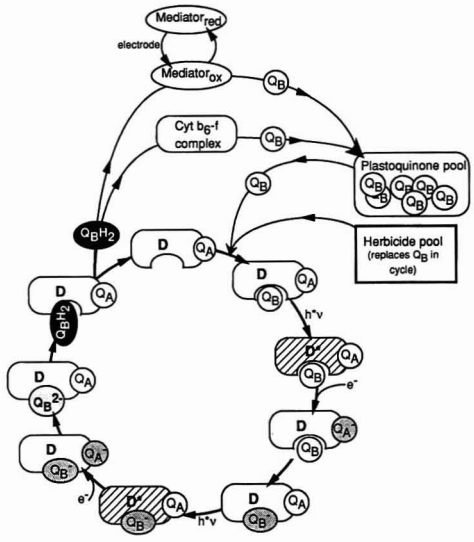

inhibition is thus a route toward their assay.[5-7] In a previous paper, we reported the detection of PET activity in cells from the cyanobacteria *Synechoccus sp.*, as a photoinitiated current resulting from the interception of charge in the PET with an electroactive mediator, diaminodurene (DAD).[8] The lipophilic character of DAD enables penetration of the cell membrane and interaction with the PET at the reducing sites of both PSI and PSII or the oxidizing site of PSI.[8] Any inhibition of PET "upstream" of the mediator interception could be detected as a reduction of the photocurrent. The use of this mediator appeared to offer levels of detection for triazines and ureas in the low-ppb range, and thus, the analytical method was considered for further development as a biosensor, and a novel emulsion immobilization method was developed, compatible with whole cells.[9]

Further information is now required concerning the result of the interaction of different herbicides with the PET system, such that the signal due to the inhibition of the photocurrent can be decoded. Herbicides which are, or have been, commonly deployed and are active at PSII include the triazines, ureas, *p*-quinones, uracils, ketonitriles, and N- and O-heterocyclic ketones. This paper looks at the mode and kinetics for inhibition of the photocurrent by two herbicides, namely, atrazine and diuron, in a diaminodurene-mediated PET from *Synechoccus sp.*, which has been assembled in a biosensor format. These herbicides have been chosen for this study since they have been in wide use and their inhibition of the photosystem is reported as noncompetitive with respect to each other,[3] which infers that they involve a different binding site or mode of inhibition.

(5) Purcell, M.; Carpentier, R.; Berlanger, D.; Fortler, G. *Biotechnol. Tech.* **1990**, *4*, 363–368.

(6) Rawson, D. M.; Willmer, A. J.; Cardosi, M. F. *Toxic. Assess.* **1987**, *2*, 325–340.

(7) Rawson, D. M.; Willmer, A. J.; Turner, A. P. F. *Biosensors* **1989**, *4*, 299–311.

(8) Martens, N.; Hall, E. A. H. *Photochem. Photobiol.* **1994**, *59*, 91–98.

EXPERIMENTAL SECTION

Chemicals required for the preparation of the electrolyte, immobilization medium, or BG 11 medium were of analytical grade and supplied by Sigma or Aldrich. The mediator was used as received from Aldrich in 97% purity and dissolved in 70% (w/v) ethanol. The herbicides atrazine and diuron were supplied by Sigma and prepared as stock solutions of different concentrations by dissolving them in methanol (absolute). The cyanobacterium *Synechococcus* (PCC 6301) was provided by Dr. Peter Rowell University of Dundee, Dundee, Scotland.

Fresh stock solutions of mediator, 10 mg/mL 2,3,5,6-Tetramethyl-1,4-phenylenediamine (diaminodurene, DAD) in 70% (w/v) ethanol, were prepared on a daily basis. An appropriate aliquot, leading to a final concentration of 0.1 mmol/L DAD, was added to the electrolyte. In order to prevent the oxidative destruction of DAD, the air-saturated electrolyte was purged with nitrogen and maintained under nitrogen during the experiments.

Synechococcus was grown in batch cultures in 250 mL conical flasks using BG 11 medium. The liquid cultures were grown at 25 °C with 100 oscillations/min in an orbital shaker with warm fluorescent light. Stock cultures were maintained using the same medium with the addition of 1.5% agar.

The cultures were grown to the midexponential phase with an optical density of $OD_{663} = \sim 1.0$ and harvested in 1 mL aliquots by rapid centrifugation for 5 min at 13 000 rpm in a desk-top centrifuge (Microcentauer MSE UK). The supernatant was removed, and the cell pellets were frozen in liquid nitrogen and then stored at −18 °C. There was no significant loss of activity over a period of 1 week of storage.[8]

The photosynthetic cells were immobilized in a calcium alginate matrix. The cell pellet obtained after centrifugation was thawed and resuspended in 20 μL of a 1% sodium alginate solution in BG 11 medium. A total of 3 μL of this suspension was then applied onto the surface of a glassy carbon electrode with a surface area of 0.071 cm^2. This drop-coated electrode was then dried for 30 min at room temperature. The formation of the calcium alginate matrix was achieved by incubating the "dry" electrode for 30 min in a 50 mM $CaCl_2$ solution of BG 11 medium containing 50 mM MOPS buffered at pH 7.0. In order to prevent the matrix from being washed off the electrode surface, the layer was covered with a dialysis membrane and secured with a rubber O-ring to keep the cells in place.

The dialysis membrane was prepared by boiling in a 1% (w/v) solution of sodium carbonate for 10 min and was subsequently rinsed thoroughly with purified water and stored at −18 °C.

All electrodes for one experimental series were prepared from the same batch of culture. Prior to use, the assembled electrodes were conditioned by soaking them in BG 11 medium containing 50 mM KCl and 50 mM MOPS buffered at pH 7.0 for ~10 min.

It is important that the cells are immobilized in a thin layer in contact with the electrode. Thicker cell layers fail to achieve the same resolution for two reasons. First, the outer layer of cells "masks" the underlayers from the incident light. Second, DAD is supplied into the solution in the reduced form, but for interaction with PSII (Schemes 1 and 2), it is required in the oxidized form. The electrode is held at the oxidizing potential, so that DAD_{ox} is produced at the electrode, supplying the cells close to the electrode. In the presence of light, the cell "output" from PSII is DAD_{red}, so that flux of DAD_{red} to the electrode increases, giving

(9) Martens, N.; Hall, E. A. H. *Anal. Chim. Acta* **1994**, *292*, 49–63.

Scheme 2. Photoelectron Transport between PSII and PSI and Interaction of Mediator DAD

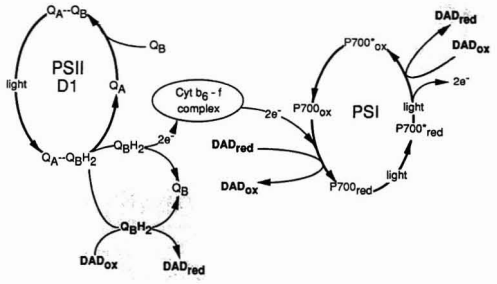

rise to a photocurrent. The magnitude of this current may also be modulated by intracellular interaction with PSI either by the oxidized DAD or by the reduced DAD, the latter supplied from the bulk solution or the "output" from PSII (Scheme 2). If the electrode is held at the reduction potential, it responds to the net flux of DAD_{ox} to the electrode; this is supplied from PSI only.[8] In the absence of DAD, there is no photocurrent recorded at either the oxidizing or reducing potential.[8]

All measurements were performed in a stirred water-jacketed electrochemical cell of 15 mL working volume, adjusted to 25 °C. In order to exclude light, the vessel was coated with black tape and sealed with a rubber lid through which the electrodes were inserted into the cell. The electrochemical cell was operated in a three-electrode mode with a glassy carbon (surface area, 0.071 cm^2) working electrode, a platinum flag (surface area, 1.5 cm^2) counter electrode, and a saturated calomel electrode (SCE) as the reference electrode.

Additions of herbicide into the sample solution were made directly via a fine injection channel through the lid of the electrochemical cell. After an addition, the solution was stirred briefly with a magnetic stirrer. Inhibition is seen after two or three light pulses following addition of herbicide, depending on the reproducibility of stirring (compare parts a and b of Figure 4).

Photosynthetic stimulation of the immobilized microorganisms on the working electrode was provided by a halogen lamp (1 W, 12 V) in combination with a UV filter to eliminate photochemical destruction of the light-sensitive mediator itself. This external light source was positioned beneath the electrochemical cell such that direct illumination of the working electrode was achieved. During the photocurrent measurements, the electrode was exposed to constant illumination in order to monitor the current/time response of both the uninhibited and inhibited systems. The light intensity in these experiments was set to a relatively low supply of 4.5 V with respect to the power source. This was selected to prevent a current decrease due to photoinhibition and photobleaching of the pigments of the photosynthetic electron transfer chain.

In other experiments, the photosynthetic activity of the biocatalyst was monitored during alternating periods of illumination and a dark period of 2.5 or 5 min. The light pulses were controlled by an "in-house" constructed timer, producing variable pulses between 68 ms and 1.24 s length. Unless otherwise stated, pulses of 1.24 s length (at 4.5 V) were applied with a dark period of 2.5 min. The current generated with this standard pulse length showed an anodic photocurrent of approximately 70–80% with respect to the maximal current achieved with constant illumination of the same light intensity. Alternatively, light pulses of 250 ms, but of an increased supply of 8 V at the light source, were applied.

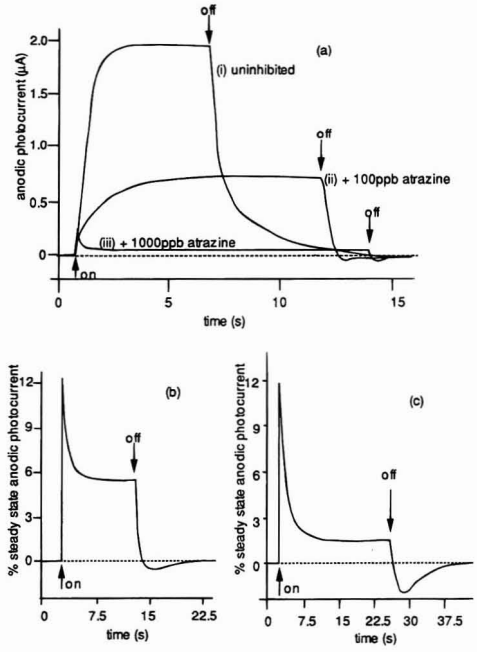

Figure 1. Diaminodurene-mediated anodic photocurrent, generated by cells of *Synechoccus sp.* immobilized at a carbon electrode. Commencement and termination of illumination is indicated by the arrows: (a) DAD oxidation recorded at **200** mV vs SCE (i) in the absence of herbicide, (ii) in the presence of 100 ppb atrazine, and (iii) in the presence of 1000 ppb atrazine. Expansion of the residual photocurrent in the presence of (b) 1000 ppb atrazine and (c) 1000 ppb diuron.

Electrochemical measurements were performed using a Model 273 potentiostat/galvanostat (EG&G Princeton Applied Research). Mediator oxidation was monitored at +200 mV and reduction at −200 mV. All potentials are referenced to the SCE. The current/time response was recorded on a $Y-t$ chart recorder (Gould BS-273). Cyclic voltammograms were recorded on a $X-Y$ plotter (Philips PM 8043).

RESULTS AND DISCUSSION

Interaction with the Photosystem. In principle, the mediator current resulting from the photoactivation of the PET increases with light intensity. However, high light intensities or prolonged light exposure also leads to photobleaching of the light-harvesting pigments and photoinhibition. This problem was addressed earlier[8] and an illumination regime, consisting of a series of light pulses, was proposed and shown to be efficient in terms of both excitation of PET and its stability, but in order to identify the mechanism of herbicide interaction in the light and dark regimes, the response of the photosystem to a light pulse was reexamined. In Figure 1, the attainment of a steady-state response of the photosystem to a light stimulus is shown in the presence and absence of atrazine. The photocurrent recorded in Figure 1 is achieved by intercepting the charge transport in the PET cycle

with an electron-accepting mediator, in this case DAD, which is then oxidized at an electrode, producing a current signal. However, it is not immediately clear whether the mediator acts itself by replacing Q_B in the cycle or whether it accepts electrons from the reduced quinone Q_BH_2, which is expelled from the cycle (Scheme 1).

Its close resemblance to Q_B (or other herbicides acting at D1) makes DAD a likely candidate for occupying the hydrophobic Q_B pocket of D1 and thus interacting directly with the PET as a competitor with Q_B. However, the general behavior seems more in favor of the oxidation of the expelled Q_BH_2, since, simply because of the higher concentration (10^3-fold) of the mediator, it would exclude any effect from a further competition by traces of herbicide, dominating the binding of vacant sites in a competitive binding with Q_B at the D1 protein. As can be seen in Figure 1, this is clearly not the case, and herbicides are able to inhibit the photocurrent, even at low concentrations. If the mediator oxidizes the Q_BH_2, which is expelled from the cycle, it interrupts the link between PSII and PSI, which normally occurs via the action of Q_BH_2 on the cytochrome b_6–f complex (Scheme 2).

From Schemes 1 and 2, we can deduce several possible effects which may be caused by the presence of an inhibitor acting at the D1 site. In considering this, it has to be remembered that the site is normally only vacated by the expulsion of Q_BH_2, and this chain is initiated by light. However, the D1 binding site is altered in the "dark" and "light" cycles, so that there will be different affinity constants for each of the binding competitors, depending on whether it is in the dark or light cycle. In the presence of inhibitor (INH), the competition for D1 sites can thus have different results: the D1 sites vacated by Q_BH_2 on each cycle can be (i) irreversibly filled with INH; (ii) filled by INH, which accepts electrons and is expelled at the end of the cycle where it is able to (a) to transfer electrons into the PSI or (b) is unable to transfer electrons into PSI; or (iii) not filled by INH, but influenced by its binding adjacent to the D1 site. These mechanisms can also be further complicated by different binding affinities in the excited (light) and unexcited (dark) states.

If the mediator reports on the output of Q_BH_2 on each cycle, and thus the turnover of Q_B in D1 sites, then Figure 1 shows either a decrease in D1 sites occupied by the plastoquinone or a decrease in its turnover, in the presence of herbicide as an inhibitor. However, DAD also catalyzes a cyclic electron transport around PSI (Scheme 2), so that even when the D1 sites are totally inhibited, a photocurrent results from the PSI interaction. The measured anodic DAD-mediated photocurrent can thus be represented as

$$i_{tot} = i_{PSII_{ox}} + i_{PSI_{ox}} - i_{PSI_{red}}$$

where in the absence of inhibitor the reduction of PSI may be achieved by a competition between DAD_{red} and the electrons transferred from Q_BH_2 via cytochrome b_6–f. As can be seen in Figure 1, the fast initial photocurrent response following onset of illumination is less dependent on herbicide concentration and probably represents the initial oxidation of the excited PSI state by DAD ($i_{PSI_{ox}}$).

If the inhibitor shows no activity toward PSI, then as the output of Q_BH_2 decreases with increase in INH, the reduction of PSI by DAD_{red} becomes more favored and $i_{PSI_{red}}$ will increase. On the other hand, if the inhibitor can also transfer electrons to PSI, there may be no net change in $i_{PSI_{red}}$, or if it is a better electron transfer

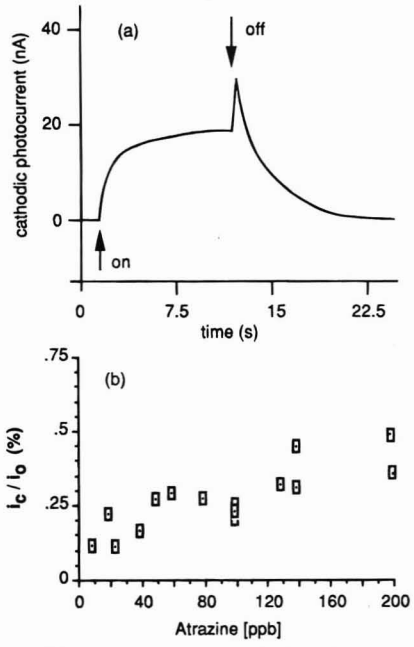

Figure 2. Diaminodurene-mediated cathodic photocurrent, generated by cells of *Synechoccus sp.* immobilized at a carbon electrode: (a) DAD reduction recorded at −200 mV vs SCE in the presence of 1000 ppb atrazine. Commencement and termination of illumination is indicated by the arrows. (b) Increase in cathodic photocurrent with atrazine concentration.

agent to PSI than DAD, $i_{PSI_{red}}$ may even decrease; similar arguments also apply to $i_{PSI_{ox}}$ if the inhibitor can accept electrons from PSI. Comparing parts b and c of Figure 1, it would appear that at high herbicide concentrations, where $i_{PSII_{ox}}$ is eliminated, a residual photocurrent is still obtained due to ($i_{PSI_{ox}} - i_{PSI_{red}}$), but the residual photocurrent for diuron is less than for atrazine:

$$(i_{PSI_{ox}} - i_{PSI_{red}})_{atr} > (i_{PSI_{ox}} - i_{PSI_{red}})_{diu}$$

From this it would be inferred that the oxidation of PSI by DAD is greater during atrazine inhibition, the reduction of PSI by DAD is less during atrazine inhibition, or both. If PSII is *totally* inhibited in both these examples, the former may suggest that atrazine is capable of interacting with the PSI cycle to a greater extent than diuron.

In the system employed here, an increase in $i_{PSI_{red}}$ seems also to be indicated by the current dropping below the baseline following the termination of illumination in the presence of both atrazine and diuron (Figure 1b,c). As the PSI_{ox}* returns to the ground state it becomes fully reduced, normally by the Q_BH_2 electron output from the previous light cycle. However, in the absence of this reducing agent transferred from the PSII cycle, DAD_{red} performs the step as illumination ceases, giving rise to a transient decrease in the concentration of DAD_{red}, so that the current falls below the background "dark" level.

The ability of DAD to reduce PSI, and thus maintain some output from the photocycle even in the presence of PSII inhibitors, may account for the longevity of the cells in the presence of DAD[8] compared with other mediators that have been proposed, such

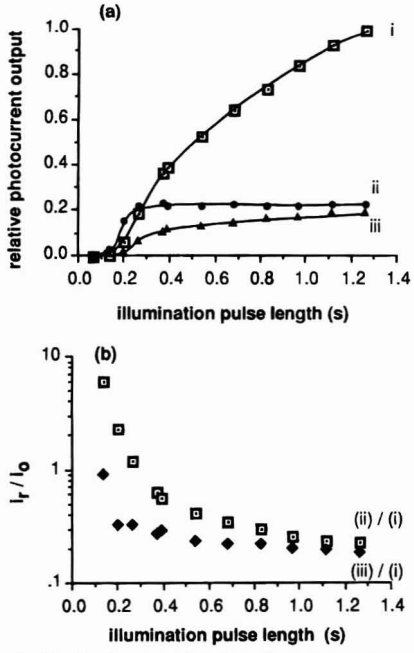

Figure 3. Diaminodurene-mediated anodic photocurrent, generated by cells of *Synechoccus sp.* immobilized at a carbon electrode: (a) a DAD oxidation recorded at +200 mV vs SCE as a function of illumination time, in a light/dark cycle employing variable illumination time (*x* axis) and fixed 2.5 min dark regime (i) in the absence of herbicide, (ii) after inhibition with 1000 ppb atrazine for 1 h, and (iii) after inhibition with 1000 ppb diuron for 1 h. Photocurrent is recorded at the end of the illumination period and includes the total contribution from PSI and PSII at that time. (b) Relative change in photocurrent as a function of illumination time due to inhibition by atrazine and diuron from data in (a).

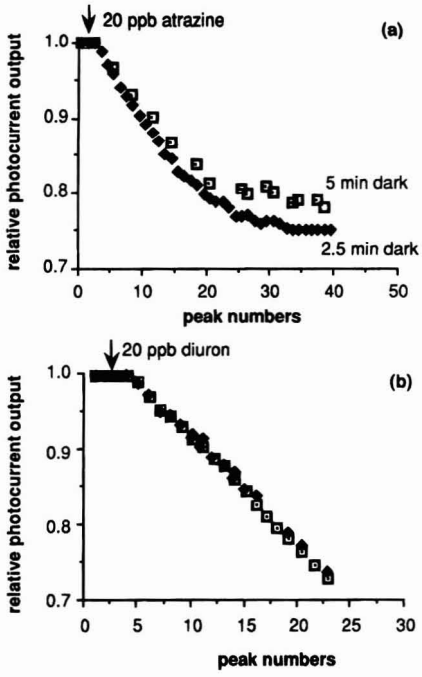

Figure 4. Effect of inhibition of the diaminodurene-mediated anodic photocurrent, generated by cells of *Synechoccus sp.* immobilized at a carbon electrode. DAD oxidation is recorded at +200 mV vs SCE for a light/dark cycle employing 1.24 s light regime and 2.5 or 5 min dark intervals. The photocurrent for in each 1.24 s light pulse is recorded and plotted against number of pulses (peak number) applied: (a) effect of addition of 20 ppb atrazine; (b) effect of addition of 20 ppb diuron.

as benzoquinone or ferricyanide, where PSI activity has not been reported. However, even though DAD may be able to promote the electron output from PET, it cannot replicate the vital H^+ gradient that is normally created by the Q_B cycle, so that indefinite operation seems unlikely.

In principle, the interaction of DAD_{red} with PSI could also be monitored as a reduction current, giving an indirect indication of PSII inhibition. However, as can be seen in Figure 2, the currents involved are less than 1% of the anodic photocurrent, so that the resolution is poor. The lower current is expected, since under these conditions the electrode is held at a reducing potential, and DAD_{ox} is not produced at the electrode, to interact with Q_BH_2 from PSII; thus Q_BH_2 reduces the cytochrome b_6–f and the charge is carried into PSI. The photocurrent measured here then represents only the DAD that is able to compete with this charge transfer into the PSI (Scheme 2). Nevertheless, the anticipated trend is confirmed, with DAD contributing to the reduction of PSI ($i_{PSI_{red}}$) more as the concentration of inhibitor increases and the Q_BH_2 output is reduced.

Investigation of the Anodic Photocurrent. Atrazine and diuron are reported to be reversible inhibition processes,[7] with the system coming into dynamic equilibrium when the cycle ceases, during the dark period. If the inhibitor enters the vacant D1 sites in PSII during the light cycle, then for a given dark (equilibration) period, it would be expected that the steady-state photocurrent inhibition would be a function of illumination period. Figure 3a compares the residual photocurrent (i_r) with the uninhibited photocurrent (i_0), as a function of illumination time, following 1 h exposure to 1 ppm atrazine and diuron. It is clear from this figure that maximum photocurrent output from the uninhibited system is achieved only for illumination times in excess of 1 s, which must be associated with the slow attainment of a steady-state cycling of Q_BH_2 from PSII. In the presence of diuron, the same time scale is involved in achieving steady state, so that a plot of i_r/i_0 (Figure 3b) is nearly independent of pulse length. On the other hand, in the presence of atrazine, the photocurrent even shows an initial *increase*, compared with the uninhibited photocurrent; this may be caused by the interaction of atrazine with *PSI*, so that $i_{PSI_{ox}}$ is seen to increase. In any case, the photocurrent reaches its maximum output within 300 ms following illumination and then becomes independent of time, well before the expected steady-state cycling of PSII is achieved in excess of 1 s. This offers two interpretations: the atrazine is either bound at the D1 site during the dark period, so that Q_B is already excluded at the start of the light cycle, or the Q_B/atrazine competition favors atrazine binding in the light cycle, so that once the initial flux of "dark bound" Q_B is expelled, it is replaced with atrazine.

In the former case, the results for atrazine should be consistent with a "dark" inhibition mechanism at the D1 site, reflecting a

Scheme 3. Mechanistic Pathways of Inhibition of the Photocycle at D1 by (a) Atrazine and (b) Diuron

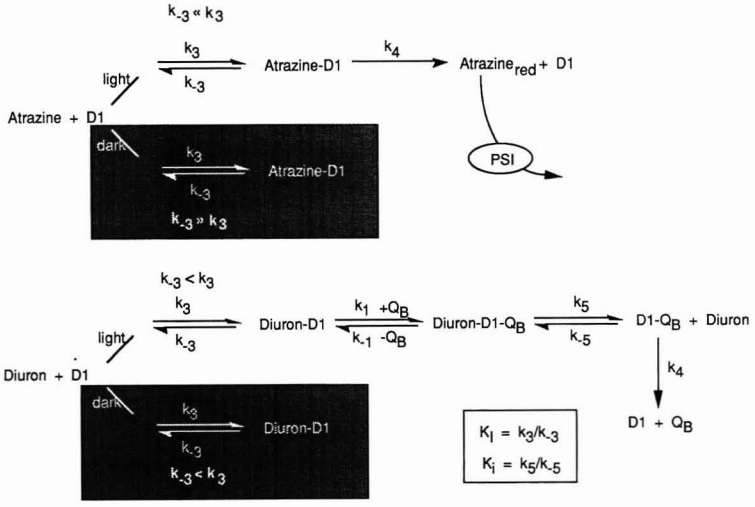

lower "dark" affinity constant for Q_B than the inhibitor, and it would be anticipated that the inhibition would increase with the length of the dark period. Conversely, if atrazine is bound only weakly or not at all during the dark period, but strongly in the light period, then inhibition would decrease with the length of the dark period. The latter mechanism is confirmed by altering the dark period over a range of atrazine concentrations. For example, Figure 4a shows a 4% increase in residual photocurrent after inhibition by 20 ppb atrazine, when the dark period is extended from 2.5 to 5 min.

No influence on the rate of inhibition could be found by altering the dark regime in the presence of diuron (Figure 4b), and together with the apparent independence of i_f/i_0 with illumination time, this seems to indicate that the diuron is bound similarly in both the light and the dark periods. Atrazine and diuron are reported as being noncompetitive with respect to one another,[3] with diuron being proposed as a noncompetitive inhibitor of the D1 site, binding adjacent to the Q_B site. The results reported here are thus consistent with this view, and the behavior of atrazine and diuron can be distinguished: atrazine is bound preferentially in the light cycle and is expelled at the end of the light cycle. It is able to interact with PSI, thus enhancing the initial photocurrent response due to $i_{PSI_{ox}}$. Conversely, diuron binding occurs adjacent to the D1 site; it is less influenced by the light/dark cycle and once bound is lost only very slowly from the site. These proposals are summarized in Scheme 3.

Kinetics of Inhibition. If the system can be approximated by a simple model of "active site"-catalyzed redox then the following mechanistic pathway follows:

$$D1 + Q_B \underset{k_{-1}}{\overset{k_1}{\rightleftharpoons}} (D1{-}Q_B \rightleftharpoons D1{-}Q_BH_2) \xrightarrow{k_2} D1 + Q_BH_2$$

This leads to

$$\frac{d[Q_BH_2]}{dt} = k_2[DQ] = \frac{k_2[D1_t][Q_B]}{K_Q + [Q_B]} \qquad (1)$$

where $[D1_t]$ is the total D1 sites, [DQ] is the plastoquinone–D1 complex (irrespective of oxidation state of the quinone), and $K_Q = (k_{-1} + k_2)/k_1$. If the mediator (DAD) reports the output of Q_BH_2, then the current measured is related to the flux described by eq 1. This allows the following relationship to be derived:

$$i_0 = \frac{i_{max}[Q_B]}{K_Q + [Q_B]} \qquad (2)$$

where $i_{max} \propto k_2[D1_t]$, and when $K_Q \gg [Q_B]$, then a first-order relationship between i_0 and Q_B would be anticipated, if Q_B could be varied.

In an earlier study it was shown that the photocurrent output increases linearly with both the concentration of DAD and the amount of chlorophyll applied to the electrode.[4] These observations lead to the rate equation

$$\text{rate} = k_a[\text{Chl}][\text{Med}] \qquad (3)$$

where [Chl] and [Med] are the concentrations of chlorophyll and mediator, respectively. k_a, the pseudo-second-order rate constant, was estimated as 2.9×10^8 mol^{-1} s^{-1} from which the rate constant with respect to reaction centers can also be deduced (ratio between chlorophyll and reaction centers is ~200:1 [10]). k_a also contains variables such as illumination time and intensity, but for a given illumination and with other experimental parameters held constant, the rate is equivalent to the peak current on illumination.

In the experiment described here, the current value prior to inhibition by herbicide (i_0) was standardized by keeping [Chl] (and thus D1 sites) and [Med] constant. Focusing on the PSII, then the current, $i_{PSII_{ox}}$, due to the output of Q_BH_2, is followed, but in the presence of atrazine or diuron, this output decreases as the inhibition site (D1 or adjacent) becomes occupied by the herbicide. In the case of competitive inhibition of the D1 site, the change in peak current (i_p) with time could therefore be related to the apparent decrease in $[D1_t]$ due to the filling of vacant sites with the inhibitor. Thus the initial rate of current decrease following addition of the inhibitor will be given by

(10) Streyer, L. *Biochemistry*; Freeman: San Francisco, 1981.

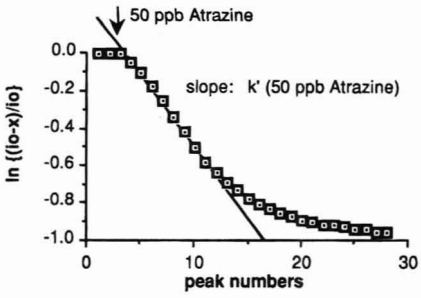

Figure 5. Diaminodurene-mediated anodic photocurrent, generated by cells of *Synechoccus sp.* immobilized at a carbon electrode. DAD oxidation is recorded at +200 mV vs SCE during a light/dark cycle employing 1.24 s light interval and 2.5 min dark regime. Typical response to herbicide inhibition is shown here for 50 ppb atrazine.

$$-\frac{di_p}{dt} = k_i[\mathrm{INH}]^n \tag{4}$$

where k_i is the pseudo-nth-order rate constant describing the inhibition mechanism and [INH] is the concentration of inhibitor. If

$$\mathrm{D1} + \mathrm{INH} \xrightarrow{k_3} \mathrm{DI}$$

where DI is the D1−inhibitor complex, then according to this scheme k_i also contains the concentration of vacated D1 sites, which should remain a constant if the inhibitor is expelled in the PSII cycle in the same way as Q_BH_2. On the other hand, if it is bound but not expelled, the number of vacated D1 sites will also diminish with inhibition time. If in the absence of inhibition the photocurrent is given by i_0, then at time t, for a given concentration of inhibitor, the effective number of D1 sites occupied by Q_B has decreased by x:

$$-\frac{di_p}{dt} = -\frac{d(i_0 - x)}{dt} = \frac{dx}{dt} = -k'(i_0 - x) \tag{5}$$

$$\ln\frac{i_0}{(i_0 - x)} = k't \tag{6}$$

where

$$k' = k_i[\mathrm{INH}]^n \tag{7}$$

so that k' and k_i can be obtained as shown in Figures 5 and 6. As can be seen in Figure 5, for short inhibition times the data fit the first-order relationship well (eq 6), but the residual current due to the PSI interaction at longer inhibition times becomes significant compared with the total current and is not accommodated by this simple mechanistic description. At these times, the approximation that the number of vacated D1 sites remains a constant may also not be valid.

The validation of the data taken at shorter times (Figure 6) can be confirmed by comparing with that obtained by estimating the initial rate (Figure 7) since from eq 4 n and k_i can be extracted (Figure 8)

$$-\log\frac{di_p}{dt} = \log k_i + n \log [\mathrm{INH}] \tag{8}$$

However, this method has a general disadvantage in that it is usually less accurate, due to the difficulty in drawing accurate tangents to represent the initial rate. Nevertheless, Table 1 shows a good correlation of the constants obtained for the inhibition of atrazine and linuron, which leads to a prediction of an order of ~1 with respect to the inhibition mechanism for both herbicides.

In the case of diuron, a noncompetitive inhibition mechanism would lead to the D1−INH−Q_B complex, which cannot release Q_BH_2 directly. If diuron is a reversible inhibitor, then the complex can dissociate to yield D1−Q_B (Scheme 3). However, if the rate of dissociation is slow, then the result as far as output of Q_BH_2 is concerned is the same as seen above for the competitive case, since the inhibitor complex effectively reduces effective D1 sites. Thus, data for diuron also gives an order with respect to the herbicide of ~1, but a rate constant much higher than that for atrazine. This is consistent with the stronger inhibition reported with the noncompetitive diuron mechanism.

Predicted Levels of Detection. For the purposes of a biosensor able to detect levels of a herbicide in field or potable waters, the minimum level that can be detected is of extreme importance. The higher binding kinetics for diuron indicates that low levels of diuron would be more easily detected as a change in signal (i_p). Nevertheless, in the case of atrazine, the inhibition was significant even at 5 ppb and above 100 ppb maximum inhibition was observed.

Taking the "active-site" redox model, then for a competitive inhibitor (Scheme 3a) the residual current should be given by

$$i_r = \frac{i_{max}[Q_B]}{[Q_B] + K_Q[1 + [I]/K_I]} \tag{9}$$

which gives

$$\frac{i_0}{i_r} = 1 + \frac{K_Q[I]}{([Q_B] + K_Q)K_I} \tag{10}$$

If the inhibition can be described by this model, therefore, a plot of i_0/i_r should intercept the y axis at $i_0 = i_r$ and if $K_Q \gg [Q_B]$ (i.e., there are free binding sites at D1) then the intercept on the x axis gives K_I ($K_I = (k_4 + k_3)/k_3$).

Figure 9 shows the results of this analysis for illumination times of 1.24 s and 250 ms. In the former case (Figure 9a), the model intercepts the y axis as predicted, at 1, and leads to an estimate of K_I of 29 ppb. This value predicts the concentration of atrazine required to reduce the current to half its initial value (representing 50% inhibition). For i_0 of 2 μA and a signal resolution of 1%, this would indicate a resolution of better than 1 ppb atrazine. However, as can be seen from the data reported, the ability to reproduce the same electrode produces a scatter that is greater than 1 ppb.

From the data analyzed for a shorter illumination time in the light/dark cycle, it can be seen in Figure 9b that the y axis intercept is >1 and there is deviation from the prediction of K_I above. However, according to the discussion above (Figure 3), this short illumination pulse is dominated by the fast $i_{PSI_{ox}}$ during atrazine inhibition, not $i_{PSII_{ox}}$. At 250 ms, the faster $i_{PSI_{ox}}$ photocurrent is up to 80% of i_0, whereas for illumination times greater than 1 s it contributes less than 10% of i_0. Figure 9c shows the i_0/i_r ratio corrected for the PSI current contribution, and it can now be seen that these data agree closely with the prediction for K_I at 1.24s.

In the case of diuron, a noncompetitive binding inhibition (Scheme 3b) leads to

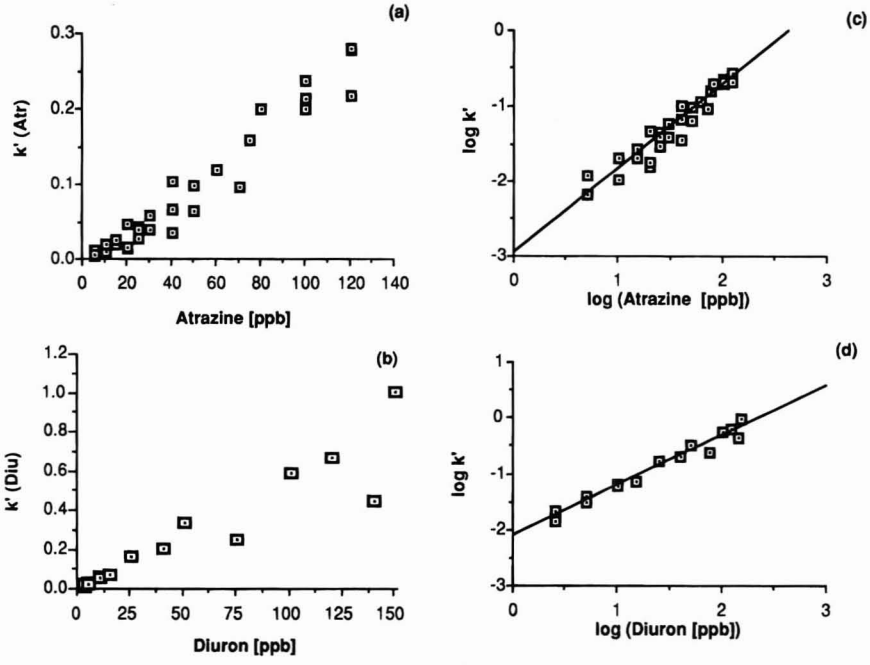

Figure 6. Initial rate of inhibition of photocurrent due to (a) atrazine and (b) diuron, showing approximate linear relationship, obtained from the slope of the diaminodurene-mediated anodic photocurrent, generated by cells of *Synechoccus sp.* immobilized at a carbon electrode as shown in Figure 5. log/log plot for (c) atrazine, obtained from (a), and (d) diuron, obtained from (b), in order to obtain order and rate constant of inhibition.

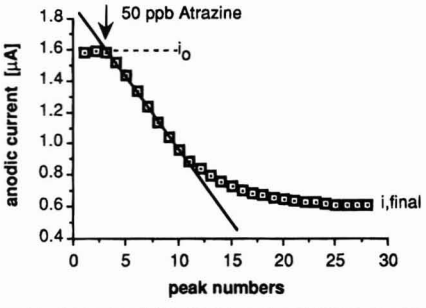

Figure 7. First-order plot for the interaction of 50 ppb atrazine with cells of *Synechoccus sp.* immobilized at a carbon electrode, mediated by diaminodurene. DAD oxidation is recorded at +200 mV vs SCE.

$$\frac{i_0}{i_r} = 1 + \frac{K_Q[I]}{([Q_B] + K_Q)K_I} + \frac{Q_B[I]}{([Q_B] + K_Q)K_i} \qquad (11)$$

so that only in cases where $K_i \sim K_I$ does a simple relationship between the x axis intercept and the equilibrium constant for the inhibitor binding exist. In any case, the inhibition by diuron was greater than by atrazine, so that only data at low diuron concentration gave a residual current that was dependent on concentration. This would indicate a very small K_I, but as a result of the strong inhibition, insufficient data could be obtained across a large enough concentration range to extract accurate information, and 50% inhibition at ~5 ppb is estimated.

The value of K_I predicted for atrazine is much lower than that obtained (~1700 ppb) in an oxygen-mediated detection of the photosystem isolated from thyalkoid membranes.[5] However, the mediation by oxygen is not directly related to the redox processes at D1, and the higher value may reflect a "compensation" effect achieved by the photosystem as a whole during the inhibition. The value is closer to the range reported previously[7] for the inhibition of *Synochoccus* with 2,5-dibromo-3-methyl-6-isopropyl-*p*-benzoquinone and linuron (20–50 ppb), although in our work, we have found that linuron shows inhibition similar to that seen by diuron,[11] so we would predict a lower apparent K_I here. However, the values extracted will be strongly dependent on the mediation mechanism and may be a result of the different mediator used in this study. Mediators that are able to interact themselves, directly with the D1 site, or else "report" on a PET species other than Q_BH_2 will not give direct information about the inhibitor–Q_B competition.

Table 1. Comparison of n and k_i for Atrazine and Diuron[a]

	initial rate method		Q_B filled D1 sites method	
	n	k_i	n	k_i
atrazine	1.02	1.23	1.11	1.15
diuron	0.84	7.30	0.89	8.27

CONCLUSION

In the development of a system for the detection of herbicides, the results with the DAD-mediated photocurrent from *Synochoccus*

(11) Martens, N. Aspects of mediated amperometric biosensors. Ph.D. Thesis, University of Cambridge, Cambridge, U.K., 1994.

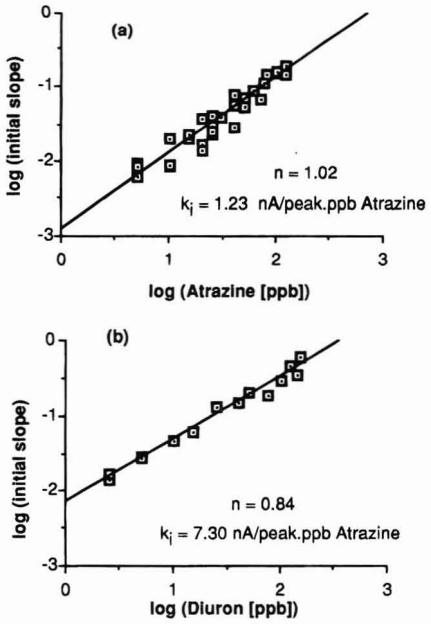

Figure 8. Pseudo-first-order rate constant from the inhibition of photocurrent due to (a) atrazine and (b) diuron, obtained as shown in Figure 7. log/log plot for (c) atrazine, obtained from (a), and (d) diuron, obtained from (b), in order to obtain the rate constant of inhibition.

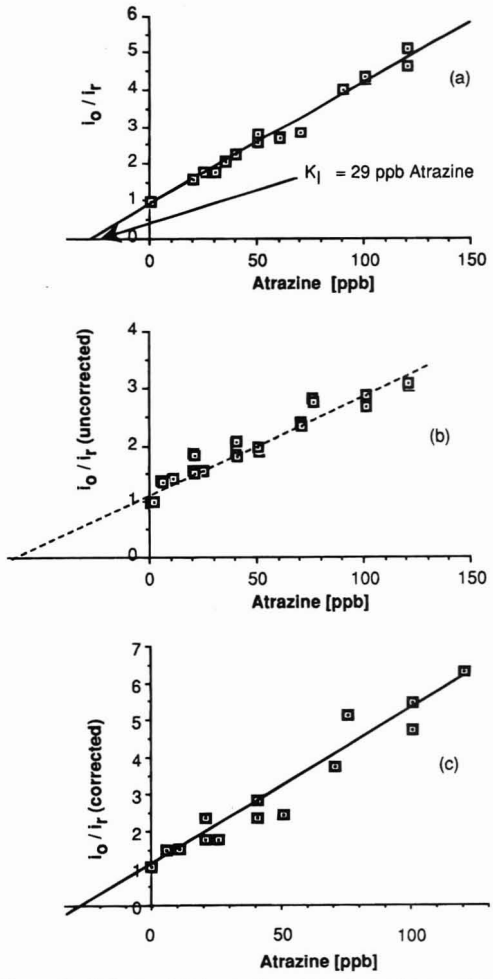

Figure 9. Estimate of K_i for atrazine. Data obtained from a light/dark cycle of (a) 1.24 s/2.5 min, K_i = 29 ppb; (b) 250 ms/2.5 min, without correction for $i_{PSI_{ox}}$, K_i = 61 ppb; and (c) 250 ms/2.5 min, with correction for $i_{PSI_{ox}}$, K_i = 28 ppb.

give a detection level within the ppb range, compared with the oxygen-mediated ppm levels obtainable with spinach thylakoid membranes. The mediator reports on the PET production of Q_BH_2, probably oxidizing the reduced plastoquinone, Q_BH_2, which is expelled from the D1 site in the light cycle, and thus the photocurrent is sensitive to inhibitors of the D1 site in PSII, where they act competitively or noncompetitively with the oxidized plastoquinone Q_B for binding.

The binding kinetics for different herbicides active at D1 may be influenced by both the dark and light affinity constants and the expulsion of the herbicide (possibly in a reduced form) during the light cycle. Atrazine, for example, is a competitive inhibitor of D1, which is released from the active site during the dark cycle and has a much enhanced binding affinity during the light regime, but it is cycled by the PSII, so that D1 sites are vacated as it is expelled. This leads to a "large" K_I (29 ppb) and large dynamic range of detection. On the other hand, diuron is bound noncompetitively during both the light and dark regimes and has a strong affinity, but does not appear to be expelled to any significant extent during the light cycle, thus causing a small K_I and smaller but lower dynamic range of detection.

By considering the rate of inhibition following exposure to a herbicide, the kinetics can be studied even for concentrations outside the dynamic range predicted by K_I. A trend similar to that seen in the K_I estimates was obtained, with a first-order inhibition constant for diuron that was ~7 times that of atrazine, but the full derivation and comparison of these rate constants is complicated by their dependency on light and dark cycles, so the differences may vary if compared exclusively within a light or dark period. For example, since the binding of atrazine is reversed during the dark period, the apparent rate of inhibition following exposure will depend on the light/dark cycle. On the other hand, since the inhibition by diuron was independent of the light and dark regimes, the apparent first-order rate constant should not vary and, in principle, could be obtained in independent units.

The variation in affinity of different herbicides during the light and dark regimes has extreme potential has a means of identifying individual herbicides from the families active at D1. The application of complex light and dark cycles is readily achieved by simple light switching control. In addition, further specificity can be gained from monitoring the DAD-mediated $i_{PSI_{red}}$ current at the reduction potential for DAD. This current measurement is less attractive than the oxidation current, since it is only equivalent to less than 1% of the anodic current. Nevertheless, it gives diagnostic information, in particular about the ability of the herbicide to interact with PSI. In the case of atrazine, there is evidence that it is able to reduce PSI (either directly or via electron

transfer to Cyt b_6–f), but diuron does not show this activity. This information may be better exploited with a PSI-exclusive mediator, where the photocurrent is only influenced by the PSI interactions and cannot be short-circuited by interaction at PSII/Q_BH_2. In such an arrangement, the PSII inhibition and resultant effect on PSI would be measured independently with different mediators at an electrode array.

In conclusion, however, this study has shown that the mediated photocurrent is able to report on the inhibition of the D1 site and that it has the potential for further deconvolution, in order to achieve a more precise identification of the inhibition species.

Received for review February 9, 1995. Accepted April 18, 1995.[⊗]

AC950147M

[⊗] Abstract published in *Advance ACS Abstracts,* May 15, 1995.

Anal. Chem. **1995,** *67,* 1950–1954

High-Resolution Matrix-Assisted Laser Desorption/Ionization in a Linear Time-of-Flight Mass Spectrometer

Randy M. Whittal and Liang Li*

Department of Chemistry, University of Alberta, Edmonton, Alberta, Canada T6G 2G2

A time-lag focusing method is developed for the improvement of mass resolution in a linear time-of-flight mass spectrometer for matrix-assisted laser desorption/ionization (MALDI). In this technique, the ions generated by the MALDI process are extracted by a pulsed voltage. A short time delay (280 ns) is inserted in between the laser desorption/ionization event and the ion extraction. The region between the repeller and extraction grid is field-free during the delay. The time-lag extraction allows the ions generated in the region between the repeller and the extraction grid to separate according to their velocity (energy). Application, to the repeller, of the appropriate pulse voltage provides the energy correction necessary to simultaneously detect all ions of the same mass/charge regardless of their initial energy, resulting in improved mass resolution. It is demonstrated that mass resolution in the range of 3000–6000 fwhm can be obtained. With this mass resolution, isotopically resolved mass spectra are observed for peptides with masses up to 3000 Da. For proteins, such as bovine insulin, cytochrome *c*, and apomyoglobin, resolution in the range of 800–1000 fwhm is observed with a mass measurement accuracy better than 0.01%.

Matrix-assisted laser desorption/ionization (MALDI) has become an increasingly important technique for the detection of biopolymers.[1,2] At present, the ions generated by the MALDI process are commonly analyzed with the use of a time-of-flight mass spectrometer (TOFMS). A TOFMS is inexpensive to construct and simple to operate. It has no theoretical mass limit. The sensitivity of TOFMS can be very high due to its efficient ion transmission and ion extraction duty cycle with a pulsed ionization source. A major drawback of TOFMS is the low mass resolving power for the detection of ions in MALDI. Low mass resolution can be attributed to several factors including the initial spatial, temporal, and kinetic energy distribution of the ions. Metastable decay in the flight tube may also play a significant role.[3] Several approaches have been developed to reduce the contribution of one or more of these factors in order to enhance the mass resolution of MALDI TOFMS. For example, a TOFMS that is equipped with an ion reflector for compensation of the kinetic energy distribution provides much improved mass resolution.[3] Resolution as high as 6000 fwhm (defined as $t/(2\Delta t)$, where t is the flight time of the ion and Δt is the peak width at half height) has been reported for peptides with masses up to 3000 Da in a commercial system.[4] In contrast, a simple linear TOFMS normally provides a mass resolution of no greater than 1000 fwhm.

Reported here is the observation of mass resolution in the range of 3,000–6,000 fwhm in a simple linear TOFMS. With this high resolution, isotopically resolved mass spectra are observed for peptides with masses up to 3000 Da. To attain this resolution, a time-lag focusing (TLF) method is used for ion extraction. In conventional MALDI instruments, the ions generated by the laser beam near the surface of the sample probe are extracted by a dc potential. In TLF, a short time delay (<300 ns) is inserted between the laser ionization and ion extraction events. The region between the repeller and extraction grid is field-free during the delay. Following the delay, a pulsed potential is applied to the repeller. Application of the appropriate pulse voltage provides the energy correction necessary to simultaneously detect all ions of the same mass/charge regardless of their initial energy. The initially less energetic ions closer to the repeller receive more energy (from the pulsed potential) than the initially more energetic ions further from the repeller at the time the pulse is applied. An energy/spatial correction is thus provided such that all ions of the same mass/charge reach the detector plane simultaneously. The optimal pulse potential is mass dependent; higher pulse potentials are required for ions of higher mass.

The time-lag focusing concept was first reported by Wiley and McLaren[5] for improving mass resolution in electron impact ionization TOFMS. Shortly after the report of the first MALDI experiment, Spengler and Cotter used the TLF method for MALDI in an orthogonal TOFMS system.[6] We have also been involved in developing the TLF method, primarily for our continuous-flow, liquid chromatography MALDI interface. We observed a significant improvement in mass resolution over DC ion extraction. Recently, Lennon and Brown[7] reported the use of pulsed ion acceleration in a conventional parallel ion extraction configuration. Mass resolution of up to 1600 fwhm was reported in their linear system. Reilly et al.[8] have developed a pulsed spatial/velocity

(1) Chait, B. T.; Kent, S. B. H. *Science* **1992,** *257,* 1885–1894.
(2) Hillenkamp, F.; Karas, M.; Beavis, R. C.; Chait, B. T. *Anal. Chem.* **1991,** *63,* 1193–1203.
(3) Cotter, R. J. In *Time-of-Flight Mass Spectrometry;* Cotter, R. J., Ed.; ACS Symposium Series 549; American Chemical Society: Washington DC, 1994; pp 16–48.
(4) Ingendoh, A.; Karas, M.; Hillenkamp, F.; Giessmann, U. *Int. J. Mass Spectrom. Ion Processes* **1994,** *131,* 345–354.
(5) Wiley, W. C.; McLaren, I. H. *Rev. Sci. Instrum.* **1955,** *26,* 1150–1157.
(6) Spengler, B.; Cotter, R. J. *Anal. Chem.* **1990,** *62,* 793–796.
(7) Lennon, J. J.; Brown, R. S. In *Proceedings of the 42nd ASMS Conference on Mass Spectrometry and Allied Topics,* Chicago, IL, May 29–June 3, 1994; p 501.
(8) Colby, S. M.; King, T. B.; Reilly, J. P. *Rapid Commun. Mass Spectrom.* **1994,** *8,* 865–868.

0003-2700/95/0367-1950$9.00/0 © 1995 American Chemical Society

focusing instrument to achieve similar results. It is further noted by Hillenkamp et al.[9] that pulsed ion extraction improves the sensitivity for the detection of MALDI-generated ions. Herein we present a study of the TLF method for improving mass resolution in a linear MALDI TOFMS. We demonstrate that a simple linear system with TLF can provide mass resolution similar to that obtained with a reflectron TOFMS.

EXPERIMENTAL SECTION

The MALDI TOFMS is constructed at the University of Alberta. The ionization region is housed in a 22 × 22 × 22 cm cubic stainless steel vacuum chamber pumped with a 15-cm diffusion pump (Varian). Additional pumping is provided by a 10-cm diffusion pump (Edwards) connected to the middle of the flight tube. The flight tube is made from 10-cm-diameter stainless steel tubing, providing a total flight path of ~1 m. The vacuum pressure of the instrument in the flight tube is 2 to 5 × 10^{-8} Torr. The ion optics design is facilitated with the Simion ion trajectory simulation program. The ionization and ion extraction regions consist of four stainless steel plates separated with 5-mm ruby balls which provide a plate separation of 4.5 mm. The ion repeller plate has a 4.2-mm hole in the center for insertion of the sample probe. The two extraction plates are gridless with a 12-mm-diameter hole. The ground plate has a 1-cm-diameter center hole covered with a stainless steel grid. Following the ground plate is a pair of ion deflectors. For all the experimental results shown here, the ion deflectors are grounded. The detector is a 1.8-cm-diameter Chevron multichannel plate assembly (R. M. Jordan Co.) operated with the front plate set to −2 kV.

A nitrogen laser (Photochemical Research Associates LN1000) is used to generate the MALDI ions. The laser temporal width is not measured, but it is reported to be 800 ps by the laser manufacturer. The laser power used for each sample is adjusted to just above the threshold for ion production.

For ion extraction in DC mode, the voltage applied to the ion source is typically 12, 8, and 4 kV for the repeller and two extraction plates, respectively. For pulsed ion extraction, a custom-built power supply is used to power the repeller plate. This power supply is capable of delivering a 5-kV pulsed potential with a rise and fall time of 30 ns and adjustable pulse width from 300 ns to 3 ms. The pulsed potential used for ion extraction is typically 1−3 kV. This potential can be varied to achieve optimal ion focusing for the analyte of interest. Up to 20 kV can be applied as a DC offset to the pulse. The offset is adjusted to 12 kV DC for all the spectra shown below. An independent DC power supply is used to match the potential applied to the first extraction plate to that of the repeller voltage. The potential applied to the second extraction plate is 6 kV. The timing sequence in the time-lag focusing experiment is as follows. A portion of the laser beam from the nitrogen laser strikes a photodiode to generate a trigger pulse. This pulse is used to trigger a pulse generator that in turn triggers the high-voltage pulse power supply. An induction signal from the high-voltage pulse is used to trigger the oscilloscope.

The minimum time delay between the ionization and ion extraction events is 230 ns, which is set by the propagation delay time of triggering and pulsing circuitry. In order to achieve the high mass resolution reported here, we find that a minimum delay time of 280 ns is required. Further decrease in the delay time does not provide improvement in mass resolution. However, the width of the mass range where isotopically resolved peptide peaks can be achieved is also found to be dependent upon the delay time. Shorter delay times narrow the range. Thus, a 280-ns delay time is used throughout the work presented herein.

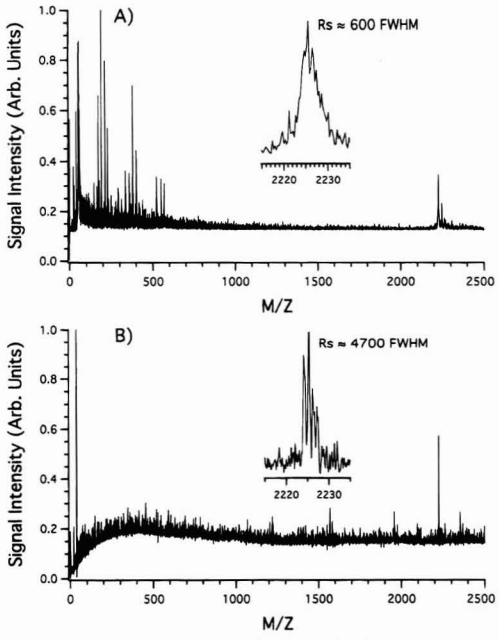

Figure 1. MALDI mass spectra for a total loading of 1 pmol of a synthetic peptide, Ac-ELEKLLKELEKLLKEAEK-Am (monoisotopic, $(M + H)^+ = 2224.317$ Da), obtained by using (A) dc ion extraction and (B) time-lag focusing ion extraction with a 2.00-kV pulse. Each spectrum is the result of signal averaging of 100 shots on the oscilloscope.

The ion signal is first amplified with a 500-MHz (3 dB), 20-dB amplifier (CLC 100, Comlinear Corp.). A spectrum is captured using either a LeCroy 9354M or 9350M digital oscilloscope. The major difference is the sampling rate. The 9354M oscilloscope provides a sampling rate of up to 2 × 10^9 samples/s or a time resolution of 0.5 ns/point whereas the 9350M oscilloscope has a time resolution of 1 ns/point. In most TLF experiments, we find that the 9350M oscilloscope is adequate. Single-shot spectra may have peak widths as narrow as 2.0 ns; thus, undersampling is observed in some cases. All mass spectra, with exceptions noted, are the result of signal averaging of 100 laser shots. Signal averaging is performed on the oscilloscope without selection. The averaged mass spectrum is then downloaded to a PC for processing.

Bradykinin, insulin, cytochrome *c*, and myoglobin were purchased from Sigma. The synthetic peptides were a gift from the Center of Excellence in Protein Engineering at the University of Alberta. The α-cyano-4-hydroxycinnamic acid (CHCA) and sinapinic acid (SA) were purchased from Aldrich. All solvents were purchased from BDH Laboratories Inc. Trifluoroacetic acid (TFA) was purchased from Caledon Laboratories. Water used throughout the experiment was from a NANOpure water system (Barnstead/Thermolyne).

(9) Wang, B. H.; Dreisewerd, K.; Bahr, U.; Karas, M.; Hillenkamp, F. *J. Am. Soc. Mass Spectrom.* **1993**, *4*, 393−398.

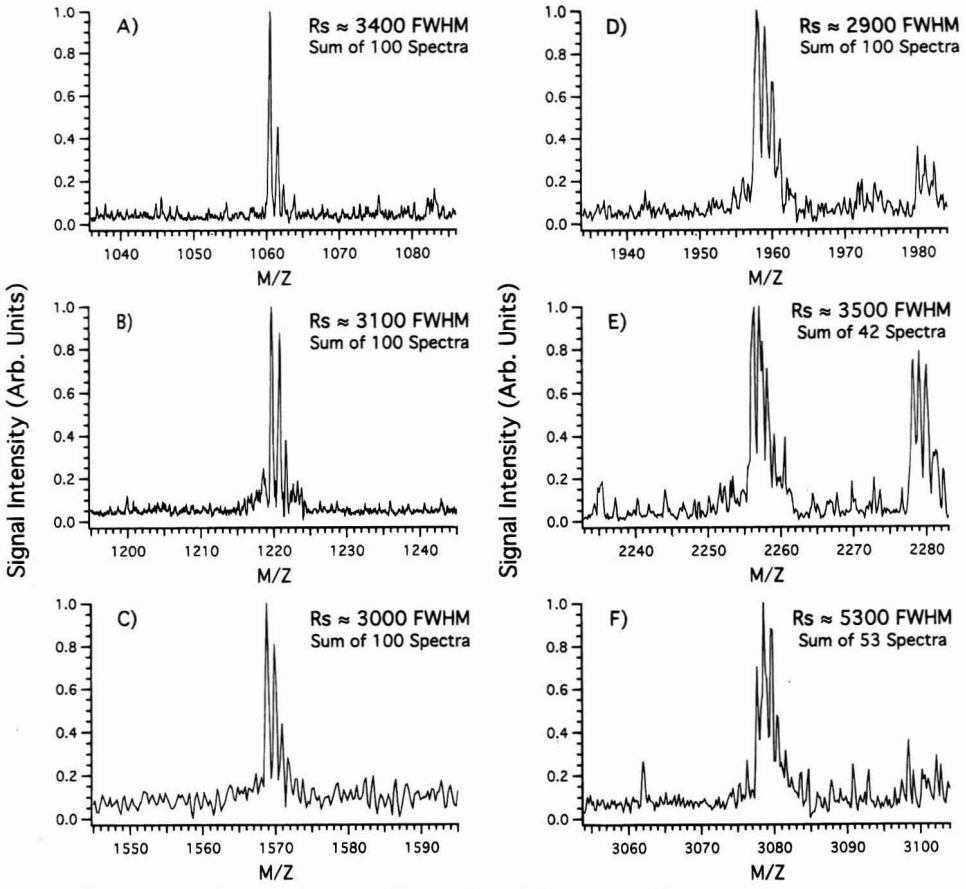

Figure 2. TLF MALDI mass spectra for a total loading of 1 pmol of peptide for several peptides using CHCA as matrix. The pulse potential used is given in parentheses: (A) bradykinin, $(M + H)^+ = 1060.569$ Da (0.90 kV); (B) LYPVKLYPVK, $(M + H)^+ = 1219.746$ Da (1.00 kV); (C) Ac-KLEALEAKLEALEA-Am, $(M + H)^+ = 1568.290$ Da (1.30 kV). (D) Ac-EAEKAAKEAEKGAKEAEK-Am, $(M + H)^+ = 1958.020$ Da (1.75 kV). (E) Ac-ELEKLLKECEKLLKELEK-Am, $(M + H)^+ = 2256.289$ Da (2.05 kV); (F) Ac-KLEALEAKLEALEAKLEALEAKLEALEA-Am, $(M + H)^+ = 3077.735$ Da (2.50 kV).

Standard preparation techniques are used to prepare samples.[10] A saturated solution of matrix is prepared in 30% methanol/0.1% TFA with the aid of vortex mixing. The matrix solution is then centrifuged to eliminate suspended solids. Peptide and protein samples are prepared at a concentration of 1–5 μM in 0.1% TFA. A 1.0-μL drop of matrix and 1.0-μL drop of sample are mixed together on the probe tip and allowed to dry. Alternatively, the method of Vorm et al.[11,12] was used. In this case, matrix solutions are prepared in acetone at a concentration of 0.12 M. A 0.5-μL drop of matrix solution is applied to the probe tip. The droplet spreads and dries very quickly, leaving a thin layer of matrix crystals. Peptide samples are prepared in 0.1% TFA at a concentration of 1.0 μM. A 1.0-μL drop of peptide solution is placed on top of the matrix layer and allowed to dry. The sample is then washed by placing 10 μL of room temperature water on the probe tip. After 20 s the water is absorbed by placing a Kimwipe at the edge of the probe tip.

RESULTS AND DISCUSSION

Figure 1A shows a typical MALDI mass spectrum for 1 pmol of a synthetic peptide (monoisotopic mass of 2224.317 Da) acquired with the application of a DC potential. Figure 1B is the mass spectrum of the same peptide, obtained under the same experimental conditions with the exception of the application of TLF. The molecular ion region of each spectrum is shown in the inset. The observed mass resolution for Figure 1A is ~600 fwhm. Figure 1B shows that the isotope peaks of this compound are well resolved with TLF MALDI. The mass resolution is calculated to be 4700 fwhm. Using a two-point external mass calibration, the mass of the monoisotopic peak is determined to be 2224.790 Da, representing a mass measurement accuracy of 0.02%. With the use of a two-point internal calibration, the molecular ion mass is found to be 2224.302 Da. This shows a mass accuracy of 7 ppm. The internal calibrant peaks in this case, as shown in Figure

(10) Karas, M.; Bahr, U.; Giebmann, U. *Mass Spectrom. Rev.* **1991**, *10*, 335–357.
(11) Vorm, O.; Roepstorff, P.; Mann, M. In *Proceedings of the 42nd ASMS Conference on Mass Spectrometry and Allied Topics*, Chicago, IL, May 29–June 3, 1994; p 9.
(12) Vorm, O.; Roepstorff, P.; Mann, M. *Anal. Chem.* **1994**, *66*, 3281–3287.

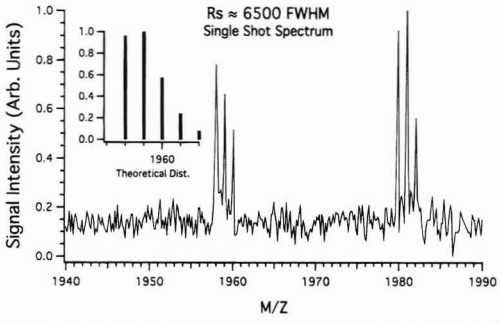

Figure 3. Single-shot mass spectrum for a total loading of 1 pmol of synthetic peptide Ac-EAEKAAKEAEKGAKEAK-Am using CHCA as matrix. The pulse potential used is 1.75 kV.

1B, are the peaks at m/z 1569 and 1959 corresponding to the synthetic peptides Ac-KLEALEAKLEALEA-Am and Ac-EAEKAAKE-AEKGAKEAEK-Am, respectively.

Figure 2 A shows the molecular ion region of several peptides with molecular masses in the range of 1000–3000 Da. The observed mass resolution of each spectrum is listed in the figures and exceeds 3000 fwhm in most cases. The temporal peak width is generally in the range of 3.0–4.5 ns fwhm. The theoretical minimum peak width is the combination of the detector response, oscilloscope and amplifier bandwidths and jitter in the trigger electronics.[13] A dual-microchannel plate detector has a pulse width of ~2 ns. The LeCroy 9350M and 9354M oscilloscopes and Comlinear's CLC 100 preamplifier have a bandwidth of 500 MHz. A 500-MHz bandwidth should have an insignificant broadening effect upon a 2-ns peak. Electronic jitter in the acquisition starting point and trigger relays broadens peaks when performing spectral summing. The extent of jitter-induced peak broadening is not known for the system but one should expect it to be significant. As an example, Figure 3 shows the $(M + H)^+ = 1958.02$ Da and $(M + Na)^+$ molecular ions for a single-shot mass spectrum of a synthetic peptide. The peak widths vary from 1.8 to 2.3 ns. Therefore, the calculated mass resolution for this single-shot spectrum also varies from 5700 to 7300 fwhm. The inset in Figure 3 shows the theoretical isotopic distribution for this peptide. One should note that although the mass accuracy is better than 33 ppm for all peaks, the isotopic distribution is not accurately represented in a single-shot spectrum.

Further investigation of Figure 3 reveals that small peaks are observed on the high-mass side of most of the peaks, preventing baseline separation. These small peaks cannot be due to electronic jitter but must be the result of other experimentally induced parameters. Specifically, the major contribution to peak broadening for a summed spectrum may be the kinetic energy and spatial distribution of the ions at the time the potential pulse is applied. The initial kinetic energy distribution is converted into an energy and spatial distribution which may be corrected in the ion source.[5] Selection of the appropriate pulse voltage provides focusing such that the slower ions closer to the repeller impact the detector at the same time as the faster ions further from the repeller. But this correction may not be perfect. If this is the case, improvement in the ion optics design and the pulse shape, rise time, etc., of the extraction pulse may be necessary. Further

(13) Guilhaus, M. *J. Am. Soc. Mass Spectrom.* **1994**, *5*, 588–595.

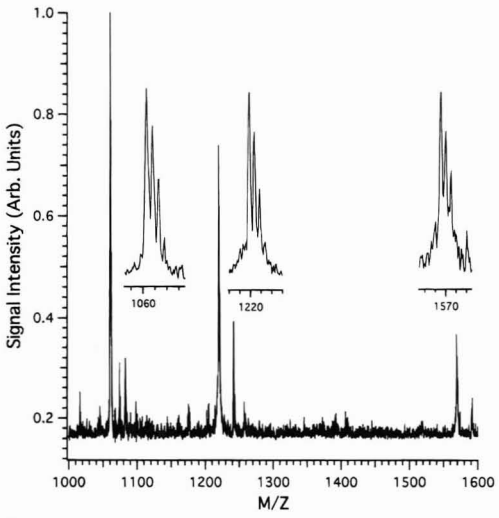

Figure 4. TLF MALDI mass spectrum of a mixture of peptides (1 pmol of each peptide is loaded to the sample probe) using CHCA as matrix. The pulse potential used is 1.20 kV. The peptide sequence of the two synthetic peptides is given in Figure 2.

ion energy correction for ions of the same mass to charge can only be corrected with the use of a reflectron instrument. While it is yet unknown what factor limits the observed peak width, isotopic resolution can be achieved, as shown in Figure 2, for small peptides with masses up to 3000 Da in a linear 1-m TOFMS using moderate acceleration voltages.

In achieving high mass resolution in TLF TOFMS, the pulse applied to the repeller requires optimization to provide energy/spatial focusing at the detector plane. Although the pulse potential may not be optimal for each individual species, a given pulse potential is sufficient for a range of mass values. Figure 4 shows the mass spectrum of a mixture of bradykinin and two synthetic peptides. The molecular ion region of each peptide is shown in the inset. The mass resolution for each peptide is 1600, 2000, and 2600 fwhm for bradykinin, synthetic peptide 1, and synthetic peptide 2, respectively. As Figure 4 illustrates, the resolution obtained is adequate to resolve the isotopic peaks of each peptide. In addition, the mass measurement accuracy for these isotopically resolved peptides is generally in the range of 5–70 ppm from repeat measurement, with an average value of 30–50 ppm.

We have also examined several larger peptides and proteins using this TLF TOFMS method. Figure 5 shows the mass spectra of bovine insulin, equine cytochrome *c*, and equine apomyoglobin. Broader molecular ion peaks are observed. However, compared with DC ion extraction, the TLF method provides much improved mass resolution. For example, the observed mass resolution is 1000 fwhm for insulin, 800 fwhm for cytochrome *c*, and 900 fwhm for apomyoglobin. In general, we find that for high-mass ions (MW >3000), the mass resolution enhancement is ~3-fold. The reduction of the apparent mass resolution for larger ions can likely be attributed to the increased kinetic energy distribution for ions of higher mass.[14,15] Increasing the pulse potential to correct for

(14) Beavis, R. C.; Chait, B. T. *Chem. Phys. Lett.* **1991**, *181*, 479–484.
(15) Pan, Y.; Cotter, R. J. *Org. Mass Spectrom.* **1992**, *27*, 3–8.

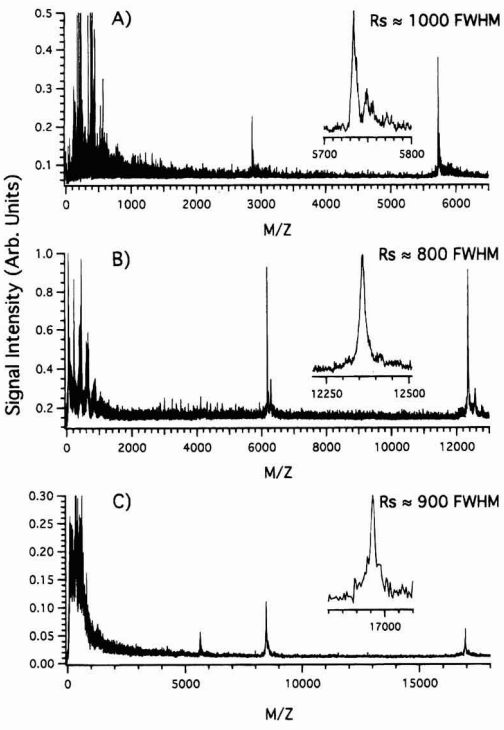

Figure 5. TLF MALDI mass spectra for a total loading of 1 pmol of (A) bovine insulin $(M + H)^+ = 5734.37$ Da using CHCA as matrix, pulse potential 2.75 kV, (B) equine cytochrome *c* using SA as matrix, pulse potential 3.50 kV, and (C) equine apomyoglobin using CHCA as matrix, pulse potential 4.50 kV.

the increased kinetic energy distribution does not appear to provide complete compensation. However, the mass measurement accuracy is good for proteins. Using a two-point external calibration, the mass obtained for insulin, cytochrome *c*, and apomyoglobin is 5734.37, 12362.6, and 16959.1 Da, representing a mass measurement accuracy of 0.002, 0.01, and 0.04%, respectively. The calibrants for bovine insulin are a synthetic peptide (average MW 3079) and equine cytochrome *c*. The calibrants for cytochrome *c* are bovine insulin chain B and bovine insulin. The calibrants for equine apomyoglobin are bovine insulin and equine cytochrome *c*. With internal calibration (spectra not shown), the mass obtained for cytochrome *c* and apomyoglobin is 12361.8 (57 ppm accuracy) and 16954.7 Da (130 ppm accuracy), respectively.

In summary, with a standard 1-m flight tube TOFMS, we demonstrate that a linear system can be used to achieve unit mass resolution for peptides up to m/z 3000. High resolution and mass measurement accuracy are also obtained for larger peptides and proteins with masses up to ~17 000 Da. This type of simple system should be very useful for many applications. Indeed, while we continue to optimize the current system, this technique has been routinely used for the detection of small peptides and oligosaccharides with isotope resolution for analytical applications. Detailed studies on the focusing capability of the TLF MALDI system for larger proteins and glycoproteins will be reported in the future.

ACKNOWLEDGMENT

This work was in part supported by the Natural Sciences and Engineering Research Council of Canada (NSERC). R.M.W. thanks NSERC for a postgraduate scholarship. We thank Allan Crawford Associates for the loan of the 9354M oscilloscope. We thank P. Semchuk at the Center of Excellence in Protein Engineering at the University of Alberta for the generous gift of the synthetically generated peptides.

Received for review April 5, 1995. Accepted May 3, 1995.[⊗]

AC950339H

[⊗] Abstract published in *Advance ACS Abstracts*, June 1, 1995.

Articles

Anal. Chem. **1995,** *67,* 1955–1962

Characterization of a Perfluorotetradecahydrophenanthrene Oligomer

William H. Tuminello,* Ioannis V. Bletsos, Fredric Davidson, and Frank J. Weigert

The Dupont Company, Experimental Station, P.O. Box 80356, Wilmington, Delaware 19880-0356

Nigel Simpson† and David Slinn‡

Rhône-Poulenc Chemicals, P.O. Box 46, St. Andrews Road, Bristol BS11 9YF, United Kingdom

A complex mixture of oligomeric perfluorocarbons was characterized primarily by nuclear magnetic resonance spectroscopy, electron spectroscopy for chemical analysis, and time-of-flight secondary ion mass spectrometry. Supporting tools were infrared and ultraviolet/visible spectrometry, plus elemental analysis and conventional gas chromatography/mass spectrometry. The following distribution of carbon and fluorine groups (expressed as the percentage of total carbons) was determined: olefinic carbon, 8%; CF_3, 8%; CF_2, 51%; and CF, 33%. A general structural framework is proposed with the chemical formula $C_{14}F_{23}(C_{14}F_{22})_nC_{14}F_{23}$, where $n = 0$, 1, and 2 for dimer, trimer, and tetramer, respectively. The monomer has the structure of perfluorotetradecahydrophenanthrene. A wide diversity of structures was created during synthesis by (1) loss of fluorine atom pairs to create further ring closure or unsaturated carbon–carbon bonds and (2) ring opening to obtained perfluoroalkyl side chains.

Perfluorocarbon oligomers are byproducts in the commercial synthesis of perfluorotetradecahydrophenanthrene ($C_{14}F_{24}$). The synthesis involves the fluorination of phenanthrene via cofeeding elemental fluorine and the hydrocarbon in the gaseous state over a bed of cobalt(III) fluoride.[1] $C_{14}F_{24}$ manufactured by this route is sold commercially as Flutec PP11, primarily used for vapor phase soldering of printed circuit boards. Formerly this was carried out by Rhône-Poulenc, but the manufacture and sales have now been taken over by BNFL Fluorochemicals Ltd. Part of the manufacturing process requires separation of the Flutec PP11 from the oligomeric byproducts by fractional distillation. The oligomers are the "still bottoms".

It was recently reported[2] that the oligomeric byproducts are excellent atmospheric pressure solvents for PTFE, which opens the door to unique new characterization and processing possibilities for this polymer. Our objective in characterizing this material was to identify it sufficiently for government certification, strengthening of any patents referring to the oligomer, formulation of a basis for manufacturing specifications, and a deeper understanding in further research efforts.

EXPERIMENTAL SECTION

It was believed that the as-synthesized oligomers contain small amounts of hydrogen and olefinic carbon (by olefinic carbon we mean trigonal sp^2). One or more fluorines might be attached to this olefinic carbon. Postfluorination was used to reduce the unsaturation and hydrogen content. The material we are characterizing is one of these postfluorinated substances. During the postfluorination process, the "crude" oligomer was stirred at ~200 °C in a vessel while free elemental fluorine, diluted 3:1 with nitrogen, was bubbled through the liquid for several hours. The process was continued until about 1.5 mol of fluorine/mol of oligomer had passed through the reactor.

The oligomers have never been a controlled product, so there is expected to be variability from lot to lot. This particular oligomer sample has an atmospheric pressure boiling point of about 322 °C. Its components have boiling ranges from about 280 to 400 °C. The whole oligomer is an exceedingly viscous, transparent, colorless liquid at room temperature which flows easily at about 60 °C. Higher boiling fractions are more viscous. The highest boiling fractions are brittle glasses at room temperature. All fractions observed thus far are transparent and nearly colorless. Discoloration occurred after several hours above 330 °C.

The following solvents were used as received. HPLC grade 99.9% pure Freon 113 (1,1,2-trichlorotrifluoroethane), HPLC grade 99.9+% carbon tetrachloride, 99.8% deuterated chloroform, and 99+% Freon 11 (fluorotrichloromethane) were all obtained from Aldrich. The chloroform, obtained from EM Science, was glass distilled, hydrocarbon stabilized, and 99.97% pure.

^{19}F NMR. ^{19}F NMR spectra were obtained on a Nicolet NT-200 FT-NMR instrument. Both deuteriochloroform and carbon tetrachloride were used as solvents. The oligomer was only marginally soluble in deuteriochloroform. Solubility was improved in carbon tetrachloride but was still limited to about 1%. Since deuteriochloroform was used as a "lock", it was added (about 10%)

† Current address: Fluoro Systems Ltd., Honeysuckle Cottage, Tidenham Chase, Nr. Chepstow, Gwent NP6 7JW, U.K.

‡ Current address: Fluoro Systems Ltd., Cotswold House, Manor Road, Abbots Leigh, Bristol BS8 3RP, U.K.

(1) Joyner, B. D. *J. Fluorine Chem.* **1986,** *33,* 337.

(2) Tuminello, W. H.; Dee, G. T. *Macromolecules* **1994,** *27,* 669.

0003-2700/95/0367-1955$9.00/0 © 1995 American Chemical Society

to the CCl_4 solutions. Freon 11 was used as a reference. About 5 cm^3 of Freon 11 vapor was added to the NMR tube and mixed with the sample by shaking.

^{19}F-Decoupled ^{13}C NMR. Two types of experiments were performed on a GE Omega 300 NMR instrument. A quantitative inverse-gated $^{13}C\{^{19}F\}$ experiment using GARP decoupling was performed to determine the relative concentrations of the different types of carbons present. The ^{13}C APT-like, ^{19}F-decoupled experiment allowed the assignment of the number of fluorines attached to each type of carbon. (Although APT is the acronym for "attached proton test", in our case we were using fluorine in place of protons.) Solutions were prepared by using very small amounts of Freon 113 to make the oligomer mobile enough to be added to an NMR tube. A smaller bore tube containing dimethyl sulfoxide (DMSO) was placed inside the tube containing the plasticized oligomer and acted as the NMR deuterium lock.

^{1}H NMR. Proton NMR spectra were obtained to quantitatively determine the hydrogen content. A GE QE 300 MHz NMR instrument was used. The oligomer was dissolved in Freon 113 (23 wt% oligomer), and a known amount (~0.01 wt %) of chloroform was added as an internal proton reference. The relative amounts of protons in the chloroform were compared to those in the oligomer by spectral integration.

TOF-SIMS. Very thin films (~100 nm) of the oligomer were prepared by rubbing a drop of the heat-softened material (with a Kimwipe tissue) onto a silver foil etched with nitric acid (20% v/v). These coated silver samples were placed in a reflectron time-of-flight selected ion mass spectrometry (TOF-SIMS) instrument (IX23S) manufactured by Fisons, Inc. It has been shown[3,4] that molecular and fragment ions of considerable size (up to m/z = 10 000) are desorbed and separated by mass. In this way, structural characterization and molecular weight distributions can be obtained. We operated in the static mode at a mass resolution of $m/\Delta m = 1000$. Positive and negative ion spectra were obtained without charge compensation. In this report, we present the negative ion spectra, which are the most revealing in terms of the structures of the oligomers and their molecular weight distributions.

ESCA. Very thin films (~100 nm) of oligomer were prepared by rubbing a drop of heat-softened material (with a Kimwipe tissue) onto a clean indium foil. The oligomer film thus obtained was continuous and thick enough to prevent indium from being detected by electron spectroscopy for chemical analysis (ESCA). The analysis was performed using a Perkin-Elmer Physical Electronics 5000 LS ESCA instrument (Mg Kα X-rays at 1253.6 eV and 45° take-off angle). Charge compensation was not used; therefore, the peaks in the ESCA spectrum were shifted due to charging. Peak assignments were based on binding energy differences between peaks and referencing to the peak at the highest binding energy in the carbon 1s spectrum, assuming $-CF_3$ is at 293.7 eV.[5,6] The absence of an aliphatic hydrocarbon peak did not allow the usual referencing to C−C at 284.6 eV.

Verification of structural group assignments (based on binding energy differences) were made using Flutec PP11 and a Fisons ESCA LAB MKII instrument equipped with a cold probe. The PP11 was kept at liquid nitrogen temperatures to minimize evaporation in the ultrahigh vacuum of the instrument.

GC/MS. Freon 113 solutions were injected into a Hewlett-Packard Model 5890 gas chromatograph, and the effluent was directly fed into a Fisons Model VG-70SE mass spectrometer. A DB-1 capillary was used in the gas chromatograph programmed to heat from 60 to 280 °C at 10 deg/min. The mass spectrometry was done in the negative ion mode using electron capture mass spectrometry. Argon gas was used to thermalize the electrons.

It might seem odd that our gas chromatograph was programmed to heat to only 280 °C when we have already stated that some components of the oligomer mixture boil as high as 400 °C. However, we have found that perfluorocarbons are extremely volatile at temperatures far below their boiling points. For example, all of these oligomers will evaporate completely at temperatures below 300 °C. This is due to the very low intermolecular forces acting in these systems. In short, at 280 °C, all the oligomer had evaporated.

IR. IR spectra were obtained on samples of both Flutec PP11 and the oligomer as a film between potassium bromide plates and in a calcium fluoride liquid cell. The instrument was a Nicolet 20SX FT-IR spectrophotometer run at 2 cm^{-1} resolution with 100 scans coadded.

UV/Vis. Measurements were made on the neat liquid in a 1.0 mm length cell using a Cary 2300 spectrophotometer.

Elemental Analysis. The sample was sent to a contract lab, Micro-Analysis, Inc., for the non-fluorine analyses. The fluorine analysis was done using a Wickbold torch ion selective electrode.

Vapor Pressure Osmometry. A Perkin-Elmer 115 vapor pressure osmometer was used to determine the number average molecular weight, $\bar{M}_n$, of the oligomer. Measurements were taken in Freon 113 at 39.5 °C. Benzil was used as a standard. Considerable scatter was observed in the measurements which we attribute to the high vapor pressure of the solvent at the experimental conditions. We estimate the error to be ~5%.

RESULTS

IR, GC/MS, and UV/vis measurements confirm that the oligomer is a complex mixture of many components containing a low level of unsaturation and possibly some hydrogen. The GC trace in Figure 1 indicates a complex mixture of components. We were not able to find conditions permitting the resolution of any peaks, nor could we make any structural determinations from the mass spectra. One can, however, decipher three to four broad bands of intensity suggesting the presence of dimers, trimers, and tetramers. On first reflection, one might consider it odd that this chromatogram in Figure 1 is so complex. However, the building block of these oligomers, pure perfluorotetradecahydrophenanthrene, has six structurally distinct isomers. Each isomer has at least 12 distinct fluorines. Thus hundreds of dimers can result from coupling two monomers. Hundreds of dimers imply thousands of trimers. These counts do not even consider the possibility of anthracene ring connection isomers, ring opening, and ring contraction. Even if only a fraction of these isomers are actually present, the gas chromatograph can be complex and unresolved.

IR spectra for Flutec PP11 and the oligomer are compared in Figure 2 for a limited portion of the IR range. As is true for the entire spectral range, all major bands roughly correspond in both materials. The lack of sharp bands for the oligomer is consistent

(3) Bletsos, I. V.; Hercules, D. M.; Fowler, D.; vanLeyen, D.; Benninghoven, A. *Anal. Chem.* **1990**, *62*, 1275.
(4) Bletsos, I. V.; Hercules, D. M.; vanLeyen, D.; Hagenhoff, B.; Niehuis, E.; Benninghoven, A. *Anal. Chem.* **1991**, *63*, 1953.
(5) Clark, D. T. In *Structural Studies of Macromolecules by Spectroscopic Methods*; Ivin, K. J., Ed.; John Wiley and Sons: London, 1976; pp 111−179.
(6) Chambers, R. D.; Clark, D. T.; Kilcast, D.; Partington, S. *J. Polym. Sci., Polym. Chem. Ed.* **1974**, *12*, 1647.

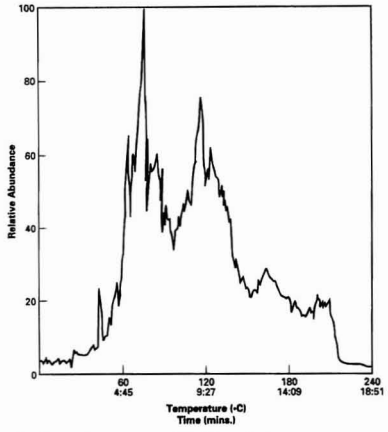

Figure 1. Gas chromatograph of the oligomer.

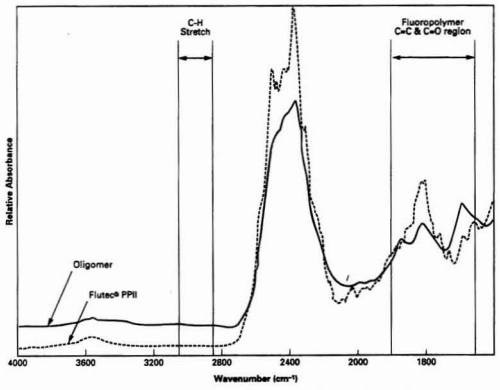

Figure 2. Comparison of the IR spectra for perfluorotetradecahydrophenanthrene and the oligomer, showing the regions where absorptions due to the presence of C–H and C=C bonds are expected in fluoropolymers.

with a mixture of similar compounds with overlapping bands. As is illustrated in Figure 2, there is no significant absorption in the C–H stretch region for either material. There are some weak bands in the 1650–1900 cm^{-1} region which may be due to unsaturation.

More evidence of unsaturation was obtained with UV/vis spectrometry. Figure 3 shows much more absorption at lower wavelengths for the oligomer than for the chlorotrifluoroethylene oligomer (trade name Fluorolube) and water. Neither of the latter materials has unsaturation. Elemental analysis (amounts given in wt %) indicates the presence of carbon (26.3), hydrogen (0.25), nitrogen (4.0), and fluorine (67.9). (More will be said of this later.) The ^1H NMR analyses revealed that hydrogen was present in only trace quantities ($\sim 2 \times 10^{-7}$ mol of hydrogen/g of oligomer). More detailed reporting using the remaining techniques follows.

^{19}F NMR. The ^{19}F NMR spectrum in deuteriochloroform is shown in Figure 4. The reference peak (0 ppm chemical shift) represents the single fluorine in $CFCl_3$. Although there are few sharp resonances, there is considerable structural information in this spectrum. Clear regions of resonance attributable to CF, CF_2, and CF_3 were identified. These are summarized in Table 1. The

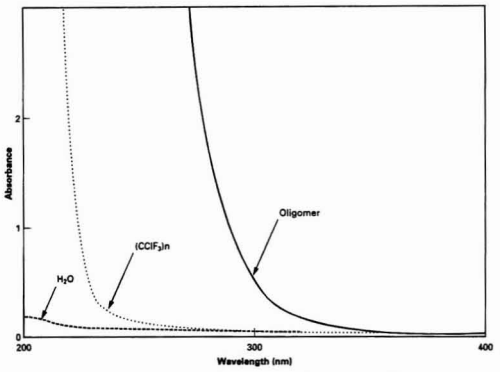

Figure 3. UV/vis spectra for water, the chlorotrifluoroethylene oligomer, and the Flutec PP11 oligomer.

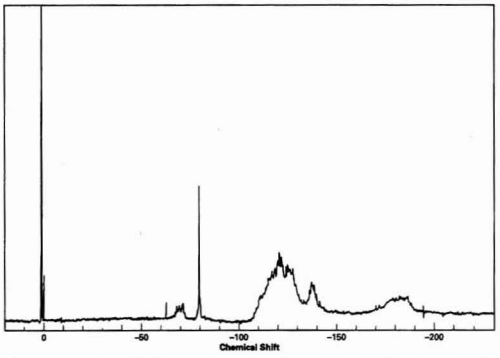

Figure 4. ^{19}F NMR spectrum for the Flutec PP11 oligomer in deuteriochloroform with $CFCl_3$ as a reference.

Table 1. Structural Assignments for ^{19}F NMR Spectrum of Oligomer in $CDCl_3$[a]

chemical shift (ppm)	description	structural assignment[a]
−68.5 to −74.0	broad	$CF_3CF<$, $CF_3CF=$
−81	sharp	CF_3CF_2-
−106 to −134	broad	$-CF_2$(ring), CF_3CF_2-, $CF_3CF_2C(RF)=$, $CF_3CF=$
−134 to −144	moderately broad	axial $-CF_2-$
−168 to −192	broad	$CF_iCF(CF_j)CF_k$[b]

[a] From ref 7. The fluorines responsible for the signal are shown in italics. [b] Except for $i = 1$ or 2 and $j = k = 0$.

assignments were made on the basis of compilations by Weigert and Karel.[7]

Two types of CF_3 were identified accounting for ~8 atom % of the total fluorine. There is a broad band from −68.5 to −74.0 ppm and a very sharp resonance at −81 ppm. The broad band can be assigned to either $CF_3CF<$ or $CF_3CF=$, where the italic type indicates the resonating fluorines. The unsaturation would have to be in a side chain and not a ring structure since a single fluorine attached to a single olefinic carbon in a 5- or 6-membered ring would resonate at 150 or 146 ppm, respectively. We observed no such chemical shifts. The very sharp peak is due to CF_3CF_2-.

(7) Weigert, F. J.; Karel, K. J. *J. Fluorine Chem.* **1987**, *37*, 125.

Table 2. Abundance of Fluorine-Containing Groups by ^{19}F NMR

solvent	CF_3[a]	CF_2[a]	CF[a]	E + A[b]
$CDCl_3$	5	69	26	18.5
CCl_4	5	66	29	15.9

[a] Molar ratio of groups normalized to 100. [b] Fluorine atom % of equatorial and axial fluorines in 6-membered rings.

There are (within experimental error) equal amounts of fluorines in both resonance ranges. No $CF_3C(RF_i)(RF_j)(RF_k)$ signals were observed, with chemical shifts reported at −58 to −68 ppm.

Primarily CF_2 groups are assigned to the chemical shifts observed in the −106 to −144 ppm region. Assuming that all the resonance is due to CF_2 groups, this accounts for about 77 atom % of the total fluorine. The presence of 6-membered rings is consistent with the observation of peaks at about −142 and −124 ppm. These are due to the axial and equatorial fluorines in CF_2 groups not adjacent to trisubstituted carbons. About 18.5 atom % of the total fluorine is either axial or equatorial. This assumes that the region from −134 to −144 ppm is due to axial fluorine resonance only. Chemical shifts from −106 to −134 ppm can be attributed to CF_2 fluorines in 5- or 7-membered rings, equatorial fluorines, CF_2 in 6-membered rings adjacent to trisubstituted carbons, or in alkyl or olefinic side chains as listed in Table 1. One also cannot rule out the presence of CF in $CF_3CF{=}$, which has a reported chemical shift in the range −98 to −162 ppm.

CF resonance is attributed to the observed chemical shifts in the −168 to −192 ppm range. This accounts for the remaining 15 atom % of fluorines observed. The only CF resonances not observed are for those groups adjacent to two tetrasubstituted carbons, reported to occur at −154 and −158 ppm.

The presence of aromatic fluorine is doubtful. Chemical shifts for fluorine in the meta and para positions of monosubstituted pentafluorophenyl rings are reported to be at −144 to −152 and −160 to −162 ppm, where we observe no resonance.

Virtually identical spectra were obtained for two higher boiling distillation cuts of the oligomer. Since deuteriochloroform is such a poor solvent for the oligomer, we feared that the lower boiling fractions may have been preferentially extracted. A nearly identical spectrum was obtained in a better (but not good) solvent, carbon tetrachloride. The positions of the resonances varied very slightly, presumably from well-known solvent effects. The magnitudes also varied slightly, possibly due to the preferential extraction that we feared, but the differences in abundance are not greater than the experimental error (estimated to be ~10%). The molar ratios of the different groups as determined in carbon tetrachloride are compared with the results in deuteriochloroform in Table 2.

^{19}F-Decoupled ^{13}C NMR. Figure 5 is a quantitative spectrum of the inverse-gated fluorine-decoupled ^{13}C experiment. The relative molar amounts of each type of carbon are shown in the peak integrations. The chemical shift for the DMSO ("lock") carbons is well out of the field of this spectrum at about 40 ppm. The fluorine-decoupled ^{13}C APT-like experiment gave the assignments for the oligomer carbons listed in Table 3. The very sharp resonances at 114 and 122 ppm are due to the Freon 113 solvent. Since only a small amount of solvent was used, the resonances represent only a small fraction of the total carbons. There is a very broad resonance of low amplitude (between about 130 and

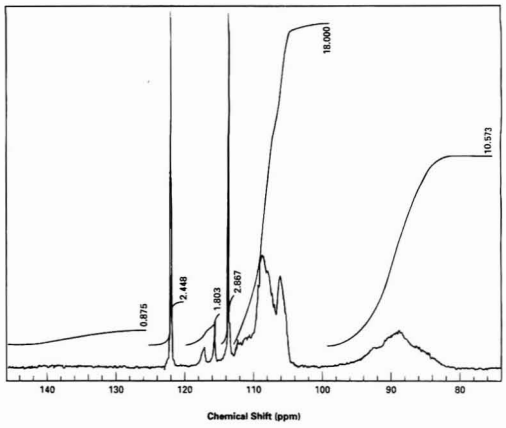

Figure 5. Fluorine-decoupled ^{13}C NMR spectrum of the oligomer from a gated experiment.

Table 3. Structural Assignments for ^{19}F-Decoupled ^{13}C NMR Spectrum of Oligomer in CCl_2FCClF_2

chemical shift (ppm)	description	structural assignment
−130 to 140	extremely broad	>C=, −CF=
−117 to −118	moderately sharp	CF_3
−116	sharp	CF_3
−105 to −113	moderately broad	CF_2
−81 to −98	broad	CF

140 ppm) which is only clearly observed through the integration. It is assigned to olefinic carbons, primarily bonded to other carbons only. The abundance of these carbons is estimated to be 2.8 atom % of the total. The very low signal to noise ratio make this estimate highly ambiguous, with an error estimate of well over 100%. The carbons in the aliphatic CF_3 (~116 and 118 ppm) and CF_2 (~105−113 ppm) groups have resonances that slightly overlap each other and the 114 ppm solvent resonance. The error estimate for the abundances of these carbons is estimated to be 10−20%. The somewhat broad nature of the CF resonance centered on ~90 ppm would give approximately the same error of 10−20%. There was no evidence of tetrasubstituted carbon (chemical shift, 70 ppm). If for some strange reason a quaternary carbon did happen to fall in our observed range, the comparison of the coupled and decoupled experiments would also have indicated their presence. Since aromatic carbon resonances overlap those of olefinic carbon signals, we cannot make a differentiation.

The fluorine-decoupled ^{13}C NMR experiments result in the following quantitative assessment (atom % of total oligomer carbons): >C=, 3%; CF_3, 6%; CF_2, 57%; and CF, 34%. These results are within experimental error of the uncoupled ^{19}F experiments in $CDCl_3$ and CCl_4. It should be remembered, however, that the presence of any $CF_3CF{=}$ would result in a false high value for the CF_2 concentration. This would be due to the resonance of the single fluorine in this group overlapping the region normally dominated by CF_2 resonances. There is also the possibility that preferential dissolution of low molecular weight fractions by the poorer solvents ($CDCl_3$ and CCl_4) also contributed to the quantitative differences.

ESCA. The curve-fitted ESCA carbon 1s spectrum is shown in Figure 6. Four types of carbons were detected. Reasonably

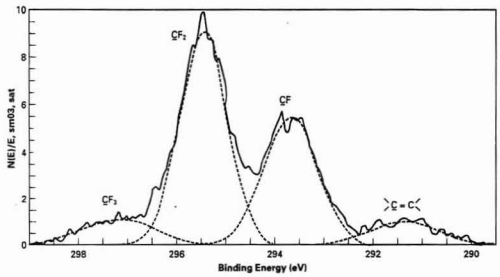

Figure 6. ESCA spectrum for the oligomer.

Table 4. Carbon Atom % Abundance of Oligomer Groups

technique	>C=	CF_3	CF_2	CF
decoupled NMR	3	6	57	34
ESCA	8	10	48	34

broad peaks at about 291.4 and 297.2 eV were assigned to >*C*=*C*< and *C*F_3, respectively. Sharper peaks at 293.6 and 295.5 eV were assigned to *C*F and *C*F_2, respectively.

Nitrogen was not detected (detection limit, ~0.5 atom %). Oxygen was detected at the detection limit but could be the result of adsorption. Hydrocarbons were not detected. Atom % abundances based on total carbon are listed in Table 4 and compared with the values obtained by decoupled NMR. The differences are within experimental error. Atom % calculation errors are probably of the order of 10–20%, whereas for the broader peaks, greater errors (~20%) are expected. The precision in determining the degree of unsaturation is so much poorer by NMR that the ESCA figure will be used as the best number available. Using the cold probe ESCA did not give significantly different results.

Double- and triple-distilled Flutec PP11 samples were analyzed with the cold probe ESCA. CF, CF_2, and CF_3 were detected in the following respective abundances (carbon atom %): 25–27%, 68–71%, and 3–8%. Carbon to fluorine ratios of 32:68 were calculated. If Flutec PP11 consists of pure perfluorotetradecahydrophenanthrene, only CF and CF_2 should be detected at concentrations of 29 and 71% and C/F ratios of 37:63. However, P. Coe of Birmingham University has deduced that 6–10% of $C_{14}F_{26}$ is present on the basis of mass spectrographic analyses.[8] Coe proposed that this corresponds with one of the rings opening by the addition of two fluorines and thus at least one CF_3 group per $C_{14}F_{26}$ molecule. This material should be very difficult to separate from the $C_{14}F_{24}$ by fractional distillation, accounting for its presence in the doubly and triply distilled samples. Also, traces of oligomer were detected by TOF-SIMS in these fractions. After correction for the CF_3, the composition of the PP11 sample becomes identical to the theoretical.

TOF-SIMS. Earlier in this section, we reported that ESCA and NMR determined that the oligomers consist of >C=C<, CF, CF_2, and CF_3 functional groups. Both analyses are in good agreement, but they are not specific enough to determine oligomeric structure. Although gas chromatography revealed the presence of an exceedingly complex mixture, individual component resolution was not obtained. Electron impact mass spectrometry produces low mass ions characteristic of fluoropolymers but not specific to a particular structure. We have used TOF-SIMS to determine nearly exact molecular weights of the components (for structural determination) as well as molecular weight distributions.

The negative TOF-SIMS spectra are shown in Figures 7 in the mass range m/z = 950–2350. These spectra are plotted as ion intensity versus atomic mass. The ion intensity is proportional to the number of moles of ions of a particular mass. These figures reveal three distinct distributions centered around m/z 1150, 1680, and 2190. The mass difference between consecutive distributions is nearly 624, the molecular weight of $C_{14}F_{24}$. TOF-SIMS thus provides the first evidence that the oligomers consist of the dimer, trimer, and tetramer of $C_{14}F_{24}$. Judging from the intensity of the distributions, the most abundant species is the dimer, followed by trimer with minute amounts of tetramer. It must, of course, be emphasized that any of the structural possibilities presented below can be represented by many other isomers.

A general structural framework of $C_{14}F_{24}$ building blocks can account for the distribution of masses observed. The structural framework we envision would have the general formula $C_{14}F_{23}$-$(C_{14}F_{22})_nC_{14}F_{23}$, where n = 0, 1, and 2 for dimer trimer, and tetramer, respectively. A pictorial representation would be

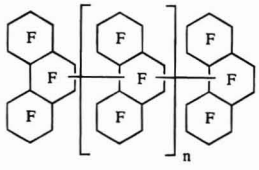

This picture is simplified since we do not represent the myriad of possibilities with anthracene-like ring structures. Not only can our data not rule out these possibilities, but the literature[7] indicates that the anthracene structure is possibly present in $C_{14}F_{24}$ in sizeable concentrations. The distribution of masses separated by multiples of 19 mass units is probably due to losses of fluorine. Loss of two fluorines at a time would occur with an additional ring closure or the formation of a carbon–carbon double bond. Opening a ring would give perfluoroalkyl side chains. Thus a wide variety of structures is possible within this framework which would be consistent with the ESCA and NMR results.

Figure 7b shows the fragments with masses centered around m/z = 1150. There appear to be two overlapping distributions in this region offset by 19 mass units. We believe this is, in fact, one distribution. The higher mass peak of adjacent pairs represents the molecular ion. We believe the lower mass peak is a fragment of the molecular ion resulting from the loss of a fluorine atom. Our average MW calculations, discussed later in this paper, did not take this into account because it could only reduce the value by 19 mass units at most.

The dimer framework structure is represented below, having the chemical formula $C_{28}F_{46}$. The molecular possibilities of modifying this structure by removing fluorine atom pairs are listed in Table 5. Each of these possibilities can be accounted for by the major peaks observed; the observed peaks are listed in the last column of Table 5. The structures represented by MW = 1248 ($C_{28}F_{48}$) would result from the opening of one of the rings in the framework structure (designated −1 for the number of

(8) Rhône-Poulenc files; European registration documents for Flutec PP11.

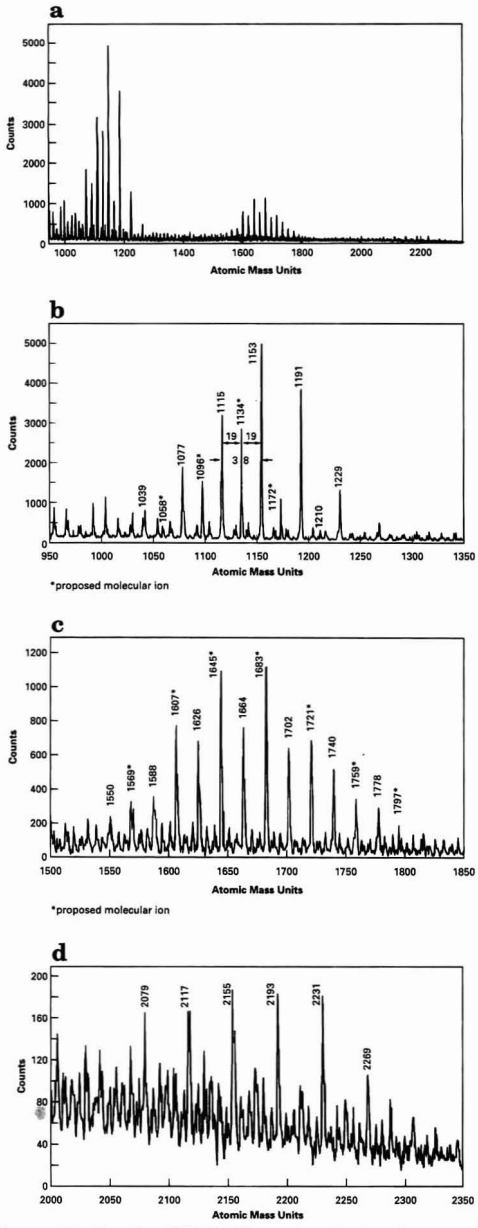

Figure 7. Negative TOF-SIMS spectra for the oligomer: (a) complete spectrum, (b) dimer distribution, (c) trimer distribution, and (d) tetramer distribution. Parameters for each spectrum are as follows: primary beam, Ga; primary energy, 30.00 kV; primary current, 1.700 nA; channel width, 0.500 amu; pulse width, 30 ns; total pulses, 1.638×10^{-6}; no. of ions/cm^2, 2.267×10^{11}.

additional rings). The highest intensity peaks appear centered around $m/z = 1172$. As explained in the previous paragraph, the parent ion at $m/z = 1172$ is represented by peaks at $m/z = 1153$ (fragment ion) and 1172. Structure I, shown below, is one possibility for the component with molecular weight 1134.

Table 5. Dimer Possibilities

formula	MW	no. of rings[a]	TOF-SIMS peaks (m/z)
$C_{28}F_{48}$	1248	−1	1229
$C_{28}F_{46}$	1210	0	1191, 1210
$C_{28}F_{44}$	1172	1	1153, 1172
$C_{28}F_{42}$	1134	2	1115, 1134
$C_{28}F_{40}$	1096	3	1077, 1096
$C_{28}F_{38}$	1058	4	1039, 1058

[a] The number of additional rings or unsaturated bonds versus the framework structure.

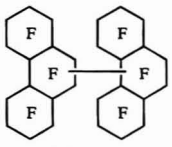

Dimer

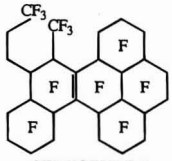

STRUCTURE I

The presence of trimers explains the distribution of peaks in Figure 7c centered around m/z 1680. As for the case of the dimers, we interpret pairs of peaks separated by 19 mass units as representing a molecualr ion and its fragment less a fluorine atom. With the trimers, we generally observe that the more intense peaks are assigned to the molecular ions. With the dimers, however, we notice the opposite trend: the less intense peaks are more likely assigned to the molecular ions. The trimer framework structure is shown below, having the chemical formula $C_{42}F_{68}$. Molecular possibilities resulting from removing pairs of

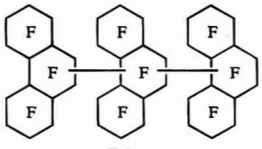

Trimer

fluorine atoms are listed in Table 6. Structure II, shown below, is a possibility based on this framework for the species with MW = 1720. We assumed that the peaks in Figure 7c were actually 1 mass unit less than the labeled value, which is well within instrument precision. This allowed us to assign the "trimer framework structure", shown immediately above, to the parent ion peak at m/z 1796 (labeled 1797).

We will assume that tetramers account for the low-intensity peaks centered around $m/z = 2190$ illustrated in Figure 7d. The general oligomeric framework formula would be $C_{56}F_{90}$. Table 7 lists the possibilities for removing two fluorines at a time. We assign the only peaks identified with any certainty to molecular ions between m/z = 2078 and 2268. A potential molecular structure assignable to the peak at $m/z = 2154$ is shown below

Table 6. Trimer Possibilities

formula	MW	no. of rings[a]	TOF-SIMS peaks (m/z)
$C_{42}F_{68}$	1796	0	1778, 1797
$C_{42}F_{66}$	1758	1	1740, 1759
$C_{42}F_{64}$	1720	2	1702, 1721
$C_{42}F_{62}$	1682	3	1664, 1683
$C_{42}F_{60}$	1644	4	1626, 1645
$C_{42}F_{58}$	1606	5	1588, 1607
$C_{42}F_{56}$	1568	6	1550, 1569

[a] The number of additional rings or unsaturated bonds versus the framework structure.

Table 7. Trimer Possibilities

formula	MW	no. of rings[a]	TOF-SIMS peaks (m/z)
$C_{56}F_{90}$	2382	0	none detected
$C_{56}F_{84}$	2268	3	2269
$C_{56}F_{82}$	2230	4	2231
$C_{56}F_{80}$	2193	5	2193
$C_{56}F_{78}$	2154	6	2155
$C_{56}F_{76}$	2116	7	2117
$C_{56}F_{74}$	2078	8	2079

[a] The number of additional rings or unsaturated bonds versus the framework structure.

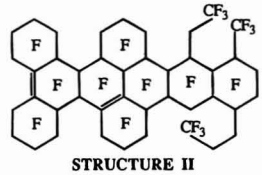

STRUCTURE II

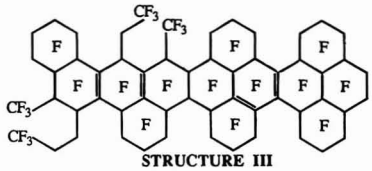

STRUCTURE III

DISCUSSION

Based on the ESCA and ^{1}H NMR results, we conclude that only carbon and fluorine are present in these samples in significant amounts. Elemental analysis indicated significant concentrations of nitrogen and hydrogen. It is known, however, that highly fluorinated materials are difficult to combust. Analyzers which assume that an inert component of the combustion gas is nitrogen give erroneously high nitrogen values because incomplete combustion products of fluorine compounds escape absorption in the sorbents. In fluorinated compounds, such a low level of hydrogen (0.25%) may be insignificant.[9] If no hydrogen and nitrogen are present, elemental analysis cannot account for 6% of the oligomer's weight. The missing material could be (1) carbon, because of incomplete combustion; (2) low fluorine; or (3) another element. The amount of carbon determined by elemental analysis and ESCA is identical. We indicated earlier that oxygen was detected by ESCA at the limit of detection (~0.5 atom %), but this is too low a concentration to account for the missing material. We must assume that the fluorine analysis was in error, although fluorine recovery should be above 97%.[9] Also, as mentioned earlier, the IR spectrum substantiates the ESCA and ^{1}H NMR results that no significant amounts of hydrogen are present.

(9) Kissa, E. Private communication.

Table 8. Abundance of Groups in Possible Oligomer Structures

structure	>C=[a]	CF_3[a]	CF_2[a]	CF[a]	E + A[b]
exptl[c]	8	8	51	33	17
I	7	7	50	36	18
II	10	7	48	36	16
III	14	7	43	36	16

[a] Carbon atom %. [b] Fluorine atom % of equatorial and axial fluorines in 6-membered rings. [c] Average of fluorine-decoupled NMR and ESCA results.

We would now like to make structural assignments consistent with the ESCA, NMR, and TOF-SIMS results. The results from NMR and ESCA summarized in Tables 2 and 4 indicate the following mole ratios of carbons: 8% unsaturated, 8% CF_3, 51% CF_2, and 33% CF. In addition, about 17 atom % of the total fluorine is of the equatorial and axial type in 6-membered rings. Also, half of the CF_3 groups are attached to CF_2 groups.

The general structural framework we described in the TOF-SIMS Results section is intuitively sensible because (1) it is based on $C_{14}F_{21}$ building blocks and (2) one can imagine the rings connecting and opening in the suggested ways during the harsh fluorination conditions. There is precedence for polymerization in the way we suggest. Laatsch et al.[10] reported the trimerization of anthracene 1,4-quinones. When considered in conjunction with the known dimerization of hexafluorobenzene in the presence of elemental fluorine,[11] polymerization of the phenanthrene seems plausible.

The structures I, II, and III (for dimer, trimer, and tetramer, respectively) drawn in this report are only a few of the myriad of possibilities. A comparison of these suggested structures with the experimental results for the groups detected is given in Table 8. It is most important that the dimer structure compares favorably (and it does) with the experimental results since it is present in the largest quantities. Also, one can easily imagine dimer structures on either side of the MW of structure I which would give the proper balance of group concentrations when averaged together. Although they do not affect the average concentration of groups as much as the dimer, the trimer and tetramer structures suggested are reasonably close to the experimental findings as well.

The unsaturation suggested in structures I, II, and III is always "buried" in the molecule and of the form (RF1)(RF2)C=C(RF3)-(RF4). We feel that any unsaturation not sterically protected in this way would easily have been fluorinated either by the initial CoF_3 reaction or by the subsequent reaction with elemental fluorine.

There are two remaining questions concerning the TOF-SIMS experiment: (1) Are the masses of the observed peaks near those of the parent ions (or are they predominantly much lower mass fragments)? (2) Is the TOF-SIMS distribution skewed by loss of

(10) Laatsch, H.; Beck, H.; Egert, E. *Liebigs Ann. Chem.* **1992**, *11*, 1125.
(11) Hotchkiss, I. J.; Stephens, R.; Tatlow, J. C. *J. Fluorine Chem.* **1975**, *6*, 135.

Table 9. Molecular Weight Calculation for TOF-SIMS Data[a]

M_i [b]	N_i [c]	M_i [b]	N_i [c]	M_i [b]	N_i [c]
1001	170	1569	310	1816	115
1039	516	1588	340	2079	77
1058	318	1607	752	2098	62
1077	1789	1626	663	2117	80
1096	1437	1645	1074	2136	65
1115	3117	1664	741	2155	155
1134	2771	1683	1098	2174	79
1153	4926	1702	623	2193	149
1172	1004	1721	667	2212	62
1191	3776	1740	500	2231	147
1210	241	1759	326	2250	48
1229	1239	1778	274	2269	72
1267	428	1797	100	2288	48
1550	130				

[a] $\bar{M}_n$ = 1313. [b] Molecular mass of the TOF-SIMS peak. [c] Intensity of the TOF-SIMS peak.

lower mass volatiles? Two sets of experiments have shown that the peaks are predominantly due to oligomer ions. First, we obtained TOF-SIMS spectra of $C_{14}F_{24}$ the same way as we did for the oligomers. Even though this material is quite volatile under the high-vacuum conditions of the experiment, apparently enough remained on the silver foil to allow us to successfully make the measurements. In the negative ion TOF-SIMS spectrum of this material, the principal peak was obtained at $m/z = 624$ and was due to the parent ion $C_{14}F_{24}^-$. The peak at $m/z = 586$, only about 15% the intensity of the parent ion peak, was due to the fragment $C_{14}F_{22}^-$.

We also compared the $\bar{M}_n$ determined by TOF-SIMS with that obtained by vapor pressure osmometry (VPO). The intensity (N_i) and molecular mass (M_i) of each peak used in the calculation are listed in Table 9. $\bar{M}_n$ calculated from the TOF-SIMS data is 1313. This is considerably higher than the value of 869 determined by VPO. It must be remembered, however, that the TOF-SIMS experiment is performed under a vacuum of $\sim 10^{-8}$ Torr. Under these conditions, the lower MW oligomer fractions would probably vaporize and not be recorded, thus biasing the molecular weight distribution to the high end. If this is true, one would expect the VPO analysis to give a lower MW. This is also consistent with the species observed by ToF-SIMS being molecular ions or nearly so. If the peaks used in the $\bar{M}_n$ calculation were due to fragments of substantially lower mass than molecular ions, the calculated $\bar{M}_n$ would have been lower than the VPO result.

Although the discrepancies between the ESCA and NMR results were within experimental error, one could expect differences if the lower MW components were structurally different from the higher MW components and they vaporized during the ESCA experiment. Like TOF-SIMS, ESCA was performed at $\sim 10^{-8}$ Torr, possibily rendering the lower boilers volatile.

ACKNOWLEDGMENT

The authors gratefully acknowledge the skilled assistance of R. McKay under the guidance of Dr. F. Kitson and Dr. C. N. Mc Ewen for the GC/MS analysis, C. Bowers under the guidance of Dr. E. Kissa for the elemental analysis, S. Krakowski for the ^1H NMR spectra, K. Raffell for the ^{19}F NMR spectra, and B. Bennett under the guidance of R. Fuller for the VPO analysis. We would also like to acknowledge the skilled assistance of W. Justison under the guidance of Dr. K. G. Lloyd for the TOF-SIMS. We also thank Dr. E. Matthews for the UV/vis and Dr. D. Kasprzak for the FT-IR analyses. D. Davidson and J. Wyre should be thanked, as well, for their skilled assistance in performing the ESCA experiments. Parts of the TOF-SIMS analysis reported herein were reported previously at the SIMS IX Conference, Yokohama, Japan, November 7–12, 1993.

Received for review September 15, 1994. Accepted March 30, 1995.[⊗]

AC940923A

[⊗] Abstract published in *Advance ACS Abstracts,* May 15, 1995.

Anal. Chem. **1995,** *67,* 1963–1967

Matrix-Assisted Laser Desorption Ionization of Neutral Clusters Composed of Matrix and Analyte Molecules

Andrew N. Krutchinsky, Anatoli I. Dolguine, and Mikhail A. Khodorkovski*

LEPTA-Petersburg Ltd., 197198 St. Petersburg, Russia

A new version of the matrix-assisted laser desorption ionization experiment is described. Composed clusters created by laser desorption of a mixture of analyte and matrix material were injected into a supersonic jet and then analyzed by multiphoton ionization time-of-flight mass spectrometry. Selective two-photon ionization of matrix molecules of a cluster component caused their dissociation, followed by intercluster proton or cation transfer to an analyte that is transparent for the wavelength of ionizing radiation. The intercluster charge transfer reactions are the only pathway for analyte ion formation under these conditions, as can be concluded from analysis of the mass spectra of a variety of substances.

With the introduction of pulsed direct laser desorption (LD), mass spectrometry got a powerful tool for analysis of labile organic compounds.[1–3] It has been shown[4,5] that LD allows transformation of condensed phase molecules into gas phase ions or neutrals. However, the widespread application of LD appears to be limited to the analysis of intact molecules with masses less then a few thousand Daltons. Either resonant or nonresonant excitation of analyte molecules by desorbing laser shots left the possibility of uncontrollable energy transfer into dissociative channels of such molecules.[6] Many efforts have been made to overcome this limitation. It has been shown in recent years that the addition of some organic substrates to create a matrix for analyte molecules allows the introduction of much larger ions into the gas phase.[7,8] The following development of this matrix-assisted laser desorption ionization (MALDI) technique, mainly directed toward extending the mass range and the list of compounds as well as substances applicable for matrix prepration,[9–12] gave rise to a number of models proposed to explain MALDI.[13–15] Based upon either empirical or gas dynamic approaches, the requirements for a matrix material and the rules of sample preparation have been determined.[16,17]

Among numerous experimental works, some have been carried out in a way different from that which became a standard method for MALDI experiments. In these experiments, a "dynamic" rather than a "static" target of the sample layer was laser irradiated to produce the quasimolecular ions of the analytes. Murray and Russel[18] irradiated a beam of particles of dried eluent from the output of a chromatograph. Apparently because of the aerosol character of the target, they called this approach "aerosol MALDI". The addition to an eluent of nitroaniline as a matrix strongly absorbing at the wavelength of the ionizing laser caused the protonation of analyte molecules. Thus, it was concluded that the proton transfer from nitroaniline molecules to analyte molecules was the key mechanism of ion formation. In other work, Langridge-Smith and co-workers[19] performed two-photon ionization (2PI) of a number of dyes desorbed by laser shots into a supersonic jet. They have shown that, together with radical cations, protonated or cationated ions of analytes were formed under the specific conditions of the experiment. However, the authors have not proposed any clear explanation of quasimolecular ion formation.

A common feature of these experiments is the laser irradiation of the dynamic target consisting of either pieces of a dried-from-eluent sample or laser-desorbed neutral species to produce the quasimolecular ions of anlaytes. The 2PI of desorbed species such as clusters might not only cause the formation of radical cations of an analyte but also initiate intercluster charge transfer reactions, leading to formation of quasimolecular ions. Similar processes have been studied by Nishi and Shinohara.[20] Ammonium clusters as the model objects were ionized by UV radiation. It has been shown that a competition between intercluster proton transfer and electron-removing reactions generated the protonated ions and radical cations, respectively. However, it is reasonable to expect that this competition may be excluded in the case of photoion-

(1) Unsold, E.; Hillenkamp, F.; Nitsche, R. *Analysis* **1976,** *4,* 115.
(2) Posthumus, M. A.; Kistemaker, P. G.; Meusellaar, H. L. C.; ten Noever de Brauw, M. C. *Anal. Chem.* **1978,** *50,* 985.
(3) Conzemius, R. J.; Capellon, J. M. *Int. J. Mass Spectrom. Ion Processes* **1980,** *34,* 197.
(4) Cotter, R. J. *Anal. Chem.* **1980,** *52,* 1767.
(5) Vastova, F. J.; Pirone, A. J. *Adv. Mass Spectrom.* **1968,** *4,* 107.
(6) Antonov, V. S.; Letokhov, V. S.; Shibanov, A. N. *Appl. Phys.* **1981,** *25,* 71.
(7) Karas, M.; Bachmann, D.; Bahr, U.; Hillenkamp, F. *Int. J. Mass Spectrom. Ion Processes* **1987,** *78,* 53.
(8) Tanaka, K.; Waki, H.; Ido, Y.; Akita, S.; Yoshida, Y.; Yoshida, T. *Rapid Commun. Mass Spectrom.* **1988,** *2,* 151.
(9) Karas, M.; Bahr, U.; Ingendoh, A.; Hillenkamp, F. *Angew. Chem., Int. Ed. Engl.* **1989,** *28,* 760.
(10) Beavis, R. C.; Chait, B. T. *Org. Mass Spectrom.* **1992,** *27,* 156.
(11) Chan, T.-W. D.; Colburn, A. W.; Derrick, P. G. *Org. Mass Spectrom.* **1992,** *27,* 53.
(12) Fitzgerald, M. C.; Parr, G. R.; Smith, L. M. *Anal. Chem.* **1993,** *65,* 3204.
(13) Vertes, A.; Levine, R. D. *Rapid Commun. Mass Spectrom.* **1990,** *4,* 233.
(14) Vertes, A. *Microbeam. Anal.* **1991,** *25,* (special issue, Howitt, D. G., Ed.).
(15) Ens, W.; Mao, Y.; Mayer, F.; Standing, K. G. *Rapid Commun. Mass Spectrom.* **1991,** *5,* 117.
(16) Beavis, R. C.; Chait, B. T. Proceedings of the 38th ASMS Conference on Mass Spectrometry and Allied Topics, Tuscon, AZ, 1990; Caprioli, R. M., Ed.; p 152.
(17) Hillekamp, F.; Karas, M.; Beavis, R. C.; Chait, B. T. *Anal. Chem.* **1991,** *63,* 1993A.
(18) Murray, K. K.; Russel, D. H. *Anal. Chem.* **1993,** *65,* 2534.
(19) Dale, M. J.; Jones, A. C.; Langridge-Smith, P. R. R.; Costello, K. F.; Cummins, P. G. *Anal. Chem.* **1993,** *65,* 793.
(20) Shinohara, H.; Nishi, N. *J. Chem. Phys.* **1985,** *83* (4), 1939.

0003-2700/95/0367-1963$9.00/0 © 1995 American Chemical Society

ization of clusters composed at least of two components, with the proviso that one of the components absorbs strongly at the wavelength of ionizing radiation and the other one does not. The selective photoionization of an absorbing component may be followed by dissociation, with subsequent charge transfer to the other component transparent for the wavelength of ionizing radiation. Thus, this seems to be it the only probable path for analyte ion formation along charge transfer reaction coordinates.

In this paper we present the results of 2PI of neutral clusters composed of matrix and analyte molecules. The clusters were prepared by IR-LD of a matrix material containing analyte molecules. The products of desorption were injected into a supersonic jet. The wavelengths and power density of ionizing radiation were chosen to allow selective 2PI of matrix molecules from neutral clusters. The time-of-flight mass spectra of a number of substances such as synthetic polymers, sugars, and peptides have been obtained under the conditions at which the analytes did not absorb at the wavelengths of ionizing radiation.

EXPERIMENTAL SECTION

Materials and Sample Preparation. The reagents used were poly(ethylene glycols) (PEGS), pentaphenylalanine, poly(L-valine), alanylglysylglysine (AGG), dalargin (Tyr-D-Ala-Gly-Phe-Gly-Arg, aminobenzoic acid sodium salt, caffeic acid, 3,4-dyhydroxy-*trans*-cinnamic acid (all from Sigma, St. Louis, MO). All of the sugars used were from Reachim, Russia. Other chemicals and solvents were reagent grade.

The solution of an analyte in ethanol/benzene, ethanol/water, or methanol/0.1% acetic acid, typically of 1 mg/mL concentration, was mixed with a 1 mg/mL solution of the aminobenzoic acid sodium salt or caffeic acid (3,4-dyhydroxy-*trans*-cinnamic acid) in methanol to prepare the matrix with the desired molar ratio of the components (1:1−1:10). An aliquot of 10 μL of the mixture was applied on the steel surface of a probe tip, dried, and introduced into the desorption chamber of the mass spectrometer. The products of laser desorption injected into a supersonic jet were examined by 2PI/TOF MS.

Instrumentation. All experiments were performed using the reflection time-of-flight mass spectrometer TOF-1 (Bruker-Franzen Analytik, Bremen, Germany) with MUPI ion source.[21−23] The principal scheme and main parameters of the experimental setup were described elsewhere.[21,27] Briefly, a stainless steel pulsed valve (General Valve Co., Fairfield, NJ) of 0.2 mm orifice diameter was used as a supersonic beam source. In the experiments, Ar with a backing pressure of 4−5 bar was the carrier gas; the background pressure remained at 1×10^{-7} Torr. The jet was skimmed 35 mm downstream by a skimmer with a 1 mm orifice. The samples were desorbed by an Altec AL 854 pulse CO_2 laser (Altec, Luebeck, Germany) directly in front of an expending gas jet. The rate of desorption could be controlled by adjusting the CO_2 laser power density on the sample surface. Based on the known beam profile, the power density of the desorbing beam was held at (1−10) $\times$ 10^5 W/cm^2. The laser ionization was performed 75 mm downstream from the desorption area by a frequency-doubled dye laser, FL 3002 (Lambda Physik, Hottingen, Germany), pumped by a LPX 200 excimer laser (308 nm, 15 ns) (Lambda Physik). The delay time between desorbing and ionizing laser shots could be changed within 1−1500 μs. The ionizing laser beam was collimated with a 20 cm focal length lens to produce a laser beam 1−2 mm in diameter. The power density in the ionization region was typically on the order of 10^5−10^6 W/cm^2. The ion signals were recorded by an RTD-710 200 MHz transient digitizer (Sony-Tektronix, Beaverton, OR) and stored via a GPIB interface on a Motorola 68000 fast computer system. Up to 100 laser shots were averaged to produce a mass spectrum.

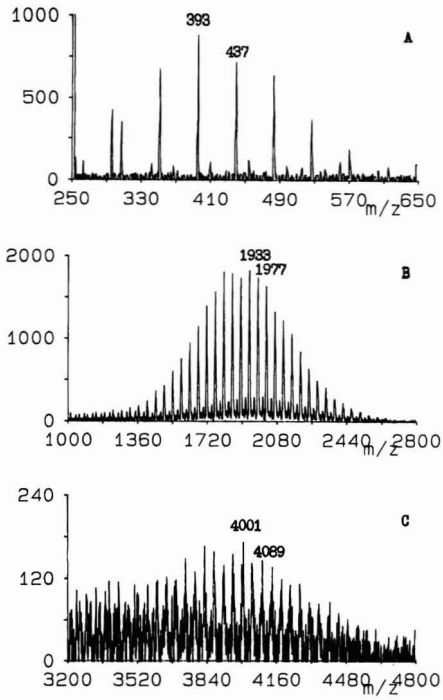

Figure 1. Mass spectra of PEG 400 (A), 2000 (B), and 4000 (C) obtained by 2PI (262 nm) of neutral clusters composed of aminobenzoic acid sodium salt and analyte molecules.

RESULTS AND DISCUSSION

Synthetic Polymers. The mass spectra of PEGS 400, 2000, and 4000 are shown in Figure 1, parts A−C, respectively. All polymers were desorbed from the sodium salt of aminobenzoic acid matrix. 2PI at 262 nm of desorbed products caused the sodiumation of molecules of linear polymers transparent for the wavelength of ionizing radiation. Little formation of the cationated ions occurred by attachment of gas phase sodium ions because of the very low probability of two-body collisions in the ionization region. However, this probability might be increased sufficiently if the process of charge transfer occurred within a cluster. The appearance of charges was promoted via 2PI of a cluster

(21) Frey, R.; Holle, A.; Weiss, G.; Franzen, J.; Koch, D. Proceedings of the 36th Annual Conference on Mass Spectrometry and Allied Topics, San Francisco, CA, 1988; p 185.
(22) Krutchinsky, A. N.; Dolgin, A. T., Khodorkovski, M. A. *J. Mass Spectrom.* **1995**, *30*, 375.
(23) Beavis, R. C.; Lindner, J.; Grotemeyer, J.; Schlag, E. W. *Chem. Phys. Lett.* **1988**, *146*, 310.
(24) Li, L.; Lubmun, D. M. *Appl. Spectrosc.* **1989**, *43*, 543.
(25) Yu, W.; Vath, J. E.; Huberty, M. C.; Martin, S. A. *Anal. Chem.* **1993**, *65*, 3015.
(26) Walter, K.; Boesl, U.; Schlag, E. W. *Int. J. Mass Spectrom. Ion Processes* **1986**, *71*, 309.
(27) Boesl, V.; Grotemayer, J.; Walter, K.; Shlag, E. W. *Anal. Instrum.* **1987**, *16*, 151.

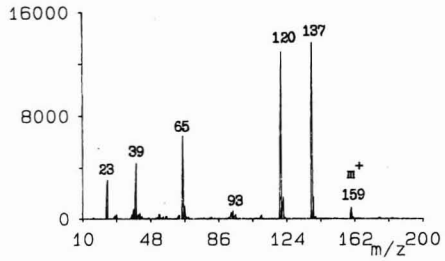

Figure 2. LD (10.6 μm)/2PI (262 nm) spectrum of aminobenzoic acid sodium salt (m = 159 *m/z*).

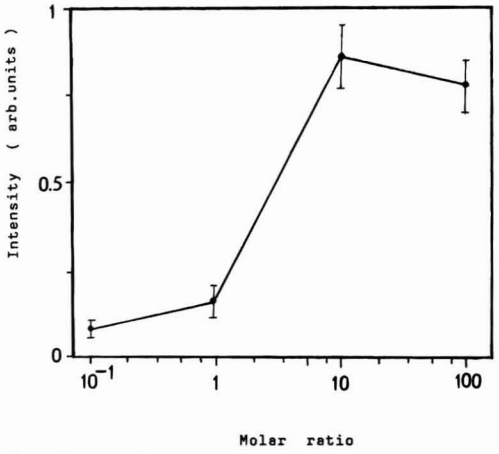

Figure 3. Dependence of the intensity of the mass peak (*m/z* 2021) in mass spectra of PEG 2000 on the molar ratio of the matrix of the analyte.

components. The ion signal of two-photon ionization of pure sodium, which might be presented as an impurity, was not as abundant as in the 2PI mass spectrum of sodium salt of aminobenzoic acid (see Figure 2). Thus, the most probable process occurring within a neutral composed cluster after ionization of the matrix molecules was Na^+ detachment and transfer to an analyte molecule with subsequent reorganization and dissociation of the clusters.

The investigation was carried out to determine the optimal matrix to analyte molar ratio. For this, a series of mass spectra were obtained for PEG 2000 desorbed from the matrices with different relative concentrations of aminobenzoic acid sodium salt and the polymer. The normalized amplitude values of the mass peak at *m/z* 2021 near the maximum of the polymer distribution as a function of the matrix to analyte molar ratio by constant amount of the polymer applied onto a probe tip (~2 μg, ~1 nmol) are shown in Figure 3. It can be seen in this figure that the signals were increased by increasing the molar ratio until the ratio was approximately equal to 10. We did not use any system to deflect low-weight ions, so the drop of the signal was not due to the deviation from the optimal ratio but was caused by charging of the microchannel plates because of a large number of matrix ions incident upon its surface. However, from these results, it may be concluded that the greater the molar ratio, the more effectively the matrix assisted desorption, apparently both as a heat buffer for excessive desorption energy and as a cation donor.

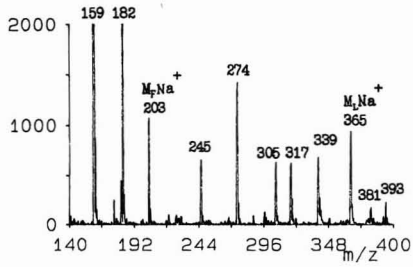

Figure 4. Mass spectrum of a mixture of fructose and lactose obtained by 2PI (262 nm) of neutral clusters composed of aminobenzoic acid sodium salt and analyte molecules. M_FNa^+, sodiumated fructose (M_F = 180 *m/z*); M_LNa^+, sodiumated lactose (M_L = 342 *m/z*).

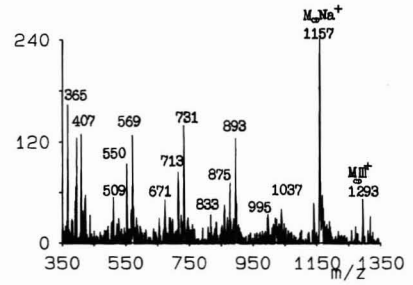

Figure 5. Mass spectrum of β-cyclodextrin obtained by 2PI (262 nm) of neutral clusters composed of aminobenzoic acid sodium salt and analyte molecules. $M_{CD}Na^+$, sodiumated β-cyclodextrin (M_{CD} = 1134 *m/z*); $M_{CD}m^+$, ions of composed clusters.

This approach was successfully applied for analysis of a number of synthesized polymers, such as poly(ethylene glycols), poly(propylene glycols), and polyfurans, not only to determine the final products but also to optimize the conditions of polymerization.

Sugars. The process of cation transfer appears to be effective also for a number of sugars. Sodium salt of aminobenzoic acid was appropriated as matrix material to obtain the mass spectra of fructose, lactose, glucose, and sucrose. Figure 4 shows the mass spectrum of fructose (*m/z* 180) and lactose (*m/z* 342). Although in the mass spectrum there are many peaks that can be identified with the ions of clusters composed of the fragments of matrix molecules, the sodiumated ions are clearly recognizable. Analysis of the mass spectrum of β-cyclodextrin (*m/z* 1134) in Figure 5 shows that the mechanism described above was involved in the processes of cationated ion formation.

Peptides. The mass spectra of a number of peptides containing no aromatic amino acid residues were obtained by 2PI of caffeic acid molecules of a composed cluster component. The dissociative ionization at 262 nm of the matrix molecules was followed by proton transfer to the analyte molecules. The mass spectra of the AGG (*m/z* 203) and caffeic acid matrix shown in parts A and B of Figure 6 were obtained at ~5 × 10^5 and ~10^8 W/cm^2 power densities of the ionizing laser radiation, respectively. The ultimate high-power density of UV radiation used for ionization of clusters did not cause any fragmentation of the peptide transparent at 262 nm. The dissipation of UV radiation energy occurred along dissociative ionization reaction coordinates of the matrix molecules which acted as a buffer for excessive energy.

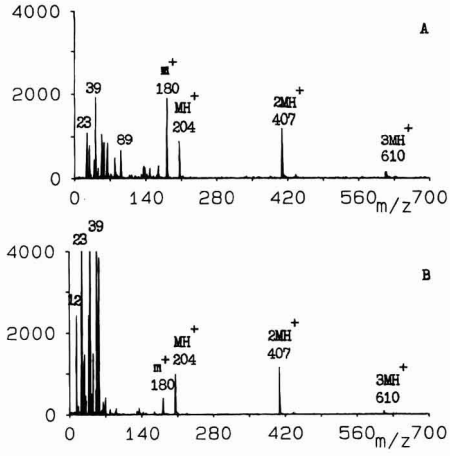

Figure 6. Mass spectra of AGG peptide (M = 203 *m/z*) obtained by 2PI (262 nm) of neutral clusters composed from caffeic acid (m = 180 *m/z*) and analyte molecules. Power density of the ionizing radiation: (A) 5×10^5 and (B) $\sim 10^8$ W/cm^2.

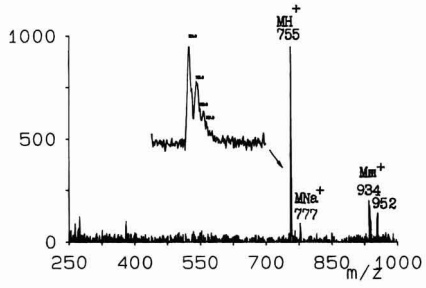

Figure 7. Mass spectrum of pentaphenylalanine obtained by 2PI (308 nm) of neutral clusters composed of caffeic acid and analyte molecules. MH^+, protonated analyte (M = 754 *m/z*); Mm^+, ions of composed clusters.

However, no clear, recognizable effects of intercluster charge transfer have been observed upon study of the compounds having aromatic groups strongly absorbing at 262 nm. This can be explained by a low dilution factor of an analyte in the matrix (obviously, the numbers of analyte and matrix molecules in a composed cluster were comparable) and by the competition between the intercluster charge transfer reactions and the electron-removing reactions which generate the protonated (or cationated) ions and radical cations, respectively.[20] To avoid competition between two possible reaction channels for those compounds that have absorption maxima in the region of 260–290 nm, the wavelength of ionizing laser radiation should be above 300 nm. On this assumption, the mass spectrum of pentaphenylalanine (*m/z* 754) was obtained by 2PI of caffeic acid molecules of a cluster component. The 2PI of the matrix was performed at 322 nm, where the weak absorbency band of the gas phase molecules had been found. The resonance 2PI of the proton-donated matrix molecules can be also induced at 308 nm, where the absorbency of the matrix molecules was stronger (Figure 7). Thus, the caffeic acid matrix appeared to be very convenient for the selective photoionization of matrix molecules of a cluster component using the 308 nm wavelength of an XeCl excimer laser.

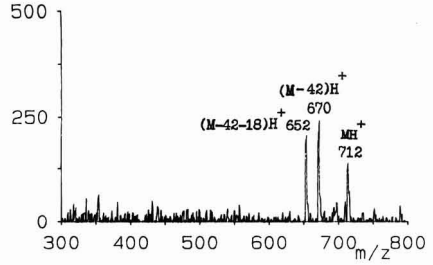

Figure 8. Mass spectrum of acetyldalargin (CH_3-CO-YAGFGR) obtained by 2PI (308 nm) of neutral clusters composed of caffeic acid and analyte molecules. MH^+, protonated analyte (M = 711 *m/z*); (M − 42)H^+ and (M − 42 − 18)H^+, protonated pyrolytic fragments of the original peptide.

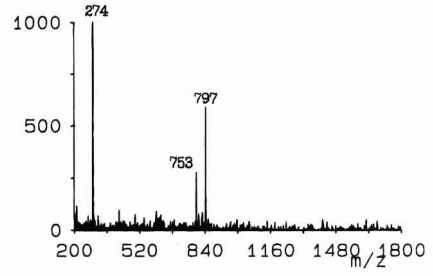

Figure 9. Mass spectrum of SPPTSTPDPKPKNNT peptide (*m/z* = 1579) obtained by 2PI (262 nm) of neutral clusters composed from caffeic acid and analyte molecules. The mass peak at *m/z* 797 is identified with the (-DPKPKNNT)H^+ fragment ion formed due to the breaking of the labile -P···D- bond of the peptide.

It should be pointed out that, whereas the processes of direct deposition of the ionizing radiation energy can be excluded by causing matrix-assisted ionization, the processes of molecule excitation during laser desorption still might occur. The processes of thermopyrolyses were clearly discerned in the mass spectrum of acetyldalargin (CH_3-CO-YAGFGR, *m/z* 711, Figure 8). The intensive protonated fragment ions correspond to the loss of the guanidine group of the arginine residue, reduction (*m/z* 669), and loss of water (*m/z* 651), the typical pyrolytic fragments.[23,24] Probably, the excitation of the SPPTSTPDPKPKNNT (*m/z* 1579) molecules during laser desorption caused the gas phase cleavage of the -P···D- labile bond of the peptide, which was clearly observed in the mass spectrum (see Figure 9). This evidence is in good agreement with the recent results of a study of some peptides having the -P···D- (-Pro-Asp-) bond.[25] It has been proposed that the gas phase cleavage of the peptide is due to the rather short lifetime of the excited quasimolecular ions.

For some polypeptides, the process of cationation seemed to be preferable over protonation. The poly(L-valine) mass spectrum obtained by using aminobenzoic acid sodium salt as a matrix is shown in Figure 10; the yield of the protonated ions appeared to be very low when the proton-donated matrix was used.

All mass spectra were obtained at a time delay between IR and UV laser shots of 250–260 μs. The measured time delay spectra for almost all of the compounds showed that the maximum of the distribution was within mentioned values and the fwhm was less than 50 μs. Figure 11 shows the normalized time delay spectra for a number of AGG protonated clusters. The spectra

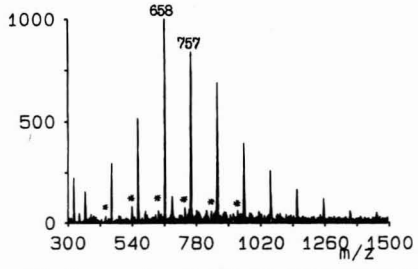

Figure 10. Mass spectrum of poly(L-valine) obtained by 2PI (262 nm) of neutral clusters composed of aminobenzoic acid sodium salt and analyte molecules. The main set of mass peaks corresponds to $(H(C_5H_9NO)_nOH)2Na^+$; peaks labeled with asterisk correspond to $(H(C_5H_9NO)_nOH)Na^+$.

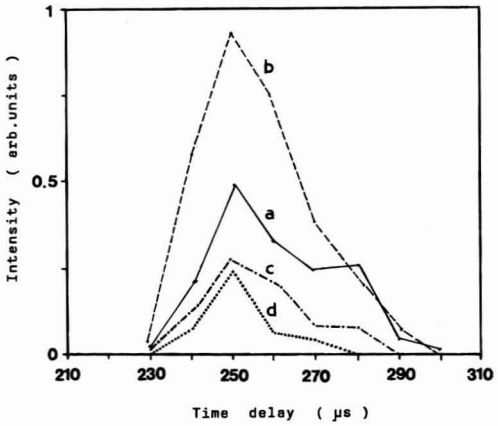

Figure 11. Time delay spectra of $(AGG)_n$ peptide clusters. $n = 1$ (a), 2 (b), 3 (c), and 4 (d).

were obtained by integrating the ion signals of corresponding masses, scanning the delay time between desorbing and ionizing laser shots. We suppose that the emission of clusters occurred within a short period of time, comparable with the duration of desorbing laser pulse ($\tau = 4\,\mu$s). If this is true, then the full time for clusters to reach the ionization area was mainly determined by the velocity of the jet, not the time of cluster emission. Thus, the time delay distribution can be interpreted as the velocity distribution of the clusters in the ionization area. The mass resolution of 1000–1500 obtained for almost all of the compounds studied (see, for example, Figure 7) was typical of the resolution achieved in our experiments with 2PI of neutral molecules. It may imply that the initial velocity distribution of ions resulting from charge transfer with subsequent cluster reorganization is similar to the measured velocity distribution of neutral clusters. Thus, it seems that the maximum and width of the initial velocity distribution of quasimolecular ions in the ionization area are much lower and narrower than were determined by irradiation of "static" matrix layers.[15] We did not make efforts to improve the mass resolution, but it is believed that the resolution might be improved sufficiently due to the properties inherent in the experiments by separately performing desorption into a supersonic jet and multiphoton ionization.[26]

CONCLUSIONS

The LD of various analyte compounds embedded in a matrix of aminobenzoic acid sodium salt or caffeic acid and 2PI of desorbed products showed that the ionization of analyte molecules had occurred via selective photodissociative ionization of a matrix component of the neutral clusters, followed by charge transfer reactions with subsequent cluster reorganization and fragmentation. The wavelengths of ionizing radiation, chosen on the basis of knowledge of the absorption bands of the matrix molecules in the gas phase, allowed the selective deposition of laser energy into these molecules but not into the analytes that are transparent for these wavelengths. Under this condition, the only possible route for analyte ion formation was along charge transfer coordinates.

The ionization of composed cluster may be viewed as a simplest model of an irradiated target. Because of the small number of the components involved in photochemical reactions, all possible paths of deposition and dissipation of the energy of laser radiation can be easily traced. Obviously, there is a direct analogy between the processes occurring upon irradiation of the composed clusters and in the "static" matrix layers. One can consider this analogy to elucidate the basis principles underyling the physical processes involved in MALDI.

ACKNOWLEDGMENT

We gratefully acknowledge the support of this work by Bruker-Franzen Analytik GmbH (Bremen) and the helpful discussions with Drs. R. Frey, C. Köster, A. Holle, and J. Franzen.

Received for review August 29, 1994. Accepted January 4, 1995.[⊗]

AC940855S

[⊗] Abstract published in *Advance ACS Abstracts,* February 1, 1995.

Anal. Chem. **1995,** *67,* 1968–1975

Determination of Acidic Pesticides in Water by a Benchtop Electrospray Liquid Chromatography Mass Spectrometer

Carlo Crescenzi, Antonio Di Corcia,* Stefano Marchese, and Roberto Samperi

Dipartimento di Chimica, Università "La Sapienza", Piazza Aldo Moro 5, 00185 Roma, Italy

A very sensitive and specific analytical procedure for determining 20 acidic pesticides in aqueous environmental samples using pneumatically assisted electrospray (ES) LC/MS is presented. This procedure involves passing 1- and 4-L river water and drinking water samples, respectively, through a 1-g graphitized carbon black (GCB) extraction cartridge. By exploiting the presence of positively charged active centers on the GCB surface, isolation of the acidic pesticides from base/neutral species was made possible by differential elution. Recoveries of the analytes were higher than 85%, irrespective of the aqueous matrix in which they were dissolved. Adoption of the ion pair technique by addition of 0.1 mmol/L K_2HPO_4 and 0.2 mmol/L tetrabutylammonium fluoride to the mobile phase allowed analytes to be analyzed as preformed ions. A conventional 4.6-mm-i.d. reversed-phase LC C-18 column operating with a 1 mL/min flow of the mobile phase was used for chromatographing the analytes. A flow of 30 μL/min of the column effluent was diverted to the ES source, while the rest of the mobile phase was delivered to a UV detector set at 220-nm wavelength. The effects of the nature of the ion pair forming agent and its counterion as well as its concentration in the mobile phase on the response of the ES/MS detector were investigated. The effects of varying the skimmer cone voltage on the production of diagnostic fragments and the response of the MS detector were also evaluated. For the analytes considered, the response of the mass detector was linearly related to the amount of the analytes injected between 2.5 and 200 ng. A certain variation of the ion signal for the analytes considered occurred after several hours of continuous use of the LC/ES/MS instrumentation. For routine use, then, analyte quantitation could be better performed by the UV trace method while entrusting unambiguous identification of the analytes to the MS detector. The limits of sensitivity (signal-to-noise ratio = 3) of the method for the pesticides considered in drinking water and surface water samples were estimated to be about 2–6 and 8–25 ng/L, respectively.

A number of liquid chromatographic methods have been proposed for determining those analytes of environmental interest that are not amenable to analysis by the gas chromatography/mass spectrometry technique. However, because of the legal implications of many environmental data, coupling LC with MS is a key element for the future of LC procedures.

Electrospray (ES) ionization has rapidly emerged as a very promising technique for interfacing LC to MS. Similarly to thermospray, ES ionization produces ions at atmospheric pressure, but without the need for high temperatures that could decompose labile compounds. Briefly, the sequence of events in the electrospray process leading to generation of gas phase ions involves formation of charged small droplets by an electrical field. The droplets are gradually reduced in size by heat transfer and repeated Coulombic explosion until the radius of curvature of the daughter droplets becomes so small that field-assisted ion "evaporation" competes with further droplet disintegration. The LC/ES/MS system has proven to be a sensitive technique for analyzing compounds of environmental interest that exist as ions in solution.[1,2]

Notably, although the electrospray process generates gas phase ions in a gentle way, structural information on analytes can also be easily achieved by collision-induced fragmentation with a suitable adjustment of the electrical field existing in the intermediate-pressure desolvation chamber located between the ionization source and the mass analyzer region. By suitably exploiting this possibility, Voyksner and Pack[3] showed that a single mass analyzer can provide structural information very similar to that obtained by the much more costly tandem MS technique.

Recent legislation enacted in many european countries (members of the European Community, EC) states that pesticides must not exceed the 100 ng/L level in waters intended for human consumption. In order to judge with sufficient confidence whether a water sample is in compliance with this EC Directive, analytical methods able to detect pesticides at 20–30 ng/L levels are needed. In the recent past, we elaborated a very sensitive and rapid LC/UV method able to analyze more than 120 pesticides in aqueous environmental samples at the ng/L level.[4–6] This method involves the use of a 1-g graphitized carbon black (GCB) reversible cartridge for extracting pesticides from water samples. Passing sequentially through the cartridge two suitable solvent systems, isolation of acidic pesticides from nonacidic ones was successfully achieved by differential elution. Class fractionation was made possible because the GCB surface framework is contaminated by

(1) Conboy, J. J.; Henion, J. D.; Martin, M. W.; Zweigeinbaum, J. A. *Anal. Chem.* **1990,** *62,* 800–807.
(2) Popenoe, D. D.; Morris, S. J.; Horn, P. S.; Norwood, K. T. *Anal. Chem.* **1994,** *66,* 1620–1629.
(3) Voykner, R. D.; Pack, T. *Rapid Commun. Mass Spectrom.* **1991,** *5,* 263–268.
(4) Di Corcia, A.; Marchetti, M. *Anal. Chem.* **1991,** *63,* 580–585.
(5) Di Corcia, A.; Marchetti, M. *Environ. Sci. Technol.* **1992,** *26,* 66–74.
(6) Di Corcia, A.; Marcomini, A.; Samperi, R.; Stelluto, S. *Anal. Chem.* **1993,** *65,* 907–912.

0003-2700/95/0367-1968$9.00/0 © 1995 American Chemical Society

some positively charged adsorption sites that enable this material to behave as both a nonspecific sorbent and an anion exchanger.[7,8]

The purpose of this work has been to evaluate the potentiality of coupling our sample preparation procedure with the high confirmational power of the LC/ES/MS system for monitoring unambiguously acidic pesticides in drinking water and surface water samples.

EXPERIMENTAL SECTION

Reagents and Chemicals. Authentic acidic pesticides were purchased in part fom Eurobase (Milano, Italy) and in part from Riedel-de Haen (Seelze, Germany). The compounds considered in this work are listed below, together with their common names and pK_a values (in parentheses): 3,6-dichloro-2-methoxybenzoic acid (dicamba, 1.9); 2-isopropyl-(1*H*)-benzo-2,1,3-thiadiazin-4(3*H*)-one 2,2′-dioxide (bentazone, 3.2); 2,4-dinitrophenol (2,4-DNPh, 4.5); 4-chloro-2-oxo-3(2*H*)-benzothiazoleacetic acid (benazolin, 3.6); 3-(α-acetonylfurfuryl)-4-hydroxycoumarin (coumafuryl, 4.9); 3,5-dibromo-4-hydroxybenzonitrile (bromoxynil, 4.1); 4,6-dinitro-*o*-cresol (DNOC, 4.7); 4-hydroxy-3-(3-oxo-1-phenylbutyl)coumarin (warfarin, 4.9); 2-methyl-4-chlorophenoxyacetic acid (MCPA, 3.1); 2,4-dichlorophenoxyacetic acid (2,4-D, 2.6); 3,5-diiodo-2-hydroxybenzonitrile (ioxynil, 3.96); 2-(2-methyl-4-chlorophenoxy)propionic acid (mecoprop, 3.8); 2-(2,4-dichlorophenoxy)propionic acid (dichlorprop, 3.0); 2,4,5-trichlorophenoxyacetic acid (2,4,5-T, 2.1); 2-methyl-4-chlorophenoxybutyric acid (MCPB, 4.8); 2,4-dichlorophenoxybutyric acid (2,4-DB, 4.8); 2-(2,4,5-trichlorophenoxy)propionic acid (2,4,5-TP, 3.3); 2-*sec*-butyl-4,6-dinitrophenol (dinoseb, 4.6); 2-*tert*-butyl-4,6-dinitrophenol (dinoterb, 4.6); and pentachlorophenol (PCP, 4.7). Although 2,4-DNPh is not used in agriculture as a pesticide, it was included in this study as it is a metabolite of pesticides largely used in agriculture. Linear octyl benzenesulfonate (C-8 LAS) sodium salt was from Fluka AG (Buchs, Switzerland) and was used as internal standard (IS). Linear alkyl benzenesulfonate (LAS) compounds are important surfactants that can be present in environmental waters. In spite of this, C-8 LAS was chosen as IS as commercial formulations invariably contain C-10 through C-14 LAS mixtures. Individual standard solutions were prepared by dissolving 50 mg of each pesticide in 50 mL of acetonitrile. A composite working standard solution was prepared by mixing 0.5 mL of each pesticide standard solution and diluting to 50 mL with acetonitrile.

For LC, distilled water was further purified by the Milli-Q RG apparatus (Millipore, Bedford, MA). Methanol "plus" and acetonitrile "plus" of LC grade were from Carlo Erba (Milano, Italy). K_2HPO_4, trifluoroacetic acid (TFA), and various quaternary ammonium salts were from Fluka AG. All other solvents were of reagent grade and were used as supplied.

GCB, commercially referred to as Carbograph 1 or Carbopack B, was kindly supplied by Alltech (Deerfield, IL), while the other materials for preparing extraction cartridges were from Supelco (Bellefonte, PA). The preparation and pretreatment of the 1-g reversible extraction cartridges were carried out as previously reported.[9] With respect to this work, the design of the cartridge was sligthly modified in that the Teflon piston had a Luer tip and was inserted into the syringe-type cartridge after water extraction and washings before the base/neutral fraction was eluted.

The trap was fitted into a side-arm filtering flask, and liquids were forced to pass through the cartridge by vacuum from a water pump.

Grab samples of river water (from the Tiber River) were collected in empty solvent bottles and stored at 4 °C until used.

Procedure. The extraction of the analytes from aqueous samples was accomplished in a manner similar to that previously described.[6,9] After water sample extraction, the cartridge was sequentially washed with 6 mL of distilled water and 1 mL of methanol. Thereafter, a Teflon piston was forced to enter the cartridge that was turned upside down. The cartridge was firstly back-flushed with another 1 mL of methanol, followed by 6 mL of a methylene chloride/methanol (80/20 v/v) solution to wash out coextracted base/neutral subtances, and then with 6 mL of methylene chloride/methanol (80/20 v/v) acidified with 0.2% (v/v) TFA to elute acidic species. Before solvent removal, the acid-containing extract was partially neutralized by addition of 50 μL of a water/methanol solution of ammonia obtained by diluting 2 mL of concentrated ammonia to 10 mL with methanol. When the acidic extract was dried without the addition of ammonia, severe losses of those pesticides that are more readily esterified by methanol in an acidic ambient, especially coumafuryl and warfarin, were noted. Furthermore, 100 μL of a 15 ng/μL C-8 LAS methanolic solution was added as internal standard. After exhaustively drying the extract in a water bath at 40 °C under a stream of nitrogen, the residue was reconstituted with 200 μL of a water/methanol (70/30 v/v) solution containing 4 mmol/L K_2HPO_4 and 0.2 mmol/L tetrabutylammonium fluoride (TBAF). A 50-μL portion of the final extract was injected into the LC column.

LC/UV/ES/MS Analysis. Liquid chromatography was carried out with a Varian (Walnut Creek, CA) Model 9010 instrument equipped with a Rheodyne Model 7125 injector having a 50-μL loop. The analytes were chromatographed on an Alltima 25-cm × 4.6-mm-i.d. column filled with 5-mμ C-18 reversed-phase packing (Alltech). Phase A was a methanol/acetonitrile mixture (85/15 v/v), and phase B was water. Both phases contained 0.1 mmol/L K_2HPO_4 and 0.2 mmol/L TBAF. The initial composition of the mobile phase was 30% A, increased linearly to 75% A over 40 min. The flow rate of the mobile phase was 1 mL/min. A 30-μL portion of the column effluent was diverted to the ES source, while the rest of the mobile phase was delivered to a Model 2550 UV detector (Varian) set at 220-nm wavelength. A Fisons VG Platform benchtop mass spectrometer (Fisons Instruments/VG BioTech, Milano, Italy) equipped with a pneumatically assisted electrospray LC/MS interface and a single quadrupole was used for analyzing target compounds in the column effluent. This was introduced into the ES interface through a 40-cm length of 75-μm-diameter poly(ether ether ketone) (PEEK) capillary tube. The mass spectrometer was operated in the negative ion mode by applying to the capillary a voltage of 2.9 kV, while the skimmer cone voltage was set at 20 V. Mass spectra collected in full-scan mode were obtained by scanning over the range $139 \leq m/z \leq 380$ in 2 s. The source temperature was maintained at 60 °C. Ions were generated using highly pure air as drying and nebulizing gas. The optimum flow rates of the drying and nebulizing gas were found to be 300 L/h and 13 mL/min, respectively.

On a weekly basis, the counter electrode and the sampling cone were cleaned with a concentrated nitric acid/water (1/1 v/v)

(7) Campanella, L.; Di Corcia, A.; Samperi, R.; Gambacorta, A. *Mater. Chem.* **1982**, *7*, 429–438.

(8) Di Corcia, A.; Marchese, S.; Samperi, R. *J. Chromatogr.* **1993**, *642*, 163–174.

(9) Di Corcia, A.; Marchese, S.; Samperi R. *J. Assoc. Off. Anal. Chem.* **1994**, *77*, 446–453.

mixture and 10 min of sonication. Thereafter, they were extensively washed with distilled water, followed by acetone and methanol. The entire cleaning procedure required no more than 25 min/week.

For recovery studies, the concentrations of pesticides in water were calculated by measuring the peak area for each analyte relative to that of the IS and comparing those results with those obtained from standard solutions. The standards were prepared by dissolving known and appropriate volumes of the working standard solution in the eluant phase used for desorbing acidic pesticides from the Carbograph surface and then following the procedure reported above. For those pesticides producing overlapping peaks, recoveries were calculated by measuring peak areas obtained after extracting chromatograms for selected *m/z* values.

The mass spectrometry data handling system used was the Mass Lynkx software from Fisons Instruments.

RESULTS AND DISCUSSION

In our previous work,[4] LC fractionation of acidic pesticides was performed by using the ion suppression technique with addition of a suitable amount of TFA to the mobile phase. Under this chromatographic condition and with the ES/MS detector operating in the positive mode, however, very low signals for the analytes were obtained because of the scarce tendency that un-ionized acids have to form adducts with positive ions. Thus, the ion suppression technique was replaced with the ion pair (IP) technique by adding suitable amounts of HPO_4^{2-} and a quaternary ammonium salt. In this way, the analytes were delivered to the ES source operating in the negative mode as "preformed" ions.

Typical IP-LC methods discussed in the literature involve concentrations of buffers and quaternary ammonium salts in the mobile phase between 5 and 20 mmol/L. It is known that a severe limitation of the ES interface is that it cannot afford mobile phases containing such relatively high salt concentrations, as they provoke signal instability and, ultimately, electrical breakage.[10] Also, mobile phases rich in salts can rapidly occlude the sampling cone orifice, thus precluding ions from reaching the mass analyzer region. Therefore, our efforts were devoted to minimizing the concentrations of both the buffer and the quaternary ammonium salts dissolved in the mobile phase while still obtaining sharp and well-retained peaks for the target compounds.

The addition of only 0.1 mmol/L K_2HPO_4 to the mobile phase sufficed to give a pH of 7.1, thus ensuring dissociation of the acidic species considered.

With the view of optimizing the chromatographic performance of the analytical column and achieving well-defined ion signals for the analytes, the effects of the nature of the ion pair forming agent and its counterion as well as its concentration in the mobile phase on the two parameters discussed above were investigated.

The effect of varying the alkyl chain length of the quaternary ammonium salt, i.e., tetramethyl, tetraethyl, tetrapropyl, tetrabutyl, and tetrapentylammonium chloride, dissolved in the column effluent on the ion signals is shown in Figure 1. This experiment was conducted by dissolving 0.2 mmol/L of the various quaternary ammonium salts considered in 0.1 mmol/L HPO_4^{2-} buffered water/methanol (50/50 v/v) mixtures and measuring the ion signal intensities relative to known amounts of three selected

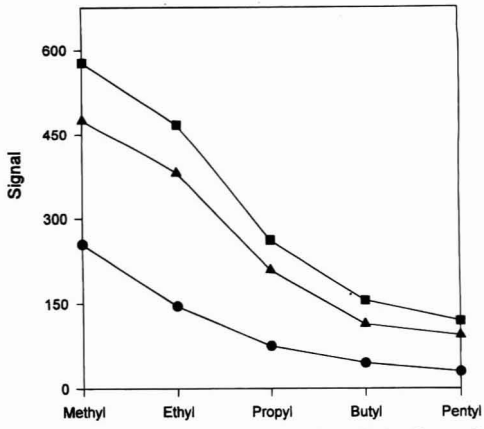

Figure 1. Ion signal for three selected analytes obtained by varying the alkyl chain length of the quaternary ammonium ion dissolved in the mobile phase. (■) Bromoxynil, (▲) 2,4-D, and (●) dicamba.

pesticides. These compounds were separately and directly injected into the ES source by the flow injection analysis (FIA) technique. Measurements were made in duplicate. As can be seen, a steady decrease in the signals was observed as the alkyl chain length was increased. This result may be explained on the basis of two considerations. One is that the extent of solvation of the quaternary ammonium ion decreases as the alkyl chain length increases, with the result that more and more stable ion pairs with analyte anions are formed. The other is that the electrospray process produces only a partial charge separation, so that the electrosprayed solution still maintains, during the sequence of events leading ultimately to gas phase ion formation, a certain amount of quaternary ammonium ions. Thus, anions leave the charged liquid droplets in part as such and in part recombined with the quaternary ammonium ions. From these two considerations, it follows that the recombination process will decrease the ion signal intensity to the extent that quaternary ammonium ions are able to form stable ion pairs with analyte anions.

It is worth noting that the ion signal intensity was also dependent on the nature of the analyte. This effect could be accounted for by considering that, as found by Hiraoka et al.,[11] the less volatile the organic ion, the more is its tendency to recombine with quaternary ammonium ions. Thus, less volatile ions will be detected with lower sensitivity by the ES/MS system.

From a chromatographic point of view, it was observed that mobile phases containing quaternary ammonium ions with short alkyl chains were unfortunately unable to elute the most polar analytes with sufficiently high retention times or to produce untailed peaks for the early-eluting phenol derivative analytes, such as 2,4-DNPh, DNOC, bromoxynil, and, to a lesser extent, ioxynil. These two adverse effects could be in part lessened by both decreasing the organic modifier percentage and increasing the ion pair forming agent concentration in the mobile phase. Under these conditions, however, a significantly weaker and less stable ion signal for the analytes was observed. Definitively, the best compromise was reached by adding to the buffered mobile phase a suitable amount of tetrabutylammonium (TBA) ions.

(10) Hopfgartner, G.; Wachs, T.; Bean, K.; Henion, J. *Anal. Chem.* **1993**, *65*, 439–446.

(11) Hiraoka, K.; Murata, K.; Kudaka, I. *Rapid Commun. Mass Spectrom.* **1993**, *7*, 363–373.

Table 1. Effect of the Nature of the Counterion of the Ion Pair Agent on the Ion Signals of Some Selected Analytes

	ion signal[a]			
compound	F^-	Cl^-	Br^-	I^-
2,4-D	68	38	25	20
mecoprop	65	32	20	15
bromoxynil	139	108	113	105
PCP	86	60	64	55

[a] Arbitrary units.

The effect of the nature of the counterion of the quaternary ammonium salt on the response of the ES/MS detector for the analytes considered was evaluated. These experiments were conducted under FIA conditions by introducing separately into the ES source equal amounts of some selected analytes, namely, 2,4-D, mecoprop, bromoxynil, and PCP. The liquid phases were 0.1 mmol/L HPO_4^{2-} buffered water/methanol (50/50 v/v) mixtures containing equal concentrations (0.2 mmol/L) of various TBA salts having respectively F^-, Cl^-, Br^-, and I^- as counterions. Measurements were made in duplicate. Results are reported in Table 1. As can be seen, for the conjugated bases of the two phenoxyacids, 2,4-D and mecoprop, a remarkable decrease in the signal was observed on changing from F^- to Cl^- as counterion. Although to a lesser extent, this trend was maintained by further increasing the counterion size. The behaviors exhibited by bromoxynil and PCP were counterintuitive. On steadily increasing the size of the counterion, their signals first decreased and then increased. These findings could be explained by making some assumptions. One is that competition effects occurring between halide ions and analyte ions in forming stable ion pairs with residual tetrabutylammonium ions present in the electrosprayed aerosol can affect the transition efficiency of organic anions to the gas phase. Among the counterions considered, the fluoride ion has the highest charge density, and thus a second reasonable assumption is that it forms the most stable ion pair with a quaternary ammonium ion. When these assumptions are accepted, the highest analyte ion signals obtained with F^- as counterion can be accounted for by a decrease in the actual concentration of residual TBA^+ ions in the electrosprayed solution. With respect to 2,4-D and mecoprop, differences in the behaviors of the ionized forms of bromoxynil and PCP could be explained assuming that the latter two species are more volatile, and so their transition to the gas phase is less affected by recombination processes. Studies performed by Raffaelli and Bruins[12] with the view of assessing whether the nature of the counterion could affect the transition efficiency of quaternary ammonium ions from an extremely diluted electrosprayed methanol solution to the gas phase led these authors to the conclusion that the small differences observed could not be considered significant. Nevertheless, their experimental results appear to partially substantiate the first two assumptions reported above, as they obtained a definite decrease in the ion current for the TBA^+ ion on replacing Cl^- with F^- as counterion.

The dependence of the ion signal for some selected analytes on the concentration of TBAF present in the mobile phase was assessed. For this experiment, increasing concentrations of TBAF were added to buffered water/methanol (50/50 v/v) mixtures. Measurements were made in duplicate. Results reported in Figure 2 show that the ion signal intensities were severely affected even by the presence of a small concentration of TBAF in the buffered solution. This indicated once more that significant recombination effects taking place between the ion pair forming agent and the analyte ions in the electrosprayed droplets deeply influence the ion transition yield to the gas phase. From a chromatographic point of view, the addition of 0.2 mmol/L TBAF to the mobile phase sufficed to satisfy the requirement of well-retained and sharp peaks for the analytes considered.

Under the chromatographic conditions adopted, the linear dynamic range and the absolute sensitivity of the ES/MS detector were estimated. These measurements were performed by injecting in triplicate into the LC column known and variable amounts of bromoxynil and 2,4-D and measuring their peak areas by extracting chromatograms relative to m/z 274–279 (2,6-dibromo-4-cyanophenoxy ion) and 161–166 (2,4-dichlorophenoxy ion) +

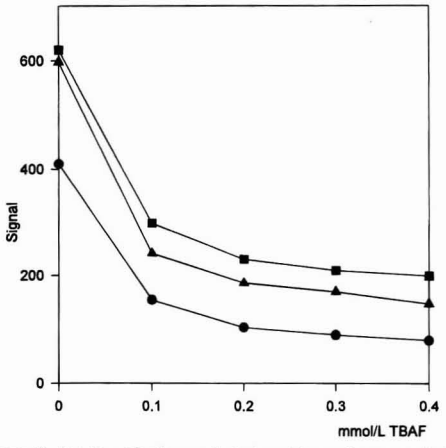

Figure 2. Ion signal for three selected analytes vs the concentration of tetrabutylammonium fluoride in the mobile phase. (■) loxynil, (▲) mecoprop, and (●) MCPA.

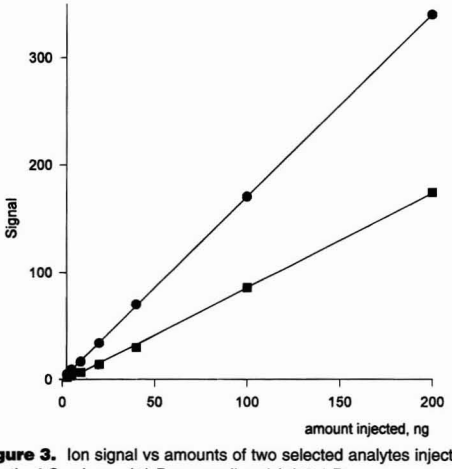

Figure 3. Ion signal vs amounts of two selected analytes injected into the LC column. (●) Bromoxynil and (■) 2,4-D.

(12) Raffaelli, A.; Bruins, A. P. *Rapid Commun. Mass Spectrom.* **1991**, *5*, 269–275.

Table 2. Variation of the Ion Signal Intensity and the Relative Abundance of Diagnostic Fragments for Some Selected Analytes on Varying the Voltage Applied to the Skimmer Cone

	signal/noise [*m/z* (relative abundance)]			
compound	10 V	20 V	30 V	40 V
dicamba	125 [*220*[a] (90), 176[b] (100)]	270 [*220* (10), 176 (100)]	124 [*220* (6), 176 (100)]	45 [*220* (10), 176 (100)]
bentazone	145 [*239* (100)]	360 [*239* (100)]	560 [*239* (100)]	530 [*239* (100) 196[c] (20)]
ioxynil	420 [*370* (100)]	970 [*370* (100)]	1080 [*370* (100)]	900 [*370* (100)]
2,4-D	110 [*220* (100), 161[d] (5)]	283 [*220* (100), 161 (90)]	530 [*220* (100), 161 (90)]	715 [*220* (10), 161 (100)]
dichlorprop	100 [*234* (100), 161 (5)]	360 [*234* (60), 161 (100)]	584 [*234* (10), 161 (100)]	650 [*234* (5), 161 (100)]
2,4 DB	40 [*248* (100), 161(50)]	280 [*248* (10), 161(100)]	320 [*248* (5), 161(100)]	380 [*248* (3), 161 (100)]
dinoseb	200 [*239* (100)]	650 [*239* (100)]	940 [*239* (100)]	1040 [*239* (100), 193[e] (20)]
PCP	190 [*265* (100)]	400 [*265* (100)]	548 [*265* (100), 230[f] (10)]	420 [*265* (100), 230 (20)]

[a] The value for the molecular ion is indicated in italic type. [b] *m/z* relative to 3,6-dichloro-2-methoxyphenoxy ion. [c] *m/z* relative to 1H-benzo-2,1,3-thiadiazin-4-one 2,2-dioxide ion. [d] *m/z* relative to 2,4-dichlorophenoxy ion. [e] *m/z* relative to 2-*sec*-butylnitrophenoxy ion. [f] *m/z* relative to tetrachlorophenoxy ion.

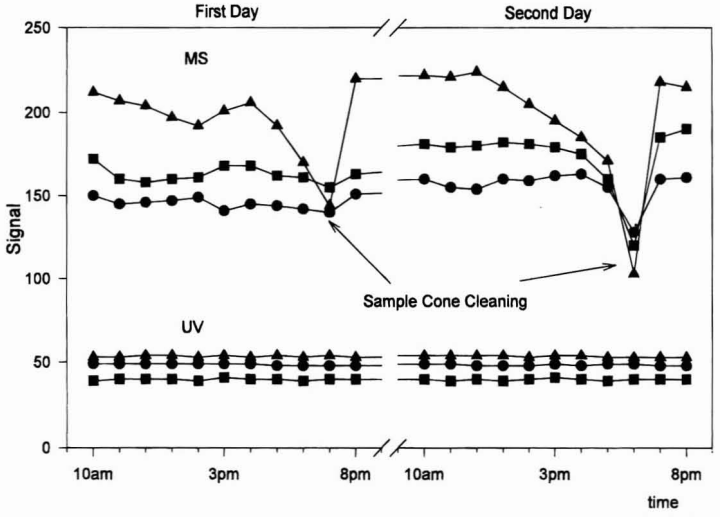

Figure 4. Variation of the MS and UV signals for three selected analytes over 2 working days. (▲) loxynil, (■) dichlorprop, and (●), 2,4-D.

219–225 (2,4-dichlorophenoxyacetate ion). The column was operated isocratically with 50% of the organic modifier. As can be seen from the plot in Figure 3, the response of the ES/MS detector was linearly related to injected amounts of the two model compounds from 2.5 to 200 ng. By measuring the signal-to-noise ratio (S/N) from extracted chromatograms relative to the lowest injected amounts of both bromoxynil and 2,4-D, the absolute limits of sensitivity (S/N = 3) of the ES/MS were set at about 0.3 and 1 ng, respectively. As the response of the ES/MS detector is related to the analyte concentration in the mobile phase, the absolute limits of detection reported above could be significantly decreased by adopting narrower LC columns. However, in our experience and as already extensively discussed by Hopfgartner et al.,[13] the use of small-bore LC columns does not offer practical advantages, since lower extract volumes of actual samples must be injected into these columns to avoid overloading effects and retention time variations of the early-eluting analytes.

For unambiguous confirmation of the presence of a certain target compound in complex matrices, a spectrum having at least one diagnostic daughter ion in addition to the corresponding molecular ion is desirable. As mentioned above, structural information on analytes can be simply obtained by suitably adjusting the potential difference set between the extraction and skimmer cones to produce collision-induced dissociation (CID) of ions in the region of intermediate pressure. In addition, an increase of the skimmer cone voltage usually enhances the S/N for an analyte by reducing the background ion current and

(13) Hopfgartner, G.; Bean, K.; Henion, J.; Henry, R. *J. Chromatogr.* **1993**, *647*, 51–61.

Table 3. Percentage Recovery (n = 6) of 20 Acidic Pesticides Added to 1-L River Water and 4-L Drinking Water Samples[a]

	recovery ± RSD,[b] %	
compound	drinking water	river water
dicamba	99 ± 3	94 ± 2
bentazone	96 ± 3	101 ± 3
2,4-DNPh	97 ± 4	98 ± 4
benazolin	93 ± 4	96 ± 3
coumafuryl	86 ± 6	94 ± 4
bromoxynil	98 ± 3	99 ± 2
DNOC	102 ± 4	97 ± 5
warfarin	86 ± 7	93 ± 3
MCPA	97 ± 3	98 ± 4
2,4-D	94 ± 4	100 ± 4
ioxynil	96 ± 3	97 ± 6
mecoprop	95 ± 4	95 ± 5
dichlorprop	96 ± 3	97 ± 4
2,4,5-T	97 ± 4	94 ± 5
MCPB	96 ± 3	93 ± 4
2,4-DB	97 ± 4	94 ± 5
2,4,5-TP	97 ± 4	96 ± 3
dinoseb	94 ± 4	95 ± 3
dinoterb	95 ± 3	94 ± 4
PCP	99 ± 3	97 ± 3

[a] Spike levels: 1 μg/L for river water and 0.1 μg/L for drinking water. [b] RSD = relative standard deviation.

improving the ion focusing effect.[14] The effects of increasing the cone voltage on both the response of the MS detector and the production of diagnostic ions were investigated. This experiment was conducted by introducing into the source known amounts of eight selected analytes via FIA using a water/methanol (50/50 v/v) mixture containing 0.1 mmol/L K_2HPO_4 and 0.2 mmol/L TBFA and calculating S/N values at an extraction cone voltage increasing from 10 to 40 V. Measurements were made in triplicate. Results are reported in Table 2. Except for dicamba, significant increases of the S/N values for the other species considered in this experiment were obtained on increasing the skimmer cone voltage from 10 to 30 V. As expected, this increase was due to both lower background noise and higher peak heights. By further increasing the cone voltage from 30 to 40 V, the S/N for some of the analytes decreased, presumably due to the fact that high-energy collisions generated small daughter ions having m/z out of the mass scan range selected (see the Experimental Section). For dicamba, the CID process generated Cl^- ions whose abundance increased as the cone voltage was increased from 20 to 40 V, as observed by decreasing the lower limit of the m/z scan range down to 30. Large differences were noted in the stability of the analyte ions. Within the cone voltage range reported in the Table 2, no daughter ion was obtained for ioxynil. Only by setting the cone voltage at 50 V was it possible to detect a fragment produced by the loss of a iodine atom. At 40 V, the fragmentation of the dinoseb and bentazone parent ions by the CID process generated two diagnostic ions, resulting from the respective losses of a nitro group and an isopropyl group. From the fragmentation of the ionized forms of the three phenoxyacids included in this experiment, i.e., 2,4-D, 2,4-dichlorprop, and (2,4-DB), the same daughter ion, i.e., 2,4-dichlorophenoxy ion, was generated by CID. The relative abundance of this charged fragment was dependent upon the nature of the parent ion and

(14) Duffin, K. L.; Wachs, T.; Henion, J. D. *Anal. Chem.* **1992**, *64*, 61–68.

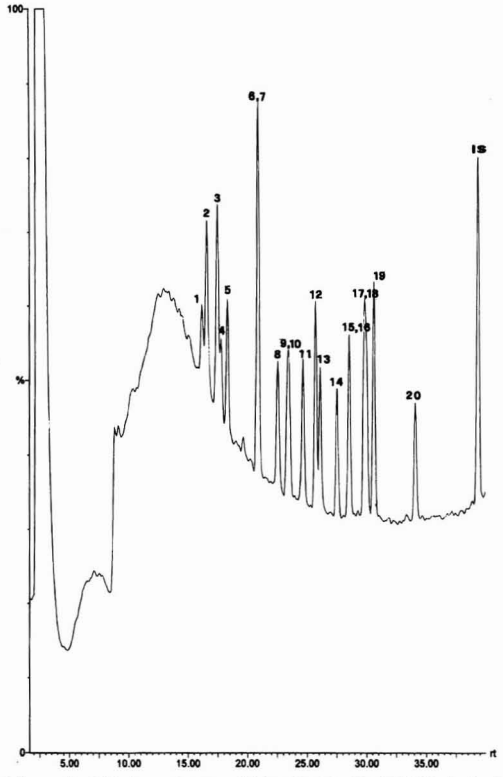

Figure 5. TIC chromatogram obtained by injecting 50/200 of a final extract relative to 1 L of a river water sample (from the Tiber River) spiked with the acidic pesticides at the level of 0.5 μg/L each: (1) dicamba; (2) bentazone, (3), 2,4-DNPh, (4) benazolin, (5) coumafuryl, (6) bromoxynil, (7) DNOC, (8) warfarin, (9) MCPA, (10) 2,4-D, (11) ioxynil, (12) mecoprop, (13) dichlorprop, (14) 2,4,5-T, (15) MCPB, (16) 2,4-DB, (17) dinoseb, (18) 2,4,5-TP, (19) dinoterb, and (20) PCP; IS, C-8 LAS.

the voltage applied to the skimmer cone. Analogous behavior was exhibited by the three ionized forms of three phenoxyacids (MCPA, mecoprop, and MCPB), differing from those mentioned above in that one chlorine is replaced by a methyl group. In this case, the CID process produced a daughter ion at m/z 141, corresponding to the 2-methyl-4-chlorophenoxy ion. To obtain a good response of the MS detector for all of the analytes considered, we chose to set the skimmer cone voltage at 20 V. To obtain diagnostic ions even from the most stable analytes considered, the only way could be to appropriately modify the cone voltage during the chromatographic run.

The robustness of this method was tested over two uninterrupted working days. This investigation was conducted by injecting at 1-h intervals 25 μL of a solution containing 2,4-D, ioxynil, and dichlorprop at the level of 4 ng/L each into the LC column and measuring the peak areas produced by both the MS and UV detectors for the three model compounds. The column was operated isocratically with 50% of the organic modifier. Between injections, the colum effluent was continuously delivered to the ES source. Signals were plotted vs time, and the resulting graph is shown in Figure 4. Over the initial 10 h of the first

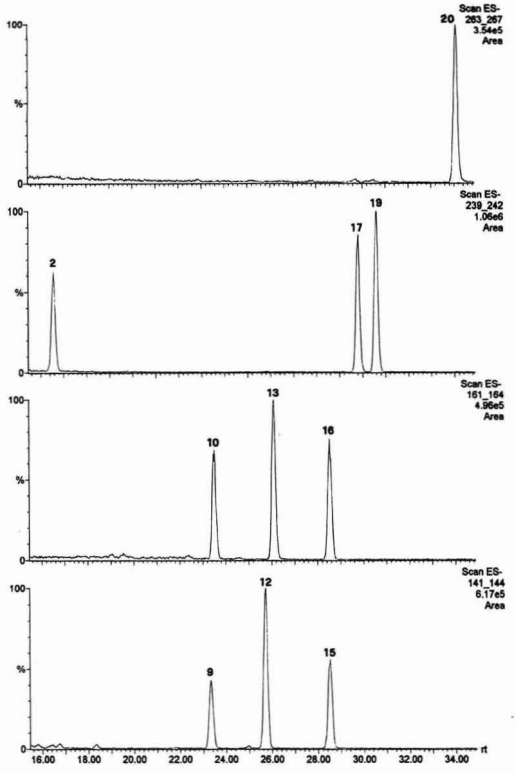

Figure 6. Selected ion current chromatograms for selected *m/z* values extracted from the chromatogram in Figure 5.

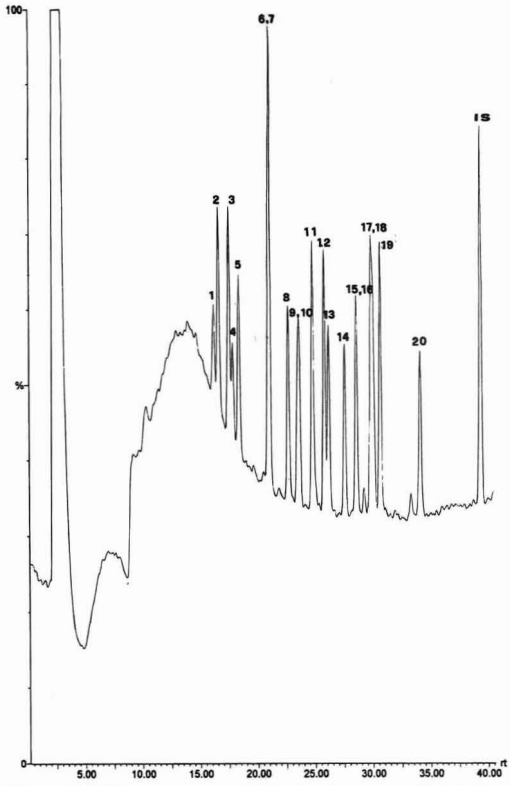

Figure 7. TIC chromatogram obtained by injecting 50/200 of a final extract relative to 4 L of a drinking water sample spiked with the acidic pesticides at the level of 100 ng/L each. Peak numbering is the same as in Figure 5.

Table 4. Time-Scheduled SIM Conditions for Monitoring 20 Acidic Pesticides in Drinking Water Samples[a]

compound	selected *m/z*	start–end times (min)
dicamba	176	14.0–19.0
bentazone	239	
2,4-DNPh	183	
benazolin	170, 198	
coumafouryl	297	
bromoxynil	275	19.0–26.6
DNOC	197	
warfarin	307	
MCPA	142, 200	
2,4-D	162, 220	
ioxynil	370	
mecoprop	142, 213	
dichlorprop	162, 234	
2,4,5-T	255	26.6–31.5
MCPB	142	
2,4-DB	162	
2,4,5-TP	196	
dinoseb	239	
dinoterb	239	
PCP	265	31.5–36.0

[a] Dwell time, 0.1 s; span, 1.

working day, ion signals for 2,4-D and dichlorprop did not show significant variations. Conversely, a steady signal loss for ioxynil was observed after the instrumentation was operated uninterrupted for 8 h. After 10 working hours, a 50% signal loss for ioxynil was observed. This difference in behaviors between the two phenoxyacids and ioxynil was unclear to us. A check of the sample cone revealed the presence of a very thin salt layer. With the system beyond the cone still under vacuum, cleaning the sample cone was easily addressed with use of a methanol-imbibed paper, taking care to pass it repeatedly over the cone orifice to dissolve salt particles that could partially obstruct the opening. As a result of this cleaning procedure, the ion signal for ioxynil was restored. A similar behavior was observed on the second day, with the difference that, after 9 working hours, a significant signal decrease occurred even for 2,4-D and dichlorprop. In addition, this signal loss was accompanied by a largely unstable background current. Again, the initial condition in terms of S/N was restored after the extraction cone cleaning procedure mentioned above. As expected, the UV signals for the three model compounds did not show any significant variation over the two working days. For a routine application of the method under evaluation, the results obtained by the test described above indicate that the best solution could be to exploit the UV signals for analyte quantitation while entrusting unambiguous analyte identification to the ES/MS detector.

The present analytical procedure was applied to the determination of acidic pesticides in drinking water and river water samples.

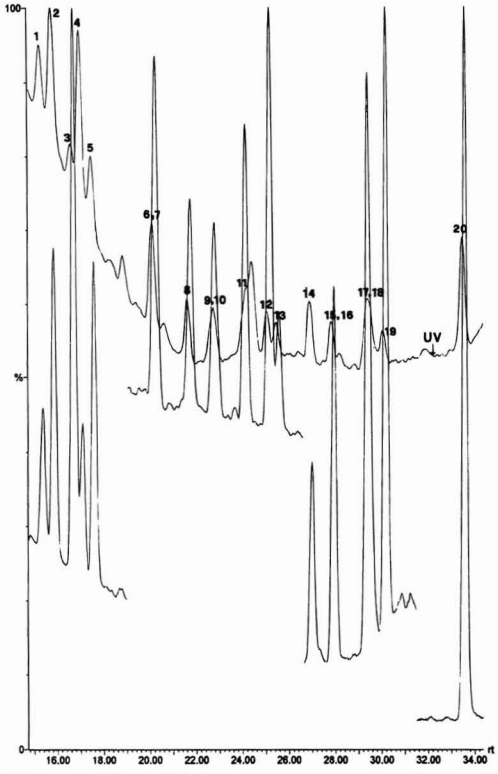

Figure 8. UV and SIM chromatograms obtained by injecting 50/200 of a final extract relative to 4 L of a drinking water sample spiked with the acidic pesticides at the level of 10 ng/L each. Peak numbering is the same as in Figure 5.

The spike recoveries of the overall isolation and chromatographic procedure are reported in Table 3. Pesticides were added at the indicated concentrations to six individual samples of each of the two matrices considered and analyzed. When recovery experiments were performed in hypochlorite-containing tap water samples, 0.5 g of $Na_2S_2O_3 \cdot 5H_2O$/L of water was added before addition of the analytes, to prevent their oxidation and other unwelcome effects previously discussed.[4]

Figure 5 shows a TIC mass chromatogram obtained by spiking 1 L of a pesticide-free river water sample fortified with the 20 analytes considered at the level of 0.5 μg/L and analyzing this sample by the procedure described above. As can be seen, distinct peaks were obtained for all of the analytes included in this study. By extracting chromatograms for selected *m/z* values corresponding to some selected analytes, Figure 6 shows that the specific determination of acidic pesticides in surface water samples can be achieved at concentrations far below 0.5 μg/L.

A 4-L drinking water sample was spiked with the pesticides under evaluation at the level of 100 ng/L each and analyzed by the procedure described above. The TIC mass chromatogram shown in Figure 7 demonstrates that this method can satisfy the stringent requirements imposed by the EC Directive mentioned above. In terms of sensitivity and specificity, the potentiality of the ES/MS instrumentation used was fully exploited by extracting a 4-L drinking water sample fortified with the analytes at the level of 10 ng/L each and analyzing the final extract by a time-scheduled, selected ion monitoring (SIM) scheme, the results of which are reported in Table 4. The SIM mass chromatogram obtained by following this procedure (Figure 8) shows that unambiguous identification of acidic pesticides in water can be performed even at concentrations below 1 ng/L. The corresponding UV trace reported in the same figure shows that distinct peaks can be obtained for few a nanograms of any injected pesticide under study.

For the acidic pesticides under evaluation, considering the analysis of 4 L of drinking water, reconstituting the residue with 200 μL, and injecting 50 μL of this, the quantification limits estimated from the UV signals (5 times the limits of detection) ranged between 8 and 30 ng/L. For pesticides in surface water samples, the figures reported above should be increased of a factor 4, as only 1 L of surface water can be extracted by this procedure without loss of the most polar pesticides.

ACKNOWLEDGMENT

We wish to thank the Consiglio Nazionale delle Ricerche for financially supporting this work.

Received for review November 30, 1994. Accepted March 1, 1995.[⊗]

AC9411637

[⊗] Abstract published in *Advance ACS Abstracts,* May 1, 1995.

Anal. Chem. **1995,** *67,* 1976–1980

Determination of 4-Nonylphenol in Effluent and Sludge from Sewage Treatment Plants

Hing-Biu Lee* and Thomas E. Peart

Priority Substances Project, Aquatic Ecosystem Protection Branch, National Water Research Institute, Environment Canada, P.O. Box 5050, Burlington, Ontario L7R 4A6, Canada

Quantitative and efficient methods for the determination of 4-nonylphenol (4-NP) in sewage treatment plant (STP) effluent and sludge samples were developed. For effluent, the 4-NP was converted, in situ, into its acetyl derivative with acetic anhydride in the presence of a base. In the case of sewage sludge, 4-NP was subjected to supercritical carbon dioxide extraction and on-line acetylation during the extraction stage. After a silica gel column cleanup, sample extract was analyzed by capillary column gas chromatography/mass spectrometry in the selected ion monitoring mode. Recoveries of 4-NP in spiked samples (1 and 10 μg/L for effluent and 5 and 50 μg/g for sludge) were 93% or above with relative standard deviations better than 5%. Detection limits for 4-NP were 0.1 μg/L for effluent and 0.1 μg/g for sludge. These methods were applied to the determination of 4-NP in samples collected from Toronto and vicinity STPs. Concentrations of 4-NP from <1 to 30 μg/L in the effluent and >100 μg/g in sludge were found.

Nonylphenol ethoxylates (NPEs) are a major class of nonionic surfactant used across Canada. NPEs are derived from the addition of ethylene oxide to nonylphenol and may have 1–20 ethoxy units per molecule.[1] Nonylphenol, manufactured by the alkylation of phenol with nonene, consists mainly of a mixture of 4-substituted monoalkylphenols with various isomeric, branched nonyl groups. The demand for NPEs in Canada was 4.1 kton in 1990. While the use of NPEs in household detergents has diminished in recent years, the textile and pulp and paper industries are presently the major users of these surfactants. Under anaerobic conditions,[2–4] NPEs ultimately biodegrade into 4-nonylphenol (4-NP), which is persistent, lipophilic, and more toxic than the ethoxylates to fish and other aquatic organisms. Its 96-h LC_{50} values for salmon and trout ranged from 0.13 to 0.23 mg/L.[5]

The occurrence of NPEs and their metabolites including 4-NP has been monitored in sewage treatment plant (STP) samples in some European countries since the early 1980s. Concentrations of 4-NP varied from <1 to 100 μg/L in effluent[2–4,6] and from 100 to 1000 μg/g in sludge.[3,7] With a log K_{ow} (octanol–water partition coefficient) of 4.48,[8] 4-NP is expected to be adsorbed on sediments. To date, very little information regarding the levels of 4-NP in Canadian STP effluent and sludge is available. The main environmental cause of NPEs and their metabolite 4-NP is from the use of detergents derived from this surfactant. Inputs from the other industrial applications of 4-NP, such as pesticide adjuvants and polymerization emulsifiers, are relatively minor.

The presence of 4-NP in the environment has recently become of increasing concern since it has been shown to be a strongly estrogenic compound that can cause feminization of male fish downstream of STPs,[9] resulting in a lack of reproductive success. While the evidence is still fragmentary, these environmental estrogens, including compounds such as DDE, DDT, Kepone, some polychlorinated biphenyls, and alkylphenols, particularly nonyl- and octylphenols, are also linked to fertility problems in men and cancer in humans.[9] In one study, 4-NP at 10 μM was shown to exhibit estrogenic effects similar to 30 pM of 17β-estradiol in inducing the proliferation of MCF_7 human breast cancer cells.[10]

In the past, several extraction methods, including continuous solvent extraction, exhaustive steam distillation, and gaseous stripping with nitrogen into ethyl acetate using the Wickbold procedure, have been used for the enrichment of 4-NP in wastewaters and sewage effluent.[2,3,11] The steam distillation method was also used for the extraction of 4-NP in sewage sludge and soil samples after the solids were suspended in water.[3] While other chromatographic methods were developed,[2,11] quantitative analysis of 4-NP was usually carried out by normal phase HPLC analysis using an UV detector at 277 nm since this technique was more amenable to the simultaneous analysis of the polyethoxylates.[3] In this work, we validate an in situ derivatization technique for the simultaneous extraction and acetylation of 4-NP in effluent, sludge, and sediment samples. Sample extracts were quantified by GC/MS operating in selected ion monitoring mode for sensitive detection and positive identification. The application of this technique to the determination of 4-NP and 4-*tert*-octylphenol (4-tOP) in effluent and sludge samples collected from nearby municipal STPs, as well as in some aquatic sediments, is also described.

EXPERIMENTAL SECTION

Chemicals. 4-NP, 4-tOP 4-(1,1,3,3-tetramethylbutyl)phenol, 4-*n*-octylphenol, acetic anhydride, and triethylamine were obtained from Aldrich (Milwaukee, WI). Stock solutions of the phenols at

(1) Ahel, M.; Giger, W. *Anal. Chem.* **1985**, *57*, 2584–2590.
(2) Stephanou, E.; Giger, W. *Environ. Sci. Technol.* **1982**, *16*, 800–805.
(3) Ahel, M.; Giger, W. *Anal. Chem.* **1985**, *57*, 1577–1583.
(4) Ahel, M.; Giger, W.; Koch, M. *Water Res.* **1994**, *28*, 1131–1142.
(5) McLeese, D. W.; Zitko, V.; Sergeant, D. B.; Burridge, L.; Metcalfe, C. D. *Chemosphere* **1981**, *10*, 723–730.
(6) Ahel, M.; Conrad, T.; Giger, W. *Environ. Sci. Technol.* **1987**, *21*, 697–703.
(7) Giger, W.; Brunner, P. H.; Schaffner, C. *Science* **1984**, *225*, 623–625.
(8) Ahel, M.; Giger, W. *Chemosphere* **1993**, *26*, 1471–1478.
(9) Hileman, B. *Chem. Eng. News* **1994**, Jan 31, 19–23.
(10) Soto, A. M.; Justicia, H.; Wray, J. W.; Sonnenschein, C. *Environ. Health Perspect.* **1991**, *92*, 167–173.
(11) Giger, W.; Stephanou, E.; Schaffner, C. *Chemosphere* **1981**, *10*, 1253–1263.

0003-2700/95/0367-1976$9.00/0 © 1995 American Chemical Society

1000 μg/mL were prepared in acetone and stored in crimped top vials at 4 °C. Non-acid-washed Celite 545, anhydrous sodium sulfate, potassium carbonate, and silica gel (GC grade 950, 60–200 mesh) were purchased from Fisher Scientific Co. (Toronto, Canada). Acetic anhydride was triply distilled in our laboratory and kept at −20 °C. Sodium sulfate was heated to 500 °C overnight, cooled, and stored in glass bottles before use. Silica gel was activated at 200 °C overnight and then deactivated by adding 5 mL of water to 95 g of the adsorbent. Solvents (hexane, petroleum ether 30–60 °C, acetone, and isooctane) were distilled-in-glass grade available from Baxter (Burdick and Jackson, Muskegon, WI). Supercritical fluid extraction (SFE) grade carbon dioxide without a helium head pressure was obtained from Air Products (Nepean, Canada).

Effluent and Sludge Samples. Samples from STPs in metropolitan Toronto (four sites: Leslie, Humber, Highland Creek, and North Toronto) and Mississauga (Lakeview) were tested in this work. Up to three effluent samples (1–4 L grab) were collected at each site: primary effluent, final effluent before chlorination, and final effluent after chlorination. Heat-treated sludges were collected from the Leslie and Highland Creek plants. No preservative was used for these samples. After collection, each effluent was filtered through 0.45 μm Whatman GF/C filters, kept at 4 °C, and extracted the following day. Sludge and sediments were air-dried at 22 °C, ground, and passed through a 30 mesh sieve to remove extraneous matters such as hair, wood chips, and gravel. The homogenized powder was used for SFE work.

In Situ Acetylation of 4-NP in Effluent. To 250 mL of a filtered effluent was added 1 g of potassium carbonate to bring the pH to 10 or above. To this was added 1 mL of the triple distilled acetic anhydride was added, followed by 30 mL of petroleum ether, and the sample was stirred on a magnetic stirrer for 30 min. The layers were then separated in a separatory funnel, and the aqueous layer was returned to its original container. The acetylation was repeated twice with an additional 100 μL of acetic anhydride and 30 mL of petroleum ether for 15 min each time. The combined organic extract was partitioned with 30 mL of 1% potassium carbonate solution to remove the coextracted acetic acid. After the base was discarded, the organic layer was dehydrated by passing through a 2.5 cm layer of anhydrous sodium sulfate in a filter funnel and concentrated to ~5 mL with a rotary evaporator and a 40 °C bath. The concentrated extract was quantitatively transferred to a 15 mL test tube and further evaporated, by a gentle stream of nitrogen, to 1 mL in the presence of 1 mL of isooctane as a keeper.

In Situ Acetylation and SFE of 4-NP from STP Sludge. All SFE was carried out with a Hewlett-Packard 7680T supercritical fluid extractor. The extraction thimble was prepared as follows. First, a layer of Whatman GF/C filter paper cut to the diameter of the thimble was placed at the bottom of the thimble, making sure that it did not interfere with the sealing surface of the cap. Next, 200 mg of Celite followed by 250 mg of a dry sludge or 1 g of a dry sediment was added. A 30 μL portion of triethylamine was then spiked onto the sample, followed by another layer of Celite (200 mg) and 100 μL of acetic anhydride. Another layer of GF/C filter paper was placed on top. The void volume of the extraction thimble was filled by a glass rod of 1 cm diameter and a suitable length (3–5 cm, depending on the sample size).

The samples were extracted with supercritical carbon dioxide at 80 °C and a density of 0.79 g/mL (5096 psi) at a flow rate of 2 mL/min. The extraction times were 15 min static and 10 min dynamic. The variable restrictor nozzle was kept at 50 °C to prevent freezing. The acetyl derivative of 4-NP formed during the static extraction was removed from the sample matrix in the dynamic extraction stage. After depressurization of the supercritical fluid, the extract was adsorbed on an octadecyl functionalized silica gel (ODS) trap which was maintained at 5 °C during extraction. At the end of the extraction, the trap was heated to 40 °C before the derivatives were eluted from the trap by 1.5 and 1.0 mL aliquots of hexane into two vials. The extracts were combined in a 15 mL tube and partitioned with 3 mL of 1% potassium carbonate solution to remove the coextracted acetic acid. The organic layer was then dried with anhydrous sodium sulfate and concentrated to 1 mL with nitrogen in a 40 °C bath.

Silica Gel Column Cleanup. To clean up all derivatized effluent and sludge extracts, a column made of a 7 mm i.d. disposable Pasteur pipet with a piece of glass wool plug at the bottom was prepared. The column was filled 5 cm of 5% deactivated silica gel and then with 5 mm of anhydrous sodium sulfate. After pre-elution with 3 mL of petroleum ether, the concentrated sample extract was quantitatively applied to the column. It was then sequentially eluted by the following: (1) 5 mL of 5% dichloromethane in petroleum ether, (2) 10 mL of 50% dichloromethane in petroleum ether, and (3) 10 mL of 1% methanol in dichloromethane. Fraction 1 was discarded. Fractions 2 and 3 were collected separately, and each fraction was solvent exchanged into 1 mL of isooctane.

Gas Chromatography/Mass Spectrometry (GC/MS) Analysis. GC/MS analysis of sample extracts was performed with a Hewlett-Packard (HP) 5972 mass selective detector (MSD) interfaced to a HP5890 Series II gas chromatograph (GC). For most samples, only fraction 2 from the silica gel column cleanup that contained the acetyl derivative of 4-NP was analyzed. Sample injection was made, in the splitless mode, by the HP7673A autosampler onto a 30 m × 0.25 mm i.d. × 0.25 μm HP-5-MS column. Injection port and detector interface temperatures were 250 and 280 °C, respectively. The GC oven temperature program was 70 °C initial (kept for 1 min), increased to 160 °C at 30 °C/min, then increased to 240 °C at 5 °C/min. Carrier gas (helium) linear velocity was held constant at 39.8 cm/s by means of an electronic pressure controller. The electron energy and electron multiplier voltage were 70 eV and 2000 V, respectively. Confirmation of samples was carried out in full scan mode, and data were acquired from *m/z* 40 to 300. Quantitative analysis of the 4-nonylphenyl acetate was performed by monitoring the ions at *m/z* 107, 121, 135, 163, 191, and 262 in selected ion monitoring (SIM) mode. For 4-*tert*-octylphenyl acetate, the ions at *m/z* 135, 177, and 248 were monitored.

Calibration Standards and Quantification. Calibration standards were prepared by acetylation of a mixture of 4-NP (100 μg) and 4-tOP (10 μg) in 30 mL of 1% K_2CO_3 in the presence of acetic anhydride as described above for effluent samples. Further dilutions of the product were made in isooctane to prepare standard solutions at 10, 1, and 0.1 μg/mL for 4-nonylphenyl acetate and 1, 0.1, and 0.01 μg/mL for 4-*tert*-octylphenyl acetate. Confirmation of peak identity was achieved by the observation of molecular ions at *m/z* 248 (for 4-tOP) and 262 (for 4-NP). Quantification of the phenols in sample extracts was carried out by the external standard method using response factors generated by the authentic standards prepared above. Each sample extract

was injected twice, and the average result was used. For extracts with 4-NP and 4-tOP concentrations higher than the calibration standards, the samples were further diluted and reanalyzed. Response factors were recalibrated once every three samples. For 4-NP, summation of areas was performed for those peaks that had the same retention times as the calibration standard as well as the presence of the confirmation ion *m/z* 262 in the SIM traces.

RESULTS AND DISCUSSION

In Situ Acetylation of 4-NP. A wide range of phenolic compounds of environmental importance react readily and quantitatively with acetic anhydride to form the acetyl derivatives. These include priority pollutants such as chlorophenols,[12–14] methylphenols,[12] and nitrophenols[15] as well as the chlorinated guaiacols, catechols, and syringols found in effluent from chlorine-bleaching pulp and paper mills.[16] Even though gas chromatographic methods have been established for underivatized 4-NP, the less polar acetyl derivative is our choice for this work since it offers better chromatographic separation of the 4-NP isomers as well as a lower (~4-fold) detection limit by GC/MS in SIM mode. The extraction of 4-nonylphenyl acetate in effluent could be effected by a nonpolar solvent such as petroleum ether, and the emulsion formed during the extraction steps was never severe enough to affect phase separation. Further, the derivative is more readily separated from the more polar coextractives by the silica gel cleanup column, and it is therefore advantageous in the analysis of highly contaminated effluent and sludge samples. While the derivatization route has an extra step in the procedure, it does not require any extra time since the extraction and acetylation of 4-NP can be carried out simultaneously.

Electron Impact Mass Spectra of Acetyl Derivatives of 4-NP. Figure 1A is a total ion current (TIC) profile of the acetyl derivatives 4-tOP and 4-NP chromatographed on a 5% phenyl methyl polysiloxane phase capillary column. Peak 1, with a retention time of 8.70 min, was derived from 4-tOP, while those peaks from 9.8 to 10.9 min (peaks 2–11) were attributed to the different isomers of 4-nonylphenyl acetate. Under the GC conditions described earlier, 10 peaks were resolved for the derivatized 4-NP, and they all had retention times longer than the free phenol. The mass spectra of these peaks exhibited the same molecular ion of *m/z* 262 with a relative intensity of 5% or less, confirming the formation of acetyl derivatives. Other than the molecular ion, the mass spectra of the derivatives are very similar to those of the free phenol, with intense fragment ions at *m/z* 107, 121, 135, 149, and 191.[2,11]

A closer inspection of these mass spectra indicated that, with the exception of peaks 7 and 8, the nonylphenol isomers could be classified into three groups. The mass spectrum of the group 1 isomer (peak 2 in Figure 1A) is shown in Figure 1B. With a base peak at *m/z* 121 ($[M - COCH_2 - C_7H_{15}]^+$), it is consistent with a resonance stabilized, substituted benzyl ion having the α-methyl structure on the alkyl chain. The group 2 isomers (peaks 3, 5, and 9) exhibited mass spectra with a base peak at

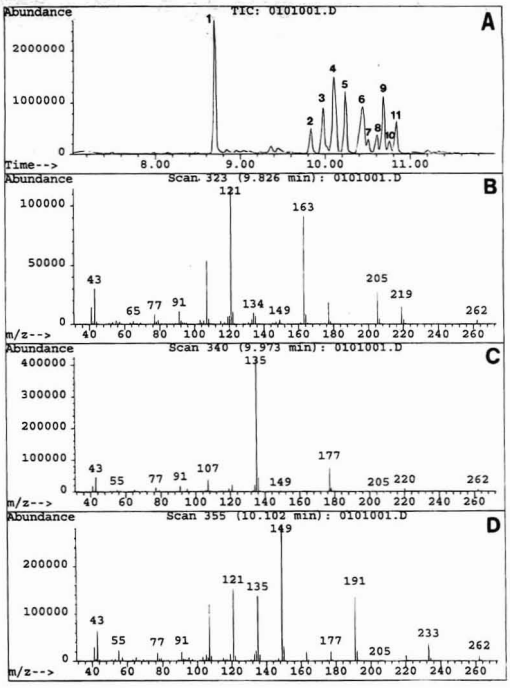

Figure 1. (A) Total ion current chromatogram of the acetyl derivatives of 4-*tert*-octylphenol (retention time, 8.70 min) and 4-NP (retention times, 9.8–10.9 min). (B) Mass spectrum of peak 2 in the TIC chromatogram. (C) Mass spectrum of peak 3 in the TIC chromatogram. Those for peaks 5 and 9 are similar. (D) Mass spectrum of peak 4 in the TIC chromatogram. Those for peaks 6, 10 and 11 are similar.

m/z 135 ($[M - COCH_2 - C_6H_{13}]^+$), suggesting that they have an α,α-dimethyl structure (Figure 1C). The third group of isomers (peaks 4, 6, 10, and 11) had a base peak at *m/z* 149 ($[M - COCH_2 - C_5H_{11}]^+$) and are consistent with structures having α-methyl-α-ethyl side chains (Figure 1D). The mass spectrum of peak 7 had major fragments at *m/z* 219, 177 (base peak, $[M - COCH_2 - C_3H_7]^+$), 135, 121, and 107 in addition to the weak M^+. Since the first three ions were 42 mass units apart and the last three were 14 mass units apart, a C_9 side chain with two propyl groups and an ethyl group attached to the benzylic carbon was assigned to this isomer. On the basis of the presence of major fragments at *m/z* 205 ($[M - COCH_2 - CH_3]^+$), 163 (base peak, $[M - COCH_2 - C_4H_9]^+$), 121, and 107 in the mass spectrum of peak 8, an alkyl structure with a methyl, a propyl, and a butyl substitution at the α carbon was tentatively assigned to this nonylphenol isomer. The mass spectrum of 4-*tert*-octylphenyl acetate closely resembled that in Figure 1C, with the exception of the molecular ion occurring at *m/z* 248. With a base peak at *m/z* 135, it was again consistent with an α,α-dimethyl structure. Meanwhile, the mass spectrum of 4-*n*-octylphenyl acetate exhibited a base peak at *m/z* 107, indicating no branched alkyl substitution at the α carbon.

The GC/MS selected ion monitoring technique offers selective detection and confirmative results for 4-NP in highly contaminated STP samples, goals that could not be achieved by the previously reported GC-FID and HPLC methods. Furthermore, the high resolution of the capillary column also permitted the simultaneous

(12) Coutts, R. T.; Hargesheimer, E. E.; Pasutto, F. M. *J. Chromatogr.* **1979**, *179*, 291–299.
(13) Abrahamsson, K.; Xie, T. M. *J. Chromatogr.* **1983**, *279*, 199–208.
(14) Lee, H. B.; Weng, L. D.; Chau, A. S. Y. *J. Assoc. Off. Anal. Chem.* **1984**, *67*, 789–794.
(15) Coutts, R. T.; Hargesheimer, E. E.; Pasutto, F. M. *J. Chromatogr.* **1980**, *195*, 105–112.
(16) Lee, H. B.; Hong-You, R. L.; Fowlie, P. J. A. *J. Assoc. Off. Anal. Chem.* **1989**, *72*, 979–984.

Table 1. Recovery of 4-Nonylphenol from Spiked Water and Sediment Samples[a]

matrix	spiking level	mean recovery, %	RSD, %
lake water	10 μg/L	93	3.2
lake water	1 μg/L	97	4.1
lake sediment	50 μg/g	96	4.5
lake sediment	5 μg/g	98	5.3

[a] Four replicates at each spiking level.

determination of octylphenol; the latter coeluted with nonylphenol under normal phase HPLC conditions.

Supercritical Carbon Dioxide Extraction and in Situ Acetylation of 4-NP from Sludge and Sediments. A few years ago, we developed a highly efficient and selective extraction method for the determination of pentachlorophenol and other chlorophenols in contaminated soil and sediment samples.[17] In that procedure, chlorophenols were first extracted by supercritical carbon dioxide and then acetylated by acetic anhydride in the presence of triethylamine under SFE conditions. This single-step procedure was later applied to the online SFE and acetylation of phenolics such as chlorinated guaiacols, catechols, and syringols in sediments collected downstream of chlorine-bleaching pulp and paper mills.[18] Unpublished work from our laboratory also indicated that the same procedure could be extended to the determination of priority pollutants such as methylphenols and nitrophenols in soils and sediments.

4-NP in sludge and sediments was readily extracted and acetylated by supercritical carbon dioxide of 0.79 g/mL density at a temperature of 80 °C. Using an air-dried and homogenized sludge collected from a Toronto STP as a reference sample for method development, quantitative recovery of 4-NP was achieved by a 15 min static extraction followed by a 10 min dynamic extraction at a flow rate of 2 mL/min. These SFE conditions were used for the subsequent determination of 4-NP in sludge and sediments since higher extraction temperature (100 °C) and higher carbon dioxide density (0.87 g/mL), as well as a doubling in extraction times (static and dynamic) or the amount of derivatization reagents, all failed to yield more 4-NP. A second extraction of the same sample recovered less than 0.5% more 4-NP. The entire extraction/acetylation cycle required ~45 min. For comparison, 1 g of the same sludge used for SFE work was dispersed in 300 mL of water and then steam distilled for 3 h into 3 mL of cyclohexane.[19] The organic layer was subsequently acetylated and the products were cleaned up as described before. However, in three trials, the recovery of 4-NP obtained by steam distillation was less than 8% of the SFE results.

Recovery of 4-NP from Spiked Samples. Subsamples of a Burlington Bay water spiked with 4-NP were extracted by the in situ acetylation procedure described above. Replicate analyses at 1 and 10 μg/L levels produced recoveries of ≥93% with relative standard deviation better than 5% (Table 1). These results are similar to those obtained for the di- and trimethylphenols in our laboratory. In the case of sludge, a lake sediment free from 4-NP contamination was used for spiking purpose. Replicate analyses at spiking levels of 5 and 50 μg/g also produced results with acceptable precision and accuracy (Table 1). The detection limits of 4-NP were estimated as 0.1 μg/L for effluent (based on a concentration factor of 1000) and 0.1 μg/g for sludge and sediment (based on a concentration factor of 1). With the same concentration factors, the detection limits for 4-tOP were 0.005 μg/L (effluent) and 0.005 μg/g (sludge and sediment). These detection limits easily attained the purposes of monitoring 4-NP in STP samples.

Table 2. Levels of 4-Nonylphenol and 4-*tert*-Octylphenol in Municipal Sewage Treatment Plant Effluent

sewage treatment plant	effluent type[a]	[4-NP], μg/L	[4-tOP], μg/L
Mississauga (Lakeview)	primary	12.7	0.9
Toronto (Leslie)	primary	30.0	2.5
	final A	15.1	1.6
	final B	15.0	1.7
Toronto (Highland Creek)	primary	4.0	1.1
	final A	1.9	0.77
	final B	1.4	0.69
North Toronto	primary	2.8	0.48
	final A	3.0	0.23
	final B	1.2	0.17
Toronto (Humber River)	primary	4.4	0.41
	final A	1.0	0.12
	final B	0.8	0.19

[a] A, prechlorination; B, postchlorination.

Occurrence and Levels of 4-NP in STP Samples and Some Aquatic Sediments. Effluent samples from four STPs in metropolitan Toronto and another STP in the nearby city of Mississauga were collected and analyzed for 4-NP. The results (Table 2) indicated that the phenol was found in all samples and its level varied from 2.8 to 30 μg/L in the primary effluent and from 0.8 to 15 μg/L in the postchlorination final effluent. There was a 2- to 5-fold decrease in 4-NP between the primary and final effluent tested. Chlorination of the final effluent did not seem to have a significant impact on the level of 4-NP since its level was virtually the same before and after this process. In addition to 4-NP, 4-tOP was also present in all effluent samples, with concentrations varying from 0.12 to 2.5 μg/L. The environmental occurrence of 4-tOP ethoxylate, possibly a minor component in NPE formulations, in the Delaware River has been reported.[20] In contrast, 4-*n*-octylphenol was not detected in the effluent samples tested. It was noted that, in a spiked water sample, the recoveries for 4-*n*-octylphenol, 4-NP, and 4-tOP were similar. Under the same GC conditions, the retention time for 4-*n*-octylphenyl acetate, 11.10 min, was longer than those for 4-nonylphenyl acetate.

The two sludge samples collected inside the Toronto STPs are contaminated with very high levels of 4-NP, 470 and 137 μg/g on a dry weight basis (Table 3). A Hamilton Bay sediment that was collected near the Burlington STP effluent outlet was found to have 41 μg/g 4-NP. Another sediment in the nearby Windermere Basin, which receives STP effluent from the city of Hamilton, had 6.73 μg/g 4-NP. Three river sediments, collected at various sites downstream of pulp and paper mills in Thunder Bay in 1991, were also shown to be contaminated by 4-NP, although the levels were low (0.29–1.28 μg/g) in comparison with the STP related samples.

(17) Lee, H. B.; Peart, T. E.; Hong-You, R. L. *J. Chromatogr.* **1992**, *605*, 109–113.
(18) Lee, H. B.; Peart, T. E.; Hong-You, R. L. *J. Chromatogr.* **1993**, *636*, 263–270.
(19) Veith, G. P.; Kiwus, L. M. *Bull. Environ. Contam. Toxicol.* **1977**, *17*, 631–636.
(20) Sheldon, L. S.; Hites, R. A. *Sci. Total Environ.* **1979**, *11*, 279–286.

Table 3. Concentrations of 4-Nonylphenol and 4-*tert*-Octylphenol in Sewage Treatment Plant Sludge and Aquatic Sediments

location	sample type	[4-NP], μg/g	[4-tOP], μg/g
Toronto (Leslie)	STP sludge	470 ± 22 (n = 6)	9.2 ± 0.4 (n = 6)
Toronto (Highland Creek)	STP sludge	137 ± 7.7 (n = 3)	12.1 ± 0.5 (n = 3)
Hamilton Bay near the Burlington STP outlet	sludge/sediment mix	41.1	0.91
Hamilton Bay (Windermere Basin)	sediment	6.73 ± 0.19 (n = 3)	0.40 ± 0.02 (n = 3)
Hamilton Bay (the "deep hole")	sediment	1.29	0.07
Humber River	sediment	0.78	<0.005
Kaministiquia River (site A)	sediment	0.29	<0.005
Kaministiquia River (site B)	sediment	0.41	0.006
Kaministiquia River (site C)	sediment	1.28	0.028

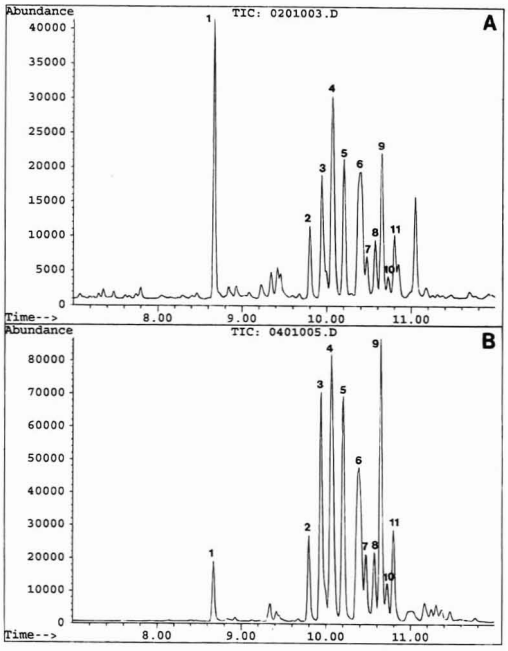

Figure 2. (A) Total ion current chromatogram of the acetyl derivatives of (A) a STP primary effluent contaminated by 4-NP and (B) a STP sludge.

Again, 4-tOP was found in many of these sludges and sediments, with concentrations varying from <0.005 to 12.1 μg/g. As a further test of the precision of the present SFE procedure applied to naturally contaminated samples, replicate analyses were performed on some sludge and sediment samples. The relative standard deviations of the 4-NP and 4-tOP results in those cases varied from 2.8% to 5.6%, indicating that this new technique is capable of generating reproducible results for these phenols. The TIC chromatograms of the acetylated extract for the primary effluent and the sludge obtained from the Leslie plant are depicted in Figure 2 parts A and B, respectively. It should be noted that, in these chromatograms, all 10 peaks for 4-NP not only were observed but also closely resembled, in relative abundance, those for the authentic standard. The same observation also applied to the extracts of other effluent, sludge, and sediment samples with lower concentrations of 4-NP, indicating the integrity of the phenol in these samples.

We have also analyzed, by GC/MS, the third fraction from the silica gel column cleanup of the two sludge samples as well as the two effluent samples that had the highest levels of 4-NP. A group of peaks with retention times from 12 to 15 min was observed in each of those extracts. They were tentatively assigned as the nonylphenol monoethoxylates due to the presence of major fragmentation ions at m/z 165, 179, 193, 207, and 264 reported earlier for these compounds.[2,11] Because of the lack of an authentic standard, their concentrations were not determined.

In conclusion, the in situ acetylation procedure was an effective alternative for the preconcentration of 4-NP in STP effluents. For sludge and sediment samples, the SFE approach was faster and produced much higher yields than steam distillation. GC/MS analysis in SIM mode produced superior chromatography for the acetyl derivatives and was more sensitive and selective than the existing HPLC method developed for the underivatized phenol. The presence of 4-NP in all STP-derived samples confirmed the widespread occurrence of this compound in municipal sewage. Although there was a decrease in the 4-NP concentration in the final effluent by a factor of 2–5 in comparison to the primary effluent, this compound was still easily detectable (at low μg/L levels) in the treated effluent. As reported earlier by Giger et al.,[7] extremely high concentrations of 4-NP in anaerobically digested sewage sludge were observed. Therefore, discharges of the sewage effluent into rivers and lakes and the disposal of sludge onto soil are likely to cause contamination of 4-NP in the aquatic environment. Further work on the survey of 4-NP in effluent and sludge samples from other STPs across Canada is underway.

ACKNOWLEDGMENT

We thank Mr. Jack Chan, Metropolitan Toronto Public Works, for the collection of the sewage treatment plant samples and Dr. R. James Maguire, NWRI, for reviewing the manuscript.

Received for review November 28, 1994. Accepted March 30, 1995.[⊗]

AC941149U

[⊗] Abstract published in *Advance ACS Abstracts,* May 15, 1995.

Anal. Chem. **1995**, *67*, 1981–1986

Aerosol Matrix-Assisted Laser Desorption Ionization: Effects of Analyte Concentration and Matrix-to-Analyte Ratio

Michelle D. Beeson, Kermit K. Murray,† and David H. Russell*

Department of Chemistry, Texas A&M University, College Station, Texas 77843-3255

We have recently developed an aerosol–liquid introduction interface for matrix-assisted laser desorption ionization (MALDI) mass spectrometry. In this study, we examine the effect of matrix-to-analyte ratio and analyte concentration on analyte ion yield. These studies were performed using bradykinin, gramicidin S, bovine insulin, and myoglobin as analytes and α-cyano-4-hydroxycinnamic acid and 4-nitroaniline as matrices. The optimum matrix-to-analyte molar ratio for aerosol MALDI was determined to be 10–100:1, which is lower than that typically used for conventional surface MALDI (100–10 000:1). The ion yield was found to be a nonlinear function of analyte concentration. Possible explanations for these observations are discussed.

The ability to introduce solutions directly into a mass spectrometer affords many opportunities for the study of solution phase species. Applications of mass spectrometric liquid introduction include coupling high-performance liquid chromatography to mass spectrometry (LC/MS),[1] investigating biomolecule associations in solution,[2–4] and probing protein behavior in solution.[5] The primary difficulty in developing liquid interfaces for mass spectrometry is the incompatibility of solvent with the vacuum requirements of the mass spectrometer. This is particularly true in the case of LC/MS, where typical column effluent flows are in the range of 1–2 mL/min. Various techniques have been developed to decrease the amount of chromatographic solvent introduced into the mass spectrometer by either splitting off some of the eluent before it enters the spectrometer[6] or removing the eluent before ionization.[7] A continuous liquid beam method has also been reported.[8]

Two common methods of liquid sample introduction use aerosols formed either in a corona discharge (electrospray)[9,10] or by pneumatic or ultrasonic nebulization followed by chemical or electron impact ionization.[11,12] Of these two methods, electrospray ionization (ESI) is the best suited for ionization of large biomolecules. The multiply-charged ions formed in the electrospray process reduce the mass-to-charge ratio to less than 2000, and this enables routine mass measurement accuracy of 0.01% using quadrupole mass analyzers.[13] Mass resolution of 10^6 has been obtained for proteins with molecular masses up to 30 kDa using Fourier transform ion cyclotron resonance (FTICR) instruments.[14] Although great progress has been made with ESI, it can be difficult to interpret ESI mass spectra of mixtures,[13] and the presence of salts and buffers reduces the sensitivity and complicates quantification.[15]

We recently developed a method for liquid sample introduction that is compatible with matrix-assisted laser desorption ionization (MALDI).[16,17] MALDI is potentially useful for mass spectrometric analysis of liquid samples because the predominant ions produced correspond to the protonated molecule[18,19] and the abundance of fragment ions can be varied by judicious matrix selection.[20–22] Most MALDI experiments are performed by applying a solution containing the matrix and analyte to a metal surface. The solvent is evaporated before the sample is inserted into the mass spectrometer, where the matrix and analyte are then ablated and ionized using a pulsed laser. The typical matrix used for MALDI is a low molecular weight organic compound which absorbs at the wavelength of the pulsed UV laser. For optimum analyte ion signal, the matrix is present in large molar excess over the analyte, usually by 2–4 orders of magnitude.[18,23] One limitation for

† Present address: Department of Chemistry, Emory University, Atlanta, GA 30322.

(1) Arpino, P. J.; Guiochon, G. *Anal. Chem.* **1979**, *51*, 682A–701A.
(2) Ganem, B.; Li, Y. T.; Henion, J. D. *J. Am. Chem. Soc.* **1991**, *113*, 6294–6296.
(3) Ganem, B.; Henion, J. D. *Chemtracts* **1993**, *6*, 1–22 and references therein.
(4) Smith, R. D.; Light-Wahl, K. J. *Biol. Mass Spectrom.* **1993**, *22*, 493–501 and references therein.
(5) Miranker, A.; Robinson, C. V.; Radford, S. E.; Aplin, R. T.; Dobson, C. M. *Science* **1993**, *262*, 896–900.
(6) Emary, W. B.; Lys, I.; Cotter, R. J.; Simpson, R.; Hoffman, A. *Anal. Chem.* **1990**, *62*, 1319–1324.
(7) McFadden, W. H.; Schwarz, H. L.; Evans, S. *J. Chromatogr.* **1976**, *122*, 389–396.
(8) Mafuné, F.; Takeda, Y.; Nagata, T.; Kondow, T. *Chem. Phys. Lett.* **1992**, *199*, 615–620.
(9) Fenn, J. B.; Mann, M.; Meng, C. K.; Wong, S. F.; Whitehouse, C. M. *Mass Spectrom. Rev.* **1990**, *9*, 37–70.
(10) Bruins, A. P.; Covey, T. R.; Henion, J. D. *Anal. Chem.* **1987**, *59*, 2642–2646.
(11) Browner, R. F. *Microchem. J.* **1989**, *40*, 4–29.
(12) Willoughby, R. C.; Browner, R. F. *Anal. Chem.* **1984**, *56*, 2626–2631.
(13) Bieman, K. *Annu. Rev. Biochem.* **1992**, *61*, 977–1010.
(14) Senko, M. W.; McLafferty, F. W. *Annu. Rev. Biophys. Biomol. Struct.* **1994**, *23*, 763–785.
(15) Moseley, M. A.; Jorgenson, J. W.; Shabanowitz, J.; Hunt, D. F.; Tomer, K. B. *J. Am. Soc. Mass. Spectrom.* **1992**, *3*, 289–300.
(16) Murray, K. K.; Russell, D. H. *Anal. Chem.* **1993**, *65*, 2534–2537.
(17) Murray, K. K.; Russell, D. H. *J. Am. Soc. Mass Spectrom.* **1994**, *5*, 1–9.
(18) Hillenkamp, F.; Karas, M.; Beavis, R. C.; Chait, B. T. *Anal. Chem.* **1991**, *63*, 1193A–1202A.
(19) Karas, M.; Hillenkamp, F. *Anal. Chem.* **1988**, *60*, 2299–2301.
(20) Solouki, T.; Oriedo, J. V. B.; Russell, D. H. Proceedings of the 40th ASMS Conference on Mass Spectrometry and Allied Topics, Washington, DC, May, 1992; pp 89–90.
(21) Preston Schaffter, L. M. Ph.D. Thesis, Texas A&M University, College Station, TX, 1994.
(22) Spengler, B.; Kirsch, D.; Kaufmann, R. *J. Phys. Chem.* **1992**, *96*, 9678–9684.
(23) Strupat, K.; Karas, M.; Hillenkamp, F. *Int. J. Mass Spectrom. Ion Processes* **1991**, *111*, 89–102.

0003-2700/95/0367-1981$9.00/0 © 1995 American Chemical Society

developing MALDI LC/MS is the incompatibility of the mass spectrometer with high flow rate liquid sample introduction. To overcome this limitation, Li and co-workers developed an interface for MALDI LC/MS similar to flow FAB.[24] In our laboratory we developed a pneumatic nebulizer to form aerosol particles that are sprayed into the vacuum. The aerosol particles are ablated by irradiation from the 355 nm output of a Nd:YAG laser, and ionization of the molecules that constitute the aerosol is enhanced by the presence of matrix and solvent.[17] For LC/aerosol MALDI-MS, the matrix is mixed postcolumn with the LC effluent using a mixing tee.[25] The utility of aerosol MALDI for LC/MS and for investigating the association behavior of proteins in solution[25] has been demonstrated.

Our current work on aerosol MALDI is focused on developing a better understanding of the experimental parameters that effect the ionization process. The objective of this work is to determine the parameters that most strongly affect ion yield and limit our ability to make quantitative measurements under a range of chromatographic conditions, including solvents systems and the type and presence of buffers. The experimental parameters of laser intensity, sample preparation, matrix, and molar ratio of the matrix and analyte influence the ion yield in the aerosol MALDI experiment.[26] The work described in this paper focuses on two of these parameters: (1) analyte concentration and (2) matrix-to-analyte ratio. In addition, we address the differences observed in optimum matrix-to-analyte ratio between aerosol MALDI and surface MALDI.

EXPERIMENTAL SECTION

The aerosol MALDI apparatus has been described in detail.[17] A solution of analyte and matrix is delivered by a syringe pump to a pneumatic nebulizer where nitrogen gas sprays the aerosol into a vacuum chamber. The chamber is evacuated by a 300 L/s roots blower and rotary piston backing pump. The aerosol beam is skimmed as it enters a 25 cm long, 4 mm i.d. drying tube heated to 500 °C. The dried aerosol particles enter the ion formation region and are irradiated by the pulsed 355 nm output of a frequency tripled Nd:YAG. The laser beam is focused using a cylindrical lens to 7 mm × 0.2 mm, with the long axis parallel to the aerosol beam. For the experiments described here, the laser energy was 13 mJ/pulse (160 MW/cm^2). Ions formed by the laser are extracted by a repeller plate held at 10 kV with the extraction grid at ground. Mass separation is achieved in a differentially pumped 1.1 m flight tube, and ions are detected with a micro-channel plate particle multiplier. The ion formation chamber is evacuated by a 2400 L/s, liquid nitrogen-trapped 6 in. diffusion pump, and the flight tube is evacuated by a 1200 L/s, 4 in. diffusion pump. Mass spectra are acquired and averaged with a digital oscilloscope and transferred to a microcomputer for analysis.

All mass spectra presented here were an average of 1000 laser shots, containing 40 000 data points at 5 ns/data point. The spectra were averaged and smoothed using procedures described previously.[17,25] The integrated peak area was determined by summing the ion signal in the region of the protonated molecule and subtracting an estimated baseline signal. Because the peaks resulting from adducts with the analyte molecule, for example $[M + Na]^+$, were not completely resolved in the bovine insulin and myoglobin spectra, adduct signals are included in the peak area integration for these analytes. For consistency, adduct signals are also included in integrations of spectra in which the peaks are resolved. The integrated peak areas are taken to be indicative of the analyte ion $[M + H]^+$ yield.

Mass calibration was performed as described previously.[17] Briefly, this method uses solvent clusters of the type $(ROH)_n{\cdot}H^+$ and $(ROH)_n{\cdot}Na^+$, where ROH denotes the alcohol solvent used and $n = 1-6$, to calibrate the mass spectra to approximately m/z 200. The calibration is then extended to high m/z ratios using reference compounds such as bradykinin or gramicidin S. For example, extrapolation of the low mass calibration data to include peptide standards typically results in mass measurement accuracy of ± 2 m/z units up to approximately m/z 1500. Using reference compounds, extrapolation of the mass calibration to m/z values of 5000–10 000 typically yields mass measurement accuracy of ± 20 m/z units. The mass measurement accuracy can be as good as ± 2 m/z units if internal standards are used.

The analyte and matrix solutions were prepared in a methanol solvent containing 6% (v/v) trifluoroacetic acid. For the studies that examined the effects of matrix-to-analyte molar ratios, the matrix concentrations were 6 mg/mL, and the analyte concentrations were varied. The limited solubility of bovine insulin and myoglobin prevented studies of these analytes at matrix-to-analyte molar ratios lower than 100:1. The bradykinin acetate salt, bovine insulin, horse heart myoglobin (95–100%, Sigma Chemical Co., St. Louis, MO), and gramicidin S hydrochloride from *Bacillus brevis* (Fluka Chemika-BioChemika, Ronkonkoma, NY) were used without further purification. The solvents used were trifluoroacetic acid (Sigma) and anhydrous 99.8% spectrophotometric grade methanol (Mallinckrodt, Paris, KY). The compounds α-cyano-4-hydroxycinnamic acid (97%) and 4-nitroaniline (99+%, both from Aldrich Chemical Co., Milwaukee, WI) were used as matrices without further purification.

RESULTS

The studies described in this paper focus on two parameters that influence aerosol MALDI ion signal: analyte concentration and matrix-to-analyte molar ratio. The analytes were chosen to provide a range of molecular masses and analyte characteristics. Bradykinin (1060.2 Da) is a linear nonapeptide which contains basic residues on both the N- and C-terminus; gramicidin S (1141.5 Da) is a cyclic decapeptide; bovine insulin (5733.6 Da) is a globular protein containing intramolecular disulfide bonds; and myoglobin (16 890 Da), also a globular protein, contains a heme group with an iron center. α-Cyano-4-hydroxycinnamic acid and 4-nitroaniline were chosen as matrices because in previous studies they provided the largest signals of several matrices studied.[17]

Figure 1 contains the aerosol MALDI mass spectra of the four analytes. The mass spectrum of bradykinin shows characteristics typical of an aerosol MALDI mass spectrum. The protonated molecule, denoted $[M + H]^+$, is observed at approximately m/z 1050. The sodium adduct ion, $[M + Na]^+$, is also present, and it is only partially resolved from the $[M + H]^+$ ion. In spectra where the $[M + H]^+$ and $[M + Na]^+$ ion signals are resolved, the largest signal is due to the protonated molecule.[25] We assume that the sodium contribution is constant for all matrix and analyte combinations. The validity of this assumption is supported by

(24) Li, L.; Wang, A. P. L.; Coulson, L. D. *Anal. Chem.* **1993**, *65*, 493–495.
(25) Murray, K. K.; Lewis, T. M.; Beeson, M. D.; Russell, D. H. *Anal. Chem.* **1994**, *66*, 1601–1609.
(26) Murray, K. K.; Russell, D. H. In *Laser Ablation: Mechanisms and Applications II*; Miller, J. C., Geohegan, D. B., Eds.; American Institute of Physics: New York, 1994; pp 459–464.

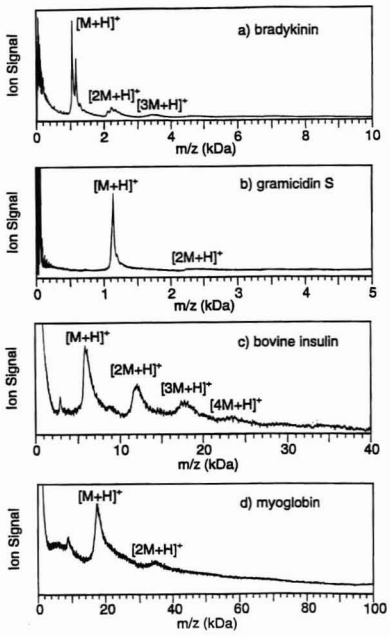

Figure 1. Aerosol MALDI mass spectra of the analytes used. (a) A 1.5 mM solution of bradykinin with 4-nitroaniline at a ratio of 30:1. (b) A 4.4 mM solution of gramicidin S with α-cyano-4-hydroxycinnamic acid at a 5:1 matrix-to-analyte ratio. (c) A 0.3 mM solution of bovine insulin with 4-nitroaniline at a ratio of 100:1. (d) A 0.1 mM solution of myoglobin with α-cyano-4-hydroxycinnamic acid at a ratio of 90:1.

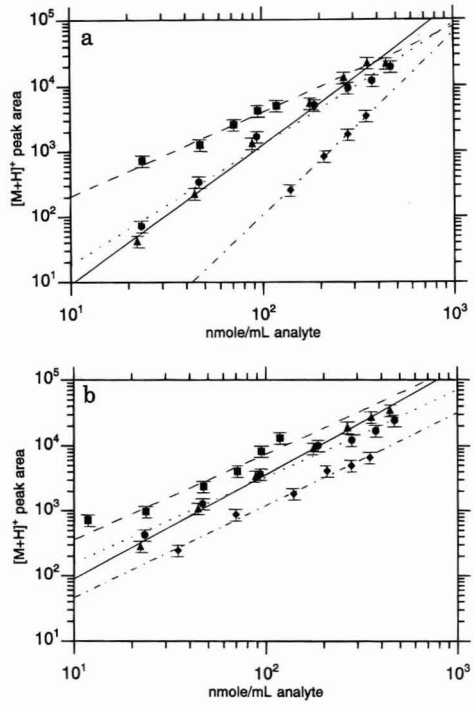

Figure 2. Log/log plots of the $[M + H]^+$ peak area as a function of analyte concentration at a matrix-to-analyte ratio of 100:1 for (a) 4-nitroaniline and (b) α-cyano-4-hydroxycinnamic acid matrices. ◆ corresponds to bovine insulin, ■ to myoglobin, ▲ to gramicidin S, and ● to bradykinin. The error bars represent 20% variation.

atomic absorption data which indicate that sodium impurities come primarily from the methanol solvent. Adducts of matrix fragments with bradykinin are also resolved. Protonated clusters of bradykinin are also observed, denoted $[2M + H]^+$ and $[3M + H]^+$ for clusters of two and three bradykinin molecules, respectively. The intense peaks below *m/z* 300 are always observed in the aerosol MALDI mass spectra and result from solvent clusters of the form $(ROH)_n{\cdot}H^+$ and $(ROH)_n{\cdot}Na^+$,[17] where ROH denotes the alcohol solvent used.

Figure 1b–d contains mass spectra of gramicidin S, bovine insulin, and myoglobin, respectively. These spectra are similar to that noted in Figure 1a. The sodium adduct, $[M + Na]^+$, is partially resolved for gramicidin S but is unresolved for bovine insulin and myoglobin. The presence of $[M + Na]^+$ in the mass spectrum is indicated by a shift of the analyte peak centroid to *m/z* values higher than the molecular weight of the singly protonated analyte. The analyte peak in the mass spectra is labeled $[M + H]^+$ because this is the largest peak.[25] Doubly protonated analytes are also observed for bovine insulin and myoglobin. Although the myoglobin and bovine insulin signals appear smaller than the gramicidin S and bradykinin signals, the integrated peak areas are similar. For example, the peak height of the myoglobin $[M + H]^+$ is less than 4% of the bradykinin $[M + H]^+$ peak height, whereas the myoglobin peak area is about 50% that of bradykinin. Also note that if the peaks in the bovine insulin spectrum labeled $[M + H]^+$, $[2M + H]^+$, and $[3M + H]^+$ are integrated together, the signal intensity increases by a factor of 2.

Table 1. Values of *n* from a Least-Squares Fit to $S = Ac^n$, Where *S* is the $[M + H]^+$ Signal from Figure 2, *c* is the Analyte Concentration, and *A* is a Proportionality Constant

	matrix	
analyte	4-nitroaniline	α-cyano-4-hydroxycinnamic acid
bradykinin	1.84	1.32
gramicidin S	2.14	1.61
bovine insulin	2.78	1.42
myoglobin	1.29	1.32

Figure 2 contains log–log plots of the integrated peak area for each analyte as a function of analyte concentration. The error bars represent the instability of the aerosol generator over time, variations in the laser pulse energy, and the error in estimating the baseline in the area determinations. The error was estimated by repetitive area determinations to be 20%. The lines through the data points are the results of a least-squares fit to the function $S = Ac^n$, where *S* is the integrated peak area, *A* is a scaling factor, *c* is the analyte concentration, and *n* is the power to which the concentration is raised. The parameters *A* and *n* were varied in the fit. The *n* values from the fit are shown in Table 1 and are discussed below. Figure 2a contains a plot of the integrated $[M + H]^+$ signal as a function of the analyte concentration using the matrix 4-nitroaniline. The signals for gramicidin S and bradykinin are similar in relative abundance throughout the concentration

range studied. The lines fit to the data points for bovine insulin have a slope similar to those for gramicidin S and bradykinin, although the bovine insulin signal is lower. At low concentrations, the $[M + H]^+$ signals for myoglobin indicate greater relative abundance than the $[M + H]^+$ signals for the other analytes. Figure 2b contains a plot of the $[M + H]^+$ peak area as a function of the analyte concentration using the matrix α-cyano-4-hydroxycinnamic acid. In this plot, the slopes of the lines are similar, and the $[M + H]^+$ signals show less variance than those in Figure 2a. In both plots, the relative ion yield is myoglobin > gramicidin S ≈ bradykinin > bovine insulin. Comparison of the plots in Figure 2, parts a and b, reveals that the signals are larger with the α-cyano-4-hydroxycinnamic acid matrix than with the 4-nitroaniline matrix. The fact that α-cyano-4-hydroxycinnamic acid produces greater ion signal than 4-nitroaniline with aerosol MALDI has been observed previously with bovine insulin.[17]

Table 1 summarizes the results of the least-squares fit to $S = Ac^n$ for the data in Figure 2. A value of $n = 1$ indicates that the ion signal is linearly dependent on the analyte concentration. In general, the n values are smaller for α-cyano-4-hydroxycinnamic acid than for 4-nitroaniline, indicating that the ion signal is less strongly dependent on concentration with α-cyano-4-hydroxycinnamic acid than with 4-nitroaniline. However, the n values for myoglobin are nearly identical for both matrices. For all analytes and with both matrices, n is greater than unity, indicating a nonlinear dependence of $[M + H]^+$ signal on analyte concentration.

Figure 3 contains log–log plots of the integrated $[M + H]^+$ peak area as a function of the matrix-to-analyte molar ratio. The limited solubility of myoglobin and bovine insulin prohibits measurements of $[M + H]^+$ signal for these analytes at matrix-to-analyte ratios lower than 100:1. Figure 3a contains a plot of the integrated $[M + H]^+$ signal as a function of the matrix-to-analyte ratio for the matrix 4-nitroaniline. Note that the $[M + H]^+$ ion signal decreases at matrix-to-analyte ratios larger than 100:1. This is particularly noticeable for bradykinin, which has an optimum matrix-to-analyte ratio in the range 30–100:1. Figure 3b contains a plot of the integrated $[M + H]^+$ signal as a function of the matrix-to-analyte ratio for the matrix α-cyano-4-hydroxycinnamic acid. The maximum bradykinin $[M + H]^+$ signal occurs at matrix-to-analyte ratios between 10 and 30:1. The bovine insulin $[M + H]^+$ signal is optimum at a matrix-to-analyte ratio of approximately 100:1, and the myoglobin $[M + H]^+$ signal is optimum for matrix-to-analyte ratios of 100:1 or less. It appears that for the matrices and analytes used, the optimum matrix-to-analyte ratio lies in the range of 10–100:1.

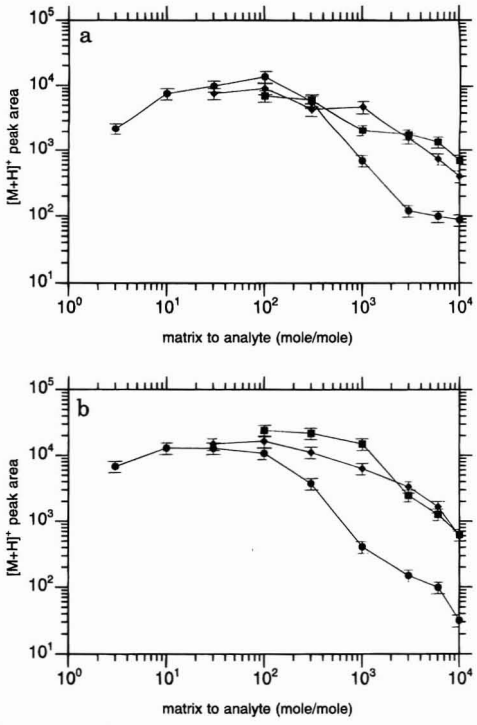

Figure 3. Log/log plots of the $[M + H]^+$ peak area as a function of matrix-to-analyte ratio for (a) 4-nitroaniline and (b) α-cyano-4-hydroxycinnamic acid matrices. ◆ corresponds to bovine insulin, ■ to myoglobin, and ● to bradykinin. The error bars represent 20% variation.

DISCUSSION

The ionization of samples introduced into the mass spectrometer from a solution is a complicated process, especially if the sample is still in a condensed phase environment. For example, it is known that aerosol particles sampled in the aerosol MALDI experiment retain significant amounts of solvent because clusters of the solvent are observed in the mass spectra.[17] Because the aerosol particles are composed of analyte, matrix, residual solvent, and other species in the solution (salts, buffers, trifluoroacetic acid), the formation of gas phase ionic forms of the analyte requires separation of the charged species from the matrix and solvent. The ionization process occurs concurrently with separation from the matrix and solvent. Thus, it would be surprising if matrix and solvent effects did not influence the ionization process.

One of the more striking differences between surface MALDI and aerosol MALDI is the optimum matrix-to-analyte ratio. In surface MALDI, the optimum matrix-to-analyte ratio is typically 10^2–10^4.[19,23] In a previous study,[26] we found that the *best* ion signal for bovine insulin with 4-nitroaniline matrix was obtained at a matrix-to-analyte ratio of 50:1, whereas a typical matrix-to-analyte ratio for surface MALDI of bovine insulin is 500–1000:1. No other matrix and analyte combinations were studied, and no matrix-to-analyte ratios below 50:1 were investigated. We suggested that differences in optimum matrix-to-analyte ratio between surface MALDI and aerosol MALDI are related to the rate of crystal formation.[17,26] Fast crystallization forces the matrix and analyte into contact and favors a low matrix-to-analyte ratio. The lower matrix-to-analyte ratio for aerosol MALDI may also be due to the particle size. For example, we find that optimum matrix-to-analyte ratios for aerosol spray sample deposition of bovine insulin are 100–500:1, which is lower than the matrix-to-analyte ratio required for evaporation deposition.[26]

The idea of fast crystallization promoting MALDI ion yields is not limited to aerosol MALDI or aerosol sample deposition. Vorm and co-workers described a sample preparation method for surface MALDI which uses rapid evaporation of solvent to prepare matrix deposits onto which the analyte-containing solution is deposited.

This preparation method results in improved ion yield and mass resolution.[27] Nuwaysir and Wilkins also reported improved ion yield and better signal reproducibility for surface MALDI samples formed using a matrix–analyte "redeposition" method.[28] In this method, acetone is used to redissolve the matrix and analyte after deposition from a methanol or water solvent. Xiang and Beavis also reported improved ion yield from surface MALDI sample deposits formed by rapid evaporation of the solvent.[29]

Aerosol spray methods and solvent evaporation to deposit matrix–analyte films produce crystalline particles with a range of sizes. Deposits from slowly evaporating solvents form large matrix crystals and result in segregation of matrix and analyte.[23] Thus, the inclusion of analyte into the matrix crystal lattice is diminished. Under these conditions, analyte deposits may be formed at defect sites within the matrix crystal lattice. Matrix–analyte deposits formed from rapidly evaporating solvent systems result in the formation of smaller crystalline particles and more homogeneous matrix–analyte deposits. Thus, matrix–analyte deposits formed during the evaporation of volatile solvents should favor more uniform distribution of matrix and analyte. In the aerosol MALDI experiment, the solvent quickly evaporates from the droplet, possibly causing the remaining solvent to freeze due to evaporative cooling.[30,31] Matrix–analyte crystal formation occurs in a steep concentration gradient as the volume of the solvent is decreased. Although it may be difficult to develop a temperature-dependent quantitative model that describes the crystal growth within an evaporating liquid droplet,[32] the contrast between slowly evaporating solvents and rapidly evaporating systems appears rather obvious. Specifically, matrix–matrix, matrix–analyte, and analyte–analyte interactions in the solution phase more directly influence the distribution of the matrix and analyte in the solid phase, whereas solid phase matrix–matrix, matrix–analyte, and analyte–analyte interactions are more important for deposits formed via a slow crystallization process.[33,34]

The data contained in Figure 2 show that the aerosol MALDI ion signal is nonlinear in analyte concentration. We attribute the nonlinear responses to residual solvent present in the aerosol particle. At a constant matrix-to-analyte ratio, the analyte concentration is proportional to the ratio of solute to solvent. Thus, in Figure 2, the analyte concentration axis reflects the average solvent content of the aerosol particles, with the amount of solvent decreasing from left to right. Figure 2 shows that as the aerosol solvent content increases, the ion signal decreases nonlinearly. The best signal is obtained with the least solvent, in agreement with earlier observations that drier aerosol particles produce better ion signal.[17]

If our interpretation of the data contained in Figure 2 is correct, the effects of residual solvent on the ion yield are not the same for the matrices and analytes studied. One interpretation of the n values given in Table 1 is that the sensitivities of matrix and analyte to solvent in the aerosol particle are not constant. For example, 4-nitroaniline is more sensitive to solvent than is α-cyano-4-hydroxycinnamic acid, because 4-nitroaniline has the larger value of n. Bovine insulin seems particularly sensitive and myoglobin particularly insensitive to the presence of solvent. Previous studies of nonlinear signal response implicate mass transport effects.[35] However, we interpret the differences observed for matrix and analyte as evidence that some portion of the nonlinear response is related to the solvent content of the aerosol particles. If the nonlinear signal response were due only to mass transport, the effects should not vary with matrix and analyte, unless chemical properties affect particle size.

The data in Figure 2 suggest that the $[M + H]^+$ ion yields are analyte dependent; the relative sensitivities of the various analytes are myoglobin > gramicidin S ≈ bradykinin > bovine insulin. Factors that might cause such an effect include analyte surface area, hydrophobicities, and basic residues. The simplest view would be that the surface area of the analyte could be related to the probability for protonation. In the case of peptides and proteins, the surface area increases with increasing molecular weight.[36] The molecular weights of the analytes are as follow: bradykinin, 1060.2; gramicidin S, 1141.5; bovine insulin, 5733.6; and myoglobin, 16 890. With the exception of bovine insulin, ion signal increases with increasing molecular weight. It seems unlikely that the surface area of bovine insulin in methanol is less than that of gramicidin S and bradykinin. Although the relative surface area of bovine insulin may be diminished by the formation of oligomers, summing the integrated areas for bovine insulin $[M + H]^+$, $[2M + H]^+$, and $[3M + H]^+$ increases the total signal only by a factor of 2. This does not change the order of the relative sensitivities of the analytes.

Analyte hydrophobicities may also affect the matrix–analyte interaction and thus the ion yield and sensitivities.[37,38] Average hydrophobicities for bradykinin, gramicidin S, bovine insulin, and myoglobin were calculated from amino acid compositions using tabulated hydrophobicities of individual amino acids.[39] The estimated hydrophobicity of gramicidin S is 1980 cal/mol, bradykinin is 1556 cal/mol, myoglobin is 1023 cal/mol, and bovine insulin is 1020 cal/mol. Thus, the hydrophobicity ordering of gramicidin S > bradykinin > myoglobin ≈ bovine insulin does not correlate with the data from Figure 2. This suggests that analyte hydrophobicities alone do not determine the ion yield and sensitivities.

Another parameter that could affect the analyte ion yield and sensitivity is the number of basic residues. Basic amino acid residues may act as proton acceptor groups for MALDI proton transfer. (Basic residues are defined here as residues that are positively charged at pH 7.0.) Bradykinin is composed of 22% basic residues, myoglobin of 21%, bovine insulin of 8%, and gramicidin S has no basic residues. This ordering does not correlate with the observed order of analyte ion yield and suggests that the

(27) Vorm, O.; Roepstorff, P.; Mann, M. *Anal. Chem.* **1994**, *66*, 3281–3287.
(28) Nuwaysir, L. M.; Wilkins, C. L. In *Applied Spectroscopy in Materials Science*; Saperstein, D. D., Ed.; Proceedings of SPIE 1437; The International Society for Optical Engineering: Bellingham, WA, 1991; pp 112–123.
(29) Xiang, F.; Beavis, R. C. *Rapid Commun. Mass Spectrom.* **1994**, *8*, 199–204.
(30) Klots, C. E. *J. Chem. Phys.* **1985**, *83*, 5854–5860.
(31) Engelking, P. C. *J. Chem. Phys.* **1986**, *85*, 3103–3110.
(32) Boorn, A. W.; Cresser, M. S.; Browner, R. F. *Spectrochim. Acta* **1980**, *35B*, 823–832.
(33) Mattiasson, B.; Kaul, R. In *Molecular Interactions in Bioseparations*; Nago, T. T., Ed.; Plenum Publishing: New York, 1993; pp 469–478.
(34) Kopperschlager, G.; Birkenmeier, G. In *Molecular Interactions in Bioseparations*; Nago, T. T., Ed.; Plenum Publishing: New York, 1993; pp 499–509.
(35) Ho, J. S.; Behymer, T. D.; Budde, W. L.; Bellar, T. A. *J. Am. Soc. Mass Spectrom.* **1992**, *3*, 662–671.
(36) Janin, J.; Miller, S.; Chothia, C. *J. Mol. Biol.* **1988**, *204*, 155–164.
(37) Naylor, S.; Findeis, A. F.; Gibson, B. W.; Williams, D. H. *J. Am. Chem. Soc.* **1986**, *108*, 6359–6363.
(38) Caldwell, K. A.; Gross, M. L. *Anal. Chem.* **1989**, *61*, 494–496.
(39) Bigelow, C. C.; Channon, M. In *Handbook of Biochemistry and Molecular Biology. Proteins; Vol. I*, 3rd ed.; Fasman, G. D, Ed.; CRC: Cleveland, OH, 1976; pp 209–243.

number of basic residues is not a significant factor in determining ion yield and sensitivity.

The observation that the analyte ion yield depends on the nature of the analyte and the solvent content of the aerosol particle suggests that quantification may require the use of internal standards. This study was limited to methanol, but it seems logical that different solvents may have different effects on individual biomolecules. For example, it may be possible that matrix–analyte interactions are sensitive to solvent type. Solvents affect the rates of crystallization, which strongly influence inclusion of the analyte in the matrix crystal lattice. Both noncovalent and hydrogen bonding interactions between the matrix and analyte would be expected to change as the solvent characteristics change. Thus, solvent would be expected to affect the MALDI ion yield and quantification.

It is also important to consider how changing the matrix and analyte concentrations affect the aerosol particle size. Particle size is important for two reasons: (1) aerosol particle transport efficiency depends on particle size[40,41] and (2) aerosol MALDI ion yields may depend on particle size. Within the mass spectrometer, large and small aerosol particles are not transported with the same efficiencies. Consequently, large and small aerosol particles may not be sampled identically in the time-of-flight source region. Particle size may also influence the ion yield. Under conditions of complete desolvation, higher concentrations of matrix and analyte produce aerosol particles with larger diameters.[42,43] However, because desolvation is incomplete in the aerosol MALDI experiment, it is not clear whether the aerosol particle size and the resulting ion yield are strongly affected by the concentrations of the matrix and analyte. To determine if the matrix and analyte concentrations influence the size distribution of the aerosol particles requires direct particle size measurements.

In summary, three observations concerning aerosol MALDI ion yields can be made from the results presented here. (1) The optimum matrix-to-analyte ratio in aerosol MALDI is in the range 10–100:1 for the analytes and matrices studied. This optimum matrix-to-analyte ratio is smaller than the optimum matrix-to-analyte ratio observed in surface MALDI. We postulate that the lower optimum matrix-to-analyte ratio is a result of rapid desolvation occurring in aerosol MALDI, forcing the matrix and analyte into contact with each other. Rapid desolvation promotes more efficient matrix–analyte interactions. (2) Desolvation also influences the $[M + H]^+$ ion signal. We interpret the observation that the $[M + H]^+$ ion signal is a nonlinear function of the analyte concentration as an indication of the importance of aerosol desolvation. Drier aerosol particles produce larger aerosol MALDI ion signal. (3) The relative sensitivities for the different analytes are due to the chemical properties of the analyte. The order of the $[M + H]^+$ ion yields is myoglobin > gramicidin S ≈ bradykinin > bovine insulin. After examining the hydrophobicities, number of basic residues, and surface areas of each analyte, we tentatively suggest a correlation between analyte size and ion yield.

(40) Winkler, P. C.; Perkins, D. D.; Williams, W. K.; Browner, R. F. *Anal. Chem.* **1988**, *60*, 489–493.
(41) Browner, R. F.; Boorn, A. W.; Smith, D. D. *Anal. Chem.* **1982**, *54*, 1411–1419.
(42) Allen, L. B.; Koropchak, J. A. *Anal. Chem.* **1993**, *65*, 841–844.
(43) Charlesworth, J. M. *Anal. Chem.* **1978**, *50*, 1414–1420.

ACKNOWLEDGMENT

This research was funded by the Texas Advanced Technology Program and by the Division of Chemical Sciences, Office of Basic Energy Sciences, U.S. Department of Energy under Grant No. DE-FG05-85ER-13434. The Nd:YAG laser and additional equipment were purchased with funds provided by the National Science Foundation under Grant No. CHE-9223629.

Received for review September 19, 1994. Accepted April 6, 1995.[⊗]

AC9409344

[⊗] Abstract published in *Advance ACS Abstracts,* May 15, 1995.

Anal. Chem. **1995,** *67,* 1987–1991

Static SIMS Detection of Gold and Gold Cyanide Complexes on Carbon Using Crown Ether Enhancement

G. S. Groenewold,* J. C. Ingram, A. D. Appelhans, and J. E. Delmore

Idaho National Engineering Laboratory, P.O. Box 1625, Idaho Falls, Idaho 83415-2208

B. Pesic

College of Mines and Earth Resources, University of Idaho, Moscow, Idaho 83843

Determination of the nature of adsorbed gold cyanide species on activated carbon is difficult with presently available surface analysis techniques. Efforts toward the development of new, more specific analytical techniques are described in this paper. It is shown that static secondary ion mass spectrometry can be used for the detection of gold on carbon surfaces and for the identification of cyanide species present. The method described relies on two features: (1) the instrumentation employed utilizes pulsed secondary ion extraction, which mitigates the buildup of surface charge (a major problem in the bombardment of carbon) and permits the acquisition of the anion and cation spectra during the same analysis; (2) the surface of the carbon samples is doped with a crown ether, which results in the facile observation of $Au(CN)_2^-$, $[M + crown]^+$ (where M is Na^+ or K^+), and in some cases Au^-. It is hypothesized that the crown ether facilitates the formation of gold cyanide ions by forming complexes with Na^+ and K^+ present on the surface of the charcoal, thereby loosening or freeing the $Au(CN)_2^-$.

Sodium cyanide is the main lixiviant for the recovery of gold from gold-bearing ores. Once solubilized, gold can be recovered from solution either by precipitation with zinc powder or by adsorption on activated carbon. While zinc precipitation has been the dominant method, recent interest has focused on the use of activated carbon for the recovery of gold from cyanide leach solutions. At present, there is little agreement on the mechanisms by which aurocyanide is adsorbed onto activated carbon, because of an inability to characterize the relevant chemical species hosted by the surface of activated carbon. Mechanistic investigations have been based on the analysis of solutions in contact with carbon and have produced equilibrium and kinetic information.[1-6] Adsorption has also been investigated using appropriate model compounds.[2-4] However, direct information on the gold cyanide species present on the carbon surfaces is lacking.

In the present paper, we describe the direct detection of $Au(CN)_2^-$ on the surface of carbon used for the adsorption of gold cyanide complexes. The detection scheme was based upon static secondary ion mass spectrometry (SIMS), in which the carbon surface was doped with a crown ether solution and allowed to dry prior to SIMS analysis. The crown ether facilitates the observation of $Au(CN)_2^-$, most likely by complexing counterions present on the surface of the carbon, thereby facilitating ion formation from $Au(CN)_2^-$ complexes.

Previous investigations of crown ethers supported the expectation that they might be useful for altering the surface ion chemistry important in a SIMS experiment. Crown ethers have been long known for their ability to complex alkali metal cations in solution[7,8] and have also been the subject of several mass spectrometric investigations, in which the affinities of different crowns for different cations were evaluated.[9-13]

Static SIMS has been under investigation because the technique has very good sensitivity for molecular species present on sample surfaces.[14] The sensitivity is augmented by the use of a molecular primary beam, such as ReO_4^-, which is used in the instruments in our laboratory.[15] Another attractive attribute of static SIMS is that it requires minimal sample preparation and minimizes waste generation, which is particularly advantageous when analysis of hazardous samples is required. Finally, static SIMS is capable of accommodating sample types that develop surface charge by using pulsed secondary ion extraction[16] or electron flooding.[17] These techniques make SIMS amenable to virtually any sample type that is vacuum compatible.

(1) Dixon, S.; Cho, E. H.; Pitt, C. H. *AIChE Symp. Ser.* **1978**, *74* (173), 75–83.
(2) McDougall, G. J.; Adams, M. D.; Hancock, R. D. *Hydrometallurgy* **1987**, *18*, 125–138.
(3) Adams, M. D.; McDougall, G. J.; Hancock, R. D. *Hydrometallurgy* **1987**, *18*, 139–154.
(4) Adams, M. D.; McDougall, G. J.; Hancock, R. D. *Hydrometallurgy* **1987**, *19*, 95–115.
(5) Cook, R.; Crathorne, E. A.; Monhemius, A. J.; Perry, D. L. *Hydrometallurgy* **1989**, *22*, 171–182.
(6) Cook, R.; Crathorne, E. A.; Monhemius, A. J.; Perry, D. L. *Hydrometallurgy* **1990**, *25*, 394–396.
(7) Huheey, J. E. *Inorganic Chemistry Principles of Structure and Reactivity*, 3rd ed.; Harper & Row Publishers: New York, 1983; pp 527–533.
(8) Izatt, R. M.; Pawlak, K.; Bradshaw, J. S.; Bruening, R. L. *Chem. Rev.* **1991**, *91*, 1721–2085.
(9) Maleknia, S.; Brodbelt, J. *J. Am. Chem. Soc.* **1992**, *114*, 4295–4298.
(10) (a) Chu, I. H.; Zhang, H.; Dearden, D. V. *J. Am. Chem. Soc.* **1993**, *115*, 5736–5744. (b) Zhang, J.; Chu, I.-H.; Leming, S.; Dearden, D. V. *J. Am. Chem. Soc.* **1991**, *113*, 7415–7417.
(11) Johnstone, R. A. W.; Lewis, J. A. S. *Int. J. Mass Spectrom Ion Phys.* **1983**, *46*, 451.
(12) Johnstone, R. A. W.; Lewis, J. A. S. *Tetrahedron* **1983**, *39*, 1597.
(13) Man, V. F.; Lin, J. D.; Cook, K. D. *J. Am. Chem. Soc.* **1985**, *107*, 4635–4640.
(14) Benninghoven, A. *Surf. Sci.* **1973**, *35*, 427–457.
(15) Delmore, J. E.; Appelhans, A. D.; Peterson, E. S. *Int. J. Mass Spectrom Ion Processes* **1991**, *108*, 179.
(16) Appelhans, A. D.; Dahl, D. A.; Delmore, J. E. *Anal. Chem.* **1990**, *62*, 1679.

0003-2700/95/0367-1987$9.00/0 © 1995 American Chemical Society

The issue of analyzing gold in refractory or otherwise difficult matrices has been addressed using dynamic SIMS, which is capable of detecting gold at sub-ppm concentrations in a variety of refractory ore types.[18,19] Speciation of gold has been studied using XPS, but the interpretation of the data has been difficult because of severe charging occurring in the samples studied.[5,6,20] The analytical efforts to date have not been able to provide information on the identity of the gold species present on sample surfaces. One approach for facilitating the observation of metal species on surfaces is to dope the surface with a complexing agent. This strategy was employed for the imaging of galena (high lead content) samples doped with diisobutyl dithiophosphinate, but the images of the dopant and Pb^+ did not exactly correlate, and hence the chemical nature of Pb on the doped galena surface could not be surmised.[21] Nevertheless, it was felt that doping the sample surface with a crown ether might work in the present study, because of the presence of substantial quantities of group I cations on the surface.

EXPERIMENTAL SECTION

Preparation of Carbon Samples Exposed to Gold Cyanide Solutions. Activated carbon with adsorbed gold was prepared by agitation of 100 mg of 10X14 mesh PICA carbon (coconut shell carbon) in 100 mL of solution containing 1 mg of gold in the form of gold cyanide complex. The solution pH, adjusted with NaOH, was 11.5. Total time of adsorption was 24 h. After adsorption was completed, the carbon was separated by filtration, rinsed with deionized water, air-dried, and stored in a glass vial for future use. The concentration of gold in the solution was analyzed to determine the amount of adsorbed gold. It was found that 80% of the gold was adsorbed, producing a sample containing 8 mg of gold/g of activated carbon.

Preparation of Carbon Samples for SIMS Analysis. The carbon granules were crushed using a mortar and pestle prior to analysis. Normally, one carbon granule was crushed at a time; a typical sample mass was thus on the order of 1–3 mg. A wire sample holder fitted with double-sided tape was then used to "swab" the bottom of the mortar, thereby collecting the crushed carbon sample. Enough carbon was collected to completely cover the double-sided tape.

For the crown ether complexation experiments, 30–70 μL of crown ether/methanol solution (12-crown-4 or 18-crown-6 (Aldrich)) was added to the carbon during crushing. The typical molarity used for the crown ether solutions was in the range of 0.05–0.2 M, although in one study the molarity of the 18-crown-6 was varied from 0.005 to 0.5. The sample was applied either by applying a droplet of the slurry to a sample holder fitted with double-sided tape and allowing it to dry or by swabbing the bottom of the mortar. Either method produced observable $Au(CN)_2^-$ complexes.

Secondary Ion Mass Spectrometry. The instrument used for the SIMS analyses described in this paper has been described previously;[16] a brief description will be provided here. The instrument uses ReO_4^- as the primary bombarding particle, which is produced by heating a $Ba(ReO_4)_2$ ceramic in vacuum.[15] The ceramic was synthesized in our laboratories and processed in a form that could be used as an ion source. ReO_4^- ions that are emitted upon heating are accelerated to 10 keV. The ion gun was typically operated at 95 pA (the ion current from the gun could be continuously adjusted by adjusting the current passing through the heating element that supported the ceramic). The focusing of the primary ion gun was adjusted so that the sample was just silhouetted on an image intensifier located behind the sample. Thus, most of the primary ion beam is directed onto the target. Typical acquisition required 203 s, and a typical sample had an area of about 0.03 cm^2; thus a normal primary ion dose was 4.0×10^{12} ions/cm^2, which is below the commonly accepted static SIMS limit.[22]

The secondary anions and cations were extracted from the sample target region using pulsed secondary ion extraction.[16] This technique alternately extracts anions and cations from the sample surface by alternating the polarity of the secondary ion extraction lens. The alternating anion/cation extraction mitigates charge buildup on the surface of the sample and thus permits facile analysis of electrically insulating samples. The ratio of [time extracting cations]/[time extracting anions] is adjustable in this instrument, and in the case of the charcoal samples, a value of 6 worked well. The total period for the pulsed extraction sequence was 140 ms, divided as follows: cation extraction, 113 ms; electronic settle time, 4 ms; anion extraction, 19 ms; electronic settle time, 4 ms. This sequence was repeated for each 0.2 u step of the scan of the quadrupole secondary mass spectrometer, which was scanned from 10 to 310 u. The quadrupole was a m/z 2–2000 instrument, manufactured by Extrel (Pittsburgh) and modified in our laboratory. The quadrupole was tuned for unit mass resolution and optimum sensitivity for m/z 81^- and 198^+ in the SIMS spectrum of tetrahexylammonium bromide.[23]

The observation and abundance of the gold-bearing ions were subject to some variability. For most chips analyzed, CN^- and $Au(CN)_2^-$ could be readily observed, although for a fraction of the chips (20–30%), these ions were very low abundance or not observable. Furthermore, the abundance of the aurocyanide ions was variable for samples analyzed from the same carbon chip: for example, the abundance of m/z 249^- ($Au(CN)_2^-$) varied from 400 to 1500 counts/s in replicate analyses of the same crushed carbon sample. The source of the variability is not instrumental: the abundances of the non-gold-bearing ions were repeatable to within 20% of the mean absolute abundance. An example of this is the abundance of m/z 25^- (C_2H^-), which ranged from 4000 to 5000 counts/s in the same set of analyses. This variation is consistent with relative standard deviation values (10–30%) for other amorphous samples analyzed using this instrumentation.[24] Hence the variability is probably due to inhomogeneous distribution of gold in the carbon samples, since sample preparation was identical for all samples. A consequence of the variability is that the technique is qualitative at this time.

(17) Benninghoven, A.; Rudenauer, F. G.; Werner, H. W. *Secondary Ion Mass Spectrometry*; John Wiley and Sons: New York, 1987; pp 881–889.

(18) Chryssoulis, S. L.; Cabri, L. J.; Salter, R. S. *Proceedings of the International Symposium on Gold Metallurgy*; Pergamon Press: New York, 1987; pp 235–244.

(19) Stephens, J. D.; Bryan, S. R.; Rothbard, D. R. In *Gold '90*; Hausen, D. M., Ed.; Society for Mining, Metallurgy, and Exploration, Inc.: Littleton, CO, 1990; Chapter 31, pages 333–339.

(20) Klauber, C.; Vernon, C. F. *Hydrometallurgy* **1990**, *25*, 387–393.

(21) Brinen, J. S.; Reich, F. *Analysis* **1992**, *18*, 448–452.

(22) Briggs, D.; Hearn, M. J. *Vacuum* **1986**, *36*, 1005.

(23) Winger, B. E.; Hand, O. W.; Cooks, R. G. *Int. J. Mass Spectrom. Ion Processes* **1988**, *84*, 89.

(24) Groenewold, G. S.; Ingram, J. C.; Delmore J. E.; Appelhans, A. D. *J. Am. Soc. Mass Spectrom.* in press.

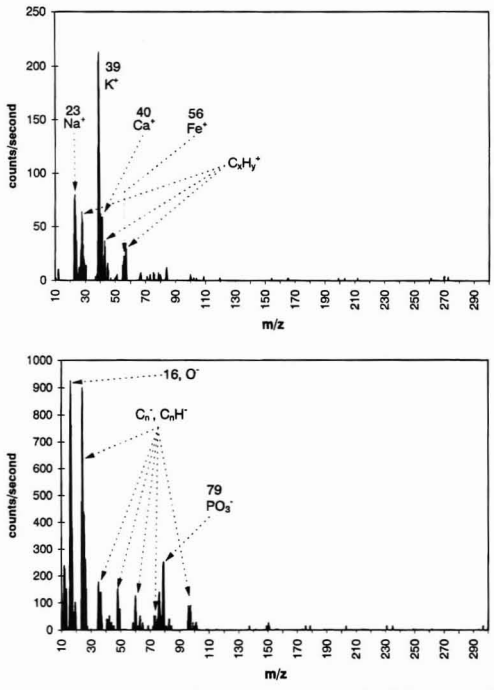

Figure 1. Cation (a, top) and anion (b, bottom) SIMS spectra of carbon.

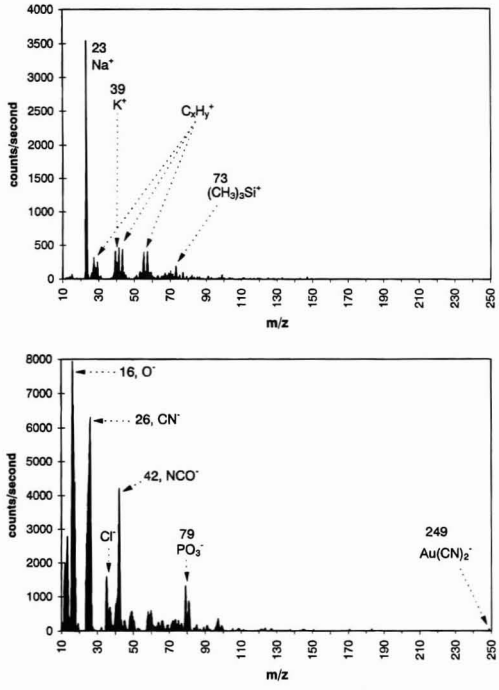

Figure 2. Cation (a, top) and anion (b, bottom) SIMS spectra of carbon exposed to 10 mg/L gold cyanide solution.

RESULTS AND DISCUSSION

SIMS Spectra of Unexposed Carbon. The analysis of benchmark carbon was difficult because of surface charging that occurs when carbon samples are crushed and bombarded. This difficulty was reflected in low ion abundances recorded in the SIMS spectra of this sample (Figure 1). Nevertheless the sample charging was manageable using pulsed extraction, such that anion and cation spectra could be recorded (see Experimental Section).

The SIMS spectra of unexposed carbon (Figure 1a) was relatively simple: cations corresponding to K^+, Na^+, Ca^+, and Fe^+ were clearly observed, as were a few low-abundance hydrocarbon ions. These latter ions are observed at odd masses and are common for static SIMS spectra.[14] The anion spectrum is also simple: O^- accounts for the most abundant peak, and C_n^- and C_nH^- ions are also prevalent for $n = 1-5$. The abundance of CN^- is low (m/z 26$^-$). The ion observed at m/z 79$^-$ has been attributed to PO_3^-, which may be indigenous to the carbon sample (phosphorus is present) or may be the result of the adsorption of trace quantities of atmospheric tributyl phosphate, which is occasionally present in our laboratory.[24]

SIMS Spectra of Carbon Exposed to Gold Cyanide. The carbon was exposed to the gold cyanide solution (10 mg/L), washed with distilled water, air-dried, and then analyzed using SIMS. The resulting SIMS spectrum was markedly different from that of the unexposed carbon. The absolute ion abundances (both anion and cation) are significantly greater than in the spectra of the unexposed carbon. This observation is partly due to the fact that the exposed carbon samples are not as susceptible to surface charging, which is characterized by the sample deflecting the incoming primary ion beam. At the present time, the physical or chemical properties responsible for exacerbating or mitigating surface charging during primary ion bombardment of carbon have not been identified for carbon samples.

Na^+ is the most abundant peak in the cation spectrum, which is consistent with the fact that the carbon was exposed to a solution containing a significant quantity of Na^+ (Figure 2a). The other abundant ions observed in this spectrum are readily explainable in terms of K^+, hydrocarbon, and siloxane contamination. In the anion spectrum, the abundances of CN^- and NCO^- were markedly enhanced compared to the spectrum of the unexposed sample, which reflects the fact that the carbon had been exposed to cyanide. A very low abundance ion could occasionally be observed at m/z 249$^-$, which is consistent with $Au(CN)_2^-$, but the abundance of this ion was too low to be analytically useful.

SIMS Spectra of Carbon Exposed to Gold Cyanide, Treated with 12-Crown-4. The very low abundances of the gold-containing ions in the static SIMS analysis of the exposed carbon were surprising, because the concentration of gold in the sample was relatively high (8 parts per thousand). It was hypothesized that poor ionization efficiency was responsible and hence, means to assist dissociation of ionic complexes on the carbon surface were investigated. 12-Crown-4 was chosen because the compound forms stable adduct ions with Na^+ in solution and in the gas phase.[7,9,10] If similar behavior occurred on the surface of the carbon, then $Au(CN)_2^-$ present on the surface would be less tightly bound to Na^+ and more amenable to sputtering as an ion.

The carbon samples were spiked with a 12-crown-4/methanol solution (0.05–0.08 M) and crushed wet using mortar and pestle.

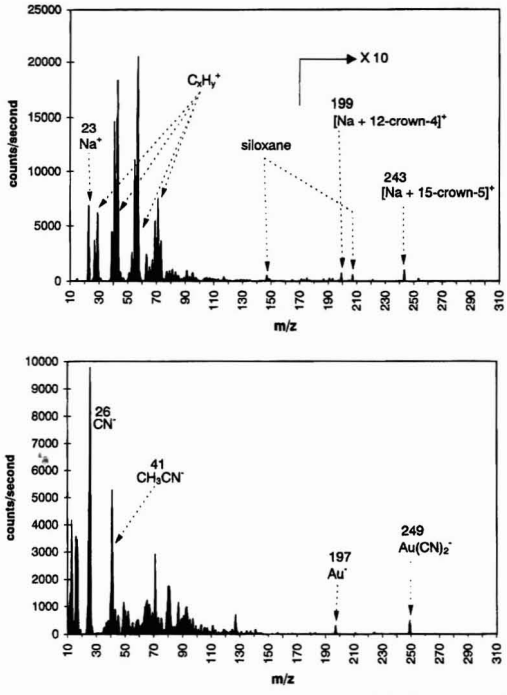

Figure 3. Cation (a, top) and anion (b, bottom) SIMS spectra of carbon exposed to 10 mg/L gold cyanide solution, treated with 12-crown-4 (with 15-crown-5 impurity in (a)).

A droplet of the resulting slurry was then placed on a sample holder that had been fitted with double-sided tape and was allowed to dry. Subsequent SIMS analyses resulted in anion and cation spectra that contained ions that were much more abundant than either the unexposed or exposed carbon samples. *m/z* 249$^-$ and 197$^-$ were readily observed in the anion spectrum; these ions must correspond to Au^- and $Au(CN)_2^-$ (Figure 3b). These ion assignments are supported by control experiments in which carbon samples unexposed to gold (unwashed and washed with water) were treated with crown ether solution and analyzed: *m/z* 249$^-$ and 197$^-$ were not observed. The possibility that the methanol might be enhancing the observation of the gold-bearing ions was eliminated by analyzing gold cyanide-exposed carbon crushed with methanol: again, the gold-bearing ions were not observed.

In the lower mass region of the anion spectrum, abundant CN^- is observed as before, but the abundant NCO^- at *m/z* 42$^-$ has been supplanted by an abundant *m/z* 41$^-$, which may correspond to CH_3CN^-, although other assignments cannot be ruled out. The appearance of an abundant *m/z* 41$^-$ is related to the presence of the crown ether, as this ion was also observed in the 18-crown-6 spectrum (Figure 4b).

The appearance of the cation spectrum (Figure 3a) was also significantly different: a higher mass cation was observed at *m/z* 199$^+$, which corresponds to [Na + 12-crown-4]$^+$, and another cation was observed at *m/z* 243$^+$. The *m/z* 243$^+$ is interpreted in terms of [Na + 15-crown-5]$^+$, where the 15-crown-5 is an impurity in the 12-crown-4. GC/MS analysis of the 12-crown-4 revealed the presence of 15-crown-5, but at a concentration <1% 12-crown-4, which is not consistent with the abundance of [Na + 15-crown-5]$^+$ in the SIMS analysis (comparable to that of [Na + 12-crown-4]$^+$). The abundance of the [Na + 15-crown-5]$^+$ relative to [Na + 12-crown-4]$^+$ probably reflects higher Na^+ affinity of 15-crown-5 in solution[7,8] or in the gas phase.[10] No kalliated crown adducts were observed, because Na^+ is by far the dominant group I cation on the surface. We estimate the ratio of Na^+ to K^+ to be about 17 by comparing the absolute abundance of Na^+ in the spectrum of the gold cyanide-treated carbon (Figure 2a) with the abundance of K^+ in the spectrum of the untreated carbon (Figure 1a). (Note that it was not possible to directly compare the *m/z* 23$^+$ abundance with that of *m/z* 39$^+$ in the spectrum of the 12-crown-4 + gold cyanide treated sample, because *m/z* 39$^+$ has a substantial component corresponding to $C_3H_3^+$ which could not be resolved.)

In the lower mass regions of the cation spectra, abundant hydrocarbons are observed. A simplistic explanation for the presence of these abundant ions is that they are derived from the crown ether, but there is little evidence for oxygen in these ions (e.g., the abundance of *m/z* 45$^+$ (normally $C_2H_4OH^+$) is low). Further, it is difficult to rationalize C_3, C_4, and higher ions in terms of the crown ether, whose repeating unit is (C_2H_4O). Alternative explanations are that the hydrocarbon ions are either derived from an atmospheric source or are indigenous to carbon surfaces. The observation of these ions may be facilitated by the presence of the crown ether.

SIMS Spectra of Carbon Exposed to Gold Cyanide, Treated with 18-Crown-6. The carbon exposed to gold cyanide was crushed wet with an 18-crown-6 solution, because it was felt that more abundant complex ions might be observable using a larger crown, which is capable of efficiently complexing K^+ and more efficiently complexing Na^+. $Au(CN)_2^-$ was observed in the anion spectrum, as was CN^- and CH_3CN^- (Figures 4b and 5b). The abundances of these ions were similar to those observed in the spectra of carbon doped with 12-crown-4. In the cation spectrum, adduct ions corresponding to [Na + 18-crown-6]$^+$ and [K + 18-crown-6]$^+$ were observed at *m/z* 287$^+$ and 303$^+$ (Figures 4a and 5a). The lower mass region again contained very abundant hydrocarbon ions.

It was surprising that the 12-crown-4 worked as well as the 18-crown-6 in promoting the sputtering of $Au(CN)_2^-$, because the larger ligand is known to be a more effective complexing agent.[8,10] An equimolar solution of both crown ethers (0.049 M) was applied to a carbon chip, which was then crushed and analyzed. This experiment showed that 18-crown-6 was indeed much more effective at complexing Na^+ than 12-crown-4: the ratio of [Na + 18-crown-6]$^+$/[Na + 12-crown-4]$^+$ was at least 49.

The role of the crown ether concentration was evaluated by analyzing carbon chips that had been crushed in 50 mL of 18-crown-6 solutions having concentrations ranging from 0.0049 to 0.49 M. At the lowest concentrations, a very low abundance [Na + 18-crown-6]$^+$ ion could be observed, but no $Au(CN)_2^-$. Thus, insufficient 18-crown-6 defeats attempts to observe $Au(CN)_2^-$. When 0.049 or 0.18 M crown solutions were used, good abundances of the [Na + 18-crown-6]$^+$ and $Au(CN)_2^-$ were observed. The higher concentration crown solution appeared to work better, but the precision of the measurements do not permit a firm conclusion to be drawn at this time. Interestingly, when a 0.49 M solution was used, the abundances of the complex ions were markedly decreased, perhaps because the organic had thoroughly

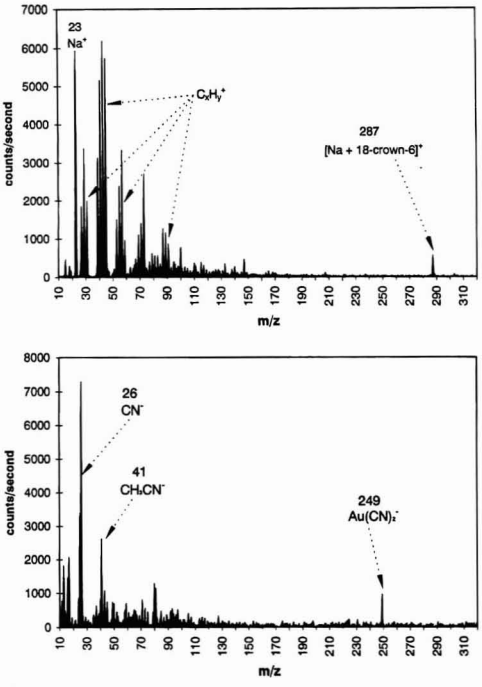

Figure 4. Cation (a, top) and anion (b, bottom) SIMS spectra of carbon exposed to 10 mg/L gold cyanide solution, treated with 18-crown-6.

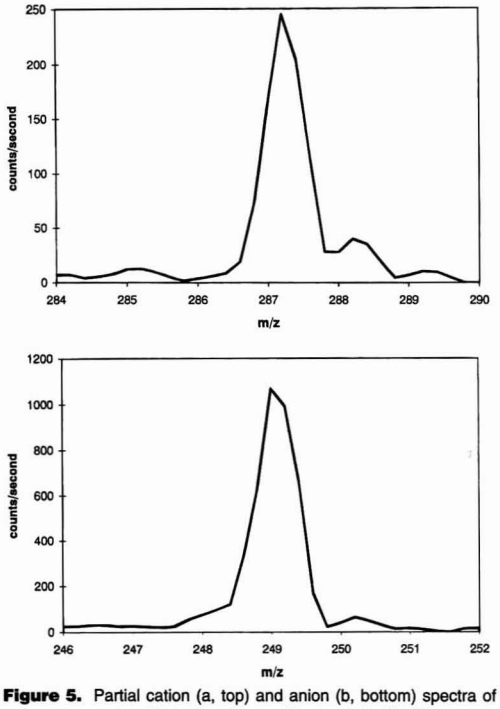

Figure 5. Partial cation (a, top) and anion (b, bottom) spectra of carbon exposed to 10 mg/L gold cyanide, treated with 18-crown-6.

coated the surface and thus obscured ions originating from the carbon surface.

Discussion. The 18-crown-6 and 12-crown-4 results show that $Au(CN)_2^-$ may be readily observed on carbon surfaces by treating the surface with a crown ether. It is hypothesized that the crown ether enhances the sputtering of $Au(CN)_2^-$ and other ions by complexing the group I cation, thereby weakening $MAu(CN)_2$ compounds present on the carbon surface (where $M = Na^+$ or K^+), and facilitating subsequent formation of gas-phase $Au(CN)_2^-$ upon sputtering with ReO_4^-. The observation of $[M + crown]^+$ is consistent with this hypothesis, which if correct generally implies that secondary ion sputtering can be facilitated by manipulation of the surface chemistry.

Although SIMS does not provide direct spectral information on adsorbed surface species, the present observations are consistent with the notion that gold is extant as the $Au(CN)_2^-$ complex on the carbon surface. A less likely alternative is that Au and CN^- are independently present on the carbon surface and then combine to form $Au(CN)_2^-$ in the "selvedge" region upon ion bombardment. This type of process would be similar to the formation of M_2^+ ions observed by Rabalais and co-workers (M = alkali metal).[25] We do not favor clustering as an explanation for $Au(CN)_2^-$, because if this were occurring, then $Au(CN)_2^-$ should be observable irrespective of the presence of the crown ether. The fact that the crown ether promotes $Au(CN)_2^-$ sputtering also suggests strongly that $Au(CN)_2^-$ is tightly complexed on the surface with sodium.

The presence of crown ethers on the carbon surface also appear to promote the formation of Au^- (Figure 3b). One explanation for the auride ions is that nascent or actual $[Na + crown]^+Au^-$ complexes are formed on the carbon surface; the component ions are then sputtered into the gas phase upon SIMS bombardment. This idea is supported by the fact that crown ethers are known to promote the formation and stabilization of Au^- in the presence of sodium.[7] A second plausible explanation is that Au^- is formed by a SIMS-induced decomposition of $Au(CN)_2^-$. This draws support from the SIMS spectrum of $KAu(CN)_2$, which contains Au^-. A third possibility is that Au^- is formed directly from SIMS bombardment of Au^0; however, this does not account for the enhancing effect of the crown ether. At the present time, Au^0 cannot be identified in the presence of $Au(CN)_2^-$ on carbon surfaces, but an improved understanding of the relationship between the two ionic species may permit this distinction in the future.

ACKNOWLEDGMENT

The authors thank Marnie Cortez for assistance with SIMS data acquisition, and Cathy Rae for GC/MS analysis. This work was supported by the U.S. Department of Energy, Idaho Operations Office Contract DE-AC-07-76IDO1570.

Received for review January 17, 1995. Accepted April 6, 1995.[⊗]

AC950053C

(25) Honda, F.; Fukuda, Y.; Rabalais, J. W. *J. Chem. Phys.* **1979**, *70*, 4834–4836.

[⊗] Abstract published in *Advance ACS Abstracts,* May 15, 1995.

Anal. Chem. **1995,** *67,* 1992–1997

High-Precision Determination of $^2H/^1H$ in H_2 and H_2O by Continuous-Flow Isotope Ratio Mass Spectrometry

Simon J. Prosser*,† and Charles M. Scrimgeour‡

Europa Scientific Ltd., Electra Way, Crewe CW1 1ZA, U.K. and Chemistry Department, Scottish Crop Research Institute, Invergowrie, Dundee DD2 5DA, U.K.

The major obstacle to accurate and precise measurement of $^2H/^1H$ in H_2 by continuous-flow, isotope ratio mass spectrometry has been the interference of the $^4He^+$ carrier peak with the neighboring $^2H^1H^+$ peak. This has been overcome using a novel mass spectrometer with high dispersion, giving an abundance sensitivity at *m/z* 3 of <1 ppm. Samples of H_2 with natural abundance $^2H/^1H$ can be analyzed routinely in <2 min with a precision of ±1.5‰. In combination with the equilibration of H_2O with H_2, this technique provides a fast, accurate method of analysis of water, with a precision of ±3.0‰ at natural abundance. There is no measurable memory between samples of either water or H_2 gas. The technique is accurate over a wide range of enrichment and is useful for tracer experiments as well as natural abundance studies.

Continuous-flow isotope ratio mass spectrometry (CF-IRMS) has simplified the measurement of many of the so-called 'light element' stable isotopes (H, C, N, O, and S) for a large number of applications. Analysis of ^{15}N, ^{13}C, and ^{18}O to a precision of 0.1–0.2‰ is now routine for CF-IRMS.[1,2] For many applications this challenges the precision available by traditional, dual-inlet isotope ratio mass spectrometry (DI-IRMS), once the variability due to off-line sample preparation is taken into account. Measurement of ^{34}S by CF-IRMS to ~0.5‰ has also been reported.[3,4] The only light element hitherto unmeasured by CF-IRMS is H. There are a number of reasons for this. Low-resolution mass spectrometers designed for DI-IRMS of H_2 often had an extra, shorter spur added to an existing IRMS and were unable satisfactorily to resolve the $^2H^1H^+$ ion beam from the 10^4–10^5 times larger $^4He^+$ ion beam. Neither was there a suitably fast and simple method of preparing H_2 from H_2O that would benefit from the speed and simplicity of CF-IRMS. The interference of $^3He^+$ on the $^2H^1H^+$ ion beam is not important—it is a constant (and very small) proportion of the He carrier and is easily corrected for by a background subtraction. A simple mathematical proof demonstrates that there is no effect on δ values caused by the suppression of the $^3He^+$ background during the introduction of a pulse of H_2.

Traditionally, $^2H/^1H$ has been measured in H_2O by reduction of the H_2O to H_2 over a heated metal, either in a batch process using zinc[5,6] or by on-line reduction in a uranium furnace.[7] The on-line technique is subject to memory effects and can require up to 10 replicate samples to be analyzed to achieve reliable results. The results achieved using the batch preparation with Zn are variable across different batches of Zn reagent, although much progress has been made in making the Zn reduction technique more reliable.[8–10] A further complication of reduction techniques is that they require pure water; any dissolved material can contaminate the metal surface and prevent complete reaction. Samples must either be pre-prepared by distillation[11] or kept physically separate until evaporated during the heating process.[12] The Zn batch technique is also less satisfactory for enriched samples due to the presence of occluded natural abundance waters.

A fundamentally different approach is to equilibrate H_2O with H_2. This equilibration needs a catalyst in order to proceed quickly enough to be viable. Platinum is known to catalyze the equilibration; however, it operates on the vapor/gas interface and must be kept dry to work. This has been accomplished using Pt supported on a porous hydrophobic polymer (Hokko beads, Shoko Corp., Tokyo, Japan).[13,14] This achieves equilibration within 1 h and has been used as the basis of an automated batch preparation method.[15] The fractionation factor between H_2O and H_2 is highly temperature-dependent, the δ^2H of H_2 gas in equilibration with H_2O changes by ~6‰ per degree,[16] and so temperature control to ± 0.01 °C is necessary. The equilibration technique allows a wide variety of aqueous fluids to be analyzed without the need

† Europa Scientific, Ltd.

‡ Scottish Crop Research Institute.

(1) Prosser, S. J. *Int. J. Mass Spectrom. Ion Processes* **1993**, *125*, 241–266.

(2) Barrie, A.; Debney, S.; Workman, C. T.; Pullan, C. In *International Symposium on Nuclear and Related Techniques in Soil/Plant Studies on Sustainable Agriculture and Environmental Preservation*; IAEA: Vienna, 1994; IAEA-SM-334/37.

(3) Haystead, A. In *Stable Isotopes in Plant Nutrition, Soil Fertility and Environmental Studies*; IAEA: Vienna, 1991; pp 3–25.

(4) Geisemann, A.; Jäger H.-J.; Norman, A. L.; Krouse, H. R.; Brand, W. A. *Anal. Chem.* **1994**, *66*, 2816–2819.

(5) Coleman, M. L.; Shepard, T. J.; Durham, J. J.; Rouse, J. E.; Moore, G. R. *Anal. Chem.* **1982**, *54*, 993–995.

(6) Kendall, C.; Coplen, T. B. *Anal. Chem.* **1985**, *57*, 1437–1440.

(7) Barrie, A.; Coward, W. A. *Biomed. Mass Spectrom.* **1985**, *12*, 535–541.

(8) Tanweer, A.; Hut, G.; Burgman, J. O. *Chem. Geol.* **1988**, *73*, 199–203.

(9) Tanweer, A. *Anal. Chem.* **1990**, *62*, 2158–2160.

(10) Hayes, J. M.; Johnson, M. W. Indiana University, Bloomington, IN, 1988. Unpublished work.

(11) Penman, A. D.; Wright, I. A. *Biomed. Environ. Mass Spectrom.* **1987**, *14*, 339–342.

(12) Wong, W. W.; Cochran, W. J.; Klish, W. J.; Smith, E. O.; Lee, L. S.; Klein, P. D. *Am. J. Clin. Nutr.* **1987**, 905–913.

(13) Horita, J. *Chem. Geol.* **1988**, *72*, 89–94.

(14) Horita, J. *Chem. Geol.* **1989**, *79*, 107–112.

(15) Coplen, T. B.; Wildman, J. D.; Chen, J. *Anal. Chem.* **1991**, *63*, 910–912.

(16) Rolston, J. H.; Hartog, J. den; Butler, J. P. *J. Phys. Chem.* **1976**, *80*, 1064–1067.

0003-2700/95/0367-1992$9.00/0 © 1995 American Chemical Society

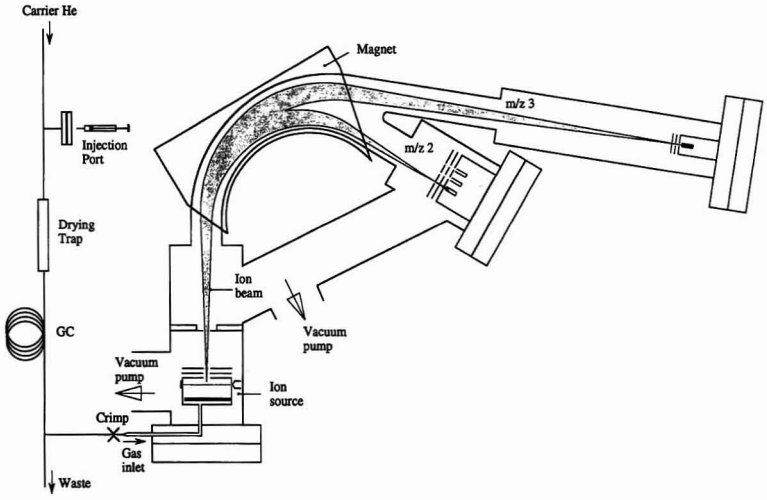

Figure 1. Schematic of the modified 20–20 mass spectrometer showing the extra spur and large separation between $^1H^1H^+$ and $^2H^1H^+$. Also shown is a simplified schematic of the gas inlet system.

for pre-distillation. An alternative method,[17] described in greater detail below, uses a readily available, Pt-on-alumina, catalyst that slows the equilibration time. The effect of temperature fluctuations is greatly reduced by the long equilibration time as they are averaged out, and temperature control of the equilibration process has been found not to be necessary. The slow equilibration also allows samples with bound water, e.g., plant tissue and soil, to be analyzed without pre-extraction of the water, at least for tracer studies.[18]

Despite some advantages of equilibration over the reduction method, it does have some shortcomings. Compared with reduction methods, equilibration requires more sample; 0.1–1 mL versus 1–10 μL. Hydrogen in isotopic equilibrium with H_2O at room temperature has a $^2H/^1H$ ratio some four times less than that of the H_2O.[16] The natural abundance ratio is already very low ($^2H/^1H$ = ~0.00015, m/z 3/2 = ~0.0003), so any further depletion of ^2H makes precise measurement even more problematic.

All the methods of determining δ^2H have relied on DI-IRMS to analyze the prepared gas. The internal precision (~0.15‰, 2σ10) of such IRMS is overkill for the reproducibility of the preparation methods, ~1–2‰, and requires ~20 min to analyze each sample. A simpler, faster measurement technique employing CF-IRMS is described below.

EXPERIMENTAL SECTION

Instrumentation. A 20–20 isotope ratio mass spectrometer[1] (Europa Scientific, Crewe, U.K.) was modified to allow simultaneous collection of m/z 2 ($^1H^1H^+$) and 3 ($^1H^2H^+$) ions. The large relative mass difference between the two ions of interest results in a large difference in the radius of their paths through the analyzer. The flight tube of the mass spectrometer was 'flared' to accommodate the larger outer radius of the m/z 3 ion beam, and an extra collector spur was added (Figure 1). A magnetic field strength of 0.12 T with accelerating potential of ~4 × 10^3 V allowed m/z 2 to be collected in the major collector of the standard triple collector assembly, radius 10.9 cm, while the additional single collector assembly, radius 13.3 cm, measured m/z 3. The standard collector is placed with a sector angle of 120° and a focal length of 9.6 cm; the additional collector is placed with a sector angle of 98.8° and a focal length of 31.7 cm. The distance between the focal points of the two ion beams of m/z 2 and m/z 3 is 24.0 cm; it is this large dispersion that ensures that there is no interference at m/z 3 from m/z 2 or from the He carrier at m/z 4.

Gas samples were introduced to the mass spectrometer via the continuous-flow gas injection interface described by Prosser et al.,[19] a simplified schematic is shown in Figure 1. In brief, sample gas was injected into a flow of He carrier gas (~60 mL min^{-1}); the sample swept through a drying tube [$Mg(ClO_4)_2$, 0.2 m long, 5 mm i.d.) and packed-column GC (Carboseive-G, 0.5 m long, 5 mm i.d.). A small amount of the eluent (~0.05 mL min^{-1}) flowed via a crimp into the ion source of the mass spectrometer. The ratio of m/z 3 to m/z 2 of injected pulses of H_2 entering the mass spectrometer were measured by simultaneous integration of the ion beams over time.

Procedures. Hydrogen gas was taken from a high-pressure cylinder of 99.999% H_2 (Electrochem Ltd., Stoke-on-Trent, U.K.) and transferred into a 0.5 L foil gas bag (Becton Dickinson Ltd., Cowley, Oxford, U.K.) fitted with a three-way valve. Aliquots were drawn from the foil bag, using a 2 mL gas-tight syringe fitted with an isolation valve, and injected into the CF interface.

Water samples were equilibrated with H_2 using the method described by Scrimgeour et al.;[17] 0.4 mL of water was equilibrated with ~13 mL of the tank H_2 gas in 13 mL, septum-topped vials in the presence of a Pt-on-alumina catalyst for 3 days at room temperature. After equilibration, gas was withdrawn from the vials using a 2 mL gas-tight syringe and injected into the CF interface.

Hydrogen in equilibrium with water is very depleted in ^2H; at 20 °C the fractionation factor is 3.9688; H_2 in equilibrium with

(17) Scrimgeour, C. M.; Rollo, M. M.; Mudambo, S. M. K. T.; Handley, L. L.; Prosser, S. J. *Biol. Mass Spectrom.* **1993**, *22*, 383–387.

(18) Scrimgeour, C. M. *J. Hydrol.*, in press.

(19) Prosser, S. J.; Brookes, S. T.; Linton, A.; Preston, T. *Biol. Mass Spectrom.* **1991**, *20*, 724–730.

V-SMOW at this temperature would have $\delta^2H = -748.0‰$. If such gas were measured against a natural abundance standard, the accuracy would suffer because of the large isotopic difference between the gases. Because the permil scale of the H_2 is apparently compressed by the large fractionation during equilibration and must be re-expanded to obtain the isotopic composition of the original water, the precision also suffers as the analytical uncertainty is expanded by the same factor as the permil scale. To overcome these problems, samples were measured against H_2 equilibrated with a reference water.

The fractionation factor, α, is given by

$$\alpha = R_w/R_g \quad (1)$$

where R_w is the $^2H/^1H$ of the water after equilibration and R_g is the $^2H/^1H$ of the H_2 gas in equilibrium with it. The isotopic composition of a water sample is given by

$$\delta^2H_w = (R_{w(sample)}/R_{w(reference)} - 1) \times 100 \ (‰) \quad (2)$$

combining this with eq 1

$$\delta^2H_w = ((\alpha R_{g(sample)})/(\alpha R_{g(reference)}) - 1) \times 1000 \ (‰) \quad (3)$$

Equation 3 demonstrates that if reference and sample waters are equilibrated at the same temperature so that α is constant, then α cancels from the top and bottom of the equation and the δ^2H_w of the sample versus reference water is equivalent to the δ^2H_g between the H_2 in equilibrium with the waters. This removes the errors associated with re-expanding the permil scale and, most importantly, makes the measurement entirely independent of the fractionation factor and thus temperature. It is not necessary to know the value of the fractionation factor or temperature so long as it is constant across a batch of samples and references. The effect of any temporal temperature variation is minimized by the fast analysis time and slow equilibration process. The effects of spatial variations are minimized by keeping the vials close together during the equilibration process, at the place where they will be sampled.

Equation 3 gives the isotopic composition of the water at the end of the equilibration, δ^2H_w, which is governed by the original isotopic composition of the water (δ^2H_{ow}) and H_2 (δ^2H_{og}) and the molar ratio of H_2 to H_2O (ϱ):

$$\delta^2H_{ow} = \delta^2H_w - \varrho(\delta^2H_{og} - \delta^2H_g) \quad (4)$$

If the molar ratio of H_2 to H_2O is low enough, the isotopic composition of the water does not change significantly during the equilibration, and no correction for the original isotopic composition of the H_2 is necessary. Due to an oversight, the procedure described above provides a molar ratio above 0.02, which results in a 2.5% scaling error. We now recommend only 1 mL of H_2 for 0.4 mL of H_2O, which brings the scaling error within the overall precision of the technique. A balance of He is used to raise the vial slightly above atmospheric pressure to help guard against ingress of air.

The equilibration method was used to prepare a dilution series from ~99% ^2H_2O and reference water at $\delta^2H_{V\text{-}SMOW} = 32.0‰$ (160.7 ppm). The dilution series extended to ~920 ppm excess over the reference water (defined as 0 ppm excess) in six steps. Samples of the international standards V-SMOW and V-SLAP were also prepared using this method.

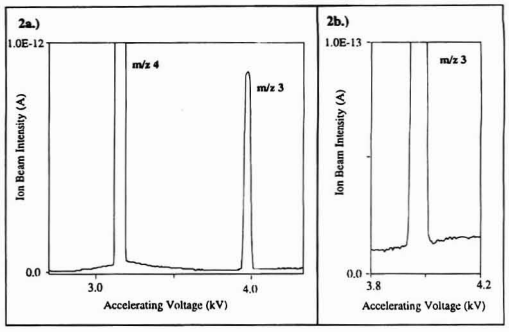

Figure 2. (a) $^4He^+$ and $^2H^1H^+$ peaks as they are scanned across the outer spur collector using the acceleration voltage. (b) Expanded scale for the *m/z* 3 peak from which the upper limits of the abundance sensitivity were determined.

RESULTS AND DISCUSSION

Mass Spectrometer Performance Characteristics. The mass spectrum between *m/z* 4 and 3, scanned across the single collector spur, is shown in Figure 2a. The trace was obtained under normal continuous-flow conditions with a mix of approximately 20:1 of He to H_2 bleeding into the mass spectrometer. The indicated pressure in the source housing was 4×10^{-6} mbar, and ion beam intensities were *m/z* 2, 2.27×10^{-9} A; *m/z* 3, 8.42×10^{-13} A; and *m/z* 4, 1.39×10^{-8} A. The dispersion was measured at *m/z* 3 as 9.1 cm, equivalent to an effective dispersion radius of 27.3 cm. The resolution was measured as 40 using the '5% peak height' definition, which is given by

$$R = m/\Delta m_y \quad (5)$$

where R is resolution, m is the mass of the ion in amu, and Δm_y is the width of the peak in amu at 5% of the peak height. This is technically equivalent to the '10% valley' definition that is given by the highest mass of two adjacent ion beam peaks of equal intensity, differing in mass by 1 amu, which shows a valley between the peaks of 10% of the peak height. In practice, the '5% peak height' method is easier to use.

The mass spectrum shown in Figure 2a is magnified in Figure 2b to show greater detail around *m/z* 3. The large physical separation between the ion beams has resulted in negligible interference between them. The upper limit for the abundance sensitivity of the tailing from *m/z* 2 under the *m/z* 3 beam is 1 ppm; the upper limit for *m/z* 4 tailing under *m/z* 3 is 0.5 ppm.

Figure 3 shows the peak shapes for *m/z* 2 and 3 as they are simultaneously scanned across their respective collectors. Also shown is the ratio between these two beams. The flat tops and steep sides of the peaks indicate well-focused ion beams; the flat top of the ratio trace shows excellent stability over a range of 25 V.

Gas Samples. Measurement of isotopes using H_2 gas is complicated by ion/molecule reactions forming H_3^+ ions in the ion source. These are collected with the $^2H^1H^+$ ions and result

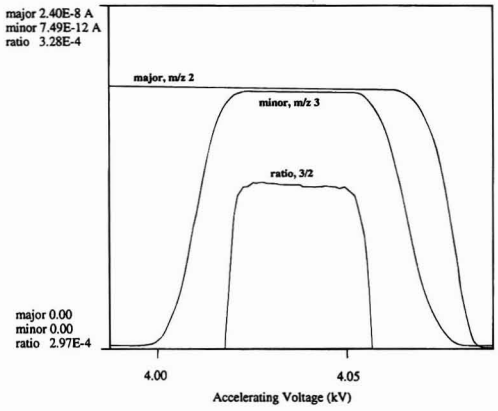

Figure 3. Peak scan of *m/z* 2 and 3 and the 3/2 ratio showing the quality of focusing and coincidence of the ion beams and the 25 V range of acceleration potential for which the ratio remains stable.

Table 1. Analytical Precision for Injection of Natural Abundance H_2 Gas

sample size (mL)	major beam area (% ref)	δ^2H_{raw} (‰)	mean	SD	δ^2H_{corr} (‰)	mean	SD
1.0	100.07	−1.76			−1.40		
1.0	100.95	2.39			0.47		
1.0	101.52	3.70			0.30		
1.0	102.14	4.46			−0.55		
1.0	102.63	5.66	**3.0**	**2.9**	−0.62	**−0.4**	**0.8**
0.5	51.89	−123.91			1.38		
0.75	78.08	−57.64			−0.26		
1.0	93.32	−16.18			1.68		
1.25	128.48	73.34			0.03		
1.50	150.70	132.60	**1.64**	**102.3**	1.67	**0.9**	**0.9**

in an overestimation of the measured $^2H/^1H$ ratio. The amount of H_3^+ formed is proportional to the square of the amount of H_2, and so there is a linear relationship between the measured $^2H/^1H$ ratio and the pressure of H_2 (intensity of the *m/z* 2 ion beam) in the mass spectrometer. Theoretically, if this relationship is extrapolated back to zero ion beam intensity, the ratio is then correct. Using traditional DI-IRMS, the problems of H_3^+ are overcome by using a linear correction for major ion beam (*m/z* 2) intensity in conjunction with accurate matching of the major ion beam intensities of reference and sample gases. Using CF-IRMS, it is not always possible to match the sizes of samples and references, and so mathematical correction must be relied upon.

Table 1 shows the extent of the 'H_3^+ effect' for a particular source tuning condition. The major beam area and δ^2H_{raw} are the original experimental data.

$$\delta^2H_{raw} = (R_{ms}/R_{mr} - 1) \times 1000\ (‰) \qquad (6)$$

where R_{ms} is the measured ratio for the sample and R_{mr} is the measured ratio for the reference. Without correction, even variations of a few percent of major beam area greatly change the δ^2H_{raw} and render the technique useless.

The ratio values were then corrected by linear regression through the data series of measured ratios (R_m) versus major ion beam intensity (I_m) to find the proportionality constant (k) from

$$R_m = kI_m + R_0 \qquad (7)$$

This constant was then used to extrapolate to major ion beam intensity $I_m = 0$ for each point to find the offset ratio, R_0. A δ value corrected for the H_3^+ effect was then calculated:

$$\delta^2H_{corr} = (R_{0s}/R_{0r} - 1) \times 1000\ (‰) \qquad (8)$$

where R_{0s} is the offset ratio for the sample and R_{0r} is the offset ratio for the reference. These corrected values (δ^2H_{corr}) show how predictable the effect is. There is no significant difference in analytical precision for sample sizes varying by ±50%, and sample sizes matched as closely as the injection technique would allow (Table 1). CF-IRMS is capable of measuring the $^2H/^1H$ of natural abundance H_2 with a precision of ±1‰.

In order to measure the proportionality constant (k) using DI-IRMS, it is necessary to vary the pressure in the inlet and note the change in ratio. Using CF-IRMS, each peak provides intensity *versus* ratio data as the peak rises and falls. The possibility of using this information to perform an individual H_3^+ correction on each peak was investigated. However, it was found that differences in transport times for light and heavy molecules through the injection interface and mass spectrometer crimp resulted in a time dependence of the ratio, which was superimposed on the pressure dependence; the two effects proving difficult to deconvolute. In practice, with a measurement cycle of <2 min, it was found easier to measure reference gas of three different sizes to determine k.

Water Samples. An important precondition, if the technique is to be accurate, is that the proportionality constant k is both reasonably constant in time and independent of enrichment. These two conditions were investigated by analyzing a sequence of water samples of different enrichments, from the dilution series, at three different injection sizes. To prevent possible variations from sample preparation, all three samples were taken from the same equilibration vial. The k factor for each different enrichment was compared to that of the H_2 tank gas. The results are shown in Figure 4, where the measured ratio is plotted against major beam intensity. All least squares fit lines for each of the data sets are reasonably parallel to that for the tank gas. The k factors obtained from the regression analysis and the analytical precision for the three points are given in Table 2. The k factor for the tank gas measured at the end is not significantly different from that measured at the beginning, and there is little variation of k with time; for periods of the same order as that of the experiment, ~45 min, k may be considered to be constant.

However, there is systematic variation of k with enrichment, R_0, i.e., the H_3^+ effect changes its magnitude with enrichment; this dependence is plotted in Figure 5. Assuming a linear relationship between k and R_0, the effect is relatively small and may be corrected for

$$k = aR_0 + b \qquad (9)$$

combining this with eq 7 yields

$$R_0 = (R_m - bI)/(1 + aI) \qquad (10)$$

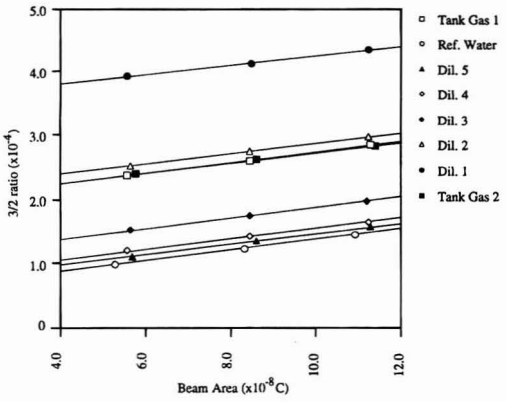

Figure 4. H_3^+ effect for samples of differing enrichment. Beam area is given in coulombs (C) = amperes × s.

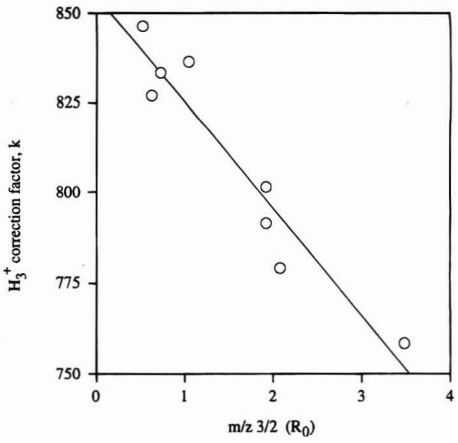

Figure 5. Relationship between H_3^+ correction factor and $^2H/^1H$. The correction factor k, eq 7, is plotted against the average of the three R_0 values given in Table 2.

Table 2. H_3^+ Correction Factors for Varying Enrichment and Precision of Measurement

sample	beam area ($\times10^{-8}$ C[a])	$^2H/^1H$ (R_m) ($\times10^{-4}$)	k	R_0 ($\times10^{-4}$)	$\delta^2H_{V\text{-}SMOW}$[b] (‰)	SD
tank gas	11.286	2.8269		1.92289		
	8.4145	2.5954		1.92140		
	5.5381	2.3664	**801.2**	1.92280	**2842.9**	**1.9**
ref water	10.912	1.4410		0.51675		
	8.3152	1.2193		0.51500		
	5.2850	0.9646	**846.5**	0.51696	**32.0**	**2.2**
Dil 5	11.256	1.5529		0.62203		
	8.5705	1.3278		0.61902		
	5.6519	1.0894	**826.9**	0.62199	**241.4**	**3.4**
Dil 4	11.224	1.6491		0.71414		
	8.4427	1.4152		0.71192		
	5.5653	1.1776	**833.2**	0.71401	**426.1**	**2.5**
Dil 3	11.180	1.9743		1.03965		
	8.4273	1.7395		1.03498		
	5.6174	1.5092	**836.1**	1.03959	**1075.2**	**5.2**
Dil 2	11.248	2.9517		2.07548		
	8.4341	2.7270		2.06998		
	5.6229	2.5137	**778.7**	2.07568	**3145.5**	**6.3**
Dil 1	11.224	4.3323		3.48152		
	8.4727	4.1207		3.47847		
	5.5474	3.9017	**758.4**	3.48121	**5957.6**	**3.3**
tank gas	11.371	2.8223		1.92285		
	8.6093	2.6003		1.91930		
	5.7443	2.3771	**791.2**	1.92273	**2841.5**	**4.0**

[a] Beam area given in coulombs (C). [b] Calculated using the sample R_0 against the average ref water, R_0, as in eq 8 and then converting to the V-SMOW scale using $\delta^2H_{V\text{-}SMOW}$ Ref water = 32.0‰ and the formula given in ref 22.

A similar correction is necessary for DI-IRMS and is performed by using a scaling factor derived from two-point calibration from V-SLAP and V-SMOW to achieve the accepted difference.[20] The dependence of the H_3^+ effect on enrichment is likely to be the reason for the necessity of the DI-IRMS correction also. If sample sizes are kept constant, eq 10 implies that when performing a differential δ measurement a simple linear scaling factor is all that is required. This is the case for DI-IRMS where the major ion beam intensities for sample and reference are closely matched. For CF-IRMS of varying sample sizes, to get the best absolute accuracy, it is necessary to perform the full correction as described by eq 10, and so the H_3^+ effect must be measured for two references of differing isotopic composition in order to determine constants m and c. However, if sample sizes are matched to within ±10%, which is reasonably easy with many CF techniques, then this second-order correction is not significant within the precision of the technique, and H_3^+ correction followed by linear scaling can be relied upon.

This is demonstrated in Table 3, showing the analysis of the dilution series against the reference water. Three further samples of reference water were used to determine k at the start of the analysis, and three replicates of each sample were analyzed. This time similarly sized samples (±10%) were injected, and each aliquot was taken from a separate vial. A linear scaling factor between 'ref water' and 'Dil 1' is used to correct the data (the value determined for Dil 1 in Table 2 being taken as correct). The values obtained are compared with calculated values, assuming a starting enrichment of 99% ^2H_2O, in Figure 6. The excellent agreement over a very wide range of enrichment (~6000 ‰) demonstrates the accuracy of the technique. The data can also be compared to those obtained using individual H_3^+ correction factors for each sample (Table 2); no significant difference is seen. The precision given here is the overall precision of the entire technique, including sample preparation; although there is a slight worsening in precision at very high enrichment, it is still well within the limits required by most tracer experiments. The precision achieved at lower enrichments is adequate for many natural abundance studies. The data are presented in the order in which they were analyzed; there is no discernible memory effect between samples.

To further investigate absolute accuracy, V-SLAP was analyzed versus V-SMOW using the same equilibration method. The H_3^+ k factor was determined from three aliquots of V-SMOW, and V-SLAP was corrected using the same factor, with no scaling applied. Table 4 shows two analyses performed 11 days apart. In common with DI-IRMS systems, as discussed above, a small scaling factor is required to achieve the accepted value of −428‰; this scaling factor appears to be reasonably constant in time. The overall precision is similar to that achieved by DI-IRMS with Zn

(20) Gonfiantini, R. *Nature (London)* **1978**, *271*, 534–536.

Table 3. Reproducibility of Measurement for Natural Abundance and Enriched Waters Using CF-IRMS Combined with the H_2O/H_2 Equilibration Technique

sample	$\delta^2H_{V\text{-}SMOW}$ (‰)	mean (‰)	SD (‰)	abundance ^2H (ppm excess)	SD (ppm)	expected ^2H (ppm excess)
ref water	37.6					
	31.3					
	31.2	**33.4**	**3.7**	**0.2**	**0.6**	**0.0**
Dil 5	224.1					
	223.7					
	227.5	**225.1**	**2.1**	**30.1**	**0.3**	**29.5**
Dil 2	3153.4					
	3159.5					
	3147.5	**3153.5**	**6.0**	**485.8**	**0.9**	**489.0**
Dil 4	413.6					
	410.6					
	407.8	**410.7**	**2.9**	**59.8**	**0.2**	**54.7**
Dil 1	5969.5					
	5949.0					
	5954.5	**5957.6**	**10.6**	**921.8**	**1.6**	**919.2**
Dil 3	1074.6					
	1072.1					
	1073.7	**1073.5**	**1.2**	**162.1**	**0.2**	**163.6**

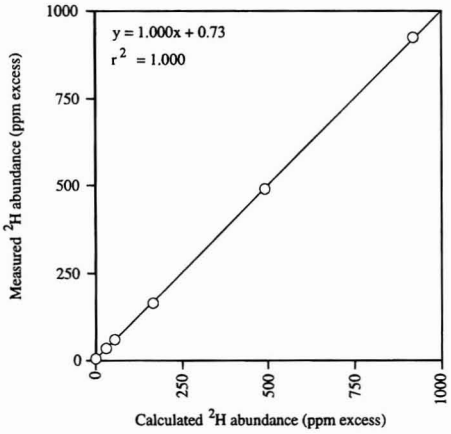

Figure 6. Relationship between measured and nominal deuterium abundance for the range of enrichment 0–920 ppm excess (δ = ~6000‰).

Table 4. V-SLAP versus V-SMOW

	δ^2H (‰)	mean	SD
day 1	−436.7		
	−444.6		
	−443.7	−441.7	4.3
day 12	−437.2		
	−442.3		
	−438.3	−439.3	2.7

reduction of H_2O despite the very low amounts of ^2H in the equilibrated H_2, only ~24 ppm for V-SLAP.

CONCLUSIONS

A new instrument has been described which, for the first time, allows precise measurement of $^2H/^1H$ by CF-IRMS, by removing the interference of $^4He^+$ from the $^2H^1H^+$ ion beam.

Hydrogen isotopes in natural abundance H_2 may be routinely measured with a precision of ±1.5‰, with no discernible memory and with an analysis time of <2 min. When coupled to the technique of H_2/H_2O equilibration, the δ^2H of even highly ^2H-depleted waters, such as V-SLAP, may be measured with a reproducibility of ±4‰. While this precision is ample for tracer studies and for many natural abundance studies, in order to take full advantage of the precision available by the CF-IRMS technique, it would be desirable to find an alternative method of preparing H_2 from H_2O and other samples that did not result in such severe depletion of the $^2H/^1H$ ratio.

Now that the major obstacle to measuring hydrogen isotopes by CF-IRMS has been overcome, many further developments become possible. Automation is easily achieved using a previously described gas injection system.[19] The equilibration technique described allows for the simultaneous equilibration of H_2O with CO_2 and H_2 so that both δ^2H and $\delta^{18}O$ could be measured from the same sample in ~7 min in the same manner that sequential measurement of $\delta^{15}N$ and $\delta^{13}C$ from the same sample has already been described.[21] There is now the incentive to develop a suitable reaction chemistry that would enable a vast array of applications for δ^2H measurement in organic compounds by GC-IRMS.

Now that the problem of measuring H isotopes in an He carrier has been solved, the entire suite of light element stable isotopes (C, N, O, S, and H) can be analyzed by CF-IRMS.

ACKNOWLEDGMENT

This work was carried out jointly as part of a program funded by the Scottish Office Agriculture and Fisheries Department and by Europa Scientific Ltd.

Received for review February 15, 1995. Accepted April 19, 1995.[⊗]

AC950166W

[⊗] Abstract published in *Advance ACS Abstracts,* June 1, 1995.

(21) Brookes, S. T.; Davies, J. E.; Scrimgeour, C. M.; Smith, K.; Watt, P. W. In *Frontiers and New Horizons in Amino Acid Research*; Takai, K., Ed.; Elsevier: Amsterdam, 1992; pp 411–415.

(22) Craig, H. *Geochim. Cosmoschim. Acta* **1957**, *12*, 133–149.

Anal. Chem. **1995,** *67,* 1998–2003

Mass Resolution Improvement by Incorporation of Pulsed Ion Extraction in a Matrix-Assisted Laser Desorption/Ionization Linear Time-of-Flight Mass Spectrometer

Robert S. Brown* and John J. Lennon

Department of Chemistry and Biochemistry, Utah State University, Logan, Utah 84322-0300

A linear time-of-flight mass spectrometer has been modified to incorporate pulsed ion extraction of matrix-assisted laser desorption/ionization (MALDI) generated ions. A unique aspect of the experiments presented is the combination of pulsed extraction with very high source potentials (up to 25 kV) which allows improved mass resolution while maintaining excellent sensitivity for the large *m/z* ions generated by the MALDI technique. Mass resolution in excess of 1000 (fwhm) is demonstrated for cytochrome *c* (12 361.1 Da) with the pulsed ion extraction linear time-of-flight mass spectrometer described. The influence on obtainable mass resolution of experimental variables such as delay time between laser ionization and ion extraction, amplitude of the pulsed voltage employed, and the source bias voltage are presented. It is shown that, for any given source potential, the optimum pulsed extraction voltage is a linear function of the mass of the analyte. This is consistent with the observation that the initial ion velocity distribution for MALDI-generated ions is independent of mass.

Matrix-assisted laser desorption/ionization (MALDI) has developed into one of the more important mass spectrometric methods for the analysis of large biologically relevant molecules.[1–5] While this ionization technique has been coupled to a variety of mass analyzers including scanning sector instruments equipped with array detectors[6] and magnetic ion traps,[7,8] by far the most popular mass analyzers for this technique have been those which utilize time-of-flight (TOF) mass analysis. This is due to both their relatively simple and inexpensive design and their excellent sensitivity and high-mass capability. Both linear and reflectron-based TOF mass spectrometers (MS) are widely employed. Linear systems combine excellent sensitivity and simple operation with demonstrated upper mass limits in excess of 200 000 Da.[9] Linear systems also provide adequate mass resolution ($m/\Delta m \approx$ 500 or less depending on the ion m/z) for many applications. TOF-MS, which incorporates an ion mirror[10] to correct for the initial ion velocity spread of MALDI-generated ions, can produce a mass resolution of several thousand for ions up to several thousand[11] m/z units. An ion mirror based system's mass resolution becomes limited by the increased isotopic distribution of larger m/z ions and, with larger m/z MALDI-generated ions, the high degree of metastable fragmentation which occurs after ion acceleration and prior to the ion mirror. The loss in sensitivity often encountered with a reflecting TOF-MS relative to a linear TOF-MS must also be considered when deciding upon which mode to employ.

Current MALDI TOF-MS (both linear and reflector) designs rely on the short laser pulse (typically 1–5 ns, depending on the laser) to produce discrete ion packets in the ion source, which are then continuously extracted from the ion source by the application of a large static electric potential (25–30 kV). The resulting high ion velocity provides for good ion detection efficiency and, especially in the case of the linear design, minimizes the effect on mass resolution of the initial velocity distribution. Utilization of dynamic extraction fields has historically been employed for improved mass resolution in TOF-MS.[12–14] Pulsed ion extraction methods have also been utilized[15–17] with laser desorption TOF-MS to compensate for the initial velocity and temporal and spatial distributions of the ions produced. While useful for smaller m/z ions, this approach has generally been abandoned for large m/z MALDI-generated ions in favor of the better mass resolution and sensitivity afforded by continuous ion extraction at high accelerating potentials.

A TOF-MS design that can combine both the advantages of pulsed ion extraction and high ion source accelerating potentials offers significant advantages over conventional designs. In this

(1) Karas, M.; Ingendoh, A.; Bahr, U.; Hillenkamp, F. *Biomed. Environ. Mass Spectrom.* **1989**, *18*, 841–843.
(2) Karas, M.; Bahr, U.; Ingendoh, A.; Nordhoff, E.; Stahl, B.; Strupat, K.; Hillenkamp, F. *Anal. Chim. Acta* **1990**, *241*, 175–185.
(3) Beavis, R. C.; Chait, B. T. *Rapid Commun. Mass Spectrom.* **1989**, *3*, 432–435.
(4) Beavis R. C.; Chait, B. T. *Proc. Natl. Acad. Sci. U.S.A.* **1990**, *87*, 6873–6877.
(5) Stahl, B.; Steup, M.; Karas, M.; Hillenkamp, F. *Anal. Chem.* **1991**, *63*, 1463–1466.
(6) Hill, J. A.; Annan, R. S.; Biemann, K. *Rapid Commun. Mass Spectrom.* **1991**, *5*, 395–399.
(7) Castoro, J. A.; Köster C.; Wilkins, C. L. *Rapid Commun. Mass Spectrom.* **1992**, *6*, 239–241.
(8) Castoro, J. A.; Wilkins, C. L. *Anal. Chem.* **1993**, *65*, 2621–2627.
(9) Karas, M.; Bahr, U.; Ingendoh, A.; Hillenkamp, F. *Angew. Chem., Int. Ed. Engl.* **1989**, *28*, 760–761.
(10) Mamyrin, B. A.; Karatajev, V. J.; Shmikk, D. V.; Zagulin, V. A. *Sov. Phys. JETP* **1973**, *37*, 45–48.
(11) Spengler, B.; Kaufmann, R. *Analusis* **1992**, *20*, 91–101.
(12) Wiley, W. C.; McLaren, I. H. *Rev. Sci. Instrum.* **1955**, *26*, 1150–1157.
(13) Browder, J. A.; Miller, R. L.; Thomas, W. A.; Sanzone, G. *Int. J. Mass Spectrom. Ion Phys.* **1981**, *37*, 99–108.
(14) Kinsel, G. R.; Grundwuermer, J. M.; Grotemeyer, J. *J. Am. Soc. Mass Spectrom.* **1993**, *4*, 2–10.
(15) Spengler, B.; Pan, Y.; Cotter, R. J.; Kan, L.-S. *Rapid Commun. Mass Spectrom.* **1990**, *4*, 99–102.
(16) Wang, B. H.; Dreisewerd, K.; Bahr, U.; Karas, M.; Hillenkamp, F. *J. Am. Soc. Mass Spectrom.* **1993**, *4*, 393–398.
(17) Colby, S. M.; King, T. B.; Reilly, J. P. *Rapid Commun. Mass Spectrom.* **1994**, *8*, 869–875.

0003-2700/95/0367-1998$9.00/0 © 1995 American Chemical Society

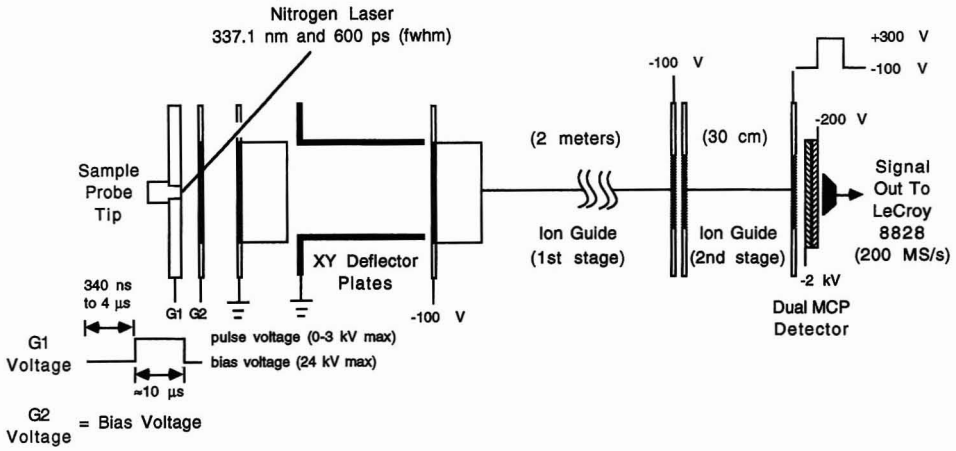

Figure 1. Schematic representation of linear TOF-MS used for pulsed ion extraction studies.

paper, the technical design and performance of a high-voltage (0–3 kV) pulsed extraction system capable of being biased at up to 30 kV coupled to an otherwise conventional linear TOF-MS is described. The effect of various fundamental experimental variables (pulse voltage, bias voltage, delay time, analyte m/z) on the obtainable mass resolution of MALDI-generated ions has been studied, and optimal experimental parameters have been determined. Direct comparison of the mass spectra obtained with the same linear TOF-MS operating in conventional continuous ion and optimized pulsed ion extraction (both at equivalent total ion energies) is presented.

EXPERIMENTAL SECTION

Instrumentation. The general design of the linear TOF-MS employed in these studies has been described previously.[18] Modifications to the system to facilitate pulsed ion extraction include the use of a dual-microchannel plate detector (R. M. Jordan Co., Grass Valley, CA) for improved time response. The single-stage wire ion guide previously described[19] has been modified by the addition of a short (30 cm) second stage prior to the detector to facilitate pulsed ion deflection and prevent detector saturation. Total flight path is now ~2.3 m. The transient digitizer's sampling rate has been increased to 200 MS/s (LeCroy Model 8828A, Chestnut Ridge, NY). The current ion source design utilized for both continuous and pulsed ion extraction is shown in Figure 1. It is a standard three-grid design with spacings of 4 mm between the pulsed grids and 16 mm between the second and third (grounded) grids. Each grid utilizes 90% transmissive mesh to ensure uniform electrostatic extraction fields. As in the previous design, sample is applied to a spring-loaded stainless steel probe tip which mates flush with the first solid ion grid. Limitations in the current electrical isolation of the ion source limits operation to a maximum source bias potential of 24 kV without intermittent arcing. The remainder of the system is capable of operation up to the 30-kV design limit of the pulsed ion extraction electronics (see below). Typical background pressures in the TOF-MS ion source during operation are 2×10^{-7} Torr. A pulsed nitrogen laser (Model PL2300, PTI Lasers, Princeton, NJ) producing 600-ps (fwhm) laser pulses at 337.1 nm was used for all of the studies presented.

Pulsed ion extraction was accomplished by the use of a variable-amplitude (0–3 kV) pulser board (Model GRX 3.0K, Directed Energy, Inc., Fort Collins, CO) biased at high voltage (±30 kV maximum). A 30-kV isolation transformer provides floated 110 VAC power for both the pulser and the auxiliary 0–3 kV high-voltage power supply (Series 602C, Bertan High Voltage, Hicksville, NY). All components (except the 0–30-kV bias power supply) are in an electrically isolated enclosure. The bias voltage from the variable 30-kV power supply serves as the ground reference for all components. The 0–3-kV pulse voltage for positive ion extraction is connected with ~2 ft of RG-59 cable via a high-voltage vacuum feedthrough to the first source grid, and the variable bias voltage is connected to the second grid. Pulse rise times with this arrangement and the GRX 3.0K pulser (unbiased) were measured to be ~20 ns. In the positive ion mode experiments described here, when the pulser is triggered after a variable delay period relative to ion formation, the increased positive potential on the first source plate repels the ions out of the first source region. They are then accelerated to their final velocity through the second grid region, which is held at a constant potential difference (equal to the bias voltage employed). Although not demonstrated here, negative ion spectra can be generated by the use of a negative polarity biasing supply and interchange of the potentials applied to the first two source grids.

The pulse voltage employed can be varied (0–3 kV) by adjusting an electrically isolated potentiometer. The pulser itself is triggered via a fiber-optic cable and a simple circuit which provides for control of the pulse delay after ion formation and the pulse duration. The pulse duration employed for all experiments was 10 µs, which ensured all of the ions formed had been accelerated out of the ion source. Pulse delays between 320 and 1060 ns were utilized. All events (digitizer and pulser) were triggered from the response of a dc biased silicon pin diode (<1-ns rise time; Model DET2-Si, Thor Labs, Newton, NJ) exposed to a deflected (via a quartz window beam splitter) portion of the

(18) Brown, R. S.; Gilfrich, N. L. *Rapid Commun. Mass Spectrom.* **1992**, *6*, 697–701.

(19) Brown, R. S.; Gilfrich, N. L. *Anal. Chim. Acta* **1991**, *248*, 541–552.

laser beam. Propagation time delays in both the pulser and its trigger circuitry currently prevent investigation of time delays shorter than 320 ns.

Sample Preparation. All proteins and peptides used in these studies were obtained from Sigma Chemical Co. (St. Louis, MO) and used without further purification. All matrices employed were obtained from Aldrich Chemical Co. (Milwaukee, WI) and were also used without further purification. Protein/peptide samples were prepared as 10 μM solutions in distilled, deionized water. Matrix solutions were prepared as 10 mM solutions in 30% (v/v) acetonitrile and 70% distilled, deionized water with 0.1% TFA. These two solutions were mixed in a 2:1 ratio and 2.5 μL (~10 pmol) was applied to a 7-mm^2 stainless steel probe surface and allowed to air-dry. Laser spot size as determined from the image produced on thermal paper applied to the probe tip and inserted into the laser beam focus was approximately 100 μm by 250 μm. The laser power employed for each sample/matrix combination was attenuated via a combination of a fixed concentration dye solution and an adjustable iris aperture, to a point just above the threshold irradiance where a good S/N for the analyte was obtained. The mass spectra presented represent the signal produced (5 ns/point time resolution) and averaged from 50 individual laser shots on a single surface of the sample. Both pulsed and continuous time-of-flight spectra are mass calibrated by a standard two-point linear fit from two known masses.[20]

RESULTS AND DISCUSSION

Several unique experimental aspects of the MALDI process make it an attractive candidate for pulsed ion extraction TOF-MS. For surface-based desorption/ionization techniques such as MALDI, the primary contribution to resolution loss in TOF-MS is the flight time spread caused by ions being produced with different initial velocities. This initial ion velocity distribution is in addition to the constant velocity that the ions of a particular m/z value attain as they are accelerated out of the ion source and into the field-free drift region of the TOF-MS. Ion mirrors correct for this initial velocity distribution by forcing the faster ions to travel a slightly longer angular path to the detector than slower ions of the same m/z value. The result when properly implemented is that ions of the same m/z arrive simultaneously at the detector. With delayed pulsed ion extraction, the initial velocity differences of MALDI-generated ions allow any ions (same m/z) with higher initial velocities to travel further toward the second grid of the ion source than those with lower initial velocities during the initial pulse delay period. When the extraction field is pulsed on, an electrostatic field gradient is established between the two source plates. The slower moving ions will experience a larger electrostatic extraction field than the faster moving ions. This results in the slower moving ions achieving a slightly higher final velocity upon exiting the ion source than those ions which were initially moving faster. By appropriate choice of delay time and pulse voltage amplitude, slower ions can be made to catch up to faster ions exactly at the plane of the detector.

An additional advantage with this type of ion velocity focusing scheme is the fact that MALDI-generated ions have been shown[21] to have very similar velocity distributions that are independent of the mass of the ion. This means that the optimal pulsed voltage to achieve ion arrival time focusing at the detector for a given source bias voltage and ion extraction delay time should be a simple linear function of the m/z of the ion being focused. Given the same initial velocities and velocity spread, ions of different m/z will travel the same distance between the source grids during the initial ion extraction delay period. Thus, ions of different m/z values and the same initial velocity will experience the same potential gradient upon establishment of the extraction field. To optimally correct for this equivalent spatial spread in the ion source, ions with different m/z values will require an optimal extraction potential that is a linear function of an ion's m/z. As will be shown below, this MALDI characteristic allows a predictable adjustment of the pulse amplitude necessary to optimally focus different m/z analyte ions.

In addition to the mass resolution improvement expected from the above ion velocity compensation, some actual decrease in the width of the initial ion velocity distribution might be expected with delayed pulsed ion extraction. Significant ion energy deficits have been observed experimentally[22] for MALDI-generated ions under continuous ion extraction conditions. One possible explanation for this observed ion energy loss involves collisions and an associated kinetic energy exchange between ions and neutrals. Some MALDI models postulate an initially dense laser plume produced early in the desorption event. With continuous ion extraction, significant ion kinetic energy exchange might be occurring though highly energetic ion/neutral collisions early in the desorption event. This would also be expected to broaden the apparent initial velocity distribution of the ions, which would be expected to lower the mass resolution that was obtainable with a linear TOF instrument. If an ion is given some time to expand away from the surface prior to the application of an extraction field, the ion's available kinetic energy for transfer in these early collisions would be greatly limited, thus potentially decreasing the width of the ion's actual velocity distribution. This should lead to an improvement in the obtainable mass resolution for the ion. A combination of these factors is believed to be responsible for the significant mass resolution enhancement with pulsed ion extraction that is demonstrated below.

In order to determine the effectiveness of delayed pulsed ion extraction TOF-MS for mass resolution improvement of MALDI-generated ions, a systematic study of the experimental variables (source bias voltage, ion extraction delay time, pulse voltage amplitude) associated with the technique was conducted. These systematic studies were all performed by utilizing the common MALDI matrix α-cyano-4-hydroxycinnamic acid and the ion source geometry described in the Experimental Section. Laser irradiance was adjusted just above threshold irradiance to ensure that adequate and sustained ion signals would be produced by each sample.

In the first set of experiments, the mass resolution for the singly protonated molecular ion of three different peptides (oxidized B chain of bovine insulin, bovine insulin, bovine ubiquitin) was utilized as a probe for the effect of the applied pulse voltage amplitude on the mass resolution observed at a fixed bias voltage and pulsed delay time. Bias voltages of 15, 20, and 24 kV were utilized along with pulse delays of approximately 300, 600, and 1000 ns (exact delays given in the appropriate figure). The amplitude of the pulse voltage was varied over an appropriate range for each set of fixed conditions to produce an adequate

(20) Beavis, R. C.; Chait, B. T. *Anal. Chem.* **1990**, *62*, 1836–1840.
(21) Beavis. R. C.; Chait, B. T. *Chem. Phys. Lett.* 1991, *5*, 479–484.
(22) Zhou, J.; Ens, W.; Standing, K. G.; Verentchikov, A. *Rapid Commun. Mass Spectrom.* **1992**, *6*, 671–678.

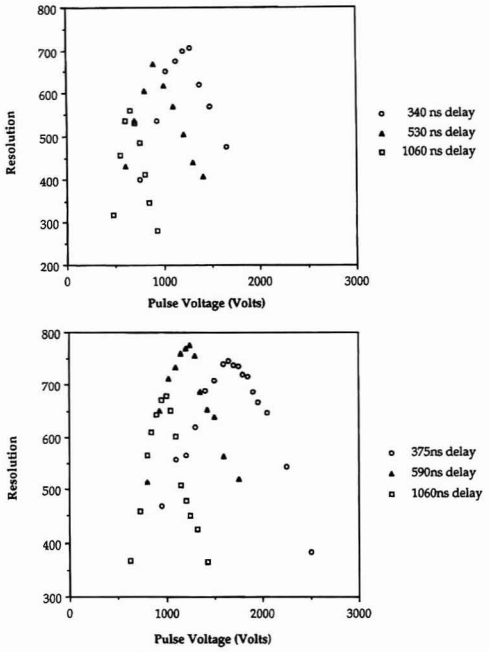

Figure 2. Typical observed mass resolution for the protonated molecular ion of bovine insulin as a function of the applied pulsed voltage at 15 (top) and 24 kV (bottom) source bias voltage and various pulsed extraction delay times.

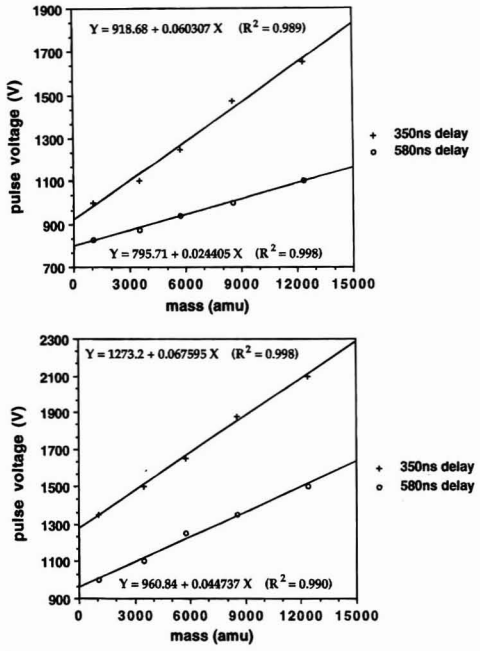

Figure 3. Pulsed voltage required for optimal mass resolution as a function of analyte *m/z* and pulsed delay time employed with 15 (top) and 24 kV (bottom) source bias voltage.

profile of this experimental parameter's effect on mass resolution. For each of the fixed set of experimental conditions (i.e., ion *m/z*, accelerating voltage, and pulse delay time), the pulse voltage employed was varied and the mass resolution ($t/2\Delta t$, fwhm) determined for the average of 10 laser shots on a sample surface. This was repeated for each pulse voltage studied. This entire procedure was repeated for three independently prepared samples, and all results were averaged to produce a series of pulse voltage versus mass resolution graphs for a given probe analyte and source bias voltage.

While the best mass resolution (and the best sensitivity) was obtained in all cases with the highest source bias voltage utilized, the general trends observed were the same for all of the bias voltages studied. For this reason, only representative plots of the data for bovine insulin are presented. Figure 2 (top) demonstrates the dependence of the applied pulse amplitude on the obtained mass resolution for the insulin probe analyte (singly protonated molecular ion) at a 24-kV bias voltage. The three curves shown are the results obtained for the three different pulsed delay times studied. The data in Figure 2 (bottom) is for bovine insulin and a source bias of 15 kV and demonstrates the general effect of the ion source bias voltage on the optimal conditions for mass resolution.

From the above results, along with the additional data from the lower source bias voltage and different probe analyte experiments not shown, the following trends can be discerned. Mass resolution for any given *m/z* ion increases with higher ion source bias voltage and shorter pulse delay times. However, as the pulse delay time is shortened, the bias voltage increased, or both, the pulse voltage amplitude required for optimal mass resolution also increases. If the pulse delay time is increased, a lower pulse voltage can be employed for a given *m/z* ion. This apparent advantage is offset by the fact that a narrower range of *m/z* values will be effectively focused. The maximum obtainable mass resolution for a selected *m/z* ion also decreases somewhat relative to that obtained for the same *m/z* ion with a shorter pulse delay. The reason for this poorer focusing at longer pulse delay times is not immediately evident. It may result from a velocity spread induced by radial expansion of the desorbed ions or be associated with larger extraction field inhomogeneities farther away from the initial grid surface. Utilization of a lower ion source bias voltage also lowers the pulse voltage required for a particular *m/z* ion at any given pulse delay time. However, this is achieved at the expense of sensitivity and mass resolution. For any given set of experimental parameters, the greater the *m/z* of the ion, the higher the pulse voltage needed for optimal mass resolution.

A second set of systematic experiments were performed to examine the mass dependence on the optimal pulse voltage for different delay times. In addition to the previous analyte probes, angiotensin II and cytochrome *c* were included in order to cover the mass range between approximately 1000 and 12 000 Da. For these experiments, the pulse voltage that produced the maximum mass resolution was determined for each sample under various sets of source bias voltage and pulse delay times. Pulse delay times of 350 and 580 ns and ion source bias voltages of 15 and 24 kV were utilized. These data are presented in Figure 3 (top, 15-kV bias voltage; bottom, 24-kV bias voltage). These data can be used to determine the optimum pulse voltage to be used for a given *m/z* analyte ion and a given pulse delay and source bias

voltage. The dependence on mass is extremely linear over the mass range studied and is consistent with the previously discussed property of MALDI and its observed independence of initial ion velocity distribution with analyte mass. While this mass dependence prevents optimum mass resolution improvement from being simultaneously realized for all *m/z* ions generated in a MALDI spectrum under a single set of pulsed extraction conditions, in practice, this is not a problem except for very low *m/z* ions (i.e., matrix ions). For example, if an optimal pulse voltage for cytochrome *c* of 1500 V is employed (580 ns, 24 kV from Figure 3), the expected mass resolution for bovine insulin (Figure 2) would be at least 650. This is a 44% improvement in mass resolution relative to the mass resolution of 450 that can be achieved under optimal continuous ion extraction conditions for bovine insulin with the same instrument and equivalent ion kinetic energies.

If the 24-kV bias voltage plot in Figure 3 is extrapolated to higher *m/z and* assuming the linear trend of the data holds, these results suggest that given the 3.0-kV maximum pulser voltage possible and the shortest currently possible pulse delay time (~350 ns) combined with the maximum current source bias voltage, an upper limit for ion focusing would occur at a *m/z* of a little over 25 000. If the delay was increased to 580 ns, a narrower mass range could be focused up to a *m/z* of approximately ~45 000. Alternatively, a substantially higher extraction field gradient could be developed by simply reducing the pulsed grid spacing to 2 mm. As the maximum residence time of an unaccelerated ion in the (2 mm) region between the first two source grids would be about ~2 μs (estimating ~1000 m/s initial ion velocity), no ions should exit from the pulsed source region during the pulse delays used in these studies. The higher extraction field gradient produced with this grid spacing (i.e., 1500 V/mm instead of 750 V/mm) would be equivalent to a pulse voltage of 6000 V with the current grid spacing and should allow (again by extrapolating the data in Figure 3 to 6000 V) ions with a *m/z* of almost 70 000 to be focused utilizing the shortest (350 ns) pulse delay time. Current sensitivity limitations of our present microchannel plate detector have restricted our initial studies to ions with *m/z* below ~20 000. Future experiments will explore the area of pulsed ion extraction focusing by utilization of a discrete dynode detector.

While the above data was all collected utilizing α-cyano-4-hydroxycinnamic acid as the matrix, it has been found that all of the other common MALDI matrices examined to date have also produced optimized mass resolution with essentially identical focusing parameters as long as laser irradiance is kept somewhere near the threshold for desorption. Even at levels substantially above the desorption threshold, little deterioration in mass resolution is observed with delayed pulsed ion extraction. Some of the matrices examined have included: α-phenyl-4-hydroxycinnamic acid, 2,5-dihydroxybenzoic acid, ferulic acid, sinapinic acid, caffeic acid, 3,4,5-trimethoxycinnamic acid, and 7-hydroxycoumarin. This implies very similar ion velocity distributions are produced from each of these matrices. It also suggests the probability that very similar ion production mechanisms are likely involved with all of these matrices. More detailed studies of pulsed ion extraction with different matrices are currently underway.

The singly protonated molecular ion region for a MALDI mass spectrum of bovine insulin (sinapinic acid matrix) generated under

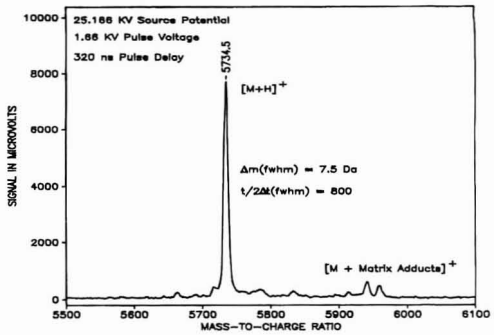

Figure 4. Typical MALDI (sinapinic acid matrix) mass spectrum showing the protonated molecular ion region of bovine insulin obtained with pulsed ion extraction and demonstrating an obtainable mass resolution of 800 (fwhm).

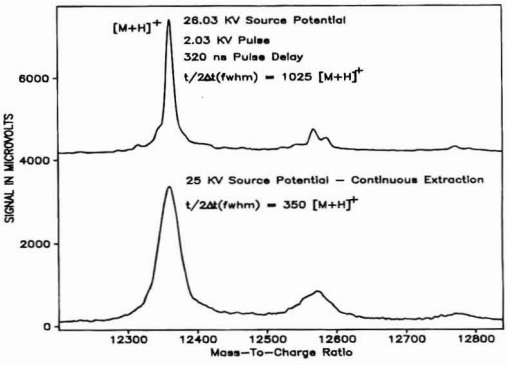

Figure 5. Typical MALDI (sinapinic acid matrix) mass spectra comparing the protonated molecular ion region of cytochrome *c* obtained with pulsed ion extraction (top) versus continuous ion extraction (bottom).

optimized pulsed extracted conditions (24-kV bias voltage, 320-ns delay) is shown in Figure 4. A mass resolution of 800 (fwhm) is easily obtained, and the matrix adduct peaks can be clearly resolved (intact matrix, dehydration of matrix and decarboxylation of matrix). Maximum mass resolution ($t/2\Delta t$, fwhm) with continuous ion extraction (optimal laser fluence near threshold irradiance) for this sample on the same instrument with source bias voltage of 25 kV would typically be 450. Pulsed ion extraction thus produces a 78% improvement in mass resolution over what could optimally be obtained with continuous ion extraction and similar ion kinetic energies. Although not shown, the sensitivity of the technique under conditions that produce the maximum mass resolution is also much better with pulsed ion extraction. This is because higher laser fluence can be utilized with pulsed ion extraction without sacrificing mass resolution as is typically observed with linear TOF-MS.

Even more impressive mass resolution improvement is obtained for cytochrome *c* with delayed pulsed ion extraction (Figure 5, upper mass spectrum) when compared to continuous ion extraction under similar total ion kinetic energies (Figure 5, lower mass spectrum). For the delayed pulsed ion extraction experiment, the singly protonated molecular ion is resolved with a mass resolution ($t/2\Delta t$, fwhm) of 1025. This compares to a mass resolution of only 350 obtained from the identical sample under

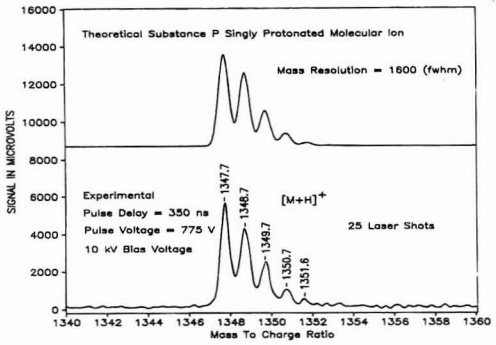

Figure 6. MALDI (sinapinic acid matrix) mass spectrum showing the protonated molecular ion region of substance P obtained with pulsed ion extraction (bottom) and the expected theoretical isotopic distribution (top) at a mass resolution (fwhm) of 1600.

the same laser fluence conditions (near threshold) with the same linear TOF instrument operated in continuous ion extraction mode with a source bias voltage of 25 kV.

Lower m/z ions can also benefit substantially from pulsed ion extraction. Because of the very narrow arrival time distributions for lower m/z ions and the limited time resolution (5 ns/point) of the transient digitizer employed, it is beneficial to utilize a lower ion source bias voltage for small peptides or matrix ions. The resulting lower ion velocities produce longer ion flight times and broader ion arrival time distributions. This means that mass resolution is not as limited by the digitizer's time resolution. By lowering the source bias voltage to only 10 kV, the unit mass isotopic distribution can now be resolved for molecules whose ions have m/z values up to ~2000. This is demonstrated for the protonated molecular ion of the small peptide substance P (Figure 6). The individual isotopic multiplet is now resolved and shows good agreement with the expected theoretical spectrum of the protonated molecular ion calculated for a mass resolution of 1600 (fwhm). It is believed that even higher mass resolution could be obtained with a faster transient digitizer sampling rate and the use of a higher source bias voltage (24 kV).

CONCLUSIONS

Pulsed ion extraction coupled with high ion source bias voltages has been shown to be an effective and simple technique for mass resolution enhancement in MALDI. In the case of larger m/z ions such as cytochrome c, it begins to approach the performance of ion mirror based TOF-MS. Metastable ion decay of larger m/z ions in the field-free drift region, which often limits the obtainable mass resolution in ion mirror based TOF-MS, is not a problem with delayed pulsed ion extraction as long as no postsource acceleration/deceleration fields (such as at the detector) are employed. Our current design has a small (1 mm) −2-kV acceleration region just prior to the detector which produces some signal broadening (slight fronting and tailing observed in Figure 5). This postsource accelerating region can be eliminated by capacitive coupling of the detector's output signal, which would allow the top plate of the dual MCP detector to be biased at the same potential as the particle guide. This modification is planned in the near future as is incorporation of a higher time resolution transient digitizer (500 MS/s).

An aspect of delayed pulsed ion extraction not discussed in the present paper is the ability to observe very rapid (<300 ns) metastable ion decay in the source which occurs during the imposed pulsed extraction delay period. This aspect of pulsed ion extraction will be discussed in detail in a subsequent paper, which will examine the prompt metastable fragmentation of MALDI-generated ions from peptides and proteins, their use for obtaining sequence structural information, and the implications to the ionization processes involved in MALDI of these metastable decay ions. Further improvements in pulsed ion extraction mass resolution enhancement are expected from planned improvements in transient digitizer time resolution and optimization of the ion source geometry. Modifications are also planned to allow investigation of delay times less than 300 ns. This is expected to provide additional improvement in obtainable mass resolution and in the m/z range optimally focused by this technique.

ACKNOWLEDGMENT

The authors greatly acknowledge the assistance of Directed Energy, Inc., both for donation of the initial GRX 3.0K pulser and for helpful discussions with the staff concerning its use for this project. This research was supported, in part, by grants from the National Institutes of Health, Divisions of Research Resources (RR05311) and General Medical (GM47914), and with funds provided by Utah State University.

Received for review January 25, 1995. Accepted April 19, 1995.[⊗]

AC950086S

[⊗] Abstract published in *Advance ACS Abstracts*, June 1, 1995.

Anal. Chem. **1995,** *67,* 2004–2009

Electrospray Liquid Chromatography–Mass Spectrometry of Carotenoids

Richard B. van Breemen

Department of Medicinal Chemistry and Pharmacognosy, College of Pharmacy, University of Illinois at Chicago, 833 South Wood Street, M/C 781, Chicago, Illinois 60612-7231

The first method for electrospray liquid chromatography–mass spectrometry (LC–MS) of carotenoids is reported, which uses a C_{30} reversed-phase HPLC column and a gradient solvent system containing methanol/methyl *tert*-butyl ether/ammonium acetate at a flow rate of 1.0 mL/min. The entire HPLC column effluent passes through a photodiode array absorbance detector and then into the electrospray LC–MS interface without solvent splitting. In this way, maximum sensitivity is achieved for both the photodiode array detector, which records the UV/vis spectra of each carotenoid, and the mass spectrometer, which measures the molecular ions of each carotenoid. Molecular ions, $M^{\cdot+}$, without evidence of any fragmentation, were observed in the electrospray mass spectra of both xanthophylls and carotenes. In order to enhance the formation of molecular ions, solution-phase carotenoid oxidation was carried out by means of postcolumn addition of a halogenated solvent to the HPLC effluent. Several different halogenated solvents were evaluated, including chloroform, 2,2,3,3,4,4,4-heptafluoro-1-butanol, 2,2,3,3,4,4,4-heptafluorobutyric acid, 1,1,1,3,3,3-hexafluoro-2-propanol, and trifluoroacetic acid. Among these halogenated solvents, 2,2,3,3,4,4,4-heptafluoro-1-butanol at a concentration of 0.1% (v/v) was found to produce the best combination of carotenoid molecular ion abundance and reproducibility. The limits of detection for lutein and β-carotene were between 1 and 2 pmol each, which was 100-fold lower than the detection limit of the photodiode array detector signal.

The nutritional importance of certain carotenoids as metabolic precursors of vitamin A in man is well known.[1] Additional functions for carotenoids, including some non-provitamin A carotenoids, have been suggested to include cancer prevention and treatment,[2] immunoenhancers,[3] and in vivo antioxidants.[4] Increased interest in carotenoids, coupled with frequently inadequate analytical determination of these compounds when present in many biological tissues, such as serum, liver, and foods, emphasizes the need for new methods which can positively identify individual carotenoids (see carotenoid structures in Figure 1).

High-performance liquid chromatography (HPLC) is regarded as the preferred method for the separation, identification, and quantitation of carotenoids found in biological tissues.[5] Unfortunately, complex mixtures of carotenoids, many of which are closely related structurally, are often present in biological matrices, rendering unequivocal identification by HPLC using retention and fixed wavelength data alone unacceptable. The advent of photodiode array detection, allowing for continuous collection of spectral data during HPLC analysis, has provided a powerful tool for carotenoid research.[5] However, tentative identification of carotenoids using HPLC with photodiode array detection requires retention time measurement, complete chromatographic resolution of absorbing species so that spectrophotometric data for the analyte alone are observed, and comparison of UV/vis spectra and retention times with those of authentic standards. Mass spectrometric and tandem mass spectrometric analyses,[6] which provide molecular weight and characteristic fragmentation pat-

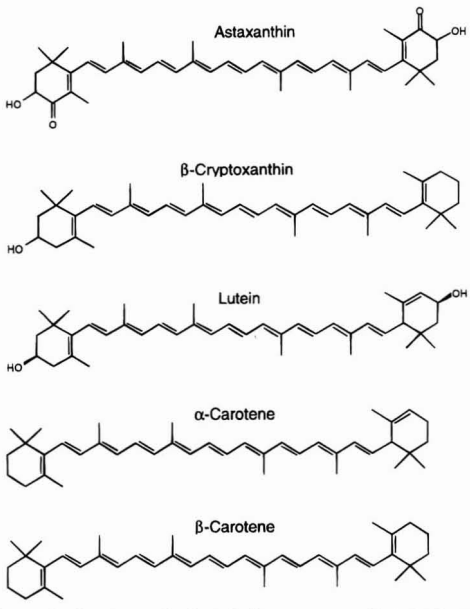

Figure 1. Structures of selected all-trans carotenoids including the xanthophylls astaxanthin, β-cryptoxanthin, and lutein and the carotenes α-carotene and β-carotene.

(1) Sporn, M. B.; Clamon, G. H.; Dunlop, N. M.; Newton, D. L.; Smith, J. M.; Saffiotti, U. *Nature (London)* **1975,** *253,* 47–50.
(2) Ziegler, R. G. *Am. J. Clin. Nutr.* **1991,** *53,* S251–S259.
(3) Bendich, A.; Olson, J. A. *FASEB J.* **1989,** *3,* 1927–1932.
(4) Malone, W. F. *Am. J. Clin. Nutr.* **1991,** *53,* S305–S313.
(5) Taylor, R. F.; Farrow, P. E.; Yelle, L. M.; Harris, J. C.; Marenchic, I. G. In *Carotenoids: Chemistry and Biology;* Krinsky, N. I., et al., Eds.; Plenum Press: New York, 1990; pp 105–123.
(6) van Breemen, R. B.; Schmitz, H. H.; Schwartz, S. J. *J. Agric. Food Chem.* **1995,** *43,* 384–389.

0003-2700/95/0367-2004$9.00/0 © 1995 American Chemical Society

terns, may then provide final confirmation of individual carotenoid identities when used in conjunction with retention and spectral characteristics.[7]

Several ionization methods have been reported for mass spectrometric analysis of carotenoids, including electron impact[8] and fast atom bombardment (FAB).[9] Electron impact requires sample vaporization prior to ionization, which is a disadvantage in the analysis of the thermally labile and nonvolatile carotenoids. Recently, a positive ion electrospray mass spectrum of β-carotene was obtained by Van Berkel and Zhou[10] using solution-phase oxidation, which showed a doubly charged molecular ion and $[M^{2+} - H^+]^+$. However, electrospray LC–MS was not demonstrated in their investigation.[10]

Previous reports from our own laboratory and others exploring the application of LC–MS to carotenoid analysis used a heated moving belt interface with electron impact ionization,[5] a particle beam interface with chemical ionization and a heated ion source,[11] or continuous-flow FAB mass spectrometry.[7,12] Among these methods, only continuous-flow FAB does not require the use of gas-phase ionization or a heated ion source, which might lead to carotenoid pyrolysis. However, the flow rate of continuous-flow FAB is limited to <10 μL/min, so capillary HPLC columns must be used or solvent splitting of the analytical scale HPLC effluent must be carried out prior to mass spectrometric analysis. In the present investigation, we report development of an electrospray LC–MS method that is compatible with analytical scale HPLC column flow rates of 1.0 mL/min. Furthermore, compatibility of this new electrospray LC–MS method will be demonstrated with the C_{30} reversed-phase HPLC stationary phase recently engineered by Sander et al.[13] for the separation of carotenoids and carotenoid isomers.

EXPERIMENTAL SECTION

Mass spectra were obtained using a Hewlett-Packard (Palo Alto, CA) 5989B MS engine quadrupole mass spectrometer equipped with a ChemStation data system and high-flow (i.e., 1 mL/min) pneumatic nebulizer-assisted electrospray LC–MS interface. The mass spectrometer was interfaced to a Hewlett-Packard 1090L gradient HPLC system equipped with an autoinjector and a photodiode array UV/vis absorbance detector. The quadrupole analyzer was maintained at 120 °C, and unit resolution was used for all measurements. Nitrogen at a pressure of 80 psi was used for nebulization of the HPLC effluent, and nitrogen bath gas at 350 °C and a flow rate of 1.0 L/min was used for evaporation of solvent from the electrospray. The electrospray needle was maintained at ground potential, while the counterelectrode was at −5100 V. The range *m/z* 200–610 was scanned over ~2 s during LC–MS.

HPLC separations were carried out using a reversed-phase column, 4.6 mm × 12.5 cm, containing a C_{30} silica stationary phase, which was engineered specifically for carotenoid separations.[13] The solvent system consisted of a 60 min linear gradient from 85:15 to 10:90 methanol/methyl *tert*-butyl ether containing 1.0 mM ammonium acetate at a flow rate of 1 mL/min. Absorbance spectra were recorded from 250 to 600 nm using a photodiode array detector located in-line between the HPLC column and the electrospray LC–MS interface. Based on the method of Van Berkel and Zhou,[10] carotenoids were oxidized in solution by postcolumn addition of methanol/methyl *tert*-butyl ether solution (50:50 v/v) containing a halogenated oxidant (i.e., 2% v/v 2,2,3,3,4,4,4-heptafluoro-1-butanol) at a flow rate of 50 μL/min. Optimization experiments were carried out in which different halogenated compounds at various concentrations were evaluated.

During some experiments, flow injection of carotenoid solutions was used in combination with selected ion monitoring, in order to measure the abundance of $M^{\bullet+}$ ions, such as *m/z* 536 for β-carotene or *m/z* 568 for lutein. The selected ion monitoring dwell time was 100 ms/ion. Carotenoid standards were injected using a Rheodyne (Cotati, CA) Model 7725 injector equipped with a custom-made 1.5 μL fused silica capillary sample loop that was completely filled for each injection. An Applied Biosystems (Foster City, CA) Model 140A dual syringe HPLC pump was used for delivery of methanol (or acetonitrile)/methyl *tert*-butyl ether (70:30 v/v) containing the appropriate halogenated oxidant (typically 0.1% v/v 2,2,3,3,4,4,4-heptafluoro-1-butanol) during flow injection measurements at a flow rate of 5 or 10 μL/min. Other carrier solvents investigated included methanol/methyl *tert*-butyl ether/water (containing 10 mM ammonia or 0.1% v/v glacial acetic acid) (50:46:4 v/v/v) or methanol/ethyl acetate/water (with or without 10 mM sodium acetate) (30:69:1 v/v/v).

HPLC solvents were purchased from Fisher Scientific (Springfield, NJ). The halogenated compounds chloroform, 2,2,3,3,4,4,4-heptafluoro-1-butanol, 2,2,3,3,4,4,4-heptafluorobutyric acid, 1,1,1,3,3,3-hexafluoro-2-propanol, and trifluoroacetic acid were reagent grade or HPLC grade and were obtained from Aldrich Chemical Co. (Milwaukee, WI). Lutein, α-carotene, and β-carotene standards were purchased from Sigma Chemical Co. (St. Louis, MO) and purified as necessary by using HPLC, and the purity of each standard was confirmed by using HPLC with photodiode array absorbance detection. Standard solutions of lutein, α-carotene, and/or β-carotene with concentrations up to 25 ng/mL were prepared in methyl *tert*-butyl ether/methanol (or acetonitrile) (50:50 v/v). Processed, canned sweet potatoes were extracted and prepared in an analogous manner to carrot and tomato extracts, which was previously described.[7]

RESULTS AND DISCUSSION

In order to develop an electrospray liquid chromatography–mass spectrometry (LC–MS) method, flow injection analyses were carried out to determine suitable electrospray parameters and mobile phase composition. Initially, negative ion electrospray mass spectra were obtained while flow-injecting carotenoids into a solution of methanol, methyl *tert*-butyl ether, and water. Under these conditions, deprotonated molecules of polar xanthophylls such as astaxanthin at *m/z* 595 were observed, but no signals were detected for the hydrocarbon carotenes (see carotenoid structures in Figure 1). Addition of ammonia to the carrier solution increased the abundance of deprotonated xanthophyll molecules, but no carotene ions were observed.

Positive ion electrospray mass spectrometry of carotenoids was investigated using a mobile phase containing methanol, ethyl acetate, and water. Protonated molecules and traces of sodium

(7) Schmitz, H. H.; van Breemen, R. B.; Schwartz, S. J. *Methods Enzymol.* **1992**, *213*, 322–336.
(8) Vetter, W.; Meister, W. *Org. Mass Spectrom.* **1985**, *20*, 266.
(9) Caccamese, S.; Garozzo, D. *Org. Mass Spectrom.* **1990**, *25*, 137–140.
(10) Van Berkel, G. J.; Zhou, F. *Anal. Chem.* **1994**, *66*, 3408–3415.
(11) Khachik, F.; Beecher, G. R.; Goli, M. B.; Lusby, W. R.; Smith, J. C., Jr. *Anal. Chem.* **1992**, *64*, 2111–2122.
(12) van Breemen, R. B.; Schmitz, H. H.; Schwartz, S. J. *Anal. Chem.* **1993**, *65*, 965–969.
(13) Sander, L. C.; Sharpless, K. E.; Craft, N. E.; Wise, S. A. *Anal. Chem.* **1994**, *66*, 1667–1674.

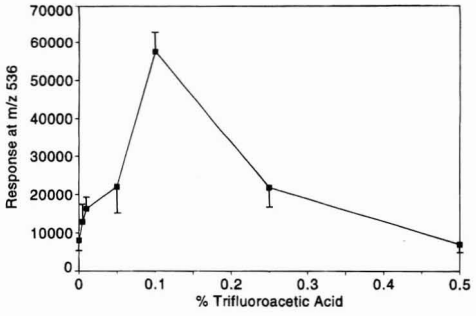

Figure 2. Optimization of trifluoroacetic acid content during solution-phase oxidation of β-carotene. The abundance of the molecular ion of β-carotene (0.25 μg/injection) was monitored at *m/z* 536 during flow injection positive ion electrospray mass spectrometry. The carrier solvent was acetonitrile/methyl *tert*-butyl ether (70:30 v/v) at 10 μL/min. Each data point represents the average of at least three measurements (± standard deviation).

adducts were observed for xanthophylls but not carotenes. Acidification of the solution by addition of acetic acid slightly increased the abundance of protonated molecules, but sodium adducts were still observed. When sodium acetate was added to the mobile phase instead of acetic acid, no protonated molecules were observed; instead, abundant $[M + Na]^+$ ions were detected for xanthophylls such as astaxanthin (Figure 1). Because carotenes lack any heteroatoms such as oxygen to which protons or sodium cations might attach, no ions were detected for these hydrocarbons during electrospray under these conditions.

In order to ionize carotenes such as β-carotene during electrospray LC–MS, trifluoroacetic acid was added postcolumn to the mobile phase in order to carry out solution-phase oxidation as described by Van Berkel and Zhou.[10] Although Van Berkel and Zhou observed doubly charged molecular ions and $[M - H]^+$ species during solution-phase oxidation of β-carotene, only molecular ion radicals, $M^{\bullet+}$, were observed for the carotenoids investigated during the present investigation. The primary differences between these two studies were the composition of the mobile phase and the use of a quadrupole instead of an ion trap mass spectrometer. Previously,[10] methylene chloride was used as the carrier solvent for flow injection electrospray mass spectrometry, which might have been at least partly responsible for oxidation of β-carotene to a doubly charged molecular ion. Methanol and methyl *tert*-butyl ether were used instead of methylene chloride in the present LC–MS study for optimum carotenoid chromatography using the C_{30} silica HPLC column developed by Sander et al.[13] Because molecular ions, $M^{\bullet+}$, were preferred over doubly charged species or $[M - H]^+$ ions, no further attempts were made to reproduce the results of Van Berkel and Zhou.[10]

A range of trifluoroacetic acid concentrations, including 0.01%, 0.02%, 0.05%, 0.1%, 0.25%, and 0.5%, were evaluated for the solution-phase oxidation of β-carotene, and the most effective composition was found to contain 0.1% trifluoroacetic acid (v/v) (see Figure 2). The highest level of trifluoroacetic acid investigated, 0.5%, was as ineffective as no trifluoroacetic acid at all, which suggested that the electrospray was not forming efficiently in the presence of higher concentrations of trifluoroacetic acid,[14] β-carotene ions were being quenched in the gas phase by trifluoroacetic acid, or β-carotene ions could not evaporate from charged droplets containing high concentrations of acid. As the conductivity of the mobile phase increases with increasing concentrations of trifluoroacetic acid, the "Taylor cone" from which charged droplets are emitted can become unstable so that sensitivity decreases.[14] This source of interference with the formation of a stable electrospray might account for the loss of sensitivity at 0.25% and 0.5% trifluoroacetic acid compared to lower concentrations of acid.

Because molecular ions of β-carotene were observed in the absence of solution-phase oxidants such as trifluoroacetic acid, the electrospray process itself was shown to contribute to the oxidation and ionization of β-carotene. Electrospray ionization of neutral carotenoids probably occurs by electrophoretic charging and field ionization at the metal–liquid interface of the electrospray capillary, as described by Blades et al.[15] In this manner, the electrospray interface may be viewed as an electrolytic cell. The formation of carotenoid molecular ions by electrochemical oxidation is also similar to oxidation of metallocenes reported by Xu et al.,[16] who concluded that formation of metallocene ions occurred either in solution or at the needle–solution interface. Like in the electrospray mass spectra of carotenoids reported here, Xu et al. observed primarily molecular ions, $M^{\bullet+}$, and no doubly charged ions. Although Xu et al. found that addition of trifluoroacetic acid had no effect upon formation of metallocene ions,[16] carotenoid ionization was enhanced by the addition of trifluoroacetic acid, as described by Van Berkel et al.[10,17]

In order to determine what properties of trifluoroacetic acid were important for the formation of molecular ions of carotenoids during electrospray and to possibly identify a superior halogenated oxidant for this application, several other halogenated solvents were investigated as solution-phase oxidants, including chloroform, 2,2,3,3,4,4,4-heptafluorobutyric acid, 2,2,3,3,4,4,4-heptafluoro-1-butanol, and 1,1,1,3,3,3-hexafluoro-2-propanol. A comparison of the abundances of β-carotene molecular ions at two different concentrations of each solution-phase oxidant is shown in Figure 3. Acidification of the solution with 0.1% acetic acid resulted in no molecular ion formation, so the acidity of trifluoroacetic acid was probably not beneficial for oxidation and ionization of β-carotene. A comparison of heptafluorobutyric acid and heptafluorobutanol (Figure 3) also shows that the presence of the carboxylic acid group in the oxidant does not contribute to and probably suppresses the ionization of β-carotene. Among the oxidants evaluated, hexafluoropropanol and heptafluorobutanol facilitated production of the most abundant molecular ions of β-carotene.

Because heptafluorobutanol at either 0.1% or 0.5% produced abundant molecular ions of β-carotene with high reproducibility (see standard deviations of the measurements in Figure 3), the optimum concentration of this oxidant was determined, and the results are shown in Figure 4. A plateau of maximum molecular ion formation of β-carotene was reached from 0.02% to 0.25% heptafluorobutanol (Figure 4). All subsequent electrospray analyses of carotenoids were carried out using heptafluorobutanol at

(14) Eshraghi, J.; Chowdhury, S. K. *Anal. Chem.* **1993**, *65*, 3528–3533.
(15) Blades, A. T.; Ikonomou, M. G.; Kebarle, P. *Anal. Chem.* **1991**, *63*, 2109–2114.
(16) Xu, X.; Nolan, S. P.; Cole, R. B. *Anal. Chem.* **1994**, *66*, 119–125.
(17) Van Berkel, G. J.; McLuckey, S. A.; Glish, G. L. *Anal. Chem.* **1992**, *64*, 1586–1593.

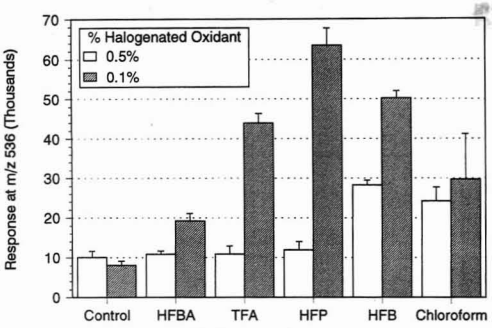

Figure 3. Comparison of halogenated solvents as oxidants during positive ion electrospray mass spectrometry of β-carotene. Selected ion monitoring was used to measure the abundance of the molecular ion of β-carotene (0.25 μg) introduced by flow injection into a solution of acetonitrile/methyl *tert*-butyl ether (70:30 v/v). Each value represents the average of three measurements (± standard deviation).

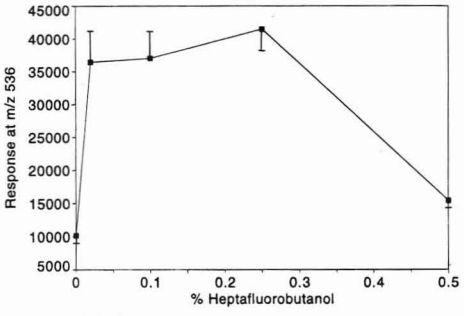

Figure 4. Optimization of heptafluorobutanol content during solution-phase oxidation of β-carotene. Using selected ion monitoring, the abundance of the molecular ion of β-carotene (0.25 μg/injection) was monitored at *m/z* 536 during flow injection positive ion electrospray mass spectrometry. The carrier solvent was acetonitrile/methyl *tert*-butyl ether (70:30 v/v) at 10 μL/min. Each data point represents the average of at least three measurements (± standard deviation).

0.1% (the middle of the plateau region in Figure 4) as the solution-phase oxidant.

The limit of detection of positive ion electrospray mass spectrometry for carotenoid analysis was determined using the xanthophyll, lutein, and the carotene, β-carotene, as standards (Figure 5). Because the electrospray mass spectra of lutein and β-carotene (and all other carotenoids used in this study) contained no fragment ions, selected ion monitoring was carried out of the molecular ions at *m/z* 568 and 536, respectively. Serial dilutions of each carotenoid were prepared and flow-injected. The limits of detection of lutein and β-carotene were determined to be between 1 and 2 pmol (Figure 5). These limits of detection are comparable to those obtained of continuous-flow FAB, which were reported to be ~9.0 and 28 pmol for lutein and α-carotene, respectively.[12] Note that the continuous-flow FAB detection limits were determined using an HPLC column while scanning the mass spectrometer, whereas the electrospray detection limit was measured using flow injection with selected ion monitoring.

Although acetonitrile and methyl *tert*-butyl ether were used as cosolvents during the limit of detection measurements with the expectation that protic solvents might interfere with ionization and should be avoided, substitution of methanol for acetonitrile

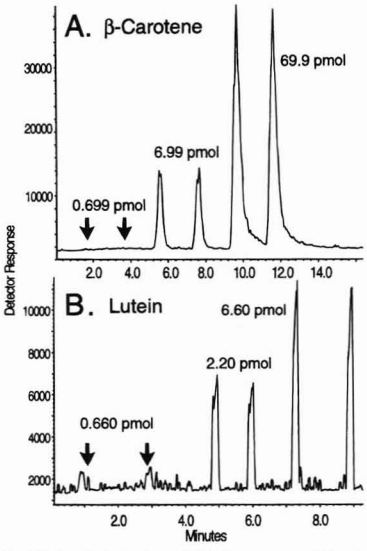

Figure 5. Limits of detection of (A) β-carotene, $M^{\cdot+}$ at *m/z* 536, and (B) lutein, $M^{\cdot+}$ at *m/z* 568, using positive ion electrospray mass spectrometry with selected ion monitoring. After serial dilution, 1.5 μL aliquots of each standard were flow-injected into a solution of acetonitrile/methyl *tert*-butyl ether/heptafluorobutanol (70:30:0.1 v/v/v) at 10 μL/min.

produced similar limits of detection. This result is consistent with those of Xu et al.,[16] who found that protic solvents did not interfere with metallocene ionization during electrospray. In contrast, Van Berkel et al.[17] reported that protic and/or nucleophilic solvents such as methanol would quench molecular ions and should be avoided. Because gradients of methanol to methyl *tert*-butyl ether produced carotenoid separations that were superior to those obtained with gradients using acetonitrile, methanol was used in all LC–MS analyses using the C_{30} reversed-phase column.

The LC–MS analysis of a mixture of α-carotene and β-carotene standards (20 ng each) is shown in Figure 6. Both the electrospray mass spectrometer and the photodiode array absorbance detector detected the all-trans isomers of α- and β-carotene (Figure 6 panels A and B). However, only the mass spectrometer detected the cis isomers eluting between 8–10 and 13–14 min. Compared to the absorbance chromatogram at 450 nm, the signal-to-noise ratio was considerably higher in the computer reconstructed mass chromatogram of the molecular ions at *m/z* 536. The mass spectrum of α-carotene, which was recorded at an elution time of 10.8 min, contained an abundant molecular ion at *m/z* 536 and no fragment ions (see mass spectrum in Figure 6C).

Next, an extract of heat processed, canned sweet potatoes was analyzed by using electrospray LC–MS. When ~20 ng of β-carotene was injected onto the C_{30} reversed-phase HPLC column, a mixture of cis and trans isomers of β-carotene was chromatographically resolved and detected by positive ion electrospray mass spectrometry (see the computer reconstructed mass chromatogram in Figure 7A). However, only the more abundant all-trans isomers were detected during the same analysis using the on-line photodiode array absorbance detector (Figure 7D). When 100-fold more sample was injected onto the HPLC column, the absorbance chromatogram resembled the reconstructed mass

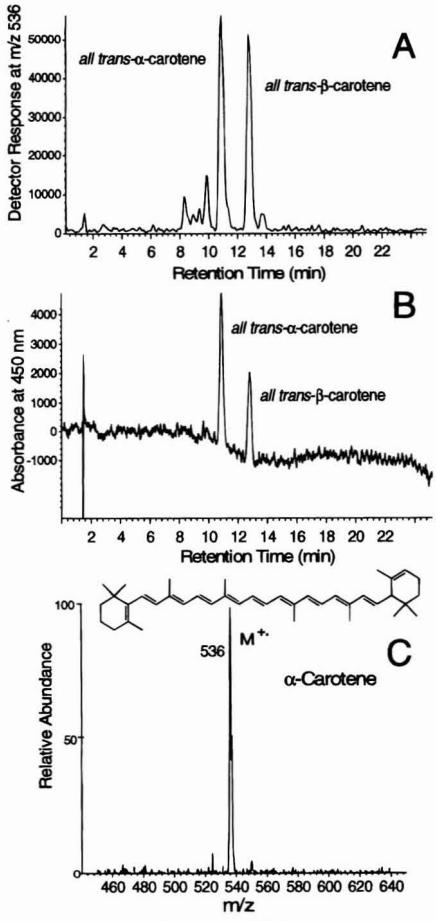

Figure 6. Positive ion electrospray LC–MS analysis of a mixture of α-carotene and β-carotene (20 ng each) using a C_{30} reversed-phase HPLC column with postcolumn addition of heptafluorobutanol as oxidant. (A) Computer-reconstructed mass chromatogram of the molecular ions at *m/z* 536. (B) Absorbance chromatogram at 450 nm recorded on-line using a photodiode array detector. (C) Electrospray mass spectrum of α-carotene recorded at a retention time of 10.8 min.

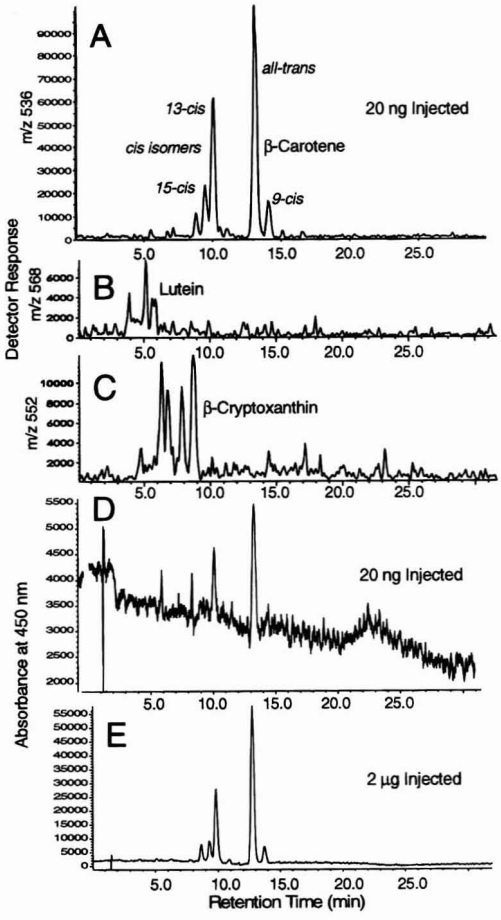

Figure 7. Positive ion electrospray LC–MS analysis of an extract of heat-processed, canned sweet potatoes using a C_{30} reversed-phase HPLC column with postcolumn addition of heptafluorobutanol. (A) Computer-reconstructed mass chromatogram of the β-carotene molecular ion at *m/z* 536 following injection of ~20 ng of extract. (B) Computer-reconstructed mass chromatogram of the ion at *m/z* 568 corresponding to lutein. (C) Computer-reconstructed mass chromatogram of *m/z* 552 showing isomers of β-cryptoxanthin. (D) HPLC photodiode array detector absorbance chromatogram at 450 nm recorded on-line during the analysis shown in (A). (E) HPLC absorbance chromatogram for the analysis of 2 μg of sweet potato extract.

chromatogram with respect to signal-to-noise and detection of the cis isomers (Figure 7E). Therefore, the sensitivity of electrospray mass spectrometry for the detection of carotenoids was found to be ~100-fold higher than that of the photodiode array detector used during this investigation. Although β-carotene was the most abundant carotenoid in the sweet potato extract, molecular ions corresponding to other more polar carotenoids were detected at lower abundance, including ions of *m/z* 568 and 552 which probably corresponded to isomers of lutein and β-cryptoxanthin (see Figure 7, parts B and C). Because no corresponding absorbance spectra for these compounds could be obtained at this concentration using the photodiode array detector, the assignment of these structures is based only on HPLC retention times and molecular weight.

CONCLUSIONS

Although negative ion electrospray mass spectrometry may be used to detect polar xanthophylls, positive ion electrospray LC–MS was shown to be useful for the analysis of both xanthophylls and carotenes. Molecular ions, $M^{\cdot+}$, were observed for all carotenoids investigated, and the mechanisms of ionization included solution-phase oxidation using heptafluorobutanol and electrophoretic charging and field ionization at the metal–liquid interface. This electrospray LC–MS method is compatible with solvents used for the C_{30} reversed-phase HPLC column and can be used on-line with photodiode array absorbance detection for additional characterization of carotenoids eluting from the HPLC column. Because no solvent splitting of the 1 mL/min HPLC

effluent is necessary, postcolumn band broadening is minimized.

ACKNOWLEDGMENT

Alexander Schilling and Steven Fischer provided fruitful discussions and technical assistance with mass spectrometry. Use of the electrospray mass spectrometer was generously provided by the Hewlett-Packard Co. The C_{30} HPLC column was a gift from Lane Sander of the National Institute of Science and Technology.

Received for review December 12, 1994. Accepted April 19, 1995.[⊗]

AC9411987

[⊗] Abstract published in *Advance ACS Abstracts,* June 1, 1995.

Anal. Chem. **1995,** *67,* 2010–2014

A Capillary Cartridge with an On-line Desalting Device That Allows Fast Sampling for Capillary Isoelectric Focusing

Jiaqi Wu† and Janusz Pawliszyn*

Department of Chemistry, University of Waterloo, Waterloo, Ontario, Canada N2L 3G1

The capillary isoelectric focusing (CIEF) cartridge uses a 4 cm long, 75 μm i.d., 150 μm o.d. capillary. The two ends of the capillary are connected to two pieces of 3 mm long, 150 μm i.d., 170 μm o.d. dialysis hollow fibers. These pieces are inserted into electrolyte reservoirs attached to the two ends of the capillary. The fibers isolate the sample solution inside the capillary from the electrolytes in the reservoirs but allow small ions to pass freely, so that the isoelectric focusing process can take place normally inside the capillary. With this cartridge, samples can be injected conveniently and quickly from one end of the capillary. After the sample injection, the separation voltage is turned on and the focusing process begins. When the cartridge is combined with a real-time, on-line absorption imaging detector, the analysis time of the instrument for a sample is only 4 min, including sample injection. The analysis time can be further reduced to about 30 s by using a 1 cm long capillary as the separation column. To preserve the fast speed of this CIEF instrument, a fast, on-line desalting and carrier ampholyte mixing device using a dialysis hollow fiber was also designed. Protein samples 1–10 μL in volume can be desalted and mixed with carrier ampholytes and injected into the separation column in an on-line fashion in 2 min. The new CIEF-desalting device was also developed with multiple capillaries, which increases the sample throughput of the CIEF method. A three capillary cartridge was constructed and tested. Total analysis time for three samples in the three capillaries is only 5 min.

Capillary isoelectric focusing (CIEF) is becoming recognized as a powerful separation technique for proteins and peptides due to its fast separation speed and ease of use for quantitative determination.[1] Until now, most applications of CIEF have used commercial capillary electrophoresis (CE) instruments. These instruments have a 20–60 cm long capillary and an on-column UV absorption detector. When these instruments are used for CIEF, all protein zones separated by the focusing process must be moved through the detection point of the on-column detector located at one end of the capillary. Isoelectric focusing can be done in commercial CE instruments by a two-step method or a one-step method.

In the two-step method, the capillary inner wall is coated with non-cross-linked acrylamide to eliminate electroosmotic flow.[2] The capillary is first filled with a mixture of sample and carrier ampholytes, and two electrolyte reservoirs connected to the capillary ends are filled with anolyte and catholyte, respectively. A dc voltage is then applied across the capillary. After the focusing process, all protein zones are stationary inside the capillary. Finally, a mobilization process is used to move all these zones through the detection point. Mobilization can be achieved by using hydrodynamic force[2] or adding salts[2,3] to one end of the capillary column.

In the one-step method, an uncoated capillary is used as the separation column. A plug of sample and carrier ampholytes solution is introduced into the capillary between anolyte and catholyte. Additives, such as methylcellulose, are mixed into sample and electrolyte solutions to increase viscosity of the solution and reduce the electroosmotic flow.[4,5] Upon application of a dc voltage, protein components are focused inside the capillary, while the whole volume of solutions inside the capillary is mobilized slowly from the anodic end to the cathodic end.

The one-step method appears to have advantages over the two-step method since it overcomes many problems of the two-step method, such as the blind section in the capillary[3] and the instability of the coating on the capillary inner wall.[4] The one-step method is more compatible with current commercial CE instruments. However, CIEF performed in commerical CE instruments using the mobilization process has problems. Mobilization causes uneven resolution along the capillary column and makes the pH gradient nonlinear so that isoelectric point (pI) values of protein samples are difficult to estimate from their elution times. The mobilization process lengthens analysis time, since focusing takes 2–6 min, while mobilization usually takes 10–30 min.[3–5] During the whole process, all protein zones remain focused at the positions where their pI values are the same as the pH values.[3–5] Keeping proteins at high concentration and in a state of zero net charge for a long time increases their chance of precipitation. In the one-step CIEF method, concentrations of carrier ampholytes and additives, capillary length, and sample plug length have to be optimized to adjust the mobilization speed in order to obtain the best resolution for different samples.[4,5]

All these problems associated with the mobilization process can be overcome simply by eliminating the process. This can be

† Present address: SCIEX, 55 Glen Cameron Road, Thornhill, Ontario, Canada L3T 1P2.

(1) Wehr, T.; Zhu, M.; Rodriguez, R.; Burke, D.; Duncan, K. *Am. Biotechnol. Lab.* **1990**, *8*, 22–29.
(2) Hjerten, S.; Zhu, M. *J. Chromatogr.* **1985**, *346*, 265–270.
(3) Zhu, M.; Rodriguez, R.; Wehr, T. *J. Chromatogr.* **1991**, *559*, 479–488.
(4) Mazzeo, J. R.; Krull, I. S. *Anal. Chem.* **1991**, *63*, 2852–2857.
(5) Thormann, W.; Caslavska, J.; Molteni, S.; Chmelik, J. *J. Chromatogr.* **1992**, *589*, 321–327.

0003-2700/95/0367-2010$9.00/0 © 1995 American Chemical Society

accomplished by using an on-line, real-time imaging detector to replace the on-column detectors. In our laboratory, several imaging detection systems have been developed for CIEF: a universal refractive index gradient imaging detector,[6,7] an optical absorption imaging detector,[7,8] and a fluorescence imaging detector.[9] To accommodate an imaging detector system in the CIEF instrument, short capillaries, 4 cm long, were employed. Isoelectric focusing performed in the 4 cm long capillaries showed the same resolution as for CIEF performed in 20–60 cm long capillaries.[7] Analyzing a protein sample takes only 2–4 min using the imaging detection system. Isoelectric points of components can be determined directly from their positions along the capillary column. The CIEF imaging detector system was also developed into a multichannel separation and detection method,[10,11] which overcomes the low sample throughput problem of conventional CIEF. This fast and high throughput separation technique would benefit from a fast method for sample preparation and injection.

The sample injection procedure of the CIEF imaging detector instruments follows. The mixture of sample and carrier ampholytes are first forced into the capillary with a syringe, and then both electrolyte reservoirs connected to the two ends of the capillary are filled with anolyte and catholyte, respectively. Skill is required to ensure that no bubbles are inside the capillary and the sample solution inside the capillary is not mixed with the electrolytes in the reservoirs.[7] Each time a sample is changed, both electrolytes in the two reservoirs also must be changed. This sampling procedure takes 2–5 min for one capillary instruments.

To simplify the sample injection procedure, in our laboratory a new capillary cartridge was designed that has sections of dialysis hollow fibers to isolate the sample solution inside the capillary from the electrolytes in the reservoirs. With this new cartridge, samples can be continuously injected into the capillary without changing electrolytes. The injection procedure is fast and can be automated, which is especially advantageous for a cartridge holding multiple capillaries. When this cartridge is combined with the imaging detector, the total analysis time for samples in three capillaries, including the sampling procedure, is only 4 min. The sampling volume of this fast CIEF instrument is less than 0.5 μL.

Sample preparation for CIEF separation usually includes desalting and mixing samples with carrier ampholytes. A high concentration of salt will distort or even destroy the linear pH gradient during the focusing process.[3] An ideal method of sample preparation for CIEF would be to use an on-line desalting, carrier ampholytes mixing device which can handle samples with volumes of 1–10 μL. We designed a desalting, carrier ampholytes mixing device for our CIEF imaging detector instrument. This on-line device is also based on dialysis hollow fibers.

In this paper, the construction of the new capillary cartridge and the on-line desalting, carrier ampholytes mixing device will be described, and preliminary results of their application will be discussed.

EXPERIMENTAL SECTION

Instrumental Procedure. The configuration of the capillary cartridge, as shown in Figure 1, is similar to that used in previous

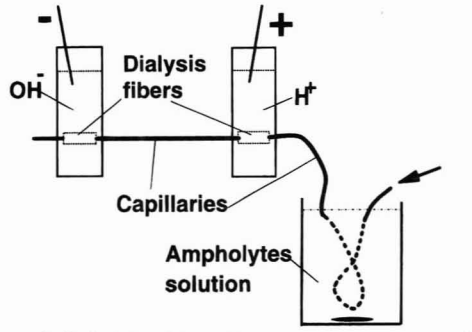

Figure 1. Basic design of the capillary cartridge with dialysis hollow fibers and the on-line desalting, carrier ampholyte mixing device.

experiments.[7] The separation column is a 4 cm long, 75 μm i.d., 150 μm o.d. silica capillary (Polymicro Technologies, Tucson, AZ). The coatings on the outside of the capillary were removed for detection. The capillary inner wall was coated with non-cross-linked acrylamide to eliminate electroosmotic flow by the reported way.[2] The two ends of the capillary are connected to two pieces of 3 mm long dialysis hollow fiber membranes (Spectrum Medical Industries, Inc., Los Angeles, CA). The i.d. of the fiber is 150 μm, and the o.d. is 170 μm. Its molecular weight cutoff value is 9000. The two sections of fiber are inserted into the two electrolyte reservoirs, one filled with anolyte, 10 mM H_3PO_4, and the other catholyte, 20 mM NaOH.

As shown in Figure 1, the desalting device consisted of a 10 cm long dialysis fiber immersed in a 100 mL breaker containing 4% carrier ampholytes solution. One end of the fiber was connected to the inlet of the separation column through a 75 μm i.d. capillary, and the other end was connected to a syringe pump. Protein samples were injected into the separation column through the desalting device.

The detection system is an absorption imaging detector using a CCD camera. The design of the detector was explained in a previous paper.[11] A monochromatic light beam at 410 nm was obtained by passing the light beam from a tungsten lamp through a 410 nm, 40 nm bandpass filter. The light beam was directed through the capillary column by a bundle of 300, 200 μm o.d. optical fibers.

Reagents. All chemicals were reagent grade. Hemoglobin samples (Hemo AFSC, Hemo AA_2, and Hemo AS) were purchased from Helena Laboratories (Beaumont, TX). Horse myoglobin and carrier ampholytes (Pharmalyte 3–10) were obtained from Sigma Chemical Co. Solutions were prepared in deionized water and filtered using 0.2 μm pore size cellulose acetate filters (Sartorius, Gottingen, Germany) prior to use.

Desalting and Isoelectric Focusing Process. First, the two reservoirs at the two ends of the capillary column were filled with anolyte and catholyte, respectively, and sample was pumped into the desalting device. The carrier ampholytes solution in the 100 mL beaker was stirred by a magnetic stir bar. Small salt molecules in the sample were washed away through the wall of the dialysis hollow fiber in the beaker, and at the same time small carrier ampholyte molecules (molecular weights less than 3000) were added to the sample through the wall of the fiber. The flow rate was adjusted to about 1 μL/min. A 500 V dc voltage was applied to the two reservoirs, and current passing through the separation

(6) Wu, J.; Pawliszyn, J. *Anal. Chem.* **1992**, *64*, 224–227.
(7) Wu, J.; Pawliszyn, J. *Anal. Chem.* **1994**, *66*, 867–873.
(8) Wu, J.; Pawliszyn, J. *J. Liq. Chromatogr.* **1993**, *16*, 1891–1902.
(9) Wu, J.; Pawliszyn, J. *Am. Lab.* **1994**, October, 48–52.
(10) Wu, J.; Pawliszyn, J. *Electrophoresis* **1993**, *14*, 469–474.
(11) Wu, J.; Pawliszyn, J. *Analyst* **1995**, *120*, 1567–1572.

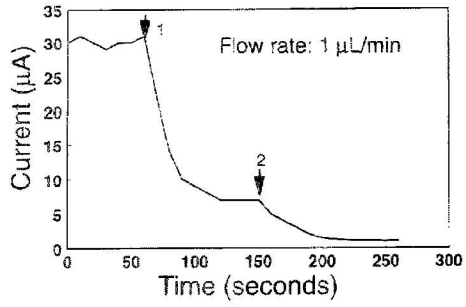

Figure 2. Current measured during the desalting process for a myoglobin sample in 100 mM Tris buffer solution.

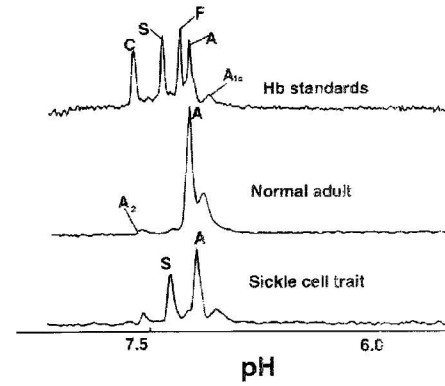

Figure 3. Electropherograms of three hemoglobin samples injected consecutively into the CIEF instrument shown in Figure 1.

column was monitored during the desalting process. When the current dropped to about 1 μA in 1–2 min, the syringe pump was stopped, and the capillary column was blocked at the other end to stop the hydrodynamic flow inside the column. The separation voltage (3 kV) was then turned on. The focusing process was monitored by the absorption imaging detector, and the detection was completed when focusing finished. The total analysis time is usually 2–4 min. After an analysis, the whole system was washed with deionized water for about 20 s, and it was ready for the next sample.

RESULTS AND DISCUSSION

The dialysis hollow fibers in the cartridge isolate the sample solution inside the capillary from the electrolytes in the reservoirs. However, small molecules, such as H^+ and OH^- ions, can pass through the wall of the hollow fiber freely. Thus, isoelectric focusing can take place normally inside the capillary held by the cartridge. With this cartridge, sample injection is a simple procedure. Sample solution can be injected from one end of the capillary column without withdrawing the electrolytes inside the two reservoirs. This procedure is much simpler than the sample injection method for conventional one-step or two-step CIEF performed in commercial CE instruments.

The efficiency of the desalting device was investigated. Myoglobin dissolved in 100 mM Tris buffer was used as the sample in the experiment. The salt concentration in the sample during the desalting process was monitored by measuring the current passing through the separation column. As shown in Figure 2, when there is no solution in the 100 mL beaker, the current passing through the capillary is about 30 μA for the 500 V voltage applied. This current shows that the 100 mM salt concentration is too high. Usually, the voltage applied to the 4 cm long capillary during the focusing process is 3–4 kV. The current under that voltage would have been about 0.2 mA, which is high enough to boil the solution inside the 75 μm i.d. capillary. The linear pH gradient would also be destroyed by the high concentration of salt. Isoelectric focusing cannot be performed with this salt concentration. Next, a solution of 4% carrier ampholytes is added to the beaker (arrow 1 in Figure 2). The current drops quickly from 30 μA to about 8 μA and stabilizes in about 1 min. This result shows that diffusion of salt from inside the fiber to outside the fiber is very fast, as expected, due to the narrow diameter of the dialysis hollow fiber. Thus, passing a sample through the fiber before it enters the separation column can desalt the sample effectively. The residual of salt in the sample can be better washed away by stirring the solution inside the beaker. Arrow 2 in Figure 2 indicates the time when the stirring starts. After the stirring starts, the current reduces to 1 μA and stabilizes in 50 s.

In the device, the desalted protein sample is also mixed with carrier ampholytes in the 10 cm long dialysis hollow fiber immersed in the 100 mL beaker. So, after the current stabilizes, the pump can be stopped, a 3 kV dc voltage applied, and the sample focused inside the separation column between the two electrolyte reservoirs. Since in the instrument a real time absorption imaging detector is used, the focusing process can be monitored, and detection finishes when focusing is complete, which takes only about 3 min. The whole analysis time for a sample using this instrument is less than 4 min, including the desalting procedure. This is the first report of an on-line desalting and carrier ampholyte mixing device for CIEF.

Figure 3 shows electropherograms of three hemoglobin samples injected consecutively. The reproducibility of focusing patterns with this instrument is good for the consecutively injected samples, which shows that the salts in the sample are adequately washed away and that the carrier ampholytes are effectively mixed into the sample. All three samples were analyzed by the instrument shown in Figure 1 in 15 min, including sampling times. This speed is about 3 times higher than that of a conventional CIEF analysis.[3-5] The resolution, when the pH 3–10 carrier ampholytes are used, is estimated to be 0.02 pH units from the distance between hemoglobin A and F (pI difference between them is 0.05 pH units). The CIEF instrument can be used for fast screening of abnormal hemoglobins, such as hemoglobins from sickle cell anemia patients. Also, variants separated by CIEF can be determined quantitatively with this instrument by their absorption peak areas, e.g., the ratio of variants A and A_2 can be determined from the ratio of their peak areas, as shown in Figure 3.[12]

Isoelectric focusing performed in the cartridge has advantages for reproducible sample injection over conventional CIEF and other CE methods. In CE and CIEF with one-step methods, the length of the sample plug has to be accurately (standard deviation less than 10%) controlled for quantitative determination. Usually, the plug is introduced into the capillary by hydrodynamic or

(12) Wu, J.; Pawliszyn, J. *Electrophoresis*, in press.

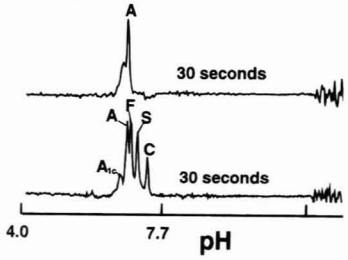

Figure 4. Electropherograms of two hemoglobin samples run consecutively in a 1 cm long capillary. The first sample is hemoglobin from a normal adult, and the second one is hemoglobin standard.

electrokinetic methods,[13] which cannot be easily controlled when a narrow capillary is used. However, with our cartridge, the amount of sample injected into the capillary does not need to be controlled. When the dc voltage is turned on for the cartridge shown in Figure 1, only the part of the sample between the two dialysis hollow fibers is focused. The sampling volume equals the capillary column volume between the two fibers, which guarantees the high accuracy in the sampling volume. The preliminary results of quantitative determination of proteins using our new instrument have high precision. The results are discussed in another paper.[12]

The separation speed of CIEF can be further increased with this new capillary cartridge since its speed is no longer limited by sampling. Fast CIEF may be useful for two-dimensional separations (2-D separation). 2-D separation usually requires that the sample injection intervals to the second separation step be short and that the second step be a fast one, so that the second separation can sample a peak eluted from the first separation dimension several times across the peak's width.[14] Although the analysis time of the CIEF with the cartridge and imaging detector reaches 2–4 min for a sample, this speed is still not high enough for CIEF to couple with high-performance liquid chromatography (HPLC) methods, since the peak widths of HPLC are usually in the few minutes range. With the new cartridge design, the speed of CIEF can be further increased by using a short capillary column. Figure 4 shows electropherograms of two hemoglobin samples separated consecutively in a 1 cm long capillary using the design shown in Figure 1. The focusing time is only 30 s, and analysis time for the two samples is 2 min, including the sampling for the two runs. The resolution of the separation is not bad for the 1 cm long capillary column. The peaks of hemoglobin A and F which have a pI difference of 0.05 pH units can be resolved. This resolution can be enhanced by using narrower pH range carrier ampholytes,[11] such as pH 6–8, if the ranges of samples' pI values are known. This speed allows CIEF to be coupled with HPLC separation to form a 2-D separation scheme.

Since the desalting device and the sample injection step for the cartridge could be automated with an autosampler, CIEF could be performed in multiple capillaries fixed on a single cartridge automatically, including sample preparation. Multicapillary CIEF can be detected with the absorption imaging detector.[11] Figure 5 shows the structure of a multicapillary instrument, which is

(13) Li, S. F. Y. *Capillary Electrophoresis, Principles, Practice and Applications*; Elsevier: Amsterdam, 1992.
(14) Bushey, M. M.; Jorgenson, J. W. *Anal. Chem.* **1990**, *62*, 978–984.

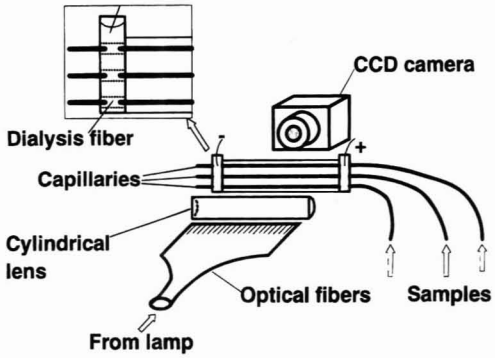

Figure 5. Basic design of the cartridge that has multiple capillaries with dialysis hollow fibers for CIEF with absorption imaging detection.

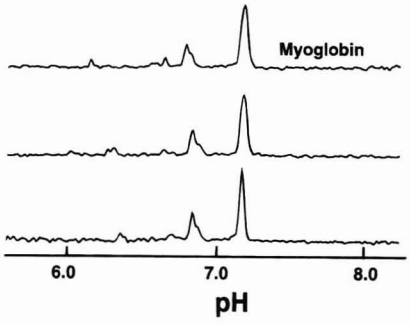

Figure 6. Electropherograms of three myoglobin samples separated in the three capillary cartridge, detected by an absorption imaging detector operated at 410 nm wavelength.

similar to that of a single capillary instrument and can be coupled with a multichannel on-line desalting device. The light beam from a tungsten lamp is sent into a bundle of optical fibers and then is projected onto the capillary cartridge by a 5 cm focal length cylindrical lens. The sample zones focused inside the capillaries are monitored by the CCD camera. In the present experiment, three capillaries are used in the instrument, although technically more than three capillaries could be in the cartridge.

The use of multicapillaries greatly increases the sample throughput of CIEF, making it comparable to gel slab isoelectric focusing, in which several samples and standards can be separated in different lanes simultaneously. But the speed of CIEF is much faster than that of gel slab isoelectric focusing, which needs hours for a separation.

The sampling procedure for the three capillaries takes less than 2 min, even manually. This speed could be increased by using an autosampler. After three samples are injected into the capillaries, the separation dc voltage is applied to the two electrolyte reservoirs, and focusing begins in the three capillaries. Focusing and detection are complete for samples in all three capillaries in 3 min. Figure 6 shows an example application of the multicapillary CIEF instrument. The separated zones inside the three capillaries are monitored by the absorption imaging detector operated at 410 nm. Three replicate myoglobin samples are focused in the three capillaries. The whole analysis time for all three samples, including the sampling procedure, is only about 5 min. The result shows good reproducibility of the focused

pattern. Because of the good reproducibility, unknown samples could be run with a standard simultaneously, and zones in the unknown sample can be identified by comparing their positions along the capillary with those in the standard. This comparison between a standard and a sample is difficult with a conventional single channel CIEF instrument.

ACKNOWLEDGMENT

This work was supported by the National Sciences and Engineering Research Council of Canada and SCIEX, a division of MDS Health Group Limited, Canada. We thank M. Adams for his editorial assistance in preparing this manuscript.

Received for review February 15, 1995. Accepted March 16, 1995.[⊗]

AC950163J

[⊗] Abstract published in *Advance ACS Abstracts,* April 15, 1995.

Anal. Chem. **1995**, *67*, 2015–2019

Determination of Aromatic Hydrocarbons in Gasolines by Gas Chromatography/Fourier Transform Infrared Spectroscopy

John W. Diehl,* John W. Finkbeiner, and Frank P. DiSanzo

Mobil Research and Development Corporation, Paulsboro Research Laboratory, Paulsboro, New Jersey 08066

The total aromatic contents of gasolines as well as 25 individual gasoline-range aromatic hydrocarbons were quantitated by GC/FT-IR with 1,2-dimethoxyethane as internal standard. Reconstructed selective wavelength chromatograms (SWCs) were used for each analyte to give good selectivities over respective coeluting hydrocarbons. Calibrations and quantitations were based on the peak areas from these SWCs, and all calibration curves were linear. An average relative standard deviation of 0.9% and an average accuracy of 0.9% were found. GC/FT-IR provided analyses comparable to the current EPA-specified GC/MS method with less sample preparation than GC/MS and with the added advantage of the simultaneous measurement of the ethers and alcohols (oxygenates) in the fuels.

As a result of clean fuel legislation, the levels of two classes of compounds present in reformulated gasolines currently are or soon will be regulated in many parts of the United States. These two classes of compounds are oxygenates, mainly ethers and/or alcohols added to reduce exhaust emissions, and aromatic hydrocarbons. The U.S. Environmental Protection Agency (EPA) currently mandates[1] a gas chromatography/oxygen flame ionization (GC/O-FID) method,[1,2] to determine the oxygenates, a gas chromatography/mass spectrometric (GC/MS) method[1,3] to determine approximately 25 individual aromatic compounds typically found in gasolines and to estimate the total aromatic levels, and American Standard of Testing Materials method D3606 to determine benzene. A complete analysis requires three instruments and the addition of five internal standards to each sample. The proposed inclusion of benzene in the GC/MS analysis[3] may eliminate method D3606, but the amount of instrumentation and sample preparation will still be substantial.

We have recently published methods for the determination of oxygenates[4] and benzene, toluene, ethylbenzene, and *m*-, *p*-, and *o*-xylenes (BTEX)[5] in gasolines by GC/FT-IR. These methods used selective wavelength chromatograms (SWCs) at the analytes' respective unique infrared absorbances (the C–O stretching region for the ethers and alcohols and the aryl C–H out-of-plane bending region for the aromatics) to obtain selectivity over coeluting hydrocarbons. The work below expands upon this GC/FT-IR approach for quantitation to include the aromatic hydrocarbons specified by the EPA, to provide a means to estimate the total aromatic levels in fuels, and to provide simultaneous determination of the oxygenates along with the aromatics.

EXPERIMENTAL SECTION

GC/FT-IR System. A Hewlett Packard Model 5890 Series II GC/5965B IRD FT-IR spectrometer was configured as follows.

GC Column. Hewlett Packard 60 m × 0.53 mm i.d. × 5.0 μm film HP-1.

Carrier. H_2, 42 cm/s (5.1 psi) set at 300 °C.

Injector. Electronic pressure controlled on-column with a Hewlett Packard 7673B autosampler. Injection volume was 0.5 μL. Injector was not heated but lagged the oven temperature by ~5 °C.

Oven Temperature Program. From 40 °C (0 min), 2 deg/min to 190 °C (0 min), then 30 deg/min to 300 °C (1.0 min). All of the analytes and the internal standard (ISTD) eluted before the oven reached 190 °C. The fast temperature ramp to 300 °C was to eliminate any carryover between samples.

Electronic Pressure Program. From 5.1 psi (75 min), 99 psi/min to 60 psi (until end of oven temperature program). All of the analytes and the ISTD eluted at 5.1 psi column head pressure. The fast ramp to 60 psi was to eliminate carryover between samples.

FT-IR Spectrometer Detector. Wide band (4000–550 cm^{-1}) MCT (nominal $D^* = 1 \times 10^{10}$ cm Hz 0.5/W).

Light Pipe Temperature. 300 °C.

Transfer Line Temperatures. 300 °C. The flow cell exit line was connected to vent outside the GC oven with a 0.25 m × 0.53 mm i.d. section of fused silica tubing. Narrower i.d. tubing caused back pressure in the light pipe, especially when the column head pressure was increased to 60 psi.

Resolution. 8 cm^{-1}.

Scan Rate. Six interferograms were coadded for 1 spectrum/s.

Selective Wavelength Chromatogram Reconstructions. The second difference type was used[6,7] (derivative function width, 75). A reference spectrum for the reconstructions was obtained by averaging the spectra from 0.1 to 0.5 min of each chromatogram. No compounds eluted during this period. As part of the SWC reconstruction, the software produced an absorbance spectrum

(1) Environmental Protection Agency, 40 CFR Part 80, Dec. 13, 1993.
(2) DiSanzo, F. P. *J. Chromatogr. Sci.* **1990**, *28*, 73–74.
(3) Proposed ASTM GC/MS method for determining aromatics in reformulated gasolines.
(4) Diehl, J. W.; Finkbeiner, J. W.; DiSanzo, F. P. *Anal Chem.* **1992**, *64*, 3202–3205.
(5) Diehl, J. W.; Finkbeiner, J. W.; DiSanzo, F. P. *Anal. Chem.* **1993**, *65*, 2493–2496.
(6) de Haseth, J. A.; Isenhours, T. L. *Anal. Chem.* **1977**, *49*, 49.
(7) Bowater, I. C.; Brown, R. S.; Cooper, J. R.; Wilkins, C. L. *Anal. Chem.* **1986**, *58*, 2195.

0003-2700/95/0367-2015$9.00/0 © 1995 American Chemical Society

Table 1. Selective Wavelength Chromatogram Reconstruction Frequencies

compound	frequency range (cm^{-1})
1,2-dimethoxyethane (ISTD)	1123–1131
benzene	670–678
toluene	724–732
ethylbenzene	694–702
m-xylene	687–695
p-xylene	790–798
o-xylene	736–744
isopropylbenzene	695–703
n-propylbenzene	695–703
1-ethyl-3-methylbenzene	775–783
1-ethyl-4-methylbenzene	807–815
1,3,5-trimethylbenzene	831–839
1-ethyl-2-methylbenzene	741–749
1,2,4-trimethylbenzene	801–809
1,2,3-trimethylbenzene	762–770
indan	739–747
1,3-diethylbenzene	698–706
1,4-diethylbenzene	826–834
n-butylbenzene	694–702
1,2-diethylbenzene	748–756
1,2,4,5-tetramethylbenzene	863–871
1,2,3,5-tetramethylbenzene	844–852
1,2,3,4-tetramethylbenzene	798–806
naphthalene	777–785
2-methylnaphthalene	803–811
1-methylnaphthalene	782–790

for each chromatographic data point by ratioing the reference spectrum against the spectrum stored for each point. Table 1 contains a list of the wavelengths used for the analytes and the ISTD, 1,2-dimethoxyethane. These corresponded to the analytes' aryl C–H out-of-plane bending frequencies ±4 cm^{-1}. All compounds were identified by retention time matching and spiking with pure standards (when available) as well as spectroscopically by GC/FT-IR/MS.[8,9] Figure 1 shows a 600–900 cm^{-1} SWC of a typical gasoline with the analytes labeled.

Spectrometer Purge. Dry N_2, 40 psi (100 L/min), was used. The restrictors were removed from the spectrometer's purge gas lines. This high purge rate greatly reduced any danger of explosion if H_2 reached the IR source because of a light pipe leak. No leaks were observed in 3 years of operation.

Data System. Data were processed on a Dell 4560XE IBM-compatible personal computer with Hewlett Packard Petro-IRD GC/FT-IR quantitation software.

Materials. Pure compounds were purchased from Aldrich Chemical Co. and Wiley Organics. Calibration solutions were prepared in 100 mL volumetric flasks with *n*-heptane as solvent. Concentrations of the calibration solutions were analyte dependent, and the procedure is described for each below.

Benzene. Into respective volumetric flasks were added 0.1, 0.5, 1.0, 3.0, and 5.0 mL of benzene along with 10.0 mL of ISTD, 1,2-dimethoxyethane while the weights of the benzene and ISTD were accurately recorded. The flasks were then diluted to the mark with solvent.

Toluene. Into respective flasks were added 1.0, 3.0, 5.0, 10.0, 20.0, and 25.0 mL of toluene along with 10.0 mL of ISTD while the weights were accurately recorded. The flasks were then diluted to the mark with solvent.

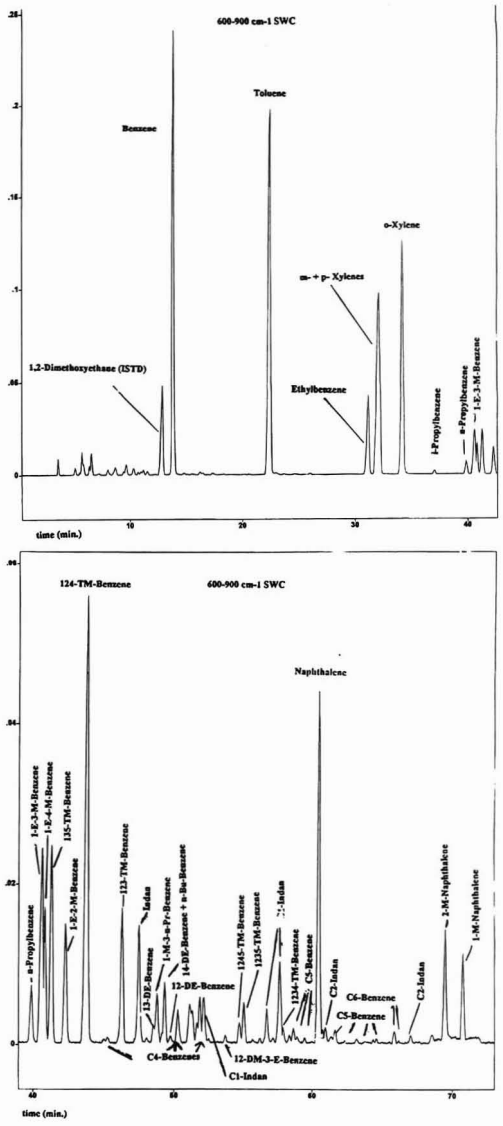

Figure 1. GC/FT-IR selective wavelength chromatograms showing the aromatics found in gasoline: (top) 0–40 min; (bottom) 40–75 min.

C2-Benzenes. Into respective flasks were added 0.5, 1.0, 3.0, 5.0, and 10.0 mL of each compound along with 10.0 mL ISTD while the weights were accurately recorded. The flasks were then diluted to the mark with solvent.

C3-Benzenes, C4-Benzenes, C5-Benzenes, Indan, and Naphthalenes. Into respective flasks were added 0.1, 0.5, 1.0, 3.0, and 5.0 g of each compound along with 10.0 mL of ISTD while the weights were accurately recorded. The flasks were then diluted to the mark with solvent.

These solutions bracketed the concentration ranges over which the analytes occurred in gasolines. The manner in which the compounds were combined in solutions was not critical for calibration as long as no compound contained an impurity which

(8) Wilkins, C. L.; Giss, G. N.; White, R. L.; Brissey, G. M.; Onyiriuka, E. C. *Anal. Chem.* **1982**, *54*, 2260–2264.
(9) Laude, D. A.; Brissey, G. M.; Ijames, C. F.; Brown, R. S.; Wilkins, C. L. *Anal. Chem.* **1984**, *56*, 1163–1168.

Table 2. GC/FT-IR Selectivities of Coeluting Aromatic Compounds

compounds	selectivity
m-xylene over *p*-xylene	>1000
p-xylene over *m*-xylene	14
1-ethyl-3-methylbenzene over 1-ethyl-4-methylbenzene	7
1-ethyl-4-methylbenzene over 1-ethyl-3-methylbenzene	35
1,4-diethylbenzene over *n*-butylbenzene	>1000
n-butylbenzene over 1,4-diethylbenzene	>1000

Table 3. Precision and Accuracy Data[a]

compound	actual	determined (mean)	RSD ($n-1$)	accuracy (%)
benzene	1.75	1.76	0.6	0.6
toluene	11.19	11.40	1.1	1.9
ethylbenzene	4.31	4.36	1.5	1.2
m-xylene	4.31	4.37	2.1	1.4
p-xylene	4.28	4.27	0.2	0.2
o-xylene	4.37	4.42	0.7	1.1
isopropylbenzene	11.50	11.55	0.7	0.4
n-propylbenzene	11.72	11.80	0.8	0.7
1-ethyl-3-methylbenzene	11.76	11.85	1.0	0.8
1-ethyl-4-methylbenzene	12.01	12.01	0.9	0.0
1,3,5-trimethylbenzene	34.53	35.01	0.7	1.4
1-ethyl-2-methylbenzene	11.98	12.10	0.9	1.0
1,2,4-trimethylbenzene	34.91	35.41	0.8	1.4
1,2,3-trimethylbenzene	35.17	35.76	0.5	1.7
indan	11.61	11.79	0.7	1.6
1,3-diethylbenzene	11.63	11.48	1.1	1.3
1,4-diethylbenzene	11.56	11.51	1.1	0.5
n-butylbenzene	11.44	11.37	1.0	0.6
1,2-diethylbenzene	11.91	11.86	1.1	0.4
1,2,4,5-tetramethylbenzene	11.59	11.60	0.9	0.1
1,2,3,5-tetramethylbenzene	11.72	11.70	1.1	0.2
1,2,3,4-tetramethylbenzene	11.62	11.66	0.9	0.4
naphthalene	11.20	11.25	1.0	0.5
2-methylnaphthalene	11.67	11.77	1.1	0.9
1-methylnaphthalene	11.59	11.79	1.1	1.7

[a] Results are in mg/mL. $n = 10$ over 48 h. Average accuracy, 0.9%. Average RSD, 0.9%.

would interfere with another aromatic in the same solution. In this case, BTEX were added together in one set of five solutions, the C3-benzenes and indan were added together in another set of five solutions, and the other compounds were added together in another set of five solutions. Each of these solutions contained 10.0 mL (~8.6 g) of ISTD.

Calibration curves were the plots of the respective selective wavelength (SW) chromatographic peak area of the analyte divided by the SW chromatographic peak area of the ISTD vs the weight of the analyte in the calibration solution divided by the weight of the ISTD in the solution (i.e., A_a/A_i vs W_a/W_i, where a is analyte and i is ISTD). All calibration and quantitation routines were performed with the commercial software provided with the FT-IR spectrometer.

Gasolines were prepared by adding 1.0 mL of ISTD to 9.0 mL of sample while the weights were accurately recorded. After GC/FT-IR data acquisition, the weights of the analytes were determined from the calibration curves. Weight % was calculated by dividing the determined weight of an analyte by the sample weight and multiplying by 100.

GC/MS Analyses. The GC/MS analyses were performed according to the method outlined in ref 3. Gasoline samples were prepared by accurately weighing 0.10 g each of four internal

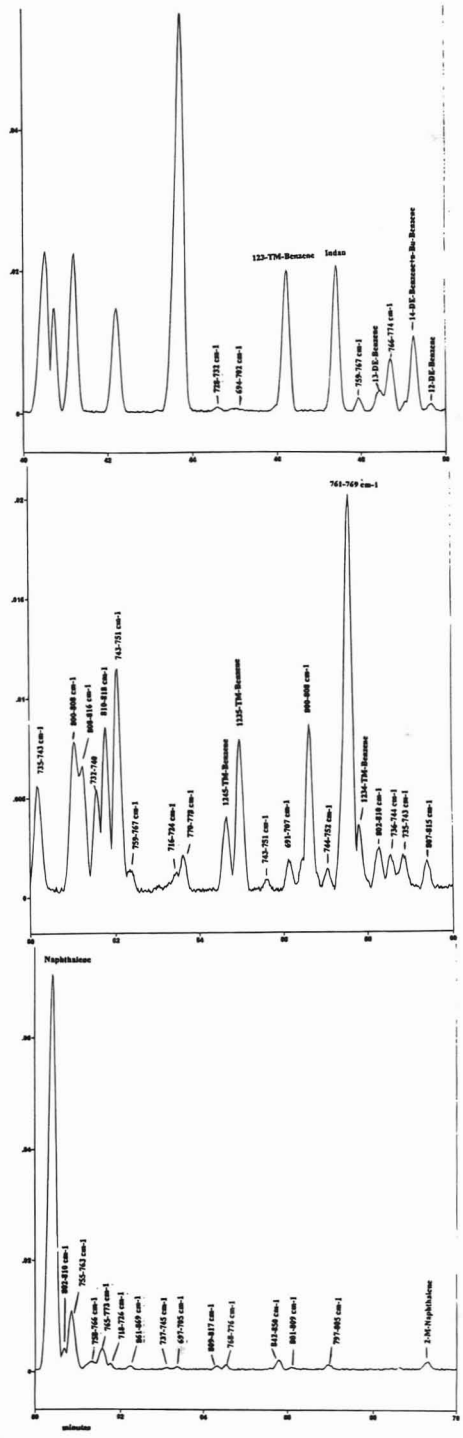

Figure 2. GC/FT-IR chromatograms showing the SWC frequencies used for the estimated aromatics: (top) 40–50 min; (middle) 50–60 min; and (bottom) 60–70 min.

Table 4. Analysis of a Full Range Gasoline[a]

compound/class	GC/FT-IR	GC/MS[b]
MTBE[c]	10.7 ± 0.10[d]	nr[f]
benzene	1.15 ± 0.02[e]	1.20[g]
toluene	8.41 ± 0.14	8.35
ethylbenzene	2.35 ± 0.07	2.29
m-xylene	3.61 ± 0.12	nr
p-xylene	1.50 ± 0.01	nr
m- + *p*-xylene	5.11 ± 0.13	5.12
o-xylene	1.77 ± 0.02	1.72
isopropylbenzene	0.09 ± 0.01	0.05
n-propylbenzene	0.37 ± 0.01	0.38
1-ethyl-3-methylbenzene	1.56 ± 0.04	1.46
1-ethyl-4-methylbenzene	0.55 ± 0.02	0.58
1,3,5-trimethylbenzene	0.63 ± 0.02	0.66
1-ethyl-2-methylbenzene	0.42 ± 0.01	0.41
1,2,4-trimethylbenzene	1.84 ± 0.05	1.63
1,2,3-trimethylbenzene	0.33 ± 0.01	0.45
indan	0.15 ± 0.01	0.19
1,3-diethylbenzene	0.09 ± 0.01	0.10
1,4-diethylbenzene	0.25 ± 0.01	nr
n-butylbenzene	0.21 ± 0.01	nr
1,4-diethyl + *n*-butylbenzene	0.46 ± 0.02	0.48
1,2-diethylbenzene	0.04 ± 0.01	0.03
1,2,4,5-tetramethylbenzene	0.09 ± 0.01	0.13
1,2,3,5-tetramethylbenzene	0.19 ± 0.01	0.26
1,2,3,4-tetramethylbenzene	0.30 ± 0.01	0.29
naphthalene	0.18 ± 0.01	0.25
2-methylnaphthalene	0.18 ± 0.01	0.23
1-methylnaphthalene	0.08 ± 0.01	0.11
estimated C10+ aromatics	1.31 ± 0.03	1.20
total aromatics	27.4	27.6

[a] Results are in wt %. [b] GC/MS analyses were performed according to the method described in ref 3. [c] SWC frequencies were 1205–1213 cm^{-1} as specified in ref 10. [d] ±2 times the SD provided in ref 4. [e] ±2 times the SD listed in Table 3. [f] Not reported. [g] GC/MS precision not listed in ref 1 or 3.

Table 5. GC/FT-IR Analyses of the Same Gasoline Performed 6 Weeks Apart but with the Same Calibration Curves

compound/class	8/16/94	9/30/94	rel diff (%)[b]
benzene	0.94	0.94	0.0
toluene	4.85	4.82	0.6
ethylbenzene	1.28	1.23	4.0
m-xylene	3.86	3.84	0.5
p-xylene	1.36	1.34	1.5
o-xylene	2.02	2.00	1.0
isopropylbenzene	0.05	0.04	20.0
n-propylbenzene	0.37	0.35	8.0
1-ethyl-3-methylbenzene	2.30	2.22	3.5
1-ethyl-4-methylbenzene	0.57	0.51	10.5
1,3,5-trimethylbenzene	0.83	0.83	0.0
1-ethyl-2-methylbenzene	0.58	0.59	1.7
1,2,4-trimethylbenzene	2.88	2.87	0.3
1,2,3-trimethylbenzene	0.68	0.69	1.5
indan	0.44	0.44	0.0
1,3-diethylbenzene	0.21	0.21	0.0
1,4-diethylbenzene	0.40	0.42	5.0
n-butylbenzene	0.54	0.49	9.3
1,2-diethylbenzene	0.03	0.06	100.0
1,2,4,5-tetramethylbenzene	0.31	0.34	9.7
1,2,3,5-tetramethylbenzene	0.57	0.62	8.8
1,2,3,4-tetramethylbenzene	0.13	0.13	0.0
naphthalene	0.65	0.64	1.5
2-methylnaphthalene	0.05	0.05	0.0
1-methylnaphthalene	0.05	0.07	40.0
estd C10+ aromatics	10.70	11.00	2.8
total aromatics	37.0	36.7	0.8

[a] Results are in wt %. [b] Absolute value of (8/16/94 result − 9/30/94 result)/8/16/94 result × 100. Average relative difference, 8.6%.

standards, benzene-d_6, toluene-d_8, ethylbenzene-d_{10}, and naphthalene-d_8, into 10.00 g of a sample.

RESULTS AND DISCUSSION

Note that, in Figure 1, 1-ethyl-3-methylbenzene was only partially resolved from 1-ethyl-4-methylbenzene, *m*-xylene was unresolved from *p*-xylene, and 1,4-diethylbenzene was unresolved from *n*-butylbenzene. Table 2 shows the selectivities of these compounds over the respective coeluting compounds. Selectivity was calculated by dividing the respective SW chromatographic peak area of the analyte at 10 mg/mL concentration by the area of the peak produced by 10 mg/mL of the coeluting compound after reconstruction at the analyte's wavelength region.

All calibration curves were linear. Precision and accuracy data are shown in Table 3. The average relative standard deviation was 0.9%, and the average accuracy was 0.9%. The detection limits for BTEX have been presented previously.[5] The detection limits for the other aromatics were ~0.05 wt % (50 ng injected), with a signal to noise ratio of 10. It should be noted that although multiple perdeuterated internal standards have been used for GC/FT-IR quantitation,[5] only 1,2-dimethoxyethane, the same ISTD used to determine oxygenates by GC/FT-IR,[4,10] was needed for this work. This differed from the GC/MS approach, which required multiple internal standards.[1,2]

A major difficulty in analyzing petroleum streams is that there are usually many isomers present for which pure standards are difficult or impossible to obtain. This was the case for gasoline range aromatics with carbon numbers above nine, as can be readily seen in the 600–900 cm^{-1} SWC in Figure 1. Some method of estimating these compounds must be employed such that, when this estimate is added to the sum of the levels of the known analytes, a total aromatics value is obtained. The GC/MS approach[1,2] used one C4-benzene isomer's calibration curves to estimate other C4-benzenes, one C5-benzene isomer for other C5-benzenes, etc.

In this work, 1,2,3,5-tetramethylbenzene's 844–852 cm^{-1} calibration curve was used to estimate the aromatic compounds for which standards were unavailable. SWCs were generated at the estimated compounds' respective wavelengths, and the respective amounts were calculated from the areas of the peaks and the 1,2,3,5-tetramethylbenzene curve's slope and intercept. Figure 2 is a 600–900 cm^{-1} SWC which shows the estimated compounds with the respective reconstruction frequencies labeled. These frequencies were obtained from examination of each compound's vapor phase infrared spectrum. The mass spectrum was also examined to ensure that the infrared absorbances were definitely due to an aromatic hydrocarbon. The sum of the estimated compounds' results was the total estimated amount of C10+ aromatics. This was added to the sum of the determined amounts of analytes to provide the total amount of aromatics in the gasoline.

Table 4 shows the GC/FT-IR results of the analysis of a full boiling range (C4–C12) gasoline compared to GC/MS results. There was good agreement between GC/FT-IR and GC/MS results for the measurement of the individual isomers as well as for the total. This agreement indicated that the SWC approach

(10) Proposed ASTM GC/FT-IR method for determining oxygenates and aromatics in reformulated gasolines.

for GC/FT-IR provided selectivity over the hydrocarbons, primarily paraffins, olefins, and naphthenes,[11] which coeluted with the aromatics comparable to that of the reconstructed ion chromatograms (RIC) used by the GC/MS approach.[2] Note that GC/MS did not report methyl *tert*-butyl ether. Determination of ethers and alcohols in gasolines by GC/MS may be possible, but the use of GC/MS for this application is not widespread. Since molecular ions are not very abundant in these compounds' electron impact spectra,[12] chemical or some other mode of ionization may be needed to obtain good selectivity over the coeluting hydrocarbons. Also note that GC/MS reported the coeluting pairs of *m*-xylene/*p*-xylene and 1,4-diethylbenzene/*n*-butylbenzene as sums because the pairs were not spectroscopically distinguished. Using different ions for the RICs or changing chromatographic conditions (such as a higher resolution column, a different phase, etc.) may address this GC/MS limitation, but these improvements may also increase analysis time, decrease loading capacity/detection limits, or cause other problems avoided by the GC/FT-IR approach.

(11) DiSanzo, F. P.; Giarrocco, V. J. *J. Chromatogr. Sci.* **1988**, *26*, 258.
(12) Silverstein, R. M.; Bassler, G. C. *Spectrometric Identification of Organic Compounds*, 2nd ed.; John Wiley & Sons, Inc.: New York, 1967.

GC/FT-IR calibration curves were found to be very stable, as can be seen in Table 5. A gasoline was analyzed twice over a 6 week period without recalibrating the instrument. Despite the time lapse, the results were essentially unchanged. The average relative difference was 8.6%, which included a number of analytes at <0.1 wt % which had 95% confidence limits of >10% of the determined value.

CONCLUSION

GC/FT-IR was definitely a precise and accurate technique for measuring aromatic hydrocarbons in gasolines which provided results comparable to those obtained with GC/MS. The proper choice of selective wavelength chromatogram reconstruction frequencies eliminated interferences from coeluting compounds and produced linear and stable calibration curves. Unlike GC/MS, GC/FT-IR could also simultaneously measure oxygenates along with the aromatic compounds.

Received for review January 23, 1995. Accepted March 23, 1995.[⊗]

AC950072M

[⊗] Abstract published in *Advance ACS Abstracts,* May 15, 1995.

Anal. Chem. **1995**, *67*, 2020–2025

Capillary Electrophoresis Coupled On-Line with Inductively Coupled Plasma Mass Spectrometry for Elemental Speciation

Yan Liu and Viorica Lopez-Avila*

California Operations, Midwest Research Institute, 625-B Clyde Avenue, Mountain View, California 94043

Jim J. Zhu and Daniel R. Wiederin

CETAC Technologies Inc., 5600 South 42nd Street, Omaha, Nebraska 68107

Werner F. Beckert

Environmental Monitoring System Laboratory, U.S. Environmental Protection Agency, 944 East Harmon Avenue, Las Vegas, Nevada 89119

A novel interface to connect a capillary electrophoresis (CE) system with an inductively coupled plasma mass spectrometric (ICPMS) detector is reported here. The interface was built using a direct injection nebulizer (DIN) system. In this interface, the CE capillary was placed concentrically inside the fused-silica DIN sample introduction capillary. A makeup liquid was pumped at a flow rate of 15 μL/min into the fused-silica DIN sample transfer capillary via a connector. The makeup liquid flowing outside the CE capillary served two purposes: (a) it established continuous and stable electrical contact at the exit (grounding) terminus of the CE capillary, and (b) it allowed the DIN system to be optimized independently of the CE system for efficient sample introduction to the ICPMS system. The makeup liquid along with the liquid from the electroosmotic flow generated inside the CE capillary was nebulized by the DIN system directly into the ICP torch. The CE/DIN-ICPMS system was evaluated using test samples containing selected alkali, alkaline-earth, and heavy metal ions, as well as selenium [Se(IV) and Se(VI)], and various inorganic and organic arsenic species. The preliminary results show that the CE/DIN-ICPMS system can be used to determine metal species at parts-per-trillion to parts-per-billion levels.

Capillary electrophoresis (CE) has become a powerful analytical technique for the separation of a variety of analytes ranging from small inorganic ions to large biomolecules such as proteins and nucleic acids.[1–4] The development of highly sensitive and selective detectors for CE has been one of the most important and challenging prerequisites for the growth of CE. On-column UV and fluorescence detectors are commonly used to determine the analytes separated by CE. However, these detectors are often not very sensitive; the analyte concentrations that can be detected with these detectors are on the order of 10^{-5}–10^{-6} M.[5] The use of other detection techniques such as mass spectrometry, laser-induced fluorescence, amperometry, and conductometry has been investigated to provide more sensitive and selective detection of the target analytes separated by CE.[5–12]

Some of the most sensitive and selective techniques for the determination of metals include plasma atomic spectrometry techniques such as microwave-induced plasma atomic emission spectrometry (MIP-AES), inductively coupled plasma atomic emission spectrometry (ICP-AES), and inductively coupled plasma mass spectrometry (ICPMS). These detection techniques have been successfully combined with separation techniques such as gas chromatography, liquid chromatography, and supercritical fluid chromatography.[13–16] However, relatively few studies have been published on the use of plasma atomic spectrometry or mass spectrometry techniques as a means of detection in CE separations.[17,18] In 1993, a CE system was interfaced with a microwave-induced helium plasma atomic emission detector (MIP-AED) and it was demonstrated, in principle, to be useful for element-specific detection of organotin compounds.[17] The results also indicated, however, that the helium plasma of the MIP-AED system did not have sufficient energy to vaporize and atomize the analytes contained in the aqueous buffer solution. The detection limit was

(1) Jorgenson, J.; Lukacs, K. D. *Anal. Chem.* **1981**, *53*, 1298–1302.
(2) Jorgenson, J.; Lukacs, K. D. *Science* **1983**, *222*, 266–272.
(3) Ewing, A. G.; Wallingford, R. A.; Olefirowicz, T. M. *Anal. Chem.* **1989**, *61*, 292A–303A.
(4) Monnig, C. A.; Kennedy, R. T. *Anal. Chem.* **1994**, *66*, 280R–314R.
(5) Smith, R. D.; Wahl, J. H.; Goodlett, D. R.; Hofstadler, S. A. *Anal. Chem.* **1993**, *65*, 574A–584A.
(6) Smith, R. D.; Udseth, H. R.; Barinaga, C. J.; Edmonds, C. G. *J. Chromatogr.* **1991**, *559*, 197–208.
(7) Olivares, J. A.; Nguyen, N. T.; Yonker, C. R.; Smith, R. D. *Anal. Chem.* **1987**, *59*, 1230–1232.
(8) Gassman, E.; Kuo, J. E.; Zare, R. N. *Science* **1985**, *230*, 813–814.
(9) Wallingford, R. A.; Ewing, A. G. *Anal. Chem.* **1987**, *59*, 1762–1766.
(10) Huang, X.; Pang, T.-K. J.; Gordon, M. J.; Zare, R. N. *Anal. Chem.* **1987**, *59*, 2747–2749.
(11) Dasgupta, P. K.; Bao, L. *Anal. Chem.* **1993**, *65*, 1003–1011.
(12) Albin, M.; Grossman, P. D.; Moring, S. E. *Anal. Chem.* **1993**, *65*, 489A–497A.
(13) Donard, O. F. X.; Martin, F. M. *Trends Anal. Chem.* **1992**, *11*, 17–26.
(14) Vela, N. P.; Olson, L. K.; Caruso, J. A. *Anal. Chem.* **1993**, *65*, 585A–597A.
(15) Hill, S. J.; Bloxham, M. J.; Worsfold, P. J. *J. Anal. At. Spectrom.* **1993**, *8*, 499–515.
(16) Lobinski, R.; Adams F. C. *Trends Anal. Chem.* **1993**, *12*, 41–49.
(17) Liu, Y.; Lopez-Avila, V. *J. High Resolut. Chromatogr.* **1993**, *16*, 717–720.
(18) Olesik, J. W.; Kinzer, J. A.; Olesik, S. V. *Anal. Chem.* **1995**, *67*, 1–12.

0003-2700/95/0367-2020$9.00/0 © 1995 American Chemical Society

thus rather poor (about 1 mg/mL for trimethyltin). More recently, Olesik and co-workers reported on interfacing CE with ICPAES and ICPMS and demonstrated that CE/ICPAES and CE/ICPMS could be used to speciate metals at parts-per-billion levels in aqueous solutions.[18]

Designing an efficient interface to connect the end of the CE separation capillary with the plasma is critical to the success of any CE/plasma atomic spectrometry or mass spectrometry technique. In the interface reported by Olesik and co-workers, the CE capillary exit terminus, which was coated with silver paint (serving as a conductor to complete the electrophoresis circuit), was fitted into the center tube of a concentric, pneumatic nebulizer with a spray chamber. These workers reported that silver contamination could occur under some conditions,[18] and their results also indicated that the interface caused some band broadening (probably due to the dead volume of the spray chamber used in the study).

The direct injection nebulizer (DIN) is a microconcentric pneumatic nebulizer with no spray chamber; it nebulizes the liquid sample directly into the central channel of the ICP torch.[19-22] Compared with conventional nebulizers, important advantages of DIN include (a) 100% sample introduction efficiency into the ICP, (b) accommodation of low sample introduction flow rates (10–100 μL/min), (c) an extremely small internal volume (<2 μL), and (d) fast sample washout with minimal memory effects. DIN has been successfully used as an interface to connect microbore column LC with ICPMS in the speciation of trace metals such as lead, mercury, arsenic, selenium, and chromium in various samples.[23-26]

As part of a continuing development and evaluation program of new analytical and sample preparation techniques conducted by the U.S. Environmental Protection Agency (EPA) through the Environmental Monitoring Systems Laboratory—Las Vegas (EMSL-LV), the use of ICPMS as an on-line detection technique for CE was investigated and a novel CE/ICPMS interface was developed using a commercially available, but modified, DIN system. In this paper, the performance characteristics of the CE/DIN-ICPMS system are discussed, and the preliminary results on the use of the CE/DIN-ICPMS technique for the determination of selected alkali, alkaline-earth, and heavy metal ions and for the speciation of selenium(IV)/selenium(VI) and various inorganic and organic arsenic species are presented.

EXPERIMENTAL SECTION

Reagents and Materials. Individual standard stock solutions containing Li^+, K^+, Cs^+, Cd^{2+}, Co^{2+}, Mn^{2+}, Pb^{2+}, Sr^{2+}, Tl^+, and Y^{3+} at 1000 μg/mL per metal in 2% nitric acid were obtained from Inorganic Ventures Inc. (Lakewood, NJ) or Fisher Scientific (Fair Lawn, NJ). Sodium arsenite ($NaAsO_2$), potassium hydrogen arsenate (KH_2AsO_4), monomethylarsonic acid ($CH_3H_2AsO_3$, MMA), dimethylarsinic acid [$(CH_3)_2HAsO_2$, DMA], disodium selenite (Na_2SeO_3), disodium selenate (Na_2SeO_4), 1,10-phenanthroline, and ammonium nitrate were obtained from Sigma Chemical Co. (St. Louis, MO). Ultrex-grade ultrapure nitric acid was obtained from J. T. Baker (Philipsburg, NJ). Trace metal-grade ammonium hydroxide was obtained from Fisher Scientific.

A multielement stock solution containing Li^+, K^+, Cs^+, Cd^{2+}, Co^{2+}, Mn^{2+}, Pb^{2+}, Sr^{2+}, and Tl^+ at 10 μg/mL per metal was prepared by compositing the individual standard stock solutions and diluting the composite solution with deionized water. Multielement test solutions at lower concentrations were prepared by diluting the 10 μg/mL multielement stock solution with deionized water as needed.

Individual stock solutions of $NaAsO_2$, KH_2AsO_4, MMA, DMA, Na_2SeO_3, and Na_2SeO_4 at 100 μg/mL (as As or Se) were prepared by dissolving the appropriate amounts of the corresponding salts in deionized water. Test solutions containing selenium and arsenic species at lower concentrations were prepared by compositing the individual stock solutions and diluting the composite solution with deionized water as needed.

For the CE separation of the selected alkali, alkaline-earth, and heavy metal ions, an electrophoresis buffer solution of 10 mM ammonium nitrate, 5 mM phenanthroline, and 50 ng/mL Cs^+ was prepared by dissolving appropriate amounts of the chemicals in deionized water and adjusting the pH of the solution to 8.75 with 0.1 M ammonium hydroxide. An electrophoresis buffer solution of 2.3 mM pyromellitic acid, 6.5 mM sodium hydroxide, 1.6 mM triethanolamine, and 0.75 mM hexamethonium hydroxide (pH 7.7), which was used in the CE separation of selenium and arsenic species, was obtained from Dionex Corp. (Catalog No. 044138, Sunnyvale, CA). A solution of 50 ng/mL Y^{3+} in 2% nitric acid was used as the makeup liquid for the CE/DIN-ICPMS.

Uncoated fused-silica capillaries (50- and 125-μm i.d., 100- and 175-μm o.d.), purchased from Polymicro Technologies, Inc. (Phoenix, AZ) were used as the separation and interfacing capillaries, respectively.

CE/ICPMS System. An Isco Model 3850 electrophoresis system (Isco, Inc., Lincoln, NE) and a Hewlett-Packard Model 4500 ICPMS system (Hewlett-Packard Co., Wilmington, DE) were used in this study. The operation of the HP 4500 ICPMS system was controlled through the HP 4500 ICPMS Chemstation computer and software. The ICPMS data acquisition during the CE/ICPMS analyses was performed in a time-resolved mode with multiple-mass monitoring, and the dwell time for each mass was set at 100 μs. The ICPMS operating conditions are summarized in Table 1.

The CE/ICPMS interface was built using a modified Microneb 2000 DIN system (Cetac Technologies Inc., Omaha, NE). The Microneb 2000 DIN torch insert was fitted with a PEEK cross-connector that was specially fabricated for this study (Figure 1). The fused-silica DIN sample introduction capillary (25-cm length × 125-μm i.d. × 175-μm o.d.) was connected to the PEEK cross-connector using a $^1/_{16}$-in. o.d. Teflon sleeve. The CE capillary (75-cm length × 50-μm i.d. × 100-μm o.d.) was inserted (through the PEEK cross-connector) concentrically inside the fused-silica DIN sample introduction capillary, and the grounding terminus of the CE capillary was positioned about 1 mm from the exiting terminus of the DIN sample transfer capillary. A platinum electrode (i.e., CE grounding electrode) was connected to one

(19) Lawrence, K. E.; Rice, G. W.; Fassel, V. A. *Anal. Chem.* **1984**, *56*, 289–292.
(20) LaFreniere, K. E.; Fassel, V. A.; Eckels, D. E. *Anal. Chem.* **1987**, *59*, 879–887.
(21) Wiederin, D. R.; Smith, F. G.; Houk, R. S. *Anal. Chem.* **1991**, *63*, 219–225.
(22) Houk, R. S.; Shum, S. C. K.; Wiederin, D. R. *Anal. Chim. Acta* **1991**, *250*, 61–70.
(23) Shum, S. C. K.; Pang, H. M.; Houk, R. S. *Anal. Chem.* **1992**, *64*, 2444–2450.
(24) Shum, S. C. K.; Neddersen, R.; Houk, R. S. *Analyst* **1992**, *117*, 577–582.
(25) Gjerde, D. T.; Wiederin, D. R.; Smith, F. G.; Mattson, B. M. *J. Chromatogr.* **1993**, *640*, 73–78.
(26) Shum, S. C. K.; Houk, R. S. *Anal. Chem.* **1993**, *65*, 2972–2976.

Table 1. DIN-ICPMS Operating Conditions

DIN and ICP Parameters	
DIN	Microneb 2000
rf power, W	1300
rf matching, V	1.98
sample depth, mm	7
torch-H, mm	−0.7
torch-V, mm	0
coolant gas flow rate, L/min	15
auxiliary gas flow rate, L/min	0.7
carrier gas flow rate, L/min	0.3
DIN nebulizer gas pressure, psi	70
DIN nebulizer gas flow rate, L/min	0.6
DIN sample liquid flow rate, μL/min	15
MS Parameters	
sample core, copper, mm orifice	0.4
skimmer, copper, mm orifice	1.0
first-stage pressure, Torr	1.0
second-stage pressure, Torr	5×10^{-4}
third-stage pressure, Torr	5×10^{-5}
extract 1, V	−244
extract 2, V	−157
Einzel 1, 3, V	−168
Einzel 2, V	32.7
ω bias, V	−54
ω (+), V	22
ω (−), V	−7
QP focus, V	8
ion def, V	30
amu gain	128
amu offset	179
axis gain	0.9965
axis offset	−0.05
plate bias, V	−9
pole bias, V	0
discriminator, mV	12.5
EM voltage, V	−2620
last dynode, V	−300
P/A factor 1	106
P/A factor 2	106
P/A factor 3	79

port of the PEEK cross-connector using a $^1/_{16}$-in. o.d. Teflon sleeve. The gas displacement pump of the Microneb 2000 DIN system was used to add a constant and pulse-free makeup liquid (a solution of 50 ng/L Y^{3+} in 2% nitric acid) at a flow rate of 15 μL/min to the fused-silica DIN sample transfer capillary through one port of the PEEK cross-connector. The makeup liquid flowing through the DIN sample transfer capillary (outside the CE capillary) established the CE electrical contact at the grounding terminus of the CE capillary. The makeup liquid flow, along with the electroosmotic flow generated inside the CE capillary, was nebulized by the DIN directly into the ICP torch. The typical DIN operating conditions used in this study are summarized in Table 1.

The voltage applied in the CE separation of the selected alkali, alkaline-earth, and heavy metal ions was +25 kV, and the electrophoresis current was 15 μA. For CE separation of selenium and arsenic species, the applied voltage was −30 kV and the electrophoresis current was 10 μA. The test samples were injected manually using either the electromigration injection method (5 s at 20 kV) or the hydrodynamic injection method by elevating the sample vial at the injection end of the CE capillary (20 s at 25 cm).

RESULTS AND DISCUSSION

Characteristics of the CE/DIN-ICPMS Interface. In the CE/DIN-ICPMS interface developed in this study (Figure 1), the makeup liquid serves two purposes. First, the makeup liquid flowing through the DIN sample introduction capillary (outside the CE separation capillary) provides a continuous and stable electrical contact at the exit (grounding) terminus of the CE capillary so that the complete electrophoresis circuit can be established. Second, the addition of makeup liquid at a flow rate of 15 μL/min ensures that the DIN system can be operated independently of the CE system for efficient sample introduction to the ICPMS. The electroosmotic flow generated inside the CE capillary under the experimental conditions used in this study was approximately 100 nL/min, which is significantly lower than the minimal liquid flow of 10 μL/min required for continuous and stable operation of the DIN. With the addition of makeup liquid, the operation of the DIN system became largely independent of the electroosmotic flow generated by the electrophoresis process. This allowed us to use different electrophoresis buffers and applied voltages to achieve efficient and rapid separation of target analytes.

To reduce the dead volume and to avoid convective band broadening, the makeup liquid flow and the electroosmotic flow from the CE capillary were combined inside a 1-mm-long section of the DIN sample introduction capillary at the exiting terminus

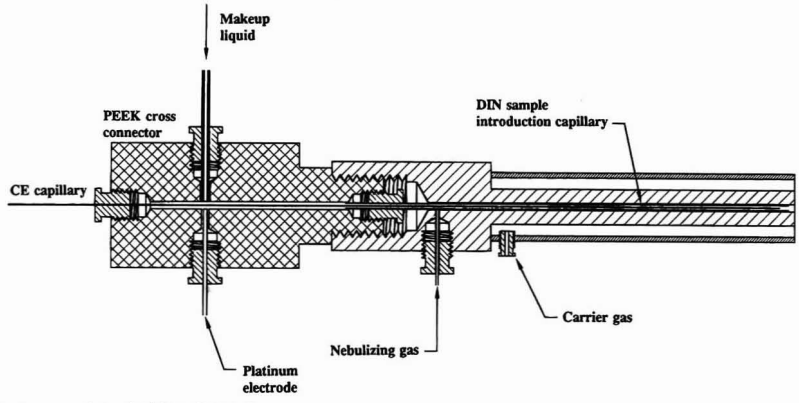

Figure 1. Block diagram of the CE/ICPMS interface.

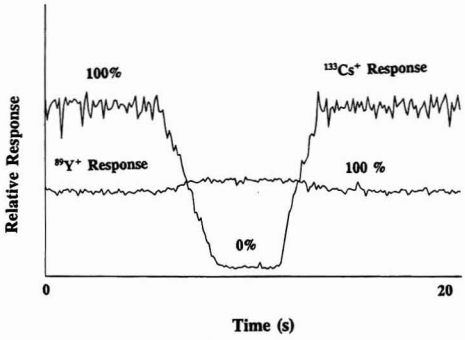

Figure 2. Time plots of $^{133}Cs^+$ and $^{89}Y^+$ responses obtained during the ICPMS system tuning step, indicative of electrosmotic flow and makeup liquid flow, respectively.

before they were nebulized by the DIN directly into the central channel of the ICP torch. The volume of this 1-mm section of the DIN sample introduction capillary at the exiting terminus was approximately 18 nL and could be swept by the makeup liquid in about 0.7 s at a flow rate of 15 μL/min. The DIN tip is usually placed only a few millimeters from the base of the ICP plasma. The nebulized sample aerosol leaves the DIN at a velocity of about 120 m/s, and the sample enters the plasma as a tight plume.[21]

The direct injection nebulization did not cause any noticable suction or back pressure during the CE separation. Using this interface, CE sample injection can be accomplished by the electrokinetic injection or hydrodynamic injection method. For efficient nebulization, it is preferred that the DIN sample introduction capillary have a wall thickness of less than 50 μm and an outer diameter of less than 200 μm. When the CE capillary is positioned concentrically inside the DIN sample introduction capillary, the outer diameter of the fused-silica capillary used for CE separation should match the inner diameter of the DIN sample introduction capillary. A CE capillary with an inner diameter of 50 μm and an outer diameter of 100 μm was used in this study.

Evaluation of CE/DIN-ICPMS System. A preliminary evaluation of the CE/DIN-ICPMS system was carried out by analyzing test samples containing selected alkali, alkaline-earth, and heavy metal ions at concentrations ranging from 2 to 100 ng/mL. To take advantage of the multielemental capability of the ICPMS system, Y^{3+} ions were added to the makeup liquid (50 ng/mL Y^{3+} in 2% nitric acid) and the operation of the DIN and ICPMS systems was monitored from the $^{89}Y^+$response. Cs^+ ions were also added to the electrophoresis buffer to monitor the stability of the electroosmotic flow. A typical example of the time plots of $^{133}Cs^+$ and $^{89}Y^+$responses obtained during the ICPMS system tuning step is shown in Figure 2. When the electrophoresis voltage was turned off, the $^{133}Cs^+$ response diminished and the $^{89}Y^+$response remained relatively stable. The results suggest that the electrophoresis process had little effect on the operation of the DIN.

Figure 3 shows the CE/DIN-ICPMS electropherograms obtained for a test sample containing Li^+, K^+, Mn^{2+}, Co^{2+}, Sr^{2+}, Cd^{2+}, Tl^+, and Pb^{2+} at 2.0 ng/mL per metal ion. Baseline resolution of Li^+, K^+, Sr^{2+}, and Tl^+ was achieved with the following elution order: $K^+ < Tl^+ < Li^+ < Sr^{2+}$; these four metal ions were separated in less than 210 s. The divalent heavy metal ions Cd^{2+},

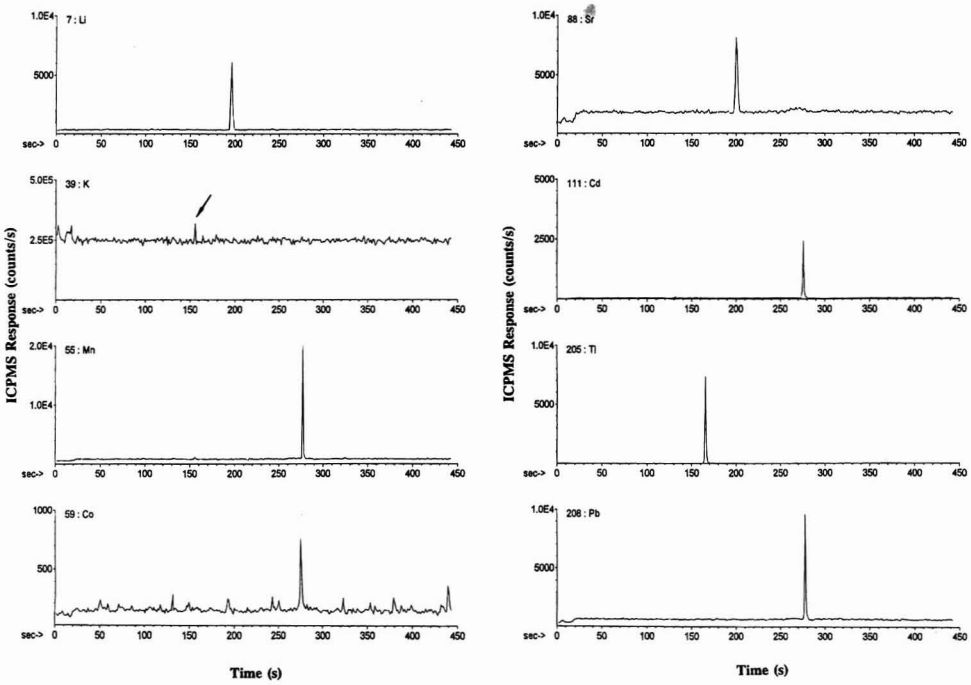

Figure 3. CE/DIN-ICPMS electropherograms obtained for a test sample containing Li^+, K^+, Mn^{2+}, Co^{2+}, Sr^{2+}, Cd^{2+}, Tl^+, and Pb^{2+} at 2.0 ng/mL per metal. All electropherograms were obtained with a single injection of the multielement test sample.

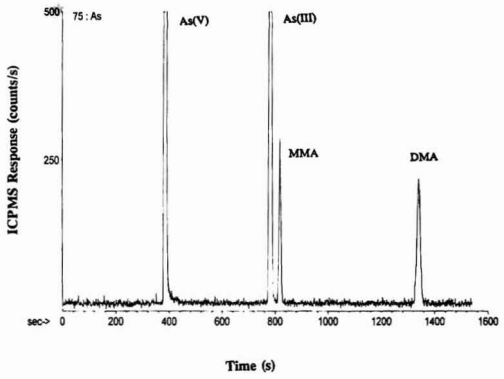

Figure 4. CE/DIN-ICPMS electropherogram obtained for a test sample containing As(III), As(V), MMA, and DMA at 500 ng/mL.

Co^{2+}, Mn^{2+}, and Pb^{2+} formed complexes with phenanthroline, which was added to the electrophoresis buffer to prevent the formation of metal hydroxide species at the pH of the buffer (pH 8.75). Although the metal complexes eluting later in the CE run around 280 s were not completely resolved, the elution peak of the Pb(II)−phenanthroline complex had a theoretical plate count of 10^5, indicating that the CE/DIN-ICPMS interface did not cause any significant band broadening.

The feasibility of using the CE/DIN-ICPMS system to speciate selenium [Se(IV), Se(VI)] and arsenic [As(III), As(V), DMA, MMA] was also demonstrated. In the CE separation of the selenium and arsenic species, hexamethonium hydroxide was used as the cationic surface modifier in the electrophoresis buffer to reverse the direction of electroosmotic flow so that faster separation of anionic selenium and arsenic species could be obtained. Figure 4 shows the CE/DIN-ICPMS electropherogram obtained for a test sample containing As(III), As(V), MMA, and DMA at 500 ng/mL; the four arsenic species eluting in the order As(V) < As(III) < MMA < DMA were completely resolved. Figure 5 shows the CE/DIN-ICPMS separation of a test sample containing As(III), As(V), Se(IV), and Se(VI) at 2.0 ng/mL. The electropherograms obtained with the CE/DIN-ICPMS system show excellent peak shapes and good sensitivities for the arsenic and selenium species.

Table 2 summarizes the detection limits obtained with DIN-ICPMS and CE/DIN-ICPMS for metal species tested in this study. The DIN-ICPMS detection limits for the target metal species were obtained with continuous DIN sample introduction at a flow rate of 100 μL/min. The CE/DIN-ICPMS detection limits were estimated from the data shown in Figures 3 and 5. For the metal ions investigated in this study, the CE/DIN-ICPMS detection limits ranged from 7 pg/mL for Tl^+ to 1000 pg/mL for K^+. These detection limits were up to 600 times as high as those obtained with DIN-ICPMS, although the majority were only up to 15 times as high. It is not clear why the ratios of the continuous DIN-ICPMS and CE/DIN-ICPMS detection limits vary to the extent observed; further investigation is needed.

CONCLUSIONS

The CE/DIN-ICPMS interface developed in this study, which is based on a commercially available DIN system, allows the DIN system to be optimized independently of the CE system for efficient sample introduction to the ICPMS system. The interface can be used under different CE conditions (e.g., different electrophoresis buffers and applied voltages). The preliminary results reported here demonstrate that CE/DIN-ICPMS can be used to speciate metals at parts-per-trillion to parts-per-billion levels. The CE/DIN-ICPMS system combines the high separation efficiency of CE with the high elemental sensitivity and selectivity of the ICPMS, making it a potentially powerful analytical technique for

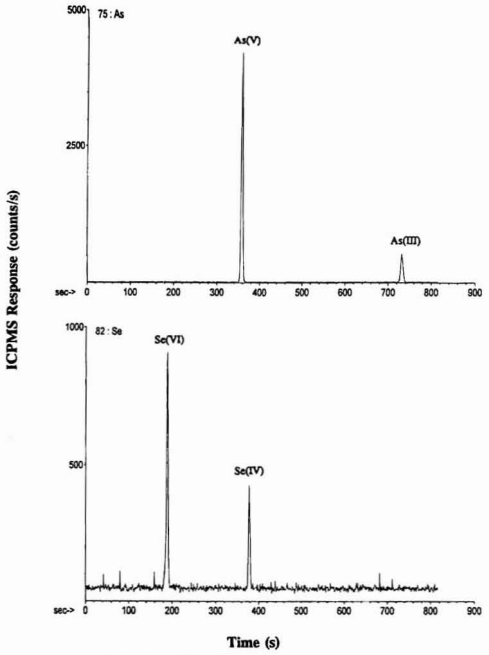

Figure 5. CE/DIN-ICPMS electropherograms obtained for a test sample containing As(III), As(V), Se(IV), and Se(VI) at 2.0 ng/mL. All electropherograms were obtained with a single injection of the multielement test sample.

Table 2. Detection Limits for Metal Species Investigated in This Study[a]

metal species	continuous DIN-ICPMS, pg/mL	CE/DIN-ICPMS, pg/mL
Li^+	3	50
K^+	100	1000
Cd^{2+}	6	60
Co^{2+}	1	420
Mn^{2+}	3	30
Pb^{2+}	0.9	600
Sr^{2+}	0.3	180
Tl^+	0.4	7
As(III)	20	100
As(V)	20	20
Se(IV)	80	300
Se(VI)	80	100

[a] The detection limits for the DIN-ICPMS and the CE/DIN-ICPMS techniques are defined as the analyte concentrations giving a signal of 3 times the standard deviation of the background noise. The ICPMS data acquisition for the continuous DIN-ICPMS experiments was performed in a continuous-signal mode with multiple-mass monitoring. The ICPMS data acquisition for the CE/DIN-ICPMS experiments was performed in a time-resolved mode with multiple-mass monitoring.

the determination and speciation of trace metals in various sample matrices.

ACKNOWLEDGMENT

The U.S. Environmental Protection Agency (EPA), through its Office of Research and Development (ORD), partially funded and collaborated in the research described here. This manuscript has been subjected to the Agency's peer review and has been approved as an EPA publication. The U.S. Government has a nonexclusive, royalty-free license in and to any copyright covering this article. Mention of trade names or commercial products does not constitute endorsement or recommendation for use. The authors thank Kevin Patt and Warren Stueben of Isco, Inc., for making available the CE system for use in this study.

Received for review November 4, 1994. Accepted March 28, 1995.[⊗]

AC941072+

[⊗] Abstract published in *Advance ACS Abstracts,* May 15, 1995.

Anal. Chem. **1995,** *67,* 2026–2029

Capillary Electrochromatography: Analysis of Polycyclic Aromatic Hydrocarbons

Chao Yan, Rajeev Dadoo, Hui Zhao, and Richard N. Zare*

Department of Chemistry, Stanford University, Stanford, California 94305

David J. Rakestraw

Sandia National Laboratories, Livermore, California 94551

Electrochromatography is utilized to separate a mixture of 16 different polycyclic aromatic hydrocarbons (PAHs). Fused-silica capillary columns ranging in size from 50 to 150 μm i.d. were packed (20–40-cm sections) with 3-μm octadecylsilica particles. A potential of 15–30 kV is applied across the 30–50-cm total length capillary column to generate electroosmotic flow that carries the PAHs through the stationary phase. An intracavity-doubled argon ion laser operating at 257 nm is used to detect the PAHs by laser-induced fluorescence. Efficiencies up to 400 000 theoretical plates/m are obtained when detection is performed within the column packing and up to 150 000 theoretical plates/m when detection is performed following a frit (used to hold the packing). The reproducibility of the peak retention times is better than 2% (RSD). The limits of detection for individual PAHs range between 10^{-17} and 10^{-20} mol (10^{-9}–10^{-11} M), with a linear response spanning 4 orders of magnitude in concentration.

The quest to gain an understanding at the molecular level of various biochemical phenomena and the necessity created by the trend toward strict monitoring of processes that lead to environmental pollution have placed stringent demands on the methods used for such analysis. Because of the complexity of the sample mixtures and often the low levels of compounds present in them, the analytical technique must possess good separation capabilities (high efficiency and high selectivity) and also good detection sensitivity.

Electrokinetic separations performed in capillary columns provide high-resolution and high-efficiency analyses of complex samples.[1] Capillary zone electrophoresis (CZE),[1] in which the capillary column is open and the walls of the capillary serve to establish electroosmotic flow, is useful in separating charged species via their different electrophoretic mobilities but is unable to resolve neutral components. As demonstrated by Terabe et al.,[2] the introduction of micelles into the separation electrolyte (called micellar electrokinetic capillary chromatography (MECC)) results in the separation of some uncharged species. This separation is based on the partitioning of the uncharged analytes between the electrolyte and the micelles that serve as a pseudostationary phase. Although easy to implement, MECC currently lacks selectivity, and it does not offer the choice in stationary phases that is available in high-performance liquid chromatography (HPLC). Consequently, MECC has not yet emerged as a routinely used technique in the laboratory.

As first shown in 1974 by Pretorius, Hopkins, and Schieke,[3] by applying an electric field across columns packed with microparticulates, electroosmotic flow can be made to act as a pump for chromatographic separations. This technique is referred to as capillary electrochromatography (CEC). They demonstrated that the efficiency of a separation obtained by electroosmotic propulsion is superior to that obtained by pressure-driven flow (as is the case in HPLC). CEC has since been applied by Jorgenson and Lukacs[4] in 1981 and by Tsuda, Nomura, and Nakagawa[5] in 1982 to analyze neutral aromatic compounds that could not be separated by CZE. Knox and Grant[6] have pointed out that CEC promises efficiencies comparable to those obtained with capillary gas chromatography if the capillary can be packed with submicrometer-sized particles. They have demonstrated the increase in efficiency that is obtained with particle sizes down to 1.5 μm using a few polycyclic aromatic hydrocarbons (PAHs) as model analytes. Recently, Smith and Evans[7] utilized a pressurized electrochromatographic system to separate certain pharmaceutical compounds. The pressurized system was used to minimize bubble formation in the capillaries that was significantly interfering with the electrochromatographic separations. In spite of these demonstrations, CEC has received relatively little attention because of the difficulty in fabricating and operating the packed capillary columns.

In this study we utilize a methodology developed previously by Yan[8] for the production of packed capillary columns and demonstrate that CEC can be used in a routine manner. In addition, we expand on the high-sensitivity CZE work of Nie, Dadoo, and Zare[9] for the analysis of PAHs by UV laser-excited native fluorescence. We report the use of CEC combined with UV laser-induced fluorescence (LIF) detection for the high-efficiency, high-sensitivity analysis of 16 PAHs classified by the U.S. Environmental Protection Agency (EPA) as priority pollutants. Because capillary separation techniques are so well suited for analyzing ultrasmall volumes (<1 nL), this methodology is expected to be particularly applicable to any study requiring high resolution and high efficiency in the analysis of analytes in a limited volume.

(1) Weinberger, R. *Practical Capillary Electrophoresis*; Academic Press, Inc.: San Diego, 1993.
(2) Terabe, S.; Otsuka, K.; Ichikawa, K.; Tsuchiya, A.; Ando, T. *Anal. Chem.* **1984**, *56*, 113.
(3) Pretorius, V.; Hopkins, B. J.; Schieke, J. D. *J. Chromatogr.* **1974**, *99*, 23.
(4) Jorgenson, J. W.; Lukacs, K. D. *J. Chromatogr.* **1981**, *218*, 209.
(5) Tsuda, T.; Nomura, K.; Nakagawa, G. *J. Chromatogr.* **1982**, *248*, 241.
(6) Knox, J. H.; Grant, I. H. *Chromatographia* **1991**, *32*, 317.
(7) Smith, N. W.; Evans, M. B. *Chromatographia* **1994**, *38*, 649.
(8) Yan, C. Electrokinetic Packing of Capillary Columns. U.S. Patent Appl. 08/142, 917, October 29, 1993.
(9) Nie, S.; Dadoo, R.; Zare, R. N. *Anal. Chem.* **1993**, *65*, 3571.

0003-2700/95/0367-2026$9.00/0 © 1995 American Chemical Society

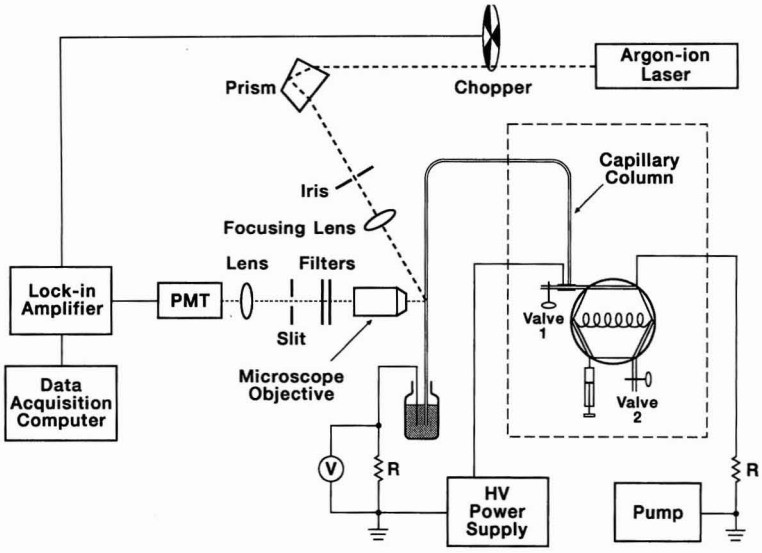

Figure 1. Schematic of the CEC-LIF apparatus.

EXPERIMENTAL SECTION

CEC and Micro-HPLC Apparatus. The apparatus used to perform the separations is similar to that described by Yan, Schaufelberger, and Erni[10] but was modified for our purposes. A schematic of the apparatus is shown in Figure 1. A stainless-steel six-port rotary valve fitted with a 20-μL sample loop (Model 7010, Rheodyne, Inc., Cotati, CA) was used as an injection manifold. The valve was used primarily for hydrodynamic injections with micro-HPLC runs. A pump capable of delivering 0.1–1250 μL/min (Micro-Tech Scientific, Sunnyvale, CA) was connected to the rotary valve and was used for initially filling the capillary column with the mobile phase and for the micro-HPLC experiments. A 0–50-kV high-voltage power supply (Glassman High Voltage, Inc., Whitehouse Station, NJ) provided the electric field for the electrochromatography. A fan was used to assist the heat dissipation of the capillary during the separations.

Detection Apparatus. The confocal-design UV-LIF apparatus described earlier[9] was adapted for electrochromatography. The 257-nm line from an intracavity-doubled argon ion laser (Coherent, Inc., Santa Clara, CA) was used for excitation of the PAHs. A prism was used to separate residual 514-nm light in the laser beam from the 257-nm light. A fused-silica lens (50-mm focal length; Melles Griot, Irvine, CA) focused the laser beam onto the capillary. The fluorescence was collected by using a high-numerical-aperture (NA) microscope objective (40× magnification, NA = 0.85, 0.37-mm working distance; Nikon, Melville, NY) and then sent through a set of filters (a 280-nm longpass in combination with two 600-nm shortpass filters or a 70-nm bandpass filter centered at 400 nm) and a variable slit (Newport Corp., Fountain Valley, CA) onto a photomultiplier tube (PMT) (Model R955, Hamamatsu, San Jose, CA) operated between 500 and 600 V. A lock-in amplifier (Stanford Research Systems, Sunnyvale, CA) was used in conjunction with a chopper (operating at 250 Hz) in the path of the laser beam to measure the output of the PMT. Commercial software (LabCalc, Galactic Industries Corp., Salem, NH) run on an IBM personal computer was used for data acquisition at a rate of 1 Hz.

Preparation of Packed Capillary Columns. Capillary columns with different inside diameters (50–150 μm) were packed using the procedure developed previously.[8] A suspension of 3-μm octyldecylsilica (ODS) particles (90%) and 1-μm silica gel (10%) in methanol containing 2 mM sodium phosphate (pH 4.5) was electrokinetically packed into the column after an initial frit was created by sintering 5-μm silica gel (using a microflame torch). A second frit consisting of fused-ODS particles (~10 cm from the outlet) was made in the column after the packing procedure to hold the particles firmly in place. A thermal wire stripper was used to make the second frit. The wire stripper gently heated the particles in a controlled fashion which minimized disturbance of the adjacent ODS particles. Extraneous particles between the frit and the outlet of the column were then flushed out because passing the laser beam through the particles generated significant background scatter. A narrow window (2–5 mm) for detection was created within 1–2 mm after the packed portion of the column. The column was flushed with the selected mobile phase (by pressurizing the column inlet to 1000 psi) for ~1 h prior to performing the separations.

Materials and Reagents. The fused-silica capillary columns were purchased from Polymicro Technologies, Inc. (Phoenix, AZ). The 3-μm ODS and the 1-μm silica particles were obtained from SynChrom, Inc. (Lafayette, IN) and Phase Separation, Inc. (Norwalk, NJ), respectively. The 5-μm silica gel for creating the frits was graciously provided by John O'Gara from Waters Corp. (Milford, MA). The priority pollutant PAH mixture (standard reference material, SRM 1647c) was a gift from Dr. Lane Sander at the National Institute of Standards and Technology. Sodium tetraborate, acetonitrile (HPLC grade), methanol, and individual PAHs were purchased from Aldrich Chemical Co. (Milwaukee, WI). The mobile phase was prepared by mixing the appropriate percentage of acetonitrile in 4 mM sodium tetraborate solution

(10) Yan, C.; Schaufelberger, D.; Erni, F. *J. Chromatogr.* **1994**, *670*, 15.

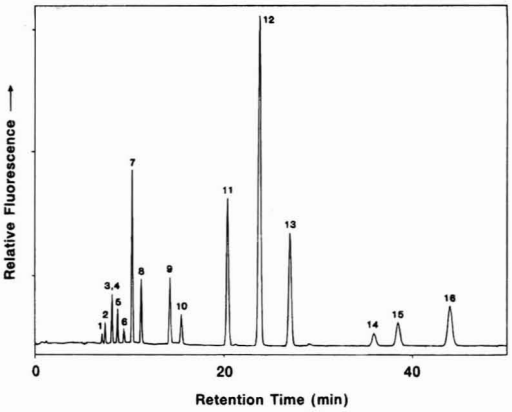

Figure 2. Electrochromatogram showing the capillary electrochromatographic separation of the 16 PAHs. The column dimensions were 75 μm i.d. × 365 μm o.d. (33-cm packed length). The mobile phase consisted of 80% acetonitrile in a 4 mM sodium borate solution. The applied voltage was 15 kV. Injection was performed electrokinetically at 5 kV for 5 s. The peaks are identified as follows (~10^{-6}–10^{-8} M of each compound): (1) naphthalene, (2) acenaphthylene, (3) acenaphthene, (4) fluorene, (5) phenanthrene, (6) anthracene, (7) fluoranthene, (8) pyrene, (9) benz[*a*]anthracene, (10) chrysene, (11) benzo[*b*]fluoranthene, (12) benzo[*k*]fluoranthene, (13) benzo[*a*]pyrene, (14) dibenz[*a,h*]anthracene, (15) benzo[*ghi*]perylene, and (16) indeno-[1,2,3-*cd*]pyrene.

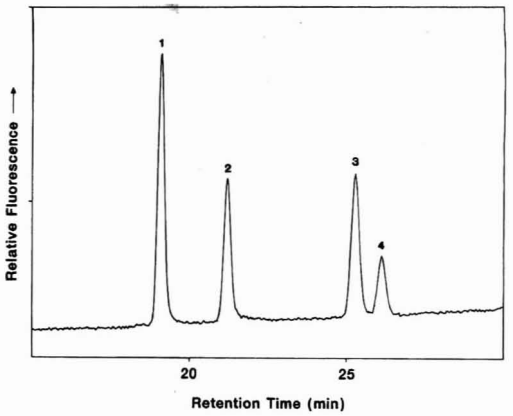

Figure 3. Electrochromatogram showing the separation of the first four PAHs. The conditions are the same as in Figure 2, except that the acetonitrile in the mobile phase has been changed to 60%.

and degassed before use. Water was purified with an Ultra-Pure water system from Millipore (Milford, MA). Stock solutions (1–10 mM) of the individual PAHs were first made in acetonitrile and then diluted to the desired levels in the mobile phase.

RESULTS AND DISCUSSION

Packing Capillary Columns. We found several factors to be important in consistently producing the packed capillary columns. The quality of the frits played a significant role in creating columns that generated reliable results. Overheating the frits caused blockage of the column, resulting in a reduction or elimination of the mobile phase flow, whereas insufficient heating caused the stationary phase particles to migrate through the frits. Initial efforts attempted to create a frit in a second piece of capillary that was attached to the outlet end of the packed column with a Teflon sleeve. Achieving a good connection was tedious and difficult. Therefore, we focused our attention on creating the outlet frit on-column, as described in the Experimental Section. In our experience, packing the columns electrokinetically[8] was more effective than packing the columns with a pump. We also added 1-μm pure silica particles (10%) to the 3-μm ODS particles (90%) in the column packing. This addition may have aided in stabilizing the electroosmotic flow, but no detailed studies were carried out. In addition, particular attention was paid to formulating the mobile phase, degassing it thoroughly to prevent bubble formation, and equilibrating the column before running the samples.

Efficiency and Selectivity. Figure 2 shows a typical electrochromatogram of the 16 PAHs and demonstrates the high efficiency of CEC. (The peaks were identified by comparing their retention times with those of standards run individually.) The numbers of theoretical plates per meter (calculated using the equation $N = 5.54(t_R/w_{0.5})^2$, where N, t_R, and $w_{0.5}$ represent the number of theoretical plates, the retention time of the analyte, and the width at half-height of the peak, respectively, and normalized per meter of column length) for acenaphthalene, fluoranthene, and benzo[*k*]fluoranthene, for example, are 110 000, 120 000, and 150 000, respectively. Because the detection window was created approximately 1–2 mm after the outlet frit, some dispersion of the peaks may result when the solutes pass from the packed section of the column to the unpacked section. Using a 150-μm-i.d. column (20-cm packed length) with a window created immediately prior to the outlet frit, efficiencies up to 400 000 theoretical plates/m were obtained. The higher efficiencies were obtained, however, at the expense of lower detection sensitivities caused by excessive light scattering from the packing particles.

Under the isocratic mobile phase conditions used in the run (80% acetonitrile in the 4 mM sodium tetraborate solution), 15 of the 16 components were baseline resolved. Two of the components, acenaphthene and fluorene, coeluted under these conditions. When the fraction of acetonitrile in the mobile phase was changed to 60%, we were able to separate these two peaks from each other (shown in Figure 3). Using the lower percentage of acetonitrile in the mobile phase, however, resulted in a large increase in the retention times for the later-eluting peaks. It is expected that a gradient elution procedure should allow the separation of acenaphthene and fluorene without significant expense in the total time of analysis.

Sensitivity, Linearity, and Reproducibility. Serial dilutions (10 times to 100 000 times) of the standard reference mixture were run to determine the minimum detection limits of the system. Table 1 lists the values of the detection limits for the PAHs obtained using the UV-LIF detection scheme.[11] The addition of acetonitrile to the mobile phase significantly enhanced the fluorescence intensities observed for the PAHs. Because the fluorescence wavelengths of the different PAHs vary greatly, a broad wavelength window (280–600 nm) was used to detect the emission. A slit was utilized to prevent background luminescence from the capillary walls from reaching the PMT. This luminescence from the fused-silica capillary wall occurs at >600 nm (measurements peformed using a monochromator). Conse-

(11) The values of the mass detection limits of the PAHs were calculated on the assumption that the packing particles occupied 75% of the volume in the packed section of the column.

Table 1. Detection Limits of the 16 PAHs Using UV-LIF[a]

PAH	concn (M × 10^{-10}) I	concn (M × 10^{-10}) II	mass (mol × 10^{-19}) I	mass (mol × 10^{-19}) II
naphthalene	32	64	220	450
acenaphthylene	30	40	210	280
acenaphthene	12	13	84	91
fluorene	5.3	5.8	37	41
phenanthrene	3.5	2.7	25	19
anthracene	1.7	0.73	12	5.1
fluoranthene	1.1	1.4	7.7	9.8
pyrene	3.3	2.0	23	14
benz[*a*]anthracene	1.3	0.50	9.1	3.5
chrysene	2.4	1.5	17	11
benzo[*b*]fluoranthene	0.57	0.53	4.0	3.7
benzo[*k*]fluoranthene	0.20	0.09	1.4	0.63
benzo[*a*]pyrene	0.43	0.27	3.0	3.0
dibenz[*a,h*]anthracene	3.7	2.2	26	15
benzo[*ghi*]perylene	2.0	1.3	14	9.1
indeno[1,2,3-*cd*]pyrene	1.2	15	8.4	110

[a] Two different filter arrangements were used: (I) a 280-nm longpass filter and two 600-nm shortpass filters and (II) a 70-nm (fwhm) bandpass filter centered at 400 nm.

quently, it may be more difficult to detect large PAHs that fluoresce in this region. It was observed that a 70-nm (fwhm) bandpass filter centered at 400 nm gave better limits of detection for most of the PAHs compared to the limits of detection obtained using the broader wavelength range (280–600 nm). The large variation in the limits of detection for the PAHs is caused by the difference in absorption of the PAHs at 257 nm and their different fluorescence quantum efficiencies. We believe that the sensitivity of our detection system was limited by background fluorescence from the mobile phase. This problem may be minimized in the future by using appropriate cleaning procedures (e.g., distillation of solvents) or by photobleaching the mobile phase before use.

The reproducibility in the peak heights of the PAHs and the linearity in the fluorescence response of the detection system were also measured. The variation in the peak heights ($n = 3$) was less than 5%. To measure the linearity, benzo[*k*]fluoranthene was chosen as a model analyte. The response was found to be linear between 2×10^{-7} and 2×10^{-11} M, with a correlation coefficient of 0.9995.

The reproducibilty in the retention times of the PAHs is demonstrated in Figure 4. The four electrochromatograms shown were taken over a period of 1 week with the same column. The relative standard deviations for the retention times of the peaks were less than 2%. We have obtained similar results with numerous other columns.

Comparison of CEC with Micro-HPLC and MECC. It is expected that efficiencies obtained in CEC should be higher than those obtained in micro-HPLC because of the pluglike profile of electroosmotic flow.[6] We compared the efficiencies obtained with a column run electrokinetically and the same column run with pressure (75-μm-i.d. column with a 33-cm packed length). The results are shown in Table 2. Under our experimental conditions, up to 75% higher efficiencies were obtained with CEC.

Terabe et al.[12] have also attempted the separation of these 16 PAHs with MECC. By using a high concentration of surfactant (100 mM SDS) in combination with cyclodextrins and urea, partial resolution between the components was achieved. The use of the high concentration of SDS and urea prevented us from taking advantage of LIF detection because of excessive fluorescence background.

(12) Terabe, S.; Miyashita, Y.; Ishihama, Y.; Shibata, O. *J. Chromatogr.* **1993**, *636*, 47.

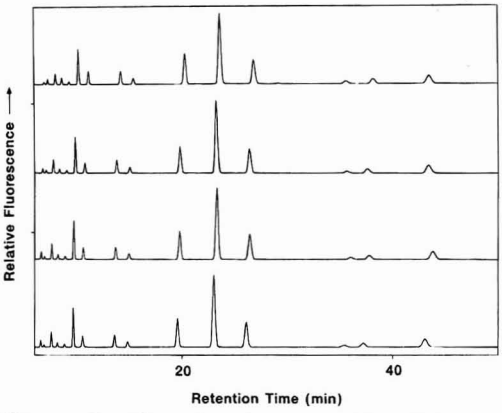

Figure 4. Four different electrochromatograms taken with the same column during the period of 1 week. The separation conditions are similar to those in Figure 2.

Table 2. Comparison of Efficiencies between CEC and Micro-HPLC

PAH	no. of theoretical plates (*N*)/m CEC	no. of theoretical plates (*N*)/m micro-HPLC
naphthalene	102 000	67 000
fluoranthene	132 000	85 000
benz[*a*]anthracene	137 000	89 000
benzo[*k*]fluoranthene	138 000	103 000

CONCLUSION

We have demonstrated that CEC can be used effectively in the laboratory to obtain high-efficiency, high-selectivity separations of neutral molecules. It combines the benefits of high-resolution capillary electrokinetic separations with the universality of liquid chromatography. In combination with a LIF detection system, subattomole detection limits can be achieved for PAHs on the basis of their native fluorescence following UV excitation. We believe the production of packed capillary columns can be achieved in a routine manner. This capability might allow CEC to achieve a growth rate that is similar to that which CZE has experienced over the past decade.

ACKNOWLEDGMENT

We would like to thank Gary Hux and Judy Rognlien for technical assistance. R.D. is grateful to Eli Lilly and Co. for sponsoring his ACS Analytical Division Summer Fellowship. This work was supported by a grant from the Defense Programs Technology Transfer Initiative, U.S. Department of Energy.

NOTE ADDED IN PROOF

Since this paper was accepted for publication, Prof. T. Tsuda has kindly informed us of his use of electrokinetic forces in preparing packed capillaries. See: Inagaki, M.; Kitagawa, S.; Tsuda, T. *Chromatography* **1993**, *14*, 55R–60R.

Received for review January 3, 1995. Accepted March 28, 1995.[⊗]
AC9500038

[⊗] Abstract published in *Advance ACS Abstracts,* May 15, 1995.

Anal. Chem. **1995,** *67,* 2030–2036

Solid Phase Trapping Mechanisms Involved in the Supercritical Fluid Extraction of Digitalis Glycosides with Modified Carbon Dioxide

W. N. Moore and L. T. Taylor*

Department of Chemistry, Virginia Polytechnic Institute and State University, Blacksburg, Virginia 24061

Understanding and optimizing the variables involved in the collection of the extracted analytes are as important as understanding and optimizing the extraction variables themselves. It has been shown here that the method by which the modifier is introduced can have an effect on one's ability to trap the components quantitatively. The ability of the solid phase to quantitatively trap extracted components at high modifier percentages, as well as the type of mechanism that gives rise to sample loss from a tandem trapping system, has been shown to be dependent on flow rate and trapping temperature. It is further shown that the optimum trap temperature and flow rate combination for extractions where high modifier levels are employed exists at high trap temperature, to boil away any modifier, and low flow rates, to maximize contact time with the trap.

The success of supercritical fluid extraction (SFE) with liquid trapping is limited by the ability to (1) remove the analytes of interest from the matrix, (2) quantitatively trap the extracted components, and (3) accurately assay the resulting solution. For successful SFE with solid phase trapping, the additional step of thoroughly rinsing the analytes from the trap prior to analysis is required. Failure to optimize each of these steps will limit the success of SFE. The removal of the analytes from the matrix is viewed as the most complex and complicated of the steps presented and is achieved by optimizing extraction parameters such as fluid density, static and dynamic extraction time periods, flow rate, and fluid composition. If the fluid has insufficient solvating power for the analytes in question, and if one is restricted to a particular fluid, modification of the supercritical fluid with a polar liquid is required.

At first glance, the collection of the analytes in SFE seems fairly simple and straightforward. The analytes can be collected via two basic trapping techniques. The first and most popular to date is liquid trapping, in which the analyte-containing CO_2 is decompressed into a compatible organic solvent such as methanol or hexane. Its popularity is due largely to the fact that it is mechanically simple to carry out. However, liquid trapping does possess many variables which must be optimized to ensure quantitative trapping. Such variables include the type and volume of organic solvent, depth of the restrictor or transfer tube into the collection solvent, geometry of the collection vessel, temperature of the restrictor and liquid, and flow rate of the fluid. Since a liquid CO_2 flow rate of 1 mL/min results in a decompressed gaseous flow rate of ~500 mL/min, low flow rates must be employed which decrease the chance of analyte loss due to its being purged or vented from the collection solvent. Also, Joule–Thompson cooling is associated with the expansion of the gas, which can result in plugging of the restrictor by the extracted analyte, although instrumentation advances have minimized and in some cases eliminated this problem. There have been many extractions which have employed liquid trapping when 100% CO_2 was used as the extraction fluid. Burford et al. have given a detailed review of liquid trapping employing 100% CO_2.[1] Hawthorne and Miller have reported high recoveries of PAHs from a variety of matrices, including urban dust, river sediment, and fly ash, employing a liquid trap of methylene chloride (2 mL).[2] Also, liquid trapping has been successful in the trapping of PAHs and organochlorine pesticides with hexane as the collection solvent.[3] However, when an organic modifier is incorporated into the extraction protocol, a considerable effect on the trapping efficiency of a liquid solvent may be realized. Since modifier will be trapped along with the analytes and will become an integral part of the trapping medium, the compatibility between the modifier and the collection solvent should be addressed. In other words, optimum trap conditions for 100% CO_2 would not necessarily be optimum for modified CO_2. Our literature search has not revealed a detailed study of simple liquid trapping alone when modified fluids are employed. However, there have been many published applications where liquid trapping has been employed in conjunction with modifiers and with a variety of matrices, such as plant materials, soils, sludges, and cell media.[2,4–8]

The second type of SFE collection technique which is rapidly growing in popularity and is expected to surpass liquid trapping in the future is known as solid phase trapping. In this case, the analyte-containing CO_2 is decompressed onto an inert solid phase such as stainless steel beads or onto a solid sorbent which is often a chromatographic stationary phase such as octadecylsilica or silica itself. The analyte must then be rinsed off the solid surface with a suitable solvent. For 100% CO_2 systems, Mulcahey et al. have provided a detailed study of solid phase trapping.[9] The trap temperature was found to be critical for certain analytes (e.g.,

(1) Burford, M. D.; Hawthorne, S. B.; Miller, D. J.; Braggins, T. J. *J. Chromatogr.* **1992,** *609,* 321.
(2) Hawthorne, S. B.; Miller, D. J. *Anal. Chem.* **1987,** *59,* 1705–1708.
(3) Lopez-Avilla, V.; Dodhiwala, N. S.; Beckert, W. S. *J. Chromatogr. Sci.* **1990,** *28,* 468–476.
(4) Hawthorne, S. B.; Miller, D. J. *J. Chromatrogr. Sci.* **1986,** *24,* 258–264.
(5) Dooley, K. M.; Ghonasgi, D.; Knopf, F. C. *Environ. Prog.* **1990,** *9,* 197–203.
(6) Campbell, R. M.; Meunier, D. M.; Cortes, H. J. *J. Microcolumn Sep.* **1989,** *1,* 302–308.
(7) Janda, V.; Steenbeke, F.; Sandra, P. *J. Chromatogr.* **1989,** *479,* 200–205.
(8) McNally, M. E. P.; Wheeler, J. R. *J. Chromatrogr.* **1988,** *435,* 63–71.
(9) Mulcahey, L. J.; Hedrick, J. L.; Taylor, L. T. *Anal. Chem.* **1991,** *63,* 2225–2232.

0003-2700/95/0367-2030$9.00/0 © 1995 American Chemical Society

acetophenone and *N,N*-dimethylaniline), but for others it did not seem to matter (e.g., tetracosane, decanoic acid, and 2-naphthol). Trapping with a solid phase when 100% CO_2 is employed is easier to achieve and less complicated than in systems which incorporate modifier; however, there are numerous matrices/analytes where modifier will be required.

Mulcahey and Taylor have shown, for example, that both volatile and nonvolatile components of a test mixture are lost from a C-18 sorbent trap when modifier in excess of 4% is utilized.[10] It is believed that this analyte loss stems from aerosol formation with the expanding SF mixture of CO_2 and condensed organic solvent.[11-13] Yoo and Taylor reported that an increased trap temperature aids in the recovery of an array of compounds at higher (4–16%) modifier percentages, but percent recoveries plateau when the trap can no longer boil away the condensed modifier.[14] Currently, it is believed that the ability to trap compounds on a solid sorbent at high (>4%) modifier concentrations is directly related to the trap temperature during extraction and the supercritical fluid flow rate.

For some applications, a single trap may be insufficient for quantitative purposes, in which case a third and less common form of trapping in SFE known as tandem trapping could be employed. This type of trapping system may employ sequential solid and liquid trapping schemes in order to maximize the collection of analytes. Dionex (Sunnyvale, CA) manufactures a supercritical fluid extractor which employs in tandem a glass surface plus a liquid trapping system. This device employs a fully heated restrictor housed within a glass tube that extends into the liquid. The glass tube serves as the solid phase trap, while a variety of different organic solvents can be utilized in the liquid trap. Work has been performed on this instrument which shows that tandem trapping is more efficient in trapping some compounds than conventional liquid trapping alone.[11,15] In cases where the fluid employed with this type of tandem trapping system was 100% CO_2, several applications and studies have revealed recoveries of PAHs, for example, from marine sediment that are comparable to that of Soxhlet extraction.[15] Also, Thompson and Taylor reported on the tandem solid/liquid collection of an array of nonpolar and polar compounds using the aforementioned Dionex SFE system.[16] For analytes of varying polarity, a solvent mix composed of hexane and chloroform proved best.

Detailed studies involving tandem solid/liquid trapping when modified CO_2 was employed have recently been reported by these same workers.[17] When modifier was employed, recoveries were generally poor, regardless of the modifier amount and identity when the 100% CO_2 optimum collection solvent mixture was employed. In cases where modifier was used, pure hexane surprisingly was found to work best. Meyer et al. have also reported that high recoveries of PAHs from soils have been achieved with Dionex tandem solid/liquid trap when employing modifier.[11]

As was previously stated, to increase the polar nature of the fluid for solvating more polar compounds and to overcome any analyte–matrix interaction which may be present, a polar liquid modifier is added to the SF. There has been an ongoing debate concerning the various ways in which modifier can be introduced into the SFE experiment. Modifier introduction may be of three types: (1) addition of premixed modified fluid, (2) modifier addition to CO_2 in-line with the aid of a micro-HPLC pump, and (3) direct modifier addition to the matrix via spiking. While premixed tanks are still in use, they pose problems, as the modifier concentration has been shown to vary with respect to the amount of fluid used. Consequently, the latter two techniques are gaining in popularity.

It is known but not widely studied that the mode of modifier introduction into SFE can have a profound effect on the extraction efficiency. Knipe et al.[18] have suggested that matrix modification rather than fluid modification is more effective for the extraction of atrazine, cyanazine, and diuron from Celite and soil. We believe that the mode of modifier introduction can have a significant effect on trapping in SFE as well.

The focus of the work reported here is twofold. First, the effect of the mode of modifier introduction on solid phase trapping in SFE is investigated. Second, the various types of mechanisms which can lead to analyte loss at the solid phase trap when high levels of modifier are used are considered. Three possible mechanisms are given whereby analytes may be lost from a solid phase trap when employing modified CO_2. Trapping and extraction conditions which favor each particular mechanism are presented, and the degree of success achieved when a tandem liquid trap is employed under each scenario is investigated. Recommendations for successful trapping are also given in concert with modified fluids.

EXPERIMENTAL SECTION

All supercritical fluid extractions were performed on the Suprex Prepmaster (Suprex Corp., Pittsburgh, PA), which employs an automated variable restrictor. The Accutrap (Suprex Corp.), which is a module used for off-line collection of the analytes via either solid, liquid, or tandem trapping, was employed. This component can achieve solid trap temperatures from −50 to +100 °C, and its automated restrictor can also achieve a temperature of 100 °C, which further helps to reduce clogging. The extractor employs a dual-head reciprocating pump which can deliver up to 7 mL/min liquid flow while achieving a maximum pressure of 500 atm (7348 psi). The oven can achieve temperatures up to 150 °C. The extraction fluid was SFE/SFC grade CO_2 and was obtained from Air Products and Chemicals, Inc. (Allentown, PA). Modifier was either introduced in-line with an HPLC pump obtained from SSI (State College, PA) or added directly to the vessel. All solvents were HPLC grade purchased from EM Science (Gibbstown, NJ). All samples for extraction were prepared by spiking 0.5 mg (1 mL of a 0.5 mg/mL solution in methanol) of each of the three analytes, digoxin, gitoxin, and digitoxin, onto Celite (Supelco, Bellefonte, PA) in a 3.7 mL vessel obtained from Dionex (Sunnyvale, CA). The methanol was completely evaporated prior to each extraction. The glycoside

(10) Mulcahey, L. J.; Taylor, L. T. *Anal. Chem.* **1992**, *64*, 2352–2356.
(11) Meyer, A.; Kleibohmer, W.; Cammann, K. *J. High Resolut. Chromatogr.* **1993**, *16*, 491–494.
(12) Vannoort, R. W.; Chervet, J.-P.; Lingeman, H.; de Jong, G. J.; Brinkman, U. A. Th. *J. Chromatrogr.* **1990**, *505*, 45–77.
(13) Wright, B. W.; Wright, C. W.; Gale, R. W.; Smith, R. D. *Anal. Chem.* **1991**, *63*, 38–44.
(14) Yoo, W. J.; Taylor, L. T. Air Products Application Note, 1994.
(15) Meyer, A. *J. Chromatrogr.* **1993**, *657*, 327–335.
(16) Thompson, P. G.; Taylor, L. T. *J. High Resolut. Chromatogr.* **1993**, *16*, 713–716.
(17) Thompson, P. G.; Taylor, L. T. *J. High Resolut. Chromatogr.* **1994**, *17*, 759–764.
(18) Knipe, C. R.; Gere, D. R.; McNally, M. E. P. *ACS Symp. Ser.* **1992**, *488*, 251–265.

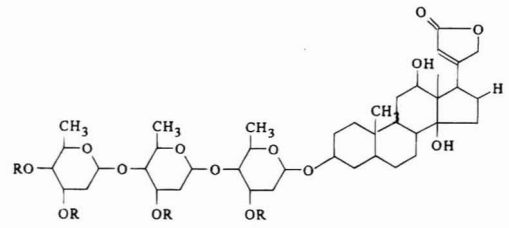

DIGOXIN

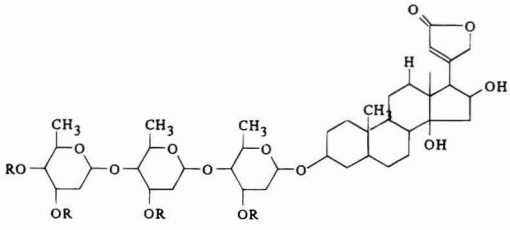

GITOXIN

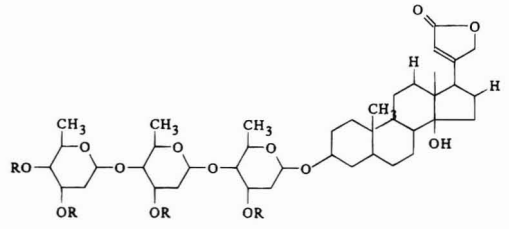

DIGITOXIN

Figure 1. Structures of the three glycoside compounds used for the trapping study. Molecular weights are ~800, while the melting points of each are ~300 °C.

standards were purchased from Sigma Chemical Co. (St. Louis, MO) (Figure 1).

All extractions were performed at a pressure of 450 atm and an oven temperature of 50 °C. The solid phase trap was packed with stainless steel beads obtained from Suprex, and a liquid trap of 3 mL of methanol in a 10 mL sealed microcollection flask (Supelco) was employed in tandem (Figure 2). Following each extraction, the liquid trap was assayed for percent recovery, followed by an assay of the solid trap rinse, which was 5 mL of methanol at 25 °C. The restrictor during extraction was heated to either 50 or 100 °C, and the solid phase trap during rinsing was held at 25 °C. Flow rates and modifier concentration were varied throughout the experimental process.

An HPLC–UV assay of the glycoside standards was performed on a 1050 Series HPLC system (Hewlett-Packard, Avondale, PA), which incorporates a quaternary gradient pump and a variable wavelength UV detector. A gradient 75/25 water/acetonitrile–100% acetonitrile program was employed. A model EQ-60 LC six-port external loop injection valve (Valco, Houston, TX) was used with a 10 μL sample loop. A 4.6 × 250 mm Hypersil ODS (5 μm) (Keystone Scientific Inc., Bellefonte, PA) liquid chromatographic column was employed. The wavelength of detection was 215 nm, and the flow rate employed was 1.5 mL/min. All samples were

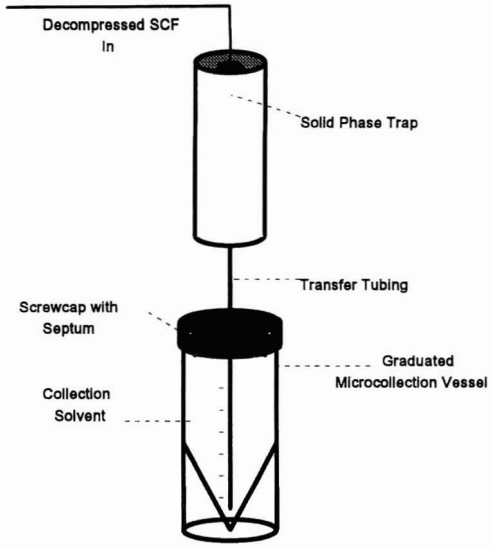

Figure 2. Diagram of the tandem trapping system employed throughout the study.

filtered through a 0.45 μm filter (Millipore, Bedford, MA) prior to injection.

Extraction profiles were obtained by carrying out a stepwise extraction in which the liquid and solid phase traps were periodically assayed and their cumulative recoveries plotted as a function of extraction time. During each of the trap rinsing steps, the extraction vessel was maintained under supercritical conditions with the aid of a six-port static/dynamic valve.

Analyte recoveries relative to an external standard were calculated on the basis of a four-point calibration curve of each glycoside compound, in which the correlation coefficient for each curve was ≥0.9995. Relative standard deviations of the chromatographic method were found to be ≤1% for $n = 3$ for each of the three compounds when employing the separation method discussed above.

RESULTS AND DISCUSSION

1. Modifier Concentration and Introduction. <senThis portion of our trapping study focuses on the effect of modifier concentration and the manner in which the modifier is introduced. The benefit of employing a tandem liquid trap was also examined. A liquid CO_2 flow rate of 1 mL/min was used. The solid trap and restrictor temperatures were maintained at 100 °C, and the liquid phase of the tandem trap was at 25 °C. It should be noted that a solid phase trap of 100 °C is unusually high, but since our analytes have molecular weights around 800 amu, no decomposition of analytes was anticipated. Initially, methanol modifier was introduced in-line to the fortified matrix. Increasing percentages (0–30%) of methanol-modified CO_2 were used in each dynamic extraction, which lasted 30 min (Figure 3a). Recovery increased for all three analytes as the methanol concentration increased. This was surprising, because in the past just the opposite had been observed because of decreased trap efficiency with higher modifier levels, but in these previous cases, the solid phase trap temperature was below the boiling point of the modifier.[5]

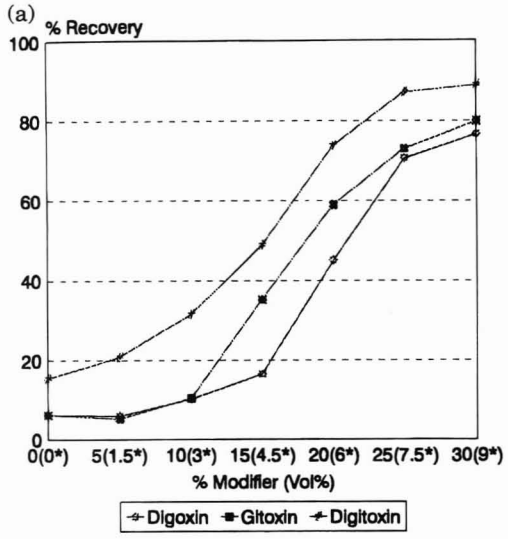

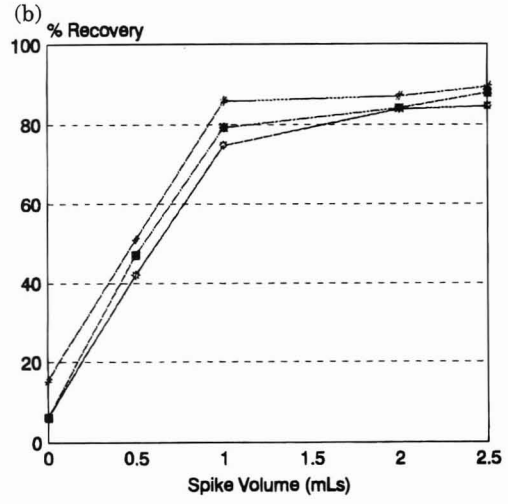

Figure 3. Plots of combined recoveries of solid and liquid trapping versus time for the two extractions by which the method of modifier introduction was varied. (a) The plot for the in-line modifier addition. The numbers in parentheses on the *x*-axis indicate the volume (mL) of modifier used. (b) The plot for the spiking of the modifier in the vessel. In this extraction, >95% of all material was trapped on the solid phase.

<senSince the solid phase trap was at 100 °C, no liquid methanol should have accumulated on the stainless steel trap. The large percentage (30%) of methanol was deemed to be needed to solubilize these high molecular weight analytes. In a second extraction, the modifier was introduced into the system by spiking the fortified matrix with methanol just prior to extracting with 100% CO_2 for 10 min in the static mode, followed by 20 min in the dynamic mode (Figure 3b). A comparison of both parts a and b of Figure 3 naively suggests that approximately the same (but less than quantitative) recovery is obtained with either a total of

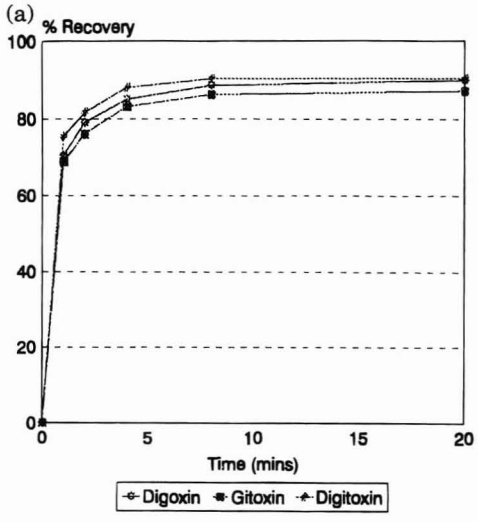

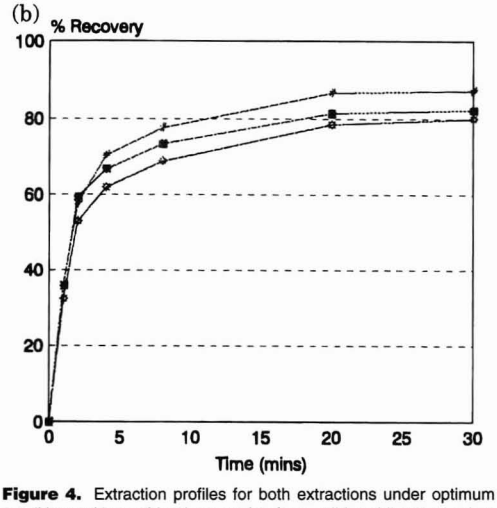

Figure 4. Extraction profiles for both extractions under optimum conditions with combined recoveries from solid and liquid trapping.

9 mL of methanol (in-line/30 min dynamic) in the modified fluid case or 2.0 mL of methanol (spike/10 min static–20 min dynamic) in the modified matrix case.

Extraction profiles were next constructed under optimum conditions for both "in-line" and "spiked" extractions (Figure 4) in order to gain some insight as to why a larger amount of modifier for the in-line extraction was required for a comparable extraction of the three glycosides. Both extraction profiles appeared somewhat similar in that initial slopes were rather steep but each profile quickly reached a plateau. This type of extraction profile is indicative of minimal analyte–matrix interaction, which was expected since the matrix was inert. Surprisingly, the in-line modifier (30%) profile (Figure 4a) showed a greater recovery in 5 min than was seen after 30 min with 30% in-line modifier (Figure 3a) under identical dynamic extraction conditions. The only difference in the two experiments was that the stainless steel trap

was rinsed after every 2.5 min for the in-line extraction profile data, whereas the trap was rinsed only once after 30 min dynamic extraction in the other (Figure 3a). The in-line 30% modifier extraction profile (Figure 4a) also showed a greater initial recovery of the analytes after 5 min when compared to the extraction profile results when an optimum methanol matrix spike was employed (2 mL) (Figure 4b). This finding can be explained by the idea that solvent breaks through the trap, taking analyte with it during the initial stages of the spiked matrix extraction, when modifier levels are high. This large amount of methanol which condenses on the trap is believed to form an aerosol in the initial stages of the extraction, resulting in lower recoveries for the spike extraction throughout the extraction profile. This aerosol formation was subsequently proven to increase when the CO_2 flow rate increased (Figure 5). It appears that the solid trap, when heated to 100 °C, is able to boil away the 0.3 mL/min of methanol introduced by in-line modifier addition, but it is unable to boil away the larger initial cascade of 2 mL of methanol introduced through matrix spiking.

The lower recoveries witnessed initially with the in-line 30% modifier 30 min extraction compared with a 5 min in-line 30% modifier extraction under identical conditions can be attributed to analyte loss from the solid phase trap by physical removal of the analytes from the stainless steel trap over the 30 min extraction period as decompressed supercritical fluid continued to enter the solid trap. It was thought originally that the tandem liquid trap under these conditions (i.e., continuous 30 min extraction) would have trapped any compounds which were not trapped on the solid phase, but this proved not to be the case, as <5% of the total recovery could be attributed to the liquid trap. For the spiked matrix study, the liquid trap in tandem with the solid phase trap did accumulate some analyte with increasing CO_2 flow, but the overall result was lower recoveries with increasing flow. This observation once again points out the ineffectiveness of the tandem liquid trap.

2. Trapping Loss Mechanisms. There appear to be three possible mechanisms responsible for analyte loss from a solid phase trap: (1) blowing off of the solid phase trap due to the force generated by the decompressed gas (i.e., blow-by), (2) blowing by the trap in the form of an aerosol generated by the decompression of the mixture of CO_2 and modifier (i.e., aerosol formation), and (3) analyte being mechanically rinsed from the solid phase trap by condensed modifier which is produced during the SF decompression (i.e., modifier elution). Three experiments are described here in which one of the mechanisms appears to be in effect. In each case, it is believed that each of the three mechanisms contributes to analyte loss from the trap; however, for each scenario given, one mechanism is predominant.

Blow-By. This particular experiment was described in detail in the previous section (Modifier Concentration and Introduction). An extraction profile was constructed with the "in-line modifier addition" extraction (Figure 4a), and a greater overall recovery in 5 min was seen compared with a 30 min extraction under identical extraction (Figure 3a) conditions, with the only difference being the frequency of washing of the solid phase trap. The lower recoveries witnessed initially with the in-line modifier extraction for 30 min (~80%) compared with a 5 min (~90%) extraction under identical conditions can be attributed to analyte loss from the solid phase trap by physical blow-by of the analytes from the stainless steel trap over the 30 min extraction period. Analytes which are

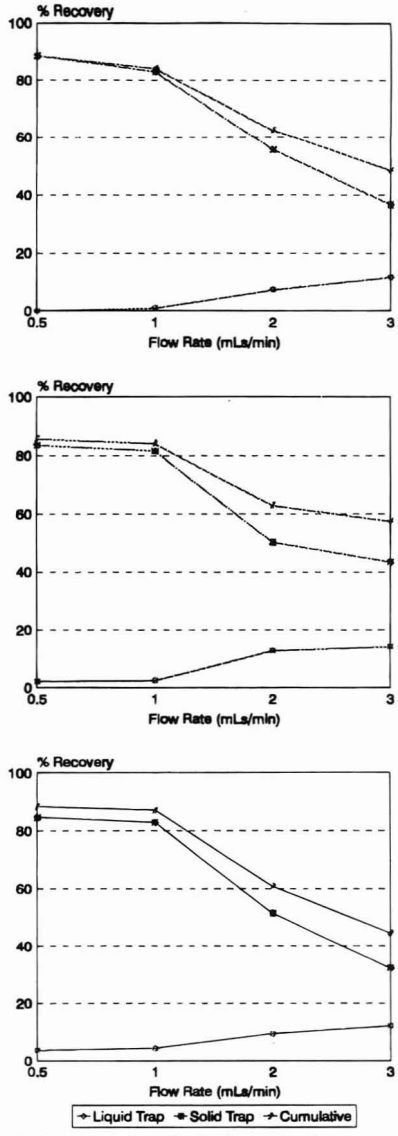

Figure 5. Plot showing the effect of increasing flow rate on trapping efficiency after matrix modification of the solid and liquid phase traps for each of the three probe analytes, digoxin (top), gitoxin (middle), and digitoxin (bottom).

lost from the solid trap as a result of being mechanically forced off due to SF decompression appear to be surprisingly unretained by even the liquid trap (e.g., <5% of the glycosides were found in the in-line liquid trap).

Aerosol Formation. Methanol (2 mL) was spiked onto the matrix and extracted as in the previous experiment. The solid phase trap during extraction was kept at 30 °C, the restrictor at 50 °C, and the flow rate was increased from 0.5 to 2 mL/min. Under these conditions, extracted methanol would condense onto the trap. Decompressed carbon dioxide thus flowing past the stainless steel surface on which the methanol had condensed

would no doubt blow off the methanol which contained the dissolved analytes. Proof for this comes from the fact that <5% of the recoveries could be attributed to solid phase trapping at the highest flow rate, as was expected. In addition, a dramatic decrease in the amount of analyte trapped within the liquid trap was observed (relative to the lower flow rate in the previous experiment), indicating an increased amount of blow-by of both traps due to aerosol formation. Recoveries of combined solid and liquid traps were below 40% for each of the three analytes. It is believed that higher flow rates propel the aerosol farther than lower flow rates, thereby resulting in less analyte being trapped in the liquid trap.

Modifier Elution. Varying amounts of methanol were spiked into the vessel, and the fortified matrix was extracted statically 10 min, followed by a 20 min dynamic extraction wherein 15 mL of extraction fluid was used. The conditions of the extraction were kept the same as above, with the exception that the solid phase trap temperature during extraction was lowered from 100 to 30 °C, the restrictor temperature was set at 50 °C, and the flow rate was set at 0.5 mL/min. The ability of the solid phase trap to retain the extracted analyte was very poor at low trap temperatures and all spiked modifier levels (Figure 6). For example, a 2.5 mL modifier spike essentially had nothing trapped on the solid phase. While the liquid trap appeared to exhibit increasing efficiency with increasing level of spiked modifier, a less than quantitative cumulative recovery was found. At low spike levels, the combined solid and liquid traps are probably efficient, but the level of modifier is too low to achieve sufficient solubility. For example, ~45% recovery was found for a 0.5 mL modifier spike. At high modifier levels, a relatively large amount of modifier condenses on the solid phase, such that one can observe liquid modifier dripping from the solid trap. Under these conditions, it is clear that the presence of the tandem liquid trap is very important, as it trapped components which were ineffectively trapped on the solid sorbent.

A final experiment was performed to prove the hypothesis that high trap temperature and low flow rate would provide the highest recoveries thus far with the stainless steel trap. Methanol (2 mL) was spiked onto the matrix and extracted for 10 min in the static mode, followed by 20 min in the dynamic mode. The liquid flow rate was 0.5 mL/min, and the trap temperature was held at 100 °C throughout the extraction. These extraction parameters represent optimum high-temperature/low-flow conditions, and quantitative recoveries were obtained on each analyte, as shown in Figure 7. The recoveries, along with the RSDs, of the three compounds were as follows: digoxin, 93.8% (3.2%); gitoxin, 95.9% (5.1%); digitoxin, 93.5% (2.9%).

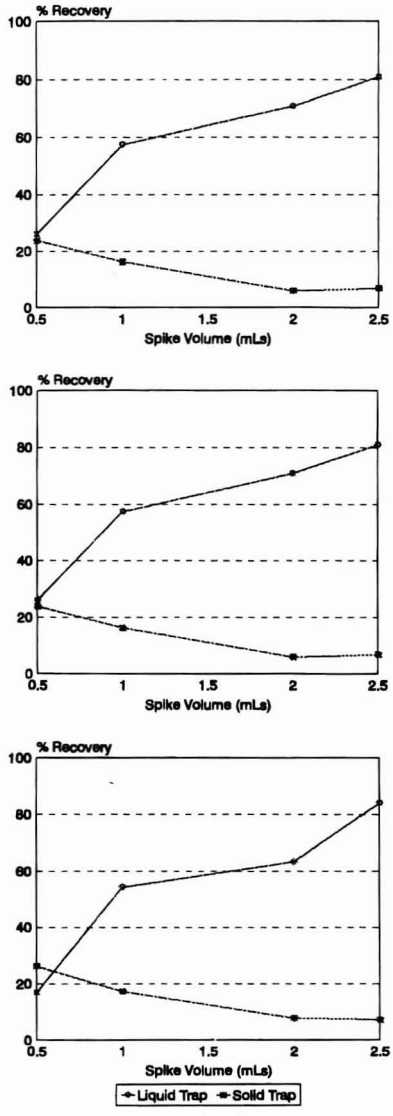

Figure 6. Plot showing how matrix spike volume affects where the target analytes [digoxin (top), gitoxin (bottom), and digitoxin (middle)] are trapped within the tandem trapping system.

CONCLUSION

The use of modified CO_2 adds another dimension to SFE in the trapping process as well as in the extraction step. When employing modifier, the user should be aware that low recoveries may not be due to the fluid's inability to solvate and remove the analyte of interest from the matrix, but rather a problem exists in the ability to trap the extracted components effectively. It is known that the method by which modifier is introduced into the SFE system affects the extraction efficiency of different matrices, and it can also have an effect on the ability to trap the components effectively. While larger initial amounts of modifier may help to solvate more of the analytes within the vessel, problems with trapping are observed at these higher spiked modifier percentages which cannot be eliminated totally even at high trap temperatures.

For extractions which exhibit matrix effects, a modified matrix may be preferred over a modified fluid, depending on the amount of modifier employed. However, a large volume of modifier added to the vessel may actually lead to lower net recoveries than in-line modifier addition, even at high trap temperatures, because of aerosol formation at the trap. Extractions that use high flows and that place lots of decompressed CO_2 through the stainless steel trap (between trap rinses) run the risk of analytes blowing off the trap. For this reason, it may prove beneficial to use frequent rinse steps. For the best recoveries when modifier

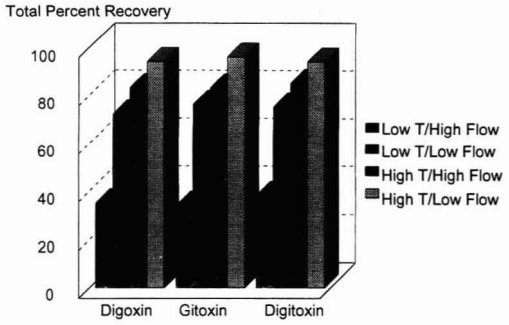

Figure 7. Bar graph showing the cumulative recoveries after matrix modification as a function of the four combinations of high/low trap temperature and high/low liquid flow rate.

concentration is high, regardless of the mode of modifier introduction, it is believed that high trap temperatures, low flow rates, and periodic trap rinsing are preferred.

The ability of the solid phase to quantitatively trap extracted components at high modifier percentages, as well as the type of mechanism that gives rise to sample loss from the tandem trapping system, has been shown to be dependent on flow rate and trapping temperature. Tandem trapping proved to be beneficial in instances where modifier elution was occurring (low trap temperature/low flow rate/modifier condensation); however, in instances where the analyte was being lost due to aerosol formation (low trap temperature/high flow rate/modifier condensation) and/or physical blow-by of the analyte (high trap temperature/high flow rate/no modifier condensation) due to the force of the decompressed gas, the liquid trap in tandem provided very little benefit, even for the nonvolatile, higher molecular weight glycosides. It was shown that the optimum trap temperature and flow rate combination for extractions where high modifier levels are employed exists at high trap temperature, to boil away any modifier, and low flow rates, to maximize contact time with the tandem liquid trap. Under these high modifier conditions, a sorbent trap should be investigated, but one should verify with a tandem trap (at high/low trap temperature and high/low decompressed flow rate), as was performed here, the sufficiency of a single solid phase trap.

ACKNOWLEDGMENT

We appreciate and would like to thank Air Products and Chemicals, Inc. for providing the gases employed in the extractions and Suprex Corp. for providing the supercritical fluid extractor.

Received for review February 13, 1995. Accepted April 12, 1995.[⊗]

AC9501598

[⊗] Abstract published in *Advance ACS Abstracts,* June 1, 1995.

Anal. Chem. **1995**, *67*, 2037–2041

Evaluation of a Dual-Cyclodextrin Phase Variant of Capillary Electrokinetic Chromatography for Separations of Nonionizable Solutes

Michael J. Sepaniak,* Christine L. Copper, Kylen W. Whitaker, and Vincent C. Anigbogu†

Department of Chemistry, University of Tennessee, Knoxville, Tennessee 37996-1600

A capillary electrokinetic chromatography technique is described that employs neutral cyclodextrins (CDs) as a primary phase, transported with electroosmotic flow, and charged CDs as an electrophoretically mediated secondary phase. Neutral, hydrophobic solutes are separated on the basis of their differential distribution between these CD phases. The technique resembles micellar electrokinetic capillary chromatography (MECC) with regard to instrumentation and the fundamental relationships for resolution and capacity factor, which are influenced by the existence of a finite elution window. Conversely, the CD technique offers unique and beneficial characteristics when compared to MECC. Efficiency, selectivity, and system retention are evaluated on the basis of separations of polyaromatic hydrocarbons (PAHs). Efficiency is comparable to that of MECC (>10^5 plates/m). The specificity associated with solute–CD inclusion complexation provides elution orders for PAHs that do not follow the hydrophobicity trends of MECC. Moreover, since the CD phases are largely noninteractive, complex CD systems can be used to enhance selectivity. Capacity factors can be altered in a convenient and predictable fashion simply by changing the CD phase ratio. The technique is rather robust with regard to the use of running buffers containing organic solvents; the effects or organic modifier and pH on system retention are demonstrated.

The hallmark of capillary electrophoresis (CE) is exceptional efficiency. Plate counts exceeding 10^6 plates/m are not unusual. The facile addition of a wide variety of reagents to CE running buffers provides for unique selectivities and renders the technique fairly versatile. Nevertheless, a substantial limitation of CE is its inability to separate neutral species. Because of the preponderance of neutral compounds in samples of biological, environmental, and industrial origin, this limitation is particularly significant to current CE technology. Neutral compounds can be separated if they acquire an effective mobility due to association with charged running buffer additives. This can be accomplished via solvophobic interactions with organic ions.[1] However, the most successful and general approach involves the addition of surfactants at concentrations exceeding the critical micelle concentration. This technique was first introduced by Terabe[2] and is sometimes dubbed micellar electrokinetic capillary chromatography (MECC).[3] Instrumental and operational aspects of MECC are virtually indistinguishable from those of CE. However, MECC also shares many of the features of chromatography. The running buffer assumes the role of the "primary phase", and the micelles constitute a "secondary phase". The running buffer is transported through the capillary by electroosmotic flow (EOF), and, in general, the micelles are retarded due to electrophoretic effects. Injected solutes are separated on the basis of a differential distribution between these phases. The MECC technique is characterized by a finite "elution window" which can limit peak capacity and hinder the separation of hydrophobic species.[3] Otherwise, the retention characteristics of MECC resemble those of reversed phase HPLC, albeit with much improved efficiency.

Mixed aqueous–organic running buffers expand the utility of MECC for separations of hydropobic molecules by extending the elution window,[3,4] which increases peak capacity, and by reducing capacity factors (k' values), for which optimum values are generally <5.[5] Unfortunately, organic modifier concentrations greater than about 25% inhibit micelle formation. Separations of hydrophobic molecules in MECC are also facilitated through the use of running buffers that contain cyclodextrins (CDs).

Native CDs are neutral, cylindrically shaped, macrocyclic sugar molecules that possess a hydrophobic cavity and a hydrophillic exterior.[6] Cavity diameters for these chiral reagents vary depending on the number of glucopyranose units (6, 7, and 8 units for α-CD, β-CD, and γ-CD, respectively) in the structure. Native CDs have been derivatized with a wide variety of neutral and ionizable functional groups.[7] Inclusion complex formation between guest solutes and the cavity of the CD host is influenced by the geometry, size, and physiochemical properties of the solute. Inclusion complexation can be highly selective and serves to reduce k' values in MECC by hindering the association of solutes with micelles. We have found CD-modified MECC to be an effective method for efficient separations of many hydrophobic polyaromatic hydrocarbons (PAHs).[8,9] Computational molecular modeling techniques provided insights into the mechanisms by which CDs discriminated between PAH geometrical isomers.[9]

† Visiting summer faculty program participant. Current address: Department of Chemistry, Agnes Scott College, Decatur, GA 30030.

(1) Walbroehl, Y.; Jorgenson, J. W. *Anal. Chem.* **1986**, *58*, 479–481.
(2) Terabe, S.; Otsuka, K.; Ichikawa, K.; Tsuchiya, A.; Ando, T. *Anal. Chem.* **1984**, *56*, 111–113.
(3) Sepaniak, M. J.; Swaile, D. F.; Powell, A. C.; Cole, R. O. In *Capillary Electrophoresis: Theory and Practice*; Grossman, P., Colburn, J., Eds.; Academic Press, Inc.: New York, 1992; Chapter 6.
(4) Balchunas, A. T.; Sepaniak, M. J. *Anal. Chem.* **1987**, *59*, 1466–1470.
(5) Terabe, S.; Otsuka, K.; Ando, T. *Anal. Chem.* **1985**, *57*, 834–841.
(6) Strattan, C. *BioPharm* **1991**, *4*, 44–51.
(7) Terabe, S.; Otsuka, K.; Nishi, H. *J. Chromatogr. A* **1994**, *666*, 295–319.
(8) Copper, C. L.; Staller, T. D.; Sepaniak, M. J. *Polycyclic Aromat. Compds.* **1993**, *3*, 121–135.
(9) Copper, C. L.; Sepaniak, M. J. *Anal. Chem.* **1994**, *66*, 147–154.

0003-2700/95/0367-2037$9.00/0 © 1995 American Chemical Society

CD type and concentration influence separation performance. Derivatized CDs generally provide less selectivity in CD-modified MECC, i.e., they function largely as organic modifiers.[9] Terabe and co-workers first demonstrated that carboxylated CDs can function in a manner similar to negatively charged micelles (as the secondary phase described above) for separations of water soluble neutral compounds.[10] More recently, enantiomeric separations of water soluble compounds (mostly chiral drugs) have been facilitated using running buffers containing charged CDs.[11–14] Migration behavior depends on the ionic state of the drug and the magnitude of EOF.[11] Lurie et al. recently reported the use of mixtures of neutral and anionic CDs to facilitate separations of cationic drugs of forensic interest.[15] In that work, the charged and neutral CDs served to selectively modify the mobilities of the charged drugs in what is largely an electrophoretic mode of operation.

The work described herein differs from the approaches discussed above in two significant regards. First, we address the separation of hydrophobic PAH molecules that are essentially insoluble in the running buffer. Second, the electrokinetic chromatography phase system is comprised of a secondary phase that is charged CD and a primary phase that is neutral CD, rather than running buffer as with other approaches; i.e., the running buffer functions solely as a carrier fluid. Separations are based on a differential distribution between these distinct CD phases. Hence, we will refer herein to this CE variant as cyclodextrin distribution capillary electrochromatography (CDCE). A preliminary evaluation of the technique is presented that focuses on efficiency, selectivity, and system retention characteristics, with an emphasis on comparisons with MECC.

EXPERIMENTAL SECTION

Apparatus. The component-based CE apparatus used in this work has been described in detail elsewhere.[8] Briefly, it consisted of a Hipotronics (Brewster, NY) Model 840A high-voltage power supply, fused-silica capillaries (typically 50 cm, 40 cm to the detection zone, 50 μm i.d.) provided by Polymicro Technologies, Inc. (Phoenix, AZ), and inlet and outlet reservoirs comprised of microcentrifuge tubes with platinum wire electrodes. Laser-induced fluorescence detection was accomplished using an Omnichrome (Chino, CA) Model 3074-20M He–Cd laser (20 mW, 325 nm) for excitation and a Hammamatsu (Bridgewater, NJ) Model R1516 photomultiplier tube and Pacific Photonics (Concord, CA) photometer to acquire and process signals. Details concerning the optical arrangement can be found in ref 8.

Reagents. All CDs used in these studies were gifts from American Maize Products (Hammond, IN) or CTD, Inc. (Gainesville, FL). Carboxymethyl-β-CD (CM-β-CD) was used exclusively as the charged CD phase, and various native and hydroxypropyl (HP) CDs were used as the neutral CD phases. CD concentrations were in the range of 1–15 mM. HPLC grade solvents were obtained from Baxter Scientific (McGraw, IL). PAHs, buffer salts, and surfactants were purchased from Sigma Chemical Co. (St. Louis, MO). Buffers were comprised of 10 mM sodium phosphate and 6 mM sodium borate, with pH adjusted by using phosphoric acid (normally pH 6 for CDCE and pH 9 for MECC). The running buffer for MECC separations contained 50 mM sodium dodecyl sulfate (SDS).

Procedures and Operating Conditions. The capillaries were initially rinsed with 100 mM NaOH. As a general observation, we find that capillary lifetime in CE degrades if excessive rinsing is employed. In this CDCE work, rinsing every several injections with a weak base solution (10 mM NaOH), followed by a water rinse, resulted in good reproducibility. In particular, coefficients of variation in retention time for quadruplicate injections of pyrene and anthracene were consistently <2.0%. Stock solutions of the PAHs were prepared in tetrahydrofuran and then diluted with running buffer to prepare working sample solutions with PAH concentrations in the low micromolar range. Peak identity was based on peak height increase upon spiking of the working solution with the PAH of interest. Separations were accomplished without temperature control at applied voltages of 15–20 kV. Hydrostatic injections were performed using an inlet elevation of 10 cm and an injection time of 10 s. The void time of each run was marked by a solvent disturbance. This was taken to represent the effective elution time of the neutral CDs in the system. It should be noted that high concentrations of CD reduced EOF slightly. The retention time of anthracene was used as a rough indication of the effective retention time of the charged CD phase (see Results and Discussion). Theoretical plate counts (N) were determined from stripchart recordings using the standard equation involving peak baseline width and retention time.

Safety. Benzo[*a*]pyrene and certain other PAHs are known carcinogens, so caution should be exercised when working with them. PAH solutions were prepared under a ventilated hood. Disposable latex gloves were worn while working with these compounds. Care was taken to dispose of waste solutions properly.

RESULTS AND DISCUSSION

By analogy with the expressions derived by Terabe for capillary electrokinetic chromatography,[5,10] the values for resolution (R_s) and k' in CDCE are given by eqs 1 and 2, respectively. In these

$$R_s = \frac{N^{1/2}}{4}\frac{\alpha - 1}{\alpha}\frac{k_2'}{1 + k_2'}\frac{1 - t_{ne}/t_{ch}}{1 - (t_{ne}/t_{ch})k_1'} \quad (1)$$

$$k' = \frac{t_R - t_{ne}}{t_{ne}(1 - t_R/t_{ch})} = \frac{V_{charged}}{V_{neutral}}K_D \quad (2)$$

equations, α is a selectivity factor (k_2'/k_1'), $V_{charged}/V_{neutral}$ is the CD volume phase ratio for the system, and K_D is the distribution coefficient of the solute between the CD phases. The times appearing in the equations, t_{ne}, t_{ch}, and t_R, are the effective retention times of the neutral CD, charged CD, and injected solute, respectively. Because the charged CD sample used in this work is very polydisperse (see below) and, unlike normal micelles, is a "fixed" organized assembly (i.e., does not exchange between its various derivatized forms), the value of t_{ch} is not well-defined. Nevertheless, we have used the t_R of the PAH anthracene, in a system without neutral CD, as a means to determine t_{ch}. This is

(10) Terabe, S.; Ozaki, H.; Otsuka, K.; Ando, T. *J. Chromatogr.* **1985**, *332*, 211–217.
(11) Schmitt, T.; Engelhardt, H. *Chromatographia* **1993**, *37*, 475–481.
(12) Smith, N. *J. Chromatogr. A* **1993**, *652*, 259–262.
(13) Nardi, A.; Eliseev, A.; Bocek, P.; Fanali, S. *J. Chromatogr.* **1993**, *638*, 247–253.
(14) Tait, R. J.; Thompson, D. O.; Stella, V. J.; Stobaugh, J. F. *Anal. Chem.* **1994**, *66*, 4013–4018.
(15) Lurie, I. S.; Klein, R. F. X.; Dal Cason, T. A.; LeBelle, M. J.; Brenneisen, R.; Weinberger, R. E. *Anal. Chem.* **1994**, *66*, 4019–4026.

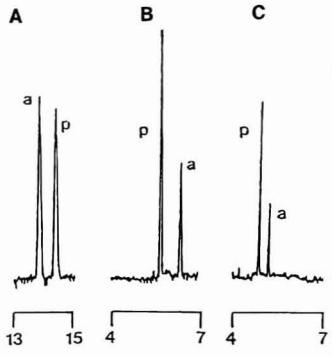

Figure 1. Separations of anthracene (a) and pyrene (p) using a standard capillary and running buffer (see Experimental Section) with 20% CH_3CN as organic modifier and (A) 50 mM SDS, MECC system; (B) 5 mM β-CD:10 mM CM-β-CD, CDCE system; and (C) 5 mM HP-β-CD:10 mM CM-β-CD, CDCE system. Separations performed at 15 kV.

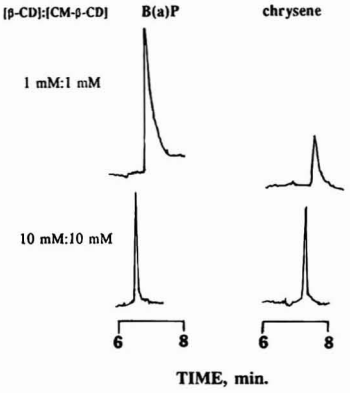

Figure 2. CDCE peak profiles for B(a)P and chrysene at low and high CD concentrations using standard capillary and running buffer with 30% CH_3OH as organic modifier. Profiles obtained at 20 kV.

based on the observation that without neutral CD in the running buffer, the effective electrophoretic mobility of the anthracene–CM-β-CD complex did not change as the concentration of CM-β-CD was varied from 1 to 15 mM (i.e., anthracene appears to have a very large inclusion complexation constant with CM-β-CD). This mobility is taken to approximate an aggregate electrophoretic mobility of the many forms of CM-β-CD. The CM-β-CD mobility obtained in this manner is assumed to be constant and is used to calculate t_{ch} for certain of the CDCE systems used in this work. Subsequent discussion is organized around efficiency, selectivity, and system retention, which are represented in eq 1 by the first, second, and last two terms, respectively.

Efficiency. Sources of band dispersion in MECC have been studied extensively.[16–18] The ultimate limit of efficiency in all forms of CE is axial diffusion. However, resistance to mass transfer (the association–dissociation of solutes with micelles or CDs and mass transport between micelles or CDs) can be an important source of band dispersion in capillary electrokinetic chromatography. The fact that micelles and charged CDs are polydisperse can exacerbate problems with slow mass transfer. The problem in MECC is lessened by the fact that normal micelles are dynamic assemblies and are rapidly exchanging with free surfactant. Conversely, the CM-β-CD used in this work contains a complex mixture of CDs derivatized to varying degrees and at various hydroxyl positions (21 such hydroxyl positions exist on β-CD[6]). The manufacturer quotes an average of three CMs per β-CD. However, our mass spectral investigation of this CD indicated a wide distribution in the degree of substitution. Thus, rapid association–dissociation kinetics and transport between CDs is expected to be very important in achieving high efficiency.

Figure 1 reveals that efficiency in CDCE can be comparable to that of MECC. The efficiencies for the pyrene peaks in that figure are 210 000 plates/m for the MECC case and 150 000 and 220 000 plates/m for the CDCE cases that employ β-CD and HP-β-CD, respectively, as the neutral CD. The effective diffusion coefficients of the solutes in the CDCE separations should be very low since they are associated with bulky CD molecules. Thus, the observed efficiency is probably too low for axial diffusion to be a significant source of dispersion.

The CD concentration can be important in providing high efficiency, as demonstrated in Figure 2. Benzo[*a*]pyrene (B(a)P) and chrysene are unresolved with the simple CDCE system employed and thus are shown separately in the figure. When the CD concentrations are increased from 1 to 10 mM, efficiency is improved dramatically. A possible increase in temperature, due to a greater thermal load, and improved solubility may contribute to the observed efficiency effect. However, running currents and PAH concentrations were fairly low in that experiment. It is more likely that improved mass transfer is responsible for the superior efficiency at the higher CD concentration. Since the PAHs are essentially insoluble in the aqueous phase, CDs must get very close in order to exchange solute. Assuming a uniform distribution of CD within the running buffer, the average inter-CD distance is small for both systems (22 and 8 nm calculated for the small and large CD concentrations, respectively). Thus, the frequency of CD encounters is extremely high in each system and should not prohibit mass transfer. However, the better proximity of CDs for the high concentration case could influence the orientation for solute exchange between CDs and/or the association–dissociation kinetics. In any event, increases in CD concentration can improve efficiency but were limited in this work to CD-β-CD concentration less than about 15 mM due to the onset of thermal dispersion.

In some runs, the current was observed to increase. In those cases, the flow rate appeared to change and peaks exhibited severe tailing. This indicates interaction between the CD phase and the capillary wall. Given the like charges of the silica surface and the CM-β-CD, this is somewhat surprising. In most cases, a base (10 mM NaOH) rinse restored separation performance.

Selectivity. The unique selectivity afforded by the CDCE technique is evidenced by a reversal of elution order, relative to MECC, of pyrene and anthracene in Figure 1. The CDCE system used for Figure 1B involves native and charged β-CD. If the CM derivatization did not alter the complexation characteristics of the β-CD, there would be no separation of these PAHs, even though

(16) Sepaniak, M. J.; Cole, R. O. *Anal. Chem.* **1987**, *59*, 472–476.
(17) Terabe, S.; Otsuka, K.; Ando, T. *Anal. Chem.* **1989**, *61*, 251–260.
(18) Davis, J. M. *Anal. Chem.* **1989**, *61*, 2455–2461.

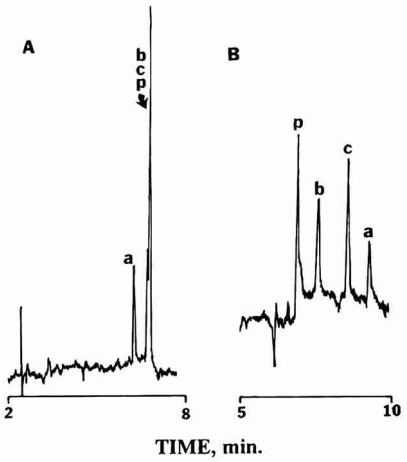

Figure 3. Separations of anthracene (a), pyrene (p), chrysene (c), and B(a)P (b) using standard capillary and running buffer and (A) 50 mM SDS, 8 mM γ-CD, 8 mM β-CD, CD-modified MECC system; and (B) 8 mM β-CD and 1 mM γ-CD:10 mM CM-β-CD with 30% organic modifier, complex CDCE system. Separations performed at 20 kV.

they have very different complexation constants. In fact, K_D values would be expected to be the same for all compounds. Obviously, the derivatization of β-CD with CM in this particular commercial product strongly enhances the inclusion complexation with anthracene relative to pyrene. Since dozens of derivatized CDs are commercially available, CDCE systems with diverse selectivities should be possible.

Another illustration of unique selectivity is shown in Figure 3. It is intriguing that the elution order for the CDCE separation is pyrene (four fused benzene rings), B(a)P (five rings), chrysene (four rings), and anthracene (three rings). Unlike micellar systems, which can form mixed micelles when multiple surfactants are used and may interact with the CD when CD-modified MECC is performed, the CDs in the CDCE technique act independently. Thus, complex systems can be designed in CDCE with predictable effects on selectivity. For example, in order to resolve B(a)P and chrysene (see Figure 3B), it was necessary to employ a ternary CD system that contained a low concentration of γ-CD; prior work had revealed a strong association between B(a)P and γ-CD.[9]

We have also employed a CDCE system to separate the enantiomers of a neutral drug.[19] In that work, the use of charged CD alone did not result in enantioselectivity. However, a system comprised of β-CD−CM-β-CD provided baseline resolution.

System Retention. The optimum capacity factor for the MECC technique depends on the width of the elution window and generally falls in the range of 1−5.[4] Hydrophobic molecules exhibit excessive k' values and tend to coelute near the end of the window. Thus, it is possible to improve R_s without improving selectivity simply by reducing k' and/or extending the elution window. The elution window in CDCE is defined by t_{ne} and t_{ch} and, as such, depends on EOF and the electrophoretic mobility of the charged CD. Low EOF and a high degree of CM-β-CD substitution favor a wide elution window but can result in long separation time and can influence CD inclusion. Because t_{ch} is not well-defined in CDCE (see above), the width of the elution window is also not well-defined. In fact, since substitution of the CD is shown in this work to influence solute−CD inclusion, it is possible for compounds with different distributions in their affinities for the CM-β-CD "mixture" to experience different effective windows under the same set of operating conditions. In general, the windows for the CDCE systems investigated in this work are smaller than those in MECC. This can be seen from inspection of Figure 3.

Table 1 presents the effects of organic modifier (CH_3OH) and pH on the retention times of pyrene and anthracene, which elute near the beginning and the end of the window, respectively. As the v/v content of CH_3OH (%) is increased, the EOF decreases and the spacing between the compounds increases. It is possible that an increase in the solubility of anthracene in the high organic content running buffer may partially mask the extension of the window. In related CDCE work,[19] we observed an increase in resolution from about 0.6 to 1.1 for the enantiomers of a neutral drug as CH_3OH concentration was increased from 0 to 50%. This illustrates both the influence of the width of the elution window on resolution and the ability of the CDCE technique to tolerate

Table 1. Effect of Organic Modifier and pH on System Retention (in Min)

conditions[a]	t_{pyrene}	$t_{anthracene}$	Δt
organic modifier			
a + 10% CH_3OH	6.3	8.1	1.8
a + 20% CH_3OH	6.8	9.1	2.3
a + 30% CH_3OH	12.5	15.5	3.0
a + 40% CH_3OH	15.3	18.8	3.5
pH			
b at pH 6.4	5.1	6.6	1.5
b at pH 3.3	9.1	14.5	5.4
b at pH 2.5	10.6	10.6	0

[a] Conditions: **a**, standard capillary and running buffer, 8 mM β-CD, 1 mM γ-CD:10 mM CM-β-CD system, applied voltage of 15 kV; **b**, standard capillary and running buffer, pH adjusted with phosphoric acid, 5 mM β-CD:10 mM CM-β-CD system, applied voltage of 20 kV.

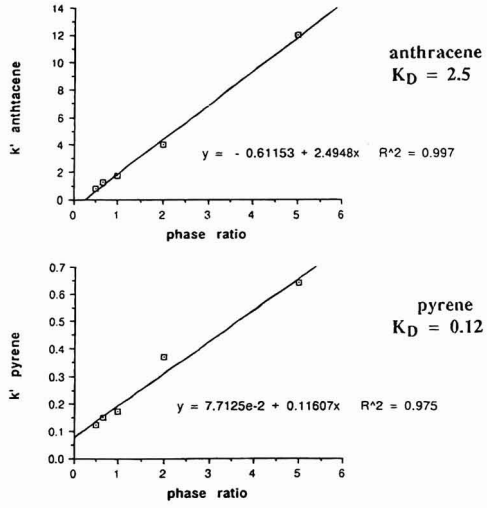

Figure 4. Plots of phase ratio (approximated as concentration ratio [CM-β-CD]/[β-CD]) versus approximate K' (see text for details).

(19) Anigbogu, V. C.; Copper, C. L.; Sepaniak, M. J. *J. Chromatogr. A*, in press.

high concentrations of organic solvents. Table 1 also demonstrates a pH related increase in the width of the window, due to a reduction in EOF as pH is decreased, and the eventual collapse of the window as the charged CD phase is neutralized.

Because of its strong influence on R_s, it would be desirable to exert close control over k' in capillary electrokinetic chromatography. This is easily accomplished in CDCE. Equation 2 illustrates the relationship between k' and the CD phase ratio. This equation assumes no direct interaction between the solutes and the running buffer. Since $V_{charged}/V_{neutral}$ is proportional (and roughly equal to) to [CM-β-CD]/[β-CD], a plot of the concentration ratio versus k' should be linear with a slope approximately equal to the distribution coefficient. Plots for anthracene and pyrene are presented in Figure 4. Phase ratio is approximated by the CD concentration ratio. CM-β-CD concentration was held constant at 5 mM, and β-CD concentration was changed from 0 to 10 mM. The no β-CD case, with an injection of anthracene, was used to establish t_{ch} (see Experimental Section), and solvent disturbances were used to mark t_{ne}. The plots are reasonably linear, and the K_D values are consistent with the stronger association of anthracene with CM-β-CD.

In summary, the dual-CD variant of capillary electrokinetic chromatography described in this report adds new versatility to CE. While it resembles MECC in many regards, it provides unique selectivity and should be particularly useful in isomeric separations, where the geometrical and chiral characteristics of CD inclusion can be exploited. Convenient control over k' and the ability to employ complex CD systems and high concentrations of organic solvents represent other desirable traits of this approach.

ACKNOWLEDGMENT

This work was sponsored by the Division of Chemical Sciences, Office of Basic Energy Science, U.S. Department of Energy, under Grant DE-FG05-86ER13613 with The University of Tennessee, Knoxville. Support was also contributed by The Procter & Gamble Co. and Merck & Co., Inc. The authors are grateful to G. A. Reed of American Maize Products and S. Herschleb of CTD, Inc. for providing cyclodextrin samples used in this work.

Received for review February 1, 1995. Accepted April 12, 1995.[⊗]

AC9501147

[⊗] Abstract published in *Advance ACS Abstracts,* June 1, 1995.

Anal. Chem. **1995,** *67,* 2042–2049

Liquid Droplet. A Renewable Gas Sampling Interface

Shaorong Liu and Purnendu K. Dasgupta*

Department of Chemistry and Biochemistry, Texas Tech University, Lubbock, Texas 79409-1061

As a gas stream flows across a liquid droplet, the soluble constituents contained in the gas diffuse to and dissolve in the liquid drop. From the viewpoint of analytical chemistry, this droplet is thus a potential sampling interface for such soluble constituents. The problem that needs to be solved relates to the manner of its incorporation in a chemical analysis system. This paper describes the coupling of this sampling interface with a sequential analysis system, demonstration of its applicability for the measurement of parts-per-billion levels of gaseous NH_3, and a characterization of the performance of this experimental arrangement. Various aspects of the behavior of the liquid droplet as a collection interface are theoretically discussed and experimentally examined using NH_3 and SO_2 as test gases.

It is often necessary to discriminate between gases and particles by some physical means because the same analyte may be present in both phases. Because the diffusion coefficient of a gas is typically 4 orders of magnitude greater than the smallest atmospheric aerosol of significance, diffusive discrimination provides a noninvasive means. Diffusion denuders, tubes with interior walls coated to function as a sink for the desired gases, were originally described by Townsend.[1] They have been used since the late 1970s for the collection of gases.[2] The original implementation was labor-intensive, wetted denuders in which a (flowing) liquid is used as the collection surface and their membrane-based counterparts called diffusion scrubbers now permit automated continuous collector/analyzers; recent reviews are available.[3,4]

A droplet of water is a natural collector for soluble gases. Allusions to the freshness of air after drops of rain fall through the atmosphere has long been a favorite of the literati. The physical process of rainout of soluble gases like SO_2, HNO_3, etc., has been mathematically described.[5] Additionally, droplets of atmospheric water, in the form of clouds, rain, fog, dew, etc., serve as efficient atmospheric reactors. An interesting aspect of using a droplet as a collector for gases is that as the liquid evaporates from the droplet surface, the flux of the molecules leaving the surface inhibits the approach of particles (but not of soluble gases). This is referred to as *diffusiophoresis* due to *Stefan flow* in the aerosol science literature.[6]

The world of analytical chemistry increasingly involves smaller scales and miniature devices. The use of capillary-based analysis systems is presently enjoying an exponential growth. Membrane-interfaced capillary systems have already been reported for gas analysis.[7,8] A liquid drop, deployed as a collector at the end of a tube, may not only eliminate interference from particles, it may also constitute an effective interface for gas analysis by a capillary-based analysis system. Since such a droplet is readily renewable, there should be no fouling problems as with membranes. The design, characteristics, and deployment of a droplet-based gas analysis system is addressed in this paper.

EXPERIMENTAL SECTION

Collection Device. A droplet-based sampler is schematically shown in Figure 1. One end of a silica capillary tube is supported in the center of a larger tube; the latter serves as the sample gas conduit. A suitable solution is pumped through the capillary, and a droplet is formed at its tip for collection of the gas. As sample gas flows around the drop, gas molecules diffuse to its surface and are collected by the droplet. The analyte concentration can be determined by aspirating the droplet solution back to an in-line automated analysis system. After one collection analysis cycle, a new droplet is formed and the cycle is begun anew.

Trace Gas Generation and Sampling. Most of the work reported in this paper is related to the sampling and determination of ammonia at sub-parts-per-million (ppm) levels. The standard NH_3 gas generation system is schematically shown in Figure 2; The principle has been previously described.[9,10] Compressed house air was fed through a pressure regulator (G), a particle filter (F1, Mini Capsule filter, 0.2 μm, P/N 12122, Gelman Sciences Inc., Ann Arbor, MI), and an NH_3 filter (F2, a column filled with H_2SO_4-washed silica gel). The flow rate of each line was controlled by a mass flowmeter and controller (FC1–3, Model FC-280, Tylan General, Torrance, CA). One line was connected to a porous Teflon tube (M, 60 cm × 5.5 mm i.d., Accurel, V8/2, mean pore size 0.2 μm, Akzo Inc., Wuppertal, Germany) which was completely immersed in the NH_3 generation solution in a sealed plastic bottle. Ammonia was transported from the aqueous solution into the gas phase through the pores in the tube M. At the flow rate (0.12 L/min) used in this experiment, Henry's law equilibration is achieved.[10] Thus, a constant NH_3 concentration was generated in the gas phase as long as the $[NH_{3(aq)}]$ in the generation solution

(1) Townsend, J. S. *Philos. Trans. R. Soc. London, Sect. A* **1900**, *193*, 129–158.
(2) Ferm, M. *Atmos. Environ.* **1979**, *13*, 1385–1393.
(3) Dagupta, P. K. *ACS Adv. Chem. Ser.* **1993,** *No. 232*, 41–90.
(4) Ali, Z.; Paul Thomas, C. L.; Alder, J. F. *Analyst (London)* **1989,** *114*, 759–769.
(5) Butler, J. D. *Air Pollution Chemistry*; Academic Press: New York, 1979; pp 102–106.
(6) Hinds, W. C. *Aerosol Technology*; Wiley: New York, 1982; p 161.
(7) Bao, L.; Dasgupta, P. K. *Anal. Chem.* **1992**, *64*, 991–996.
(8) Liu, S.; Dasgupta, P. K. *Anal. Chim. Acta*, in press.
(9) Hwang, H.; Dasgupta, P. K. *Environ. Sci. Technol.* **1985**, *19*, 255–258.
(10) Dasgupta, P. K.; Dong, S. *Atmos. Environ.* **1986**, *20*, 565–570.

0003-2700/95/0367-2042$9.00/0 © 1995 American Chemical Society

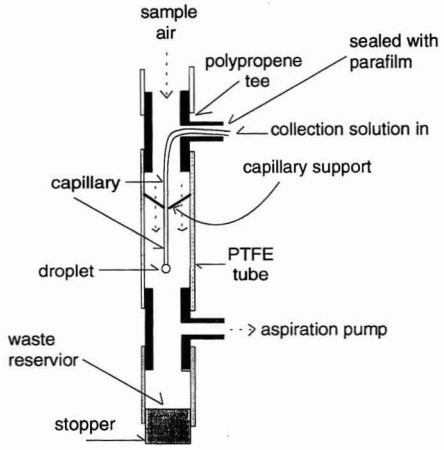

Figure 1. Schematic diagram of the droplet collector construction. The capillary is 0.15 mm i.d. and 0.35 mm o.d. The internal diameter of the PTFE tube is 8 mm.

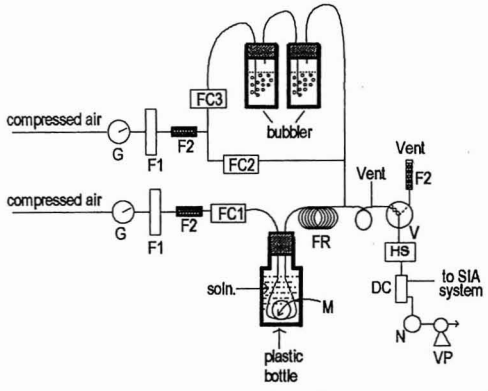

Figure 2. NH_3 gas generation system: G, pressure gauge and regulator; F1, aerosol filter; F2, ammonia filter; FC1, FC2, and FC3, mass flowmeter and controller; FR, flow resistor; V, pneumatic valve; soln., 5 mM NH_4Cl at pH 7; M, porous PTFE membrane; N, needle valve; HS, humidity sensor; VP, vacuum pump; DC, droplet collector.

was maintained constant. A coiled PVC tube (1.5 m × 2 mm i.d.) served as a flow resistor to minimize the influences of flow fluctuations from the dilution air line on the NH_3 source flow rate. The dilution air line was divided into two after the NH_3 filter. One stream, passing through FC3, was fully humidified by passage through two sequential water-filled bubblers. The relative humidity of the dilution airstream was thus controlled by the adjustment of the relative flow rates through FC2 and FC3. The concentration of NH_3 directly in the source output was determined by sampling through a bubbler filled with 10 mM H_2SO_4 and subsequent colorimetric analysis (vide infra) and agreed closely with previously published data.[10] The concentrations of NH_3 in the sample gas was varied by appropriate dilution. If the three-way valve (V) is directed to F2, all the sample is vented. When V is directed to the sample gas line, a portion of the sample is aspirated through the droplet collector (DC); the exact flow rate is controlled by

(11) Huang, H.; Dasgupta, P. K. *Anal. Chem.* **1990**, *62*, 1935–1942.

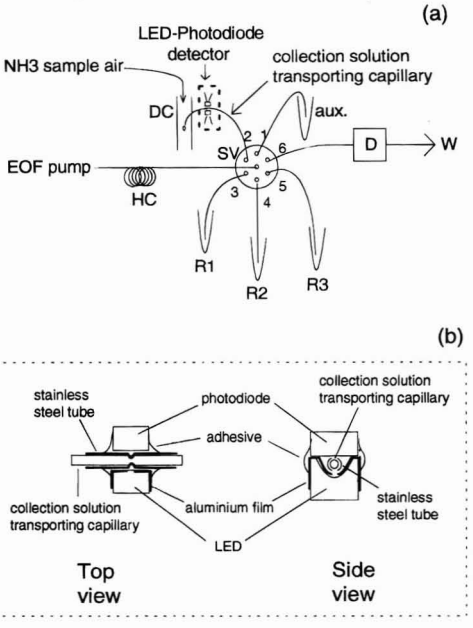

Figure 3. Schematic diagram of the SIA detection scheme: DC, droplet collector; HC, collection solution holding coil; SV, selector valve; R1, R2, and R3, chemical reagents; aux., collection solution; W, waste; D, spectrophotometric detector with wavelength set at 630 nm. Detail constructions of the LED photodiode detector are schematically shown in the bottom panel.

the needle valve (N) before the vacuum pump (VP). A microsized humidity sensor[11] was incorporated after V to determine the relative humidity of the sample gas through DC.

Ammonia-bearing sample air was initially aspirated through DC in a bottom-to-top direction; later results were obtained with flow in the reverse direction as well. The collector droplet is formed as the collection solution is pumped out of the capillary tip. After the desired sampling period, the droplet is aspirated back to a capillary format sequential injection analysis (SIA) system[12] for analysis. Sample carry-over was minimized by propelling the collection solution through the transporting capillary until a drop of the solution (~5 μL) dropped freely from the capillary tip. The volume of this drop is comparable to the volume of the capillary up to the SIA selector valve. A new droplet is then generated. The size of the droplet is controlled by the solution pumping time. An electroosmotic pump[13] was used; however, this is not a requirement.

Analysis System. The SIA system involves electroosmotic pumping and is schematically shown in Figure 3a. The main system was described previously.[12] Briefly, the transporting capillary comprises two segments of capillaries, a ~5 cm × 250 μm i.d. and a 15 cm × 150 μm i.d. capillary. The two segments are butt-jointed with a piece of PVC tubing as a sleeve.

For this work, an LED photodiode detector was put on the transporting capillary to monitor when the meniscus of the

(12) Liu, S.; Dasgupta, P. K. *Talanta* **1994**, *41*, 1903–1910.
(13) Dasgupta, P. K.; Liu, S. *Anal. Chem.* **1994**, *66*, 3997–4004.

Table 1. Protocol for Sample Collection and Detection for the Droplet Collection System

step[a]	time, s	HV,[b] kV	comments
1 (2)	90	+20	generation of a 90 s droplet
2 (2)	330	0	collection of NH_3
3 (2)	~120	−20	aspiration of the solution[c] in the transporting capillary
4 (2)	10	−20	aspiration of NH_3 collected droplet solution
5 (3)	3	−20	aspiration of R1
6 (4)	5	−20	aspiration of R2
7 (5)	15	−20	aspiration of R3
8 (6)	240	+20	propulsion of the reaction product to detector and then cycle from steps 4 to 8 until all the droplet solution is consumed
9 (2)[d]	~300	+20	washing of the transporting capillary until a full drop of the collection solution is dislodged. Return to step 1

[a] This is the high voltage on the EOF pump. [b] The number in parenthesis indicates the selector valve position. [c] The volume of the solution between the collection droplet and the selector valve should be minimized by minimizing the volume of the connecting tubing. [d] From steps 8 to 9, selector valve stopped at position 1 for 0.5 s.

collection solution passed across it (and thence to determine the aspirated droplet volume, vide infra). The detector is shown in Figure 3b. The plastic head of a T-1$^3/_4$ size red LED (650 nm, HLMP-8104, Hewlett-Packard) was filed to flatness. Then a U notch (~1 mm wide × ~1 mm deep) was cut on top with the light-emitting source in the center of the notch. This was covered with a piece of aluminum film with a ~200 μm diameter opening to allow the LED output to shine through. A stainless steel tube segment (~10 mm × ~400 μm i.d. × ~600 μm o.d.) was filed with a hole (~1 mm long × ~300 μm wide) each on opposing sides. This was placed in the U notch on the LED head with its holes in line with the opening of the aluminum film. A photodiode was put the other side of the stainless steel tube. The LED was powered with a constant-current source. The photocurrent was measured with a switched integrator-based detector.[14] For the present purpose, the polyimide coating on the transporting capillary need not be removed; even with the coating intact, there is sufficient photocurrent. Since the inner diameter of the stainless steel tube is slightly bigger than the outer diameter of the transporting capillary, the LED photodiode detector can be easily moved along the capillary and placed anywhere between the selector valve SV and the droplet collector DC.

The chemistry involved in the determination of ammonia utilizes the Berthelot reaction using the sequential mixing of a phenol/sodium nitroprusside reagent (R1, Figure 3a), alkaline EDTA (R2), and sodium hypochlorite (R3). The protocol is listed in Table 1. The absorbance of the indophenol blue product is measured at 630 nm using a linear PHD detector designed for capillary systems (Thermo Separation Products).

A set of experiments was also conducted with SO_2 as the test gas. For the determination of SO_2, a conductivity detector[15] was placed at the joint of two segmented capillaries in the transporting conduit. Using Mn-catalyzed oxidation by H_2O_2 in the collecting droplet, the collected SO_2 was converted to sulfuric acid. The conductivity of the collecting droplet increases in direct proportion to the H_2SO_4 content. After collection, as the droplet is aspirated through the conductivity detector, the H_2SO_4 concentration in the liquid can be directly monitored by conductivity as a function of aspiration time.

Reagents. Reagents used for analysis have been described.[12] For the NH_3 generation solution, 0.26 g of NH_4Cl was dissolved in ~100 mL of 0.1 M Na_2HPO_4; 0.1 M KH_2PO_4 was used to adjust the pH to ~7.0 and the solution was made up to a final volume to 500 mL. This solution has a C_{NH_3} of 10 mM and a $C_{PO_4^{3-}}$ of 0.1 M. The pH of the final solution was measured to be 7.10.

SO_2 Generation Solution. A solution of 5.0 mM $NaHSO_3$ in 0.20 M phthalate buffer (pH ~4) was prepared by dissolving 0.30 g of $NaHSO_3$ in 500 mL of 0.2 M potassium hydrogen phthalate aqueous solution.

Collection Solution for NH_3. Except as stated, 1.0 mM H_2SO_4 was used. As the collection solution for SO_2, 500 μM H_2O_2 in 10 μM $MnSO_4$ was prepared by adding 29 μL of 3% H_2O_2 solution to 50 mL of 10 μM $MnSO_4$ solution. This solution is prepared immediately before use. $Na_2B_4O_7$ (2 mM), used as the electroosmotic pump fluid, was diluted from a 0.5 M stock solution.

RESULTS AND DISCUSSION

Direction of Flow. Statistically, there was no significant difference between results obtained with the sample gas flowing downwards or upwards. Collection occurs by diffusion in a direction transverse to the flow direction in either case, and no difference is expected. However, if the capillary is not exactly centered and a dislodged wash droplet happens to end up on the wall, sample loss will occur with upward flow. With this in mind, a top downwards sampling arrangement was adopted.

Diffusion and Collection of NH_3. The collection of gaseous NH_3 by the droplet involves the following sequential steps, similar to that outlined by Schwartz and Freiberg[16] for the collection of SO_2 by a cloud droplet: (a) diffusion of NH_3 molecules within the gas phase to the gas/liquid interface; (b) Establishment of Henry's law equilibrium at the interface; (c) hydration of NH_3 and partial ionization of NH_4OH (or protonation of $NH_{3(aq)}$ by extant H^+); (d) transport of NH_4^+ within the aqueous phase. Based on previous work on cloud droplets,[16] steps a−c are fast relative to step d. The present experiments use droplet sizes close to 2.0 mm in diameter, substantially larger than cloud droplets, so step d can be safely assumed as the rate-limiting step for the absorption of NH_3.

As NH_3 dissolves, the pH of the interfacial solution increases. Henry's law equilibrium at the interface is very quickly established. A steady state in NH_4^+ concentration in the interfacial solution can be assumed between its production by dissolution/ionization and transport from the interface. If we assume that the droplet is spherical and NH_3 dissolution occurs with spherical symmetry around the droplet, and that the droplet solution is stagnant (no convective mixing), the NH_4^+ concentration within the droplet can be described as[17]

$$C_{r,t} = C_0\frac{r}{R} + \frac{2C_0}{\pi}\sum_n \frac{(-1)^n}{n}\sin\frac{n\pi r}{R}\exp\left(-\frac{n^2}{R^2}Dt\right) \quad (1)$$

where $C_{r,t}$ is the NH_4^+ concentration within the droplet at a

(14) Liu, H.; Dasgupta, P. K.; Zheng, H. J. *Talanta* **1993**, *40*, 1331−1338.
(15) Kar, S.; Dasgupta, P. K.; Liu, H.; Hwang, H. *Anal. Chem.* **1994**, *66*, 2537−2543.
(16) Schwartz, S. E.; Freiberg, J. E. *Atmos. Environ.* **1981**, *15*, 1129−1144.
(17) Vergnaud, J. M. *Liquid Transport Processes in Polymeric Materials, Modeling and Industrial Applications;* Prentice Hall: Englewood Cliffs, NJ, 1991; p 32.

distance of r from the center of the droplet and after a sampling time of t, C_0 is the interfacial solution concentration, R is the droplet radius, and D is the diffusion coefficient of NH_4^+ in the droplet. Normally, terms with $n \geq 2$ are negligible; eq 1 simplifies to

$$C_{r,t} = C_0\frac{r}{R} - \frac{2C_0}{\pi}\sin\frac{\pi r}{R}\exp\left(-\frac{\pi^2}{R^2}Dt\right) \qquad (2)$$

The process of the aspiration of the droplet solution back into the capillary can be envisioned as the droplet being squeezed by the surface tension of the liquid. The solution in the center of the drop closest to the capillary tip is aspirated first while the solution at the surface of the droplet is the last to enter the capillary. For simplicity, we assume that any incremental aspiration results in a spherical volume of radius r' being withdrawn into the capillary, the spherical volume being originally located tangential to the capillary tip (Figure 4). The volume elements 1, 2, 3, 4, etc., in the original droplet may, for example, be aspirated in sequence as aspiration is commenced. In a spherical coordinate system, the NH_4^+ concentration at the exit can be expressed as a function of r':

$$C(r') = \frac{\int_{0\to r'+\delta}\int\int\int C_{r,t}\,dV - \int_{0\to r'}\int\int\int C_{r,t}\,dV}{\frac{4}{3}\pi(r'+\delta)^3 - \frac{4}{3}\pi r'^3} \qquad (3)$$

where δ is a small increment of r'.

For $2r' \leq R$

$$\int_{0\to r'}\int\int\int C_{r,t}\,dV =$$

$$\int_0^{2\pi} d\theta \int_0^{\arcsin r'/(R-r')} \sin\varphi\, d\varphi \int_{(R-r')\cos\varphi-\sqrt{r'^2-(R-r')^2\sin^2\varphi}}^{(R-r')\cos\varphi+\sqrt{r'^2-(R-r')^2\sin^2\varphi}} \left[C_0\frac{r}{R} - \frac{2C_0}{\pi}\sin\frac{\pi r}{R}\exp\left(-\frac{\pi^2}{R^2}Dt\right)\right] r^2\, dr \quad (4a)$$

and for $2r' \geq R$

$$\int_{0\to r'}\int\int\int C_{r,t}\,dV =$$

$$\int_0^{2\pi} d\theta \int_0^{\arcsin r'/(R-r')} \sin\varphi\, d\varphi \int_0^{(R-r')\cos\varphi+\sqrt{r'^2-(R-r')^2\sin^2\varphi}} \left[C_0\frac{r}{R} - \frac{2C_0}{\pi}\sin\frac{\pi r}{R}\exp\left(-\frac{\pi^2}{R^2}Dt\right)\right] r^2\, dr \quad (4b)$$

For typical experimental parameters, $R = \sim 1.0$ mm, $t = 330$ s (sampling time), $Q = \sim 1.5\ \mu$L/min, and NH_4^+ diffusion coefficient in dilute aqueous solutions is 2.0×10^{-5} cm/s (calculated from its infinite dilution equivalent conductance[18] at 25 °C); we can numerically integrate eqs 4a or 4b by iterative stepped integration methods.

A value of $^1/_2\pi$ was used for C_0 for computational purposes. Since both eqs 4a and 4b scale linearly with C_0, the *profile* of $C(r')$ is unaltered by the specific choice of C_0. Numerical integration was carried out with a r' step size of 2 μm, that is, $\delta = 2\ \mu$m. This value was chosen after determining that, for $R = 1000\ \mu$m, the results no longer change below a step size of 4 μm for r'.

(18) Lide, D. R., Ed. *CRC Handbook of Chemistry and Physics*, 73rd ed.; CRC Press, Inc.: Boca Raton, FL, 1992; p 5–111.

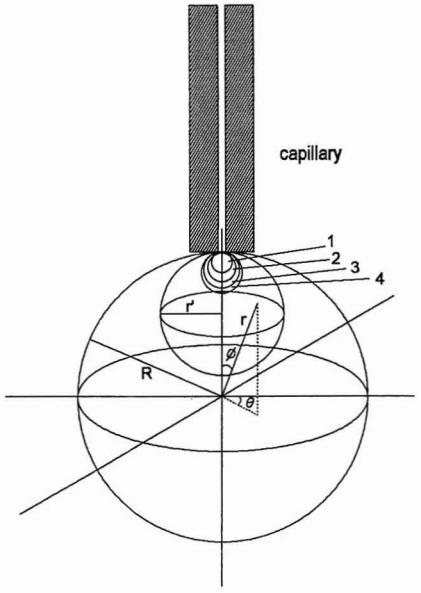

Figure 4. Spherical coordinate system for the solution aspirated back: R, the radius of the whole droplet solution; r', the radius of the solution aspirated back; r, φ, and θ are the spherical coordinates.

Since r' can be expressed in terms of experimental parameters from the relationship

$$r' = \left(\frac{3t'Q}{4\pi}\right)^{1/3} \qquad (5)$$

where t' is the aspiration time and Q is the aspiration rate, the concentration profile $C(r')$ can be converted as a function of the aspiration time t'.

In our experiment, the sample requirements of the SIA system is such that a single droplet of 1 mm radius allows many sequential aliquots to be taken for analysis. We aspirated the droplet in 18 successive aliquots, analyzing each aliquot separately. Figure 5 shows the comparison of the theoretical computations vs the experimental results. In general, at longer aspiration times, that is, for the results from the outer surface of the droplet, the experimental data match the theoretical expectations quite well. For earlier times, especially during the very beginning of the aspiration period, the solution represents mostly the volume element near the capillary tip; the experimental concentrations are increasingly below the theoretical model. This is readily understandable; the theoretical model does not account for the presence of the capillary tip on the surface of the sphere but assumes a uniform input flux of ammonia to the entire surface area of the sphere. In reality, a 0.35 mm diameter capillary occupies a significant portion of the surface area of a 1 mm radius sphere and blocks any input flux over this area. Indeed, the

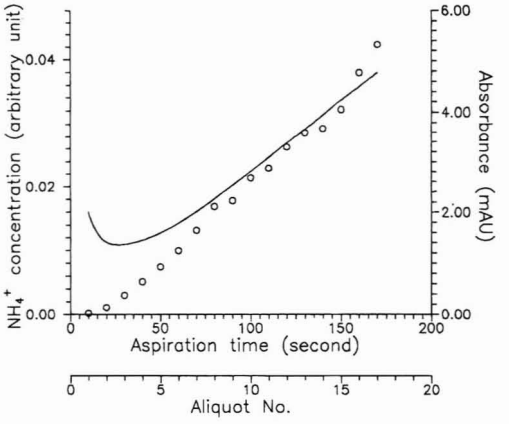

Figure 5. NH_4^+ concentration profile as being aspirated back into the transporting capillary. The solid curve is computed from eqs 4a and 4b, corresponding to the left ordinate and the top abscissa. The points are experimental data, corresponding to the right ordinate and the bottom abscissa; one aliquot is equivalent to 10 s aspiration time. The experiment was done with a HV of ±15 kV on the EOF pump and for a droplet size of 4.5 μL. The experimental procedure is similar to that described in Table 1, with some changes in individual step intervals; 250 ppbv NH_3, ~80% relative humidity, and sampling rate 0.12 L/min.

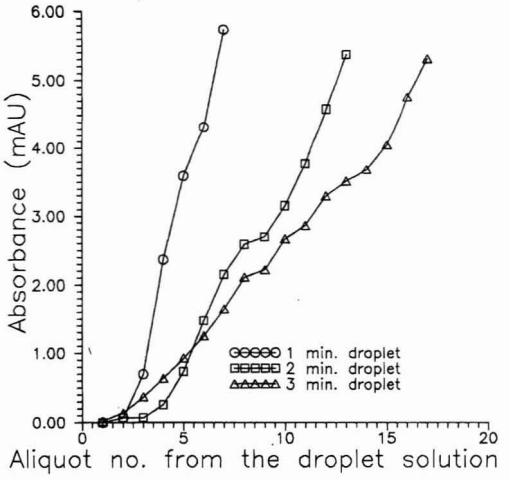

Figure 6. NH_4^+ concentration profiles as a function of the aspiration aliquot number for different droplet sizes. Experimental conditions as in Figure 5.

volume element at the immediate tip of the capillary is virtually fully sheltered and the first aliquot contains almost no NH_4^+.

A second feature of the experimental data becomes apparent after a closer examination of Figure 5. After the first couple of aliquots, the absorbance increases nearly linearly until aliquot 12; then there is a virtual plateau until aliquot 14, and following this, the absorbance increases again linearly, with a greater slope than in the first step. This is a pattern we observe consistently. Close visual examination of the droplet during the sampling experiment clearly shows that the surface of the droplet is not stagnant. A circulatory motion of the surface layer, presumably caused by the frictional drag of the air moving past the droplet, results in better uptake than that predicted by a stagnant boundary layer. We believe this is responsible for the observed results.

Effect of Droplet Size. The concentration of NH_4^+ as a function of aliquot number was determined for different droplet sizes; the results are shown in Figure 6. Droplets with a radius of 0.65, 0.81, and 0.93 mm were formed by pumping the absorbing solution for 1, 2, and 3 min, respectively. Given the same analytical sample size, the number of aliquots that can be withdrawn from droplets of different size is naturally dependent on the size of the droplet. However, in all cases, the final aliquot represents the solution on the surface of the droplet. It is noteworthy that the final aliquot composition is virtually identical in all three droplet sizes. (The smallest droplet has a only slightly higher final aliquot concentration than the rest. This can be readily attributed to a sampling artifact: a longer time and a larger total aspirated volume are needed to get to the final aliquot for the larger droplets and this leads to greater mixing.) This validates that C_0 is constant regardless of the droplet size.

The area under each curve in Figure 6, hereinafter referred to as the integrated absorbance signal (IAS), is proportional to the total mass of ammonia collected. As long as the surface of the droplet still behaves as an effective sink for the exposed surface area S of the droplet, which can be approximated as

$$S = 4\pi R^2 - \pi r_c^2 \qquad (6)$$

where r_c is the outer radius of the capillary, the IAS for the three cases in Figure 6 is indeed linearly related to the value of S with a linear correlation coefficient (r^2) value of 0.9936.

Sampling Time and Initial Droplet Conditions. The total mass of an analyte gas collected will increase linearly with the sampling time as long as the sink efficiency of the droplet surface remains the same. In the present case, $NH_{3(aq)}$ is protonated by H^+ supplied by H_2SO_4 originally present in the droplet; this removal of un-ionized $NH_{3(aq)}$ by protonation keeps the droplet surface an effective sink for NH_3. The initial amount of H^+ available for this purpose is that present in the surface layer (the thickness of which is defined by the circulatory mixing), and as the H^+ is consumed by the influx of NH_3, it is also replenished by outward radial diffusion of H^+ from the interior of the droplet. However, depending on the ammonia concentration and its flow rate, diffusive replenishment from the interior may be inadequate to maintain a sufficient H^+ concentration on the surface and thus limit the effectiveness of the surface to capture NH_3.

Figure 7 shows the amount of NH_3 collected (at a constant NH_3 concentration and sampling rate) as a function of sampling time for different concentrations of acid initially present in the droplet. The collection efficiency decreases with increasing sampling time, but better results are obtained with increasing initial acid content. Although not specifically shown here, it is intuitively obvious that, under otherwise fixed conditions, the collection efficiency will be less affected with a decreasing total flux of NH_3 to the droplet, i.e., with a lower NH_3 concentration. A similar effect may be expected for the sample flow rate; however, in the present situation, increasing sample flow rate also results in greater circulatory mixing of the surface layer and may thus mitigate, at least partially, the effect of the increasing flux.

Collection Efficiency. The absolute collection efficiency of the droplet was estimated by measuring the relative amounts of

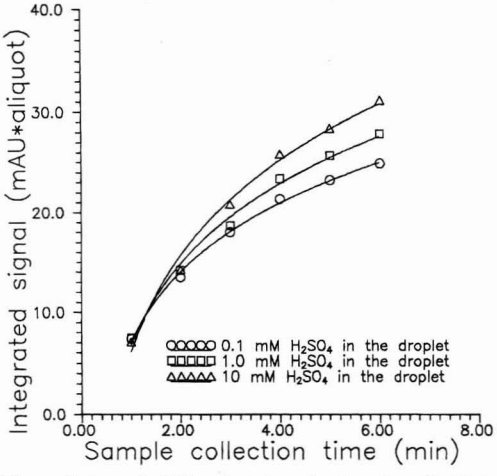

Figure 7. Amount of NH_3 collected as a function of sampling time. The experimental procedure is as in Table 1, except the time for step 2. Other conditions are as in Figure 5.

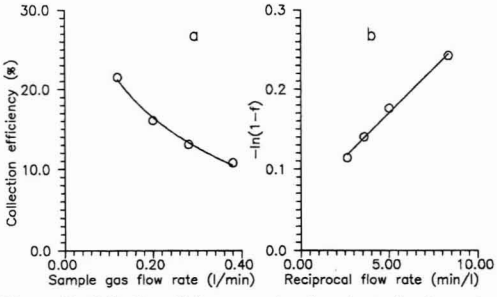

Figure 8. Collection efficiency as a function of sampling flow rate. The experimental procedure and conditions are as in Table 1 and Figure 5. See text for detail.

ammonia collected in the presence and absence of another identical droplet upstream. Referring to Figure 1, another capillary (not shown) was inserted into the top part of the DC so that a second droplet could be deployed, in series after the first one. The amount of NH_3 collected by the principal droplet was measured with and without the second droplet. From these data, the NH_3 removal efficiency of the auxiliary droplet (and thus the identical, principal droplet) is readily calculated. Figure 8a shows the collection efficiency as a function of sampling flow rate.

For a diffusion-based collector, the collection efficiency f exhibits the general form[3]

$$\ln(1 - f) = (b/Q) + \ln a \qquad (7)$$

where a and b are constants and Q is the sampling flow rate. Figure 8b shows that the linear behavior predicted by eq 7 is indeed observed.

Effect of Sample Relative Humidity. The sample relative humidity (RH) can have two different effects on the amount of the analyte collected. The first is related to the evaporative loss of water from the droplet. This can be substantial, especially at low sample relative humidity values and for extended sampling

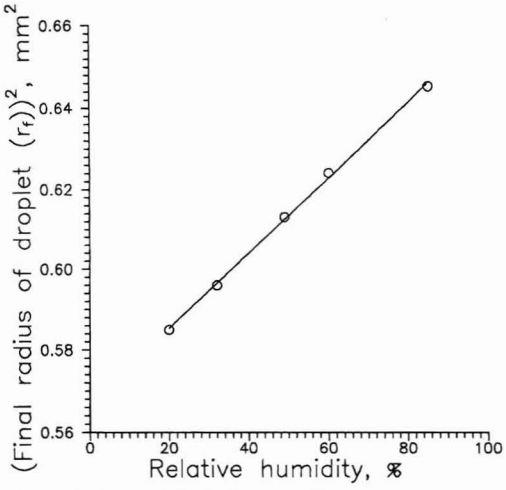

Figure 9. Square of the final droplet radius as a function of the sample gas relative humidity.

periods. Concerning the rate of evaporation from a spherical water droplet in a stream of flowing air, Frossling[19] previously derived the droplet radius R changes as a function of time, as

$$\frac{d(R^2)}{dt} = -k(1 - \mathrm{RH})\sqrt{Re} \qquad (8)$$

where k is a constant and Re is the Reynolds number. If the experimental conditions are fixed, integration of eq 8 yields

$$r_f^2 = r_o^2 - k(1 - \mathrm{RH})\sqrt{Re}\, t \qquad (9)$$

where r_o and r_f are the initial and final droplet radius. Under given experimental conditions, r_f^2 is therefore linearly related to the sample relative humidity. The experimental data (Figure 9) show that this relationship holds very well in our experimental system. The consequence of this behavior is that the droplet surface area decrease during sampling is directly proportional to the relative humidity of the sample gas. Because the gaseous analyte dissolution flux is proportional to the available surface, the amount of the analyte collected is expected to increase with the sample gas relative humidity. As detailed below, an experiment was designed to determine the collection of SO_2 as a function of sample relative humidity with a fixed initial droplet size.

As a result of 5.5 min sample collection (90, 70, 50, and 30% RH) at a flow rate of 0.12 L/min, the initial droplet volume (2.25 μL) decreased in size to 2.15, 2.10, 2.02_5 and 1.92_5 μL, respectively. The integrated conductance signal, linearly proportional to the amount of SO_2 collected, also decreased (0.287, 0.285, 0.272, 0.268, respectively). These data show reasonable linear correlation (r = 0.96, 0.99 with one point omitted) with the mean surface area value over the sampling period. In any case, these data also show that, for modest sampling periods (single digit minutes) and at flow rates typically used in this work, the relative humidity effect is not prohibitively large.

(19) Frossling, N. *Gerlands Beitr. Geophys.* **1938**, *52*, 170.

Sample relative humidity can also affect the collection of a gaseous analyte in an altogether different manner. In diffusion scrubber-based measurements of ammonia, it has been observed that sample collection efficiency decreases with increasing sample relative humidity; this presumably occurs due to the formation of ammonia hydrates, $NH_3(H_2O)_n$, in the gas phase.[20] The effective diffusion coefficient of NH_3 as an analyte thus decreases with increasing relative humidity. The resulting decrease in collection efficiency may overshadow any droplet evaporation effects. The experimental results for the collection of NH_3 as a function of relative humidity (Figure 10) shows this behavior; not only is this effect opposite to that observed for SO_2, it is substantially larger in magnitude.

Nevertheless, at any given sample relative humidity, there is always a characteristic calibration curve. The relative humidity effects can therefore be corrected by establishing a set of calibration curves at different relative humidity levels. The NH_3 content can be calculated based on the calibration curve for the appropriate relative humidity level. However, the relative humidity of the sample is not routinely measured. Since the extent of evaporation of the droplet is related to the relative humidity, the relative humidity of the sample gas can actually be obtained from the droplet size change during sampling. From eq 9, we have

$$(V_f)^{2/3} = (V_o)^{2/3} - (4\pi/3)^{2/3}k(1 - \mathrm{RH})\sqrt{Re}\, t \quad (10)$$

where V_f and V_0 are the final and initial volumes of the droplet.

V_f can be easily determined based on the aspiration time, t_a, needed to aspirate the final droplet solution back into the transporting capillary and the aspiration flow rate, F

$$(t_a)^{2/3} = k'RH + C \quad (11)$$

where

$$k' = (4\pi/3F)^{2/3}k\sqrt{Re}\, t \quad (12)$$

and

$$C = V_0^{2/3} - (4\pi/3F)^{2/3}k\sqrt{Re}\, t \quad (13)$$

For a given system and a set of fixed experimental parameters, k' and C are constants. They can be calculated from the experimental parameters and information such as that presented in Figure 9. In this work, the aspiration time is determined from the LED Photodiode detector (see Figure 3) while the NH_3 absorbance signal is measured by the in-line SIA system. Alternatively and perhaps more conveniently, instead of designating different humidities, sets of calibration curves can be constructed, each corresponding to the length of time needed to aspirate the entire droplet. Such a set of data is shown in Figure 11. After the aspiration time and the NH_3 absorbance signal are obtained, one can go directly to such calibration data for determining the NH_3 concentration.

CONCLUSIONS AND FUTURE POSSIBILITIES

We have demonstrated the feasibility of a new type of gaseous analyte collection system, a droplet collector. As may be apparent,

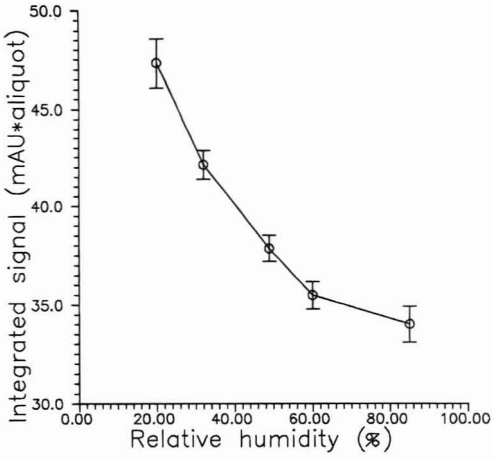

Figure 10. Amount of NH_3 collected as a function of relative humidity. The experimental procedure and conditions are as in Table 1 and Figure 5.

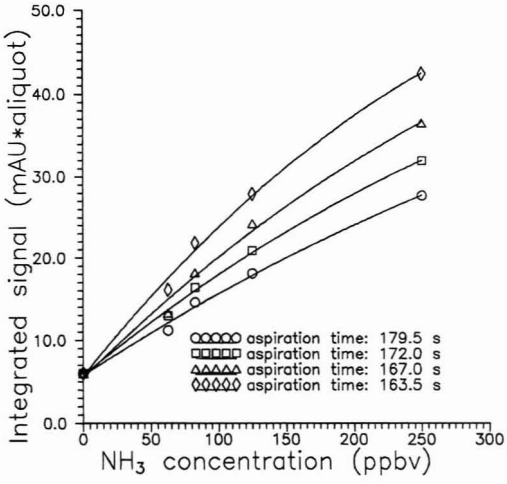

Figure 11. Calibration curves of the droplet collector for NH_3 at different relative humidity values. Aspiration times of 179.5 ± 2.4, 172.0 ± 1.8, 167.0 ± 2.3, and 163.5 ± 1.3 s, respectively, correspond to 90, 70, 50, and 30% relative humidity.

SIA is hardly the perfect system to measure the collected analyte. A more straightforward approach would be to deploy sensing probes in the form of microelectrodes, optical fibers directly in the droplet for continuous or periodic interrogation. If chemical treatment is required before detection, a multiplicity of capillaries bundled together can be used, with one of them transporting the collection solution and others for various reagents, all temini sharing a common droplet. For some analytes, reagents can also be introduced from the gas phase. For SO_2 collection for example, oxidant reagents such as gaseous H_2O_2 or O_3 may be introduced. When postsampling reaction with other reagents is used, satisfactory mixing can be attained with a simultaneously bundled empty capillary by repeated withdrawal and expulsion of the droplet solution. When the droplet needs to be discarded or replaced, more collection solution is delivered. As discussed, the collection

(20) Genfa, Z.; Dasgupta, P. K.; Dong, S. *Environ. Sci. Technol.* **1989**, *23*, 1467–1474.

efficiency change resulting from different sample gas humidities can be corrected for on the basis of the experimental data. If the change is a function of only the evaporation of the droplet solution, it will be relatively small and correction may not be necessary.

The "droplet" need not be spherical or ovoid. Such geometries are in fact disadvantageous if concentration, rather than the total amount collected, is measured (as may be the case with in situ probes) because of the low surface/volume ratio. Ongoing experiments with in situ probes in this laboratory utilize circular or U-shaped wire loops to form a filmlike "droplet" at the terminus of the liquid delivery conduit.

The disadvantage of a droplet interface is that it is not a quantitative collector, except at very low flow rates. Consequently, some constancy of temperature, to maintain a stable collection efficiency, may be essential.

The apparent advantages of the proposed technique over other types of gaseous analyte collection system are (1) its simplicity and low cost, (2) facile replacement or regeneration of the collection solution, (3) convenient introduction of reagent(s) to carry out reaction(s), (4) potential of real-time detection of the analyte of interest in the collection solution or in situ detection immediately after sample collection, and (5) facility of automation.

In terms of providing a readily renewable surface, the droplet interface for sampling gases has certain obvious similarities with a dropping mercury electrode (DME) or a hanging mercury drop electrode (HMDE). The present concept is obviously not limited to the gaseous samples; the sampling and sampled phases merely need be immiscible. It would be most gratifying to the authors if its usefulness attains even a small fraction of what the DME and HMDE have contributed to electroanalysis.

ACKNOWLEDGMENT

This work was sponsored in part by the Office of Exploratory research, US Environmental Protection Agency through Grant R 821117-01-0. However, this paper has not been subjected to review by the agency and no official endorsement should be inferred. We are grateful to Steve Gluck, Dow Chemical Co., for his keen interest.

Received for review January 13, 1995. Accepted April 12, 1995.[⊗]

AC950046O

[⊗] Abstract published in *Advance ACS Abstracts,* June 1, 1995.

Anal. Chem. **1995,** *67,* 2050–2053

Charged Polyacrylamide Gels for Capillary Electrochromatographic Separations of Uncharged, Low Molecular Weight Compounds

Chuzo Fujimoto

Department of Chemistry, Hamamatsu University School of Medicine, Hamamatsu 431-31, Japan

The polyacrylamide gels described here have the ability to separate uncharged substances of comparatively low molecular weight due to the built-in, negatively charged functional groups. The functional groups permit the development of electroosmotic flow under the influence of a high voltage, which makes possible capillary electrochromatographic separations of uncharged compounds. The effects of gel compositions on the column performance were examined. Migration time reproducibilities of 0.43% RSD or less were found with the gel-filled capillary columns. Possible insight into the separation mechanisms is discussed.

Due to its potential to increase chromatographic performance, the feasibility of electoosmotic pumping of the mobile phase in capillary liquid chromatography has been extensively investigated. Recently, Yan et al.[1] and Knox and Grant[2,3] described a chromatographic method in which the mobile phase is transported through a stationary phase in a microbore or capillary column by electroosmotic flow (EOF) using an electric field, termed capillary electrochromatography (CEC). Originally, the use of the term electrochromatography was restricted to *electrophoretic* procedures where separation is effected by sorptive interaction with the stationary phase.[4] According to this original definition, separation of uncharged analytes with the aid of EOF, that is, electroosmotically driven chromatography (or electroosmotic chromatography), is excluded. Tsuda approved of the inclusion of electroosmotic chromatography in the term electrochromatography as one of its extreme cases.[5] Further, Tsuda introduced the concept of pressurized flow in electrochromatography[6–8] and collectively called these techniques "high-performance electrochromatography".[5] Every capillary liquid chromatography performed under the influence of an electric field will henceforth be termed CEC, without any consideration to the presence of EOF or analyte charges. In CEC, the stationary phase can be polymer networks used in capillary gel electrophoresis (CGE) and capillary affinity gel electrophoresis (CAGE) as well as packing material utilized for high-performance liquid chromatography (HPLC). (This paper has few references to CGE and CAGE in that the EOF of the gel columns is suppressed in these types of chromatography or it is insufficient for effective separation of uncharged compounds, unlike the columns described here.) Alternatively, some interactive materials attached to the capillary wall may be used in the open-tubular format. Normal chromatographic distribution (including size-selective distribution) between a mobile phase and a stationary phase is utilized to separate charged and uncharged compounds with higher resolution and superior efficiency, compared with micro-HPLC using an identical column.[1–3,5–23]

CEC has been performed with several types of columns. As early as 1974, Pretorius et al.[9] proposed the use of EOF with a packed column and an open tube (both 1 mm i.d. × 50 cm) to improve the efficiencies of the chromatographic system, but the idea remained dormant until Jorgenson and Lukacs[10] reported the results obtained with a glass capillary (170 μm i.d. × 68 cm) packed with a 10-μm reversed-phase packing. In 1982, Tsuda[11] employed an octadecylsilane-bonded, open-tubular capillary column (30 μm i.d.) for the separations of aromatic compounds. The use of packed fused-silica capillary columns in CE was demonstrated by Knox and Grant[2,3] and Tsuda.[6–8,11,12] Recently, Jacobson et al.[13] reported CEC on a glass microchip having a narrow channel (5.6 μm × 66 μm).

In this article, we report the results of our investigations on CEC with charged polyacrylamide gel columns. In contrast to polyacrylamide gels which have been used in CGE, the gels are prepared using three kinds of acrylamide monomers, that is, straight acrylamide (AA), *N,N'*-methylenebisacrylamide (BIS), and 2-acrylamido-2-methyl-1-propanesulfonic acid (AMPS); the last component is incorporated into the common binary acrylamide gel to give an EOF. In the case of conventional CEC, the surfaces of HPLC packings or capillary walls can exhibit sufficient SiO^- groups to generate an EOF; in our approach, the sulfo group of AMPS immobilized into the cross-linked polymer is ionized in solutions of a wide range of pH so that the generated EOF

(1) Yan, C.; Schaufelberger, D.; Erni, F. *J. Chromatogr. A* **1994**, *670*, 15–23.
(2) Knox, J. H.; Grant, I. H. *Chromatographia* **1987**, *24*, 135–143.
(3) Knox, J. H.; Grant, I. H. *Chromatographia* **1991**, *32*, 317–328.
(4) Wieme, R. J. In *Chromatography—A Laboratory Handbook of Chromatographic and Electrophoretic Methods*, 3rd ed.; Heftmann, E., Ed.; Van Nostrand Reinhold Co.: New York, 1975; Chapter 10, and references therein.
(5) Tsuda, T. *LC-GC Int.* **1992**, *5*, 26–36.
(6) Tsuda, T. *Anal. Chem.* **1987**, *59*, 521–523.
(7) Tsuda, T. *Anal. Chem.* **1988**, *60*, 1677–1680.
(8) Tsuda, T.; Muramatsu, Y. *J. Chromatogr.* **1990**, *515*, 645–652.
(9) Pretorius, V.; Hopkins, B. J.; Schieke J. D. *J. Chromtogr.* **1974**, *99*, 23–30.
(10) Jorgenson, J. W.; Lukacs, K. D. *J. Chromatogr.* **1981**, *218*, 209–216.
(11) Tsuda, T.; Nomura, K.; Nakagawa, G. *J. Chromatogr.* **1982**, *248*, 241–247.
(12) Tsuda, T. *Nippon Kagakukaishi*, **1986**, 937–942.
(13) Jacobson, S. C.; Hergenröder, R.; Koutny, L. B.; Ramsey, J. M. *Anal. Chem.* **1994**, *66*, 2369–2373.
(14) Pfeffer, W. D.; Yeung, E. S. *Anal. Chem.* **1990**, *62*, 2178–2182.
(15) Pfeffer, W. D.; Yeung, E. S. *J. Chromatogr.* **1991**, *557*, 125–136.
(16) Garner, T. W.; Yeung, E. S. *J. Chromatogr.* **1993**, *640*, 397–402.
(17) Ymamoto, H.; Baumann, J.; Erni, F. *J. Chromatogr.* **1992**, *593*, 313–319.
(18) Mayer, S.; Schurig, V. *J. High. Resolut. Chromatogr.* **1992**, *15*, 129–131.
(19) Bruin, B. J. M.; Tock, P. P. H.; Kraak, J. C.; Poppe, H. *J. Chromatogr.* **1990**, *517*, 557–572.
(20) Li, S.; Lloyd, D. K. *Anal. Chem.* **1993**, *65*, 3684–3690.
(21) Ng, C. L.; Ong, C. P.; Lee, H. K.; Li, S. F. Y. *J. Chromatogr. Sci.* **1994**, *32*, 121–125.
(22) Martin, M.; Guiochon, G.; Walbroehl, Y.; Jorgenson, J. W. *Anal. Chem.* **1985**, *57*, 559–561.
(23) Martin, M.; Guiochon, G. *Anal. Chem.* **1984**, *56*, 614–620.

0003-2700/95/0367-2050$9.00/0 © 1995 American Chemical Society

transports uncharged compounds as well as charged compounds through a bed of polyacrylamide gel. The presence of such ionized groups in polyacrylamide gels has been unfavorable to CGE because of the possible electrostatic interactions between ionized analytes (usually, large molecules such as proteins and DNA fragments) and the built-in, ionized groups, resulting in ruined separations. However, it should be possible to advantageously use EOF when uncharged molecules are being separated. We examined the separation performance of the gels using uncharged, low molecular weight compounds (<200).

Thus far, the potential of polyacrylamide for separating ionized or ionizable, large molecules has been well documented. However, to our knowledge, polyacrylamide gels have not been intentionally used for CEC separations of uncharged, small molecules. The earliest demonstration of this type of separation was by Synge and Tiselius[24] in 1950. They separated uncharged starch derivatives in an agar gel by applying an electric field. After this work, granulated gels (e.g., agar gel, polyacrylamide gel, and Sephadex beads) were examined in either columns or thin layers under an electric field.[4] Unfortunately, the results were disappointment: the zones were much broader than expected in electrophoresis, due to the intervention of the "nonequilibrium term" in determining zone spreading.[4]

EXPERIMENTAL SECTION

Apparatus. The experiments were performed in a laboratory-made apparatus. A 30-kV direct-current power supply equipped with an interlock mechanism (Model HCZE-30PN0.25; Matsusada Precision Devices, Kusatsu, Japan) was used to generate a potential drop across the column. A UV detector (Model 870-CE; Jasco, Tokyo, Japan) was used at 254 nm. Separations were performed in fused-silica tubing (GL Sciences, Tokyo, Japan) of 0.075 mm i.d. and 0.375 mm o.d., which had a ~1-mm portion of the polyimide coating removed for UV detection. Each end of the column was placed in a buffer reservoir (4-mL volume) with a platinum wire electrode. The high-voltage end of the system was encased in a Plexiglas box equipped with an interlock system. The chromatograms were acquired and stored on an integrator (Model Labchart 180, System Instruments, Tokyo, Japan) or recorded on a strip-chart recorder (Model FBR-251A, TOA Electronics, Tokyo, Japan). Samples were dissolved in the buffer and introduced onto the gel-filled columns by electrokinetic injection: high voltage was applied for a carefully timed interval (typically 5 s). Calculations of plate numbers were made using the software originally supplied with the integrator.

Chemicals. AA, BIS, ammonium persulfate (APS), and *N,N,N′,N′*-tetramethylenediamine (TEMED) were purchased from Nacalai Tesque (Kyoto, Japan). 3-(Trimethoxysilyl)propyl ester and AMPS were obtained from Tokyo Kasei Kogyo (Tokyo, Japan). Tris(hydroxymethyl)aminomethane (Tris) was purchased from Merck (Darmstadt, Germany). Boric acid, acetone, and acetophenone were obtained from Kishida Chemical (Osaka, Japan). Buffer solutions were prepared with deionized, distilled water which was obtained from an Autostil WG 23 (Yamato, Tokyo, Japan). All other chemicals were of analytical reagent grade from several sources and were used without further purification.

Preparation of Columns. The internal walls of capillaries were treated with a reagent mixture consisting of 40 μL of methacrylic acid 3-(trimethoxysilyl)propyl ester mixed with 10 mL of 6 mM acetic acid at room temperature overnight, as described by Hjertén.[25] After rinsing thoroughly with distilled, deionized water, a mixture of AA, BIS, and AMPS in the buffer containing 0.5–1.0 mg/mL APS and 3 μL/mL TEMED was introduced into a precut fused-silica tube and stored at room temperature for >3 h. All columns were preelectrophoresed until the baseline of the detector output remained stable: during this time the applied voltage was increased in a stepwise manner until the separation voltage was reached.

Polyacrylamide gels with varying compositions were prepared using the mixtures of different amounts of AA, BIS, and AMPS through linear and cross-linking procedures.

The nomenclature introduced by Hjertén[26] was used to represent the total acrylamide concentration (% *T*) and the degree of cross-linking (% *C*):

$$\%\ T = 100\ (a + B + c)/V,\quad \%\ C = 100b/(a + b + c)$$

where *a*, *b*, and *c* are the masses of AA, BIS, and AMPS (in g), respectively, and *V* is the volume (in mL). For the sake of convenience, the mole percentage of AMPS (% *S*) is defined in the present work as

$$\%\ S = 100\gamma/(\alpha + \beta + \gamma)$$

where α, β, and γ are the molarities of AA, BIS, and AMPS, respectively.

RESULTS AND DISCUSSION

Separation of Various Compounds. Figure 1 shows an example of CEC separations of uncharged compounds on a charged polyacrylamide gel column. A column of 12.0% *T*, 5.8% *C*, 7.8% *S* gel composition was used. The separation was carried out using an effective length of 51.0 cm with a 100 mM Tris–100 mM boric acid buffer (pH 8.4) at an applied voltage of 22.0 kV. Some of the solutes are typical neutral markers, which have been used for estimation of the velocity of EOF in free-solution capillary electrophoresis, and they differ in size and functionality. In this figure, individual components are clearly separated, indicating the high resolving power of the charged gel column. The plate count for benzaldehyde was found to be 5.16×10^4 (corresponding to a plate height of 9.9 μm): this value is comparable or superior to those normally encountered in HPLC separations using a pressure-driven flow with a column of the same length. However, the plate count on the 12.0% *T*, 5.8% *C* column is smaller than previously reported, lower % *T* columns (e.g., refs 27 and 28).

Dependence of Migration Velocity and Plate Height on AMPS Concentration. In order to evaluate the electroosmotic elution system in CEC, the AMPS content in gel was varied from 1.5 to 12.3% *S* while the concentrations of AA and BIS remained constant (% $T = 6.0$, % $C = 9.17$). For this purpose, a mixture of acetone and acetophenone was separated using a 100 mM Tris–150 mM boric acid buffer (pH 8.1) with an applied voltage of 13.0 kV. The effective length was 15.0 cm. Figure 2A shows the effect of increasing the AMPS concentration on the migration velocities of the test solutes. It can be seen that the migration times vary approximately linearly to the AMPS content. Taking acetone as

(24) Synge, R. L. M.; Tiselius, A. *Biochem. J.* **1950**, *46*, xli.

(25) Hjertén, S. *J. Chromatogr.* **1985**, *347*, 191–198.
(26) Hjertén, S. *Arch. Biochem. Biophys.* **1962**, (Suppl. 1), 147–151.
(27) Guttman, A.; Cohen, A. S.; Heiger, D. N.; Karger, B. L. *Anal. Chem.* **1990**, *62*, 137–141.
(28) Liu, J.; Dolnik, V.; Hsieh, Y.-Z.; Novotny M. *Anal. Chem.* **1992**, *64*, 1328–1336.

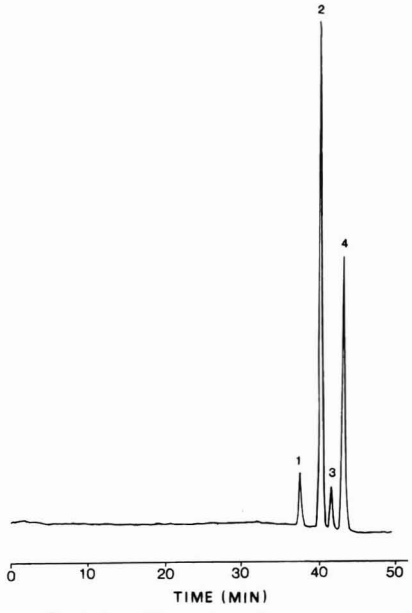

Figure 1. Separation of five uncharged compounds on a charged polyacrylamide gel column: mobile phase, 100 mM Tris–100 mM boric acid (pH 8.4); capillary, 67.9 cm × 0.075 mm i.d. (51.0-cm effective length); applied voltage (current), 22.0 kV; detection wavelength, 254 nm. Peaks: (1) acetone, (2)mesityl oxide and thiourea, (3) benzyl alcohol, and (4) benzaldehyde.

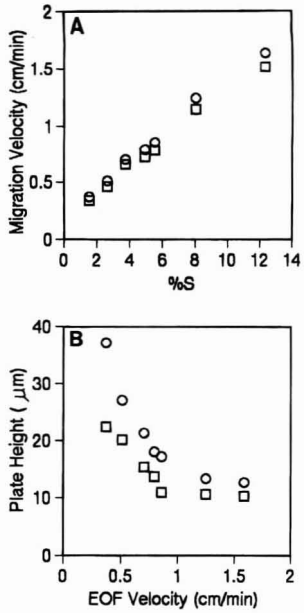

Figure 2. Effect of AMPS concentration on migration velocity (A) and plate height (B): (○) acetone (an EOF marker); (□) acetophenone. Conditions: % *T*, 6.0; % *C*, 9.2; capillary, 65.0 cm × 0.075 mm i.d. (15.0 cm effective length); mobile phase, 100 mM Tris–150 mM boric acid (pH 8.1); applied voltage, 13.0 kV; detection wavelength, 254 nm.

an unretained solute marker, the EOF velocity was calculated. At a field strength of 200 V/cm, EOF ranged from 0.37 to 1.64 cm/min. The velocities of EOF obtained at higher values of % *S* are on the same order as those obtained with conventional CEC columns unless either additives[14] or remarkably high field strengths[17] are used. With the proposed columns, higher EOF velocities can be obtained at higher field strengths (see Table 2). In general, the composition of the polymer (gel) would differ from that in the polymerization solution, and hence, the approximate linear relationship in this range may be fortuitous. Current was found to increase with increasing the AMPS content, ranging from 4.0 μA at 1.5% *S* to 22.5 μA at 12.3% *S*.

The separation performance can be evaluated in terms of plate height as a function of the velocity of EOF. The results are shown in Figure 2B. Although plate height decreases with increasing % *S* (or mobile-phase velocity), there is no significant change in plate height above 8%. No minimum can be seen in the plot of plate height vs the velocity of EOF within the measured range.

Dependence of Migration Time on Concentrations of AA and BIS. Table 1 shows the effect of changing the concentration of AA and BIS in a polymerization solution on the migration times of the test solutes. The effective length was 15.0 cm, and the field strength was 200 V/cm. In all cases, % *S* was held at 2.4. The migration times increase with increasing the concentration of acrylamide monomers (% *T*) at a constant % *C*. On the other hand, at a constant % *T*, the migration times change irregularly with % *C*. It appears that the migration times are related to the pore size of the gel rather than the concentrations of monomers: the smaller the pore size, the longer is the migration times. This indicates that the polyacrylamide gel exerts molecular sieving even

Table 1. Effect of Concentrations of AA and BIS on the Migration Times of Acetone and Acetophenone[a]

% *T*	% *C*	pore diameter[b] (Å)	migration time (min)	
			acetone	acetophenone
6.5	5.0		37.72	41.73
8.0	1.0	46	28.6	33.38
8.0	5.0	32	43.78	49.44
8.0	15.0	48	29.94	34.08
10.0	5.0	28	47.51	55.48
12.0	5.0	18	49.31	58.05

[a] Conditions: % *S*, 2.4; effective length, 15.0 cm; total length, 65.0 cm; applied voltage, 13.0 kV; buffer, 100 mM Tris–150 mM boric acid (pH 8.1); detection, 254 nm. [b] Data taken from ref 30.

on such small molecules. According to the recent paper by Righetti et al.,[29] though there is reasonable agreement that the average pore diameter in a standard gel is of the order of a few tens of angstroms, it differs significantly from source to source. Here, the data listed in Table 1 were taken from ref 30 somewhat arbitrarily, assuming that the presence of AMPS does not affect the accessible pore size. Pore diameters ranging from 18 to 48 Å are likely to be adequately small to hinder the migration of the solutes through the gel. In this connection, one may recall the work by Hjertén et al.[31] in 1989. They observed the retardation of basic drugs on a 6% *T*, 3% *C* polyacrylamide gel column, where it is not the gel but the analyte that is charged. However, the difference in the appearance of electropherograms in the absence

(29) Righetti, P. G.; Caglio, S.; Saracchi, M.; Quaroni, S. *Electrophoresis*, **1992**, *13*, 587–595.
(30) Chrambach, A.; Rodbard, D. *Science* **1971**, *172*, 440–451.
(31) Hjertén, S.; Valtcheva, L.; Elenbring, K.; Eaker D. *J. Liq. Chromatogr.* **1989**, *12*, 2471–2499.

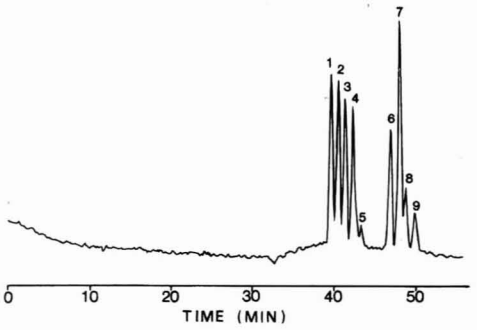

Figure 3. Chromatogram of ketones on a charged polyacrylamide gel column: mobile phase, 100 mM Tris−150 mM boric acid (pH 8.1); capillary, 65.0 cm × 0.075 mm i.d. (50.0 cm effective length); % *T*, 13.7; % *C*, 5.1; % *S*, 10.0; applied voltage, 20.0 kV; detection wavelength, 254 nm. Peaks: (1) dimethyl ketone, (2)methyl ethyl ketone, (3) methyl *n*-propyl ketone, (4) methyl *n*-butyl ketone, (5) methyl *n*-pentyl ketone, (6) methy phenyl ketone, (7) ethyl phenyl ketone, (8) *n*-propyl phenyl ketone, and (9) *n*-butyl phenyl ketone.

and presence of polyacrylamide was ascribed to "aromatic adsorption" which is an inherent property of most polymers, but not to size selectivity.

Separation of Homologous Ketones. To further explore the separation mechanism, we obtained a chromatogram of homologous ketones using a 13.7% *T*, 5.1% *C*, 10.0% *S* column, which is shown in Figure 3. In this chromatogram, the components elute in the order of molecular size, so it is apparent that the gel acts as a molecular sieve while the solutes are carried by EOF. In the sense that size exclusion chromatography (SEC) is admitted among liquid chromatography, this type of chromatography can be regarded as a variant of CEC, though the elution order is opposite to that in SEC. Additionally, it is no doubt that some sorptive interaction has played a role for these separations: as evidence of that, thiourea and mesityl oxide, which differ in size, coelute (see Figure 1); the injection of a mixture of benzamide, benzaldehyde, and acetophenone results in a single peak (the data are not shown). Consequently, we prefer to use the term CEC rather than CGE to describe the method. When some functional group, which can interact overwhelmingly with analytes, is introduced into the gel, the method will be termed CEC without any objection.

Dependence of Migration Velocity, Current, and Plate Height on Applied Potential. A means of developing a substantial EOF is to increase the AMPS content, as shown in Figure 2. Another practice is to use higher applied potentials. Table 2 lists migration velocity, current, and plate height, which were obtained in a 150−450 V/cm range for a 6.0% *T*, 9.2% *C*, 8.0% *S* column. A plate height as low as 6.9 μm were obtained for acetophenone ($k' = 0.087$) at 350 V/cm. The migration velocities of both solutes and current increase with increasing field strength over the measured range. In contrast, there was little change in plate count (or plate height) above 300 V/cm. Although no attempt to clarify this point has been done here, it may be worth mentioning that a similar phenomenon was noted previously for charged compounds separated on both cross-linked and linear polymer columns.[32]

(32) Liu, J., Dolnik, V.; Hsieh, Y.-Z.; Novotny, M. *Anal. Chem.* **1992**, *64*, 1328−1336.

Table 2. Effect of Field Strength on the Migration Velocity, Current, and Plate Height[a]

field strength (V/cm)	current (μA)	migration velocity (cm/min)	plate height (μm)
150	9.8	0.82	12.1
200	13.0	1.11	10.2
250	19.0	1.46	8.2
300	24.5	1.87	7.0
350	30.5	2.36	6.9
450	48−51[b]	3.60	9.5

[a] Conditions: % *T*, 6.0; % *C*, 9.2; % *S*, 8.0; effective length, 49.4 cm; total length, 65.0 cm; sample, 0.002% acetophenone; injection, 5 s at 13.0 kV; detection, 254 nm; buffer, 100 mM Tris−150 mM boric acid (pH 8.1). [b] Current increased with time during the run.

Table 3. Reproducibility of Migration Time ($n = 6$)[a]

	column 1 (6.0% *T*, 3.3% *C*, 2.4% *S*)		column 2 (6.0% *T*, 9.2% *C*, 12.3% *S*)	
	acetone	acetophenone	acetone	acetophenone
av time (min)	98.25	107.58	8.84	9.57
SD	0.21	0.24	0.038	0.041
RSD (%)	0.21	0.22	0.43	0.43

[a] Conditions: effective length, 15.0 cm; total length, 65.0 cm; applied voltage, 13.0 kV; buffer, 100 mM Tris−150 mM boric acid (pH 8.1); sample, mixture of 2% acetone and 0.002% acetophenone.

Stability and Migration Time Reproducibility. Under electrophoretic conditions, the columns discussed here were usable for a long period of time (up to several weeks) without noticeable change in the separation properties. The run-to-run reproducibility of migration time for two columns having a different gel composition is shown in Table 3. The data on the 6.0% *T*, 3.3% *C*, 2.4% *S* column was obtained by conducting the experiments over the whole day, during which the variation in surrounding temperature is significant (~10 °C) and no temperature control was available. Nevertheless, the RSD values were as small as 0.43 or less, indicating the excellent repeatability of this method. Column-to-column reproducibility has not been evaluated.

In summary, we have demonstrated that charged polyacrylamide gel columns are useful for chromatographic separation of uncharged, low molecular compounds under the application of a high electric potential, in spite of the fact that the experimental conditions were not optimized. The columns can of course separate both uncharged and charged compounds. Molecular sieving seems to be a dominant separation mechanism in the above separations. However, using a column filled with gel having more interactive functionality, the method could become a general CEC technique. Further investigation in this direction is already in progress in our laboratory.

ACKNOWLEDGMENT

We thank Jun Kino and Shigeki Kuroishi for their assistance during the course of this research. This work was supported by the Research Foundation of Hamamatsu University School of Medicine.

Received for review January 23, 1995. Accepted April 21, 1995.[⊗]

AC9500803

[⊗] Abstract published in *Advance ACS Abstracts*, June 1, 1995.

Anal. Chem. **1995**, *67*, 2054–2058

Chiral Separation and Detection of Terbutaline and Ephedrine by Capillary Electrophoresis Coupled with Ion Spray Mass Spectrometry

Robin L. Sheppard,† Xinchun Tong, Jianyi Cai, and Jack D. Henion*

Analytical Toxicology, Diagnostic Laboratory, Cornell University, 927 Warren Drive, Ithaca, New York 14850

The enantiomers of both terbutaline and ephedrine were separated by capillary electrophoresis using electrolyte solutions of heptakis(2,6-di-*O*-methyl)-β-cyclodextrin in low pH buffers. The analytes were detected by ion spray mass spectrometry using selected ion monitoring or by selected reaction monitoring in the positive ion mode. Both the free drug enantiomers and the noncovalent enantiomer–cyclodextrin inclusion complexes for terbutaline can be detected simultaneously using this method. The feasibility of using CE/MS for chiral purity determination is demonstrated. In addition, a comparison of UV detection versus mass spectrometry detection for a spiked urine sample is included to demonstrate the selectivity and sensitivity advantages of the mass spectrometer as a CE detector.

The characterization of chiral drugs is important because many drugs have only one active enantiomer while the other is either inactive or, in some cases, potentially harmful. The U.S. Food and Drug Administration (FDA) has set guidelines for marketing chiral drugs which require pharmaceutical companies to show proof of chiral composition.[1] Currently, many chiral separations for thermally labile compounds are accomplished by HPLC. There are some drawbacks to this approach which include either multistep derivatizations,[2] low separation efficiency,[3] or expensive derivatizing agents, chiral stationary phases, or chiral selectors added to the mobile phase.[2–4] In many cases, the mobile phase compositions would preclude detection by on-line mass spectrometry due to the presence of relatively high concentrations of involatile additives.

Alternatively, capillary electrophoresis (CE) has recently been shown to be a powerful separation technique for chiral drugs because of its increased separation efficiency compared to HPLC.[5,6] In particular, the chiral selectivity achieved by adding various cyclodextrins to the running buffer has been demonstrated by several groups,[7,8] and the theoretical basis of this technique has been discussed.[9–13] Often, relatively high concentrations of involatile additives including the cyclodextrins are necessary to achieve separations in CE. This would seem to pose the same problems for CE/MS as for LC/MS. While the additives may compete with the analyte for available charge and thus affect the sensitivity of the mass spectrometer, the flow rate of the CE running buffer is usually only on the order of a few nanoliters per minute. Therefore, the absolute amount of involatile buffers introduced into the mass spectrometer is extremely low and causes no apparent problems for the instrumentation.

Because of the very low sample sizes (picomoles and lower) used in the small diameter capillaries, detection in CE remains an important challenge. Ultraviolet absorbance is by far the most commonly used detection method because an in-line UV cell is easily made by burning off a short section of the polyimide coating on the fused-silica capillary. However, this tiny flow cell limits the detection sensitivity of even UV-absorbing analytes. More importantly, UV is not a specific detector that can provide structural information suitable for characterization of organic compounds.

Mass spectrometry can provide the structural characterization that is desirable in any separation science mode including CE.[14] The use of mass spectrometry as a detector for CE was first reported in 1987 by Smith and co-workers.[15] Variations on approaches to CE/MS including the use of liquid sheath[16] and the liquid junction interface[17] rapidly followed. Excellent review articles on the background and development of CE/MS have recently been published.[18,19] Improved sensitivity can be achieved using selected ion monitoring or ion trap MS,[14] but the additional analytical power of selected reaction monitoring can be used to selectively detect the target compound even in a complex matrix such as a biological fluid.[20] In this work, we describe the

† On sabbatical from Xerox Corp., 800 Phillips Rd., 139-64A, Webster, NY 14580.

(1) U.S. Food and Drug Administration. *Chirality* **1992**, *4*, 338–340.
(2) Pirkle, W. H.; Burke, J. A. *J. Chromatogr.* **1992**, *598*, 159–167.
(3) Witte, D. T.; Ahnoff, M.; Karlsson, K.-E.; Franke, J.-P.; de Zeeuw, R. A. *J. Chromatogr.* **1993**, *641*, 39–48.
(4) Shimada, K.; Mitamura, K.; Morita, M.; Hirakata, K. *J. Liq.Chromatogr.* **1993**, *16*, 3311–3320.
(5) Ward, T. J. *Anal. Chem.* **1994**, *66*, 633A–640A.
(6) Novotny, M.; Soini, H.; Stefansson, M. *Anal. Chem.* **1994**, *66*, 647A–655A.
(7) Fanali, S. *J. Chromatogr.* **1989**, *674*, 441–446.
(8) Fanali, S. *J. Chromatogr.* **1991**, *545*, 437–444.
(9) Rawjee, Y. Y.; Vigh, G. *Anal. Chem.* **1994**, *66*, 619–627.
(10) Wren, S. A. C.; Rowe, R. C. *J. Chromatogr.* **1992**, *609*, 363–367.
(11) Wren, S. A. C.; Rowe, R. C. *J. Chromatogr.* **1992**, *603*, 235–241.
(12) Rawjee, Y. Y.; Williams, R. L.; Vigh, G. *J. Chromatogr.* **1993**, *635*, 291–306.
(13) Rawjee, Y. Y.; Williams, R. L.; Vigh, G. *J. Chromatogr.* **1993**, *652*, 233–245.
(14) Henion, J. D.; Mordehai, A. V.; Cai, J. *Anal. Chem.* **1994**, *66*, 2103–2109.
(15) Olivares, J. A.; Nguyen, N. T.; Yonker, C. R.; Smith, R. D. *Anal. Chem.* **1987**, *59*, 1230–1232.
(16) Smith, R. D.; Baringa, C. J.; Udseth, H. R. *Anal. Chem.* **1988**, *60*, 1948–1952.
(17) Lee, E. D.; Mück, W. M.; Henion, J. D.; Covey, T. R. *J. Chromatogr.* **1988**, *458*, 313–321.
(18) Cai, J.; Henion, J. *J. Chromatogr.* In press.
(19) Smith, R. D.; Wahl, J. H.; Goodlett, D. R.; Hofstadler, S. A. *Anal. Chem.* **1993**, *65*, 574A–584A.

0003-2700/95/0367-2054$9.00/0 © 1995 American Chemical Society

combination of CE and ion spray mass spectrometry to analyze three chiral drug mixtures and a spiked urine sample using cyclodextrin-based electrolyte solutions.

EXPERIMENTAL SECTION

Racemic 2-*tert*-butylamino-1-(3,5-dihydroxyphenyl)ethanol (common name terbutaline), heptakis(2,6-di-*O*-methyl)-β-cyclodextrin, and tris(hydroxymethyl)aminomethane (Tris) were obtained from Sigma Chemical Co. (St. Louis, MO). The individual enantiomers (1*R*,2*S*)-(−)-ephedrine hydrochloride and (1*S*,2*R*)-(+)-ephedrine hydrochloride were purchased from Aldrich Chemical Co. (Milwaukee, WI). Phosphate buffer (0.1 M, pH 2.5) and Capillary Wash solution (20 mM phosphoric acid) were obtained from Bio-Rad Laboratories (Hercules, CA). Formic acid (88%), glacial acetic acid, and ammonium acetate were obtained from Fisher Scientific (Pittsburgh, PA). Water was purified with an in-house Barnstead Nanopure ultrapure water system (Dubuque, IA). Concentrations of sample solutions are indicated in the text.

Capillary electrophoresis was carried out on a Beckman P/ACE Model 2050 using uncoated 75 μm i.d. fused-silica capillaries that were 120 cm in length. Separations were performed at room temperature. The separation capillary was rinsed with Bio-Rad Capillary Wash solution followed by water before equilibration with the separation buffer. The electrolyte solutions contained heptakis(2,6-di-*O*-methyl)-β-cyclodextrin and either phosphate or Tris/formic acid at pH 2.5–3.0. Samples were loaded using either electrokinetic injection at 10 kV or pressure injection for 5–10 s duration. The sample amounts are calculated by first running a separation under the injection conditions used (either low pressure or 10 kV). The calculation has been described previously.[14] The CE voltage was maintained at 30 kV for all analyses described, but the effective running voltage was between 25.5 and 26.5 kV when the ion spray tip voltage was maintained between 4.5 and 3.5 kV. The CE capillary was threaded through a home-made ion spray interface, in which the end of the CE capillary slightly protrudes from the ends of two coaxial stainless steel tubes which carry the sheath liquid flow and the nebulizing gas. A schematic diagram of the interface can be found elsewhere.[21] A sheath liquid flow of 50:50 to 90:10 methanol/water with or without 2 mM ammonium acetate was maintained coaxial to the central CE capillary at 2–4 μL/min. The ion spray nebulizing gas was nitrogen maintained at 35 psi. Mass spectrometry in the positive ion mode was performed on a Sciex TAGA 6000E upgraded to an API III operated with unit mass resolution. MS/MS experiments used argon for the collision gas at a thickness of 200×10^{12} atoms/cm^2 with a collision energy of 100 eV. Data acquisition and presentation were performed using the standard proprietary Macintosh-based system provided by Sciex.

The use of heptakis(2,6-di-*O*-methyl)-β-cyclodextrin in the CE buffer caused no apparent problems for the stability or overall sensitivity of the mass spectrometer. This cyclodextrin is neutral in solution, and therefore it migrates only under the influence of the extremely low electroosmotic flow rates of the buffer systems used. Precautions need to be taken to turn off the sprayer voltage and nebulizing gas when the CE capillary is flushed with buffer so that the cyclodextrin is not pumped into the mass spectrometer at unnecessarily high flow rates. The mass spectrometer was not cleaned any more frequently than usual.

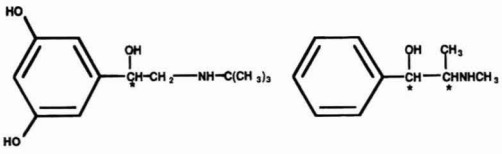

Terbutaline MW 225.1 Ephedrine MW 165.1

Figure 1. Structures of terbutaline and ephedrine with indication of chiral centers (*) and molecular weights.

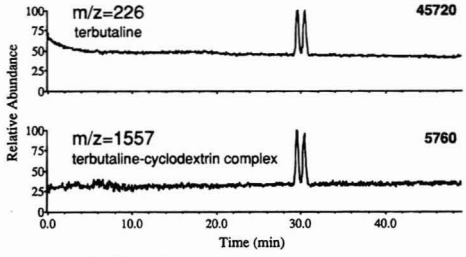

Figure 2. SIM/CE/MS electropherogram of racemic terbutaline mixture, monitoring *m/z* 226 (protonated molecule of terbutaline) and 1557 (terbutaline–cyclodextrin host–guest inclusion complex). Total ion abundance is indicated in the upper right-hand corner of each electropherogram.

RESULTS AND DISCUSSION

Structures of the two enantiomeric drugs studied in this work are shown in Figure 1. An enantiomeric mixture of terbutaline was separated using a running buffer solution containing 5 mM heptakis(2,6-di-*O*-methyl)-β-cyclodextrin (MW 1330.6) and 5 mM sodium phosphate buffer at pH 2.5. Terbutaline was purchased as a racemic mixture, and a sample solution was prepared at a concentration of 0.1 mM of each enantiomer in the separation buffer. The sample amounts injected were calculated to be 1.9 pmol of each terbutaline enantiomer. The running current for this separation was constant at about 9 μA, as measured with the P/ACE 2050 system. The resulting electropherograms obtained in the selected ion monitoring (SIM) mode are shown in Figure 2. The upper electropherogram represents the *m/z* 226 ion current profile for the protonated molecule of terbutaline. The lower electropherogram represents the *m/z* 1557 ion current profile expected for the protonated terbutaline–cyclodextrin host–guest inclusion complex. The ion current abundance observed for the protonated free drug is about 8 times that of the protonated drug–cyclodextrin complex (Figure 2). While some of the free drug is probably due to dissociation of the complex during vaporization,[22] the fact that the two species comigrate suggests that the drug may be in dynamic equilibrium with the cyclodextrin as it migrates through the capillary. The difference in the abundance between the free drug and the complex is probably related in part to the effective binding constant for the drug–cyclodextrin complex in this system.[12,13,22] It is difficult to demonstrate unequivocally whether the observed drug–cyclodextrin inclusion complex was derived from solution or was in fact formed during the spraying process. In order to address this problem, one approach is to perform infusion studies at a constant cyclodextrin concentration while varying the drug concentration

(20) Mück, W. M.; Henion, J. D. *J. Chromatogr.* **1989**, *495*, 41–59.
(21) Hsieh, F. Y. L.; Cai, J.; Henion, J. D. *J. Chromatog. A* **1994**, *679*, 206–211.
(22) Ganem, B.; Li, Y.-T.; Henion, J. D. *J. Am. Chem. Soc.* **1991**, *113*, 6294–6296.

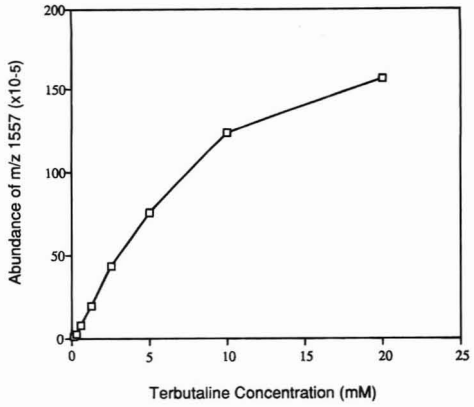

Figure 3. Calibration plot of SIM abundance of terbutaline–cyclodextrin noncovalent inclusion complex at *m/z* 1557 at constant cyclodextrin concentration (0.5 mM) and varying terbutaline concentration.

and observing the abundance of the inclusion complex.[23] These experiments were performed for terbutaline in 0.5 mM heptakis-(2,6-di-*O*-methyl)-β-cyclodextrin, 1 mM phosphate buffer adjusted to pH 2.5 with acetic acid. The resulting calibration plot of terbutaline concentration versus the abundance of the terbutaline–cycodextrin complex at m/z 1557 is shown in Figure 3. We cannot plot the ratio of the ion abundances of the drug and the complex because the drug ion current is saturated almost as soon as the complex ion current is at a detectable level. Nonetheless, the intensity of m/z 1557 with respect to the terbutaline concentration appears to be linear up to a 5:1 molar ratio of drug to cyclodextrin under these experimental conditions. These data provide supporting evidence that the complex may be derived from solution chemistry and is not simply an artifact of the spray process.

The abundance of the drug–cyclodextrin complex can also be shown to increase when the cyclodextrin is infused via the CE capillary and the terbutaline is introduced separately via the sheath capillary. However, the two solutions still have to mix for a short time in the liquid phase to complete the electrical circuit at the sprayer tip before they are sprayed. Therefore, it is not possible to convincingly demonstrate that the complex is not formed by gas phase chemistry with this experiment. Since neither a solution phase-derived drug–cyclodextrin complex nor a gas phase–derived drug–cyclodextrin adduct has been unequivocally proven thus far, these matters will be investigated further in future work.

The drugs were detected in the SIM mode in these experiments due to significant chemical interference from the running buffer additives. As an example of this interference, a representative full-scan mass spectrum at unit mass resolution of terbutaline in the running buffer is shown in Figure 4. CE detection in full-scan mass spectral mode may be more available in the future by the use of ion spray on an atmospheric pressure ionization ion trap mass spectrometer. This technology can provide significantly improved sensitivity,[14] while chemical interference problems associated with the buffer additives may be solved by resonance ion ejection techniques which have been reported for ion trap MS.[24]

Figure 5 shows the same separation as in Figure 3, but under selected reaction monitoring (SRM) conditions. Two precursor–product ion reactions were monitored. In the upper electropherogram, the protonated molecule for terbutaline at m/z 226 is used as the precursor ion. The dominant fragment for m/z 226 is the product ion m/z 152, which was previously confirmed by direct infusion of terbutaline in the full-scan mode (data not shown).[25] In the lower electropherogram (Figure 5), the protonated drug–cyclodextrin noncovalent inclusion complex at m/z 1557 is used as the precursor ion. The dissociation of the complex is readily demonstrated by the observation of its product ion at m/z 226 for the protonated molecule of free terbutaline. This dissociation is barely detectable in this second trace because of the limited amount of complex that is present and the ion transmission losses common to MS/MS using a triple quadrupole mass spectrometer. However, the detection of this transition documents for the first time the on-line CE/MS/MS detection and dissociation of a

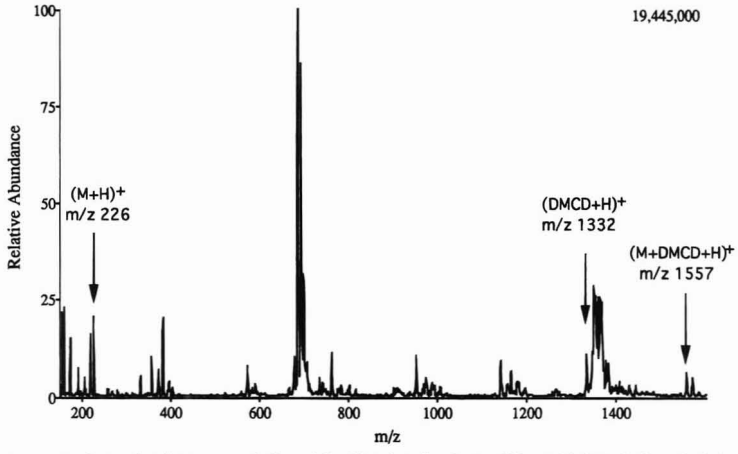

Figure 4. Full-scan mass spectrum at unit mass resolution of 2 mM terbutaline in 5 mM heptakis(2,6-di-*O*-methyl)-β-cyclodextrin and 5 mM sodium phosphate buffer at pH 2.5. The notation $(M + H)^+$ represents the protonated molecular ion for terbutaline, $(DMCD + H)^+$ represents the protonated molecular ion of heptakis(2,6-di-*O*-methyl)-β-cyclodextrin, and $(M + DMCD + H)^+$ represents the protonated noncovalent complex of terbutaline and heptakis(2,6-di-*O*-methyl)-β-cyclodextrin.

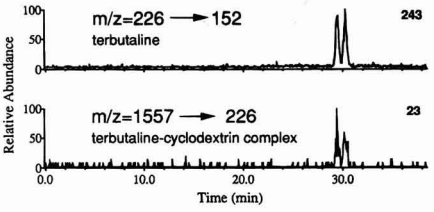

Figure 5. SRM/CE/MS electropherogram of racemic terbutaline mixture, monitoring the reactions *m/z* 226 (protonated molecule of terbutaline) fragmenting to 152, and *m/z* 1557 (protonated terbutaline–cyclodextrin host–guest inclusion complex) dissociating to 226. Total ion abundance is indicated in the upper right-hand corner of each electropherogram.

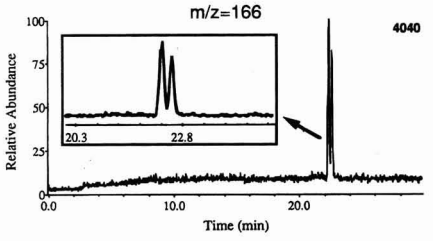

Figure 6. SIM/CE/MS electropherogram of the enantiomers (1*R*,2*S*)-(−)-ephedrine and (1*S*,2*R*)-(+)-ephedrine, monitoring the protonated molecules at *m/z* 266. Total ion abundance is indicated in the upper right-hand corner of the electropherogram.

β-cyclodextrin host–guest noncovalent inclusion complex.

An enantiomeric mixture of ephedrine was also separated using a running buffer containing 20 mM heptakis(2,6-di-*O*-methyl)-β-cyclodextrin and 10 mM tris(hydroxymethyl)aminomethane adjusted to pH 3.0 with formic acid (88% solution). The drug mixture was prepared in water at a concentration of 4.2 mM (1*R*,2*S*)-(−)-ephedrine and 3.4 mM (1*S*,2*R*)-(+)-ephedrine. The sample amounts injected were calculated to be 65 pmol of (1*R*,2*S*)-(−)-ephedrine and 50 pmol of (1*S*,2*R*)-(+)-ephedrine. The running current for this separation was constant at 20 μA. The resulting SIM electropherogram shown in Figure 6 was obtained for the protonated molecule for each enantiomer at *m/z* 166. The inset is an expansion of the time scale for the same peaks which shows nearly baseline separation for each ephedrine enantiomer. Figure 7 is a SIM electropherogram under the same separation conditions but with 0.44 pmol of (1*R*,2*S*)-(−)-ephedrine and 44 pmol of (1*S*,2*R*)-(+)-ephedrine injected from a solution of 0.03 mM (1*R*,2*S*)-(−)-ephedrine and 3 mM (1*S*,2*R*)-(+)-ephedrine. The inset is a 28× magnification of the *y*-axis in Figure 7 and demonstrates the detection of 1% of the (−)-*E* enantiomer in the presence of the (+)-*E* enantiomer.

In order to compare the sensitivity and illustrate the selectivity of the mass spectrometer versus a UV detector, a sample of male urine was spiked with 27 μg/mL of each terbutaline enantiomer. The spiked urine was simply filtered prior to analysis. No extraction method was used to clean up the sample prior to injection into the CE capillary. In Figure 8, electropherogram a

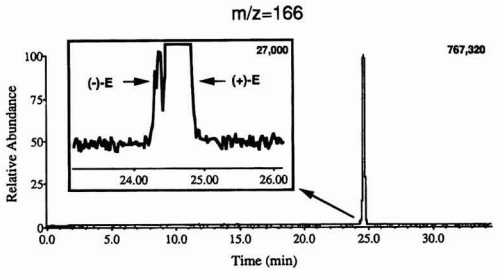

Figure 7. SIM/CE/MS electropherogram of 1% (1*R*,2*S*)-(−)-ephedrine present in (1*S*,2*R*)-(+)-ephedrine. (−)-*E* indicates (1*R*,2*S*)-(−)-ephedrine and (+)-*E* indicates (1*S*,2*R*)-(+)-ephedrine. Total ion abundance is indicated in the upper right-hand corners of the electropherogram and the magnified inset.

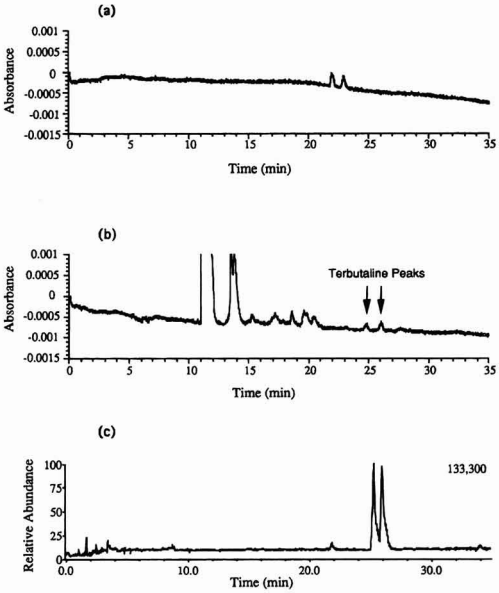

Figure 8. (a) CE/UV electropherogram at 200 nm of racemic terbutaline mixture in water at 27 μg/mL of each enantiomer. (b) CE/UV electropherogram at 200 nm of urine spiked to 27 μg/mL of each terbutaline enantiomer. (c) SIM/CE/MS electropherogram of a urine sample spiked to 27 μg/mL of each terbutaline enantiomer. Total ion abundance is indicated in the upper right-hand corner of electropherogram c.

was obtained with UV detection at 200 nm and represents a 110 pg injection of an analytical standard solution of terbutaline in water obtained using the same separation conditions as shown in Figure 2. Electropherogram b was also obtained with UV detection at 200 nm using spiked male urine at the same concentration as the analytical standard solution (110 pg injected) shown in electropherogram a. Electropherogram c shows an identical analysis of the same spiked urine using MS detection in the SIM mode while monitoring the protonated terbutaline ion at m/z 226. The slight migration time shifts observed between electropherogram a and electropherograms b and c in Figure 8 appear to be due to the higher ionic strength and higher pH of the urine compared to the CE buffer. The slight differences in

(23) Krull, I. S.; Mhatre, R.; Cunniff, J. *LC·GC* **1994**, *12*, 914–919.
(24) McLuckey, S. A.; Van Berkel, G. J.; Goeringer, D. E.; Glish, G. L. *Anal. Chem.* **1994**, *66*, 689A–696A.
(25) Debrauwer, L.; Bories, G. *Rapid Commun. Mass Spectrom.* **1992**, *6*, 382–387.

electrophoretic resolution and time scale between electropherograms b and c are typical of the day-to-day reproducibility variances that we encountered. These variances are not as important for identification purposes as when UV or fluorescence detection are used due to the high specificity afforded by mass spectrometry. This comparison shows that ion spray mass spectrometry used in the SIM mode provides a 1000-fold improvement in the signal-to-noise ratio compared with UV detection. The significantly reduced baseline obtained with the mass spectrometer also illustrates the selectivity that can be achieved in a complex matrix such as this filtered urine. While common levels of some β-agonists in human urine at therapeutic dosage are in the 1−100 ng/mL range, we did not attempt to achieve this level of sensitivity. It should be possible to inject larger volumes of more dilute sample in order to detect these low levels. If additional specificity were needed, selected reaction monitoring could be used as well.

CONCLUSIONS

Capillary electrophoresis combined with ion spray mass spectrometry is potentially useful for the determination of chiral composition and enantiomeric purity and the determination of chiral drugs in complex matrices. The selectivity provided by mass spectrometry gives unequivocal support needed to verify chiral composition of enantiomeric mixtures. Although SIM/CE/MS was sufficient to selectively detect terbutaline in urine, the additional specificity provided by CE/MS/MS should be extremely useful in the determination and characterization of chiral drugs in biological samples and pharmaceutical formulations. Future efforts in this laboratory will explore improved buffer compositions and ion trap mass spectrometry detection for these types of capillary electrophoresis applications.

ACKNOWLEDGMENT

We thank Beckman Instruments for the loan of the P/ACE 2050 capillary electrophoresis instrument and PE Sciex for partial financial support of this work. We are grateful to Cornell research group members Dr. Tim Wachs and Ms. Karen Bean for their technical assistance. This research was supported in part by the National Institutes of Health through Grants GM 47931 and GM 36712. R.S. would especially like to thank Xerox Corp. for this unique educational opportunity.

Received for review February 27, 1995. Accepted April 10, 1995.[⊗]

AC9502099

[⊗] Abstract published in *Advance ACS Abstracts,* June 1, 1995.

Anal. Chem. **1995**, *67*, 2059–2063

Fused Quartz Substrates for Microchip Electrophoresis

Stephen C. Jacobson,* Alvin W. Moore, and J. Michael Ramsey

Chemical and Analytical Sciences Division, Oak Ridge National Laboratory, P.O. Box 2008 Oak Ridge, Tennessee 37831-6142

A fused quartz microchip is fabricated to perform capillary electrophoresis of metal ions complexed with 8-hydroxyquinoline-5-sulfonic acid (HQS). The channel manifold on the quartz substrate is fabricated using standard photolithographic, etching, and deposition techniques. By incorporating a direct bonding technique during the fabrication of the microchip, the substrate and cover plate can be fused together below the melting temperature for fused quartz. To enhance the resolution for the separation, the electroosmotic flow is minimized by covalently bonding polyacrylamide to the channel walls. A separation length of 16.5 mm and separation field strength of 870 V/cm enable separations to be performed in ≤15 s. By increasing the concentration of HQS from 5 mM to 20 mM, the separation efficiency improves by ~3 times. The low background signal from the fused quartz substrate results in mass detection limits of 85, 61, and 134 amol and concentration detection limits of 46, 57, and 30 ppb for Zn, Cd, and Al, respectively.

Miniaturized chemical analysis instruments fabricated using micromachining techniques are receiving increasing attention. The more successful demonstrations for miniaturized instruments incorporate liquid phase separation techniques. Devices have been demonstrated for capillary electrophoresis,[1–6] free-flow electrophoresis,[7] open channel electrochromatography,[8] and capillary electrophoresis with pre- and postcolumn derivatization.[9,10] All of the previously demonstrated devices utilize glass substrates. By moving to quartz substrates, the superior optical properties of quartz especially in the UV region can be exploited. For both capillary electrophoresis and liquid chromatography, the most useful wavelength range for the purpose of optical detection is 200–400 nm, and the ability to fabricate fused quartz microchips permits investigation of similar detection scenarios.

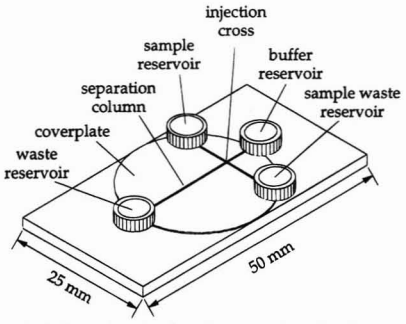

Figure 1. Schematic of the fused quartz microchip. The reservoirs are affixed on the microchip via epoxy.

To test the performance of fused quartz substrates, metal ions complexed with 8-hydroxyquinoline-5-sulfonic acid (HQS) are separated by electrophoresis and detected with UV laser-induced fluorescence. HQS has been widely used as a ligand for optical determinations of metal ions following initial work by Fiegl and Heisig.[11] The optical properties and the solubility of HQS in aqueous media have recently been used for detection of metal ions separated by ion chromatography[12] and capillary electrophoresis.[13] Because uncomplexed HQS does not fluoresce, excess ligand is added to the buffer to maintain the complexation equilibria during the separation without contributing a large background signal. This benefits both the efficiency of the separation and the detectability of the sample.

In this paper, the fabrication of fused quartz microchips is described. Direct bonding of the cover plate to the substrate enables covalent bonding to be performed below the melting temperature of fused quartz. A simple cross channel manifold (Figure 1) is constructed to perform electrophoretic analysis of metal ions complexed with HQS. The electroosmotic flow of the microchip is minimized by covalently bonding polyacrylamide to the surface of the channels. This enables a higher resolution to be achieved in a shorter separation time and length. Improved efficiency with increasing HQS concentration is also discussed.

EXPERIMENTAL SECTION

The microchips are fabricated using standard photolithographic, wet chemical etching and bonding techniques.[14] First,

(1) Harrison, D. J.; Manz, A.; Fan, Z.; Lüdi, H.; Widmer, H. M. *Anal. Chem.* **1992**, *64*, 1926.
(2) Manz, A.; Harrison, J.; Verpoorte, E. M. J.; Fettinger, J. C.; Paulus, A.; Lüdi, H.; Widmer, H. M. *J. Chromatogr.* **1992**, *593*, 253.
(3) Seiler, K.; Harrison, D. J.; Manz, A. *Anal. Chem.* **1993**, *65*, 1481.
(4) Harrison, D. J.; Fluri, K.; Seiler, K.; Fan, Z.; Effenhauser, C. S.; Manz, A. *Science* **1993**, *261*, 895.
(5) Jacobson, S. C.; Hergenröder, R.; Koutny, L. B.; Warmack, R. J.; Ramsey, J. M. *Anal. Chem.* **1994**, *66*, 1107.
(6) Jacobson, S. C.; Hergenröder, R.; Koutny, L. B.; Ramsey, J. M. *Anal. Chem.* **1994**, *66*, 1114.
(7) Raymond, D. E.; Manz, A.; Widmer, H. M. *Anal. Chem.* **1994**, *66*, 2858.
(8) Jacobson, S. C.; Hergenröder, R.; Koutny, L. B.; Ramsey, J. M. *Anal. Chem.* **1994**, *66*, 2369.
(9) Jacobson, S. C.; Hergenröder, R.; Moore, A. W., Jr.; Ramsey, J. M. *Anal. Chem.* **1994**, *66*, 4127.
(10) Jacobson, S. C.; Koutny, L. B.; Hergenröder, R.; Moore, A. W., Jr.; Ramsey, J. M. *Anal. Chem.* **1994**, *66*, 3472.
(11) Fiegl, F.; Heisig, G. B. *Anal. Chim. Acta* **1949**, *3*, 561.
(12) Soroka, K.; Vithanage, R. S.; Phillips, D. A.; Walker, B.; Dasgupta, P. K. *Anal. Chem.* **1987**, *59*, 629.
(13) Swaile, D. F.; Sepaniak, M. J. *Anal. Chem.* **1991**, *63*, 179.
(14) For example: Ko, W. H.; Suminto, J. T. In *Sensors*; Gopel, W., Hasse, J., Zemmel, J. N., Eds.; VCH: Weinhein, Germany, 1989; Vol. 1, pp 107–168.

0003-2700/95/0367-2059$9.00/0 © 1995 American Chemical Society

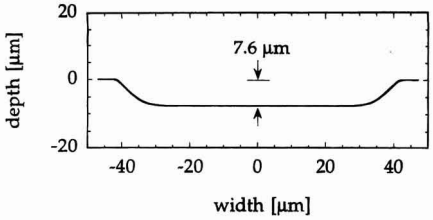

Figure 2. Profile of separation channel machined on a fused quartz substrate.

the fused quartz substrates (50 mm × 25 mm × 1 mm; Esco Products, Inc. R120110) are sputtered with metal films of chromium (30 nm) and gold (400 nm). A positive photoresist (Shipley 1811) is then spin-coated on top of the Au film, and the column design (Figure 1) is transferred to the substrate using an e-beam written photomask (Institute of Advanced Manufacturing Sciences, Inc.). Following exposure, the metal films are etched using KI/I_2 for Au and $K_3Fe(CN)_6/NaOH$ for Cr. Finally, the channels are etched into the substrate in a dilute, stirred HF/NH_4F bath at 50 °C. Due to the isotropic etch of amorphous materials, the channel profile is trapezoidal. Figure 2 shows the cross section of the quartz channel measured by a profilometer (Alpha Step 200, Tencor Instruments) prior to bonding the cover plate. The channel depth is 7.6 μm, and the channel width at half-depth is 75 μm. To form the closed network of channels, a circular cover plate (25 mm diameter; Esco Products, Inc. R525000) is bonded to the substrate over the etched channels. The substrate and cover plate are first hydrolyzed in NH_4OH/H_2O_2 at 50 °C, rinsed in H_2O, joined, and then annealed at 1100 °C for 5 h. Cylindrical glass reservoirs are affixed on the substrate using epoxy. The channel walls are then coated with polyacrylamide to minimize electroosmotic flow.[15] First, the channels of the microchip are filled with a solution of [γ-(methacryloxy)propyl]trimethoxysilane 0.4% (v/v) in water (pH 3.5, adjusted with acetic acid) for 30 min. The channels are then flushed with water and filled with a 3% (w/v) solution of acrylamide in water with 0.1% (v/v) *N,N,N′,N′*-tetramethylethylenediamine and 0.1% (w/v) potassium persulfate for 30 min. The excess acrylamide solution is removed, and the channels are rinsed sequentially with water and separation buffer.

Column performance and separations are monitored on-microchip using a single-point detection scheme via laser-induced fluorescence (LIF). An argon ion laser (351.1–363.8 nm, 10 mW; Coherent Innova 90) is used for excitation and focused to a spot on the microchip using a lens (100 mm focal length). The fluorescence signal is collected using a 21× microscope objective, followed by spatial filtering (0.6 mm diameter pinhole) and spectral filtering (425 nm cutoff; Corning 3-73), and measured using a photomultiplier tube (PMT; Oriel 77340). The data acquisition/voltage switching apparatus is computer controlled using programs written in-house in Labview 3.0 (National Instruments). Platinum electrodes provide electrical contact from the power supply (Spellman CZE1000R) to the solutions in the reservoirs. The compounds used for the experiments are zinc sulfate, cadmium nitrate, and aluminum nitrate. The buffer is sodium phosphate (60 mM, pH 6.9) with 8-hydroxyquinoline-5-sulfonic acid (20 mM for all experiments except that in Figure 5; Sigma Chemical Co.). At least 50 mM sodium phosphate buffer is needed to dissolve up to 20 mM HQS.

(15) Hjerten, S. *J. Chromatogr.* **1985**, *347*, 191.

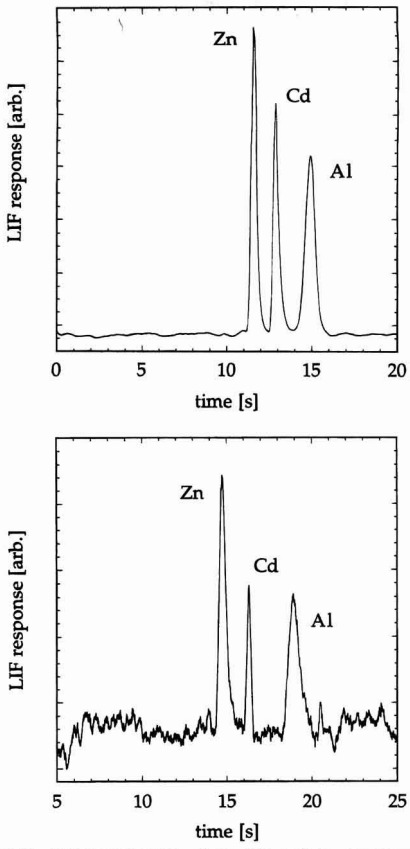

Figure 3. Electropherogram of Zn, Cd, and Al complexed with HQS: (a, top) E_{sep} = 870 V/cm and L_{sep} = 16.5 mm. The injected concentrations are 8.5 (130), 6.7 (60), and 4.3 ppm (160 μM) for Zn, Cd, and Al, respectively (b, bottom) E_{sep} = 720 V/cm and L_{sep} = 16.5 mm. The injected concentrations are 260 (4.0), 210 (1.9), and 130 ppb (4.9 μM) for Zn, Cd, and Al, respectively.

The microchip is operated in either a sample loading or separation mode. The floating sample loading, described previously,[4] is used to transport the sample to the injection cross, enabling a larger volume sample plug to be injected onto the separation column than with the pinched sample loading. The average sample plug volume for the floating sample loading is estimated to be 120 pL compared to 65 pL for the pinched sample loading. These volumes are determined by measuring injected plug widths 0.1 mm downstream from the injection cross. For comparison, the volume of the injection cross is 43 pL. With the floating sample loading, the injected plug has no electrophoretic bias, but the volume of sample is a function of the sample loading time. Because the sample loading time is inversely proportional to the field strength used, for high sample loading field strengths a shorter sample loading time is used than for low injection field strengths. For example, for a sample loading field strength of 630 V/cm (Figure 3a), the sample loading time is 12 s, and for a sample loading field strength of 520 V/cm (Figure 3b), the sample loading time is 14.5 s. Both the pinched and floating sample loadings can be used with and without suppression of the electroosmotic flow. To implement the floating sample loading,

Table 1. Data for Figure 3a

metal ion	electrophoretic mobility (10^4 cm^2 V^{-1} s^{-1})	plate no.	resolution
Zn	1.65	8200	
			2.26
Cd	1.49	6500	
			2.86
Al	1.28	3200	

a voltage is applied to the sample reservoir with the sample waste reservoir grounded and the buffer and waste reservoirs floating. After the slowest moving ion, e.g., Al, passes through the injection cross, the applied potentials are reconfigured for the separation mode. In the separation mode, the voltage is applied to the buffer reservoir with the waste reservoir grounded and with sample and sample waste reservoirs at 60% of the buffer reservoir potential. Having a voltage applied to the sample and sample waste reservoirs at a fraction of the buffer reservoir voltage prevents excess sample from bleeding into the separation column.

RESULTS AND DISCUSSION

Figure 3 shows the separation of three metal ions complexed with 8-hydroxyquinoline-5-sulfonic acid. All three complexes have a net negative charge. With the electroosmotic flow minimized by the covalent bonding of polyacrylamide to the channel walls, negative potentials relative to ground are used to manipulate the complexes during sample loading and separation. In panels a and b of Figure 3, the separation channel field strength is 870 and 720 V/cm, respectively, and the separation length is 16.5 mm. The volume of the injection plug is 120 pL, which corresponds to 16, 7, and 19 fmol injected for Zn, Cd, and Al, respectively, for Figure 3a. In Figure 3b, 0.48, 0.23, and 0.59 fmol of Zn, Cd, and Al, respectively, are injected onto the separation column. The average reproducibility of the amounts injected is 1.6% relative standard deviation (rsd) as measured by peak areas (six replicate analyses). The stability of the laser used to excite the complexes is ~1% rsd.

The primary purpose of eliminating the electroosmotic flow is to enhance the resolution of the separation. For electrophoretic separations, the resolution between two components can be written[16]

$$R_s = \frac{\sqrt{N}}{4}\left(\frac{\mu_A - \mu_B}{\mu_{AV} + \mu_{EO}}\right) \quad (1)$$

where N is the average number of theoretical plates, μ_A and μ_B are the electrophoretic mobilities for components A and B, respectively, μ_{AV} is the average electrophoretic mobility for A and B, and μ_{EO} is the electroosmotic mobility. Electroosmosis does not contribute to the separation. To maximize the resolution, electroosmosis must be eliminated or precisely controlled, e.g., application of an external field.[17] For simplicity, electroosmosis is minimized by covalently bonding polyacrylamide to the channel surface.

Table 1 lists the efficiencies and resolution (eq 1) generated for each complex in Figure 3a. The resolution obtained between Zn/Cd and Cd/Al is 2.25 and 2.86, respectively. To obtain a comparable resolution, e.g., 2.25, with electroosmotic flow would require a longer separation column and analysis time. For example, with an electroosmotic mobility of 5.7×10^{-4} cm^2 V^{-1} s^{-1} (measured on a microchip without the electroosmotic flow minimized), a field strength of 870 V/cm and a resolution of 2.25, a separation length of 11.5 cm is required to resolve these three metal ion complexes, and the total analysis time increases to 33 s. Also, to produce the equivalent separation field strength, a 9.9 kV power supply is required compared to 1.4 kV for this separation. The smaller power supply is more amenable to miniaturization.

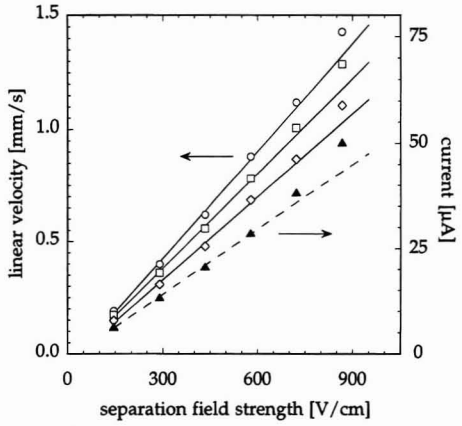

Figure 4. Variation of linear velocity for Zn (○), Cd (□), and Al (◇) and separation column current (▲) with separation field strength. Lines represent linear fits for separation field strengths from 140 to 580 V/cm and extrapolated to 870 V/cm.

The analysis time can be reduced by increasing the separation field strength and, consequently, the linear velocity of the sample[16]

$$u = \mu E_{sep} \quad (2)$$

where μ is the electrophoretic mobility and E_{sep} is the separation field strength. The electrophoretic mobility depends on the viscosity of the buffer. If the heat generated in the separation column is not dissipated efficiently during a separation, the viscosity of the buffer decreases, leading to higher than predicted linear velocities for the sample zones. In Figure 4 the linear velocity of the sample zones are plotted versus the electric field strength. For separation field strengths of ≥720 V/cm, a deviation from linear behavior is observed. Also, plotted in Figure 4 is the current measured in the separation column. As expected, the current in the separation column exhibits the same nonlinear behavior for field strengths of ≥720 V/cm. For separation field strengths of 720 and 870 V/cm, the microchip required ~2 min for the linear velocities to stabilize. The reproducibility of the linear velocities is 0.1% rsd (six replicate analyses). To reduce this heating effect at comparable separation field strengths, channels with smaller cross-sectional areas or lower concentration (lower conductivity) buffers are two possibilities. Optimum HQS concentration for detection and separation (discussed below) is determined to be 20 mM, which requires at least 50 mM phosphate buffer for dissolution. Thus, 80 mM for a total buffer concentration is near the operating limit for these experiments.

(16) Jorgenson, J. W.; Lukacs, K. D. *Anal. Chem.* **1981**, *53*, 1298.
(17) Lee, C. S.; Banchard, W. C.; Wu, C. T. *Anal. Chem.* **1990**, *62*, 1550.

Table 2. Detection Limits

metal ion	concentration μM	concentration ppb	mass[a] (amol)
Zn	0.71	46	85
Cd	0.51	57	61
Al	1.12	30	134

[a] 120 pL injection volume.

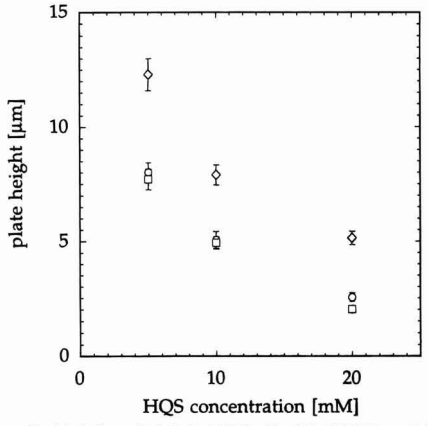

Figure 5. Variation of plate height for Zn (○), Cd (□), and Al (◇) with concentration of HQS. Error bars are $\pm\sigma$ for three analyses.

In addition to resolving power and analysis time, detection must also be considered in an analytical procedure. Detection limits are measured using serial dilutions of a stock solution of the metal ions. The measurements are performed by separating the mixture of the metal ions, using the experimental conditions in Figure 3b. The data are then extrapolated to a signal-to-noise ratio (S/N) of 2, to give the concentration and mass detection limits listed in Table 2. Figure 3b shows the electropherogram at the lowest concentration injected for the mixture during the detection limit study. The peaks correspond to an average S/N for 3 runs of 16.4, 10.7, and 8.6 for Zn, Cd, and Al, respectively, which are within 1 order of magnitude of the estimated detection limits (Table 2). A pH 6.9 separation buffer is near the optimum conditions for fluorescence detection of the complexes with Zn, Cd, and Al.[11] Detection limits are improved by using a fused quartz substrate as opposed to a glass substrate. The observed background signal from the experimental apparatus with the fused quartz substrate inserted is 30% of the background signal observed for glass. The primary contributions to the background signal include stray room light, scattered laser light, and inelastic scattering from the microscope objective and microchip substrate. Further reductions in background signals are expected by improving the quality of the optical components.

A substantial decrease in the plate height is observed with increasing concentrations of HQS in the separation buffer. Figure 5 shows the variation of the plate height with concentration of the HQS. The Al complex exhibits the poorest efficiency. The formation constants for Zn, Cd, and Al are $10^{16.2}$, $10^{14.2}$,[18] and 10^{9},[19] respectively. Because of the large formation constants, the dominant form for Zn and Cd is a 2:1 ligand–metal complex, and for Al a 3:1 complex. The Al complex with a 3– charge might undergo an ion-pairing phenomena. If two or more species exist in the sample band for Al, additional band dispersion results because the species will migrate at different velocities, yet cannot be resolved under these conditions. For HQS concentrations of >20 mM, significant improvements in the efficiency are not observed. The relationships between HQS concentration, the complex formation constant, and band broadening associated with HQS–metal complexes in capillary electrophoresis have been investigated.[12] Additional band broadening was previously attributed to nonequilibrium conditions at injection, various HQS-metal species in the sample band, and competing equilibria with supporting electrolyte.[12] For these experiments, nonequilibrium conditions at injection do not occur because the sample and separation buffers are the same. With the magnitude of the formation constants listed above and the large excess of HQS, multiple metal–HQS species seems improbable.

For electrophoresis, the contributions to the total plate height from the injection plug length, detector observation length,[20] axial diffusion,[21] and Joule heating[22] are

$$H = \frac{l_{inj}^2}{16L_{sep}} + \frac{l_{det}^2}{16L_{sep}} + \frac{2D_m}{\mu E_{sep}} + \frac{7 \times 10^{-9}\mu E_{sep}^5 d_c^6 \lambda^2 C^2}{D_m \kappa^2} \quad (3)$$

where l_{inj} is the injection plug length, l_{det} is the detector observation length, L_{sep} is the separation length, D_m is the diffusion coefficient, d_c is the channel depth,[23] λ is the molar conductivity of the buffer, C is the buffer concentration, and κ is the thermal conductivity of the buffer. The contributions from the injection plug length and detector observation length assume Gaussian distributions. The lengths of the injection plug and the detector observation are constant for all experiments. If these time-independent contributions predominate in their contribution to the plate height, then the total plate height decreases as the separation length increases. The contribution from axial diffusion to the plate height is reduced by increasing the separation field strength and, consequently, reducing the analysis time. The contribution from Joule heating can be minimized by controlling the channel dimensions, separation field strength, and buffer concentration.

In Figure 6, the variation of the total plate height with the electric field strength is plotted. For these experiments, the injection plug length is 330 μm and the detector observation length is 80 μm. The corresponding contributions to the plate height from the injection plug length and detector observation length are 0.41 μm and 24 nm, respectively. These contributions are small relative to the measured plate heights. The contribution from axial diffusion decreases with increasing field strength.

(18) *Lange's Handbook of Chemistry*, 14th ed.; Dean, J. A., Ed.; McGraw-Hill Book Co.: New York, 1992.

(19) Bishop, J. A. *Anal. Chem. Acta* **1973**, *63*, 305.
(20) Sternberg, J. C. *Adv. Chromatogr.* **1966**, *2*, 205.
(21) Giddings, J. C. *Dynamics of Chromatography, Part I: Principles and Theory*; Marcel Dekker: New York, 1965; Chapter 2.
(22) Knox, J. H.; Grant, I. H. *Chromatographia* **1987**, *24*, 135.
(23) d_c usually corresponds to the capillary diameter. In this case, a channel with a trapezoidal cross section is under consideration, and the channel depth will be used for estimating the contribution of Joule heating to the plate height.
(24) Monnig, C. A.; Jorgenson, J. W. *Anal. Chem.* **1991**, *63*, 802.
(25) Hjertén, S.; Elenbring, K.; Kilár, F.; Liao, J.-L.; Chen, A.; Siebert, C. J.; Zhu, M.-D. *J. Chromatogr.* **1987**, *403*, 47.
(26) Aebersold, R.; Morrison, H. D. *J. Chromatogr.* **1990**, *516*, 79.
(27) Jandik, P.; Jones, W. R. *J. Chromatogr.* **1991**, *546*, 431.

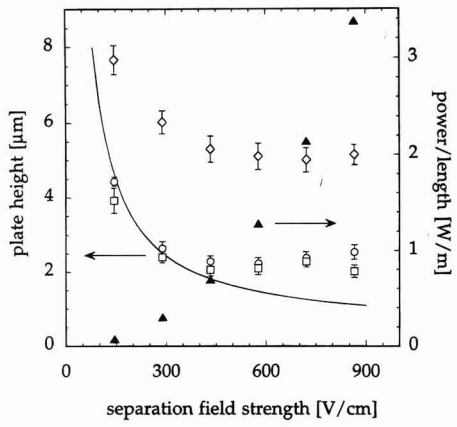

Figure 6. Variation of plate height for Zn (○), Cd (□), and Al (◇) and power/length (▲) with the separation field strength complexed with HQS. The solid line is the calculated plate height for Zn using eq 3. Error bars are $\pm\sigma$ for three analyses.

However, the experimental plate height data do not asymptotically approach the sum of the time-independent contributions at high field strengths. In Figure 6, the calculated plate height for Zn using eq 3 ($\mu_{Zn} = 1.65 \times 10^{-4}$ cm^2 V^{-1} s^{-1}, $D_m = 5 \times 10^{-6}$ cm^2 s^{-1}) is plotted. For separation field strengths of ≤430 V/cm, the experimental data correspond well with the calculated values, but for separation field strengths of ≥580 V/cm, the agreement is poor. This difference could be due to heating of the microchip, as observed in the nonlinear behavior of the linear velocities (Figure 4). The power/length in the separation column is also plotted in Figure 6 for the corresponding field strengths. Typically for electrophoretic systems, when the power/length remains below 1 W/m,[24] Joule heating does not interfere with the separation performance. For separation field strengths of ≥580 V/cm, the power/length is >1 W/m. Using the last term for Joule heating in eq 3, this contribution can be estimated. For μ(Zn) = 1.65×10^{-4} cm^2 V^{-1} s^{-1}, $E_{sep} = 870$ V/cm, $d_c = 7.6$ μm, $\lambda = 0.015$ m^2 mol^{-1} Ω^{-1}, $C = 80$ mM, $D_m = 5 \times 10^{-6}$ cm^2 s^{-1}, and $\kappa = 0.6$ W m^{-1} K^{-1}; the contribution of Joule heating to the plate height is 6.5 pm. As calculated, this contribution is insignificant relative to the plate height data. An alternative explanation for this discrepancy in the experimental and calculated plate height might be due to geometrical fluctuations in the channel over the length of the separation channel. As fabrication techniques for glass and quartz substrates improve, this discrepancy is likely to decrease as was the case for silica capillaries.

In conclusion, metal ions complexed with 8-hydroxyquinoline-5-sulfonic acid are resolved in less than 15 s using microchip electrophoresis, and detection limits are in the range of 30–60 ppb. To enhance the detection limits for these complexes, a preconcentration step can be added prior to the separation. A sample preconcentration method that can be easily incorporated with electrophoretic analyses is field-amplified sample injection and sample stacking.[25–28] Enhancements in detection limits up to 10^3 times have been observed using stacking methods with conventional capillary electrophoresis.[29] Similar stacking procedures have been demonstrated on microchips[30] and may allow sub-ppb detection limits for metal ions.

ACKNOWLEDGMENT

This research is sponsored by the U.S. Department of Energy (DOE), Office of Research and Development. Oak Ridge National Laboratory is managed by Martin Marietta Energy Systems, Inc. for the U.S. Department of Energy under Contract DE-AC05-84OR21400. Also, this research is sponsored in part by an appointment for A.W.M. to the ORNL Postdoctoral Research Associates Program. These postdoctoral programs are administered by the Oak Ridge Institute for Science and Education and ORNL.

Received for review December 13, 1994. Accepted April 10, 1995.

AC9412037

[⊗] Abstract published in *Advance ACS Abstracts,* June 1, 1995.

(28) Chien, R.-L.; Burgi, D. S. *J. Chromatogr.* **1991**, *559*, 141.
(29) Chien, R.-L.; Burgi, D. S. *J. Chromatogr.* **1991**, *559*, 153.
(30) Jacobson, S. C.; Ramsey, J. M. *Electrophoresis,* in press.

Anal. Chem. **1995**, *67*, 2064–2069

Experimental Design Approach for the Extraction of Polycyclic Aromatic Hydrocarbons from Soil Using Supercritical Carbon Dioxide

Ian J. Barnabas, John R. Dean,* William R. Tomlinson, and Susan P. Owen†

Department of Chemical and Life Sciences, Ellison Building, University of Northumbria at Newcastle, Newcastle-upon-Tyne, NE1 8ST U.K.

Polycyclic aromatic hydrocarbons (PAHs) have been extracted from contaminated land samples by supercritical fluid extraction (SFE) with both pure and modified carbon dioxide. An experimental design approach, based on a central composite design, was used to determine which SFE operating variables affect the total recovery of 16 PAHS. Four parametes were chosen for evaluation: pressure, temperature, extraction time, and percent methanol modifier addition. Accessible levels of each parameter were dependent on instrumental constraints. A statistical treatment of the results indicated that extraction time and percent modifier addition were the only variables to significantly affect PAH recovery. The levels of these variables were then set at their maximum values, while the pressure and temperature were maintained at their midpoint values in the design. These conditions were used in a repeatability study ($n = 7$), which extracted an average of 458.0 mg kg^{-1} total PAHs from the contaminated land sample with an RSD of 3.1%. Sequential extractions on three of these samples, using identical operating conditions, did not show the presence of any PAHs. The result was compared with Soxhlet extraction and microwave-assisted extraction of the sample, which recovered an average of 297.4 (RSD 10.0%) and 422.9 mg kg^{-1} (RSD 2.4%), respectively. Extraction of an interlaboratory test soil yielded high RSD values because of the presence of elemental sulfur.

Supercritical fluid extraction (SFE) has increasingly been used to extract low-polarity pollutants from environmental samples because of both its potential to reduce the time required for extraction and the absence of large amounts of organic solvents.[1,2] Supercritical CO_2 as an extracting fluid has several advantageous features: low cost, low toxicity, and low critical parameters. It has the ability to dissolve a variety of nonpolar and moderately polar substances. These characteristics have meant that SFE using CO_2 has been extensively used to extract nonpolar analytes and thus has prompted much research into the extraction of polycyclic aromatic hydrocarbons (PAHs) by supercritical CO_2.[3] Although PAHs are sufficiently soluble in supercritical CO_2, their efficient recovery from environmental solids is greatly dependent on the nature of the matrix. Often, organic modifiers are required in conjunction with CO_2[4,5] to effectively remove the PAHs, which can vary substantially in their molecular weights. Other supercritical fluids have been used to aid PAH extraction, including N_2O, $CHClF_2$,[6] and water,[7] but they are often more difficult to use than conventional CO_2, having additional safety requirements. High extraction temperatures have also been used to increase the efficiency of PAH extraction from environmental solids.[8] These factors add to the complex nature of SFE, even for low-polarity analytes, and make the elucidation of the most efficient extraction parameters a difficult task. The variables which affect the efficiency of SFE are still poorly understood and perhaps can be investigated best by using an experimental design approach.[9,10] This allows several variables to be studied simultaneously and uses subsequent statistical analysis to validate the procedure and results. This approach also allows a reduction in the number of experiments required to fully understand a system and to ascertain the existence of any interactions between variables. This, in turn, can greatly simplify the optimization procedure. The resultant procedure requires far fewer experiments to be carried out which are now capable of giving more information than the conventional "alter one factor at a time" evaluation.

This paper discusses the extraction of native PAHs from samples of contaminated soil, which can represent one of the most difficult environmental matrices from which to extract, because of the often diverse and heterogeneous nature of the sample. The use of a "real" contaminated soil sample is favored over normal spiking methods to assess the efficiency of the extraction procedure, as recoveries obtained from spiked samples do not effectively represent the effects of the matrix.[11] A central

† Analytical and Environmental Services, Northumberland Dock Road, Wallsend, Tyne and Wear, NE28 0QD U.K.

(1) Hawthorne, S. B.; Miller, D. J. *Anal. Chem.* **1987**, *59*, 1705.
(2) Lopez-Avila, Dodhiwala, N. S.; Beckert, W. F. *J. Chromatogr. Sci.* **1990**, *28*, 468.
(3) Barnabas, I. J.; Dean, J. R.; Owen, S. P. *Analyst* **1994**, *119*, 2381.
(4) Hill, J. W.; Hill, H. H. *J. Chromatogr. Sci.* **1993**, *31*, 6.
(5) Dankers, J.; Groenenboom, M.; Scholtis, L. H. A.; van der Heiden, C. *J. Chromatogr.* **1993**, *641*, 357.
(6) Hawthorne, S. B.; Langenfeld, J. J.; Miller, D. J.; Burford, M. D. *Anal. Chem.* **1992**, *64*, 1614.
(7) Hawthorne, S. B.; Yang, Y.; Miller, D. J. *Anal. Chem.* **1994**, *66*, 2912.
(8) Langenfeld, J. J.; Hawthorne, S. B.; Miller, D. J.; Pawliszyn, J. *Anal. Chem.* **1993**, *65*, 338.
(9) Brereton, R. G. *Chemometrics: Applications of Mathematics and Statistics to Laboratory Systems*; Ellis Horwood: Sussex, England, 1990; Chapter 2.
(10) Kane, M.; Dean, J. R.; Hitchen, S. M.; Dowle, C. J.; Tranter, R. L. *Anal. Chim. Acta* **1993**, *271*, 83.
(11) Burford, M. D.; Hawthorne, S. B.; Miller, D. J. *Anal. Chem.* **1993**, *65*, 1497.

0003-2700/95/0367-2064$9.00/0 © 1995 American Chemical Society

composite design[12,13] has been used to elucidate the optimum operating conditions for the removal of the maximum amount of PAHs from the contaminated soil sample. The combination of statistically designed experiments with the versatility of SFE allows a significant reduction in extraction time and method development.

EXPERIMENTAL SECTION

Samples. All of the contaminated land samples used are native and contain relatively high levels of total PAHs (several hundred mg kg^{-1}). The preparation of the bulk sample used throughout the central composite design is described in detail elsewhere[14] and consists of a drying stage followed by removal of stones and other large aggregates and blending of the sample in a commercial blender. The CONTEST soil sample used was supplied by the Laboratory of the Government Chemist (LGC), Department of Environment, U.K., and is part of an interlaboratory study. This soil was used as received without any pretreatment.

Supercritical Fluid Extraction. All of the extractions were performed on a Jasco SFE (Mettler-Toledo Ltd., Halstead, Essex) instrument which possesses a second pump for modifier addition. The back-pressure regulator with the system allows independent control of both the flow rate and the extraction pressure (details described elsewhere[15]). SFC grade CO_2 (≥99.995% purity) was purchased from Air Products Ltd. (Sunderland, U.K.) and combined with methanol modifier by mixing in a pressure relief valve. The CO_2 flow rate was kept constant at 1 mL min^{-1} throughout the experimentation. The sample (1 ± 0.01 g) was accurately weighed into 4.6 mm i.d. stainless steel extraction cells having a volume of 2.5 mL (Phase Separations Ltd., Clwyd, U.K.) and placed inside the extraction oven, where the cells were allowed to equilibriate at the set temperature before sample extraction. Once the cell had reached the set extraction temperature and pressure, the pumps were switched off, and each sample was extracted for 5 min in the static mode, after which the pumps were switched on and the dynamic extraction time period was begun. All extracts were collected by inserting the end of the back-pressure regulator through a PTFE-lined septum into a vial containing 5 mL of methylene chloride. The collection vial was placed in an ice–water batch to aid trapping. In addition, the escaping CO_2 was vented via a hypodermic needle into a C_{18} solid-phase extraction (SPE) cartridge (Bond-Elut, Phase Separations Ltd.), which prevented any of the PAHs from escaping in the aerosol formed by the CO_2 (Figure 1). To obtain quantitative recoveries, the SPE cartridge was back-flushed into the collection vial using methanol. The combined extract was made up to a final volume of 25 mL in methylene chloride to await analysis.

Soxhlet Extraction and Microwave-Assisted Extraction. The recovery obtained by SFE of the contaminated land sample was compared with those from conventional Soxhlet extraction and microwave-assisted extraction. The 6 h solid–liquid extraction with 100 mL of methylene chloride and the 20 min microwave-assisted extraction using either acetone or dichloromethane is detailed in other work.[14]

Analysis of Extracts. All of the SFE and Soxhlet extracts were analyzed without the need for any preconcentration or cleanup, using a Hewlett Packard (Bracknell, U.K.) 5890 Series II + capillary GC fitted with a 5972 A mass selective detector (MSD) and 7673 autosampler. The GC was equipped with a 30 m J & W DB-5 column (0.25 mm i.d. × 0.25 μm film thickness) supplied by Phase Separations Ltd. The split/splitless injector was held at 280 °C and operated in splitless mode with the split valve held closed for 1 min following sample injection (2 μL). The split flow was set at 40 mL min^{-1}. The initial oven was maintained at 85 °C for 3 min, followed by a temperature ramp of 6 °C/min to 300 °C, where it remained for 10 min. The transfer nozzle of the GC was kept at 290 °C throughout the analysis, with an electron energy of 70 eV. Quantification was achieved using the selected ion monitoring (SIM) mode by viewing only the most abundant ion present in each species. The instrument was calibrated using a five-point calibration curve from the serial dilution of a stock standard containing 16 PAHs in methylene chloride/benzene (1:1), supplied by Sigma Chemical Ltd. (Dorset, U.K.). Prior to analysis, 5 μg portions of the internal standards (3,6-dimethylphenanthrene and 6-ethylchrysene), purchased from Lancaster Chemicals Ltd. (Lancashire, U.K.), were added to 0.5 mL aliquots of all extracts and standards.

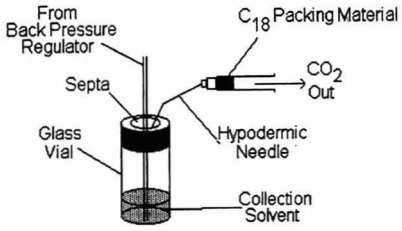

Figure 1. Schematic diagram of the supercritical fluid collection device.

Experimental Design. If we are to fully understand the way in which SFE operating variables affect an extraction, we must consider possible interactions between multiple variables and nonlinear effects. In this study, the variables which have been chosen are extraction pressure and temperature, time of dynamic extraction, and percent addition of methanol modifier. Methanol was chosen as the modifier because it has been shown to have the greatest affect on PAH extraction efficiency from native soils.[16] The increase in recovery from native samples is most likely due to matrix–modifier interactions and/or the swelling of the matrix by the polar modifier. The flow rate of CO_2 was kept constant throughout the experiments (1 mL min^{-1}) since it has been postulated that it does not affect extraction efficiency if the analytes are sufficiently soluble in the extraction fluid.[17] The four variables were studied using a full second-order central composite design.[18] Each of the variables had levels set at five separate coded levels: $-\alpha$, -1, 0, $+1$, and $+\alpha$, requiring 30 experiments in total. The design can be broken down into three groups of design points, a two-level factorial design (coded ±1), "star" or axial points (coded $\pm\alpha$), and center points (coded 0). The "star" points allow estimation of the curvature in the model. In a four-factor

(12) Cochran, W. G.; Cox, G. M. *Experimental Designs*, 2nd ed.; J. Wiley and Sons: New York, 1957; Chapter 8.
(13) Adasoglu, N.; Dincer, S.; Bolat, E. *J. Supercrit. Fluids* **1994**, *7*, 93.
(14) Barnabas, I. J.; Dean, J. R.; Fowlis, I. A.; Owen, S. P. *Analyst*, in press.
(15) Barnabas, I. J.; Dean, J. R.; Hitchen, S. M.; Owen, S. P. *J. Chromatogr. Sci.* **1994**, *32*, 547.
(16) Tena, M. T.; Luque de Castro, M. D.; Valcarcel, M. *Chromatographic* **1994**, *38*, 431.
(17) Hawthorne, S. B. In *Supercritical Fluid Extraction and Its Use in Chromatographic Sample Preparation*; Westwood, S. A., ed.; Blackie Acedemic and Professional: London, 1993.
(18) Box, G. E. P.; Wilson, K. B. *J. R. Stat. Soc.* **1951**, *13*, 1.

Table 1. Values of the Four Variables at Five Levels Used for the Central Composite Design

level	pressure (kg cm^{-2})	temp (°C)	extrctn time (min)	methanol content (%)
$-\alpha$	100	40	10	0
−1	150	55	22.5	5
0	200	70	35	10
+1	250	85	47.5	15
$+\alpha$	300	100	60	20

(variables) central composite design, the coded values α are ±2.00. The center points allow an estimation of the "pure error" in the system. The results from a central composite design can be fitted to a linear model (or response surface), which is adequate for describing a wide variety of multifactor chemical systems,[19] of the following form:

$$Y_1 = \beta_0 + \sum_{i=1}^{\alpha} \beta_i x_i + \sum_{i=1}^{q} \beta_{ii} x_i^2 + \sum_{i=1}^{q} \sum_{j=1}^{q} \beta_{ij} x_i x_j$$

In this case, Y_1 (the response) is the overall total amount of PAHs extracted and β_0 (the intercept) is the value of the fitted response at the center of the design. Each variable was assigned limits set because of experimental and instrumental limitations. The pressure variable was given ranges between 100 and 300 kg cm^{-2} (x_1), temperature between 40 and 100 °C (x_2), extraction time between 10 and 60 min (x_3), and methanol modifier content between 0% and 20% (x_4). The extraction time was fixed at a maximum of 1 h to aid a relatively high sample throughput. These values were input into a statistical experimental design computer program (Design Expert, Version 3.0, Stat-Ease, Inc., Minneapolis, MN) which used the values to create a central composite design matrix where the outer limits of the variables were used as the star points. The +1, −1 levels and the center points were then calculated from these levels and used to complete the design.[20] The final values for the design variables are shown in Table 1. The large number of experiments required for the design (30) necessitated that they be performed on three successive days, and the design was blocked into three sets of 10 experiments. The experimental blocking also has the advantage of allowing some assessment of reproducibility to be introduced into the model. The individual experiments in the blocks were then randomized to remove any systematic error, and the extractions were performed in that random order.[21]

RESULTS AND DISCUSSION

Central Composite Design Results. The responses for the central composite design experiment, together with the full design, are shown in Table 2. Each of the responses consisted of the summed totals for 16 individual PAHs routinely analyzed in EPA Method 8100.[22] The summed totals for the PAHs were used to reduce the statistical evaluation which would be required if individual PAHs were considered. The reproducibility of extraction of the PAHs was determined, using the center points of the blocked experiments, to be 396.2 mg kg^{-1} (RSD 7.06%), based on six repeat extractions over a 3 day period. Analysis of variance (ANOVA) was performed on the design to assess the significance of the model with the initial summary of the model statistics depicted in Table 3a. It should be noted that with this design, a possible cubic model exhibits alaising (all β coefficients cannot be uniquely described) because of an insufficient number of experiments and cannot be considered.

Table 2. Full Coded Central Composite Design with Total PAH Extracted[a]

run order	block	pressure	temp	extrctn time	MeOH content	total PAH extrcd (mg kg^{-1})
1	1	+1	−1	1	1	391.8
2	1	−1	1	1	1	413.6
3	1	1	−1	−1	−1	68.7
4	1	1	1	1	−1	143.0
5	1	−1	1	−1	−1	104.0
6	1	−1	−1	−1	1	309.1
7	1	0	0	0	0	400.6
8	1	1	1	−1	1	402.5
9	1	−1	−1	1	−1	77.7
10	1	0	0	0	0	426.5
11	2	1	1	1	1	457.5
12	2	−1	−1	−1	−1	56.9
13	2	1	1	−1	−1	94.1
14	2	1	−1	−1	1	409.7
15	2	−1	−1	1	1	410.9
16	2	−1	1	−1	1	375.8
17	2	−1	1	1	−1	110.5
18	2	0	0	0	0	387.8
19	2	1	−1	1	−1	103.0
20	2	0	0	0	0	399.1
21	3	0	0	0	0	416.9
22	3	0	−α	0	0	359.8
23	3	0	0	−α	0	276.1
24	3	0	0	+α	0	462.3
25	3	−α	0	0	0	311.5
26	3	0	0	0	0	346.5
27	3	0	0	0	−α	46.8
28	3	0	0	0	+α	418.7
29	3	0	+α	0	0	413.9
30	3	+α	0	0	0	429.4

[a] Design response, Y_1.

Table 3. Summary of (a) the ANOVA Model Statistics and (b) the Lack of Fit of the Models

(a) ANOVA Model Statistics

source	sum of squares	DF[a]	mean square	F value	prob > F
mean	2715 321.7	1	2715 321.7		
blocks	33 851.4	2	16 925.7		
linear	447 599.3	4	111 899.8	17.72	0.0001
quadratic	100 176.6	10	10 017.7	2.89	0.0382
cubic	26 912.5	8	3 364.1	0.93	0.5611
residual	18 142.0	5	3 628.4		
total	3342 003.6	30			

(b) Lack of Fit of the Models

model	sum of squares	DF	mean square	F value	prob > F
linear	142 353.8	20	7117.7	7.421	0.0618
quadratic	42 177.2	10	4217.7	4.398	0.1248
cubic	15 264.7	2	7632.4	7.958	0.0632
pure error	2 877.3	3	959.1		

[a] Number of degrees of freedom.

(19) Palasota, J. A.; Deming, S. N. *J. Chem. Educ.* **1992**, *69*, 560.

(20) *Design Expert Training Manual*, Version 3.0; Stat-Ease Inc.: Minneapolis, MN, 1992.

(21) Cox, D. R. *Planning of Experiments*; J. Wiley and Sons: New York, 1992; Chapter 5.

(22) *Determination of Polycyclic Aromatic Hydrocarbons in Solid Waste by Gas Chromatography*, U.S. EPA Method 8100; U.S. Government Printing Office: Washington, DC, 1986.

Table 4. Results of Significance Test on Quadratic Model Coefficients[a]

indepndt variable	coeff estimate	std error	*t* for null hypothesis	prob > |*t*|
intercept	396.2	24.0	16.490	
block 1	−27.1			
block 2	−20.2			
block 3	47.3			
x_1[b]	18.7	12.0	1.555	0.1440
x_2[c]	15.9	12.0	1.320	0.2097
x_3[d]	*27.5*	*12.0*	*2.290*	*0.0394*
x_4[e]	*131.5*	*12.0*	*10.940*	*0.0001*
x_1^2	−22.1	11.2	−1.970	0.0705
x_2^2	−18.0	11.2	−1.606	0.1324
x_3^2	−22.5	11.2	−1.998	0.0671
x_4^2	*−56.6*	*11.2*	*−5.033*	*0.0002*
x_1x_2	−1.6	14.7	−0.111	0.9131
x_1x_3	−2.9	14.7	−0.195	0.8488
x_1x_4	5.7	14.7	0.389	0.7036
x_2x_3	0.5	14.7	3.57×10^{-2}	0.9721
x_2x_4	−1.0	14.7	-7.05×10^{-2}	0.9449
x_3x_4	4.1	14.7	0.278	0.7856

[a] Significant values are shown in italic type. [b] Pressure (kg cm^{-2}). [c] Temperature (°C). [d] Extraction time (min). [e] MeOH content (%).

The *F* value in Table 3a is the ratio between the mean-squared error (*lack of fit of the model*) and the pure error obtained from the replicates at the design center. The significance of the *F* value, which is dependent on the number of degrees of freedom (DF) in the model, is shown by the final column in the table (prob > *F*) (at the 95% significance level) and represents the effect of adding the linear, quadratic, and cubic terms sequentially to the intercept and block terms.[20] The summary statistics indicate that the quadratic model should be further investigated since the quadratic terms are significant (<0.05) when added to the mean, intercept, and linear terms of the model.

The *lack of fit each model* is summarized in Table 3b and indicates how well each of the full models fits the experimental data. This is achieved by comparing the residual error to the pure error from the replicated design points. The prob > *F* value in the final column of the table again indicates any significant (95%) *lack of fit of each model*. In this case, none of the models show any significant lack of fit at the 95% confidence level to the experimental data points, but the quadratic model exhibits the least significant lack of fit. The quadratic model was then fully evaluated using ANOVA to determine which variables, if any, had a significant effect on PAH recovery. This was achieved by dividing each coefficient by its associated standard error to obtain a Student's value *t*, which tests whether the coefficient is different from zero, the null hypothesis. The associated *p* values (prob > |*t*|) are interpreted as the probability of getting a coefficient as large as that observed when the true coefficient equals zero. Therefore, small values of *p* (<0.05 at the 95% significance level) indicate significant coefficients in the model. The significance test results are shown in Table 4.

Table 4 shows that there are only three significant coefficients which affect total PAH recovery: extraction time (x_3), percent methanol modifier (x_4), and the squared term of modifier addition (x_4^2). By far, the most statistically significant of these coefficients are the methanol modifier terms. No other coefficients were found to have an effect on PAH extraction efficiency, and the extremely low significance of the cross-product terms suggests no interaction between variables is likely. The final second-order polynomial in terms of actual values was calculated using the software (Design Expert) and is shown below:

$$\text{total PAH} = -1239.1 + 4.0015P + 12.764T + 12.330t + 65.658(\text{MeOH}) - 0.0089P^2 - 0.0802T^2 - 0.1438t^2 - 2.269(\text{MeOH})^2 - 0.0022PT - 0.0046Pt + 0.0229P(\text{MeOH}) + 0.0028Tt - 0.0138T(\text{MeOH}) + 0.0654t(\text{MeOH})$$

where *P* represents pressure, *T* is temperature, *t* is extraction time, and (MeOH) is methanol content.

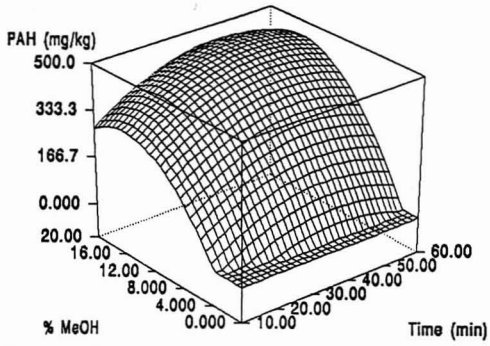

Figure 2. Response surface for PAH recovery from contaminated land samples showing the effect of percent methanol modifier and extraction time on the extraction efficiency at 200 kg cm^{-2} and 70 °C.

The effect of the two significant variables (extraction time and percent modifier) on the overall PAH recovery is illustrated with a response surface (Figure 2). Obviously, only two independent variables can be visualized using a 3-D response surface, with the third axis as the dependent response. The other two variables (pressure and temperature) were kept constant at their midpoint values. The surface graphically shows that percent modifier has, by far, the greatest influence on PAH recovery.

An analysis of the residuals (actual values versus those predicted by the model) was performed to reveal any problems with the ANOVA model. The analysis included a normal probability plot (normal probability vs Studentized residuals), a plot of Student residuals vs the predicted response, and two other residual plots designed to check for any systematic errors in the experiment. In all cases, the diagnostic plots indicated that the chosen quadratic model fits the data correctly.

Optimum Conditions for PAH Recovery by SFE. The results from the central composite design were then used to predict the SFE operating conditions which would result in the most efficient extraction of PAHs from the contaminated sample. The final model indicated that both the pressure and the temperature used in the extraction had no statistical significance on PAH recovery. Consequently, both of these parameters were kept at their midpoint values (200 kg cm^{-2} and 70 °C, respectively) for extraction under optimum conditions. The remaining two variables (extraction time and percent methanol modifier) were operated at their maximum values since the model predicted that both had a direct influence on the total PAH recovery. The final optimum extraction conditions chosen were pressure, 200

Table 5. Repeatability Study (Contaminated Land Sample) Using the Central Composite Design Optimum Conditions[a]

compound	1	2	3	4	5	6	7	average	SD	RSD (%)
naphthalene	10.8	11.0	10.8	9.9	9.8	11.3	10.2	10.5	0.58	5.5
acenaphthylene	3.5	3.5	3.7	3.8	3.5	4.2	3.3	3.6	0.29	8.1
acenaphthalene	15.4	17.1	17.9	16.1	16.2	17.2	16.2	16.6	0.85	5.1
fluorene	12.5	14.5	15.7	14.3	14.0	15.7	13.3	14.3	1.18	8.2
phenanthrene	83.9	91.4	96.3	83.8	86.3	91.2	83.8	88.1	4.93	5.6
anthracene	30.5	35.4	35.8	30.8	31.0	35.1	30.2	32.7	2.59	7.9
fluoranthene	78.7	84.5	87.5	75.6	81.2	75.3	77.9	80.1	4.57	5.7
pyrene	58.6	62.8	64.5	59.6	60.7	61.9	63.6	61.7	2.15	3.5
benz[*a*]anthracene	27.3	28.5	29.3	27.7	27.7	28.1	26.7	27.9	0.84	3.0
chrysene	28.3	29.1	29.8	28.9	28.6	29.4	27.7	28.8	0.70	2.4
benzo[*b*]fluoranthene	27.4	18.0	13.6	18.4	18.9	20.3	22.6	19.9	4.29	2.2
benzo[*k*]fluoranthene	19.6	12.9	17.1	13.2	13.6	14.5	16.2	15.3	2.46	16.1
benzo[*a*]pyrene	24.4	26.3	25.7	25.2	25.7	24.6	23.7	25.1	0.90	3.6
indeno[1,2,3-*cd*]pyrene	16.6	18.4	17.7	17.5	18.6	16.9	16.2	17.4	0.90	5.2
dibenz[*a,h*]anthracene	1.8	2.0	2.7	3.9	3.1	2.9	1.8	2.6	0.78	30.1
benz[*ghi*]perylene	12.6	13.9	13.6	13.3	14.3	13.1	12.5	13.3	0.66	5.0
total	452.0	469.4	481.9	441.9	453.2	461.8	446.1	458.0	14.0	3.1

[a] Pressure, 200 kg cm^{-2}; temperature, 70 °C; time, 5 min static, 60 min dynamic; MeOH content, 20%; flow rate, 1 mL min^{-1}.

Table 6. Recoveries (mg kg^{-1}) of Individual PAHs Using Microwave-Assisted Extraction with 100% Acetone and Soxhlet Extraction with Methylene Chloride[14]

compound	microwave-assisted extraction ($n = 6$)[a]	RSD (%)	Soxhlet extraction ($n = 5$)[b]	RSD (%)
naphthalene	12.0	5.4	4.2	22.4
acenaphthylene	3.7	0.0	2.6	19.5
acenaphthene	14.5	4.2	6.4	20.1
fluorene	13.4	3.8	8.6	15.9
phenanthrene	74.8	2.8	53.4	11.2
anthracene	24.2	2.9	13.6	8.2
fluoranthene	73.7	2.5	54.1	6.1
pyrene	56.8	2.5	43.0	7.1
benz[*a*]anthracene	26.3	3.3	25.3	7.6
chrysene	27.3	2.5	26.6	4.9
benzo[*b*]fluoranthene	19.8	5.3	15.1	19.2
benzo[*k*]fluoranthene	18.3	5.7	11.0	12.0
benzo[*a*]pyrene	24.2	3.8	15.3	16.6
indeno[1,2,3-*cd*]pyrene	15.3	4.0	7.2	27.4
dibenz[*a,h*]anthracene	3.7	0.0	3.4	58.3
benzo[*ghi*]perylene	14.9	4.7	7.6	23.0
total	422.9	2.4	297.4	10.0

[a] Extracted at 120 °C for 20 min. [b] Extracted for 6 h.

kg cm^{-2}; temperature, 70 °C, extraction time, 60 min; and methanol content, 20%. These conditions were used in a repeatability study to assess the effectiveness of the model's prediction. The results of the study, shown in Table 5, show an overall average recovery of 458.0 mg kg^{-1} (RSD 3.1%). This recovery is very similar to the maximum obtained during the design experiments (run 24 in Table 2), indicating the correct choice of operating conditions. Sequential repeat extractions were also carried out on the samples from the first three experiments in the repeatability study to investigate whether the initial extractions were exhaustive. If possible, in sequentially extracting samples, it is important to increase the strength of the second extraction to test the efficiency of the first. Unfortunately, it was not possible to increase the percent methanol added to the sample because of the detrimental effect the polar solvent has on the gas chromatograph with nonpolar columns. It would also not be practical to increase the time of extraction if still desiring a high sample throughput. The sequential extractions were therefore performed under identical operating conditions as the first. GC/MS analysis failed to detect PAHs present in any of the second extracts, which indicates that the first extraction is exhaustive, in terms of SFE, under the optimized operating conditions.

The results of the optimized SFE extraction were compared with those from a 6 h methylene chloride Soxhlet extraction and a 20 min microwave-assisted extraction using acetone performed on the contaminated sample in a previous study.[14] The average total concentration of PAHs extracted by Soxhlet extraction was 297.4 mg kg^{-1}, with an RSD of 10.0% ($n = 5$), and that by microwave-assisted extraction was 422.9 mg kg^{-1}, with an RSD of 2.4% ($n = 6$). The results for the individual PAHs are shown in Table 6. The lower recoveries for the individual PAHs by Soxhlet extraction are probably indicative of (a) the choice of solvent and (b) the nature of the native soil.

Extraction and Analysis of the CONTEST Soil Sample. An interlaboratory test sample, containing a concentration of PAHs similar to that of the previous native sample, was also extracted using the optimized SFE conditions. The soil was extracted under conditions identical to those already used. However, during the dynamic extraction period, the CO_2 pump periodically reached its maximum pressure with the back-pressure regulator reading

Table 7. Repeatability Study (CONTEST Soil Sample) Using the Central Composite Design Optimum Conditions[a]

compound	1	2	3	4	average	SD	RSD (%)
naphthalene	3.6	1.0	2.7	1.0	2.1	1.29	62.4
acenaphthylene	0.6	0.7	0.5	0.6	0.6	0.08	13.6
acenaphthene	0.3	0.9	0.7	0.6	0.6	0.25	40.0
fluorene	0.2	0.3	0.2	0.2	0.2	0.05	22.2
phenanthrene	74.6	70.0	45.4	64.5	63.6	12.83	20.2
anthracene	70.3	69.9	53.8	75.2	67.3	9.32	13.8
fluoranthene	49.0	49.3	39.4	53.1	47.7	5.84	12.2
pyrene	31.8	31.3	26.0	34.6	30.9	3.59	11.6
benz[*a*]anthracene	8.8	7.8	6.1	8.7	7.9	1.25	15.9
chrysene	13.9	14.4	12.0	15.0	13.8	1.30	9.4
benzo[*b*]fluoranthene	14.5	6.4	4.7	9.1	8.7	4.29	49.4
benzo[*k*]fluoranthene	10.4	12.6	10.0	11.4	11.1	1.16	10.5
benzo[*a*]pyrene	2.1	1.7	1.3	8.4	3.4	3.37	99.7
indeno[1,2,3-*cd*]pyrene	9.1	20.1	14.6	20.1	16.0	5.27	33.0
dibenz[*a*,*h*]anthracene	1.7	1.0	1.1	0.9	1.2	0.36	30.6
benzo[*ghi*]perylene	6.6	6.3	4.2	6.2	5.8	1.10	18.8
total	297.4	293.7	222.7	309.6	280.9	39.4	14.0

[a] Pressure, 200 kg cm^{-2}; temperature, 70 °C; time, 5 min static, 60 min dynamic; MeOH content, 20%; flow rate, 1 mL min^{-1}.

as normal. This indicated some blockage in the system by coextractives. Each time this occurred, the blockage was cleared by flushing the entire system with solvent, and a new extraction was performed. Upon analysis by GC/MS in total ion mode, large amounts of elemental sulfur were found in the chromatogram, in much higher concentrations than the extracted PAHs, which may account for the system blockage. Problems with elemental sulfur are well known, and samples containing percent levels of sulfur have been successfully extracted by SFE by using copper as a scavenger to remove the sulfur before it is allowed to cause blockages or interfere with chromatographic detection.[23,24] The results of the repeatability study (Table 7), obtained when the SFE instrument did not block, show quite widely varying total PAH concentrations with associated high RSD values. This compares poorly with results from Soxhlet and microwave-assisted extractions performed previously[14] (Soxhlet extraction 242.7 mg kg^{-1} (RSD 1.0%, $n = 3$); microwave-assisted extraction, 241.7 mg kg^{-1}, with individual recoveries of 242.2 and 241.1 mg kg^{-1} using acetone, and 247.5 mg kg^{-1}, with individual recoveries of 249.5 and 245.5 mg kg^{-1} using dichloromethane).

CONCLUSIONS

An experimental design approach has been used to successfully optimized the SFE operating parameters for the extraction of PAHs from a native contaminated land sample. A statistical analysis using the resultant data indicated that only methanol modifier content and extraction time have a significant effect on extraction. It should be noted that the significance of each of the parameters may alter with changes in the sample matrix, and therefore any optimum operating conditions may require re-examination if different matrices are to be efficiently extracted. Repeatability studies using the optimum conditions have shown SFE, using CO_2 and methanol modifier, to be a rapid extraction technique capable of extracting greater total amounts of PAHs, with better precision than the conventional Soxhlet. The extraction of an interlaboratory test soil has proved difficult because of the presence of elemental sulfur in the sample, which caused SFE instrument blockages. The problem may be overcome in further work with the use of copper as a sulfur scavenger.

ACKNOWLEDGMENT

We gratefully acknowledge the financial support of Analytical and Environmental Services Ltd., Northumbria Water Group plc.

Received for review February 9, 1995. Accepted April 12, 1995.[⊗]

AC950144+

(23) Pyle, S. M.; Setty, M. M. *Talanta* **1991**, *38*, 1125.
(24) Bowadt, S.; Johansson, B. *Anal. Chem.* **1994**, *66*, 667.

[⊗] Abstract published in *Advance ACS Abstracts,* June 1, 1995.

Anal. Chem. **1995**, *67*, 2070–2077

Separation of Hydrophobic, Positively Chargeable Substances by Capillary Electrophoresis

Chao-Xuan Zhang, Franz von Heeren, and Wolfgang Thormann*

Department of Clinical Pharmacology, University of Bern, Murtenstrasse 35, CH-3010 Bern, Switzerland

The electrokinetic separation behavior of positively chargeable substances with various hydrophobicities over the pH range 2–11 is described, using plain aqueous buffers, binary media with organic solvents, and systems with surfactants at concentrations between 0.0005 and 75 mM or other buffer additives. Examples studied include dextromethorphan, methadone, ketoconazole, itraconazole, amiodarone, and desethylamiodarone, compounds that play an important role in pharmacotherapy. Electrokinetic chromatography systems comprising dynamically formed micelles or ionic buffer additives that can form ion pairs with the solutes are shown to be unsuitable for the separation of highly hydrophobic, positively chargeable compounds, including the latter three drugs investigated. However, capillary zone electrophoresis (CZE) in binary systems with organic solvents (40–80%, v/v) at a buffer pH near or lower the solute's pK_a values or CZE at low pH in the presence of an electrically neutral complexing agent, such as β-cyclodextrin, can be employed effectively. Data presented illustrate that pK_a values in binary systems with organic solvents that are more basic than water are smaller than those in aqueous media. Furthermore, somewhat less hydrophobic and positively chargeable compounds can be sufficiently dissolved in aqueous buffer at pH < pK_a and can therefore be analyzed by CZE without any buffer additives.

Capillary electrophoresis (CE) has been shown to be a powerful analytical tool for a wide range of samples, including many applications to the analysis of drugs.[1,2] The electrokinetic separation behavior of hydrophobic drugs is not yet fully understood. Using micellar electrokinetic chromatography (MEKC), many hydrophobic compounds have been shown to be totally incorporated into the micelles and thus cannot be separated. To reduce the large values of the capacity factors, urea[3–5] and cyclodextrin[4,5] have been added to the micellar solutions, as well as bile salts[6] of weaker solvation capability compared to dodecyl sulfate, have been employed. The addition of organic solvents has also been shown to reduce the capacity factor of a solute,[7–9] and the separation of hydrophobic polyaromatic hydrocarbons by MEKC with 30–50% (v/v) organic solvents has been described.[10] With ionic buffer additives, such as tetraalkylammonium ions[11–13] or surfactants[14] to buffers containing typically 50% (v/v) of an organic solvent, single molecules are acting as carriers and separation is based upon differences in the interaction of neutral solutes with the ionic carriers. This technique can be called ionic electrokinetic chromatography, another mode of electrokinetic chromatography.[15] With these techniques, nice separations for selected classes of molecules have been achieved. As of today, however, no general rules for the selection of CE separation conditions have been elucidated. Thus, failures in attempted separations are mostly based upon inadequate use of a running buffer.[16]

Thus far, CE investigations dealing with hydrophobic substances have mostly been focused on electrically neutral solutes. The work described here is concerned with the electrokinetic separation behavior of positively chargeable, highly hydrophobic drugs, including itraconazole, amiodarone, and desethylamiodarone (Figure 1). Moderately hydrophobic drugs (ketoconazole, methadone, dextromethorphan), as well as three hydrophilic compounds (theophylline, caffeine, naproxen), have also been investigated. These compounds represent pharmaceuticals that are widely applied for pharmacotherapy, and with the exception of naproxen, they have nitrogen in their chemical structures (Figure 1) and are therefore positively chargeable. Although CE methods for the determinations of methadone,[17] dextromethorphan,[18] theophylline,[19,20] and naproxen[20,21] were previously developed for clinical purposes, these compounds have been included to provide better insight into selection of separation conditions.

(1) Guzman, N. A., Ed. *Capillary Electrophoresis Technology;* Marcel Dekker: New York, 1993.
(2) Thormann, W.; Molteni, S.; Caslavska, J.; Schmutz, A. *Electrophoresis* **1994**, *15*, 3–12.
(3) Terabe, S.; Ishihama, Y.; Nishi, H.; Fukuyama, T.; Otsuka, K. *J. Chromatogr.* **1991**, *545*, 359–168.
(4) Terabe, S.; Miyashita, Y.; Ishihama, Y.; Shibata, O. *J. Chromatogr.* **1993**, *636*, 47–55.
(5) Terabe, S.; Miyashita, Y.; Shibata, O.; Barnhart, E. R.; Alexander, L. R.; Patterson, D. G.; Karger, B. L.; Hosoya, K.; Tanaka, N. *J. Chromatogr.* **1990**, *516*, 23–31.
(6) Nishi, H.; Fukuyama, T.; Matsuo, M.; Terabe, S. *J. Chromatogr.* **1990**, *513*, 279–295.
(7) Balchunas, A. T.; Sepaniak, M. J. *Anal. Chem.* **1988**, *60*, 617–621.
(8) Thormann, W.; Lienhard, S.; Wernly, P. *J. Chromatogr.* **1993**, *636*, 137–148.
(9) Kaneta, T.; Yamashita, T.; Imasaka, T. *Electrophoresis* **1994**, *15*, 1276–1279.
(10) Otsuka, K.; Higashimori, M.; Koike, R.; Karuhaka, K.; Okada, Y.; Terabe, S. *Electrophoresis* **1994**, *15*, 1280–1283.
(11) Walbroehl, Y.; Jorgenson, J. W. *J. Chromatogr.* **1984**, *315*, 135–143.
(12) Walbroehl, Y.; Jorgenson, J. W. *Anal. Chem.* **1986**, *58*, 479–481.
(13) Shi, Y.; Fritz, J. S. *J. High Resolut. Chromatogr.* **1994**, *17*, 1–6.
(14) Ahuja, E. S.; Foley, J. P. *J. Chromatogr.* **1994**, *680*, 73–83.
(15) Terabe, S. In *Capillary Electrophoresis Technology*; Guzman, N. A., Ed.; Marcel Dekker: New York, 1993; pp 66–88.
(16) Brumley, W. C.; Jones, W. J. *J. Chromatogr.* **1994**, *680*, 163–173.
(17) Molteni, S.; Caslavska, J.; Allemann, D.; Thormann, W. *J. Chromatogr.* **1994**, *658*, 355–367.
(18) Caslavska, J.; Hufschmid, E.; Theurillat, R.; Desiderio, C.; Wolfisberg, H.; Thormann, W. *J. Chromatogr.* **1994**, *656*, 219–231.
(19) Thormann, W.; Minger, A.; Molteni, S.; Caslavska, J.; Gebauer, P. *J. Chromatogr.* **1992**, *593*, 275–288.
(20) Zhang, C.-X.; Thormann, W. *J. Capillary Electrophoresis* **1994**, *1*, 208–218.
(21) Schmutz, A.; Thormann, W. *Electrophoresis* **1994**, *15*, 1295–1303.

0003-2700/95/0367-2070$9.00/0 © 1995 American Chemical Society

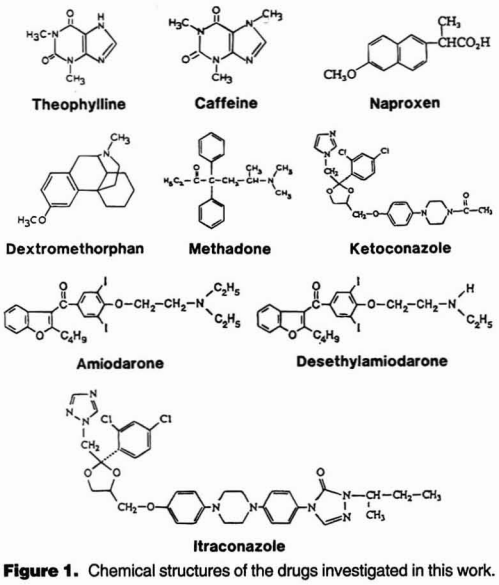

Figure 1. Chemical structures of the drugs investigated in this work.

EXPERIMENTAL SECTION

Chemicals and Drugs. All chemicals were of analytical reagent grade and the organic solvents methanol, ethanol, 1-propanol, 2-propanol, acetonitrile, and tetrahydrofuran (THF) were of HPLC grade. Sodium dodecyl sulfate (SDS) was purchased from Bioprobe System (Montreuil-Sous-Bois, France), β-cyclodextrin (β-CD) from Fluka (Buchs, Switzerland), sodium taurocholate (STC) from Calbiochem (La Jolla, CA), sodium deoxycholate from Merck (Darmstadt, Germany), cetyltrimethylammonium bromide (CTAB) from Sigma (St. Louis, MO), and urea from Aristar (BDH Limited, Poole, Great Britain). Itraconazole and ketoconazole were obtained from Janssen Research Foundation (Beerse, Belgium), and naproxen from Grünenthal (Mitlödi, Switzerland). Theophylline, caffeine, and methadone hydrochloride were of European Pharmacopoeia quality and were supplied by the university hospital pharmacy (Bern, Switzerland). Dextromethorphan hydrobromide was a kind gift of F. Hoffmann-La Roche (Basel, Switzerland). Amiodarone hydrochloride and desethylamiodarone hydrochloride were received from Sanofi (Basel, Switzerland).

Preparation of Sample Solutions and Running Buffers. Stock solutions of drugs were prepared in different solvents, namely, in THF for itraconazole (0.49 mg/mL); in methanol for amiodarone hydrochloride (0.61 mg/mL), desethylamiodarone hydrochloride (0.79 mg/mL), and naproxen (1.37 mg/mL); in 0.04 M phosphate buffer (pH 2.2) for ketoconazole (0.96 mg/mL); or in water for methadone hydrochloride (1.22 mg/mL), dextromethorphan hydrobromide (1.86 mg/mL), theophylline (0.76 mg/mL), caffeine (0.75 mg/mL), and phenol (4.68 mg/mL). The sample solutions were prepared by adding appropriate aliquots of the stock solutions to methanol, resulting in solute concentrations of 30–130 μg/mL. The phosphate running buffer was prepared by adding appropriate aliquots of 0.2 M H_3PO_4, 0.2 M NaH_2PO_4, 0.2 M Na_2HPO_4, and 0.1 M NaOH stock solutions into water or into mixtures of water and organic solvents. Additives such as surfactants, cyclodextrin, or urea were directly dissolved in the running phosphate buffers. The pH of buffers without organic solvents was determined by a Ross combination pH electrode (Orion, Boston, MA). For the binary systems, the pH value given refers to that of an aqueous buffer with the same phosphate composition.

Capillary Electrophoresis. CE was carried out in two instruments. The experiments with organic solvents were performed on a BioFocus 3000 capillary electrophoresis system (Bio-Rad Labs, Hercules, CA) and all other experiments on a Prince apparatus (Lauerlabs, Emmen, The Netherlands). In both instruments, a constant voltage of 20 (anode on sampling end) or −20 kV (cathode on sampling side) was applied, and absorbance detection toward the capillary end was effected at 220 nm. In the Prince instrument, a fused-silica capillary (Polymicro Technologies, Phoenix, AZ) of 50 μm i.d. and 44.5 cm (55.5 cm) effective (total) length was employed. The temperature of the capillary was kept at 35 °C. Capillary conditioning was effected by rinsing with running buffer for 5 min using a positive pressure of 3000 mbar. Sample injection was carried out by applying a positive pressure of 20 mbar for 0.1 min. The signal from the UV absorbance detector was recorded by a Model D-2000 chromatointegrator (Merck-Hitachi, Darmstadt, Germany). For the experiments with the BioFocus 3000, the capillary (Polymicro Technologies) was of 50 μm i.d. and 35.4 cm (40.0 cm) effective (total) length. The temperatures of capillary and sample carousel were kept at 20 °C. Sample injection occurred by a positive pressure at 5 psi (4 psi·s). Capillary conditioning between runs was effected by rinsing with 0.1 M NaOH (1 min) and running buffer (2 min) applying positive pressure of ~100 psi. The electropherograms were evaluated using the BioFocus 3000 postrun software version 3.10 (Bio-Rad).

RESULTS AND DISCUSSION

Capillary Zone Electrophoresis in Aqueous Solution. All drugs investigated have one or several nitrogen-containing groups or a carboxylic function (naproxen) in their chemical structures (Figure 1). Thus, depending on pH, these compounds can be charged, and thereby possibly separated on the basis of differences in electrophoretic mobilities. The electrophoretic behavior of all nine drugs was studied in the pH range 2–9, the pH dependence of the determined electrophoretic mobilities being shown in Figure 2. The effective electrophoretic mobility (for definition refer to ref 22) was calculated using the solvent peak as a marker of the electroosmotic flow.[23,24] A positive (negative) electrophoretic mobility means that the solute has a positive (negative) charge and migrates electrophoretically toward the cathode (anode).

The electrophoretic behavior observed is closely related to the durgs' structures (Figure 1). At pH >6.8 theophylline (**8**) was found to have a negative charge, which can be ascribed to the dissociation of hydrogen in the imidazole ring. Caffeine (**7**) does not have such a proton and therefore no negative mobility was observed for this substance. The sharp change in theophylline mobility between pH 7 and 9 is in agreement with the reported

(22) Karger, B. L.; Foret, F. In *Capillary Electrophoresis Technology*; Guzman, N. A., Ed.; Marcel Dekker: New York, 1993; pp 3–64.
(23) Quang, C.; Strasters, J. K.; Khaledi, M. G. *Anal. Chem.* **1994**, *66*, 1646–1653.
(24) Copper, C. L.; Sepaniak, M. J. *Anal. Chem.* **1994**, *66*, 147–154.

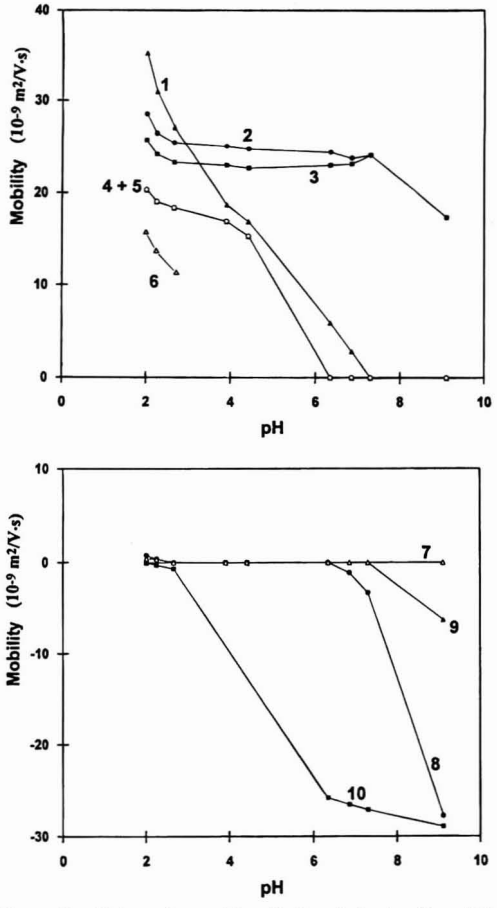

Figure 2. pH dependence of the effective electrophoretic mobility in 0.04 M aqueous phosphate buffer. The data were obtained with the Prince instrument. The applied voltage was a constant 20 kV, and depending on pH, the currents were between 26 and 72 μA. Other conditions are given in the Experimental Section. Key: **1**, ketoconazole; **2**, dextromethorphan; **3**, methadone; **4**, desethylamiodarone; **5**, amiodarone; **6**, itraconazole; **7**, caffeine; **8**, theophylline; **9**, phenol; **10**, naproxen.

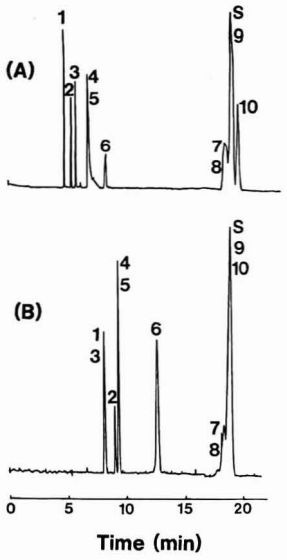

Figure 3. Typical electropherograms obtained with the Prince instrument. The running buffers were (A) 0.04 M phosphate solution (pH 2.2) and (B) the same as in (A) and containing 20 mM β-CD. The applied voltage was 20 kV, and the current was ~30 μA. Other conditions as in the Experimental Section. The symbol "s" indicates the solvent peak. The key is given in Figure 2.

pK_a value of 8.8[25] and with the pH-dependent elution in MEKC with SDS.[26] The pK_a for the cationic acid is 2.5,[25] explaining the fact that small positive mobilities were observed for both theophylline and caffeine at pH <2.2. Naproxen (**10** in Figure 2) has a pK_a of 4.8.[21] Therefore, a drastic change in mobility is expected to occur between pH 4 and 6. However, naproxen was not detected at pH 4.4 and 3.9, because in this range the electroosmotic mobility was reduced to such an extent that it could not compensate for its electrophoretic migration in the opposite direction. In fact naproxen was detected at pH 4.4 when a negative voltage was applied. With decreasing degree of dissociation, however, naproxen was monitored at buffer pH values of <2.6.

Phenol (**9**) always coeluted with solvent unless buffer pH was >7.3, thus it could easily be used as the marker of electroosmotic flow at low pH.[27] According to the literature, the saturated aliphatic amine pK_a values are between 10 and 11,[28] and such molecules are therefore positively charged when pH is <10. As shown in Figure 2, dextromethorphan (**2**) and methadone (**3**) mobilities were found to remain almost unchanged when pH was <7.3. The slight increase in mobility observed at pH <2.6 can be attributed to a decrease in ionic strength associated with a decrease in pH, because the total phosphate concentration was kept identical in all experiments. This is in agreement with theory, which predicts an electrophoretic mobility decrease with increasing ionic strength.[29] The increase of the mobility of ketoconazole (**1**) associated with decreasing pH suggests that this substance is gradually charged.

According to the chemical structures (Figure 1), it is expected that itraconazole, amiodarone, and desethylamiodarone can also be positively charged in the examined pH range. Due to the high hydrophobicity, however, itraconazole (**6** of Figure 2) could be detected only at pH <2.6. Desethylamiodarone and amiodarone (**4** and **5**, respectively) appeared as broad and tailing peaks at a buffer pH of <4.4. A typical electropherogram obtained at pH 2.2 is presented in Figure 3A. It is assumed that the hydrophobic substances cannot dissolve well in the separation medium and therefore tend to adsorb onto the capillary wall. With addition of

(25) Budavari, S., O'Neil, M. J., Smith, A., Heckelman, P. E., Eds. *The Merck Index*, 11th ed.; Merck & Co.: Rahway, NJ, 1989.
(26) Dang, Q.-X.; Yan, L.-X.; Sun, Z.-P.; Ling, D.-K. *J. Chromatogr.* **1993**, *630*, 363–369.
(27) Zhang, C.-X.; Sun, Z.-P.; Ling, D.-K.; Zhang, Y.-J. *J. Chromatogr.* **1992**, *627*, 281–286.
(28) Weast, R. C., Astle, M. J., Beyer, W. H., Eds. *CRC Handbook of Chemistry and Physics*, 67th ed.; CRC Press: Boca Raton, FL, 1986.
(29) Grossman, P. D. In *Capillary Electrophoresis: Theory and Practice;* Grossman, P. D., Colburn, J. C., Eds.; Academic Press: San Diego, CA, 1992; pp 111–132.

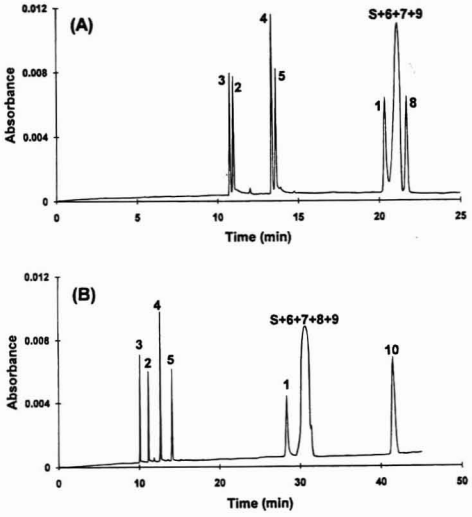

Figure 4. Typical electropherograms obtained in the binary systems. The running buffers were (A) a mixture of water with 1-propanol (40% v/v) containing 0.1 M phosphate (pH 6.3) and (B) the binary system with 60% (v/v) THF containing 0.04 M phosphate (pH 5.2). The experiments were performed with the Bio-Rad instrument. Applied voltage, 20 kV. Current, (A) 29 and (B) 7 μA. Other conditions as for Figure 3.

20 mM β-CD to the phosphate buffer (pH 2.2), sharp peaks were observed for all solutes (Figure 3B). The hydrophobic substances, not unlike other solutes, can be incorporated into the cavity of β-CD, thus enhancing solvation and preventing adsorption onto the capillary wall. Comparison of parts A and B of Figure 3 reveals that β-CD is reducing the mobility of both cations and anions (naproxen). Complexation with β-CD increases the solutes' sizes without altering their charge, thus reducing electrophoretic migration. Furthermore, β-CD has little effect on the electroosmotic flow. It is worth noting that with addition of β-CD the elution order of methadone and dextromethorphan changed, indicating that the latter drug is more easily entering the cavity of β-CD. At pH <5, amiodarone and desethylamiodarone could not be separated. In this pH range, the two compounds are completely ionized (see below) and the difference in chemical structure appears to insufficiently impact the electrophoretic mobilities. However, the tertiary and secondary amines should be characterized by different pK_a values. Thus, the two compounds might separate at a pH that is close to their pK_a's, i.e., in an environment within which differences of electrophoretic mobilities are expected to be largest. Unfortunately, at pH >5 amiodarone and desethylamiodarone became too hydrophobic so that small and tailing peaks or no peaks at all were observed. The same was the case with the addition of 20 mM β-CD. Working with a 0.02 M phosphate buffer at pH 11.2, ketoconazole, methadone, and dextromethorphan (all uncharged molecules at that pH) were found to coelute with the solvent (data not shown). At this pH, itraconazole, amiodarone, and desethylamiodarone must be uncharged as well, but could not be detected. Insufficient solubility of these compounds is assumed to be the reason for that (see below).

Capillary Zone Electrophoresis in Binary Systems with Organic Solvents. In order to explore the electrophoretic behavior of the hydrophobic drugs at pH values that were not accessible in aqueous solution, the use of organic solvents was taken into account. Typical electropherograms obtained in binary systems with 1-propanol (40% v/v, pH 6.3) and THF (60% v/v, pH 5.2) are presented in parts A and B of Figure 4, respectively. Addition of large amounts of the organic solvents provided sharp peaks for both amiodarone and desethylamiodarone, and the two substances could easily be separated. The separation behavior for other solutes was also profoundly modified. Caffeine and itraconazole comigrated with solvent because they were electroneutral at the investigated pH values. Using 1-propanol and a pH of 6.3, effects of the organic fraction and ionic strength are presented in Figure 5. The data presented in Figure 5A reveal that the mobilities of the cations gradually decrease with increasing volume fraction of 1-propanol. According to the theory described in ref 29, this behavior is mainly attributed to the concomitant increase in viscosity. Similar data were obtained in regard to the absolute mobility values for the anions naproxen and theophylline (data not shown). It should be noted that when

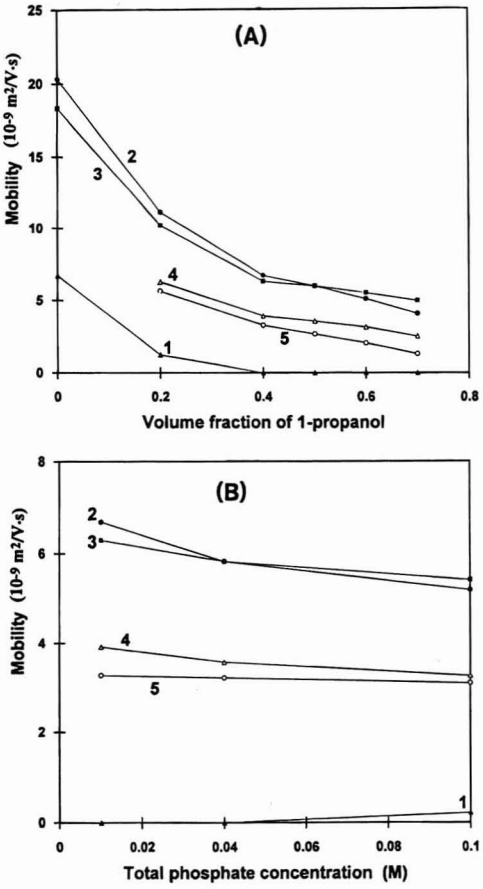

Figure 5. Dependence of the effective electrophoretic mobility on (A) the volume fraction of 1-propanol in the binary systems containing 0.01 M phosphate (pH 6.3) and (B) the phosphate concentration in the mixtures with 40% (v/v) 1-propanol and pH 6.3. Other conditions as for Figure 4.

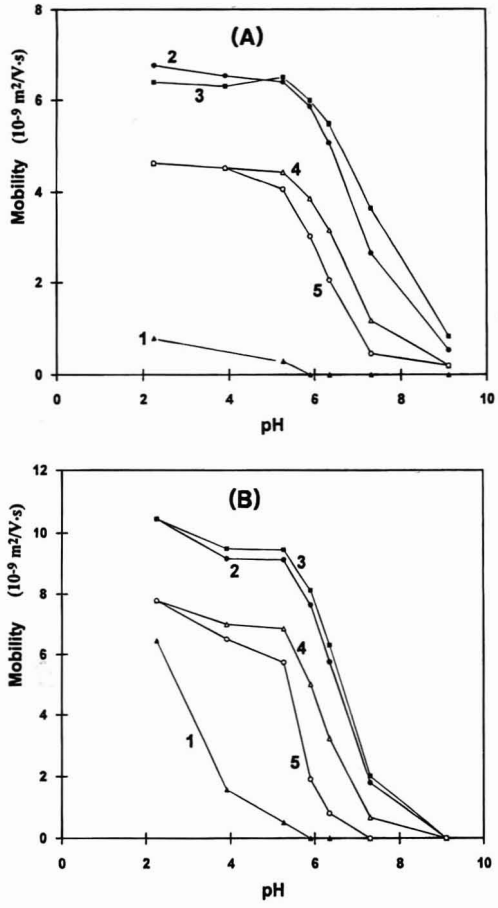

Figure 6. pH dependence of the effective electrophoretic mobility in binary systems with 0.01 M phosphate containing (A) 60% (v/v) 1-propanol and (B) 60% (v/v) THF. Other conditions as for Figure 4.

the volume fraction of 1-propanol was below 0.2, itraconazole, amiodarone, and desethylamiodarone showed broad and tailing peaks or no peak at all. The content of organic solvents required for sufficient dissolution of the hydrophobic drugs was determined to be >30% (v/v). Pure organic solvents were not employed, because traces of water were reported to significantly affect their properties.[30] With increasing amounts of 1-propanol, the selectivity for amiodarone and desethylamiodarone improved and the detection order of methadone and dextromethorphan became reversed, an effect attributed to a change in pK_a values (see below). Surprisingly, detection order could also be changed through an increase in ionic strength (Figure 5B). Generally, with an increase in phosphate concentration a small decrease of the mobilities was noted, this being qualitatively in agreement with theory.[29] Thus far no explanation could be found for the small electrophoretic mobility of ketoconazole (**1** in Figure 5B) observed at a high phosphate concentration.

In addition to the volume fraction and ionic strength, the most important factor in CE with binary systems remains the buffer pH. It is inadequate to determine the pH values of binary mixtures of water with organic solvents using a glass electrode standardized with aqueous buffer systems.[31] For convenience, the pH value in a binary system given here is equal to the value of an aqueous buffer having the same phosphate composition. Data on the pH dependency of the electrophoretic mobility in binary systems with 60% (v/v) 1-propanol and 60% THF are presented in parts A and B of Figure 6, respectively. Due to complete ionization at pH <5, the mobilities of amiodarone, desethylamiodarone, methadone, and dextromethorphan were found to be almost independent of pH. In the pH interval 6–8, which essentially includes the pK_a values, mobilities were determined to decrease rapidly as pH was increased to ~8. As was observed at low pH in purely aqueous buffer, amiodarone and desethylamiodarone in their fully ionized form were found to be inseparable. At intermediate pH (6–7) where these compounds are partly ionized, however, full separation was obtained. Itraconazole coeluted with the solvent in the two binary systems and over the whole pH range, except with THF at pH 2.2 where it showed a small positive electrophoretic mobilty (1×10^{-10} m²/V·s), which suggested that its pK_a value was greatly reduced (data not shown). Comparison of the data presented in Figure 6 with those of Figure 2 also suggests that the pK_a values of the cationic acids are smaller in the binary systems. The pK_a value can be simply estimated by the mobility data measured at two pH values at which the compound is partly ionized.[32] Furthermore, because of the small effect of ionic strength on mobility (Figure 5B), the variation of ionic strength due to the pH change was neglected. The calculated pK_a values of the drugs and the pH intervals used are listed in Table 1. Few pK_a data of these drugs in aqueous solutions are available in the literature, nor could any values be found for the binary systems. By comparing the literature pK_a values of naproxen (4.8 [21]) and theophylline (8.77 [25]) in water with our values of 5.0 and 8.3, respectively, an error range of ±0.5 pH unit can be expected with this kind of pK_a determination. Thus, the values listed in Table 1 can only be employed for a qualitative discussion.

Table 1. Estimated pK_a Values in Different Media[a]

compound		solvent: water	water–1-propanol (4:6 v/v)	water–tetrahydrofuran (4:6 v/v)
methadone	pK_a	9.5	7.5	6.8
	pH	7.3–9.1	6.3–7.3	6.3–7.3
dextromethorphan	pK_a	9.5	7.2	6.8
	pH	7.3–9.1	6.3–7.3	6.3–7.3
desethylamiodarone	pK_a		6.8	6.3
	pH		5.9–6.3	5.9–6.3
amiodarone	pK_a		6.4	5.4
	pH		5.9–6.3	5.9–6.3
ketoconazole	pK_a	6.4	5.0	4.9
	pH	6.3–6.8	2.2–5.2	3.9–5.2
theophylline	pK_a	8.3	7.4	7.5
	pH	7.3–9.1	6.3–7.3	6.3–7.3
naproxen	pK_a	5.0		4.0
	pH	6.3–6.8		5.2–3.9

[a] pH refers to the two pH values with which the mobility data used for the pK_a calculation were determined. The data for water and the binary systems were obtained with the Prince and the BioFocus 3000, respectively.

(30) Kenndler, E.; Jenner, P. *J. Chromatogr.* **1987**, *390*, 169–183.

(31) Kenndler, E. In *Capillary Electrophoresis Technology*; Guzman, N. A., Ed.; Marcel Dekker: New York, 1993; pp 161–186.

(32) Jacquier, J. C.; Rony, C.; Desbene, P. L. *J. Chromatogr.* **1993**, *652*, 337–345.

Ketoconazole has two amine functions, and the pK_a in Table 1 should be regarded as pK_{a_2}. Both amine functions are directly connected to electron-attracting phenyl and acetyl groups (Figure 1). Thus, the ability to attract a proton is weakened and its pK_a is smaller than that of methadone and dextromethorphan. The pK_a values of amiodarone and desethylamiodarone could not be determined by CE in aqueous solution. Having their values in binary systems (Table 1), however, permits an estimation for aqueous buffers. The pK_a values of amiodarone and desethylamiodarone are expected to be between those of methadone/dextromethorphan and ketoconazole. Furthermore, the presence of an electron-attracting phenolic group in the β position of the amine function, as well as the literature value of 6.56,[33] supports this assumption. According to its chemical structure, itraconazole is expected to have a smaller pK_a than ketoconazole, which explains the difficulty in protonation of that compound (see above). This is in agreement with the pK_a value of 3.7 given in the literature.[34] The pK_a data in aqueous buffer and binary systems were determined on different instruments and thereby at different temperatures (35 and 20 °C, respectively). This difference does not prevent a discussion about the effect of the buffer medium on pK_a, because the impact of temperature on pK_a is typically much smaller than the differences listed in Table 1.[28] The pK_a values of all evaluated compounds were found to be larger in aqueous solutions compared to those determined for the mixed media. Furthermore, pK_a values of the cationic acids are smaller in the THF–water mixture than in the 1-propanol–water system (Table 1).

A total of six organic solvents were explored for the possibility of separating hydrophobic drugs. The mobility data presented in Figure 7A were obtained with an organic solvent content of 60% (v/v) and a phosphate buffer concentration of 0.01 M (pH 5.2). In these systems, itraconazole was determined to coelute with solvent (data not shown). Amiodarone and desethylamiodarone could not be separated with methanol and acetonitrile, whereas baseline resolution of these two compounds was obtained with all other organic solvents. The significant differences in mobility values observed between different binary systems can mainly be attributed to the viscosity of the organic solvents. The data presented in Figure 7A were obtained under a constant ionic strength. If changes caused by the different dielectric constants are neglected and if it is assumed that the solvated radius of a solute is not differing much in the different binary systems, the change in the product of electrophoretic mobility and viscosity can be regarded as the change in the net charge of the solute.[29] Data reflecting this treatment are presented in Figure 7B. The viscosity data for the THF–water and acetonitrile–water mixtures were taken from refs 35 and 36, respectively, and those for the other mixtures from ref 28. The data given in Figure 7B reveal that the net charge (or the degree of protonation) of the cationic acids gradually decreases in the order from acetonitrile to THF. This is in agreement with the basicity increase of organic solvents in the order acetonitrile < methanol < ethanol < 1-propanol < 2-propanol < THF and is thus additional support for the evidence

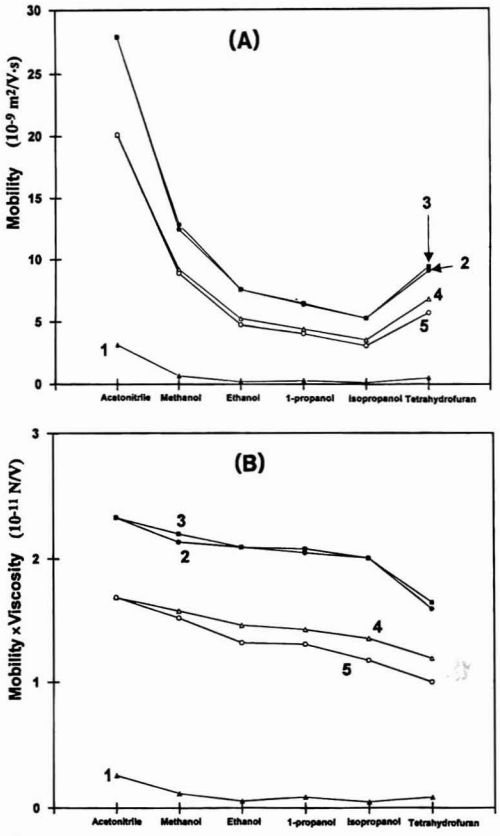

Figure 7. Impact of different organic solvents on (A) the effective electrophoretic mobility of solutes and (B) the product of mobility and viscosity. The running buffer consisted of 60% (v/v) organic solvent and 0.01 M phosphate (pH 5.2). Other conditions as for Figure 4.

that the more basic the solvent, the smaller the pK_a values of cationic acids.

Capillary Zone Electrophoresis in the Presence of a Surfactant and Micellar Electrokinetic Chromatography. Data obtained at pH 2.2 using a buffer containing 20 mM SDS are presented in Figure 8. In this configuration, the electrophoretic velocity (toward the anode) of the negatively charged dodecyl sulfate micelles is larger than the electroosmotic velocity (toward cathode). Therefore, compounds with a low capacity factor could be detected upon application of 20 kV (Figure 8A). Drugs with high capacity factors, such itraconazole, amiodarone, desethylamiodarone, ketoconazole, methadone, and dextromethorphan, are carried by the micelle in the direction opposite to electroosmosis. They could only be detected via reversal of the electric field and were found to coelute (Figure 8B). This corresponds to the situation referred to as case VIII according to the general classification of MEKC modes,[37] a configuration in which solutes are detected in the order of decreasing capacity factors. Capacity factors can be reduced by lowering the surfactant concentration,[38] and dodecyl sulfate is known to affect the separation behavior of

(33) Bonati, M.; Gaspari, F.; D'Aranno, V.; Benfenati, E.; Neyroz, P.; Galletti, F.; Tognoni, G. *J. Pharm. Sci.* **1984**, *73*, 829–831.
(34) Heykants, J.; Van Peer, A.; Van de Velde, V.; Van Rooy, P.; Meuldermans, W.; Lavrijsen, K.; Woestenborghs, R.; Van Cutsem, J.; Cauwenbergh, G. *Mycoses* **1989**, *32* (Suppl. 1), 67–87.
(35) Melander, W. R.; Horvath, C. In *High-Performance Liquid Chromatography*; Horvath, C., Ed.; Academic Press: New York, 1980; pp 113–319.
(36) Snyder, L. R. *J. Chromatogr. Sci.* **1977**, *15*, 441–449.
(37) Zhang, C.-X.; Sun, Z.-P.; Ling, D.-K. *J. Chromatogr.* **1993**, *655*, 309–316.
(38) Terabe, S.; Otsuka, K.; Ando, T. *Anal. Chem.* **1985**, *57*, 834–841.

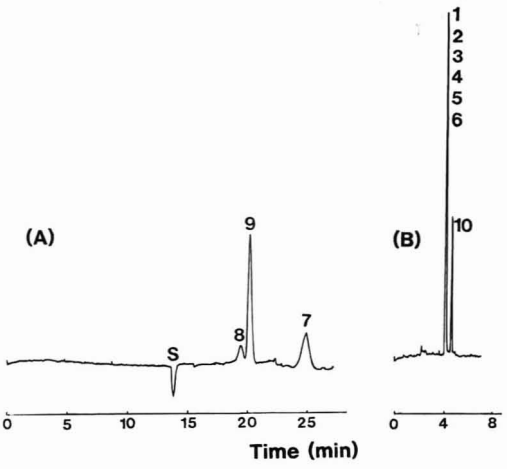

Figure 8. MEKC electrochromatograms (Prince instrument) with a running buffer composed of 0.04 M phosphate and 20 mM SDS (pH 2.2). Applied voltages were (A) 20 and (B) −20 kV. The current was ~40 μA. Other conditions as for Figure 3.

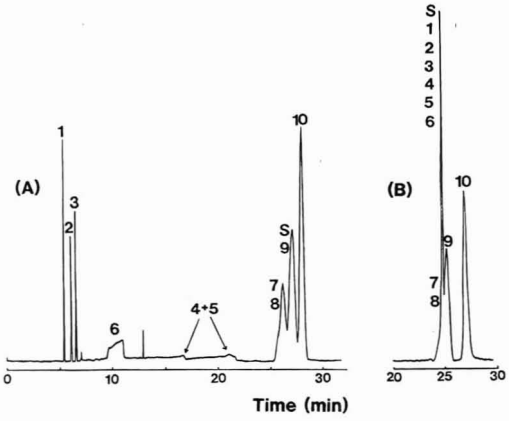

Figure 9. Electrochromatograms (Prince instrument) obtained in the presence of low amounts of SDS. The running buffers were composed of 0.04 M phosphate (pH 2.2) containing (A) 10 μM and (B) 1 mM SDS. Applied voltage, 20 kV. Current, (A) 30 and (B) 31 μA. Other conditions as for Figure 3.

hydrophobic or cationic substances when applied below its critical micellar concentration (cmc; ~8 mM SDS[14]).[39] At pH 2.2, the interaction between dodecyl sulfate and itraconazole, amiodarone, and desethylamiodarone was already noticed when the running buffer contained 2 μM SDS. With an SDS concentration of <50 μM, the peak shapes were distorted (Figure 9A) whereas with a concentration of 50 μM sharp peaks were observed and the three compounds coeluted as neutral ion pairs with the solvent (data not shown). In contrast, at or below 50 μM SDS, the separation behavior of all other solutes remained unaffected. With 1 mM SDS, however, ketoconazole, methadone, and dextromethorphan were also found to form neutral ion pairs. Thus, all six cationic drugs coeluted with the solvent (Figure 9B) and only naproxen

(39) Zhang, C.-X.; Sun, Z.-P.; Ling, D.-K.; Zheng, J.-S.; Guo, J.; Li, X.-Y. *J. Chromatogr.* **1993**, *612*, 287–294.

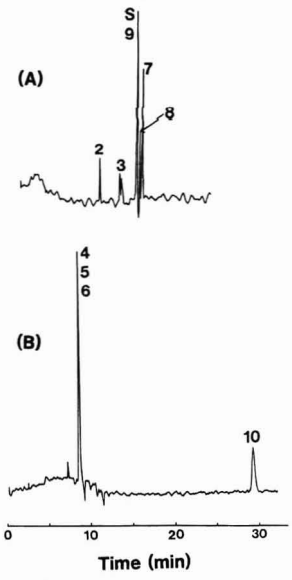

Figure 10. MEKC electrochromatograms with a running buffer comprising 0.04 M phosphate and 20 mM STC (pH 2.2). The applied voltages were (A) 20 and (B) −20 kV. The current was ~43 μA. Other conditions as for Figure 3.

was completely resolved. Using 5 mM or larger SDS concentrations, the cationic drugs were determined to migrate toward the positive electrode and to coelute as is shown with the data presented in Figure 8B. Thus, the conclusion can be reached that the cationic and hydrophobic substances examined here cannot be separated by reducing the SDS concentration.

Although cyclodextrin has been reported to reduce the capacity factor by hosting the solutes,[4,5] no improvement for the hydrophobic and positively charged drugs has been observed. By addition of 20 mM β-CD to the 20 mM SDS micellar solution (pH 2.2), the six drugs were found to coelute, much the same way as was the case without β-CD (Figure 8B). The retention time of naproxen, however, was determined to be much larger in the presence of cyclodextrin. On the other hand, with a decreased SDS concentration and keeping the β-CD concentration at 20 mM, broad and tailing peaks comparable to those shown in Figure 9A were observed (data not shown). Using taurocholate as a micelle-forming agent and a buffer pH of 2.2, methadone, dextromethorphan, and other solutes were found to have very little interaction with the micelles (Figure 10A). This is in contrast to the situation observed with SDS (Figure 8B). Itraconazole, amiodarone, and desethylamiodarone were found to coelute and could only be detected by reversing the polarity (Figure 10B). In analogy to the data presented in Figure 8B, the three compounds are shown to have large capacity factors and possibly coelute with the micelle. Methadone produced a double peak, which could be attributed to the separation of its enantiomers (Figure 10A). Ketoconazole could not be detected within 60 min in both polarity modes, corresponding to case VII of the general classification of MEKC[37] in which the capacity factor is close to $-t_{mc}/t_0$ and the retention time is approaching infinity. Addition of 20 mM β-CD to the 20 mM STC micellar solution (pH 2.2) led to distortion of peak shape for itraconazole, amiodarone, and desethylamiodarone. Further-

more, using a buffer composed of 50 mM sodium deoxycholate at pH 9.1, itraconazole and methadone could be separated while being transported in the direction of electroosmosis. These experiments indicate that the use of bile salts instead of SDS results in a sufficient reduction of the capacity factor for moderately hydrophobic compounds (including methadone and dextromethorphan) but not for highly hydrophobic substances.

The strong electrostatic attraction between positively charged molecules and anionic micelles is one of the reasons that the six drugs coelute in MEKC at pH 2.2. The pK_a values of the cationic acids were determined to be below 10 (Table 1). Thus, their charge is drastically reduced or vanishes completely at pH >11. The data presented in Figure 11A were obtained with a 0.02 M phosphate buffer containing 20 mM SDS and having pH 11.2. In that system, six uncharged drugs coeluted. Similar behavior was observed with a buffer at pH 9.2 comprising 75 mM SDS (data not shown). With addition of 20 mM β-CD, some peaks became somewhat distorted and ketoconazole, methadone, and dextromethorphan eluted relatively early (Figure 11B). Furthermore, addition of urea was found not to improve peak formation and the use of a cationic surfactant (50 mM CTAB at pH 9.2; elimination of the electrostatic attraction between micelles and cationic solutes) also resulted in coelution of amiodarone and desethylamiodarone (data not shown). Thus, in order to be able to use a micellar system with either anionic or cationic micelles, suitable buffer additives that sufficiently enhance the solubility of the highly hydrophobic substances in the aqueous phase should be found.

CONCLUSIONS

In contrast to electrokinetic capillary methods with ionic surfactants, CE in binary systems with high amounts of organic solvents (>30% (v/v)) at a buffer pH near or lower the solute's pK_a values or CE in the presence of β-CD (or another electrically neutral complexing agent) at low pH can be effective approaches for the separation of highly hydrophobic (log P value of >4 [33,34,40]) and positively chargeable substances. Moderately hydrophobic and positively chargeable compounds can be sufficiently dissolved in aqueous media for their separation by CE at pH < pK_a. Compared to aqueous chemistry, pK_a values of cationic acids become lower in binary systems with organic solvents which are more basic than water. Amiodarone and desethylamiodarone, which have very similar chemical structures, separate well using binary systems with THF, 2-propanol, 1-propanol, or ethanol, when a buffer pH of ~6 (close to their pK_a's) is employed. Itraconazole with its much lower pK_a is difficult to analyze in binary systems but can be determined in an aqueous buffer with β-CD at pH 2–3. Application of these methods for determination of serum drug levels is currently under investigation.

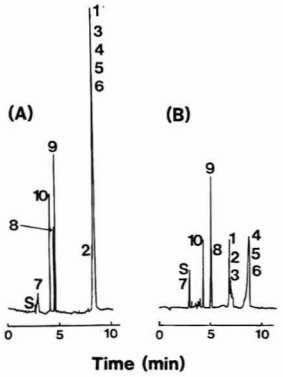

Figure 11. Separation by MEKC at high pH. The running buffers were composed of (A) 0.02 M phosphate containing 20 mM SDS (pH 11.2) and (B) the same buffer supplemented with 20 mM β-CD. The applied voltage (current) was 20 kV (47 μA). Other conditions as for Figure 3.

ACKNOWLEDGMENT

The authors gratefully acknowledge the generous loan of a BioFocus 3000 from its manufacturer, Bio-Rad Laboratories, Life Science Group, Hercules, CA. C.-X.Z. is grateful to his employer for granting study leave. This work was sponsored by the Swiss National Science Foundation.

Received for review January 5, 1995. Accepted April 21, 1995.[⊗]

AC950020X

(40) Herbert, B. J.; Dorsey, J. G. *Anal. Chem.* **1995**, *67*, 744–749.

[⊗] Abstract published in *Advance ACS Abstracts*, June 1, 1995.

Anal. Chem. **1995**, *67*, 2078–2087

Superposition of Chromatographic Retention Patterns

Attila Felinger

Department of Analytical Chemistry, University of Veszprém, Veszprém, P.O. Box 158, H-8201 Hungary

The retention pattern of multicomponent chromatograms is studied. When the sample being analyzed is a mixture of some structured series of compounds, the simplest models fail to characterize the interval distribution of adjacent peaks. In this study, the effect of superposition is explained, showing that even the mixture of samples that give strictly deterministic chromatograms individually turns disordered. The resultant interval distribution rapidly approaches the exponential distribution. For this reason, a second-order property (the variance–time curve) is needed to recognize the fact of superposition. The variance–time curve also allows the determination of the number of individual chromatograms, i.e., the number of families of compounds. The model was applied to two sharply different multicomponent chromatograms: that of a chamomile flower extract and a naphtha sample, proving that the former one is a true disordered sample while the latter one is the product of the superposition of structured sources.

The total chromatographic analysis of a multicomponent mixture is an extremely tedious task.[1] During the past decade, different statistical methods have been elaborated in order to enhance the information obtained from a multicomponent chromatogram. These methods give macroscopic information about the mixture, in a sense that they provide the average statistical attributes but say nothing about individual peaks or peak homogeneity.

The first of these methods, the statistical model of peak overlap, was originally developed[2] and modified[3,4] by assuming a totally random retention pattern. Such a behavior can be characterized by a Poissonian process that results in exponentially distributed intervals between adjacent peaks.[2] As this theory is based on the assumption that each single-component peak occupies the same amount of space on the time scale, it is strictly valid only when all peaks are of equal height and width. However, extensive numerical calculations[5] and processing real chromatograms[6–10] demonstrated that, despite these limitations, the method works well for the estimation of the number of components from both simulated and real chromatograms.

The subsequently elaborated Fourier analysis of multicomponent chromatograms[11,12] was able to account for the peak height dispersion and for the retention pattern as well. Furthermore, by means of Fourier analysis, the nonconstancy of the single-component peak widths can also be accounted for.[13] By applying this method, it turned out that in some cases interdistance models different from the Poissonian one give more realistic picture of the retention pattern,[14] because when the sample contains some structured series of components or members of homologous series, the retention times cannot be regarded completely random. By the Fourier analysis approach, many other interdistance models can be taken into account.[15] The statistical model of peak overlap was also extended accordingly[16] in order to be able to estimate the significance of peak overlap for the above situations.

Recently, Davis[17] extended the statistical model of peak overlap to nonstationary Poissonian cases, i.e., to chromatograms where the peak density is the function of time but the behavior is locally Poissonian. Surprisingly, although extremely different peak density models were considered, the extent of peak overlap, i.e., the number of singlets, doublets, etc., and the number of observable peaks were found to be fairly insensitive to the density, except for highly saturated chromatograms.

Whereas, when the sample is a mixture of a great number homologous series the assumption of randomness is sound, a recent analysis of PCB chromatograms[18] showed that the most common interval distributions do not model well the retention pattern in all cases. For this reason, it is necessary to study more deeply what happens when different retention patterns overlap, i.e., the sample is a mixture of some individual series, and the chromatogram of the mixture can be regarded as a superposition of the different particular chromatograms.

THEORY

Rentention Patterns. The retention pattern is characterized by the probability density function of the intervals between adjacent peaks. For the most disordered random chromatogram,

(1) Kováts, E. sz. *J. Chromatogr.* **1987**, *406*, 185–222.
(2) Davis, J. M.; Giddings, J. C. *Anal. Chem.* **1983**, *55*, 418–424.
(3) Herman, D. P.; Gonnord, M.-F.; Guiochon, G. *Anal. Chem.* **1984**, *56*, 995–1003.
(4) Martin, M.; Herman, D. P.; Guiochon, G. *Anal. Chem.* **1986**, *58*, 2200–2207.
(5) Davis, J. M.; Giddings, J. C. *Anal. Chem.* **1985**, *57*, 2168–2177.
(6) Davis, J. M.; Giddings, J. C. *Anal. Chem.* **1985**, *57*, 2178–2182.
(7) Dondi, F.; Kahie, Y. D.; Lodi, G.; Remelli, M.; Reschiglian, P.; Bighi, C. *Anal. Chim. Acta* **1986**, *191*, 261–273.
(8) Davis, J. M. *J. Chromatogr.* **1988**, *449*, 41–52.
(9) Coppi, S.; Betti, A.; Dondi, F. *Anal. Chim. Acta* **1988**, *212*, 165–170.
(10) Delinger, S. L.; Davis, J. M. *Anal. Chem.* **1990**, *62*, 436–443.
(11) Felinger, A. Pasti, L.; Dondi, F. *Anal. Chem.* **1990**, *62*, 1846–1853.
(12) Felinger, A.; Pasti, L.; Reschiglian, P.; Dondi, F. *Anal. Chem.* **1990**, *62*, 1854–1860.
(13) Felinger, A.; Pasti, L.; Dondi, F. *Anal. Chem.* **1991**, *63*, 2627–2633.
(14) Dondi, F.; Betti, A.; Pasti, L.; Pietrogrande, M. C.; Felinger, A. *Anal. Chem.* **1993**, *65*, 2209–2222.
(15) Felinger, A.; Pasti, L.; Dondi, F. *Anal. Chem.* **1992**, *64*, 2164–2174.
(16) Pietrogrande, M. C.; Dondi, F.; Felinger, A.; Davis, J. M. *Chemom. Intell. Lab. Syst.*, in press.
(17) Davis, J. M. *Anal. Chem.* **1994**, *66*, 735–746.
(18) Pietrogrande, M. C.; Bollain-Rodriguez, M. H.; Carro-Diaz, M. A.; Pasti, L.; Dondi, F. *J. High Resolut. Chromatogr.* **1994**, *17*, 839.

0003-2700/95/0367-2078$9.00/0 © 1995 American Chemical Society

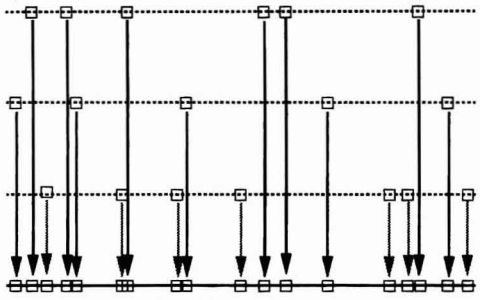

Figure 1. Superposition of three point processes.

which is considered to be the result of a Poissonian process, the interval distribution is exponential

$$f(t) = (1/T)e^{-t/T} \tag{1}$$

where T is the mean interval.

A totally ordered chromatogram—when all the retention time increments are constant—is described by the δ function, which can also be handled as a limit $\sigma_T \to 0$ of the normal distribution

$$f(t) = \frac{1}{\sqrt{2\pi}\sigma_T} e^{-(t-T)^2/2\sigma_T^2} \tag{2}$$

The normal interdistance model plays a special role, as by simply increasing its σ_T parameter—i.e., the standard deviation of the mean intervals—it can model many different behaviors from the totally ordered to the totally disordered chromatogram.

A couple of other interdistance models have also been used for describing the retention patterns:[14,15] the Γ and the uniform distributions. The Γ model is also flexible: when its shape parameter is equal to $p = 1$, it is identical to the exponential distribution. On the other hand, when p increases, it approaches the normal distribution.

$$f(t) = \frac{\tau^{-p} t^{p-1} e^{-t/\tau}}{\Gamma(p)}, \quad t \geq 0 \tag{3}$$

where $\tau = T/p$ and the relative standard deviation of the distances is RSD $= 1/(p)^{1/2}$.

By means of these flexible distributions, many various behaviors can be modeled. Numerical simulations proved that when Fourier analysis is applied to multicomponent chromatograms, the correct retention pattern is not always identified, especially when the chromatogram is saturated and the long-distance correlations are suppressed.[15] However, even in this case the Fourier method is able to give a reliable estimate for both the number of components and its variance. For this reason, a good fit is not the proof of finding the correct interdistance model. In order to give a more reliable estimation for the retention pattern, we have to understand what happens when different retention patterns overlap, i.e., when a *mixture of mixtures* is being analyzed.

Superposition of Point Processes. The superposition of point processes is demonstrated in Figure 1. The pooled process is the result of the superposition of three component processes. The objective of analyzing the superposition is to determine the interval distribution of the superposed process from the individual processes, as well as to recognize the presence of superposition and to estimate the number of individual processes.

For the derivation of the superposed retention pattern, we will regard the chromatogram as a point process; i.e., one component is characterized by only its retention time. The process is defined by the intervals $\{t_1, t_2, ...\}$ distributed with the density $f(t)$. There is a strong requirement that the intervals between successive events be mutually independent. We will consider an individual chromatogram as an equilibrium renewal process;[19] i.e., we assume that the density of the first interval is given by the equilibrium delay function

$$f_i^{(1)}(t) = \frac{1 - F_i(t)}{T_i} = \frac{\mathcal{F}_i(t)}{T_i} \tag{4}$$

where $f_i^{(1)}(t)$ is the probability density function of the delay of the first event, $\mathcal{F}_i(t) = 1 - F_i(t)$ is the survival function corresponding to the density $f_i(t)$, and T_i is the mean of the density $f_i(t)$, i.e., the mean interval.

In order to calculate the probability density function of the intervals in the superposed process when k independent point processes are superposed, we will consider the equilibrium behavior a long time after the start of the process. For any time t, we can define Y_i delay random variable as the length of time measured backwards from t to the last event before t in the ith source.[20] Then in the superposed process, the corresponding variable Y is

$$Y = \min(Y_1, ..., Y_k) \tag{5}$$

As the individual processes are independent, the probability that $Y > t$ is the product of the individual probabilities.

$$P(Y>t) = \prod_{i=1}^{k} P(Y_i>t) = \prod_{i=1}^{k} \int_t^\infty \frac{\mathcal{F}_i(u)}{T_i}\,du \tag{6}$$

Since Y exceeds t only if the delay variable in process i exceeds t, for the interval survival function we can write

$$\frac{\mathcal{F}(t)}{T} = -\frac{d}{dt}\prod_{i=1}^{k} \int_t^\infty \frac{\mathcal{F}_i(u)}{T_i}\,du \tag{7}$$

The mean interval in the superposed process can be calculated from the average intervals in the individual chromatograms

$$\frac{1}{T} = \sum_{i=1}^{k} \frac{1}{T_i} \tag{8}$$

The density function of the intervals $f(t)$ can be calculated by differentiating the interval survival function given in eq 7.

(19) Cox, D. R.; Isham, V. *Point Processes*; Chapman and Hall: London, 1980.
(20) Cox, D. R.; Smith, W. L. *Biometrika* **1954**, *41*, 91–99.

$$f(t) = \left(\sum_{i=1}^{k} \frac{1}{T_i}\right)^{-1} \frac{d^2}{dt^2} \prod_{i=1}^{k} \frac{1}{T_i} \int_t^\infty \mathcal{F}_i(u)\, du \qquad (9)$$

This equation models the interval probability density in the superposed chromatogram and serves as the basis of subsequent calculations.

When two individual renewal processes are superposed, the above equation simplifies to[19]

$$f(t) = \frac{1}{T_1 + T_2}(2\mathcal{F}_1(t)\mathcal{F}_2(t) + f_1(t) \int_t^\infty \mathcal{F}_2(u)\, du + f_2(t) \int_t^\infty \mathcal{F}_1(u)\, du) \qquad (10)$$

When k identical distributions are superposed ($T_1 = ... = T_i = ... = T_k$), the pooled chromatogram will have the following interval distribution:[20,21]

$$f(t) = -\frac{d}{dt}\left[\mathcal{F}_i(t)\left(\frac{1}{T_i}\int_t^\infty \mathcal{F}_i(u)\, du\right)^{k-1}\right] \qquad (11)$$

We can easily calculate the above interval distribution for the distributions summarized in Table 1. Writing the appropriate terms of Table 1 into eq 11, we will get for the case of the exponential distribution that

$$f(t) = (k/T_i)e^{-kt/T_i} \qquad (12)$$

If we want to keep the resultant interval at constant T, the interval in the individual chromatograms should be kT_i. Taking this into account, the above equation will be identical to eq 1, since $T = T_i/k$. Equations 1 and 12 show that superposing any number of Poissonian chromatograms will always result in Poissonian chromatograms. This holds true not only in the case of equal mean intervals but also when the T_i mean intervals of the individual chromatograms differ (see the second equation of Table 2).

When we repeat the same procedure for uniform interval distribution, we will get

$$f(t) = \frac{2k-1}{2T_i}\left(1 - \frac{t}{2T_i}\right)^{2k-2} = \frac{2k-1}{2kT}\left(1 - \frac{t}{2kT}\right)^{2k-2} \qquad (13)$$

which shows that the superposition of uniform interval distributions gives polynomial distributions whose limit as k increases is

$$\lim_{k\to\infty} \frac{2k-1}{2kT}\left(1 - \frac{t}{2kT}\right)^{2k-2} = \frac{1}{T}e^{-t/T} \qquad (14)$$

which is the same Poissonian chromatogram that is given in eq 1.

When we superpose deterministic individual chromatograms without any randomness, we will get the density function for the intervals as

$$f(t) = \frac{k-1}{T_i}\left(1 - \frac{t}{T_i}\right)^{k-2} = \frac{k-1}{kT}\left(1 - \frac{t}{kT}\right)^{k-2} \qquad (15)$$

The only randomness in superposing identical deterministic point processes is in the starting time of the ith individual process, which is given by the survival function in the case of equilibrium processes; i.e., for a deterministic chromatogram we assume that the starting time of the first events in each individual process are distributed uniformly. The limit of this function is also

$$\lim_{k\to\infty} \frac{k-1}{kT}\left(1 - \frac{t}{kT}\right)^{k-2} = \frac{1}{T}e^{-t/T} \qquad (16)$$

since the only difference between eqs 14 and 16 is that eq 14 contains parameter $2k$ where eq 16 contains parameter k. This means that superposing two identical deterministic chromatograms will give a uniform interval distribution; moreover, superposing $2k$ identical deterministic chromatograms will result in the same retention pattern as superposing k chromatograms of uniform interval distribution. Figure 2a demonstrates the rate of convergence when superposing deterministic chromatograms. It is obvious that superposing even only a few deterministic chromatograms results in an exponential-like interval density.

When a minor randomness is introduced—which corresponds better to real-life situations—the normal distribution with small standard deviation can be used as an interval model. Figure 2b shows that superposing such chromatograms will exhibit the same behavior except for a small shoulder at T_i when two sources are superposed.

Generally, whatever the component distributions are, as k tends to infinity, the limit is always the disordered Poissonian chromatogram and the corresponding exponential distribution of the intervals. For large k, the superposed chromatogram is locally random, provided that we consider intervals that are short compared to the individual mean intervals T_i.

Determination of the Retention Pattern. The above results demonstrated that the interval distribution is very close to the exponential even if the number of the individual component chromatograms is small. For this reason, any method that is based on the model of the interval distribution is not sensitive enough to detect the slight differences. Moreover, the fluctuations that arise from the sampling of a finite number of points hinder the correct estimation of the interdistance model.

We have to use second-order properties in order to estimate the interval distribution. For this purpose, instead of the intervals previously used for the characterization of the retention pattern, the properties of counts will be used. The series of points are considered as a stationary counting process $\{N_t\}$. $\{N_t\}$ indicates the number of points (counts) up to time t. The expected number of points is

$$M(t) = E(N_t) = t/T \qquad (17)$$

The variance–time curve, i.e., the variance of the number of points in an interval t

$$V(t) = E(N_t^2) - \{E(N_t)\}^2 \qquad (18)$$

is a very suitable means to analyze the retention pattern. For a Poissonian process, the variance–time curve is a straight line

(21) Cox, D. R. *Renewal Theory*; Methuen & Co. Ltd.: London, 1962.

Table 1. The Frequency Function, the Survival Function, and Its Integral for Some Distributions

distribution	$f_i(t)$	$\mathcal{F}_i(t)$	$\int_t^\infty \mathcal{F}_i(u)\,du$
δ $(t < T_i)$	$\delta(t - T_i)$	1	$T_i - t$
exponential $(t \geq 0)$	$(1/T_i)e^{-t/T_i}$	e^{-t/T_i}	$T_i e^{-t/T_i}$
uniform $(t < 2T_i)$	$1/2T_i$	$1 - t/2T_i$	$T_i(1 - t/2T_i)^2$
normal	$\frac{1}{\sqrt{2\pi}\sigma_i} e^{-(t-T_i)^2/2\sigma_i^2}$	$\frac{1}{2} - \frac{1}{2}\mathrm{erf}\left(\frac{t - T_i}{\sqrt{2}\sigma_i}\right)$	$\frac{\sigma_i}{\sqrt{2\pi}} e^{-(t-T_i)^2/2\sigma_i^2} + \frac{t - T_i}{2}\left[\mathrm{erf}\left(\frac{t - T_i}{\sqrt{2}\sigma_i}\right) - 1\right]$

$$V(t) = M(t) = \Lambda t = t/T \tag{19}$$

For distributions less dispersed than the exponential, the slope of the variance–time curve is smaller than the value given by the above equation.

The following method can be used to determine the variance-time curve from experimental data,[22,23] which is a moving average over a number of possible intervals of length t. First the point series should be divided into short intervals of length τ so that preferably at most two points n_i are in the ith interval. Then the number of points in each interval should be counted, resulting in a discrete time series $[n_1, ..., n_m]$, where n_i is the number of points in $(i - 1)\tau \leq t < i\tau$. Then the n's are added together in blocks of r giving

$$\begin{aligned} U_1^{(r)} &= n_1 + ... + n_r \\ U_2^{(r)} &= n_2 + ... + n_{r+1} \\ &\vdots \\ U_{m-r+1}^{(r)} &= n_{m-r+1} + ... + n_m \end{aligned} \tag{20}$$

The $U^{(r)}$'s are the numbers of points occurring in the intervals of length $t = r\tau$, so they can be used for the estimation of the variance–time curve[22,23]

$$\hat{V}(r\tau) = \frac{3M}{3M^2 - 3Mr + r^2 - 1}\left\{\prod_{i=1}^{M}(U_i^{(r)})^2 - \frac{1}{M}\left(\prod_{i=1}^{M} U_i^{(r)}\right)^2\right\} \tag{21}$$

where $M = m - r + 1$. The divisor in the above equation was chosen so that if the series is a Poissonian process with constant mean $r\lambda$ then

$$E[\hat{V}(r\tau)] = V(r\tau) = r\tau\lambda \tag{22}$$

provided that $r < m/2$.[23]

If the sources are not Poissonian processes, $V(t)$ will depart from eq 19 at times comparable with or larger than the mean interval in the component processes.

The asymptote of the variance–time can be used for estimating the number of component chromatograms that build up the superposed one.[20,23] If the asymptotic form of the variance–time curve is $\hat{a}t + \hat{b}$, the estimate for the number of component processes is

$$\hat{k} = \frac{6\hat{b}}{1 - (\hat{a}T)^2} \tag{23}$$

When deriving the above relationship, Cox[23] made the assumption that the intervals in the individual processes have Γ distribution. However, when the term $\hat{a}T$ is much smaller than 1, the estimate is insensitive to the form of the interval distribution as long as it is not fairly dispersed.[23]

RESULTS AND DISCUSSION

Interval Distribution of Superposed Chromatograms. Calculations were carried out in order to assure that the equations derived for the superposed retention patterns describe correctly the process. For this reason, line chromatograms of different interval distributions were generated numerically. A line chromatogram is a series of spikes (or δ functions), i.e., peaks of zero width. The computer simulation of line chromatograms consists of generating random retention times and peak heights by means of an appropriate interval and peak height model. The individual chromatograms were superposed, restructured, and the interval histograms of the resultant chromatograms (containing 8000 peaks, respectively) were compared to the interval model calculated from eq 10. The superposition of individual chromatograms of normal interval distribution is shown in Figure 3. The mean interval of the component chromatograms is $T_1 = T_2 = 1$. Apparently, the derived model (solid line) matches well the numerically computed histograms in all cases.

In Figure 3a, where the component chromatograms are nearly deterministic (RSD = 0.05), the interval distribution of the superposed chromatogram is very close to the uniform distribution. The superposition has dramatically increased the number of short intervals. Consequently, the number of observable peaks will strongly decrease as the consequence of the superposition. Similar behavior can be observed when superposing more dispersed chromatograms of normal interval distributions (see Figure 3b–d).

The increase of the short interdistances is not so enhanced when superposing an already disordered (Poissonian) chromatogram and a strictly periodic one. The superposition of an exponential interval distribution ($T_1 = 1$) and that of a deterministic one ($T_2 = 1$) is shown in Figure 4a. Since all the interdistances are equal in the deterministic chromatogram, superposing this one and an exponential one, the $T_2 = 1$ intervals will cut the intervals of the exponential model, and in the resultant chromato-

(22) Cox, D. R.; Smith, W. L. *Biometrika* **1953**, *40*, 1–11.
(23) Cox, D. R.; Lewis, P. A. W. *The Statistical Analysis of Series of Events*; Methuen & Co. Ltd.; London, 1966.

Table 2. Superposition of Some Distributions

1. uniform–uniform

$$f(t) = \frac{3t^2 - 6t(T_1 + T_2) + 2(T_1^2 + 4T_1T_2 + T_2^2)}{4(T_1 + T_2)T_1T_2} \qquad T_1 < T_2,\ t < 2T_1$$

2. exponential–exponential

$$f(t) = \frac{T_1 + T_2}{T_1T_2} e^{-t(1/T_1 + 1/T_2)}$$

3. uniform–exponential

$$f(t) = \frac{t^2 - 4t(T_1 + T_2) + 4(T_1 + T_2)^2}{4T_1T_2(T_1 + T_2)} e^{-t/T_2} \qquad t < 2T_1$$

4. exponential–δ

$$f(t) = \frac{e^{-t/T_1}}{T_1 + T_2}\left[2 + \frac{T_2 - t}{T_1} + \delta(t - T_2)\right]$$

5. uniform–δ

$f(t) =$

$$\begin{cases} \dfrac{1}{T_1 + T_2}\left[2 + \dfrac{T_2 - 3t}{2T_1} + T_1\left(1 - \dfrac{t}{2T_1}\right)^2 \delta(t - T_2)\right] & \text{if } t < T_2 < T_1 \\ \dfrac{4T_1 - T_2 - 3t}{2T_1(T_1 + T_2)} & \text{if } t < T_1 < T_2 \end{cases}$$

6. δ–δ

$$f(t) = \frac{1}{T_1 + T_2}[2 + (T_2 - t)\delta(t - T_1)] \qquad t < T_1 < T_2$$

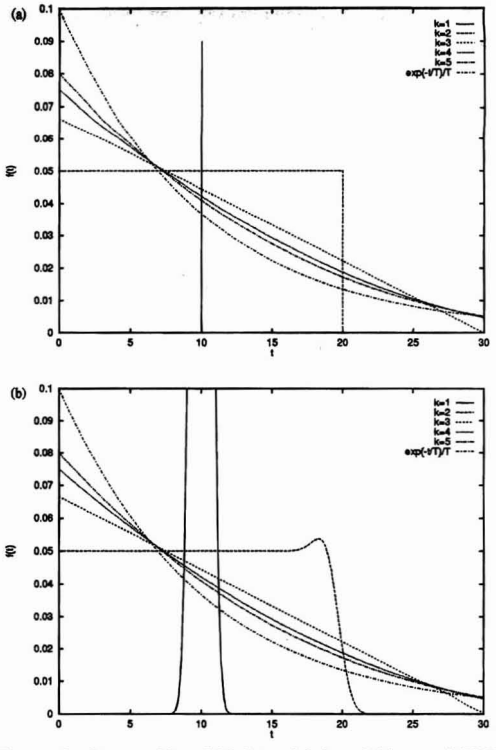

Figure 2. Superposition of (a) deterministic and (b) normal (RSD = 0.05) interval distributions; $T = 10$.

gram, no interdistance above $t = 1$ will appear. The same effect can be observed in Figure 4b, except here the mean interval of the Poissonian line chromatogram is half that of the strictly periodic chromatogram, so the Poissonian chromatogram originally contained fewer intervals for which $t > 1$ than in the previous case. An important feature of superposing these kinds of chromatograms is the multitude of intervals exactly at the intervals of the deterministic chromatogram. This occurs, since in the resultant chromatogram, many times two adjacent points belong to the same source, i.e., here to the deterministic one. The occurrence of this is less frequent in Figure 4b, because in that case the number of interdistances longer than 1 is smaller in the Poissonian chromatogram.

A comparison of the theoretically calculated interval distributions (solid lines) and the histograms calculated by numerical simulation shows that the model developed here models very well the aftermath of superposition in each case.

Variance–Time Curve. As was discussed in the previous section, the variance–time curve can be used to characterize the retention pattern. A series of variance–time curves are shown in Figure 5 for some basic interval models. For each point process, the mean interval is $T = 1$. From the bottom to the top, the individual curves (symbols) correspond to the following interval distributions: deterministic (◇); normal with RSD = 0.2 (×); Γ with $p = 5$ (+); normal with RSD = 0.5 (△); uniform (+); Γ with $p = 2$ (◇); normal with RSD = 1 (*); exponential (□). The solid line indicates the theoretical variance–time curve for a Poissonian process. The long-time values of all variance–time curves are characterized by the dispersion of the interval distribution; i.e., the variance–time curves of more dispersed interval models are plotted from the bottom to the top of the figure. It is interesting to see that the exponential model coincides with the normal model of RSD = 1. Although the relative standard deviation of the exponential distribution is also RSD = 1, even the extremely sensitive variance–time method is unable to distinguish them.

The discriminative power of the variance–time curve is demonstrated in Figure 6. In this figure, the numerically obtained interval histogram is plotted for the superposed chromatogram of five sources, with normal interval distribution of RSD = 0.2 each. The dotted line shows the theoretical interval distribution calculated by eq 11. We also indicate the best fit Poissonian model with a solid line. Although it is obvious that the Poissonian model overestimates the number of short intervals, and underestimates the longer ones, there cannot be seen much difference between the histogram and either theoretical model.

On the other hand, the two models mentioned above can be very well separated by calculating their variance–time curves. Figure 7 shows the variance–time curve of superposed normal intervals of RSD = 0.2. From the bottom to the top in Figure 7a, 1, 2, 5, and 10 point processes are superposed, and the chain line indicates the Poissonian process. Figure 7b enlarges the variance–time curve for short time. The variance–time curve in the middle of Figure 7b (dotted line and symbols □) corresponds to the interval distribution labeled as Correct model in Figure 6, while the chain line to the Poissonian model. While

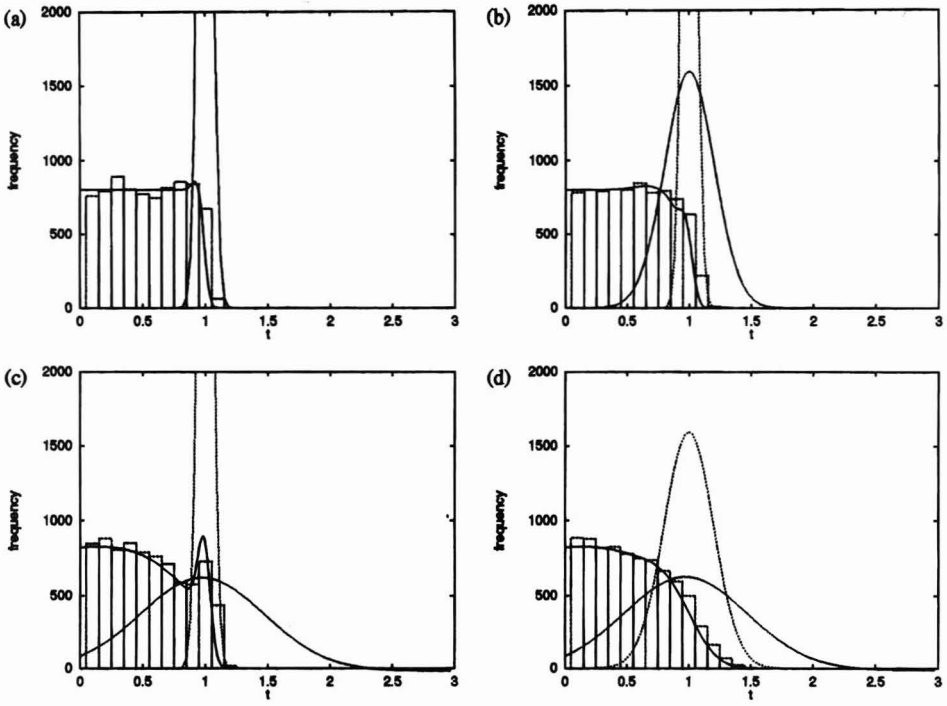

Figure 3. Superposition of two normal interval distributions ($T_1 = T_2 = 1$): (a) $RSD_1 = RSD_2 = 0.05$; (b) $RSD_1 = 0.05$, $RSD_2 = 0.20$; (c) $RSD_1 = 0.05$, $RSD_2 = 0.50$; (d) $RSD_1 = 0.20$, $RSD_2 = 0.50$. Dotted line, original interval models; solid lines, estimation by the model of superposition; bars, results of numberical simulation.

the interval density functions of these two models are very close to each other, their variance–time curves are amazingly separated.

Another interesting feature of the variance–time curve can also be observed in Figure 7b: the oscillation at short intervals. The variance–time curve oscillates with a periodicity determined by the number of superposed component chromatograms. The curves are plotted in such a way that the mean interval of the pooled chromatogram is equal to $T = 1$. Because the mean interval of the sources is T/k when k line chromatograms overlap, the variance of the number of points is small when exactly this interval is spanned over for the variance calculation. For this reason, the variance–time curve can be useful in order to estimate the number of sources, for instance, the number of homologous series or number of families of compounds present in a mixture chromatographed, provided that the individual distributions are not fairly dispersed.

Another attribute of the variance–time curve is that it follows the Poissonian model up to $t = T/k$, that is, the mean interval of the sources. This means that *any chromatogram is locally Poissonian* (random); the structure cannot be seen at intervals shorter than the mean interval of the source chromatogram.

The oscillations are more enhanced in the case of strictly deterministic behavior (Figure 8), since this circumstance means that the number of points in an interval of T/k is always constant and suggests that the variance–time curve is zero at this point and its integer multiples.

Increasing the dispersion of the interval density of the sources, the oscillation of the variance–time curve disappears, as is shown in Figure 9 for the case of superposed chromatograms with a normal interval distribution of RSD = 0.5. In this case, the randomness is present even in the sources,so the number of sources cannot be determined from the oscillations.

Equation 23 can serve as another means to calculate the number of sources from the asymptote of the variance–time curve. In Table 3, we summarized the parameters of the asymptotes estimated from the curves in Figures 7b and 9b, and the calculated number of sources. Because of the oscillations, it was impossible to determine the asymptote for $k = 10$ and RSD = 0.2, but in all other cases the estimation is very good.

When real chromatograms are analyzed, the short distance information is lost due to peak overlap. Numerical simulation was carried out in order to see how the peak width influences the variance–time curve. Poissonian chromatograms were generated at two different saturation factors: $\alpha = {}^1/_6$, and $\alpha = {}^1/_3$, respectively. The saturation of the chromatogram is the number of components over the peak capacity: $\alpha = m/N_c$. The peak capacity is defined at peak resolution $R_s = 0.5$. The peak heights of the individual peaks were generated by exponentially distributed random numbers. The higher the saturation factor of the chromatogram, the fewer the number of peaks detected. At $\alpha = {}^1/_6$, only about 80% of the component peaks can be detected, whereas at $\alpha = {}^1/_3$, 65% is the ratio of the detected peaks. The effect of overlap on the variance–time curve is demonstrated in

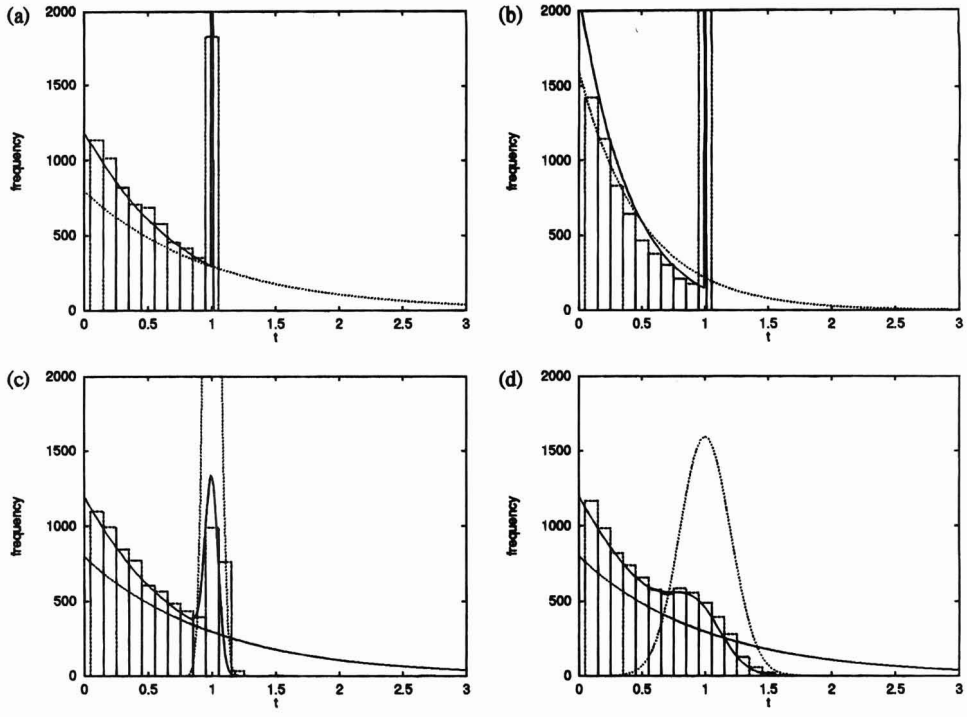

Figure 4. Superposition of an exponential and a normal interval distribution: (a) $T_{exp} = 1$, $T_{norm} = 1$ $RSD_{norm} = 0$ (deterministic); (b) $T_{exp} = 0.5$, $T_{norm} = 1$ $RSD_{norm} = 0$ (deterministic); (c) $T_{exp} = 0.1$, $T_{norm} = 1$ $RSD_{norm} = 0.2$; (d) $T_{exp} = 0.1$, $T_{norm} = 1$ $RSD_{norm} = 0.5$. Dotted line, original interval models; solid lines, estimation by the model of superposition; bars, results of numerical simulation.

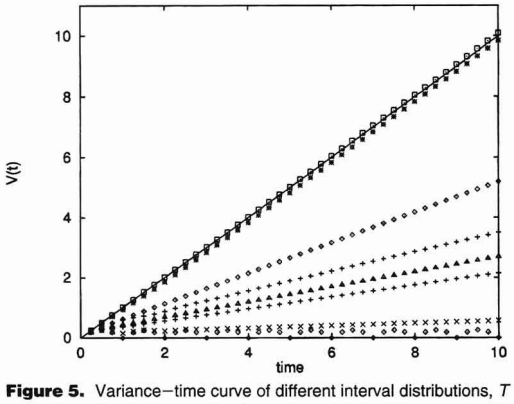

Figure 5. Variance–time curve of different interval distributions, $T = 1$. From the bottom to the top: deterministic (◇); normal with RSD = 0.2 (×); Γ with $p = 5$ (+); normal with RSD = 0.5 (△); uniform (+); Γ with $p = 2$ (◇); normal with RSD = 1 (*); exponential (□). Solid line, the theoretical variance–time curve for a Poissonian process.

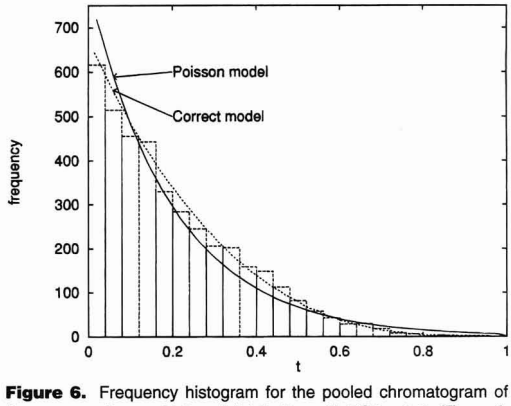

Figure 6. Frequency histogram for the pooled chromatogram of five sources of normal interval distribution with RSD = 0.2. Theoretical probability density function (dashed line) calculated by eq 11; the best fit Poissonian model (solid line).

Figure 10. Some deviation can be observed from the theoretical curve, but considering the resolution power of the variance–time curve, the calculated curves are very close to the theoretical one. However, the higher the saturation factor, the higher the deviation.

Experimental Check. Recently two very different samples were examined by Fourier analysis.[14] One of them was a chamomile lipophilic extract and the other a naphtha sample. The handling of the samples, the experimental conditions, and an extensive analysis of the multicomponent chromatograms can be found elsewhere.[14] During the numerical evaluation of real chromatograms, peaks were detected by means of their maxima. Five consecutive data points were compared, and a maximum was detected if the first three points were increasing and the last three points were decreasing. A threshold level was defined as 1% of the height of the largest peak and all maxima below this level were rejected.

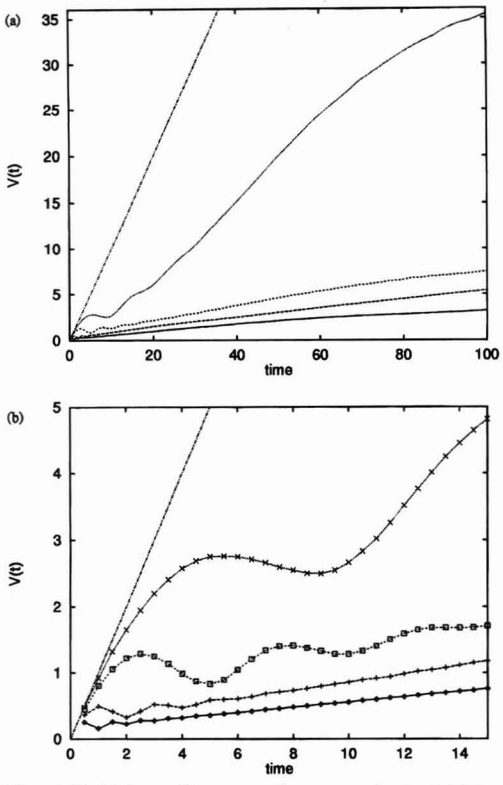

Figure 7. Variance–time curve of superposed normal interval distributions (RSD = 0.2): original line chromatogram (solid line and ◇), superposition of 2 (dashed line and +), 5 (dashed line and □) and 10 (dotted line and ×) sources. Chain line, the variance–time curve of a Poissonian process.

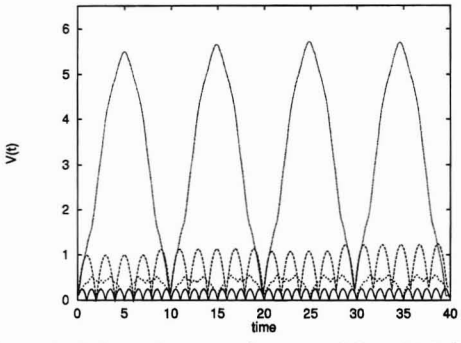

Figure 8. Variance–time curve of superposed deterministic line chromatograms: original line chromatogram (solid line), superposition of 2 (dashed line), 5 (dashed line) and 10 (dotted line) sources.

In this study, the two chromatograms were taken in order to check the hypothesis that the chamomile chromatogram is a disordered one, having components without meaningful structural relationship, while the naphtha chromatogram is supposed to be a mixture of different hydrocarbon families having structured chromatograms, individually.

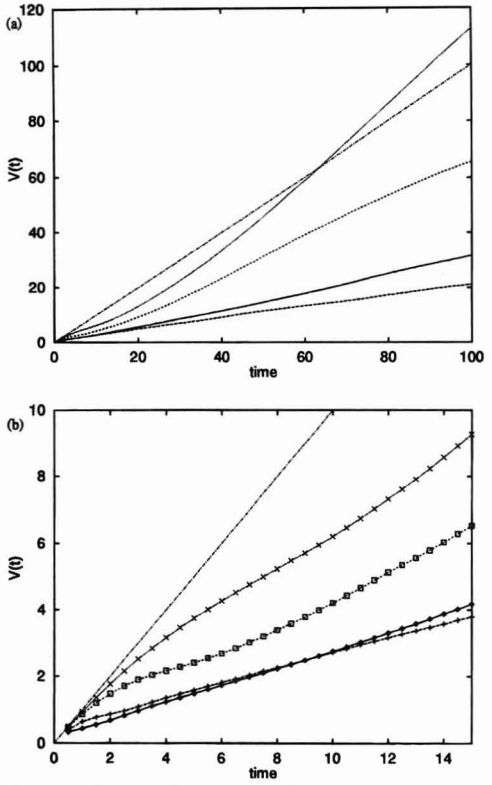

Figure 9. Same as Figure 7, except RSD = 0.5.

Table 3. Parameters of the Asymptote of the Variance–Time Curve and the Estimated Number of Individual Chromatograms of Normal Interval Densities

RSD	k	$\hat{a}$	$\hat{b}$	$\hat{k}$
0.2	1	0.04	0.16	0.96
0.2	2	0.06	0.26	1.58
0.2	5	0.08	0.62	3.76
0.2	10			
0.5	1	0.25	0.19	1.24
0.5	2	0.23	0.41	2.60
0.5	5	0.26	1.13	7.27
0.5	10	0.48	1.42	11.1

The chamomile and the naphtha chromatograms are shown in Figures 11a and 12a, respectively. In Figures 11b and 12b, the cumulative number of peaks detected is plotted against time. This is an important step in order to make sure that the peak density is constant along the time axis. The dots at the beginning of the chamomile and at the end of the naphtha chromatograms indicate regions where the peak density is different from the one indicated by solid line in the rest of the figures.

If the peak density $\lambda(t)$ is changing along the time, the time axis should be transformed into a new time scale that results in homogeneous process with constant peak density:[23]

$$t' = \int \lambda(t)\, dt \qquad (24)$$

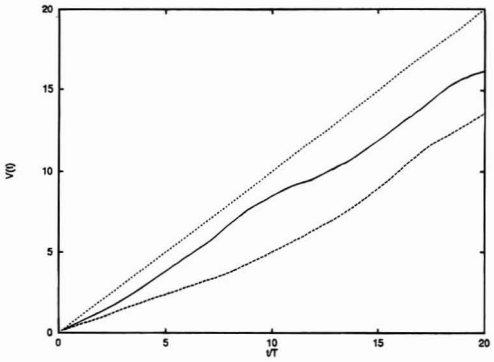

Figure 10. Variance–time curve of Poissonian chromatograms: theoretical curve of a Poissonian process (upper dashed line); calculated curve at $\alpha = 1/6$ (solid line); calculated curve at $\alpha = 1/3$ (lower dashed line);

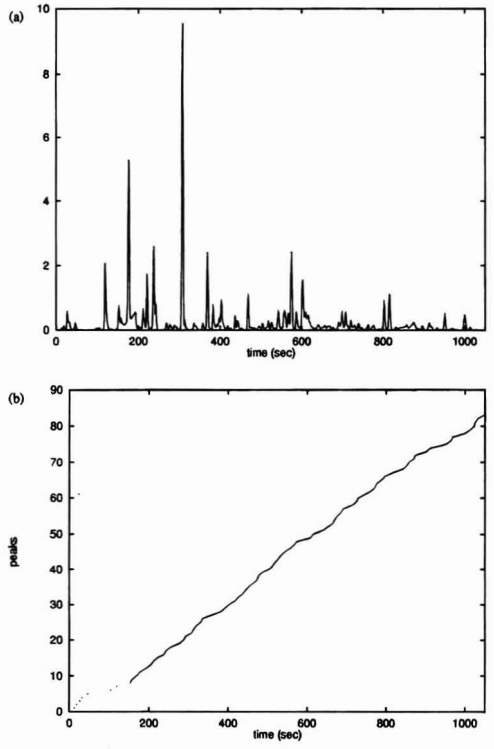

Figure 11. (a) Chromatogram of the chamomile extract. (b) Cumulative number of detected peaks.

The variance–time curve of the number of detected peaks was then calculated; the result is shown in Figure 13. The fact that both variance–time curves lie below the straight line of the Poissonian process indicates that both chromatograms are more ordered that the Poissonian one. The naphtha chromatogram is more ordered, while the chamomile chromatogram is very close to the Poissonian one, considering the discriminative power of the variance–time curve (recall Figures 6 and 7).

The asymptote of each variance time curve was determined. For the chamomile chromatogram parameters $\hat{a} = 0.305$ and $\hat{b} = 0.208$ were found. These parameters give an estimated number of individual chromatograms $\hat{k} = 1.48$. The meaning of this number is that the variance–time curve is not able to detect the effect of superposition of individual chromatograms; i.e., the chamomile sample can be regarded as a *true* disordered one. Moreover, the variance–time curve of the chamomile chromatogram is very close to that of a Poissonian chromatogram, which is another proof of a true disordered sample.

The analysis of the variance–time curve of the naphtha chromatogram resulted in asymptote parameters: $\hat{a} = 0.094$ and $\hat{b} = 0.863$, giving $\hat{k} = 5.22$. On the bases of these values, the naphtha chromatogram is supposed to consist of five different

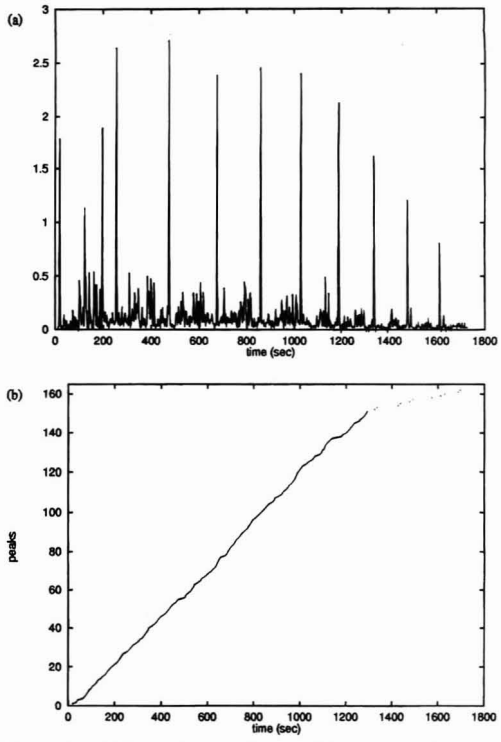

Figure 12. (a) Chromatogram of the naphtha sample. (b) Cumulative number of detected peaks.

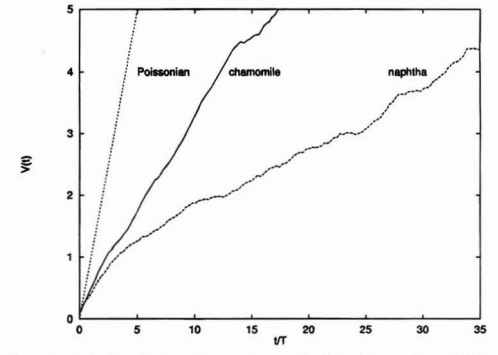

Figure 13. Variance–time curves of the chamomile and the naphtha chromatograms.

sources of components. However, at this point it is very important to emphasize that this latter number should be handled very cautiously. Only in the case when different sources overlap that have similar retention pattern, peak density, and number of components can we say that the number of families of compounds is equal to five. The real sample is much more complex. The Fourier analysis of this chromatogram estimated that the number of single components present in the sample is $m = 272$. Considering that this sample contains a C_9–C_{18} fraction, around 27 sources might overlap in the chromatogram. However, this assumption would express that the number of components is identical (10) in each sources. Most probably this is not the case; the sample may contain incomplete homologue series or components that do not belong to any series may give disordered retention pattern.

On the above grounds, at this moment it is impossible to attribute quantitative meaning to the estimated number of sources $\hat{k} = 5.22$. The major result of the variance–time curve analysis is that it is able to distinguish between disordered and structured chromatograms. By means of this method, we are able to recognize whether a seemingly disordered chromatogram is a true Poissonian one or the result of the superposition effect. Although, when the results indicate that the chromatogram is the superposition of many different sources, the estimated number of sources should be dealt with special care.

A comparison of Figures 7b and 13 shows that the variance-time curve of the naphtha chromatograms lies close to that of a superposed chromatogram of five normally distributed (RSD = 0.2) sources. The oscillations present in Figure 7b cannot be detected in Figure 13, which indicates that the individual sources of the naphtha chromatogram are not as nicely behaving as in the case of numerical simulation.

It is important to note that the above analysis was performed solely on the basis of retention times. The Fourier analysis of multicomponent chromatograms utilizes all the accessible information, such as peak shape and peak height dispersion. When looking at the naphtha chromatogram, the constant repetition suggests that we are faced with a structured sample, but the variance–time method is able to detect it plainly from the retention time data.

CONCLUSIONS

The model derived for the retention pattern of superposed individual chromatograms fits very well to the experimentally calculated interval histograms whether the individual chromatograms are disordered or structured. As was shown, when we superpose structured individual chromatograms, i.e., we mix different homologue series, the distribution of the intervals between adjacent peaks becomes very close to the exponential distribution. This fact indicates that we will be faced with a seemingly disordered chromatogram, a so-called pseudo-Poissonian chromatogram. The interval histogram is not able to distinguish between a true disordered chromatogram resulting from the lack of structural relationship between the components of a multicomponent sample and a structured chromatogram resulting from mixing some structured mixtures. A second-order property, the variance–time curve was found to be exceptionally sensitive for detecting the presence of overlap of structured chromatograms, and it can be used in order to differentiate ordered and disordered cases. The asymptote of the variance–time curve can be utilized to determine the number of overlapping individual chromatograms; however, we have to be cautious about the number estimated since this approach assumes equal contribution from each sources. In real multicomponent samples, when not all the possible members of a homologue series are present, this assumption may falsify the results, since a given family of compounds may occupy only a fragment of the total chromatographic space. Nevertheless, if the estimated number of sources is close to one, and the variance–time curve lies close to that of the Poissonian process, we can be convinced that the chromatogram is a true disordered chromatogram. Moreover, by means of the variance–time curve, qualitative information can be extracted about the amount of structuredness of the multicomponent sample.

The models of retention patterns that are the results of superposition can be implemented into the statistical model of peak overlap or Fourier analysis. The models elaborated here provide the interdistance models needed to apply the statistical analysis of multicomponent chromatograms in the case of many complex retention patterns.

ACKNOWLEDGMENT

The author gratefully acknowledges fruitful discussions with Francesco Dondi (University of Ferrara, Ferrara, Italy).

Received for review November 28, 1994. Accepted April 10, 1995.[⊗]

AC9411379

[⊗] Abstract published in *Advance ACS Abstracts*, June 1, 1995.

Anal. Chem. **1995,** *67,* 2088–2095

Effect of Micelles and Mixed Micelles on Efficiency and Selectivity of Antibiotic-Based Capillary Electrophoretic Enantioseparations

Kimber L. Rundlett and Daniel W. Armstrong*

University of Missouri–Rolla, Rolla, Missouri, 65401

Vancomycin (an oligophenolic, glycopeptide, macrocyclic antibiotic) has been shown to be a superb chiral selector for anionic and neutral compounds. It was found that adding sodium dodecyl sulfate to the run buffer increased efficiency by over 1 order of magnitude, decreased analysis times, and reversed the elution order of the enantiomers. This allows for control of the retention order as well as the resolution of enantiomers in complex mixtures in a single run. A mechanism is proposed which explains all of the observed effects and is verified experimentally. Since vancomycin is present in both the micelle and in free solution, previously proposed micelle–selector models are, at best, limiting cases. A general equation is derived which can be used to describe all possible interactions, including those with the capillary wall, if needed. Also, it is shown that electrophoretic mobilities and not migration times must be used to calculate binding constants of a solute to the micelle, the chiral selector, or both. Furthermore, it is shown that a neutral marker molecule cannot be used to accurately correct mobilities that have been altered due to changes in solution viscosity. While this work utilizes the practical vancomycin–micelle system, the general conclusions and theory apply to most other analogous CE systems as well.

Micellar electrokinetic separations are a mode of capillary electrophoresis (CE) which is used for the separation of neutral compounds that cannot be separated using conventional CE buffers. This technique was developed by Terabe et al.[1,2] by combining micellar chromatography[3–6] with capillary electrophoresis.[7] In micellar CE, the neutral solutes partition between the aqueous phase and the micellar phase during the separation process. The mobilities of a solute are different when in the aqueous and micellar phases, resulting in an overall mobility that is related to the partition coefficient of the solute. The separation of a mixture of neutral compounds is based on the different partition coefficients of the solutes between aqueous and micellar pseudophases. As in LC, micelles have also been used in CE to increase the solubility of hydrophobic compounds in aqueous buffers and to improve the selectivity of charged compounds[8–10] including peptides.[11] A comprehensive review on micelles in separations described many of these phenomena.[12]

The number of chiral separations by capillary electrophoresis reported in the literature has increased dramatically in the last few years. Cyclodextrins and their derivatives have been the most common buffer additives used for enantioresolution of many classes of compounds.[13,14] Although charged derivatives of cyclodextrins can be used to resolve neutral compounds, enantioseparation of neutral hydrophobic compounds with neutral cyclodextrins requires the addition of surfactants to the cyclodextrin run buffer. This results in a system that has been defined by a model consisting of micellar and aqueous cyclodextrin phases.[15,16] In this two-phase model, the cyclodextrin is assumed to have no interaction with the micelle phase and the equations for calculation of capacity factors for compounds separated by cyclodextrin–micelles are the same as those using only surfactant. This model only strictly applies to hydrophobic analytes which do not partition between the cyclodextrin or micelle phases to the water phase.[17] However, it should be noted that if the micelles associate with the chiral selector, or if the analytes partition to the aqueous buffer from the selector or micelle, the proposed model and equations are incorrect or, at best, a limiting case. CE chiral separations with micelles have also been performed using other chiral micelle-forming compounds such as bile salts,[18–20] as well as mixtures of chiral compounds and nonchiral surfactants.[21–23] The equations describing these systems are the same as those for conventional micellar separations.

(1) Terabe, S.; Otsuka, K.; Ichikawa, K.; Tasuchya, A.; Ando, T. *Anal. Chem.* **1984**, *56*, 111–3.
(2) Terabe, S.; Otsuka, K.; Ando, T. *Anal. Chem.* **1985**, *57*, 834–41.
(3) Armstrong, D. W.; Terrill, R. Q. *Anal. Chem.* **1979**, *51*, 2160–3.
(4) Armstrong, D. W.; Henry, S. J. *J. Liq. Chromatogr.* **1980**, *3*, 657–62.
(5) Armstrong, D. W.; Nome, F. *Anal. Chem.* **1981**, *53*, 1662–6.
(6) Armstrong, D. W.; Stine, G. Y. *J. Am. Chem. Soc.* **1983**, *105*, 2962–4.
(7) Jorgenson, J. W.; Lucas, K. D. *Anal. Chem.* **1981**, *53*, 1298–302.
(8) Cohen, A. S.; Terabe, S.; Smith, J.; Karger, B. L. *Anal. Chem.* **1987**, *59*, 1021–7.
(9) Otsuka, K.; Terabe, S.; Ando, A. *J. Chromatogr.* **1985**, *332*, 219–26.
(10) Otsuka, K.; Terabe, S.; Ando, A. *J. Chromatogr.* **1985**, *348*, 39–47.
(11) Liu, J.; Cobb, K. A.; Novotony, M. *J. Chromatogr.* **1990**, *519*, 189–97.
(12) Armstrong, D. W. *Sep. Purif. Methods* **1985**, *14*, 213–304.
(13) Ward, T. J. *Anal. Chem.* **1994**, *66*, 633A–40A.
(14) Bereuter, T. *LC-GC INT.* **1994**, *7*, 78–93.
(15) Nishi, H.; Fukuyama, T.; Terabe, S. *J. Chromatogr.* **1991**, *553*, 503–16.
(16) Otsuka, K.; Terabe, S. *J. Liq. Chromatogr.* **1993**, *16*, 945–53.
(17) Terabe, S.; Miyashita, Y.; Shibata, O.; Barnhart, E. R.; Alexander, L. R.; Patterson, D. G.; Karger, B. L.; Hosoya, K.; Tanaka, N. *J. Chromatogr.* **1990**, *516*, 23–31.
(18) Terabe, S.; Shibata, M.; Miyashita, Y. *J. Chromatogr.* **1989**, *480*, 403–11.
(19) Cole, R. O.; Sepaniak, M. J.; Hinze, W. L.; Gorse, J. *J. Chromatogr.* **1991**, *557*, 113–23.
(20) Nishi, H.; Fukuyama, T.; Matsuo, M.; Terabe, S. *J. Chromatogr.* **1990**, *515*, 233–43.
(21) Otsuka, K.; Kawahara, J.; Tatekawa, K.; Terabe, S. *J. Chromatogr.* **1991**, *559*, 209–14.
(22) Dobashi, A.; Ono, T.; Hara, S.; Yamaguchi, J. *Anal. Chem.* **1989**, *61*, 1986–8.
(23) Otsuka, K.; Terabe, S. *J. Chromatogr.* **1990**, *515*, 221–6.

0003-2700/95/0367-2088$9.00/0 © 1995 American Chemical Society

While the most common chiral selectors are cyclodextrins and their derivatives, many new types of chiral selectors have been introduced such as heparin[24] and the macrocyclic antibiotics rifamycin B,[25] vancomycin,[26] ristocetin A,[27] and teicoplanin.[28] The oligophenolic glycopeptides, vancomycin, ristocetin, and teicoplanin, exhibit exceptional enantioselectivity for many chiral compounds at low selector concentrations. Some of these chiral selectors tend to interact with the capillary walls, causing decreased electroosmotic flow (eof) velocities, increased analysis times, and less than optimum efficiency. Of the three glycopeptides investigated, vancomycin appears to interact most strongly with the capillary wall.[26-28]

In this work we demonstrate the beneficial effect of the addition of sodium dodecyl sulfate (SDS) micelles to vancomycin solutions on the efficiency, analysis time, and resolution of enantiomers. Since the chiral selector binds strongly to the micelle and acts in conjunction with it, previously postulated model systems (i.e., for micelles and cyclodextrins) and treatments are not applicable. An equation is derived to calculate the binding constants of the solutes for the antibiotic–SDS mixed micelles, and the binding constants are compared. This general model and treatment applies to any case where there is association between the micelle and chiral selector. As will be shown in later work, this model and treatment may be more appropriate for the micelle–cyclodextrin system as well.

EXPERIMENTAL SECTION

Materials. All dansyl-amino acids and nonsteroidal antiinflammatory compounds were purchased from Sigma (St. Louis, MO). The sodium hydroxide, potassium hydroxide, and sodium monohydrogen phosphate were purchased from Aldrich (Milwaukee, WI). Vancomycin was provided by ASTEC (Whippany, NJ). Nylon filters, 0.45 μm, were from Alltech (Deerfield, IL). Electrophoresis grade SDS was purchased from Bio-Rad (Richmond, CA).

Methods. Separations were performed using a Beckman P/ACE 2000 with a 50 μm × 37 cm (30 cm to detector) capillary monitored at 254 nm and thermostated at 20 °C. Data were collected and analyzed with System Gold software (Beckman, Palo Alto, CA). The capillary was pretreated daily with 0.5 M potassium hydroxide for 5 min and then flushed with water for 10 min. Run buffer was passed through the column for 10 min prior to beginning the first run. Between runs, the capillary was rinsed with 0.1 M potassium hydroxide, water, and run buffer for 2 min each. Rinsing with potassium hydroxide helps to prevent the buildup of vancomycin on the capillary wall and maintain eof reproducibility. Samples were prepared at ~0.1 mg/mL in 50 mM, pH 7.0 phosphate buffer and injected using the pressure mode at 0.5 psi for 1.0 s. Vancomycin and SDS solutions were prepared by weighing the appropriate amounts of the compounds together in volumetric flasks and diluting with phosphate buffer. Dissolution was aided by sonication, but the solutions were not allowed to warm during sonication since the decomposition of vancomycin is greatly accelerated at temperatures only slightly higher than room temperature. Separations were performed at +5 kV, which is low compared to most CE separations. Operation at higher voltages produced an unstable baseline due to the background absorbance of the selector. In addition, the lifetime of the selector is reduced at higher run voltages because of greater Joule heating. All solutions were filtered with 0.45 μm nylon filters prior to analysis. The eof and micellar velocities were determined using methanol or mesityl oxide as the neutral marker and quinine hydrochloride as the micellar marker.[29] Elution orders were determined by spiking racemic mixtures with the pure single enantiomers. Electrophoretic mobilities were calculated by subtracting the eof mobilities from the measured mobilities.

Table 1. Electrophoretic Data Used in Conjunction with Eq 1 To Calculate the Equilibrium Constant for the Association of Vancomycin with the SDS Micelle[a]

[SDS][b] (mM)	μ_e[c]	$(\mu_f - \mu_i)/(\mu_i - \mu_m)$
0.00	0.32	0.00
3.42	−9.80	0.843
7.14	−14.5	2.03
10.9	−16.3	3.02
18.3	−17.7	4.40

[a] The mobility of the micelle is −21.8 cm²/kV·min. From these data, $K = 253 \pm 15$ and $K_p = 1020$. [b] Concentration of SDS in the micelles. [c] Measured electrophoretic mobility of vancomycin (cm²/kV·min).

The equilibrium constant for the association of vancomycin with SDS was determined by CE by injecting vancomycin into buffer solutions containing various concentrations of SDS and followed by analysis with eq 1. Table 1 gives the experimental data used to calculate K. The partition coefficient is related to the equilibrium constant by the relationship[30] $K = (P - 1)v$, where K is the equilibrium constant, P is the partition coefficient, and v is the molar volume of SDS (0.249 L/mol). The critical micelle concentrations (cmc's) of SDS were measured using a surface tensiometer (Fisher, St. Louis, MO) and found to be 0.3 mM in 50 mM, pH 7 phosphate buffer and 1.3 mM in 2 mM vancomycin–50 mM phosphate buffer.

RESULTS AND DISCUSSION:

While vancomycin exhibits tremendous enantioselectivity for individual anionic and neutral analytes, it has been less successful in completely resolving the enantiomers in complex mixtures of these compounds. This is due to several factors including the high affinity of vancomycin for one of the two enantiomers and the less than optimum CE efficiency due to adsorption of vancomycin on the capillary wall. Figure 1 shows the effect of addition of SDS to the vancomycin run buffer on the separation of a mixture of six dansyl-amino acids. When no SDS is present (Figure 1), the D enantiomers elute together before the L enantiomers and all of the peaks are not completely resolved. In addition, the eof velocity is slow, the analysis time is somewhat longer than necessary, and the efficiency is on the order of 10^4 plates. It should be noted that the analysis time can be reduced and the efficiency can be improved somewhat if the buffer concentration is increased from 50 to 100 mM phosphate, but all compounds shown in Figure 1 will still not be completely

(24) Stalcup, A. M.; Agyei, N. M. *Anal. Chem.* **1994**, *66*, 3054–9.
(25) Armstrong, D. W.; Rundlett, K.; Reid, G. *Anal. Chem.* **1994**, *66*, 1690–5.
(26) Armstrong, D. W.; Rundlett, K. L.; Chen, J. R. *Chirality* **1994**, *6*, 496–509.
(27) Armstrong, D. W.; Gasper, M. P.; Rundlett, K. L. *J. Chromatogr., A* **1995**, *689*, 285–304.
(28) Rundlett, K. L.; Gasper, M. P.; Zhou, E.; Armstrong, D. W. *Chirality*, in press.
(29) Terabe, S. *Micellar Electrokinetic Chromatography*; Beckman Instruments Inc.: Fullteron, CA, 1992; p 12.
(30) Berezin, I. V.; Martinek, K.; Yatsimerskii, A. K. *Russ. Chem. Rev.* **1973**, *42*, 787–802.

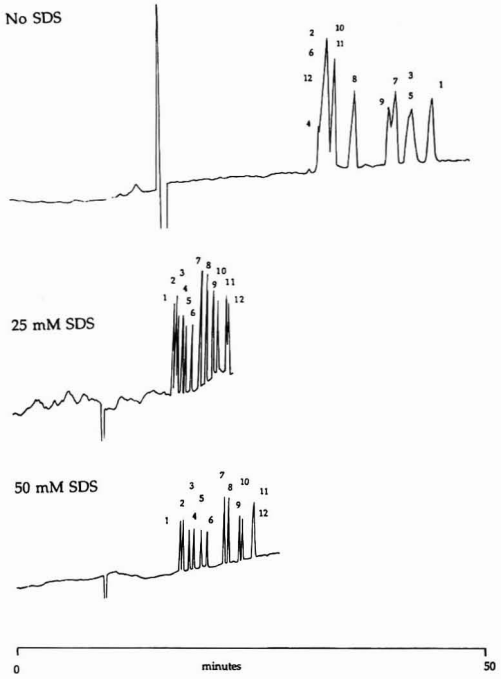

Figure 1. Electropherograms showing the effect of SDS on the enantiomeric separation of dansyl-D,L-amino acids. All separations were performed with 2 mM vancomycin in 50 mM, pH 7.0 phosphate buffer at 20 °C. The capillary was 50 μm × 30 cm (37 cm total length), the run voltage was +5 kV, and the solutes were detected at 254 nm. Peak designations: 1, (L)-α-amino-*n*-butyric acid; 2, (D)-α-amino-*n*-butyric acid; 3, (L)-valine; 4, (D)-valine; 5, (L)-norvaline; 6, (D)-norvaline; 7, (L)-leucine; 8, (D)-leucine; 9, (L)-norleucine; 10, (D)-norleucine; 11, (L)-tryptophan; 12, (D)-tryptophan.

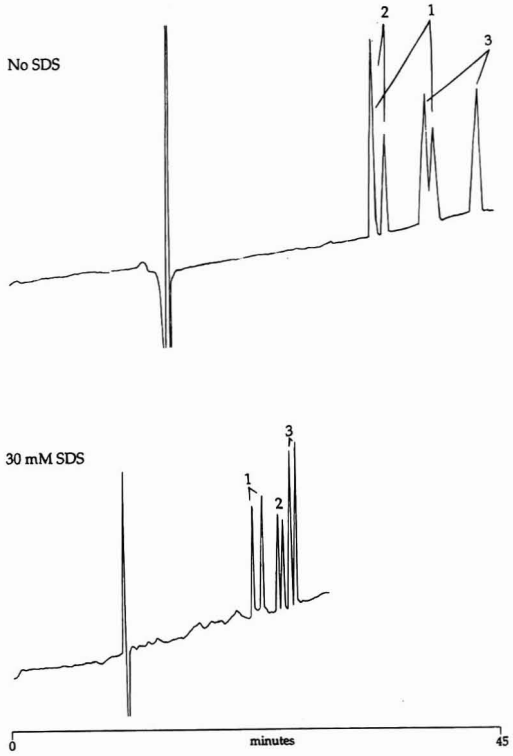

Figure 2. Electropherograms showing the effect of SDS concentration on the enantiomeric separation of nonsteroidal antiinflammatory compounds. See Figure 1 for experimental details. Peak designations: 1, ketoprofen; 2, indoprofen; 3, flurbiprofen.

separated. The buffer concentration for this study was chosen for optimum separation conditions for the SDS systems. The same phenomenon is demonstrated in Figure 2 for nonsteroidal anti-inflammatory compounds.

When SDS is added to the run buffer containing vancomycin, the efficiency improves by 1 order of magnitude, the eof velocity increases, and the analysis time decreases. These improvements in separation conditions are due in large part to the interaction between the positively charged vancomycin and the negatively charged SDS, which reduces the interaction of vancomycin with the capillary walls. However, from this information alone it cannot be determined whether vancomycin associates with the micelles or whether it forms ion pairs with the surfactant monomers.

Other notable features of the electropherograms in Figure 1 are the change in relative elution order of the amino acid derivatives and the reversal of elution order for all enantiomers that occurs when SDS is added. The relative elution order of the compounds changes from one based on electrophoretic mobility in the vancomycin system to an elution order based on partitioning to the SDS micelle. The reversal of elution order of enantiomers can be attributed to the change in the electrophoretic mobility of vancomycin that occurs when vancomycin complexes with the SDS micelle. The extent of this interaction was measured (Table 1), and the partition coefficient for vancomycin to SDS micelles was found to be 1020. Using this value and the molar volume of SDS as 0.249 L/mol,[6] ~90% of the vancomycin is bound to SDS under these experimental conditions. (This value is only an approximation since the binding constant was calculated from data at near-infinite dilution conditions for vancomycin while the CE enantioseparations with mixed micelles were not conducted under these exact conditions.) Figure 3 is a pictorial model of the system studied. At pH 7, vancomycin carries a slight positive charge and migrates toward the cathode with the eof (Figure 3A).[26] The carboxylic acid enantiomers migrate in the opposite direction, and upon complexation with vancomycin, they travel faster through the capillary. Therefore, the enantiomers that interact most strongly with vancomycin (e.g., the D enantiomers of amino acids) elute first. Upon binding to SDS (Figure 3B), the mobility of vancomycin changes from positive (i.e., migration in the same direction as the eof) to negative (migration against the eof). Because the electrophoretic mobility of the vancomycin–SDS mixed micelle is now more negative than the analytes, complexation of the analytes with the selector now retards the migration of the analytes through the capillary and the D enantiomer elutes last. The simple mechanism, in which vancomycin associates with the micelle rather than with the monomers, explains the reversal of enantiomeric retention order in this system. It also provides a very easy way for the analyst to reverse the retention order of enantiomers. Figure 3C shows the complete partitioning or binding behavior of a carboxylic acid analyte among the three

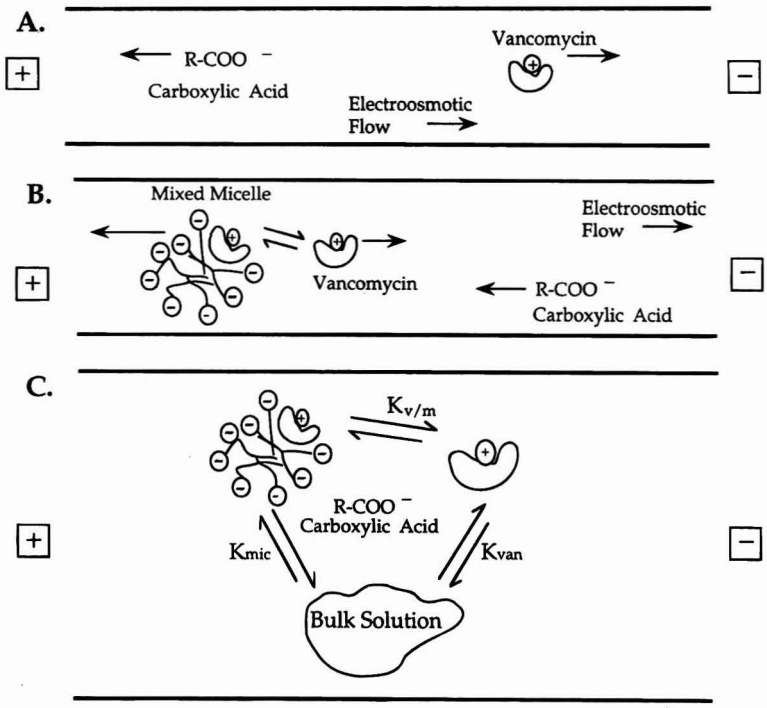

Figure 3. Representation of the electrophoretic mobilities of the analytes, chiral selector and mixed micelles in (A) buffer containing vancomycin (relative migration times: $t_{vancomycin} < t_{eof} < t_{acid}$) and (B) buffer containing vancomycin and SDS (relative migration times: $t_{eof} < t_{acid} < t_{vancomycin} < t_{SDS}$). Note that the migration time of vancomycin changes from ~8.8 min in phosphate buffer to 33.8 min in 21 mM SDS. (C) Shows the equilibria of acid analytes (between the bulk solution and free vancomycin or mixed micelle) considered for derivation of eq 6.

pseudophases: the bulk solution, the mixed micelle, and the free selector. It cannot be ascertained from these data whether the solute partitions directly to the mixed micelles or whether the vancomycin–solute complex partitions to the micelle together. It is likely that both can occur. This pseudophase model, as well as those proposed for other CE systems, is analogous to those used for some time with a variety of separation methods.[6,31,32]

Table 2 lists the effects of SDS and vancomycin concentrations on the resolution, eof times, migration times, and mobilities of enantiomers of dansyl-amino acids and nonsteroidal antiinflammatory compounds. At 2 mM vancomycin and concentrations of SDS less than 20 mM, there were large system peaks and an unstable baseline. The eof times were quite long (~15 min) in the buffer containing vancomycin, and the eof times showed more variation than with the SDS + vancomycin systems. The eof time was reduced to ~9 min (which is close to the eof time in phosphate buffer) in the presence of SDS. Compared to phosphate buffer alone, the effective mobilities of the analytes are less negative in the buffer containing vancomycin (indicating faster migration toward the detector). As the concentration of SDS increases, the migration times of the analytes increase and the effective mobilities become more negative as the compounds partition into the micelles. Figure 4 shows the effect of SDS concentration on the resolution of dansyl-norvaline. The enantioresolutions obtained with the buffer containing only vancomycin are far greater than those in analogous systems containing micelles. The resolution drops dramatically when SDS is first added and then gradually increases with increasing SDS concentration. For most compounds, the resolution then goes through a maximum (at ~49 mM for most compounds) and then decreases at high micelle concentrations. The decrease in enantioresolution with SDS may be due to the competition of SDS monomer with the analyte for the chiral selector. The enantioresolutions of dansyl-tryptophan and dansyl-phenylalanine, the amino acids having the greatest affinity for SDS, decrease with increasing SDS concentration.

The equation developed to calculate binding constants for a 1:1 association for solutes to a single ligand is

$$K_m[M] = \left(\frac{\mu_f - \mu_a}{\mu_a - \mu_m}\right) \quad (1)$$

where K_m is the equilibrium constant for a solute to a ligand, M. Also, μ_f and μ_m are the electrophoretic mobilities of the free solute and of solute bound to the ligand, and μ_a is the measured electrophoretic mobility of a solute in a buffer containing free ligand concentration [M]. This relationship was first used for calculation of equilibrium constants by conventional elec-

(31) Armstrong, D. W.; Fendler, J. H. *Biochim. Biophys. Acta* **1977**, *478*, 75–80.
(32) Berthod, A.; Armstrong, D. W.; Meyers, M. N.; Giddings, J. C. *Anal. Chem.* **1988**, *60*, 2138–41.

Table 2. Resolution, Analysis Times, and Mobilities of Enantiomers Separated with SDS–Vancomycin Buffers

compound	SDS concn (mM)	vancomycin concn (mM)	resoln	t_{eof} (min)	t_1 (min)	t_2 (min)	μ_{e1} ($cm^2/kV \cdot min$)	μ_{e2} ($cm^2/kV \cdot min$)
flurbiprofen	0	0		9.3	16.4	16.4	−10.2	−10.2
	0	2.0	3.3	14.9	42.1	47.9	−9.7	−10.3
	21	2.0	0.9	9.5	19.0	19.2	−11.7	−11.8
	36	2.0	1.0	9.4	21.3	21.7	−13.2	−13.4
	49	2.0	1.1	9.5	24.4	24.8	−14.3	−14.4
	49	0		9.4	23.2	23.2	−14.0	−14.0
	103	2.0	0.9	9.6	37.0	37.6	−17.1	−17.2
ketoprofen	0	0		9.2	15.5	15.5	−9.7	−9.7
	0	2.0	6.2	15.1	36.0	43.0	−8.5	−9.5
	21	2.0	1.7	9.5	17.4	17.8	−10.6	−10.6
	36	2.0	2.3	9.4	18.8	19.5	−11.8	−12.2
	49	2.0	3.2	9.5	20.8	21.7	−12.7	−13.1
	49	0		9.4	19.7	19.7	−12.3	−12.3
	103	2.0	2.7	9.6	29.2	30.5	−15.5	−15.5
carprofen	0	0		9.2	15.7	15.7	−9.9	−9.9
	0	2.0	1.9	14.7	37.7	40.1	−9.2	−9.6
	21	2.0	1.3	9.5	23.7	24.1	−14.0	−14.2
	36	2.0	1.3	9.4	29.1	29.4	−16.0	−16.1
	49	2.0	1.5	9.5	36.4	37.2	−17.3	−17.4
	49	0		9.4	39.7	39.7	−18.0	−18.0
	103	2.0	0.0	9.4	55.0	55.0	−19.6	−19.6
indoprofen	0	0		9.2	14.9	14.9	−9.3	−9.3
	0	2.0	2.0	19.0	55.7	58.8	−7.7	−7.9
	21	2.0	1.0	9.5	18.3	18.5	−11.2	−11.4
	36	2.0	1.0	9.4	20.6	20.9	−12.8	−13.0
	49	2.0	1.2	9.4	23.4	23.8	−14.1	−14.3
	49	0.0		9.4	22.2	22.2	−13.6	−13.6
	103	2.0	1.0	9.5	35.3	35.7	−17.1	−17.1
suprofen	0	0		9.2	15.5	15.5	−9.9	−9.9
	0	2.0	2.4	17.3	54.0	58.4	−8.7	−9.0
	21	2.0	0.0	9.8	16.7	16.7	−9.4	−9.4
	36	2.0	0.5	9.4	18.4	18.6	−11.6	−11.7
	49	2.0	0.5	9.5	20.1	20.3	−12.3	−12.4
	49	0		9.5	18.7	18.7	−11.8	−11.8
	103	2.0	0.5	9.6	26.9	27.2	−14.9	−15.0
dansyl-valine	0	0		9.4	14.4	14.4	−8.3	−8.3
	0	2.0	9.1	16.5	37.7	50.6	−7.6	−9.1
	21	2.0	2.1	9.4	16.5	16.9	−10.2	−10.5
	36	2.0	2.1	9.4	18.5	19.1	−11.6	−12.0
	49	2.0	2.2	9.6	21.9	22.6	−13.0	−13.3
	49	0		8.9	20.4	24.9	−14.1	−14.1
	103	2.0	1.9	9.4	31.0	31.9	−16.5	−16.7
dansy-tryptophan	0	0		9.1	13.3	13.3	−7.8	−7.8
	0	2.0	1.0	18.4	38.6	41.1	−6.3	−6.7
	21	2.0	0.5	9.5	20.2	20.4	−12.4	−12.5
	36	2.0	0.5	9.4	25.0	25.2	−14.7	−14.8
	49	2.0	0.0	9.6	31.8	31.8	−16.1	−16.1
	49	0		9.1	34.3	34.3	−17.9	−17.9
	103	2.0	0.0	9.4	47.8	47.8	−19.0	−19.0
dansyl-norleucine	0	0		9.4	14.3	14.3	−8.1	−8.1
	0	2.0	6.0	19.8	50.7	65.3	−6.8	−7.8
	21	2.0	1.8	9.5	19.1	19.6	−11.7	−12.0
	36	2.0	1.7	9.4	23.8	24.2	−14.3	−14.4
	49	2.0	1.2	9.6	29.3	29.8	−15.5	−15.7
	49	0		9.0	31.1	31.1	−17.5	−17.5
	103	2.0	0.4	9.4	44.8	45.1	−18.7	−18.7
dansyl-norvaline	0	0		9.4	14.4	14.4	−8.3	−8.3
	0	2.0	9.8	19.1	43.8	62.5	−6.6	−8.1
	21	2.0	1.8	9.7	17.9	18.5	−10.5	−10.9
	36	2.0	2.4	9.5	19.9	20.7	−12.2	−12.6
	49	2.0	2.3	9.5	23.1	23.9	−13.8	−14.1
	49	0		9.0	22.7	22.7	−14.9	−14.9
	103	2.0	1.7	9.4	34.3	35.1	−17.1	−17.3
dansyl-leucine	0	0		9.4	14.2	14.2	−8.0	−8.0
	0	2.0	4.9	18.4	42.1	48.1	−6.8	−7.4
	21	2.0	2.6	9.6	18.4	19.0	−11.1	−11.4
	36	2.0	2.0	9.4	21.8	22.5	−13.4	−13.8
	49	2.0	1.6	9.5	26.3	27.0	−14.9	−15.1
	49	0.0		8.9	26.3	26.3	−16.5	−16.5
	103	2.0	1.0	9.4	41.2	41.8	−18.2	−18.3
dansyl-α-amino-*n*-butyric acid	0	0		9.1	14.7	14.7	−9.2	−9.2
	0	2.0	9.8	18.2	37.9	51.7	−6.3	−7.9
	21	2.0	0.8	9.4	16.0	16.2	−9.7	−9.9
	36	2.0	1.4	9.4	17.8	18.1	−11.1	−11.4
	49	2.0	1.4	9.5	19.9	20.3	−12.2	−12.4
	49	0		9.4	21.1	21.1	−13.1	−13.1
	103	2.0	1.2	9.5	27.9	28.4	−15.4	−15.6
dansyl-phenylalanine	0	0		9.4	14.4	14.4	−8.3	−8.3
	0	2.0	9.8	19.1	43.8	62.5	−6.6	−8.1
	21	2.0	1.8	9.7	17.9	18.5	−10.5	−10.9
	36	2.0	2.4	9.5	19.9	20.7	−12.2	−12.6
	49	2.0	2.3	9.5	23.1	23.9	−13.8	−14.1
	49	0		9.0	22.7	22.7	−14.9	−14.9
	103	2.0	1.7	9.4	34.3	35.1	−17.1	−17.3

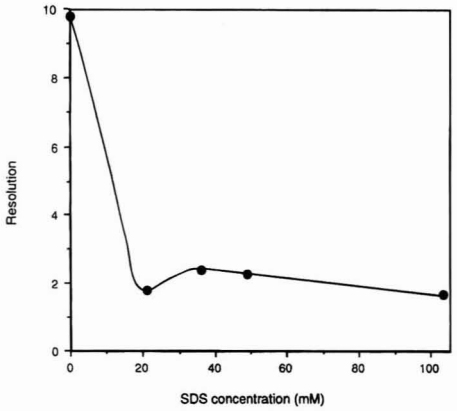

Figure 4. Plot of the resolution of enantiomers of dansyl-norvaline as a function of SDS concentration. All separations were performed using 2 mM SDS in 50 mM, pH 7.0 phosphate buffer. See Figure 1 for more details.

trophoresis[33–38] and subsequently reintroduced for capillary electrophoresis.[1,2,39–41] This equation cannot be used to calculate the binding constants of solutes in this system since it is limited to a single binding scenario where the solute associates only with one selector or ligand. It does not consider the binding of solutes to both free and micellized vancomycin. It also cannot be used to describe systems where the solute binds or partitions to more than one ligand or selector, such as a selector–pseudophase complex. A more general mathematical treatment must account for the existence of both the free selector and pseudophase-associated selector. In essence, a variation on the original three-phase model for pseudophase separations is needed to properly describe this and analogous systems.[5,12]

The binding constants for the solutes to the mixed-micelle system were calculated by considering the different mobilities of an analyte in aqueous buffer, bound to vancomycin–SDS mixed micelles and bound to free unmicellized vancomycin, respectively. Following the derivation of eq 1,[33–41] the measured mobility, μ_a, can be considered to be a weighted average of the mobilities of the analyte in each phase:

$$\mu_a = \chi_f \mu_f + \chi_v \mu_v + \chi_m \mu_m \quad (2)$$

where χ_f, χ_m, and χ_v are the mole fractions of the solute in the aqueous, vancomycin, and mixed-micelle phases. μ_f is the mobility of free solute in the aqueous phase, μ_v is the mobility of the solute–vancomycin complex, and μ_m is the solute–mixed-micelle mobility. Equation 2 can be written in terms of the equilibrium concentrations of the solute in each phase:

$$\mu_a = \frac{[A]_f}{[A]_f + [A]_v + [A]_m}\mu_f + \frac{[A]_v}{[A]_f + [A]_v + [A]_m}\mu_v + \frac{[A]_m}{[A]_f + [A]_v + [A]_m}\mu_m \quad (3)$$

where $[A]_f$, $[A]_v$, and $[A]_m$ are the equilibrium concentrations of solute in free aqueous solution, bound to unmicellized vancomycin, and bound to the mixed micelle, respectively. The equilibrium constant expressions for solute binding with vancomycin, K_{van}, and binding with the vancomycin–SDS micelle, K_{mic}, can be substituted into eq 3:

$$K_{mic} = [A]_m/[A]_f[M]_f \quad (4)$$

$$K_{van} = [A]_v/[A]_f[V]_f \quad (5)$$

The equation can be rearranged to give

$$K_{mic} = \frac{1}{[M]_f}\left(\frac{\mu_f - \mu_a}{\mu_a - \mu_m}\right) + \frac{K_{van}[V]_f}{[M]_f}\left(\frac{\mu_v - \mu_a}{\mu_a - \mu_m}\right) \quad (6)$$

$[M]_f$ is the equilibrium concentration of micelle not bound to solute, and $[V]_f$ is the equilibrium concentration of free unmicellized vancomycin. $[V]_f$ was calculated from the partition coefficient of vancomycin between aqueous solution and SDS micelles and from the SDS concentration and molar volume (see Table 1). This equation assumes a 1:1 association between the analyte and vancomycin[42,43] and that the equilibrium constants remain unchanged in all systems studied. When compared to eq 1, eq 6 reveals that an additional term is needed when the chiral selector exists in both free and bound states (which occurs in the case of glycopeptide antibiotics with micelles). This equation may also be used in other cases, which will be discussed subsequently.

Equations 1 and 6 require the measurement of μ_v, the mobility of the unmicellized vancomycin–solute complex, which is usually measured as the limiting mobility reached at high selector concentration (i.e., at complete saturation of analyte with selector). Wall adsorption of vancomycin and changes in the solution properties at high concentrations result in unreliable values of μ_v if this method is used. Therefore, μ_v was approximated using compounds of known charge and molecular weight along with the relationship for peptides:[44]

$$\mu \propto f/M^{2/3} \quad (7)$$

f is the fraction of charge on the compound, and M is the molecular weight. μ_v was estimated by plotting the mobility vs $f/M^{2/3}$ for standards of known charge and molecular weight. The fraction of charge values for vancomycin and analytes were calculated from the determined mobility and known molecular weights. The mobility of the complex was calculated from

$$\mu \propto (f_1 + f_2)/(M_1 + M_2)^{2/3} \quad (8)$$

where f_1 and f_2 are the fractions of charge on the selector and solute and M_1 and M_2 are the molecular weights of selector and complex. All the data and other information used for this method are given in Table 3. Also, the reproducibility of the determined slopes and intercepts is indicated in Table 3C. The values of the complex mobility, μ_v, were determined from eq 8 and used in eqs 1 and 6.

(33) Tiselius, A. *Nova Acta Reg. Soc. Sci. Uppsaliensis, Ser. IV* **1930**, *7*, 1–107.
(34) Alberty, R. A.; King, E. L. *J. Am. Chem. Soc.* **1951**, *73*, 517–23.
(35) Jokl, V. *J. Chromatogr.* **1964**, *13*, 451–8.
(36) Jokl, V. *J. Chromatogr.* **1972**, *71*, 523–31.
(37) Yavada, P. C.; Ghouse, A. K.; Yavada, K. L.; Dey, A. K. *Chromatographia* **1976**, *9*, 410–2.
(38) Sakanoue, M.; Nakatani, M. *Bull. Chem. Soc. Jpn.* **1972**, *45*, 3429–33.
(39) Guttman, A.; Paulus, A.; Cohen, S.; Grinberg, N.; Karger, B. L. *J. Chromatogr.* **1988**, *488*, 41–53.
(40) Wren, S. A. *J. Chromatogr.* **1993**, *636*, 57–62.
(41) Wren, S. A.; Rowe, R. C. *J. Chromatogr.* **1992**, *603*, 235–41.
(42) Perkins, H. R. *Biochem. J.* **1969**, *111*, 195–205.
(43) Popieniek, P. H.; Pratt, R. F. *J. Am. Chem. Soc.* **1988**, *110*, 1285–6.
(44) Compton, B. J.; O'Grady, E. A. *Anal. Chem.* **1991**, *63*, 28–33.

Table 3. Representative Data Treatment for the Calculation of the Mobilities of the Complex Formed from Selector and Solute Using Equations 7 and 8

A. Standards

compound	K_a	f[a]	MW[b]	$1/t$[c]	$(f/M^{2/3})$[d]	slope[e]	intercept[e]
ephedrine	7.25×10^{-11}	+0.999	166.2	0.1587	0.03304		
phenol	1.28×10^{-10}	−0.0013	93.1	0.1134	-6.32×10^{-5}		
o-toluic acid	1.22×10^{-4}	−0.999	135.1	0.05112	−0.03794		
2-naphthoic acid	6.8×10^{-5}	−0.999	171.2	0.04890	−0.03240	1.605	0.1080

B. Solute and Selector

compound	$1/t$[c]	$(f/M^{2/3})$[f]	MW[b]	f[g]	$(f/M^{2/3})_{complex}$[h]	$\mu_{complex}$[i]
dansyl-valine	0.07698	−0.01933	349	−0.958		
vancomycin	0.1145	0.004050	1449	+0.522		
dansyl-valine−vancomycin					-2.95×10^{-3}	−1.05

C. Fraction of Charge, f, Calculated for Analyte Ions from Equation 7

compound	MW	$1/t$	slope[j]	intercept[k]	f[f]
flurbiprofen	244	0.0668	1.602	0.1074	−0.989
carprofen	273	0.0687	1.602	0.1074	−1.00
ketoprofen	254	0.0704	1.602	0.1074	−0.927
naproxen	230	0.0664	1.602	0.1074	−0.961
indoprofen	281	0.0723	1.599	0.1077	−0.950
dansyl-methionine	383	0.0772	1.605	0.1077	−1.00
dansyl-norleucine	363	0.0775	1.605	0.1077	−0.958
dansyl-α-amino-*n*-butyric acid	335	0.0760	1.605	0.1080	−0.963
dansyl-norvaline	349	0.0772	1.605	0.1080	−0.953
dansyl-tryptophan	436	0.0790	1.603	0.1079	−1.00
dansyl-leucine	363	0.0760	1.605	0.1076	−1.00
vancomycin	1449	0.1145	1.605	0.1080	+0.522

[a] The fraction of charge, f, was calculated from K_a. [b] Molecular weight of the ions. [c] t is the migration time measured in minutes. $1/t$ is proportional to mobility. [d] Calculated from charge and molecular weight of ion. [e] Slope and intercept from plot of $1/t$ vs $(f/M^{2/3})$ ($r^2 = 0.995$). [f] Determined from measured migration time and slope and intercept in (A). [g] Fraction of charge determined experimentally. [h] Complex $f/M^{2/3}$ calculated from the experimentally determined f and known MW. [i] Electrophotetic mobility of complex (in cm²/kV·min). The eof mobility has been subtracted. [j] Average slope, 1.603 ± 0.002. [k] Average intercept, 0.1077 ± 0.0002.

Table 4. Representative Calculation of the Binding Constants for Dansyl-leucine to the Mixed Micelles Using Equation 6

compound	μ_a[a]	μ_f[b]	μ_{mic}[c]	μ_v[d]	[M][e]	$[V_f]$[f]	K_{van}[g]	K_{mic}[h]
dansyl-L-leucine	−15.09	−7.98	−18.01	−1.05	50.6	0.15	19 ± 1	48 ± 3
dansyl-D-Leucine	−15.31	−7.98	−18.01	−1.05	50.6	0.15	68 ± 5	55 ± 4

[a] Measured electrophoretic mobility of solute in mixed micelle system. [b] Electrophoretic mobility of free solute measured in phosphate buffer. [c] Electrophoretic mobility of mixed micelle. [d] Electrophoretic mobility of vancomycin:solute complex (see Table 3). [e] Mixed micelle concentration (in mM). [f] Free vancomycin concentration (in mM) calculated from the partition coefficient of vancomycin between aqueous solution and micelles (see Table 1). [g] Binding constant of solute to vancomycin (see Table 5). The listed uncertainties were calculated from the standard deviations in the binding constants calculated at different vancomycin concentrations. [h] Binding constant of solute to mixed micelle. The uncertainties were calculated from the uncertainties in K_{van}. Experimental conditions are the same as in Table 5.

It should be noted that there are other possible ways to estimate the value of the vancomycin−solute complex mobility, μ_v. Perhaps the best of these is linear[45] or nonlinear[46,47] plotting and curve fitting of the CE binding isotherm. Other possible approaches include devising a special wall-coated capillary that does not interact with vancomycin or adding the solute to the run buffer and injecting vancomycin. Both of these latter methods assume that the experimental limitations of background UV absorbance and devising an inert coating can be overcome.

Equation 1 was used to calculate the binding constants of solutes to vancomycin, K_{van}, and to SDS micelles, K_{SDS}. In the vancomycin system, the solute concentration was significant compared to the vancomycin concentration so that the free vancomycin concentration could not be estimated as the added concentration. Therefore, an iterative procedure was used to calculate the free selector concentration and binding constants.[48] The binding constants to the mixed micelle, K_{mic}, were calculated with eq 6, and representative data and treatments are given in Table 4. The concentration of all species forming the mixed micelles, $[M]_f$, was estimated as the sum of the SDS concentration in the micelles ($C_{added} - C_{cmc}$) and the micellar bound vancomycin concentration. The migration times used to calculate the electrophoretic mobilities were adjusted to the same reference state using the eof times as described previously.[41,46]

For the vancomycin system, uncorrected electrophoretic mobilities were used to calculate the equilibrium constant, K_{van}. While it has been reported that calculation of binding constants from electrophoretic data for cyclodextrin ligands requires a

(45) Rundlett, K. L., Armstrong, D. W. *J. Chromatogr., A.*, in press.

(46) Shibukawa, A.; Lloyd, D. K.; Wainer, I. W. *Chromatographia* **1993**, *35*, 419–29.

(47) Penn, S. G.; Bergström, E. T.; Goodall, D. M.; Loran, J. S. *Anal. Chem.* **1994**, *66*, 2866–73.

(48) Connors, K. A. *Binding Constants. The Measurement of Molecular Complex Stability*; Wiley: New York, 1987; pp 42–3.

Table 5. Equilibrium Constants Calculated for Solutes with SDS Systems, Vancomycin Systems, and Mixed-Micelle Systems[a]

	equilibrium constants[b] (M^{-1})						
		K_{van}			K_{mic}[c]		
compound	K_{SDS}	K_1	K_2	α	K_1	K_2	α
dansyl-α-amino-*n*-butyric acid	8.8	146	9.7	15.1	16	14	1.2
dansyl-leucine	35	68	19	3.6	55	48	1.1
dansyl-tryptophan	72	83	78	1.1	107	107	1.0
dansyl-methionine	21	127	20	6.4	31	28	1.1
dansyl-norvaline	20	144	22	6.6	33	28	1.2
dansyl-valine	12	143	13	11.0	25	21	1.2
dansyl-norleucine	50	118	32	3.7	81	73	1.1
ketoprofen	6.3	99	28	3.5	16	12	1.3
suprofen	4.4	32	16	2.0	10	10	1.0
carprofen	80	120	95	1.2	296	232	1.3
flurbiprofen	12	121	81	1.5	26	24	1.1
naproxen	4.5	43	17	2.6	12	11	1.1
indoprofen	13	79	71	1.1	28	26	1.1

[a] All measurements were made in 50 mM phosphate buffer, pH 7.0. See the Experimental Section for further details. [b] The uncertainties, calculated from the standard deviations of the data, varied from 1 to 25% relative. Most uncertainties were 10% or less. [c] These binding constants were estimated from a single mixed-micelle composition of 2 mM vancomycin−49 mM SDS.

correction for solution viscosity,[41,46] these corrections were not made with the vancomycin system. Low concentrations of vancomycin were used to calculate the binding constants and the current changed very little over the vancomycin concentration range. In 50 mM, pH 7.0 phosphate buffer, the currents were 18.9, 19.1, 18.9, and 18.8 μA for 0, 0.61, 1.1, and 1.5 mM vancomycin, respectively. However, the eof time changed dramatically over this same at concentration range (from ~8.7 min in phosphate buffer to 14 min in 1.5 mM vancomycin) due to wall adsorption of vancomycin. Therefore, migration times cannot be used directly to calculate the binding constants and a neutral marker, which is used to correct for changes in solution viscosity, cannot be used to correct the mobilities to a desired reference state. Since there is little change in run current (and presumably solution viscosity) uncorrected electrophoretic mobilities were used to calculate binding constants to vancomycin.

It should be noted that the binding constants to vancomycin are calculated by assuming that the solute interaction with the wall-bound vancomycin is negligible. In calculating the mixed-micelle binding constants listed in Table 5, the second term on the right side of eq 6 is small compared to the first term due to the low free vancomycin concentration. Therefore, neglect of the wall interactions has little effect on the K_{mic} values.

Enantioselectivities were calculated from the binding constants:

$$\alpha = K_1/K_2 \tag{9}$$

Table 5 lists the binding constants and selectivities calculated for the analytes with SDS, vancomycin, and the mixed micelle. The presence of vancomycin appears to increase the affinity of the negatively charged analytes for the negatively charged micelle for all analytes studied. The binding constants for the analytes to vancomycin are much larger than those to the SDS micelle. Also, the analyte binding to the mixed micelle is closer to that of the SDS micelle than to vancomycin. It appears that the repulsion between the negatively charged SDS and the analyte in the mixed system is a significant factor in the association equilibria. The enantioselectivities exhibited by vancomycin for many analytes are quite large; for example, α = 15.1 for dansyl-α-amino-*n*-butyric acid and 11.0 for dansyl-valine. However, these enantioselectivities decrease in the presence of SDS to 1.2 for both compounds. Clearly the benefits of shorter analysis time and improved efficiency provided by the SDS are gained at the expense of enantioselectivity.

Equation 3 can be expressed in a general form to include all possible types of interactions between the solute and i number of species capable of binding with the solute:[33]

$$\mu_{measured} = \frac{\sum[A]_i \mu_i}{\sum[A]_i} = \frac{[A]_1 \mu_1 + [A]_2 \mu_2 + ... + [A]_i \mu_i}{[A]_1 + [A]_2 + ... + [A]} \tag{10}$$

Substituting expressions for the equilibrium constants into eq 10 allows it to be used to determine the binding constants for a system containing many species that interact with the analyte. This relationship assumes that the equilibrium constants remain constant in all systems. Some examples of other systems where this relationship could be used include those where the solute binds to both a free and wall-bound selector (essentially a type of stationary phase), where two or more chiral selectors are used in conjunction (for example, cyclodextrins with crown ethers), or where any combination of chiral selector and surfactant is used with analytes that also partition to the bulk solution.

CONCLUSIONS

Four basic factors were addressed in this paper. First, a practical and simple approach was described for enhancing efficiency, decreasing analysis time, and controlling enantiomeric elution order. Second, a general model that described this system and many other pseudophase systems in CE was proposed and supported. Third, this model provided a unified approach for the use of secondary equilibria and pseudophase systems in both CE and other separation methods that utilized these approaches over of the last two decades. Finally, it was clearly shown that migration times should not directly be used to calculate association constants in CE and that neutral marker molecules cannot be used to correct mobilities for changes in solution viscosity in some cases.

ACKNOWLEDGMENT

Support of this work by the Department of Energy, Office of Basic Sciences (Grant DE FG02 88ER13819) is gratefully acknowledged. Thanks are extended to Dr. Nuran Ercal for the use of the P/ACE 2000 capillary electrophoresis unit.

Received for review January 26, 1995. Accepted April 21, 1995.[⊗]

AC950091W

[⊗] Abstract published in *Advance ACS Abstracts,* June 1, 1995.

Anal. Chem. **1995,** *67,* 2096–2102

Extraction of Organic Pollutants from Solid Samples Using Microwave Energy

Viorica Lopez-Avila,* Richard Young, Janet Benedicto, Pauline Ho, and Robert Kim

Midwest Research Institute, California Operations, 625-B Clyde Avenue, Mountain View, California 94043

Werner F. Beckert

U.S. Environmental Protection Agency, Environmental Monitoring Systems Laboratory, 944 East Harmon Avenue, Las Vegas, Nevada 89119

This study, which is part of an ongoing U.S. Environmental Protection Agency (EPA) research program, carried out by the Environmental Monitoring Systems Laboratory—Las Vegas, addresses new sample preparation techniques that (a) prevent or minimize pollution in analytical laboratories, (b) improve target analyte recoveries, and (c) reduce sample preparation costs. We present here additional evaluation results of the microwave-assisted extraction (MAE) procedure (described previously in this journal) for 187 compounds and four Aroclors listed in the EPA Methods 8250, 8081, and 8141A. Our results demonstrate that most of these compounds can be recovered in good yields from the matrices investigated. For example, recoveries ranged from 80 to 120% for 79 of the 95 compounds listed in Method 8250, 38 of the 45 organochlorine pesticides listed in Method 8081, and 34 of the 47 organophosphorus pesticides listed in Method 8141A. When recoveries from freshly spiked soil samples were compared with those from aged samples, we found that recoveries usually decreased; as expected, there was more spread in recoveries with increased aging time. For 15 compounds in a reference soil, the recoveries of 14 compounds by MAE were equal to or better than recoveries obtained by Soxhlet extraction (naphthalene being the exception); for selected organochlorine pesticides, recoveries from spiked soil samples were at least 7% higher for MAE than for either Soxhlet or sonication extraction.

In earlier studies,[1–3] we investigated a microwave-assisted extraction (MAE) technique for extracting polynuclear aromatic hydrocarbons and some base/neutral/acidic compounds, of interest to the U.S. Environmental Protection Agency (EPA), from certified reference soils and marine sediments. These materials were subjected to MAE in a closed-vessel microwave system with hexane–acetone (1:1) as the extraction solvent at 80, 115, or 145 °C for 5, 10, or 20 min. For comparison, the same samples were subjected to (i) room temperature extraction by allowing the solvent mixture to stay in contact with the solid matrix the same amount of time as the microwave-extracted sample (including any cooling time) and (ii) simple heating with solvent in a closed container using a convection oven.[3] Our results indicated that MAE compares favorably with Soxhlet/Soxtec and sonication extraction techniques. Moreover, MAE requires smaller volumes of organic solvents than the conventional techniques, and sample processing time is increased by shorter extraction times (10 min) and simultaneous extraction of up to 12 samples.

In this study, which is part of an ongoing EPA program, carried out by the Environmental Monitoring Systems Laboratory (Las Vegas, NV), to evaluate sample preparation techniques that (a) prevent or minimize pollution in analytical laboratories, (b) improve target analyte recoveries, and (c) reduce sample preparation costs, we have evaluated the extractability under MAE conditions of 95 compounds (including six surrogate compounds) listed in Method 8250,[4] 45 organochlorine pesticides (OCPs) and four Aroclors listed in Method 8081,[5] and 47 organophosphorus pesticides (OPPs) listed in Method 8141A.[6] Freshly spiked soil samples, spiked soil samples that were aged for 24 h, 14 days, or 21 days, and a few standard reference materials were extracted with hexane–acetone (1:1) at 115 °C for 10 min. The extracts were analyzed by gas chromatography/mass spectrometry (GC/MS), gas chromatography with electron capture detection (GC/ECD), or gas chromatography with nitrogen-phosphorus detection (GC/NPD), as specified in the respective EPA methods.

We present here the recovery data for 187 compounds (including six surrogate compounds) and four Aroclors listed in Methods 8250, 8081, and 8141A. These compounds were spiked into topsoil samples, and the samples were either extracted immediately or aged for 24 h, 14 days, or 21 days and then extracted by MAE.

EXPERIMENTAL SECTION

Microwave-Assisted Extraction Procedure. All MAEs were performed with a MES-1000 microwave sample extraction system (CEM Corp., Matthews, NC) described in ref 2.

(1) Beckert, W. F.; Lopez-Avila, V. Proceedings of the International Conference and Exhibition on Pollution Prevention in the Laboratory, Boston, MA, June 1993.

(2) Lopez-Avila, V.; Young, R.; Beckert, W. F. *Anal. Chem.* **1994**, *66*, 1097–1106.

(3) Lopez-Avila, V.; Young, R. *Application of Microwave Energy to the Extraction of Organic Compounds from Solid Samples*; EPA Report 600/R-94/031; U.S. Environmental Protection Agency, Environmental Monitoring Systems Laboratory: Las Vegas, NV, March 1994.

(4) Method 8250 (Revision 1, November 1992). In *Test Methods for Evaluating Solid Waste*, 3rd ed.; SW-846, Proposed Update II; U.S. Environmental Protection Agency: Washington, DC, 1986.

(5) Method 8081 (Revision 0, November 1992). In *Test Methods for Evaluating Solid Waste*, 3rd ed.; SW-846, Proposed Update II; U.S. Environmental Protection Agency: Washington, DC, 1986.

(6) Method 8141A (Revision 1, November 1992). In *Test Methods for Evaluating Solid Waste*, 3rd ed.; SW-846, Proposed Update II; U.S. Environmental Protection Agency: Washington, DC, 1986.

0003-2700/95/0367-2096$9.00/0 © 1995 American Chemical Society

A 5-g portion of the spiked soil or the certified material was accurately weighed into an aluminum dish and was transferred quantitatively to the Teflon-lined extraction vessel. For the wet samples, the calculated volume of water was added to the sample in the extraction vessel and allowed to equilibrate with the matrix for ~10 min. A solution containing the surrogate compounds (i.e., 2-fluorobiphenyl, 2-fluorophenol, nitrobenzene-d_5, phenol-d_5, terphenyl-d_{14}, and 2,4,6-tribromophenol) was added to each sample immediately before the hexane–acetone (1:1) solvent (30 mL) was added. No surrogate compounds were used with the compounds listed in Methods 8081 and 8141A. After ensuring that a new rupture membrane was in place, the extraction vessel was closed. Extractions were performed at 115 °C for 10 min at 100% power. After extraction, the vessels were allowed to cool to room temperature for ~20 min before they were opened. The supernatant was filtered through glass wool prewashed with hexane–acetone and was then combined with the 2- to 3-mL hexane–acetone rinse of the extracted sample. The extract was concentrated to ~5 mL using nitrogen blowdown evaporation and was centrifuged twice for 10 min at 2300 rpm to separate the fine particulates. The extract was concentrated to 1 mL for GC/MS, GC/ECD, or GC/NPD analysis.

Spiking Procedure. Spiking of the topsoil samples with the target compounds was performed as follows. The sample was weighed into an aluminum cup, and 50–250 μL of a concentrated stock solution (prepared by compositing the various mixtures and diluting with methylene chloride) containing either the compounds listed in Method 8250, 8081, or 8141A, was added to the sample with a syringe, ensuring that the solution did not contact the aluminum cup. Polychlorinated biphenyls (PCBs) were spiked separately from the OCPs. The concentrations of the spiking solutions were 125 μg/mL for the compounds listed in Method 8250, 2–20 μg/mL for those listed in Method 8081 (OCPs), 5 μg/mL for PCBs, and 20–40 μg/mL (except thionazin and HMPA at 10 μg/mL) for the compounds listed in Method 8141A (OPPs). The individual spiking levels and results are given in the tables in the supporting information. The spiked samples were allowed to dry for ~10 min and were then transferred to the MAE vessels.

The topsoil samples identified as "aged" samples were spiked as described above. Water (2 mL) was added to each sample after the spiked soil samples had been transferred to the extraction vessels. The vessels were capped and were stored in a refrigerator at 4 °C for 24 h, 14 days, or 21 days. The six surrogate compounds were added to the respective soil samples immediately prior to extraction.

Analysis of Extracts. The analyses of the extracts containing the compounds listed in Method 8250 were performed on a Hewlett-Packard 5890 Series II gas chromatograph interfaced to a Hewlett-Packard 5971A mass spectrometer MSD/DOS Chemstation (Hewlett Packard, Palo Alto, CA) and equipped with a Hewlett-Packard 5973A autoinjector. The samples were introduced via a 30-m length × 0.25-mm i.d. × 0.25-μm film thickness DB-5 fused-silica open-tubular column (J&W Scientific, Folsom, CA) with helium as carrier gas at a flow rate of ~1 mL/min. The column temperature was held at 40 °C for 4 min and then increased at 8 °C/min to a final temperature of 300 °C, where it was held for 10 min. The injection volume was 1 μL, and the injector temperature was 250 °C. The injector was set in the splitless mode for 1 min after the injection. The electron energy was set at 70 eV and the electron multiplier voltage at 2160 V. Spectral data were acquired at a rate of 1 s/scan (scanning range 35–500 amu). The instrument was tuned daily with DFTPP introduced via the GC inlet. A 5-point internal standard calibration using standards at 5, 10, 25, 50, and 100 μg/mL was performed daily to establish the GC/MS linear range. The six internal standards specified below were spiked into every calibration standard and sample extract that was analyzed by GC/MS. For quantification, we used the average relative response factors from the multilevel calibration.

For OCP and PCB analyses, we used a Hewlett-Packard 5890 Series II gas chromatograph equipped with two ECDs and a Hewlett-Packard 5973A autoinjector. Samples were introduced via a splitless injector into a retention gap (20-cm length × 0.53-mm i.d.) connected through a fused-silica Y-shaped inlet splitter to two 30-m length × 0.32-mm i.d. × 0.25-μm film thickness fused-silica open-tubular columns (a DB-5 and a DB-1701) with helium as carrier gas at flow rates of 3.7 and 4.0 mL/min, respectively. For OCP analyses, the column temperature was increased at 5 °C/min from 80 to 275 °C (2-min hold); the injection volume was 1 μL, and the injector temperature was 250 °C. A 3-point external standard calibration using standards at 25, 50, and 100 ng/mL for the 20 μg/kg spike level and correspondingly higher concentrations for the higher spike levels was performed initially to establish the GC/ECD linear range. For PCB analyses, the column temperature was increased at 12 °C/min from 140 to 190 °C, held at 190 °C for 2 min and then increased at 4 °C/min to 275 °C; the injection volume was 1 μL, and the injector temperature was 250 °C. A 4-point external standard calibration using standards at 0.1, 0.25, 0.5, and 1 μg/mL was performed for the Aroclors. For quantification, we used the average response factors from the multilevel calibration.

For OPP analyses, we used a Hewlett-Packard 5890 Series II gas chromatograph equipped with two NPDs and a Hewlett-Packard 5973A autoinjector. Samples were introduced via a packed-column injector connected to a fused-silica retention gap (20-cm length × 0.53-mm i.d.) and a fused-silica Y-shaped inlet splitter connected to two 30-m length × 0.32-mm i.d. × 0.25-μm film fused-silica open-tubular columns (a DB-5 and a DB-1701) with helium as carrier gas at a flow rate of 3 mL/min. The column temperature was held at 120 °C for 3 min and then increased at 5 °C/min to 260 °C (hold 1 min). The injection volume was 1 μL, and the injector temperature was 250 °C. A 4-point external standard calibration using standards at 1, 2.5, 5, and 10 μg/mL for the 1 mg/kg spike level and half or twice these concentrations for the 0.5 and 2 mg/kg spike levels, respectively, was performed initially to establish the GC/NPD linear range. For quantification, we used the average response factors for the multilevel calibration.

Solvents. All solvents used in this study were distilled-in-glass pesticide grade and were obtained from Baxter Scientific (McGaw Park, IL).

Standards. Analytical reference standards of the 89 semivolatile compounds listed in Method 8250, 45 OCPs listed in Method 8081, and 47 compounds listed in Method 8141 were purchased as composite solutions in various solvents.

The compounds listed in Method 8250 were purchased from Absolute Standards, Inc. (Camden, CT), as eight composite solutions in methylene chloride (mix 1 consisting of 14 ethers, phthalates, and nitrosamines; mix 2 of 14 compounds consisting mostly of chlorinated benzenes, nitrobenzene, and nitrotoluenes;

Table 1. MAE Method Performance for Selected Compounds Listed in Method 8250[a]

compd	compound name	ERA certified concn (mg/kg)[b]	typical recovery using EPA method[b]	average recovery[c] uncorrected[d]	average recovery[c] corrected[e]	RSD (%)	blowdown evaporation recovery
6	anthracene	1.01	54.7	60.6	68.6	4.7	88.3
9	benzo[*a*]anthracene	2.03	56.2	91.1	103	6.7	88.3
18	bis(2-ethylhexyl) phthalate	7.12	85.8	125	150	11.2	83.5
20	butyl benzyl phthalate	10.6	80.8	109	128	10.8	84.8
25	2-chlorophenol	5.08	56.1	52.3	76.2	15.7	68.6
27	chrysene	2.35	60.4	99.8	114	8.5	87.9
30	dibenzofuran	6.79	66.7	75.6	88.8	1.9	85.1
46	2,4-dinitrotoluene	5.0	63.4	80.6	83.0	4.2	97.1
52	fluorene	6.06	61.4	60.2	72.1	1.0	83.5
64	naphthalene	1.64	64.0	43.3	64.3	15.7	67.3
78	pentachlorophenol	12.2	42.8	81.8	85.0	6.8	96.2
80	phenanthrene	1.57	69.4	95.8	110	6.8	87.1
84	pyrene	8.03	56.9	95.3	110	12.8	86.7
88	2,4,5-trichlorophenol	7.99	64.7	86.4	96.9	1.3	89.2
89	2,4,6-trichlorophenol	4.56	61.0	63.6	71.1	4.7	89.4
SU-1	2-fluorobiphenyl	6.0	*f*	82.3	102	8.8	80.8
SU-2	2-fluorophenol	20.0	*f*	63.5	99.5	14.1	63.8
SU-3	nitrobenzene-d_5	5.0	*f*	61.6	87.4	15.8	70.5
SU-4	phenol-d_5	20.0	*f*	70.4	96.0	13.1	73.3
SU-5	terphenyl-d_{14}	5.0	*f*	127	142	8.4	89.6
SU-6	2,4,6-tribromophenol	20.0	*f*	96.7	94.8	3.9	102

[a] Five compounds (i.e., 1,2- and 1,4-dichlorobenzene, 2- and 4-methylphenol, and 1,2,4-trichlorobenzene) are not listed because of questionable concentrations reported by ERA. All recovery values are given in percent. [b] Certified values reported by ERA are the true spiked concentrations; the "typical recoveries" values were reported by ERA. [c] The number of determinations was four. [d] Recoveries were not corrected for losses during blowdown evaporation. [e] Recoveries were corrected for losses during blowdown evaporation. [f] Data not available.

mix 4 of three phenols and benzoic acid; mix 5 of various anilines, dibenzofuran, benzyl alcohol, and 2-methyl naphthalene; mix 8 of 13 phenols; mix 9 of eight miscellaneous compounds; mix 10 of ethyl methanesulfonate and methyl methanesulfonate; and mix 11 of 11 nitrogen-containing compounds), one composite solution in methanol (mix 6 consisting of benzidine and 3,3′-dichlorobenzidine), and one composite solution in methylene chloride–benzene (1:1) consisting of 17 polynuclear aromatic hydrocarbons. The individual concentrations of the compounds in these mixtures were 2 mg/mL. Dibenzo[*a*,*j*]acridine was purchased from Chem Service (West Chester, PA) and 1,2-diphenylhydrazine from Aldrich Chemical (Milwaukee, WI). The six surrogate compounds listed in Table 1 were purchased from Absolute Standards as two composite solutions; the acid surrogate standard contained 2-fluorophenol, phenol-d_5, and 2,4,6-tribromophenol at 2 mg/mL in methanol, and the base/neutral surrogate standard contained 2-fluorobiphenyl, terphenyl-d_{14}, and nitrobenzene-d_5 at 1 mg/mL in methylene chloride. The six internal standards listed in Method 8250 (i.e., 1,4-dichlorobenzene-d_4, naphthalene-d_8, acenaphthene-d_{10}, phenanthrene-d_{10}, chrysene-d_{12}, and perylene-d_{12}) were purchased from Supelco, Inc. (Bellefonte, PA) as a composite solution at 2 mg/mL in methylene chloride; their purities were stated to be 99%. An intermediate stock solution of the target compounds listed in Method 8250 at 125 μg/mL was prepared by combining the various composite solutions; the calibration standards at 5, 10, 15, and 50 μg/mL were prepared by serial dilution with methylene chloride of the 125 μg/mL composite solution. The six internal standards were spiked into every calibration standard and sample extract at 40 μg/mL.

Analytical reference standards of the compounds listed in Method 8081 were purchased from Absolute Standards as one composite solution in toluene–hexane (1:1) containing 18 compounds (aldrin, the four BHCs, 4,4′-DDD, 4,4′-DDE, 4,4′-DDT, dieldrin, endosulfan I, endosulfan II, endosulfan sulfate, endrin, endrin aldehyde, endrin ketone, heptachlor, heptachlor epoxide, and methoxychlor) at 2 mg/mL per compound; one composite solution from Absolute Standards in isooctane containing DBCP, etridiazole, chloroneb, propachlor, PCNB, chloropropylate, and chlorobenzilate at 100 μg/mL per compound; and one composite solution from Absolute Standards in isooctane containing dichloran, chlorothalonil, DCPA, methoxychlor, and *cis*- and *trans*-permethrin at 1 mg/mL per compound. Alachlor, hexachlorocyclopentadiene, and isodrin were purchased as individual solutions in methanol (concentration 5 mg/mL, except alachlor at 1 mg/mL) from NSI Environmental Solutions (Research Triangle Park, NC). The rest of the compounds listed in Method 8081 were obtained as neat materials from Chem Service, Ultra Scientific (North Kingstown, RI), or Aldrich Chemical. An intermediate stock solution of the compounds listed in Method 8081 at 2 μg/mL in acetone was prepared by combining the various composite stock solutions; this solution was used for spiking soil samples and for preparing the calibration standards.

Aroclors 1016 and 1260 were purchased from Supelco, Inc., as solutions at 1 mg/mL in isooctane, and Aroclors 1248 and 1254 were purchased as neat materials from Chem Service. A composite solution of Aroclors 1016 and 1260 at 5 μg/mL in acetone was prepared by combining the two individual stock solutions at 1 mg/mL; this solution was used for spiking soil samples and for preparing the calibration standards.

Analytical reference standards of the compounds listed in Method 8141A were purchased from Absolute Standards as individual solutions in either hexane or methanol, with the exceptions of aspon, azinphos ethyl, chlorofenvinphos, chlorpyrifos methyl, dichlorofenthion, ethion, and fonophos, which were obtained as neat materials from Ultra Scientific, Inc.; dicrotophos, leptophos, phosmet, trichlorfon, tri-o-cresylphosphate, and simazine, which were obtained as neat materials from Chem Service; famphur at 1 mg/mL in acetonitrile and atrazine at 1 mg/mL in methanol, which were obtained from NSI Environmental Solutions; and thionazin at 1 mg/mL in methanol, which was obtained from

Supelco. An intermediate stock solution of the compounds listed in Method 8141A (in hexane–methanol–acetonitrile) at 20 μg/mL was prepared by combining the various individual stock solutions; this solution was used for spiking soil samples and preparing the calibration standards.

Soil and Sediment Materials. The topsoil (pH 7.5; cation exchange capacity 14.6 mequiv/100 g; organic carbon content 0.1%; water content 2.6%; sand 57.6%; silt 21.8%; and clay 20.6%) used in this study was obtained from Sandoz Crop Protection (Gilroy, CA). The ERA soil (Lot 324) is a material spiked with selected semivolatile compounds and was purchased from Environmental Resource Associates (ERA, Arvada, CO). The other ERA soil (Lot 9801) was certified for PCBs. The certified values for these materials are included in Tables 1 and 3. The two reference sediments HS-1 and HS-2, certified for PCBs, are marine sediments collected from three harbors in Nova Scotia; these materials were purchased from the National Research Council of Canada, Atlantic Research Laboratory (Halifax, Canada). According to the certificate of analysis, these materials were freeze-dried, passed through a sieve (125-μm mesh size), homogenized in a cement mixer, and then subsampled into 200-g portions. Information on the physicochemical properties of these materials is not available.

Safety. The microwave unit, which incorporates several safety features described in ref 2, should be operated in accordance with CEM's recommended operating safety instructions. A new rupture membrane per vessel should be used for each extraction. Should the membrane rupture due to increased pressure inside individual vessels, the solvent vapor is unlikely to leak into the cavity because all vessels are connected to a containment vessel via the solvent rupture vent tube. To prevent pressure buildup inside individual vessels, wet samples should not be extracted simultaneously with dry samples; when 12 samples are extracted simultaneously, they should be either all dry or all wet. Likewise, solvent blanks should not be heated together with samples that are to be extracted by MAE, because the former will heat faster than the latter.

RESULTS AND DISCUSSION

Semivolatile Compounds (Method 8250). There are presently 118 semivolatile compounds listed in EPA Method 8250 (Revision 1, November 1992). We initially selected 92 compounds for our experimental work; the other 26 compounds were OCPs and PCBs, which we investigated separately with the compounds listed in Method 8081. From the 92 semivolatile compounds, we are reporting data for only 89 compounds. Benzo[*b*]fluoranthene (compound **10**) and benzo[*k*]fluoranthene (compound **11**) could not be resolved on the DB-5 column, and therefore we are reporting only one set of numbers for both compounds. We deleted *N*-nitrosodimethylamine, which was difficult to separate from the solvent under the gas chromatographic conditions used in this study, and *N*-nitrosodiphenylamine, which decomposed in the gas chromatographic inlet to diphenylamine; thus, the latter two compounds could not be reliably quantified by Method 8250 without conducting separate experiments for each compound. We also spiked the samples with six surrogate compounds; thus, the total number of compounds for which we are reporting MAE recoveries is 95.

When topsoil samples were spiked with the 95 compounds and extracted immediately by MAE, the recoveries of 79 compounds ranged from 80 to 120%; the recoveries of 14 compounds were

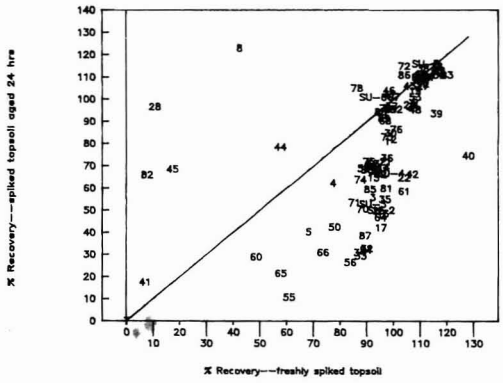

Figure 1. Distribution of recoveries for the compounds listed in Method 8250 that were spiked into topsoil samples (freshly spiked soil vs spiked soil aged for 24 h).

below 80%, and the recovery of 7,12-dimethylbenz[*a*]anthracene (compound **40**) was above 120% (Figure 1). From the 14 compounds with recoveries below 80%, five compounds had recoveries below 20%. The nine compounds with recoveries ranging from 80 to 20% were 4-aminobiphenyl (**4**), aniline (**5**), benzoic acid (**8**), 4,6-dinitro-2-methylphenol (**44**), methyl and ethyl methanesulfonates (**60** and **50**, respectively), hexachlorocyclopentadiene (**55**), and 1- and 2-naphthylamines (**65** and **66**, respectively). Of the five compounds with recoveries below 20%, benzidine (**7**) could not be recovered at all, the recovery of α,α-dimethylphenethylamine (**41**) was 7.0%, the recovery of 2-picoline (**82**) was 7.7%, the recovery of dibenzo[*a*,*j*]acridine (**28**) was 10.6%, and the recovery of 2,4-dinitrophenol (**45**) was 17.2%). When topsoil samples were spiked with the 95 compounds, aged for 24 h at 4 °C (water was added to the spiked soil to ensure good mixing of the target compounds with the matrix), and then extracted by MAE, only 46 compounds had recoveries between 80 and 120%; the recoveries of 47 compounds were below 80%, and the recovery of benzoic acid (**8**) was above 120%. As shown in Figure 1, there is a downward trend in recovery on going from freshly spiked soil samples to the aged samples as more recoveries fall below the line of equality. Recoveries of six compounds were higher when they were extracted from the wet, aged matrix. For example, the recoveries of benzoic acid (**8**) increased from 42 to 123%; dibenzo[*a*,*j*]acridine (**28**) from 11 to 97%; 2,4-dinitrophenol (**45**) from 17 to 69%; and 2-picoline (**82**) from 8 to 66%. Water appears to have a beneficial effect in this case, possibly displacing the analyte from the soil matrix into the organic solvent.

When the MAE technique was used to extract the ERA soil sample and the recoveries (Table 1) were calculated on the basis of the concentrations certified by ERA (ERA reported the true spikes as the certified concentrations), we found that recoveries obtained by MAE were higher for 11 of the 15 compounds known to be present in this matrix, as compared to recoveries reported by ERA. The recoveries of three compounds were almost identical for both techniques, and only the recoveries of naphthalene were significantly lower when MAE was used (Table 1). When comparing the MAE and "typical recovery using EPA method" data, as reported by ERA, we used the uncorrected recovery values for MAE since the values reported by ERA were also not corrected for evaporation losses from blowdown. The lower recoveries for

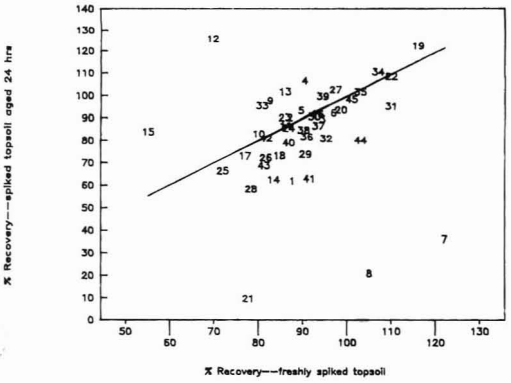

Figure 2. Distribution of recoveries for the compounds listed in Method 8081 that were spiked into topsoil samples (freshly spiked vs spiked soil aged for 24 h).

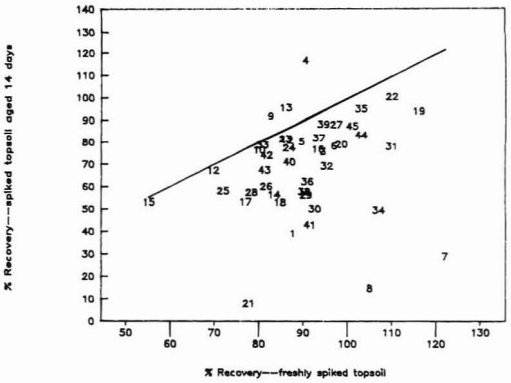

Figure 3. Distribution of recoveries for the compounds listed in Method 8081 that were spiked into topsoil samples (freshly spiked vs spiked soil aged for 14 days).

naphthalene were most probably due to losses during blowdown evaporation since in separate experiments we found that 33% of the amount of naphthalene in hexane–acetone, subjected to blowdown evaporation, was lost.

In summary, the MAE technique performed adequately for the semivolatile compounds listed in Method 8250 (the data shown in Figure 1 are also included in Table 1 of the supporting information). The RSDs for the freshly spiked topsoil were <10% for 64 of the 95 compounds given in Table 1 of the supporting information, 10–20% for 25 compounds, and 28–39% for four compounds. We are not reporting the RSDs for benzidine (0% recovery), and we report only a combined RSD value for benzo[*b*]fluoranthene and benzo[*k*]fluoranthene since these two compounds could not be resolved on the DB-5 column.

Organochlorine Pesticides and PCBs. In our previous publication[1] on the MAE technique, we reported recoveries ranging from 83 to 117% when hexane–acetone (1:1) alone spiked with 20 OCPs was heated at 115 °C using microwave energy, and slightly lower but still good recoveries (above 80%, except for γ-chlordane at 74%) when the experiments were carried out in the presence of soil. In the present study, we expanded the list of OCP compounds to 45, and we evaluated the MAE technique with soil freshly spiked with the target compounds, spiked soil aged for 24 h at 4 °C, and spiked soil aged for 14 days at 4 °C.

Table 2 of the supporting information summarizes the recovery data for the compounds listed in Method 8081, and Figures 2 and 3 illustrate the distribution of these recoveries. From the 45 compounds that were extracted by MAE from the freshly spiked soil, 38 compounds had recoveries between 80 and 120%, six compounds had recoveries between 50 and 80%, and the recovery of captafol (**7**) was above 120% (Figure 2). For the spiked soil samples aged for 24 h (Figure 2), 28 compounds had recoveries between 80 and 120%, 12 compounds had recoveries between 50 and 80%, three compounds [captafol (**7**), captan (**8**), and dichlone (**21**)] were poorly recovered and chloroneb (**12**) and 4,4′-DDT (**19**) had recoveries above 120%. For the spiked soil samples aged for 14 days (Figure 3), 14 compounds had recoveries between 80 and 120%, 24 compounds had recoveries between 50 and 80%, and seven compounds had recoveries below 50%. The seven compounds with recoveries below 50% were alachlor (**1**), captafol (**7**), captan (**8**), diallate (**21**), etridiazole (**30**), hexachlorocyclopentadiene (**34**), and propachlor (**41**).

A decrease in recovery with increased aging time (Figures 2 and 3) is also evident in the case of OCPs. This is especially apparent for captafol (**7**), captan (**8**), and dichlone (**21**) when the recoveries from freshly spiked vs spiked soil aged for 24 h are compared (i.e., the recovery of captafol dropped from 122 to 36%, the recovery of captan dropped from 105 to 21%, and the recovery of dichlone dropped from 78 to 10%). The recoveries of etridiazole (**30**) and hexachlorocyclopentadiene (**34**) were almost identical from the freshly spiked and the spiked soil aged for 24 h (Figure 2), but they dropped to 50% for the spiked soil aged for 14 days (Figure 3). The recoveries of other compounds, such as chlorothalonil (**14**) and propachlor (**41**), also decreased with increased aging time (e.g., the recovery of chlorothalonil dropped from 83% for freshly spiked soil to 63% for the spiked soil aged for 24 h to 56% for the spiked soil aged for 14 days, and the recovery of propachlor dropped from 92% for freshly spiked soil to 63% for the spiked soil aged for 24 h to 43% for the spiked soil aged for 14 days).

Despite these few occurrences in which recoveries were lower from the spiked soil aged for 24 h and the spiked soil aged for 14 days (we suspect that microbial degradation may at least partially account for the loss of compounds), the recoveries obtained by MAE are comparable to or higher than those achieved by the conventional extraction techniques.

When we compared recoveries obtained by MAE with those we reported earlier[7] for the sonication and Soxhlet extraction techniques (Table 2) for topsoil samples spiked with selected OCPs at 50 μg/kg (except hexachlorobenzene at 200 μg/kg and hexachlorocyclopentadiene at 100 μg/kg), we found that the recoveries were at least 7% higher for MAE than those for either the Soxhlet or the sonication technique [except for 4,4′-DDT, where the recoveries were above 100% for all three techniques, and for dieldrin, where the Soxhlet recoveries were 12% higher than the MAE or sonication recoveries (Table 2)]. Hexachlorocyclopentadiene exhibited the largest increase in recovery by MAE

(7) Lopez-Avila, V. *Sonication and Soxhlet Extraction in Environmental Analysis: Methods Comparison.* EPA Report 600/X-93/010; U.S. Environmental Protection Agency: Environmental Monitoring Systems Laboratory: Las Vegas, NV, February 1993.

Table 2. Comparison of MAE with Sonication and Soxhlet Extraction Techniques

		sonication[a]		Soxhlet[a]		MAE[b]	
compd no.	compound name	average recovery (%)	RSD (%)	average recovery (%)	RSD (%)	average recovery (%)	RSD (%)
2	aldrin	66.2	5.2	77.9	3.7	87	2.1
3	α-BHC	70.2	6.2	69.7	4.7	94.4	4.1
6	δ-BHC	*c*		68.2	1.7	96.9	2.8
19	4,4′-DDT	108	5.7	128	3.6	116	5.6
23	dieldrin	79.3	4.4	96.4	2.7	85.9	3.8
24	endosulfan I	68.4	3.9	69.1	3.3	86.8	3.1
25	endosulfan II	63.3	5.3	58.2	8.3	71.9	6.3
27	endrin	62.1	6.4	62.9	2.7	97.4	1.9
31	heptachlor	68.6	5.2	85.0	6.7	110	1.4
32	heptachlor epoxide	60.9	4.9	69.7	2.9	95.3	2.7
33	hexachlorobenzene	65.7	5.6	73.6	7.2	80.8	1.6
34	hexachlorocyclopentadiene	44.8	11	21.9	96	107	12

[a] The spike level was 50 μg/kg for the sonication and Soxhlet extraction experiments. The number of determinations was three. These data were taken from ref 4. [b] The number of determinations was three. The spike levels are listed in Table 2 of the supporting information. [c] Data not available.

Table 3. MAE Method Performance for PCBs

matrix	certified value or spike level (mg/kg)	Aroclor type	average recovery (%) uncorrected[a]	average recovery (%) corrected[b]	RSD (%)	blowdown evaporation recovery (%)
HS-1 marine sediment	0.022[c]	1254	93.2[d]		8.1	
HS-2 marine sediment	0.112[c]	1254	76.7[e]		6.0	
ERA soil (Lot 9801)	394[f]	1260	82.8[d]	89.9	2.6	92.1
freshly spiked topsoil	0.100[g]	1016	73.7[e]	85.9	5.6	85.8
		1260	76.0[e]	82.5	4.2	92.1
spiked topsoil aged for 24 h at 4 °C	0.100[g]	1016	79.6[e]	92.8	14	85.8
		1260	81.6[e]	88.6	10	92.1
superfund site sample 1	465[h]	1248	102[e]		3.5	
superfund site sample 2	1.13[h]	1248	157[e]		6.3	
superfund site sample 3	0.033[h]	1248	86.8[e]		35	
superfund site sample 4	6.7[h]	1248	75.3[e]		17	

[a] Recoveries were not corrected for losses during blowdown evaporation. [b] Recoveries were corrected for losses during blowdown evaporation. [c] Certified by the National Research Council of Canada. [d] The number of determinations was four. [e] The number of determinations was three. [f] Certified by ERA. [g] Spiked in our laboratory. [h] Reported by an independent laboratory that used Soxhlet extraction and GC/ECD.

as compared with the other two techniques. Method precisions (RSDs) were comparable for the three techniques, with the exception of the very high RSDs for the Soxhlet extraction of hexachlorocyclopentadiene.

The results for the performance of the method for four Aroclors are presented in Table 3. Samples of two standard reference marine sediments (HS-1 and HS-2), a standard reference soil, a freshly spiked topsoil, a spiked and aged topsoil, and four soils from a Superfund site were extracted by MAE. The recoveries of Aroclor 1016 and 1260 (corrected for blowdown evaporation losses) were in the range of 82–93%; the recoveries of Aroclor 1248 and 1254 ranged from 75–157% over a concentration range of 0.022–465 mg/kg.

Organophosphorus Pesticides. Of the 51 compounds presently listed in the Method 8141A, 47 are OPPs, two are industrial chemicals, and two are triazine herbicides. In our study, we spiked 47 of the 51 compounds into soil samples. Carbophenothion, diazinon, parathion methyl, and terbufos were not spiked, because we could not quantify them under the gas chromatographic conditions we used. Carbophenothion coelutes with famphur on the DB-5 column and with Bolstar on the DB-210 column; diazinon coelutes with disulfoton on the DB-5 column and with sulfotepp on the DB-210 column; parathion methyl coelutes with chlorpyrifos methyl on the DB-5 column and with malathion on the DB-210 column; and terbufos coelutes with fonophos on the DB-5 column and with naled on the DB-210 column.

Table 3 of the supporting information summarizes recovery data for the compounds listed in Method 8141A, and Figures 4 and 5 show the distributions of the recoveries. Of the 47 compounds listed in Method 8141A, which were extracted by MAE from the freshly spiked soil, 35 compounds had recoveries between 80 and 120%, four compounds [dichlorofenthion (**12**), dichlorvos (**13**), fensulfothion (**23**), and mevinphos (**29**)] had recoveries between 50 and 80%, six compounds [monochrotophos (**30**), naled (**31**), phosphamidon (**35**), TEPP (**39**), trichlorfon (**42**), and HMPA (**44**)] had recoveries below 20%, and azinphos ethyl (**3**) and simazine (**47**) had recoveries above 120%. For the spiked soil samples aged for 24 h (Figure 4), 37 compounds had recoveries between 80 and 120%, three compounds [demeton-S (**11**), naled (**31**), and trichlorfon (**42**)] had recoveries between 50 and 80%, two compounds [monochrotophos (**30**) and TEPP (**39**)] had recoveries below 50%, and five compounds had recoveries above 120%. For the spiked topsoil samples aged for 21 days (Figure 5), 35 compounds had recoveries between 80 and 120%, three compounds [dioxathion (**16**), phorate (**33**), and thionazin (**40**)] had recoveries between 50 and 80%, seven compounds [demeton-O (**10**), demeton-S (**11**), monochrotophos

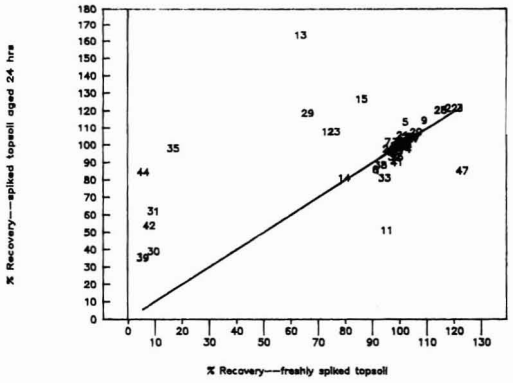

Figure 4. Distribution of recoveries for the compounds listed in Method 8141A that were spiked into topsoil samples (freshly spiked vs spiked soil aged for 24 h).

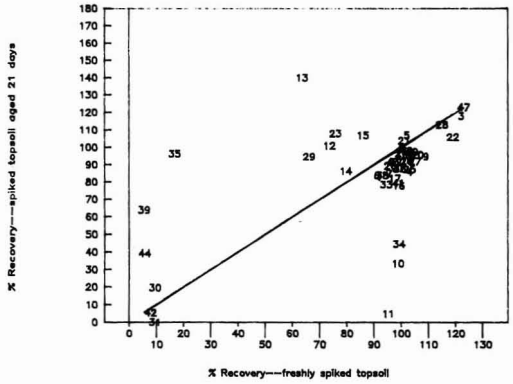

Figure 5. Distribution of recoveries for the compounds listed in Method 8141A that were spiked into topsoil samples (freshly spiked vs spiked soil aged for 21 days).

(**30**), naled (**31**), phosmet (**34**), trichlorfon (**42**), and HMPA (**44**)] had recoveries below 50%, and dichlorvos (**13**) and simazine (**47**) had recoveries above 120%.

The six compounds that exhibited recoveries below 20% from freshly spiked soil samples were monocrotophos (**30**), naled (**31**), phosphamidon (**35**), TEPP (**38**), trichlorfon (**42**), and HMPA (**44**). We found significant improvement in their recoveries when we extracted them from aged topsoil samples and attributed this to the presence of water in the matrix. For example, the average recoveries increased for monocrotophos from 9.4 to 39%, for naled from 9.4 to 62.3%, for phosphamidon from 16.6 to 98.1%, for TEPP from 5.4 to 34%, for trichlorfon from 7.8 to 54.0%, and for HMPA from 5.6 to 84.7%. The recoveries decreased, however, for the spiked soil aged for 21 days (Figure 5). We attributed the decreases mainly to microbial degradation of target compounds, although chemical transformations, such as debromination for naled and dehydrochlorination for trichlorfon, are also possible. The latter two compounds are known to be converted to dichlorvos,[6] and this may explain the very high recoveries of dichlorvos (**13**).

CONCLUSIONS

Microwave-assisted extraction of organic compounds from solid samples, including extraction of pollutants of environmental concern from soil and sediment samples, is a viable technique for sample preparation. We demonstrated in this study that many of the compounds of interest to the EPA can be extracted from spiked and spiked/aged soil samples with a relatively small volume of organic solvent (30 mL in MAE vs 300 mL in Soxhlet extraction) in 10 min. Repeated extractions with fresh solvent portions were not required, since separate experiments showed that the amounts of analytes recovered in the second fraction were insignificant. Safety issues associated with the handling of flammable solvents in a microwave system have been adequately addressed by at least one manufacturer, and work is in progress now to validate the first MAE method, proposed for the EPA, in a multilaboratory evaluation study.

ACKNOWLEDGMENT

The authors thank the CEM Corp. for the loan of the microwave unit used in this study to Midwest Research Institute. The U.S. EPA, through its Office of Research and Development (ORD), partially funded and collaborated in the research described here. It has been subjected to the Agency's review and has been approved as an EPA publication. Readers should note the existence of a patent describing the microwave-assisted extraction of biological materials. Neither the EPA nor ORD endorses or recommends any trade names or commercial products mentioned in this article; they are noted solely for the purpose of description and clarification. The U.S. Government has a nonexclusive royalty-free license in and to any copyright covering this article.

SUPPORTING INFORMATION AVAILABLE

Tables listing spike levels and MAE performance data for the compounds listed in Methods 8250, 8081, and 8141A (12 pages). Ordering information is given on any current masthead page.

Received for review November 4, 1994. Accepted March 30, 1995.[⊗]

AC9410732

[⊗] Abstract published in *Advance ACS Abstracts,* May 15, 1995.

Anal. Chem. **1995**, *67*, 2103–2109

Colloid Chemical Aspects of Slurry Packing Techniques in Microcolumn Liquid Chromatography

Johannes P. C. Vissers,*,†,§ Henk A. Claessens,† Jozua Laven,‡ and Carel A. Cramers†

Laboratory of Instrumental Analysis and Laboratory of Colloid Chemistry, Eindhoven University of Technology, P.O. Box 513, 5600 MB Eindhoven, The Netherlands

The relationship between the coagulating properties of slurry suspensions, type of packing liquids, and final performance of slurry-packed microcolumns for liquid chromatography (LC) was investigated. The colloidal stability of stationary-phase suspensions was examined by means of sedimentation and ζ-potential experiments. Expressions for the theoretical sedimentation rate of noncoagulated particle suspensions were derived for spherical particles with completely and incompletely filled pores and for irregularly shaped particles with incompletely filled pores. The performance of the slurry-packed microcolumns was predominantly determined by the selection of the packing liquid. It is shown that the packing liquid preferably has to be coagulating to obtain efficient and stable packed capillary LC columns. The selection of the slurry liquid on the column performance was of minor importance.

The relatively poor column efficiency and long-term stability of packed capillary columns have delayed the introduction and application of microcolumn liquid chromatography as an analytical technique. Possible reasons for this are the coagulating properties of slurry suspensions, containing alkyl-modified silica or poly(styrene–divinylbenzene) packing materials particles, and the physical/chemical properties of the applied packing liquids. Different packing techniques are proposed to overcome these problems.

Most of the packing procedures of columns in liquid chromatography (LC) are performed by using slurry packing techniques.[1] As a result of the dispersion of the stationary-phase particles in a solvent, the attraction between the particles is drastically reduced, resulting in favorable packing conditions compared with dry packing methods.[2,3] However, the type of slurry solvent strongly determines the stability of the slurry suspension. Bristow,[4] and more recently Shelly et al.[5,6] and Wang et al.,[7] pointed out that the colloidal stability of packing material suspensions, that is, the coagulating behavior of stationary-phase particles in a solvent, can be critically important in slurry packing methods. These effects become even more critical in packed fused-silica capillary columns of 100–350-μm internal diameter (i.d.) because of the large value for the column length to column internal diameter ratio of such columns.[5] In slurry packing methods, efforts are made to avoid coagulation of the stationary-phase particles. Currently applied slurry packing techniques are balanced and nonbalanced density methods, chemical and mechanical stabilization methods, and high- and low-slurry viscosity methods.[8]

This paper reports a quantitative method describing the colloidal stability of porous, reversed-phase particles in apolar liquids, as based on the sedimentation rate of the particles. In addition, ζ-potential measurements were performed to study slurry stabilities in more detail. The effect of the type of slurry and packing liquids on the resulting chromatographic performance (plate height, separation impedance, flow resistance parameter) is investigated extensively for nominally identical stationary phases. The results of this study were used to develop selection criteria for slurry packing techniques in microcolumn LC.

THEORY

Spherically Shaped Particles. Bristow[4] pointed out that the theoretical sedimentation rate can be used to determine the colloidal stability of slurry suspensions. Suspensions in which the particle settling rate exceeded the calculated one were regarded as coagulated. The theoretical sedimentation rate of spherical stationary-phase particle suspensions can be determined with the Stokes equation but is only valid for solid particles at infinite dilution. At present, most stationary-phase particles are porous and infinite dilutions are impractical in column packing techniques. Both effects can be corrected for by taking the particle porosity, ϵ_i, and a hindered settling function[9–11] into account, which is represented by the term $(1-\phi)^{-\kappa_2}$, resulting in a modified Stokes expression for the theoretical sedimentation rate of noncoagulated stationary-phase particles:

$$v = \frac{(1-\phi)^{-\kappa_2} d_p^2 (\varrho_{skel} - \varrho_1)(1-\epsilon_i) g}{18\eta} \qquad (1)$$

where ϕ is the volume fraction of the particles, κ_2 is a particle/

† Laboratory of Instrumental Analysis.
‡ Laboratory of Colloidal Chemistry.
§ Present address: LC Packings, Baarsjesweg 154, 1057 HM Amsterdam, The Netherlands.

(1) Bristow, P. A.; Brittain, P. N.; Riley, C. M.; Williamson, B. F. *J. Chromatogr.* **1977**, *131*, 57.
(2) Crestinni, G.; Mastrogiacomo, A. R. *J. Microcolumn Sep.* **1991**, *3*, 539.
(3) Guan, Y.; Zhou, L.; Shang, Z. *J. High Resolut. Chromatogr.* **1992**, *15*, 434.
(4) Bristow, P. A. *Liquid Chromatography in Practice*; hetp: Handforth, UK, 1977; p 34.
(5) Shelly, D. C.; Edkins, T. J. *J. Chromatogr.* **1987**, *411*, 185.
(6) Shelly, D. C.; Antonucci, L.; Edkins, T. J.; Dalton, T. J. *J. Chromatogr.* **1989**, *458*, 267.
(7) Wang, H.; Hartwick, R. A.; Miller, N. T.; Shelly, D. C. *J. Chromatogr.* **1990**, *523*, 23.
(8) Verzele, M.; Dewaele, C. *LC-GC* **1986**, *4*, 614.
(9) Khan, R. A.; Richardson, J. F. *Chem. Eng. Commun.* **1989**, *78*, 111.
(10) Davis, R. A.; Acrivos, A. *Annu. Rev. Fluid Mech.* **1985**, *17*, 91.
(11) Russel, W. B.; Saville, D. A.; Schowalter, W. R. Sedimentation. In *Colloidal Suspensions*; Russel, W. B., Saville, D. A., Schowalter, W. R., Eds.; Cambridge University Press: Cambridge, UK, 1989; p 395.

0003-2700/95/0367-2103$9.00/0 © 1995 American Chemical Society

solvent-dependent constant, ϱ_{skel} and ϱ_1 are the densities of the packing material and the liquid, respectively, η is the viscosity of the liquid, and g is the gravitational constant. ϵ_i can be expressed as[12,13]

$$\epsilon_i = \frac{V_{pore}}{V_{hydro}} = \frac{V_{pore}}{V_{pore} + 1/\varrho_{skel}} \quad (2)$$

where V_{pore} is the total pore volume per unit of mass and V_{hydro} the hydrodynamic particle volume per unit of mass. The application of ϵ_i to calculate the effective density of a particle is only valid for immiscible substances, as is the case for packing material suspensions. ϵ_i equals 0 if the particle is completely solid and theoretically equals 1 if it is completely porous, meaning no silica backbone is present anymore. As is shown later, eq 1 can only be applied for particles completely filled with slurry liquid: poly(styrene–divinylbenzene) (PS–DVB) particles. As a result of the possible inclusion of gas into the particle pores, eq 3 must be applied for alkyl-modified silicas to calculate the settling rate of noncoagulated porous particles:

$$v = \frac{(1-\phi)^{-\kappa_2} d_p^2 \{\varrho_{skel}(1-\epsilon_i) + \varrho_1(\epsilon_f - 1)\} g}{18\eta} \quad (3)$$

where ϵ_f/ϵ_i is the fraction of filled particle pores. In this equation, we assumed that the density of the gas phase was negligible for the calculation the effective mass of the particles.

Irregularly Shaped Particles. Predicting the theoretical sedimentation rate is more complicated for irregularly shaped porous packing materials than for spherically shaped particles. The description of the shape of such particles and its influence on the free-falling behavior are complicating factors.[14] The final settling velocity for irregularly shaped particles is usually determined by means of iterative calculating schemes.[14] However, the theoretical sedimentation rate of noncoagulated particles can be calculated analytically by the combination of the equations that are applied in iterative calculation schemes, resulting in

$$v = \frac{(1-\phi)^{-\kappa_2} \psi d_A^2 \{\varrho_{skel}(1-\epsilon_i) + \varrho_1(\epsilon_f - 1)\} g}{3\pi\eta} \quad (4)$$

where ψ is an empirical shape factor, which is defined as the volume of the particle divided by the volume term obtained from the mean projected area diameter of the particle.[14–17] d_A is the projected area diameter.

EXPERIMENTAL SECTION

Particle Characterization. The particle size distribution of the different stationary phases was measured with a Malvern 2600 particle sizer (Malvern Instruments, Worcestershire, UK). The skeleton density of the materials was determined with a gas (He) volume densitometer (Stereopycnometer, Quanta-chrome Corp., Greenvale, NY). Pore volumes were assessed with an automatic multipoint B.E.T. apparatus (Sorptomatic 1900, Carlo Erba Instruments, Milan, Italy). The projected area diameter of irregularly shaped particles was determined as described by Clift et al.[16] Slurry densities were measured with a 10-mL capped liquid pycnometer, after sonication for 10 min and thermostating at 20 °C for 15 min in a water bath.

Particle Settling Device. A particle settling device was constructed from 130 × 7 mm i.d. glass tubes. The stationary-phase slurries were transferred into the tubes by means of a pipet. The tubes were closed by a rubber stopper to prevent solvent evaporation and placed in a homemade tube holder to ensure they were held in a vertical position. The height of the slurry was measured from 5 min to 48 h after filling of the tubes. All sedimentation experiments were carried out twice.

ζ-Potential Measurements. The electrophoretic mobility of the packing material particles in the selected slurry liquids was measured by means of a Malvern Zetasizer 3 (Malvern Instruments) equipped with an AZ-4 cell for moderate conductivity measurements, i.e., electrophoretic experiments in solvents with a relatively high dielectric constant or an AZ-26 cell for low-conductivity measurements. The principles of detection and measurement with the AZ-26 cell are discussed by Arts et al.[18]

Column Preparation and Packing Equipment. Columns were constructed from 0.40 m × 320 μm i.d. uncoated fused silica tubing (Chrompack, Middelburg, The Netherlands). An EPM2000 glass filter frit (Whatman, Maidstone, UK) was cut out by the column. To hold the frit in position, a 0.080 m × 75 μm i.d., 280 μm outer diameter (o.d.) fused-silica capillary (LC Packings, Amsterdam, The Netherlands) was fixed into the large capillary using epoxy resin.

The packing equipment consisted of a DSTV-122 air-driven fluid pump (Haskel Engineering, Burbank, CA) for constant pressure packing and a 0.19 × 0.0020 m i.d. stainless-steel slurry reservoir. The column was connected to the slurry vessel with a 0.2 mm i.d., 0.5 mm o.d. PVDF double cone (Merck, Darmstadt, Germany).

In this study, only reversed-phase particles were used. The packing material particles were suspended at a concentration of 100 kg·m^{-3} in a slurry liquid by sonication for 10 min. Afterward, the slurry was transferred to the slurry reservoir with a syringe. The columns were unless otherwise stated packed at a pressure of 500 bar during a 1-h period.

Chromatographic Instrumentation. The HPLC system consisted of a Model 100 DM syringe pump (Isco Inc., Lincoln, NE), a microUVIS20 absorbance detector (Carlo Erba Instruments), and a 60-nL CI4W injection valve (VICI-AG Valco Europe, Schenkon, Switzerland). To ensure that no stationary phase could enter the injection valve, a 0.2-μm nylon membrane (Alltech Associates Inc., Deerfield, IL) was positioned into the valve outlet to the column. UV detection was performed at 255 nm. A 900 Series interface and Nelson 5.0 software (Perkin Elmer Nelson, Cupertine, CA) were employed for data acquisition.

Column Evaluation. The reversed-phase columns were evaluated with a test mixture containing four components: uracil (dead volume marker), naphthalene, phenanthrene, and anthracene. The concentration of all components was approximately

(12) Unger, K. K. *Porous silica: its properties and use as a support in column liquid chromatography*; Elsevier Scientific Publishing Co.: Amsterdam, 1979; p 147.
(13) Unger, K. K. Survey of Types of Chromatographic Packings and Stationary Phases and Their Role in Separation Processes. In *Packings and Stationary Phases in Chromatographic Techniques*; Unger, K. K., Ed.; Marcel Dekker Inc.: New York, 1990; p 43.
(14) Brown, N. P. The Settling Behaviour of Particles in Fluids. In *Slurry handling: design of solid–liquid systems*; Brown, N. P., Heywood, N. I., Eds.; Elsevier Applied Science: London, 1990; p 17.
(15) Turton, R.; Levenspiel, O. *Powder Technol.* **1986**, *47*, 83.
(16) Clift, R.; Grace, J. R.; Weber, M. E. *Bubbles, Drops and Particles*; Academic Press: London, 1978; p 16.
(17) Heywood, H. Uniform and Non-uniform Motion of Particles in Fluids. In *Interaction between Fluids and Particles*; Heywood, H., Ed.: Institution of Chemical Engineers: London, 1962; p 1.
(18) Arts, T. J. C.; Laven, J.; van Voorst Vader, F.; Kwaaitaal, Th. *Colloids Surf. A* **1994**, *85*, 149.

Table 1. Median Particle Diameter, d_p, Pore Volume, V_{pore}, Skeleton Density, ϱ_{skel}, and Particle Porosity, ϵ_i, of Reversed-Phase Packing Materials

stationary phase	d_p (μm)	V_{pore} (10^{-3} m^3·kg^{-1})	ϱ_{skel} (10^3 kg·m^{-3})	ϵ_i
silica-based (spherical)				
BioSil C18 HL 90-5 S	5.70	0.357	2.101	0.429
Nucleosil 100-5 C18	5.10	0.809	2.106	0.630
Spherisorb ODS-1	4.84	0.430	2.166	0.482
Zorbax ODS	4.40	0.358	1.987	0.413
Zorbax SB-C18	5.24	0.318	2.194	0.411
silica-based (irregular)				
Polygosil 60-5 C18[a]	6.39	0.658	2.077	0.577
polystyrene-based				
RoGel RP[b]	7.59	1.3	1.05	0.577

[a] Averaged projected area diameter. [b] For RoGel RP, the values for density and pore volume taken are as specified by the manufacturer.

Table 2. Fraction ϵ_f/ϵ_i of the Pores Filled with Slurry Liquid after Sonication for 10 Minutes

	ϵ_f/ϵ_i					
stationary phase	acetone	ACN	CCl_4[a]	IPA	MeOH	THF
silica-based						
BioSil C18 HL 90-5 S	0.594	0.420	0.646	0.632	0.700	0.660
Nuclosil 100-5 C18	0.817	0.765	0.837	0.837	0.778	0.832
Spherisorb ODS-1	0.782	0.730	0.795	0.871	0.865	0.836
Zorbax ODS	0.528	0.530	0.777	0.666	0.721	0.789
Zorbax SB-C18	0.591	0.564	0.708	0.752	0.740	0.718
polystyrene-based						
RoGel RP	1.0	1.0		1.0	1.0	1.0

[a] RoGel RP could not be suspended in CCl_4.

0.1 mol·m^{-3}. As the mobile phase, acetonitrile/water 70:30 (v/v) was used. The individual solvents of the mobile phase were filtered through a 0.45-μm filter. Prior to use, the mobile phase was degassed with helium. The peak of anthracene was used to calculate the column efficiencies. The reduced plate heights were calculated using an algorithm developed by Foley and Dorsey.[19] In the evaluation of the PS–DVB columns, the mobile phase was acetonitrile/water 60:40 (v/v) and the test components were benzylideneacetone and 4-aminoacetophenone. Here the plate heights were calculated for the 4-aminoacetopheneone peak.

Chemicals. Acetone, carbon tetrachloride, methanol (MeOH), 2-propanol (IPA), and 4-aminoacetophenone were purchased from Merck. Acetonitrile (ACN) and benzylideneacetone were from Janssen Chimica (Beerse, Belgium), uracil, anthracene, naphthalene, and phenanthrene were from Fluka AG (Buchs, Switzerland) and tetrahydrofuran (THF) was from Biosolve LTD (Barneveld, The Netherlands). All chemicals were of p.a. grade. Water was purified and demineralized with a Milli-Q water purification system (Waters-Millipore Milford, MA) prior to use.

The Zorbax ODS 5-μm and Zorbax SB-C18 5-μm modified silicas were obtained from Rockland Technologies Inc. (New Port, DE). Nucleosil 100-5 C18 and Polygosil 60-5 C18 were from Machery-Nagel GmbH & Co KG (Düren, Germany), and Spherisorb ODS-1 was from Phase Separations (Deerfield, UK). The PS–DVB polymer material, RoGel RP, and BioSil C18 HL 90-5 S were from BioRad RSL nv. (Nazareth, Belgium).

RESULTS AND DISCUSSION

Characterization of the Particles. The particle diameter, skeleton density of the particles, and particle porosity must be known in order to determine the theoretical sedimentation rate of porous spherically shaped particles, according to eq 3. The results of the size distribution, nitrogen absorption, and stereopycnometric measurements on six different octadecyl-bonded silicas (ODS) and a PS–DVB packing material are given in Table 1. The median, d_{50}, was taken as the average particle diameter, d_p. The particle porosity is given in Table 1, which was calculated by use of eq 2.

Application of eq 1 to suspensions of noncoagulated silica-based packing materials resulted in an overestimation of the theoretical sedimentation rate compared to empirical determined settling rates. Assuming that the silica particles pores would be completely filled with liquid after 10 min of sonication, ϱ_{skel} should compare well with values for the density obtained with a liquid pycnometer. However, average values as obtained by stereopycnometric experiments were (2.0–2.2) × 10^3 kg·m^{-3}, whereas with a liquid pycnometer, measurements values of (1.5–1.9) × 10^3 kg·m^{-3} were found. These results indicate that the pores of the ODS particles are only partly filled with liquid. During sonication of the suspensions, gas might remain entrapped in the pores of the silica particles. Additional evidence for this assumption was found with liquid pycnometer experiments carried out at elevated pressures. Compression and decompression was used to remove the gas out of the pores. As an example, with Nucleosil 100-5 C18 in acetone, skeleton densities were found of 1.6055 × 10^3, 1.6415 × 10^3, and 1.6878 × 10^3 kg·m^{-3} at pressures of 1, 6, and 20 bar, respectively. As shown by the latter results, the inclusion of air is the most likely reason for the entrapping of air in the particle pores during sonication.

The amount of entrapped air can be calculated by applying simple mass equations, knowing ϱ_{skel} from a gas pycnometer, V_{pore}, and the apparent skeleton density from a liquid pycnometer. Information about the filled pore fraction can be obtained by expressing the amount of entrapped air as a function of the particle porosity. All liquid pycnometer density measurements were duplicated. The repeatability of these experiments was found to be better than 2%. In Table 2, ϵ_f/ϵ_i is given for the different ODS particles in various liquids. Only 40–90% of the silica particle pores got filled with slurry liquid after sonication of the slurry during a 10-min period, as can been seen from the results in Table 2. With RoGel RP, the pores were completely filled with liquid in all cases.

Sedimentation Experiments. Two main types of particle suspensions can be distinguished: coagulated and noncoagulated. The former is characterized by the fact that the particles form clusters and will therefore settle faster than predicted by Stokes equation for noncoagulated particles. In noncoagulated suspensions, the particles are discrete and remain suspended for a relatively long period of time, depending on the particle size, the difference in density between particle and surrounding liquid, and liquid viscosity. Thus, coagulation of particles can be characterized by the sedimentation rate.

Experimental rates of sedimentation were measured with the ODS stationary phases and RoGel RP in a number of selected solvents. During the sedimentation experiments, the position of the height of the settling slurry was recorded. To facilitate the comparison of the sedimentation rate for the different combina-

(19) Foley, J. P.; Dorsey, J. G. *Anal. Chem.* **1983**, *55*, 730.

tions of stationary phases and liquids of varying densities and viscosities, normalized parameters were introduced.

normalized height Λ: $\Lambda = (h_{tot} - h_{clear})/h_{tot}$ (5)

where h_{clear} and h_{tot} are the heights of the clear top layer and of the total slurry, respectively.

normalized time τ: $\tau = tv/h_{tot}$ (6)

where t is time elapsed since the start of the sedimentation experiments and v the theoretical sedimentation rate of noncoagulated particles according to equation 1, 3, or 4. For the hindred settling constant κ_2, a value of -5.4 was used. A more detailed explanation about hindred settling is given elsewhere.[20] In that paper, a detailed discussion is given of the coagulating behavior of ODS particles, as based on van der Waals interactions.

An example of a graph of normalized height of a sediment vs normalized time for two different slurry liquids at three different slurry concentrations is shown in Figure 1a,b. The solid lines in this figure represent the normalized theoretical sedimentation rate for noncoagulated suspensions. As can be seen, Nucleosil 100-5 C18 in acetone clearly shows noncoagulated behavior. The theoretical and experimental sedimentation curves are in good agreement. However, the same stationary phase, Figure 1b, coagulates in CCl_4.

This approach for particle sedimentation provides information about the extent to which the particles are coagulated, whereas the sedimentation quotient as introduced by Shelly and Edkins[5] provides only relative information. Furthermore, the sedimentation rate is more sensitive toward coagulation than the sedimentation quotient, especially for low suspension concentrations. All investigated silica-based stationary phases were noncoagulated in acetone, ACN, IPA, and THF. Exceptions were BioSil C18 HL 90-5 S, which was coagulated in ACN, and Nucleosil 100-5 C18, which was coagulated in IPA. Coagulation of all silica materials took place in ACN/H_2O 70:30 (v/v), CCl_4, and MeOH. Here, Spherisorb ODS-1 and Zorbax SB-C18 were exceptions because they did not coagulate in MeOH and only moderately coagulated in ACN/H_2O 70:30 (v/v). RoGel RP coagulated in CCl_4, IPA, and MeOH.

A comparison of the theoretical rates of sedimentation of irregularly shaped particles with the experimental settling rate can be performed in a similar way. To demonstrate this, Polygosil 60-5 C18 was employed for sedimentation experiments in acetone. The shape factor, ψ, was estimated to be 0.26. The slurry concentration was 100 kg·m^{-3}. The results are shown in Figure 2. The open circles represent normalized times if a ±5% deviation in ϵ_i (the most critical sedimentation parameter) was assumed. Again, the theoretical and experimental settling rate are in fairly good agreement for irregularly shaped particles.

ζ-Potential Measurements. ζ-potentials of the particles were measured to determine whether electrostatic or steric effects play a decisive role in slurry stabilization. A measure for the degree of coagulation is the ratio α of the initial slope of the experimentally determined and the theoretically calculated sedimentation rates, this is, $\alpha = (\Delta\Lambda_{exp}/\Delta\tau_{exp})/(\Delta\Lambda_{theor}/\Delta\tau_{theor})$. $\alpha = 1$ for stable suspensions, and $\alpha > 1$ for coagulated suspensions.

In Figure 3, α is given for four types of packing material particles in MeOH as a function of the ζ-potential. With all suspensions that are stable according to the sedimentation experiments, ζ-potentials in the order of -40 to -100 mV were found. Electrostatic repulsion forces are therefore believed to be predominant in the stabilizing effects of these kinds of particles. Because of the geometry of the measuring cell and refractive index differences, it was impossible to determine the ζ-potential of unstable and CCl_4 suspensions, respectively.

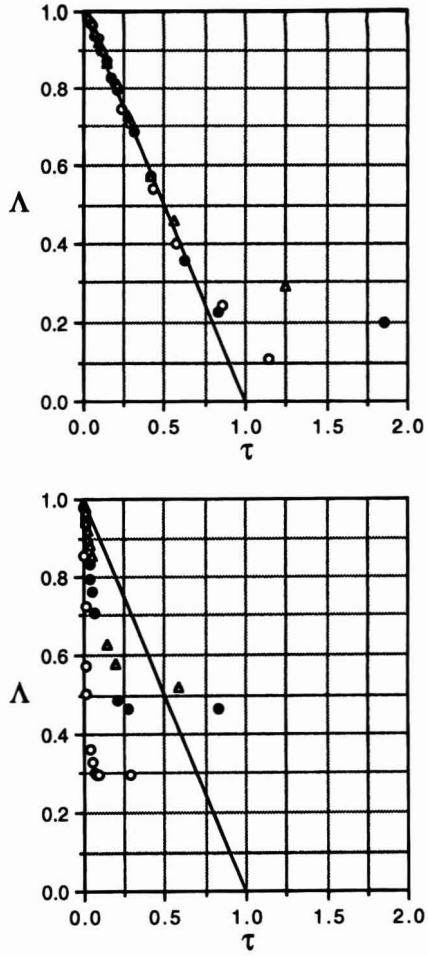

Figure 1. Normalized height of the sediment, Λ, as a function of the normalized time, τ, for Nucleosil 100-5 C18 in (a, top) acetone or CCl_4 (b, bottom) as the dispersion liquid. Slurry concentrations: (○) 50, (●) 100, and (△) 150 kg·m^{-3}. The solid line represents the theoretical rate of sedimentation for noncoagulated stationary phase particles.

Chromatographic Results. A number of solvents were selected as slurry and packing liquids in the packing procedure for the microcolumns, based on the results of the sedimentation experiments. A representative example of the results obtained is given in Table 3, where the average chromatographic performances for capillary columns packed with Nucleosil 100-5 C18 as the stationary phase are summarized. Of each type of column at least three were prepared and tested. In all LC experiments the mobile-phase velocity was 4 μL·min^{-1}, a value close to the optimum

(20) Vissers, J. P. C.; Laven, J.; Claessens, H. A.; Cramers, C. A.; Agterof, W. G. M. *Colloids Surf. A.*, submitted for publication.

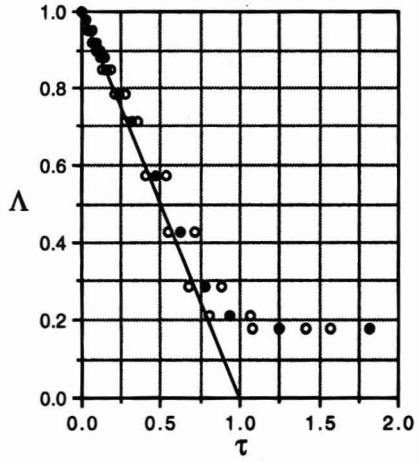

Figure 2. Normalized height of the sediment, Λ, vs the normalized time, τ, for Polygosil 60-5 C18 in acetone as the dispersion liquid: (●) ϵ_i = 0.577 and (○) ϵ_i ±5%. The solid line represents the theoretical rate of sedimentation for noncoagulated stationary-phase particles, using ϵ_i = 0.577.

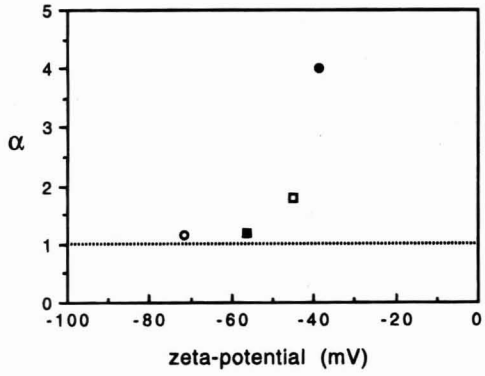

Figure 3. Degree of flocculation, α, vs the ζ-potential for (○) Spherisorb ODS-1, (■) Zorbax SB-C18, and (□) Nucleosil 100-5 C18, and (●) RoGel RP packing materials in MeOH as the dispersion liquid. The concentration of the slurry from which α was derived was 100 kg·m^{-3}.

velocity of the mobile phase for each case. From the first three rows in this table it can be seen that if the same solvent were used as the slurry and the packing liquid, low efficient columns were obtained in terms of h, Φ, and E irrespective of the coagulating properties of the suspensions. However, acetone was a clear exception in this respect. Similar results were found for other stationary phases, as shown later. For all investigated stationary phases, the lowest efficiencies were obtained for THF/THF as slurry liquid and packing liquid. Moreover, during the conditioning step of these columns, a consolidation of the chromatographic bed was observed of about 20–30 mm over a total column length of 0.40 m. An explanation of this effect is given in the next section, where attention is paid to the contradiction between h and Φ for columns packed with THF as both slurry and packing liquid.

Table 3. Column Performance of 320-μm-i.d. Capillary Columns Packed with Nucleosil 100-5 C18, Using Different Slurry and Packing Liquids[a]

slurry liquid[b]	packing liquid[b]	h	Φ	E
acetone	acetone	2.08	587	2530
MeOH	MeOH	4.25	493	11100
THF	THF	7.48	1150	68000
acetone	MeOH	2.35	639	3740
THF	MeOH	2.68	701	5320
acetone	ACN/H_2O	2.43	608	3630
ACN/H_2O	ACN/H_2O	2.42	571	3340
MeOH	ACN/H_2O	2.25	609	3100
THF	ACN/H_2O	2.34	849	4600

[a] Columns were tested with an eluent composition ACN/H_2O 70:30 (v/v). The eluent velocity was 4 μL·min^{-1}. The test compound was anthracene ($k \sim 4$). [b] ACN/H_2O 70:30 (v/v).

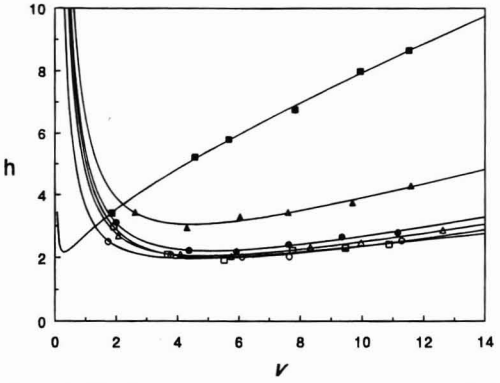

Figure 4. Knox h–ν plots for fused-silica capillary columns packed with BioSil C18 HL 90-5 S. CCl_4 was used as the slurry liquid. Packing liquids: (○) acetone, (●) ACN, (△) ACN/H_2O 70:30 (v/v), (▲) IPA, (□) MeOH, and (■) THF. Test conditions as in Table 3.

Changing the packing procedure using the same slurry and packing liquid into a system consisting of noncoagulating or moderately coagulating slurry liquids and coagulating packing liquids resulted in good quality capillary columns, as can be seen in Table 3. These results indicate that, to obtain well-packed capillary fused-silica columns, the type of slurry liquid is of minor importance compared with the type of packing liquid. No consolidation was observed for columns packed with ACN/H_2O 70:30 (v/v). In all other cases, consolidation of the chromatographic bed was moderate.

Results similar to the Nucleosil 100-5 C18 microcolumns were obtained for columns packed with BioSil C18 HL 90-5 S as the stationary phase. In the latter experiments, the slurry liquid, CCl_4, was used constantly and the packing liquids were varied. In Figure 4, the obtained Knox h–ν curves are depicted for the applied slurry solvents for the BioSil C18 HL 90-5 S stationary phase. From the results in Figure 4, it can be seen that good columns were obtained with the coagulating packing liquids, ACN, ACN/H_2O 70:30 (v/v), and MeOH. The noncoagulating packing liquids, IPA and THF, yielded columns of lower separation efficiency. In these experiments, acetone was an exception too. Although acetone showed noncoagulating properties, it yielded very good results when applied as the packing liquid. As yet, no reasonable explanation for this has been found.

Application of the results of the experiments described above to the other investigated reversed-phase packing materials showed similar results. In summary, going from a noncoagulating slurry/packing liquid system, IPA/IPA, to a noncoagulating/coagulating system, acetone/MeOH, for Spherisorb ODS-1, h-values decreased from 8.3 to 3.9. For Zorbax SB-C18, h was 19.1 in a THF/THF system; this value decreased to 4.7 for a system using acetone as the slurry liquid and MeOH as the packing liquid. For Zorbax ODS, the h-value was 3.5 for a noncoagulating/coagulating system THF/(ACN/H_2O 70:30 (v/v)). These results of reduced plate heights are moderate compared to the results obtained for Nucleosil 100-5 C18 and BioSil C18 HL 90-5 S. However, in the latter experiments, the particles coagulated moderately in the applied packing liquids. Application of more coagulating packing liquids might increase the performance of these columns. For RoGel RP an h-value of 6.4 was observed when ACN was applied as the slurry and packing liquid. For a noncoagulating/coagulating system, THF/(ACN/H_2O 70:30 (v/v)), h was reduced to 4.4. Similar results were reported recently by Cortes and Pfeiffer[21] for another PS–DVB material tested in the size exclusion chromatography mode for incompletely permeating compounds.

Chromatographic Bed Structures. The most plausible explanation for the extreme consolidation phenomena, observed in the experiments for columns packed with THF as the slurry and the packing liquid, is that the electrostatic repulsion forces between the particles during the packing process could not be overcome by the applied packing pressure. Alternatively, the particles were pushed away from each other by the same kind of electrostatic forces, after disconnecting the column from the packing equipment, both resulting in a very loosely packed bed. During conditioning of the THF/THF packed capillary columns, the loosely packed stationary-phase particles coagulate and reorganization of the chromatographic bed takes place. This consolidation process is random and results in a very disordered bed, as indicated by the reduced plate height and flow resistance parameter of the Nucleosil 100-5 C18 THF/THF packed columns. These ideas are supported by scanning electron microscope pictures of cross sections of packed capillary columns, of which examples are given in Figure 5a,b. To obtain correct information about the structure of the chromatographic bed, the particles were embedded in a low-viscosity resin[22] prior to the cutting of the column. The main demands for such a resin are a low viscosity in its monomeric state and a negligible difference in density between the monomeric and polymeric state.

Figure 5a shows the cross section of a chromatographic bed of a Nucleosil 100-5 C18 packed column, using MeOH as the slurry and packing liquid, respectively. This column showed a relative low h of 2.7 and a moderate back pressure, Δp, of 94.3 bar over a column length of 0.412 m, which is in agreement with the observed bed structure, i.e., a homogeneous tightly packed bed. In Figure 5b, a packed bed cross section is shown for a Zorbax SB-C18 packed column, using THF as the slurry and the packing liquid, respectively. This column showed a very high h of 21.9 and a Δp of 165.8 bar over a column length of 0.445 m. The reason for the low performance of the column is obvious. As can be seen from Figure 5b, the bed structure is very disordered and even channels are present. However, examination of other slices of cross sections of this column also showed tightly packed particles, explaining the very high back pressure of the column.

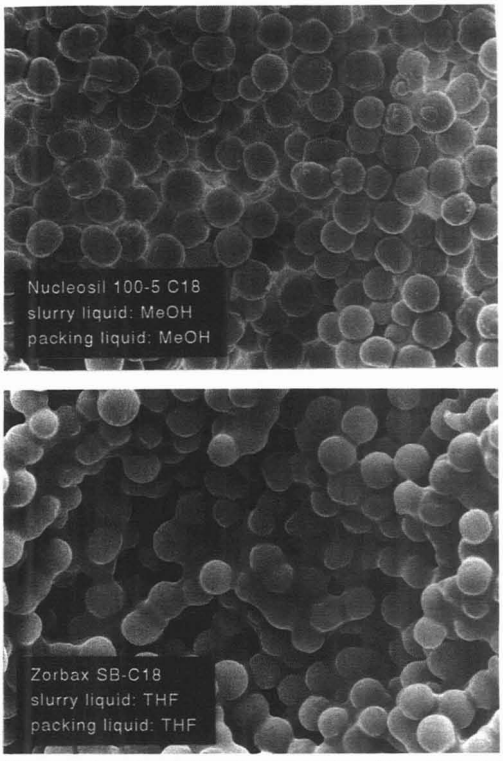

Figure 5. Scanning electron microscope picture of the cross section of a fused-silica capillary column: (a) packed with Nucleosil 100-5 C18, slurry liquid MeOH, packing liquid MeOH, $h = 2.7$, and $\Delta p = 94.3$ bar; (b) packed with Zorbax SB C18, slurry liquid THF, packing liquid THF, $h = 21.9$, and $\Delta p = 165{,}8$ bar.

Reproducibility Studies. BioSil C18 HL 90-5 S was also used to test the reproducibility of packing procedures using the same slurry and packing liquids as described in the section Chromatographic Results. Each packing procedure was repeated 5 times in order to gain statistical information about the repeatability in h, E, and Φ at the optimum mobile-phase velocity of these procedures. The results are given in Table 4.

The coagulating packing liquids ACN, ACN/H_2O 70:30 (v/v), and MeOH generally showed a better repeatability for h than the noncoagulating packing liquids acetone, IPA, and THF. The repeatibility obtained with acetone as the packing liquid was, however, only slightly higher. Far the best results were obtained with ACN/H_2O 70:30 (v/v) as the packing liquid. h, E, Φ, and the repeatability were significantly better compared to the other liquids. It is noteworthy that BioSil C18 HL 90-5 S particles in ACN/H_2O 70:30 (v/v) were more coagulated compared to the other packing liquids.

CONCLUSIONS

The theoretical free settling rate of noncoagulated spherical and irregularly shaped reversed-phase packing materials in aqueous/organic solvents can be determined by means of a modified Stokes equation that accounts for possible inclusion of

(21) Cortes, H. J.; Pfeiffer, C. D. *Anal. Chem.* **1993**, *65*, 1476.
(22) Spur, A. R. *J. Ultrastruct. Res.* **1969**, *26*, 31.

Table 4. Average Values ($n = 5$) of the Reduced Plate Height, h, Separation Impedance, E, and Flow Resistance Factor, Φ, with Relative Standard Deviation (%, in Parentheses) for 320-μm-i.d. Capillary Columns Packed with BioSil C18 HL 90-5 S[a]

packing liquid	h	E	Φ
acetone	2.37 (16.3)	3980 (32)	698 (12.7)
ACN	2.41 (14.0)	3570 (31)	600 (5.8)
ACN/H_2O 70:30 (v/v)	2.11 (2.2)	2650 (10)	595 (10.7)
IPA	2.79 (24.2)	5180 (25)	629 (4.7)
MeOH	2.32 (15.8)	3240 (31)	597 (9.3)
THF	4.05 (66.0)	19300 (12)	832 (20.6)

[a] CCl_4 was the slurry liquid; columns were tested with an eluent composition ACN/H_2O 70:30 (v/v); the test compound was anthracene ($k \sim 4$).

air in the pores of the stationary-phase particles. The degree of particle coagulation in slurry and packing liquids can be derived by comparison of the experimentally determined sedimentation rate of the particles with the theoretically calculated sedimentation rate of noncoagulated particles. No general rules for the coagulating behavior of ODS particles an be derived. However, ThF and acetone have noncoagulating properties for all investigated ODS stationary phases. The results of the stability experiments of reversed-phase particle suspensions, measured by sedimentation, were in good agreement with the ζ-potential measurements.

The chromatographic performance of a packed bed in a microcolumn is strongly influenced by the nature of the packing liquid rather than by the slurry liquid. A packing liquid must preferably have coagulating properties to obtain good results in terms of reduced plate height and flow resistance parameter. From the results of this study, the slurry liquid obviously is of minor importance for the final performance of packed capillary columns. The applied pressures are most likely large enough to overcome the attraction forces between the particles during the packing process, even in the case of the use of coagulating slurry liquids. No general rules exist for the selection of a proper slurry liquid. Finally, it can be concluded that for each stationary phase the individual packing solvent and packing condition has to be optimized to achieve satisfactory chromatographic performance. However, the results from this research provide adequate tools for the proper selection of packing liquid to be used in packing techniques for capillary LC columns.

ACKNOWLEDGMENT

The authors acknowledge E. M. van Oers (Eindhoven University of Technology, Department of Inorganic Chemistry, Eindhoven, The Netherlands), A. Spoelstra (Eindhoven University of Technology, Department of Polymer Technology, Eindhoven, The Netherlands), and M. E. H. Vanderbroeck for their technical assistance. We also thank A. B. J. M. Dams (Rockland Technologies, Inc., Nuenen, The Netherlands) and C. Dewaele (BioRad RSL nv., Nazareth, Belgium) for their generous gifts of the Zorbax SB-C18 and BioSil C18 HL 90-5 S stationary phases, respectively.

Received for review December 8, 1994. Accepted April 5, 1995.[⊗]

AC941187D

[⊗] Abstract published in *Advance ACS Abstracts,* May 15, 1995.

Anal. Chem. **1995,** *67,* 2110–2118

Two-Dimensional Conductometric Detection in Ion Chromatography. Analyte Identification, Quantitation of Very Weak Acid Anions, and Universal Calibration

Anna Sjögren and Purnendu K. Dasgupta*

Department of Chemistry and Biochemistry, Texas Tech University, Lubbock, Texas 79401-1061

A universal and sensitive detection method for anion chromatography is described. Following suppressed conductometric detection carried out with an NaOH eluent and an electrical suppressor, the eluite is transported through a microscale electrodialytic NaOH generator and a second conductivity detector. While the first detector responds primarily to strong acid anions, the second detector records a decrease in the NaOH background signal, regardless of the pK_a of the analyte. Routine detection of very weak acids at the low micromolar level is possible. The dual detection method not only constitutes the most generally applicable approach to IC by combining the detection merits of both suppressed and single-column IC, it provides possibilities of peak identification beyond retention characteristics. Area ratio values from the two detector signals provide unique signatures for each analyte ion. It is possible to estimate the limiting equivalent conductance of an unknown eluite and the analyte concentration without specific calibration. The method is also effective in diagnosing the occurrence of coelution.

A situation common to all chromatographic methods utilizing bulk property detectors is that the retention time of an eluite constitutes merely an indication of its identity. Along with refractometry, conductometry is among the most general of all liquid-phase detection methods. Conductometry is ideally suitable for ion chromatography (IC): electrical conductivity is a property shared by all ions and uncharged species cannot interfere.

In 1975, Small et al.[1] developed a method that eliminated the eluent conductivity in a postseparation H^+-exchange step termed suppression; the decrease in the background conductance allowed dramatically improved strong acid analyte detection limits. Subsequent refinements to the technique, such as electrodialytic suppression and eluent generation,[2–5] improved column technology[6] and system hardware, have made possible present day systems that can easily detect analyte signals corresponding to a change in conductance less than a tenth of the conductance of pure water.

Suppressed conductometric IC has been a resounding success in both research laboratories and the marketplace. However, for weak and especially very weak acid anions, poor sensitivity and markedly nonlinear calibration behavior constitute significant shortcomings. Also, while the technique is generally applicable for strong acid anions, it is a problem to identify the eluted ions beyond their retention behavior. Ancillary confirmation of the identity is always desirable: the validation of analytical data is increasingly important. Efforts to achieve high and relatively uniform sensitivities for all analytes have included various manipulations of the suppressed eluate.[7,8] Identification efforts have included the sequential conductance measurement of the nonsuppressed and the column-suppressed eluate.[9] On-line conversions of the analyte, first from an acid to a base and then from an acid to a salt, have been described in a series of papers.[10–12] These efforts[9–12] are all based on dual conductometric detection. New clues to the eluite identity are obtained with two signals that can be analyzed both independently and in combination. Serial indirect conductometric and UV detection have also been used to deduce the identity of an eluite ion.[13] Compared to conventional suppressed IC, another major advantage of these systems is that weak and very weak acids can also be detected. This paper presents a complete theoretical background and experimental refinements of the most successful of these approaches: NaOH eluent suppressed conductometric IC followed by on-line electrodialytic NaOH introduction and conductometric detection[12] to provide universal calibration, estimation of equivalent conductance/pK_a values, diagnostics for peak coelution, and compatibility with gradient elution.

OPERATING PRINCIPLES

When NaOH is used as the eluent, after suppression the background should theoretically be pure water. In practice, the suppressor background effluent is slightly acidic because of the presence of anionic impurities in the eluent and the intrusion of

(1) Small, H.; Stevens, T. S.; Bauman, W. C. *Anal. Chem.* **1975**, *47*, 1801–1809.
(2) Strong, D. L.; Joung, C. U.; Dasgupta, P. K. *J. Chromatogr.* **1991**, *546*, 159–173.
(3) Strong, D. L.; Dasgupta, P. K. *Anal. Chem.* **1989**, *61*, 939–945.
(4) Strong, D. L.; Dasgupta, P. K.; Friedman, K.; Stillian, J. R. *Anal. Chem.* **1991**, *63*, 480–486.
(5) Rabin, S.; Stillian, J.; Barreto, V.; Friedman, K.; Toofan, M. *J. Chromatogr.* **1993**, *640*, 97–109.
(6) Stillian, J. R.; Pohl, C. A. *J. Chromatogr.* **1990**, *499*, 249–266.
(7) Downey, S. W.; Hieftje, G. M. *Anal. Chim. Acta.* **1983**, *153*, 1–13.
(8) Shintani, H.; Dasgupta, P. K. *Anal. Chem.* **1987**, *59*, 1963–1969.
(9) Sato, H.; Shishido, Y.; Furuya, K.; Dasgupta, P. K., unpublished studies, 1992.
(10) Berglund, I.; Dasgupta, P. K. *Anal. Chem.* **1991**, *63*, 2175–2183.
(11) Berglund, I.; Dasgupta, P. K. *Anal. Chem.* **1992**, 64, 3007–3012.
(12) Berglund, I.; Dasgupta, P. K.; Lopez, J. L.; Nara, O. *Anal. Chem.* **1993**, *65*, 1192–1198.
(13) Sato, H. Keynote lecture presented at the International Symposium on Ion Chromatography, Turin, Italy, September 1994.

0003-2700/95/0367-2110$9.00/0 © 1995 American Chemical Society

omnipresent CO_2. Since un-ionized eluites are invisible to a conductivity detector, the undissociated fraction of any weak acid eluite will not elicit a detector response. The signal is thus strongly dependent on the pK_a of the eluite. This essentially means that eluite acids with $pK_a \geq 7$ cannot be detected by suppressed IC at all ($pK_a \geq 6$ for a carbonate-containing eluent) and the linear dynamic range for the determination of eluite acids in the pK_a range 3–6 is quite limited. If, however, the detector influent background was alkaline instead of slightly acidic, all but eluites of the highest pK_a values will be ionized and will thus be sensed by conductance detection. If the suppressor consistently suppressed exactly 99.9% of a 100 mM NaOH eluent, the detector influent will contain 0.1 mM NaOH (pH 10) and acid eluites with a pK_a value of $\leq\sim 10$ will be significantly ionized. While there is no known method to achieve an exact and constant degree of substoichiometric neutralization, it is possible to introduce a small and constant quantity of NaOH after quantitative neutralization and prior to the measurement of conductance. The concentration of NaOH should be limited to avoid a large (and noisy) detector background.

As previously shown,[12] the introduction of a small constant amount of NaOH is best accomplished by electrodialysis. As an eluite HX comes through, the following reaction occurs:

$$OH^- + HX \rightarrow X^- + H_2O \qquad (1)$$

with the result that OH^- is replaced by an equivalent amount of X^- and because the equivalent conductance of OH^- is greater than that of X^-, a decreased conductance (i.e., negative) signal results. Obviously, this response is not particularly analyte specific (except that extremely weak acids, $pK_a \geq 11$, are still largely undetected) and is essentially governed by the same detection principles that would be operative for an NaOH eluent, unsuppressed IC system.[14] The latter system, however, is largely impractical because the full concentration of the NaOH eluent appears as the detector background. In contrast, in the system discussed here, the detector NaOH background has no direct relationship with the eluent NaOH concentration and the user is free to choose any value for either the eluent or the detector background NaOH concentration.

The experimental arrangement is largely the same as that described previously.[12] An NaOH eluent anion chromatography system is configured with a water regenerant electrical suppressor that is followed by the first conductivity detector (D1). The background effluent from this detector is nearly pure water, containing a trace amount of acids resulting from non-hydroxide anions present in the eluent. This is followed by the microelectrodialytic NaOH generator (MENG) and a passive low-dispersion mixing device to achieve mixing of the electrodialytically introduced NaOH and the D1 effluent. A second conductivity detector (D2) then monitors the conductance again.

THEORETICAL CONSIDERATIONS

The following embodies generally applicable theoretical considerations for our experimental system. In specific cases, aprroximations and simplifications are possible; see, e.g., refs 10-12. For a strong monoprotic acid HX, the D1 signal G_{1sm} (in μS/cm) at any point in the eluite band where the eluite concentration is C molar, is given by

$$G_{1sm} = 1000C(\lambda_H + \lambda_X) \qquad (2)$$

Where λ_H and λ_X are the equivalent conductance of H^+ and X^-. For a weak monoprotic acid, the corresponding signal G_{1wm} is given by

$$G_{1wm} = 1000C'(\lambda_H + \lambda_X) \qquad (3)$$

where C' is given by

$$C' = 0.5(-K + (K^2 + 4KC)^{1/2}) \qquad (4)$$

where K is the dissociation constant of acid HX. The above expression for G_{1wm} is an approximation; it is not applicable at extreme dilutions or for values of K so low that the dissociation of HX is affected by the traces of acid present in the background suppressor effluent.

The general equation for weak polyprotic acids can be formulated as

$$G_{1wp} = 1000([H^+]\lambda_H + \sum_{i=1}^{n} iC\alpha_i\lambda_{H(n-i)X}) \qquad (5)$$

where $\lambda_{H(n-i)X}$ is the equivalent conductance value of the ion $H_{n-i}X^{i-}$ and the α values can be expressed as

$$\alpha_i = (K_0, ..., K_i[H^+]^{n-i})/\sum_{I=0}^{n}(K_0, ..., K_i[H^+]^{n-i}) \qquad (6)$$

K_1 through K_n are the first through nth dissociation constants of H_nX and K_0 has a value of 1. A polynomial in $[H^+]$, with a single unique real solution, is constituted by the charge balance expression

$$[H^+] = \sum_{i=1}^{n} iC\alpha_i \qquad (7)$$

With most polyprotic acids, the above expressions can be simplified in practice, some dissociations being negligible and other, closely spaced dissociation steps occurring to comparable degrees.

The second detector background, G_{2bgnd}, is dependent on the MENG current. It can be expressed as

$$G_{2bgnd}\ (\mu S/cm) = 1000(60Ei/96500Q)(\lambda_{Na} + \lambda_{OH}) \qquad (8)$$

where E is the faradaic efficiency (most MENG designs operate with near-unity faradaic efficiency), i is the MENG current (in mA), and Q is the chromatographic flow rate (in mL/min). Substitution of numerical values and consolidation of these lead to a simplified form of eq 8 that directly relates the D2 background to the MENG current, device efficiency, and the chromatographic flow rate:

$$G_{2bgnd} = 155Ei/Q \qquad (9)$$

(14) Okada, T.; Kuwamoto, M. *Anal. Chem.* **1985**, *57*, 829–833.

The exact background conductance will still depend on the extent of impurity anions present in the eluent. However, unless the amounts of impurities present are very significant, the precise value of G_{2bgnd} does not control the magnitude of the eluite signal; its choice is only important to us to reach an optimum value between the conflicting demands of having sufficient free NaOH available to equal or exceed the maximum eluite concentration expected and keeping the concentration low enough to maintain G_{2bgnd} low and thus minimize detector noise. A G_{2bgnd} value of 20–35 μS/cm (130–225 μA MENG current for unity efficiency at an eluent flow rate of 1 mL/min) is optimum for most purposes, providing a background NaOH concentration of ~100 μM (accounting for typical chromatographic dilution, this will accommodate injected analyte concentrations of 1 mN for each separated analyte).

For monoprotic acids with $pK_a \leq 8$ and for n-protic acids with pK_{a_n} being ≤ 8, neutralization of the eluite acid by the NaOH introduced is complete as long as modest concentrations are injected. The signal G_2 at any point in the eluite band, where the eluite concentration is C molar, is given by

$$G_{2m} = 1000C(\lambda_{OH} - \lambda_X) \quad (10)$$

$$G_{2p} = 1000Cn(\lambda_{OH} - \lambda_X{}^{n-}) \quad (11)$$

For the simplest case of a strong monoprotic acid, if the two detector signals, (eq 2) and G_{2m} (eq 10) are plotted against each other, the slope S_{sm} (or the ratio of G_{1sm} to G_{2m}) is constant, independent of the eluite concentration, and given by

$$S_{sm} = (\lambda_H + \lambda_H)/(\lambda_{OH} - \lambda_X) \quad (12)$$

Considering that λ_X values for common anions range approximately from 30 to 80, S_{sm} will range from 2.25 to 3.63. A rearranged form of eq 12 is useful for determining λ_X:

$$\lambda_X = (S_{sm}\lambda_{OH} - \lambda_H)/(S_{sm} + 1) \quad (13)$$

The caveat in determining λ_X is to be cognizant of the uncertainties caused by the propagation of errors; for an intermediate mobility anion of $\lambda_X = 50$, an uncertainty of 2% in determining G_{1sm} and G_{2m} translates to an uncertainty of 2.8% in S_{sm} and thence to ~10% in determining λ_X.

For the weak monoprotic acid case, the slope S_{wm} is going to be concentration dependent, decreasing with increasing C. Dividing eqn 3 by eq 10 yields

$$S_{wm} = (0.5S_{sm}(-K + (K^2 + 4KC)^{1/2}))/C \quad (14)$$

S_{wm} is linearly dependent on C^m where m varies from 0.5 to 1, depending on the relative magnitudes of K and C. For values of C comparable to K, e.g., put $C = 2K$ in eq 14; this yields

$$S_{wm} = 0.5S_{sm}K/C \quad (15)$$

while for $C \gg K$, eq 14 reduces to

$$S_{wm} = S_{sm}(K/C)^{1/2} \quad (16)$$

For polyprotic acids, a variety of scenarios are possible; a common one involves only the first proton being significantly, perhaps fully, dissociated in D1 ($G_1 = G_{1sm}$), while in D2, the fully ionized anion is the dominant species as given by eq 11. In this case, the slope S_{1sp} can be computed by dividing eq 2 by eq 11:

$$S_{1sp} = (\lambda_H + \lambda_{H(n-1)X})/(n(\lambda_{OH} - \lambda_X{}^{n-})) \quad (17)$$

The behavior is similar to that of strong monoprotic acids in that the slope is basically governed by the ionic mobilities. However, in this case not only the equivalent conductance of the monoanion but also that of the fully ionized polyanion is involved. Note that although $\lambda_X{}^{n-}$ is generally substantially higher than $\lambda_{H(n-1)X}$, the value of S_{1sp} will typically be lower than or, at best, equal to the range of values observed for S_{sm} in eq 12 because of the appearance of the factor n in the denominator of eq 17; i.e., the analyte exhibits a greater number of equivalents in D2 than in D1. A typical case where eq 17 applies is that of orthophosphate as analyte, the third proton of H_3PO_4 not playing any discernible role. At typical conditions used in IC, it is fully dissociated to $H_2PO_4^-$ in D1 with essentially no dissociation to HPO_4^{2-} while in D2 the only anionic form of the analyte is HPO_4^{2-}. In many other cases, there is significantly incomplete dissociation in D1 even for the first proton. In such a situation, it is necessary to modify eq 17:

$$S_{wp} = 0.5(-K + (K^2 + 4KC)^{1/2})/(C(\lambda_H + \lambda_{H(n-1)X})/(n(\lambda_{OH} - \lambda_X{}^{n-}))) \quad (18)$$

and the exact value of S_{wp} will exhibit a dependence on C similar to that previously discussed for eq 14.

One final case merits an individual discussion, that of weak acid analytes with $pK_a \geq 8$. These analytes may be incompletely ionized with a background NaOH concentration of 0.1 mM. It is sufficient to consider the case of a monoprotic acid because subsequent dissociation steps with pK_a values even higher are likely to contribute very little to the observed signal. For such analytes, e.g., borate, cyanide, silicate, etc., there is no discernible signal in D1. Consequently, the G_1/G_2 quotient is essentially zero. In the second detector, only the fraction that is ionized contributes to the D2 signal and this is a function of the amount of NaOH introduced through the MENG. The amount of NaOH introduced is available by appropriately modifying eq 9:

$$[Na^+] = 0.623Ei/Q \quad (19)$$

With the approximation that, in comparison with OH^-, H^+ is negligible in the second detector (this is reasonable under all conditions in which the amount of eluite acid does not overwhelm the amount of NaOH introduced), the D2 signal for a very weak monoprotic acid can be explicitly calculated from charge and mass balance expressions:

$$G_{2vwm} = 1000fC(\lambda_{OH} - \lambda_X) \quad (20)$$

where f is given by

$$f = 2[Na^+]K/(K(1 + C - [Na^+]) + K_w + ((K([Na^+] - C) - K_w)^2 + 4KK_w[Na^+])^{1/2}) \quad (21)$$

The consequence of eq 20 is that f varies as a function of concentration and there is a departure from linearity in the response behavior. More importantly, for $[Na^+] = 0.1$ mM, while an analyte of $pK_a = 8$ is nearly completely ionized, only ~10% is ionized for an analyte with $pK_a = 11$. Clearly, detection of even weaker acids is impractical unless $[Na^+]$ is increased.

Finally, while dual-channel chromatographic detection and detailed numerical processing of the resulting two channels of data is not a rare practice (see, e.g., the exemplary work of Aue et al. in ref 15 and citations therein), such data are usually collected simultaneously or in parallel. In the present case, there is a reactive element in between the two detectors that obligatorily results in time delay and dispersion. In taking the ratio of G_1 and G_2 signals or plotting them against each other, it will be first necessary to correct for this.

EXPERIMENTAL SECTION

The experimental setup was similar to that used previously.[12] A prototype Dionex 4000i gradient pump was used in combination with an auxiliary pulse dampener. Other parts, such as the injection valve (25 μL), the electrically operated water regenerant autosuppressor (ASRS-1, 4 mm), conductivity detectors (CDM-I), and the knitted mixing coil, were all Dionex components (Sunnyvale, CA). All chromatography was performed with NaOH eluents, prepared with 50% NaOH and Nanopure water, at a flow rate of 1.0 mL/min. The eluent concentration varied between 3 and 30 mM; generally these were prepared in situ by dilution of a 30 mM stock. Both isocratic and gradient elution were used. An anion trap column (ATC-1) was incorporated before the injection valve. The analytical column was a 4 × 250 mm AS-11 column, in combination with a 4 × 50 mm AG-11 guard column. All connecting tubing in the chromatographic line was 0.25 mm i.d. PEEK tubing. The MENG was made from Nafion and PTFE tubing as described below; it was powered by a previously described constant-current generator.[12]

The MENG design is an improvement over that previously used (Figure 3a, ref 12). It is constructed from Nafion 020 tubing (~0.4 mm i.d., 0.5 mm o.d.; Perma-Pure Products, Toms River, NJ; courtesy Dr. David Leighty), having an active length of ~15 mm. The electrodes are made of 100 μm diameter platinum wire, of which the cathode protrudes out through the wall of the PTFE tubing. The anode is wound as a spiral around the Nafion membrane. This arrangement is inserted into an outer shell, made of a segment from a disposable plastic 1 mL syringe. Feed NaOH passing through the shell was ~10 mM in concentration. The NaOH solution flowed by gravity at a rate of ~>1 mL/min. With a typical applied current level of 160 μA, G_{2bgnd} typically ranged between 23 and 27 μS/cm for NaOH eluent concentrations ranging between 3 and 50 mM. The necessary voltage was 2.2–2.5 V.

All data were acquired by a 80386-based PC using AI-450 software and an ACI interface, both from Dionex. In comparing G_1 and G_2 signals, the following algorithm was used: (a) align the two peaks at the peak maximum; (b) process the leading and trailing halves of the peaks separately, for G_1, first compute the time interval between 25% of the peak maximum at the leading edge and the peak apex and compress the corresponding time interval for G_2 to this value; (c) repeat the procedure for the trailing edge. This results in the two peaks being temporally aligned at the $h_{0.25}$ points, and the data can now be directly compared. Data below 25% of the peak height are not used. The choice of $h_{0.25}$ for alignment is not unique; any other value, e.g., $h_{0.1}$, can be used just as well. A copy of the routine for this alignment/dispersion correction, written in BASIC, is available from the authors on request.

RESULTS AND DISCUSSION

Design and Performance of the MENG. The MENG must be designed to minimize the induced dispersion and reduce detector noise. In addition to hydrodynamic dispersion caused by the physical nature and dimensions of the MENG conduit, there is also reactive dispersion in such a device. Eluite HX diffusing outward from the central region of the flow stream reacts with the NaOH diffusing inward from the membrane walls to form NaX. The latter is redistributed again because of the extant concentration gradient. In terms of noise, there are potentially several sources; variations of the constancy of the current fed to the MENG is generally not a significant source, but the constancy of the faradaic efficiency can be a factor since the exact physical rigidity of the device (interelectrode distance, membrane/electrode contact, etc.) and the formation of any gas bubbles or layers on the electrode can all affect the faradaic efficiency. The typical baseline noise (standard deviation) of the present system, operating with a G_{2bgnd} of ~25 μS/cm, is 20–25 nS/cm over a 20 min period; the value is smaller over shorter periods.

On the basis of our general experience with MENG devices, the following points are salient. It is desirable to have as low a potential as possible to achieve a given current level. If the outer electrode is further away from the membrane and is, for example, in contact with the outer jacket, the interelectrode distance is typically large and the electrical resistance of the device increases. The exact physical position of the outer electrode should not be sensitive to vibrations. Both of these increase the observed detector noise. It was found that devices with an active length shorter than 10 mm tend to be more noisy than longer devices: this is understandable in view of the fact that, at an applied current level of 200 μA, the current density is already in excess of 10 A/m^2 of membrane area, a relatively high value at such low ionic strengths. At the current levels we typically use, it is interesting that devices significantly longer than ~16 mm also produced more noise, but this appears to be related to the relative loss of rigidity as the device length increases. Noise performance of such longer devices can be increased by improving rigidity, e.g., by coiling the inner electrode on an wettable polysulfone membrane tube before the insertion of the assembly within the Nafion membrane tube or by inserting a self-expanding helix of Nylon monofilament inside the Nafion. In any case, excessively long membrane lengths in the MENG are undesirable because they increase the hydrodynamic dispersion. Layering of gas or bubbles on the inner electrode where NaOH is generated according to the reaction

$$Na^+ + H_2O + e \rightarrow NaOH + {}^1/_2H_2 \quad (22)$$

does not appear to be a significant source of noise. We studied

(15) Millier, B.; Sun, X.-Y.; Aue, W. A. *Anal. Chem.* **1993**, *65*, 104–111.

the use of a palladium wire cathode, which would have eliminated any evolution of hydrogen for a prolonged period of time; however, no baseline noise improvements could be discerned. Consideration of tabulated data on the aqueous solubilities of hydrogen (780 μM at 1 atm and 25 °C) also indicates that there should not be any evolution of *gaseous* H_2 accompanying the generation of 100 μM NaOH. Since the aqueous solubility of O_2 is much higher than that of H_2, gas evolution should obviously not be a problem at the anode.

Band dispersion was studied in detail for a MENG device incorporating a 15 mm long membrane; band dispersion was calculated as the square root of the difference between the square of the band volumes with and without the MENG device.[16] The dispersion values computed this way decrease with increasing band volumes; i.e., the same extent of dispersion affects a fast eluting, intrinsically narrower band more adversely than it affects a broader eluite band. For a chloride peak (injection volume 25 μL) that elutes relatively fast, the measured dispersion value was 67 ± 4 μL when the device was operating in the passive mode (hydrodynamic dispersion only) and 94 ± 6 μL with the device in actual operation. Since dispersion adds in a square root of sum of squares fashion, the contribution of the reactive dispersion can be computed to be 65 μL, i.e., it contributes as much as the hydrodynamic dispersion.

Analyte Overloading. With low-pK_a acids, when C in the eluite band exceeds the background NaOH concentration in the detector, the resulting peak is W-shaped, giving the misleading impression that it is a poorly resolved doublet. This happens because the decreasing conductivity and the resulting negative signal produced according to eq 1 continues only until free OH^- is available. When the NaOH is fully titrated, excess HX begins to increase the conductance again. If the overload is only slight, the peak may appear misshapen relative to the corresponding D1 peak. As the pK_a of the eluite acid increases beyond ~5, a W-shaped peak is not observed, because of the formation of a NaX/HX buffer system. At eluite p$K_a \geq 6$, after the NaOH is fully neutralized, any further amount of HX added does not dissociate significantly. Hence, analyte overload results in a flat-topped peak. Experimental observations match theoretical expectations; simulated responses for (a) a strong acid, (b) p$K = 4$, (c) p$K = 5$, and (d) p$K = 6$ are shown in Figure 1.

Any misshapen D2 peak should therefore be reexamined by injecting a more dilute sample. Unless overloaded, the D2 peak area/height is strictly linearly related to the injected concentration. Because the MENG responds very rapidly to a change in the driving current, the suspect D2 peak can also be reexamined in a more convenient fashion after increasing the MENG current and reinjecting the same sample without dilution.

Effect of Impurities in the NaOH Eluent. Thus far, we have not taken into account the effect of impurities present in the NaOH used as the chromatographic eluent. Without an electrodialytic eluent generator (EEG),[4] there will always be some degree of impurities present in the eluent. Most notably, there is always some extent of CO_2 (or carbonate) contamination. An EEG is not commercially available; in the present work we have therefore concentrated on alternatives that would be available more easily to most users. With an impurity removing column (e.g., an anion trap column, ATC-1), it was found possible to minimize (but not completely eliminate) the level of impurities in the eluent. There

(16) Dasgupta, P. K. *Anal. Chem.*, **1984**, *56*, 103–105.

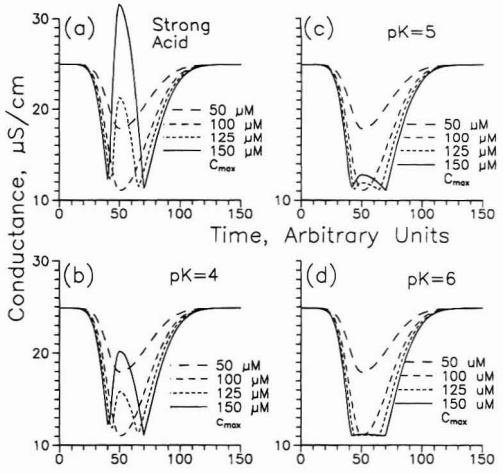

Figure 1. Responses for different concentrations (50–150 μM at the peak apex, D2 background 100 μM NaOH) of a monoprotic eluite acid ranging from (a) strong acid to (d) pK = 6. The simulated peak profile is modified Gaussian and λ_X is assumed to be 60.

can be impurities other than carbonate in the eluent. One procedure used in this laboratory for preparing NaOH eluents involved boiling high-purity water to remove any residual CO_2 and then adding high-purity solid NaOH or 50% NaOH in the desired amount. It was found that if a glass vessel is used for boiling the water and especially if the NaOH is added while the water is still hot, very substantial amounts of silicate are incorporated in the eluent. Incorporation of carbonate or silicate generally results in an increase in the eluent strength over that of pure NaOH. There is also an increase in the D1 background conductance. But the effects of these on the D1 signal are generally minor. The most important adverse effect of such impurities is their influence on the D2 signal, especially for high-pK_a analytes. In the presence of significant amounts of carbonate or silicate, the absolute value of the G_{2bgnd} is not an accurate measure of the NaOH that is free and available to react with the eluite HX. The value of G_{2bgnd} does not linearly increase with the MENG current because the initial amounts of NaOH introduced are spent in titrating the impurity acids present in the suppressed background. Indeed, G_{2bgnd} may actually first decrease with increasing MENG current and then increase in the expected fashion. Figure 2 shows simulated and actual G_{2bgnd} values at two different levels of carbonate contamination. The simulations assumed a faradaic efficiency factor of 1.075, which best fits the behavior of the particular MENG device used. The close correspondence of the simulated results with the experimental data is an indication of the validity of the experimental model.

Consider that, in the presence of carbonate, eq 1 will be replaced or augmented by

$$CO_3^{2-} + HX \rightarrow HCO_3^- + X^- \qquad (23)$$

resulting in a substantial loss of signal. Further, even the occurrence of the reaction above is compromised as the pK_a of HX approaches or exceeds the the pK_a of HCO_3^-. It is obvious that an approach substantially more complex than eq 10 or 11,

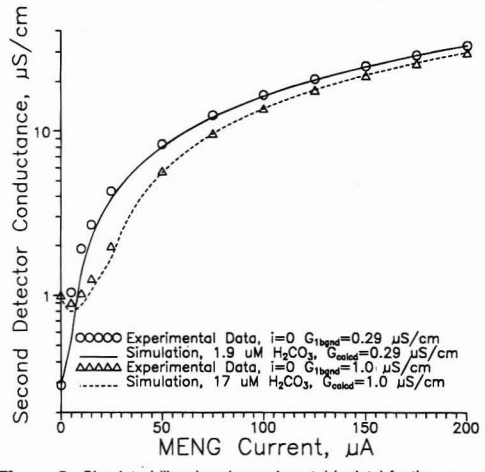

Figure 2. Simulated (lines) and experimental (points) for the second detector background conductance at two different carbonate contamination levels. The carbonate concentration used in the simulation was computed from the first detector background conductance, assuming it to be solely due to H_2CO_3.

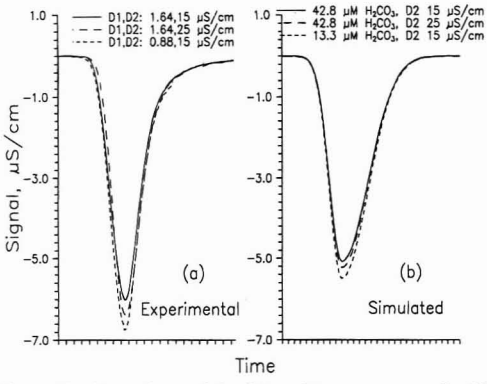

Figure 3. Dependence of the D2 analyte response on the D2 background conductance in the presence of significant eluent impurity levels. (a) Experimental and (b) theoretically simulated results are shown for 100 μM phthalate as sample at two different carbonate contamination levels (at two different D2 background conductance values for the higher contamination level).

that takes into account the presence of the various carbonate species and their redistribution upon reaction with HX, is necessary to appropriately simulate the system. Figure 3a shows the experimental results for 100 μM phthalate as the injected sample and 30 mM NaOH as the eluent. The presence or absence of an impurity trap column made a significant difference in the D1 background conductance (0.88 vs 1.64 μS/cm). The results at two different MENG current levels (to obtain G_{2bgnd} values of ~15 and 25 μS/cm) for the higher carbonate contamination level and for a single MENG current level (G_{2bgnd} ~15 μS/cm) at the lower carbonate contamination level are presented. A numerical simulation of the same system is shown in Figure 3b. The carbonate contamination levels were calculated to be 13.3 and 42.8 μM, respectively, with and without the impurity trap column, assuming that the D1 background conductance is solely due to H_2CO_3. An exponentially modified Gaussian peak profile was assumed. The limiting equivalent conductance of the hydrogen phthalate monoanion and the phthalate dianion are not available in the literature and were respectively assumed to be 29 and 57 μS/cm. The exact peak width is different in the experimental vs the simulated system; also, experimental detector calibration may not have been exact. With this in mind, the agreement between theory and experiment is excellent.

Since the presence of carbonate in D2 is detrimental, we wished to determine whether the choice of the MENG feed solution has any effect on the system performance. It was thought that the choice of a neutral salt solution such as 10 mM Na_2SO_4 instead of the NaOH as the Na^+ feed solution may reduce the amount of carbonate that is introduced through the MENG, if any is introduced through this route. Analyte peak heights were unchanged whether NaOH or Na_2SO_4 was used as the MENG feed. The use of Na_2SO_4 or similar other salt solution, however, electrodialytically generates acid on the feed side, and the H^+ thus generated competes with Na^+ for passage to the cathode side (very effectively, since λ_H is 7 times greater than λ_{Na}). The electrodialytic NaOH generation efficiency is thus markedly decreased relative to the use of a NaOH feed. Consequently, a higher MENG current is needed to attain the same G_{2bgnd} with a concomitant rise in the noise level. Therefore, the use of NaOH as the Na^+ feed is preferred.

As long as electrodialytically generated NaOH is unavailable, we find that minimum carbonate contamination is achieved by diluting a more concentrated stock eluent solution (maintained in a bottle with a soda lime-based CO_2 trap) in line with high-purity water if a gradient pump that allows in situ mixing is available. Typically 10–20% of the stock eluent should be diluted with 80–90% water; satisfactory performance is then obtained in the presence of an impurity trapping column. The presence of the latter is still critical, however. As a general rule, optimum performance can be expected from the system as long as the D1 background conductance is ≤ 1 μS/cm.

System Noise and Limits Of Detection. The limits of detection for various anions at the second detector, based on a signal equal to 3 times the standard deviation of the background signal, is listed below (in micromolar, followed by retention time in minutes in parentheses): azide, 3.0 (4.58); arsenite, 3.2 (2.85); borate, 8.6 (3.65); bromate, 1.65 (3.63); bromide, 1.7 (4.25); chloride, 1.5 (2.48); malate, 1.9 (7.22); nitrate, 2.7 (5.98); nitrite, 2.1 (3.28); phthalate, 1.2 (5.03); silicate, 4.0 (2.68); succinate, 1.7 (7.00); sulfate, 2.1 (8.08), and sulfide, 5.1 (3.03).

There is some indication that thermostating the entire setup results in significant further improvement of signal/noise; detailed results will be published in the future. Borate and cyanide peaks show significant tailing and broadening on the stationary phase used; this adversely affects the attainable limit of detection. For volatile weak acids such as HCN and H_2S, transmembrane loss in the suppressor can also occur.[17]

Calibration Behavior. Second detector calibration shows excellent linearity for a variety of anions tested across the pK_a range. Coefficient of determination (linear r^2, peak area vs injected concentration at a G_{2bgnd} level of 25–27 μS/cm) values for arsenite, chloride, monochloroacetate, nitrate, nitrite, phthalate, silicate, succinate, and sulfate were respectively determined to

(17) Dasgupta, P. K. *J. Chromatogr. Sci.* **1989**, *27*, 422–448.

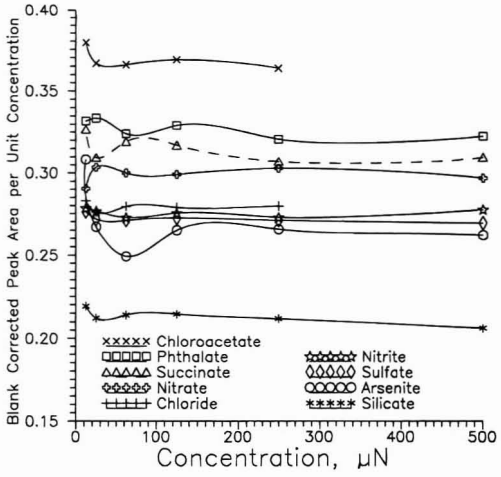

Figure 4. Analytical sensitivity as a function of concentration. A perfectly linear calibration response will result in a perfectly flat line.

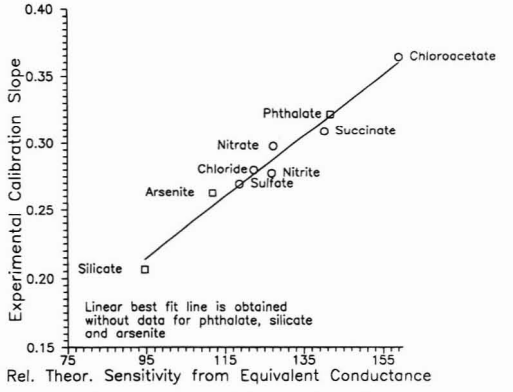

Figure 5. Correspondence of the experimental analyte response sensitivity to that calculated from pK_a and λ values. For arsenite, phthalate, and silicate, the λ values are not tabulated; these were estimated (see text).

be 1.0000, 0.9999, 1.0000, 0.9999, 0.9999, 1.0000, 0.9998, 0.9999, and 1.0000, over the 0–500 μN injected sample concentration range. Linearity of calibration for several of these analytes is much worse on the first detector; some are not even seen by the first detector. The response linearity observed for silicate is slightly worse because at the high end of the injected sample concentration the extent of ionization for silicate at the second detector is concentration dependent, decreasing at higher concentrations, as elaborated in eqs 20 and 21. Figure 4 shows a sensitivity plot as a function of concentration. Essentially uniform sensitivity is seen for all the analytes tested (with the recognition that at low concentrations, blank correction becomes increasingly important) with the exception of arsenite. In the arsenite case, oxidation to arsenate, either on-column or in the prepared standards, to a relatively greater extent at lower sample concentrations, is the likely reason.

The calibration slopes for the various analytes in the above experiment are shown plotted in Figure 5 against relative theoretical sensitivities obtained from eqs 10, 11, 20, and 21. The theoretical values were calculated based on an assumed injected concentration of 125 μM, a 10-fold dilution (at the peak apex) during the chromatographic process, a D2 background of 100 μM NaOH, pK_a values of the acids, and the limiting equivalent ionic conductance values. The latter data are not available in the literature for phthalate, silicate, and arsenite. These values were initially estimated from their size and shape with later experimental verification by ion-exchange/conductance measurement techniques as detailed in ref 18. The values used were 67, 44.5, and 57 μS/cm for the arsenite and silicate monoanions and the phthalate dianion, respectively. The pK_a value(s) and any assumption regarding dilution in the chromatographic process are needed only for the very weak acids because of the potentially nonlinear relationship of the signal with concentration represented by eqs 20 and 21.

The linear relationship observed between theoretical predictions and experimental data suggests that if pK_a and equivalent conductance values are known, reasonably good results can be obtained without actual calibration with analyte standards. This can be a real advantage where standards are difficult to prepare, expensive, or degrade rapidly, e.g., by oxidation. It is important to note that the best-fit line in Figure 5 was drawn without considering the data for arsenite, silicate, and phthalate for which the equivalent conductance values were not tabulated. It is remarkable as to how well the predicted values in these cases fall on the best-fit line. Nevertheless, the approach should be implemented with caution for the anions of very weak acids where the pK_a values are comparable to or greater than the pH of the D2 background. Not only is it necessary to use the correct equivalent conductance value but the results can be particularly sensitive to the choice of the pK_a value. In a significant number of cases, the reported pK_a value spans a significant range; Perrin's compilation of pK_a values[19] show, for example, the pK_a value for $HAsO_2$ at 25 °C to range from 9.08 to 9.28. There are other cases where the tabulated equivalent conductance value may bear reexamination. As Figure 5 shows, nitrate and nitrite have tabulated equivalent conductance values that are almost the same but have perceptibly different experimental calibration slopes. It is interesting that we have previously observed, in a totally disparate experiment, that there is also a discrepancy between the behavior of nitrite and nitrate when the electrophoretic mobilities are plotted against the tabulated equivalent conductance.[20]

Estimation of Limiting Equivalent Conductance. The present experimental setup permits the estimation of the equivalent conductance in a unique manner if the sample concentration in equivalents per liter is known (a knowledge of the relevant pK_a value(s) is also necessary if very weak acids are involved). Equations 10, 11, and 20 indicate that the peak area is proportional to the injected concentration C (in equiv/L; for very weak acids the fraction ionized f can be computed from eq 21) and the difference in the equivalent conductance between the hydroxide ion and the test analyte. Consider eq 10; if the area response values for different analyte ions at the same concentration are plotted

(18) Dasgupta, P. K.; Nara, O. *Anal. Chem.* **1990**, *62*, 1117–1122.

(19) Perrin. D. D. *Ionisation Constants of Inorganic Acids and Bases in Aqueous Solution*; 2nd ed.; Pergamon: New York, 1986.

(20) Dasgupta, P. K.; Bao, L. *Anal. Chem.* **1993**, *65*, 1003–1011.

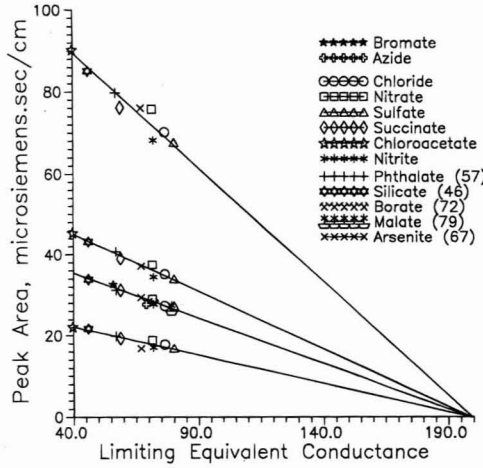

Figure 6. Peak conductance area vs limiting equivalent conductance. If the concentration (and pK_a for very weak acids) is known, the second detector peak area at a given injected concentration can be used for the estimation of the λ value (of the fully ionized species); see text. The lines from bottom up are for injected concentrations of 62.5, 100, 125, and 250 μN analyte, respectively. The λ values for some ions are not in the literature; the independently estimated values for these are shown in parentheses; note their excellent correspondence on the respective lines.

against the respective λ values, a straight line will be observed. If the process is repeated at a different concentration, a straight line with a different slope, proportional to the concentration C (or fC, for very weak acids, according to eq 21), will result. Further, all such lines should intersect the abscissa at a value corresponding to λ_{OH}. Such a plot is shown in Figure 6 at four different concentration levels. Some ions with unknown λ values are also plotted as indicated; for very weak acids, f was calculated from eq 21 based on a listed pK_a value. The λ values obtained for those analytes with unknown λ values correspond well with what we can independently estimate or measure for them (vide supra). While the method admittedly requires a knowledge of the pK_a for very weak acids, it nevertheless provides a novel and interesting way of determining limiting equivalent conductance values.

Diagnosis of Coelution. Consideration of the two-dimensional data (appropriately corrected for the time lag and the dispersion between the two detectors) as a whole can yield valuable information about the equivalent conductance for an analyte anion, pK_a of the corresponding acid, and occurrence of peak overlap (if such overlapping analyte peaks have different pK_a values, limiting equivalent conductance values, or both). Consider first the case for pure analyte peaks where the signals for four individual pure analytes are plotted in Figure 7; with the first detector signal as the ordinate and the second detector signal as the abscissa. Note that insets in each figure show the individual responses of the first and the second detectors. The signals for the leading and trailing halves (ascending and descending parts) of the peak are individually shown; ideally these should be identical for a pure analyte peak. The scale ratios (x/y) for all of the individual analytes are the same. It is immediately noticeable that the observed slopes are a strong function of the pK_a, as would be predicted by eqs 10 and 12–14. Ideally the slope for sulfide should be essentially zero—the small but discernible response that

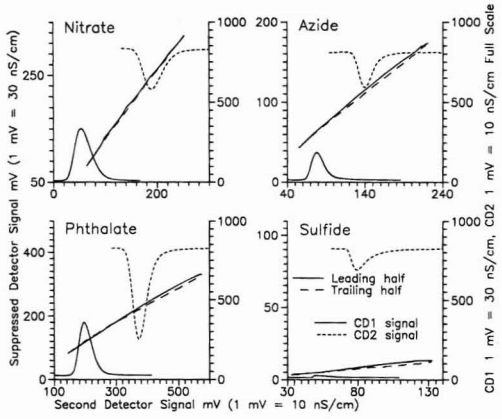

Figure 7. D1 output vs D2 output. The peak at the bottom left is the D1 output, the negative peak at the top right is the D2 output (right ordinate applies to both and the time (abscissa) is the same for both outputs but in arbitrary units. The principal item of interest in each panel, representing the depicted analyte, is the D1 output plotted against the D2 output (left ordinate and bottom abscissa scales, respectively) with the solid and dashed lines depicting the leading and trailing halves of each peak, respectively. The slope of this line is an indication of the analyte pK_a, value and the concordance of the solid and the dashed lines is an indication of the purity of the peak.

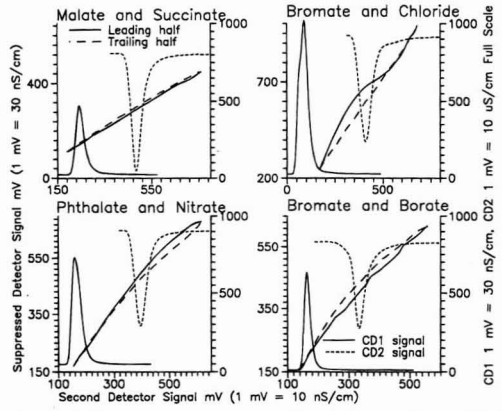

Figure 8. Same as Figure 11, except mixtures that result in coeluted peaks used.

is observed in the first detector is likely caused by on-column or in-suppressor partial oxidation of sulfide. Closer examination of the plots further shows that the plots are really not perfect straight lines, except for nitrate. For the other analytes, the slope decreases as the peak apex is approached (as the signal increases). This is expected for weak acids: as concentration increases toward the peak apex, the degree of dissociation decreases, resulting in a proportionally lower signal at higher concentrations.

Figure 8 shows similar plots for four pairs of analytes: in each case, the eluent strength was deliberately increased to cause coelution. However, in no case can a presence of more than one analyte be discerned if the individual detector responses are examined. If there is anything short of a perfect peak overlap, the composition of the leading and trailing halves will be different,

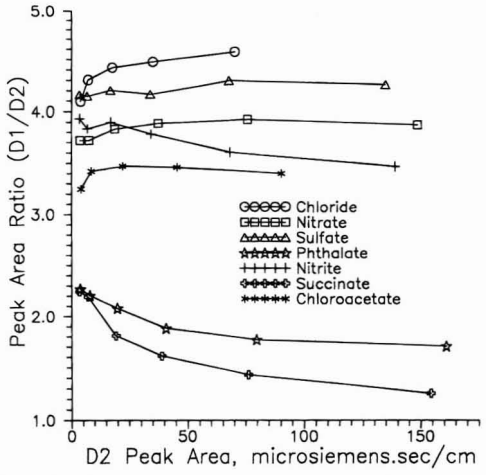

Figure 9. Area ratio of first vs second detector peaks for selected analytes as a function of second detector peak area. This can be used as a quick index for the verification of the identity of a peak.

leading to a difference in the nature of the lines plotted for the ascending and the descending parts. This is clearly evident for the bromate/chloride (both are fully ionized under the conditions of the experiment but λ values are significantly different) and bromate/borate (marked difference in the pK_a values) pairs. The diagnosis of coelution is less apparent at first sight in the case of the nitrate/phthalate pair, but closer examination reveals a clue (other than the difference in the plots for the ascending and descending parts near the peak apex): the initial slope is high and is typical of a strong acid; however, nonlinearity becomes quite pronounced toward the peak apex, not expected for strong acid analytes. The diagnosis of coelution is not foolproof; the completely overlapped peak pair of malate and succinate have similar pK_a and λ values, and the present method fails to diagnose coelution in this case.

Peak Identity Verification. The validation of the identity of an eluite peak, beyond its retention time, through the consideration of the two individual detector signals and the estimation of the pK_a and the λ values has been suggested in the foregoing. A superior and much faster alternative is to match the observed ratio of the areas of the two peaks registered by the two detectors against an internal library of such values. The area ratio reflects the effect of both the pK_a and the λ value. This comparison is preferably done as a function of one of the detector signals, e.g., that from the second detector, since the degree of dissociation in the first detector and thus the peak area ratio for weak acids can be dependent on the concentration injected. We have also observed some variation in the area ratio for some strong acid ions at low injected concentrations; the reason for this is not fully understood but is likely due to changes in peak shapes as a function of injected concentrations and the nature of the integration algorithm. Figure 9 shows such a plot; it is obvious that the availability of such data can greatly aid rapid confirmation of the identity of an eluite.

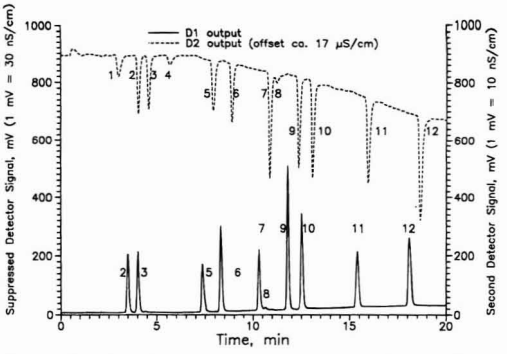

Figure 10. Two-channel gradient chromatogram for a multicomponent sample: 25 μL injection, 50 μM each analyte, 0–2.5 min, 3 mM NaOH, linearly ramped to 30 mM NaOH over 2.5–15 min and held there till the end of the run. Peak identities: (1) silicate, (2) monochloroacetate, (3) bromate, (4) cyanide, (5) trifluoroacetate, (6) bromide, (7) succinate, (8) carbonate (contamination), (9) sulfate, (10) fumarate, (11) phthalate, and (12) citrate.

Gradient Elution Chromatography. The method is generally applicable to both isocratic and gradient elutions. It should be noted, however, that the use of an impurity trap column is essential with gradient systems. An illustrative gradient elution chromatogram with each analyte at the 50 μM level is shown in Figure 10. The eluent concentration was varied 10-fold over the elution program (3 → 30 mM NaOH) and resulted in a change in G_{1bgnd} and G_{2bgnd} of 0.17 → 0.90 and 26.4 → 24.3 μS/cm, respectively. The test sample consists of representative very weak, weak (mono- and divalent), and strong (mono- and divalent) acids. Even a simple visual examination of the two detector outputs allows one to reach some conclusion about the nature of a particular eluite peak.

Although it has not been specifically demonstrated, it is obvious that a approach similar to that described here for anions will be of value in the analysis of cationic substances, notably amines and amino compounds.

ACKNOWLEDGMENT

This research was supported by a grant from the Dionex Corp. We would particularly like to acknowledge the help and encouragement offered by Steve Rabin, John Stillian, and Nebojsa Avdalovic.

Received for review January 9, 1995. Accepted April 12, 1995.[⊗]

AC950026M

[⊗] Abstract published in *Advance ACS Abstracts,* June 1, 1995.

Anal. Chem. **1995,** *67,* 2119–2128

Thermodynamics of Solute Partitioning into Immobilized Artificial Membranes

Shaowei Ong and Charles Pidgeon*

Department of Medicinal Chemistry, School of Pharmacy, Purdue University, West Lafayette, Indiana 47907

The solute retention mechanism on immobilized artificial membranes (IAMs) was studied using three different IAM.PC phases. IAMs were prepared by immobilizing either single-chain or double-chain phosphatidylcholine (PC) ligands. Solute affinity for the single-chain IAM.PC columns (with a ligand density of 127 μmol of PC/g of IAM) was 3-fold lower compared to solute affinity on the double-chain IAM.PC column (with a ligand density of 98 μmol of PC/g of IAM). This suggests that the solute retention on IAMs is dominated by a solute partitioning mechanism. Temperature-dependent studies indicated that the thermodynamics of solute partitioning is similar on both the single-chain and double-chain IAM.PC surfaces. For a set of phenol derivatives, the partitioning into IAM.PC surfaces is both enthalpy and entropy driven. For β-blockers, the partitioning into IAM.PC surfaces is entropy driven. The free energy of solute partitioning into IAMs correlates very well with the free energy of solute partitioning into liposomes.

Immobilized artificial membrane (IAM) chromatography surfaces have been used in a variety of chemical and biological applications.[1–12] One of the most promising applications of IAM surfaces resides in their ability to predict drug permeability through membranes and drug absorption in tissues and animals.[3,5] In addition, a recent report demonstrated that IAMs can predict pharmacokinetic parameters including drug binding to proteins,[13] which was unexpected because IAMs emulate lipid surfaces not protein surfaces. Nevertheless, these applications of IAMs involve the chromatography of small drug molecules on IAM high-performance liquid chromatography surfaces. Elucidating the molecular reasons responsible for IAM predictions of drug transport and drug partitioning requires that the mechanism of solute retention on IAMs be understood from a fundamental perspective.

Solute retention on IAMs and all other chromatographic surfaces is facilitated by understanding the temperature-dependent solute retention of the capacity factor, k'_{IAM}, that is calculated according to

$$k'_{IAM} = (t_r - t_o)/t_o \quad (1)$$

where t_o is the retention time for an unretained compound and t_r is the retention time of solute. During the chromatographic process, there is an equilibrium between the solute in the mobile phase and solute in the stationary phase; for IAM surfaces, this equilibrium constant or distribution constant is denoted as K'_{IAM}. The k'_{IAM} capacity factor is proportional to the K'_{IAM} partition coefficient,

$$k'_{IAM} = \phi K'_{IAM} = \phi(C_{IAM}/C_M) \quad (2)$$

where $\phi = V_s/V_m$, V_s is the stationary phase volume, and V_m is the mobile phase volume in the column. In eq 2, C_{IAM} is the molar solute concentration in the IAM interphase and C_M is the molar solute concentration in the mobile phase. Equation 2 defines the relationship between the chromatographically measured k'_{IAM} value to the biologically relevant immobilized artificial membrane equilibrium constant K'_{IAM}.

The key concept is that when solute retention is dominated by a partitioning mechanism, the distribution constant K_{IAM} is called the IAM partition coefficient. The Gibbs free energy of transfer, $\Delta G°$, of solute transfer from the mobile phase to the stationary phase is related to K_{IAM} as follows:[14]

$$\Delta G° = -RT \ln K_{IAM} \quad (3)$$

where R is the gas constant and T is temperature. Equation 4 shows how the temperature dependence of a solute's capacity factor k'_{IAM} can be used to obtain thermodyamic quantities

$$\ln k'_{IAM} = -\frac{\Delta H°}{RT} + \frac{\Delta S°}{R} + \ln \phi \quad (4)$$

where $\Delta H°$ is the partial molar enthalpy change for the transfer of the solute from the mobile phase to the stationary phase and $\Delta S°$ is the associated change in entropy. If $\Delta H°$ and $\Delta S°$ are independent of temperature, a linear plot of $\ln k'$ vs $1/T$ (the van't Hoff plot) is obtained, the slope equals $\Delta H°$, and the intercept

(1) Pidgeon, C. U.S. Patent 4,931,498, 1990.
(2) Pidgeon, C.; Stevens, J.; Otto, S.; Jefcoate, C.; Marcus, C. *Anal. Biochem.* **1991**, *194*, 163–173.
(3) Ong, S.; Liu, H.; Qiu, X.; Bhat, G.; Pidgeon, C. *Anal. Chem.* **1995**, *67*, 755–762.
(4) Pidgeon, C. U.S. Patent 4,927,879, 1990.
(5) Pidgeon, C.; Ong, S.; Liu, H.; Qiu, X.; Pidgeon, M.; Dantzig, A. H.; Munroe, J.; Hornback, W. J.; Kasher, J. S.; Glunz, L.; Szczerba, T. *J. Med. Chem.* **1995**, *38*, 590–594.
(6) Ong, S.; Cai, S. J.; Bernal, C.; Rhee, D.; Qiu, X.; Pidgeon, C. *Anal. Chem.* **1994**, *66*, 782–792.
(7) Qiu, X.; Ong, S.; Bernal, C.; Rhee, D.; Pidgeon, C. *J. Org. Chem.* **1994**, *59*, 537–543.
(8) Rhee, D.; R., M.; Chae, W. G.; Qiu, X.; Pidgeon, C. *Anal. Chim. Acta* **1994**, *297*, 377–386.
(9) Thurnhofer, H.; Schnabel, J.; Betz, M.; Lipka, G.; Pidgeon, C.; Hauser, H. *Biochim. Biophys. Acta* **1991**, *1064*, 275–286.
(10) Cohen, D. E.; Leonard, M. R.; Leonard, A. N.; Donovan; Carrey, M. C. *Gastroenterology* **1993**, *104*, A889.
(11) Pidgeon, C.; Cai, S.; Bernal, C., submitted for publication in *J. Chromatogr., A.*
(12) Pidgeon, C.; Venkatarum, U. V. *Anal. Biochem.* **1989**, *176*, 36–47.
(13) Kaliszan, R.; Nasal, A.; Bucinski, A. *Eur. J. Med. Chem.* **1994**, *29*, 163–170.
(14) See, for example: Edsall, J. T.; Gutfreund, H. *Biothermodynamics: The Study of Biochemical Processes at Equilibrium*; Wiley: New York, 1983.

0003-2700/95/0367-2119$9.00/0 © 1995 American Chemical Society

Chart 1. Structures of Three Different IAM.PC Bonded Phases[a]

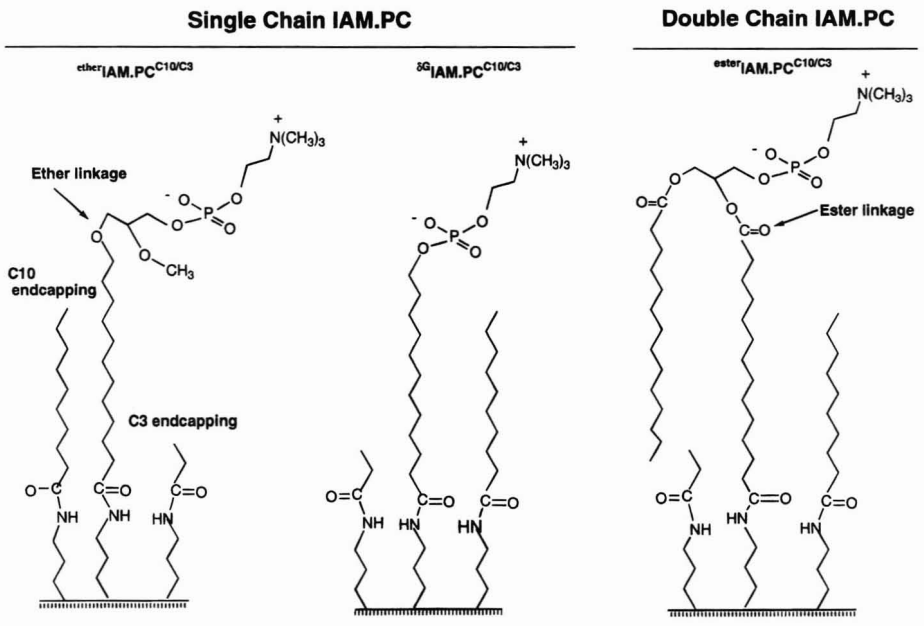

[a] The double-chain IAM.PC has a nonbonded, conformationally free hydrocarbon chain.

equals the sum of $\Delta S°/R$ plus a constant that depends on the phase ratio ($\ln \phi$). These thermodynamic constants ($\Delta H°$, $\Delta S°$) are useful in assessing the thermodynamic driving force responsible for solute retention. Our goal is to obtain thermodynamic parameters to elucidate solute retention on IAM surfaces. The intent is to understand why IAM surfaces are more accurate than all existing experimental models in predicting drug membrane partitioning.

The effect of the lipid structure on the thermodynamics of solute partitioning was studied. Differences in lipid structure are shown in Chart 1. One of the major factors influencing solute retention is the number of alkyl/acyl chains on the immobilized phospholipid ligands shown in Chart 1. The IAM bonded phases were (i) a single-chain ether PC ligand (^{ether}IAM.PC$^{C10/C3}$), (ii) a single-chain PC ligand that lacks a glycerol backbone ($^{\delta G}$IAM.PC$^{C10/C3}$), and (iii) a diacylated or double-chain PC ligand (^{ester}IAM.PC$^{C10/C3}$). Single-chain IAM.PC denotes either ^{ether}IAM.PC$^{C10/C3}$ or $^{\delta G}$IAM.PC$^{C10/C3}$; double-chain IAM.PC denotes ^{ester}IAM.PC$^{C10/C3}$.

EXPERIMENTAL SECTION

Chemicals. The following chemicals were purchased from Sigma: phenol, *p*-cresol, *p*-ethylphenol, *p*-*n*-propylphenol, *p*-florophenol, *p*-chlorophenol, *p*-bromophenol, *p*-iodophenol, propranolol, alprenolol, oxprenolol, metoprolol, pindolol, nadolol, atenolol, and phosphate-buffered saline (PBS). *p*-*n*-butylphenol was purchased from Lancaster.

Synthesis of IAM.PC Bonded Phases. Detailed procedures for the synthesis of IAM.PC bonded phases have been described for the ^{ether}IAM.PC$^{C10/C3}$ phase,[8] the $^{\delta G}$IAM.PC$^{C10/C3}$ phase,[3] and the ^{ester}IAM.PC$^{C10/C3}$ phase.[12] $^{\delta G}$IAM.PC$^{C10/C3}$ is currently commercialized as an IAM.PC.DD column (Regis Chemical Co.). The ligand densities (in μmol/g of IAM; PC:C10:C3) are 127:28:60 for ^{ether}IAM.PC$^{C10/C3}$, 127:48:36 for $^{\delta G}$IAM.PC$^{C10/C3}$, and 98:48.6:28 for ^{ester}IAM.PC$^{C10/C3}$. The ligand densities (in mg/g of IAM; (PC:C10:C3) are 59.7:3.9:2.5 for ^{ether}IAM.PC$^{C10/C3}$, 48.5:6.7:1.5 for $^{\delta G}$IAM.PC$^{C10/C3}$, and 70.0:6.7:1.2 for ^{ester}IAM.PC$^{C10/C3}$. The bonded ligand densities on IAMs were measured as described.[6]

IAM Chromatography. IAM.PC chromatographic particles suspended in acetone (10% w/v) were packed at Regis Chemical Co. All IAM HPLC columns were 0.46 × 3 cm and contained a void volume V_m of ~0.415 mL. For water-soluble solutes, the injection volume was ~10 μL of the solute solution (1 μg/μL) in aqueous solsution. The two solutes *p*-iodophenol and *p*-*n*-butylphenol have low solubility in water and were dissolved in methanol; these compounds were injected in ~10 μL of methanol (1 μg/μL). The flow rate was 1 mL/min for ^{ether}IAM.PC$^{C10/C3}$ and $^{\delta G}$IAM.PC$^{C10/C3}$ columns and 3 mL/min for an ^{ester}IAM.PC$^{C10/C3}$ column. High flow rates were needed for the ^{ester}IAM.PC$^{C10/C3}$ column because the solute retention times are longer on a double-chain ester IAM.PC column compared to the single-chain IAM.PC columns. Solute detection was at 220 nm. The buffered aqueous mobile phase was 0.01 M PBS at pH 7.4 (which contains 0.027 M KCl and 0.137 M NaCl). Chromatograms were obtained as described.[3]

The volume of the stationary phase (V_s) is assumed to be the sum of the volume of bonded PC ligands (V_s^{PC}), the volume of bonded C10 groups (V_s^{C10}) and the volume of bonded C3 groups (V_s^{C3}). The IAM interfacial thickness is unknown, and it is therefore difficult to accurately calculate V_s; approximations are thus made. To calculate V_s on IAMs, we used Cole's method of

Table 1. Chemical Structures of Phenol Derivitives and β-Blockers

Group 1	phenol	cresol	Et-phenol	Pr-phenol	Bu-phenol		
Structure	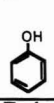						
Group 2	F-phenol	Cl-phenol	Br-phenol	I-phenol			
Structure		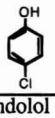	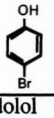				
Group 3	atenolol	pindolol	nadolol	metoprolol	oxprenolol	alprenolol	propranolol
Structure		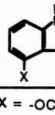	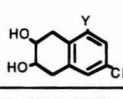	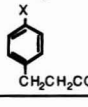	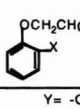	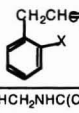	

X = -OCH$_2$CHCH$_2$NHCH(CH$_3$)$_2$ (OH)

Y= -OCH$_2$CHCH$_2$NHC(CH$_3$)$_3$ (OH)

calculating V_s on C18 columns.[15] The volume of each individual bonded ligands was thus calculated as the weight of the ligand divided by ligand's density.

$$V_s = V_s^{PC} + V_s^{C10} + V_s^{C3} = \frac{W^{PC}}{\varrho^{PC}} + \frac{W^{C10}}{\varrho^{C10}} + \frac{W^{C3}}{\varrho^{C3}} \qquad (5)$$

The density of the PC ligands (ϱ^{PC}) is ~1.01 g/mL.[16] The density of hydrocarbons (ϱ^{C10}, ϱ^{C3}) is ~0.86 g/mL.[17] A typical 0.46 × 3 cm IAM.PC column contains 0.277 g of packing material. Based on the ligand densities, the calculated values of V_s are 0.0189 mL for ^{ether}IAM.PC$^{C10/C3}$, 0.0144 mL for $^{\delta G}$IAM.PC$^{C10/C3}$, and 0.0220 mL for ^{ester}IAM.PC$^{C10/C3}$. The dead volume (V_m) in a 0.46 × 3 cm IAM.PC column is 0.415 mL, and approximate values of the phase ratio ($\phi = V_s/V_m$) are 0.046 for ^{ether}IAM.PC$^{C10/C3}$, 0.035 for $^{\delta G}$IAM.PC$^{C10/C3}$, and 0.053 for ^{ester}IAM.PC$^{C10/C3}$.

The temperature dependence of solute retention on IAM columns was performed by placing the IAM column in a Rainin Eldex CH-150 temperature controller. Temperature was varied from 25 to 50 °C. The temperature was controlled to an accuracy of 0.1 °C, and the time allowed for temperature equilibration was always greater than 30 min.

RESULTS AND DISCUSSION

Sixteen solutes used in this study are shown in Table 1. Group 1 solutes are a homologous series of *p*-alkylphenols including phenol, *p*-cresol, *p*-ethylphenol, *p*-*n*-propylphenol, and *p*-*n*-butylphenol; the only structural difference is the hydrocarbon chain length. Group 2 solutes are a homologous set of *p*-halophenols including *p*-florophenol, *p*-chlorophenol, *p*-bromophenol, and *p*-iodophenol; the only structural difference is a halogen atom. Group 3 solutes are a set of β-blockers including atenolol, pindolol, nadolol, metoprolol, oxprenolol, alprenolol, and propranolol.

Figure 1A–C compares the retention k'_{IAM} values of these 16 solutes on three different IAM.PC columns at 298 K. There is almost a perfect correlation ($r^2 > 0.99$) between k'_{IAM} values obtained on the ^{ether}IAM.PC$^{C10/C3}$ column and k'_{IAM} values obtained on the $^{\delta G}$AM.PC$^{C10/C3}$ column (Figure 1A). Similar results were found when correlating solute retention between ^{ester}IAM.PC$^{C10/C3}$ and ^{ether}IAM.PC$^{C10/C3}$ columns (Figure 1B) and ^{ester}IAM.PC$^{C10/C3}$ and $^{\delta G}$AM.PC$^{C10/C3}$ columns (Figure 1C). More important, the slope of 0.91 in Figure 1A indicates that k'_{IAM} retention factors measured on single-chain $^{\delta G}$AM.PC$^{C10/C3}$ and ^{ether}IAM.PC$^{C10/C3}$ columns are virtually identical. However, the slopes of ~4 in (B) and (C) indicate that the double-chain ^{ester}IAM.PC$^{C10/C3}$ column has ~4-fold higher k'_{IAM} values compared to the single-chain IAM columns.

The K_{IAM} value reflects the distribution of solute between the stationary phase and the mobile phase. The phase ratio and k'_{IAM} were used to calculate K_{IAM} according to eq 2. At pH 7.4, phenols exist mostly in un-ionized form whereas both ionized and un-ionized forms of β-blockers exist. β-blockers contain ionizable functional groups (i.e., the amino groups), and the pK_a values are 9.55 for atenolol, 8.80 for pindolol, 9.67 for nadolol, 9.70 for metoprolol, 9.50 for oxprenolol, 9.70 for alprenolol, and 9.45 for propranolol.[18] The ionized species usually does not participate in membrane binding or partitioning. Thus, for β-blockers K'_{IAM} only measures the partitioning of the un-ionized forms and needs to be corrected as follows:[18]

$$K_{IAM} = K'_{IAM}(1 + 10^{pK_a - 7.4}) \qquad (6)$$

The K_{IAM} values obtained on each IAM column correlate with the K_{IAM} values obtained with the other two IAM columns (Figure 1D–F); excellent linear correlations (r^2 = 0.982–0.998) were always obtained. It should be noted that the affinity of solutes for the ^{ester}IAM.PC$^{C10/C3}$ surface is ~3 times the affinity of solutes for the ^{ether}IAM.PC$^{C10/C3}$ surface (Figure 1E,F). These results are significant and provide insight into the mechanism of solute retention as further discussed below.

Solute–IAM interactions may be dominated by partitioning, adsorption, or both. Partitioning implies that the solute molecule penetrates the head-group region of IAM and is embedded within the hydrocarbon region, whereas adsorption implies that the solute molecule is simply in surface contact with the polar lipid

(15) Cole, L. A.; Dorsey, J. G. *Anal. Chem.* **1992**, *64*, 1317–1323.
(16) Katz, Y.; Diamond, J. M. *J. Membr. Biol.* **1974**, *17*, 69–86.
(17) Cheng, W. *Anal. Chem.* **1985**, *57*, 2409–2412.
(18) Betageri, G. V.; Rogers, J. A. *Int. J. Pharm.* **1987**, *36*, 165–173.

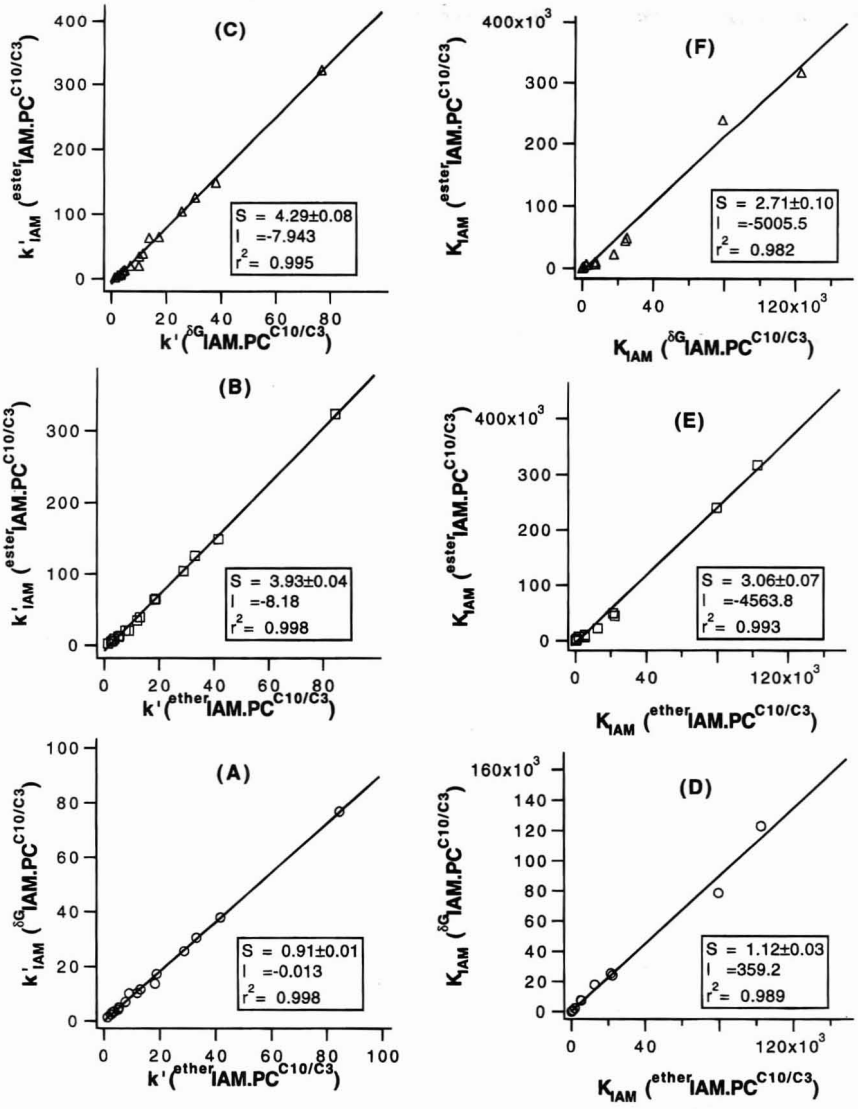

Figure 1. (A–C) Correlation of the IAM capacity factors (k'_{IAM}) of 16 solutes on the single-chain and double-chain IAM.PC columns at 298 K. (D–F) Correlation of the equilibrium distribution constants of 16 solutes on the single-chain and double-chain IAM.PC columns at 298 K.

Chart 2. Partitioning: The Dominating Retention Mechanism on IAMs

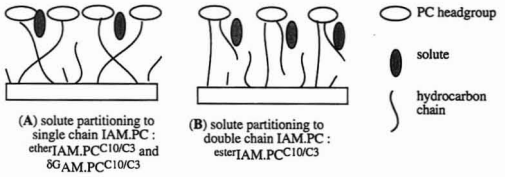

head groups. The outer most surface of IAM.PC contains a monolayer of PC head groups, and underneath these polar lipid head groups resides the hydrocarbon chains of the immobilized PC ligands and the C10 or C3 alkyl groups as shown in Chart 2.

If solute adsorption dominates retention, then the amount of immobilized PC head groups determines k'_{IAM}. The density of PC head groups on the ^{ester}IAM.PC$^{C10/C3}$ column (98 μmol of PC/g of IAM, Table 1) is lower than the densities of PC head groups on ^{ether}IAM.PC$^{C10/C3}$ or $^{\delta G}$IAM.PC$^{C10/C3}$ (127 μmol of PC/g of IAM). Based on PC head-group density, an adsorption retention mechanism predicts that the ^{ester}IAM.PC$^{C10/C3}$ column should have the shortest solute retention values. However, Figure 1A–C demonstrated the opposite effect; i.e., the ^{ester}IAM.PC$^{C10/C3}$ column has the longest retention factors. This indicates that, for these solutes, a partitioning mechanism controls solute retention on the IAM phase and not solute adsorption. Thus, the solute actually

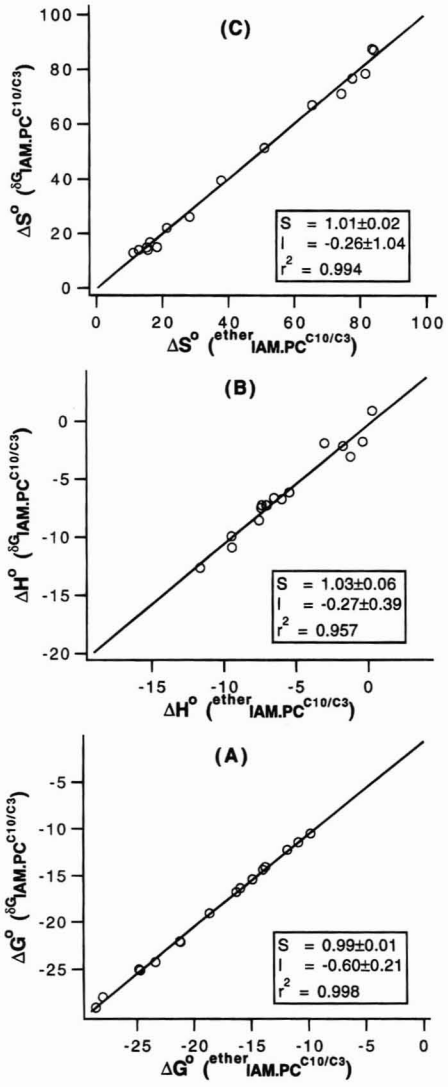

Figure 2. Correlation of thermodynamic properties ($\Delta G°$ at 298 K, $\Delta H°$, $\Delta S°$) of 16 solutes partitioning on the single-chain IAM.PC columns.

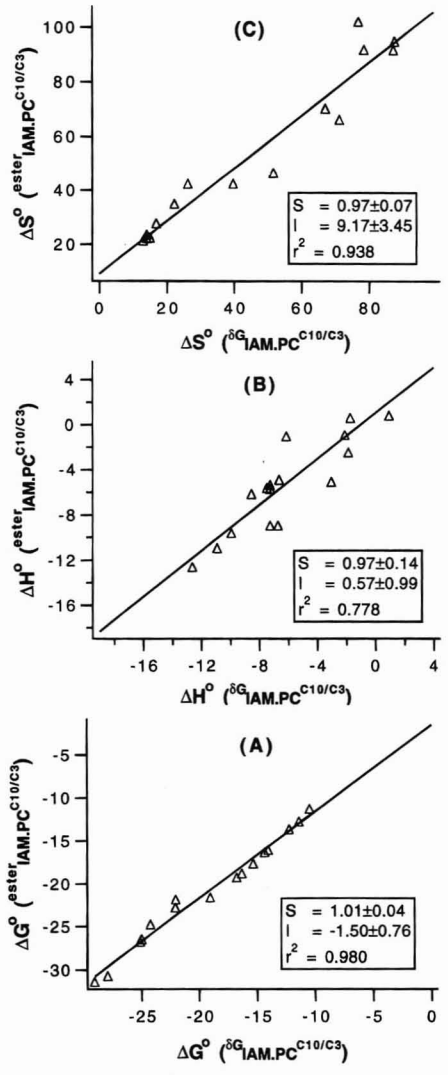

Figure 3. Correlation of thermodynamic properties ($\Delta G°$ at 298 K, $\Delta H°$, $\Delta S°$) for partitioning of 16 solutes between a single-chain $^{\delta G}$IAM.PC$^{C10/C3}$ column and a double-chain ^{ester}IAM.PC$^{C10/C3}$ column.

penetrates beyond the interfacial PC head groups and is embedded within the IAM.PC bonded phase (Chart 2). For this reason, the distribution constant K_{IAM} of a solute between IAMs and mobile phase is the partition coefficient of the solute between IAMs and the mobile phase.

As discussed above, Figure 1E,F demonstrated that solute partitioning into the double-chain ester PC column is ~3 fold more favorable compared to solute partitioning into the single-chain IAM column. The higher partitioning on the ester column may be the result of the following: (i) a lower immobilized PC density exhibits a lower interfacial barrier to solute transport into the IAM hydrocarbon region, and (ii) immobilized double-chain ester PC ligands (98 μmol of PC/g of IAM) contain ~50% more hydrocarbon compared to the single-chain PC ligands (both were 127 μmol of PC/g of IAM). The higher hydrocarbon density on the ^{ester}IAM.PC$^{C10/C3}$ column would increase the Van der Waals interactions between the hydrophobic solutes and the bonded phases and, therefore, increase the solute affinity to the bonded phase.

Using eq 4, the K_{IAM} values measured at $T = 298$ K were used for calculating the free energy $\Delta G°$ of solute partitioning into IAM columns. Temperature-dependent solute retention was used to obtain $\Delta H°$ and $\Delta S°$ for the partitioning process. $\Delta H°$ was obtained from the slope of van't Hoff plots, which are plots of ln k'_{IAM} vs $1/T$. The values for $\Delta S°$ were calculated as follows:

Table 2. Thermodynamics of Partitioning of Group 1 Solutes (*p*-Alkylphenols), Group 2 Solutes (*p*-Halophenols), and Group 3 Solutes (*β*-Blockers) into IAM.PC Columns[a,b]

	^{ether}IAM.PC$^{C10/C3}$				$^{\delta G}$IAM.PC$^{C10/C3}$				^{ester}IAM.PC$^{C10/C3}$			
solute	K_{IAM}	$\Delta G°$ (kJ/mol)	$\Delta H°$ (kJ/mol)	$\Delta S°$ (J/mol K)	K_{IAM}	$\Delta G°$ (kJ/mol)	$\Delta H°$ (kJ/mol)	$\Delta S°$ (J/mol K)	K_{IAM}	$\Delta G°$ (kJ/mol)	$\Delta H°$ (kJ/mol)	$\Delta S°$ (J/mol K)
					Group 1							
phenol	52.9	−9.83	−6.54	11.04	69.1	−10.50	−6.65	12.90	94.1	−11.26	−4.90	21.32
cresol	118.2	−11.82	−7.02	16.10	140.6	−12.25	−7.26	16.76	244.6	−13.63	−5.35	27.79
p-ethylphenol	258.7	−13.77	−7.42	21.31	293.1	−14.07	−7.48	22.12	653.5	−16.06	−5.61	35.06
p-*n*-propylphenol	626.7	−15.96	−7.57	28.16	733.2	−16.35	−8.56	26.14	1960.7	−18.78	−6.14	42.44
p-*n*-butylphenol	1838.2	−18.62	−7.38	37.72	2194.3	−19.06	−7.26	39.61	6102.5	−21.60	−8.95	42.45
					Group 2							
p-fluorophenol	80.4	−10.87	−7.07	12.76	100.4	−11.42	−7.27	13.94	171.1	−12.74	−5.70	23.64
p-chlorophenol	282.4	−13.98	−9.48	15.11	330.1	−14.37	−9.94	14.88	733.5	−16.35	−9.62	22.58
p-bromophenol	409.0	−14.90	−9.44	18.31	494.7	−15.37	−10.92	14.95	1221.1	−17.61	−10.96	22.32
p-iodophenol	719.0	−16.30	−11.66	15.57	870.7	−16.77	−12.63	13.90	2364.3	−19.25	−12.63	22.20
					Group 3							
atenolol	5316.1	−21.25	−1.76	65.41	7375.5	−22.06	−2.12	66.93	6710.9	−21.83	−0.93	70.14
pindolol	5122.0	−21.16	−5.99	59.93	7505.9	−22.11	−6.73	51.59	9924.6	−22.80	−8.94	46.49
nadolol	12536.9	−23.38	−1.26	74.24	17786.0	−24.25	−3.05	71.12	22040.1	−24.78	−5.06	66.16
metoprolol	22250.2	−24.80	0.22	84.06	24128.5	−25.00	0.93	87.02	44210.9	−26.50	1.96	91.62
oxprenolol	21336.4	−24.70	−0.42	81.48	25206.8	−25.11	−1.74	78.43	48621.1	−26.74	0.58	91.68
alprenolol	79741.4	−27.96	−3.06	83.57	78745.8	−27.93	−1.88	87.43	240600.0	−30.70	−2.49	94.68
propranolol	102642.7	−28.59	−5.46	77.61	122935.8	−29.04	−6.16	76.76	317686.2	−31.39	−1.03	101.87

[a] K_{IAM} and $\Delta G°$ are the values at $T = 298$ K (25 °C). [b] $\Delta H°$ and $\Delta S°$ were obtained from the linear regression of van't Hoff plots. The fitting parameters for linear regressions of van't Hoff plots (i.e., slopes, intercepts, and linear correlations) are available as supplementary material.

$$\Delta S° = (\Delta H° - \Delta G°)/T \quad (7)$$

Table 2 shows $\Delta G°$, $\Delta H°$, and $\Delta S°$ values for solute partitioning into three different IAM.PC columns.

For all solutes tested, increasing the temperature causes a decrease in k'_{IAM} (data not shown). With few exceptions, the test solute gave excellent correlations on van't Hoff plots regardless of the IAM.PC column used for the analysis ($r^2 \sim 0.9$–0.99, data not shown). The compounds that give a poor correlation are oxprenolol and metoprolol on ^{ether}IAM.PC$^{C10/C3}$, alprenolol on $^{\delta G}$IAM.PC$^{C10/C3}$, and oxprenolol, metoprolol, and atenolol on ^{ester}IAM.PC$^{C10/C3}$ (data not shown). Poor correlations occurred for these compounds because a very weak temperature dependence of retention was observed. Weak temperature dependence results in small slopes for van't Hoff plots and small $\Delta H°$ values, which cause the poor correlation. Nevertheless, decreasing k'_{IAM} with increasing temperature results in positive slopes for van't Hoff plots, and positive slopes on van't Hoff plots correspond to negative values for $\Delta H°$. Most of the compounds tested had a negative value for $\Delta H°$.

The thermodynamic parameters ($\Delta G°$, $\Delta H°$, $\Delta S°$) for solute partitioning on the two different single-chain IAM.PC surfaces are compared in Figure 2; for all parameters, a perfect correlation between the two single-chain IAM.PC columns was obtained (i.e., ^{ether}IAM.PC$^{C10/C3}$ and $^{\delta G}$IAM.PC$^{C10/C3}$ columns). Most important, the intercepts are almost zero and the slopes for all of the plots are very close to unity. When intercepts are ~0, and slopes are ~1, eqs 8–10 indicate that the values of $\Delta G°$, $\Delta H°$, and $\Delta S°$ are similar on the two columns,

$$\Delta G°_{column\text{-}1} = \text{slope} \times (\Delta G°_{column\text{-}2}) + \text{intercept} \quad (8)$$

$$\Delta H°_{column\text{-}1} = \text{slope} \times (\Delta H°_{column\text{-}2}) + \text{intercept} \quad (9)$$

$$\Delta S°_{column\text{-}1} = \text{slope} \times (\Delta S°_{column\text{-}2}) + \text{intercept} \quad (10)$$

The structural difference between the two single-chain IAM.PC columns is that the ^{ether}IAM.PC$^{C10/C3}$ surface contains immobilized PC ligands that contain a glycerol backbone and an *O*-methyl tethered to the glycerol backbone, whereas the $^{\delta G}$IAM.PC$^{C10/C3}$ surface lacks these structural features. However, since $\Delta G°$, $\Delta H°$, and $\Delta S°$ are similar on the ^{ether}IAM.PC$^{C10/C3}$ vs $^{\delta G}$IAM.PC$^{C10/C3}$ columns (Figure 2), these structural differences are apparently unimportant regarding the solute partitioning process.

Thermodynamic properties between single-chain and double-chain IAM.PC columns were also compared. Figure 3 compares the ^{ester}IAM.PC$^{C10/C3}$ vs $^{\delta G}$IAM.PC$^{C10/C3}$ column. For all parameters ($\Delta G°$, $\Delta H°$, $\Delta S°$) there is almost a perfect correlation and the slopes are ~1. However, unlike the comparison of the single-chain IAM.PC columns where the intercepts were ~0, the intercepts in Figure 3 significantly deviate from zero. Equation 11 applies to the data in Figure 3, which compares the double-chain ester IAM.PC column to the single-chain δGIAM.PC column.

$$\Delta G°_{ester} = \text{slope} \times (\Delta G°\delta G) + \text{intercept} \quad (11)$$

The intercept of −1.50± 0.76 kJ/mol in Figure 3 indicates that the ester column has −1.50 ± 0.76 kJ/mol more favorable free energy of partitioning compared to the single-chain δG column. The thermodynamic reason for the more favorable free energy of partitioning is attributed to a more favorable entropy contribution on the double-chain ester column. This is based on the intercepts of the plots in Figure 4B and C. Equations for the $\Delta H°$ data shown in Figure 4B are

$$\Delta H°_{ester} = \text{slope} \times (\Delta H°\delta G) + \text{intercept}\ \Delta H°_{ester} = \text{slope} \times (\Delta H°\delta G) + (0.57 \pm 0.99) \quad (12)$$

and equations for $\Delta S°$ data shown in Figure 4C are

$$\Delta S°_{ester} = \text{slope} \times (\Delta S°\delta G) + \text{intercept}$$

$$\Delta S°_{ester} = \text{slope} \times (\Delta S°\delta G) + (9.17 \pm 3.45) \quad (13)$$

The intercept of + 0.57± 0.99 kJ/mol for $\Delta H°$ corresponds to a small difference in the $\Delta H°$ between ester and δG columns. However, the intercept of 9.17 ± 3.45 for $\Delta S°$ corresponds to a

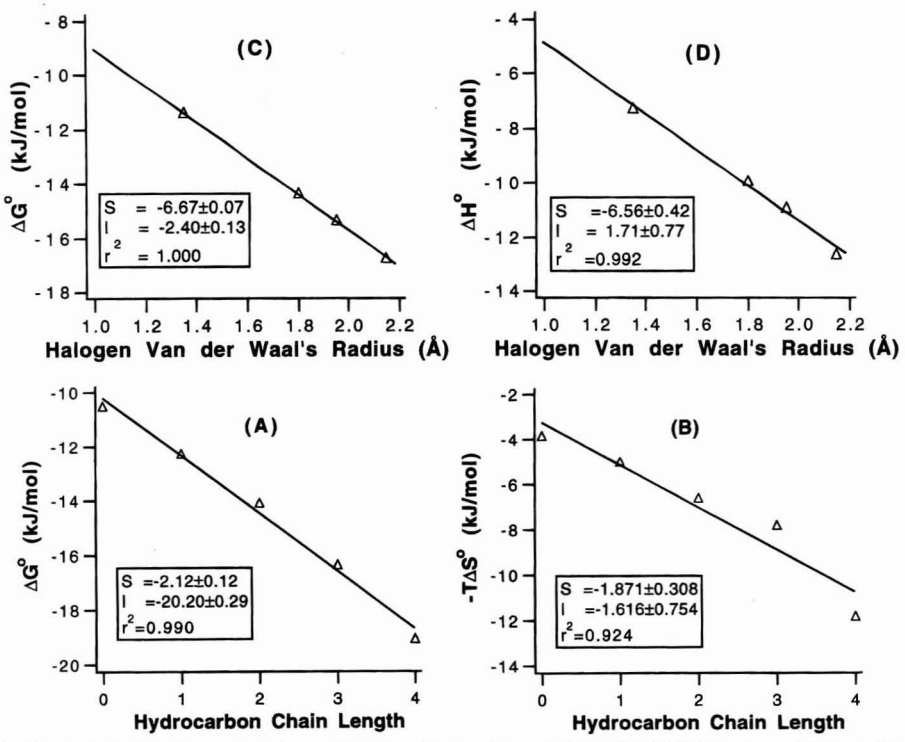

Figure 4. Structural effects on thermodynamic properties of partitioning of phenols into a $^{\delta G}$IAM.PC$^{C10/C3}$ column: (A) dependence of free energy of partitioning, $\Delta G°$ at 298 K, on hydrocarbon chain length for group 1 solutes (*p*-alkylphenols); (B) dependence of entropy contributions to partitioning, $T\Delta S°$ at 298 K on hydrocarbon chain length for group 1 solutes (*p*-alkylphenols); (C) dependence of free energy of partitioning, $\Delta G°$ at 298 K, on the halogen size of group 2 solutes (*p*-halophenols); (D) dependence of enthalpy, $\Delta H°$, on the halogen size of group 2 solutes (*p*-halophenols).

2.73 ± 1.01 kJ/mol ($T\Delta S°$) difference in the entropy contribution to the partitioning process between the ester and the δG column. Thus, there is a significant entropy contribution $T\Delta S°$ that favors solute partitioning into double-chain IAM columns. Similar results were obtained for comparisons between ^{ester}IAM.PC$^{C10/C3}$ and ^{ether}IAM.PC$^{C10/C3}$. In other words, both single-chain IAM.PC columns give virtually identical results when compared to the double-chain IAM.PC ester column. Thus, the key finding from these results is that the more favorable solute partitioning is into double-chain IAM columns compared to single-chain columns, which is probably due to an increase in entropy of the double-chain surface during the partitioning process.

Solute partitioning can be discussed relative to the functional groups associated with each solute. Three groups of solutes were studied, and within each group the compounds were rank ordered according to their $\Delta G°$ values, as shown in Table 2. The general rank order of solute partitioning into the IAM surfaces is

	group 1	~	group 2	<	group 3
	p-alkylphenol	~	*p*-halophenols	<	β-blockers
$-\Delta G°$ (kJ/mol)	9.83–21.60	~	10.87–19.25	<	21.16–31.39

Group 1 and group 2 exhibit similar free energies of partitioning whereas group 3 exhibits a large negative free energy of partitioning.

Regardless of single- or double-chain immobilized PC ligands on IAM.PC columns, chromatography of group 1 compounds demonstrated that increasing the hydrocarbon chain length of the solute results in a more negative $\Delta G°$ for the partition process of ~2 kJ/methylene group (compare $\Delta G°$ values for group 1 compounds in Table 2). This is more clearly shown in Figure 4A where $\Delta G°$ for the solute partitioning process is plotted vs the alkyl chain length of the group 1 solutes for the $^{\delta G}$IAM.PC$^{C10/C3}$ column. Similar linear plots were also obtained for ^{ether}IAM.PC$^{C10/C3}$ and ^{ester}IAM.PC$^{C10/C3}$ columns but are not shown here. The slope of Figure 4A corresponds to the $\Delta G°$/methylene group for the partitioning process, and the value is $-2.123 \pm 0.0.118$ kJ/mol for $^{\delta G}$IAM.PC$^{C10/C3}$. Similarly, the values of $\Delta G°$/methylene group for the partitioning process are -2.171 ± 0.082 kJ/mol for ^{ether}IAM.PC$^{C10/C3}$ and -2.583 ± 0.059 kJ/mol for ^{ester}IAM.PC$^{C10/C3}$. These $\Delta G°$/methylene values are similar to the $\Delta G°$/methylene of 2.51 ± 0.54 kJ/mol for *p*-alkylphenol partitioning into DMPC liposomes in the gel phase (i.e., below the phase transition temperature, T_m). However, we note that $\Delta G°$/methylene is only 1.63 ± 0.79 kJ/mol for *p*-alkylphenol partitioning into DMPC liposomes in the liquid-crystalline phase (above T_m).[19]

The contribution of $\Delta S°$ and $\Delta H°$ to the free energy of the partitioning process for group 1 solutes was also evaluated. Both

(19) Rogers, J. A.; Davis, S. S. *Biochim. Biophys. Acta* **1980**, *598*, 392–404.

Table 3. Contributions of Enthalpy and Entropy to the Free Energy for Partitioning of *p*-Alkylphenols, *p*-Halophenols, and β-Blockers in ^{ether}IAM.PC$^{C10/C3}$, $^{\delta G}$IAM.PC$^{C10/C3}$, and ^{ester}IAM.PC$^{C10/C3}$ and in DMPC Liposomes[a]

	^{ether}IAM.PC$^{C10/C3}$		$^{\delta G}$IAM.PC$^{C10/C3}$		^{ester}IAM.PC$^{C10/C3}$		DMPC liposome[b]			
							above T_m		below T_m	
solute	% $\Delta H°$	% $T\Delta S°$	% $\Delta H°$	% $T\Delta S°$	% $\Delta H°$	% $T\Delta S°$	% $\Delta H°$	% $T\Delta S°$	% $\Delta H°$	% $T\Delta S°$
				Group 1 Solutes						
phenol	66.5	33.5	63.4	36.6	43.6	56.4				
cresol	59.4	40.6	59.2	40.8	39.2	60.8	233.2	−133.2	−80.9	180.9
p-ethylphenol	53.9	46.1	53.2	46.8	34.9	65.1	245.3	−145.3	−64.2	164.2
p-*n*-propylphenol	47.4	52.6	52.3	47.7	32.7	67.3	500.9	−400.9	−34.1	134.1
p-*n*-butylphenol	39.6	60.4	38.1	61.9	41.4	58.6	523.1	−423.1	−4.4	104.4
				Group 2 Solutes						
p-florophenol	65.0	35.0	63.6	36.4	44.7	55.3	−170.7	270.7	−170.7	270.7
p-chlorophenol	67.8	32.2	69.1	30.9	58.8	41.1	122.9	−22.9	−75.3	175.3
p-bromophenol	63.4	36.6	71.0	29.0	62.2	37.8	219.4	−119.4	−19.3	119.3
p-iodophenol	71.5	28.5	75.3	24.7	65.6	34.4	217.8	−117.8	53.6	46.4
				Group 3 Solutes						
propranolol	19.1	80.9	21.2	78.8	3.3	96.7	24.1	75.9	49.1	50.9
alprenolol	10.9	89.1	6.7	93.3	8.1	91.9	−7.3	107.3	−21.6	121.6
oxprenolol	1.7	98.3	6.9	93.1	−2.2	102.2	−50.0	150.5	175.0	−75.0
metoprolol	−1.0	101.0	−3.7	103.7	−3.0	103.0	−144.5	244.5	−166.3	266.3
atenolol	8.3	91.7	9.6	90.4	4.3	95.7	−106.5	206.5	1642.9	−1542.9
pindolol	28.3	71.7	30.5	69.5	39.2	60.8	−129.9	229.9	66.9	33.1
nadolol	5.4	94.6	12.6	87.4	20.4	79.6	417.1	−317.1	0.0	0.0

[a] Note that contribution of entropy to $\Delta G°$ is represented by $T\Delta S°$. % $\Delta H°$ or % $T\Delta S°$ was calculated by dividing $\Delta H°$ or $T\Delta S°$ by $\Delta G°$ in Table 2, where T is 298 K. Positive values represent favorable contributions to $\Delta G°$, whereas negative values represent unfavorable contributions to $\Delta G°$. [b] Calculated from the data of Rogers and Davis;[19] T_m = 21 °C is the phase transition temperature of DMPC liposomes.

$\Delta S°$ and $\Delta H°$ contribute favorably to the free energy of partitioning; partitioning of group 1 solutes is thus both an enthalpy- and entropy-driven process. Regardless of the IAM.PC column used for the analysis, as the solute hydrocarbon chain length increases, $\Delta H°$ remains almost constant (Table 2), which is unexpected. Intuitively, as the solute hydrocarbon chain increases, one might have expected an increase in $\Delta H°$. However, the net $\Delta H°$ from transferring solute from a water phase into the IAM interphase can be described by eq 14.

$$\Delta H° = (\Delta H°_{gas} - \Delta H°_{water}) + (\Delta H°_{IAM} + \Delta H°_{gas}) \quad (14)$$

where $\Delta H°_{IAM}$ is the enthalpy due to solute-IAM interactions, $\Delta H°_{water}$ is the solute hydration enthalpy, and $\Delta H°_{gas}$ is the enthalpy of the solute in the gas phase (imaginary standard state). As the hydrocarbon chain length increases, it is known that $\Delta H°_{water}$ becomes more negative as the hydrocarbon chain length increases,[20,21] whereas $\Delta H°_{IAM}$ also becomes more negative due to the increased nonpolar interactions between the hydrocarbon chains of IAMs and the solute with a longer hydrocarbon chain. In other words, increased hydrocarbon tethered to the solutes causes a decrease in $\Delta H°_{water}$ and a decrease in $\Delta H°_{IAM}$, and therefore, the net enthalpy of partitioning $\Delta H°$ does not necessarily change. The net negative enthalpies most likely arise from the hydrogen bondings between the hydroxyls on *p*-alkylphenols and the polar PC head groups of IAM surfaces.

The constant $\Delta H°$ values for group 1 compounds should be compared to the decreasing value of $\Delta G°$ during the partitioning process. As the alkyl chain increases $\Delta G°$ becomes more negative, and since $\Delta H°$ does not change, the decrease in $\Delta G°$ is from an entropy-driven process. In other words, group 1 solutes have increased partitioning with increased chain length and the reason is an entropy effect instead of an enthalpy effect. The positive entropy change ($\Delta S°$) is due to the removal of hydrocarbon (i.e., the benzene ring and the hydrocarbon chain of the group 1 solutes) from the aqueous phase into the IAM interphase as described by many others.[21]

The entropy contribution to the free energy of partitioning ($T\Delta S°$) increases linearly as hydrocarbon chain length increases in group 1 solutes, which is demonstrated in Figure 4B for the $^{\delta G}$IAM.PC$^{C10/C3}$ column. Similar linear plots were also obtained for ^{ether}IAM.PC$^{C10/C3}$ and ^{ester}IAM.PC$^{C10/C3}$ columns but are not shown here. The slope in Figure 4B corresponds to the energy change per methylene group ($-T\Delta S°/CH_2$ group). The value of $-T\Delta S°/CH_2$ is −1.871 ± 0.0.118 kJ/mol for $^{\delta G}$IAM.PC$^{C10/C3}$. Similarly, The value of $-T\Delta S°/CH_2$ are −1.949 ± 0.161 kJ/mol for ^{ether}IAM.PC$^{C10/C3}$ and −2.104 ± 0.047 kJ/mol for ^{ester}IAM.PC$^{C10/C3}$. The $-T\Delta S°/CH_2$ energy is similar to $\Delta G°/CH_2$ for each IAM.PC column. This can be seen by comparing the slope ($=\Delta G°/CH_2$) of Figure 4A and the slope ($=-T\Delta S°/CH_2$) of Figure 4B for the $^{\delta G}$IAM.PC$^{C10/C3}$ column. The key finding is that partitioning becomes more favorable as the hydrocarbon chain length increases in group 1 solutes because of an increase in $\Delta S°$ ($\Delta H°$ does not change), and the increase in $\Delta S°$ is linearly related to the number of methylene groups in the solute.

Thermodynamic properties were also studied for group 2 solutes, which are a homologous set of halogen-substituted phenols. The most important structural difference among group 2 solutes is the size of each halogen substituent. Halogen van der Waals radii are 1.35 Å for F, 1.80 Å for Cl, 1.95 Å for Br, and 2.15 Å for I. As the halogen size increases, the magnitude of $\Delta G°$ for the partitioning process linearly decreases (i.e., more favorable partitioning). This decreased $\Delta G°$ with increasing halogen size is shown in Figure 4C for the $^{\delta G}$IAM.PC$^{C10/C3}$ column. Similar linear plots were also obtained for ^{ether}IAM.PC$^{C10/C3}$ and ^{ester}IAM.PC$^{C10/C3}$ columns but are not shown here.

(20) Butler, J. A. V. *J. Chem. Soc.* **1933**, 229–236.
(21) Tanford, C. *The Hydrophobic Effect*; John Wiley & Sons: New York, 1980.

Similar to group 1 compounds, both enthalpy and entropy contribute favorably to the partitioning process in group 2 solutes; i.e, $\Delta H°$ is negative and $\Delta S°$ is positive. As halogen size increases, $T\Delta S°$ remains almost unchanged, whereas $\Delta H°$ linearly increases. This is in contrast to group 1 solute partitioning in which the enthalpy contribution remained unchanged during the partitioning process on all IAM.PC columns tested. The constant value for $\Delta S°$ in group 2 compounds can be clearly seen in Table 2. Although $\Delta S°$ is constant on all IAM.PC columns, the numerical value for $\Delta S°$ is largest on the ^{ester}IAM.PC$^{C10/C3}$ column (Table 2), and in addition, the $\Delta S°$ is approximately the same for the partitioning process on both of the single-chain IAM.PC columns (Table 2). We interpret the $\Delta S°$ contribution to partitioning on the single-chain IAMs to be primarily from desolvation of the hydrophobic solute as the solute enters the IAM interphase. The increased entropy on the double-chain IAM column is the result of additional chain fluctuations in the immobilized double-chain PC ligand. In other words, only one of the acyl chains of the double-chain PC ligand is immobilized and the second chain has substantial conformational freedom compared to the tethered chain. Solute partitioning apparently creates a solute cavity in the IAM interphase that allows conformational freedom of the nonbonded acyl chain of the double-chain PC. This results in increased $\Delta S°$ for this phase.

As stated above, entropy contributions to the free energy of partitioning are virtually constant for group 2 compounds chromatographed on each IAM.PC surface. However, as halogen size increases (i.e., I > Br > Cl > F), the enthalpy contribution to the partitioning process increases, which is demonstrated in Figure 4B for the $^{\delta G}$IAM.PC$^{C10/C3}$ column. Similar linear plots were also obtained for ^{ether}IAM.PC$^{C10/C3}$ and ^{ester}IAM.PC$^{C10/C3}$ columns but are not shown here. Thus, the increased partitioning of group 2 solutes with increasing size of the halogen is the result of a more favorable enthalpy contribution. This is in contrast to group 1 compounds in which an increase in $\Delta S°$ was responsible for the increase in $\Delta G°$ as the size of the hydrocarbon chain increased.

In contrast to group 1 and group 2 compounds, group 3 compounds are a chemically diverse set of β-blockers (Table 2). The chemical diversity eliminated the ability to identify any trends in $\Delta G°$, $\Delta H°$, or $\Delta S°$ for the partitioning process. The general features of partitioning of β-blockers into IAM.PC phases is that $\Delta G°$ is usually large and negative ($-21.16 \sim -31.39$ kJ/mol). This can be clearly seen by comparing the $\Delta G°$ values for group 3 compounds in Table 2 for the single-chain IAM.PC surfaces. In addition, Table 2 also shows that $\Delta G°$ for each solute in group 3 is more negative on the double-chain IAM.PC column compared to the single-chain IAM.PC columns. This indicates that the group 3 β-blockers are very lipophilic compounds and solute partitioning is more favored for the double-chain IAM.PC column compared to the single-chain IAM.PC columns. Furthermore, for all IAM.PC columns, the enthalpy contribution to the partitioning process is very small compared to the entropy contribution to the partitioning process (Compare % ΔH to % $T\Delta$S for group 3 compounds in Table 3). Therefore, the partioning of β-blockers into the IAM.PC phase is an entropy-driven process.

The solutes of groups 1–3 were also used to compare the thermodynamics of solute partitioning on IAMs with solute partitioning into fluid liposome membranes. Figure 5 demonstrates that $\Delta G°$ for solute partitioning into IAM.PC phases correlates well ($r^2 = 0.848–0.901$)with the $\Delta G°$ of solute partitioning to DMPC liposomes. Compared to the single-chain IAM.PC columns, the double-chain ^{ester}IAM.PC$^{C10/C3}$ column is chemically most similar to the lipids comprising DMPC liposomes, and, thus the ^{ester}IAM.PC$^{C10/C3}$ column gave the best correlation (Figure 5C, $r^2 = 0.901$). However, IAM columns prepared from the single-chain PC ligands give almost equally good correlations (Figure 5A, $r^2 = 0.868$ for the ^{ether}IAM.PC$^{C10/C3}$ column; Figure 5B, $r^2 = 0.848$ for the $^{\delta G}$IAM.PC$^{C10/C3}$ column). The key finding from this comparison is that the structure of the immobilized lipid is not critical for correlating the free energy of solute partitioning into fluid membranes with the free energy of solute partitioning into immobilized membranes. We have previously demonstrated that log k'_{IAM} measured using IAM chromatography correlates very well with the logarithm of liposome partition coefficient (log K'_m).[3]

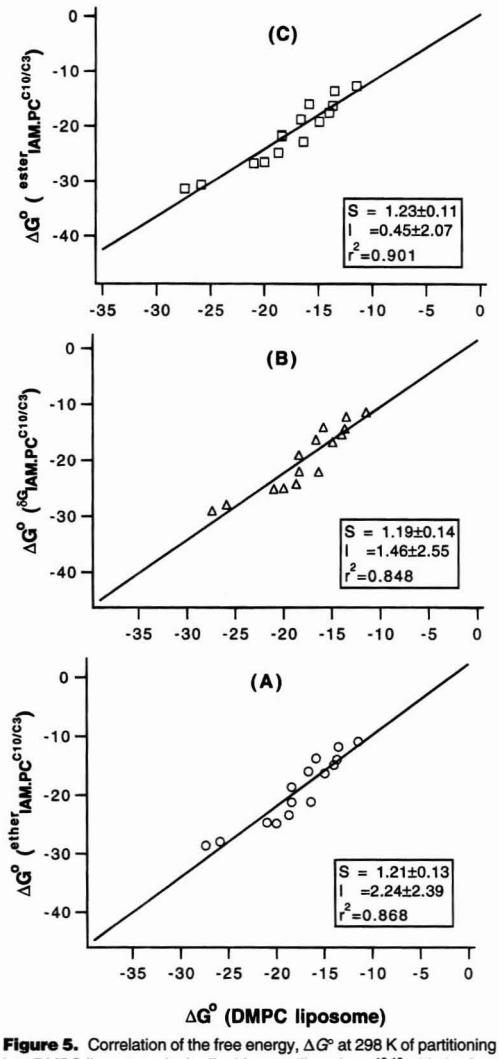

Figure 5. Correlation of the free energy, $\Delta G°$ at 298 K of partitioning into DMPC liposomes in the liquid-crystalline phase[18,19] with the free energy of solute partitioning into IAM.PC columns, for all 16 solutes.

Table 3 compares the contributions of $\Delta H°$ and $\Delta S°$ to $\Delta G°$ associated with solute partitioning into single- and double-chain IAMs with these parameters measured for solute partitioning into liposomes. Most interesting, no general trend was found regarding entropy or enthalpy dominating the partitioning process for both IAMs and liposomes but $\Delta G°$ for IAM always correlates well with the $\Delta G°$ of the partitioning process using liposomes. Comparing solute partitioning into immobilized membranes to solute partitioning into fluid liposome membranes cannot be done with regard to trends in $\Delta H°$ and $\Delta S°$. This is because for some solutes $\Delta H°$ dominates the free energy of partitioning to fluid membranes and for the same solutes $\Delta S°$ dominates the retention. The converse is also true. However, the most important comparison that can be made is that $\Delta G°$ for solute partitioning into fluid membranes always correlates with $\Delta G°$ for solute partitioning into immobilized artificial membranes. Thus, even though there may be different underlying thermodynamic reasons for the solute partitioning process between IAMs and liposomes, the free energy of solute partitioning correlates very well between IAMs and liposomes.

ACKNOWLEDGMENT

We are very grateful for the support from Eli Lilly and Co. This work was also supported by NSF (Grant CTS 9214794), NIH (Grant AI33031), and Regis Chemical Co. (2R446M3022-02).

SUPPORTING INFORMATION AVAILABLE

Tables of fitting parameters for linear regressions of van't Hoff plots (3 pages). Ordering information is available on any current masthead page.

GLOSSARY

C3	proprionyl
C10	decanoyl
DMPC	dimyristoylphosphatidylcholine
HPLC	high-performance liquid chromatography
I	intercept in linear least-squares fitting
IAM	immobilized artificial membrane
k'	capacity factor
k'_{IAM}	capacity factor on an IAM column
K_{IAM}	equilibrium distribution constant between IAMs and an aqueous phase, also denotes solute IAM partition coefficient
K_m	membrane partition coefficient
K'_m	liposome partition coefficient
PBS	phosphate-buffered saline
PC	phosphatidylcholine
S	slope in linear least-squares fitting
SPA	silica propylamine

Received for review December 12, 1994. Accepted March 30, 1995.[⊗]

AC9411942

[⊗] Abstract published in *Advance ACS Abstracts,* May 15, 1995.

Anal. Chem. **1995,** *67,* 2129–2135

Use of Vibrational Spectroscopy To Determine Oxide Content of Alkali Metal Fluoride–Tantalum Melts

N. J. Bjerrum,* R. W. Berg, E. Christensen, and D. H. Kerridge

Materials Science Group, Chemistry Department A, Technical University of Denmark, DK-2800 Lyngby, Denmark

J. H. von Barner

Institute of Mineral Industry, Building 204, Technical University of Denmark, DK-2800 Lyngby, Denmark

Infrared and Raman spectroscopic measurements on a series of quenched alkali metal fluoride (Flinak) melts containing tantalum and oxide have led to the development of new methods of oxide analysis, which have an important use in the field of molten fluoride chemistry. The tantalum concentration was maintained at 2.7 mol %, with the oxide concentration varying from 0 to 5.4 mol %, over 22 samples. The oxide content of a melt can be determined to within ±0.1 mol % from the intensity ratio of two vibrations. For example, a melt consisting of purified Flinak, after addition of K_2TaF_7 and heating to 700 °C for 5 h for equilibration, was shown by infrared spectroscopy to contain 0.3 ± 0.1 mol % oxide and by Raman spectroscopy to contain 0.2 ± 0.1 mol %. The frequency and relative intensities of the bands enable the assignment of Ta–F and Ta–O bands for both fluorotantalate and oxofluorotantalate entities. In addition a new, dimeric, species with a Ta–O–Ta unit is postulated. Raman spectra of molten samples showed bands of the same frequency and relative intensities, indicating that crystal effects were not important and that the equilibrium melt species were retained on quenching.

Upgrading the properties of cheaper materials is clearly needed as the resources of rarer and more exotic materials become progressively exhausted. A primary way to enhance desirable properties of a low-cost base material such as steel is to plate it with high-melting and chemically inert metallic layers.

The use of molten fluoride solutions, e.g., eutectic LiF–NaF–KF (Flinak), for the electrolytical deposition of refractory metals has been known for many years.[1] Despite their toxicities and high melting points, such melts are still important, in some cases irreplaceable, for plating of certain metals, including niobium and tantalum. Numerous studies on the electrochemical reactions of refractory metals in halide melts have been done. It is of great importance in this connection to know the content of oxide in the melts since this strongly influences which species are formed (i.e., fluoro or oxofluoro complexes), as discussed in detail by Christensen et al.[2] for the case of niobium in Flinak. Many electrochemical investigations are performed with minor concentrations of the solute refractory metal, which makes it even more important to know the amount of oxide present. If the oxide content is not taken into account, erroneous conclusions may easily be drawn. Such problems are very common for investigations in molten salts, because these solvents are in most cases hygroscopic. However, the number of papers describing methods for oxide determination in melts or solidified melts is very small. Important examples (for chloroaluminate melts) are given by Kurayasu and Inokuma[3] and Laher et al.[4] In the latter investigation,[4] Ta(V) was used as a probe for oxide.

However, the plating of niobium and tantalum has proved to be a complex process and difficult to optimize. Among the parameters that are important is the oxide content of the fluoride melt. In the case of tantalum solutions, the oxide is present as oxofluoro species which would seem to be electrochemically active. Because of the importance of electrodeposition of tantalum onto steel from a melt of fixed oxide content, and the inherent variability of residual oxide in a purified eutectic melt of Flinak, two rapid quantitative analytical methods were devised, based on the intensity ratios of chosen vibrational bands to give the tantalum/oxide ratio.

Much of our current knowledge concerning tantalum oxofluoride species is derived from crystalline solids. Much less is known about such species in solution and especially in high-temperature melt solutions. Vibrational spectroscopy, both infrared and Raman, is particularly useful in these cases because it can be applied both to melts and to their quenched solids at room temperature. In this study, a large number of samples of closely spaced compositions were prepared under conditions excluding both moisture and gaseous oxygen. In this way the appearance of vibrational bands with increasing oxide content could be followed closely and deductions made from their relative intensities about the tantalum/oxide ratios present. The intensity ratios also clearly indicate which bands arise from the same, or closely related, species.

EXPERIMENTAL SECTION

All handling and weighing was carried out in gloveboxes filled with dry nitrogen (dew point ~−45 °C).

Each alkali metal fluoride was purified separately by recrystallization from the melt. The salt, contained in a platinum crucible, was evacuated for 8 h at 400 °C to remove moisture and then heated to 20 °C above its melting point. The salt was then

(1) Senderoff, S.; Mellors, G. W. *J. Electrochem. Soc.* **1965,** *77,* 266.
(2) Christensen, E.; Xindong Wang; von Barner, J. H.; Østvold, T.; Bjerrum, N. J. *J. Electrochem. Soc.* **1994,** *141,* 1212.
(3) Kurayasu, H.; Inokuma, Y. *Anal. Chem.* **1993,** *65,* 1210.
(4) Laher, T. M.; McCurry, L. E.; Mamantov, G. *Anal. Chem.* **1985,** *57,* 500.

0003-2700/95/0367-2129$9.00/0 © 1995 American Chemical Society

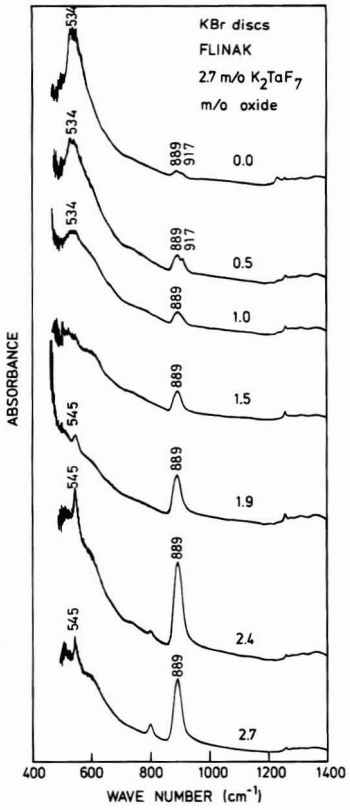

Figure 1. Infrared absorption spectra of KBr disks containing solidified K_2TaF_7/Flinak samples with added oxide (m/o, mol %). O^{2-}/Ta(V) molar ratios ≤1. The maximum absorption (at 534 or 545 cm^{-1}) is typically in the range of 2.0.

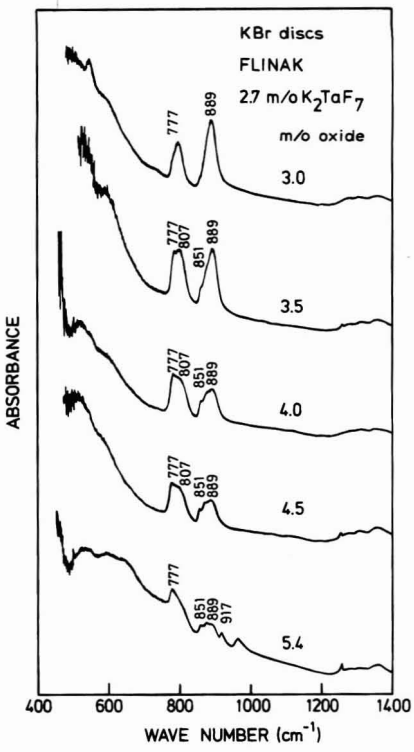

Figure 2. Infrared absorption spectra of KBr disks containing solidified K_2TaF_7/Flinak samples with added oxide (m/o, mol %). O^{2-}/Ta(V) molar ratios >1.

cooled slowly (4 °C/h), until 20 °C below the freezing point, from which temperature cooling was more rapid. The solidified lump was broken up, and the outer pure crystals were removed manually from the impurities concentrated at the center.

Flinak was weighed out, in the glovebox, in the required proportions (LiF 46.5 mol %, NaF 11.5 mol %, KF 42.0 mol %). Sodium monoxide was obtained by heating sodium peroxide (Merck, AR) in an alumina crucible at 700 °C for 12 h under vacuum; analysis by titration gave 98.0% of the theoretical amount for Na_2O. Potassium heptafluorotantalate (Phaltz and Bauer) was analyzed potentiometrically (Found: F, 33.4. Calcd for K_2TaF_7: F, 33.9). K_2TaF_7 was also prepared at our laboratory by mixing hot solutions of Ta_2O_5 in 40 wt % HF and of KF in 15 wt % HF. A white precipitate was obtained, which was then recrystallized in 40 wt % HF. Analytical results for this material were very similar to those obtained for the commercial product.

Glassy carbon crucibles (V25, Carbone Lorraine) were filled with the appropriate Na_2O/K_2TaF_7/Flinak mixture, in that order, to promote homogenity after melting, heated under dried argon for 5 h at 700 °C, and then cooled.

The solidified pellet was broken up and stored in a glass ampule that was sealed under purified argon. For infrared measurements, 15 mg samples were taken, well ground, mixed with 300 mg of KBr (SpectraTech), and pressed at 17 tons for 3 min. Infrared spectra were taken from the disks (12.5 mm in diameter) immediately, using a Bomem DA3.01 interferometer, averaging 500 scans. Spectra of samples taken from different places in the same solidified melt (top and bottom) were identical. The spectrum of pure Flinak was also recorded. From this spectrum, baselines could be estimated for the spectra of the tantalum species. The absorption intensities of the maxima of the bands were measured relative to these baselines. Disks made from Flinak heated with oxide, but without tantalum, showed the same absorptions as Flinak alone.

Raman spectra were measured on coarsely crushed samples in sealed ampules with a JEOL JRS-400D spectrometer using filtered 514.5 nm argon ion laser radiation. Signals were detected with a cooled extended S-20 PM tube and a photon counting system. The excitation power was ~500 mW. The spectra were recorded in the depolarized mode, digitized every 2 cm^{-1}, and then stored in a computer for calculations and plotting.

RESULTS

Infrared Spectra. The infrared spectra of a series of 22 solid samples, formed by cooling melts containing 2.7 mol % tantalum (added as K_2TaF_7) and varying amounts of oxide (0.0–5.4 mol % O, added as Na_2O) were found to form a regular series, with bands growing, or diminishing, relative to each other as the tantalum/oxide ratio changed. Some of the spectral curves are given in Figures 1 and 2. Unavoidably there was some variation in the

Table 1. Variation of Ratios of Intensities of Infrared Bands with Oxide Concentration in Flinak Containing 2.7 Mol % K_2TaF_7 and Na_2O

	band ratios					
% oxide	889/534	889/545	889/732	889/777	889/851	889/917
0.0	0.067		0.75			0.80
0.0	0.25		1.7			6.0
0.0	0.062		3.0			1.5
0.25	0.27		2.2			0.82
0.5	0.25		2.4			1.2
0.5	0.29		3.0			1.1
0.75	0.54		6.5			1.4
0.8	0.30		10			1.2
1.0	1.4		5.0			1.7
1.2	1.2		21			
1.5	3.0		5.0			
1.7	4.1	2.4	5.8			
1.9		17	17			
2.1		1.9	4.2			
2.4		1.1	19			
2.7		3.0				
3.0		2.0				
3.5		0.90		1.4	2.7	
4.0		2.8		0.81	1.9	
4.5		0.87		0.87	1.7	
5.0		0.81		0.81	1.2	
5.4		5.7		0.61	1.1	

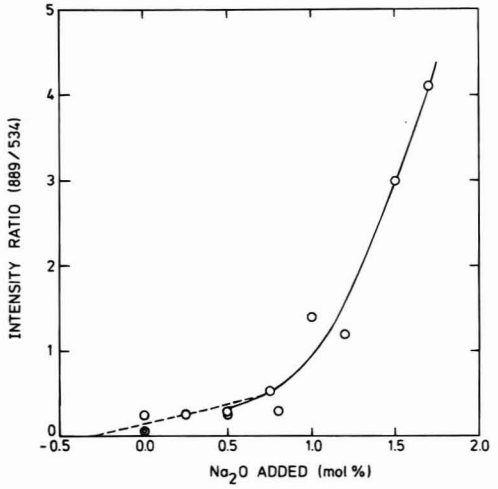

Figure 3. Ratios of the intensities of the 889 and 534 cm^{-1} infrared absorption bands against added oxide. The doughnut signature represents a coincidence of two data points.

intensities of the bands due to physical factors, such as differences in number, orientation, and size of particles, surface configuration, disk formation, etc. To standardize comparison, the ratios of the intensities of two bands from the same spectrum were employed. The intensity of the 889 cm^{-1} band was used, in each case, as the numerator since this band arises from an oxofluoro species and was the only absorption that persisted throughout the whole range of oxide concentrations. Several bands were tested as denominators. Average values of the ratios obtained are given in Table 1.

Plotting these ratios against the percentage of added oxide shows that the 889/534 ratio is by far the best measure of low oxide concentrations. This curve (Figure 3) could be used to estimate the total oxide content of an unknown sample after similar thermal treatment as discussed below.

The effect of moisture on the infrared spectrum of a melt has been studied by Fordyce and Baum,[5] who reported that a 900 cm^{-1} band due to the formation of tantalum oxofluoride products was found for fluoride melts (equimolar LiF/KF) containing tantalum pentafluoride that have been in contact with water. In our work, the absorption background from 900 to 1400 cm^{-1} increased when a disk was aged for 2 months in a closed tube, with definite bands appearing at 1230 and 1255 cm^{-1}. With freshly prepared disks, the background absorption over this range was very small.

The absorption bands may be assigned as follows. The 534 cm^{-1} band is in the range expected for tantalum–fluoride stretching vibrations, and it probably arises from a species not containing oxygen, because it is closest to that found by other workers for heptafluorotantalate anions in the solid potassium compound (535 cm^{-1} in K_2TaF_7 [6–8]) and the solid sodium compound (530 cm^{-1} in Na_2TaF_7 [9]). The regular octahedral anion (TaF_6^-) has an absorption at rather higher frequencies (581 and 590 cm^{-1} [10,11]) and is, in any case, unlikely to be found in the presence of excess fluoride, as is the case here where it is diluted with Flinak, because the equilibrium should be displaced toward the heptafluoro species.[11] The eight-coordinated anion (TaF_8^{3-}) absorbs at 510 cm^{-1}.[12,13]

Similarly, the bands at high frequencies (889 and 917 cm^{-1}, which could not be completely resolved, even at the highest sensitivity) are attributed to tantalum–oxide double bond vibrations, possibly arising from two different tantalum oxofluoro species. In view of their appearance at low oxide content, the suggestion can be made that the oxide/tantalum ratio is unlikely to be higher than 1. A very weak absorption band at 732 cm^{-1} (Table 1) may also arise from the tantalum–fluoride vibrations of such a species.

The 545, 777, 807, and 851 cm^{-1} bands all evidently increase in intensity with oxide/tantalum ratios greater than 1 and are thus to be attributed to tantalum oxofluoro compounds, with the first arising from a tantalum–fluoride vibration. However, the number of fluorides in these species is more conjectural. Two bands (545 and 889 cm^{-1}) are close to those of known oxohexafluorides and oxopentafluorides: $(NH_4)_3TaOF_6$ shows Raman bands at 540 and 862 cm^{-1},[10] and Cs_2TaOF_5 absorbs at 898, 590, 540, and 520 cm^{-1} [14] in the infrared wavenumber range investigated here (Raman bands for $CsTaOF_5$ occur at 898 and 595 cm^{-1} [14]). In contrast to this, the two bands mentioned are less close to those of an oxotetrafluoride ($CsTaOF_4$, bands at 475, 530, 580, 730, and 955 cm^{-1} [15]).

(5) Fordyce, J. S.; Baum, R. L. *J Phys. Chem.* **1965**, *69*, 4335.
(6) Agulyanskii, A. I.; Kirillov, S. A.; Prisyazhnyi, V. D. *Ukr. Khim. Zh.* **1980**, *46*, 457.
(7) Fordyce, J. S.; Baum, R. L. *J. Chem. Phys.* **1966**, *44*, 1159.
(8) Agulyanskii, A. I.; Zalkind, O. A.; Masloboev, V. A. *Zh. Prikl. Spektrosk.* **1993**, *39*, 960.
(9) Agulyanskii, A. I. *Zh. Neorg. Khim.* **1980**, *25*, 2998.
(10) Keller, O. L.; Chetham-Strode, A. *Inorg. Chem.* **1966**, *5*, 367.
(11) Matwiyoff, N. A.; Asprey, L. B.; Wageman, W. E. *Inorg. Chem.* **1970**, *9*, 2014.
(12) Hartman, K. O; Miller, F. A. *Spectrochim. Acta* **1968**, *24A*, 669.
(13) Tsikaeva, D. V.; Nikitina, S. D.; Agulyanskii, A. I.; Kalinnikov, V. T. *Koord. Khim.* **1986**, *12*, 929.
(14) Pausewang, G.; Schmitt, R.; Dehnicke, K. *Z. Anorg. Allg. Chem.* **1974**, *408*, 1.

A number of species are likely to be present in a particular solution depending on the tantalum/oxide/fluoride ratio. Also, structural isomers may be present in some cases. The equilibria are also sensitive to temperature and to the kind of alkali metal cation. (These points may be illustrated by TaF_7^{2-}, which is probably the most studied anion, whose 535 cm^{-1} band moves to 546 cm^{-1} on melting[6] and then to 610 cm^{-1} at 850 °C due to its dissociation to TaF_6^-. With added KF, the band moves to 550 cm^{-1}. Addition of other alkali metal fluorides gives a different pattern of band shifts.[9] In the present case with Flinak it seems that the absorption bands are closest to those found for the potassium salt, perhaps indicating that these cations surround the tantalate anion.

Despite this complicated situation and the uncertainty concerning the species actually present, the ratios of the various absorption bands offer a method of linking several bands to a particular species. If the ratio of two intensities remains approximately constant as concentration is varied (in this case oxide concentration is varied while tantalum concentration and other conditions are held constant), then it follows that both bands arise from the same species, or at least from two closely related species, with the same tantalum/oxide ratio and related by a simple equilibrium such as

$$TaOF_5^{2-} + F^- \rightleftharpoons TaOF_6^{3-} \qquad (1)$$

From Table 1 it seems likely that the 889 and 917 cm^{-1} bands fall into this category. Likewise, the 777 and 851 cm^{-1} bands, which possibly arise from a species with an oxide/tantalum ratio of 2, are probably also closely related since the ratio of their intensities is almost independent of concentration (Table 1).

In Figure 4 are shown infrared spectra of different samples containing K_2TaF_7 at room temperature. It is interesting to note that the pure salt, when it has not been heated, shows no IR bands due to vibrations of the Ta=O bond, i.e., no Ta(V)−oxofluoro complexes are present. However, if the salt is heated to 750 °C for 5 h under an argon atmosphere and subsequently cooled to ambient temperature, bands appear at 889 and 917 cm^{-1}. Since IR bands around 900 cm^{-1} are indicative of Ta=O vibrations, a part of the salt must have undergone a transformation to a Ta(V) oxofluoro compound. In this light, it is likely that the bands at 889 and 917 cm^{-1} observed for 2.7 mol % K_2TaF_7 dissolved in Flinak at 700 °C do not arise from the Flinak solvent itself, but rather have their origin from an oxide impurity (e.g., H_2O) in the K_2TaF_7. This view is supported by the last spectrum shown in Figure 4, where the K_2TaF_7 concentration has been increased to 8.1 mol % K_2TaF_7 (dissolved in Flinak at 750 °C). In this case, it appears that the 889 and ~917 cm^{-1} bands increase in intensity (absolute value). If the oxide impurity originated from the solvent, band intensities similar to those seen at the lower concentration should have been observed.

If we now plot the intensity ratio of the 889 and 534 cm^{-1} bands as obtained from Table 1 vs the concentration of added oxide, an almost linear relationship is obtained (Figure 3). The straight line drawn under this assumption allows us to carry out an extrapolation, so that the oxide impurity in the chemicals used (Flinak solvent and K_2TaF_7) can be estimated from the intersection of this line with the abcissa. If the purpose is to determine the amount of oxide in the Flinak solvent alone, it is important to subtract any amount of oxide originating from the K_2TaF_7 salt, as previously discussed.

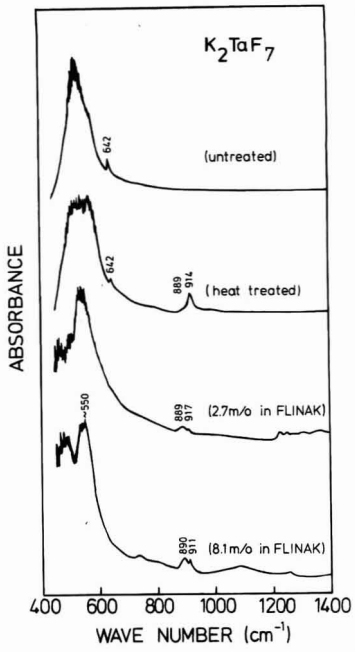

Figure 4. Infrared absorption spectra of K_2TaF_7 treated in different ways (KBr disks at room temperature).

In this particular case, the error in the data is not only related to the intensity ratio measured but also to the composition of the melts. This is because during preparation of the melts, and also during preparation of the KBr pellets, there is always a risk of contamination with oxide by hydrolysis. Because of this, we carried out linear regression according to the method of Bartlett[16] in which the oxide content and the intensity ratio both have error variance. The resulting line for the seven points of lowest oxide content is shown in Figure 3 as a dashed line. Thus, the oxide impurity level after addition of K_2TaF_7 is estimated to be 0.3 ± 0.1 mol %.

If the chemicals are purified in an appropriate way, the oxide content in the solvent melt is normally rather low. However, for electrochemical investigations, where low concentrations (often in the range of 0.1 mol % or less) are usually applied, the oxide content should be almost negligible. In such cases it is the data for the lower range of oxide concentrations, i.e., the linear range in Figure 3, that are the most useful. It is also important to note that oxide contents in the order of magnitude of 0.1 mol % (in total) will easily be detected.

Taking into account the correction for the oxide impurity arising from K_2TaF_7 (0.3 mol %), a standard curve for the oxide content in the Flinak melt can now be obtained by changing the starting point of the curve to 0.0 mol %.

Raman Spectra. It was evident that the Raman spectra of the same tantalum/oxide/fluoride solidified samples showed a

(15) Buslaev, Y. A.; Kokunov, Y. V. *Izv. Akad. Nauk. SSSR Neorg. Mater.* **1968**, *4*, 537.

(16) Bartlett, M. S. *Biometrics* **1949**, 207.

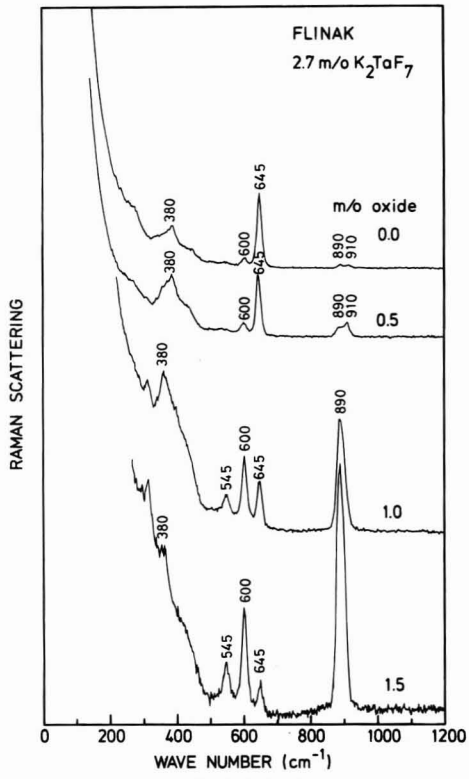

Figure 5. Raman spectra of solid K_2TaF_7/Flinak samples with added oxide (m/o, mol %). O^{2-}/Ta(V) molar ratios ≤0.56.

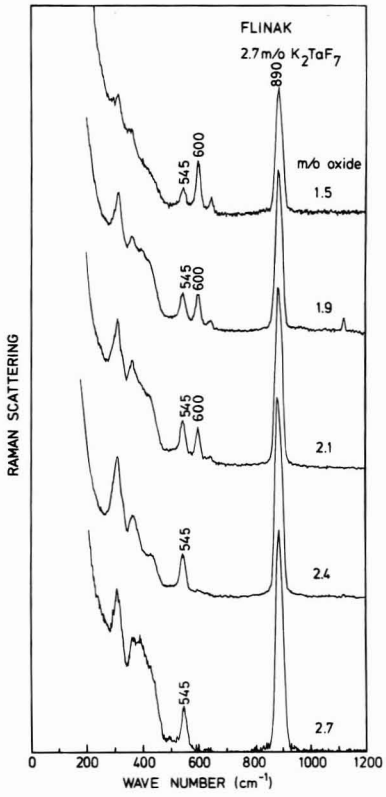

Figure 6. Raman spectra of solid tantalum/Flinak samples with added oxide (m/o, mol %). O^{2-}/Ta(V) molar ratios in the range 0.56–1.0.

similar regular pattern of the intensity ratios for 13 frequencies as a function of the oxide content (Figures 5–7). The chief difference is the complete absence of the 534 cm^{-1} band, which is evidently Raman inactive. Interestingly, similar spectra were obtained from these samples in the molten state,[17] so that the solid state signals cannot be ascribed purely to crystal effects. There was some small variation in the intensity ratios obtained from spectra of different crystal fragments of the same sample. Probably this is due to orientation effects or some segregation of component compounds occurring during the cooling and freezing of the melt solutions. Spectra of several crystal fragments of a sample were summed and normalized to provide representative values. Ratios of these intensities again illustrate a regular pattern of variations (Table 2), which can assist the assignment of the vibrations to particular tantalum/oxide ratios as well as be used to estimate the oxide content, for example, of supposedly pure Flinak. Again the measured intensities of several bands were tried as the denominator, and the 890 cm^{-1} band, which was present over almost the whole oxide concentration range studied, turned out to be most usefully employed as the numerator.

The signal at 645 cm^{-1} is clearly a Ta–F vibration and has a maximum intensity at 0 mol % added oxide, diminishing to zero intensity at 2.4 mol %. Hence it is ascribed to a tantalum fluoride species without oxide, most probably the symmetric stretch vibration of potassium heptafluorotantalate (reported to give bands at 641,[7,10] 645,[11,18,19] and 635 cm^{-1} [20]). The heptafluoride is more likely than either the hexafluoride anion (with a stretch vibration band at 692 cm^{-1} for $CsTaF_6$ [10,20]) or the octafluoride anion (371, 411, and 614 cm^{-1} [10] or 377, 426, and 622 cm^{-1},[12] both for Na_3TaF_8). A similar assignment is made for the vibration at 280 cm^{-1} observed at the same frequency by Torardi et al.[19] for a Ta–F bending mode. It may be noted that Fordyce and Baum[5] found a strong infrared band at 285 cm^{-1} for solid K_2TaF_7 and at 292 cm^{-1} for Ta(V) in LiF/KF melts.[7] The vibration at 380 cm^{-1} may also be due to a Ta–F species without oxide (cf. 392[10] and 395 cm^{-1},[19] both for K_2TaF_7), but interference from a signal due to pyrex glass sometimes occurred near this frequency and also at 420 cm^{-1}. This was confirmed using an empty tube. Thus, these vibrations and their ratios were not used for oxide estimations.

The positions of the 890 and 910 cm^{-1} bands clearly show that they are due to tantalum–oxide double bond vibrations (e.g., 888 cm^{-1} was found for K_3TaOF_6,[5] and 890 cm^{-1} for $(NH_4)_3TaOF_5$ [10]

(17) von Barner, J. H.; Berg, R. W.; Bjerrum, N. J., Christensen, E., Rasmussen, F. *Mater. Sci. Forum* **1991**, *73–75*, 279.

(18) Tsikaeva, D. V.; Nikitina, S. D.; Agulyanskii, A. I.; Kalinnikov, V. T. *Zh. Obshch. Khim.* **1987**, *57*, 974.

(19) Torardi, C. C.; Blixner, L. H.; Blasse, G. *J. Solid State Chem.* **1987**, *67*, 21.

(20) Babkin, A. G.; Nikolaev, A. I.; Shevyreva, E. V. *Zh. Neorg. Khim.* **1986**, *31*, 2444.

Table 2. Variations of Ratios of Intensities of Raman Bands with Oxide Concentration in Flinak Containing 2.7 Mol % K_2TaF_7 and Na_2O

	band ratios								
% oxide	890/910	890/645	890/600	890/545	890/310	890/280	870/795	870/565	870/310
0.0	0.50	0.03	0.37	∞	∞	0.15			
0.0	0.71	0.12	0.80	4.0	∞	0.80			
0.0	1.0	0.03	0.36	2.0	∞	0.17			
0.25	1.0	0.18	0.70	4.7	∞	1.8			
0.50	1.4	0.29	1.3	7.3	∞	4.4			
0.50	0.83	0.20	1.0	5.0	∞	1.2			
0.75		1.3	1.5	5.5	6.6	11			
0.80		0.64	1.2	4.4	∞	∞			
1.0		2.6	1.7	6.0	4.1	54			
1.2		1.9	1.5	5.1	5.8	∞			
1.5		8.3	2.5	6.4	3.8	9.2			
1.7		12	2.8	5.0	4.8	∞			
1.9		23	4.1	5.9	2.8	31			
2.1		36	5.4	5.1	2.4	25			
2.4		∞	61	5.4	2.6	∞			
2.7		∞	∞	5.5	3.4	55			
3.0		∞	49	5.8	3.8	∞			
3.5		∞	∞	7.9	2.5	∞	7.9		
4.0		∞	∞	10	2.8	∞	7.0		
4.5							6.7	9.4	2.3
5.0							6.9	11	3.8
5.4							5.6	∞	∞

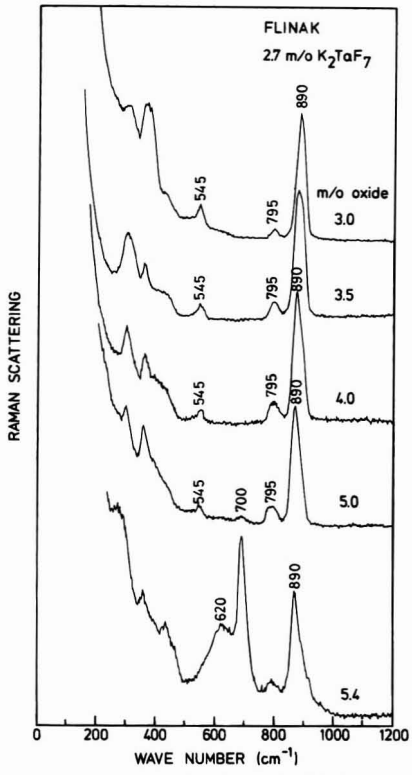

Figure 7. Raman spectra of solid tantalum/Flinak samples with added oxide (m/o, mol %). O^{2-}/Ta(V) molar rarios >1.

(880 cm^{-1} was quoted for $(Et_4N)_2Ta_2OF_{10}$,[21] but this may well be due to impurities containing tantalum terminal oxygen groups)).

(21) Sala-Pala, J.; Calves, J. Y.; Guerchais, J. E.; Brownstein, S.; Dewan, J. C.; Edwards, A. J. *Can. J. Chem.* **1978**, *56*, 1545.

The 890 and 910 cm^{-1} bands may be due to very similar species in slightly different environments. The band at 545 cm^{-1} varies in its intensity from very small for 0.0 mol % added oxide, through a maximum at 2.4 mol %, and decreases to zero for 5.4 mol %, respectively. Hence, this band seems to be associated with a species with a 1:1 tantalum/oxide ratio. A band at 540 cm^{-1} has been reported by Keller and Chetham-Strode[10] for solid $(NH_4)_3TaOF_6$. The constant intensity ratios found for the 545 cm^{-1} band to the 890 cm^{-1} band support the suggestion that they arise from the same species.

The vibration at 600 cm^{-1} was present from 0.0 to 2.4 mol % added oxide and very clearly reaches a maximum around 1.4 mol % in the normalized spectra. This change is also seen in Table 2 as a ratio (890/600) vs oxide concentration break; i.e., when the intensity ratios are plotted, a distinct break between two nearly straight lines is seen. The simplest explanation of this tantalum/oxide ratio equal to 2:1 is the existence of a dimer species containing an oxygen bridge (Ta−O−Ta) and with the 600 cm^{-1} band due to a tantalum−fluoro stretch vibration. The formation of such a species would also explain the very rapid decrease of the tantalum−fluoride stretching band intensity (at 645 cm^{-1}, attributed to the TaF_7^{2-} anion), as was also found for the infrared stretch at 534 cm^{-1} attributed to the same species.

In Figures 5 and 6 the summed experimental spectra have been rescaled so that the characteristic vibration of the presumed predominant species in the sample is proportional to the concentration of that species. Thus Figure 5 is drawn so that the tantalum−fluoride vibration at 645 cm^{-1} (considered to be due to a Ta−F stretch of a species without oxide) is normalized to the concentration of oxide-free tantalum (i.e., to Ta mol % minus oxide mol %), whereas Figure 6 is drawn with the 890 cm^{-1} vibration (considered to be due to a Ta=O vibration of a monooxo $TaOF_x^{(x-3)}$ species) made proportional to the concentration of TaOF species (i.e., to mole percent oxide).

At high added oxide contents, e.g., above 4.0 mol %, new vibrations appear, at 620, 700, and 795 cm^{-1}, while the hitherto ubiquitous 890 cm^{-1} signal shifts to 870 cm^{-1}, as can be seen in

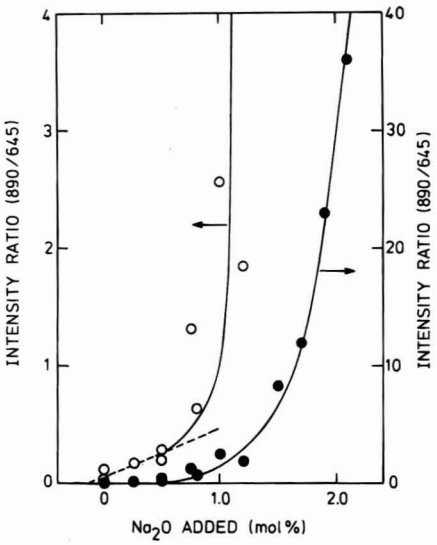

Figure 8. Ratios of the intensities of 890 and 645 cm^{-1} Raman bands against added oxide. For convenience, two different scales are used. Filled circles refer to the ordinate on the right side; open circles refer to the ordinate on the left side.

Figure 7 where the spectra have been rescaled so that the 870 or 890 cm^{-1} vibration (i.e., of Ta=O in a TaOF species) is of constant height. These vibrations are all attributed to new tantalum–oxofluoro species with a tantalum/oxide ratio of 1:2. It is inherent in the above discussion of all spectra that the melts (both liquid and solidified) contain more than one kind of species, and probably often more than two kinds, of different stoichiometries and/or geometries, particularly when the oxide/tantalum ratios are high.

The intensity ratios from different species may again be used for quantitative determination of the oxide content of fluoride melts or of Flinak itself. In the case of Flinak, the 890/600 and 890/645 ratios were found to be particularly useful. The latter ratio is shown in Figure 8. The linear regression[16] was carried out on the first six points, and the confidence limits were calculated for the first seven points as in the case of the infrared ratio.

From this analysis (dashed line, Figure 8), the oxide impurity level in Flinak with K_2TaF_7 added is estimated to be 0.2 ± 0.1 mol %. It can be seen that the values obtained from the two vibrational methods are closely similar. As for the infrared spectra, a standard curve starting from 0.0 mol % oxide can also be obtained by displacement of the curve in Figure 8 by an amount corresponding to the background impurity, here 0.2 mol %.

CONCLUSION

Both infrared and Raman spectroscopies can be used for the determination of oxide contents of fluoride melts if suitable additions of tantalum(V) are made and the melts equilibrated.

The two techniques give identical values for the oxide content of the purified Flinak with K_2TaF_7 added. By comparison of the spectra used for the standard curves with the spectra of pure K_2TaF_7, or of Flinak with K_2TaF_7 added in a higher concentration, it can be stated that the oxide is mainly introduced via the K_2TaF_7 salt.

Thus, the standard curves obtained can be used in different ways: By correcting for the amount of oxide arising from the tantalum salt, a standard curve for determination of oxide in the Flinak can be obtained. Alternatively, by using very pure alkali fluorides, the oxide content in the K_2TaF_7 may be determined. The total oxide content, i.e., in Flinak and K_2TaF_7, may of course also be determined, when proper correction is carried out.

The infrared method has an inherent advantage because it measures an average of several crystallites whereas the Raman method requires recording of at least two spectra to minimize crystal orientation effects or inhomogenities.

Received for review October 20, 1994. Accepted March 9, 1995.[⊗]

AC9410272

[⊗] Abstract published in *Advance ACS Abstracts,* April 15, 1995.

Anal. Chem. **1995,** *67,* 2136–2141

Carius Tube Digestion for Low-Blank Rhenium–Osmium Analysis

Steven B. Shirey*

Department of Terrestrial Magnetism, Carnegie Institution of Washington, 5241 Broad Branch Road, NW, Washington, D.C. 20015

Richard J. Walker

Department of Geology, Isotope Geochemistry Lab, University of Maryland, College Park, College Park, Maryland 20742

A relatively high-temperature oxidizing digestion using aqua regia has been developed for <0.1–5 g size samples of various types of rocks including silicates, sulfides, and metals prior to Re–Os isotopic analysis. Reactions are accomplished in sealed, thick-walled Pyrex tubes (Carius tubes) at 240 °C and elevated pressures for ~12 h. This digestion technique dissolves platinum-group element minerals, metals, and sulfides and evidently sufficiently reacts with silicates to release most or all Re and Os contained in a silicate matrix. The procedure also leads to the oxidation of Re and Os to their highest valences and, therefore, promotes the complete chemical equilibration of sample Re and Os with enriched isotopes of Re and Os that are added for isotope dilution analysis. Once sample digestion and equilibration are complete, subsequent Os separation is accomplished by conventional double distillation from sulfuric acid, and Re is separated by anion exchange chromatography. Comparison of conventional Teflon vessel digestions and Carius tube digestions for a diverse suite of geological samples shows that the Carius tube digestion both liberates more Os from most matrices and also is a much more robust method for reproducibly measuring the isotopic composition of a sample.

The Re–Os isotopic system (^{187}Re decays to ^{187}Os via $^{-}\beta$ decay with a ~42 Ma half-life) has seen increasing use in solid Earth geochemistry as a tracer with chalcophilic and siderophilic properties and thus forms a unique complement to the other long-lived, lithophilic radioisotope systems. The system has proven useful for a variety of applications including constraining the ages of subcontinental lithospheric mantle[1,2] and magmatic iron meteorite groups,[3] examining the recycling of oceanic crust into the mantle,[4] determining the origin of platinum-group elements in certain ores,[5] and constraining the influx of extraterrestrial and continental components into the oceans.[6]

The increased use of the Re–Os system has been spurred by advances in measurement sensitivity and analytical accuracy. The technique of choice for high-precision Re–Os analysis is isotope dilution mass spectrometry using negative thermal ionization (NTIMS).[7] To optimize Re and Os data on geologically old samples and obtain accurate Re–Os isochrons, full equilibration of the Re and Os in the spike and sample during isotope dilution is paramount. Unfortunately, improvements in spike–sample equilibration have lagged behind the other advances and now serve as the limiting factor in Re–Os isotopic work. We report here a new adaptation of an old technique that has proven superior, in many ways, to the commonly used techniques.

EXPERIMENTAL SECTION

The Carius tube method described here has been developed to improve on and thus replace the Teflon vessel digestion procedure described by Walker.[8] Some of the same reagents (e.g., HF, HCl, HNO_3, ethanol, and enriched isotope spikes of ^{190}Os and ^{185}Re) are used in both procedures so their preparation has been described previously.[8] Further, it has been found that double distillation[9] yields cleaner Os for NTIMS and is recommended for improved mass spectrometry.

Carius Tube Loading Procedure. The original design for high-temperature, thick-walled glass tubes for sample digestion was described by Carius in 1865.[10] The modern redesign and employment of the Carius combustion tube for the digestion of platinum-group metals and other refractory materials was accomplished at the U.S. National Bureau of Standards during the 1940s.[11–13] Carius tubes of similar design have been refined more recently by Kelly at the National Institute of Standards and Technology to digest samples for sulfur analysis by thermal ionization mass spectrometry[14] and to dissolve metallic Os.[8] The Carius tube design used in this work and instructions for Carius

(1) Walker, R. J.; Carlson, R. W.; Shirey, S. B.; Boyd, F. R. *Geochim. Cosmochim. Acta* **1989,** *53,* 1583–1595.
(2) Carlson, R. W.; Irving, A. J. *Earth Planet. Sci. Lett.* **1994,** *126,* 456–472.
(3) Horan, M. F.; Morgan, J. W.; Walker, R. J.; Grossman, J. N. *Science* **1992,** *255,* 1118–1121.
(4) Hauri E. H.; Hart, S. R. *Earth Planet. Sci. Lett.* **1993,** *114,* 353–371.
(5) Walker, R. J.; Morgan, J. W.; Naldrett, A. J.; Li, C.; Fassett, J. D. *Earth Planet. Science Lett.* **1991,** *105,* 416–429.
(6) Esser, B. K.; Turekian, K. K. *Geochim. Cosmochim. Acta* **1988,** *52,* 1383–1388.
(7) Creaser, R. A.; Papanastassiou, D. A.; Wasserburg, G. J. *Geochim. Cosmochim. Acta* **1991,** *55,* 397–401.
(8) Walker, R. J. *Anal. Chem.* **1988,** *60,* 1231–1234.
(9) Morgan, J. W.; Walker, R. J. *Anal. Chim. Acta* **1989,** *222,* 291–300.
(10) Carius, L. *Liebigs Ann. Chem.* **1865,** *136,* 129.
(11) Gordon, C. L. *J. Res. Natl. Bur. Stand.* **1943,** *30,* 107–111.
(12) Wichers, E.; Schlecht, W. G.; Gordon, C. L. *J. Res. Natl. Bur. Stand.* **1944,** *33,* 363–381.
(13) Gordon, C. L.; Schlecht, W. G.; Wichers, E. *J. Res. Natl. Bur. Stand.* **1944,** *33,* 457–470.
(14) Paulsen, P. J.; Kelly, W. R. *Anal. Chem.* **1984,** *56,* 708–713.

0003-2700/95/0367-2136$9.00/0 © 1995 American Chemical Society

tube fabrication have been described previously.[11-14] The Carius tubes used in this study have a body 20 cm long fabricated from 1.3 cm inner diameter (i.d.), 1.9 cm outer diameter (o.d.) borosilicate glass tubing with a sample introduction neck 5 cm long fabricated from 0.6 cm i.d., 0.9 cm o.d. tubing. The tubes are cleaned by boiling in CrO_3–H_2SO_4 and reagent grade 12 M HNO_3 each for 4 h, multiply rinsed with high-purity water, and then thoroughly dried. As a safety precaution, even empty, new tubes should be handled with care. Sharp blows to the outside of the tube or surface scratches can cause premature breakage when the tubes are heated and at high pressure.

When loading, the lower half of the tube is immersed in an ethanol–dry ice slush so that sample, enriched isotopes (spikes), and reagents are chilled upon addition to the tube. Chilling is desirable because it reduces the vapor pressure of the reagents and makes the sealing of the tube easier and more reliable. Also, the reagents can oxidize both Re and Os, and both form moderately volatile oxides. The chilling precludes the possibility of Re or Os loss from the tube during loading, prior to sealing. Note that tubes should *never* be chilled in liquid nitrogen because once sealed they will overpressure and explode as soon as they warm up slightly.

Sample powders are introduced into the tube via Teflon or glass funnels sized to fit into the sample loading neck and extend into the main portion of the tube (~5.5 cm long). ^{190}Os and ^{185}Re spikes in 6 N HCl solutions are weighed and quantitatively transferred through the funnel into the tube and allowed to freeze in the bottom of the tube. Then 4 mL of 10 M HCl and 2 mL of 16 M HNO_3 to make aqua regia are introduced through the funnel and allowed to freeze. As a precaution against bursting, it is very important to leave at least half to two-thirds of the tube volume unfilled. While the bottom is still frozen, the tube is sealed by drawing-in the neck using an oxygen–propane torch.

With silicates, it is also possible to reduce the volume of the sample by driving off the silica. The desilicification procedure, discussed previously[8] and used here as a comparison for the Carius tube attacks alone (Table 1), may be added to the sample processing steps before the sample is inserted into the Carius tube to reduce the volume of especially large samples by driving off silica. In some types of samples this has improved the liberation of the Re and Os that either is structurally bound or occurs as inclusions in silicate minerals. However, if this procedure is used, it is important to fully remove residual HF to avoid etching of the tube and to remove any residual ethanol to avoid explosion of the tube.

Sample Digestion and Tube Opening. Once sealed, the tube is permitted to warm to room temperature. The tube is placed in a 3.3 cm o.d., 2.7 i.d., 28 cm long stainless-steel jacket. The jacket is welded at the bottom and has a threaded cap at the top. Notches are cut just above the threads so that the cap cannot form a tight seal. The internal volume of the stainless steel jacket is about twice the external volume of the Carius tube so that if it bursts, the jacket does not become overpressured. The purpose of this jacket to confine the glass and sample if the tube should burst.

The tube is heated in an oven at 220–260 °C for ~12 h. Agitation in between multiple heating cycles can aid in sample digestion. It should be noted that, once heated, the inside of the tube may be pressurized even when the temperature is reduced to room conditions. Hence, the tubes should be treated gently, they should not be scratched or bumped, and protective face and body shielding should be worn during subsequent handling.

After one heating cycle, 1–2 g samples of ultramafic to mafic rocks will often give clear solutions, particularly if they have been treated to an HF–HCl digestion step in a Teflon bomb first. However, larger samples and those that have not been treated with HF before the Carius tube step rarely give clear solutions. As discussed below, this does not appear to be critical to extraction of all of the Re and Os. Carius tubes containing digested samples can be stored indefinitely.

Sample Extraction and Re–Os Purification. Upon cooling, the sample-bearing Carius tube is immersed in an ethanol–dry ice slush and frozen. The tube can be vented by gently heating the filler neck with a torch until a hole forms and pressure is vented. This step should be done behind a safety shield and while wearing a face mask. The upper portion of the tube can then be broken off by scoring and touching the score with a hot glass rod. The tube is then placed in ice water until the contents thaw and the tube and its contents come fully up to 0 °C. This last step is important to assure no Os remains frozen to the wall of the tube when it is poured into the distillation flask.

Samples are distilled following procedures and apparatus hybridized from those described previously.[8,9] The sample is introduced into the distillation flask by cutting and breaking the thick-walled part of the tube and pouring into the flask directly. Residue is washed-in with 30–40 mL of 2.5 M H_2SO_4. Several boiling chips can be added at this stage to aid in the smooth generation of bubbles during boiling. Osmium is distilled as the tetraoxide using a nitrogen flow with no additional oxidants apart from the aqua regia already in the Carius tube. The OsO_4 is trapped in 5–10 mL of 6 M NaOH that is chilled with ice. Distillation is continued for ~2 h with a flask temperature of 108–112 °C. Nitrogen flow should be such that several bubbles are emitted per second in the trap. Ground glass joints in the distillation apparatus are sealed with water.

When the first-stage distillation is complete, the flask is removed and the residual Re-bearing solution is poured off to be subsequently centrifuged. The NaOH trap solution is added to the now-empty flask and acidified with 2 mL of 10 M H_2SO_4 per 1 mL of trap solution. The mixture is distilled again for 2 h at ~108 °C and trapped in ~3 mL of either 10 M HBr or a 3:1 mixture (by volume) of 10 M HCl and ethanol. We use a smaller second trap for this distillation because of the difficulty in removing all traces of NaOH from the original trap and because of the lesser volume of trap solution used. After distillation, the trap solution is transferred into a 7.5 mL Savillex Teflon container and placed in an oven at 90 °C for 1 h. This step reduces the Os to a nonvolatile bromide or chloride species. The solution is then dried-down and can either be loaded into the mass spectrometer or further purified using anion exchange chromatography.

The Re-containing pot solution is centrifuged to remove solids, loaded onto a 1 mL anion column (AG-1 X8 200–400 mesh), and eluted using previously published guidelines.[15] A second smaller anion column is used for additional purification.[9]

Average Re and Os blanks for the total Carius tube procedure as described above are less than 10 and 5 pg, respectively, with an Os yield of 80% or greater.

(15) Morgan, J. W.; Golightly, D. W.; Dorrzapf, A. F. *Talanta* **1991**, *38*, 259–265.

Table 1. Replicate Re–Os Isotopic Analyses Carried Out by Acid Digestion with HCl–HF–Ethanol in Teflon Vessels (TV) and Aqua Regia Digestion in Carius Tubes (CT)[a]

sample no.	rock type	locality	age (Ma)	digest. method	Re (ng/g)	Os (ng/g)	$^{187}Re/^{188}Os$	$^{187}Os/^{188}Os$
SMB-3	alkali basalt	Sao Miguel, Azores	0	TV		0.148		0.1308
				CT		0.316		0.1305
WKH-111A	HAOT	western U.S.	0	TV	0.384	0.050	37.3	0.1531
				CT	0.387	0.208	9.00	0.1550
WKH-27	HAOT	western U. S.	0	TV	0.474	0.045	51.1	0.2068
				CT	0.472	0.067	34.3	0.2192
WKH-6A	HAOT	western U. S.	0	TV	0.297	0.047	30.8	0.1864
				CT	0.295	0.091	15.7	0.1877
WKH-1	HAOT	western U. S.	0	TV[b]	0.559	0.021	130.7	0.1711
				CT	0.557	0.083	32.7	0.1707
PC-3	lamproite	Prairie Creek, AK	100	TV[b]	0.056	0.379	0.711	0.1130
				CT	0.027	1.755	0.075	0.1226
MH-1	lamproite	Prairie Creek, AK	100	TV		0.241		0.1140
				CT	0.055	1.324	0.202	0.1232
PHN2600	spinel peridotite	Kaapvaal craton, SA	90	TV	0.035	0.625	0.267	0.1081
				CT	0.044	0.679	0.312	0.1088
PHN5239	garnet peridotite	Kaapvaal craton, SA	90	TV	0.100	1.540	0.311	0.1104
				CT	0.065	1.324	0.235	0.1100
PHN5275	spinel peridotite	Kaapvaal craton, SA	90	TV	0.103	8.230	0.060	0.1117
				CT	0.085	6.900	0.059	0.1115
UV564/89	spinel peridotite	Siberian craton	350	TV	0.469	1.580	1.439	0.1235
				CT	0.459	1.520	1.455	0.1233
UV179/86	eclogite	Siberian craton	350	TV	1.650	0.088	204.5	9.8080
				CT	1.583	0.082	203.0	9.1410
218324	komatiite	Pyke Hill, ON	2715	TV	1.093	0.751	7.214	0.3221
				CT	0.998	0.892	5.506	0.2833
218326	komatiite	Pyke Hill, ON	2715	TV[c]	3.652	1.661	10.97	0.3682
				CT	0.943	1.369	3.386	0.2564
218357	komatiite	Pyke Hill, ON	2715	TV	0.381	1.028	1.802	0.1749
				CT	0.383	1.520	1.218	0.1501
218357	komatiite	Pyke Hill, ON	2715	TV	0.379	1.109	1.656	0.1696
				CT	0.373	1.699	1.060	0.1498
218357	komatiite	Pyke Hill, ON	2715	TV	0.393	1.221	1.565	0.1743
				CT	0.366	1.871	0.947	0.1477
218358	komatiite	Pyke Hill, ON	2715	TV	0.577	1.153	2.421	0.1887
				CT	0.544	1.812	1.467	0.1610
218358	komatiite	Pyke Hill, ON	2715	TV	0.539	1.131	2.316	0.1901
				CT	0.652	1.573	1.997	0.1747
218358	komatiite	Pyke Hill, ON	2715	TV[c]	2.222	0.758	14.38	0.2424
				CT	0.569	1.810	1.525	0.1630
SJ-101	basaltic komatiite	Cape Smith, QUE	1930	TV	0.660	0.373	8.824	0.3889
				CT	0.660	0.550	5.912	0.2881
BV-6	basaltic komatiite	Cape Smith, QUE	1930	TV	1.914	2.037	4.589	0.2311
				CT	2.288	3.372	3.096	0.2076
SJ-102	basaltic komatiite	Cape Smith, QUE	1930	TV	0.184	0.392	2.306	0.2838
				CT	0.200	0.403	2.433	0.2697

[a] All analyses except two are by negative thermal ionization mass spectrometry. HAOT, high alumina olivine tholeiite. Samples collected as follows: Azores alkali basalt, E. Widom; HOATs, W. K. Hart; lamproites, S. C. Bergman; Kaapvaal peridotites, P. H. Nixon; Siberian xenoliths, N. Pohilenko; komatiites, O. Stecher and basaltic komatiites, S.-J. Barnes. Analysts inlude E. Widom, W. K. Hart, D. G. Pearson, S. B. Shirey and R. J. Walker. [b] Analysis carried out by much lower precision resonance ionization mass spectrometry. [c] Apparent Re and/or Os spike loss. Age given for peridotites and eclogite in table is kimberlite eruption age.

RESULTS AND DISCUSSION

Comparison of results for samples from Teflon vessel digestions[8] with results for the Carius tube procedure described above (with no acid pretreatment) for some 23 pairs of a wide variety of igneous whole-rock samples are given in Table 1 and Figures 1–4. The absolute reproducibility of the Carius tube technique was tested via the analysis of four to eight repeat analyses of powder aliquots of three 2715 Ma old komatiites and five separate pieces of a ~4540 Ma old iron meteorite, Filomena (Table 2). Sizes for samples given in Tables 1 and 2 ranged from 0.1–2 g for the Teflon vessel and Carius tube digestion of mantle peridotites, komatiites, and the iron meteorite to 5–7 g for the Teflon vessel digestion of basaltic composition rocks. Sample sizes for Carius tube digestions of basaltic rocks were held to less than 4 g because of Carius tube volume limits.

Table 1 and Figure 1 compare Re and Os concentrations for the Teflon vessel and Carius tube procedures. The two techniques give very similar Re concentrations. The only exceptions are at Re concentrations below 100 ppt, where some of the lack of agreement may be due to Re blank corrections. The agreement between the two techniques for Os concentrations varies considerably as a consequence of rock type. Mantle xenoliths, regardless whether they are garnet or spinel peridotites, or eclogites, give nearly identical Os concentrations with both methods. In contrast, the volcanic rocks of a variety of ages show from 3 to 400% higher Os content for the Carius tube digested samples. There is only one example, of the 18 volcanic rock pairs studied, where the Carius tube digestions gave lower Os concentrations compared to Teflon vessel digestions.

Table 2. Repeat Re–Os Isotopic Analyses of Three Komatiites and One Iron Meteorite[a]

sample	lab	Re (ng/g)	Os (ng/g)	$^{187}Re/^{188}Os$	$^{187}Os/^{188}Os$	$^{187}Os/^{188}Os_I$
KAL-1	USGS	0.695	1.922	1.755	0.1806	0.1007
KAL-1	USGS	0.785	2.100	1.813	0.1835	0.1010
KAL-1	UMd	0.504	2.025	1.203	0.1560	0.1012
KAL-1	DTM	0.443	1.803	1.221	0.1629	0.1073
KAL-1	DTM	0.439	2.117	1.035	0.1552	0.1081
218357	UMd	0.366	1.871	0.947	0.1477	0.1046
218357	DTM	0.395	1.708	1.125	0.1565	0.1056
218357	DTM	0.383	1.520	1.218	0.1501	0.0946
218357	DTM	0.373	1.699	1.060	0.1498	0.1015
218358	UMd	0.611	1.839	1.613	0.1666	0.0931
218358	UMd	0.601	1.641	1.779	0.1726	0.0916
218358	UMd	0.569	1.810	1.525	0.1630	0.0935
218358	UMd	0.592	2.471	1.161	0.1484	0.0955
218358	UMd	0.536	1.921	1.356	0.1596	0.0979
218358	DTM	0.544	1.812	1.466	0.1610	0.0942
218358	DTM	0.652	1.573	1.997	0.1747	0.0838
218358	DTM	0.547	1.813	1.482	0.1611	0.0936
Filomena	UMd	201.8	1036.5	0.94311	0.16928	
Filomena	UMd	201.7	1038.7	0.94049	0.16931	
Filomena	UMd	201.6	1040.1	0.93885	0.16926	
Filomena	UMd	201.8	1040.6	0.93934	0.16917	

[a] Samples KAL-1, 218357, 218358 are Archean komatiites, Filomena is a IIA iron meteorite. Sample KAL-1 was collected by N. Arndt at Alexo, ON, and Filomena was donated by R. Clarke of the USMNH of the Smithsonian Institution. All analyses carried out by aqua regia digestion in Carius tubes with the exception of the two carried out at the USGS by M. F. Horan using $NaOH–Na_2O_2$ flux fusion. The komatiite powder aliquots were all in the 1–2 g size range; the iron metoerite pieces weighed 0.1 g and were obtained as sawed chunks from the same porion of the meteorite. Iron meteorite analyses were carried out by M. Smoliar. Initial Os compositions were calculated using a ^{187}Re decay constant of 1.64×10^{-11} and ages of 2715 Ma for the komatiites.

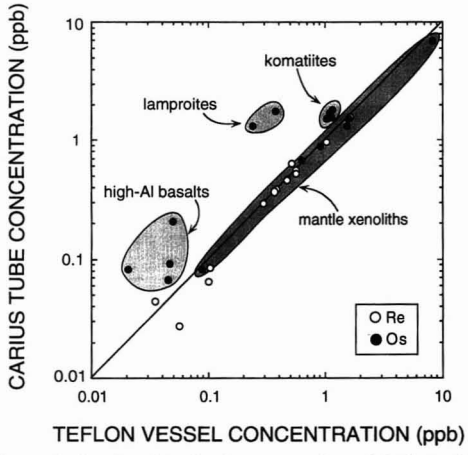

Figure 1. log–log plots showing a comparison of duplicate data for a variety of different rock types and rocks of different age as given in Table 1. Re data are generally in good agreement between the Teflon vessel and Carius tube digestion methods, whereas komatiites, lamproites, and basalts generally show similar to significantly higher Os concentrations by Carius tube digestion.

Osmium isotopic compositions ($^{187}Os/^{188}Os$) also show similar systematic differences in behavior between the rock suites (Table 1, Figure 2). Very young volcanic rocks show a good correspondence between Teflon vessel digestions and Carius tube digestions; agreement on analyses of different powder aliquots by the two methods in some instances is better than 1%. With the exception of one very radiogenic eclogite, agreement between the different analyses of mantle xenoliths is often excellent, being at the ±0.1% level regardless of age or xenolith type. In contrast, the results for older volcanic rocks (100–2700 Ma) are more variable. For the two lamproites from Prairie Creek, AR, the Carius tube digested samples have isotopic compositions ~10% less radiogenic than the Teflon vessel digestion. The 11 significantly older basaltic komatiites and komatiites have routinely lower Os isotopic compositions with the differences between the two techniques ranging from 10 to 30%.

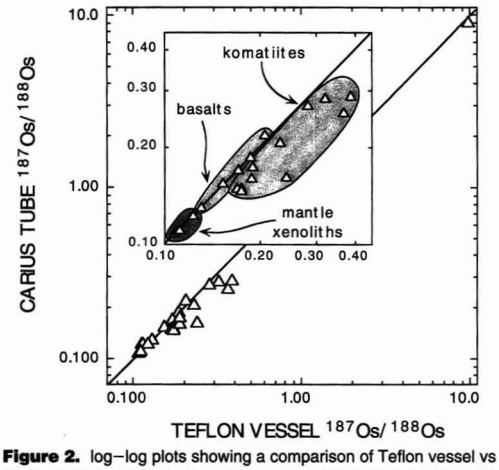

Figure 2. log–log plots showing a comparison of Teflon vessel vs Carius tube Os isotopic data. Inset shows detail for the rocks with lower isotopic compositions. The Os isotopic compositions of mantle xenoliths and young volcanic rocks agree well with both procedures. Os isotopic compositions are systematically lower for the 1.9–2.7 Ga old picrites and komatiites when the rocks are dissolved by the Carius tube procedure.

When Os concentrations are combined with Os isotopic compositions for comparison of the two techniques (Figure 3), the distinction between the suites of rocks is even clearer. The mantle xenoliths show good reproducibility in both Os concentration and Os isotopic composition. For the young volcanic rocks, the large increase in Os concentration with the Carius tube method is not accompanied by any significant change in their isotopic composition. The Proterozoic to Archean komatiites, on the other hand, show that their higher Os concentrations are usually accompanied by systematically lower $^{187}Os/^{188}Os$. In only three cases is there a decrease in the $^{187}Os/^{188}Os$ with little change in Os concentration.

The Re–Os isotopic data for the two dissolution techniques is a function of the age and mineralogy of the rocks. Xenoliths of mantle peridotite and eclogite are quite reproducible regardless of digestion method. This reproducibility is surprising because of the old Os model age of the xenoliths.[16] Re and Os in mantle peridotites are likely to be contained primarily in sulfides, as has been shown petrographically for other platinum-group elements.[17] Sulfides also would be expected to be soluble in both reducing

(16) Pearson, D. G.; Shirey, S. B., Carlson, R. W.; Boyd, F. R., Pokhilenko, N. P.; Shimizu, N. *Geochim. Cosmochim. Acta* **1995**, *59*, 959–978.

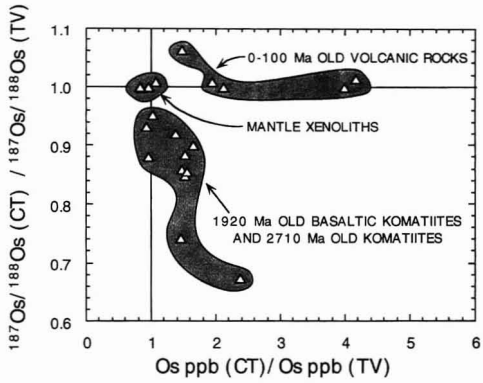

Figure 3. Os isotopic compositions obtained via the Carius tube method normalized to that obtained via Teflon bomb digestion vs Os concentration compared in the same way between the two methods: CT, Carius tube; TV, Teflon vessel digestion. Samples plot in distinct fields on this plot, emphasizing the different dissolution behavior between mantle samples and volcanic rocks and between volcanic rocks of different ages.

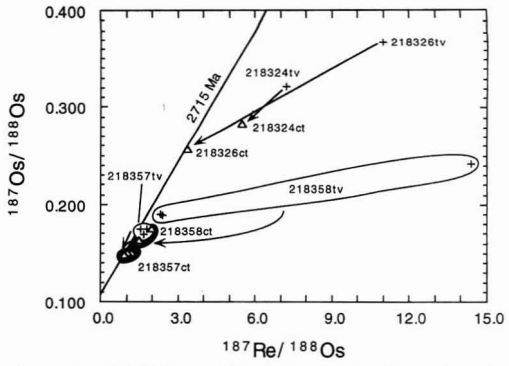

Figure 4. $^{187}Re/^{188}Os$ vs $^{187}Os/^{188}Os$ plot showing Carius tube digested and corresponding Teflon vessel digested whole-rock samples of komatiites from Pyke Hill, Munro Township, ON, compared to a 2715 Ma old isochron with a chondritic initial $^{187}Os/^{188}Os$. Crosses are Teflon vessel digestions, and triangles are Carius tube digestions. Note the poor adherence to the isochron for the Teflon vessel digestions and the reasonably good adherence for the Carius tube digestions.

Teflon vessel techniques and the higher temperature, oxidizing Carius tube method.

The Proterozoic–Archean komatiites are metamorphosed ultramafic volcanic rocks. With three exceptions, lower Os isotopic compositions correlate with higher Os contents in the Carius tube digestions as compared to the Teflon vessel digestions (Table 1, Figure 3), while Re concentrations remain similar. This is a clear indication that, in the metamorphic assemblage, Re is sited in phases equally soluble to both techniques, probably silicates or primary or secondary sulfides. In contrast, Os must be sited in some dissolution-resistant phase that has a low Re/Os. The most likely candidate is chromite or microinclusions within chromite. Chromite is essentially insoluble in the HCl–HF Teflon vessel digestion reagents.

Incomplete digestion of phases such as chromite would pose no problem if the metamorphism of the komatiites followed closely (e.g., <50 Ma) on their crystallization and the rocks remained closed to the movement of Re and Os on the scale of sampling since that time. In this case, data sets would only be affected by moving individual analyses up and down along isochrons of slope equal to the crystallization age and that have indistinguishable initial Os isotopic compositions. These natural variations in Re and Os abundance known as the *"nugget effect"* in sampling different aliquots of sample powder will have little affect on the results for geological purposes except to produce additional variation along the isochron. But in cases where other isotope systems such as Rb–Sr demonstrate a much later reequilibration,[18] there is no way a technique that does not dissolve that mineral can be trusted to produce accurate Os initial isotopic composition. The partial dissolution produced by Teflon vessel digestions would produce spurious initial Os isotopic compositions.

The problem is especially pernicious when the effect of incomplete Os extraction becomes combined with incomplete spike–sample equilibration, spike–sample loss, or both, during sample digestion as an isochron plot for the meta-komatiites from Pyke Hill, Munro Township shows (Figure 4). Teflon vessel digestions of samples 218324, 218326, and 218358 plot far off the isochron whereas two of the 218358 replicates and all of the 218357 replicates plot quite near the reference isochron. In all cases, Carius tube digestions produce data closer to an isochron of the accepted age, at lower $^{187}Re/^{188}Os$ and $^{187}Os/^{188}Os$, and in all cases except one with the expected, slightly subchondritic initial $^{187}Os/^{188}Os$. There is a large reduction in analytical scatter compared to the Teflon vessel digested samples. Also striking is the sample-dependent nature of these differences. Sample 218357 produces reasonable adherence to isochron systematics with both dissolution techniques whereas sample 218358 shows large improvement in the Carius tube vs the Teflon vessel digestions. Both samples have similar major element composition and metamorphic mineralogy and occur side by side in the outcrop. This is a concern because it would be impossible to predict a priori which samples would behave well during Teflon vessel digestions.

Numerous other failed Teflon vessel digestions (not shown) of these komatiites vary primarily in their $^{187}Re/^{188}Os$, falling in near-horizontal arrays with much less variability in their $^{187}Os/^{188}Os$. This is primarily due to large (sometimes >100%) variability in Os content that must be from a combination of effects. Incomplete Os extractions will produce analyses with systematically low Os and high $^{187}Re/^{188}Os$. These samples will give artificially low initial $^{187}Os/^{188}Os$ that could be interpreted erroneously as a subchondritic mantle source. Loss of Os from the spike during digestion will produce artificially high Os content, low $^{187}Re/^{188}Os$, and artificially high $^{187}Os/^{188}Os$ that could be interpreted erroneously as crustal contamination.

Generating an isochron using a dissolution technique equally effective for Re and Os is viewed as a prerequisite to accurately assessing the isotopic compositions of various mantle sources in the past. But without rigorously testing the Re–Os data using isochron systematics (e.g., correct age and geologically reasonable initial $^{187}Os/^{188}Os$), and employing severe dissolution techniques

(17) Mitchell, R. H.; Keays, R. R. *Geochim. Cosmochim. Acta* **1981**, *45*, 2425–2442.
(18) Walker, R. J.; Shirey, S. B.; Stecher, O. *Earth Planet. Sci. Lett.* **1988**, *87*, 1–12.

such as the Carius tube or Na_2O_2–NaOH fusion techniques, highly erroneous age-corrected Os initial ratios may be obtained.

Young volcanic rocks clearly have the same dissolution problems in achieving accurate Os concentrations as older komatiitic volcanic rocks (Table 1, Figure 1). But since there is not enough time for decay of ^{187}Re to affect the $^{187}Os/^{188}Os$, Teflon vessel dissolution techniques are adequate for determining Os isotopic compositions on young rocks. However, the Os concentrations will not be accurate.

We have tested the absolute reproducibility of the Carius tube technique reported here on rocks with multiple replicate analyses of three komatiites and one iron meteorite (Table 2). The komatiite powders, aliquotted at the 1–2 g sample size are clearly more heterogeneous in Re and Os content, $^{187}Re/^{188}Os$, and measured $^{187}Os/^{188}Os$ than the 0.1 g iron meteorite pieces even though they were 10–20 times larger. For the komatiites, variability in Re abundance as measured by the 2σ standard deviation of the population of replicates, expressed as a percentage of the mean, ranges from 7 to 61%, Os 9 to 26%, $^{187}Re/^{188}Os$ 14 to 24%, and $^{187}Os/^{188}Os$ 4 to 8%. For sample KAL-1, Re abundance, $^{187}Re/^{188}Os$, and measured $^{187}Os/^{188}Os$ are higher for the fusions compared to the Carius tube digestions. The difference between fusion and Carius tube results is not likely due to equilibration differences since both methods should be equally good at equilibrating spike and sample Re and Os. Further, Re blanks are likely not the factor even though Re blanks are higher for the fusion technique because all data reported here have been blank corrected; uncertainties in Re concentration due to Re blank correction would lead to age-corrected $^{187}Os/^{188}Os$ with comparable uncertainty to the $^{187}Re/^{188}Os$, and measured $^{187}Os/^{188}Os$ also is higher in these two samples. The age-corrected $^{187}Os/^{188}Os$ for the fusions are quite close to the Carius tube determinations, leading us to conclude that the there are real differences in the ability of the two methods to attack Re-bearing phases in metamorphic rocks. The Carius tube method, used alone, may not liberate all the Re and hence all of the radiogenic Os in this sample.

The eight separate dissolutions of sample 218358 give age-corrected $^{187}Os/^{188}Os$ with variability that is much less than the variability on Re, Os, $^{187}Re/^{188}Os$, or measured $^{187}Os/^{188}Os$. This suggests that there are slight differences in each aliquot of powder in parent to daughter isotopic abundances which are supported by radioactive decay since the rock crystallized 2715 Ma ago (i.e., closed-system isochron behavior but with nugget effects). For sample 218357, the variability in age-corrected $^{187}Os/^{188}Os$ is substantially less than the variability in Re or Os abundance and $^{187}Re/^{188}Os$ but only slightly less than the measured $^{187}Os/^{188}Os$, suggesting uncertainties in spike–sample mixing using independent Re and Os spikes plays a role as well as slight powder aliquot differences along a 2715 Ma isochron. These conclusions for samples 218357 and KAL-1 must be tempered by the fact that, for statistical purposes, only small numbers of replicates (4–5) were analyzed.

Compared to the metamorphosed volcanic rocks, the group IIA iron meteorite Filomena is very homogeneous. Replicate analyses show total variability in Re of 0.08%, Os of 0.3%, $^{187}Re/^{188}Os$ of 0.4%, and measured $^{187}Os/^{188}Os$ of 0.06%. This is a better than factor of 2 improvement relative to the alkaline fusion (Na_2O_2–NaOH) technique. The variability in Os concentration, and also $^{187}Re/^{188}Os$, is most likely due to minor heterogeneity in the meteorite, as the Re/Os correlates positively with $^{187}Os/^{188}Os$. Thus, the Filomena replicates clearly represent a lower limit to the variability that would be expected on old metamorphosed terrestrial samples and demonstrate the potential of the Carius tube technique on homogeneous samples.

ACKNOWLEDGMENT

M. F. Horan, W. K. Hart, D. G. Pearson, M. Smoliar, and E. Widom are thanked for contributing Re–Os isotopic analyses in advance of publication. W. R. Kelly of NIST was very helpful with advice on Carius tube techniques. Discussions with W. R. Kelly, R. W. Carlson, D. D. Lambert, J. Morgan, and D. Kuentz were highly useful. This work would not have been possible without the assistance of M. Trembly (UMCP Chemistry Department glass shop) or J. Emler and N. McWhorter (DTM). NSF Grants EAR 9005412 and EAR 9204718 to S.B.S. and Richard Carlson at DTM, and NSF Grant EAR 9117684 and NASA Grant NAGW 3625 to R.J.W. at UMCP have supported Re–Os development work.

Received for review January 30, 1995. Accepted April 11, 1995.[⊗]

AC950102L

[⊗] Abstract published in *Advance ACS Abstracts,* June 1, 1995.

Anal. Chem. **1995,** *67,* 2142–2144

Introducing Biomimetic Sensors Based on Molecularly Imprinted Polymers as Recognition Elements

Dario Kriz, Olof Ramström, Anders Svensson, and Klaus Mosbach*

Department of Pure and Applied Biochemistry, Chemical Center, University of Lund, P.O. Box 124, S-221 00 Lund, Sweden

The construction and operation of fiber-optic sensing devices based on molecularly imprinted polymers are reported. Fiber-optic detection of an amino acid derivatized with a fluorescent labeling group (dansyl-L-phenylalanine) is demonstrated. The advantages of using molecularly imprinted polymers as artificial recognition systems in sensor technology are discussed.

Biosensor technology is now highly developed and widely applied in the specific detection and measurement of analytes.[1–4] As the name implies, the recognition element is of biological origin, measuring interactions such as antigen–antibody or utilizing the substrate specificity obtained with enzymes. However, for a number of potential applications, no biocomponent is available or requirements such as stability cannot be met using a biocomponent.

Parallel to this development, the technique of molecular imprinting has emerged, which provides synthetic polymers with specific binding properties.[5] This methodology is based on the prearrangement of print molecules and functional monomers prior to initiation of polymerization. A rigid, cross-linked, macroporous polymer is formed which contains sites complementary to the print molecule both in shape and in the arrangement of functional groups. Removal of the print molecule by extraction leaves sites specific for print molecules and free for binding. Many imprinted polymers specific for different compounds have been prepared in several laboratories over the last few years, including theophylline-specific polymers which have been used as antibody mimics.[6] Most polymers, though, have been used in chromatographic application in the HPLC mode, as particles or continuous rod,[7] and recently also as coatings for thin-layer chromatography (TLC).[8]

The recognition properties of the imprinted synthetic polymers should not be affected by acid, base, heat, or organic phase treatment. This, together with the frequent lack of suitable biological recognition elements mentioned above, suggests that such imprints in connection with suitable transducers would have potential as biosensor-like biomimetic sensors. Although we have previously published preliminary attempts in this direction,[9] it is only in the investigation presented here that for the first time a unit is described in which the sensing and measuring elements are in direct proximity to one another and which allow quantitative determination assessment to analytes. After further development, this should permit fast and sensitive measurements as in a "true" biosensor. As a model system we have chosen to measure fluorescence using optical fibers, as this method is growing in importance.[10]

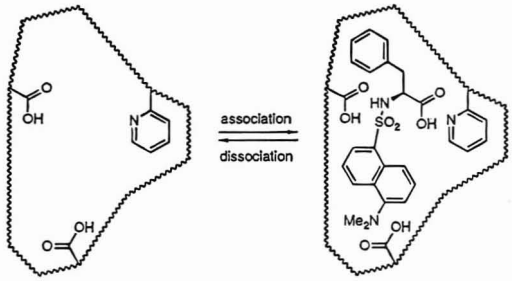

Figure 1. Schematic picture of the association and dissociation of dansylphenylalanine to a binding cavity in the molecularly imprinted polymer.

We present here some results obtained using a fiber-optic sensing device showing some enantiospecificity for a fluorescence-labeled amino acid (dansyl-L-phenylalanine) based on molecularly imprinted polymers (MIPs). The polymers[11] used in our model system exhibited strong binding to the imprint species, dansylphenylalanine; a schematic picture of the association with and dissociation from a binding cavity in the MIP is shown in Figure 1.

MATERIALS AND METHODS

Materials. Methacrylic acid (MAA) was obtained from Janssen Chimica (Belgium). Ethylene glycol dimethacrylate (EDMA) and 2,2′-azobis(2,4-dimethylvaleronitrile) (ABDV) were purchased from Polysciences Inc. The enantiomers of dansylphenylalanine (dansyl-Phe-OH) were obtained from Sigma, and 2-vinylpyridine (2VPy) was purchased from Merck.

(1) Turner, A. P. F. *Curr. Opin. Biotechnol.* **1994**, *5*, 49–53.
(2) Scheller, F.; Schubert, F. *Biosensors*; Elsevier: Amsterdam, 1992.
(3) Guilbault, G. G. *Curr. Opin. Biotechnol.* **1991**, *2*, 3–8.
(4) Karube, I.; Sode, K. In *Biotechnology Focus*, 2nd ed.; Finn, R. E., Prave, P., Eds.; Hanser Publishers: Munich, Germany, 1990; pp 175–197.
(5) Mosbach, K. *Trends Biochem. Sci.* **1994**, *19*, 9–14 and references cited therein.
(6) Vlatakis, G.; Andersson, L. I.; Müller, R.; Mosbach, K. *Nature* **1993**, *361*, 645–647.
(7) Matsui, J.; Kato, T.; Takeuchi, T.; Suzuki, M.; Yokoyama, K.; Tamiya, E.; Karube, I. *Anal. Chem.* **1993**, *65*, 2223–2224.
(8) Kriz, D.; Kriz Berggren, C.; Andersson, L. I.; Mosbach, K. *Anal. Chem.* **1994**, *66*, 2636–2639.
(9) Hedborg, E.; Winquist, F.; Lundström, I.; Andersson, L. I.; Mosbach, K. *Sens. Actuators A* **1993**, *37–38*, 796–799.
(10) Janata, J.; Josowicz, M.; Devaney, D. M. *Anal. Chem.* **1994**, *66*, 207R–228R.
(11) Ramström, O.; Andersson, L. I.; Mosbach, K. *J. Org. Chem.*, **1993**, *58*, 7562–7564.

0003-2700/95/0367-2142$9.00/0 © 1995 American Chemical Society

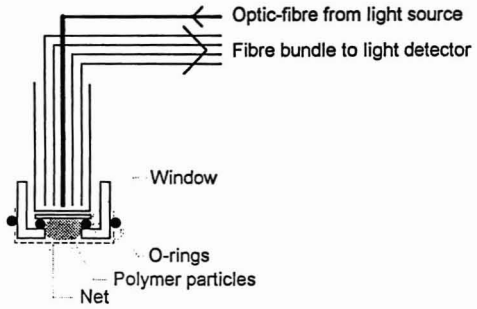

Figure 2. Fiber-optic sensing device configuration. A layer consisting of 2 mg of polymer particles (L-MIP or D-MIP) was held below the quartz glass window. The layer was kept in place by a nylon net (20 μm pores) and an O-ring. An optical fiber was connected through a monochromator (350 nm) to a light source (xenon lamp). The excitation light from this fiber passed through the quartz window onto the polymer surface. A part of the total light emitted from the polymer was collected and guided through the fiber bundle to the detector (visible light-sensitive photodiode).

The visible light-sensitive photodiode, TSL 250, was obtained from Texas Instruments. The optofiber bundle, Fibroflex No. 3, was purchased from ELFA, and the UV–vis optical fiber, Model 77514, was obtained from Oriel.

Preparation of the Imprinted Polymers. The molecularly imprinted polymers against dansyl-L-Phe-OH (L-MIPs) were prepared according to a method similar to that reported previously.[11] In order to obtain particles in the range of 75–105 μm, a modified procedure was used. To a suspension of 56.4 mg (0.164 mmol) of dansyl-L-Phe-OH in 2.0 mL of acetonitrile were added 69.0 mg (0.656 mmol) of freshly distilled 2VPy, 56.5 mg (0.656 mmol) of MAA, 1.305 g (6.56 mmol) of EDMA, and 15 mg of ABDV. The solution was thoroughly purged with nitrogen and polymerized in a water bath at 45 °C overnight (15 h). The polymer was subsequently ground in a mechanical mortar (Retsch, Haan, FRG) and wet-sieved with water to a particle size of 75–105 μm. A reference polymer (D-MIP) was prepared with dansyl-D-Phe-OH according to the same protocol.

Both polymers (L-MIP and D-MIP) were washed with a mixture of methanol and acetic acid (9:1) on a glass filter until no fluorescence could be detected in the wash solution. Finally they were washed with acetone and dried in air.

Fluorescence Measurements in a Batchwise Mode. The binding properties of the polymers were investigated by fluorescence measurements. Suspensions containing 50 mg of polymer particles (L-MIP or D-MIP) in 5 mL of acetonitrile were prepared. An increasing amount of either one of the enantiomers of dansyl-Phe-OH was added. The fluorescence (λ_{ex} 350 nm, λ_{em} 485 nm) of the supernatant, after centrifugation (14 000 rpm, 6 min), was measured using a fluorescence spectrophotometer (Hitachi F-3000), and the amount of bound analyte was determined. All measurements were performed at equilibrium after incubation overnight at room temperature.

Fluorescence Measurements with the Fiber-Optic Device. Polymer particles of 75–105 μm (2 mg) of L-MIP or D-MIP were put in front of the quartz window of a fiber-optic device and held in place by a nylon net (see Figure 2). The system was allowed to equilibrate for 4 h at 20 °C in 10 mL of acetonitrile, whereupon the light detector reading was set to zero. An increasing amount of dansyl-Phe-OH (0–500 μg) was added. After each addition, the signal (in mV) was allowed to reach a constant value and then recorded.

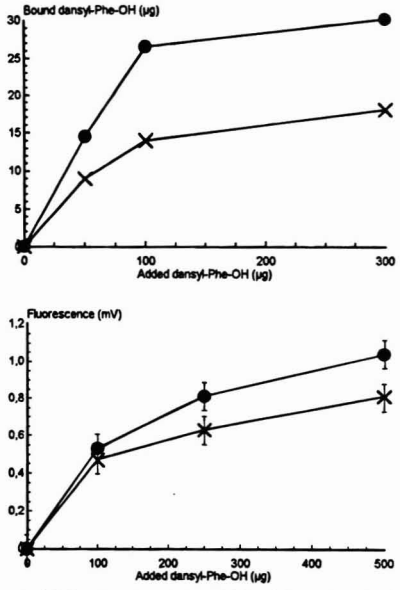

Figure 3. (a) Total binding of dansyl-Phe-OH (L- or D-enantiomers) to 50 mg of imprinted polymer (L-MIP) in 5 mL of acetonitrile as a function of the amount of added enantiomer. The mass of analyte bound to the polymer was calculated on the basis of fluorescence measurements of the supernatant. (b) Fiber-optic measurements of the dansyl-L-Phe-OH-imprinted polymers (L-MIPs) in the presence of increasing amounts of enantiomers. ●, Dansyl-L-Phe-OH. ×, Dansyl-D-Phe-OH.

RESULTS

First, the stereoselectivity toward binding of the enantiomers of the print molecule was tested. It was shown that the L-MIP bound the L-enantiomer more than the D-enantiomer (see Figure 3a). The D-MIP showed a similar ability to distinguish between the D- L-enantiomers, the D-enantiomer being more strongly bound.

Subsequently, fiber-optic measurements with the dansyl-L-Phe-OH-imprinted polymer (L-MIP) and the reference polymer (D-MIP) were carried out using the device shown in Figure 2. It was found that the fluorescence signal when the L-MIP-based device was added to dansyl-L-Phe-OH and dansyl-D-Phe-OH in acetonitrile was dependent on the concentration of the analyte and the enantiomer used (see Figure 3b). A higher fluorescence signal was obtained with the L-enantiomer of the analyte. Conversely, as anticipated, with the device containing D-MIP, a higher fluorescence was instead observed with the D-enantiomer. These results agree with the data obtained from the characterization of these two polymer types by fluorescence measurements of the supernatant after incubation.

The signal-to-noise ratio for the fiber-optic device is worse, which can be attributed to the contribution of free analyte present in the pores and between the polymer particles. For the measurements of the bulk supernatant, interference, caused by the unbound analyte, is eliminated as the calculation is based on the

concentration of the analyte in the bulk solution (which equals the analyte concentration in the interstitial volume and the polymer void volume). In conclusion, the sensing device thus shows some degree of chiral specificity for the analyte in solution. In addition, the binding process could be followed in real time. The time required for a steady response was 4 h. This response time stands in correlation to the time the binding needs to reach equilibrium, which in its turn is dependent on at least two steps, the diffusion of the analyte from the bulk solution through the pores to the binding cavities and the actual binding kinetics between the analyte and the cavities. It should be possible to vastly reduce the response time by using either smaller particles or membranes.[9]

DISCUSSION

Summarizing, it was possible to follow the increased fluorescence (due to local enrichment of the analyte) as a function of the concentration of the fluorescence-labeled amino acid derivative. Furthermore, the fiber-optic device showed some enantiospecific discrimination of the analyte. These results demonstrate the promising features of MIPs in sensing devices. These artificial recognition systems in sensor technology provide an opportunity for the development of sensors exhibiting both selectivity and stability. At present, stability is one of the major drawbacks of biosensor technology. Imprinted polymers offer a solution to this problem. An additional advantage in developing MIP-based sensors is that recognition systems can be manufactured for which there are no biological alternatives.

For the more immediate future, we will study fluorescent drugs such as acetylsalicylic acid and chinidin in plasma, using the described approach. In addition, fluorescent-labeled antigens will be prepared and assayed in a competitive mode using imprints of the conjugates. Our future research will also involve development of MIPs with catalytic properties. Both approaches could provide the basis for widening the application of biosensors and chemical sensors.

ACKNOWLEDGMENT

Financial support from the Swedish Research Council for Engineering Sciences (the Micronics project) and technical support from the Chemel Research Institute, Malmö, Sweden, are gratefully acknowledged. We would also like to thank Dr. Richard Ansell for linguistic advice.

Received for review December 9, 1994. Accepted March 28, 1995.[⊗]

AC941190X

[⊗] Abstract published in *Advance ACS Abstracts,* May 15, 1995.

Anal. Chem. **1995**, *67*, 2145–2153

Influence of the Chain Length and Surface Density on the Conformation and Mobility of *n*-Alkyl Ligands Chemically Immobilized onto a Silica Surface

Irene Yarovsky, Marie-Isabel Aguilar, and Milton T. W. Hearn*

Centre for Bioprocess Technology, Department of Biochemistry and Molecular Biology, Monash University, Wellington Road, Clayton, Victoria 3168, Australia

Molecular dynamics procedures have been used to investigate the conformation and mobility of *n*-alkyl ligands immobilized onto an amorphous silica surface, analogous to those utilized with silica-based RP-HPLC sorbents. Molecular models were constructed for *n*-octyl and *n*-octadecyl bonded phases with ligand densities of 1.64, 2.67, and 3.69 μmol/m^2 for each ligand length. The hydrocarbon layer thickness, gauche–trans statistics, end-to-end distance distribution of the *n*-alkyl chains, and diffusion coefficients of individual atoms in the *n*-alkyl ligands were determined for each system. The results have been compared with data previously obtained with an *n*-butyl bonded phase. The conformation of the chains, their positions with respect to the surface, and the chain mobilities were characterized as a function of ligand length and surface density. The results demonstrated that the most ordered part of the chain is always the segment that is anchored closest to the silica surface. With decreasing density, the ligands become more bent, with more gauche defects occurring in the middle and at the free end of the chains. This behavior leads to a dramatic decrease in the thickness of the hydrocarbon layer at minimum surface loading. Potentially, this behavior could result in stronger surface interactions with a prospective solute. These simulation studies also indicate that both short and long *n*-alkyl ligands can layer over the surface at lower ligand density, thus creating additional protection of unreacted surface silanols, with this effect being more pronounced for the longer *n*-alkyl chains. In terms of ligand dynamics, the simulated structures indicated that the *n*-octyl chain exhibits the highest overall mobility at all studied densities, while the *n*-octadecyl ligands possess the lowest motional freedom. The degree of mobility for any length ligand decreased with increasing surface density. The mobility of individual carbon atoms within the chains also increased with distance from the silica surface for all ligand lengths and densities. These simulated properties of *n*-alkyl ligands immobilized onto a silica surface correlated well with other results obtained by FTIR or ^{13}C-cross polarization magic angle spinning NMR experimental methods and statistical predictions of the behavior of immobilized chains.

Reversed phase high-performance liquid chromatography (RP-HPLC) is currently one of the most powerful separation techniques for the analysis and purification of a wide range of compounds. Despite the widespread use of RP-HPLC in both analytical and preparative applications, method development and optimization are still, however, often based on empirical "trial-and-error" approaches. Some notable exceptions exist with low molecular weight solutes, where the retention behavior can be adequately predicted under a variety of conditions using computer-assisted optimization procedures relying on, for example, first-order analysis of the chromatographic response functions. However, much more empirical approaches generally prevail with solutes which do not exhibit such regular or ideal retention behavior. This situation currently exists as a consequence of incomplete understanding of the chromatographic process at the molecular level. Detailed mechanistic models are therefore required to describe in precise molecular terms the nature of the interaction between the immobilized stationary phase ligands, the mobile phase, and the solute.

Critical to the development of physically relevant molecular retention models is knowledge of the interactive structure of the immobilized ligands. In the case of RP-HPLC adsorbents, a number of recent studies have described the use of NMR[1–6] and fluorescence[7,8] techniques to study the relative dynamics of *n*-alkyl ligands immobilized onto the silica-based stationary phases. These studies have demonstrated that the mobility of the immobilized *n*-alkyl chains is dependent on the degree of functionalization of the silanol groups, the composition of the *n*-alkyl groups, the extent of endcapping, and the composition of the mobile phase. In addition, the behavior of the mobile phase components at the sorbent surface has also been studied by NMR techniques,[9,10] thus providing important information on the influence of the mobile phase on the structure of the reversed phase

(1) Pfleiderer, B.; Albert, K.; Lork, K. D.; Unger, K. K.; Bruckner, H.; Bayer, E. *Angew. Chem., Int. Ed. Engl.* **1989**, *28*, 327.
(2) Buszewski, B.; Suprynowicz, Z.; Staszczuk, P.; Albert, K.; Pfleiderer, B.; Bayer, E. *J. Chromatogr.* **1990**, *499*, 305.
(3) Bayer, E.; Paulus, A.; Peters, B.; Laupp, G.; Reiners, J.; Albert, K. *J. Chromatogr.* **1986**, *364*, 25.
(4) Lindgren, G.; Lundstrom, B.; Kallman, I.; Hansson, K.-A. *J. Chromatogr.* **1984**, *296*, 83.
(5) Claessens, H. A.; De Haan, J. W.; Van de Ven, L. J. M.; De Bruyn, P. C.; Cramers, C. A. *J. Chromatogr.* **1988**, *436*, 345.
(6) Zeigler, R. C.; Maciel, G. E. *J. Am. Chem. Soc.* **1991**, *113*, 6349.
(7) Wright, P. B.; Lamb, E.; Dorsey, J. G.; Kooser, R. G. *Anal. Chem.* **1992**, *64*, 785.
(8) Montgomery, M. E., Jr.; Green, M. A.; Wirth, M. J. *Anal. Chem.* **1992**, *64*, 1170.
(9) Bleisner, D. M.; Sentell, K. B. *J. Chromatogr.* **1993**, *631*, 23.
(10) Bleisner, D. M.; Sentell, K. B. *Anal. Chem.* **1993**, *65*, 1819.

0003-2700/95/0367-2145$9.00/0 © 1995 American Chemical Society

ligands. Infrared spectroscopy has also been used[11,12] with *n*-alkylsilicas to study the conformational disorder of immobilized *n*-alkyldimethyl ligands and has revealed a significant increase in the molecular ordering of the immobilized hydrocarbon ligands compared to the situation found with the corresponding noncovalently bonded but chemisorbed silanes.

A number of theories have been developed to describe the mechanism of retention of small molecules with *n*-alkyl ligands used in RP-HPLC.[13–19] The statistically based partition models[13–17] describe the formation of a solute-sized cavity in the stationary phase, which is followed by transfer of the solute from the aqueous cavity in the mobile phase to the stationary phase and closure of the cavity in the mobile phase. As a consequence, the partition model, in contrast to the adsorption model,[19] predicts a critical role of the *n*-alkyl ligand density. These studies have also led to the prediction that the segments of the chain nearest to the silica surface are the most highly ordered and are thus aligned perpendicular to the surface, and that increasing the surface density of the chains leads to increased ordering of the entire chain. A major conclusion arising from this statistical theory is that the chain organization of the stationary phase plays a major role in the retention,[20] which can be contrasted with predictions of the adsorption theory,[19] which does not incorporate the entropic role of the stationary phase ligand structure. In practical terms, it is known that the *n*-alkyl chain length and *n*-alkyl surface concentration are two critical parameters that determine the hydrophobicity of a packing material and hence the retention and selectivity characteristics.[21,22] Moreover, the hydrophobic and hydrophilic properties of a stationary phase depend not only on the ratio of the number of micromoles of ligands and residual silanol groups per square meter, but also on the accessibility and type of silanol groups.[23–25]

As part of our ongoing studies of the mechanism of the reversed phase retention process, we recently reported the application of molecular dynamics procedures to investigate the conformation of *n*-butyl ligands immobilized onto an amorphous silica surface.[26] A number of parameters related to the structure and dynamics of the bonded phases were derived in order to characterize the molecular properties of each system. In the present study, this molecular simulation approach has been extended to include *n*-octyl and *n*-octadecyl ligands immobilized onto the silica surface at three different ligand densities. The results are discussed in terms of the influence of chain length and surface density on the conformation and the dynamics of each

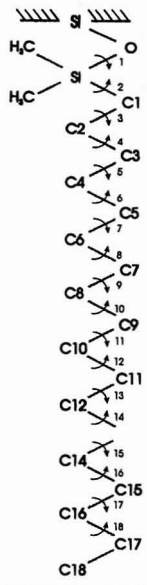

Figure 1. Schematic structure of an *n*-octadecyldimethylsilyl ligand attached to a silica surface indicating the torsion angles.

n-alkyl ligand. The aim of these investigations is to develop a physically realistic molecular model of the characteristics of *n*-alkyl ligands immobilized onto a silica surface and to compare the derived simulated results with other experimental data derived, for example, from spectroscopic techniques. The present study thus represents the first stage of a multistage strategy to develop a comprehensive molecular model capable of simulating the reversed phase retention process involving molecular modeling of (1) the ligand structure, (2) the solute structure, and (3) the interaction between solute molecules and the ligands in a solvated state.

EXPERIMENTAL SECTION

Molecular Model. Two different *n*-alkyldimethyl ligands, *n*-octyl (C8) and *n*-octadecyl (C18), were covalently bonded to a model amorphous silica surface[27,28] using three different surface densities according to criteria previously described for the *n*-butyl (C4) ligand.[26] The structure of a single attached *n*-octadecyldimethyl ligand is shown in Figure 1. The silica lattice contained 285 silicon and 570 oxygen atoms, with the total hydroxyl groups surface density of the unmodified support equal to 6.57 μmol/m^2. Atomic coordinates for the silica matrix determined previously[27,28] were fixed during the simulation.

Three molecular systems designated A, B, and C and corresponding to the surface ligand densities of 3.69, 2.67, and 1.64 μmol/m^2 respectively, were investigated. Periodic boundary conditions with unit cell dimensions [28.5 × 28.5 × (25.0, 30.0, 40.0) Å] for the C4, C8, and C18 ligands, respectively, were applied to mimic an infinite *n*-alkyl-modified chromatographic surface. The

(11) Sander, L. C.; Callis, J. B.; Field, L. R. *Anal. Chem.* **1983**, *55*, 1068.
(12) Leyden, D. E.; Kendall, D. S.; Burggraf, L. W.; Pern F. J.; DeBello, M. *Anal. Chem.* **1982**, *54*, 101.
(13) Dill, K. A.; Flory, P. J. *Proc. Natl. Acad. Sci. U.S.A.* **1980**, *77*, 3115.
(14) Dill, K. A. *J. Phys. Chem.* **1987**, *91*, 1980.
(15) Dorsey, J. G.; Dill, K. A. *Chem. Rev.* **1989**, *89*, 331.
(16) Jaroniec, M.; Martire, D. E. *J. Chromatogr.* **1987**, *387*, 55.
(17) Martire, D. E.; Boehm, R. E. *J. Phys. Chem.* **1983**, *87*, 1045.
(18) Katz, E. D.; Ogan, K.; Scott, R. P. W. *J. Chromatogr.* **1986**, *352*, 67.
(19) Horvath, Cs.; Melander, W.; Molnar, I. *J. Chromatogr.* **1976**, *125*, 125.
(20) Sentell, K. B.; Dorsey, J. G. *Anal. Chem.* **1989**, *61*, 930.
(21) Lork, K. D.; Unger, K. K.; Bruckner, H.; Hearn, M. T. W. *J. Chromatogr.* **1989**, *476*, 135.
(22) Hemetsberger, H.; Behrensmeyer, P.; Henning, J.; Ricker, H. *Chromatographia* **1979**, *12*, 71.
(23) Kohler, J.; Chase, D. B.; Failee, R. D.; Vega, A. J.; Kirkland, J. J. *J. Chromatogr.* **1986**, *352*, 275.
(24) Roumeliotis, P.; Unger, K. K. *J. Chromatogr.* **1978**, *149*, 211.
(25) Kirkland, J. J.; Glajch, J. L.; Farbe, R. D. *Anal. Chem.* **1989**, *61*, 2.
(26) Yarovsky, I. Yu.; Aguilar, M. I.; Hearn, M. T. W. *J. Chromatogr.* **1994**, *660*, 75.
(27) Levine, S. M.; Garofalini, S. H. *Surf. Sci.* **1985**, *163*, 59.
(28) Levine, S. M.; Garofalini, S. H. In *Defects in Glasses*; Galeener, F. L., Griscom, D. L., Weber, M. J., Eds., Proceedings of the Material Research Society Symposia 61; Materials Research Society Press: Pittsburgh, PA, 1986; pp 29–37.

Table 1. Molecular Details of Simulated Sorbent Systems

system name	ligand density, μmol/m^2	surface hydroxyl density, μmol/m^2	surface area per ligand, Å^2	average near-neighbor spacing, Å	number of atoms		
					C4	C8	C18
A	3.69	2.88	45.12	6.71	1420	1636	2176
B	2.67	3.90	62.48	7.90	1315	1471	1861
C	1.64	4.93	101.53	10.08	1210	1306	1546

initial conformation of the chains was all-trans, and the chains were oriented normal to the surface. Chains were randomly positioned on the silica surface according to a specific surface density to yield the average interchain distances listed in Table 1. Table 1 also summarizes the other main molecular properties of the simulated systems. Computational results were obtained using software programs from Biosym Technologies (San Diego, CA), with dynamics calculations performed with Discover and graphical displays created using InsightII. All calculations were performed on a CONVEX C210 supercomputer.

Computational Method. A molecular dynamics (MD) simulation method was applied to the molecular systems described above. The Consistent Valence Forcefield[29] from the Biosym Library, which was parametrized for the silicon atom, was used to approximate the potential energy of the simulated systems. The potential energy function of each system was calculated as the sum of the bond length, bond angle, and torsion angle terms as well as the terms representing the nonbonded van der Waals and electrostatic interactions. The nonbonded interactions for pairs of atoms separated by distances greater than a cutoff value of 12 Å were neglected. The neighbor list was updated every 20 steps.

To avoid bad contacts arising from the initial model building, the energy of each system was first minimized by steepest descents, followed by conjugate gradients method until the derivatives decreased to 1 kcal mol^{-1} Å^{-1}. The systems were then subjected to the constant volume MD simulation with periodic boundary conditions. The temperature of simulation was set to 300 K. Initial velocities were randomly assigned according to a Maxwell–Boltzmann distribution for the given temperature. The equations of motion were solved using the Verlet algorithm[30] with the integration time step of 1 fs. The initial equilibration stage, in which the temperature was adjusted by scaling the velocities, was continued until such properties as total energy, temperature, and trans fraction of chain torsion angles had stabilized. The length of equilibration runs was 20–40 ps (20 000–40 000 time steps), depending on the size of the system. An equilibration period was followed by a data collection stage of 100 ps (100 000 time steps), in which Berendsen's method of a weak coupling of the system to a temperature bath at 300 K was applied.[31] The atomic coordinates were stored on disk every 100 time steps for analysis.

RESULTS AND DISCUSSION

Hydrocarbon Layer Thickness and Surface Accessibility. Following MD simulation, a number of physical parameters were derived to characterize the molecular properties of each simulated sorbent system. The overall position of the ligands with respect to the surface as well as the accessibility of the unreacted surface silanols to either solvent or solute molecules can be initially characterized from the thickness of the hydrocarbon layer. The average hydrocarbon layer thicknesses in the systems under investigation were estimated by calculating the average distances between the terminal methyl group and the mean Si plane. The mean Si plane was constructed as an average plane containing Si atoms from the upper layer of the surface of each molecular model exemplified by the models displayed in Figures 2 and 3.

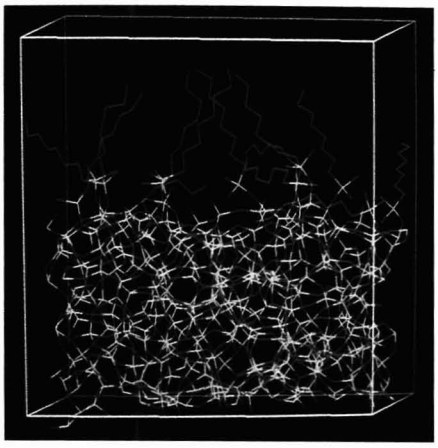

Figure 2. Instantaneous conformation of *n*-octyl ligands immobilized onto amorphous silica with ligand density of 2.67 μmol/m^2 taken from the later stages of the dynamics run of different ligand systems. Atoms are color-coded as follows: silicon, yellow; oxygen, red; carbon, green. Hydrogens are not displayed.

The average hydrocarbon thickness values for the systems under investigation, together with the results obtained previously for the *n*-butyl ligands,[26] are presented in Table 2. The values of the bonded phase thickness obtained from small angle neutron scattering experiments[32] for the maximum phase coverage are also included for comparison. A number of important conclusions can be made from the results listed in Table 2. First, it can be seen that values for the hydrocarbon thickness obtained from the MD simulations are in the same range as experimentally observed values. Second, the hydrocarbon thickness values for the more dense systems (A,B) are substantially higher than those for the lowest density systems (C) for all three ligand lengths. This result indicates that the equilibrium positions of the chains at high or intermediate density are normal to the surface or slightly tilted (as shown in Figures 2 and 3), which in turn is a consequence of the steric restrictions imposed on each chain by the neighboring ligands. This excluded volume effect was observed by Schure,[33] who carried out a MD simulation of an *n*-octadecylsilica with an

(29) *Discover User Guide*, Version 2.9.0; Biosym Technology: San Diego, CA, 1993.
(30) Verlet, L. *Phys. Rev.* **1967**, *159*, 98.
(31) Berendsen, H. J. C.; Postma, J. P. M.; van Gunsteren, W. F.; DiNola, A.; Haak, J. R. *J. Chem. Phys.* **1984**, *81*, 3684.
(32) Sander, L. C.; Glinka, C. J.; Wise, S. A. *Anal. Chem.* **1990**, *62*, 1099.

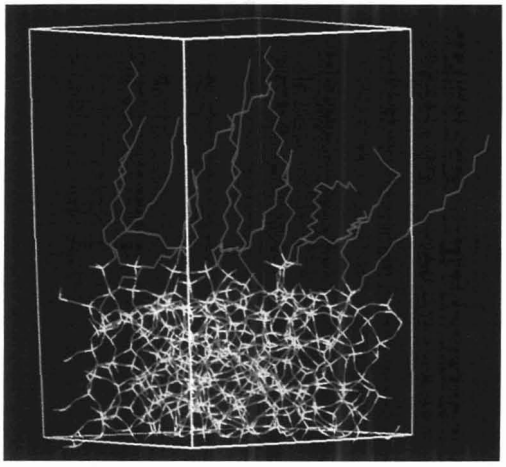

Figure 3. Instantaneous conformation of *n*-octadecyl ligands immobilized onto amorphous silica with ligand density of 2.67 μmol/m^2 taken from the later stages of the dynamics run. See Figure 2 for color codes.

Table 2. Hydrocarbon Layer Thickness Values for Simulated Systems

system	ligand density, μmol/m^2	hydrocarbon layer thickness, Å		
		C4	C8	C18
A	3.69	5.63	9.08 10 ± 2^a	17.67 17 ± 3^a
B	2.67	5.45	7.53	17.49
C	1.64	3.43	3.98	7.87

[a] Data from small angle neutron scattering experiments.[32]

average chain loading of 2.1 μmol/m^2 using analogous periodic boundary conditions. For the low ligand density system C with the C4, C8, and C18 ligands, the hydrocarbon layer thickness in each case drops dramatically, demonstrating that the *n*-alkyl chains are bent or highly tilted, with part of the chain lying almost parallel to the silica surface. The near-neighbor spacing (Table 1) for each low-density system C is 2.18 Å larger than for the intermediate system B, while there is a much smaller difference between systems A and B, i.e., 1.19 Å. For the short C4 ligands, the near-neighbor spacing is larger than the ligand chain length, while the distance between the C8 chains is comparable to the C8 chain length. It is therefore possible for the whole C8 chain to adopt a position which is almost parallel to the surface, resulting in very similar values for the hydrocarbon layer thickness for the C4 and C8 ligands for the lowest density systems C (Table 2). For the much longer C18 ligands, the near neighbor spacing does not allow the whole chain to lie parallel to the surface. The initial part of the C18 chain is still perpendicular to the surface, even at the lowest surface density, while the more remote part of the ligand runs parallel to the surface due to the bend in the middle of the chain. This picture of chain geometry is further analyzed below in terms of the distribution of gauche defects along the ligands. Thus, for the lowest ligand density system, the *n*-alkyl

(33) Schure, M. R. In *Chemically Modified Surfaces*; Pesek, J. J., Legg, I. E., Eds.; Royal Society of Chemistry: London, 1994.

Table 3. Percentage Decrease in Accessible Surface Area of Silica as a Function of Ligand Density following Molecular Dynamics

system	ligand density, μmol/m^2	decrease in accessible surface area (%)		
		C4	C8	C18
A	3.69	11.20	13.70	8.28
B	2.67	6.63	15.89	11.97
C	1.64	1.38	13.68	15.11

chains possess much more space for movement, which results in their ability to cover the silica surface. Similar conclusions have been reached from ^{2}H-NMR data,[6] suggesting that this motional constraint has its origin in van der Waals interactions between the *n*-alkyl chains and the silica surface. As the ligand density of the *n*-alkyl chains increases, the motion becomes more constrained due to the van der Waals interaction between the chains themselves.

A further consequence of the differences in surface coverage of the ligands is that with the higher ligand density systems a solute molecule cannot approach the surface as closely as it could with the lowest density case. This coverage effect will significantly decrease the extent of solute interaction with unreacted silanols and thus directly influence the retention behavior. At the same, time the ability of the *n*-alkyl chains to form a bent structure at low density and to cover the surface will create an additional protection for unreacted silanols. In order to further characterize the effective surface coverage, the total solvent accessible surface area of the silica was calculated for each system using the Connolly algorithm[34] with a probe radius of 1.4 Å (i.e., a probe with a radius of a water molecule). The total accessible area with chains in the starting conformations (i.e., all-trans and perpendicular to the silica surface) was compared to the average surface accessibility of equilibrium conformations stored during the dynamics run. The percentage decrease in surface accessibility was then calculated, and the values are summarized in Table 3. For the high-density system A, the percentage decrease in surface accessibility was 11.20% for C4, 13.70% for C8, and 8.28% for the C18 ligand. For the intermediate density system B, the relative surface accessibility increased for the C8 and the C18 ligands, while the corresponding value for the C4 ligands decreased almost by a factor of 2. At the lowest ligand density (system C), the surface coverage for the C8 ligands decreases again, while the surface coverage for the C18 ligand, increased further. These results are in contrast to the results for the C4 ligand where the percentage decrease in surface accessibility was only 1.38%. Thus, at 3.69 μmol/m^2, the high ligand density affords a significant degree of protection of the silica surface. However, as the ligand density decreases, the ability of the longer C8 and C18 ligands to lie over the silica surface maintains the level of silica protection observed at the high ligand densities. In contrast, the C4 ligands are unable to layer over the silica surface, and there is a sharp decline in the degree of surface protection at the lowest ligand density.

Trans–Gauche Statistics. More detailed information on the relative conformation of the *n*-alkyl ligands was obtained from analysis of the trans–gauche statistics of each molecular system. The state of the internal dihedral angles of a molecule is the factor

(34) Connolly, M. L. *Science* **1983**, *221*, 709.

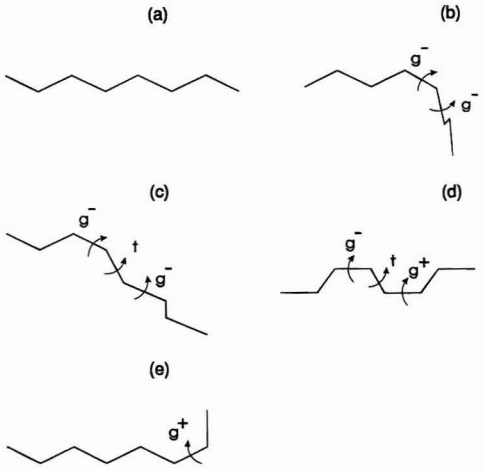

Figure 4. 4. Schematic representation of different types of gauche-defects in an *n*-alkyl chain: (a) all-trans (tt), (b) double-gauche (g±g±), (c) gauche-trans-gauche (g±tg±), (d) kink (g±tg∓), and (e) end kink (g±t).

which determines both the degree and the location of chain disorder as well as the overall orientation of the molecule with respect to the surface. The codes used for assignment of the hydrocarbon chain dihedral angles were the customary g^+, t, and g^-, corresponding to the three intervals, (0° to 120°), (120° to −120°), and (−120° to 0°), respectively. The following types of trans−gauche sequences, which are shown diagrammatically in Figure 4, were considered in the conformational analysis of the *n*-alkyl chain molecules: (a) all-trans (tt) conformation, which predominates in the low-temperature crystalline structures of long hydrocarbon chains; (b) double-gauche (g±,g±) conformation, where two consecutive gauche bonds result in a severe departure from the planar conformation, changing the chain direction; (c) gauche-trans-gauche (g±tg±) triple sequence with the same gauche signs, which also changes the direction of the chain and is therefore highly nonplanar; (d) kink (g±tg∓) triple sequence with different gauche, signs which connects parallel but laterally displaced planar segments of a chain and does not change the chain direction; and (e) end-gauche (g±t), in which the last torsion of a chain is characterized by g±. An *n*-alkyl chain which is highly constrained under the imposed conditions will sample predominantly trans conformations during a MD simulation. Conversely, *n*-alkyl chains which have the ability to overcome the torsion energy barrier associated with the gauche−trans energy difference of 500−600 cal/mol may be considered as flexible. Figure 1 presents the system used for assigning the torsion numbers of a C18 ligand; a similar system was applied to the C8 and C4 ligands.

Typical molecular configurations for the systems under investigation are shown in Figures 2 and 3 for the C8 and C18 ligands, respectively, at a ligand density of 2.67 μmol/m^2. The overall proportion of gauche conformation in the systems is shown in Table 4. There is a significant decrease in gauche population in comparison with pure liquid *n*-alkanes (where up to 40% of torsions are gauche), especially for the high-density systems. At the same time, it can be seen that for all ligand lengths, the number of gauche defects increases with decreasing surface density, i.e., as the spacing between the ligands increases, a liquid-like behavior

Table 4. Fraction of Gauche Dihedral Angles in *n*-Alkyl Ligands

		gauche fraction		
system	ligand density, μmol/m^2	C4	C8	C18
A	3.69	0.14	0.17	0.18
B	2.67	0.15	0.19	0.18
C	1.64	0.25	0.28	0.21

is observed for the low-density phases. This finding is easily explained in terms of steric restrictions on chain geometries imposed by neighboring ligands at higher densities and is in agreement with earlier theoretical predictions.[15] The increase in gauche conformations for less dense systems results in a more bent structure of the chains, which in turn allows them to lie closer to the silica surface. This effect was also manifested by a decrease in the hydrocarbon layer thickness and is also further analyzed below in terms of the end-to-end distribution function of the chains. It is surprising to note that the proportion of gauche dihedrals is higher for the C8 ligands than for the C18 ligands at low density, particularly at 1.64 μmol/m^2. This observation suggests that the longer C18 chains are more constrained by their interactions with their nearest neighbors than the shorter C8 and C4 chains for which the average near-neighbor distance (Table 1) allows more bent chain conformations to exist. The fraction of gauche conformations observed for the C8 ligands is lower than that reported by Klatte and Beck,[35] who performed a MD simulation of the temperature dependence of the physical properties of a tethered C8 system. However, these workers did not include an explicit silica surface in their model, and the chain conformation would not be influenced by van der Waals interactions, which may result in the higher gauche proportion.

To analyze the predominant positions along the chains at which the chain direction changed, the average fractions of the gauche conformation for each dihedral angle along each *n*-alkyl ligand were also calculated and are shown in Figure 5 for the different ligand lengths and densities. Torsion angles 1 and 2 describe the geometry of ligand attachment to the silica surface. It can be seen from Figure 5 that a relatively high proportion of gauche conformation for torsion 1 occurs for all systems. This conformation leads to a perpendicular orientation of the O−Si bond relative to the silica surface. The frequency of gauche conformations at this position also increases with ligand density. This result indicates that the probability of chain orientation perpendicular to the surface at this position is higher for high-density systems, which would be anticipated from steric considerations. Torsion number 2 is predominantly in a trans conformation, thus maintaining the same chain orientation to the surface created by the conformation of torsion number 1.

The relative statistics of the remaining torsion angles are determined by an energetically inexpensive internal rotation about single C−C bonds. Theoretically, the chain structure at a higher chain density will prefer either an all-trans or a kink conformation which sterically allows denser packing of the chains. As the ligand density decreases, greater steric freedom of the chains will result in a higher frequency of gauche conformations in a greater proportion of the chain. This steric effect is reflected in the MD simulation by an increase in the gauche population for the low-

(35) Klatte, S. J.; Beck, T. L. *J. Phys. Chem.* **1993**, *97*, 5727.

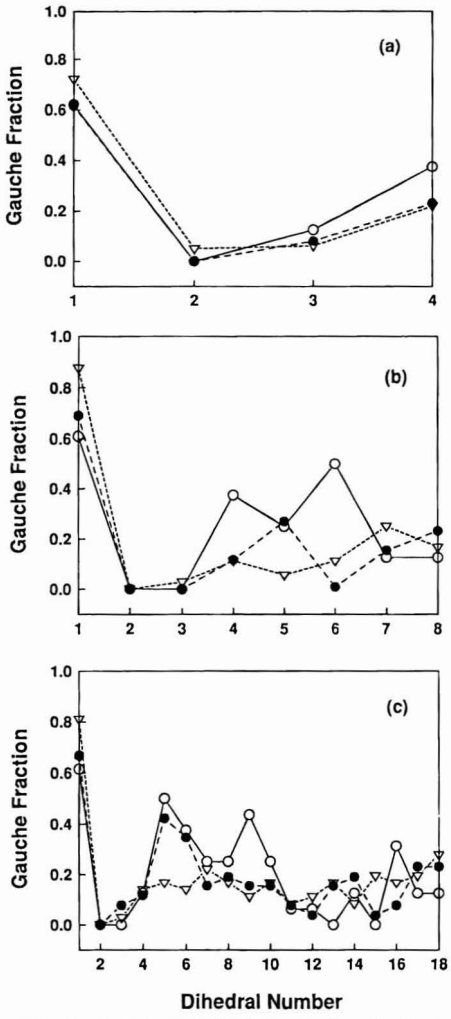

Figure 5. Fraction of gauche dihedral angles in *n*-alkyl ligands as a function of dihedral number and surface density: (a) *n*-butyl,[26] (b) *n*-octyl, and (c) *n*-octadecyl ligands. (○) 1.64, (●) 2.67, and (▽) 3.69 μmol/m^2.

density system for dihedral numbers greater than 4 for the C8 and C18 ligands. In particular, it can be seen from Figure 5 that most of the gauche conformations occur for the torsion number 4 for C4 ligands (Figure 5a), torsions 4–6 for the C8 ligands (Figure 5b), and torsions number 5–10 for the C18 ligands (Figure 5c). The predominance of the trans conformation for the first few C–C–C–C torsions along the chains allows the perpendicular chain orientation created by the conformation of torsion number 1 to be maintained with respect to the surface. This finding also demonstrates that the degree of order of the carbon chains increases near the silica surface for all chain lengths and ligand densities and is in agreement with the theoretical "motional disorder gradient" model,[15] where the chain segments nearest to the surface are predicted to be the most ordered (i.e., aligned perpendicular to the surface).

In terms of overall chain conformation, the end-gauche defect was found to be the most probable for the C4 ligands,[26] which is in agreement with the Fourier transform infrared spectroscopy studies of *n*-butylsilicas[11] and is consistent with the theoretical treatment of Dorsey and Dill.[15] For the C8 and C18 ligands there exists an increase in the gauche population in the middle of the chain which is more pronounced for the low ligand density. This increase in gauche conformation frequency demonstrates that the most probable position for a chain to be bent at 1.64 μmol/m^2 is in the middle of the C8 and C18 chains. For the higher density systems of 2.67 and 3.69 μmol/m^2, a smooth increase in the gauche population toward the end of the chain was observed, although a decrease in the end-gauche population was observed for the low-density C8 and C18 ligands. These longer *n*-alkyl chains are capable of changing their perpendicular orientation with respect to the surface, exhibiting a bend in the middle, and then running parallel or toward the surface. For the low-density C8 and C18 systems, this effect was apparent with the double-gauche (g±,g±) and triple (g±tg±) conformational defects being predominant. For the higher density C8 and C18 systems, kinks and all-trans conformations predominate in the middle of the chains, with an increase in the end-gauche population. Clearly, the presence of neighboring chains restricts the number and types of possible chain conformations at the high density. Our estimation of chain conformations based on these MD results is in qualitative agreement with FT-IR results[11] for *n*-alkyl ligands chemically bonded to a chromatographic surface at a density of 2 bonded groups/nm^2, corresponding to our highest density systems A. These experiments have shown that although the *n*-alkyl groups of the bonded materials are more ordered than those in the corresponding liquids, they still contain several gauche bonds per chain. The results for high-density systems support the model of Riedo et al.[36] who described the unwetted long chains (C14–C22) as "swollen brushes". For the low-density systems, a "collapsed droplet like" model[37] can be applied. Ziegler and Maciel[6] have studied the structure and dynamics of dimethyloctadecylsilyl-modified silica by solid state ^{2}H-NMR techniques. Their data demonstrated that the C18 chains in sterically crowded high-density sorbents are more constrained than those in low-density sorbents, with the mobility of an individual C18 chain impeded by interactions with adjacent C18 chains.

Distribution Functions. The average length of the hydrocarbon chains was further characterized by constructing the distribution functions of the end-to-end distance, i.e., the distance between the C_1 and C_N atoms ($N = 8$ or 18) of the ligands. These distribution functions are shown in Figure 6, together with the corresponding data for the C4 ligands.[26] For the C4 ligands, the maximum possible end-to-end distance which corresponds to the all-trans conformation is ~4 Å. As is evident in Figure 6a, two peaks were observed for the C4 ligands which correspond to distances of 3.25 and 3.95 Å between C_1 and C_4. The first peak of this distribution function ($r = 3.25$ Å) corresponds to the gauche conformation for the C_1–C_2–C_3–C_4 torsion angle, and the probability of this gauche conformation was highest for the lowest density system C. In contrast, the probability of the second peak at 3.95 Å, which corresponds to the all-trans conformation, was higher for the high-density systems A and B.

(36) Riedo, F.; Czencz, M.; Liardou, I; Kovats, E. *Helv. Chim. Acta* **1978**, *61*, 1912.
(37) Lochmuller, C. H.; Wilder, D. R. *J. Chromatogr. Sci.* **1979**, *17*, 574.

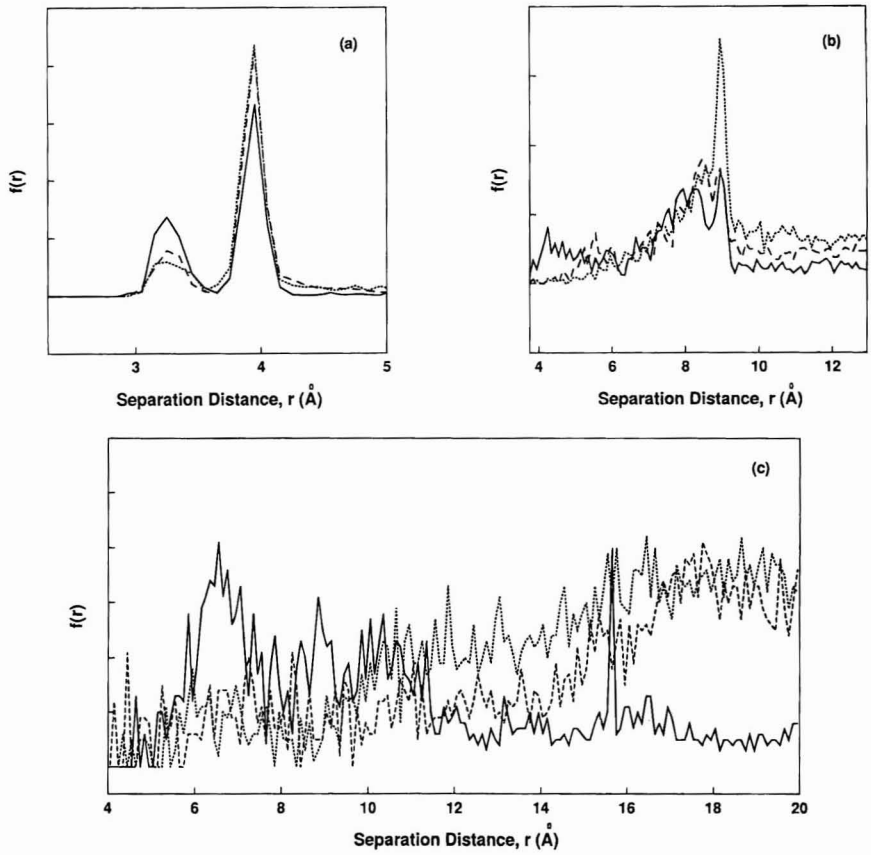

Figure 6. End-to-end distance distribution of *n*-alkyl ligands at different ligand densities: (a) *n*-butyl,[26] (b) *n*-octyl, and (c) *n*-octadecyl ligands. (—) 1.64, (– – –) 2.67, and (• • •) 3.69 μmol/m^2.

For the C8 ligands, the maximum end-to-end distance corresponding to the all-trans conformation is about 9 Å. It can be seen from Figure 6b that fully extended chains predominate at the highest density of 3.69 μmol/m^2. At the lowest density there is a much lower proportion of the all-trans conformation, while the proportion of collapsed chains with an end-to-end distance in the range of 4–6 Å is increased. This result reflects the higher proportion of gauche dihedrals for lower ligand densities which was discussed above in the trans–gauche analysis.

The maximum end-to-end distance for the C18 ligands in an all-trans conformation is about 22 Å. Inspection of the data presented in Figure 6c reveals that there is also a similar increase in the probability of the *n*-alkyl chains existing in a more extended arrangement (end-to-end distance of about 20 Å or more) for the higher density systems A and B. In contrast, for the lowest density system C, much shorter end-to-end chain lengths in the range of 6–12 Å occur with the highest probability, while the arrangement corresponding to more extended chains has a very low probability. This observation also indicates that collapsed geometries are more probable at lower ligand density but that the extended chain conformations predominate for both intermediate and high densities.

Chain Mobility. Differences in the mobilities of the *n*-alkyl ligands can be characterized by studying the dynamic behavior of each carbon atom. The time dependence of the average mean-squared displacements (MSDs) of individual carbon atoms over all the chains in the simulation and multiple time origins, t_0, were calculated as previously described[23] according to the following relationship:

$$\mathrm{MSD} = (\Delta R(t))^2 = \sum \langle |r_i(t + t_0) - r_i(t_0)|^2 \rangle \qquad (1)$$

where R is the average distance travelled and r_i represents the coordinates of atom i. To estimate the relative mobilities of individual carbon atoms, diffusion coefficients (D) for these atoms were calculated using the Einstein relation[38] as follows:

$$2tD = {}^1/_3 \lim_{t \to \infty} \langle (\Delta R(t))^2 \rangle \qquad (2)$$

Plots of the calculated diffusion coefficients for individual carbon

(38) Allen, M. P.; Tildesley, D. J. *Computer Simulation of Liquids*; Clarendon Press, Oxford Science Publications: Oxford, U.K., 1987.

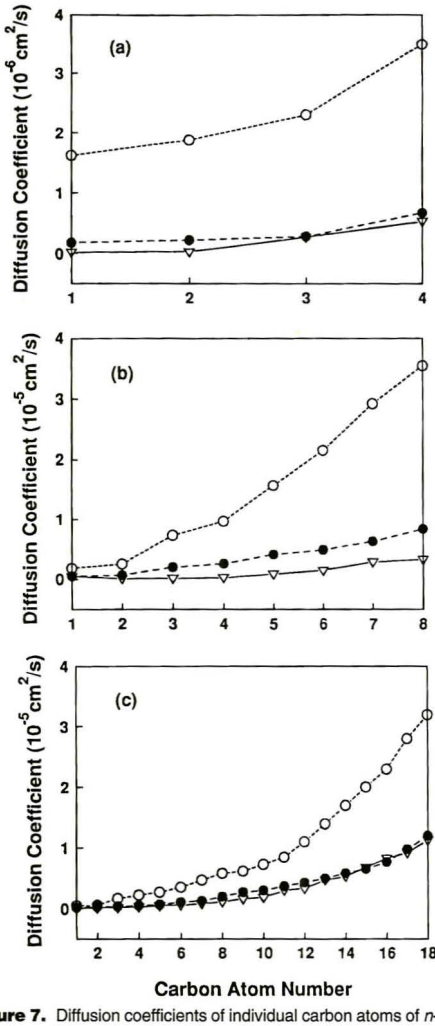

Figure 7. Diffusion coefficients of individual carbon atoms of *n*-alkyl ligands at different ligand densities: (a) *n*-butyl,[26] (b) *n*-octyl, and (c) *n*-octadecyl ligands. (○) 1.64, (●) 2.67, (▽) 3.69 μmol/m^2.

atoms in each system are given in Figure 7. It can be seen from Figure 7 that for the C4, C8, and C18 ligands at all ligand densities, the mobility increases from the C_1 atom to the C_N ($N = 4$, 8, or 18) atom, i.e., the atoms closer to the surface are more restricted by immobilization than the atoms which are remote from the surface. This increase in mobility of the atoms remote from the surface also correlates with the increased number of gauche defects located around these atoms, i.e., for dihedral angles 2–4 for C4, 3–7 for C8, and 5–11 and 15–18 for C18 ligands. These results are in agreement with ^{13}C-CP/MAS NMR spectroscopy measurements of the proton relaxation times in the rotating coordinate system, which have been used as a measure of mobility of the alkyl chains.[1] In addition, Ziegler and Maciel[6] demonstrated that the mobility of carbon atoms at the nonimmobilized end of a C18 chain is higher than the mobility of the carbon atoms which are closer to the silica surface.

It is also evident from the data in Figure 7 for the three ligand types that the mobilities of all atoms in the low-density systems (i.e., 1.64 μmol/m^2) are much higher than those of the atoms in the two higher density systems. This observation again reflects the degree of steric restrictions arising from the different near-neighbor ligand spacing at different densities. The mobility of ligands in systems A and B is very low but increases dramatically in the lowest density system C, where the *n*-alkyl chains possess much more space for movement, resulting in a higher diffusion coefficient for individual carbon atoms. This result also correlates with previous NMR studies[3] which showed that *n*-alkyl chain mobility is dependent on the degree of functionalization of silanol groups. The diffusion coefficients observed for the C8 ligands in this study are an order of magnitude lower than the values reported by Klatte and Beck.[35] These differences in chain mobility may again be due to the absence of an explicit silica surface where the influence of van der Waals interactions between the chains and the silica surface on the mobility of the tethered chains will be excluded.

It is also interesting to compare the relative mobilities of different chains at the same surface density. Figure 8 presents the diffusion coefficients of individual carbon atoms of the C4, C8, and C18 ligands in systems A, B, and C. Surprisingly, at all surface densities the mobility of carbons in the C8 ligands are the highest. Moreover, the terminal carbon atom in the C4 ligands is more mobile than the corresponding C_4 atom of the C18 ligands in all systems, and at low density (Figure 8c), the mobilities of all carbons in the C4 ligands are higher than the corresponding mobilities of the C_1–C_4 atoms in the C18 ligands. At the same time, it should be noted that with the high-density system A (Figure 8a), the mobilities of the terminal atoms of the C18 ligands are higher than those of the C8 ligands, while with the intermediate density system B (Figure 8b), the mobilities of terminal atoms of the C8 and C18 ligands are similar. With the low-density system C (Figure 8c), the terminal atoms of the C8 ligands are more mobile than those of the C18 ligands. Thus, several conclusions may be made: (i) with all surface densities, the *n*-octyl chains exhibit the highest overall motional freedom; (ii) with decreasing surface density, the mobility of the C4 ligands becomes higher than the mobility of the C18 ligands; and (iii) the mobility of terminal carbon atoms of the C18 ligands is higher than that of the C8 ligands at the same high density but is lower at the low density. This result, taken together with the observations of Ziegler and Maciel,[6] can be explained by the ability of the long C18 chains to form numerous van der Waals contacts with the silica surface at low ligand density, which also reduces the overall atomic mobility. In contrast, there is less opportunity for the shorter C8 ligands to form interchain van der Waals contacts, which then results in a higher mobility than observed for the C18 ligands. Finally, the mobility of the C4 ligands is largely constrained by their covalent attachment to the silica surface.

It is apparent from the experimental results presented in Figures 7 and 8 that the mobility of the bonded *n*-alkyl chains is strongly dependent on both the ligand density and the ligand chain length. As a consequence, the conformational freedom of each chain is a result of the interplay between the restrictions of both intrachain and surface–chain interactions and the mobility afforded by the surrounding free space. On one hand, the chain mobility increases with decreasing ligand density since the

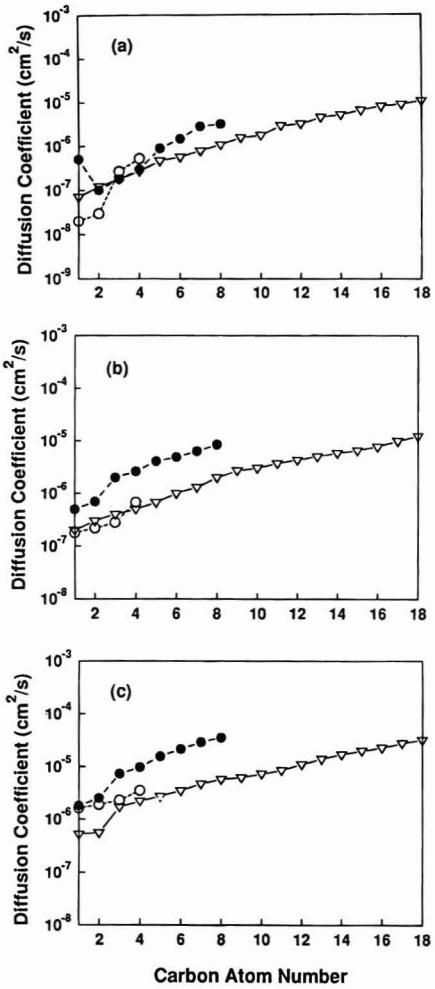

Figure 8. Diffusion coefficients of individual carbon atoms of different ligand chain lengths: (a) 3.69, (b) 2.67, and (c) 1.64 μmol/m². (○) *n*-Butyl ligand,[26] (●) *n*-octyl, (▽) *n*-octadecyl ligands.

available space increases for each chain. However, the increase in the interchain distance at low ligand density also favors the formation of van der Waals contacts between methylene groups of the *n*-alkyl chain and the surface atoms of the amorphous silica, which tend to decrease the chain mobility. The longer *n*-alkyl chains will be more susceptible to this second phenomenon than the shorter *n*-alkyl chains, as they are able to self-assemble and to participate in stronger van der Waals interactions with the silica surface. Importantly, these mobility effects with low ligand density systems will result, on a time-averaged basis, in greater accessibility of the underlying silica surface to solvent or solute molecules, particularly for the C4 and C8 chains. The influence of these ligand density–ligand mobility effects has been noted previously in a range of chromatographic investigations comparing the retention properties of nonpolar compounds with the experimental data obtained with polar compounds of similar molecular size but capable of hydrogen donor–hydrogen acceptor interactions with the accessible silanol groups on the *n*-alkyl-modified silica surface.[39,40]

CONCLUSIONS

In the present study, a molecular model of several *n*-alkylsilica sorbents has been constructed and subjected to a detailed molecular dynamics simulation. The molecular properties of the model have been characterized in terms of a number of physical parameters. The results of the conformational analysis indicate that the simulated structures for the *n*-alkylsilica surface reproduce the behavior of the *n*-alkyl ligands chemically immobilized onto silica in a manner which is qualitatively consistent with published spectroscopic data and chromatographic measurements. However, a complete understanding of the molecular basis of RP-HPLC also involves the analysis of ligand–solvent interactions followed by molecular docking of solute molecules to the solvent-modified *n*-alkylsilicas. The model presented in this study is currently being used in our on-going investigations on the molecular basis of peptide–sorbent–solvent interactions which occur during the chromatographic process in RP-HPLC. The results of these investigations will be described in associated publications.

ACKNOWLEDGMENT

The support of the Australian Research Council is gratefully acknowledged. The molecular dynamics simulations were carried out on a CONVEX C210 computer located at the Biomolecular Research Institute (Parkville, Australia).

Received for review September 19, 1994. Accepted March 17, 1995.[⊗]

AC940925V

[⊗] Abstract published in *Advance ACS Abstracts,* May 1, 1995.

39) Scott, R. P. W.; Simpson, C. F. *J. Chromatogr.* **1980**, *197*, 11.
40) Alvarez-Zepeda, A.; Martire, D. E. *J. Chromatogr.* **1991**, *550*, 285.

Anal. Chem. **1995,** *67,* 2154–2161

Modeling of Property Prediction from Multicomponent Analytical Data Using Different Neural Networks

Nineta Majcen

CINKARNA, p.o., SLO-63000 Celje, Slovenia & Department of Chemistry and Chemical Technology, University of Ljubljana, Slovenia

Karmen Rajer-Kanduč

CINKARNA, p.o., SLO-63000 Celje, Slovenia

Marjana Novič and Jure Zupan*

National Institute of Chemistry, SLO-61115 Ljubljana, Slovenia

Two different artificial neural network (ANN) strategies for building a model for the quantitative prediction of the property called "total color difference" are described. The models in the study are based on eight different complex oxide concentration measurements. The models obtained by the ANNs are compared with the multivariate linear regression model. Besides the two ANN strategies used for building the models (the error backpropagation and the counterpropagation), the Kohonen learning strategy is used to make a partial experimental design, i.e., to select data most suitable for building the models. An additional goal, building a rule or "formal knowledge", about the quality of the product, is achieved by overlapping eight two-dimensional maps of weights obtained in the counterpropagation neural network.

Modeling of certain properties of interest is one of the most frequently used tasks in handling complex multivariate analytical data. In recent years, research on modeling of the complex multivariate and multiresponse systems in chemistry using artificial neural networks (ANNs) has becoming increasingly intensive.[1–8] Modeling by classical methods requires supervised learning,[9–11] a procedure in which the input and the output (response or target) variables must be known in advance. For "learning" the system uses the difference between the predicted output and the actual response to correct its parameters in order to achieve better performance. The training lasts until the responses to all inputs are within adequate tolerance limits or until the iteration quota or number of learning attempts is exceeded. The three most widely recognized advantages of ANNs over the classical modeling approaches are the following: no explicit knowledge about the form of the model function is necessary; continuous and discrete valued variables can be handled at the same time, and the same "model", i.e. the same ANN architecture, can be used for all response variables.

The disadvantage of the models obtained by the error backpropagation learning strategy is that the relevance of weights in the trained ANN to the problem the model is supposed to solve cannot be bound to one weight (as it can be associated with any of the parameters in the classical modeling) but can be (if at all) bound to the entire assembly of weights obtained in a given training. This deficiency is not so damaging if the model is used as a black box—just to obtain the sought answer. The difficulty becomes more serious if deeper knowledge about the modelled variable(s) is pursued. In such cases, the internal parameters of the model can serve to obtain the measure of the quality of the entire model. The problem of correlating ANNs weights with the responses is discussed under Experimental Design.

In the ANN approach, until recently, the modeling problem was almost exclusively solved by the so-called "error backpropagation" learning strategy,[1–6,12,13] while in this paper the use of the counterpropagation ANNs[5,14–16] is shown.

THE LEARNING STRATEGIES

To explore the advantages and drawbacks of the ANN methods, the same set of experimental data is treated by a number of ANNs, each having a different architecture. For each learning

(1) Zupan, J.; Gasteiger, J. *Anal. Chim. Acta* **1991**, *248*, 1–30.
(2) Gasteiger, J.; Zupan, J. *Angew. Chem.* **1993**, *105*, 510–536; *Angew. Chem., Intl. Ed. Engl.*, **1993**, *32*, 503–527.
(3) Kateman, G. *Chemom. Intell. Lab. Sys.* **1993**, *19*, 135–142.
(4) Harrington, P. de B. *Chemom. Intell. Lab. Sys.* **1993**, *19*, 142–154.
(5) Zupan, J.; Gasteiger, J. *Neural Networks for Chemists: An Introduction*; VCH: Weinheim, Germany 1993.
(6) Smits, J. R. M.; Melssen, W. J.; Buydens, L. M. C.; Kateman, G. *Chemom. Intell. Lab. Sys.* **1994**, *22*, 165–189.
(7) Melssen, W. J.; Smits, J. R. M.; Buydens, L. M. C.; Kateman, G. *Chemom. Intell. Lab. Sys.* **1994**, *23*, 267–291.
(8) Gasteiger, J.; Li, X.; Rudolph, C.; Sadowski, J.; Zupan, J. *J. Am. Chem. Soc.* **1994**, *116*, 4608–4620.
(9) Massart, D. L.; Vandeginste, B. G. M.; Deming, S. N.; Michotte, Y.; Kaufman, L. *Chemometrics: a Textbook*; Elsevier: Amsterdam, 1988.
(10) Varmuza, K. *Pattern Recognition in Chemistry*; Springer Verlag: Berlin, 1980.
(11) Zupan, J. *Algorithms for Chemists*; John Wiley: Chichester, U.K., 1989.
(12) Rumelhart, D. E.; Hinton, G. E.; Williams, R. J. In *Microstructures of Cognition*; Rumelhart, D. E., McClelland, J. L., Eds.; MIT Press: Cambridge, MA, 1986; Vol. 1, pp 318–362.
(13) Lipmann, R. P. *IEEE ASSP Mag.* **1987**, (April) 155–162.
(14) Hecht-Nielsen, R. *Appl. Opt.* **1987**, *26*, 4979–4984.
(15) Stork, D. G. *Synapse Connection* **1988**, *1*(2), 9–17.
(16) Dayhoff, J. *Neural Network Architectures, An Introduction*; Van Nostrand Reinhold: New York, 1990; Chapter 10.

0003-2700/95/0367-2154$9.00/0 © 1995 American Chemical Society

strategy, several ANNs with different architectures are tested and compared.

Both the error backpropagation and counterpropagation ANNs employ the supervised learning strategy. The backpropagation of errors uses only the supervised learning (correction of weights based on the error between the desired target and the actual output). On the other hand, the counterpropagation learning combines two strategies: the supervised and the unsupervised learning in the output and in the input layer, respectively.

The learning in any ANN strategy is achieved by correction of weights after one object (represented as a multivariate signal) passes through the network. Different ANN learning strategies employ different ways in which the weights for correction are selected and different equations for calculating the amount of corrections.

The backpropagation of errors is well described in the literature;[2,5,6,12,13] hence, we shall give here only the main equation for the corrections of weights:

$$\Delta w_{ji}^{\ l} = \eta \delta_j^{\ l}\ \mathrm{out}_i^{\ l-1} + \mu \Delta w_{ji}^{\ l(\mathrm{previous})} \qquad (1)$$

The weights Δw_{ji}^{l} on the lth layer of neurons are corrected by two terms: δ-rule and momentum term. Coefficients η and μ are the learning rate and momentum, respectively, δ_j^{l} is the error obtained on the neuron j at the layer l, out_i^{l-1} is the output from the neuron i on the layer $l-1$, i.e., the input to all neurons on layer l, and $\Delta w_{ji}^{l(\mathrm{previous})}$ is the correction of the same weight w_{ji}^{l} on the same level l in the previous iteration step.

Because counterpropagation[5,14-17] is a less commonly used ANN learning strategy, we shall describe it here in more detail. The counterpropagation ANN always has two layers having exactly the same number and layout of neurons: the Kohonen layer to which the objects represented as m-dimensional vectors $\mathbf{X}_s$ are input and the output layer to which the n-dimensional target or response vector $\mathbf{Y}_s$ is input. The name "counterpropagation" comes from the fact that the input target pair $\{\mathbf{X}_s,\mathbf{Y}_s\}$ is input from opposite sides of the ANN: $\mathbf{X}_s$ from the input and $\mathbf{Y}_s$ from the output side.

Neurons in the Kohonen layer[18-19] have the same number of weights as there are components in the input vector $\mathbf{X}_s$, while the number of weights in the output layer neurons corresponds to the number of components in the target $\mathbf{Y}_s$. The counterpropagation learning is performed in N_{it} iteration steps. In each iteration step t, $t = 1, 2 \ldots, N_{\mathrm{it}}$, one input vector $\mathbf{X}_s$ is taken into the account and two actions are carried out.

(1) The neuron W_c^{K} in the Kohonen layer that has its weights w_{ci}^{K} most similar to the input variables is found:

$$\text{neuron } c \leftarrow \min\left\{\sum_{i=1}^{m}(x_{si} - w_{ji}^{\mathrm{K}})^2\right\} \qquad (2)$$

(2) The weights w_{ji}^{K} and w_{ji}^{O} in the Kohonen and in the output layers, respectively, are corrected using

$$\Delta w_{ji}^{\mathrm{K(new)}} = \eta(d,t)\,(x_{si} - w_{ji}^{\mathrm{K(old)}}) \quad \text{for} \quad i = 1, \ldots, m \qquad (3)$$

and

$$\Delta w_{ji}^{\mathrm{O(new)}} = \eta(d,t)\,(y_{si} - w_{ji}^{\mathrm{O(old)}}) \quad \text{for} \quad i = 1, \ldots, n \qquad (4)$$

with

$$\eta(d,t) = [(a_b - a_f)(N_{\mathrm{it}} - t)/(N_{\mathrm{it}} - 1) + a_f] \times [1 - d/[(N_{\mathrm{it}} - t)N/(N_{\mathrm{it}} - 1) + 1]] \qquad (5)$$

for all d = 0 , 1, 2, ..., $(N_{\mathrm{it}} - t)N/(N_{\mathrm{it}} - 1)$.

Both eqs 3 and 4 are virtually the same except that in eq 3 (Kohonen layer, superscript K) the weight correction is calculated using the components x_{sj} of the input vector $\mathbf{X}_s$, while in the case of the output neurons (superscript O), the corrections are calculated from the components y_{sj} of the corresponding target $\mathbf{Y}_s$ (eq 4).

Expression $\eta(d,t)$ is a monotonically decreasing function of two parameters d and t. Parameter d is the topological distance of the neighboring rings of neurons from the central neuron c. Topological distance as shown in eq 5 always runs from $d = 0$, meaning the central neuron to the furthest topological distance still to be corrected. The furthermost topological distance or the neighborhood ring of neurons $(N_{\mathrm{it}} - t)N/(N_{\mathrm{it}} - 1)$, to which the corrections of weights (eqs 3 and 4) are applied shrinks with the increasing number of iterations t. At the same time, the initial correction factor a_b (at the beginning of the training, $t = 0$) shrinks to its final value a_f at training's end ($t = N_{\mathrm{it}}$). This reduction is implemented via the term $(N_{\mathrm{it}} - t)N/(N_{\mathrm{it}} - 1)$, where N_{it} is the number of iterations (prespecified by the user) and N is the number of neurons at the larger edge of the rectangular ANN layout. In all our experiments, a_b and a_f were set to 0.5 and 0.01, respectively.

Within each neighboring ring at the topological distance d from the central neuron c, and at the same iteration steps t, all neurons j are corrected (eqs 3 and 4) using the same value of function $\eta(d,t)$ (eq 5).

Once all $\{\mathbf{X}_s,\mathbf{Y}_s\}$ pairs of the training set are sent through the network, one epoch of learning is accomplished. The prespecified maximal number of iteration steps, N_{it}, should be a multiple number of $\{\mathbf{X}_s,\mathbf{Y}_s\}$ pairs, assuring that all objects enter the training procedure the same number of times.

All ANNs calculations were executed on the personal computers (IBM PC/387/486) using the NEURON[20] and K-CTR[21] programs for error backpropagation and Kohonen counterpropagation learning, respectively.

DATA

The coloring agent in products defined as "white emulsion paints for inside" is titanium dioxide with pigment. Besides depending on the components (different oxides and hydrates of

(17) Zupan, J.; Novič, M. In *Further Advances in Chemical Information*; Collier, H., Ed.; Royal Society of Chemistry: Cambridge, U.K., 1994; pp 92 −108.
(18) Kohonen, T. *Self-Organisation and Associative Memory*, 3rd ed.; Springer Verlag: Berlin, 1989.
(19) Kohonen, T. *Neural Networks* **1988**, *1*, 3−16.
(20) Tušar, M.; Zupan, J. In *Software Developments in Chemistry 4*; Gasteiger, J., Ed.; Springer: Berlin, 1990; pp 363−376.
(21) Zupan, J. Report-KI DN-1452, 1994.

Table 1. Parameters Used in Different ANN Experiments

network	backpropagation	Kohonen ANN	counterpropagation
purpose	model for predictions	selection of the training set	model, display of variables, rules
architecture	$8 \times 2 \times 1$	$12 \times 12 \times 8$	$6 \times 6 \times (8 + 1)$
	$8 \times 4 \times 1$		$10 \times 10 \times (8 + 1)$
	$8 \times 6 \times 1$		$12 \times 12 \times (8 + 1)$
	$8 \times 8 \times 1$		$15 \times 15 \times (8 + 1)$
	$8 \times 10 \times 1$		
learning parameters	η 0.2, 0.5, 0.8; μ 0.2, 0.4, 0.8	$a_b = 0.5$, $a_f = 0.01$	$a_b = 0.5$, $a_f = 0.01$
learning "time" in epochs	1500–5000, 15 000	300	300
	50 000		
scaling			
input	each variable scaled in the range of this variable for the entire data set	each variable scaled in the range of this variable for the entire data set	each variable scaled in the range of this variable for the entire data set
output	original values divided by 2.		original data

aluminium, silicium, potassium, and phosphorus) added during the production process, the properties of the product depend on the impurities (different oxides of iron, niobium, antimmonium and sulfur). In order to maintain the desired level of quality and properties of the final product we must consider different concentrations of impurities imported by the changing quality of the ore (illmenite and/or titanium slag). Therefore, various amounts of the main components should be added at different stages of the production process. For each sample lot of the finished product, the concentrations of the eight most important impurities and additives are regularly measured by our analytical laboratory.

During a certain period of time, some of these products (after they are applied) start to change color. This, understandably, is an extremely undesired property. In order to test the products for the possibility of developing this effect, quite time-consuming and rather expensive experiments for measuring the total color difference, ΔE^*, must be performed. For carrying out one such test, two testing samples should be taken from the product lot. Both samples are painted on white wall paper and dried. One of the two samples is exposed to severe conditions of "ageing", i.e. to the UV light, high moisture, higher temperature, etc. After this treatment the ΔE^* between the samples (the one exposed to the severe conditions and the one dried regularly) is measured. The measurements performed on a number of titanium dioxide white pigment samples treated by the described procedure clearly indicate that the total color difference, ΔE^*, depends on the sample's chemical composition.

The instrument in this study used for the total color difference measurement was the ACS spectro-sensor II.[22] The reflectance measurement aperture size was 25 mm, the gloss trap was closed, the measuring range was 400–700 nm, the standard illuminate D65 was used, the geometry of measurement was $d/8°$, and SS II was calibrated with black, gray, and white standards. The equation for the determination of the ΔE^* is the following:

$$\Delta E^* = (\Delta L^{*2} + \Delta a^{*2} + \Delta b^{*2})^{0.5} \qquad (6)$$

where ΔL^* is the difference in the lightness, while Δa^* and Δb^* are the color differences along the red/green and the yellow/blue axes of both samples, respectively.

In order to assure the quality of the product, the appearance of such undesirable property should be *predicted in advance,* before the product leaves the factory and without too many expensive experiments. Therefore, the idea was to find a model based on standard analytical data, i.e., to check whether the ΔE^*, can be predicted from the concentration of eight oxides measured regularly.

Hence, the following data scheme was proposed: the set of concentrations of the eight oxide ingredients in the sample s, Al_2O_3, P_2O_5, K_2O, Fe_2O_3/FeO, SiO_2, Sb_2O_3, Nb_2O_5, and SO_3, are taken as the input vector, $\mathbf{X}_s$ while the output vector $\mathbf{Y}_s$ associated with each input vector of the sample $\mathbf{X}_s$ is sample's total color difference, ΔE^*. The output vector has thus only one component; i.e., $\mathbf{Y}_s = (y_{s1})$. All components x_{sj} (the concentrations of the mentioned oxides $j = 1, ..., 8$) of the input vector $\mathbf{X}_s$ are normalized between 0 and 1. The measured responses of the total color difference, ΔE^*, is between 0 and 2. The value of $\Delta E^* = 1$ is the quality control threshold. If a sample has a ΔE^* value lower than 1, it is accepted as passable, otherwise the sample is not acceptable for the resale and is either reprocessed or rejected. In the actual measurements of the present data set, the smallest and the largest ΔE^* values were 0.3 and 1.4, respectively. For the learning with error backpropagation ANNs, the ΔE^* values were divided by 2, while for the counterpropagation experiments, the ΔE^* values were not changed at all.

EXPERIMENTAL DESIGN

Altogether the complete analyses and measurements of the total color difference, ΔE^*, of 36 products were available. The correlation matrix between eight input variables (oxide concentrations) and response value shows that the variables are not highly correlated among themselves (all correlation coefficients are lower than $|0.84|$), nor are they highly correlated to the total color difference ΔE^* ($<|0.80|$). This indicates that most of the eight variables should be considered in the modeling process and that nonlinear models would be probably better than the linear ones. In order to verify this implication, two multivariate linear calibration techniques (principal regression analysis, PCR, and partial least squares, PLS1) were applied to the described problem. The correlation coefficients obtained with the linear models are higher ($r_{PCR} = 0.92$, $r_{PLS1} = 0.93$) than those achieved by the ANN model; however, it should be stressed that both these methods have classified four samples as outliers and were therefore not used for building the model.

Therefore, the ANN approach was chosen for modeling. All relevant parameters used in the presented ANN experiments are shown in Table 1.

(22) COLOR-CALC, Quality Control Manual, 1400/2800 ACS Part No. 4201/0001, Dietikon/Zürich, Switzerland, 1993.

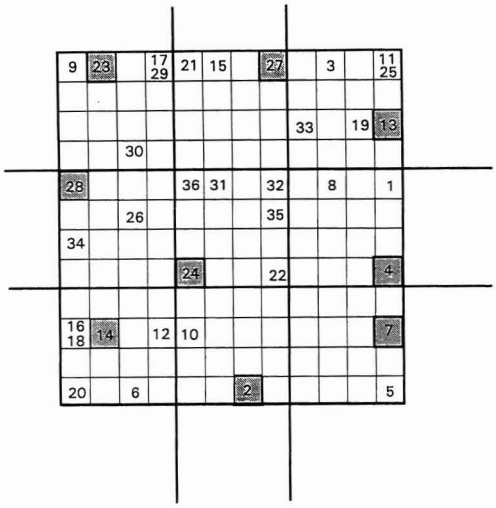

Figure 1. Mapping of all 36 objects into the 12 × 12 Kohonen map. The objects are scattered quite evenly over the entire map. Only three fields contain two objects. After the map is cut into nine rectangles (bold lines), nine objects (one from each square) is selected for building the model. The selected objects: 2, 4, 7, 13, 14, 23, 24, 27, and 28 are in the shaded boxes.

In order to obtain a reliable model, the set of 36 eight-component analyses has to be divided into the training and the test set of input/output pairs $\{\mathbf{X}_s,\mathbf{Y}_s\}^{\text{train}}$ and $\{\mathbf{X}_s,\mathbf{Y}_s\}^{\text{test}}$, respectively. Because we had a relatively small set of data we have chosen the approach first mentioned by Simon et al.[23] and later described in detail in ref 24. Using the Kohonen mapping procedure,[18,19,25] all 36 samples were mapped from eight-dimensional measurements space into a two-dimensional map consisting 144 (12 × 12) neurons each having eight weights (Figure 1).

As shown in Figure 1, the 12 × 12 Kohonen map consisting of ID labels of objects was cut into nine areas of 4 × 4 neurons each. From each of these 4 × 4 neuron squares, only one object was chosen for modeling. The selected objects were 2, 4, 7, 13, 14, 23, 24, 27, and 28, respectively. These nine objects, $\mathbf{X}_s$ ($s = 1, \ldots, 9$), each described by eight-dimensional vector $\mathbf{X}_s$ and one-dimensional response $\mathbf{Y}_s$, were then employed in all learning procedures made in the present work as input target pairs $\{\mathbf{X}_s,\mathbf{Y}_s\}$.

We tried to do the selection of the training set data in a similar way by using the PCA.[9-11] However, the two main components PC1 and PC2 contain only 35 and 27% of the total variance, respectively. Hence, the displayed cluster of points was irregular and we were not able to divide the PC1/PC2 plane into nine more or less equally populated areas. This was one of the main reasons why we have decided to chose the Kohonen map for the selection of the training set.

LEARNING TO MAKE PREDICTIONS

All backpropagation of errors learning procedures were carried out on five different networks (8 × 2 × 1, 8 × 4 × 1, 8 x 6 × 1, 8 × 8 × 1, 8 × 10 × 1). At the beginning, as the best ANN architecture was sought, the values of 0.2 and 0.4 for the learning rate η and for the momentum μ, respectively, were used. For each of the five different ANNs, 10 different random sequences for initializing the weights of neurons were tried. The three larger ANNs (with 6, 8, and 10 hidden nodes) performed slightly better than the two smallest ones (2 and 4 hidden neurons). The correlation coefficients r between the predicted and experimentally determined total color differences, ΔE^*, of 27 test samples were virtually the same ($r = 0.90 \pm 0.01$) for all three larger ANNs trained with 10 different weight randomizations each. However, a slight decline was noticed ($r = 0.85 \pm 0.02$ and $r = 0.88 \pm 0.01$) for the two smaller ANNs. The error of the correlation coefficient shows dispersion of results obtained on the ANNs with the same architecture but with different initial randomization of weights. Therefore, the smallest of the three larger ANNs, the 8 × 6 × 1 network, was chosen as the one on which the model would be built.

Table 2. Root-Mean-Square Errors for Nine Different Training Processes and the Corresponding Correlation Coefficients, r_i, for the Test Samples[a]

η	μ	rms	r_i
0.2	0.2	0.0178	0.90
0.2	0.4	0.0132	0.91
0.2	0.8	0.0059	0.90
0.5	0.2	0.0073	0.90
0.5	0.4	0.0063	0.91
0.5	0.8	0.0032	0.91
0.8	0.2	0.0060	0.91
0.8	0.4	0.0054	0.91
0.8	0.8	0.0014	0.91

[a] Each training process was carried out on the same 8 × 6 × 1 ANN using a different learning rate and momentum, η and μ pair. All training procedures were 3000 epochs long.

The selection of the best ANN should be guided by the quest after the network yielding the highest correlation coefficient in the minimal architecture (minimal number of neurons). Because the correlation coefficients were virtually the same, the test blank root-mean-square (rms) values were considered ultimately for the selection of the best ANN. After the 8 × 6 × 1 ANN layout was selected, different values for the learning rate η and momentum μ were tested in order to see how this ANN behaves under different learning conditions. As it can be seen from Table 2, after 3000 epochs of training considerably different rms values were achieved when different learning rates η and moments μ were applied. The lowest test rms value as well as the highest correlation coefficient ($r = 0.91$) was obtained when both the learning rate η and the momentum μ were equal to 0.8.

When setting up a model by the error backpropagation (or any other type of classical model), we have to be aware of the so-called overtraining effect. This effect occurs if the model (ANN) is trained too long, i.e., trained with an excessive number of learning epochs. If overtrained, the model adapts to the training data "too well" in a sense that by improving the fitting of the model on the training data the predictions on the test data do not improve anymore.

To check whether our ANNs show an overtraining effect or not, the training was run on two ANNs: first, on the optimal (8 × 6 × 1, $\eta = \mu = 0.8$) and, second, on a larger one (8 × 10 × 1, η

(23) Simon, V.; Gasteiger, J.; Zupan, J. *J. Am. Chem. Soc.*, **1993**, *115*, 9148–9159.
(24) Zupan, J. *Acta Chim. Slov.* **1994**, *41*, 327–352.
(25) Li, X.; Gasteiger, J.; Zupan, J. *Biol. Cybern.* **1993**, *70*, 189–198.

Table 3. Changes of Root-Mean-Square Errors during Training on Two Networks[a]

	network			
	$8 \times 6 \times 1$ $\eta = 0.8, \mu = 0.8$		$8 \times 10 \times 1$ $\eta = 0.2, \mu = 0.4$)	
no. of epochs	rms_{tr}	rms_{test}	rms_{tr}	rms_{test}
1500	0.0041	0.287	0.0369	0.311
2000	0.0030	0.287	0.0283	0.310
2500	0.0021	0.286	0.0215	0.308
3000	0.0014	0.287	0.0162	0.306
3500	0.0010	0.287	0.0122	0.305
4000	0.0007	0.287	0.0092	0.304
4500	0.0004	0.287	0.0070	0.304
5000	0.0003	0.287	0.0056	0.304
15000			0.0002	0.302
50000			0.0001	0.302

[a] rms_{train} is recorded automatically each epoch. Learning was stopped each 500 epochs, and the test set of 27 objects was run through each ANN to obtain the rms_{test}.

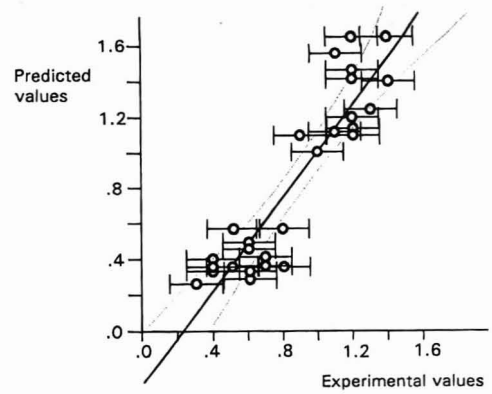

Figure 2. Prediction of the total color differences $\Delta E^* = Y_s$ for 27 products by the $8 \times 6 \times 1$ error backpropagation ANN trained on nine products. The training parameters are $\eta = \mu = 0.8$; the training was 2500 epochs long. The correlation coefficient $r = 0.91$. The regression line (0.95 confidence interval) has the slope of 1.32 ± 0.24 and the intercept -0.29 ± 0.22.

$= 0.2, \mu = 0.4$). Both ANNs were trained for 5000 epochs and the larger one even to 50 000 epochs. Although the training-rms errors fell in both cases below 0.0003, the absolute minimal test-rms error achieved was 0.287 on the $8 \times 6 \times 1$ ANN. The training-rms error (fit of the model) and the test-rms error for the predictions were recorded every 500 epochs. The results are given in Table 3.

In all tested ANNs, an asymptotic approach to a certain test-rms value was observed with the test-rms value of 0.287 as the lowest among all of them. By always testing the same set of 27 samples, this effect can be attributed to the experimental error (± 0.2) of the measured target values, t_i^{exp}, to which the predictions, t_i^{ANN}, were compared. Because the test-rms value is defined as

$$rms_{test} = \left(\sum_{i=1}^{27} (1/27) (t_i^{ANN} - t_i^{exp})^2 \right)^{1/2} \qquad (7)$$

the theoretical minimum test-rms value obtained on a much larger set of test data should be 0.2.

The final predictions obtained on the $8 \times 6 \times 1$ ANN trained with learning rate η and momentum μ both equal to 0.8 and with a 2500 epochs long sequence are shown in Figure 2. The correlation coefficient r between the predicted and experimental data is 0.91.

To see what can be obtained by standard methods, a linear multivariate regression was tried. A heavy restriction due to the small number of experiments available allows us to use only linear models for the standard statistical approach. Because the linear regression plane for an eight-variate problem requires nine parameters, a minimum of 10 measurements is necessary to determine them. Nevertheless, the eight-variate linear regression was tried on 10 experimental pairs $\{\mathbf{X}_s \mathbf{Y}_s\}$. This set of 10 experiments consisted of the same nine objects (2, 4, 7, 13, 14, 23, 24, 27, and 28, respectively) as used in the previous example, plus one additional experimental point. The agreement between the 10 experimentally determined total color differences, ΔE_i^*, on which the model was built and the values yielded by the linear regression model was within 5%. However, the predictions of the ΔE^* for the remaining 26 objects on the basis of this eight-variate linear regression model were not satisfactory in any way. The correlation coefficient, r, between the experimental and predicted data was only 0.64, compared with the $r = 0.91$ obtained by the error backpropagation model for the same data.

In general, the most serious disadvantage of the ANN approach is the lack of a plausible explanation of the model. The users, besides being mainly interested in the model predictions, are nevertheless eager to understand why the model yields such results. In classical polynomial models, this information can be deduced by inspection of the parameters of the model. In the error backpropagation ANN models, however, the parameters are the weights of neurons from which such information is hard to deduce. Specifically, there is no correlation between individual weights and the responses; however, this does not mean that there is no correspondence between the entire ensemble of weights and the responses of the ANN. As it was already shown elsewhere,[5,26] the same set of data trained on the same ANN architecture can produce two or more different sets of weights yielding practically identical responses over the entire measurement space. Such assembles of weights can be regarded as different models, yielding the same result. In order to deduce the influence of a single weight on the ANN responses, one may assume that any weight under consideration can be forcefully set to zero and the response of such network after varying only one input variable and holding all other inputs constant should be compared to the output of the nonmodified ANN. Unfortunately, each weight below the input layer *is* influenced by all inputs, and vice versa, each input influences all weights in the ANN. This means that different response behavior can be obtained for each and every set of constant inputs at which the selected input variable has been varied. Such an analysis for all weights is very hard to carry out even for the smallest ANNs.

In order to overcome this deficiency of error backpropagation ANNs, we have built a model using a two-layer ANN with the counterpropagation learning strategy. The models generated by the counterpropagation learning are look-up tables rather than

(26) Tušar, M.; Zupan, J.; Gasteiger, J. *J. Chim. Phys.* **1992**, *89*, 1517–1529.

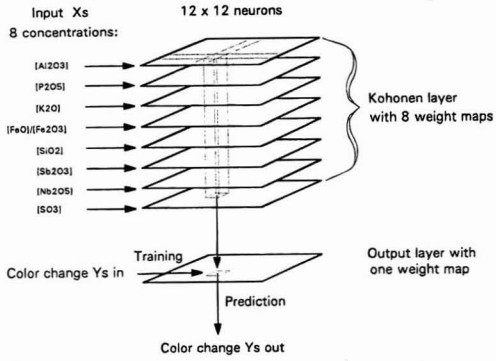

Figure 3. Counterpropagation ANN used in the present study. Each neuron is represented as an eight-weight column (dotted block). The neurons are ordered in two 12 × 12 layers. The weights in both layers (in the Kohonen and in the output layer) are arranged in levels. There are as many levels as there are variables. In the *training* phase, the target values are *input* into the output layer, while during the *testing and predictions* the answers are *taken out* of the output layer.

models providing continuous values as the response. Therefore, we were not interested in generating better models compared to those obtained by the error backpropagation learning. Instead, we were aiming at exploring an interesting feature of counterpropagation ANNs, namely, the two-dimensional maps formed on different weight levels (Figure 3).

During the training, the counterpropagation network develops as many two-dimensional maps as there are different input variables and output responses. In the Kohonen and in the output layer, the two-dimensional maps for each input and each output variable, respectively, are formed. Each two-dimensional map shows a planar distribution of values belonging to one variable obtained on the basis of the objects from the training set. The lines marking the positions of the same concentration values on the map are called the isovalue lines (contour lines). The shape of the isovalue lines depends on the location of the Kohonen neurons in the ANN excited by the training objects and on the values of the particular variable associated with each object. Additionally, the shapes of the isovalue lines at each point (neuron) on the map are influenced by the objects exciting the neighboring locations as well. The extent of this influence varies during the entire training procedure (eq 5).

According to eqs 3 and 4, at the end of the training all weights in each weight level tend to approximate the values of the particular variable that enters this specific weight level and at the same time reflect the spatial distribution of the training objects on the Kohonen ANN.

By overlapping any output map with any maps from the input layer, the relation between the corresponding response (output variable) and input variables can be obtained.

In the present investigation, four different counterpropagation ANNs having the neurons distributed in two equal rectangular blocks each containing 36, 100, 144, and 225 neurons (6 × 6, 10 × 10, 12 × 12, and 15 × 15) were tested. The learning was performed by means of eqs 2–5.

The same nine objects as used for training the error backpropagation ANNs (2, 4, 7, 13, 14, 23, 24, 27, and 28, respectively) were employed for training the counterpropagation ANNs. To make the results comparable, in all four ANNs, a 300 epoch (i.e.,

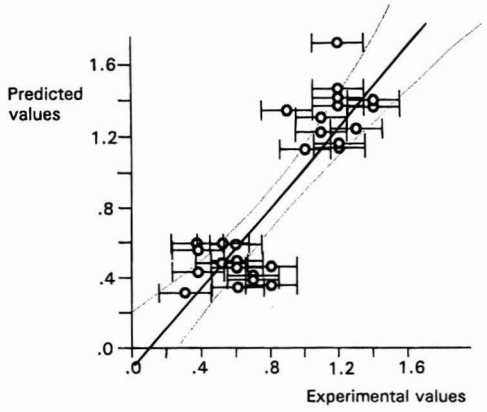

Figure 4. Prediction of the total color difference $\Delta E^*=Y_s$ for 27 products by the (12 × 12 × 8 + 12 × 12 × 1) counterpropagation ANN. The model is obtained on nine products. The training parameters are 300 epochs of training, a_b = 0.5, and a_f = 0.01. The correlation coefficient r = 0.87. The regression line (0.95 confidence interval) has the slope of 1.13 ± 0.26 and the intercept −0.10 ± 0.24.

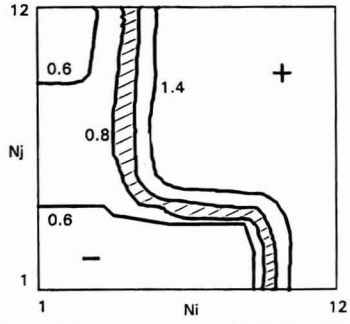

Figure 5. Resulting output map of 144 weights containing the "smoothed" values of nine Y_s, i.e., the corresponding total color differences, $\Delta E^*=Y_s$. The lines indicate the interpolated isovalues Y_s. The shaded narrow strip shows the region between the good (Y_s < 0.8) and bad (Y_s > 1.2) samples.

$N_{it} = 2700 = 9 \times 300$) long learning sequence was used. For the parameters a_b and a_f (eqs 3 and 4) the values 0.5 and 0.01, were employed. The choice of the parameters, a_b and a_f, mainly influences the convergence speed and not the form of the maps. Because the counterpropagation ANNs in general require a factor of ~10 less epochs for learning than the backpropagation ANNs, the choice of a_b and a_f is not such a crucial issue.

After testing all four ANNs, the layout of 12 × 12 neurons in each of the two layers was found to produce the best model with the most informative maps. The "best" ANN was considered the one that yields the predictions of the total color difference, ΔE^*, in the best agreements with the experimental values. For the set of 27 samples, the best correlation coefficient between the experimental and predicted values of r = 0.87 was achieved (Figure 4). This value can be well compared with the correlation coefficient of r = 0.91 obtained by the best error backpropagation model on the same set of test data.

USE OF THE WEIGHT MAPS

In the case of modeling the total color difference, ΔE^*, there is only one output map. This 12 × 12 response map (Figure 5),

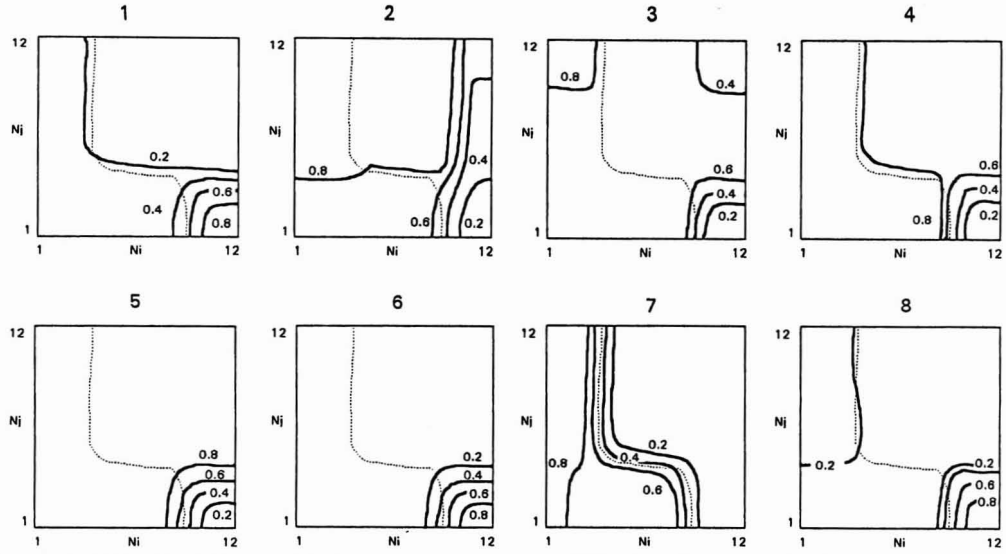

Figure 6. Eight 12 × 12 weight maps obtained after the counterpropagation ANN is trained. On each map, four isoconcentration lines at 0.2, 0.4, 0.6, and 0.8 values are drawn. The shaded region in Figure 5 is shown in each map as a dashed line. By overlapping the Y_s output map with each input map, the influence of the particular oxide on the total color difference ΔE^* can be deduced.

shows a clear separation (contour $Y_s = 1$) between two regions: the acceptable ($Y_s < 1$) and the unacceptable ($Y_s > 1$) products, respectively. All acceptable samples excite the neurons lying in the left part of the map and the unacceptable ones, having total color difference parameter $\Delta E^* = Y_s > 1$, excite the neurons in the right side of the map. Besides offering the qualitative decision rule for discrimination between good and bad samples, the 144 look-up cells of this table or map provide the data for quantitative predictions of ΔE^* within the errors of the experimental data. The results of a look-up table can be further improved by interpolation between the neighboring cells.

Because, the response map is obtained on the basis of the input variables which are mapped into the input weight maps, it is possible to obtain the correlation between the response ΔE^* and any input variable by overlapping the response map with the particular input weight maps. In Figure 6, the all eight input maps overlapped by the response map are shown.

By copying the narrow 0.8−1.2 strip (shown shaded on Figure 5), on all eight maps from Figure 6, the decision rules or formal knowledge about the influence of different oxide concentrations can be obtained. The rule for obtaining good products, for example, is obtained by the following deduction. The area in the Y_s map (see Figure 6) covering above-average good products ($Y_s < 0.4$) is situated in the lower left corner. Hence, the concentration intervals occupying the lower left corners on the eight maps (Figure 6) determine the range of oxide concentrations allowed for good products: 0.2−0.4, 0.6−0.8, 0.6−0.8, 0.8−1.0, 0.8−1.0, 0.0−0.2, 0.6−1.0, and 0.0−0.2, for oxides 1 to 8, respectively. Note, that this rule is valid only if all conditions are satisfied. If these conditions are true then the sample will be good; however, the rule does not predict that only under these conditions good samples can be obtained. Specifically, good samples (clustering in the upper right corner) can be obtained if the concentration of the oxide 8 is higher than 0.2, but then the concentration of oxides 3 and 7 should be above 0.8, etc.

Such rules can be obtained for any region formed on the response map. Even more, if the problem is a multiresponse one, complex rules for more responses can be formed in the described way simultaneously. Hence, it can be safely said that besides yielding a good and robust model in the form of a look-up table, the counterpropagation ANN has the ability to produce complex decision rules as well.

CONCLUSIONS

Both models obtained by ANNs are now used for controlling the final products, while the obtained rule has already had a feedback on those phases of the production process where the concentration of the most critical oxide impurities can be controlled. Due to the fact that the experimental error of the ΔE^* measurements on the product is quite high, i.e., ±0.2 (more than 10%), both models (the error backpropagation and the counterpropagation) predict the quantitative values of the Y_s well.

It was shown that the ANNs are capable of yielding reliable models for some problems where the conventional methods fail to do so. For building good models, the error backpropagation ANNs are well particularly well suited, providing that a thorough preliminary study of the choice of the ANNs' architecture and the learning parameters is made. Additionally, it is shown that the models can be built by the counterpropagation learning technique as well. This second method, although not giving such good quantitative results, offers the possibility of acquiring formal knowledge about complex multivariate multiresponse systems.

The models yielding continuous answers in the entire range of the measurement space seem to have an edge over the "models" generated by the counterpropagation ANNs, which are actually the look-up tables limited to a finite and rather small number of different answers. However, more important than the number of possible answers is the size of the error of these answers. If the predicted response varies from 0 to 1, then 100 answers that can be stored in the 10 × 10 network can cover this

range in 0.01 wide intervals. Such precision is more than enough if the predictions can be experimentally verified only within 5−10% error. In the case where better experimental precision is required, larger ANNs containing more "look-up cells" where more different answers can be stored should be chosen for training. The entire problem of obtaining the correct answer is thus reduced to finding a box in the look-up table (spreadsheet) with the most appropriate answer. We are aware that a set of 37 complex analytical measurements is not enough to obtain a good quantitative model to predict exact values over the entire region of a desired color change variable. What we have achieved is an excellent predictive model which can predict whether the product will develop the undesired effect of ageing or not. Additionally, the model can predict (within its limitation and the limitation of experimental error) how close the product is to the acceptance limit. The obtained ANN model is now in permanent use for the prediction of the color change ΔE in the routine quality control check of the produced paints. Further research in this promising area is underway.

ACKNOWLEDGMENT

The authors acknowledge the financial support of this work by the Ministry of Science and Technology of Slovenia. N.M and K.R-K. are highly indebted to Mrs. Mija Marin, Head of the QC Department, for standing support of this research.

Received for review October 20, 1994. Accepted March 24, 1995.[⊗]

AC941026+

[⊗] Abstract published in *Advance ACS Abstracts,* June 1, 1995.

Anal. Chem. **1995,** *67,* 2162–2169

Method for Estimating Polymer-Coated Acoustic Wave Vapor Sensor Responses

Jay W. Grate* and Samuel J. Patrash

Environmental Molecular Sciences Laboratory, Pacific Northwest Laboratory, Richland, Washington 99352

Michael H. Abraham*

Chemistry Department, University College London, London, WCIH OAJ United Kingdom

A method for estimating the responses of polymer-coated acoustic wave vapor sensors has been developed. Polymer/gas partition coefficients, determined experimentally for at least 20–30 solute vapors by a simple gas chromatographic method, are used to construct linear solvation energy relationships that correlate partition coefficients on a given polymer with various solute solvation parameters. Since these parameters are known for over 2000 compounds, it is possible to estimate polymer/gas partition coefficient values for thousands of vapor/polymer pairs. It is shown how these partition coefficients can, in turn, be used to estimate acoustic wave vapor sensor responses. Comparisons of predicted surface acoustic wave vapor sensor sensitivities with observed responses confirm the general validity of the approach. The approach can be used to select polymers offering the best sensitivities for particular vapors. Limits of detection have been calculated and compared with permissible exposure limits and threshhold limit values for a variety of vapors of interest in environmental remediation and occupational safety. These results indicate that polymer-coated surface acoustic wave vapor sensors are capable of detecting the majority of the vapors considered at concentrations of interest.

Polymer-coated acoustic wave vapor sensors respond to the vapor absorbed by a polymer layer on the device surface. This approach can be used with several acoustic wave devices, including the surface acoustic wave (SAW) device, the flexural plate wave (FPW) device, and the thickness shear mode (TSM) device (also known as the quartz crystal microbalance or QCM).[1,2] The amount of vapor sorbed by the polymer layer and hence the sensor's response depend on the interactions between the vapor and the polymer. Given an understanding of these interactions and the transduction mechanism(s) of the device, it should be possible to estimate the responses of such a sensor. In this paper, we present progress toward achieving this goal. The ability to make such estimations provides a tool for choosing sorbent polymers when designing sensors for particular applications and provides information for making decisions on the most appropriate applications for such sensors.

It has long been recognized that acoustic wave vapor sensors coated with an absorbent material produce responses proportional to the partition coefficient defined according to eq 1.[1-7] The partition coefficient, K, is the ratio of the concentration of sorbed vapor in the absorbent material, C_s, to the concentration of vapor in the gas phase, C_v. Partition coefficients are actually relevant to any sensor whose response depends on the absorption of vapors by a selective layer. In a typical laboratory experiment, a sensor response, Q, is measured in response to a calibrated concentration of vapor in the gas phase, as shown in eq 2.

$$K = C_s/C_v \quad (1)$$

$$Q = f(C_v) \quad (2)$$

Mechanistically, however, the sensor's response depends more directly on the amount of vapor taken up in the sorbent layer, as indicated by eq 3.

$$Q = f(C_s) \quad (3)$$

It follows that experimental sensor responses will be related to KC_v as shown in eq 4.

$$Q = f(KC_v) \quad (4)$$

This equation emphasizes the sorption aspect of the sensor's response; the transduction process is represented by the function that operates on KC_v.

We proposed in 1988 that linear solvation energy relationships (LSERs) could be used to model sorption of vapors by polymer layers on SAW sensors.[8] We described the approach in detail in a review in 1991 and in recent articles.[9-12] This approach is based on a solubility model where the vapor is a solute and the polymer is the solvent. Solubility properties of the vapor are given by a set of solvation parameters that are used in an LSER that takes the form of eq 5 for the sorption of a solute vapor from the gas phase into an absorbent material.[13] This LSER models the sorption process as a linear combination of terms representing the contributions of particular interactions to the overall sorption

$$\log K = c + rR_2 + s\pi_2^H + a\Sigma\alpha_2^H + b\Sigma\beta_2^H + l \log L^{16} \quad (5)$$

(1) Grate, J. W.; Martin, S. J.; White, R. M. *Anal. Chem.* **1993**, *65*, 940A–948A.

(2) Grate, J. W.; Martin, S. J.; White, R. M. *Anal. Chem.* **1993**, *65*, 987A–996A.

(3) Janghorbani, M.; Freund, H. *Anal. Chem.* **1973**, *45*, 325–332.

(4) Edmunds, T. E.; West, T. S. *Anal. Chim. Acta* **1980**, *117*, 147–157.

(5) McCallum, J. J.; Fielden, P. R.; Volkan, M.; Alder, J. F. *Anal. Chim. Acta* **1984**, *162*, 75–83.

(6) Wohltjen, H. *Sens. Actuators* **1984**, *5*, 307–325.

(7) Grate, J. W.; Wenzel, S. W.; White, R. M. *Anal. Chem.* **1991**, *63*, 1552–1561.

(8) Grate, J. W.; Snow, A.; Ballantine, D. S.; Wohltjen, H.; Abraham, M. H.; McGill, R. A.; Sasson, P. *Anal. Chem.* **1988**, *60*, 869–875.

(9) Grate, J. W.; Abraham, M. H. *Sens. Actuators B* **1991**, *3*, 85–111.

(10) McGill, R. A.; Abraham, M. H.; Grate, J. W. *CHEMTECH* **1994**, *24* (9), 27–37.

(11) Grate, J. W.; Abraham, M. H.; McGill, R. A. In *Handbook of Biosensors: Medicine, Food, and the Environment*; Kress-Rogers, E., Nicklin, S., Eds.; CRC Press: Boca Raton, FL, 1995; (in press).

0003-2700/95/0367-2162$9.00/0 © 1995 American Chemical Society

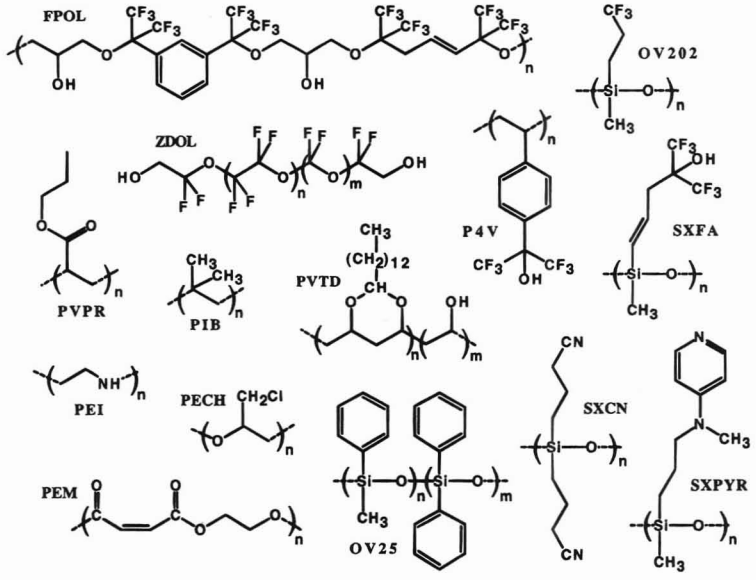

Figure 1. Structural units of the sorbent polymers and oligomers characterized by the LSER method. The polymers are fluoropolyol (FPOL), Fomblin-ZDOL (ZDOL), a 75% phenyl/25% methylpolysiloxane (OV25), an alkylaminopyridyl-substituted polysiloxane (SXPYR), poly(4-vinylhexafluorocumyl alcohol) (P4V), a hexafluoro-2-propanol-substituted polysiloxane (SXFA), poly(epichlorohydrin) (PECH), polybis(cyanopropyl)-siloxane (SXCN), poly(vinyl tetradecanal) (PVTD), poly(isobutylene) (PIB), poly(trifluoropropyl)methylsiloxane (OV-202), poly(ethylene maleate) (PEM), poly(vinyl propionate) (PVPR), and poly(ethylenimine) (PEI).

process. The solvation parameters R_2, π_2^H, $\Sigma\alpha_2^H$, $\Sigma\beta_2^H$, and log L[16] characterize the solubility properties of the vapor, where R_2 is a calculated excess molar refraction parameter;[14] π_2^H measures solute dipolarity/polarizability;[15] $\Sigma\alpha_2^H$ and $\Sigma\beta_2^H$ are effective hydrogen bond acidity and basicity parameters, respectively;[13,16] and L[16] is the gas/liquid partition coefficient of the solute on hexadecane at 25 °C.[17] These solvation parameters have been determined for some 2000 compounds, and those for several hundred organic solutes have recently been compiled in papers.[13,18] All the parameters except R_2 are derived from thermodynamic measurements of complexation or partitioning equilibria.

In order to construct an LSER equation for a particular sorbent material, at least 20–30 log K values are determined experimentally, usually by a gas chromatographic method where the sorbent material is the stationary phase.[17,19–22] Equation 5 is then solved by the method of multiple linear regression to obtain the coefficients c, r, s, a, b, and l. These coefficients characterize the properties of the sorbent material that are complementary to the corresponding vapor properties.[23] For many materials, not all the terms in eq 5 are required,[24] and statistical procedures such as the t-test or F-statistic are used to test the significance of each term.

We recently published LSER equations characterizing the sorbent properties of 14 oligomers or polymers of quite diverse structures at 298 K.[10,20] Included in these studies were materials with strong hydrogen bond acidity, strong hydrogen bond basicity, and high dipolarity as well as a selection of low polarity materials. The repeat units of the polymer structures are shown in Figure 1, and the coefficients of their LSER equations are given in Table 1. These equations in combination with available solvation parameters[13,18] permit the calculation of literally thousands of polymer/gas partition coefficients at 298 K. (LSER equations derived from SAW sensor responses have also been reported, but these do not predict thermodynamic partition coefficients.[25])

These calculated partition coefficients could be used to estimate polymer-coated acoustic wave vapor sensor responses if the full functional form of eq 4 were known. If the acoustic wave device responds solely to the mass loading of the surface by the absorbed

(12) Grate, J. W.; Abraham, M. H.; McGill, R. A. In *Polymer Films and Sensor Technologies*; Harsanyi, G., Ed.; Technomic Publishing Co.: Lancaster, PA, 1995; pp 136-149.
(13) Abraham, M. H. *Chem. Soc. Rev.* **1993**, *22*, 73–83.
(14) Abraham, M. H.; Whiting, G. S.; Doherty, R. M.; Shuely, W. J. *J. Chem. Soc., Perkin Trans. 2* **1990**, 1451–1460.
(15) Abraham, M. H.; Whiting, G. S.; Doherty, R. M.; Shuely, W. J. *J. Chromatogr.* **1991**, *587*, 213–228.
(16) Abraham, M. H. *J. Phys. Org. Chem.* **1993**, *6*, 660–684.
(17) Abraham, M. H.; Grellier, P. L.; McGill, R. A. *J. Chem. Soc., Perkin Trans. 2* **1987**, 797–803.
(18) Abraham, M. H.; Andonian-Haftvan, J.; Whiting, G.; Leo, A.; Taft, R. W. *J. Chem. Soc., Perkin Trans. 2* **1994**, 1777–1791.
(19) Abraham, M. H.; Whiting, G. S.; Andonian-Haftvan, J.; Steed, J. W.; Grate, J. W. *J. Chromatogr.* **1991**, *588*, 361–364.
(20) Abraham, M. H.; Andonian-Haftvan, J.; Du, C. M.; Diart, V.; Whiting, G.; Grate, J. W.; McGill, R. A. *J. Chem. Soc., Perkin Trans. 2* **1995**, 369–368.
(21) Abraham, M. H.; Hamerton, I.; Rose, J. B.; Grate, J. W. *J. Chem. Soc., Perkin Trans. 2* **1991**, 1417–1423.
(22) Abraham, M. H.; Fuchs, R. *J. Chem. Soc., Perkin Trans. 2* **1988**, 523–527.
(23) The a and b coefficients, being complementary to the vapor hydrogen bond acidity and basicity, represent the sorbent material hydrogen bond basicity and acidity, respectively. The s coefficient is related to the sorbent material dipolarity/polarizability. The l coefficient is related to dispersion interactions and the cost of forming a cavity. Larger values of the l coefficient indicate that differences between partition coefficients in a homologous series of vapors will be larger (L[16] values increase with chain length). The r coefficient refers to the ability of the material to interact with solute n and π electron pairs and provides an indication of polarizability.

Table 1. LSER Coefficients for 14 Polymers and Oligomers[a]

polymer[b]	r	s	a	b	l	c	statistics[c] n	R	SD	F
PIB	−0.077	0.366	0.180	0.000	1.016	−0.766	36	0.9959	0.073	941.9
PECH	0.096	1.628	1.450	0.707	0.831	−0.749	50	0.9964	0.068	1209.0
OV25	0.177	1.287	0.556	0.440	0.885	−0.846	40	0.9943	0.089	590.2
OV202	−0.480	1.298	0.441	0.705	0.807	−0.391	50	0.9967	0.071	1319.5
PVPR	0.674	0.828	2.246	1.026	0.718	−0.571	33	0.9958	0.081	646.2
PVTD	−0.016	0.736	2.436	0.224	0.919	−0.591	42	0.9951	0.073	722.3
PEM	−1.032	2.754	4.226	0.000	0.865	−1.653	31	0.9787	0.201	148.1
SXCN	0.000	2.283	3.032	0.516	0.773	−1.630	52	0.9916	0.102	537.5
PEI	0.495	1.516	7.018	0.000	0.770	−1.580	51	0.9873	0.151	443.2
SXPYR	−0.189	2.425	6.780	0.000	1.016	−1.938	39	0.9886	0.120	365.8
SXFA	−0.417	0.602	0.698	4.250	0.718	−0.084	36	0.9885	0.119	256.8
FPOL	−0.672	1.446	1.494	4.086	0.810	−1.207	26	0.9887	0.151	173.8
P4V	−1.538	2.493	1.507	5.877	0.904	−1.329	26	0.9610	0.342	47.7
ZDOL	−0.750	0.606	1.441	3.668	0.709	−0.486	46	0.9952	0.086	831.7

[a] Data are from ref 20. See ref 23 for definitions of the coefficients. [b] The polymers are fluoropolyol (FPOL), Fomblin-ZDOL (ZDOL), a 75% phenyl/25% methylpolysiloxane (OV25), an alkylaminopyridyl-substituted polysiloxane (SXPYR), poly(4-vinylhexafluorocumyl alcohol) (P4V), a hexafluoro-2-propanol-substituted polysiloxane (SXFA), poly(epichlorohydrin) (PECH), polybis(cyanopropyl)siloxane (SXCN), poly(vinyl tetradecanal) (PVTD), poly(isobutylene) (PIB), poly(trifluoropropyl)methylsiloxane (OV-202), poly(ethylene maleate) (PEM), poly(vinyl propionate) (PVPR), and poly(ethylenimine) (PEI). The repeat units of the structures of these polymers are illustrated in Figure 1. [c] Statistics are as follows: n, the number of observations; R, the correlation coefficient; SD, the standard deviation; and F, the Fisher F-statistic.

vapor, then eq 4 takes the form of eq 6.[8,26]

$$\Delta f_v(\text{mass}) = \Delta f_s C_v K/\varrho_S \quad (6)$$

The sensor's response to the mass of the vapor, a shift in frequency, is given by Δf_v(mass). The parameter Δf_s is the frequency shift that occurred when the polymer layer was applied to the bare sensor; this provides a measure of the amount of sorbent polymer on the sensor's surface. The density of the sorbent polymer material is given by ϱ_S. If the partition coefficient K is known (by experiment or calculation), then the response Δf_v of a polymer-coated SAW vapor sensor (Δf_s and ϱ_S known) exposed to a calibrated vapor stream (C_v known) can be calculated, assuming the response is only due to mass-loading effects. This equation was derived for SAW vapor sensors but applies equally well to other mass-sensitive acoustic wave devices.[1]

Recent studies have demonstrated that polymer-coated SAW vapor sensors also respond to polymer modulus changes induced by the vapor. It was recognized in early studies that such changes might contribute, but the potential contribution was difficult to evaluate because actual high-frequency moduli of the polymers before and after vapor absorption were not known.[6,26,27] Some of the first definitive evidence for polymer viscoelastic effects in response to vapor absorption was obtained by Martin and Frye[28] when they observed large attenuation changes in response to vapor sorption. Since mass-loading effects do not result in changes in attenuation, these results demonstrated that the viscoelastic properties of the polymer were changing significantly. In subsequent studies, Martin et al. presented a comprehensive treatment of polymer modulus effects on polymer-coated sensor responses to temperature and vapor concentration changes.[29] This treatment considered both thin and thick polymer films and wide ranges of vapor concentrations. In addition to providing further evidence for the importance of polymer modulus effects in vapor sensor responses, this study described film resonance effects (first reported in refs 30 and 31). Film resonance effects are most likely to be observed at high frequencies using thick films and high vapor concentrations.

We examined the issue of modulus change contributions to vapor sensor responses by comparing observed polymer-coated SAW vapor sensor responses, Δf_v(obs), with those predicted according to eq 6 for mass loading.[26] These comparisons were made for several vapors on each of three separate polymers; the polymer films were thin, and the vapor concentrations were low (~15% of saturation at room temperature). Observed responses were 3−6 times larger than the calculated mass-loading responses for 15 of the 18 vapor/polymer pairs. We concluded that polymer modulus changes contributed to the observed sensor responses and that the modulus effect was larger than the mass-loading effect. We also derived a semiempirical model in which modulus changes were related to polymer volume changes and used this model to assess whether the conclusion indicated by our experimental results was reasonable. This model predicted that the swelling-induced modulus effect is 4−6 times larger than the mass effect (i.e., observed responses fitting this model would be 5−7 times larger than mass-loading responses). Although this model may slightly overestimate responses, it does indicate that observed responses ought to be at least a few times larger than mass-loading responses. As a general rule of thumb, we found that the simple model in eq 7 provided approximate agreement with observed SAW sensor responses.[26]

$$\Delta f_v = 4\Delta f_s C_v K/\varrho_S \quad (7)$$

In this paper, we illustrate how the LSER method can be combined with models for acoustic wave sensor response (eqs 6 and 7) to estimate polymer-coated acoustic wave vapor sensor responses. These estimations are not intended to be regarded as precise predictions; rather, they are intended to help guide experimental sensor development. This paper will emphasize the uses of this approach to investigate sensitivities of polymer-coated

(24) The individual terms in eq 5 represent particular interactions, where $s\pi_2^H$ is a polarity term; rR_2 is a polarizability term; $a\Sigma\alpha_2^H$ is a hydrogen-bonding term in which the vapor is the hydrogen-bond acid; $b\Sigma\beta_2^H$ is a hydrogen-bonding term in which the vapor is the hydrogen-bond base; and l log L^{16} is a combined dispersion interaction and cavity term.

(25) Patrash, S. J.; Zellers, E. T. *Anal. Chem.* **1993**, *65*, 2055−2066.
(26) Grate, J. W.; Klusty, M.; McGill, R. A.; Abraham, M. H.; Whiting, G.; Andonian-Haftvan, J. *Anal. Chem.* **1992**, *64*, 610−624.
(27) Zellers, E. T.; White, R. M.; Wenzel, S. W. *Sens. Actuators* **1988**, *14*, 35−45.
(28) Martin, S. J.; Frye, G. C. *Appl. Phys. Lett.* **1990**, *57*, 1867−1869.

SAW vapor sensors. Selectivity issues will occasionally be mentioned, but these will be explored in a more systematic way in future work. In this paper, all estimated responses are calculated for sensors operating in a regime where film resonance effects are not significant. This is expected to be true for thin polymer films on sensors used primarily for detection of trace concentrations of vapors.

RESULTS AND DISCUSSION

Approach. The approach we have developed to estimate sensor responses consists of calculating partition coefficients by the LSER method of eq 5, and then using these partition coefficients in equations such as 6 and 7. In order to implement this approach, it was first necessary to determine LSER equations for a number of polymers using experimental values of log K, as described in the introduction. Gas chromatography is a well-established method for making these experimental measurements,[32] and we have described our method and its accuracy in previous publications.[17,26] Since we have now determined such equations for a diverse set of polymers (see Table 1 and Figure 1), and solvation parameters used in the calculation of log K values are available for some 2000 compounds, a vast number of polymer/gas partition coefficients and hence sensor responses can be estimated.[10,13,18–20]

In order to direct our work, we selected vapors of concern in occupational safety and environmental remediation. The Code of Federal Regulations and a report on contaminated DOE sites were consulted to help make this selection.[33,34] Partition coefficients for 12 polymers against 100 selected vapors were then calculated according to eq 5, the LSER coefficients in Table 1, and the solvation parameters for the vapors. Two of the 14 materials in Table 1 were eliminated from consideration in our study on the basis of their physical properties. P4V is glassy at room temperature,[35] resulting in slow sensor response times. ZDOL has an observable volatility resulting in SAW sensor drift. From the calculated partition coefficients, various measures of sensor performance such as sensitivity and limits of detection were calculated, assuming certain sensor characteristics. Selected results from these calculations are presented in this paper to illustrate our method and its use. All our results assume that sensors are operated at 298 K.

Estimated Mass-Loading Sensitivities. Mass-loading sensitivities, S(mass), were calculated from the partition coefficients according to eq 6 and expressed as Hertz response per 100 kHz of applied polymer coating per 100 mg m^{-3} of vapor concentration. These mass-loading sensitivity results do not assume any particular type of acoustic wave device. Because the methodology is based on infinite dilution partition coefficients, it is implicitly assumed that sorption isotherms are linear. The results were examined to determine which polymers yield the most sensitive sensors for each vapor, based on mass sensitivity. S(mass) values for representatives of several compound classes are given in Table 2. At least three of the most sorbent polymers are listed for each vapor. In most cases, the three polymers yielding the most sensitive polymers are listed in order of sensitivity. This rule is disregarded in certain cases where vapors of low polarity are predicted to be detected with significant sensitivity by very strongly hydrogen-bonding polymers. In these cases, the three most sensitive low polarity polymers are listed followed by a fourth column with the very polar polymer.

The polymers selected by this approach are usually those that would be expected. Alkanes are best detected using the least polar polymer, PIB. Basic vapors such as ethers, ketones, and amines are best detected by hydrogen bond acidic polymers such as SXFA and FPOL. Alcohols, which are both basic and acidic, can be best detected by coatings that are either acidic or basic (i.e., SXFA and FPOL as acidic polymers and SXPYR and PEI as basic polymers). Aromatic vapors are best detected by moderate to low polarity polymers such as PECH, OV25, and PVTD. Similar coatings are predicted to be good for detecting chlorinated hydrocarbons.

It is noteworthy that, for many vapors, the best polymers are materials that are not commercially available. This is particularly evident for the basic vapors such as ethers, ketones, and amines. The third polymer listed for each of these is a commercially available material that affords much less sensitivity than the two hydrogen bond acidic polymers that are not commercially available. These results indicate that, for some applications, sensors cannot be optimized without material synthesis and development. For nonpolar vapors, good commercial materials are available.

In the case of aromatics, chlorinated hydrocarbons, and alkenes, it is particularly interesting to note the very polar polymers that are predicted to be useful, as shown in the fourth pair of polymer/sensitivity column in Table 2. SXFA is indicated to be a good coating for alkenes. From the solvation parameters and LSER coefficients, it is apparent that this result is due to the weak basicity of the alkenes interacting with the very strong acidity of SXFA. This suggests that alkenes might be distinguished from alkanes where no such hydrogen-bonding interaction is possible. Similarly, the aromatics have weak basicity giving rise to significant interactions with SXFA. In these cases, SXFA is never predicted to be the most sensitive coating, but its sensitivity is significant. Many of the chlorinated hydrocarbons have weak acidity, as is well-known for trichloromethane. As a result, the strongly basic coating SXPYR is predicted to be good for most of these vapors, and in many cases it is estimated to be better than any of the low polarity coatings. The large l coefficient, as large as that of PIB, is also favorable in this case, as is the s coefficient.

In general, the low polarity coatings selected for aromatics and chlorinated hydrocarbons are similar. These compound classes might be difficult to distinguish using a sensor array with only such coatings. However, among the polar coatings giving significant responses to these vapors, SXFA is better for aromatics, and SXPYR is better for chlorinated hydrocarbons. These results suggest the novel hypothesis that sensor arrays for these low polarity vapors will be best if they include very high polarity coatings. This remains to be tested experimentally.

As a final note on sensitivities, the mass-loading sensitivities are based on Δf_s in eq 6, where Δf_s is assumed to be entirely due

(29) Martin, S. J.; Frye, G. C.; Senturia, S. D. *Anal. Chem.* **1994**, *66*, 2201–2219.
(30) Martin, S. J.; Frye, G. C. *Proc. IEEE Ultrason. Symp.* **1991**, 393–398.
(31) Martin, S. J.; Frye, G. C. *Proceedings of the 1992 Solid State Sensor and Actuator Workshop*; 1992; pp 27–31.
(32) Conder, J. R.; Young, C. L. *Physicochemical Measurements by Gas Chromatography*; John Wiley & Sons: New York, 1979.
(33) Riley, R. G.; Zachara, J. M.; Wobber, F. J. U.S. Department of Energy DOE/ER-0547T, 1992.
(34) *Code of Federal Regulations*; U.S. Government Printing Office: Washington, DC, 1993.
(35) Snow, A. W.; Sprague, L. G.; Soulen, R. L.; Grate, J. W.; Wohltjen, H. *J. Appl. Poly. Sci.* **1991**, *43*, 1659–1671.

Table 2. Estimated Mass Sensitivities[a] by Compound Class

	polymer	S(mass)	polymer	S(mass)	polymer	S(mass)	polymer	S(mass)
alkanes								
n-hexane	PIB	0.957	PVTD	0.756	OV202	0.463		
n-octane	PIB	10.1	PVTD	6.40	OV202	3.02		
2,2,4-trimethylpentane	PIB	2.67	PVTD	1.91	OV202	1.04		
alkenes								
1-hexene	PIB	0.807	PVTD	0.731	OV202	0.505	SXFA	0.805
1,3-butadiene	PVPR	0.110	PVTD	0.107	OV202	0.094	SXFA	0.192
chlorinated hydrocarbons								
dichloromethane	PVTD	0.892	PECH	0.872	PVPR	0.764	SXPYR	1.26
trichloromethane	PVTD	2.69	PVPR	1.80	PECH	1.77	SXPYR	5.09
tetrachloromethane	PVTD	1.96	PIB	1.75	OV25	1.45		
1,1-dichloroethane	PVTD	1.50	PECH	1.22	PVPR	1.09	SXPYR	1.66
1,2-dichloroethane	PECH	3.63	PVTD	3.34	PVPR	2.63	SXPYR	6.72
1,1,1-trichloroethane	PVTD	1.80	PIB	1.47	PECH	1.43		
1,1,2,2-tetrachloroethane	PECH	77.4	PVTD	77.3	OV25	48.3	SXPYR	551
1,1-dichloroethene	PVTD	0.418	OV202	0.329	PVPR	0.328		
cis-1,2-dichloroethene	PVTD	2.45	PECH	2.37	PVPR	1.88	SXPYR	4.82
trans-1,2,-dichloroethene	PVTD	1.11	PVPR	0.870	PECH	0.767	SXPYR	0.795
trichloroethene	PVTD	4.43	PVPR	2.78	PIB	2.66	SXPYR	2.81
tetrachloroethene	PVTD	10.8	PIB	10.6	OV25	8.80	SXPYR	4.46
ethers								
diethyl ether	SXFA	17.3	FPOL	2.40	OV202	0.576		
methyl *tert*-butyl ether	SXFA	23.3	FPOL	2.25	OV202	0.579		
tetrahydrofuran	SXFA	74.3	FPOL	17.0	PECH	3.32		
1,4-dioxane	SXFA	719	FPOL	249	PECH	16.8		
ketones								
propanone	SXFA	26.3	FPOL	8.00	PECH	1.23		
butanone	SXFA	80.8	FPOL	25.9	OV202	3.52		
amines								
ethylamine	SXFA	58.4	FPOL	10.3	PVPR	1.16		
diethylamine	SXFA	372	FPOL	60.9	PVPR	2.42		
triethylamine	SXFA	2160	FPOL	260	OV202	4.66		
alcohols								
methanol	SXPYR	9.49	PEI	9.20	SXFA	7.74	FPOL	2.36
ethanol	SXFA	18.2	SXPYR	11.3	PEI	7.82	FPOL	5.43
1-propanol	SXFA	45.4	SXPYR	40.6	PEI	20.4	FPOL	15.3
2-propanol	SXFA	56.4	FPOL	14.6	SXPYR	8.41	PEI	5.24
aromatics								
benzene	PECH	2.73	OV25	2.50	PVTD	2.46	SXFA	2.51
toluene	PVTD	7.71	PECH	7.65	OV25	7.47	SXFA	6.17
ethylbenzene	PVTD	19.9	OV25	18.5	PECH	17.9	SXFA	14.0
o-xylene	OV25	30.7	PVTD	30.5	PECH	30.1	SXFA	20.6
m-xylene	PVTD	23.1	OV25	21.9	PECH	21.2	SXFA	17.2
p-xylene	PVTD	23.1	OV25	21.8	PECH	21.2	SXFA	17.4

[a] Senstivities, S(mass) estimated in Hz response (100 kHz of polymer coating)$^{-1}$ (100 mg m^{-3} of vapor concentration)$^{-1}$ using eqs 5 and 6.

to mass loading. If the Δf_s observed when a sensor is coated is influenced by modulus effects as well, then the mass-loading vapor sensitivities predicted from eq 6 will be slightly off. The modulus effect upon applying a typical polymer film to a SAW device is predicted reduce the observed Δf_s by 10−15% at most.[36] Therefore, using such an observed Δf_s would underpredict mass-loading sensitivity of the sensor by up to 10−15%.

Comparisons of Sensitivity Estimates with Observed SAW Responses. The validity of our sensitivity estimation techniques can be determined by comparing them with measured sensor responses involving the same polymer/vapor pairs. We have made these comparisons for polymer-coated SAW vapor sensors using published data from studies in two laboratories. In recent work, Grate and co-workers have reported SAW sensor data for several vapors on each of four polymers, PIB, PECH, FPOL, and PVTD.[26,36] Patrash and Zellers have reported SAW data for tens of vapors on PIB, PECH, and OV25.[25,37] In addition, they have reported results for tens of vapors on OV275, which has similar structural features and properties to SXCN (i.e., nitrile groups appended to a polysiloxane backbone).[25,37]

The plots in Figure 2 compare the observed SAW sensor sensitivities, S(obs), from Patrash and Zellers with mass-loading sensitivities predicted according to eq 6, S(mass). Sensitivities are expressed as Hertz response per 100 kHz of applied polymer coating per 100 mg m^{-3} of vapor concentration. The corner-to-corner diagonal line indicates where the observed SAW sensitivities would fall if they agreed with mass sensitivities according to eq 6. The steeper diagonal line with a slope of 4 indicates where the experimental data would fall if they were in agreement with the SAW sensor model in eq 7.

In every case, the data are above the line for eq 6 and more closely fit the model for SAW sensor sensitivity given by eq 7. Agreement with the SAW sensor model is generally good for vapor/polymer pairs giving sensitivities below 150 Hz (100 kHz)$^{-1}$ (100 mg m^{-3})$^{-1}$. These results are consistent with our own previous conclusion that observed responses are larger than mass-loading effects alone can account for.[26] It is noteworthy that these comparisons use SAW sensor data from an independent laboratory that were not published when our model (eq 7) was developed. In addition, Patrash and Zellers examined different test vapor concentrations than those in our study where we derived our model.[26] The plotted data in Figure 2 demonstrate that eq 7 is a

(36) Grate, J. W.; Klusty, M. *Anal. Chem.* **1991**, *63*, 1719−1727.
(37) Patrash, S. J. Ph.D. Thesis, University of Michigan, 1994.

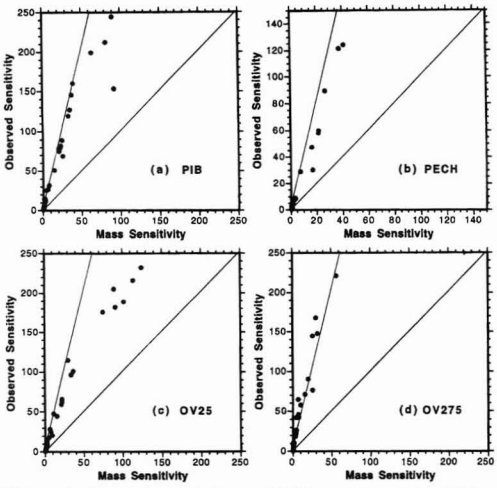

Figure 2. Comparisons of observed SAW vapor sensor sensitivities with calculated mass-loading sensitivities. The corner to corner diagonal lines represent the mass-loading model given by eq 6. The steeper diagonal line represents the SAW sensor model given by eq 7. SAW sensor data are taken from refs 21 and 35: (a) PIB, (b) PECH, (c) OV25, and (d) OV275 SAW sensor responses compared with mass-loading sensitivities calculated for SCXN.

reasonable and useful model for estimating SAW sensor responses.

Comparisons of Estimated Detection Limits with Permissible Exposure Limits and Threshold Limit Values. SAW vapor sensor sensitivities calculated from eqs 5 and 7 can be used to estimate limits of detection if the coating thickness and the minimum detectable signal of the sensor are defined. We assumed minimal detectable signals of 10 Hz and polymer layers applied to thicknesses where $\Delta f_s = 250$ kHz.[36] For each vapor of interest, a polymer was selected that provides good sensitivity. Calculated limits of detection for a variety of vapors are given in Table 3. Also presented in Table 3 are the permissable exposure limits (PEL) for these vapors from the Code of Federal Regulations (CFR) and threshold limit values (TLV) adopted by the American Conference of Governmental Industrial Hygienists (ACGIH).[34,38] It is striking how many vapors can be detected at relevant concentrations with polymer-coated SAW devices. Even if the estimated limits of detection are too optimistic by a factor of 2, this conclusion remains valid. In some cases, the TLV adopted by the ACGIH are significantly lower than the PEL in the CFR. Changes in government regulations may affect the usefulness of SAW sensors in some applications.

Estimated detection limits can help to guide the development of vapor detectors using polymer-coated SAW sensors as the detection elements. If sufficient sensitivity is available to meet the required detection limits, then there is the possibility of successful detector development, provided that selectivity issues can be resolved for the particular application. For polymer-coated SAW sensors, this will usually require arrays and pattern recognition.[39-47] If detection limits estimated by this approach are not adequate for the application, a number of options are available. A reduction in the minimum detectable signal would translate directly to better detection limits. Minimum detectable signal depends on sensor noise, drift, and the precision with which

Table 3. Comparisons of Estimated SAW Vapor Sensor Limits of Detection with Permissible Exposure Limits and Threshold Limit Values

vapor	polymer	LOD[a] (mg/m³)	PEL (CFR)[b] (mg/m³)	TLV (ACGIH)[c] (mg/m³)
n-pentane	PIB	340	2950	1770
n-hexane	PIB	100	1800	176
n-heptane	PIB	32	2000	1640
n-octane	PIB	9.9	2350	1400
cyclohexane	PIB	51	1050	1030
1,3-butadiene	SXFA	520	2200	22*
cyclohexene	SXFA	51	1015	1010
dichloromethane	PECH	120	1737 (Z2)	174
trichloromethane	PECH	56	240	49
tetrachloromethane	PIB	57	63 (Z2)	31
1,1-dichloroethane	PECH	82	400	405
1,2-dichloroethane	PECH	28	202 (Z2)	40
1,1,1-trichloroethane	PECH	70	1900	1910
1,1,2-trichloroethane	PECH	5.6	45	55
tetrachloroethane	PECH	1.3	35	6.9
vinyl chloride	OV202	890	2.6 (D)	13
1,1-dichloroethene	OV202	300		20
cis-1,2-dichloroethene	PECH	42	790	793*
trans-1,2-dichloroethene	PECH	130	790	793*
trichloroethene	PIB	38	537 (Z2)	269
tetrachloroethene	PIB	9.5	678 (Z2)	170
ethylene oxide	SXFA	34	1.8 (A)	1.8
propylene oxide	SXFA	6.7	240	48
tetrahydrofuran	SXFA	1.4	590	590
1,4-dioxane	SXFA	0.14	360	90
formaldehyde	SXFA	100	0.92 (B)	0.37(CL)
acetaldehyde	SXFA	14	360	45 (CL)
propenal (acrolein)	SXFA	7.2	0.25	0.23
propanone	SXFA	3.8	2400	1780
butanone	SXFA	1.2	590	590
4-methyl-2-pentanone	SXFA	0.33	410	205
ethyl acetate	SXFA	2.3	1400	1440
methyl acrylate	SXFA	3.0	35	35
methyl methacrylate	SXFA	1.0	410	410
acetonitrile	SXFA	14.	70	67
ethylamine	SXFA	1.7	18	9.2*
diethylamine	SXFA	0.27	75	15*
triethylamine	SXFA	0.046	100	41*
N,N-dimethylformamide	SXFA	0.016	30	30
N,N-dimethylacetamide	SXFA	0.0042	35	36
methanol	SXFA	13	260	262
ethanol	SXFA	5.5	1900	1880
propan-1-ol	SXFA	2.2	500	492
propan-2-ol	SXFA	1.8	980	983
butan-1-ol	SXFA	0.85	300	152 (CL)
ethylene glycol	SXFA	0.018		127 (CL)
carbon disulfide	OV25	200	62 (Z2)	31
benzene	PECH	37	3.2 (C)	32*
toluene	PECH	13	754 (Z2)	188
ethylbenzene	OV25	5.4	435	
o-xylene	OV25	3.3	435	434
m-xylene	OV25	4.6	435	434
p-xylene	OV25	4.6	435	434
styrene	OV25	2.7	426 (Z2)	213
aniline	SXFA	0.21	19	7.6
pyridine	SXFA	0.43	15	16

[a] Limits of detection (LOD) are calculated assuming a coating "thickness" of 250 kHz, a minimum detectable signal of 10 Hz, and responses modeled by eqs 7 and 5. [b] Permissible exposure limits (PEL) from the Code of Federal Regulations (ref 34). All values represent time-weighted 8-h averages except for the ceiling limit listed for trichloromethane. The values were taken from 49 CFR1910.1000 Table Z1 except for compunds designated Z2 (taken from Table Z2 1910.100) and the compounds designated A (29 CFR 1910.1047), B (29 CFR 1910.1048), C (29 CFR 1910.1027), and D (29 CFR 1910.1017). [c] Adopted threshold limit values (TLV) listed are those recommended by the American Conference of Governmental Industrial Hygienists in ref 38. These values represent time-weighted 8-h average exposure limits except for those compounds with the CL designation, which is a maximumum, instantaneous ceiling limit. Compounds designated with an asterisk have intended changes under propo-sal.

the zero baseline of the sensor can be defined. Sensitivity and detection limits may be improved by increasing the coating thickness, provided that this does not cause other problems such as loss of oscillation.[36] Temperature is also an important governing factor: lower temperatures increase sorption and sensor sensitivity, while higher temperatures can significantly decrease sensitivity. One may seek to develop a coating material providing greater sensitivity than the polymers in this study. However, it is anticipated that it may be difficult to obtain materials that provide more sensitivity than the polymers in this study while still maintaining other desirable sensor characteristics, such as reversibility and rapid response and recovery times. This could be particularly challenging for nonpolar vapors. If reversibility is not required, then materials providing nonreversible interactions may provide greater sensitivity, particularly if the response is integrated over time.[48-51] It is also possible to use an acoustic wave sensor as part of a sensing system that incorporates a preconcentration method.[45,52] This can greatly improve sensitivity and detection limits. If acoustic wave sensors do not provide adequate sensitivity, and none of the possible improvements just noted are feasible, then the ability to estimate detection limits may serve as the basis for choosing another sensing technology or analytical method for the application.

Reexamination of the Contribution of Modulus Effects. Although the main purpose of this paper is to illustrate our method for estimating sensor responses, the data available permit a reexamination of the contribution of modulus effects to the transduction mechanism. The factor of 4 in eq 7 can be compared to the slopes of fitted lines correlating observed sensitivities, S(obs), with calculated mass sensitivities, S(mass). These slopes were determined from linear regressions on S(obs) data from Patrash and Zellers (see Figure 2), after eliminating outliers at high sensitivities that would unduly leverage the slopes; these regression results are presented in eqs 8–11:

PIB $\quad S(\text{obs}) = 3.63S(\text{mass}) + 2.1 \quad (8)$

$n = 32, R = 0.991$

PECH $\quad S(\text{obs}) = 3.06S(\text{mass}) - 1.0 \quad (9)$

$n = 17, R = 0.988$

OV25 $\quad S(\text{obsd}) = 2.95S(\text{mass}) + 2.7 \quad (10)$

$n = 28, R = 0.9822$

OV275 $\quad S(\text{obs}) = 4.24S(\text{mass}) + 6.4 \quad (11)$

$n = 35, R = 0.971$

The number of observations is given by n and the correlation coefficient is given by R. Standard errors of the slopes of these equations are 0.1–0.2. The standard errors for the intercepts are 1.5–2.6, similar to the values of the intercepts, indicating that the lines pass through the origin as they should.

Similarly, the more limited data from recent studies by Grate and co-workers[26,36] were regressed to obtain eqs 12–15:

PIB $\quad S(\text{obs}) = 4.63S(\text{mass}) + 1.2 \quad (12)$

$n = 6, R = 0.995$

PECH $\quad S(\text{obs}) = 3.87S(\text{mass}) + 1.3 \quad (13)$

$n = 7, R = 0.929$

FPOL $\quad S(\text{obs}) = 2.22S(\text{mass}) - 0.8 \quad (14)$

$n = 6, R = 0.928$

PVTD $\quad S(\text{obs}) = 2.35S(\text{mass}) + 1.6 \quad (15)$

$n = 7, R = 0.929$

The equation for PIB omits the data for 1-butanol, a significant outlier.

The regressions in eqs 8–11 suggest that a factor of 3–3.6 may be more appropriate than a factor of 4 in eq 7. The more limited data in eqs 12 and 13 for some of the same polymers suggest that the factor of 4 is reasonable, although the fits are not particularly good. Equations 14 and 15 indicate much lower slopes for FPOL and PVTD. (The slope in eq 11 is not pertinent to this discussion since it actually compares observed sensitivities of the OV275-coated SAW sensor with sensitivities estimated for a similar but not identical polymer, SXCN.) Assuming that the differences between observed responses and calculated mass-loading responses are due to modulus effects, the results above indicate that the modulus effect multiplies the mass-loading effect by a factor of ~3–4 for polymers such as PIB, PECH, and OV25. For FPOL and PVTD, the multiplier appears to be smaller. Pending further data, it seems reasonable to continue using eq 7 for estimations of polymer-coated SAW vapor sensor sensitivities, with the provision that it may overestimate polymer-coated SAW vapor sensitivities for polymers such as PVTD and FPOL. This is a simple approach that does not require any experimental SAW sensor measurements. Where sufficient data are available to determine slopes from plots such as those in Figure 2, it is possible to fit a simple model for each such polymer, using the determined slope instead of the factor of 4 in eq 7. It is worth noting that, for any given polymer, the exact value of the multiplier is unimportant with regard to predicting the relative sensitivities to different vapors.

In a previous section of this paper (and Table 2), we ranked polymers for their sensitivities to particular vapors on the basis of their calculated mass-loading sensitivities. If modulus effects are a significant contribution to the observed sensitivities, as is the case for SAW vapor sensors, and if the modulus contribution varies from polymer to polymer, then mass sensitivities alone may

(38) *1993–1994 Threshold Limit Values for Chemical Substances and Physical Agents and Biological Exposure Indices*; American Conference of Governmental Industrial Hygienists: Cincinnati, OH, 1993.
(39) Ballantine, D. S.; Rose, S. L.; Grate, J. W.; Wohltjen, H. *Anal. Chem.* **1986**, *58*, 3058–3066.
(40) Carey, W. P.; Kowalski, B. R. *Anal. Chem.* **1986**, *58*, 3077–3084.
(41) Carey, W. P.; Beebe, K. R.; Sanchez, E.; Geladi, P.; Kowalski, B. R. *Sens. Actuators* **1986**, *9*, 223–234.
(42) Amato, I. *Science* **1991**, *251*, 1431–1432.
(43) Carey, W. P.; Beebe, K. R.; Kowalski, B. R. *Anal. Chem.* **1987**, *59*, 1529–1534.
(44) Ema, K.; Yokoyama, M.; Nakamoto, T.; Moriizumi, T. *Sens. Actuators* **1989**, *18*, 291–296.
(45) Grate, J. W.; Rose-Pehrsson, S. L.; Venezky, D. L.; Klusty, M.; Wohltjen, H. *Anal. Chem.* **1993**, *65*, 1868–1881.
(46) Rose-Pehrsson, S. L.; Grate, J. W.; Ballantine, D. S.; Jurs, P. C. *Anal. Chem.* **1988**, *60*, 2801–2811.
(47) Zellers, E. T.; Pan, T.-S.; Patrash, S. J.; Han, M.; Batterman, S. A. *Sens. Actuators B* **1993**, *12*, 123–133.
(48) Zellers, E. T.; Hassold, N.; White, R. M.; Rappaport, S. M. *Anal. Chem.* **1990**, *62*, 1227–1232.
(49) Zellers, E. T.; Zhang, G.-Z. *Anal. Chem.* **1992**, *64*, 1277–1284.
(50) Zellers, E. T.; Zhang, G.-Z. *Anal. Chim. Acta* **1993**, *280*, 1–13.
(51) Zhang, G.-Z.; Zellers, E. T. *Anal. Chem.* **1993**, *65*, 1340–1349.
(52) Kindlund, A.; Sundgren, H.; Lundstrom, I. *Sens. Actuators* **1984**, *6*, 1–17.

not correctly predict the polymer that will yield the most sensitive SAW vapor sensor. As an example, PVTD is often predicted to be the most sensitive polymer for low polarity vapors based on mass-loading sensitivities. But if the correct multiplier in eq 7 is 2.35 for PVTD (see eq 15), whereas that for PIB or PECH is closer to 4 (see eqs 8, 9, 12, and 13), then the latter polymers may actually yield more sensitive sensors when used on a SAW device. This is why polymers like PIB, PECH, and OV25 were selected in preference to PVTD for the limits of detection in Table 3. This argument also indicates another reason for suggesting multiple polymers for each vapor in Table 2, and why the estimations described in this paper should be regarded as guidance for experimental work.

We noted in a previous paper that the potential for modulus effects to contribute to a SAW vapor sensor response depended on the initial modulus of the polymer without sorbed vapor.[25] For acoustically thin films, vapor sensor frequency changes due to modulus effects depend on the difference between the initial modulus of the film without vapor and the modulus of the film containing the vapor, where the latter is a lower modulus. The maximum possible contribution due to film softening becomes smaller as the initial modulus decreases, but this factor does not affect the mass-loading response. We suspect that smaller multiplying factors for FPOL and PVTD may be due to smaller initial moduli. FPOL is an oligomer compared to the other polymers and may have a lower modulus than the others. Similarly, PVTD is internally plasticized by the long side chains and is likley to have a lower modulus than polymers like PIB and PECH.

In terms of polymer selection and development, this hypothesis suggests that the initial modulus of the polymer, which determines the sensitivity of a SAW device to perturbations in the modulus,[26] may be a factor worth considering when optimizing a polymer material for sensitivity. For nonpolar vapors, there are typically several polymer candidates offering approximately similar mass sensitivities (see Table 2). For example, in the detection of chlorinated hydrocarbons and aromatic hydrocarbons, mass sensitivities vary by less than a factor of 2 across the first three polymers listed in Table 2. Therefore, the optimal polymer will depend on the initial modulus, which the results above suggest could contribute a factor of 2 in sensitivity from one polymer to another. On the other hand, for hydrogen-bonding vapors such as ethers, ketones, and amines, the sorbent properties of the polymers as determined by hydrogen-bonding functionalities are of the greatest importance. These functionalities can result in sensitivity increases of over 20 times relative to materials without them (see Table 2). In these cases, sorbent properties are much more important in material development than material properties like modulus.

Summary. Our method for estimating the responses of polymer-coated acoustic wave vapor sensors dissects the response into two steps, sorption and transduction. The transduction step can involve multiple contributions, such as mass-loading and modulus effects. This approach allows the calculation of thousands of vapor sensor responses, and the results provide insights into a number of issues relevant to sensor development and application. To our knowledge, the ability to estimate such a large number of responses for a gas-phase chemical microsensor is unprecedented.

ACKNOWLEDGMENT

The authors gratefully acknowledge our students and coworkers who have participated in the development of sorbent polymers for chemical sensors and in the determination of LSER relationships, including Arthur Snow, R. Andrew McGill, Gary S. Whiting, Jenik Andonian-Haftvan, Jonathan W. Steed, Ian Hamerton, and Pnina Sasson. We would also like to thank those who generously provided polymer samples for our analysis, including Wilmer Fife and Martel Zeldin for the SXPYR sample, Arthur Snow for PEM and P4V samples, and Jim Griffith for the FPOL sample. The authors thank Greg Frye of Sandia National Laboratories for helpful comments on our draft manuscript. The Pacific Northwest Laboratory is a multiprogram national laboratory operated for the U.S. Department of Energy by Battelle Memorial Institute under Contract DE-AC06-76RLO 1830. This work (at PNL) was funded by the Office of Technology Development, within the Department of Energy's Office of Environmental Management, under the Characterization, Monitoring and Sensor Technology Cross-Cutting Program.

Received for review January 19, 1995. Accepted April 20, 1995.[⊗]

AC950058+

[⊗] Abstract published in *Advance ACS Abstracts,* June 1, 1995.

Anal. Chem. **1995**, *67*, 2170–2179

On-Line Detection and Identification of Interferences in Multivariate Predictions of Organic Gases Using FT-IR Spectroscopy

Marco M. A. Ruyken* and Joop A. Visser

Analytical Development Department, Solvay Duphar B.V., P.O. Box 900, 1380 DA Weesp, The Netherlands

Age K. Smilde

Laboratory for Analytical Chemistry, University of Amsterdam, Nieuwe Achtergracht 166, 1018 WV Amsterdam, The Netherlands

One of the most serious problems that can occur when a multivariate model is used for the compositional analysis of an unknown mixture is the presence of an unexpected constituent, not modeled in the calibration phase. The interferent will almost certainly influence the predicted concentrations of the modeled constituents, which leads to erroneous and, more seriously, misleading results. Usually, a recalibration—building a new calibration model in which the interferent is included—will be necessary. However, in many applications of multivariate calibration, recalibration will be possible only if an unambiguous identification of the interferent can be made. In this paper, we describe how spectral residuals resulting from a multivariate prediction can be used to detect and identify unknown interferents. The identification of the interferent is performed by matching the residual spectrum with a library of residual spectra. This library was built by processing the members of a regular spectral library by the calibration model and storing the resulting residual spectra. After successful identification, a straightforward procedure can be used to correct the concentrations of the modeled constituents, without the need for a recalibration. The methods are demonstrated using a relatively simple principal component calibration model to predict the concentrations of organic vapors and gases in ambient air with FT-IR spectroscopy. In addition, the influence of different interferents on the predicted concentrations of the modeled constituents is described.

Multivariate calibration can be regarded as a general tool to solve selectivity problems in multichannel instruments, e.g., overlapping spectra in mixture samples. In the last decade, the number of applications using multivariate calibration has grown rapidly, especially in the field of spectroscopy. An example of this growth is the use of near-infrared (near-IR) to predict the octane number of gasoline samples[1] or glucose in blood.[2] Besides near-IR, many applications exist in which multivariate calibration is used with Fourier transform infrared (FT-IR) and UV/Vis spectroscopy. The use of multivariate calibration in spectroscopy offers a combination of little or no sample preparation with high-speed quantitative analysis, enabling real-time monitoring of chemical processes. However, monitoring and controlling processes on the basis of the results of these measurements requires that the multivariate model gives precise and reliable predictions for future incoming samples. In addition, during the prediction of these unknown samples, procedures must be available that are able to detect the occurrence of outlying samples or, more generally, situations not appropriate for the model.

Building a model in multivariate calibration consists of different steps. First, and probably most critical, is the collection of representative calibration samples that will properly span all known sources of variation, e.g., the concentration of the constituents, sample preparation procedures, instrumental variations.[3,4]

The second part of multivariate calibration is the construction and optimization of the model. This part has been the subject of much research in the last 10 years. For an excellent overview on multivariate calibration, the reader is referred to the book of Martens and Naes.[5] Important steps during optimization are data pretreatment, wavelength selection, outlier detection, validation, and choosing the calibration method. Popular calibration methods are principal component regression (PCR) and partial least-squares regression (PLS), due to the availability of software for these methods on many different instruments. Besides these linear projection methods, nonlinear methods enter the field of multivariate calibration.[6–9]

The final step in multivariate calibration is the use of the calibration model to predict the properties or concentrations of samples not included in the calibration set.

A number of problems have been encountered by investigators during the prediction of future incoming samples. One of the most serious problems is the unexpected presence of an interferent, a constituent that was unaccounted for in the calibration samples and therefore not modeled. The interferent will almost

(1) Kelly, J. J.; Barlow, C. H.; Jinguji, T. M.; Callis, J. B. *Anal. Chem.* **1989**, *61*, 313.
(2) Haaland, D. M.; Robinson, M. R.; Koepp, G. W.; Thomas E. V.; Eaton, R. P. *Appl. Spectrosc.* **1992**, *46*, 1575–1678.
(3) Gemperline, P. J.; Salt, A. J. *J. Chemom.* **1989**, *3*, 343–357.
(4) Skagerberg, B.; Bonelli, D.; Clementi, S.; Cruciani, G.; Ebert, C. *Quant. Struct.–Act. Relat.* **1989**, *8*, 32–38.
(5) Martens, H.; Naes, T. *Multivariate Calibration;* John Wiley and Sons Ltd.: Chichester, U.K., 1989.
(6) Wold, S. *Chemom. Intell. Lab. Syst.* **1992**, *14*, 71–84.
(7) Höskuldsson, A. *J. Chemom.* **1992**, *6*, 307–334.
(8) Sekulic, S.; Kowalski, B. R. *J. Chemom.* **1992**, *6*, 199–216.
(9) Gemperline, P. J.; Long, J. R.; Gregoriou, B. G. *Anal. Chem.* **1991**, *63*, 2313–2323.

0003-2700/95/0367-2170$9.00/0 © 1995 American Chemical Society

certainly invalidate the model, thereby causing errors in the predicted concentrations.

The application of multivariate calibration described in this paper was developed to analyze mixtures of organic gases and vapors in production plants for purposes of hygienic control. For most of these plants, it is well known what kind of solvents are used during production, and the calibration models (a model for each plant) are constructed on the basis of this a priori knowledge. However, from time to time, unknown interferents will be present during the measurements, and in these situations the predicted concentrations of the modeled constituents will no longer be reliable. To be able to exclude these samples from the analysis, procedures will be necessary that are capable of detecting outliers (interferents) during prediction.

Fortunately, when using calibration methods based on projections like PCR and PLS, such procedures can easily be incorporated into the software. Probably the most important outlier check procedure is to monitor the residual spectral variance of the new samples and to compare this with the residual variance of the calibration model.[10] When this spectral error exceeds a certain threshold, it indicates the presence of an interferent. Gemperline et al. found that as a guideline this spectral error should be within 3 times the spectral error of the results from a long-term reproducibility test.[3] In a recent paper, however, Karstang concluded that the residual variance alone is not a good criterion for rejecting the predicted concentrations of the model constituents.[11]

After detection of an interferent, the usual way to proceed is recalibration, building a new model which includes the interferent. In general, such a procedure consists of collecting new calibration samples from the process, recording their spectra, and analyzing the constituents of interest with the same reference method used before. These new samples are then added to the old calibration set, and the calibration procedure is repeated using this extended set. The above recalibration procedure is not possible for the application described in this paper, since the calibration samples are constructed in the laboratory by mixing pure constituents. As a consequence, recalibration in this application requires that a positive identification of the interferent can be made.

Different spectral identification techniques exist, of which a direct library search is probably the one most often used in infrared analysis. Based on a dot-product metric, a library of possible interfering constituents is matched against the sample spectrum containing the model constituents and the unknown interferent.[12] Nyden and co-workers[13,14] used an identification procedure which basically treats the search as a multicomponent analysis problem. In a series of articles, Lo and Brown[15–17] presented a number of algorithms for searching in small, medium, and large spectral libraries.

Another identification technique, well known among chemometricians, is target testing factor analysis (TTFA).[18,19] Compared to a direct library search, TTFA is certainly more powerful in mixture analysis, although disadvantages are the need for a matrix of spectra in which the constituents vary more or less independently and that an estimate must be made of the dimensionality of this matrix. Both problems require expert knowledge, prohibiting routine implementation.

The first part of this paper describes the detection of interferents, based on the spectral residual variance. In the second part, the effects of different interferents on predicted concentrations of the modeled constituents are studied by deliberately adding interferents to the sample. In the third part, a new identification method, based on spectral residuals, is described and compared with a direct library search. Finally, all three steps—detection, identification, and correction—are demonstrated in two examples using real process data.

THEORY

This section will give only a brief description of the principles and equations used in multivariate calibration. For a more detailed description of the algorithms and methods, the reader is referred to ref 5. Notation used: upper case bold characters, matrices; lowercase bold characters, column vectors; a prime denotes a transposed matrix or vector.

PCR Calibration. Principal component regression is basically a two-step procedure. The first step consists of constructing a principal component model from the calibration matrix **X**:

$$\mathbf{X} = \mathbf{TP}' + \mathbf{E} \tag{1}$$

where $\mathbf{XP} = \mathbf{T}$, $\mathbf{P}' = (\mathbf{T}'\mathbf{T})^{-1}\mathbf{T}'\mathbf{X}$, and $\mathbf{E} = \mathbf{X} - \mathbf{TP}' = \mathbf{X} - \mathbf{XPP}' = \mathbf{X}[\mathbf{I} - \mathbf{PP}']$. In the present work, the calibration matrix $\mathbf{X}_{I\times K}$ has I samples and K variables. The variables are the spectral intensities at K wavelengths taken from the infrared spectra. In eq 1, the score matrix $\mathbf{T}_{I\times A}$ has orthogonal columns, and the loading matrix $\mathbf{P}_{K\times A}$ has orthonormal columns. The matrices **T** and **P** can be obtained from the singular value decomposition of **X**. The number of factors used in the decomposition is denoted by A. In PCR, the scores from **X** are used as regressors for **Y**:

$$\mathbf{Y} = \mathbf{TQ}' + \mathbf{F} \tag{2}$$

where $\mathbf{Y}_{I\times J}$ is the matrix containing the concentrations for the J constituents and $\mathbf{Q}_{J\times A}$ represents the regression coefficients of **Y** on **T**. The residuals **E** and **F** represent the unique variation in **X** and **Y** that is not explained by the A-factor solution.

PCR Prediction. The prediction of the concentration for one single constituent $\mathbf{y}_i$ from a new sample $\mathbf{x}_i$, using the PCR algorithm, can be done in two equivalent ways. The first method is a simplified prediction using

$$\hat{\mathbf{y}}_i = \hat{\mathbf{b}}_0 + \mathbf{x}_i'\hat{\mathbf{b}} \tag{3}$$

where

$$\hat{\mathbf{b}} = \mathbf{Pq} \tag{4}$$

(10) Wold, S.; Sjostrom, M. In *Chemometrics: Theory and Applications*; Kowalski, B. R., Ed.; ACS Symposium Series 52; American Chemical Society: Washington, DC, 1977; pp 243–282.
(11) Karstang, T. V.; Toft, J.; Kvalheim, O. M. *J. Chemom.* **1992**, *6*, 177–188.
(12) Delaney, M. F.; Warren, F. V.; Hollowell, J. R. *Anal. Chem.* **1983**, *55*, 1925.
(13) Nyden, M. R. *Appl. Spectrosc.* **1986**, *40*, 868–871.
(14) Nyden, M. R.; Pallister, J. E.; Sparks, D. T.; Salari, A. *Appl. Spectrosc.* **1987**, *41*, 63–66.
(15) Lo, S.; Brown, C. W. *Appl. Spectrosc.* **1991**, *45*, 1621–1627.
(16) Lo, S.; Brown, C. W. *Appl. Spectrosc.* **1991**, *45*, 1628–1632.
(17) Lo, S.; Brown, C. W. *Appl. Spectrosc.* **1992**, *46*, 790–796.
(18) Malinowski, E. R.; Howery, D. G. *Factor Analysis in Chemistry*; Wiley: New York, 1980.
(19) Gemperline, P. J.; Boyette, S. E.; Tyndall, K. *Appl. Spectrosc.* **1987**, *41*, 454–459.

and

$$\hat{b}_0 = \bar{y} - \bar{x}'\hat{b} \quad (5)$$

The regression vector **b** weighs each wavelength according to its importance in the PCR solution. Like loading vectors, the vector **b** can be studied graphically to help in the selection of important wavelength regions.

The second prediction method is known as a full prediction; here $\mathbf{y}_i$ is estimated from

$$\hat{y}_i = \bar{y} + \sum_{a=1}^{A} t_{i,a} q_{a,j} \quad (6)$$

where

$$t_{i,a} = x_i' p_a \quad (7)$$

Spectral residuals, e.g., that part of the spectrum that is not explained by the *A*-factor solution, can only be calculated using this last algorithm. After *A*-factors, the residual spectrum $\mathbf{e}_i$ is constructed from

$$e_i' = x_i' - \sum_{a=1}^{A} t_{i,a} p_a' \quad (8)$$

Large deviations in residual spectra indicate the presence of one or more interferents, and the simplest way to test for systematic variation in the residual spectrum is visual inspection. This is, of course, not possible in on-line applications, where samples are taken from the process every minute. Therefore, the residual spectrum is transformed into a root-mean-square spectral error (RMSSPE), a single parameter that can be used to judge the magnitude of deviations in residual spectra. As will be shown,

$$\mathrm{RMSSPE}_i = \sqrt{\sum_{k=1}^{K} (e_{i,k})^2 / K} \quad (9)$$

the RMSSPE is one of the most important parameters for testing the reliability during on-line predictions. By dividing the sum of the squared residuals by the number of wavelengths *K*, RMSSPE values obtained from different models can be compared mutually, irrespective of the number of wavelengths used.

Prediction in the Presence of Interferents. If a sample is contaminated by an interferent U, its measured spectrum $\mathbf{x}_i$ contains a contribution from the spectra of the model components, $\mathbf{x}_m$, plus a contribution from the interferent, **u**. Provided that the assumption of additivity remains valid, it is possible to write

$$x_i = x_m + u \quad (10)$$

The predicted concentration $\mathbf{y}_i$ for a sample $\mathbf{x}_i$, eq 10 substituted into eq 3, will be

$$\hat{y}_i = \hat{b}_0 + (x_m' + u')\hat{b} \quad (11)$$

From eq 11 it can be seen that the error caused by the interferent is simply $\mathbf{u}'\hat{\mathbf{b}}$. This error can be large if **u** is strongly correlated with $\hat{\mathbf{b}}$. The influence of the interferent on the predicted concentrations of the modeled constituents will be zero only when $\mathbf{u}'\hat{\mathbf{b}} = 0$, i.e., when the spectrum of the interferent and the regression vector is orthogonal.

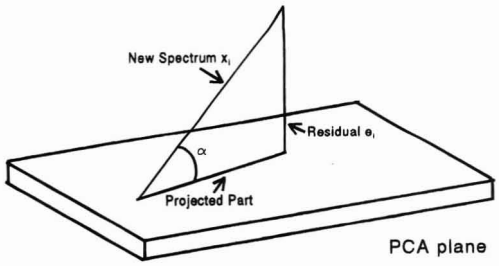

Figure 1. Illustration of the projection of the spectrum of a new sample containing an interferent on a two-factor principal component model. Because of the interferent, the sample will have a large residual spectrum, $\mathbf{e}_i$.

Identification of Interferents: Residual Library Search. Suppose two analytes A and B contribute to the multiwavelength signal. The unit spectra of these analytes are **a** and **b**, both *k*-dimensional vectors. A matrix $\mathbf{X}_{I\times K}$ contains the spectral measurements performed on mixtures of A and B with different concentrations. Under linear conditions (Lambert–Beer), the pseudorank of **X** is 2, assuming no off-set and so on. For the moment the data are not centered.

X can be modeled by

$$\mathbf{X} = \mathbf{TP}' + \mathbf{E}; \quad \text{with} \quad \mathbf{T} = [\mathbf{t}_1, \mathbf{t}_2], \quad \mathbf{P} = [\mathbf{p}_1, \mathbf{p}_2], \quad \mathbf{P}'\mathbf{P} = \mathbf{I} \quad (12)$$

The vectors $\mathbf{p}_1$ and $\mathbf{p}_2$ define the space **W** in which all the measured spectra are situated (see Figure 1). Equation 12 is often referred to as the principal component model of **X**. Obviously, span($\mathbf{p}_1$,$\mathbf{p}_2$) = span(**a**,**b**).

Suppose a new measurement becomes available containing analytes A, B, and an unknown interferent U (with unit spectrum **u**). For the sake of illustration, the concentrations of these analytes and interferents are taken as unit, but this is not necessary for the general case. Hence, the new measurement $\mathbf{x}_{new} = \mathbf{a} + \mathbf{b} + \mathbf{u}$. Calculating the residual after projection of $\mathbf{x}_{new}$ on **W** gives $\mathbf{e}'_{new} = \mathbf{x}'_{new}[\mathbf{I} - \mathbf{PP}']$. Transposing gives

$$\mathbf{e}_{new} = [\mathbf{I} - \mathbf{PP}']\mathbf{x}_{new} = [\mathbf{I} - \mathbf{PP}']\mathbf{a} + [\mathbf{I} - \mathbf{PP}']\mathbf{b} + [\mathbf{I} - \mathbf{PP}']\mathbf{u} = [\mathbf{I} - \mathbf{PP}']\mathbf{u} = \mathbf{e}_u \quad (13)$$

because **a** and **b** lie in **W** and no residual is left after projection of **a** and **b** onto **W**.

A library of spectra is available for purposes of qualitative analysis. Suppose that **z** is an arbitrary unit spectrum of this library, and calculate the residual after projection of **z** on **W**, then $\mathbf{e}_z = [\mathbf{I} - \mathbf{PP}']\mathbf{z}$, where $\mathbf{e}_z$ is the residual spectrum after projection.

As a measure of similarity between spectra, the following formula is proposed (arbitrary spectra **x** and **z**):

$$H(\mathbf{x},\mathbf{z}) = \frac{\mathbf{x}'\mathbf{z}}{||\mathbf{x}||\,||\mathbf{z}||} \quad (14)$$

Obviously, the maximum of $H = 1$ and H can be interpreted as the cosine of the angle between the spectra $\mathbf{x}$ and $\mathbf{z}$. Formula 14 is the Cauchy–Schwartz inequality and it can be proven that this maximum is attained if and only if $\mathbf{x} = \lambda\mathbf{z}$ (λ is nonzero).

Compare now the residual of $\mathbf{x}_{new}$ with all the residuals of $\mathbf{z}$ (from the library), and choose the $\mathbf{z}$ that maximizes $H(\mathbf{e}_{new},\mathbf{e}_z)$. It can easily be shown that $H(\mathbf{e}_{new},\mathbf{e}_z) = H(\mathbf{e}_u,\mathbf{e}_z) = 1$ if $\mathbf{z} = \lambda\mathbf{u}$ (or if both spectra are unit normalized, $\mathbf{z} = \mathbf{u}$). But does $H = 1$ guarantee that $\mathbf{z} = \lambda\mathbf{u}$? Suppose that $H = 1$, and hence $\mathbf{e}_z = \lambda\mathbf{e}_{new}$, then

$$\mathbf{e}_z = \lambda\mathbf{e}_{new} \rightarrow [\mathbf{I} - \mathbf{PP}']\mathbf{z} = \lambda[\mathbf{I} - \mathbf{PP}']\mathbf{u} \rightarrow \mathbf{z} - \lambda\mathbf{u} = \mathbf{PP}'(\mathbf{z} - \lambda\mathbf{u}) \quad (15)$$

which follows after elementary rearrangement. The final part of (15) shows an eigenvalue/eigenvector equation. Obviously, this equation holds if $\mathbf{z} = \lambda\mathbf{u}$ or if $\mathbf{z} - \lambda\mathbf{u}$ is an eigenvector of $\mathbf{PP}'$. The matrix $\mathbf{PP}'$ is an idempotent matrix of rank 2. Hence, $\mathbf{PP}'$ has two eigenvalues of 1 (multiplicity 2). It can easily be seen that $\mathbf{p}_1$ and $\mathbf{p}_2$ are the eigenvectors of $\mathbf{PP}'$ and since the multiplicity of the eigenvalue 1 is 2, $\mathbf{p}_1$ and $\mathbf{p}_2$ span the 2-dimensional eigenspace. Another base for this space is $\{\mathbf{a},\mathbf{b}\}$, and $\mathbf{z} - \lambda\mathbf{u}$ lies in this space if $\mathbf{z} - \lambda\mathbf{u} = \mu\mathbf{a} + \eta\mathbf{b}$, for some μ and η.

Concluding, from $H = 1$, it follows that $\mathbf{z} = \lambda\mathbf{u}$ or $\mathbf{z} = \lambda\mathbf{u} + \mu\mathbf{a} + \eta\mathbf{b}$. Therefore, the only problem arises if nonzero μ and η exist such that $\mathbf{z} = \lambda\mathbf{u} + \mu\mathbf{a} + \eta\mathbf{b}$. But $\mathbf{z} = \lambda\mathbf{u} + \mu\mathbf{a} + \eta\mathbf{b}$ is a system of K equations in three unknowns (given $\mathbf{u}$, $\mathbf{a}$, and $\mathbf{b}$) and is overdetermined. Hence, in practice with a library of approximately 50 compounds, an exact solution for $\mathbf{z} = \lambda\mathbf{u} + \mu\mathbf{a} + \eta\mathbf{b}$ does not exist, and from $H = 1$ follows $\mathbf{z} = \lambda\mathbf{u}$.

If the data matrix $\mathbf{X}$ is column-centered prior to calculating model (12), the same arguments hold if $\mathbf{x}_{new}$ and $\mathbf{z}$ are corrected with the trainingset mean prior to projection. The reasoning above is easily extended to more than two analytes in $\mathbf{X}$.

Since in PCR the residuals are obtained from a principal component analysis (PCA) model of $\mathbf{X}$, the above-mentioned reasoning applies. Hence, in PCR calibration, comparing the residuals from the first step with residuals from reference spectra obtained after projection onto the same PCA model makes identification of the unknown interferent possible.

Correction of the Data. From eq 11, it is seen that if an interferent is present, the predicted concentrations of the modeled constituents will be influenced. How great this influence will be is dependent on the spectral similarity between the spectrum of the interferent and the spectra of the constituents in the model. However, after successful identification of the interferent, the originally estimated concentrations of the constituents in the model can be corrected using the procedure below.

Suppose Z is the interferent identified from the search with spectrum $\mathbf{z}$ (arbitrary concentration), then

$$\mathbf{x}_i' = \mathbf{x}_m' + \mathbf{x}_z' = \mathbf{x}_m' + \lambda^{-1}\mathbf{z}' \quad (16)$$

in which $\mathbf{x}_i'$ is the measured spectrum, $\mathbf{x}_m'$ contains the contributions from the model components and $\mathbf{x}_z'$ is the contribution from the interferent. From the residuals it follows that

$$\left.\begin{aligned}\mathbf{e}_i &= \lambda^{-1}[\mathbf{I} - \mathbf{PP}']\mathbf{z} \\ \mathbf{e}_z &= [\mathbf{I} - \mathbf{PP}']\mathbf{z}\end{aligned}\right\} \rightarrow \mathbf{e}_z = \lambda\mathbf{e}_i \quad (17)$$

and λ can be estimated by

$$\frac{\text{RMSSPE}_z}{\text{RMSSPE}_i} = \lambda \quad (18)$$

after which the corrected spectrum is obtained by

$$\mathbf{x}_{i,corr}' = \mathbf{x}_i' - \lambda^{-1}\mathbf{z}' \quad (19)$$

The corrected spectrum $\mathbf{x}_{i,corr}$ is then predicted again with the PCR model leading to corrected concentrations, $y_{i,corr}$. From this second prediction, a new residual spectrum and RMSSPE will be obtained. This new RMSSPE can be used as a final check of whether the whole procedure has been successful.

EXPERIMENTAL SECTION

Hardware. Spectra were collected on a Bomem MB-100 Fourier transform infrared spectrometer (Bomem, Wooddale, IL) equipped with a DTGS detector and a heatable 4-m long-path gas cell (Infrared Analysis Inc., Anaheim, CA). To prevent condensation, the gas cell was heated to 60 °C by an appropriate temperature controller. For the experiments described in this paper, the system was placed in a closed loop, equipped with a metal bellow pump, into which direct injections of the different solvents could be made (total volume, 0.690 L). Before injection, the closed loop was purged with nitrogen. After 6 min, a background spectrum was collected. All spectra, averages of nine scans, were obtained with a 4-cm^{-1} resolution in the frequency range from 4000.21 to 400.68 cm^{-1}, producing 1873 discrete values. The relatively small number of scans was chosen to ensure that the total time necessary for data acquisition and data handling is less than 1 min. The 1-min sampling frequency was considered necessary in order to monitor steep and short emission peaks.

The data system was based on a Borsu 10+ portable 286 AT computer, equipped with 1 MB RAM, a coprocessor, a digital signal processing (DSP) board, a 20-MB hard disk, and a 3.5-in. floppy disk. For on-line measurements, all equipment was placed in a mobile caravan. Teflon tubes (up to 50 m) were used to connect the gas cell with a measurement site in the plant to be monitored.

Software. A special program (GasCalc) was written in SpectraCalc's Array Basic language (Galactic Industries, Salem, NH) to perform data acquisition, spectral preprocessing, PCR predictions, and presentation of the results in graphical and/or tabular form. Calibrations are performed in SpectraCalc's PLSPLUS v2.0. All offline computations were performed on a HP 386 25-MHz computer.

Spectral Library. The library used in this study consists of 41 infrared gas spectra of organic solvents measured on the same instrument under similar conditions. Before entering the library, all spectra are baseline corrected. The library contains only constituents that are used as solvents in the different production plants at the production site. All chemicals used were spectral-grade solvents.

RESULTS AND DISCUSSION

Calibration Model. To demonstrate the techniques discussed in the Theory section, a relatively simple two-component calibra-

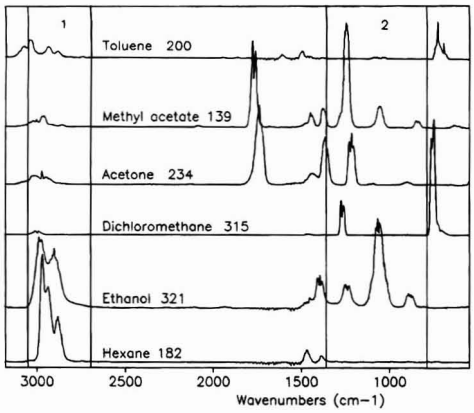

Figure 2. Fourier transform infrared spectra of hexane, ethanol, dichloromethane, acetone, methyl acetate, and toluene. The concentration of each is given in mg/m^3. Vertical lines indicate wavelength regions used for multivariate calibration.

Table 1. Composition of Hexane–Ethanol Calibration Samples[a]

mixture	hexane	ethanol
1	0.0	0.0
2	0.0	320.6
3	0.0	629.7
4	86.1	0.0
5	86.1	320.6
6	86.1	629.7
7	181.7	0.0
8	181.7	320.6
9	181.7	629.7

[a] All concentrations in mg/m^3.

tion model for hexane (HEX) and ethanol (EtOH) was constructed. This model will be used throughout this paper. Spectra of hexane and ethanol are shown in Figure 2. Also shown are two spectral regions (1 and 2) used for multivariate calibration (3079–2686 and 1359–780 cm^{-1}). The spectral limits displayed are selected in order to cut off most of the contribution from water vapor (4000–3170 and 2140–1230 cm^{-1}) and carbon dioxide (2400–2230 and 725–613 cm^{-1}).

Calibration mixtures for the two-component model were constructed according to an 3^2 experimental design yielding nine samples. The compositions of the mixtures are given in Table 1. Two PCR calibration models were built. In the first calibration model (model 1), both wavelength regions are used. The second PCR model (model 2) was built from the first spectral region only, where much less selectivity is found (comparable with IR and UV/Vis). The optimal model according to cross validation has two PCR factors for both models. Prediction errors on separate validation samples were almost completely caused by small injection inaccuracies, and ranged from 2 to 4% at the mean level. The average value of the RMSSPE for the first model is 0.7 for the calibration samples and 1.1 for the validation samples. RMSSPE values for the second model are 1.2 and 1.8, respectively.

On-Line Monitoring of Spectral Residuals. Typical collection times for monitoring production plants are in the order of 8–24 h. An example of the on-line data obtained during such a run is shown in Figure 3. The lower part displays the predicted concentrations of the model constituents hexane and ethanol as a function of time. The broken horizontal line at 90 mg/m^3 is the maximum allowable concentration (MAC) of hexane.

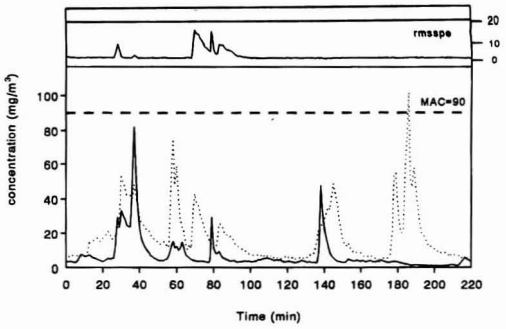

Figure 3. Example illustrating the use of the spectral residual indicator during an on-line run. Bottom: predicted values of hexane (···) and ethanol (—). Top: RMSSPE indicator.

The upper part in Figure 3 displays the (scaled) root-mean-square error indicator calculated from the spectral residuals (eq 9). The profile clearly indicates large spectral residuals (RMSSPE up to 18 compared to 0.7 for samples in the calibration set) during two periods (at around 28 min and from 70 to 95 min). Hence, predictions in these intervals are not reliable. Although the residual spectral error is a powerful indicator for outlying samples (in this case interferents), it is not clear how constituent concentrations are affected by the presence of these interferents; in other words, is there a relationship between the RMSSPE and the prediction error?

Effect of Interferents on Predictions. To test the effect of interferents on predicted concentrations of model constituents, controlled experiments were performed in which varying but known amounts of different interferents were injected into the gas cell. Before injection of the interferents, the gas cell was filled with a mixture of hexane and ethanol of a known composition. The interferents, dichloromethane (DCM), acetone (ACT), methyl acetate (MeAc), and toluene (TOL) were selected because of their mutual spectral dissimilarity. A visual comparison between the spectra of the interferents and the model constituents hexane and ethanol is possible from Figure 2. Table 2 lists correlation coefficients between the spectra calculated over the spectral ranges used for building the first and second calibration models. From a comparison between the correlation coefficients, the increase in similarities when using a narrow wavelength range (model 2) is evident.

The injection sequences and amounts of model constituents and interferents present in each of the experiments are summarized in Table 3. The first experiment consists of the sequential injection of dichloromethane causing three different concentrations. The results using dichloromethane as interferent are shown graphically in Figure 4 (top left). At the bottom, the concentration profiles obtained from model 1 for hexane and ethanol are shown; at the top, the RMSSPE profile is drawn. Until t = 15 min, the RMSSPE is almost zero, aside from a small increase at t = 10 min, due to the injection of a large amount of ethanol. Directly after the first injection of the interferent, at t = 15 min, the RMSSPE starts to rise and reaches a constant level at a value of

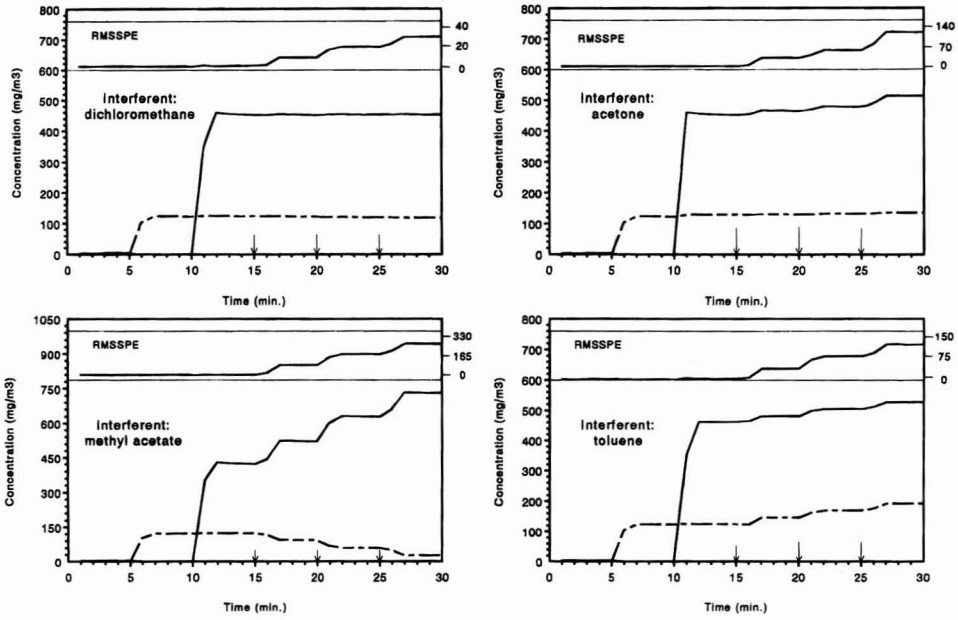

Figure 4. Concentration time plots illustrating the effect of four different interferents on the predicted concentrations of the model constituents hexane (– - –) and ethanol (—). Also shown is the RMSSPE indicator. Arrows indicate when interferents were injected.

Table 2. Correlation Coefficients of Spectra of Model Constituents and Interferents[a]

	HEX	EtOH	DCM	ACT	MeAc	TOL
HEX	1.00					
	1.00					
EtOH	0.56	1.00				
	0.84	*1.00*				
DCM	−0.03	0.01	1.00			
	0.16	*0.49*	*1.00*			
ACT	0.03	0.05	0.01	1.00		
	0.40	*0.50*	*0.78*	*1.00*		
MeAc	−0.05	0.15	0.77	0.23	1.00	
	0.50	*0.61*	*0.81*	*0.87*	*1.00*	
TOL	0.36	0.20	−0.05	0.06	−0.08	1.00
	0.12	*0.07*	*0.25*	*0.68*	*0.45*	*1.00*

[a] Correlation coefficients calculated from spectral region 1 only are shown in italic type (see text for exact wavelength ranges). All other correlation coefficients were calculated from the combined spectral regions 1 and 2.

Table 3. Concentrations of Model Constituents and Interferents Present in the Four Experiments[a]

	model constituents		interferents			
time (min)	HEX	EtOH	DCM	ACT	MeAc	TOL
0–5						
5–10	133.9					
10–15	133.9	469.4				
15–20	133.9	469.4	115.2	114.5	139.0	188.4
20–25	133.9	469.4	230.4	217.5	278.0	377.1
25–30	133.9	469.9	345.7	446.5	417.0	565.5

[a] All concentrations in mg/m^3.

10.5. The same pattern is observed for the two other injections at $t = 20$ and $t = 25$ min. Although the RMSSPE clearly indicates that predictions after $t = 15$ min are unreliable, it appears that both model constituents are not influenced by the presence of dichloromethane.

A somewhat different plot is obtained when acetone is used as interferent (Figure 4, top right, and Table 3). The RMSSPE indicator has the same pattern as before, although the actual values are now about 3 times higher. From the concentration profiles it is seen that the predicted concentration of ethanol increases each time acetone is injected. At $t = 30$ min, a 12% increase in concentration is observed. In contrast to ethanol, hexane is hardly influenced by the presence of acetone.

In the third experiment, methyl acetate was used as the interferent. Again, the residual indicator (Figure 4, bottom left) follows a pattern equivalent to the amount of interferent present. However, now both model constituents are affected by the presence of methyl acetate; most remarkable is the observed decrease of the hexane concentration. Intuitively, it is felt that an interferent should always lead to an increase of the predicted concentration of the model constituent, as is the case in univariate calibration.

Yet another pattern is observed when toluene is used as interferent. From Figure 4 (bottom right), it is seen that in this case the predictions of both model constituents increase. In the above examples, none of the predicted values of the model constituents fall outside the range of concentrations used in generating the model (see Table 1). Hence, an automated system in which the only control procedure would consist of testing whether the predicted concentrations fall inside the calibration range would not have been able to detect these outlying samples.

From eq 11, it is known that the prediction error is dependent on the amount of interferent present and the correlation between the spectrum of the interferent and the regression vector $\hat{\mathbf{b}}$. The prediction error will be unaffected by the interferent only when

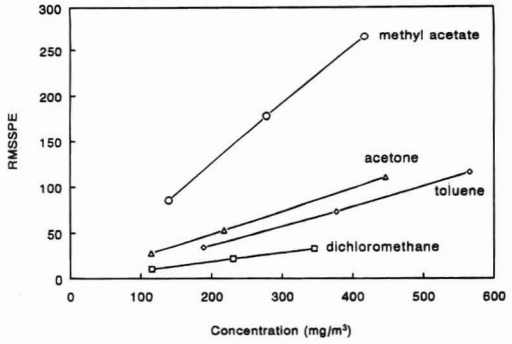

Figure 5. Relationships between the concentration of different interferents and the RMSSPE.

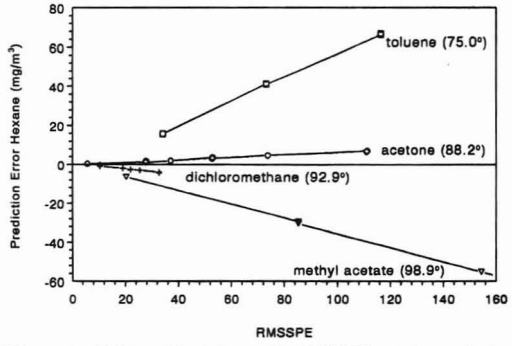

Figure 6. Relationships between the RMSSPE and the prediction error of hexane for four different interferents. Also shown are the calculated angles between the regression vector of hexane and the four interferent spectra.

the two are orthogonal to each other. Since the residual spectrum is proportional to the relative amount of interferent, there must also be a proportional relationship between the residuals and the prediction error.

For the above experiments, these relationships are shown in Figures 5 and 6. From Figure 5, it is seen that for each of the four interferents there is a perfect linear relationship between the concentration of the interferent and the RMSSPE. In Figure 6, the RMSSPE is plotted against the prediction error for hexane. Although good linear relations exist, it can be seen that for each of the interferents, the prediction error follows a different trend, depending on the overlap between the interferent spectrum and the regression vector. This overlap, calculated as the angle between both vectors, is also shown in Figure 6. Dichloromethane ($\alpha = 92.9°$) and acetone ($\alpha = 88.2°$) are almost orthogonal to the regression vector of hexane. Methyl acetate ($\alpha = 98.9°$) and toluene ($\alpha = 75.0°$) overlap much more and hence cause larger prediction errors at the same level of RMSSPE.

The trend in prediction errors can also be deduced from a direct comparison between the spectra of the interferents (see Figure 2) and the regression vectors of hexane and ethanol (Figure 7). The $\hat{\mathbf{b}}$ vector of hexane has large negative bands from 1360 to 780 cm^{-1}, a region in which hexane itself has no absorbance bands, but where the regression vector compensates for the presence of ethanol. Hence, the negative influence of methyl acetate on hexane is due to the large absorbance band

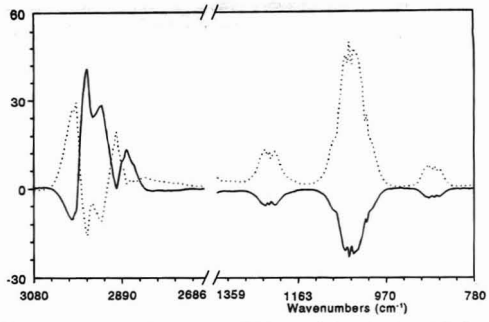

Figure 7. Regression vectors of hexane (—) and ethanol (···).

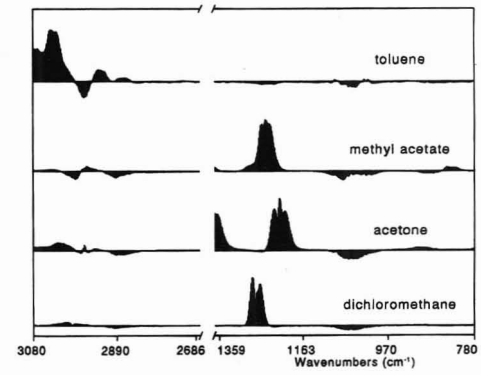

Figure 8. Spectral residuals resulting from the prediction of samples containing dichloromethane, acetone, methyl acetate, and toluene as interferents. Full calibration model (model 1) used.

from 1320 to 1160 cm^{-1}, which overlaps with the negative part of the vector $\hat{\mathbf{b}}$. In real experiments with unknown interferents, this exercise is, of course, not possible.

Identification by Visual Inspection of Residual Spectra. From Figures 5 and 6, it is concluded that the prediction error caused by interferents depends on the concentration of the interferent and the spectral overlap between interferent and regression vector. Since this overlap will be different for different interferents, it will not be possible to estimate prediction errors from spectral residuals (RMSSPE) alone. In order to be able to correct the errors, it is necessary to determine to which of the lines in Figure 6 a calculated RMSSPE belongs; i.e., the interferent must be identified uniquely.

In real predictions, however, there is only access to the raw spectrum of the sample and to the residual spectrum, $\mathbf{e}_i$, in which the last one probably gives the best estimate of the contribution of an interferent to the sample. The residual spectra extracted from the experiments described in Table 3 are shown in Figure 8. From a comparison between the residual spectrum of dichloromethane and its pure spectrum (Figure 2), it is seen that they are almost identical. The explanation is, of course, that the spectrum of dichloromethane is almost orthogonal to the two-component PCA model of hexane and ethanol (see Figure 1). In fact, if a spectrum were be truly orthogonal, then the residual spectrum would be identical to the pure spectrum of the interferent. Because dichloromethane is almost orthogonal to hexane and ethanol, the estimated concentrations are not affected, as can be seen in Figure 4 (top left).

Table 4. Results of the Residual Search on Four Mixtures[a] Predicted with Model 1

mix 1		mix 2		mix 3		mix 4	
hit name	*H*	hit name	*H*	hit name	*H*	hit name	*H*
1. DCM	0.98	1. ACT	0.99	1. MeAc	0.99	1. TOL	0.91
2. DFB	0.64	2. MFM	0.54	2. DFB	0.51	2. MXY	0.84
3. N2O5	0.59	3. MBE	0.48	3. DCM	0.46	3. OXY	0.83
4. MeAc	0.41	4. BTR	0.37	4. N2O5	0.31	4. PXY	0.65
5. BTR	0.32	5. MEK	0.37	5. ACT	0.28	5. ACN	0.31
Direct Library Search							
DCM (25)[b]	0.19	ACT (20)[b]	0.38	MeAc (12)[b]	0.61	TOL (17)[b]	0.39

[a] Mix 1; unknown, DCM; RMSSPE, 10.5. Mix 2: unknown, ACT; RMSSPE, 27.8. Mix 3: unknown, MeAc; RMSSPE, 87.3. Mix 4: unknown, TOL; RMSSPE, 5.8. [b] Position in hit list.

Table 5. Results of the Residual Search on Mixtures[a] Predicted with Model 2

mix 1		mix 2		mix 3		mix 4	
hit name	*H*	hit name	*H*	hit name	*H*	hit name	*H*
1. DCM	0.57	1. ACT	0.99	1. MeAc	0.98	1. TOL	0.96
2. DFB	0.55	2. ACH	0.82	2. ACT	0.77	2. MXY	0.94
3. DBE	0.52	3. DFB	0.82	3. DFB	0.76	3. OXY	0.93
4. MEK	0.50	4. MeAc	0.81	4. DCU	0.76	4. PXY	0.89
5. EtOH	0.49	5. ACN	0.72	5. ACH	0.70	5. ACH	0.84
Direct Library Search							
DCM (28)[b]	0.38	ACT (21)[b]	0.64	MeAc (19)[b]	0.72	TOL (27)[b]	0.16

[a] Mix 1: unknown, DCM; RMSSPE, 2.3 Mix 2: unknown, ACT; RMSSPE, 7.4. Mix 3: unknown, MeAC; RMSSPE, 10.4. Mix 4: unknown, TOL; RMSSPE, 5.4. [b] Position in hit list.

More complex residual are obtained for the other three interferents, and identification based on a visual inspection of the residual spectra becomes more difficult. From the examples in Figure 8, it is seen that in all cases the residual spectra have distinctive structures in spectral regions where the interferents have absorption bands. In some situations, it will be possible to deduce from the residual structure what kind of spectra need to be added to the analysis. In general, however, multivariate calibration models will be more complex than the one used in this paper, and the resulting residuals will be more distorted by contributions from the model constituents. This will make a direct identification almost impossible.

Identification of Interferents Using the Residual Library Search Technique. The capability of the residual library search method was tested on four different mixtures containing hexane (133.9 mg/m^3) and ethanol (469.4 mg/m^3) as the model constituents and one of the interferents used before. For each of these mixtures, the interferent was present at its lowest level (see Table 3). To test if the proposed procedure could also be applied to less selective spectral data, all computations on the four mixtures were repeated using the second calibration model (model 2, spectral range 1).

The results obtained by the residual search program, as well as the results from a direct search in the original library (raw spectra), are given in Tables 4 (model 1) and 5 (model 2). As a measure of similarity between the residual spectra, *H* is used (eq 14).

The first example (mix 1) is a three-component mixture containing hexane and ethanol as the model constituents and dichloromethane (115.2 mg/m^3) as the interferent. The residual spectrum of mix 1 has an RMSSPE of 10.5. The results from a search in the residual library (41 compounds) can be found in Table 4. The best hit from this list is dichloromethane ($H = 0.98$), which was indeed the constituent used as interferent. The other constituents in the list have much lower *H*-values and thus can be excluded as possible candidates. When using a direct library search, dichloromethane was number 25 in the hit list, with a very low *H*-value of 0.19. Clearly, no identification is possible when using the direct search algorithm.

When the second calibration model (Table 5) was used, the residual, which was heavily corrupted by noise, had a RMSSPE of only 2.3, which is slightly more than the noise in the data (RMSSPE of 1.8). If the RMSSPE threshold in the on-line application had been set 3 times the value calculated for the validation samples, this outlier would not have been detected, although the prediction errors caused by such a small interferent would probably also be negligible. The residual search algorithm still came up with dichloromethane having the highest *H*-value (0.57), indicating the sensitivity of the method, allthough the differences between other constituents in the list are now very small. Using the direct search method with a narrow wavelength range, dichloromethane ended up as number 28 in the hit list, with an *H*-value of 0.38.

The results for the other three samples, mix 2, mix 3, and mix 4, in which acetone (114.5 mg/m^3), methyl acetate (139.0 mg/m^3), and toluene (62.8 mg/m^3) were used as interferents, respectively, can also be found in Tables 4 and 5. All of the residual spectra from both models could be identified uniquely, since in each case *H* was higher than 0.95. In none of the above examples could the interferent be identified from a direct library search.

From a comparison between the RMSSPE values of both models, it is seen that with less selective spectral data, the residuals are in general much lower, due to the increase in spectral overlap. As a consequence of the bigger overlap, the *H*-values between the noninterfering constituents in the hit list and the residual spectrum increase, which means that the control limit on the *H*-value should be increased also.

Table 6. Results of the Residual Search on Mixtures[a] Containing Two Interferents: Model 1

mix 5		mix 6	
name	*H*	name	*H*
1. MeAc	0.91	1. MeAc	0.87
2. ACT	0.65	2. TOL	0.49
3. DFB	0.42	3. DFB	0.45
4. BTR	0.38	4. DCM	0.45
5. DCM	0.36	5. OXY	0.42
Direct Library Search			
MeAc (1)[b]	0.77	MeAc (3)[b]	0.68
ACT (3)[b]	0.68	TOL (11)[b]	0.59

[a] Mix 5: unknowns, ACT and MeAc; RMSSPE, 221.3. Mix 6: unknowns, TOL and MeAc; RMSSPE, 202.4. [b] Position in hit list.

In Table 6, the results are presented for mix 5 and mix 6, two samples representing the rather extreme case in which not one but two interferents are present at the same time. Apart from the model constituents present in the same amount as in the first four mixtures, mix 5 contains 468.0 mg/m^3 acetone and 278.0 mg/m^3 methyl acetate. Mix 6 contains 278.0 mg/m^3 methyl acetate and 490.6 mg/m^3 toluene. The concentrations of these interfer-

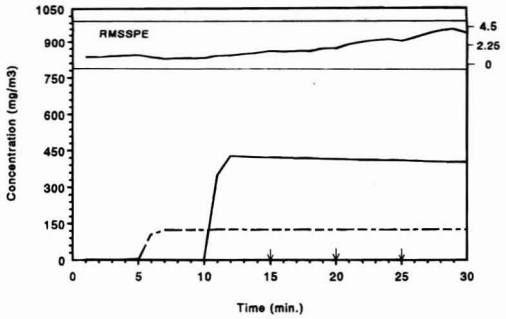

Figure 9. Updated concentration profiles for hexane (– – –) and ethanol (—) after correction of the spectra for the interferent methyl acetate (compare with Figure 4, bottom left).

ents were chosen such that their spectral contributions to the sample are in the same order. Using calibration model 1, the top hit from the residual search on the residual spectrum of mix 5 was methyl acetate, with an *H*-value of only 0.91, which is considered small compared to its large residual. The second best hit was acetone, which indeed was one of the interferents, although the *H*-value was only 0.65. From the results of the hit list, i.e., relatively small *H*-values together with large residuals (RMSSPE, 221.3), it is concluded that either the interferent is not present in the residual library or the sample is contaminated by more than one interferent. In this case, a further check will be necessary.

The last example is mix 6, containing methyl acetate and toluene as interferents. The top two hits from the residual library search correctly identify methyl acetate and toluene as the interferents. However, since the *H*-values are relatively small, no unique identification is possible, and the same conclusion as above must be made.

Correction of the Data. The final step consists of a correction of the originally estimated concentrations of the model constituents. The correction procedure was tested on data taken from the experiment in which methyl acetate was injected as the interferent (see Table 3 and Figure 4, bottom left). The predicted concentrations after correction of the spectra using eqs 18 and 19 are shown in Figure 9. As can be seen, the influence of methyl acetate on the predicted concentrations of hexane and ethanol has been successfully removed. The slight decrease in the concentration profile of ethanol is a known phenomenon and is caused by adsorption of ethanol in the gas cell. Furthermore, the RMSSPE has dropped to an acceptable level of 4.2, which is close to the noise level. The small increase in RMSSPE is most likely caused by small differences between the library spectrum of methyl acetate and its spectrum as recorded during the experiment.

Two examples using real process data will serve to illustrate the complete three-step procedure. In both examples, a PCR calibration model for methyl ethyl ketone (MEK) and toluene (TOL) was used to estimate the concentrations of both constituents in one of the production plants.

The results for the first example are shown graphically in Figure 10. From the RMSSPE profile (top) it is clear that a number of samples (57–60) have large spectral residuals, indicating the presence of an interferent. The residual library search performed on samples exceeding the RMSSPE threshold of 5.0

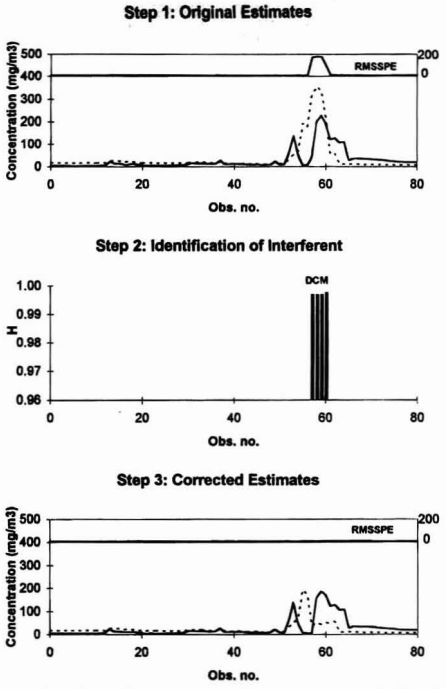

Figure 10. Example of the three-step procedure—detection, identification, and correction—for process data from on-line run 1. Top: estimated concentration profiles (uncorrected) of methyl ethyl ketone (—) and toluene (···), together with the RMSSPE. Middle: *H*-values and identification results from the residual library search. Bottom: estimated concentration profiles and RMSSPE after correction for the influence of the interferent.

(Figure 11, middle) identifies dichloromethane as the interferent present in these samples. In the last step, dichloromethane is subtracted from the raw spectra of these samples using eq 19, after which the updated concentration estimates and RMSSPE values are recalculated using the PCR calibration model. From the fact that the spectral residuals are now virtually zero, it follows that the correction procedure successfully removed the influence of the interferent dichloromethane.

The results for the second example are shown in Figure 11. From the RMSSPE profile it is concluded that an important part of the estimated concentrations is not reliable. All residual spectra from this run exceeding the RMSSPE threshold of 5.0 are used as input spectra in the residual library search (step 2). From this search it is clear that there are two regions (the first and last) in which only one interferent is present, dichloromethane (DCM) and acetone (ACT), respectively. The pattern observed in the middle region is typical for a situation where two interferents are present at the same time. However, it is also possible that the decrease in *H* is caused by the presence of an interferent not present in the library. The updated concentration profiles are shown at the bottom of Figure 11. From an analysis of the RMSSPE profile, it follows that a major part of the measurements has successfully been corrected. In addition, the part that cannot be corrected is clearly identified (samples 48–50). Once more, it is seen that the use of spectral residuals is an important tool to

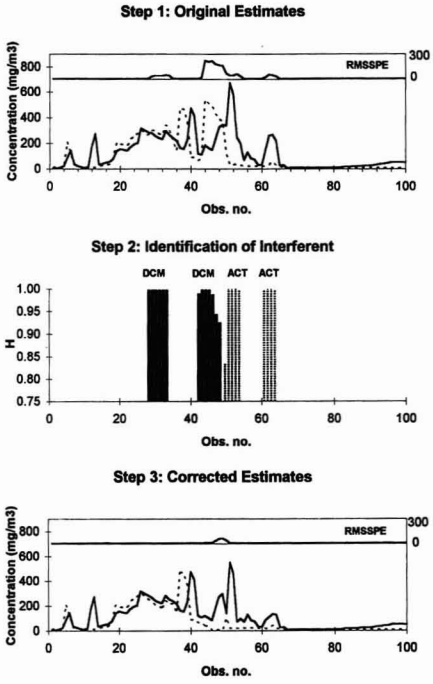

Figure 11. Example of the three-step procedure—detection, identification, and correction—for process data from on-line run 2. Top: estimated concentration profiles (uncorrected) of methyl ethyl ketone (—) and toluene (· · ·), together with the RMSSPE. Middle: *H*-values and identification results from the residual library search. Bottom: estimated concentration profiles and RMSSPE after correction for the influence of the interferents.

recognize unreliable samples. In the end, these samples have to be excluded from the final results.

Instead of performing the interferent correction as described, one could, of course, also switch to the proper three-component model. The advantages and disadvantages of both methods has yet to be proven.

CONCLUSIONS

In this paper it was demonstrated how spectral residuals resulting from the predictions of samples containing nonmodeled interferents can be used in an early warning system to control the reliability of predictions in on-line spectroscopic applications. It was shown that from the residuals alone it will not be possible to estimate to what extent the model constituents will be influenced, since in general, different interferents will lead to different prediction errors. As a consequence, all detected outliers are suspicious and should therefore be excluded from the results of the analysis. As a guideline, the RMSSPE should set at a value of 2–3 times the RMSSPE calculated from validation samples. After detection of the interferent, the residual can be used to identify the interferent by searching in a socalled residual library. In all of the examples presented in which one interferent was present, a succesful identification was possible using the above technique. No recalibration will then be necessary, since prediction errors are easily corrected. The presence of two or more interferents can be detected but not corrected whith the method described. A method to deal with that problem is under investigation.

We propose that the RMSSPE calculated from the spectral residuals should be used as an extra "constituent" in the analysis. Together with proper instrumental diagnostic procedures, it will lead to enhanced reliability of multivariate calibration methods. The advantage of using multivariate calibration methods like PLS and PCR, capable of giving outlier warnings, is, from the authors' viewpoint, of great importance in process analysis. A calibration method should be able to indicate success or failure, rather than issue an answer at any cost. The use of calibration methods even more powerful than the ones above, but without outlier detection capabilities, e.g., artificial neural networks, should be used with care when not combined with some kind of projection technique.

ACKNOWLEDGMENT

The authors wish to express their appreciation to Esseline den Nieuwenboer and Gert Klein for collecting the laboratory FT-IR data and Richard Ritsma for measuring the process data.

Received for review October 7, 1994. Accepted April 3, 1995.[⊗]

AC9409905

[⊗] Abstract published in *Advance ACS Abstracts,* May 15, 1995.

Anal. Chem. **1995**, *67*, 2180–2187

High-Performance Collision-Induced Dissociation of Peptide Ions Formed by Matrix-Assisted Laser Desorption/Ionization in a Quadrupole Ion Trap Mass Spectrometer

Vladimir M. Doroshenko and Robert J. Cotter*

Middle Atlantic Mass Spectrometry Laboratory, Department of Pharmacology and Molecular Sciences, The Johns Hopkins University School of Medicine, Baltimore, Maryland 21205

A modified ion trap detector has been utilized to obtain high-performance collision-induced dissociation (CID) mass spectra of peptide ions formed by matrix-assisted laser desorption/ionization (MALDI). MALDI ions are trapped while increasing the fundamental radio frequency field, obviating the need for elevated helium gas pressures. Molecular ion isotopic clusters are then isolated by a reverse–forward–reverse scan sequence. A single species within the isotopic cluster (generally the monoisotopic mass) is then selected for activation. Finally, modulation of the amplitude of the resonant excitation voltage on the end-cap electrodes, used previously to improve mass calibration in normal mass spectra, is now utilized to provide high mass accuracy for the product ions. The CID mass spectra of several protonated and sodium-cationized peptides are presented and are often characterized by a series of rearrangement ions that can be utilized in the determination of amino acid sequences.

Collision-induced dissociation (CID)[1] enhances the structural information available from mass spectrometry by increasing the fragmentation of molecular and fragment ions through energetic collisions with an inert gas. CID is used most effectively on tandem instruments, which also provide the opportunity for selection of a single ionic species from a mixture in the first mass analyzer and recording of its CID mass spectrum in the second. Tandem mass spectrometers currently include four-sector,[2] triple-quadrupole,[3] and hybrid[4] instruments, as well as Fourier transform mass spectrometers (FTMS)[5] and quadrupole ion traps[6] configured to carry out tandem-in-time measurements in a single mass analyzer. For the determination of complex biological structures, unit mass selection of precursor ions, high resolution, and accurate mass assignment of product ions may be required[7] and can generally be achieved only on four-sector and FTMS instruments. These high-performance instruments are, of course, the most expensive and unlikely to become the bench-top instruments that might be utilized routinely by biological scientists (for example) to determine amino acid sequences of peptides.

Mass spectrometers based upon a quadrupole ion trap have considerable potential as inexpensive tandem instruments.[8] An ion trap mass spectrometer was first produced commercially in 1983 by Finnigan MAT (San Jose, CA) as an ion trap detector (ITD) for gas chromatography with a mass range of 650 Da and limited resolution. Since that time, masses exceeding 70 000 Da have been recorded[9] by ejecting ions from the trap through axial resonance excitation,[10] while mass resolutions greater than one part in 10^7 have been achieved at very slow scan speeds.[11] Because resonance excitation increases ion velocities, it has also been used to induce fragmentation through energetic collisions for the recording of MS/MS spectra.[6] Indeed, such processes can be carried out in multiple stages, MS^n, where $n = 12$ has been demonstrated for small ions.[12] In 1990, the first CID mass spectra of peptides were obtained on an ion trap mass spectrometer, using a secondary ion mass spectrometry (SIMS) source.[13]

Because they are capable of desorbing and ionizing peptides and proteins with masses in excess of 100 kDa, electrospray ionization (ESI) and matrix-assisted laser desorption/ionization (MALDI) have also been used as ion sources for the ion trap.[14–19] Because it is a pulsed technique, MALDI is particularly attractive as an ion source. Unlike in continuous sources, in MALDI, neutral species formed during the ionization process are rapidly cleared from the trap prior to the mass measurement cycle, thus reducing

(1) Jennings, K. R. *Int. J. Mass Spectrom. Ion Phys.* **1968**, *1*, 227.
(2) Todd, P. J.; McGilvery, D. C.; Baldwin, M. A.; McLafferty, F. W. In *Tandem Mass Spectrometry*; McLafferty, F. W., Ed.; Wiley: New York, 1983; p 271.
(3) Yost, R. A.; Enke, C. G. *J. Am. Chem. Soc.* **1978**, *100*, 2274.
(4) Glish, G. L.; McLuckey, S. A.; Ridley, T. Y.; Cooks, R. G. *Int. J. Mass Spectrom. Ion Phys.* **1982**, *41*, 157.
(5) Cody, R. B.; Burnier, R. C.; Freiser, B. S. *Anal. Chem.* **1982**, *54*, 96.
(6) Louris, J. N.; Cooks, R. G.; Syka, J. E. P.; Kelley, P. E.; Stafford, G. C.; Todd, J. F. J. *Anal. Chem.* **1987**, *59*, 1677.
(7) Sato, K.; Asada, T.; Ishihara, M.; Kunihiro, F.; Kammei, Y.; Kubota, E.; Costello, C. E.; Martin, S. A.; Scoble, H. A.; Biemann, K. *Anal. Chem.* **1987**, *59*, 1652.
(8) March, R. E. *Int. J. Mass Spectrom. Ion Processes* **1992**, *118/119*, 71.
(9) Kaiser, R. E.; Cooks, R. G.; Stafford, G. C.; Syka, J. E. P.; Hemberger, P. H. *Int. J. Mass Spectrom. Ion Processes* **1991**, *106*, 79.
(10) Kaiser, R. E.; Louris, J. N.; Amy, J. W.; Cooks, R. G. *Rapid Commun. Mass Spectrom.* **1989**, *3*, 225.
(11) Londry, F. A.; Wells, G. J.; March, R. E. *Rapid Commun. Mass Spectrom.* **1993**, *7*, 43.
(12) Louris, J. N.; Brodbelt-Lustig, J. S.; Cooks, R. G.; Glish, G. L.; Van Berkel, G. J.; McLuckey, S. A. *Int. J. Mass Spectrom. Ion Processes* **1990**, *96*, 117.
(13) Kaiser, R. E.; Cooks, R. G.; Syka, J. E. P.; Stafford, G. C. *Rapid Commun. Mass Spectrom.* **1990**, *4*, 30.
(14) Van Berkel, G. J.; Glish, G. L.; McLuckey, S. A. *Anal. Chem.* **1990**, *62*, 1284.
(15) Cox, K. A.; Williams, J. D.; Cooks, R. G.; Kaiser, R. E. *Biol. Mass Spectrom.* **1992**, *21*, 226.
(16) Doroshenko, V. M.; Cornish, T. J.; Cotter, R. J. *Rapid Commun. Mass Spectrom.* **1992**, *6*, 753.
(17) Chambers, D. M.; Goeringer, D. E.; McLuckey, S. A.; Glish, G. L. *Anal. Chem.* **1993**, *65*, 14.
(18) Jonscher, K.; Currie, G.; McCormack, A. L.; Yates, J. R. *Rapid Commun. Mass Spectrom.* **1993**, *7*, 20.
(19) Schwartz, J. C.; Bier, M. E. *Rapid Commun. Mass Spectrom.* **1993**, *7*, 27.

0003-2700/95/0367-2180$9.00/0 © 1995 American Chemical Society

ion–neutral interactions and increasing the lifetime of the ions in the trap. CID mass spectra have been obtained for ion traps equipped with a MALDI source,[17,18] but not under the high-performance conditions that include unit mass selection, high resolution, and high mass measurement accuracy. CID spectra obtained on a commercial Finnigan research grade ion trap mass spectrometer (ITMS) were initially limited in mass resolution by the inability to utilize slow scan speeds.[13,17,18] Later modifications to the ITMS permitted slower scan speeds but reduced the mass recording window to only a few daltons.[9,15]

Isolation of the precursor ion in these experiments generally involved setting the direct current (dc) and radio frequency (rf) voltages so that ions of lower and higher masses are simultaneously ejected near an apex of the ion stability diagram.[13,17,18] Because this approach does not permit unit mass selection, the entire isotopic cluster was used as the precursors for CID experiments. An alternative approach utilized dc and rf voltage ramping to remove lower and higher mass ions in two consecutive stages, but this has been demonstrated only for relatively low mass ions.[20] Reverse-then-forward ejection techniques, utilizing rf-only scans in the axial resonance ejection mode, have been utilized for isolation of isotopic ion clusters[13] and (at slower scan rates) unit mass selection.[21] In addition, broad-band excitation methods have also been used.[22,23]

We recently introduced two techniques, one for trapping MALDI ions and another for recording their mass spectra, that provide considerable improvement in mass resolution and accuracy and are therefore utilized in the present work to achieve high CID performance. First, we have improved the trapping efficiency for MALDI ions by increasing the rf trapping field (from zero to its full strength) during the time that the ion pulse travels toward the center of the trap.[24,25] A similar method has been described by Nogar et al.[26] and obviates the need for using higher pressures of the helium buffer gas to stabilize and trap the ions. This, in turn, permits one to utilize pressures within the ion trap that can be optimized for high mass resolution and ion isolation. Second, while mass measurement accuracy is adversely affected by scan speeds, buffer gas pressures, and space charge effects due to large numbers of trapped ions, an apparent mass shift is often observed in the resonance ejection mode which arises from the fact that the secular frequencies of the ions are generally different from the excitation frequencies. We have previously addressed this problem by linking the ejection voltage amplitude to the fundamental rf voltage, in order to achieve a linear dependence of ejected mass on the scanned rf voltage.[27] Both of these techniques are utilized in this work to achieve high-performance mass selection and recording of CID spectra.

EXPERIMENTAL SECTION

Experiments were carried out on a Finnigan MAT ITD previously modified to accommodate MALDI ionization inside the trap.[16,25] Ions are desorbed from 0.04 in. diameter probe tip that is inserted into the ion trap cavity through the existing 0.05 in. diameter hole in the upper end-cap electrode normally used for introduction of the electron beam (Figure 1) and centered by a cylindrical Teflon spacer. Ions were desorbed by the pulsed (10 ns) laser beam from a frequency-quadrupled Quantel International (Santa Clara, CA) model YG660-10 Nd:YAG laser attenuated by a Newport (Fountain Valley, CA) model 935-5 attenuator and focused onto the sample probe through the gap between the ring and the bottom end-cap electrode by a 50 cm focal length UV quartz lens.

Ions formed by MALDI have initial kinetic energies of several electron volts[28] and, in our instrument, are trapped by increasing the fundamental rf voltage as the ions travel into the trap.[25] Thus, ions initially encounter and penetrate a weak trapping field as they enter the trap but are confined by the high trapping field present when they reach the center. The settling value of the rf trapping voltage during the storage period is generally 60–80% of the maximum value of 15 kV_{p-p}, corresponding to a mass cutoff level of 390–520 Da. This limits the number of stored ions and decreases possible effects due to space charging. Although collisions with helium are not required for trapping, a buffer gas is used to return the ions to the center of the trap and to improve sensitivity and mass resolution.[13] The buffer gas pressure, monitored by a CVC Products (Rochester, NY) GPT-450 vacuum gauge with a GIC-048-2 Penning cold cathode discharge tube, was from 4×10^{-4} to 5×10^{-4} Torr.

The mass range of the ITD was extended by isolating the end-caps from ground and applying a supplementary dipolar rf voltage across the end-caps to enable operation in the resonance ejection mode.[10] Voltages were supplied to the end-cap electrodes by two controlled voltage regulators connected to the balanced outputs of a Wavetek (San Diego, CA) model 95 arbitrary/function generator. The controlled voltage regulators provide better performance than the transformers used previously[16,24,25] and have summing amplifiers at their inputs that permit the use of multiple signal sources and independent control of the voltages on each end-cap electrode.

Instrument Control and Data Acquisition. The modified ITD was controlled by an IBM AT-486 computer using a National Instruments (Austin, TX) Lab-PC+ multifunctional input/output plug-in board and TrapWare, control software written in-house in the Turbo Pascal (Borland International, Scotts Valley, CA) language.[27] Two Lab-PC+ 12-bit resolution analog outputs were used to control the trapping rf voltage via the ITD analog board. In addition, the Lab-PC+ digital output lines were used for other ITD operations, including multiplier and rf voltage supply on/off, multiplier voltage setup, and 12-bit resolution ITD digital-to-analog converter (DAC) output control. Other Lab-PC+ outputs were used to control the Nd:YAG laser, the digital oscilloscope, and multiplexer operation, using the Lab-PC+ timers to control laser firing and to trigger the oscilloscope. These operations were all controlled by TrapWare, which was also used to set up all operational parameters, including output control voltages, excitation frequencies, and the duration between adjacent acquisition points (generally 120 μs), to transfer data (mass spectra and

(20) Gronowska, J.; Paradisi, C.; Traldi, P.; Vettori, U. *Rapid Commun. Mass Spectrom.* **1990**, *4*, 306.
(21) Schwartz, J. C.; Jardine, I. *Rapid Commun. Mass Spectrom.* **1992**, *6*, 313.
(22) Kenny, D. V.; Callahan, P. J.; Gordon, S. M.; Stiller, S. W. *Rapid Commun. Mass Spectrom.* **1993**, *7*, 1086.
(23) Soni, M. H.; Cooks, R. G. *Anal. Chem.* **1994**, *66*, 2488.
(24) Doroshenko, V. M.; Cotter, R. J. In *Laser Ablation: Mechanisms and Applications II;* Proceedings of the 2nd International Conference on Laser Ablation, Knoxville, TN, April, 1993; Miller, J. C., Geohegan, D. B., Eds.; American Institute of Physics: New York, 1993; p 513.
(25) Doroshenko, V. M.; Cotter, R. J. *Rapid Commun. Mass Spectrom.* **1993**, *7*, 822.
(26) Eiden, G. C.; Cisper, M. E.; Alexander, M. L.; Hemberger, P. H.; Nogar, N. S. *J. Am. Soc. Mass Spectrom.* **1993**, *4*, 706.
(27) Doroshenko, V. M.; Cotter, R. J. *Rapid Commun. Mass Spectrom.* **1994**, *8*, 766.
(28) Beavis, R. C.; Chait, B. T. *Chem. Phys. Lett.* **1991**, *181*, 479.

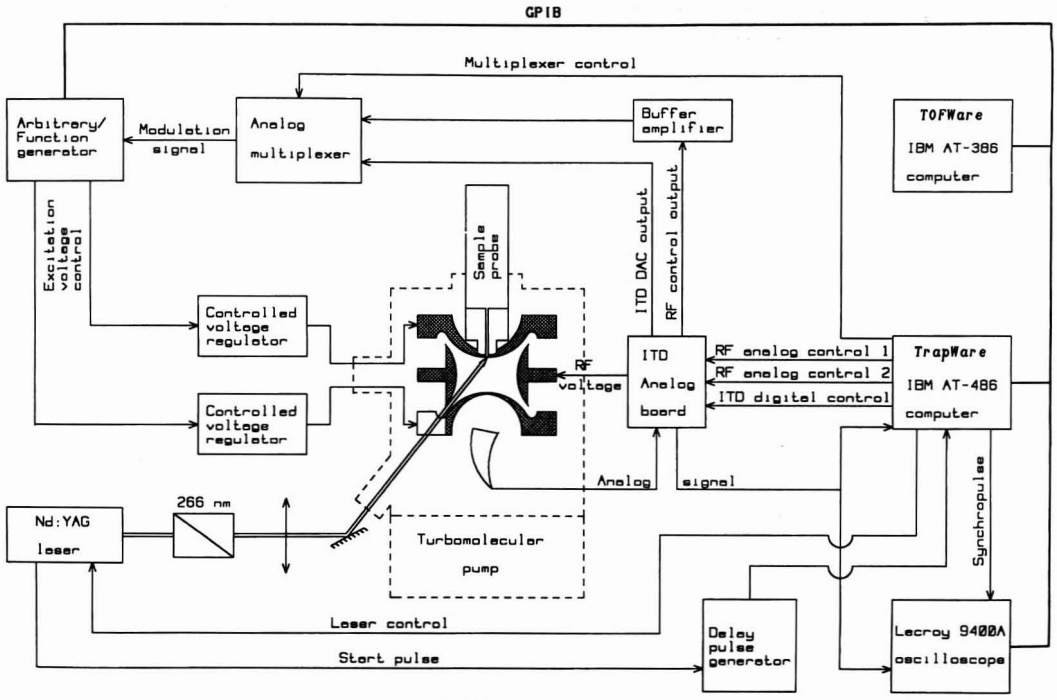

Figure 1. Block diagram of the modified ITD instrument for MALDI experiments.

calibration constants) to a second data acquisition and processing computer via a GPIB interface, and to display ejected ion mass, mass scan rate, Mathieu parameter q_z on the stability diagram, and scan functions (in graphical form) for easy and interactive programming.

In the Finnigan ITD, the DAC output from the ITD analog board controls the trapping rf voltage on the ring electrode. In the current modified instrument (Figure 1), this signal is fed to the arbitrary/function generator, which (operating in the suppressed carrier modulation mode) produces a bipolar sine wave voltage output whose amplitude is proportional to an external modulation signal. Two different modulation signal sources were used, selected by digital control of the analog multiplexer from the AT-486 computer. The first was a DAC output whose amplitude could be set independently (by software) from the rf trapping voltage. The second was an analog signal proportional to the amplitude of the rf trapping field, obtained from the rf voltage feedback line on the ITD analog board. With these two signal sources, a constant axial excitation voltage was used for isolation of the isotopic ion cluster and subsequent excitation of ions of a given m/z to obtain their CID fragments, while linear modulation of the ejection voltage was utilized in analytical microscans in which mass spectra were recorded.

Mass spectra were acquired using a 12-bit resolution analog-to-digital converter (ADC) input on the Lab-PC+ board. The analog signal from the multiplier was amplified by a preamplifier on the ITD analog board whose output was fed to the Lab-PC+ ADC and a LeCroy (Chestnut Ridge, NY) model 9400A digital oscilloscope that was used for monitoring the output signal but not for data acquisition. Mass spectra were then transferred to a second, IBM AT-386 computer via the GPIB interface, where they were displayed and processed using TOFWare, a WINDOWS-based data acquisition system available from ILYS Software (Pittsburgh, PA).[29] The data transferred through the GPIB interface contained calibration information, so the spectra were scaled according to mass.

Ion Isolation and Excitation. In the approach taken in this work, the entire isotopic cluster is isolated. However, high-performance CID is achieved by selective excitation of a single (usually monoisotopic) mass within that cluster. Peptide molecular ion clusters were isolated using a reverse–forward–reverse scan ejection method similar to the reverse–then–forward scan isolation technique reported elsewhere.[13] In the first reverse rf voltage scan, high-mass ions are ejected by scanning down to just above the highest mass of the ions to be isolated. A short forward scan is then used to move ions with masses from 100 to 150 Da below to just below the cluster. A final reverse scan then removes all-low mass ions beginning from 50–100 Da below the cluster ion mass. This scheme has a considerable advantage over the reverse-then-forward method. The 8–9 V_{0-p} used for ion ejection also results in unwanted collisional activation during the ion isolation phase, creating lower mass ions that are left in the trap during forward scans. Thus, the use of a final reverse scan produces a cleaner baseline below the cluster ion mass for later observation of CID ions of even small intensities.

Activation and subsequent CID of mass-selected ions was obtained by selective resonant excitation of ions of a given m/z

(29) Lys, I.; Chevrier, M. R.; Cotter, R. J. Proceedings of the 40th ASMS Conference on Mass Spectrometry and Allied Topics; Washington, DC, May 1992; p 1169.

in the isotopic cluster[15] for a period of 30–50 ms. The trapping voltage was tuned so that the ion resonant oscillation was equal to the excitation frequency, or within 0.25 Da on the mass scale. An excitation voltage of 0.5–1.0 V_{0-p} was used to obtain CID spectra in all cases, except for in the high-pressure experiments involving α-casein fragment 90–96, where 2.5 V_{0-p} was applied.

Mass Calibration. Using a method for obtaining mass spectra in the resonance ejection mode reported earlier,[27] the amplitude of the resonance ejection voltage applied to the end-caps was linked to the scanning rf trapping field in order to compensate for apparent mass shifts that arise because the secular frequency of oscillation for ions leaving the trap does not match the external excitation frequency. In effect, the apparent mass shift becomes proportional to the mass of the ejected ions, so the mass scale is linear, with zero trapping voltage corresponding to zero mass. Thus, we have shown earlier[27] that a single mass can be used to calibrate the mass spectrum. In MS/MS spectra, the second peak in the isotopic cluster can be used as the internal calibration point for product ion mass spectra obtained from excitation of the monoisotopic mass. At the same time, there was no loss in practical mass accuracy (±0.2 Da) when an external calibration point was used. Thus, most of the spectra reported in this work were calibrated using the monoisotopic protonated molecular ion mass of angiotensin I (*m/z* 1296.7).

In all experiments, the bipolar excitation frequency on the end-cap electrodes was 140 kHz. During mass scanning, the linearly ramped ejection voltage amplitude was set to 6 V_{0-p} at *m/z* 1296.7. The mass scan rate was 1000 Da/s, except for α-casein fragment 90–96, where the scan rate was 500 Da/s.

Operation and Sample Preparation. The experiments were generally carried out in a repetitive mode. Each scan cycle was initiated by a control signal to fire the laser. The laser electronics then output a pulse to trigger all other control and acquisition processes that was first passed through an EG&G ORTEC (Oak Ridge, TN) model 416A gate and delay generator, with the delay time set to produce optimal trapping efficiency. A typical scan cycle for obtaining CID mass spectra included (a) ion formation and trapping while increasing the rf voltage, (b) cooling of ions (20–50 ms), (c) isolation of the peptide ion cluster using the reverse–forward–reverse scan method (100–300 ms), (d) resonant excitation and subsequent CID of ions of a given *m/z* (30–50 ms), (e) cooling of product ions (30 ms), and (f) recording of CID mass spectra using the resonance ejection mode and simultaneous linear scanning of the trapping and ejection voltage amplitudes (100–1000 ms). The overall length of each scan cycle was 0.5–1.3 s, depending upon the mass range. In MS/MS/MS experiments, the isolation, excitation, and product ion cooling steps (c–e) were repeated twice before recording.

Nicotinic acid, used as an UV-absorbing matrix for MALDI, was obtained from Aldrich (Milwaukee, WI). Peptides were obtained from Sigma (St. Louis, MO). The nicotinic acid matrix solution prepared as an 0.1 M solution in 4:1 water/acetonitrile was mixed in equal volume amounts with a 5×10^{-4} M aqueous solution of analyte. Approximately 1 μL of this mixture was deposited on the probe tip to obtain several hundred single-shot spectra unless otherwise specified.

RESULTS AND DISCUSSION

Figure 2 shows the major steps used in obtaining CID mass spectra for angiotensin I (monoisotopic molecular weight, 1295.7). Figure 2a is the mass spectrum obtained after isolation of the isotopic cluster using the reverse–forward–reverse scan ejection method and shows a complete absence of ions below the molecular ion region. Figure 2b shows the results of selective excitation of the protonated monoisotopic molecular ion at *m/z* 1296.7. In addition to losses of H_2O and NH_3, major fragment ions corresponding to the b_9 and y''_9 ions[30] at *m/z* 1165.5 and 1181.6, respectively, are shown. These fragment ions are also monoisotopic, reflecting the fact that only the ions at *m/z* 1296.7 have been activated. Thus, the remaining isotopic cluster shown in Figure 2b shows only those ions with masses above the monoisotopic mass. In addition, mass resolution for both molecular and product ions is better than one part in 3000.

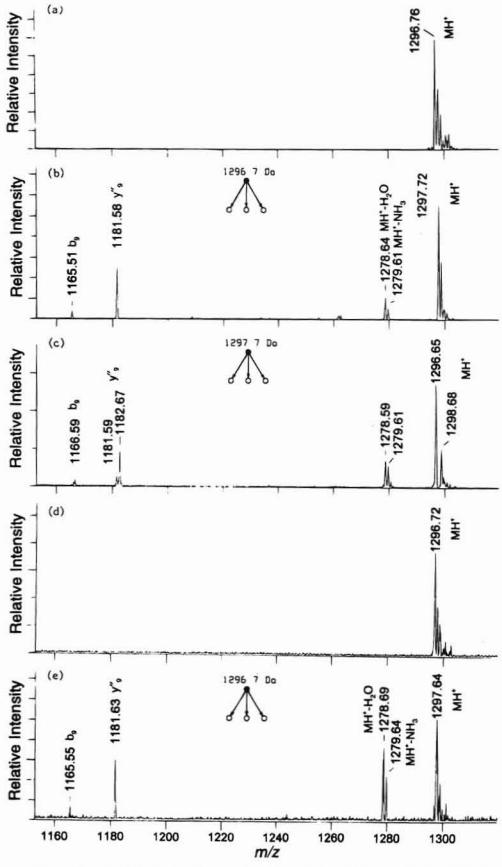

Figure 2. Isolation (a,d) of the isotopic cluster of protonated molecular ions of angiotensin I (MW = 1295.7) and CID mass spectra following excitation of the ions at *m/z* 1296.7 (b,e) and 1297.7 (c). Spectra a–c were obtained from 250 pmol of peptide, while 5 pmol was used to obtain spectra (d,e). (Note: In these and other mass spectra, the assignment of masses to several decimal places is a function of the data system. Mass accuracy, as described in the text, is ~0.2 Da.)

Figure 2c shows the results of selective excitation of the peak at *m/z* 1297.7 (which is now absent from the isotopic cluster observed in the spectrum). In this case, the b_9 and y''_9 ions at *m/z* 1166.6 and 1182.7, respectively, reflect the increase of 1 mass

(30) Roepstorff, P.; Fohlman, J. *Biomed. Environ. Mass Spectrom.* **1984**, *11*, 601.

unit in the molecular ion, while the small peak observed at *m/z* 1181.6 results from the fact that ^{13}C (which is the major isotope giving rise to the peak at *m/z* 1297.7) is found in some cases in the portion of the molecular ion that is lost as a neutral species. The peaks corresponding to the losses of H_2O and NH_3 do not show a similar shift in mass. In this case, the peaks observed at *m/z* 1278.6 and 1279.6 may result from off-resonance excitation of the protonated monoisotopic molecular ions, since it is difficult to selectively excite the species at *m/z* 1297.7 in the presence of the larger, monoisotopic species at 1296.7. (Activation of the monoisotopic species is always easier, since it is possible to excite the monoisotopic mass slightly off-center toward lower mass to obtain clean excitation.) Such off-resonance excitation would be more important in this case if the losses of H_2O and NH_3 represent fragmentation channels with lower activation energies than those resulting in the formation of b_9 and y''_9 ions. Nonetheless, excitation of the isotopic species at *m/z* 1297.7 contributes to some portion of the relative abundance of the ion at *m/z* 1279.6 and to the ion at *m/z* 1280.6. Figure 2, parts d and e, show the isolation of the isotopic cluster and excitation of *m/z* 1296.7, respectively, for a 5 pmol sample, representing the current practical sensitivity of the technique.

Ions are excited within a finite bandwidth of the excitation rf voltage applied at the end-caps, generally described as an absorption contour with a Lorentzian line shape. As described earlier,[27] this gives rise to apparent mass shifts in recording spectra and was the rationale for utilizing excitation voltage amplitudes that are proportional to the fundamental rf voltage to provide a linear mass scale and improve mass calibration. This absorption contour is broadened by higher pressures of the helium gas used to return ions to the center of the trap. Because excitation by the rf voltage applied to the end caps is involved in both ion ejection and ion activation, high pressures of helium gas will affect mass resolution, mass isolation, and selective activation, as well as mass accuracy. In Figure 3, we compare the CID mass spectra of the monoisotopic protonated molecular ion of α-casein fragment 90–96 (*m/z* 913.5) at different pressures of the helium gas. Figure 3a shows the results of excitation of the *m/z* 913.5 ion at a pressure of 0.5 mTorr. Typical of peptides containing a basic amino acid residue on the amino terminus, this spectrum reveals primarily a_n and b_n ions and no y''_n ions.[31] Small neutral losses (H_2O and NH_3) are abundant, consistent with a quasiequilibrium model for peptide decomposition during prolonged (tens of milliseconds) activation and a low rate of energy deposition by multiple low-energy collisions. This time frame also promotes rearrangement reactions, such as the b'_6 + OH ions formed by the transfer of a hydroxyl group from a terminal glutamic acid to an adjacent leucine and the formation of a stable ring structure. Such reactions have been observed only in low energy collisions[31] and verified by ^{18}O labeling experiments.[32]

Figure 3b shows the same experiment carried out at a helium gas pressure of 2.5 mTorr. The isotopic cluster is no longer resolved, so selective isolation cannot be carried out, and the peaks corresponding to losses of H_2O and NH_3 cannot be distinguished. This result also underscores the advantages of the trapping method for MALDI ions, which we have previously described,[24,25]

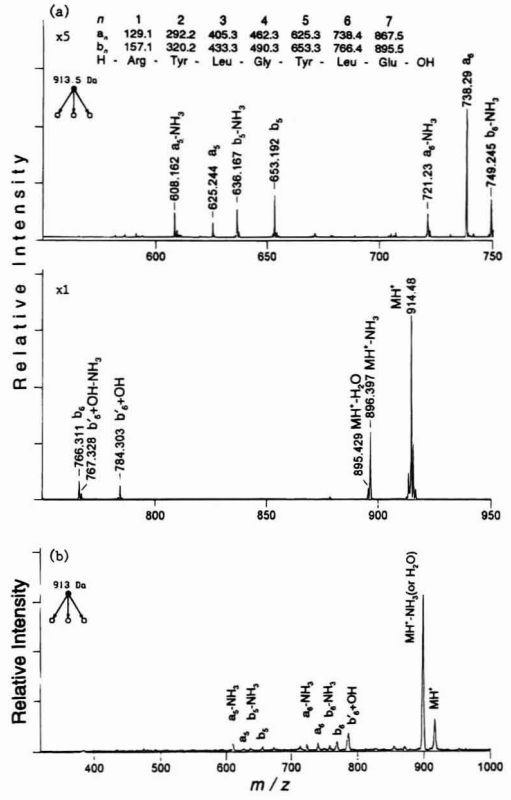

Figure 3. CID mass spectra of protonated molecular ions of α-casein fragment 90–96 (MW = 912.5) at (a) 0.5 and (b) 2.5 mTorr of helium gas.

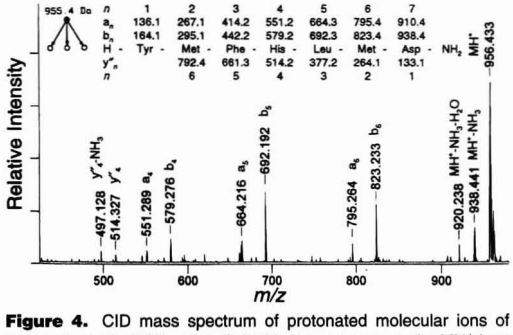

Figure 4. CID mass spectrum of protonated molecular ions of dermenkephalin (MW = 954.4). In this mass spectrum, the MH^+ ions at *m/z* 956.4 correspond to the ^{13}C isotopic peak, since the monoisotopic peak has been removed by excitation.

which utilizes ramping of the fundamental rf field rather than high pressures of helium to trap energetic ions.

Figure 4 shows the results of activation of the *m/z* 955.4 ion of dermenkephalin, which has a basic residue in the middle of the molecule. In this case, a_n and b_n ions result from cleavages of the peptide bonds to the right of the basic residue, while the y''_4 ion results from cleavage to the left of the basic residue, consistent with CID spectra of peptides with a charged center.[31] Figure 5 shows the results of activation of the protonated

(31) Gross, M. L.; Hu, P. In *Biological Mass Spectrometry: Present and Future*; Matsuo, T., Caprioli, R. M., Gross, M. L., Seyama, Y., Eds.; Wiley: New York, 1994; p 255.

(32) Thorne, G. C.; Gaskell, S. J. *Rapid Commun. Mass Spectrom.* **1989**, *3*, 217.

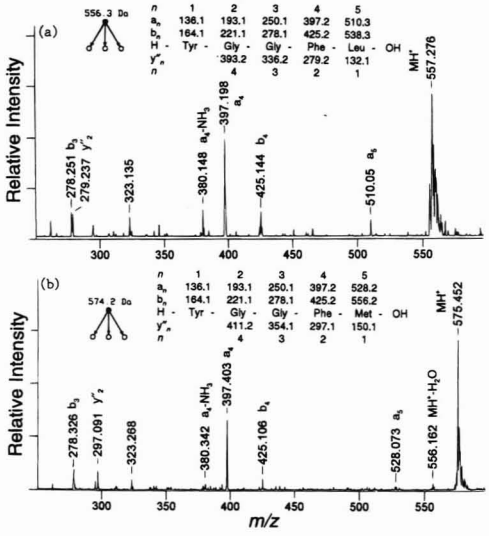

Figure 5. CID mass spectra of protonated molecular ions of (a) Leu-enkephalin (MW = 555.3) and (b) Met-enkephalin (MW = 573.2). In these spectra, the MH^+ ions at *m/z* 557.2 and 575.4 correspond to the ^{13}C isotopic peaks, since the monoisotopic peaks have been removed by excitation.

molecular ions at *m/z* 556.3 and 574.2 for the two similar peptides, Leu-enkephalin and Met-enkephalin, respectively. These peptides do not contain any basic residues, so fragmentation, primarily of the a_n and b_n types, is distributed along the peptide backbone. For Leu-enkephalin, the ratio of the y''_2 to b_3 ion has been shown to reflect the kinetic energy leading to collisional activation.[33,34] Generally, the intensity of the y''_2 ion becomes comparable to that of the b_3 ion for high-energy collisions.[33,34]

Figure 6a shows the CID spectrum for the protonated molecular ion at *m/z* 1141.7 for gramicidin S. This cyclic peptide requires at least two cleavages of the peptide backbone to produce the fragment ions that are observed. Because the first cleavage results only in opening the ring and not in a change in mass, the supplementary dipole field between the end-cap electrodes will continue to excite these ions until a second cleavage produces an ion of different mass, which then returns to the center of the trap. Gramicidin S is composed of two Leu-Phe-Pro-Val-Orn sequences connected in a head-to-tail fashion, so the peak at *m/z* 571.4 could represent any of a set of fragment ions corresponding to one-half of the molecule and is, therefore, particularly intense. Thus, in Figure 6b we have obtained the CID mass spectrum of ions with *m/z* 571.4, that is, an MS/MS/MS spectrum of gramicidin S. At the same time, the fragment ions observed in these spectra are consistent with a primary initial cleavage between ornithine and leucine, leading to the formation of an acylium ion. The b_n fragments formed from a second cleavage are also consistent with the formation of acylium ions.[35] The identity of these ions is then confirmed by the facile losses of CO observed at *m/z* 429.2, 543.3, and 803.4 in the two CID spectra.

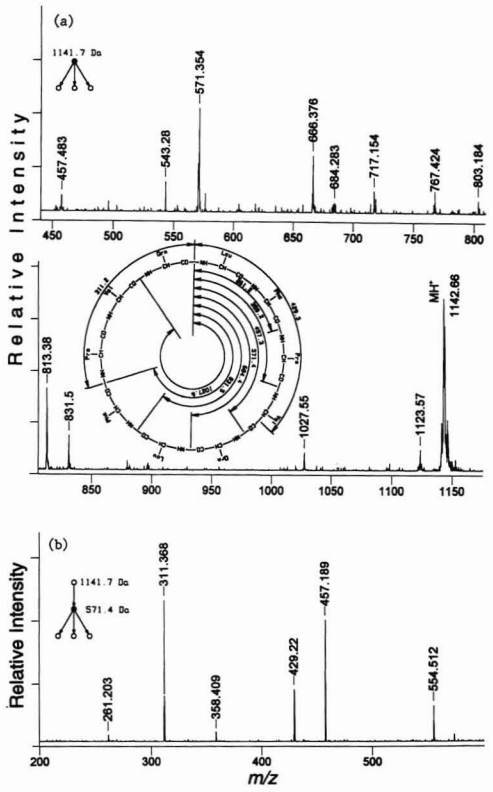

Figure 6. (a) MS/MS spectrum of protonated molecular ions of gramicidin S (MW = 1140.7). (b) MS/MS/MS spectrum obtained by excitation of the fragment at *m/z* 571.4. Ions shown in the inset were observed in the experiment. In this mass spectrum, the MH^+ ions at *m/z* 1142.7 correspond to the ^{13}C isotopic peak.

It is well known that the presence of proline residues can also direct the fragmentation of peptides.[36] Proline has a five-membered ring structure involving the amino nitrogen that reduces the bond strength of the amide bond on its N-terminal side. Thus, first cleavages at proline have often been observed for other cyclic peptides containing this residue.[37] In our spectra, the peak at *m/z* 767.4 corresponds to an initial cleavage between the Phe and Pro residues. In addition, the peak at *m/z* 311.4 in the MS/MS/MS spectrum might as well result from first and second cleavages at both Phe–Pro bonds (which would also result in the formation of an ion at half the mass of the molecular ion), followed by cleavage of the Orn–Leu bond through activation of these ions at *m/z* 571.4. However, in most instances it appears that the more basic ornithine residue directs the fragmentation, although this pattern is undoubtably dependent upon the collision energy.[38]

Figure 7 shows the CID mass spectrum of the protonated molecular ion of bombesin, which is the highest mass peptide (MW = 1618.8) presented in this work. Despite the presence of

(33) Baeten, W.; Claerboudt, J.; Van den Heuvel, H; Claeys, M. *Biomed. Environ. Mass Spectrom.* **1989**, *18*, 727.
(34) Alexander, A. J.; Boyd, R. K. *Int. J. Mass Spectrom. Ion Processes* **1989**, *90*, 211.
(35) Eckart, K. *Mass Spectrom. Rev.* **1984**, *13*, 23.
(36) Schwartz, B. L.; Bursey, M. M. *Biol. Mass Spectrom.* **1992**, *21*, 92.
(37) Tomer, K. B.; Crow, F. W.; Gross, M. L. *Anal. Chem.* **1984**, *56*, 880.
(38) Bradley, C. D.; Curtis, J. M.; Derrick, P. J.; Wright, B. *Anal. Chem.* **1992**, *64*, 2628.

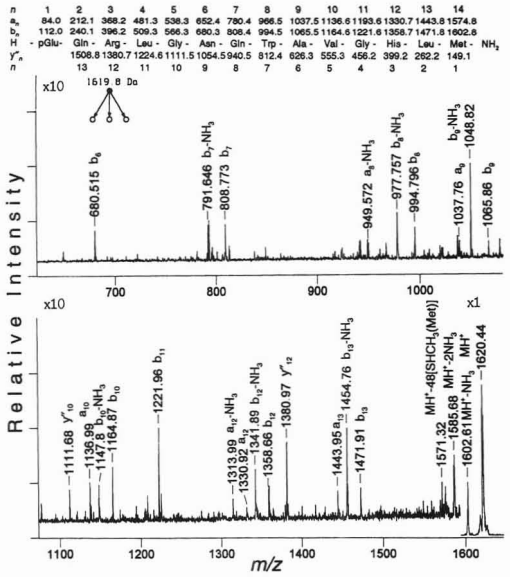

Figure 7. CID mass spectrum of protonated molecular ions of bombesin (MW = 1618.8). In this mass spectrum, the MH^+ ions at *m/z* 1620.4 correspond to the ^{13}C isotopic peak.

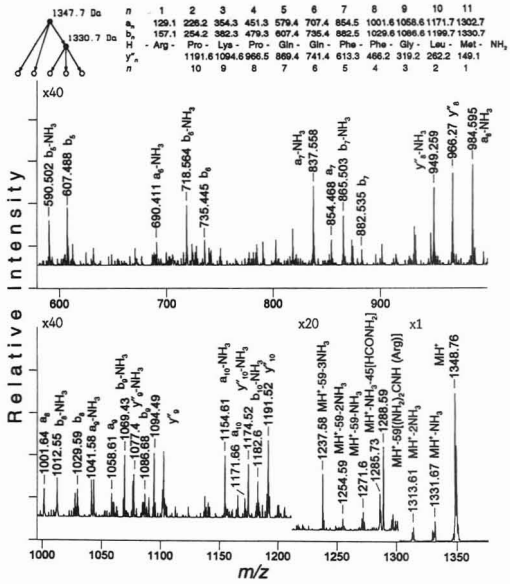

Figure 8. CID mass spectrum resulting from consecutive excitation of the monoisotopic protonated molecular ion at *m/z* 1347.7 of substance P (MW = 1346.7) and its most intense MS/MS fragment at *m/z* 1330.7. In this mass spectrum, the MH^+ ions at *m/z* 1348.8 correspond to the ^{13}C isotopic peak.

two basic residues, Arg and His, located near the amino and carboxy termini, respectively, the b_n ions (which encompass the more basic Arg residue) are more often observed than y''_n ions. a_n ions are also observed, as are extensive neutral losses (NH_3) and side-chain fragmentation.

It is often the case for larger peptides that the most abundant fragments resulting from CID of the protonated molecular ion are those corresponding to small neutral losses. This, of course, limits the information that could be obtained from lower mass, sequence-specific fragmentation. In the CID mass spectrum of substance P (MW = 1346.7), for example, the most abundant fragment ion results from the loss of neutral NH_3. In the experiment shown in Figure 8, we first isolated the protonated molecular ion cluster for substance P, activated the monoisotopic ion at *m/z* 1347.7, and then immediately activated the ion at *m/z* 1330.7 without isolating that ion. The composite CID spectrum shown in Figure 8 reveals ions resulting from the fragmentation of *m/z* 1347.7 and 1330.7. However, because of the similarity in the structures of these two precursors, the fragment ions can all be utilized to determine the amino acid structure. The presence of the basic residues, Arg and Lys, at the amino terminus results in a fragmentation pattern that consists primarily of a_n and b_n ions, as well as $a_n - NH_3$ and $b_n - NH_3$ ions arising from fragmentation of the ions at *m/z* 1330.7. In addition, y''_8, y''_9, and y''_{10} fragments reflect the presence of two proline residues.

Figure 9 shows the CID mass spectra of the sodium-cationized (MNa^+) molecules of Met-enkephalin (MW = 573.2) and Met-enkephalinamide (MW = 572.2). In these spectra a_n, b_n, and y''_n ions are replaced by their sodium cation analogs: $a_nNa - H$, b_n-$Na - H$, and y'_nNa. Although these two peptides differ only in their C-terminal groups, there are considerable differences in their CID mass spectra. For example, the rearrangement ions $b_nNa + OH$ observed at *m/z* 261.3, 318.3, and 465.4 in the CID mass

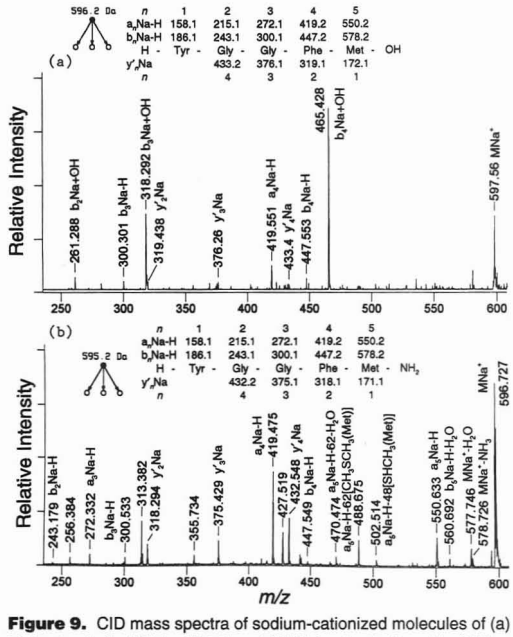

Figure 9. CID mass spectra of sodium-cationized molecules of (a) Met-enkephalin (MW = 573.2) and (b) Met-enkephalinamide (MW = 572.2). In these spectra, the MNa^+ ions at *m/z* 597.6 and 596.7 correspond to the ^{13}C isotopic peaks, since the monoisotopic peaks have been removed by excitation.

spectrum of Met-enkephalin (Figure 9a) are not observed in the CID mass spectrum of Met-enkephalinamide. These fragments are the formal equivalent to the $b'_6 + OH$ ion observed above for

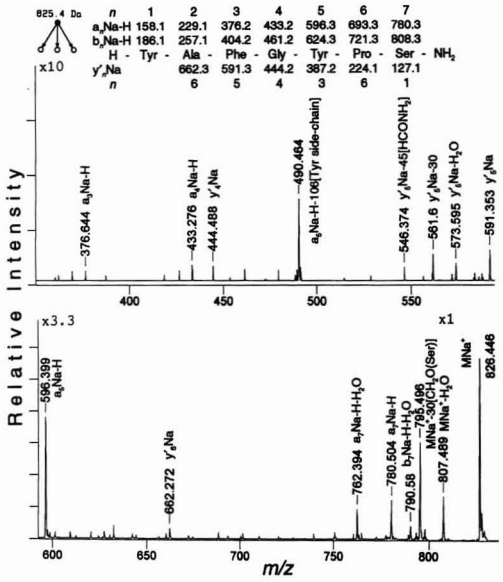

Figure 10. Tandem mass spectrum of sodium-cationized molecules of dermorphin (MW = 802.4). In this mass spectrum, the MNa^+ ions at *m/z* 826.4 correspond to the ^{13}C isotopic peak.

α-casein fragment 90–96. They have been observed in isolated cases on other mass analyzers,[31,39] while here they are observed as a series that can be used to recover the amino acid sequence. Also, in the CID mass spectrum of Met-enkephalin, the intensities of y'_nNa fragments are considerably less than those of the b_nNa + OH ions.

In the CID mass spectrum of Met-enkephalinamide (Figure 9b), the fragmentation pattern is considerably more complex and includes fragment ions formed by loss of small neutral species or side chains. Figure 10 shows that a similar result occurs in the CID mass spectrum of the MNa^+ ion of Dermorphin (MW = 802.4), which also has a C-terminal amide group. In this spectrum, there is sufficient fragmentation information to recover the full amino acid structure.

SUMMARY AND CONCLUSIONS

The technique involving modulation of the resonant ejection voltage so that it is proportional to the amplitude of the fundamental rf voltage was reported previously as a means for improving mass calibration by providing a linear dependence of the apparent mass shift on the scanned rf trapping voltage.[27] In this work, we have extended the same modulation technique to provide accurate mass assignments (within 0.2–0.3 Da down to the lowest mass) in CID product ion mass spectra. Combined with the better than unit mass resolution observed in all CID spectra (with the exception of the high-pressure spectrum), these results form the elements of high-performance CID that is normally enjoyed only on tandem sector and Fourier transform mass spectrometers. Most significant is the fact that these results are obtained for ions formed by MALDI inside the ion trap. Such ions have a high initial kinetic energy distribution, but an approach using collisions with helium at elevated pressures to assist in trapping would also compromise both mass accuracy and resolution. Thus, the use of a ramped trapping field to improve trapping efficiencies at low helium pressures[25] is as essential for high activation selectivity and mass accuracy for CID mass spectra of MALDI ions as it has been for high performance in normal mass spectra.[27]

While the CID mass spectra show abundant amino acid sequence-specific fragment ions, there are several problems in the general application of ion trap technology for peptide structure elucidation. Most prominent among these is the loss of the lower mass region. This problem is inherent in the ion trap, which is able to store only a finite region of mass for the product ions formed at the time of ion activation. In one case (gramicidin S), we addressed this problem by additional fragmentation of a prominent fragment ion of much lower mass. Alternatively, the CID mass range could be considerably extended using lower excitation frequencies. However, since the maximum energy associated with ion oscillatory motion is proportional to the square of the excitation frequency,[27] this would substantially decrease CID efficiency, which might be increased by the use of heavier buffer molecules[40] or through chemically reactive collisions.[41]

Additionally, there are a number of other techniques which, when combined with those described in this work, might significantly improve the performance of the ion trap mass spectrometer for peptide structural analysis using CID. For example, phase synchronization of the trapping and excitation voltages has been shown to improve the stability of mass calibration.[42] Additionally, isolation of isotopic clusters using broad-band excitation[22,23] might be combined with the selective activation and modulated ejection voltage methods described here. Finally, improvements in dynamic range might be achieved using selective injection of ions.[23,43,44]

ACKNOWLEDGMENT

This work was supported in part by grants from the National Science Foundation (DIR 90-16567) and National Institutes of Health (R01 RR08912-01) and was carried out at the Middle Atlantic Mass Spectrometry Laboratory, an NSF Shared Instrumentation Facility.

Received for review January 9, 1995. Accepted March 9, 1995.[⊗]

AC950030Y

[⊗] Abstract published in *Advance ACS Abstracts,* May 1, 1995.

(39) Mallis, L. M.; Russell, D. H. *Anal. Chem.* **1986**, *58*, 1076.

(40) Glish, G. L.; McLuckey, S. A.; Goeringer, D. E; Van Berkel, G. J.; Hart, K. J. Proceedings of the 39th ASMS Conference on Mass Spectrometry and Allied Topics; Nashville, TN, May 1991; p 536.

(41) Orlando, R.; Fenselau, C.; Cotter, R. J. *J. Am. Soc. Mass Spectrom.* **1992**, *2*, 189.

(42) Julian, R. K.; Reiser, H.; Cooks, R. G. *Int. J. Mass Spectrom. Ion Processes* **1993**, *123*, 85.

(43) Goeringer, D. E.; Asano, K. G.; McLuckey, S. A.; Hoekman, D.; Stiller, S. W. *Anal. Chem.* **1994**, *66*, 313.

(44) Garrett, A. W.; Cisper, M. E.; Nogar, N. S.; Hemberger, P. H. *Rapid Commun. Mass Spectrom.* **1994**, *8*, 174.

Anal. Chem. **1995**, *67*, 2188–2194

^{13}C NMR Spin–Lattice Relaxation Properties and Quantitative Analytical Methodology of ^{13}C NMR Spectroscopy for Coals

Antoni Jurkiewicz and Gary E. Maciel*

Department of Chemistry, Colorado State University, Fort Collins, Colorado 80523-0002

The quantitative reliability of ^{13}C NMR spectroscopy is examined and discussed. Studies were performed on eight Argonne Premium coals, using the nonoverlapping carbonyl peak of 4-(*N*-methylpyrrolidino)bicyclo[3.2.1]-octan-8-one triflate as an intensity reference. ^{13}C spin–lattice relaxation times measured by cross-polarization (CP) detection depend on the CP contact time. A series of experiments with different CP contact times yielded observed ^{13}C spin–lattice relaxation times that are significantly larger than those previously reported in the literature. The relaxation time characteristic of the most slowly relaxing carbons, T_{1S}, was determined for the aromatic carbons and for the aliphatic carbons of each coal. Then, if one uses repetition delays that are $>5T_{1S}$, quantitative results can be expected for the NMR-observable carbons in a direct polarization (DP) experiment. Carbon spin counting experiments performed by using DP instead of CP yielded numbers for the fraction of carbon spins that are 81–97% of those present in the sample. A relationship was observed between the number of unpaired electron spins and the fraction of ^{13}C spins detected. The role of unpaired electron spin dynamics on the effective electron magnetic moment is considered, and the corresponding influence on ^{13}C NMR detection is discussed.

The quantitative reliability of ^{13}C NMR spectroscopy as an analytical tool in studies of the chemical functionality of a complicated large macromolecular system like coal has been discussed many times since the introduction of this approach.[1–11] This topic generated a "debate" with the participation of several laboratories.[12] In this debate, the complicated spin dynamics of the ^{13}C cross polarization with magic-angle spinning (CP-MAS) experiment for coal and the role of unpaired electron spins were pointed out. There is general agreement that, in terms of the quantitative reliability of ^{13}C NMR spectroscopy in coals, the direct polarization (DP) technique, because of its simplicity and avoidance of CP, is more reliable than cross-polarization techniques. Nevertheless, in spite of a big effort to define the problems in ^{13}C NMR experiments on coal and the various ways suggested for improving the situation, the quantitative reliability of ^{13}C NMR via DP-MAS approaches still has a major obstacle that detracts from experimental accuracy and hinders definitive conclusions, uncertainty in the relevant value(s) of the ^{13}C spin–lattice relaxation time (T_1^C), which is the most important parameter in quantitative analysis by ^{13}C DP-MAS NMR. We have found significant confusion regarding the published data related to that problem; e.g., some researchers are comfortable performing ^{13}C DP-MAS analysis of Argonne Premium coals by applying a repetition delay of 20–100 s,[13] while other researchers use delays between 60 and 100 s.[14] The basis and consequences of such differences are important issues; in particular, whether or not a 20 s repetition delay is sufficient to completely relax the ^{13}C magnetization in coal is an important issue that is addressed in this paper.

This obstacle is exacerbated by the overlapping between coal peaks and the peaks of intensity standards commonly employed in ^{13}C experiments on coal, often imposing the necessity for spectral deconvolution, which inevitably introduces an additional source of error in the analysis. This kind of computer fitting process is especially uncertain and difficult in the case of a spectrum with very broad (often irregularly shaped) peaks, e.g., that of a typical coal or a humic acid.

Tetrakis(trimethylsilyl)silane (TKS),[13–15] hexamethylbenzene,[5] and Delrin[16,17] are the ^{13}C NMR intensity standards most commonly used for coal studies. To some degree, all of these compounds yield some overlap of their ^{13}C peak(s) with those of the coal spectrum. Therefore, we took advantage of the signal of the ^{13}C-enriched carbonyl position of 4(*N*-methylpyrrolidino)-bicyclo[3.2.1]loctan-8-one triflate (321-^{13}CO), for which the 217 ppm peak does not overlap with a typical coal spectrum, as an intensity standard. The synthesis and NMR characteristic of this standard have been published previously.[18]

(1) VanderHart, D. L.; Retcofsky, H. L. *Fuel* **1976**, *55*, 202.
(2) Miknis, F. P.; Sullivan, M.; Bartuska, V. J.; Maciel, G. E. *Org. Geochem.* **1981**, *3*, 19.
(3) Sullivan, M. J.; Maciel, G. E. *Anal. Chem.* **1982**, *54*, 1615.
(4) Wind, R. A.; Duijvestijn, M. J.; van der Lugt, C.; Smidt, J.; Vriend, J. *Fuel* **1987**, *66*, 1987.
(5) Botto, R. E.; Wilson, R.; Winans, R. E. *Energy Fuels* **1987**, *1*, 173.
(6) Wilson, M. A.; Pugmire, R. J.; Karas, J.; Alemany, L. B.; Woolfenden, W. R.; Grant, D. M.; Given, P. *Anal. Chem.* **1984**, *56*, 933.
(7) Dudley, R. L.; Fyfe, C. A. *Fuel* **1982**, *61*, 651.
(8) Muntean, J. V.; Stock, L. M.; Botto, R. E. *Energy Fuels* **1988**, *2*, 108.
(9) Franz, J. A.; Linehan, J. C. In *Magnetic Resonance of Carbonaceous Solids*; Botto, R. E., Sanada, Y., Eds.; Advances in Chemistry 229; American Chemical Society: Washington, DC, 1993.
(10) Wind, R. A. In *Magnetic Resonance of Carbonaceous Solids*; Botto, R. E., Sanada, Y., Eds.; Advances in Chemistry 229; American Chemical Society: Washington, DC, 1993.
(11) Jurkiewicz, A.; Leenheer, J. A.; Maciel, G. E. *Prepr. Am. Chem. Soc., Div. Environ. Chem.* **1993**, *33*, 178.
(12) Snape, C. E.; Axelson, D. E.; Botto, R. E.; Delpuech, J. J.; Tekely, P.; Gerstein, B. C.; Pruski, M.; Maciel, G. E.; Wilson, M. A. *Fuel* **1989**, *68*, 547.
(13) Muntean, J. V.; Stock, L. M.; Botto, R. E. *J. Magn. Reson.* **1988**, *76*, 540.
(14) Franz, J. A.; Garcia, R.; Linehan, J. C.; Love, G. D.; Snape, C. E. *Energy Fuels* **1992**, *6*, 598.
(15) Muntean, J. V.; Stock, L. M. *Energy Fuels* **1991**, *5*, 767.
(16) Zhang, M.; Maciel, G. E. *Fuel* **1990**, *69*, 557.
(17) Pan, V. H.; Maciel, G. E. *Fuel* **1993**, *72*, 451.

0003-2700/95/0367-2188$9.00/0 © 1995 American Chemical Society

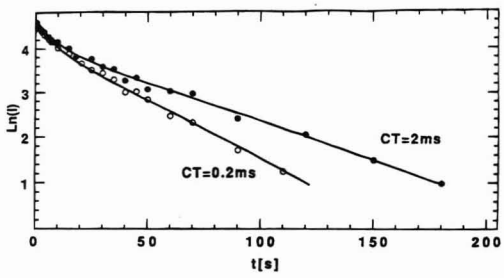

Figure 1. ^{13}C spin–lattice relaxation magnetization decays of the aromatic peak of Pocohontas no. 3 coal, recorded with two different CP contact times (CT).

^{13}C spin–lattice relaxation in Argonne Premium coals have been studied previously by techniques based on cross polarization.[13,17,19,20] Our recent studies of the spin dynamics involved in CP polarization transfer in Argonne coals led us to the view that T_1^C values determined via cross-polarization experiments depend on the length of the CP contact time employed.[21] Hence, the correct value of T_1^C might not necessarily be obtained from experiments employing only a single contact time. The resulting error in T_1^C could affect the quantitative reliability of ^{13}C NMR analysis of coals. Therefore, the goal of the investigation reported here is to improve the characterization of ^{13}C spin–lattice relaxation in coals in the sense that DP-MAS ^{13}C NMR spectroscopy can be the more quantitative analytical tool that is desired for the chemical characterization of coals. The perspective gained from these results can also be useful in assessing or developing quantitative ^{13}C NMR analysis of humic substances, polymers, biopolymers, wood, and other complex macromolecular organic systems, where quantitation is important.

EXPERIMENTAL SECTION

The solid-state ^{13}C DP-MAS and ^{13}C CP-MAS NMR experiments were carried out at 22.7 MHz on a Chemagnetics M-100/90 spectrometer. A large-volume Kel-F MAS system[16] was used with a 3.2 kHz MAS speed. The 4(*N*-methylpyrrolidino)bicyclo-[3.2.1]octa-8-one triflate intensity reference (321-^{13}C; T_1^C is 61 s at 22.7 MHz) was inserted into a Kel-F tube and placed along the rotor axis. T_1^C values were obtained by a Freeman-Hill version of the ^{13}C CP-MAS inversion recovery method. Because of poor signal-to-noise ratio, we were unable to perform accurate T_1^C measurements if cross polarization was not employed, in spite of the large-volume (2.5 cm^3) of the jumbo MAS rotor. The eight Argonne Premium coals were obtained from the Premium Coal Bank of the Argonne National Laboratory.[22]

RESULTS

1. ^{13}C Spin–Lattice Relaxation of Aromatic Resonances of Coals. Figure 1 shows ^{13}C spin–lattice relaxation magnetization decays of the aromatic resonance of Pocohontas no. 5 coal,

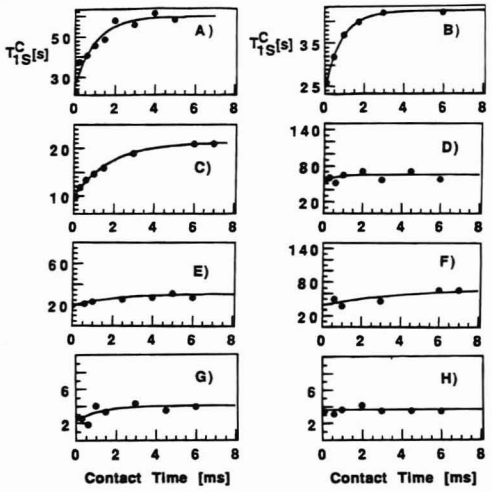

Figure 2. Plots of the spin–lattice relaxation time constant (T_{1S}^C) of the slowly relaxing component of the aromatic peak vs the CP contact time for Argonne Premium coals: (A) Pocohontas no. 3 (B) Lewiston-Stockton, (C) Blind-Canyon, (D) Upper-Freeport, (E) Illinois no. 6, (F) Pittsburgh no. 8, (G) Buelah-Zap, and (H) Wyodak-Anderson.

obtained with two different CP contact times (CT). For each curve, the magnetization decay appears to consist of two components, fast and slow, and can be described according to an equation of the following type:

$$M(t) = A_F \exp(-t/T_{1F}^C) + A_S \exp(-t/T_{1S}^C) \qquad (1)$$

where A_F and A_S are the initial amplitudes of the fast-relaxing and slowly relaxing components, respectively, and T_{1F}^C and T_{1S}^C are the corresponding magnetization decay time constants (relaxation times). It is obvious from Figure 1 that the measured spin–lattice relaxation parameters depend on the value of the CP contact time used in an experiment. On the other hand, to achieve quantitative spectral intensities in a ^{13}C DP-MAS experiment, one should choose a recycle delay that is at least 5 times greater than the largest T_1^C value.

Numerous experiments with different CP contact times were performed on each sample in order to determine the *largest* T_1^C value in each sample. The relationships between measured ^{13}C spin–lattice relaxation times of the slowly relaxing aromatic component(s), T_{1S}^C, and the CP contact time (CT) used in the T_1^C measurement is presented for all eight coals in Figure 2. For three samples, Pocohontas no. 3 (Figure 2A), Lewiston-Stockton (Figure 2B), and Blind Canyon (Figure 2C), the measured ^{13}C spin–lattice relaxation time is seen to depend strongly on the duration of the contact period. For Upper Freeport (Figure 2D), Illinois no. 6 (Figure 2E), Pittsburgh no. 8 (Figure 2F), and Buelah-Zap (Figure 2G), coals, there is still a noticeable dependence, but it is not as strong as for the first three coals mentioned. For the Wyodak-Anderson coal (Figure 2H), the measured value of T_{1S}^C does not depend substantially on the CP contact time.

Figure 3 shows the dependence of the derived T_{1F}^C values of the aromatic carbon peak upon the CP contact time. It is seen that T_{1F}^C is essentially independent of the CP contact time for the

(18) Hall, R. A.; Jurkiewicz, A.; Maciel, G. E. *Anal. Chem.* **1993**, *65*, 534.
(19) Botto, R. E.; Axelson, D. E. *Prepr. Pap.-Am. Chem. Soc., Div. Fuel Chem.* **1988**, *33*(3), 50–57.
(20) Tsiao, C.; Botto, R. E. in *Magnetic Resonance of Carbonaceous Solids*; R. E., Botto, Sanada, Y., Eds.; Advances in Chemistry 229; American Chemical Society: Washington, DC, 1993.
(21) Jurkiewicz, A.; Maciel, G. E. *Fuel* **1994**, *73*, 828.
(22) Vorres, K. S. *Energy Fuels* **1990**, *4*, 420.

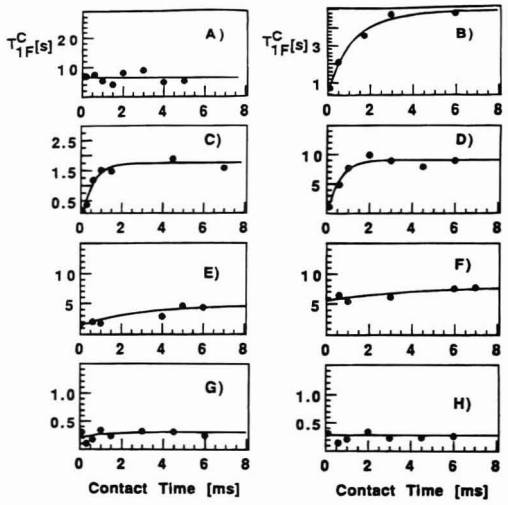

Figure 3. Plots of the spin–lattice relaxation time constant (T^c_{1F}) of the fast-relaxing component of the aromatic peak vs the CP contact time for Argonne Premium coals: (A) Pocohontas no. 3, (B) Lewiston-Stockton, (C) Blind-Canyon, (D) Upper-Freeport, (E) Illinois no. 6, (F) Pittsburgh no. 8, (G) Buelah-Zap, and (H) Wyodak-Anderson.

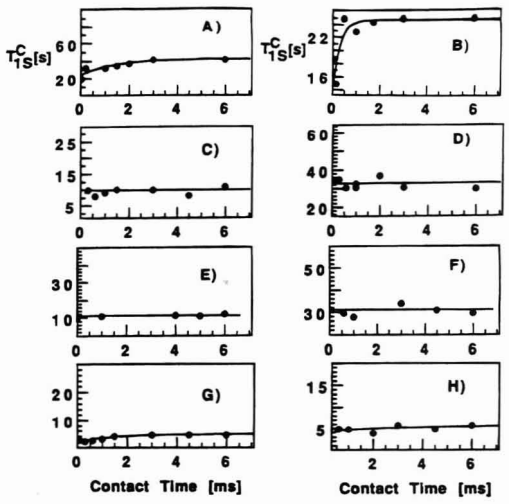

Figure 4. Plots of the spin–lattice relaxation time constant (T^c_{1S}) of the slowly relaxing component of the aliphatic peak vs the CP contact time for Argonne Premium coals: (A) Pocohontas no. 3, (B) Lewiston-Stockton, (C) Blind-Canyon, (D) Upper-Freeport, (E) Illinois no. 6, (F) Pittsburgh no. 8, (G) Buelah-Zap, and (H) Wyodak-Anderson.

Pocohontas no. 3 (Figure 3A) Wyodak-Anderson (Figure 3H), and Buelap-Zap (Figure 3G) samples. The Lewiston-Stockton (Figure 3B) and Blind-Canyon (Figure 3C) coals would apparently require a larger CP contact time than 6 or 7 ms in order to find the maximum T^c_{1F} value of the fast-relaxing component. In any case, *the time constants of these fast-relaxing components are not important in determining the recycle delay needed for quantization in DP-MAS ^{13}C experiments;* their usefulness is rather the importance for understanding details of the mechanism of spin–lattice relaxation processes in coals, not a primary goal of this paper.

2. ^{13}C Spin–Lattice Relaxation of Aliphatic Resonances in Coals. Figure 4 shows the dependence of the measured ^{13}C spin–lattice relaxation constant of the slowly relaxing aliphatic component on the CP contact time. In general, the dependence of T^c_{1S} on the CP contact time is not as strong as in the case of the aromatic resonance. The strongest dependence was observed for the Lewiston-Stockton coal (Figure 4B). Pocohontas no. 3 (Figure 4A) and Buelah-Zap (Figure 4G) coals display weak dependence of T^c_{1S} on the CP contact time. Other samples show almost no dependence of T^c_{1S} on the CP contact time.

The dependence of the T^c_1 value for the fast-relaxing component of the aliphatic peak is shown in Figure 5. The T^c_{1F} values of the Lewiston-Stockton and Beulah-Zap coals increase slightly as the CP contact time is increased, and for the aliphatic peaks of five of the remaining coals there is essentially no dependence of T^c_{1F} on CT. It is interesting to note that in one plot (Figure 5D, for the Upper-Freeport coal) the behavior is totally different from what is seen in the other plots of Figure 2–5. In this one case, the T^c_1 parameter *decreases* convincingly when the CP contact time is increased.

Figures 6 and 7 show the dependences of A_S and A_F, corresponding to the T^c_{1S} and T^c_{1F} values according to eq 1, derived from the ^{13}C CP-MAS T^c_1 measurements as a function of the CP contact time. These plots correspond to Figures 2–5 for T^c_1 values.

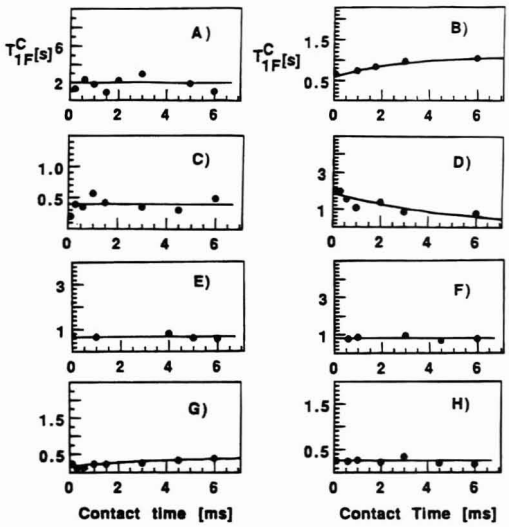

Figure 5. Plots of the spin–lattice relaxation time constant (T^c_{1F}) of the fast-relaxing component of the aliphatic peak vs the CP contact time for Argonne Premium coals: (A) Pocohontas no. 3, (B) Lewiston-Stockton, (C) Blind-Canyon, (D) Upper-Freeport, (E) Illinois no. 6, (F) Pittsburgh no. 8, (G) Buelah-Zap, and (H) Wyodak-Anderson.

3. Carbon Spin Counting Experiments. The maximum T^c_1 values for the fast-relaxing and slowly relaxing components of the aliphatic and aromatic peaks of each coal are presented in Table 1 as T^c_{1Fmax} and T^c_{1Smax}, respectively. The T^c_{1Smax} values were used as the basis for choosing appropriate values of the recycle delay (RD) for direct-polarization ^{13}C DP-MAS experiments. Such experiments were carried out for the purpose of carbon spin counting. The RD values chosen were, in each case, at least 5 times greater than the largest T^c_{1S} values derived

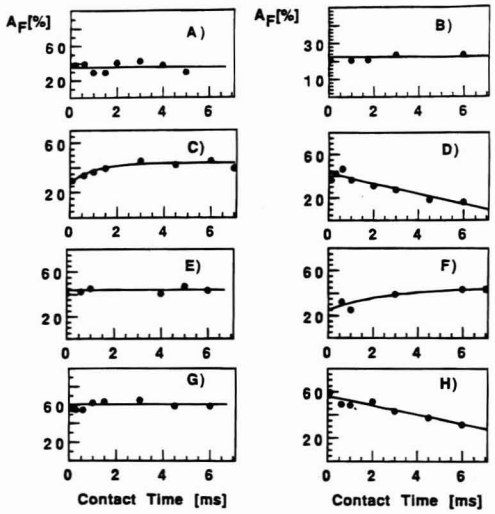

Figure 6. Plots of the weighting coefficient A_F (eq 1) for T^c_{1F} determined *via* ^{13}C CP-MAS experiments vs the CP contact time for the aromatic peaks of Argonne Premium coals: (A) Pocohontas no. 3, (B) Lewiston-Stockton, (C) Blind-Canyon, (D) Upper-Freeport, (E) Illinois no. 6, (F) Pittsburgh no. 8, (G) Buelah-Zap, and (H) Wyodak-Anderson.

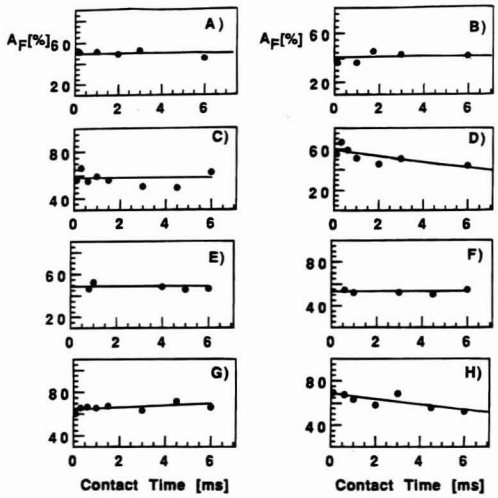

Figure 7. Plots of the weighting coefficient A_F (eq 1) for T^c_{1F} determined via ^{13}C CP-MAS experiments vs the CP contact time for the aliphatic peaks of Argonne Premium coals: (A) Pocohontas no. 3, (B) Lewiston-Stockton, (C) Blind-Canyon, (D) Upper-Freeport, (E) Illinois no. 6, (F) Pittsburgh no. 8, (G) Buelah-Zap, and (H) Wyodak-Anderson.

experimentally for the aliphatic or aromatic peaks, i.e., RD > $5T^c_{1Smax}$. For the Upper-Freeport and Pittsburgh no. 8 samples, the resulting recycle delay was rather long, 335 and 325 s, respectively. However, because of using a MAS system with a very large rotor (2.5 cm^3), we could still often obtain a good quality spectrum in a resonably short time (e.g., 8 h). A 20.5 s recycle delay was the smallest value used, to study the Beulah-Zap lignite.

Table 1. ^{13}C Spin–Lattice Relaxation Times of Argonne Premium Coals

	aromatic			aliphatic		
sample	T^c_{1Fmax} (s)	T^c_{1Smax} (s)	A_{Fmax} (%)	T^c_{1Fmax} (s)	T^c_{1Smax} (s)	A_{Fmax} (%)
Upper-Freeport	9.0	67	42	2.0	33	60
Wyodak-Anderson	0.28	5.6	55	0.28	5.8	65
Illinois no. 6	4.6	32	44	0.67	12	50
Pittsburgh no. 8	7.5	65	42	0.80	31	55
Pocohontas no. 3	6.5	59	37	2.0	42	50
Blind-Canyon	1.8	21	44	0.40	10	58
Lewiston-Stockton	4.8	42	23	1.05	25	43
Buelah-Zap	0.30	4.0	60	0.30	4.1	64

T^c_{1Fmax}, maximum value of the ^{13}C spin–lattice relaxation time of the fast-relaxing component, determined as a function of the CP contact time (CT).

T^c_{1Smax}, maximum value of the ^{13}C spin–lattice relaxation time of the slowly relaxing component, determined as a function of the CP CT.

A_F, fraction of fast-relaxing component, determined by extrapolation of the plot of A_F vs CT.

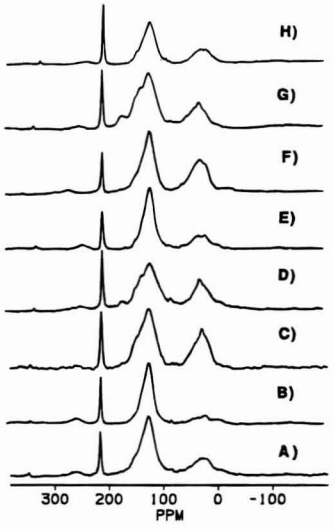

Figure 8. ^{13}C DP-MAS spectra of Argonne Premium coals obtained with the 321-^{13}CO intensity reference (217 ppm): (A) Lewiston-Stockton, (B) Pocohontas no. 3, (C) Blind-Canyon, (D) Wyodak-Anderson, (E) Upper-Freeport, (F) Illinois no. 6, (G) Buelah-Zap, and (H) Pittsburgh no. 8.

The resulting DP-MAS ^{13}C spectra of the eight coals are presented in Figure 8. The relatively sharp peak at 217 ppm in each spectrum belongs to the 321-^{13}CO intensity standard, which contains 5.806×10^{19} ^{13}C spins at the ^{13}C-enriched carbonyl position.

The weights of the coal samples examined by the ^{13}C DP-MAS measurements ranged between 1.5 and 1.8 g. The fractions of ^{13}C spins that were detected in each of these eight coals, as determined by integrated intensities, are shown in Table 2. For comparison with our results, we also include the results of similar studies reported earlier.[14,15]

DISCUSSION

The most apparent feature manifested by the results obtained from the studies described above is represented in the following

Table 2. Aromaticity (f_a) and Percent of ^{13}C Spins Observed (C_{obs}) in Argonne Premium Coals as Determined via ^{13}C DP-MAS NMR

sample	this study	C_{obs} (%) ref 13	ref 14	f_a
Upper-Freeport	96 ± 3	75	70	0.80 ± 0.03
Wyodak-Anderson	89 ± 5	95	58	0.70 ± 0.04
Illinois no. 6	97 ± 3	85	72	0.71 ± 0.03
Pittsburgh no. 8	81 ± 3	90	80	0.73 ± 0.04
Pocohontas no. 3	87 ± 6	90	82	0.86 ± 0.05
Blind-Canyon	93 ± 7	75	90	0.63 ± 0.04
Lewiston-Stockton	92 ± 6	75	84	0.71 ± 0.05
Buelah-Zap	90 ± 5	95	65	0.66 ± 0.05

statement of a well-recognized fact: there is no single T_1^C value that can adequately characterize the ^{13}C spin–lattice relaxation of any aromatic or alphatic peak of any one of the eight coals. Instead, there is a distribution of T_1^C values, which we have modeled in eq 1 by a sum of two exponential terms, and the nature of the measured distribution may depend on the CP contact time in a CP-MAS T_1^C experiment. In general, the dynamics of a specific spin set in a $^1H \rightarrow {}^{13}C$ cross-polarization experiment is governed by a pair of time constants T_{CH} and $T_{1\varrho}$,[23,24] according to the following equation:

$$M(t) = M^*/(1 - T_{CH}/T_{1\varrho})[\exp(-\tau/T_{1\varrho}) - \exp(-t/T_{CH})] \quad (2)$$

In this equation, which is valid for the case of $T_{1\varrho}^C \gg T_{CH}$, $T_{1\varrho}^H \equiv T_{1\varrho}$, $M(t)$ is the ^{13}C magnetization generated in a CP contact time t, T_{CH} is the CP cross-relaxation time constant and, $T_{1\varrho}$ is the proton rotating-frame spin–lattice relaxation time. Both time constants are related to the dipolar interaction between protons and carbons and among protons themselves, which depend on internuclear distances as well as motional dynamics. The T_{CH} value is sensitive to proton–carbon distances, and proton–proton distances are important for $T_{1\varrho}$.

In heterogeneous macromolecules like coal, we can expect a complicated distribution of proton–proton and proton–carbon distances. The distribution of proton–proton interactions has been studied theoretically by investigation of the second moment of the proton NMR spectrum for models of coal structure.[25] It was found that proton dipolar coupling depends not only on the chemical nature of the particular fragments of macromolecules but also on the spatial arrangements and proximities of such fragments within the entire structure. The contribution that comes from *inter*molecular dipolar couplings is almost twice as large as the contribution related to *intra*molecular proton–proton dipolar coupling. In the sense used here, the term *inter*molecular can apply to interactions betweeen different segments of a macromolecule, where these segments are separated by a large number of covalent bonds. In this sense, *intra*molecular applies to interactions *within* such segments. It was learned that protons separated by distances up to 9 Å yield significant contributions to the overall proton–proton dipolar coupling.[25] These results on $^1H-{}^1H$ dipolar interactions lead one to expect a complicated distribution of carbon–proton dipolar coupling in coal, which should be considered when discussing the overall strength of the carbon–proton coupling and the efficiency of energy transfer in a cross-polarization experiment.

In terms of carbon–proton dipolar strength, the following domains can be visualized:

(1) Carbons with directly attached protons in a relatively rigid framework. $^1H-{}^{13}C$ dipolar coupling is strong and only a small CP contact time is needed for cross polarization.

(2) Carbons within a rigid framework of condensed aromatic rings and therefore farther from protons. The larger intramolecular distance between a carbon and the nearest protons is large, yielding weak $^1H-{}^{13}C$ coupling. Long CP contact periods are needed for observation in a ^{13}C CP-MAS experiment. It is worth stressing that if the proton rotating-frame spin–lattice relaxation time $T_{1\varrho}$ is very small, the carbons might never be observed in a CP-MAS experiment.

(3) Carbons in a rigid structural environment that experience substantial *inter*molecular dipolar interactions with appropriately situated protons in nearly molecules. This kind of intermolecular contribution has previously been shown to be important for $^1H-{}^1H$ dipolar interactions in coal.[25]

(4) Carbons that are part of a *mobile* molecular structure or a mobile segment of a partially mobile macromolecular structure, in contrast to our view of domain types 1, 2, and 3, for which we have assumed rigid structures. From other studies on coal,[26–29] we recognize the existence of both a rigid macromolecular network and a mobile molecular part. The mobile molecules and mobile fragments of macromolecules will have resultant dipolar coupling that are dramatically reduced relative to what they would be in a corresponding rigid framework,[30] making polarization transfer more difficult and requiring longer CP contact times in a CP-MAS ^{13}C experiment.

The structural situation represented in the structural/dynamical model embodied in domain types 1–4 specified above corresponds to a sufficiently complicated heterogeneous macromolecular structure, that a CP-MAS experiment carried out with only one CP contact time is unlikely to yield a T_1^C value that would lead one to the goal of detecting all carbons in a ^{13}C DP-MAS experiment based on that T_1^C value.

The distribution of T_1^C values measured as a function of contact time can also be discussed in terms of spin temperature. In the case of a heterogeneous macromolecular structure with different local segmental dynamics, neither the ^{13}C nor ^1H spin reservoirs can be described as a system with a single homogeneous spin temperature during the cross-polarization process. A variety of strengths of dipolar couplings in different parts of the structure can give rise to spin–temperature gradients across the structure.[23,31] Each part of the structure would be detected optimally in a ^{13}C CP-MAS experiment with its own appropriate and specific cross-polarization conditions.

As we can see from Figures 2–5, more significant dependences of the measured T_1^C values on the CP contact time in a CP-MAS

(23) Mehring, M. *Principles of High Resolution NMR in Solids*, 2nd ed.; Springer-Verlag: Berlin, 1983.
(24) Demco, D. E.; Tegenfeldt, J.; Waugh, J. S. *Phys. Rev.* **1975**, *11*, 4133.
(25) Jurkiewicz, A. *J. App. Phys.* **1987**, *62*, 3892.
(26) Jurkiewicz, A.; Marzec, A.; Pislewski, N. *Fuel* **1982**, *61*, 647.
(27) Barton, W. A.; Lynch, L. J.; Webster, D. S. *Fuel* **1984**, *63*, 1262.
(28) Jurkiewicz, A.; Bronnimann, C. E.; Maciel, G. E. *Fuel* **1990**, *69*, 804.
(29) Jurkiewicz, A.; Bronnimann, C. E.; Maciel, G. E. *Fuel* **1989**, *68*, 872.
(30) Abragam, A. *The Principles of Nuclear Magnetism*; Clarendon Press: Oxford, U.K., 1961.
(31) Wu, X.; Zilm, K. W. *J. Magn. Reson.* **1991**, *93*, 265.

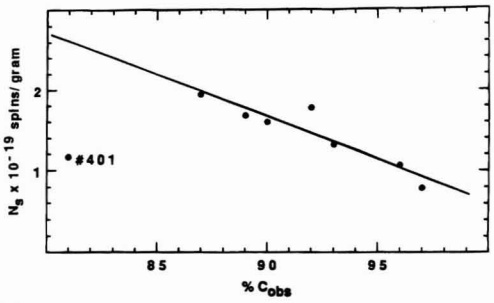

Figure 9. Plot of the concentration of unpaired electron spins N_s vs percent of observed carbons (% C_{obs}).

T_1^c experiment occur among aromatic resonances than among aliphatic resonances. Aromatic carbons on average bear fewer hydrogens than do aliphatic carbons. This situation might cause the distribution of carbon–proton distances and $^1H-^{13}C$ dipolar couplings among aromatic carbons to be broader, and optimal polarization transfer might be expected to require a broader range of CP contact times. It is also interesting that the measured T_1^c values in low-rank coals are less sensitive to the duration of cross polarization than the T_1^c values of higher rank coals. On the other hand, we know from elemental analysis that such coals contain more protons in their structure than do coals of high rank.[22] Therefore, for the same reason as indicated above, the dependence of measured T_1^c values on CP contact time might be smaller for these more proton-rich structures. Again, the intermolecular spatial arrangement of macromolecules might also be a significant factor.

The number of ^{13}C spins observed in the DP-MAS experiments represented in Figure 9 range between 81 and 97%. An important question is why, in spite of applying recycle delays that are at least $5T_{1Smax}^c$ and using a nonoverlapping intensity reference, are not all ^{13}C spins detected? Related to this question is the reason why different behaviors are observed for different coals: For Illinois no. 6, 97% of the ^{13}C can be detected, but for Pittsburgh no. 8, only 81% of the ^{13}C can be detected. In trying to find a satisfactory answer to these questions, we examined the relationship between the concentration of unpaired electrons and the percent observation of carbons by ^{13}C DP-MAS NMR. The concentrations of unpaired electrons in all eight Argonne Premium coals have been reported previously.[32–36] Silbernagel and Botto[37] presented an excellent review of those results, which are plotted vs the percent carbon observed in our spin counting experiments in Figure 9. One can see a roughly linear relationship between the concentration of unpaired electron spins and the fraction of carbons that can be observed in ^{13}C DP-MAS NMR. For seven of the coal samples there is a very good fit; only the Pittsburgh no. 8 coal deviates substantially from the correlation for the other coals.

If one attempts to explain the results summarized in Figure 9, one should consider the nature of the interactions between unpaired electrons and nuclear spins. ^{13}C nuclei located very near (e.g., <10 Å) an unpaired electron interact with it by dipolar or scalar interactions, or both, yielding a very broad NMR line that is essentially impossible to observe. Except for nuclei that are within a few covalent bonds of an unpaired electron in the same molecule, the scalar coupling is very small. Since the number of such ^{13}C nuclei in coal is a very small fraction of all the ^{13}C spins in the sample, the scalar interaction is not a major influence on ^{13}C detectability. If one considers the contribution to broadening of the ^{13}C NMR line due to dipolar interactions with electron paramagnetic centers,[25,38–40] one recognizes that it is the z-components of the magnetic moments of the paramagnetic centers that are effective in broadening the resonance of the nuclear spin. The effective electron spin magnetic moment, μ_{eff}, depends upon the angular momentum quantum number of the paramagnetic center, the temperature, the magnetic field strength (B_0), the width of the NMR peak, and the correlation time (τ_c) for fluctuations of the magnetic moment of the paramagnetic center. The parameter τ_c is usually related to the spin–lattice relaxation time of the unpaired electrons,[39,40] T_{1e}, which was measured for all Argonne Premium coals by ESR spectroscopy by Silbernagel et al.[34] for the broad and narrow organic radical ESR components. The Pittsburgh no. 8 sample was found to be uncommon among the Argonne Premium coals in terms of having by far the smallest T_{1e} value of the broad organic radical component. This might be associated with the fact that this particular coal does not follow the general relation shown in Figure 9 between the fraction of ^{13}C spins detected and the ^{13}C spin–lattice relaxation time. It might be interesting to carry out similar studies on a larger set of coals, so perhaps a relationship could be established in which one could have greater confidence.

Since the effective magnetic moment of unpaired electron spins depends linearly on B_0, it is reasonable to expect that the number of ^{13}C spins observed in ^{13}C NMR experiments carried out on different spectrometers will vary from field to field. This might be another good reason for not carrying out ^{13}C NMR studies of coals at high magnetic fields, even if problems with cross polarization and spinning side bands[12] can be solved.[10,41] Since μ_{eff} depends inversely on the temperature, a higher temperature might decrease the effective electron spin magnetic moment, thus possibly yielding a larger fraction of carbons observed. However, the electron spin correlation time τ_c should also be temperature dependent, so a reliable prediction of the effect of temperature variation on μ_{eff} would require a knowledge of τ_c's temperature dependence. Since the line broadening of the nuclear spin resonance due to dipolar interactions with unpaired electrons also

(32) Rothenberger, K. S.; Sprecher, R. F.; Castellano, S. M.; Retcofsky, H. L. In *Magnetic Resonance of Carbonaceous Solids*; Botto, R. E., Sanada, Y., Eds.; Advances in Chemistry 229; American Chemical Society: Washington, DC, 1993.

(33) Tsvetkov, Y. D.; Dzuba, S. A.; Gulin, V. I. In *Magnetic Resonance of Carbonaceous Solids*; Botto, R. E., Sanada, Y., Eds.; Advances in Chemistry 229; American Chemical Society: Washington, DC, 1993.

(34) Silbernagel, B. G.; Gebhard, L. A.; Bernardo, M.; Thoman, H. In *Magnetic Resonance of Carbonaceous Solids*; Botto, R. E., Sanada, Y., Eds.; Advances in Chemistry 229; American Chemical Society: Washington, DC, 1993.

(35) Chen, X. C.; McManus, H.; Kevin, L. In *Magnetic Resonance of Carbonaceous Solids*; Botto, R. E., Sanada, Y., Eds.; Advances in Chemistry 229; American Chemical Society: Washington, DC, 1993.

(36) Keneko, T.; Sasaki, M.; Yokono, T.; Sanada, Y. In *Magnetic Resonance of Carbonaceous Solids*; Botto, R. E., Sanada, Y., Eds.; Advances in Chemistry 229; American Chemical Society: Washington, DC, 1993.

(37) Silbernagel, B. G.; Botto, R. E. In *Magnetic Resonance of Carbonaceous Solids*; Botto, R. E., Sanada, Y., Eds.; Advances in Chemistry 229; American Chemical Society: Washington, DC, 1993.

(38) Rorschach, H. E., Jr. *Physica (Utrecht)* **1964**, *30*, 38.

(39) Pigg, A. L.; Day, S. M. *Phys. Rev.* **B1975**, *11*, 3219.

(40) Day, S. M.; Grimes, G. B., Jr.; Weatherford, W. *Phys. Rev.* **1985**, *139*, A515.

(41) Wind, R. A.; Maciel, G. E.; Botto, R. E. In *Magnetic Resonance of Carbonaceous Solids*; Botto, R. E., Sunadu, Y., Eds.; Advances in Chemistry 229; American Chemical Society: Washington, DC, 1993.

depends on the ratio of concentrations of both types of spin species, decreasing the concentration of unpaired electrons should reduce this broadening proportionately, so that a larger fraction of the carbons would be observed in a ^{13}C NMR experiment. Botto[42] and Muntean et al.,[8] in order to increase the number of observed carbons in coals, focused on the selective removal of free radicals. The coal was treated chemically by samarium(II) iodide, and a spin counting experiment showed a significant increase in the fraction of ^{13}C spins observed.

In principle, the chemical treatment of coal or other complex macromolecular organics to remove paramagnetic species might sometimes produce additional unwanted and unknown changes of their chemical structure. This kind of uncertainty can perhaps be avoided by appropriately varying other factors—B_o, T, and τ_c—which have the potential to achieve the same goal. Of course, variation in temperature should not reach a magnitude that could lead to changes in structure. We are not aware of any attempts to enhance the temperature to decrease the degree of line broadening by paramagnetic centers.

The fractions of carbon spins observed in our study are different from, and in most cases larger than, those reported by Franz et al.[14] and by Muntean and Stock.[15] All our numbers are higher, or much higher, than those measured by Muntean and Stock. Their studies were carried out using 60–100 s recycle decays, which according to our data would satisfy the ^{13}C spin–lattice relaxation requirements of only two samples, Buelah-Zap and Wyodak-Anderson coals; this range of recycle delays is far too short for the other samples (but even for the two accommodated coals, the differences between the two data sets are big). In spite of applying recycle delays shorter than $5T^c_{1Smax}$, Franz et al.[14] obtained for some coals larger fractions of observed carbon spins than we did in this study. This suggests that the recycle delay is not the only issue that gives rise to differences between laboratories. Silbernagel and Botto[37] reviewed the carbon aromaticities (f_a) of all Argonne Premium coals as determined by CP-MAS and DP-MAS techniques and generated essentially a "best set" of f_a values. Our results, obtained from integration of the DP-MAS spectra shown in Figure 8 and summarized in Table 2, agree within experimental error with those data, with one exception; our Buelah-Zap results yielded a smaller aromaticity than one would expect from reviewing the earlier DP-MAS results.

(42) Botto, R. E. In ref 12, pp 550–552.

SUMMARY AND CONCLUSIONS

The value of ^{13}C spin–lattice relaxation times (T^c_1) measured by CP-MAS experiments was found to depend strongly on the choice of the CP contact time for some Argonne Premium coals. In order to find the smallest $(T^c_1)^{-1}$ contribution, one can carry out a series of measurements in which the CP contact time is varied. The value of T^c_{1Smax} obtained in this way can be used as the basis for choosing suitable recycle delays in DP-MAS ^{13}C spin counting experiments. Values of T^c_{1Smax} were found to be substantially larger than T^c_1 values reported in the literature. In six out of the eight Argonne Premium coals, the aromatic resonance has a larger T^c_{1Smax} value than that of the aliphatic peak, but in two others (Wyodak-Anderson, Buelah-Zap) the T^c_1 characteristics of the aliphatic resonance determine the minimum satisfactory recycle delay in a DP-MAS experiment.

The fraction of ^{13}C spins observed in ^{13}C DP-MAS experiments on Argonne Premium coals range between 81 and 97%. These values are correlated with the concentrations of unpaired electrons in all but one of these coals. There are significant discrepancies between our results and existing literature data regarding the fractions of carbons that can be detected via NMR in Argonne Premium coals.

The ^{13}C NMR signal of the 4-(*N*-methylpyrrolidino)bicyclo-[3.2.1]octan-8-one triflate is suitable for use as an intensity reference standard in ^{13}C DP-NMR experiments on coals.

ACKNOWLEDGMENT

We gratefully acknowledge support of this research by DOE Grant DE-FG22-93PC93206.

Received for review March 8, 1995. Accepted March 9, 1995.®

AC950239B

® Abstract published in *Advance ACS Abstracts,* May 1, 1995.

Anal. Chem. **1995**, *67*, 2195–2200

Analytical Applications of Cylindrical Carbon Fiber Microelectrodes. Simultaneous Voltammetric Determination of Phenolic Antioxidants in Food

M. L. Agüí, A. J. Reviejo, P. Yáñez-Sedeño, and J. M. Pingarrón*

Department of Analytical Chemistry, Faculty of Chemistry, Complutense University of Madrid, 28040 Madrid, Spain

Cylindrical carbon fiber microelectrodes (CFMEs) (8 μm in diameter and 8 mm in length) have been used to determine the phenolic antioxidants *tert*-butylhydroxyanisole (BHA) and *tert*-butylhydroxytoluene (BHT) in acetonitrile medium. The electrochemical behavior of the CFMEs was tested using ferrocene in pure acetonitrile. Pretreatment of the microelectrodes was not necessary for the voltammetric analysis of the antioxidants BHA and BHT. The influence of the supporting electrolyte concentration on i_p and E_p values obtained by differential pulse voltammetry (DPV) has been evaluated. Detection limits close to 70 μg L^{-1} of BHA or BHT were achieved. Square-wave voltammetry (SWV) of these antioxidants at the CFMEs showed current densities remarkably higher than those obtained at a conventional glassy carbon disk electrode. A background current various orders of magnitude lower was also observed at the CFME. An optimization of square-wave parameters was performed in order to achieve the best sensitivity and resolution of the net current responses. Linear calibration graphs were obtained in the concentration ranges $(1.0-10.0) \times 10^{-5}$ and $(1.0-10.0) \times 10^{-6}$ mol L^{-1}, their slopes being significantly higher than those obtained by DPV. Voltammograms from mixtures of BHA and BHT showed two well-defined oxidation peaks with a difference between peak potentials of ~300 mV, which allows the simultaneous determination of both antioxidants in this medium. Interferences from other substances commonly present in commercial antioxidant mixtures were tested. The developed method by SWV was applied to determine BHA and BHT in spiked samples of dehydrated potato flakes.

Cylindrical microelectrodes have been shown to possess several advantageous properties that can be exploited in electroanalysis. Such microelectrodes can be easily fabricated from quality micrometer metallic wires or carbon fibers and are less sensitive to an imperfect seal between electrode and insulator than are disk microelectrodes.[1] Moreover, the current at cylindrical microelectrodes can be of much greater magnitude than that at disk microelectrodes. As the area of the cylinder depends not only on its radius but also on its length, the length of the microcylinder can be adjusted to obtain the desired magnitude of current without changing the diffusional characteristics.[2] This area is usually large enough to yield currents which can be measured with conventional instrumentation.[3]

In spite of these properties, cylindrical microelectrodes have not been as extensively used as would be expected. Their analytical utility seems to be limited because they cannot be polished reproducibly[4] and they can easily be damaged during work. Nevertheless, cylindrical microelectrodes have been used as sensitive detectors for liquid chromatography,[5] flow injection analysis,[6] and capillary electrophoresis,[7] as well as probe electrodes for in vivo measurements.[8]

The theory of various electrochemical techniques at microcylinder electrodes has been established, and so, the theoretical basis of chronoamperometry,[9] cyclic voltammetry,[10] square-wave voltammetry (SWV),[11] and normal and differential pulse voltammetry (DPV)[12] have been examined and verified with experimental data. Consequently, in the last few years, a better knowledge of the influence of cylindrical diffusion on the voltammetric response has been achieved, which has renewed interest in the use of these microelectrodes for analytical purposes.[13]

Most applications of cylindrical microelectrodes are referred to readily available carbon fiber electrodes, whose properties and electroanalytical applications were reviewed by Edmonds.[14] Various procedures to fabricate carbon fiber microcylinder electrodes (CFMEs) have been proposed,[15] the most popular consisting of sealing the carbon fibers into glass capillaries. SWV at a CFME has been used to determine *N*-acetylpenicillamine thionitrite with a great improvement in sensitivity with respect to conventional glassy carbon electrodes.[3] Miniaturized glucose sensors based on enzyme deposition on CFMEs have been also developed.[16] Finally, CFMEs have been used as substrates for mercury films,[1] and the preparation and some properties of these mercury coated

(1) Golás, J.; Osteryoung J. *Anal. Chim. Acta* **1986**, *186*, 1.
(2) Singleton, S. T.; O'Dea, J. J.; Osteryoung J. *Anal. Chem.* **1989**, *61*, 1211.
(3) Nuwer, M. J.; Osteryoung, J. *Anal. Chem.* **1989**, *61*, 1954.
(4) Bixler, J. W.; Bond, A. M.; Lay, P. A.; Thormann, W.; van der Bosch, P.; Fleischmann, M.; Pons, B. S. *Anal. Chim. Acta* **1986**, *187*, 67.
(5) Baur, J. E.; Wightman, R. M. *J. Chromatogr.* **1989**, *482*, 65.
(6) Wang, J.; Li, R. *Anal. Chem.* **1990**, *62*, 2414.
(7) Lu, W.; Cassidy, R. M. *Anal. Chem.* **1993**, *65*, 1649.
(8) Shannon, C.; Frank, D. G.; Hubbard, A. T. *Annu. Rev. Phys. Chem.* **1990**, *42*, 393.
(9) Aoki, K.; Honda, K.; Tokuda, K.; Matsuda, H. *J. Electroanal. Chem.* **1985**, *186*, 79.
(10) Aoki, K.; Honda, K.; Tokuda, K.; Matsuda, H. *J. Electroanal. Chem.* **1985**, *186*, 267.
(11) O'Dea, J.; Wojciechowski, M.; Osteryoung, J.; Aoki, K. *Anal. Chem.* **1985**, *57*, 954.
(12) Murphy, M. M.; O'Dea, J. J.; Osteryoung, J. *Anal. Chem.* **1991**, *63*, 2743.
(13) Peng, W.; Wang, E. *Anal. Chem.* **1993**, *65*, 2719.
(14) Edmonds, T. E. *Anal. Chim. Acta* **1985**, *175*, 1.
(15) Golás, J.; Osteryoung, J. *Anal. Chim. Acta* **1986**, *181*, 211.
(16) Wang, J.; Angnes, L. *Anal. Chem.* **1992**, *64*, 456.

0003-2700/95/0367-2195$9.00/0 © 1995 American Chemical Society

microelectrodes have been investigated.[15]

On the other hand, antioxidants are a large group of chemicals widely used in the food and pharmaceutical industries.[17] In particular, phenolic antioxidants, such as *tert*-butylhydroxyanisole (BHA) and *tert*-butylhydroxytoluene (BHT), are commonly added to food products to improve their stability and especially to prevent rancidity in products containing lipids or fats.

Several methods, usually involving separation steps, have been proposed for the determination of phenolic antioxidants.[17] Regarding electroanalytical methods, in the last few years some applications have been described. Wang and Freiha[18] studied the preconcentration and DPV of BHA at a carbon paste electrode. Liquid chromatography[19] with amperometric detection has been also used to detect some antioxidants in oil and food samples. Flow injection methods for the determination of BHA and BHT separately, and of BHA in the presence of BHT, have been described on the basis of their oxidation processes at a glassy carbon electrode.[20] Micellar and emulsified media have been also employed to carry out voltammetric studies of the BHA oxidation process and to determine this antioxidant in chewing gum samples.[21] Finally, the catalytic voltammetric determination of BHA[22] and BHT[23] at a nickel phthalocyanine-modified carbon paste electrode has been reported.

The determination of these phenolic antioxidants in food samples usually involves the extraction of the analytes with organic solvents. As it is well known, one of the most interesting analytical advantages of the use of microelectrodes is the possibility of performing measurements in highly resistive media. The aim of this work is to investigate the voltammetric behavior of the antioxidants BHA and BHT at a cylindrical carbon fiber microelectrode of relatively high length (8 mm), by applying DPV and SWV as electroanalytical techniques, in an acetonitrile medium. This organic solvent has been used to extract BHA and BHT from food samples.[24] Consequently, the voltammetric analysis has been carried out directly in the analyte extract, thus avoiding some steps of the analytical procedure, such as the solvent evaporation. The possibility of resolving mixtures of both compounds in this medium with no separation steps has also been proved, and finally, the method has been applied to the determination of these antioxidants in samples of dehydrated potato flakes.

EXPERIMENTAL SECTION

Apparatus. Experiments were performed on an EG&G PAR 273 potentiostat using the electrochemical analysis software. Two- or three-electrode configurations were employed. In the former, the reference and counter electrode connections were both attached to the Ag/AgCl (BAS MF 2063) reference electrode. A Metrohm 6.0804.010 glassy carbon electrode (3.0 mm diameter, $A = 0.0707$ cm^2) or carbon fiber microelectrodes (8 μm diameter, $A = 0.0020$ cm^2) were used as working electrodes. The auxiliary electrode consisted of a platinum wire directly immersed in the solution. A 10-mL electrochemical cell (BAS UC-2), a P-Selecta Meditronic centrifuge, and a Griffin flask shaker were also used.

Fabrication of Carbon Fiber Microelectrodes. Carbon fibers (Union Carbide Corp.) 8 μm in diameter were used to prepare the microelectrodes. The fibers were soaked, washed, and stored in acetone and dried thoroughly at room temperature. A single fiber was inserted into a 200-μL polypropylene pipet tip and sealed with epoxy resin. The pipet was backfilled with mercury, and a copper wire was used as the electrical contact. Microcylinders were cut with a scalpel to the desired length (8 mm). In a second procedure, the use of epoxy resin was suppressed, and the fiber was sealed by heating the pipet tip carefully with a red-hot steel wire. This latter procedure was demonstrated to be preferable since many electrodes can be fabricated in a very short time, and problems associated with loss of adhesion of the sealant after working with the electrode for a few hours[15] are avoided.

Reagents and Solutions. Stock 1.0×10^{-3} mol L^{-1} solutions of BHA (Sigma) and BHT (Fluka) in pure acetonitrile (Panreac) and 1.0×10^{-3} mol L^{-1} solutions of ferrocene in acetonitrile were used. In all cases, dry acetonitrile (0.01% H_2O maximum) was used as received. Tetraethylammonium perchlorate (TEAP) or tetrabutylammonium perchlorate (TBAP) (Fluka, 99%) were used as supporting electrolytes. All other chemicals were of analytical reagent grade. The water used was obtained from a Millipore Milli-Q system.

Sample. Samples analyzed were commercial dry potato flakes (Maggi), containing sodium bisulfite (E-223) and ascorbic acid (E-300) as antioxidants. These samples were spiked with BHA and/or BHT at levels of 100 mg kg^{-1} BHA and 120 mg kg^{-1} BHT.

Procedures. After use, the CFMEs were immersed in acetonitrile and stored by night in this solvent.

Determination of BHA and/or BHT in Spiked Dry Potato Flakes. About 1 g of sample previously crushed in a mortar and spiked with the appropriate volume of the BHA and/or BHT stock solution in acetonitrile was accurately weighed into a 30-mL centrifugue tube provided with a screw tap. Next, 10 mL of acetonitrile was added, and the mixture was mechanically shaken for 5 min. After centrifugation at 3500 rpm for 5 min, an aliquot of 5.0 mL of the supernatant extract was transferred to a 10-mL volummetric flask. TBAP was then added to obtain a final concentration of supporting electrolyte of 1.0×10^{-3} mol L^{-1}, diluting to the mark with acetonitrile. The determination of BHA and/or BHT was carried out by SWV using the standard additions method, which involved the addition of $(2.0-8.0) \times 10^{-5}$ mol L^{-1} of each antioxidant.

RESULTS AND DISCUSSION

In order to test the electrochemical behavior of the fabricated CFMEs, ferrocene in pure acetonitrile was used as a model of a reversible electrochemical system. Cyclic voltammograms from 0.00 to +1.00 V were registered using a two-electrode configuration. Results obtained from 1.0×10^{-3} mol L^{-1} ferrocene solutions containing 6.0×10^{-4} mol L^{-1} TEAP showed typical S-shaped curves, indicating that depletion of the electroactive species at the electrode does not occur. At potential scan rates between 10 and 60 mV s^{-1}, the forward and reverse sweeps were practically superimposed, as a result of the reversibility of the couple (Figure 1). As expected, higher scan rates, from 80 to 1000 mV s^{-1}, gave rise to the distortion of the voltammograms, which became more peak-shaped as the scan rate increased.

(17) Hudson, B. J. F., Ed. *Food Antioxidants*; Elsevier: London, 1990; pp v–vii.
(18) Wang, J.; Freiha, B. H. *Anal. Chim. Acta* **1983**, *154*, 87.
(19) Grosset, C.; Cantin, D.; Villet, A.; Alary, J. *Talanta* **1990**, *37*, 301.
(20) Yáñez-Sedeño, P.; Pingarrón, J. M.; Polo, L. M. *Anal. Chim. Acta* **1991**, *252*, 153.
(21) González, A.; Ruiz, A.; Yáñez-Sedeño, P.; Pingarrón, J. M. *Anal. Chim. Acta* **1994**, *285*, 63.
(22) Ruiz, A.; Calvo, M. P.; Pingarrón, J. M. *Talanta* **1994**, *41*, 289.
(23) Ruiz, A.; Yáñez-Sedeño, P.; Pingarrón, J. M. *Electroanalysis* **1994**, *6*, 475.
(24) *Official Methods of Analysis of the Association of Official Analytical Chemists*, 14th ed.; AOAC: Arlington, VA, 1984; Procedure 20012, p 373.

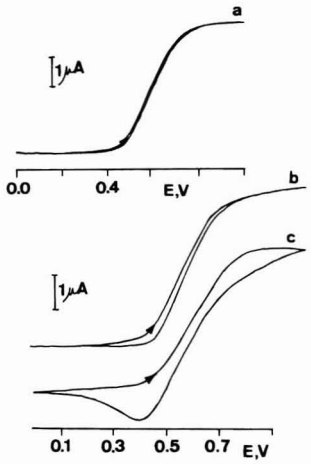

Figure 1. Cyclic voltammograms at a CFME of 1.0×10^{-3} mol L^{-1} ferrocene in acetonitrile containing 6.0×10^{-4} mol L^{-1} TEAP at scan rates of (a) 20, (b) 100, and (c) 1000 mV s^{-1}.

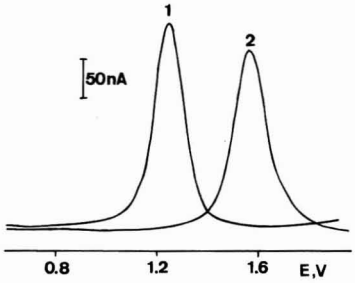

Figure 2. Differential pulse voltammograms at a CFME of (1) 1.0×10^{-4} mol L^{-1} BHA and (2) 1.0×10^{-4} mol L^{-1} BHT in acetonitrile; 1.0×10^{-3} mol L^{-1} TBAP, $\Delta E = 50$ mV.

The reproducibility of microelectrodes was tested by measuring the limiting current and half-wave potential from cyclic voltammograms of ferrocene under the same experimental conditions using a scan rate of 20 mV s^{-1}. In this case, a simple electrochemical pretreatment of the CFMEs, consisting of applying a constant potential of −0.9 V for 60 s before each scan, was necessary. Results obtained for five different CFMEs yielded limiting current and $E_{1/2}$ mean values of 3.8 ± 0.4 μA and 0.573 ± 0.013 V, respectively. These values demonstrated that there are no significative differences in the electrochemical behavior of the electrodes.

Differential Pulse Voltammetry of BHA and BHT. Differential pulse voltammograms at the CFME were obtained from BHA or BHT solutions in acetonitrile. As Figure 2 shows, a well-defined peak was obtained in each case, the peak potentials being +1.24 and +1.54 V, respectively. In order to test the reproducibility of measurements performed with the same CFME, repetitive voltammograms from 1.0×10^{-4} mol L^{-1} BHA or BHT solutions were registered. A relative standard deviation value for i_p measurements near 4% ($n = 20$) was obtained in both cases, indicating that a cleaning pretreatment of the microelectrode was not necessary for the electrochemical analysis of these antioxidants. These results constitute a great advantage of the use of CFMEs with respect to conventional carbon electrodes, especially in the case of BHT, where its strong adsorption is well known to cause fouling of the electrode surface.[18]

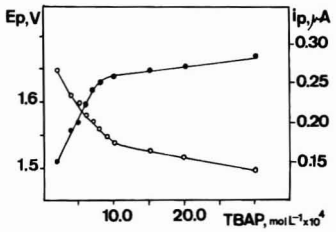

Figure 3. Influence of the supporting electrolyte concentration in acetonitrile on (○) E_p and (●) i_p for DPV at a CFME 1.0×10^{-4} mol L^{-1} BHT; $\Delta E = 50$ mV.

The influence of the supporting electrolyte concentration on the BHA and BHT DPV oxidation peaks was studied by measuring i_p and E_p from voltammograms recorded in acetonitrile solutions containing TBAP in the 1.0×10^{-4}–3.0×10^{-3} mol L^{-1} concentration range. Similar results were obtained for both antioxidants. As an example, Figure 3 shows the results obtained for BHT. As can be observed, at lower TBAP concentrations, a rapid increase in i_p together with a strong decrease in E_p values occurs when the supporting electrolyte concentration increases and, consequently, the solution resistance is reduced. At a TBAP concentration of 1.0×10^{-3} mol L^{-1}, both parameters tend to level off. Furthermore, peak width decreases monotonically with increasing TBAP concentration. A fall in the uncompensated cell resistance from 1.2 MΩ down to 270 kΩ has been reported on passing from pure acetonitrile to a 1 mM tetrabutylammonium bromide (TBAB) solution in acetonitrile.[25] Since the currents measured at the CFMEs are not very low, the ohmic potential drop (iR_s) becomes important at very low supporting electrolyte concentrations, which causes an increase of the measured peak potentials. The lower i_p values observed at these very low TBAP concentrations can be attributed to the lower conductivity of such solutions. At higher TBAP concentrations, a small peak at $E_p = +1.2$ V appears. The i_p of this peak slightly increases with increasing TBAP concentration, which suggests that, probably, the peak may be due to the presence of water in the electrolyte. As a compromise between the best sensitivity and the lower supporting electrolyte concentration, and thus, the lower water and other impurities content, a 1.0×10^{-3} mol L^{-1} TBAP concentration was chosen for subsequent studies.

Calibration Graphs for BHA and BHT by DPV. The plots of i_p versus BHA or BHT concentration were linear over the ranges $(1.0–10.0) \times 10^{-5}$ ($r = 0.9997$ in both cases) and $(1.0–10.0) \times 10^{-6}$ mol L^{-1} ($r = 0.997$ and 0.9992 for BHA and BHT, respectively). The slopes of these calibration graphs were $(2.76 \pm 0.06) \times 10^3$ and $(2.39 \pm 0.05) \times 10^3$ μA L mol^{-1} for BHA and BHT in the upper concentration range, respectively, and $(2.3 \pm 0.2) \times 10^3$ and $(1.79 \pm 0.06) \times 10^3$ μA L mol^{-1} for BHA and BHT, respectively, in the lower range of linearity. These values indicate a good sensitivity in both cases. Differences observed between the slopes in both ranges arise from the way the peak heights are measured (by drawing a baseline from the beginning of the rising portion of the peak to the portion where the peak begins

(25) Wang, J.; Wu, L.-H.; Angnes, L. *Anal. Chem.* **1991**, *63*, 2993.

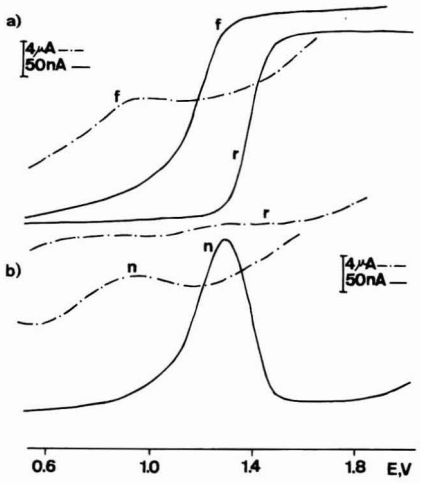

Figure 4. (a) Forward (f) and reverse (r) and (b) net (n) square-wave voltammograms at a conventional glassy carbon electrode (3 mm diameter) (– · –) and at a CFME (—) for 4.0×10^{-5} mol L^{-1} BHA in acetonitrile; 0.1 and 1.0×10^{-3} mol L^{-1} TBAP when using a glassy carbon electrode and a CFME, respectively; $f = 25$ Hz, $E_{sw} = 100$ mV, $\Delta E_s = 10$ mV.

to flatten). Intercepts were 5 ± 4 and -0.4 ± 1 nA for BHA, and -2 ± 3 and -0.1 ± 0.4 nA for BHT, respectively. Relative standard deviations of 3.7% for BHA and 2.0% for BHT were calculated for a concentration level of 5.0×10^{-5} mol L^{-1} antioxidant ($n = 10$). Limits of detection, 4.0×10^{-7} mol L^{-1} for BHA and 3.1×10^{-7} mol L^{-1} for BHT, were determined according with the $3s_b/m$ criterion, where m is the slope of the lowest calibration graph, and s_b is the standard deviation ($n = 10$) of the signals for 1.0×10^{-6} mol L^{-1} BHA or BHT. Limits of determination of 1.3×10^{-6} and 1.0×10^{-6} mol L^{-1} were calculated for BHA and BHT, respectively, according to the 10 × standard deviation criterion. Detection limits obtained, close to 70 μg L^{-1} of BHA or BHT, demonstrate the validity of the DPV methods for the determination of both antioxidants at low concentration levels.

Square-Wave Voltammetry of BHA and BHT. Nonplanar diffusion at microcylinder electrodes has been shown to give enhanced SWV signals.[2] The effect of the cylindrical diffusion is to increase the current density and, consequently, the sensitivity of the measurements. Thus, current densities at CFMEs remarkably higher than those obtained at glassy carbon disk electrodes of larger are have been reported.[3] In the case of BHA and BHT, our investigations confirmed a similar behavior. As an example, square-wave voltammograms at the CFME obtained for BHA solutions in acetonitrile are shown in Figure 4. Furthermore, voltammograms obtained at a conventional glassy carbon disk electrode ($A = 7 \times 10^{-2}$ cm^2) are also displayed. As can be observed, the net current squarewave voltammogram at the CFME shows the typical bell-shaped symmetrical peak, whereas a broad, poorly defined peak was obtained at the glassy carbon electrode. Current densities per unit concentration at the glassy carbon disk electrode were 1.09 μA/(μM cm^2) for BHA and 1.31 μA/(μM cm^2) for BHT, whereas these values at the CFME were 3.94 μA/(μM cm^2) and 3.82 μA/(μM cm^2), respectively. A background current of various orders of magnitude lower was also observed at the CFME (note the different current scales for the glassy carbon electrode and the CFME). These results agree with theoretical and experimental data which demonstrated that the shape of the net current square-wave voltammograms is unaffected by the cylindrical geometry.[2] It has been also demonstrated that, for a reversible system, the net square-wave response is independent of the electrode geometry.[2] Consequently, the shifts observed in peak potentials as well as the differences in peak width for both types of electrodes must be attributed to the nonreversibility of the oxidation process and also to the different electrode materials.[3]

Regarding individual forward and reverse currents, they have been shown to be dependent on the extent and nature of nonplanar diffusion.[2] This fact is also made clear for BHA and BHT. Thus, voltammograms registered at the glassy carbon disk electrode were typical of an irreversible electron transfer with no cathodic contribution to the reverse current. Poorly defined peaks in the forward voltammograms were obtained for both antioxidants. When these results were compared with those obtained at the CFME, noticeable differences in shape for the forward and reverse currents were observed. Now, equivalent curves, both waving in form, were obtained. This change may be attributed to the effect of the additional flux at the cylindrical fiber which does not exist in the planar diffusion to the disk electrode.[3] An optimization of square-wave voltammetric parameters was performed in order to achieve the best sensitivity and resolution of the net current responses for BHA and BHT.

The influence of the frequency was examined in the 5–300 Hz range using $\Delta E_s = 10$ mV and $E_{sw} = 50$ mV. The net current from 5 to 50 Hz was observed to increase rapidly for both antioxidants, and then level off to practically constant Δi_p values. Moreover, slight increases of the peak potential values were observed as the frequency increased, indicating the nonreversibility of the electrode process. Finally, both background current and noise also increased with increasing frequency. Taking into account the best signal-to-noise relationship, a frequency of 25 Hz was chosen for further studies.

The influence of the square-wave amplitude (E_{sw}) on the voltammetric responses was investigated within the range 5–200 mV. An increase in the net peak current and in the peak width at half-height with increasing E_{sw} was observed for both antioxidants. Thus, the resolution of the square-wave response ($\Delta i_p/W_{1/2}$) showed a maximum for a square-wave amplitude of 100 mV, which was selected for analytical purposes.

Finally, the variation of the step height (ΔE_s) in the 2–20 mV range had little effect on $W_{1/2}$ and produced a slight increase of the net current peak height. A step height of 10 mV was chosen as a reasonable value to give well-defined voltammograms.

Linear calibration graphs (r values ranging from 0.998 to 0.9995) for BHA and BHT were obtained with $f = 25$ Hz, $E_{sw} = 100$ mV, and $\Delta E_s = 10$ mV within the same concentration ranges mentioned for DPV. Slopes were $(1.25 \pm 0.03) \times 10^4$ and $(7.3 \pm 0.2) \times 10^3$ μA L mol^{-1} for BHA and BHT in the upper concentration range and $(7.3 \pm 0.4) \times 10^3$ and $(9.6 \pm 0.3) \times 10^3$ μA L mol^{-1} for BHA and BHT in the lower range of linearity. Intercept values were 0 ± 10 and 4 ± 2 nA for BHA and 10 ± 10 and 2 ± 0.2 nA for BHT, respectively. Relative standard deviations of 1.6 and 1.4% were calculated respectively for BHA or BHT concentration of 5.0×10^{-5} mol L^{-1} ($n = 10$). Limits of detection of 4.0×10^{-7} and 3.7×10^{-7} mol L^{-1} and limits of determination of 1.3×10^{-6}

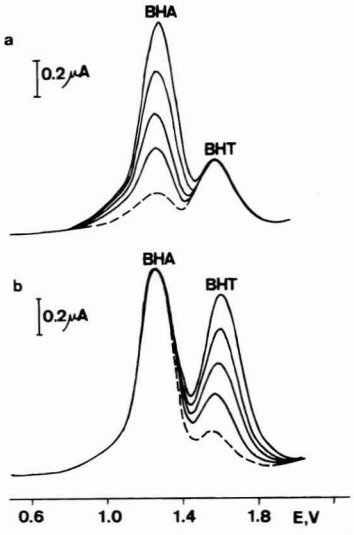

Figure 5. Net square-wave voltammograms at a CFME of BHA and BHT mixtures in acetonitrile. (a) Successive additions of 2.0×10^{-5} mol L^{-1} BHA in the presence of 4.0×10^{-5} mol L^{-1} BHT; (b) Successive additions of 2.0×10^{-5} mol L^{-1} BHT in the presence of 10.0×10^{-5} mol L^{-1} BHA; 1.0×10^{-3} mol L^{-1} TBAP; $f = 25$ Hz, $E_{sw} = 100$ mV, $\Delta E_s = 10$ mV.

and 1.2×10^{-6} mol L^{-1} for BHA and BHT, respectively, were calculated according to the same criteria as in DPV.

As can be observed, the slopes of the calibration graphs were both significantly higher than those in DPV. These results indicate an improvement in sensitivity when working with SWV. On the other hand, limits of detection were similar for both methods.

Simultaneous Determination of BHA and BHT. Voltammograms obtained from mixtures of BHA and BHT in acetonitrile showed two well-defined peaks with both DPV and SWV. The differences between peak potentials were ~300 mV in each case, which seemed to be large enough to allow the simultaneous determination of both antioxidants in this medium.

Recovery studies of each antioxidant in the presence of the other were performed by applying the standard additions method. The individual determination of BHA and BHT was accomplished in solutions containing BHA or BHT at a fixed concentration of 2.0×10^{-5} mol L^{-1}, in the presence of BHT or BHA, respectively, in the $(2.0–10.0) \times 10^{-5}$ mol L^{-1} concentration range. As an example, Figure 5 shows square-wave voltammograms obtained for the determination of BHA in the presence of 4.0×10^{-5} mol L^{-1} BHT (Figure 5a) and for the determination of BHT in the presence of 10.0×10^{-5} mol L^{-1} BHA (Figure 5b). A recovery of 96 ± 4% was found for five determinations of BHA using both DPV and SWV techniques, the slopes of the standard additions plots being $(2.2 \pm 0.1) \times 10^3$ and $(1.2 \pm 0.1) \times 10^4$ μA L mol^{-1} for DPV and SWV, respectively. Regarding BHT, recoveries of 102 ± 3% by DPV and 98 ± 3% by SWV were obtained ($n = 5$), with slopes of the standard additions graphs of $(1.76 \pm 0.05) \times 10^3$ and $(9.9 \pm 0.1) \times 10^3$ μA L mol^{-1}, respectively. All confidence intervals were calculated for a significance level of 0.05.

On the other hand, five different solutions containing 2.0×10^{-5} mol L^{-1} each of BHA and BHT were used to carry out the simultaneous determination of both antioxidants by SWV and the standard additions method. Recoveries ranging between 98 and 100% were obtained in this case.

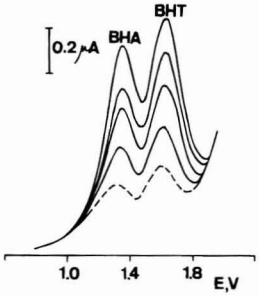

Figure 6. Net square-wave voltammograms at a CFME of the acetonitrile extract from a potato flakes sample spiked with both BHA and BHT: (– – –) spiked sample and (—) successive additions of 2.0×10^{-5} mol L^{-1} each of BHA and BHT; $f = 25$ Hz, $E_{sw} = 100$ mV, $\Delta E_s = 10$ mV.

Interferences. Different substances commonly present in commercial antioxidants mixtures (*tert*-butylhydroquinone (TBHQ), citric acid, propyl gallate, and propylene glycol) were tested by DPV in order to check for interferences with respect to the BHA and BHT peaks. Various interferent-to-analyte ratios were studied for a BHA or BHT concentration of 2.0×10^{-5} mol L^{-1}. Under the same experimental conditions used for the determination of these antioxidants, voltammograms of solutions of propylene glycol did not show any analytical peak in the +0.8 to +2.0 V potential range. Moreover, the shape of the BHA or BHT oxidation peaks did not change appreciably in the presence of this compound, which indicates that it does not interfere. In fact, in the presence of a 1:100 BHA-to-propylene glycol or BHT-to-propylene glycol ratio, the calculated concentrations of the analytes using the respective calibration graphs yielded values within the two standard deviations range for 2.0×10^{-5} mol L^{-1} BHA or BHT ($n = 10$).

Citric acid showed a poorly defined broad peak at $E_p \approx 1.4$ V which does not interfere in the determination of BHA up to a 1:100 BHA-to-citric acid concentration ratio. Nevertheless, the shape of the BHT peak changes slightly in the presence of this compound, which leads to relative errors in the concentration higher than 10% from a 1:10 BHT-to-citric acid concentration ratio.

Voltammograms from solutions of TBHQ showed a well-defined oxidation peak at +1.18 V. This E_p value is very close to that of BHA ($E_p = +1.25$ V). Thus, an overall peak was obtained from mixtures of BHA and TBHQ, whose i_p increased with increasing TBHQ concentration. Relative errors higher than 10% were obtained from a 50:1 BHA-to-TBHQ concentration ratio. On the other hand, voltammograms from BHT and TBHQ mixtures showed two well-defined peaks, with a separation between both peak potentials of about 360 mV. However, relative errors higher than 10% were obtained for the determination of BHT from a 1:2 BHT-to-TBHQ concentration ratio when the BHT calibration graph was used. In this case, the standard additions method must be used to avoid matrix effects which seem to be responsible for the aforementioned errors.

Finally, voltammograms from propyl gallate solutions showed a well-defined oxidation peak at $E_p = +1.30$ V. Results similar to those mentioned above in the case of TBHQ were obtained for

BHA and propyl gallate mixtures, which exhibited a broad overall peak. Relative errors higher than 10% were obtained for a 1:1 or lower BHA-to-propyl gallate concentration ratio. Regarding BHT, two well-defined peaks appeared in the voltammograms registered from the corresponding mixtures. No interference in the determination of BHT was found up to a 1:5 BHT-to-propyl gallate concentration ratio.

Determination of BHA and BHT in Spiked Dehydrated Potato Flakes Samples. SWV, under the experimental conditions described in the Experimental Section, was used to determine BHA and BHT in spiked samples of dehydrated potato flakes. The described procedure was applied to different samples containing (a) BHA, (b) BHT, and (c) BHA + BHT. In all cases, the final concentration of each antioxidant in the analytical solution was 2.75×10^{-5} mol L^{-1}. Voltammograms obtained from these samples exhibited well-defined peaks corresponding to the oxidation of each analyte. As an example, those registered from a sample spiked with the mixture of both antioxidants are shown in Figure 6, as well as those for the corresponding successive additions used to carry out recovery studies. As can be observed, net current increased with increasing BHA and BHT concentration. Furthermore, SW voltammograms of blank solutions obtained from unspiked samples did not show any peak in the potential range scanned. The results obtained from five samples of each type are as follow: BHA found, $(2.68 \pm 0.05) \times 10^{-5}$ mol L^{-1}, which corresponds to a recovery of 97 ± 2%; BHT found, $(2.69 \pm 0.04) \times 10^{-5}$ mol L^{-1} (recovery of 98 ± 2%); BHA + BHT found, $(2.67 \pm 0.05) \times 10^{-5} + (2.68 \pm 0.09) \times 10^{-5}$ mol L^{-1} (97 ± 2 and 97 ± 3%, respectively). The confidence intervals were calculated for a significance level of 0.05, and the relative standard deviations were ±1.5% (BHA), ±1.2% (BHT), and ±1.5 and ±2.7% for BHA and BHT, respectively.

CONCLUSION

The results obtained show fairly well that CFMEs can be used for the determination of food additives such as the antioxidants BHA and BHT in commercial samples. The advantageous properties of these microelectrodes allow this determination to be carried out directly in the antioxidants extract using acetonitrile as extraction solvent. Furthermore, the application of electroanalytical techniques such as DPV or SWV permits the sensitive determination of the analytes, and the selectivity of the proposed method is rather good when mixtures of antioxidants are present. Moreover, the CFME seems to be a suitable indicator electrode in flowing systems for electrochemical detection of phenolic antioxidants.

ACKNOWLEDGMENT

Financial support from the Spanish C.I.C.Y.T. (Project ALI 92-0049) is gratefully acknowledged.

Received for review November 28, 1994. Accepted March 21, 1995.[⊗]

AC941139T

[⊗] Abstract published in *Advance ACS Abstracts,* May 1, 1995.

Anal. Chem. **1995**, *67*, 2201–2206

Incipient Electrochemical Oxidation of Highly Oriented Pyrolytic Graphite: Correlation between Surface Blistering and Electrolyte Anion Intercalation

Kevin W. Hathcock, Jay C. Brumfield, Charles A. Goss,† Eugene A. Irene, and Royce W. Murray*

Kenan Laboratories of Chemistry, University of North Carolina, Chapel Hill, North Carolina 27599-3290

Electrochemical oxidation of highly oriented pyrolytic graphite (HOPG) electrodes in KNO_3 electrolyte solution at a carbon submonolayer level was shown in a previous paper to produce raised, bubblelike features, giving the appearance of shallow blisters. The blisters were established to be hollow, with a top surface of intact HOPG lattice and an inner one of graphitic oxide. This paper explores the relationship of the intercalating properties of the electrolyte anion to the blister formation on HOPG. Cyclic voltammetry, atomic force microscopy, optical microscopy, and in situ atomic force microscopy/electrochemistry results are presented. Surface blister formation is observed to occur in 1 M $LiClO_4$, 1 M $(NH_4)_2SO_4$, 1 M HNO_3, and 1 M H_2SO_4 aqueous electrolytes as a result of potential scans (+1.50 to +1.90 V vs SSCE, depending on the electrolyte) that pass a few carbon monolayers of charge or less. Blister formation on HOPG in 1 M KOH electrolyte is observable but at significantly higher levels of oxidative charge, whereas blisters were not observed in 1 M K_2HPO_4 and 1 M H_3PO_4 electrolytes. These results are consistent with literature Raman intercalation data that indicate phosphate does not readily intercalate into HOPG, supporting a model in which blister formation reflects electrolyte anion intercalation followed by subsurface gas evolution.

Carbon electrodes are widely employed and of technological importance, and the processes by which they become electrochemically oxidized have been widely researched.[1] A thorough understanding of carbon oxidation is hampered by the structural complexity of different carbon materials and of the associated oxidative reactions.[1-3] Highly oriented pyrolytic graphite[4] (HOPG) is a better-defined, layered structure with large crystallites and atomically flat, low defect density basal plane surfaces, and its relative structural simplicity has attracted a number of investigations of HOPG surface oxidations.[5-7]

On the basis of Raman spectroscopy, scanning electron microscopy, double-layer capacitance, electrode kinetics, and redox molecule adsorption coverage measurements, McCreery and co-workers[5] proposed that HOPG oxidation in aqueous KNO_3 leads to delamination followed by lattice strain-induced fracturing into smaller microcrystallites.[5b] Additional Raman evidence[6] showed that in aqueous 1 M H_2SO_4, 1 M $HClO_4$, and 1 M HNO_3 graphite lattice damage is preceded or accompanied by electrolyte intercalation, whereas in 1 M H_3PO_4 neither intercalation nor lattice damage was observed. These results were interpreted with a model in which the initially formed graphite intercalation compound subsequently oxidizes water or carbon to form graphite oxides. Graphite intercalation compounds have also been extensively examined by others.[2,5a,6,7,8] Gewirth and Bard[7] reported in situ scanning tunneling microscopy (STM) images during HOPG oxidation in aqueous 0.1 M H_2SO_4, documenting formation and growth of roughened areas with decreased tunneling barrier heights. They suggested that a surface graphite oxide layer forms via a nucleation and growth mechanism initiated at step and defect sites.

We became interested in the events leading up to HOPG surface damage and roughening and have described[9] potential scan experiments in aqueous KNO_3 electrolyte in which the potential limits and scan rate were adjusted so that the basal plane HOPG oxidative charge passed corresponded to that consuming, on average, only fractions or small numbers of carbon atom monolayers (Q_M is 1.23 mC/cm^2, assuming, arbitrarily, an $n = 2$ oxidation). We refer to this condition as incipient electrochemical

† Present address: Burroughs Wellcome Co., 3030 Cornwallis Rd., Research Triangle Park, NC 27709.

(1) Kinoshita, K. *Carbon: Electrochemical and Physicochemical Properties*; John Wiley & Sons: New York, 1988.

(2) Besenhard, J. O.; Fritz, H. P. *Angnew. Chem., Int. Ed. Engl.* **1983**, *22*, 950–975.

(3) Randin, J. P. In *Encyclopedia of Electrochemistry of the Elements*; Bard, A. J., Ed.; Marcel Dekker: New York, 1976; Vol. 7, pp 1–291.

(4) (a) Moore, A. W. In *Chemistry and Physics of Carbon*; Walker, P. L., Jr., Thrower, P. A., Eds.; Marcel Dekker: New York, 1981; Vol. 17, pp 233–286. (b) Moore, A. W. In *Chemistry and Physics of Carbon*; Walker, P. L., Jr., Thrower, P. A., Eds.; Marcel Dekker: New York, 1973; Vol. 11, pp 69–187.

(5) (a) McDermott, M. T.; Kneten, K.; McCreery, R. L. *J. Phys. Chem.* **1992**, *96*, 3124–3130. (b) McCreery, R. L. In *Electroanalytical Chemistry*; Bard, A. J., Ed.; Marcel Dekker: New York, 1991; Vol. 17, pp 221–374. (c) Robinson, R. S.; Sternitzke, K.; McDermott, M. T.; McCreery, R. L. *J. Electrochem. Soc.* **1991**, *138*, 2412–2418. (d) Bowling, R. J.; Packard, R. T.; McCreery, R. L. *J. Am. Chem. Soc.* **1989**, *111*, 1217–1223. (e) Bowling, R. J.; Packard, R. T.; McCreery, R. L. *Langmuir* **1989**, *5*, 683–688. (f) Bowling, R. J.; McCreery, R. L.; Pharr, C. M.; Engstrom, R. C. *Anal. Chem.* **1989**, *61*, 2763–2766. (g) Rice, R. J.; McCreery, R. L. *Anal. Chem.* **1989**, *61*, 1637–1641.

(6) Alsmeyer, D. C.; McCreery, R. L. *Anal. Chem.* **1992**, *64*, 1528–1533.

(7) Gewirth, A. A.; Bard, A. J. *J. Phys. Chem.* **1988**, *92*, 5563–5566.

(8) (a) Dresselhaus, M. S.; Dresselhaus, G. *Adv. Phys.* **1981**, *30*, 139–317. (b) Fong, R.; Sacken, U. von; Dahn, J. R. *J. Electrochem. Soc.* **1990**, *137*, 2009–2013. (c) Hennig, G. R. *Proc. Inorg. Chem.* **1959**, *1*, 126–205. (d) Inagaki, M.; Iwashita, N.; Kouno, E. *Carbon* **1990**, *28*, 49–55. (e) Krohn, H.; Beck, F.; Junge, H. *Ber. Bunsenges. Phys. Chem.* **1982**, *86*, 704–710. (f) Krohn, H. *Carbon* **1985**, *23*, 449–457. (g) Maeda, Y. *J. Electrochem. Soc.* **1990**, *137*, 3047–3052. (h) Scharff, P.; Stumpp, E. *Ber. Bunsenges. Phys. Chem.* **1991**, *95*, 58–61. (i) Ubbelohde, A. R. *Carbon* **1972**, *10*, 201–206.

(9) Goss, C. A.; Brumfield, J. C.; Irene, E. A.; Murray, R. W. *Anal. Chem.* **1993**, *65*, 1378–1389.

0003-2700/95/0367-2201$9.00/0 © 1995 American Chemical Society

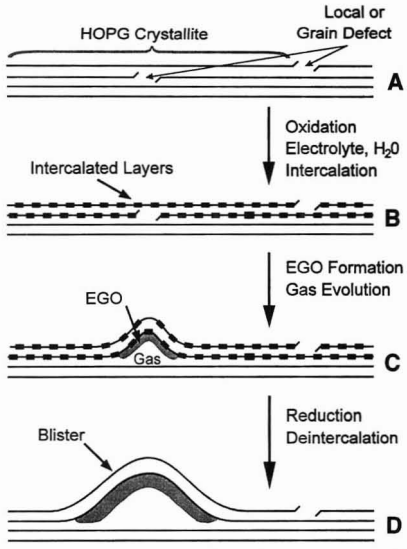

Figure 1. Schematic diagram of blister formation model: (A) cross section of basal plane HOPG electrode surface/solution interface with electrode at the initial potential prior to oxidation. Lines correspond to crystallites of HOPG, which may contain many carbon sheet layers. Length scales are arbitrary, although the longer horizontal vs vertical dimensions are intended to reflect reality. Surface and subsurface defect sites, such as crystalline grain boundaries and step edges, are also depicted. (B) After scanning the electrode potential anodically into initial oxidation wave. Dashed lines indicate areas where intercalation of electrolyte and H_2O has occurred. (C) As in (B) but showing initial blister formation. The shaded area represents electrochemically formed graphite oxide. (D) Final blister structure after scanning electrode potential back to initial value. Between (C) and (D) the blister grew due to mechanical stress attributed to gas evolution; intercalated electrolyte ions were expelled during the cathodic scan.

oxidation and found[9] that it was accompanied by the formation of blisterlike features on the basal plane surface. These blisters, observed[9] by in situ atomic force microscopy/electrochemistry[9-11] (AFM-EC), optical microscopy (OM) and SEM, are apparently the predecessor of more extensive HOPG surface damage and roughening. The blisters have essentially undisturbed HOPG lattice tops as seen by atomic resolution AFM, and as established[9] by SEM, energy-dispersive X-ray microanalysis, and Auger electron spectroscopy, are hollow with an HOPG floor, an inner roof layer of graphitic oxide, and wall thicknesses (in one example) of $\leq$300 nm. From these results, the model of Figure 1 was proposed, in which the blistering is a delamination driven by the mechanical stress of subsurface oxidation with gas formation.

Implicit in the model of Figure 1 is the reversible intercalation of electrolyte. In the previous study, only KNO_3 electrolyte was employed. The present investigation tests the blister model further by atomic force and optical microscopic observations of the propensity for blister formation on HOPG. The electrolytes include cases in which previous evidence[1,2,6,8,12] indicates intercalation does and does not occur during HOPG oxidation. The new results show that blister formation indeed is correlated with the ease of intercalation of electrolyte anions. Blistering occurs readily in 1 M $LiClO_4$, 1 M $(NH_4)_2SO_4$, 1 M HNO_3, and 1 M H_2SO_4 aqueous electrolytes, with greater difficulty in 1 M KOH electrolyte, and is not observed in 1 M K_2HPO_4 and 1 M H_3PO_4 electrolytes. While optical micrographs and AFM images have been shown previously[9] in aqueous KNO_3, images are presented here that represent the first OM, AFM, and AFM-EC images documenting blister formation in the above mentioned electrolytes.

EXPERIMENTAL SECTION

Electrodes. Approximately 1.5 cm diameter, 0.25 cm thick pieces of HOPG (supplied by Dr. Arthur W. Moore, Union Carbide Co., Parma, OH) were mounted on steel shims of the same diameter (Digital Instruments, Santa Barbara, CA) with double-sided adhesive tape. Electrical connection was made with silver epoxy (Epo-Tek H20E, Epoxy Technology Inc., Billerica, MA) cured at 110 °C for 30 min. Fresh HOPG surfaces were obtained prior to each experiment by stripping off HOPG layers with adhesive tape. The geometric electrode area as defined by a silicone o-ring was ~0.38 cm^2. In some experiments, all but a central 0.05–0.20 cm^2 area of the HOPG was masked with either clear polyurethane varnish (Servistar Corp., Butler, PA) or epoxy (Epoxy-Patch 1C, Dexter Corp., Adhesives & Structural Materials Division, Seabrook, NH) diluted with acetone. Masks were allowed to cure for 15 min at 110 °C and then several hours at ambient temperature.

Electrochemistry. Electrolyte solutions were prepared from reagent grade chemicals and purified water (Barnstead Nanopure Type I) and used undegassed at ambient temperature (~295K). Potentials cited are vs sodium-saturated calomel electrode (SSCE). Voltammetry was performed with Pine Model RDE3 or RDE4 potentiostats. Electrodes were oxidized in situ during AFM-EC experiments or ex situ in glass electrochemical o-ring cells by scanning the electrode potential between +0.135 V and the desired potential limit (+1.5 to +1.95 V), rinsing with H_2O, and drying with N_2.

Atomic Force Microscopy. Experiments were conducted using a Digital Instruments Nanoscope II AFM, Nanoprobe cantilevers (integral Si_3N_4 tips, 100 μm legs, 0.58N/m spring constant), and a "D" piezoelectric scan head (14 696 nm x–y range) using acquisition parameters: (A + B) signal ~6 V, (A − B) signal ~−2.0 V, set point voltage ~±0.75 V, integral gain 1–3, proportional gain 0–1, two-dimensional gain 0, scan rate 4.34–39.06 Hz, and filters off. The tip-sample force measured as previously described[11a] was ~60–100 nN in air and ~20–30 nN under electrolyte solution.

AFM-EC experiments were conducted using the Nanoscope glass fluid cell attachment containing the AFM tip and HOPG working, Pt auxiliary, and Ag quasi-reference electrodes as described before.[11] The cell was filled with electrolyte solution filtered through a 0.2 μm PTFE membrane (Acrodisc, Gelman Scientific). The quality of the AFM tip was typically verified, both before and after filling the cell with electrolyte solution, by

(10) (a) Chen, C.; Vesecky, S. M.; Gewirth, A. A. *J. Am. Chem. Soc.* **1992**, *114*, 451–458. (b) Manne, S.; Hansma, P. K.; Massie, J.; Elings, V. B.; Gewirth, A. A. *Science* **1991**, *251*, 183–186. (c) Manne, S.; Massie, J.; Elings, V. B.; Hansma, P. K.; Gewirth, A. A. *J. Vac. Sci. Technol.* **1991**, *9*, 950–954.

(11) (a) Goss, C. A.; Brumfield, J. C.; Irene, E. A.; Murray, R. W. *Langmuir* **1992**, *8*, 1459–1463. (b) Brumfield, J. C.; Goss, C. A.; Irene, E. A.; Murray, R. W. *Langmuir* **1992**, *8*, 2810–2817.

(12) (a) Beck, F.; Junge, H.; Krohn, H. *Electrochim. Acta* **1981**, *26*, 799–809. (b) Beck, F.; Krohn, H. *Synth. Met.* **1983**, *7*, 193–199.

obtaining stable large-area and atomically resolved images of HOPG. The tip was withdrawn 10–15 μm from the surface during filling. For oxidative voltammetry, the HOPG potential was scanned at 100 mV/s between +0.135 V and a moderate oxidizing potential, determined by scanning oxidatively to increasingly greater potentials until the onset of oxidation currents of size consistent with monolayer-level carbon oxidation were observed. To ensure that AFM images were obtained at the same location throughout an experiment, the AFM tip normally remained engaged during potential cycling, with the AFM scan rate lowered to 0.13 Hz so as to only scan one or two lines (out of 400/image) during the voltammetric scan. AFM-EC images were typically acquired with the electrode poised at +0.135 V. No evidence of tip-induced surface features was observed when the scan area was expanded. Flatten (F) and low-pass (LP) filters were utilized for some images, as indicated in figure captions.

Optical Microscopy. Oxidized electrodes were examined with a Carl Zeiss Universal M microscope equipped with a Nomarski differential interference contrast[13] attachment.

RESULTS AND DISCUSSION

Cyclic Voltammetry. The primary purpose of our voltammetric investigation of basal plane HOPG was to compare the electrochemical behavior of HOPG in electrolytes that exhibit different propensities for intercalation. Cyclic voltammetry is a useful diagnostic for this investigation because it provides information about the reversibility of reactions and is convenient in controlling the oxidation of HOPG to very small quantities. Figure 2 presents cyclic voltammetry of basal plane HOPG in the series of electrolytes indicated. Table 1 summarizes data from Figure 2, in particular the oxidative (Q_A) and reductive (Q_C) charges passed, the voltammetric reversibility and thus electrolyte intercalation as the ratio Q_C/Q_A, and the number of oxidized graphite monolayers,[9] Q_A/Q_M. Figure 2 curves A and B are from our previous investigation[9] of blister formation in 1 M KNO_3. The initial potential scan, curve A (to +1.99 V vs SSCE), exhibits oxidative wave fine structure presumably associated with electrolyte anion intercalation steps, and a small reduction peak. Subsequent potential scans (Figure 2B) exhibit a loss of most of the oxidative fine structure, a larger maximum anodic current, and a larger reduction wave (increased oxidative–reductive reversibility). Note that the oxidative charge in Figure 2A,B corresponds to an average of only one or two carbon monolayers (which, however, are probably not consumed evenly across the surface). Restricting potential scans to less positive potential limits (not shown), so as to confine the charge passed in the scan to submonolayer levels, enhances the oxidative and reductive reversibility.[9] It was in the context of such submonolayer-level voltammetry that blistering was observed[9] with the microscopies noted above, leading to the incipient oxidation model of Figure 1, in which gas evolved from intercalation and subsurface reactions accompanying electrochemical graphite oxide (EGO) formation is believed to drive the localized delamination and blister formation.

The oxidative voltammetry obtained in 1 M $LiClO_4$, 1 M $(NH_4)_2SO_4$, and 1 M H_2SO_4 (Figure 2, curves C–E) is similar to that in KNO_3. When the potential scan limit is chosen so that the charges passed amount to only submonolayer levels of carbon oxidation (see Table 1), the initial scan exhibits some fine structure and is partially reversible; subsequent scans are more reversible with less fine structure. The voltammograms for oxidations in $LiClO_4$ and $(NH_4)_2SO_4$ (Figure 2C,D) are almost completely reversible when cathodic and anodic charges are compared, while that for H_2SO_4 (Figure 2E) returns a slightly greater cathodic than anodic charge. Voltammetry in 1 M HNO_3 (not shown) is similar to that in 1 M H_2SO_4. These results are consistent with previous voltammetric investigations of natural graphite[8d,g,i,12] and HOPG[2,8h,14]

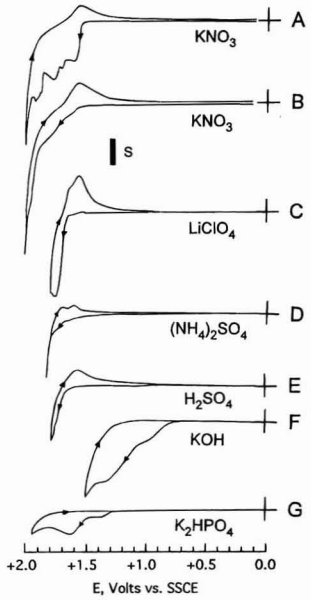

Figure 2. Cyclic voltammograms at basal plane HOPG electrode at 100 mV/s and in the following: (A) 1.0 M KNO_3 electrolyte, potential scan between +0.1 and +1.99 V, $S = 20$ μA, $Q_A/Q_M = 1.9$; (B) 1.0 M KNO_3 electrolyte, potential scan between +0.1 and +1.99 V, $S = 20$ μA, $Q_A/Q_M = 1.3$; (C) 1 M $LiClO_4$ electrolyte, potential scan between +0.1 and +1.80 V, $S = 40$ μA, $Q_A/Q_M = 0.27$; (D) 1 M $(NH_4)_2SO_4$ electrolyte, potential scan between +0.1 and +1.85 V, $S = 5$ μA, $Q_A/Q_M = 0.05$; (E) 1 M H_2SO_4 electrolyte, potential scan between +0.1 and +1.80 V, $S = 10$ μA, $Q_A/Q_M = 0.01$; (F) 1 M KOH electrolyte, potential scan between +0.1 and +1.50 V, $S = 300$ μA, $Q_A/Q_M = 3.2$; (G) 1 M K_2HPO_4 electrolyte, potential scan between +0.1 and +1.95 V, $S = 300$ μA, $Q_A/Q_M = 1.1$. Curves A and B are reproduced from an earlier investigation.[9] Q_A/Q_M is ratio of anodic charge passed to charge for $n = 2$ oxidation of a monolayer of carbon atoms.

Table 1. Voltammetric Charge Densities from Figure 2

curve[a]	electrolyte	+E limit, V	Q_A,[b] μC/cm^2	Q_C,[c] μC/cm^2	Q_C/Q_A	Q_A/Q_M[d]
A	KNO_3	+1.99	2306	278	0.12	1.9
B	KNO_3	+1.99	1578	480	0.31	1.3
C	$LiClO_4$	+1.80	328	313	0.95	0.27
D	$(NH_4)_2SO_4$	+1.85	59.7	48.4	0.81	0.05
E	H_2SO_4	+1.80	14.8	17.5	1.2	0.01
F	KOH	+1.50	4000	0	0	3.2
G	K_2HPO_4	+1.95	1366	0	0	1.1

[a] All first scan on fresh HOPG surface, except curve B. [b] Q_A, oxidative charge density. [c] Q_C, reductive charge density. [d] Q_M, monolayer equivalent charge, 1.23 mC/cm^2.

(13) McCrone, W. C.; McCrone, L. B.; Delly, J. G. *Polarized Light Microscopy*; Ann Arbor Science Publishers: Ann Arbor, MI, 1978; pp 54–57.

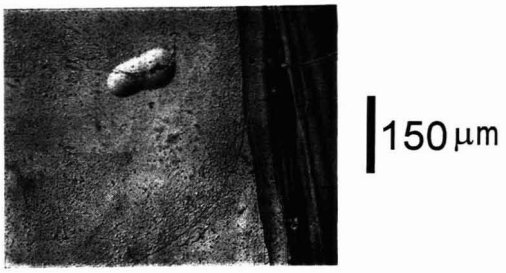

Figure 3. Optical photomicrograph of HOPG electrode oxidized in 1 M H_2SO_4 for three potential scans from +0.135 to +1.75 V at 100 mV/s, $Q_A/Q_M = 0.03$.

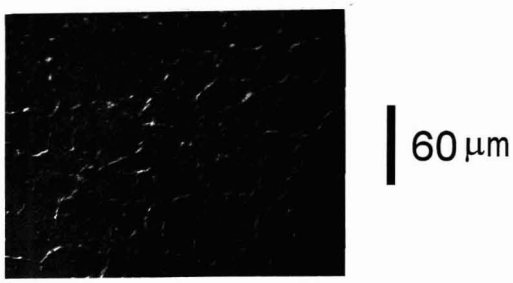

Figure 4. Optical photomicrograph of HOPG electrode oxidized in 1 M $LiClO_4$ for six potential scans from +0.135 to +1.80 V at 100 mV/s, $Q_A/Q_M = 1.2$.

Figure 5. Optical photomicrograph of HOPG electrode oxidized in 1 M $(NH_4)_2SO_4$ for four potential scans from +0.135 to +1.90 V at 100 mV/s, $Q_A/Q_M = 0.18$.

electrodes in intercalating acid electrolytes.[1] While the potentials at which submonolayer levels of oxidation occur vary in different electrolyte solutions, it is known that the anodic behavior of basal plane HOPG is complex and depends on the electrolyte, its concentration, and the pH.[1–3]

The anions of the preceding electrolytes have all been reported[1,2,6,8,12] to be capable of intercalating into the HOPG lattice during its oxidation, acting in the simplest picture as internal counterions to the radical cation-like lattice. The reduction waves in the voltammetry of Figure 2A–E reflect the rereduction of the intercalated carbon lattice with, presumably, accompanying ejection of the intercalated electrolyte anion.

Figure 2F shows voltammetry in 1 M KOH. While there have been many investigations of electrolyte intercalation and the electrochemistry of graphite in neutral and acidic media, references to graphite oxidation in basic media are rare.[1] Oxidation in Figure 2F commences at less positive potentials, consistent with the expected effect of pH. The potential limit chosen in Figure 2F corresponded to oxidation of several carbon monolayers, $Q_A/Q_M = 3.2$ (Table 1). On both the initial and subsequent potential scans in KOH, no reduction current waves are observed. An analogous result is found for phosphate electrolytes; voltammetry in K_2HPO_4 is shown in Figure 2G. That for H_3PO_4 is quite similar; again, no reduction current is seen. Alsmeyer and McCreery[6] reported from Raman evidence that oxidation of HOPG in 1 M H_3PO_4 resulted in neither intercalation nor graphite lattice damage. The result of Figure 2G is consistent with poor or no intercalation of phosphate into HOPG, and that of Figure 2F suggests that OH^- intercalation from KOH into HOPG is similarly unfavorable.

In summary, under conditions of submonolayer oxidation according to voltammetric criteria, the electrolyte anions of KNO_3, $LiClO_4$, $(NH_4)_2SO_4$, HNO_3, and H_2SO_4 appear to intercalate into HOPG during oxidation, while those of KOH, K_2HPO_4, and H_3PO_4 intercalate with difficulty or not at all.

Optical Microscopy Observations. Inspection of HOPG electrodes by optical microscopy following oxidation in $LiClO_4$, $(NH_4)_2SO_4$, HNO_3, and H_2SO_4 reveals the presence of blisters which appear identical to those previously formed and characterized in KNO_3. Figures 3, 4, and 5 are optical micrographs of electrodes oxidized in 1 M H_2SO_4 (three +0.135 to +1.75 V potential scans), 1 M $LiClO_4$ (six +0.135 to +1.80 V potential scans), and 1 M $(NH_4)_2SO_4$ (four +0.135 to +1.90 V potential scans), respectively. These micrographs show similar features, in particular larger blisters that are aligned in patterns suggesting formation near or along microcrystalline grain boundaries. This is apparent in the outlines found in Figure 4 and is especially evident in Figure 5, where blisters form in relatively high density around the edges of the tear drop-shaped cleaving defect while the remainder of the electrode surface in the micrograph appears relatively unaltered. Another common feature of the micrographs is that both large and small blisters appear in locations where there is no obvious cleaving defect. These aspects of blistering were also seen[9] in KNO_3 electrolyte and are incorporated into the model of Figure 1 in the sense that the subsurface location of gas evolution need not be visible from the HOPG surface, but that some proximity to a surface defect is nonetheless necessary for the entry of the intercalating electrolyte.

The material appearing on the right side of the image in Figure 3 is polyurethane used to mask the electrochemically accessible area of the electrode surface. Careful inspection reveals that small blisters are present underneath the polyurethane mask, extending approximately 50–100 μm from the edge of the material. These blisters could originate either from electrolyte penetration under the edge of the masking material or from subsurface processes of electrolyte intercalated from defects on the exposed electrode surface.

Another feature of micrographs like those of Figures 3–5 is that blistering is very nonuniform across the surface of any given HOPG sample. Note the single large blister ~100 μm long in Figure 3 surrounded by hundreds of much smaller blisters. It is also possible to find large regions of HOPG surface that remain relatively undisturbed and others where the blister density is quite large, as in Figures 4 and 5. An accompanying implication is that, although we confine the total oxidation charge to overall sub-

(14) Besenhard, J. O.; Wudy, E.; Möhwald, H.; Nickl, J. J.; Biberacher, W.; Foag, W. *Synth. Met.* **1983**, *7*, 185–192.

Figure 6. Optical photomicrograph of an HOPG electrode oxidized in 1 M K_2HPO_4 for three potential scans from +0.135 to +1.75 V at 100 mV/s, $Q_A/Q_M = 2.0$.

monolayer levels for the geometric HOPG surface, multiple-monolayer quantities of charge may be passed locally at sites of blistering. It is quite difficult as a result to quantify the relative extent of blistering among the electrolytes in Figures 3–5, and we do not attempt this. However, the differences between the behavior of the above electrolytes and that described next in KOH, K_2HPO_4, and H_3PO_4 are so large that we are confident of a qualitative difference in the behavior of these electrolytes.

Blister formation was observed to be possible in 1 M KOH aqueous electrolyte; however, blister formation was never observed for passage of charges as small as a few monolayers of carbon oxidation. Blisters were seen only after passages of charge from 1 to 3 orders of magnitude larger (typically 100 times $LiClO_4$) than in neutral or acidic electrolytes, and those that form are also typically larger in size and fewer in number than those that form in other aqueous electrolytes. Recall that voltammetry associated with oxidation in 1 M KOH (Figure 2F) is completely irreversible.

Attempts to produce blisters on HOPG electrodes in 1 M H_3PO_4 and 1 M K_2HPO_4 were unsuccessful at oxidation potentials as high as +1.95 V and for passage of multiple monolayers of charge (typical experiments passed charge equivalent to five or six HOPG monolayers). As in KOH oxidation, the voltammetry associated with oxidation in 1 M H_3PO_4 and 1 M K_2HPO_4 (Figure 2G) appears to be completely irreversible. The only discernable change in surface microstructure (Figure 6) from oxidation in phosphate-containing electrolytes is the appearance of fractures in the HOPG surface in patterns possibly related to graphite grain boundaries. Such features were never observed by optical microscopy on the unoxidized HOPG electrode material.

In summary, blistering is facile in KNO_3, $LiClO_4$, $(NH_4)_2SO_4$, HNO_3, and H_2SO_4 electrolytes, difficult in KOH, and unobservable in H_3PO_4 and K_2HPO_4 electrolytes.

Atomic Force Microscopy Observations. Ex situ AFM was also used to examine "blistered" electrodes as a complement to optical microscopy. AFM provides surface feature height information not readily obtained by OM, and the enhanced lateral resolution allows exploration of lattice structure and smaller surface features. Images of electrodes oxidized to a few monolayer level under 1 M HNO_3 or 1 M $(NH_4)_2SO_4$ are very similar to those shown in Figure 4 of ref 9. The 3 × 3 and 10 × 10 μm images typically show a mixture of small blisters and several large, multiple-cell blisters. Ex situ AFM was also used to obtain atom-resolved images on the tops of blisters formed in $LiClO_4$ electrolyte. As was observed in KNO_3 electrolyte,[9] these images as well as those on featureless surface regions on oxidized samples are identical to images acquired on unoxidized HOPG samples.

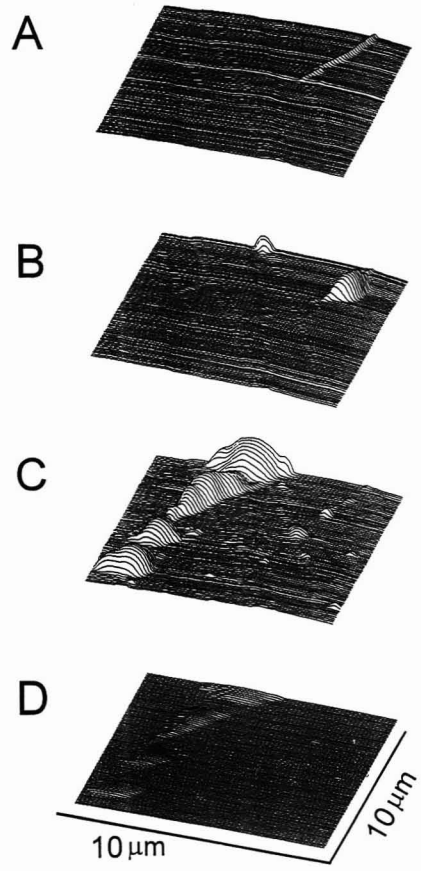

Figure 7. AFM-EC images recorded the blistering of a 10 × 10 μm region of a basal plane HOPG electrode under 1 M $LiClO_4$ electrolyte. *Z* scale for images A–C equals 100 nm: (A) Image after three potential cycles to +1.75 V; (B) image after one additional potential cycle to +1.75 V; (C) image after total seven potential cycles to +1.90 V; (D) same as (C) except that *z* scale equals 1 μm.

Atom-resolved AFM images of the blister tops gave a next nearest neighbor spacing of 0.25 ± 0.01 nm, consistent with established values.[4,15]

In situ AFM-EC experiments allow blister formation and growth to be recorded during the oxidation process. The capability of AFM to image with subnanometer resolution[9,11] under liquid makes it an ideal technique to probe incipient HOPG oxidation. By restricting oxidizing potentials to pass only sub-monolayer charges, changes in microstructure on the electrode surface can be monitored that would occur too rapidly to be followed under more oxidative conditions. Figure 7 shows a sequence of observations leading to a large multiple-cell blister using 1 M $LiClO_4$ electrolyte. The faint NW–SE diagonal features in panels A–C are cleaving defects which serve to demonstrate the absence of drift during the measurements. A small, ridgelike blister appears on the upper right corner of the 10 × 10 μm image in panel A, after three potential scans to +1.75 V. In panel B,

(15) Jolly, W. *Modern Inorganic Chemistry*; McGraw-Hill: New York, 1984; p 271.

acquired after one additional scan to +1.75 V, this blister has grown and another blister is forming at the edge of the scan area in the top center of the image. In the third image, panel C, after three additional scans to +1.90 V, the latter feature has propagated into a SW–NE diagonal chain of blisters, possibly along a subsurface defect, on the left side of the scan area. Other small features appear randomly placed in panel C, where it is also interesting that the original blister at the top right of the image has greatly diminished in size. While it is possible that it has drifted from the field of view, we think this unlikely because of the persistence of the faint cleaving defect running NW to SE from the upper left of the images in panels B and C. Panel D reproduces panel C but with *z*-axis sensitivity equal to that of the *x*–*y* planes. This picture emphasizes what is not readily evident in the previous images, that the blisters are actually quite modest elevations above the HOPG surface, like gently rounded pancakes. The modest elevation is consistent with our observations (vide supra) of an undisturbed HOPG lattice spacing; the latter is supported by simple geometrical model calculations for a typical blister.

The AFM in situ images in Figure 7 have been presented as line scans, in order to better visualize blister formation and growth. Subtle surface features, such as the cleaving defects in the in situ images, typically appear more distinct in illumination mode and as such often make interpretation difficult. While we previously presented AFM and AFM-EC images of graphite blisters formed in KNO_3, the images depicted here represent the first AFM and AFM-EC images documenting blister formation in other intercalating aqueous electrolytes.

CONCLUSIONS

The formation of graphite blisters in intercalating electrolytes, atom-resolved images of blister tops, and the lack of blister formation in nonintercalating electrolytes provide further support for the model[9] for blister formation and growth depicted in Figure 1. The development of blisters in regions far away from surface defects, the presence of undisturbed defects on top of blisters, and the formation of multiple-cell blisters are consistent with the proposed model. The voltammetry and presence or absence of blisters in particular electrolytes also corroborate the previous findings of McCreery.[6]

A number of intriguing aspects of intercalation and blister formation on HOPG remain unanswered. Our measurements give no quantitation of the extent of anion intercalation into the HOPG lattice (lateral and vertical dimensions). The processes that consume the large amount of oxidative charge in poor and nonintercalating electrolytes also deserve further study. Also, the voltammetry presented here was conducted at a moderately fast scan rate, 100 mV/s. Hence, the amount of intercalation cannot be assumed to be an equilibrium quantity and the potentially sensitive relation between current density and blister formation is unknown. It is worth noting that while the AFM-EC images shown here chronicle in situ blister formation and growth, they consist of a series of snapshots and do not provide a true sense of the blister formation process in real time.

We did not apply the array of XPS and Auger spectroscopies used in the previous study[9] to examine the composition of oxidized material within blisters formed in KNO_3 electrolyte. We presume it is similar in the other intercalating electrolytes, but there could be specific, undetermined differences. Finally, the role of intercalated solvent molecules in blister formation is of interest. If water is indeed necessary for the oxidative reactions to proceed, blistering should not be observed in nonaqueous electrolytes. In other studies,[6] evidence was observed for intercalation from $NaClO_4/CH_3CN$, but lattice damage was not seen by Raman.

ACKNOWLEDGMENT

This research was supported in part by grants from the National Science Foundation.

Received for review January 19, 1995. Accepted April 18, 1995.[⊗]

AC950066Q

[⊗] Abstract published in *Advance ACS Abstracts,* June 1, 1995.

Anal. Chem. **1995**, *67*, 2207–2211

Correlation between Permselectivity and Chemical Structure of Overoxidized Polypyrrole Membranes Used in Electroproduced Enzyme Biosensors

F. Palmisano, C. Malitesta, D. Centonze,† and P. G. Zambonin*

Dipartimento di Chimica, Università degli Studi, Via Orabona 4, 70126 Bari, Italy

The permeability (*KD*) of common electroactive interferents in H_2O_2 detecting amperometric biosensors through polypyrrole films overoxidized in aqueous solution by long-term electrolysis at low potential (+0.7 V vs Ag/AgCl) has been investigated at pH 7. *KD* values in the order of 10^{-10}–10^{-9} cm^2 s^{-1} have been obtained by rotating disk voltammetry. X-ray photoelectron spectroscopy investigation of the overoxidized polymer revealed a remarkable increment of C=O and COH functions compared to the pristine and, for the first time, revealed the presence of carboxylic groups, likely ionized under the given experimental conditions. At the same time, a transformation of positive to iminic nitrogen is observed. On this basis, the existence of two domains consisting of oxygenated functions (hydrophilic) and iminic functions (hydrophobic) can be hypothesized to explain the observed dependence of probe permeability on charge and the hydrophobicity of the probe itself. In particular, the partition of anionic hydrophilic species seems hindered in hydrophilic channels, producing low *KD* values. On the contrary, the neutral form of anionic hydrophobic species could permeate through hydrophobic channels.

Polymer-modified electrodes (PMEs) have received rather extensive interest[1] since they can be designed to provide important improvements in sensitivity and selectivity while remaining versatile enough to detect a variety of analytes. Selectivity of PMEs can be attained by different mechanisms such as size exclusion, ion exchange, and hydrophobic interactions. Nafion-modified electrodes are probably the most widely studied PMEs (see, e.g., ref 2): here the polymer acts as a cation exchanger that exclude anions; however, it exhibits a more complex selectivity pattern than the simple ion exchangers, with hydrophobic cations[3] being preferentially admitted.

Electropolymerized films have been widely used in recent years as a mean to modify electrode surfaces. PMEs obtained from the electropolymerization of pyrroles have received great attention in view of several promising applications including the development of chemical[4] and biochemical[5] sensors. In this last context, electropolymerized polypyrrole (PPY) films demonstrated suitable media for the immobilization of enzymes at the surface of an amperometric biosensor. Properties of PPY films are influenced by several factors, e.g., electrode potential,[6] solvent,[6,7] and counterion[8,9] used during electropolymerization. PPY films are also affected by the potential applied to the conducting polymer[10] after the electrosynthesis. In particular, when PPY is kept at high potentials (>0.7 V vs SCE[11]), it degrades to a new material called overoxidized polypyrrole (PPYox) with a concomitant loss of conductivity and electroactivity, usually regarded as highly desirable characteristics of PPY.

Extensive work (see, e.g., refs 12 and 13) has been performed on the chemical characterization of PPY electrochemically overoxidized in organic solvents, likely containing traces of H_2O. Less attention has been devoted to PPY electrochemically overoxidized (at potential ≥1.0 V vs SCE) in aqueous solutions,[11,14] which provides[15,16] a material showing remarkable permselective properties. The observed behavior was correlated to the hypothesized presence of carbonyl groups, already reported[14] for overoxidation at similarly high potentials.

Recently, our group[17–20] has explored a novel approach in biosensor design based on the use of electrochemically grown nonconducting, permselective polymeric films as enzyme entrapping membranes. By such an approach, glucose amperometric sensors with very peculiar and attractive features (one-step preparation, fast response, freedom from interferences) were obtained. These sensors are based on the amperometric detection

† Present address: Dipartimento di Chimica, Università della Basilicata, Via N. Sauro, 85, 85100 Potenza, Italy.

(1) Murray, R. W. In *Electroanalytical Chemistry*; Bard, A. J., Ed.; Marcel Dekker: New York, 1984; Vol. 13, pp 191–368.
(2) Nagy, G.; Gerhardt, G. A.; Oke, A. F.; Rice, M. E.; Adams, R. N.; Moore, R. B., III; Szentirmay, M. N.; Martin, C. R. *J. Electroanal. Chem.* **1985**, *188*, 85.
(3) Szentirmay, M. N.; Martin, C. R. *Anal. Chem.* **1984**, *56*, 1898.
(4) Lyons, M. E. G.; Breen, W.; Cassidy, J. *J. Chem. Soc., Faraday Trans. 1* **1991**, *87*, 115.
(5) Foulds, N. C.; Lowe, C. R. *J. Chem. Soc., Faraday Trans. 1* **1986**, *82*, 1259.
(6) Asavapiriyanont, S.; Chandler, G. K.; Gunawardena, G. A.; Pletcher, D. *J. Electroanal. Chem.* **1984**, *177*, 199.
(7) Ferreira, C. A.; Aeiyach, S.; Delamar, M.; Lacaze, P. C. *J. Electroanal. Chem.* **1990**, *284*, 351.
(8) Mammone, R. J.; Binder, M. *J. Electrochem. Soc.* **1990**, *137*, 2135.
(9) Kuwabata, S.; Nakamura, J.; Yoneyama, H. *J. Electrochem. Soc.* **1990**, *137*, 2147.
(10) Feldman, B. J.; Burgmayer, P.; Murray, R. W. *J. Am. Chem. Soc.* **1985**, *107*, 872.
(11) Christensen, P. A.; Hamnett, A. *Electrochim. Acta* **1991**, *36*, 1263.
(12) Novak, P.; Rasch, B.; Vielstich, W. *J. Electrochem. Soc.* **1991**, *138*, 3300.
(13) Schlenoff, J. B.; Xu, H. *J. Electrochem. Soc.* **1992**, *139*, 2397.
(14) Beck, F.; Braun, P.; Oberst, M. *Ber. Bunsen-Ges. Phys. Chem.* **1987**, *91*, 967.
(15) Witkowski, A.; Freund, M. S.; Brajter-Toth, A. *Anal. Chem.* **1991**, *63*, 622.
(16) Witkowski, A.; Brajter-Toth, A. *Anal. Chem.* **1992**, *64*, 635.
(17) Malitesta, C.; Palmisano, F.; Torsi, L.; Zambonin, P. G. *Anal. Chem.* **1990**, *62*, 2735.
(18) Centonze, D.; Guerrieri, A.; Malitesta, C.; Palmisano, F.; Zambonin, P. G. *Fresenius J. Anal. Chem.* **1992**, *342*, 729.
(19) Palmisano, F.; Centonze, D.; Guerrieri, A.; Zambonin, P. G. *Biosens. Bioelectron.* **1993**, *8*, 393.
(20) Centonze, D.; Guerrieri, A.; Palmisano, F.; Torsi, L.; Zambonin, P. G. *Fresenius J. Anal. Chem.* **1994**, *348*, 1673.

0003-2700/95/0367-2207$9.00/0 © 1995 American Chemical Society

of biocatalytically produced H_2O_2; in this case, any species electroactive at the detection potential as well as surface active species represent serious interferents. In this respect, it was demonstrated that, after an overoxidation process, a conducting PPY film acquires very remarkable characteristics in terms of electroactive and surface active interferents rejection both in flow injection analysis[18] and continuos flow[19,20] experiments. It is worth noting the excellent rejection obtained for acetaminophen, one of the most serious interferent; consider that 200 μM acetaminophen produced a nondetectable glucose bias at a PPYox-based sensor[19] and a glucose bias of about 7 mM at a conventional glucose biosensor.[21] Clear evidences were also obtained[18] that overoxidation of PPY can occur by long-term electrolysis during the necessary background stabilization time at the potential (+0.65 V vs SCE) of hydrogen peroxide detection at a Pt surface. In fact, following that treatment, PPY looses its electroactivity.[18] Preliminary X-ray photoelectron spectroscopy (XPS) investigations[18] demonstrated that PPYox films had a significantly increased O/C ratio compared to the pristine PPY.

In this work, the detailed chemical structure of the previously described PPYox[18] is investigated by XPS. Membrane permeability toward some endogenous (ascorbate, urate, cysteine) and exogenous (acetaminophen) electroactive interferents in glucose determination by amperometric biosensors is also reported. A correlation between the chemical structure and permeability values is attempted.

EXPERIMENTAL SECTION

Materials. Pyrrole (Aldrich) was purified just before use by vacuum distillation at 62 °C. Ascorbic acid (AA), acetaminophen (AC), and cysteine (Cys) (Sigma Chemical Co.); uric acid (UA) (Analyticals Carlo Erba); and 3,4-dihydroxyphenylacetic acid (DOPAC) (Aldrich) were used as received. All the other chemicals were of analytical grade.

Apparatus. All electrochemical experiments were carried out by a PAR 174A polarographic analyzer or a PAR 273 potentiostat-galvanostat (EG&G Princeton Applied Research) and a conventional three-electrode system with a Pt foil as counter electrode and an Ag/AgCl (KCl saturated) as the reference electrode. The working electrode was a Pt disk (1 mm diameter) embedded in a PTFE body or a Pt sheet (geometric area ca. 1 cm^2) suitable for XPS measurements. Prior to each experiment, the working electrode was mechanically polished, treated with hot HNO_3, and washed with triply distilled water.

Electrode Preparation. Polypyrrole films were prepared by potentiostatic growth at +0.7 V vs Ag/AgCl in a deareated 10 mM KCl supporting electrolyte containing 0.4 M pyrrole. A deposition charge of 300 mC/cm^2 was used; the thickness of the resulting film, ca. 0.67 μm, was estimated assuming[22] that, for PPY deposition from aqueous solutions, 45 mC/cm^2 produced a film thickness of 0.1 μm. The Pt/PPY electrode was then overoxidized[18] for 5 h at +0.7 V vs Ag/AgCl in a sodium phosphate buffer (I = 0.2 M, pH = 7).

RDE Experiments. Rotating disk electrode (RDE) experiments were carried out by an EDI-Controvit system (Tacussel, Villeurbaine, France) using a 1 mm diameter Pt disk electrode. Measurements were performed at 5000 rpm. Steady-state current (i_{ss}) was measured at +0.7 V vs Ag/AgCl. The product of K, film-solution partition constant, and D, diffusion coefficient in the film, was calculated for each test solute from the equation[23] $i_{ss} = nFAK_dC/d$, where d is the film thickness, C is the concentration, and the other symbols have the usual meaning. This equation produces accurate estimates of KD only if $(KD/d) \ll D_{soln}/\delta$ (D_{soln}, diffusion coefficient in solution; δ, solution diffusion layer), a condition which was verified by preliminary measurements that showed KD values in the range 10^{-9}–10^{-10} cm^2 s^{-1}. The δ value, at 5000 rpm, was calculated by assuming $D_{soln} = 10^{-5}$ cm^2 s^{-1} and kinematic viscosity $\nu = 0.01$ cm^2 s^{-1} for water. Then $(KD/d) = 1.5 \times (10^{-5}$–$10^{-6}) \ll 1.4 \times 10^{-2} = D_{soln}/\delta$.

XPS Experiments. XPS measurements were performed by a Leybold LHS10 spectrometer equipped with a twin anode (MgKα/AlKα) source. Both low (FRR, retarding ratio = 3) and high resolution (FAT, pass energy = 50 eV) spectra were recorded. Two software packages, both running on Compaq Deskpro 386, were employed in the data analysis of high resolution spectra. The first one[24] had the following options: smoothing, nonlinear background and radiation satellite subtraction, spectrum derivative (1st and 2nd), peak area calculus, and curve synthesis using Gaussian–Lorentzian peaks defined by the following parameters: centroid position, half-width at half maximum, peak height, and Gaussian–Lorentzian ratio (0.85).

The outputs of the first stage of curve fitting were used as initial estimates of peak parameters in the second stage, consisting of a nonlinear least-squares fitting program.[25,26]

The fitting strategy consisted of the following steps: (1) observation of the peak profiles for C1s, N1s, and O1s coupled to the use of derivatives to determine the minimum number of components present, having peak widths (fwhm) as taken from our work and literature data;[27] (2) fitting was started using the minimum number of components of the same predetermined fwhm, and that number was increased until the best fit, as evaluated by the minimum of the weighted variance, was obtained; (3) at this point, the constraint on the fwhm values was relaxed, producing the final result; (4) the coherence of the *independent* fittings of all XP signals was verified (e.g., the ratio of C=O estimates as obtained by C1s and O1s signals is 1).

Quantitation was performed by using peak areas. When a ratio between species of different elements was evaluated, the peak areas were divided by empirically derived atomic sensitivity factors (uncertainity for atomic ratio around 10%).[26] Full details of all the above calculations will be reported elsewhere.[28]

Chemical Derivatization (CD) Experiments. CD has been coupled[28] to XPS for confirming the presence of COH, C=O, and COOH groups. In particular, this was crucial to defining the presence of the small C1s (COOH) peak in PPYox. For this purpose, we used a selective derivatization method already described,[29] consisting of an esterification of COOH groups by trifluoroethanol (CF_3CH_2OH) vapors. Briefly, the sample was

(21) Moatti-Sirat, D.; Velho, G.; Reach, G. *Biosens. Bioelectron.* **1992**, *7*, 345.
(22) Fortier, G.; Brassard, E.; Bélanger, D. *Biosens. Bioelectron.* **1990**, *5*, 473.
(23) Gough, D. A.; Leypoldt, J. K. *Anal. Chem.* **1979**, *61*, 439.
(24) Desimoni, E.; Malitesta, C. *Comput. Enhanced Spectrosc.* **1986**, *3*, 107.
(25) Sherwood, P. M. A. Data Analysis in XPS and AES. In *Practical Surface Analysis*, 2nd ed.; Briggs, D., Seah, M. P., Eds.; John Wiley: Chichester, 1990; Vol. 1, Appendix 3.
(26) Malitesta, C.; Sabbatini, L.; Zambonin, P. G.; Peraldo Bicelli, L.; Maffi, V *J. Chem. Soc. Faraday Trans. 1* **1989**, *85*, 1685 and references therein.
(27) Moulder, J. F.; Stickle, W. F.; Sobol, P. E.; Bomben, K. D. *Handbook of X-ray Photoelectron Spectroscopy*; Chastain, V., Ed.; Perkin Elmer Corporation: Eden Prairie, 1992.
(28) Losito, I.; Malitesta, C.; Sabbatini, L.; Zambonin, P. G. Manuscript in preparation.
(29) Chilkoti, A.; Ratner, B. D.; Briggs, D. *Chem. Mater.* **1991**, *3*, 51.

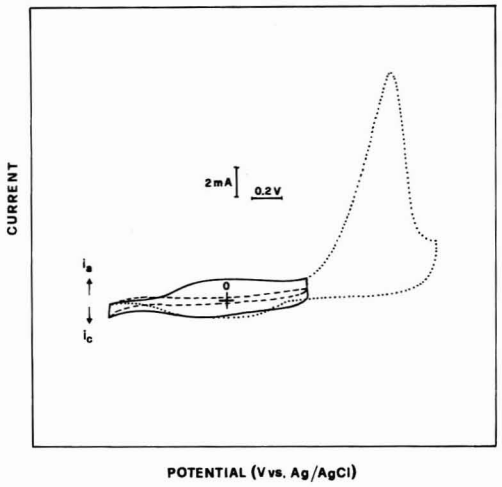

Figure 1. Cyclic voltammogram (CV) of a Pt(sheet)/PPY electrode in an aqueous 0.1 M $NaClO_4$ solution. Scan rate: 50 mV s^{-1}. The reversible behavior is represented by the continuous line (first CV scan). The overoxidation peak appears in the second cycle (dotted line) where the potential is anodically scanned up to +1.5 V. After the film was overoxidized at constant potential (+1.5 V vs Ag/AgCl) for a few minutes, the CV represented by the dashed line was finally obtained.

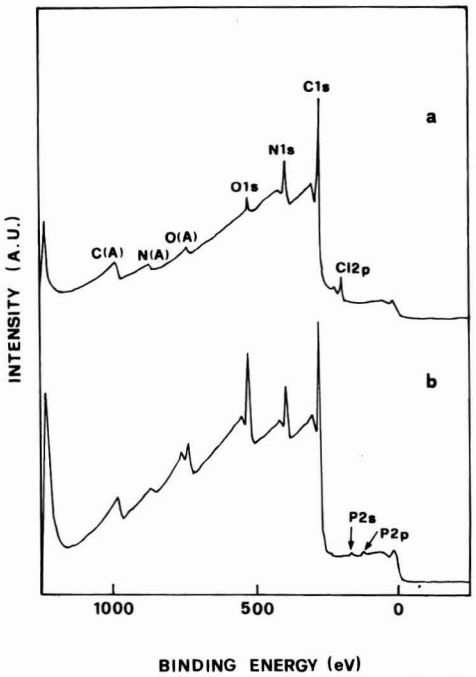

Figure 2. Low-resolution XP spectra for (a) PPY and (b) PPYox. Source Mg Kα. Na signals are not detected.

suspended in a glass test tube; trifluoroethanol (0.9 mL), pyridine (0.4 mL), and di-*tert*-butylcarbodiimide (0.3 mL) were sequentially injected into the test tube (below the sample) at 15-min intervals. The test tube was then sealed with a cap, and the reaction was allowed to proceed at ambient temperature for 12 h. The sample was then transferred to the spectrometer and analyzed.

RESULTS AND DISCUSSION

Reversible (oxidation/reduction) and irreversible (overoxidation) electrochemical processes for PPY in an aqueous solution are shown in Figure 1. The overoxidation can occur even at potential quite lower than the relevant peak potential. In fact, we could overoxidize[18] PPY by the long-term electrolysis at 0.7 V vs Ag/AgCl used for background stabilization of a PPY-entrapped glucose oxidase amperometric biosensor. Following overoxidation, PPY loses electroactivity and conductivity, acquiring a remarkable permselectivity.[18] The extent and the nature of the chemical modifications accompanying the overoxidation process have been investigated in order to gather more information about the mechanism of interferents rejection.

XPS Investigation. X-ray photoelectron spectra were collected on PPY and PPYox samples. Figure 2 shows typical low-resolution spectra for both kinds of samples. Some features are readily apparent. While the C/N ratio remains nearly constant passing from PPY to PPYox, the oxygen content (as measured by the O/N ratio) increases. At the same time, the Cl2p signal disappears. Since Cl^- ions balance positive charges of the polymer responsible for its electroactivity, this finding agrees with the disappearance of that property when PPY is overoxidized. However, a small P2p signal, likely belonging to the phosphate species of the supporting electrolyte, is present in PPYox; in any case, the phosphate content accounts only for a small part of the observed oxygen increment. The presence of phosphate species, unbalanced by supporting electrolyte cations (Na^+ not detected, see Figure 2), suggests that some positive charges are still present in the overoxidized polymer. These charges are possibly embedded in an insulating matrix so that they cannot exhibit any electroactivity. A small oxygen signal is already present in PPY, indicating that some overoxidation occurs even during the polymer growth from aqueous solution, a fact which is not surprising since the electrosynthesis and the overoxidation potentials are the same (see above).

Qualitative spectroscopic (IR, XPS) evidences of C=O and C—O groups when PPY is electrosynthesized or overoxidized in aqueous solution at high potentials (≫0.7 V vs SCE) have been already reported;[10,13] in particular, it has been suggested[13] that C=O functionalities are formed by the oxidation of COH precursors.

Details on the chemical nature of the overoxidation process were investigated by collecting high-resolution XP spectra on both PPY and PPYox samples. XPS results from several samples are reported in Figure 3 (showing the change on the distribution of C, N, and O components upon overoxidation) and in Figure 4. Some important features are apparent. The only evident anions are Cl^-, which balance N^+ species in PPY and HPO_4^{2-}, which only partially balance N^+ species in PPYox. The phosphate species is likely introduced by exchange with Cl^-. This is one of the first phenomena occurring to PPY when overoxidized in a phosphate buffer, at least in the layer sampled by XPS, as proved by an exchange experiment lasting for only 5 min. The surface anions generated by overoxidation (see below) then possibly trap phosphate species in the underlying layers. Overoxidation produces an increment of some oxygenated carbon species and the formation of new ones (COOH see Figure 5). The increment

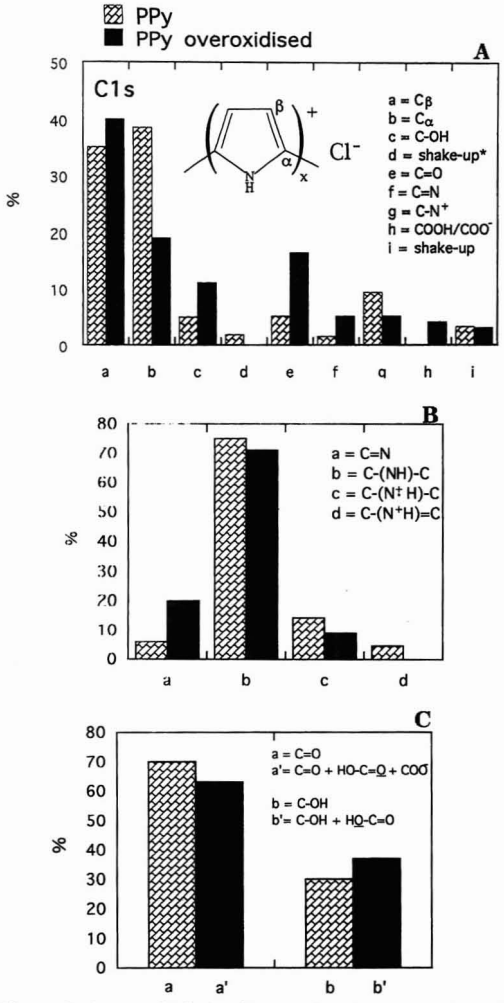

Figure 3. Average distribution (expressed as percentage of the total content of the element in each sample) of (A) carbon, (B) nitrogen, and (C) oxygen (phosphate species excluded) components for PPY and PPYox samples as measured by XPS. Contaminant species are not included. Star marks shake up at lower BE. The ideal structure of PPY, grown from a KCl solution, is included in panel A with a clear notation of α- and β-carbon atoms.

is even more pronounced at the polymer surface as evidenced by an increased O/C ratio obtained by XPS measurements at low take-off angle. Definite evidences about the presence of carboxylic functions were obtained by a selective esterification with trifluoroethanol; the occurrence of the reaction is indicated by the F signal in the spectrum (see Figure 6) of a derivatized PPYox sample.

Oxygenation of the polymer chain is not the only chemical modification occurring. In fact, positively charged N, even if still detectable in PPYox, is mostly transformed into iminic N at a large extent. The decreasing of N^+ species is again more evident at the surface. This finding, coupled to the increment of O/C ratio at the surface, suggests that the overoxidation process proceeds from the surface toward the polymer bulk. Since the residual

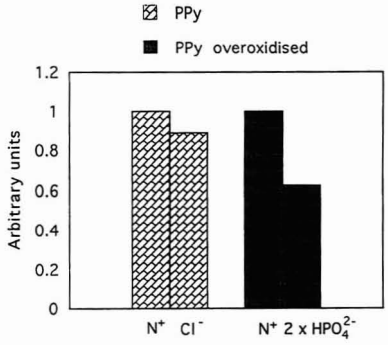

Figure 4. Charge balance: cationic and anionic species detected in PPY and PPYox. Contents normalized to the relevant N^+ species.

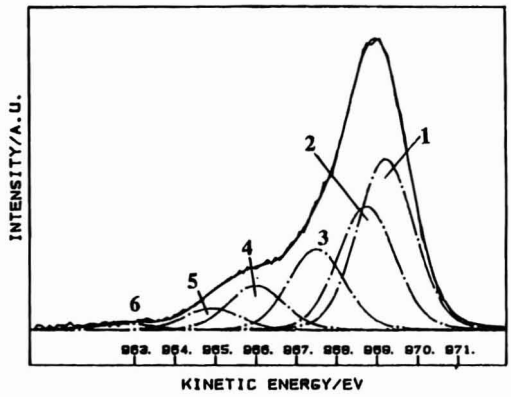

Figure 5. High-resolution XP spectrum of C1s region for a PPYox sample. The spectrum is background subtracted and fitted by the components specified in the following: 1, Cβ; 2, Cα + C (adventitious contamination); 3, C—O + C=N + CN^+; 4, C=O + $C{=}N^+$; 5, COOH + COO^-; 6, shakeup. Source Mg Kα. Energy scale not corrected for charging.

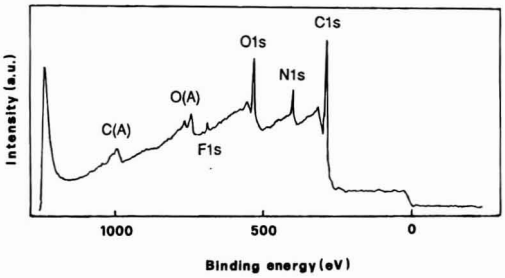

Figure 6. Low-resolution XP spectrum for a PPYox sample after derivatization by trifluoroethanol. Source Mg Kα.

positive N is not, in any case, fully balanced by HPO_4^{2-}, partial ionization of COOH groups must be invoked. The overall picture is completed by considering[28] that C atoms involved in C—O and C=O functionalities are those in the β and α position in PPY and PPYox samples, respectively. The last finding is completely new, since it is generally believed that only β positions are involved in PPY overoxidation. This implies that the observed loss of electroactivity (i.e., conjugation) in passing from PPY to PPYox is mainly due to the breakage of polymer chains. At the same

Table 1. *KD* Values As Measured by RDE in a Phosphate Buffer, pH 7, for Some Probes[a]

solute	pK_a[b]	charge[c]	log *P*[d]	*c* (mM)	*KD* ($cm^2\ s^{-1}$) $\times 10^{10}$
UA	5.4	−1	na (−1.85)	0.083	2.9
AA	4.04	−1	na (−2.88)	0.5	3.4
DOPAC	4.22	−1	na (+0.85)	0.5	13
Cys	1.92 (COOH)	0	−2.55	0.5	42
	8.37 (SH)				
	10.70 (NH_3^+)				
AC	9.71	0	+0.51	0.2	nm

[a] PPYox film thickness 0.67 μm. Errors on *KD* values ≤30%. na, not available. nm, not measurable. [b] References for pK_a values:[33] (UA, AA, Cys),[32] (DOPAC),[34] (AC). [c] The charge of the prevailing form of the probe at pH 7 is indicated. [d] log *P* is the logarithm of the 1-octanol/water partition coefficient, *P*. Values for the anionic species in the table are not available; however, they should be largely more negative[35] than values relevant to the neutral form of UA, AA, and DOPAC (reported in parentheses). The listed values are taken from refs 34–37.

time, this transformation could facilitate the formation of different microscopic chemical domains (see below).

As far as N groups are concerned, deprotonation in the overoxidation solution, i.e., in conditions more basic than those of the preparation, can be easily invoked[30,31] to explain N^+ ($N^{\cdot+}$ and $^+N=$) to iminic N transformation. The removal of fixed positive charges on the polymer and the introduction of carbonyl and carboxylic groups (likely negatively charged at the pH of permeability measurements) influences the nature of the film: the decrease of N^+ and the increase of N=C content tend to increase the hydrophobic character[32] of the film. On the other hand, the introduction of negatively charged (COO^-) and polar (C—O, C=O) groups gives a hydrophilic character to the same film.

The present picture is somewhat different from that devised for PPY overoxidized at higher potentials by other authors,[15–16] who assume that the major effect of overoxidation is the introduction of carbonyl groups as "pendant" groups into a nearly intact polymer backbone.

Permeability (*KD*) Measurements by RDE. Amperometric responses of certain solutes, mostly common electroactive interferents in H_2O_2 detecting amperometric biosensors, have been recorded at a PPYox-modified Pt electrode. The relevant *KD* values are collected in Table 1 along with other parameters such as charge and logarithm of octanol/water partition coefficient (log *P*), which provides a widely accepted hydrophobicity scale. On the basis of such a scale, some useful predictions can be made about the hydrophobic effect, which is assumed to be the driving force in several processes such as liquid–liquid partitioning, passive diffusion transport through biological membranes, drug–receptor binding, etc. As it will be shown in the following, some inferences can be drawn from Table 1 on factors affecting the permeability through PPYox for the set of substances studied.

The behavior evidenced in this case could be tentatively explained assuming the existence of two diffusion channels: hydrophilic (micropores) and hydrophobic (polymer bulk) phases, as already hypothesized by Braither-Toth et al.[16] Each probe could, in principle, permeate through both channels depending on partition and mobility in each channel. On the basis of spectroscopic evidences given above, one can hypothesize that hydrophobic paths likely contain nitrogen groups, while hydrophilic ones are crowded by C—O and C=O (properly oriented to counteract anion ingress) and COO^- groups. The presence of COO^- groups, here evidenced for the first time, could play a key role because it gives a net negative charge to the polymer. As far as the hydrophilic species listed in Table 1 are considered (monoanionic UA, AA, and DOPAC and neutral Cys), one can see that the neutral Cys displays a *KD* value considerable higher than those relevant to the monoanionic UA, AA, and DOPAC. Evidently, partition of anionic species into hydrophilic channels is considerable hindered compared to neutral ones due to unfavorable electrostatic interactions. In other words, charge as already found[15,16,18] is an important factor affecting probe permeability. Moreover, if one considers UA, AA, and DOPAC, it can be seen that the *KD* value of DOPAC is higher, by a factor ca. 4, than that of UA and AA. This behavior seems to originate from concurrence of different factors such as the existence of neutral forms of AA, UA and DOPAC at concentrations dictated by their respective pK_a values, and the different hydrophobic character of neutral AA, UA, and DOPAC, influencing partition/diffusion through the hydrophobic channels (neutral DOPAC) and hydrophilic channels (neutral AA and UA). Finally, if one considers a neutral and hydrophobic species such as AC, then probe partition/diffusion into the hydrophobic channels ultimately determines permeability; in the specific case, the *KD* value for AC is not measurable suggesting that, once partitioned, diffusion of the probe is highly inhibited due to specific (yet unknown) interactions with the polymer matrix. An extension of the study to a larger set of substances is needed to generalize the model and to interpret all effects. This aspect and others under investigation are part of a wider project going on in this laboratory aimed at investigating the correlation between chemical structure and permeability properties of specifically designed, different electrosynthesized polymeric materials.[38]

(30) Morse, N. J.; Rosseinsky, D. R.; Mortimer, R. J.; Walton, D. J. *J. Electroanal. Chem.* **1988**, *255*, 119.
(31) Kumar, S. N.; Bouyssoux, G.; Gaillard, V. *Surf. Interface Anal.* **1990**, *15*, 531.
(32) Ishimitsu, T.; Hirose, S.; Sakurai, H. *Talanta* **1977**, *24*, 555.
(33) Dawson, R. M. C.; Elliott, D. C.; Elliott, W. H.; Jones, K. M. *Data for Biochemical Research*; Clarendon Press: Oxford, 1986.
(34) Craig, V. In *Comprehensive Medicinal Chemistry*; Hansch, C., Sammes, P. G., Taylor, J. B., Eds.; Pergamon Press: Oxford, 1990; Vol. 6 pp 237–991.
(35) Leo, A.; Hansch, C.; Elkins, D. *Chem. Rev.* **1971**, *71*, 525.
(36) Hansch, C.; Leo, A. *Substituent Constants for Correlation Analysis in Chemistry and Biology*; John Wiley & Sons: New York, 1979; pp 171–330.
(37) Tawar, N. El; Tsai, R. S.; Carrupt, P. A.; Testa, B. *J. Chem. Soc., Perkin Trans. 2* **1992**, 79.
(38) Centonze, D.; Malitesta, C.; Palmisano, F.; Zambonin, P. G. *Electroanalysis* **1994**, *6*, 423.

ACKNOWLEDGMENT

Work carried out under financial support from CNR target project "Biotechnology and Bioinstrumentation" and MURST.

Received for review June 28, 1994. Accepted March 16, 1995.[⊗]

AC940649K

[⊗] Abstract published in *Advance ACS Abstracts,* May 15, 1995.

Anal. Chem. **1995,** *67,* 2212–2215

Quartz Crystal Microbalance Bioaffinity Sensor for Biotin

Már Másson, Kyusik Yun, Tetsuya Haruyama, Eiry Kobatake, and Masuo Aizawa*

Department of Bioengineering, Faculty of Bioscience and Biotechnology, Tokyo Institute of Technology, 4259 Nagatsuta, Midori-ku, Yokohama 226, Japan

A quartz crystal microbalance (QCM) bioaffinity sensor for biotin, based on the bioaffinity complex between avidin and immobilized desthiobiotin, was established. BSA–desthiobiotin conjugate was adsorbed directly onto the gold layer surface of a quartz crystal. The crystal was placed in a QCM flow cell. Avidin formed a metastable complex with the BSA–desthiobiotin conjugate on the crystal surface. When a sample solution containing biotin was injected, the avidin was released from the surface to form a more stable complex with biotin in solution. The biotin concentration corresponded to the weight change on the crystal surface that occurred when avidin desorbed. Measurements were done in the stop-flow mode with a measurement range between 0.05 and 100 μg/mL and in the continuous-flow mode with a measurement range between 0.2 and 10 000 μg/mL. The sensor was regenerated without any loss of activity by readsorbing avidin.

Two types of biosensors have been developed which involve a biocatalytic sensor and a bioaffinity sensor.[1] A biocatalytic sensor is represented by an enzyme sensor, which consists of an enzyme layer on a signal transducing device. Enzyme sensors have been forwarded into third generation of biosensors due to innovative progress. A constant variety and novel principles and technologies have emerged in the development of bioaffinity sensors which is profoundly stimulated by an enormously increased interest and demand. Bioaffinity sensors, which are based on the bioaffinity binding reaction between a ligand and a biomolecule, have a potential for a much wider range of applications than enzyme sensors. Such sensors can utilize natural bioaffinity molecules as well as a specific antibody, which is raised for a specific analyte, whereas enzyme sensors are limited in number.

Most of the research efforts in biosensors have been directed toward pursuing signal-transducing principles based on spectrophotometric and electrochemical methods. It is, however, difficult to measure the affinity binding reaction of biomolecules directly and therefore a labeling molecule has been used, and in the case of electrochemical biosensors, the labeling molecule is either an enzyme[2–4] or an electrochemically active group.[5,6] Although these bioaffinity sensors are characterized by high selectivity and sensitivity, they suffer from repeated use because of stable bioaffinity complexation.

In our group, we have proposed bioaffinity sensors based on subtle differences in the bioaffinity between an analyte and an analogue compound to the binding protein. These are easily regenerated for continuous measurement and are specifically attractive for the detection of small molecules like vitamins, hormones, and drug compounds. We have reported an electrochemical sensor for biotin based on the displacement of enzyme-labeled avidin[7] and a sensor for thyroxine based on the displacement of enzyme-labeled antibody.[8] A similar bioluminescence bioaffinity sensor for insulin based on the displacement of enzyme-labeled antibody was also reported.[9]

The binding of biomolecules can also be measured by methods which are sensitive to the physical changes that occur on a surface when a biomolecule binds. Such sensors can be based on the changes in the dielectric properties of the surface, which can be detected by impedance.[10] surface plasmon measurements,[11] or weight changes on the surface, which can be measured directly or by a quartz crystal microbalance (QCM). The QCM is an oscillating quartz crystal device whose resonance frequency changes with a change in the mass according to the formula[12]

$$\Delta f = -f_0^2(2/\sqrt{\mu_q \varrho_q})\Delta m = -f_0^2 2.3 \times 10^{-6}\Delta m$$

where Δf is the observed frequency change (in Hz), μ_q is the shear modulus, ϱ_q is the density of the crystal, and Δm is the weight change on the surface of the crystal (in g cm^{-2}).

Recently,[13] it was shown that the method is suitable for sensitive measurements in liquids as well as in air, and one of the advantages of the method is that there is a clear mathematical relationship between the adsorbed mass and the observed frequency change. Several workers have reported on the biospecific adsorption of proteins where the observed frequency change is in the 10–100 Hz order,[14–16] but to measure the binding of small molecules is more difficult. The binding of a small

(1) Aizawa, M. *Anal. Chim. Acta* **1991**, *250*, 249–256.
(2) Aizawa, M.; Morioka, A.; Matsuoka, H.; Suzuki, S.; Nagamura, Y.; Shinohara, R.; Ishiguro, I. *J. Solid-Phase Biochem.* **1976**, *1*, 319–328.
(3) Aizawa, M.; Morioka, A.; Suzuki, S. *J. Membr. Sci.* **1978**, *4*, 221–228.
(4) Aizawa, M.; Morioka, A.; Suzuki, S. *Anal. Chim. Acta* **1980**, *115*, 61–67.
(5) Gleria, K. D.; Hill, H. A. O.; McNeil, C. J.; Green, M. J. *Anal. Chem.* **1986**, *58*, 1203–1205.
(6) Yao, T.; Rechnitz, G. A. *Biosensors* **1988**, *3*, 307–312.
(7) Ikariyama, Y.; Furuki, M.; Aizawa, M. *Anal. Chem.* **1985**, *57*, 496–500.
(8) Ikariyama, Y.; Aizawa, M. *Proc. 2nd Sensor Symp.* **1982**, 97–100.
(9) Ikariyama, Y.; Aizawa, M. *Proc. 3rd Sensor Symp.* **1983**, 14–20.
(10) Bataillard, P.; Gardies, F.; Renault, M. J.; Martelet, C.; Colin, B.; Mandrand, B. *Anal. Chem.* **1988**, *60*, 2374–2379.
(11) Jonsson, U.; Fagerstam, L.; Ivarsson, B.; Johnsson, B.; Karlsson, R.; Lundh, K.; Lofas, S.; Persson, B.; Roos, H.; Ronnberg, I.; Sjolander, S.; Stenberg, E.; Stahlberg, R.; Urbaniczky, C.; Ostlin, H.; Malmqvist, M. *Biotechniques* **1991**, *11*, 620–627.
(12) Sauerbrey, G. *Z. Phys.* **1959**, *155*, 206.
(13) Bruckenstein, S.; Shay, M. *Electrochim. Acta* **1985**, *30*, 1295–1300.
(14) Ebersole, R. C.; Ward, M. D. *J. Am. Chem. Soc.* **1988**, *110*, 8623–8628.
(15) Muratsugu, M.; Ohta, F.; Miya, Y.; Hosokawa, T.; Kurosawa, S.; Kamo, N.; Ikeda, H. *Anal. Chem.* **1993**, *65*, 2933–2937.

0003-2700/95/0367-2212$9.00/0 © 1995 American Chemical Society

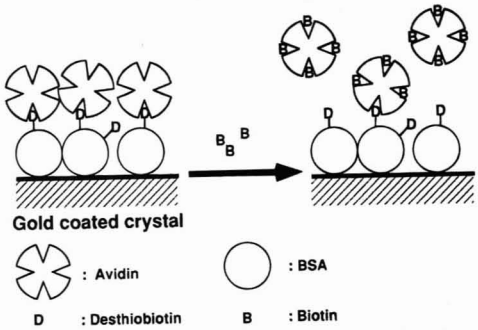

Figure 1. Principle of the QCM bioaffinity sensor based on a metastable bioaffinity complex.

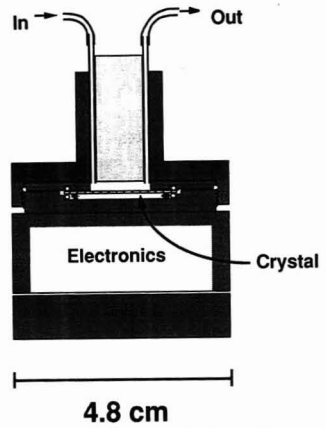

Figure 2. Cross section of the QCM flow cell.

molecule (MW ≤500) to a closed packed protein (diameter ≥10 nm) with a single binding site will give a weight change of 1 ng cm^{-2} or less. Calculation with the above formula shows that the observed frequency change of a 6 MHz-type crystal will be no more than 0.09 Hz, which is too small for detection.

In the present work, a QCM bioaffinity sensor for biotin has been developed. Biotin (MW 244, vitamin H) forms a very stable complex with avidin. Avidin also binds analogue compounds of biotin such as 2-[(4-hydroxybenzene)azo]benzoic acid (HABA), lipoic acid, and desthiobiotin. The sensing principle is shown schematically in Figure 1. Avidin binds BSA–desthiobiotin conjugate immobilized on the gold electrode layer covering the quartz crystal surface. When an analyte containing biotin is injected into the cell, the avidin might be desorbed from the surface as the binding to biotin is much stronger than the binding to desthiobiotin. The positive frequency change could then be proportional to the weight of avidin (MW 68 000) desorbed. It is noted that the measuring system could be regenerated under very mild conditions simply by reloading avidin. Fast analysis could be obtained with the continuous-flow conditions although the stop-flow conditions offered a more sensitive assay, as the reaction times were longer.

EXPERIMENTAL SECTION

Materials. D-Biotin, DL-desthiobiotin, lipoic acid, 2-[(4-hydroxybenzene)azo]benzoic acid (HABA) and *N*-hydroxy succinimide (NHS) were supplied by Nacalai Tesque, Tokyo, Japan. *p*-Nitrophenyl phosphate (PNPP), DMSO, and avidin were purchased from Wako Chemicals, Osaka, Japan. $MgCl_2$ came from Kanto Chemicals, Tokyo, Japan. 1-Ethyl-3-[3-(dimethylamino)-propyl]carbodiimide (EDC) was purchased from Dodjindo Labs, avidin-labeled alkaline phosphatase from EY Laboratories, San Mateo, CA, and BSA from Seikagaku Corp., Tokyo, Japan.

BSA–Ligand Conjugates. EDC, NHS, and the ligand (biotin, desthiobiotin, lipoic acid, or HABA) were dissolved in 1 mL of DMSO to give a 40 mM solution for each compound. The solution was stirred for 13 min and then 1 mL of 0.1 M carbonate buffer, pH 8.5, containing 30 mg of BSA was added. Precipitated protein was removed by centrifugation after a 4.7 h reaction at 37 °C. The organic solvent was removed from the remaining solution by ultrafiltration with Centricon (Amicon Inc.), concentrators and the remaining reagent molecules were removed by dialysis in 0.1 M phosphate buffer, pH 7.5. BSA–biotin and BSA–desthiobiotin conjugates were also made by overnight reaction in solutions with 50 mM reagent concentrations and 17 mg/mL BSA, containing 10% DMSO. The protein recovery was better with this method but the binding of avidin–alkaline phosphatase (Av–AP) was unchanged in the enzyme binding assay.

Assay for Ligand Content. The biotin and desthiobiotin content were determined by gradually adding 1 μL portions to 750 μL of 0.05 M phosphate solution containing 0.5 mg/mL avidin and 0.25 mM HABA, and the reduction in absorbance at 500 nm was recorded. Desthiobiotin standard solution was also measured, and the desthiobiotin content of the protein was calculated. The HABA content was calculated from the absorbance at 348 nm, where the HABA absorption peak is. The protein concentration was calculated from the absorbance at 280 nm, using a BSA standard.

Enzyme Binding Assay. The 0.16 cm^2 gold plates were cleaned by sonication for 1 h in a 2:1 ratio mixture of H_2SO_4 and H_2O_2 followed by rinsing with water. The plates were incubated for 1 h in a BSA–ligand solution, at 70 °C, rinsed with buffer, and placed in ELISA plate wells. The following incubations were done at 37 °C. The plates were incubated for 1 h in a 0.1 M phosphate buffer, pH 7.5 (PBS), containing 0.1 mg/mL avidin, and washed three times with buffer. Then they were treated with biotin solutions with 1 h before 1 h incubation in 20 μg/mL Av–AP in pH 7.4, 25 mM Tris buffer, 2 mM $ZnCl_2$, 4 mM $MgCl_2$ (TRIS-7.4) solution containing 1% BSA. When assayed for Av–Ap binding, only the last incubation was done. The enzyme reaction was carried out for 1 h in 1 M DEA, 0.5 mM $MgCl_2$, pH 9.8 (DEA-9.8), containing 1 mg/mL PNPP. The reaction was stopped by transferring the solutions from the wells with the gold plates. The absorbance of the solutions was measured at 405 nm with a Bio-Rad Model 450 microplate reader.

QCM Measurement. The QCM flow cell was made by fitting the QCM cell supplied by Hokuto Denko (Tokyo, Japan) with a rubber stopper and glass tubes as shown in Figure 2. The cell was set up in a flow system in a water bath and connected to an ECQCM Controller HQ-101B (Hokuto Denko). The crystal was an AT-cut 6 MHz crystal supplied by Hokuto Denko.

(16) Ebato, H.; Gentry, C. A.; Heron, J. N.; Muller, W.; Okahata, Y.; Ringsdorf, H.; Suci, P. A. *Anal. Chem.* **1994**, *66*, 1683–1689.

Injection in the stop-flow mode was done by pumping the solution into the cell for 3 min, with a 1.5 mL/min flow rate, and then stopping the flow. The frequency was recorded 20 min after the start of the injection, and the injection of next sample was started. After the BSA–desthiobiotin-coated crystal had been placed in the cell, the unspecific binding was blocked by two injections of 100 μg/mL BSA. One regeneration/measurement cycle constituted injection of a 100 μg/mL solution of avidin, injection of PBS buffer, injection of the biotin sample, and a final injection of buffer; the next cycle was started by injection of the avidin solution.

The cell was connected to a 1 mL injection loop (from Rheodyne) when operated in the continuous-flow mode. The flow rate was 0.5 mL/min. After blocking of the crystal with BSA, a 500 μg/mL avidin sample was injected, and 10 min later the frequency was recorded and a biotin sample was injected. Ten minutes later the frequency was recorded again and the next regeneration/measurement cycle started by injection of the avidin solution. The difference between the two frequencies was the frequency shift caused by desorption of avidin by biotin.

RESULTS AND DISCUSSION

Enzyme Binding Assay and Immobilization Procedure. In the cell supplied by Hokuto Denko, the crystal is sandwiched between two O-rings. With this cell design, a good stability was eventually achieved with less than 1 Hz drift in 1 h. However, just after a new crystal was fitted in the cell it took up to several hours for the frequency to stabilize until the measurement could be started, and it was therefore difficult to test many different conditions for the immobilization of ligand on the gold surface. A different type of cell was also tested where the O-ring was only on one side. In this case, a different pattern was observed where it generally took less than 1 h for the frequency to stabilize initially but the subsequent drift was much higher than with the present design. The cell was therefore not used for further measurements.

In order to test different immobilization procedures, an enzyme binding assay for the binding of Av–AP to modified gold plates was therefore investigated. Many different conditions could be tested in one assay, and this allowed the optimization of the conditions for the bioaffinity sensor before starting the experiment with the QCM.

Various procedures were tried, most based on thiol monolayer, and subsequent reactions to link biotin to the surface, but the best results in the enzyme binding assay were obtained when ligand-conjugated BSA was directly adsorbed to the gold surface. The advantage of this procedure was that, after the preparation of the BSA–ligand conjugate, the modified crystal could be prepared simply in a single adsorption step. High temperature (70 °C) was used for the adsorption reaction in order to maximize the binding, but denaturing of the protein should not affect the avidin binding. Enzyme binding results were not significantly different even if lower temperatures were used. The protein concentration of the conjugate in most of the experiments was 90 μg/mL but changing the concentration in the range 9–500 μg/mL did not affect the results.

Saturation binding of Av–Ap in the binding assay was obtained with 10 μg/mL concentrations or higher, but 20 μg/mL was generally used in the experiments.

Ligand Variation and Bioaffinity Assay for Biotin. The ligand to BSA ratio in the BSA–ligand conjugate for desthiobiotin and biotin was measured by a HABA displacement assay. Lipoic acid is, unlike HABA, only weakly adsorbing in the visible range and ligand content could therefore not be measured with a direct absorption measurement. The reaction conditions was the same as in the case of HABA, so similar BSA to ligand ratios should be expected.

Table 1. Ligands per Molecule and Relative Binding in the Enzyme Binding Assay

molecule	ligands per molecule	K_A for binding of ligand to avidin[a]	relative binding of Av–AP in the enzyme binding assay
BSA–biotin	4.7	1×10^{15}	0.99 ± 0.05
BSA–desthiobiotin	3.5	2×10^{12}	1.00 ± 0.13
BSA–lipoic acid		1.4×10^{6}	0.14 ± 0.05
BSA–HABA	4.1	1.7×10^{5}	0.06 ± 0.02

[a] From ref 17.

There were on average 3.5–4.7 ligands bound to each BSA molecule (Table 1). When the molecule is adsorbed on the surface, there should be at least one ligand available for binding to avidin, and nearly a monolayer binding of avidin should be possible.

The same binding of Av–AP was observed with immobilized biotin and desthiobiotin, which is consistent with the high affinity constant that avidin has for binding of these compounds. The avidin–ligand complex, on the gold surface, was therefore stable if biotin was not present in the solution. Lipoic acid and HABA have lower affinity constants for binding with avidin, and lower binding of Av–AP to these immobilized ligands was observed. This was due to either low initial binding or desorption of bound Av–AP during the washing of the gold plates, after the incubation with the avidin conjugate. Desthiobiotin was therefore found to be the most suitable ligand for the present assay method as it has 3 orders of magnitude lower affinity for avidin than biotin, but the complex on the gold surface was sufficiently stable so that the avidin was not desorbed before incubation with biotin.

The measurement range for biotin in the enzyme binding assay with desthiobiotin immobilized on gold was 0.1–1 μg/mL (data not shown) or shifted to 10 times higher concentration than in the previous work[8] with an electrochemical sensor based on the HABA–avidin complex. This shift was the result of the higher affinity of desthiobiotin.

The gold surface was flat, and the avidin should therefore be expected to bind to a single immobilized ligand through one binding site out of four available ones, as shown in Figure 1, because of the steric restriction. The three-dimensional structure of the membrane, which is used for the electrochemical sensor, will allow the avidin molecule to bind through multiple binding sites. This would explain why the complex between avidin and HABA in the membrane does not dissociate when washed with buffer, as it did when avidin was bound to HABA immobilized on flat gold surface.

QCM Bioaffinity Sensing. The typical readout for QCM bioaffinity sensing with stop flow and continuous flow is shown in Figure 3.

When the sensor was operated in the stop-flow mode, it took up to 1 h for the frequency to stabilize after the pumping was

(17) Aizawa, M. *Electrochemical Sensors in Immunological Analysis*; Plenum Press: New York, 1990; pp 268–291.
(18) Schmid, R. D.; Kunnecke, W. *J. Biotechnol.* **1990**, *14*, 3–31.

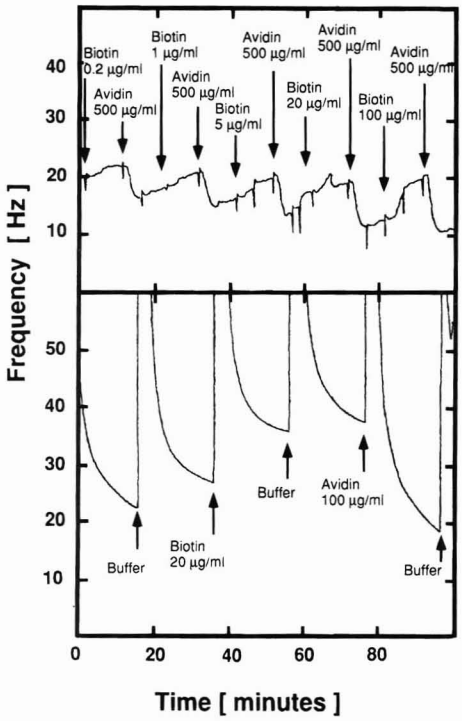

Figure 3. Typical readout for the QCM measurements. Above is the continuous-flow method, below the stop-flow method. The zero frequency was arbitrarily set for the measurements. The change in the frequency between 20 μg/mL injection of biotin and 500 μg/mL injection of avidin in the above graph is not continuous, and this was ascribed to noise.

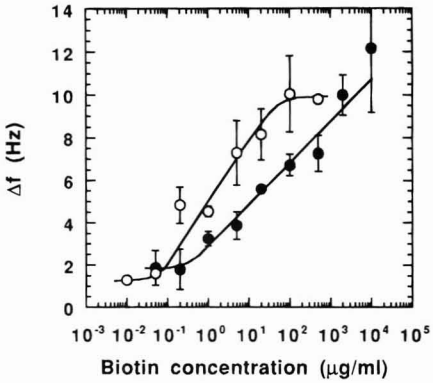

Figure 4. Result of the bioaffinity assay with the QCM bioaffinity sensor done in the stop-flow mode (○) for concentrations between 0.2 and 100 μg/mL (average of three measurements). The result of the bioaffinity assay, done in the continuous-flow mode (●), are also shown (average of three measurements).

stopped. The measurement range (Figure 4) was between 0.05 and 100 μg/mL, but the reaction time was shorter than in the enzyme binding assay. The frequency shifts shown in Figure 4 are for the change from the end of the buffer injection until the end of biotin injection, or data with a 20 min interval. Other experiments showed that biotin concentrations in the range of the measurement did not have any effects on the frequency of crystal covered with unmodified BSA. The observed frequency changes were therefore caused by changes in the mass on the crystal rather than by a change in the solution. The total time required for one measurement/regeneration cycle was 80 min.

When the sensor was regenerated by reloading avidin, the resulting frequency was always a few hertz lower than obtained during previous reloading, as is seen in Figure 3. This phenomenon was consistently observed in all the experiments done. This was not due to insufficient saturation of the binding sites. The enzyme binding assay had shown that the avidin concentration was sufficient for full saturation of the binding sites and also that the increase in frequency was constant, independent of how many times the reloading was done. The negative shift in the frequency after the reloading did not affect the positive change in frequency observed after subsequent injection of biotin.

After avidin was reloaded, it was seen with the continuous-flow operation that the frequency drifted slowly back in the positive direction, indicating that some of the bound avidin slowly being removed from the crystal. Biotin sample was injected exactly 10 min after the injection of avidin, before the frequency had fully stabilized. The frequency was read from the display of the instrument, with 0.1 Hz accuracy, at the time of the injection. Exactly 10 min later the frequency was read again and avidin injected to regenerate the sensor. The difference between the two values was taken as the frequency change caused by desorption of avidin when binding to biotin in the solution. Some biotin-complexed avidin was still desorbing when avidin was injected, as indicated by the continuous increase in the frequency. Although a chemical equilibrium has not been fully reached, the procedure offers good reproducibility, which is a general feature of flow injection systems.[18]

The measurement ranges for the continuous-flow system started from 0.2 μg/mL and continuous change was observed up to 10 000 μg/mL, but higher concentrations could not be measured because of the limited solubility of biotin. The higher limit of detection corresponds to the shorter reaction time. The frequency changes from 0.2 to 10 000 μg/mL was approximately 9 Hz or the same as the frequency change from 0.05 to 100 μg/mL in the stop-flow method. No loss of activity was detected in either the stop-flow or the continuous-flow measurement even after 3 days of operation or after 27 consecutive measurement and regeneration cycles.

CONCLUSION

A QCM bioaffinity sensor for biotin has been developed for rapid on-line FIA measurements. This bioaffinity sensor principle can be used for detection of small molecules with QCM, with regeneration of the sensor under mild conditions without any loss of activity. The approach seems promising for further application with other systems such as the antibody–antigen system.

Received for review January 11, 1995. Accepted April 7, 1995.[⊗]

AC9500388

[⊗] Abstract published in *Advance ACS Abstracts*, June 1, 1995.

Anal. Chem. **1995,** *67,* 2216–2223

Generation of Cadmium Atoms at Room Temperature Using Vesicles and Its Application to Cadmium Determination by Cold Vapor Atomic Spectrometry

A. Sanz-Medel,*,† M. C. Valdés-Hevia y Temprano,† N. Bordel García,‡ and M. R. Fernández de la Campa†

Departments of Physical and Analytical Chemistry and Physics, University of Oviedo, c/ Julián Clavería No. 8, 33006 Oviedo, Spain

The only metal recognized as able to form a monoatomic vapor at room temperature is mercury ("cold vapor" generation). This property has been widely used in many analytical techniques, particularly in atomic spectroscopy, to increase the efficiency of the transport of the metal to the measurement cell. In fact, cold vapor atomic absorption spectrometry (CV-AAS) has become the most common method for the determination of trace and ultratrace levels of mercury in the most varied samples. Evidence is shown here demonstrating that cadmium appears also to be able to form cold atomic vapor under appropriate reaction conditions. Experimental results show that some types of volatile cadmium species (most probably hydrides) can be produced by reduction with sodium borohydride of Cd^{2+} in an aqueous solution of vesicles of didodecyldimethylammonium bromide. Such volatile species are able to transport the metal to the atomic absorption measurement cell, where Cd^0 cold vapor has been detected. The absorption profile of the absorbing species at room temperature has been measured in a typical absorption quartz cell by using a spectrograph/charged coupled device arrangement. Results demonstrate the presence of monoatomic cadmium vapor in measurable concentrations in the absorption cell, the magnitude of the AAS signal being proportional to the metal concentration in the aqueous solution. This vesicular volatile species generation facilitates cadmium transport to the atomizer cell, thereby improving by about 20 times the detectability of cadmium by the cold vapor inductively coupled plasma atomic emission spectrometry technique (detection limit, 1 ng/mL Cd). Moreover, a highly sensitive determination of the metal based on these facts can be carried out by CV-AAS (detection limit, 0.08 ng/mL), and sensitivity can be further improved by working at lower temperatures for volatile species generation and transport to the absorption cell.

It is recognized worldwide that mercury is the only metal proven to be able to form at room temperature a monoatomic vapor with a measurable partial pressure. This unique property has been known since the beginning of this century, when Wood[1] and others[2] measured the absorption of the intercombination line of mercury at 253.65 nm by Hg vapor produced at temperatures around 20 °C. The volatility of this Hg^0 "cold vapor" (CV) was utilized in 1968[3] to develop an extremely sensitive cold vapor atomic absorption spectrometry (CV-AAS) technique for the determination of low levels of this metal in rocks and other pure metals. Since then, CV-AAS[4] has become the most commonly used method for determining ultratrace levels of mercury. No metal other than mercury seems to be capable of evaporating a concentration of its atoms which can be measured by atomic techniques at room temperature. However, generation of other volatile molecular species (e.g., hydrides) and final atomization (e.g., in a heated quartz tube) is a well-known alternative approach in atomic spectrometry to increase the efficiency of transport of the analyte or determinant to the measurement cell.

Moreover, it has been shown[5] that such generation of volatile species for atomic spectrometry can be facilitated by resorting to "organized media". In fact, the analytical potential of using micelles and vesicles to improve volatile species chemical generation, e.g., mercury CV or hydrides, has been demonstrated in our laboratory for Hg, As, Pb, and Cd.[5–10] Analytical sensitivity and selectivity achieved with hydride generation/atomic detection systems could be improved by the use of surfactants for the following reasons. (a) They may concentrate reactants at a molecular level and so change thermodynamic and kinetic reaction constants; thus, the analytical sensitivity can be substantially changed, and perhaps improved, in an appropriate medium. (b) Surfactants may solubilize, in a selective manner, analytes and reactants (e.g., sodium borohydride) in organized "aggregates"; thus, the special microenvironment existing in or on these aggregates may change the reactions (interferences) observed

(1) Wood, R. W. *Phil. Mag.* **1912**, *23*, 696–701.
(2) Hughes, A. L. L.; Thomas, A. R. *Phys. Rev.* **1927**, *30*, 466–472.
(3) Ronald, W.; Ott, W. L. *Anal. Chem.* **1968**, *40*, 2085–2087.
(4) Fujita, M.; Takanabe, E. *Anal. Chem.* **1983**, *55*, 454–457.
(5) Sanz-Medel, A.; Fernández de la Campa, M. R.; Valdés-Hevia y Temprano, M. C.; Aizpún Fernández, B.; Liu, Y. M. *Talanta*, **1993**, *40*, 1759–1768.
(6) Valdés-Hevia y Temprano, M. C.; Fernández de la Campa, M. R.; Sanz-Medel, A. *J. Anal. At. Spectrom.* **1993**, *8*, 847–852.
(7) Sanz-Medel, A.; Valdés-Hevia y Temprano, M. C.; Bordel García, N.; Fernández de la Campa, M. R. *Anal. Proc.* **1995**, *32*, 49–52.
(8) Aizpún Fernández, B.; Valdés-Hevia y Temprano, M. C.; Fernández de la Campa, M. R.; Sanz-Medel, A.; Neil P. *Talanta* **1992**, *39*, 1517–1523.
(9) Valdés-Hevia y Temprano, M. C.; Aizpún Fernández, B.; Fernández de la Campa, M. R.; Sanz-Medel, A. *Anal. Chim. Acta* **1993**, *283*, 175–182.
(10) Liu, Y. M.; Fernández Sánchez, M. L.; Blanco González, E.; Sanz-Medel, A. *J. Anal. At. Spectrom.* **1993**, *8*, 815–820.

† Department of Physical and Analytical Chemistry.
‡ Department of Physics.

0003-2700/95/0367-2216$9.00/0 © 1995 American Chemical Society

in the bulk aqueous phase. In other words, analytical selectivity could be favorably changed in suitable organized media.

In a previous paper,[6] we investigated in detail the continuous-flow generation of volatile Cd species, using $NaBH_4$ as the reduction agent, as a means of gaseous sample introduction for inductively coupled plasma atomic emission spectrometry (ICP-AES). In order to achieve such generation, several organized molecular assemblies have been tried, including micelles of different charge and vesicles.[6] The most promising analytical results were obtained with didodecyldimethylammonium bromide (DDAB) vesicles as the organized medium for Cd^{2+} reduction. In a recent publication, we reported on the formation of cadmium atoms at room temperature by resorting to the use of cationic vesicles of DDAB showing their potential to achieve a sensitive CV-AAS determination of the metal.[7]

In this paper, both the transport mechanism of the volatile Cd species to the atomizer and the nature of those species reaching the measurement cell are investigated by absorption measurements. Experimental evidence is given indicating that room temperature atomic absorption of the resonance radiation of cadmium (at 228.8 nm) by the volatile species formed takes place in the quartz absorption cell. In other words, Cd cold vapor generation has been demonstrated via reduction of Cd^{2+} with $NaBH_4$ in vesicular media. Factors affecting Cd^0 generation, possible transport mechanisms, and its use to develop highly sensitive CV-AAS techniques for the determination of this toxic metal are discussed in detail.

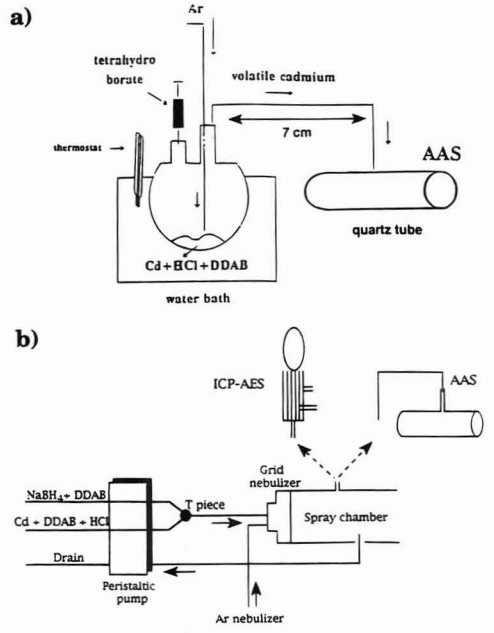

Figure 1. (a) Batch CV system. (b) Continuous CV system.

EXPERIMENTAL SECTION

Instrumentation and Analytical Procedures. A Philips Model PU7000 inductively coupled plasma atomic emission spectrometer was used for detection by ICP-AES.

A Perkin-Elmer Model 2280 atomic absorption spectrometer was used for detection by AAS.

A Perkin-Elmer Model 3030 graphite furnace atomic absorption spectrometer was used for measurements by ETA-AAS.

Batch measurements of volatile species formed were carried out using a home-made (Figure 1a) thermostated hydride generator to generate the volatile species. This device is based on a three-necked flask, where the cadmium sample is dissolved in HCl of appropriate concentration to secure a final concentration of 0.4 M in the acid for reaction and 1×10^{-2} mol/L DDAB vesicles; one entrance is for connecting to the quartz cell of the atomic absorption instrument, the second entrance is to pass a low argon flow to purge the gases to the cell from the flask, and the last entrance, closed by a septum, allows addition of tetrahydroborate solutions by syringe.

Continuous flow generation measurements of volatile species were carried out using the system shown schematically in Figure 1b.[6] The cadmium sample, dissolved in 2 M HCl and 1×10^{-2} mol/L DDAB vesicles, is continuously pumped through one of the channels of a peristaltic pump at a rate of 0.75 mL/min to merge with a 4% m/v solution of $NaBH_4$ (flow rate, 0.75 mL/min) in 1×10^{-2} mol/L DDAB vesicles. The merging solution feeds the gas–liquid separator to allow the volatile species to go to the quartz cell or the ICP. The liquid phase is continuously removed to waste (Figure 1b).

The Perkin-Elmer Model 2280 atomic absorption spectrometer, used for absorption measurements, was operated under optimum conditions suitable for the Cd 228.8 nm line (Cd hollow cathode lamp), and all these measurements were background corrected using a deuterium lamp and 228.8 nm setting.

Instrumental Setup for Absorption Profile Measurements. The absorption spectrum between 200 and 235 nm of the Cd absorbing species in the quartz cell was measured at room temperature by illumination with a continuum source (deuterium lamp) and detection with a charged coupled device (CCD; EG&G Princeton Applied Research, Princeton, NJ). Spectral dispersion (Figure 2) was secured by using a spectrometer of 0.5 m focal length with an entrance slit of 25 μm and two different grating capabilities: a ruled grating of 600 grooves/mm (0.2 nm fwhm resolution) and a holographic grating of 2400 grooves/mm (0.03 nm fwhm resolution).

The complete diagram of the instrumental setup employed to obtain such spectra is shown in Figure 2. The same instrumentation was used to measure the absorption profiles of cadmium and mercury cold vapor for comparative purposes.

Reagents. Stock standard solutions of 1000 mg/mL cadmium(II) and mercury(II) (Merck) were used. Working solutions were freshly prepared daily by diluting appropriate aliquots of the stock solutions in ultrapure water.

Sodium tetrahydroborate(III) solutions were prepared by dissolving $NaBH_4$ (Carlo Erba) in ultrapure water (Milli-Q, Millipore Corp., Bedford, MA), stabilized in 0.1% m/v sodium hydroxide solution. Solutions were prepared weekly and filtered before use.

Vesicles of didodecyldimethylammonium bromide (DDAB) were prepared by dissolving the surfactant powder (Eastman Kodak Co., Rochester, NY) in water and sonicating at room temperature at a power of 60 W for about 12 min, using the tip of a high-intensity ultrasonic processor (Sonics and Materials Inc., Danbury, CT). This procedure will be referred to as "sonication" in the text.

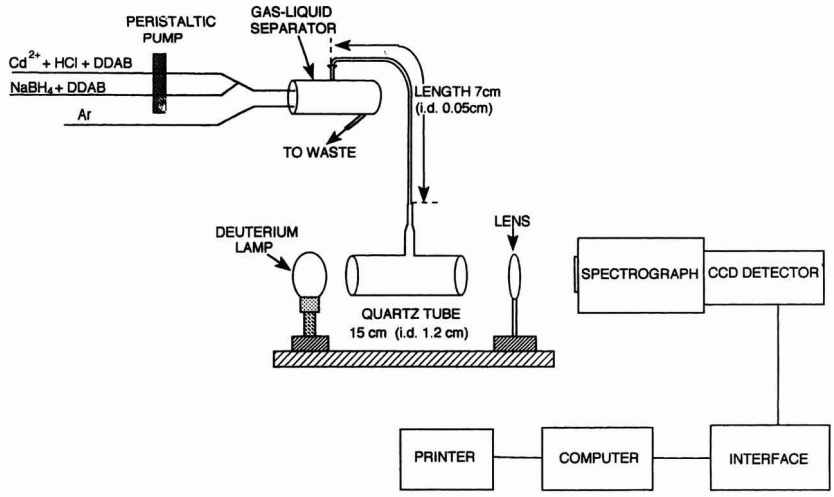

Figure 2. Instrumental setup for absorption profile measurements.

All mineral acids used were of analytical reagent grade, and ultrapure water was used throughout.

RESULTS AND DISCUSSION

A few years ago, the formation of a volatile species of cadmium by treating Cd^{2+} solutions with $NaBH_4$ in an organic medium of dimethylformamide was described.[11] Unfortunately, the nature of such species was not investigated in detail.

Experiments in our laboratory, using several organized media of different nature and $NaBH_4$ for reduction, verified the formation of a volatile Cd species. This Cd volatile species was responsible for the ICP-AES signals observed.[5,6] However, no conclusive evidence of the nature of the volatile Cd species could then be provided nor has been provided so far, to the best of our knowledge.

Preliminary efforts in our laboratory to characterize by GC/MS the Cd compound reaching the ICP-AES were unsuccessful.[6] Different experiments (e.g., leaching of tubing with diluted HCl) showed that Cd was deposited in the tubes used to "trap" the volatile species formed, preventing eventual MS detection.

The Effect of Connecting Tubing Length. The above preliminary experiments, unsuccessful at duly characterizing the Cd species formed, pointed to a prompt decomposition of the volatile compound (presumably a hydride) originally formed.

If decomposition takes place, it has been reported in the inorganic literature that cadmium hydride decomposes quickly to Cd^0 and hydrogen at temperatures around 0 °C;[12] the longer the connecting tubing to the atomizer, the longer the time available for volatile species to decompose at the 18–20 °C laboratory temperature. According to this supposition, Cd^0 coming from

$$(CdH_2)_{unstable} \rightleftharpoons Cd^0 + H_2 \qquad (1)$$

should deposit on the tubing, and ICP-AES signals for the metal should decrease with longer connecting tubings.

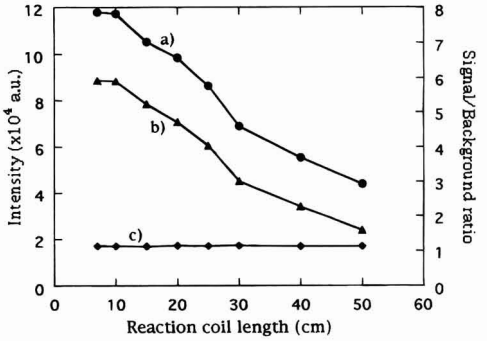

Figure 3. Effect of reaction coil length on the Cd signal measured by volatile species generation (from DDAB) - ICP-AES. (a) Total intensity of the ICP-AES signal. (b) Signal/background ratio. (c) Intensity of the background.

The observed results for such an experiment are given in Figure 3, which shows that the observed ICP-AES signal does, in fact, decrease dramatically with increasing tubing length connecting the flask to the nebulizer/spray chamber (Figure 1b) (deposition of the metal on the tubing was again proved).

Cadmium Cold Vapor Formation. In a further effort to characterize the species responsible for the cadmium signals observed, we investigated the possibility of detecting Cd^0 and CdH_2 in reaction 1. For analytical measurements of Cd^0, a batch vapor generator was designed (Figure 1a), and the cadmium volatile species generated were transported to a classical quartz cell of the conventional AAS instrument. Working at room temperature for generation, calibration AAS graphs (using increasing concentrations of Cd^{2+} in the sample vessel) were obtained independently with a heating flame and flameless in the quartz tube. Parallel experiments were carried out using the same instrumentation for the determination of Hg^{2+} (CV-AAS typical measurements).

The results obtained have been plotted, in a comparative manner, in Figure 4, parts a (Cd) and b (Hg), and are crucial to

(11) Cacho, J.; Beltrán, I.; Nerín C. *J. Anal. At. Spectrom.* **1989**, *4*, 661–663.
(12) Barbaras, G. D.; Dillard, C.; Finholt, A. E.; Wartik, T.; Willbach, K. E.; Schlesinger, H. I. *J. Am. Chem. Soc.* **1951**, *73*, 4585–4590.

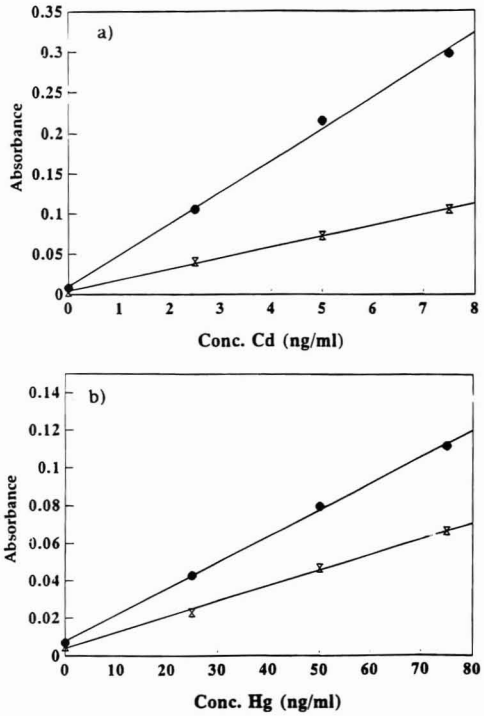

Figure 4. Calibration graph by batch CV-AAS: (a) cadmium and (b) mercury ●, flameless; ×, with flame.

understanding the transport mechanism of volatile Cd to the absorption cell by comparison with Hg^{2+} results.

Figure 4a shows clearly the presence *at room temperature in the absorption cell* of Cd atoms able to absorb their own resonance radiation (228.8 nm) coming from the Cd hollow cathode lamp. The sensitivity of the Cd calibration graph is much better without the flame than with the flame (heating the quartz tube). Figure 4b shows similar results for the parallel studies carried out on cold vapor generation of mercury. The effect of heating the quartz tube with the flame is analogous for both analytes: when the flame is on, the gases are heated in the tube. On heating, and with burning the H_2 excess, the gases expand, diluting the analyte and shortening its residence time in the beam path of the AAS instrument. Therefore, the slope of the calibration graphs decreases with the flame as compared to room temperature operation (cold vapor absorption).

Similar experiments were performed using on-line continuous-flow generation AAS detection. The results obtained showed exactly the same type of behavior illustrated in Figures 4 (for both, Cd and Hg), except that continuous operation produced a clear loss of sensitivity.

In Table 1, we have summarized the obtained analytical performance characteristics for optimized[7] cold vapor determination of Cd by quartz tube AAS, using both batch (Figure 1a) and continuous (Figure 1b) operation, both with a flame and flameless (in the latter case, a membrane drying tube from PS Analytical, Seven Oaks, OK, was used at the exit of the gas–liquid separator to prevent background from moisture and water droplets reaching

Table 1. Analytical Performance Characteristics for Cadmium by Cold Vapor Generation AAS

	batch		continuous	
	flame	flameless	flame	flameless
DL[a] (ng/mL)	0.22	0.08	2.9	1
RSD[b] (%)	2.0	1.8	2.1	1.8
slope[c]	14×10^{-3}	39×10^{-3}	1.5×10^{-3}	4×10^{-3}
Δslope[d]	1	2.8	1	2.6

[a] Detection limit, $3\sigma_b$/slope. [b] Precision (RSD, %), relative standard deviation for samples at 5 ng/mL of Cd in batch mode and 10 ng/mL of cadmium in continuous mode (n = 10) levels. [c] Slope of the calibration line (mL/ng^{-1}). [d] Slope increase (flameless/flame).

the absorption cell at room temperature.[13] It can be seen in Table 1 that extremely low levels of Cd can be analyzed, using either batch or continuous operation, by pure cold vapor quartz tube AAS measurements with good precision (2–3%). The technique can be used for the real analysis of Cd in tea infusions and lichens.[14]

In brief, those results demonstrate that the CV-AAS determination of cadmium is possible because measurable amounts of monoatomic Cd^0 vapor exist in the quartz absorption cell during measurement (in a similar manner to the well-known CV-AAS of mercury).

In the light of the above conclusions, a further question arises: Is the observed cold vapor generation of cadmium identical in nature with that of mercury?

Influence of Temperature on the Generation Reaction. In an attempt to answer the above question, the influences of temperature on the generation and transport to the absorption cell of cold vapors of Cd and Hg were investigated separately. The sample vessel (Figure 1a) was thermostated at different temperatures ranging from 0 °C to 60 °C, and the room temperature AAS signal for 100 ng/mL Cd was monitored at increasing thermostat temperatures in the flask. Similar experiments were carried out for 100 ng/mL Hg. The results observed have been plotted in Figure 5 for both metals, for comparative purposes. As can be seen, the effect of temperature on the cold vapor generation of Hg^0 is nearly opposite to what is observed for the cold vapor generation of Cd: for mercury, the higher the temperature of generation in solution, the higher the vapor pressure of Hg^0 directly formed and transported to the cell as such species (signal increases with temperature). However, the observed shape of the curve shown in Figure 5 for Cd exhibits the opposite behavior. In other words, the transport for Cd is probably mediated by the volatile unstable species (i.e., probably CdH_2, which decomposes[12] with increasing temperatures).

The Vesicular Effect. The presence of an organized medium proved to be essential for efficient formation of the observed Cd volatile species in the reaction vessel. In order to ascertain the actual role of vesicles in such Cd cold vapor generation, three series of Cd ultrafiltration experiments were carried out using ICP-AES detection: in the first series, a Cd^{2+} solution was added to DDAB vesicles already formed by sonication; in the second one, Cd^{2+} and $NaBH_4$ solutions were dissolved independently in DDAB

(13) Aizpún Fernández, B.; Fernández de la Campa, M. R.; Sanz-Medel, A. *J. Anal. At. Spectrom.* **1993**, *8*, 1097–1102.
(14) Valdés-Hevia y Temprano, M. C. Ph.D. Thesis, Universidad de Oviedo, Spain, 1994.

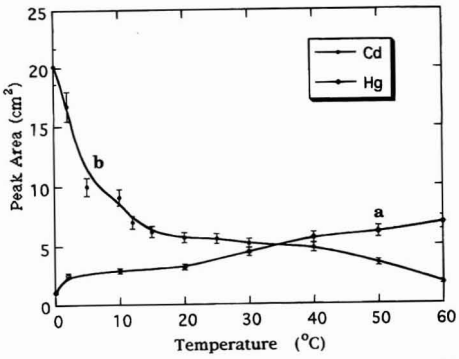

Figure 5. Temperature effect on (a) Hg signal by batch CV-AAS with the Perkin-Elmer instrument and (b) Cd signal by batch CV-AAS.

solutions and were sonicated at the same time as the surfactant solution (in order to "trap" the reagents inside the vesicles on their formation by sonication); finally, a third reference solution of pure aqueous Cd^{2+} (of the same concentration) was also prepared. For all three solutions, one fraction was directly analyzed for Cd by CV-ICP-AES,[6] and the other fraction was ultrafiltered[15] and the Cd^{2+} content in the ultrafiltrate determined by ETA-AAS. The results obtained for the three types of solutions containing 30 ng/mL Cd^{2+} are summarized as follows: when sonication of DDAB solutions is carried out in the presence of Cd^{2+}, ~50% of total cadmium added remains in the vesicles (which do not pass through the ultrafiltration membrane), as the ultrafiltered Cd was 46.7%. This sonication procedure produced the greatest CV-ICP-AES emission signals for Cd. Conversely, when Cd^{2+} solution was added to already formed (sonicated) vesicles, most of the added Cd^{2+} seemed to remain outside the vesicles in the bulk aqueous solution (93% of total Cd^{2+} added was ultrafiltrable). The observed CV-ICP-AES emission signals for this type of solution were 2.5 times lower. Pure aqueous solutions of Cd^{2+} treated with $NaBH_4$ in the conventional mode without vesicles, thus, with 100% of Cd ultrafiltrable, did not produce any CV-ICP-AES signal for Cd.

Obviously, a quantitative description of the above data is rather difficult due to the rather uncontrolled volatile compound decomposition. However, the above results support the concept that the concentration of reactants at a molecular level in the vesicles is responsible for the production of a reaction; in this case, presumably the generation a cadmium hydride compound, which does not appear to take place in the bulk aqueous solution.

The efficiency of generation of volatile cadmium at different temperatures was also calculated (measuring the residual Cd by ETA-AAS in the vesicular solutions after borohydride addition for ICP-AES analysis and relating those values to total metal added). The results obtained (Table 2) showed that the efficiency of analyte volatilization was 49.8% ± 3.4 ($n = 6$) at room temperature and 75.0% ± 3.7 ($n = 6$) at 0 °C. Therefore, this confirmed the results shown in Figure 5: lower generation temperatures favor the stabilization of volatile compound responsible for the transport of the metal. Thus, by lowering the temperature of the generation and transportation of the volatile hydride, the already high

(15) Wrobel, K.; Blanco González, E.; Sanz-Medel, A. *Trends Elem. Med.* **1993**, *10*, 97–103.

Table 2. Efficiency of the Cadium Species Generation/Volatilization

sample	Cd found by ETA-AAS (ng/mL)	efficiency[a], (%)
	Room Temperature	
1	5.4	46
2	4.5	55
3	4.8	52
4	4.9	51
5	5.2	48
6	5.3	47
$\bar{x} \pm$ SD	5.0 ± 0.3	49.8 ± 3.4
	T = 0 °C	
1	2.8	72
2	2.8	72
4	2.5	75
4	2.0	80
5	2.8	72
6	2.1	79
$\bar{x} \pm$ SD	2.5 ± 0.4	75.0 ± 3.7

[a] Efficiency, [Cd added − (10 × Cd found)/Cd added] × 100; Cd added = 100 ng/mL. Residual solutions were diluted 10 times for analysis by ETA-AAS.

sensitivity of the CV-AAS or CV-ICP determination of Cd could be increased even further to that shown in Table 1 at room temperature (i.e., detection limits better than 80 pptr Cd can be achieved).

Evidence of Room Temperature Cadmium Atoms. Absorption Profile of the Absorbing Species. All the AAS measurements given were background corrected. However, even with background correction, the presence of a net absorbance does not disprove that a molecule is absorbing the light from the hollow cathode lamp; it just may show that, as deuterium correction is being used at 228 nm, the profile of the molecular absorption band is narrow compared with the band pass of the monochromator. Therefore, in order to ascertain that the absorber is monoatomic cold vapor, we obtained the absorption profile of the absorbing species at the laboratory temperature using a continuum source (a deuterium lamp) for illumination. The light (see Figure 2) passes through the quartz tube where the absorber is present, and the emerging light is dispersed in a spectrograph of 0.5 m focal length and detected with a CCD detector, which allows us to see simultaneously the profiles of the absorption in a 10 nm range in real time when the spectrograph is used with the 2400 grooves/mm grating. Parallel experiments were carried out, using the same instrumentation, to measure the absorption profile of cold vapor of mercury. Comparative results observed are illustrated in Figure 6.

As shown in Figure 6, both Cd and Hg show a similar absorption profile: a narrow absorption at 228.80 nm for cadmium (with a half-width of 0.03 nm, Figure 6a) and a similar line for mercury at 253.65 nm (with a half-width of 0.03 nm, Figure 6b). The absorption profiles obtained demonstrate that the Cd absorber is also a monoatomic cadmium vapor. These measurements show also that on increasing the concentration of the sought elements in the sample solution, the intensity of the atomic absorption observed increases accordingly (allowing for analytical AAS determinations, as indirectly shown also by results in Figure 4 and Table 1). Using the instrumentation shown in Figure 2, we observed a linear relationship between atomic absorbance measured at 228.8 nm and Cd^{2+} concentration in the sample.

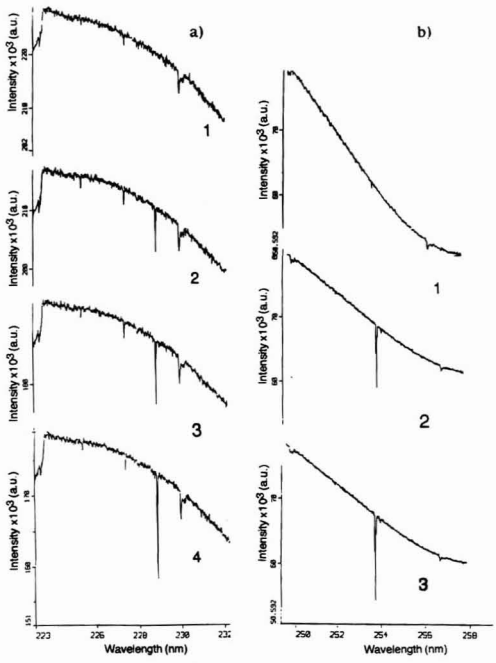

Figure 6. Absorption profile of (a) monoatomic cadmium cold vapor with (1) 0, (2) 2, (3) 5, and (4) 10 ppm cadmium, and (b) monoatomic mercury cold vapor with (1) 0, (2) 5, and (3) 10 ppm mercury.

To further confirm this approach, we tried to analyze cadmium with the conventional AAS instrument, using a nearby line of another element for illumination. By using a hollow cathode lamp of nickel (resonance line at 232.0 nm), we measured possible AAS signals for increasing Cd^{2+} concentration in the sample solutions. Results showed that the absorbance measured at 228.8 nm was a straight line ($A = 0.012 + 0.00396\,X$, $r = 0.9991$, X = cadmium concentration) with Cd^{2+} concentrations from 0 to 100 ng/mL, while measuring at 232.0 nm provided a constant absorbance ($A = 0.01$), even for a 500 ng/mL concentration of the element in the sample. This confirms once more that the absorption profile of the absorber species is very narrow and that at 3.2 nm outside the Cd resonance line, neither absorption is observed, nor is this absorption related to Cd^{2+} concentration in the samples.

Possible Molecular Absorptions. Absorption results observed with the CCD detector showed that for Cd, there is also a certain band absorption (in these CCD measurements, no background correction was used); such absorption is clearly visible on comparing blanks and samples in Figure 6a, and it is not observable in Hg^0 measurements (Figure 6b). For instance, for Hg, in the region around 253.65 nm, e.g., 252 nm, the emission of the continuum D_2 lamp was always 77×10^3 AU (emission arbitrary units) after the Hg^0 vapor was passed or even for the blank (without Hg^{2+} in the sample solution). However, for Cd in the region around 228.8 nm, e.g., 226 nm, the source emission with the blank (no Cd^{2+}) was 225×10^3 AU; if 5 ppm Cd^{2+} is volatilized and measured (Figure 6a3), an absorption band is noticed (emission $\approx 190 \times 10^3$ AU), and on volatilising 10 ppm Cd^{2+}, a further decrease of signal at 226 nm is observed.

In order to verify the assumption (according to eq 1) that the absorbing molecular species is a hydride of cadmium, absorption bands of such Cd volatile species were obtained in our CCD instrumental setup and were compared with the absorption bands obtained for arsine and selenium hydride (it is well known that those hydrides exhibit absorption bands between 200 and 240 nm.[16-19] The experimental system shown in Figure 2 was employed, but the grating of the spectrograph used for this experiment was of 600 grooves/mm, so that the CCD detector allowed simultaneous observation of the profiles of the absorption in a 50 nm range in real time.

The hydrides were generated using working 1 ppm standards of arsenic and selenium in 2 M HCl, pumping them continuously through one of the channels of the peristaltic pump to merge with 1% m/v $NaBH_4$ (stabilized in 0.5% of NaOH) introduced through other channel. The hydrides formed should reach the quartz cell (Figure 2) after passing through the gas–liquid separator. The light of the D_2 lamp should be absorbed by the hydrides along the quartz cell. The band spectra obtained for the different elements assayed are shown in Figure 7.

The "net" absorption bands (numbers 3 in Figure 7) are the result of subtracting the spectrum obtained for samples (1 ppm) (numbers 2) from the spectrum obtained for the corresponding blank (numbers 1).

In the three cases studied, the absorption bands have similar shapes; the maximum of the band for the selenium is shift toward higher wavelengths in relation to the corresponding maximum of arsine.[16,17] The observed intensity of the absorption band of the molecule of Cd is lower than those of the others, which can be explained by the unstability of this molecule: only a small part of the supposed hydride of Cd produced should be available for absorption in the quartz cell, owing to the decomposition of the hydride in accordance with reaction 1, probably enhanced by ultraviolet light photodecomposition in the cell.

In Figure 7c, the atomic absorption of the Cd^0 (228.8 nm) does not appear because of the poor resolution employed. In order to verify that there was Cd^0 in the quartz cell, for the same generation experiment we used the 2400 grooves/mm grating in the spectrometer. The spectra obtained under these higher dispersion conditions are shown in the Figure 7d. As can be seen, both the absorption line of Cd^0 and the molecular absorption, probably attributable to a Cd hydride (as is the case for As and Se), appeared on comparing the blank (Figure 7d1) and the Cd sample (Figure 7d2) spectra.

Other volatile molecules which could be present in our experimental conditions at measurable concentrations include H_2, CdH, Cd_2, and CdCl. According to available information on molecular spectra,[20] these others should have their absorption bands at wavelengths far away from the 228.8 nm regions, with the exception of Cd_2 molecule.[20] It seems that the latter molecule exhibits a broad band with a maximum at 228.8 nm, and so it could also slightly contribute to the molecular absorption observed in that spectral region (Figure 7d).

(16) Sanz, J.; Gallarta, F.; Galbán, J. *Anal Chim. Acta* **1991**, *255*, 113-120.
(17) Sanz, J.; Gallarta, F.; Galbán, J.; Castillo, J. R. *Analyst* **1988**, *113*, 1387–1391.
(18) Sanz, J.; Ortega, L. A.; Galbán, J.; Castillo, J. R. *Microchem. J.* **1990**, *41*, 29–40.
(19) Sanz, J.; Gallarta, F.; Galbán, J.; Castillo, J. R. *Fresenius Z. Anal. Chem.* **1988**, *330*, 510–515.
(20) Pearce, R. W. B.; Gaydon, A. G. *The Identification of the Molecular Spectra*, 4th ed.; Chapman and Hall: London, 1976; p 132.

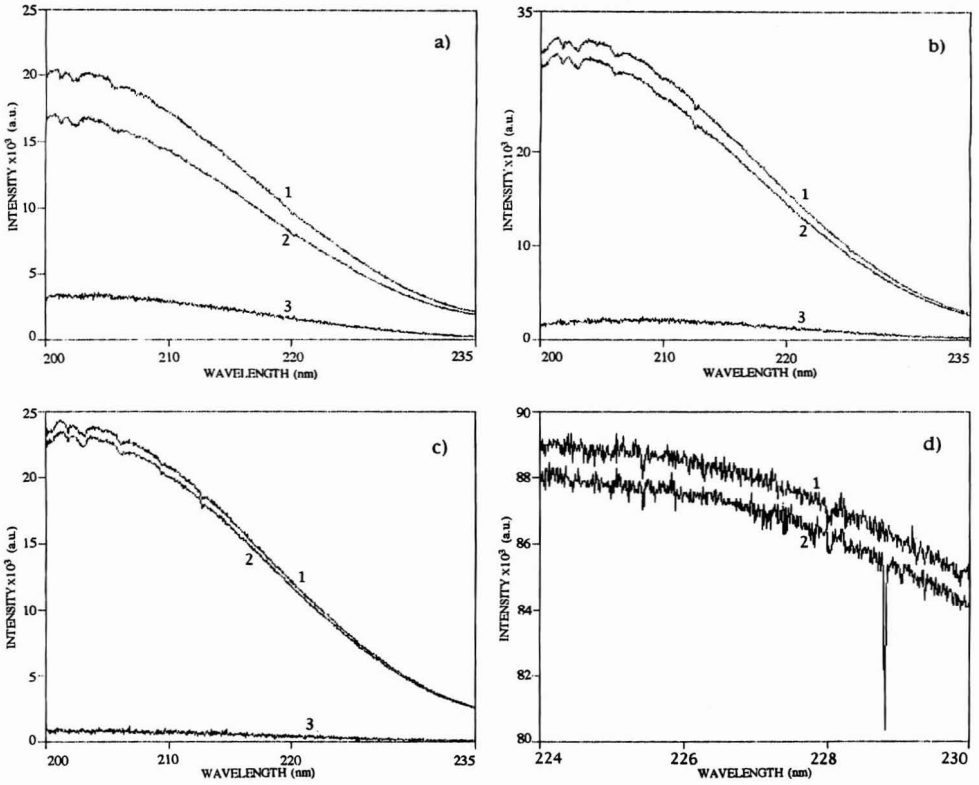

Figure 7. Absorption spectra for several hydrides: (a) As, (b) Se, and (c) Cd. (1) Blank, (2) 1 ppm sample, (3) net absorption band. Resolution of the experimental instrumentation is 0.2 nm. (d) Spectra obtained with Cd. Resolution of the experimental instrumentation is 0.03 nm.

FINAL DISCUSSION AND CONCLUSIONS

Cold vapor generation of monoatomic Cd^0 can be accomplished by reduction of Cd^{2+} solutions with $NaBH_4$ from an organized medium. However, the volatile species generated and transported to the measurement cell is probably not Cd^0. Most likely, the mechanism for generation of the Cd volatile compound is described by the following reactions:

$$BH_4^- + 3H_2O + H^+ \rightarrow H_3BO_3 + 8H^* \quad (2)$$

$$8H^* + Cd^{2+}{}_{(s)} \rightarrow (CdH_2)_{(volatile)} + 2H_{2(excess)} + 2\,H^+ \quad (3)$$

as for other better known volatile hydrides (H^* being "nascent" hydrogen). As (CdH_2) is volatile, this should be the transportation mechanism for cadmium at the temperature of the laboratory.

However, at room temperature, during transport, the formed volatile hydride would decompose according to reaction 1, and the formed Cd^0, not volatile, would deposit all along the connecting tubing. This decomposition is more efficient the higher the temperature (see Figure 5). In any case, the great excess of H_2 formed in the decomposition of BH_4^- in the acid medium of reaction will prevent the complete decomposition of the volatile hydride (see equilibrium 1). Thus, at least a certain amount of volatile cadmium will finally reach the absorption cell. Once there, according to equilibrium 1, a substantial proportion of the volatile Cd species transported seems to be able to form instantly monoatomic Cd^0 (probably favored by photodecomposition brought about by the exciting UV light), as it absorbs resonant radiation of Cd at room temperature.

The peculiar ability of Cd^0 atoms to survive in cold environments (at comparatively long distances, of the order of centimeters, from a rod glowing at 2500 °C, where those atoms were produced) has already been described.[21]

Moreover, Crabi et al.[22] used a combination of a graphite furnace and an inductively coupled plasma to study the thermal vaporization of cadmium, and they concluded that the free cadmium atoms had an extremely long lifetime near room temperature. Similarly, Kántor et al.[23] used a combined quartz furnace and flame system for the specific element detection of atomic cadmium vapor that evolved inside the furnace from the thermal decomposition of $Cd(NO_3)_2$ and $CdCl_2$. They showed that free cadmium atoms still remain in a significant amount for atomic absorption detection without flame at a considerable distance from the furnace where they were formed. They suggested that about one-ninth of the material reaching the observation zone is atomic cadmium vapor.

(21) Dean, J. R. ; Snook, R. D.; *J. Anal. At. Spectrom.* **1986**, *1*, 461–465.
(22) Crabi, G.; Cavalli, P.; Acilli, M.; Rossi, G.; Omenetto, N. *At. Spectrosc.* **1982**, *3*, 369.
(23) Kántor, T.; Bezúr, L. *J. Anal. At. Spectrom.* **1986**, *1*, 9–17.

Concerning our work here, there are two points which deserve consideration.

(1) The significantly different vapor pressures of Cd and Hg metals (e.g., at 150 °C, Cd has 1.28×10^{-5} Torr, while Hg has 2.807 Torr[24] point to different behaviors in their respective cold vapor atomic absorption process, even if a true atomic absorption is demonstrated for both metals (see Figure 6). Our results show that their CV generation behavior is totally different: while Hg is transported to the atomization/measurement cell as the cold vapor of the Hg^0 (very volatile), it seems that in the case of Cd, CdH_2 is more likely the volatile species responsible for the metal transport. This generation and transport has been possible via the use of an adequate "organized medium", vesicles, able to favorably manipulate the hydride formation reaction in solution. The chemical differences between vesicles and micelles have been stressed elsewhere.[25]

(2) Survival of Cd^0 atoms in a cold environment, as proposed in this work, is not exactly the same type of phenomenon as reported in refs 21–24. Those three papers referred to *electrothermal* formation of Cd atoms, which then survived for a while before cluster formation, condensation, or deposition occurred. Our proposition here is that we have a *chemical* formation of atoms according to the following decomposition reaction:

$$[CdH_2]_{\text{unstable}} \rightleftharpoons Cd^0{}_{\text{(monoatomic vapor)}} + H_2$$

(in a way somewhat similar to the well-known generation of atomic hydrogen, "status nascendi", by reduction of hydrogen ions, as in equilibrium 2). This decomposition process should obviously be governed by kinetics (considering the high tendency of Cd^0 atoms, instantly formed, to react, condense, and deposit eventually on the tube walls) and the possibility of photodecomposition processes induced by the UV excitation light. Notwithstanding the different mechanism of atom formation, we believe that the peculiar ability of Cd^0 atoms to survive a cold environment[21–23] still holds here and could be responsible for the appearance and transient presence of a substantial concentration of monoatomic Cd^0 cold vapor. Of course, this cold vapor would not be thermodynamically stable. However, the monoatomic Cd^0 lifetime, its ability to survive, seems to be long enough to be measured. This provides the basis for a most useful AAS measurement of Cd at room temperature.

In brief, what we propose is that in this case, *the atomizer is a chemical reaction* which on its own, or assisted by UV exciting light, provides the energy for atomization at room temperature. If the kinetics of such formation reaction, relative to those of the subsequent reactions of reactive Cd^0 atoms, are favorable, we could be able to measure surprisingly high concentrations of such transient species. In fact, we have proved here (see Table 1) that for cadmium this measurement is so sensitive and precise that CV-AAS determinations will no longer be exclusively confined to mercury.

ACKNOWLEDGMENT

Financial support from DGICYT (Spain) through project PB91-0669 is gratefully acknowledged.

Received for review December 19, 1994. Accepted March 20, 1995.[⊗]

AC941227D

(24) Weast, R. C.; Astle, M. J. Eds. *CRC Handbook of Chemistry and Physics.* 60th ed.; CRC Press Inc.: Boca Raton, FL, 1980; p D-198.

(25) Sanz-Medel, A.; Aizpún, B.; Marchante, J. M.; Segovia, E.; Fernández, M. L.; Blanco, E. *J. Chromatogr. A* **1994**, *683*, 233–243.

[⊗] Abstract published in *Advance ACS Abstracts,* May 1, 1995.

Anal. Chem. **1995**, *67*, 2224–2230

Chemiluminescent Chemical Sensors for Oxygen and Nitrogen Dioxide

Greg E. Collins* and Susan L. Rose-Pehrsson

Chemistry Division, Code 6110, Naval Research Laboratory, Washington, D.C., 20375-5342

Chemiluminescent chemical sensors for oxygen and nitrogen dioxide have been investigated via the immobilization of 3-aminophthalhydrazide (luminol) within a hydrogel or polymeric, sorbent coating that is positioned in front of a photomultiplier tube. Some selectivity is tailored into these devices by careful selection of the polymer type, pH, and metal catalyst incorporated within the film. Oxygen levels as low as 2.4 ppm in nitrogen have been detected using the oligomer fluoropolyol as the support matrix for immobilizing luminol, KOH, and the metal catalyst, $Fe_2(SO_4)_3$. For the detection of NO_2(g), the use of sorbent, polymer coatings such as fluoropolyol or polyethylenimine resulted in strong humidity dependencies, exhibiting no chemiluminescence under dry conditions. Incorporation of the chemiluminescent reagents within a hydrogel (e.g., poly(vinyl alcohol) or superabsorbing polymer Waterlock) eliminated this effect. A survey of various hydrogel immobilization matrices and metal catalysts found that, for the determination of NO_2(g), Cu(II) and the superabsorbing polymer Waterlock provided the best film performance with respect to sensitivity (0.46 ppb) and stability. Discussions center about the complete characterization of these chemiluminescent chemical sensors and an examination of specific methods used to extend the sensitivity and selectivity of these devices.

Various chemiluminescence schemes have been successfully applied to the detection of metals, polycyclic aromatic hydrocarbons, and numerous oxidizing and reducing agents.[1] These methods typically rely upon the oxidation of a chemically reactive species, e.g., luminol or lucigenin, and the subsequent emission of a photon from an electronic, excited-state intermediate. Chemiluminescent techniques are free of Raman and Rayleigh scattering, interferences associated with fluorescence techniques, and, therefore, permit the operation of a photomultiplier tube at maximum sensitivity. The primary attraction of chemiluminescence detection is the excellent sensitivity obtainable over a wide dynamic range using simple instrumentation.

The vast majority of work done in the chemiluminescence field has been devoted to solution-based, flow injection analysis formats. One of the most widely investigated chemiluminescence reagents is 3-aminophthalhydrazide, or luminol. Luminol has been effectively used for the detection of many different metals and oxidants in solution, due to the catalytic behavior these metals have on the chemiluminescent oxidation of luminol. Examples include the detection of Cr(III),[2] Co(II),[3] Fe(II),[4] H_2O_2(aq),[5] NO(aq),[6] and ClO^-(aq).[7] These methods require adequate mixing of the reagent and unknown solutions prior to passage before a photomultiplier tube (PMT), accurate control of the solution delivery to the PMT, and the consumption of a substantial amount of reagents.

Different instrumental variations, based upon the chemiluminescent oxidation of luminol, have been devised for the detection of gas-phase oxidants. Maeda et al. designed a chemiluminescent reaction compartment for the detection of NO_2(g) which collected a pool of alkaline luminol solution directly below a PMT and introduced the sampled airstream into the region above the solution.[8] Excess luminol solution and air flowed continuously out of the reaction compartment through an outlet port at the base of the system. This system was very sensitive to movements of the compartment and had a relatively slow time response. An alternate design for the chemiluminescent detection of NO_2(g) was subsequently presented by Wendel et al., wherein a length of filter paper was positioned adjacent to a PMT, and a flow of alkaline luminol solution was directed down the paper in a fine film.[9] This system has also been used for the measurement of trace levels of ambient ozone, utilizing the chemiluminescent dye eosin Y.[10] A further variation on the instrument described by Wendel et al. led to the development of a commercially available instrument devoted to the measurement of NO_2(g), the Luminox LMA-3 (Scintrex/Unisearch); a detailed description of this instrument was presented by Schiff et al.[11] The reaction cell consists of a fabric wick positioned in front of a PMT that is continually wetted with fresh luminol solution delivered via a peristaltic pump, and whose surface is exposed to a stream of the ambient air pumped through the cell. In recent years, this instrument has been utilized in combination with various pretreatment stages for the trace detection of organic nitrates.[12,13] Still another variation on the luminol chemiluminescent detector for NO_2(g) was introduced by Mikuška and Večeřa; this configuration employs a

(1) Robards, K.; Worsfold, P. J. *Anal. Chim. Acta* **1992**, *266*, 147–173.
(2) Escobar, R.; Lin, Q.; Guiraum, A.; de la Rosa, F. F. *Analyst* **1993**, *118*, 643–647.
(3) Cheng, C. A.; Patterson, H. H *Anal. Chem.* **1980**, *52*, 653–656.
(4) Seitz, W. R.; Hercules, D. M. *Anal. Chem.* **1972**, *44*, 2143–2149.
(5) Shaw, F. *Analyst* **1980**, *105*, 11–17.
(6) Kikuchi, K.; Nagano, T.; Hayakawa, H.; Hirata, Y.; Hirobe, M. *Anal. Chem.* **1993**, *65*, 1794–1799.
(7) Marino, D. F.; Ingle, J. D., Jr. *Anal. Chem.* **1981**, *53*, 455–458.
(8) Maeda, Y.; Aoki, K.; Munemori, M. *Anal. Chem.* **1980**, *52*, 307–311.
(9) Wendel, G. J.; Stedman, D. H.; Cantrell, C. A.; Damrauer, L. *Anal. Chem.* **1983**, *55*, 937–940.
(10) Ray, J. D.; Stedman, D. H.; Wendel, G. J. *Anal. Chem.* **1986**, *58*, 598–600.
(11) Schiff, H. I.; Mackay, G. I.; Castledine, C.; Harris, G. W.; Tran, Q. *Water Air Soil Pollut.* **1986**, *30*, 105–114.
(12) Blanchard, P.; Shepson, P. B.; Schiff, H. I.; Drummond, J. W. *Anal. Chem.* **1993**, *65*, 2472–2477.
(13) Hao, C.; Shepson, P. B.; Drummond, J. W.; Muthuramu, K. *Anal. Chem.* **1994**, *66*, 3737–3743.

0003-2700/95/0367-2224$9.00/0 © 1995 American Chemical Society

continuous spray of luminol solution, directed immediately below the PMT, and generated from a stream of the analyzed gas.[14] Each of the systems referenced above requires accurate and continual pumping or delivery (e.g., peristaltic pump) of an aqueous luminol solution, be it across a piece of filter paper, a wick, or mixed with an additional solution or gas containing the analyte of interest. The systems described above are not amenable to remote sensing or personal dosimeter applications because of constraints with respect to size, weight, power, or portability.

The industrial community is continually striving to develop sensor systems that are simpler, less expensive, and more compact and offer the possibility for remote sensing or personal dosimeter applications. In order to address some of these constraints, efforts were focused upon the development of a solid-phase, chemiluminescent, chemical sensor. These sensors are based upon the incorporation of the chemiluminescent reagent luminol and an appropriate metal catalyst within a polymeric thin film or hydrogel that is supported in direct view of a PMT. The objective of this work is twofold: (1) to further simplify and miniaturize the instrumental requirements for chemiluminescent measurements and (2) to introduce some selectivity, sensitivity, or both through the incorporation of the chemiluminescent reagents within a polymeric network bearing solubility characteristics altogether different from that of water. The successful incorporation of chemiluminescent reagents within polymeric matrices could lead to the formation of very compact sensor systems which consist of simply the chemiluminescent gel, a PMT, and a small pump for sampling air across the surface of the polymer or diffusion membrane. The latest development by Hamamatsu, a miniature photomultiplier tube supported on a TO-8 type metal can package (15 mm in diameter and 10 mm in height) that requires simply a 15 V power supply, is ideally suited to the development of a compact, low-power sensor system which has the possibility of being adapted for remote sensing and portable dosimeter applications.

Previous authors have demonstrated the feasibility of utilizing luminol in a reagent-less fashion, i.e., using a solid substrate support. Agranov and Reiman attempted the direct application of luminol, sodium carbonate, and copper sulfate onto indicator tape for the detection of hydrogen peroxide but were plagued by humidity and stability problems.[15] Freeman and Seitz determined hydrogen peroxide concentrations in solution by immobilizing luminol and peroxidase within a polyacrylamide gel held on the end of a fiber-optic probe.[16] The co-immobilization of dehydrogenase enzymes and luminol within a poly(vinyl alcohol) matrix has been proposed for the detection of ATP or NAD(P)H.[17] Luminol has also been covalently immobilized onto silica particles for the detection of hydrogen peroxide by flow injection analysis.[18]

Selectivity is one of the major drawbacks limiting the analytical applicability of the luminol chemiluminescence reaction. This is not true for all chemiluminescent reactions; e.g., peroxyoxalate chemiluminescence is based on the very selective reaction of an aryl oxalate ester or oxamide with hydrogen peroxide, wherein the energy produced from this chemical reaction is transferred to a fluorescent species added to the matrix and emitted in the form of light.[19] Our aim was to introduce some selectivity into the luminol-based chemiluminescent, chemical sensors discussed here by proper choice of the chemiluminescent reagent, catalyst, pH, and polymeric substrate. We have examined a number of different polymers whose sorbent properties have been characterized with respect to their hydrogen bond acidity and basicity, dipolarity, polarizability, and ability to distinguish between members of a homologous series.[20] Careful choice of the polymer used to incorporate the chemiluminescent reagents helps determine the types of analytes concentrated within the organic thin film. The selectivity of these chemical sensors can be further extended by choosing a chemiluminescent reagent, catalyst, and pH that is more responsive to the analyte of interest. This paper will discuss the development of chemiluminescent chemical sensors for oxygen and nitrogen dioxide, each of which employs specific hydrogels or polymeric thin films of luminol incorporating different catalytic metals and pH conditions.

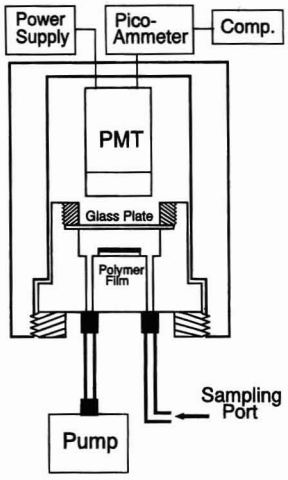

Figure 1. Experimental setup for monitoring solid-phase chemiluminescence.

EXPERIMENTAL SECTION

Apparatus. The instrumental setup consisted of a small cell supporting the polymer-coated, glass substrate behind a glass window in full view of a PMT (see Figure 1). Inlet and outlet tubes (Teflon (DuPont), PTFE) allow a vacuum pump (MSA Flow-Lite Turbo) to sample air (2 L/min) directly across the surface of the chemical sensor. For those applications in which a hydrogel substrate was utilized for immobilization of the chemiluminescent reagents, the gel was sandwiched between the glass window and a Teflon PTFE membrane (0.47 μm, Gelman Sciences). The purpose of the Teflon membrane is to permit the diffusion of analytes from the airstream into the gel while preventing the loss of water from the hydrogel. A Keithley 485 picoammeter was used to monitor the cathodic current, and National Instruments' LABView for Windows controlled the data acquisition.

Chemicals and Gas Mixtures. All chemicals were used as received from the suppliers. The following is a list of the

(14) Mikuška, P.; Večeřa, Z. *Anal. Chem.*, **1992**, *64*, 2187–2191.
(15) Agranov, Kh. I.; Reiman, L. V. *Zh. Anal. Khim.* **1979**, *34*, 1533–1538.
(16) Freeman, T. M.; Seitz, W. R. *Anal. Chem.* **1978**, *50*, 1242–1246.
(17) Coulet, P. R.; Blum, L. J.; Gautier, S. M. *Sens. Actuators B* **1993**, *11*, 57–61.
(18) Hool, K.; Nieman, T. A. *Anal. Chem.* **1988**, *60*, 834–837.
(19) Stigbrand, M.; Pontén, E.; Irgum, K. *Anal. Chem.* **1994**, *66*, 1766–1770.
(20) Rose-Pehrsson, S. L.; Grate, J. W.; Ballantine, D. S.; Jurs, P. C. *Anal. Chem.* **1988**, *60*, 2801–2811.

polymeric sorbent coatings and hydrogels examined, the abbreviation used, and the corresponding manufacturer name: polyethylenimine (PEI, Phase Separations); fluoropolyol (FPOL, synthesized in-house,[21] with the structure $[OCH_2CH(OH)CH_2OC(CF_3)_2(C_6H_4)C(CF_3)_2OCH_2CH(OH)CH_2OR\text{-}]_n$, where $n = 5-10$ and R = $CH_2(CF_2)_3CH_2$ for FPOL1, R = $(CF_3)_2CCHCHCH$ for FPOL2, and R = $(CH_2)_4$ for FPOL3; FOMBLIN Z-DOL, perfluoropolyether diol (Aldrich); polyacrylamide (PAC, synthesized from *N,N'*-methylenebis(acrylamide) and acrylamide (Aldrich) according to a previously published procedure); 4% poly(vinyl alcohol) (PVAL, Aldrich, 99% hydrolyzed) cross-linked with sodium borate; poly(ethylene oxide) (PEO, Union Carbide Corp.); SuperAbsorbing Polymer (SAP, Absorbent Technology Co.); WaterLock SuperAbsorbent polymer D-242 (Grain Processing Corp.). The 3-Aminophthalhydrazide (luminol) (97%) was purchased from Aldrich and used to prepare a 0.01 M stock solution in 0.1 M KOH. The metal salts used for the catalytic studies include $Fe_2(SO_4)_3$, $CuCl_2$, $MnSO_4$, $CoCl_2$, $K_3Fe(CN)_6$, Na_2SO_3, colloidal platinum prepared by reducing hydrogen hexachloroplatinate(IV) with ascorbic acid,[22] and colloidal platinum prepared by reducing $PtCl_4$ with sodium citrate.[23]

Gas mixtures (86 ppm NO_2 in air, 103 ppm O_2 in He, 110 ppm NO in air, 99.8 ppm SO_2 in air, and 450 ppm NH_3 in nitrogen) were obtained from either Scott Specialty Gases or Matheson and diluted with air using Matheson 8200 mass flow controllers to give varying concentration levels. The hydrazine vapor generation system has been described elsewhere and was used to generate hydrazine levels from 10 to 500 ppb in air.[24] Humidity was controlled through the use of bubblers and line mixers and quantitated using a Hygrodynamics hygrometer.

Film Preparation. The polymeric thin films were prepared by exhaustively spraying a basic methanolic solution of the polymer, luminol, and metal catalyst onto a glass substrate (8 cm^2) using an air brush (Badger Model 200-3). In general, the hydrogels were prepared by adding 1 mL of 10^{-4} M luminol (pH 13 in KOH) to 0.02 g of the resin.

RESULTS AND DISCUSSION

Shown in Figure 1 is the experimental apparatus utilized for measuring the chemiluminescence signals arising from the luminol-immobilized, polymeric films. A small, hand-held, vacuum pump was used to sample the air (2 L/min) directly across the surface of the film, and a photomultiplier tube positioned behind a glass window sensitively determined the emission of photons from the chemiluminescent film. Because the sensitivity of these sensors is directly linked to the background chemiluminescence, it was critical that all light leaks through the sampling ports be eliminated. Providing that the inlet and outlet tubes are long enough (>30 in.) and sufficiently masked with black, heat-shrink tubing, the background chemiluminescence in the absence of any analytes (i.e., in an atmosphere of ultrahigh-purity nitrogen) can be reduced to the room-temperature baseline response of the photomultiplier tube (0.5 nA).

The oxidation of luminol by oxygen results in the emission of a photon of light (~440 nm) according to the chemical reaction

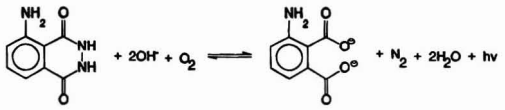

Figure 2. Chemiluminescence reaction arising from the oxidation of luminol by O_2(g).

Table 1. Sensitivities Obtained for the Detection of Oxygen in Nitrogen Utilizing a Polyethylenimine Film Incorporating Co(II) and Varying Levels of KOH onto a Glass Slide (8 cm^2)

[KOH] on glass slide (mol/cm^2)	sensitivity to O_2(g) (A/ppm × 10^{-12})
0	0.00
2.23×10^{-5}	0.00
1.15×10^{-4}	0.308
2.06×10^{-4}	0.593
2.97×10^{-4}	0.586
4.49×10^{-4}	0.200

shown in Figure 2. This reaction occurs under basic conditions and is catalyzed by numerous metal and metal cation species. The luminol-immobilized, polymeric thin films were initially characterized with respect to oxygen exposure in order to determine those substrate conditions necessary for suppressing any chemiluminescence arising from O_2(g) interactions with the film. The sensitivity of these chemiluminescent chemical sensors for NO_2(g) is dramatically improved by lowering the background chemiluminescence evident from the oxidation of luminol by the high concentration of O_2(g) in air. In addition, by suppressing the reaction of luminol with oxygen, the lifetime of these sensors is improved by maintaining the luminol and metal catalyst concentration within the polymeric film. As the next section will demonstrate, appropriate control of the polymer, relative pH, and metal catalyst can be exploited for the sensitive determination of trace levels of oxygen. Our interest in this study was to determine those conditions necessary for either completely suppressing or enhancing the O_2(g) chemiluminescence reaction with luminol.

The polymeric, luminol-immobilized, chemiluminescent films were prepared by using an air brush to exhaustively spray the contents of a methanolic solution containing the chemiluminescent reagents and polymer onto a small quartz slide (8 cm^2). Initial studies focused on the effect of KOH on the responsivity of luminol-immobilized (6.2×10^{-8} mol/cm^2) polyethylenimine (6.2×10^{-3} g/cm^2) films incorporating Co(II) as the metal catalyst (1.2×10^{-8} mol/cm^2). Shown in Table 1 are the sensitivities [A/ppm O_2(g) in N_2(g)] observed with respect to the detection of oxygen for several different polymeric films, each of which was prepared identically, with the exception of the quantity of KOH deposited onto the glass slide during spraying. It is evident from this table that the optimum concentration of KOH for the detection of oxygen is ~2×10^{-4} mol/cm^2, with the sensitivity dropping off significantly on either side of this concentration level within the polymeric film. As will be discussed in more detail later, films prepared for the detection of nitrogen dioxide utilize a much lower concentration of KOH (e.g., 2×10^{-5} mol/cm^2) within the film, in order to adequately suppress the chemiluminescence background signal arising from the direct oxidation of luminol by oxygen.

The particular metal catalyst chosen for immobilization within the polymeric film has an important impact upon the sensitivity

(21) Orear, J. G.; Griffith, J. R.; Reines, S. A. *J. Paint Technol.* **1971**, *43*, 113–119.
(22) Collins, G. E.; Latturner, S.; Rose-Pehrsson, S. L. *Talanta*, in press.
(23) Matheson, M. S.; Lee, P. C.; Meisel, D.; Pelizzetti, E. *J. Phys. Chem.* **1983**, *87*, 394–399.
(24) Grate, J. W.; Rose-Pehrsson, S.; Barger, W. R. *Langmuir* **1988**, *4*, 1293–1301.

Table 2. Chemiluminescence Sensitivities Obtained for the Detection of Oxygen While Using Various Metal Catalysts Immobilized within a Polyethylenimine Thin Film

	polymer type[b]					
metals	PEI	FPOL2	FOMBLIN	FPOL1	FPOL3	none
$Fe_2(SO_4)_3$	0.797	1.11	1.13	2.22	2.61	0.448
Co(II)	0.593					
Mn(II)	0.518					
Cu(II)	0.323					
Pt(ascorbic)	0.280					
$K_3Fe(CN)_6$	0.00					

[a] Effect of the polymer sorbent coating on the chemiluminescence sensitivity obtained for the detection of oxygen (Fe(III) used as the metal catalyst). [b] Sensitivity given in A/ppm $\times 10^{-12}$.

that film exhibits for oxygen. Table 2 summarizes the sensitivities obtained for a series of polyethylenimine films grown onto quartz slides, each incorporating identical concentrations of catalyst (1.2×10^{-8} mol/cm^2), KOH (2×10^{-4} mol/cm^2), polymer (6.2×10^{-3} g/cm^2), and luminol (6.2×10^{-8} mol/cm^2). It is interesting to note that the sensitivity for O_2(g) obtained from a film containing $Fe(CN)_6^{3-}$ is nearly unmeasurable, while the sensitivity seen using $Fe_2(SO_4)_3$ is nearly 8×10^{-13} A/ppm O_2(g) in nitrogen. Ferricyanide is certainly a catalyst to consider for situations requiring a low oxygen background, while $Fe_2(SO_4)_3$ appears to be the catalyst of choice for the detection of O_2(g).

McGill et al. have investigated the sorbent properties of a number of different polymeric coatings (including FPOL and PEI), demonstrating their ability to preferentially adsorb particular classes of analytes on the basis of the functionality groups incorporated within the polymeric backbone.[25] In fact, predictions can be made a priori concerning the type and extent of analyte adsorption into a given polymeric film by elucidating the solvation parameters for the polymer and the analyte (e.g., polarizability, dipolarity, hydrogen bond acidity, hydrogen bond basicity, etc.). In an effort to introduce some selectivity to these chemiluminescent chemical sensors, a number of different polymer coatings were investigated and compared for the detection of oxygen (see Table 2). Each of the films was prepared with identical concentrations of polymer (2.5×10^{-3} g/cm^2), KOH (2×10^{-4} mol/cm^2), metal catalyst (Fe(III), 1.2×10^{-8} mol/cm^2), and luminol (6.2×10^{-8} mol/cm^2), with the exception of the control case, in which no polymer was used. In each case, the presence of a polymeric sorbent coating on the glass slide for the immobilization of the chemiluminescent reagents resulted in an enhancement of the sensitivity. The sensor utilizing FPOL3 was found to be nearly 10 times more sensitive to oxygen. We attribute this effect to the increased chemical sorption of oxygen by the polymer on the glass slide.

From the optimization studies, a chemiluminescent chemical sensor was prepared for the sensitive determination of trace levels of oxygen via the incorporation of luminol (6.2×10^{-8} mol/cm^2), KOH (2×10^{-4} mol/cm^2) and $Fe_2(SO_4)_3$ (1.2×10^{-8} mol/cm^2) within a thin film of FPOL3 (2.5×10^{-3} g/cm^2). Figure 3 illustrates the chemiluminescent response of this sensor to increasing levels of oxygen in nitrogen. A detection limit of 2.4

(25) McGill, R. A.; Abraham, M. H.; Grate, J. W. *CHEMTECH* **1994**, *24*, 27–37.

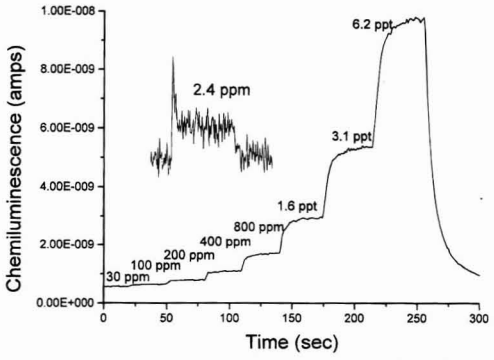

Figure 3. Introduction of varying levels of oxygen in a nitrogen carrier stream to a thin film of fluoropolyol immobilizing luminol, Fe(III), and KOH. The inset is an example of the signal/noise ratio seen for the detection of 2.4 ppm oxygen in nitrogen.

ppm O_2 in nitrogen (signal/noise = 2:1; see inset of Figure 3) was obtained with a response time of several seconds ($r > 0.99$). In a fashion similar to the films prepared for the detection of NO_2(g), which will be discussed in the following section, the sensitivity was observed to slowly decrease (1%/h) with exposure to 20 ppm O_2(g). We attribute this gradual change in the film's response to the continual and irreversible change in luminol concentration occurring at the surface of the polymeric thin film. The usable lifetime of these films is strongly dependent upon the concentration and extent of exposure to oxygen. This drawback will likely limit the applicability of this type of chemical sensor to the trace detection of oxygen within an inert atmosphere, e.g., monitoring low levels of oxygen during the fabrication of microsemiconductor devices. For monitoring low-ppm quantities of oxygen, we have found that, in general, the polymeric films should be replaced on a daily basis in order to maintain an accuracy of 10%.

Nitrogen dioxide is a strong oxidizer whose reaction with luminol results in the emission of a photon of light. Initial attempts at preparing a chemical sensor for NO_2(g) relied upon the same polymeric sorbent coatings and conditions investigated for oxygen, with the exception that a much lower concentration of KOH (2×10^{-5} mol/cm^2) was employed in order to significantly lower the background chemiluminescence evident from the oxidation of luminol by O_2(g). These polymeric films exhibited a strong humidity dependence for the detection of NO_2(g). Figure 4 is a plot of the plateau chemiluminescence response observed for the introduction of 1 ppm NO_2(g) in air to two different films, FPOL2 and PEI, while varying the relative humidity of the airstream from 0 to 100%. Both of these films immobilized identical concentrations of colloidal platinum (1.2×10^{-8} mol/cm^2) and luminol (6.2×10^{-8} mol/cm^2). Under dry conditions, no chemiluminescence response was seen for either film to the introduction of NO_2(g). As the humidity level was increased, the two polymeric matrices exhibited dynamically different behavior. For the FPOL2 film, the chemiluminescence response increased steadily with increasing relative humidity. The PEI film, on the other hand, showed a maximum in chemiluminescence at ~20% relative humidity, which decreased with increasing humidity. It is interesting to note that the peak chemiluminescence intensities observed were identical for both films, albeit at two different relative humidities.

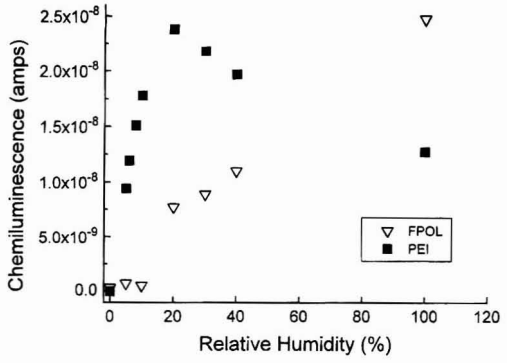

Figure 4. Effect of humidity on the chemiluminescence response of polyethylenimine and fluoropolyol thin films (immobilizing luminol and colloidal platinum) to 1.0 ppm NO_2.

These results can be better understood by examining the solubility characteristics of these polymers with respect to the adsorption of water, a property that has been previously quantitated using surface acoustic wave devices. Polyethylenimine is a polymer with hydrogen bond accepting functionalities that interact specifically with water. Fluoropolyol, on the other hand, is considered to be a hydrogen bond acid due to the fluorinated carbon atoms found along its polymer backbone and, as a result, adsorbs several times less water vapor. From Figure 4, it is evident that water absorption into these two different polymers plays a critical role in the chemiluminescent reaction scheme involving $NO_2(g)$. One explanation may be that the solvating properties of water permit the formation of free OH^- ions from KOH crystallites contained within the polymeric film. This effect is most clearly seen for the FPOL film, which exhibits a nearly linear increase in its chemiluminescence response to 1 ppm NO_2-(g) with the increase in relative humidity. The PEI film, on the other hand, strongly adsorbs water vapor into the film even at much lower relative humidities and, for this reason, exhibits a peak in the chemiluminescence at a much lower level (20% versus nearly 100%). As the relative humidity exceeds 20%, the overall chemiluminescence signal to 1 ppm $NO_2(g)$ decreases due to the competition the film expresses for the chemisorption of water vapor, as opposed to $NO_2(g)$.

From a sensor standpoint, the strong influence of humidity on the sensitivity of these chemiluminescent films limits the usefulness of these devices. In order to eliminate this effect, the chemiluminescent reagents were immobilized within polymeric hydrogels sandwiched between a quartz glass window and a Teflon PTFE membrane. The membrane serves two purposes: (1) prevents the rapid evaporation of water from the hydrogel and (2) permits the diffusion of analytes across the membrane into the hydrogel. The immobilization of luminol and a metal catalyst within a hydrogel provides a suitable matrix for supporting the chemiluminescent reaction in either dry or wet air with identical sensitivity.

Shown in Table 3 is a compilation of the sensitivities observed in the quantitation of $NO_2(g)$ and a number of other gases of analytical interest, for a series of hydrogels immobilizing the chemiluminescent reagents. Although film-to-film reproducibility was not extensively investigated for the purposes of this report, initial studies have indicated that for a given set of three films

Table 3. Compilation of the Sensitivities Observed for the Detection of $NO_2(g)$ and Other Possible Interferents While Using Various Hydrogels for Immobilizing Luminol, KOH, and Colloidal Platinum (Citrate Reduced)

	sensitivity (A/ppm × 10^{-9})				
polymer	$NO_2(g)$	$N_2H_4(g)$	$SO_2(g)$	$NO(g)$	$NH_3(g)$
SAP	76.5	0.7	0.03	0.00	0.00
PEO	52.6	0.6	0.00	0.00	0.00
PAC	4.6	0.00	0.00	0.00	0.00
Waterlock	186	0.3	0.3	0.00	0.00
Waterlock[a]	389	4.5	0.03	0.00	0.00
PVAL	48.5	0.2	0.05	0.00	0.00
PVAL[a]	806	no data	0.03	no data	0.00
PEI (20% RH)	11.2	0.06	0.00	0.00	0.00
FPOL (88% RH)	21.2	0.00	0.00	0.00	0.00

[a] 0.01 M Na_2SO_3.

Table 4. Sensitivities Observed for the Detection of $NO_2(g)$ and Other Possible Interferents While Using a Series of Transition Metal Catalysts Immobilized within a pH 13, Poly(vinyl alcohol) Film

	sensitivity (A/ppm × 10^{-9})				
metals	$NO_2(g)$	$N_2H_4(g)$	$SO_2(g)$	$NO(g)$	$NH_3(g)$
$Fe_2(SO_4)_3$	110	2.2	0.08	0.00	0.00
$K_3Fe(CN)_6$	76.3	1.6	0.06	0.00	0.00
Cu(II)	95.0	66.2	0.01	0.00	0.00
Pt(citrate)	48.5	0.2	0.05	0.00	0.00
Pt(ascorbic)	44.2	2.0	0.01	0.00	0.00
Co(II)	42.9	20.9	0.6	0.00	0.00

prepared under identical conditions, the film-to-film reproducibility is within 6–8%. We believe the reproducibility could be improved through careful control of the film thickness and placement within the sensor compartment cell. A detailed description of each hydrogel and the immobilization procedure utilized is given in the Experimental Section. Also listed for comparison are the sensitivities of two polymeric coatings, PEI and FPOL2, at their optimum relative humidity. Note first that the detection of NO_2-(g) using PEI and FPOL2 was inferior to the sensitivities observed for the majority of hydrogels examined. Just as was seen for the case of oxygen, the detection of $NO_2(g)$ is strongly dependent upon the polymeric composition of the hydrogel used to support the chemiluminescent reagents. Of the different hydrogels examined, the water-soluble resin Waterlock provided the highest sensitivity with respect to the detection of $NO_2(g)$. Wendel et al. have demonstrated that the addition of Na_2SO_3 to a solution of luminol and metal catalyst will result in a significant enhancement of the chemiluminescence signal seen for the detection of nitrogen dioxide. Our results support this observation for luminol-immobilized hydrogels, wherein the addition of sodium sulfite to an otherwise identical Waterlock hydrogel more than doubled its sensitivity to $NO_2(g)$.

In Table 4, a series of sensitivities are tabulated for the hydrogel, poly(vinyl alcohol), immobilizing luminol (5×10^{-4} mol/L) and a series of different metal catalysts (10^{-4} mol/L), all prepared under identical conditions. While $Fe_2(SO_4)_3$ seemingly provided the best sensitivity to $NO_2(g)$, the chemiluminescence response obtained using this metal catalyst was unstable, with the plateau response slowly decreasing with time. For this reason,

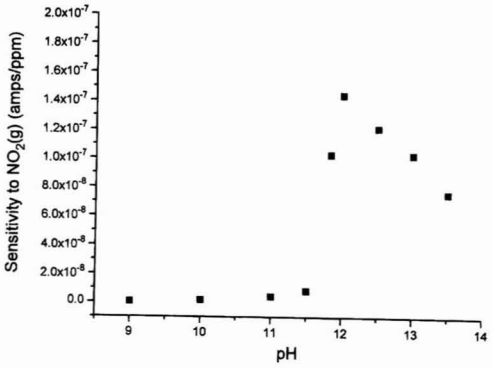

Figure 5. Influence of the pH of a Waterlock hydrogel on the sensitivity obtained for the detection of NO_2(g) (Cu(II) used as the metal catalyst).

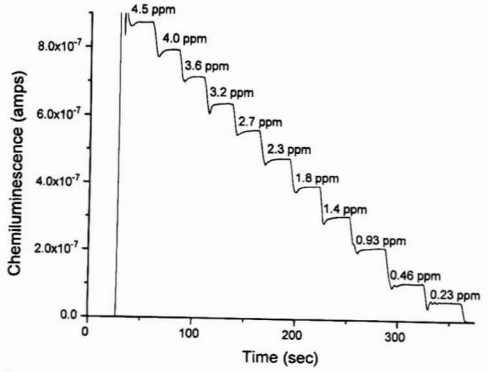

Figure 6. Response of a poly(vinyl alcohol) film immobilizing luminol and colloidal platinum (citrate reduced) to the introduction of varying levels of NO_2(g) in a carrier stream of dry air.

subsequent studies have emphasized the use of the metal catalysts colloidal platinum (citrate reduced) and Cu(II) for the quantitation of NO_2(g).

Just as was seen in the case of oxygen detection, NO_2(g) determinations using these chemiluminescent chemical sensors are strongly dependent upon the relative pH of the hydrogel. For the chemiluminescent detection of oxygen, extremely alkaline conditions were necessary on the surface of the polymer film. The optimal pH for the detection of NO_2(g), on the other hand, occurs in a pH region where the background chemiluminescence from oxygen is minimal. Figure 5 is a plot of the change in sensitivity with pH for a Waterlock polymer incorporating luminol and Cu(II) in the detection of NO_2(g). The most striking observation to be made from this figure is the sharp onset of chemiluminescence intensity above pH 11.5. The importance of this result is that some selectivity can be tailored into these devices by simply adjusting the relative pH of the hydrogel being utilized. For example, we have been examining methods for the chemiluminescence detection of chlorinated hydrocarbons that utilize a preoxidation step with a heated Pt filament.[26] This chemistry is operable at pH 11 with little loss in sensitivity for the chlorinated hydrocarbons, but with a dramatic reduction in the interference effect of NO_2(g).

The sensitive detection of part-per-trillion levels of nitrogen dioxide in air was demonstrated in a Waterlock hydrogel incorporating luminol and the metal catalyst colloidal Pt (citrate reduced) (see Figure 6). The downward spikes evident in Figure 6 are artifacts associated with the solenoid valve within the gas flow controller adjusting to the lower flow requirement for the analyte gas. Response times were on the order of seconds, with a detection limit as low as 460 ppt (signal/noise = 3:1) and error bars for point-to-point reproducibility of ±2%. While the linearity of response was excellent ($r > 0.999$), the sensitivity was observed to slowly increase or decrease depending upon the following: (1) the specific metal catalyst immobilized within the hydrogel and (2) the concentration, exposure time, and nature of the oxidant being examined. For example, when the Cu^{2+}/luminol/Waterlock gel was exposed to a constant concentration of NO_2(g) at 20 ppm, the chemiluminescence signal slowly increased at a rate of ~1%/h. This change in sensitivity is likely attributed to a change in either the catalyst or luminol concentration within the gel. The lifetime of these chemiluminescent gels is directly related to the type and concentration of the oxidant and the extent of exposure. In order to maintain accuracy (10%), we have found that, in general, the chemiluminescent gels should be replaced with fresh substrates on a daily basis.

Tables 3 and 4 also tabulate the sensitivities exhibited by each of the different hydrogels with respect to the detection of several other chemical oxidants and reductants: hydrazine, sulfur dioxide, nitrous oxide and ammonia. Each of the different film compositions was completely unresponsive to NO(g) and NH_3(g). We can attribute this result to the weak, oxidative properties of these molecules with respect to the chemiluminescent oxidation of luminol. Hydrazine and sulfur dioxide, on the other hand, were each detected to varying degrees, although nowhere near the sensitivity shown by nitrogen dioxide. Fortunately with respect to the selective detection of nitrogen dioxide, immobilization of the metal catalyst, Cu(II), resulted in the maximal suppression of any interference due to sulfur dioxide (no response seen for SO_2(g) concentrations of <3 ppm). Optimal sensitivity for sulfur dioxide was observed using the Waterlock hydrogel to immobilize the metal catalyst, Co(II), and luminol. The detection limit for sulfur dioxide under these film conditions was ~37 ppb. The time response for sulfur dioxide is comparable to that seen for nitrogen dioxide, with 90% of full scale observed within 1 min. Hydrazine is an extremely strong reducing agent whose toxic character has generated considerable interest in the development of an effective chemical sensor for this molecule. One would not expect a chemiluminescent reaction to take place between hydrazine and luminol because of the reducing character of hydrazine. Previous investigations in our laboratory with the metal catalyst colloidal platinum have suggested that hydrazine is catalytically oxidized at the surface of metal catalysts to form a radical peroxo intermediate that oxidizes luminol. The detection of hydrazine has been demonstrated to levels as low as 10 ppb in air (signal/noise = 3:1). The response obtained from this sensor for the detection of 125 and 250 ppb hydrazine in dry air is shown in Figure 7. The detection of NO_2 operated on a significantly faster time scale (several seconds) when compared to that obtained while monitoring hydrazine levels (10 min). The slow time response evident for the detection of hydrazine is likely attributed to the indirect reaction mechanism involved. In order to be

(26) Collins, G. E.; Rose-Pehrsson, S. L., document in preparation.

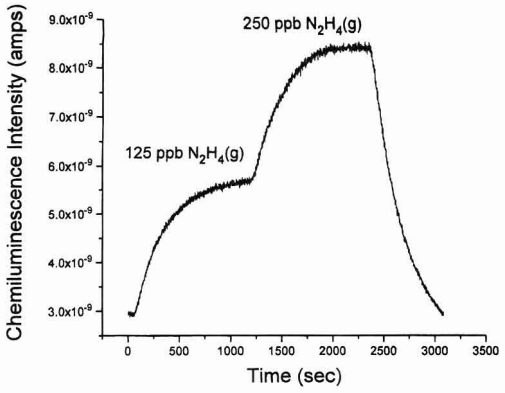

Figure 7. Example of the time response obtained for the detection of hydrazine using a Waterlock polymer immobilizing luminol, KOH, and colloidal platinum (ascorbic acid reduced).

detected, hydrazine vapor must dissolve in the hydrogel film and catalytically react at the surface of a platinum colloid to form a radical peroxo intermediate that can subsequently react with luminol to generate a photon of light. Nitrogen dioxide and oxygen, on the other hand, react with luminol directly to give a much more rapid chemiluminescent response. The time-domain signal acquired for any particular analyte can be an additional tool for introducing selectivity into these chemical sensors. Kolesar, for example, has demonstrated the ability to selectively differentiate between $NO_2(g)$ and diisopropyl methylphosphonate (DIMP) using the time- and frequency-domain responses of a copper phthalocyanine-coated IGFET.[27]

CONCLUSIONS

Chemiluminescence techniques benefit from superior sensitivity and ease of measurement, two features that are attractive to the chemical sensor arena. We are currently pursuing efforts to immobilize these chemiluminescent gels directly onto the surface of a miniature photomultiplier tube (8 mm diameter, Hamamatsu, Inc.) in order to generate a new class of portable, chemiluminescent chemical sensors. There are a number of advantages associated with the successful incorporation of this chemistry into a miniaturized format, and they include its simplicity, low power requirements (+15 V), lack of liquid waste generation (absence of a peristaltic pump—a feature common to most chemiluminescence techniques), and possibility for adaptation to remote sensing and personal dosimeter applications.

The primary drawbacks to the system described here are selectivity and stability. The selectivity can be improved by using an array of chemiluminescence chemical sensors employing different chemiluminescent reagents, pH, metal catalysts, and polymer substrates. We have demonstrated that simple changes in these parameters will significantly alter the sensitivity and selectivity of these films with respect to the detection of oxygen and nitrogen dioxide. The gradual shift in sensitivity observed in these sensors following continuous exposure to an oxidant (1%/h for 20 ppm $NO_2(g)$) is a feature associated with the irreversible character of the luminol chemiluminescence reaction, changes evident in the gel composition due to the slow evaporation of water through the Teflon membrane, or changes in pH arising from the absorption of $CO_2(g)$ into the film. Although it may be feasible to automatically adjust the calibration curve according to the integrated number of photons collected at the detector, the gradual change in sensitivity apparent in these films may ultimately limit the quantitative usefulness of these devices to either trace detection or alarm monitoring. While chemiluminescence systems that utilize continuously regenerated reagent solution have fewer problems with drift, these systems are neither compact nor suitable for remote or portable applications. The system described here sacrifices some with respect to quantitative accuracy and sensitivity, in deference to simplicity, portability, and remote sensing capability. We are currently pursuing the development of a portable, remote sensor alarm system whose daily maintenance consists of simply inserting a plug of chemiluminescence gel into the compartment cell, ensuring excellent sensitivity and reasonable quantitative accuracy over the course of a day of continuous monitoring.

ACKNOWLEDGMENT

This research was supported by NASA/Kennedy Space Center (DL-ESS-24, CC-82360A).

Received for review January 19, 1995. Accepted March 28, 1995.[⊗]

AC950065Y

(27) Kolesar, E. S. *Proceedings Sensor Expo*; Helmers Publishing, Inc.: Peterborough, NH, 1994; pp 11–30.

[⊗] Abstract published in *Advance ACS Abstracts,* May 15, 1995.

Anal. Chem. **1995,** *67,* 2231–2238

Reversible Fiber-Optic Fluorosensing of Lower Alcohols

Guillermo Orellana,*,† Ana M. Gómez-Carneros,† César de Dios,† Ana A. García-Martínez,‡ and María C. Moreno-Bondi*,‡

Laboratory of Applied Photochemistry, Department of Organic Chemistry, and Department of Analytical Chemistry, Faculty of Chemistry, Complutense University, E-28040 Madrid, Spain

Low molecular weight alcohols, such as methanol and ethanol, are optically sensed in nonhydroxylic media using the highly fluorescent dyes 5-(4-aminophenyl)-2-(2-pyrazinyl)-1,3-oxazole (appzox) or -thiazole (appzth). The novel indicator molecules display an absorption band in the blue (up to 450 nm), high emission quantum yields (up to 0.82), and small excited-state lifetimes (1–3 ns) that prevent cross-sensitivity to oxygen. Their large Stokes shift and minute emission (Φ_{em} < 0.01) in the presence of alcohols are discussed in terms of an adiabatic photoreaction that produces an intramolecular charge-transfer excited state, which constitutes the basis of the sensor response. Fabrication of a fiber-optic sensing head for reversible quantification of such analytes is possible via deposition of the indicator onto silica gel (for gas-phase monitoring) or covalent binding to cross-linked chloromethylated styrene–divinylbenzene copolymer (for both gas- and liquid-phase measurements). The performance of the optical monitoring device has been tested in the analysis of lower alcohols in hydrocarbon solvents and commercial gasoline samples. Typical response times ($t_{100\%}$) to 0.2–6% (v/v) methanol in the samples are 2–4 min at 22 °C, the relative standard deviation for repeated measurements being 1.5–3%. Of all the two- to five-carbon alcohols tested, as well as water (up to saturation), only ethanol may be regarded as interferent for methanol quantification in gasoline. Fiber-optic measurements are also insensitive to other fuel additives such as methyl *tert*-butyl ether, lead tetraethyl and colored or fluorescent stains. The temperature coefficient of the sensor in the 10–40 °C range is 0.0057/°C.

Real-time, in situ determination of certain low molecular weight alcohols (e.g., methanol, ethanol, and isopropyl alcohol) is of utmost importance in a number of industrial processes such as fermentations or distillations leading to spirituous beverages, blending of gasoline and fuel components, large-scale making of formaldehyde and esters of organic and inorganic acids, and polymer and plastics manufacturing, as well as extraction or preparation of some vitamins, alkaloids, hormones, antibiotics, and other pharmaceuticals. The majority of methods described so far to quantify lower alcohols in nonhydroxylic solvents (such as gasolines) are based on gas/liquid chromatographic analysis of samples obtained from production lines or storage containers.[1–4] Other analytical methods occasionally reported for that purpose use liquid chromatography,[5] visible[6] or infrared spectrophotometry,[7] and nuclear magnetic resonance.[8] Although most of such methods are precise enough and allow for quantification of individual alcohols, they suffer from experimental complexity, chemical interferences, or a considerable slowness of the analyte determination.

The *advantages* of fiber-optic sensors for chemical analysis, with regard to *safety* (absence of electrical signal), *size* (ease of miniaturization), *process engineering* (network integration, mechanical ruggedness, on-line continuous monitoring), and *versatility* (new working principles for novel-targeted analytes) have been widely recognized.[9] It is not surprising that commercial analyzers based on bare-fiber sensors and near-IR absorption by the O–H oscillators are already in the market.[10] Major drawbacks of the latter optical method are the lack of specificity, since most of the organic solvents and water show absorption bands in that region, and its low sensitivity due to the intrinsically small absorption coefficients and the necessary photon detectors at those wavelengths.

Passive nonselective fiber-optic sensors for liquid samples, based on determination of refractive index changes as a function of the alcohol content using either surface plasmon resonance[11] or the intensity of the associated evanescent wave,[12] have been reported as well. More recently, however, absorbance- or luminescence-based guided light sensors incorporating an *active* sensitive terminal have been developed for monitoring lower alcohols in gas or condensed phases. Thus, Seiler et al. have described selective membranes for ethanol/water optical sens-

† Laboratory of Applied Photochemistry, Department of Organic Chemistry.
‡ Department of Analytical Chemistry.

(1) Diehl, J. W.; Finkbeiner, J. W.; DiSanzo, F. P. *Anal. Chem.* **1992,** *64,* 3202–3205.
(2) *1989 Annual Book of ASTM Standards, Section 5: Petroleum Products, Lubricants, and Fossil Fuels*; Storer, R. A., Ed.; American Society for Testing and Materials: Philadelphia, PA, 1989; pp 631–634.
(3) Agarwal, V. K. *Analyst* **1988,** *113,* 907–909.
(4) Orlando, R.; Munson, B. *Anal. Chem.* **1986,** *58,* 2788–2791.
(5) Zinbo, M. *Anal. Chem.* **1984,** *56,* 244–247.
(6) Feldman, N.; Panzer, J. U.S. Pat. US 4608345, 1986.
(7) Battiste, D. R.; Fry, S. E.; White, F. T.; Scoggins, M. W.; McWilliams, T. B. *Anal. Chem.* **1981,** *53,* 1096–1099.
(8) Renzoni, G. E.; Shankland, E. G.; Gaines, J. A.; Callis, J. B. *Anal. Chem.* **1985,** *57,* 2864–2867.
(9) *Fiber-Optic Chemical Sensors and Biosensors*; Wolfbeis, O. S., Ed.; CRC Press: Boca Raton, FL, 1991; Vols. 1 and 2.
(10) For example: the UOP-Guided Wave (El Dorado Hills, CA) GW-260 spectrometer and Zeiss (Oberkochen, RFA) MCS-240, Polytech (Waldbronn, RFA) X-dap-01-IR, or Alfa-Laval Bran+Luebbe (Norderstedt, Denmark) fiber-optic analyzers.
(11) Matsubara, K.; Kawata, S.; Minami, S. *Appl. Opt.* **1988,** *27,* 1160–1164.
(12) Japanese Pat. J02236144, J02236145, and J02236146 (Hitachi), 1990.

0003-2700/95/0367-2231$9.00/0 © 1995 American Chemical Society

Table 1. Molecular Engineering of Luminescence Indicators for Alcohol Monitoring with a Fiber-Optic Sensor

aim	required or desired feature
absorption in the visible	polyaromatic ring system + auxochromes
luminescence	polyaromatic system
large Stokes shift	adiabatic photoprocess
sensitivity to polarity changes	TICT[a] excited state
high sensitivity	large emission quantum yield ($\Phi_{em} \rightarrow 1$)
no oxygen interference	shortest emission lifetimes (fluorescence)
photostability	robust molecular structure
covalent attachment to solid support	proper functional group

[a] TICT, twisted intramolecular charge transfer.

ing,[13] which incorporate lipophilic derivatives of (trifluoromethyl)-acetophenone as absorbance probes. Chemical optosensors based on the reversible decolorization of either blue thermal printer paper[14] or triphenylmethane dyes[15,16] have also been reported. Both systems are able to respond to most organic solvent vapors (including ethanol and methanol), via reflectance changes of the sensitive layer in the presence of such analytes.

A fluorescent fiber-optic sensor for the analysis of lipophilic species (almost every organic solvent including alcohols) is described by Thompson et al.[17] Their device uses a lipidic layer with an immobilized fluorophore, the emission of which varies in response to a phase transition in such layer promoted by dissolution of the analytes. On-line determination of low amounts of *water* in ethanol, based on an electrostatically immobilized fluorescent ketocyanine, has also been reported recently.[18] However, the latter device cannot be applied to monitor alcohols in nonhydroxylic solvents since the emission quantum yields of the probe are high in both media. If selectivity to ethanol is strictly required, enzymatic luminescence biosensors incorporating alcohol oxidase or alcohol dehydrogenase are the devices of choice.[19–21]

With these antecedents in mind and given the underlined importance of alcohol monitoring in process control, we set out to develop an optical fiber sensor able to respond to low molecular weight hydroxylic compounds in organic solvents or vapor phase. Given the intrinsically superior sensitivity of *luminescence* vs absorption optical measurements, the molecular engineering of novel indicators is summarized in Table 1. Excitation with visible light, strong luminescence, and a large Stokes shift between absorption and emission simplifies operation with fiber-optic devices. Nanosecond (or subnanosecond) fluorescence lifetimes ensure the absence of cross-sensitivity to oxygen, an ubiquitous

Chart 1

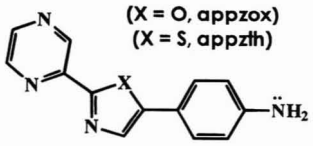

interferent present in gas samples and highly soluble in organic solvents. Covalent tethering of the indicator to a polymer support prevents leaching of the sensitive terminal and prolongs its operational lifetime compared to physical entrapment, adsorption, or electrostatic immobilization.

A screening of the literature drew our attention toward polyaromatic-substituted 1,3-oxazoles and -thiazoles.[22] Such compounds have been extensively used as scintillation counters and, more recently, as laser dyes due to their high fluorescence quantum yields, extremely fast emission decay, low photochemical fatigue, and structural tunability.[23] On the other hand, Rettig has discussed recently[24] the potential of molecules whose initially formed excited states undergo an adiabatic photoreaction as indicators of microviscosity, acidity, or polarity changes. The most important probes of the latter type are those displaying twisted intramolecular charge-transfer (TICT) excited states (see Results and Discussion).

In this way, based upon our experience in the preparation of tailored azine-substituted 1,3-azoles,[25] we describe in this paper the spectroscopic and photophysical features of two novel indicators, abbreviated appzox and appzth (Chart 1), for alcohol monitoring in nonhydroxilic media.[26] The covalent immobilization of appzth to an styrene–divinylbenzene support, and the performance of a fiber-optic fluorescent sensor constructed thereof, are reported as well. Since lower alcohols are frequently added to gasolines and fuels as octane boosters, we describe finally the application of the fabricated optical sensor to continuous monitoring of the concentration of different alcohols in fortified gasoline samples. Obviously, the possible field applications of the reported device are not limited to such examples but extend to many different nonhydroxylic liquid or gaseous media.

EXPERIMENTAL SECTION

Chemicals. The synthesis and structural characterization of the new dyes, 5-(4-aminophenyl)-2-(2-pyrazinyl)-1,3-oxazole (appzox) and 5-(4-aminophenyl)-2-(2-pyrazinyl)-1,3-thiazole (appzth), have been reported elsewhere.[27] They have been prepared by procedures similar to that for their unsubstituted analogues.[28] All the solvents used were spectroscopical grade from Aldrich (Milwaukee, WI), Merck (Darmstadt, Germany), or Scharlau

(13) Seiler, K.; Wang, K.; Kuratli, M.; Simon, W. *Anal. Chim. Acta* **1991**, *244*, 151–160.
(14) Posch, H. E.; Wolfbeis, O. S.; Pusterhoffer, J. *Talanta* **1988**, *35*, 89–94.
(15) Dickert, F. L.; Lehmann, E. H.; Scheiner, S. K.; Kimmel, H.; Mages, G. R. *Anal. Chem.* **1988**, *60*, 1377–1380.
(16) Dickert, F. L.; Scheiner, S. K.; Mages, G. R.; Kimmel, H. *Anal. Chem.* **1989**, *61*, 2306–2309.
(17) Thompson, R. B.; Yager, P.; Burgess, L. W.; Merlo, S. World Pat. Appl. WO9100510, 1991.
(18) Kessler, M. A.; Gailer, J. G.; Wolfbeis, O. S. *Sens. Actuators B* **1991**, *3*, 267–272.
(19) Völkl, K.-P.; Opitz, N.; Lübbers, D. W. *Fresenius Z. Anal. Chem.* **1980**, *301*, 162–163.
(20) Walters, B. S.; Nielsen, T. J.; Arnold, M. A. *Talanta* **1988**, *35*, 151–155.
(21) Xie, X.; Suleiman, A. A.; Guilbault, G. G.; Yang, Z.; Sun, Z. *Anal. Chim. Acta* **1992**, *266*, 325–329.
(22) Krasovitskii, B. M.; Bolotin, B. M. *Organic Luminescent Materials*; VCH: Weinheim, Germany, 1988; pp 67–93.
(23) Fletcher, A. N.; Henry, R. A.; Pietrak, M. E.; Bliss, D. E.; Hall, J. H. *Appl. Phys. B* **1987**, *43*, 155–160.
(24) Rettig, W. In *Fluorescence Spectroscopy: New Methods and Applications*; Wolfbeis, O. S., Ed.; Springer-Verlag: Berlin, Germany, 1993; pp 31–47.
(25) Orellana, G.; Moreno-Bondi, M. C.; Segovia, E.; Marazuela, M. D. *Anal. Chem.* **1992**, *64*, 2210–2215, and references therein.
(26) Orellana, G.; Moreno-Bondi, M. C.; de Dios, C.; García-Martínez, A. A.; Gómez-Carneros, A. M. Span. Pat. Appl. 9300938, 1993.
(27) de Dios, C. Ph.D. Thesis, Universidad Complutense de Madrid, Madrid, Spain, 1994.
(28) Orellana, G.; Alvarez-Ibarra, C.; Quiroga, M. L. *Bull. Soc. Chim. Belge* **1988**, *97*, 731–741.

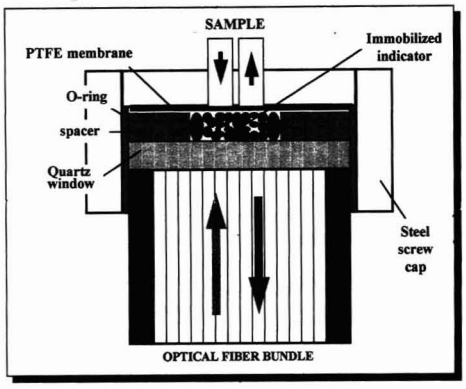

Figure 1. Custom-made flow-through cell set up used for fiber-optic measurements of lower alcohols in liquid or gas phase. The drawing has been made to approximate scale; the exact dimensions are given in the Experimental Section.

(Barcelona, Spain). Leaded and unleaded gasoline samples were kindly provided by CLH (Madrid, Spain). **WARNING**: *most of the organic solvents used are flammable and/or toxic; therefore, a well-ventilated hood must be used in the preparation of mixtures and handling of all the solutions.* The chloromethylated styrene–divinylbenzene copolymer ("Merrifield's polymer"; 2% cross-linked, 200–400 mesh, ~1 mmol of Cl/g) was purchased from Merck.

Instrumentation. Absorption spectra were recorded with a Perkin-Elmer Lambda-3 spectrophotometer (Überlingen, Germany) linked to a Perkin-Elmer 3600 data station. Emission spectra were obtained either with a Perkin-Elmer MPF-44A or a LS-50 (interfaced to an IBM PS/55SX computer for instrument control and data processing) spectrofluorometer. Emission lifetimes have been measured by the time-correlated single photon counting (TC-SPC) technique with an Edinburgh Instruments FL-900 spectrometer (Edinburgh, UK), using a hyperbaric hydrogen- or nitrogen-filled discharge lamp and a Peltier-cooled (to −29 °C) Hammamatsu R-928 red-sensitive photomultiplier. Spectrometer and multichannel analyzer (MCA) control, data collection (1024 channels), and analysis were carried out with a Comelta COP-386SX computer (Madrid, Spain). The resulting decay traces were deconvoluted and fitted to a single or double exponential using the nonlinear Marquardt algorithm contained in the Edinburg Instruments original software package. X-ray fluorescence analysis was performed with a Philips PW-2400 spectrometer.

Fiber-optic sensing experiments were carried out with a home-made stainless steel flow-through cell (Figure 1). In this cell, a poly(tetrafluorethylene) (PTFE) membrane (Millipore, Bedford, MA, FHUP 04700; 0.5-μm pore size, 175-μm thickness) separates the alcohol-sensitive fluorescent polymer layer (containing the covalently immobilized appzth dye, vide infra) from the liquid samples. A randomly distributed bifurcated bundle (25 + 25 glass fibers, 6.5-mm diameter at the common end) from Dolan-Jenner (Woburn, MA), connected to the Perkin-Elmer LS-50 spectrofluorometer via the P-E fiber-optic accessory, carries the light to and from the flow-through cell. The common end of the fiber bundle is separated from the sensitive layer by a 2-mm-thick optical glass, and the measuring chamber is made leak-proof with a 5-mm-i.d. viton O-ring. The alcohol/solvent mixtures and gasolines were continuously circulated with a Gilson Minipuls-2 peristaltic pump (Villiers-le-Bel, France). Temperature control (±0.5 °C) was provided by a Haake D8-GH circulator (Karlsruhe, Germany).

Scheme 1

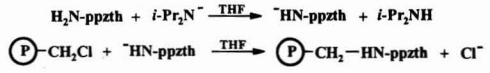

Dye Immobilization. Covalent attachment of appzth to the Merrifield's polymer was performed via the aromatic amino group of the dye. A weighted amount of appzth (6 mg, 24 μmol) was dissolved under dry argon in 1 mL of anhydrous tetrahydrofuran (THF) contained in a round-bottomed flask fitted with a rubber septum. Lithium diisopropylamide (~50 μmol) was generated under argon in a similar container, by slowly adding with a syringe (Hamilton, gas-tight) 50 μmol of butyllithium (Aldrich, 1.6 M solution in hexane; **WARNING: PYROPHORIC**) to a stirred solution of dried diisopropylamine (50 μmol, Aldrich) in 1 mL of anhydrous THF. Under argon pressure, the diisopropylamide solution was added dropwise to the appzth solution via a stainless-steel 16-gauge cannula, and the red-brown mixture was stirred 30 min. The same cannula was used to slowly transfer the mixture under argon to a round-bottomed flask, equipped with a rubber septum and a 40-cm Allihn condenser, containing 200 mg of the Merrifield's resin (previously dried at 0.05 Torr for 12 h) suspended in 3 mL of anhydrous THF. The resulting slurry was heated at reflux under argon for 18 h. After the reaction mixture was allowed to reach room temperature, and the flask was kept open for an additional hour at ambient atmosphere, the solvent was removed by filtration through a fritted-glass disk. Finally, the dyed polymer beads were carefully washed (first at room temperature and then at reflux) succesively with THF, mixtures of THF/toluene, toluene, and acetone to remove any unreacted portion of appzth. The sequence of chemical processes that lead to the covalently bound appzth is summarized as shown in Scheme 1.

RESULTS AND DISCUSSION

Solution Behavior of the Probes. The extended unsaturated ring system of appzox and appzth (Chart 1) produces a strong *absorption* in the visible region of their electronic spectra (Table 2). This feature is highly desirable when engineering luminescent probes for optical sensing since it allows for the use of cheaper excitation sources (e.g., tungsten bulbs or light-emitting diodes), and glass or plastic light guides in the construction of fiber-optic devices. The superior aromaticity of the thiazole moiety shifts the $\pi \rightarrow \pi^*$ band to the red at the expense of a lower absorption coefficient compared to the oxazole-containing probe. At it might be expected for a $\pi \rightarrow \pi^*$ transition (vide infra), the absorption of the new molecules undergoes a batho- and hypochromic shift upon an increase in the polarity of the solvent (in going from *n*-hexane to ethanol, Table 2).

The novel heterocyclic dyes have turned out to be highly luminescent as well (Table 2). Their *emission* quantum yields approach or exceed 0.8 in some solvents, making them very attractive for optical fiber sensing in terms of amount of immobilized compound required in the sensitive layer and ease of photon detection. Effects similar to those of the absorption bands are observed—even to the bare eye—in the fluorescence maxima and quantum yields upon changing the polarity of the solvent

Table 2. Spectroscopic Data and Emission Lifetimes of the Fluorescent Dyes in Solution[a]

	absorption data	emission data			
solvent	λ_{max}/nm (ϵ_{max}/M^{-1} cm^{-1})[b]	λ_{max}/nm[c]	$W_{1/2}$/nm[d]	Φ[e]	τ/ns (%)[f]
		appzox			
n-hexane	357 (26 200)	414	60	0.64	1.4 (100)
toluene	365 (22 000)	460	75	0.77	2.2 (100)
chloroform	369 (18 500)	510	102	0.26	2.9 (100)
ethanol	374 (17 600)	530, 580	131, 135	0.0045	0.3 (68), 2.7 (32)[g] 0.3 (99), 2.9 (1)[h]
		appzth			
n-hexane	367 (16 800)	443	69	0.77	1.4 (100)
toluene	380 (13 100)	471	72	0.82	2.4 (100)
chloroform	385 (11 300)	532	96	0.088	3.4 (100)
ethanol	387 (10 400)	510, 590	111, 119	0.0094	0.3 (11), 3.0 (89)[i] 0.4 (85), 3.5 (15)[j]

[a] Air-equilibrated solutions at 25 ± 1 °C. [b] λ ± 1 nm; ϵ ± 3%. [c] λ ± 1 nm, except for the widest signals where the estimated error is ±2 nm; uncorrected for instrumental response. [d] Full width at medium height; band deconvolution of overlapping emission bands has been used. [e] Emission quantum yields ±5%. [f] Excitation at the absorption maxima, except otherwise indicated; emission lifetimes ±3% for single-exponential decays and ±10% for double-exponential fittings; in parentheses, relative contribution of each component calculated by the following expression: $\% = A_m\tau_m/(A_m\tau_m + A_n\tau_n)$; 100% indicates a single-exponential decay. [g] λ_{exc} = 337 nm. [h] λ_{exc} = 381 nm. [i] λ_{exc} = 325 nm. [j] λ_{exc} = 350 nm.

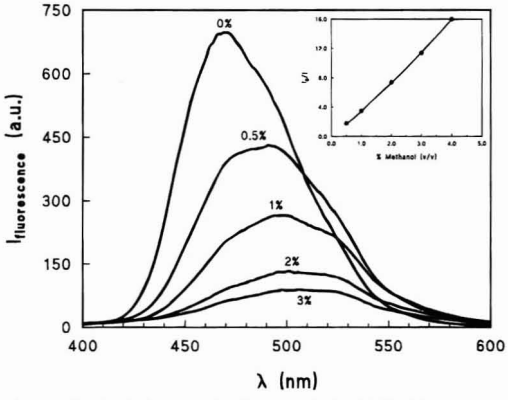

Figure 2. Emission spectra (uncorrected) of 5.0 μM appzth in toluene/methanol mixtures (percent by volume). Excitation wavelength, 387 nm; no variation in the absorption spectrum of appzth in toluene is detected within the 0–4% alcohol range. Inset: relative fluorescence of the indicator as a function of methanol concentration in toluene.

(Table 2): a pronounced red shift (up to 166 nm) and a dramatic decrease of the emission intensity have been measured when the dyes are dissolved in ethanol instead of apolar solvents. Even the addition of minute amounts of alcohol to a hydrocarbon solution of any of the dyes is readily detected by emission spectroscopy (Figure 2). Two fluorescence maxima with a larger bandwidth are always observed in pure lower alcohols. These findings, together with the wider absorption bands in such solvents, may be rationalized by assuming a strong interaction of the polar hydrogen-bonding alcohols with the probe molecules, via the unshared electron pairs of the latter (Chart 1). The interaction yields several (probably more than two) solvent-solute adducts of different stoichiometries, which will have slightly different absorption and emission properties unresolvable in full under the experimental conditions tested so far. Further confirmation of these arguments is provided by the observation of gradual changes in the relative intensity of the two fluorescence maxima in pure ethanol upon varying the excitation wavelength within the absorption band. Similar reasons have been invoked previously in order to explain the changes in the electronic spectra of certain aromatic amines such as *p*-aminobenzophenone[29] or *p*-dimethylaminobenzonitrile[30] when dissolved in lower alcohols.

The fluorescence of appzox and appzth has also been characterized by time-resolved detection. The short emission lifetimes of the probes (1–4 ns, Table 2) confirm the highly allowed nature of the radiative deactivation pathway of their singlet excited state. The deactivation rates decrease with the polarity of the solvent; however, the emission lifetime in ethanol sharply drops to a value close to the time resolution (~300 ps) of our TC-SPC fluorescence spectrometer. As expected from the solvent/dye interactions in pure ethanol discussed above (taking into account the absorption and steady-state emission data), the fluorescence decay measured in such solvent could only be fitted to a biexponential curve (Table 2), with a longer lifetime similar to that observed in polar aprotic solvents in addition to the already mentioned very short decay. The contribution of the latter to the overall decay profile increases as the excitation wavelength is moved to the red, which occurs probably as we match the absorption maxima of the most tightly associated dye–solvent adducts.

Response Mechanism. The fluorescence red shift of appzox and appzth as the polarity of the solvent increases may be justified if their π–π^* excited state reached upon light absorption is much more polar than their ground state. It is well established that different types of aromatic molecules, with both electron-donating and electron-releasing groups in conjugated positions (the prototype of which is *p*-(dimethylamino)benzonitrile), display an extremely fast (reached within a few picoseconds after light absorption) equilibrium between the initially produced planar locally excited state and the so-called TICT excited state.[31] The former is responsible for the emission wavelength in inert solvents, but in strongly solvating media and if there is no restriction to rotation around the C–N bond between the amino group and the benzene ring, an intramolecular charge transfer occurs to yield a twisted highly polar excited state (dipole moments up to 16 D have been calculated).[30] The stabilized TICT state originates the significantly red-shifted emission band and decays to the ground state via nonradiative pathways ("energy-gap" rule). A perpendicular arrangement between the donor and acceptor moieties of the indicator molecule in the TICT excited state prevents an efficient overlap between their π orbitals. This fact converts the highly allowed backward transition to the ground state into a symmetry-forbidden one, since it requires electron exchange between those orbitals centered in the two parts of the molecule (Scheme 2),[24] and would explain the dramatically lower fluorescence *quantum yield* and enhanced *lifetime* of appzox and appzth observed in alcohol (Table 2).

Our synthesized fluorescent dyes appzox and appzth carry both electron-donor and electron-acceptor moieties (the amino group and the π-deficient pyrazine ring, respectively) in conjugated positions in their molecules, linked by a suitable heteroaryl system. Therefore, it is reasonable to assume that their excited states may

(29) Hoshino, M.; Koizumi, M. *Bull. Chem. Soc. Jpn.* **1972**, *45*, 3075–3077.
(30) Wang, Y.; Eisenthal, K. B. *J. Chem. Phys.* **1982**, *77*, 6076–6082.
(31) Retig, W. *Angew. Chem., Int. Ed. Eng.* **1986**, *25*, 971–988.

Scheme 2

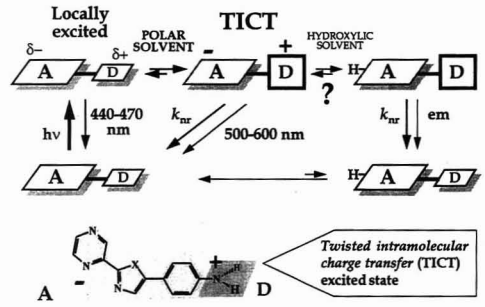

have TICT character in polar solvents. The presence of increasing amounts of lower alcohols in apolar hydrocarbons, capable of associating tightly to the polar groups of the dyes, will displace the excited-state equilibrium toward the low-fluorescent TICT form. Nevertheless, in the case of solvation by hydroxylic molecules, an intramolecular proton transfer to the TICT state might be also the cause of excited-state radiationless deactivation, via the protonated TICT form, provided the photoexcited luminophore is basic enough to react with the solvent.[32] The pyrazine moiety of the dyes would be in the present case the group responsible for the TICT excited-state acid/base behavior. An eventual proton transfer to the TICT state would also explain the features of the luminescence observed in alcohols.

The working principle of the sensing species is depicted in Scheme 2 (A, acceptor moiety, 5-aryl-2-(2-pyrazinyl)-1,3-azole; D, donor group, NH_2; wavelength data for appzth).

This mechanism explains the dual emission of both indicators observed as partially overlapping bands in hydrocarbon/alcohol mixtures (Figure 2). The working principle also explains why the measured effect on their fluorescence spectra of the alcohol concentration diminishes as the hydrocarbon chain length or branching of the latter increases (e.g., the relative fluorescence, I_0/I, of appzth for a 2% (v/v) alcohol concentration in toluene is 7.3, 3.5, 2.0, and 1.8 for methanol, ethanol, 1-butanol, and isobutyl alcohol, respectively).

Dye Immobilization. In order to fabricate a fiber-optic sensor to monitor lower alcohols in nonhydroxylic solvents or in the gas phase, it was essential to immobilize the fluorescent dye in a suitable polymer matrix to be attached to the sensitive tip. Any prospective solid support had to be compatible with the organic solvents which would constitute the analytical samples; therefore, the organic polymers poly(ethylene), poly(tetrafluoroethylene), and poly(styrene–divinylbenzene) (all as fine powders or beads for IR spectroscopy), as well as one inorganic matrix (silica gel) were initially selected. The appzth molecule was also chosen for all the subsequent fiber-optic sensor studies since its absorption and emission wavelengths appear more to the red than those of appzox, and the former shows a larger emission quantum yield. Very small amounts of the fluorescent dye were pressed into the organic polymer powders by using IR spectroscopy sample preparation dies, both with and without heating, to yield thin pellets which were tested by using the fiber-optic flow cell (see Experimental Section). Alternatively, hydrocarbon solutions of appzth were slowly evaporated in the presence of the fine-particle-sized polymer, and the dyed beads placed in the measuring chamber. In every case, the fluorescent probe was completely washed out of the polymer support after pumping the organic solvent for some time, rendering it impossible to construct a usable sensing head.

(32) Kosower, E. M.; Dodiuk, H. *J. Am. Chem. Soc.* **1976**, *98*, 924–929.

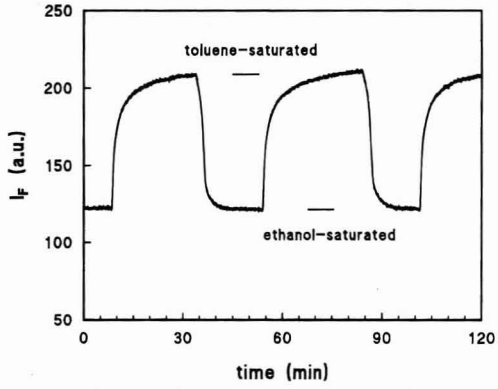

Figure 3. Response of the fiber-optic sensor fabricated with appzth immobilized onto silica gel beads, in the presence of toluene- or ethanol-saturated nitrogen (~200 mL min^{-1}) at 25 °C (λ_{exc} = 385 nm; λ_{em} = 491 nm).

Deposition of appzth onto silica gel yielded a sensitive layer also subject to continuous leaching when exposed to solvents; however, the presence of ethanol (or methanol) in the *vapor* phase can be monitored reversibly with such an indicator layer (Figure 3), although the resulting optical sensor displays a rather slow response. It is clear, at this point, that a *covalent* tethering of the appzth to a hydrophobic support was required in order to overcome the problems associated with adsorptive immobilization of the indicators for optical fiber sensing in *liquid* media.

Given the almost complete absence of reactive functional groups in the appzth molecule, the only possibility was to utilize its aromatic amino group without compromising the unshared electron pair of the nitrogen atom (required for the sensing properties of the dye, vide supra). Therefore, the replacement of an *alkyl* group for a hydrogen atom of the amino group was deemed as appropriate for covalent binding of the intact probe to a polymer support. The weak electron-releasing properties of alkyl chains would be an added bonus, since a new N substituent of this type would increase the donor character of the amino group and would favor thereby the formation of the TICT excited state.

Because of the poor nucleophylic reactivity of an aromatic amino group, carbon–nitrogen bond formation was expected to succeed only by using the amide anion (a more powerful nucleophile) of appzth and a fairly reactive electrophilic alkyl center. The latter requirement is met by the chloromethylated styrene–divinylbenzene copolymer (commercially available as Merrifield's resin), which was allowed to react with the conjugated base of appzth (formed upon hydrogen abstraction from its amino group by the strongly basic diisopropylamide anion, $pK_a > 40$). In this way, a highly fluorescent support was obtained, from which no leaching of the immobilized dye could be detected even after extensive washing with boiling THF, toluene, chloroform, or acetone. The amount of immobilized appzth (44 ± 13 μmol/g of support, which corresponds to a chemical yield of ~20%) was

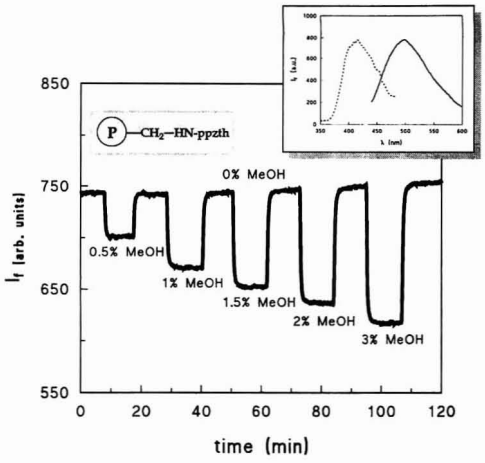

Figure 4. Response function, response time, and reversibility of the fiber-optic sensor containing covalently bound appzth (see Experimental Section), upon step changes of the methanol concentration (% by volume) in petroleum naphtha at 25 °C (λ_{exc} = 414 nm; λ_{em} = 500 nm). Inset: Uncorrected excitation and emission spectra of appzth covalently immobilized onto the styrene–divinylbenzene copolymer (see Experimental Section).

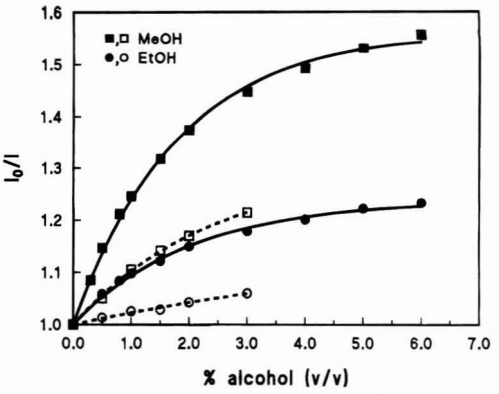

Figure 5. Dose/response plots in petroleum naphtha (open symbols; λ_{exc} = 414 nm; λ_{em} = 500 nm) and regular leaded gasoline (solid symbols; λ_{exc} = 414 nm; λ_{em} = 471 nm) at 25 °C, obtained with the optical fiber sensor containing covalently attached appzth. Curves are the best fits, using a nonlinear Marquardt algorithm, to an exponential function of the type $I_0/I = 1 + a(1-e^{-bx\%alcohol})$ (eq 1, see text). The maximum concentration attainable in each case is limited by the solubility of the alcohol in the organic phase.

evaluated by X-ray fluorescence spectroscopy from the sulfur content of the solid sample.

Fabrication and Performance of the Alcohol Sensor. The fluorescent dye has been successfully applied to the construction of a fiber-optic device for monitoring lower alcohols in gasoline samples. The sensing head is depicted in Figure 1. The polystyrene beads with the covalently immobilized appzth are separated from the liquid samples by a poly(tetrafluorethylene) membrane, which imparts mechanical stability to the reagent phase and protects it from solid impurities present in the fuels. The measuring solutions were pumped successively until a stable fluorescence signal had been attained for each of them (Figure 4).

A typical emission spectrum of the fiber-optic sensing layer when petroleum naphtha is pumped through the cell is shown in Figure 4 (inset). The maximum of the wide fluorescence band (~495 nm) is considerably red-shifted compared to that observed for the appzth in aliphatic hydrocarbon solution (Table 2). This fact may be attributed to the N alkylation of the aromatic amino group of the dye brought about by the immobilization procedure, which stabilizes further the charge-transfer excited state with respect to the free indicator molecule. Local effects of the polymer support might also play an important role in determining the spectroscopic features of the immobilized appzth. A similar emission spectrum was observed in *n*-hexane or other aliphatic hydrocarbons. The solution behavior of the dye is not affected by its covalent binding to the organic support: in the presence of small amounts of low molecular weight alcohols (0.2–6% (v/v), limited by their solubility in the selected medium) the fluorescence signal from the sensor layer decreases and the emission maximum moves to the red. Nevertheless, the extent of spectral variation observed for the *immobilized* appzth upon addition of small amounts of methanol or ethanol to a hydrocarbon solution is smaller than that shown by the free dye. This fact may be attributed to the effect of the polymer network on the formation of the TICT excited state of the indicator molecule (vide supra). A representative plot displaying the response function, response time, and reversibility of the fiber-optic sensor fabricated with appzth is shown in Figure 4. The corresponding dose/response curves for methanol and ethanol in petroleum naphtha are depicted in Figure 5. These curves turned out to be superimposable on those obtained in *n*-hexane.

The differences between the calibration curve obtained with the sensor (e.g., for methanol, Figure 5) and that measured for the indicator in homogeneous hydrocarbon solution (e.g., Figure 2, inset) might be rationalized if we assume that, after covalent attachment of the appzth to the styrene/divinyl polymer network, not all the indicator molecules can be reached by the alcohol within the excited-state lifetime of the former. Therefore, a constant fluorescent emission would contribute to every point of the dose/response curve. When a certain alcohol concentration is reached for which all the accesible molecules of the indicator are able to form a TICT excited state, no further decrease of the fluorescence is obtained and a leveling-out of the curve results.

To the contrary, the upward bending of the I_0/I vs methanol concentration curve observed in homogenous solution may be justified if ground-state alcohol–indicator adducts are formed upon increasing the methanol concentration.[30] Such an argument agrees with the absorption, emission, and TC-SPC results for the novel dyes discussed above.

A final goal of the fluorescent optical sensor described so far was its application to on-line monitorization of changes in the alcohol content of gasolines and other fuels in the production (blending) lines. In order to account for the matrix effect due to all the additives present in such samples, we decided to test and calibrate the fiber-optic device using alcohol-free leaded and unleaded real gasolines spiked with low molecular weight alcohols. The response function of the appzth-containing sensor head, as a function of methanol concentration in leaded regular gasoline, is similar to that depicted in Figure 4. Similar responses were obtained with other leaded and unleaded gasolines. Typical dose/response curves for methanol and ethanol in such media are

shown in Figure 5. Once again, as the alcohol percentage increases, the fluorescence from the immobilized indicator decreases and the emission maximum shifts to the red. The excitation wavelength was optimum at 414 nm, whereas the selected analytical wavelength was 471 nm. It must be pointed out that all the gasoline samples tested in this study were colored with a different fluorescent dye (information not available from the supplier); nevertheless, this fact has not posed any problem in monitoring their alcohol content with the optical sensor except for a very slight variation of sensitivity.

The working range of the fiber-optic device spans from 0.2 to 6.0% *methanol* (v/v) in gasolines, which includes the amounts of alcohol accepted by the current regulations on fuel substitutive components (e.g., those of the EC[33]). The response curve (Figure 5) may be fitted to the following equation:

$$I_0/I = 1 + a(1 - e^{-b\%\text{alcohol}}) \quad (1)$$

where $a = 0.57 \pm 0.02$ (±95% confidence limit) and $b = 0.55 \pm 0.04$ ($r = 0.999$) for methanol. The detection limit of the sensor, based on 3 times the standard deviation of 10 gasoline blanks,[34] has been calculated to be 0.07% (v/v) methanol, and the quantification limit amounts to 0.24% (v/v) methanol. The relative standard deviation (rsd) of the normalized emission signal (I_0/I, $n = 10$) was 2.8, 2.4, and 3.0% for 0.5, 2.0, and 4.0% (v/v) methanol in gasoline, respectively.

The figures of merit obtained for the response to *ethanol* in gasoline of the optical fiber sensor (Figure 5) are the following: $a = 0.24 \pm 0.01$ and $b = 0.49 \pm 0.06$ ($r = 0.998$) for 0.7–6.0% (v/v) ethanol in gasoline; detection limit = 0.19%; quantification limit = 0.74%; rsd (10 measurements) = 1.9 and 1.5% for 0.5 and 2.0% (v/v) ethanol concentrations, respectively.

The fiber-optic alcohol sensor displays a response time ($t_{100\%}$) of 2 min for a step change from zero to any methanol concentration in gasoline within its working range (3–3.5 min for ethanol) and 3–4.5 min for the reverse variation under the most unfavorable conditions (4 to 0% alcohol concentration jump).

Since commercial gasolines may contain also other low molecular weight alcohols (e.g., ethanol, isopropyl, isobutyl, *sec*-butyl, or *tert*-butyl alcohols) as fuel substitutive components, in addition to the most abundant methanol, the cross-sensitivity to the presence of various amounts of interfering alcohol was tested as well. Table 3 presents the relative error of two different methanol concentration determinations (0.5 and 2% (v/v); average of three measurements). On the basis of those data, only ethanol may be regarded as an interferent[35] for methanol quantification with the appzth-based fluorescent sensor. The other tested alcohols would yield an error lower than 4% of the methanol concentration in gasoline at their usual percentages added to fuel samples (0–6% v/v). Such results are in agreement with those observed for the indicator dye in solution (vide supra). Gasolines may contain as much as 0.1% water, particularly those containing alcohol components as well. Nevertheless, using a methanol content of 3% (v/v), we have observed no effect on the sensor response after addition of 0.05 or 0.1% (v/v) water to the sampled gasolines, a level for which phase segregation already occurs. It seems that the hydrophobic nature of the indicator support and the PTFE protective membrane are able to remove this possible interference.

Table 3. Effect of Different Low Molecular Weight Alcohols Added to Gasoline on the Response to Methanol of the Fiber-Optic Fluorosensor[a]

	0.5% MeOH[b]		2.0% MeOH[b]	
alcohol[c]	MeOH/ alcohol	rel sens (%)[d]	MeOH/ alcohol	rel sens (%)[d]
ethanol	1:1	103.6	1:1	99.2
	1:10	115.2	1:2	103.8
	1:20	120.5	1:5	104.7
	1:30	121.4	1:10	107.8
	1:40	123.2	1:20	109.3
i-PrOH	1:1	100.0	1:2	99.2
	1:2	100.9	1:10	96.1
	1:10	101.8	1:20	97.7
	1:20	105.4		
	1:30	106.2		
	1:40	108.0		
i-BuOH	1:1	102.7	1:2	101.6
	1:2	103.6	1:10	97.7
	1:10	105.4	1:20	98.5
	1:20	106.2		
	1:30	107.1		
	1:40	108.9		
s-BuOH	1:1	102.8	1:2	99.2
	1:2	102.6	1:10	99.2
	1:10	102.6		
	1:20	106.0		
	1:30	108.0		
	1:40	109.8		
t-BuOH	1:1	100.0	1:1	97.7
	1:2	100.0	1:2	93.8
	1:10	100.8	1:5	90.7
	1:20	101.8	1:10	86.1
	1:40	103.0		
MTBE	1:40	99.1	1:10	100.8

[a] Alcohol-fortified leaded gasoline samples at 25 ± 1 °C. [b] Volume/volume. [c] Abbreviations: EtOH, ethanol; *i*-PrOH, isopropyl alcohol; *i*-BuOH, isobutyl alcohol; *s*-BuOH, *sec*-butyl alcohol; *t*-BuOH, *tert*-butyl alcohol; MTBE, methyl *tert*-butyl ether. [d] Relative sensitivity on the normalized fluorescence intensity I_0/I, where I_0 is the emission intensity in the absence of any alcohol (gasoline blank) and I is the sensor fluorescence in the presence of the methanol/interferent alcohol mixture.

The effect of methyl *tert*-butyl ether (MTBE) on the sensitivity of the optical device was also checked since it is a common additive to both leaded and unleaded gasolines (actually, the leaded gasoline used in most of the test experiments contained 1% by volume of MTBE). Even the presence of very high concentrations of such a fuel component does not modify the sensor response to methanol (Table 3). Cross-sensitivity to tetraethyllead was not observed either.

Finally, we have also evaluated the effect of temperature on the fluorosensor response. The experiments were carried out at 10, 25, and 40 °C by repeated exposure to gasoline samples containing 0 and 2% (v/v) methanol. The relative emission intensity increases ~5.7×10^{-3}/°C in that temperature range; at the same time, the sensor response time decreases from 6 to 1 min. Enhanced availability of the analyte to the covalently bound indicator, due to swelling of the polymer support with temperature, might account for both effects. Polymer swelling could be also the cause of the different sensitivity to methanol (and ethanol) dissolved in gasoline or petroleum naphtha (Figure 5).

(33) *Official Journal of the European Communities*; L 334/20 (12.12.85), pp 14–16.
(34) Long, L. G.; Winefordner, J. D. *Anal. Chem.* **1983**, *55*, 713A–724A.
(35) Hems, R. V.; Kirkbright, G. F.; West, T. S. *Talanta* **1969**, *7*, 789–796.

CONCLUSIONS

A new method for fluorescence optosensing of low molecular weight hydroxylic compounds in nonpolar media has been established. The working principle is based on novel heterocyclic strongly fluorescent indicators which are able to form a weakly emitting twisted intramolecular charge-transfer excited state in the presence of small amounts of lower alcohols. A fiber-optic sensor has been fabricated by covalent tethering of the dye to a styrene–divinylbenzene copolymer in order to monitor the concentration of methanol or ethanol in leaded or unleaded commercial gasolines. The advantages of such a principle over existing optical devices for those analytes include (a) excitation and emission wavelengths in the visible region of the electromagnetic spectrum, (b) a substantial Stokes shift, which allows for an easy separation of the luminescence signal from the scattered excitation light, (c) enhanced sensitivity due to the large variation of the fluorescence quantum yield upon addition of alcohols to a nonpolar solvent, and (d) ease of covalent immobilization of the indicator to polymeric supports bearing electrophilic functional groups.

The performance and dynamic range of the optode constructed upon that principle makes it suitable, for example, for monitoring on-line the amount of methanol (and/or ethanol) added to the hydrocarbon mixture during the blending process that leads to commercial fuels. The optical fiber sensor has recently been employed successfully to measure the degree of humidity in the atmosphere by attaching the fluorescent dye (appzth) to a cellulosic support. Further work is now in progress in order to develop this latter field. Moreover, a new familly of related azole indicators is currently being synthesized which will make it possible to immobilize them electrostatically to solid supports or covalently to polymers functionalized with nucleophilic substituents. The possiblity of alcohol monitoring in aqueous media by using ethanol-selective permeable membranes (e.g., chitosan[36]) is currently being tested as well.

ACKNOWLEDGMENT

The authors gratefully thank the Spanish government (National R+D Plan, CICYT) for financial support of sensor research (projects no. AMB92-92-C03 and PTR91-36) and the Ministry of Education and Science for a doctoral grant to C.deD. We acknowledge also Mr. Carlos Jiménez from Philips Ibérica (Madrid) for performing the X-ray fluorescence analyses, Dr. Manuel Gómez-Marín from Compañía Logística de Hidrocarburos (CLH) for his kind supply of the many different gasoline samples used in this research, Prof. J. L. Peral (UCM) for the very helpful assistance he has provided in the statistical analysis of the results, and Prof. O. S. Wolfbeis for his invaluable suggestions.

Received for review December 28, 1994. Accepted March 24, 1995.[®]

AC941242I

(36) Kurauchi, Y.; Yanai, T.; Ohga, K. *Chem. Lett.* **1991**, 1411–1412.

[®] Abstract published in *Advance ACS Abstracts,* May 15, 1995.

Anal. Chem. **1995,** *67,* 2239–2245

Characterization of 9-Aminopyrene-1,4,6-trisulfonate-Derivatized Sugars by Capillary Electrophoresis with Laser-Induced Fluorescence Detection

Ramon A. Evangelista, Ming-Sun Liu, and Fu-Tai A. Chen*,†

Advanced Technology Center, Beckman Instruments Inc., 2500 Harbor Boulevard D-20A, Fullerton, California 92634

Mono- and oligosaccharides with reducing ends were derivatized with 9-aminopyrene-1,4,6-trisulfonate (APTS) by reductive amination. The resulting adducts were characterized by capillary electrophoresis (CE) with laser-induced fluorescence (LIF) detection. The APTS-derivatized sugars have significant absorption at 488 nm (35% of its 455 nm maximum absorption), while APTS (λ_{max} = 424 nm) has only 4% of its λ_{max} absorption. When excited at 488 nm, the APTS-derivatized sugars fluoresce at a maximum wavelength of 512 nm, while APTS itself has a much weaker fluorescence with a maximum at 501 nm. By using a 488-nm argon-ion laser for excitation and a narrow band filter at 520 nm for fluorescence emission, the APTS-derivatized sugars can be selectively detected while the signal of the excess APTS reagent is drastically suppressed. The APTS-derivatized monosaccharides were readily separated in borate buffer (pH 10.2), while the oligosaccharide ladders were analyzed using either an acidic phosphate buffer (pH 2.2) or the alkaline borate buffer for separation. The present APTS derivatization chemistry is capable of converting 2 pmol of sugar analyte to the fluorescent derivative detectable by the present CE/LIF procedure. The use of CE/LIF as a tool for the investigation of the specificity of enzyme action of glycosidases using an end-labeled oligosaccharide substrate is also demonstrated.

The analysis of carbohydrates is impeded by their lack of outstanding structural features. Traditional methods of carbohydrate analysis rely on chromatography and electrophoresis techniques.[1–3] Since most sugars do not contain chromophoric moieties, the methods of detection of sugars are thus limited. Although sugars do absorb at 185 nm,[4] the detection sensitivity is poor due to their low molar absorptivities. Amperometric detection is the preferred method for analysis for some sugar samples, but the method suffers from its nonspecific response to not only to carbohydrates but also to amines and alcohols.[5] Despite the above disadvantages in detection specificity, amperometric detection for sugars in CE has been reported to yield excellent detection sensitivity with concentrations in the micromolar region.[6]

Electrophoretic separation of carbohydrates may be achieved by using an appropriate derivatization agent. Reductive amination of sugars with 2-aminopyridine (AP), first proposed by Hase and et al.,[7] was employed by Honda et al.[8] for high resolution CE separation of mono- and oligosaccharides. Since pyridylamino sugar derivatives do not carry charge, complexation of vicinal hydroxyl groups with borate at high pH (>10) or protonation (phosphate buffer of pH 2.5 or less) of the amino moiety in the AP-sugars was utilized for electrophoretic separations.[8] A two-dimensional CE method based on a two-buffer system has been employed for the characterization of sugars.[8] Jackson[9] demonstrated that oligosaccharide ladders derivatized by reductive amination with 8-aminonaphthalene-1,3,6-trisulfonic acid (ANTS) could be resolved by polyacrylamide gel electrophoresis and detected by a CCD fluorescence imaging device.[9] Chiesa and Horvath[10] and Stefansson and Novotny[11] did exhaustive characterization of ANTS and 5-aminonaphthalene-2-sulfonate (ANA) derivatized oligosaccharides by CE technique. Liu et al.[12] aminated the reducing sugars and then derivatized them with 3-(4-carboxybenzoyl)-2-quinolinecarboxaldehyde (CBQCA) for fluorescence detection. Excellent resolution of the resulting CBQCA-derivatized sugars was demonstrated in a gel-filled capillary electrophoresis system. Schwaiger et al.[13] showed that both reducing sugars and ketohexoses, such as fructose and sorbose, can be derivatized with 4-aminobenzonitrile (ABN).

In this paper, we describe the analysis of reducing sugars and fructose, a ketohexose, by CE/LIF using a derivatization reagent, 9-aminopyrene-1,4,6-trisulfonate (APTS). Although APTS is structurally similar to ANTS, it has several distinct advantages over ANTS and other currently used reagents for the detection of sugars such as ANA, ABN, and AP. The APTS-derivatized sugars

* Corresponding author: E-mail address, afchen@ccgate.dp.beckman.com.

† This paper is dedicated to Professor Yau-Tang Lin, National Taiwan University, on his Anniversary Memorial Symposium, April 15, 1995 in Taipei, Taiwan.

(1) Hardy, M. R.; Townsend, R. R.; Lee, Y. C. *Methods Enzymol.* **1989**, *179*, 65–76.
(2) Basa, L. J.; Spellman, M. W. *J. Chromatogr.* **1990**, *499*, 205–211.
(3) Yamashida, K.; Mizuochi, T.; Kobata, A. *Methods Enzymol.* **1982**, *83*, 105–126.
(4) Hoffstetter-Kuhn, S.; Paulus, A.; Gassmann, E.; Widmer, H. M. *Anal. Chem.* **1991**, *63*, 1541–1547.
(5) Lee, Y. C. *Anal. Biochem.* **1990**, *189*, 151–62.
(6) Colon, L. A.; Dadoo, R.; Zare, R. N. *Anal. Chem.* **1993**, *65*, 476–481.
(7) Hase, S.; Hara, S.; Matsushima, Y. *J. Biochem.* **1979**, *85*, 217–777.
(8) Suzuki, S.; Kakehi, K.; Honda, S. *Anal. Biochem.* **1992**, *205*, 227–236.
(9) Jackson, P. *Biochem. J.* **1990**, *270*, 705–713.
(10) Chiesa, C.; Horvath, C. *J. Chromatogr.* **1993**, *645*, 337–352.
(11) Stefansson, M.; Novotny, M. *Anal. Chem.* **1994**, *66*, 1134–1140.
(12) Liu, J.; Shirota, O.; Novotny, M. *Anal. Chem.* **1992**, *63*, 64–78.
(13) Schwaiger, H.; Oefner, P. J.; Huber, C.; Grill, E.; Bonn, G. K. *Electrophoresis* **1994**, *15*, 941–52.

0003-2700/95/0367-2239$9.00/0 © 1995 American Chemical Society

have substantially higher molar absorptivity and quantum efficiency than ANTS-, ANA-, ABN-, and AP-saccharides. The APTS-derivatized sugars have λ_{max} at 455 nm with a significant amount of absorption at 488 nm, while APTS itself has λ_{max} at 424 nm with a relatively low absorptivity at 488 nm. When excited with a 488-nm argon-ion laser, APTS–sugar derivatives fluoresce with substantially higher intensity (em λ_{max} = 512 nm) than the APTS emission (λ_{max} = 501 nm). Using a selective emission filter, preferential detection of the APTS sugar derivatives can be achieved. Thus, the excess derivatization reagent does not produce significant interference with the signals from the sugar analytes. The use of the 488-nm argon-ion laser for excitation is more advantageous than the 325-nm He/Cd laser, which has relatively short lifetime and considerable intensity fluctuation due to the sensitivity of its output to temperature variations.[14] Excitation at 488 nm is also less likely to produce interferences due to the endogenous fluorescent compounds in biological fluids when compared with the 325-nm He/Cd laser.

While our work for this paper was in progress, a report on the use of the APTS for derivatization of sugars was published, but the experimental results on the analysis of APTS-sugars were not reported.[15]

EXPERIMENTAL SECTION

Reagents. 9-Aminopyrene-1,4,6-trisulfonate (APTS) was obtained from Lambda Fluoreszenztechnologie GmbH, Graz, Austria. 8-Aminonaphthalene-1,3,6-trisulfonic acid (ANTS) was purchased from Molecular Probes, Eugene, OR. Sodium cyanoborohydride (1.0 M solution in tetrahydrofuran) was purchased from Aldrich Chemicals, Milwaukee, WI. Dextrin 15 was obtained from Fluka, Flushing, NY. All other carbohydrates and buffer components were purchased from Sigma Chemicals, St Louis, MO. All sugars were dissolved in water and stored at −20 °C prior to use.

Capillary Electrophoresis Procedures. CE separations were performed on a P/ACE 2100 equipped with laser-induced fluorescence system and a 3-mW 488-nm argon-ion laser (Beckman Instruments, Inc., Fullerton, CA). The system was equipped with a P/ACE system software controlled by an IBM PS/2 Model 55 SX. Capillary columns, typically 27 cm in length (20 cm to detector window) × 20 or 50 μm i.d. (Polymicro Technologies, Phoenix, AZ), were assembled in the P/ACE cartridge format with an ellipsoidal mirror to collect fluorescence. Electrophoresis was performed at the voltage shown in each electropherogram. Running buffers were a sodium salt of 100 or 200 mM borate, pH 10.2, or 50 mM phosphate, pH 2.2. When using borate buffer, the capillary was sequentially washed between runs with 1.0 N sodium hydroxide and water (12 s of high pressure rinsing at 15 psi), followed by reconditioning with the running buffer, typically 1 min. Using phosphate buffer, pH 2.2, as the electrophoresis buffer, the capillary was rinsed with same buffer for 1 min prior to each sample injection. Peak areas were calculated using the Beckman System Gold Chromatography Software.

A 5-mW He/Cd laser at 325 nm and a laser headcoupler to a standard SMA-906 fiber connector to the P/ACE system with LIF detector were obtained from Omnichrome, Chino, CA. The fluorescence emission filter of 520 ± 9 nm was purchased from Oriel Corp. Stratford, CT. The laser beam was rejected either by short pass filter, cutoff at 380 nm or below, or by a notch filter at 488 nm (Barr Associates, Westford, MA).

Derivatization of Sugars with ANTS and APTS. The derivatization procedure for the monosaccharides and the oligosaccharide ladder was essentially adapted from the method first described by Jackson[9] and modified by Chiesa and Horvath.[10] Briefly, 10 μL of 0.1 M saccharide (1 μmol) in a 500-μL Eppendorf SafeLock conical microcentrifuge tube was mixed with 2 μL of 0.1 M APTS in 25% acetic acid and 10 μL of 1 M sodium cyanoborohydride in tetrahydrofuran. The reaction tube was centrifuged and then heated in a water bath at 75 °C for 1 h. For ANTS-derivatized sugars, the method was essentially the same as the above procedure. In the quantitation studies, 2 pmol–200 nmol of maltoheptaose (G_7) in 10 μL of water was reductively aminated with the same amount of APTS and sodium borohydride; for α-Glc-(1→6)-α-Glc-(1→4)-α-Glc-(1→4)-α-Glc (G_4'), the amount was 3 pmol–30 nmol in 10 μL of water. The resulting mixture was diluted in water and injected into the CE system or passed through a Sephadex G-10 column (5 mm × 100 mm, 50 mM bicarbonate buffer, pH 8.5). Derivatized oligosaccharides were collected in the void volume.

Measurement of UV/Visible and Fluorescence Spectra. UV/visible spectra of APTS and its sugar derivatives were recorded on a Beckman 7500 diode-array spectrophotometer (Fullerton, CA). Fluorescence spectra were recorded on a Perkin-Elmer LS50 luminescence spectrometer (Beaconsfield, Buckinghamshire, U.K.). The molar extinction coefficients of APTS and its sugar derivatives were determined. Samples of APTS were dissolved in 50 mM phosphate buffer, pH 7.0. The concentration of APTS used in the derivatization was based on the extinction coefficient of 14 400 M^{-1} cm^{-1} at 424 nm.[16] The ANTS- and APTS-derivatized maltoheptaose were purified through a Sephadex G-10 column (5 mm × 100 mm, 50 mM bicarbonate buffer, pH 8.5), and their molar extinction coefficients (7050 M^{-1} cm^{-1} at 367 nm and 17 160 M^{-1} cm^{-1} at 455 nm, respectively) were measured on a Beckman UV/vis DU-7500 diode-array spectrophotometer.

Polyacrylamide Gel Electrophoresis (PAGE). The APTS-labeled oligosaccharide ladder was analyzed by PAGE. The electrophoresis procedure was followed the methods described by Jackson.[9] Samples were applied to a 30% (w/v) polyacrylamide slab gel (0.5 mm × 160 mm × 200 mm) in Tris–HCl/glycine buffer.[17] The electrophoresis was performed at 4 °C at 100 V for 30 min and at 850 V for 180 min. The APTS-labeled oligosaccharide ladder was then examined on a 366-nm Fotodyne UV transilluminator, and the photoimage was taken by using Polaroid film type 667 (exposure time, 10 s).

RESULTS AND DISCUSSION

The derivatization of a reducing sugar by reductive amination with APTS is represented by eq 1 in Figure 1. The absorption λ_{max} of APTS and the APTS-derivatized sugars in buffered aqueous solution at pH 7 are 424 and 455 nm, respectively. The absorption spectra of APTS–sugar adducts were obtained from diluted reaction mixtures of APTS and 20-fold molar excess of sugar under conditions that produced complete conversion of APTS to the

(14) Yeung, E. S.; Wang, P.; Li, W.; Giese, R. W. *J. Chromatogr.* **1992**, *608*, 73–77.
(15) Linhardt R. J.; Lee, K. B.; Ali-Hakim, A.; Loganathan, D. U.S. Patent 5,284,-558, Feb 8, 1994.
(16) Koller, E.; Kriechbaum, M.; Wolfbeis, O. S. *Spectroscopy* **1988**, *3*, 37–39.
(17) Laemmli, U. K. *Nature (London)* **1970**, *227*, 248–254.

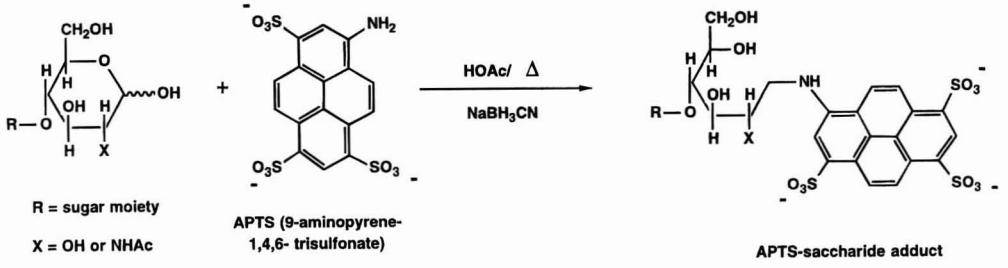

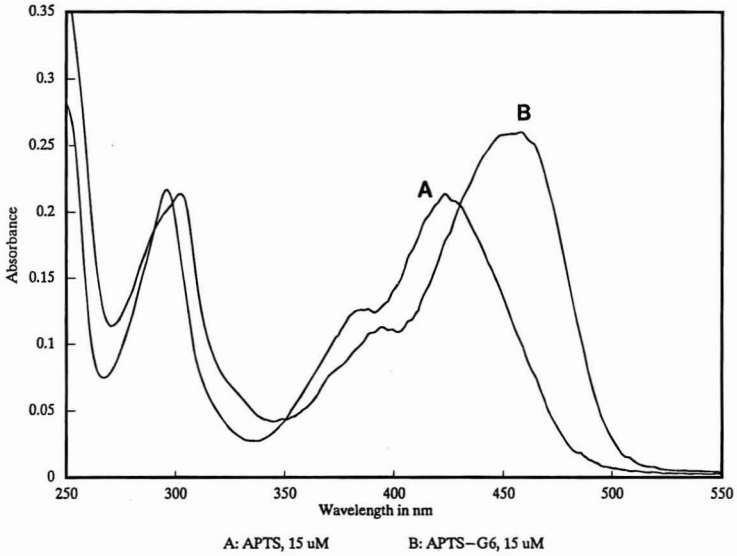

Figure 1. Equation 1: Reductive amination reaction scheme showing structures of APTS and its adduct with a reducing sugar. Spectra A and B: UV/visible spectra of APTS and its adduct with maltohexaose, respectively, at 15 μM each in 50 mM phosphate, pH 7.0.

Table 1. Comparative Fluorescence Intensities of APTS, APTS–Rhamnose (APTS-Rham), APTS-G_6, ANTS, and ANTS-G_6 at 1.0 μM each[a]

	excitation:325 nm emission λ_{max}:RFU	excitation:442 nm emission λ_{max}:RFU	excitation:488 nm emission λ_{max}:RFU
APTS	502 nm:53.5	500 nm:186.8	501 nm:11.1
APTS-G_6	511 nm:95.9	511 nm:486.1	511 nm:155.4
APTS-Rham	514 nm:85.4	513 nm:403.9	513 nm:160.1
ANTS	507 nm:2.89	509 nm:0.254	505 nm:0.098
ANTS-G_6	506 nm:3.14	520 nm:0.318	506 nm:0.096
ANTS-Rham	512 nm:2.67	520 nm:0.307	517 nm:0.085

[a] RFU, relative fluorescence unit.

sugar derivatives (electropherograms of the reaction mixtures showed the complete absence of APTS and the formation of APTS–sugar adducts). The UV/visible spectra of the APTS and APTS–maltohexaose (APTS-G_6) are exhibited in Figure 1, spectra A and B, respectively, at 15 μM each. Molar absorptivities were calculated to be 14 010 M^{-1} cm^{-1} for APTS at 424 nm, very close to the reported value of 14 400 M^{-1} cm^{-1} [16] and 17 160 M^{-1} cm^{-1} at 455 nm for APTS–sugar adducts. Both APTS and its sugar derivatives absorb at 325 nm, but with lower absorptivity relative to their absorption maxima. At 488 nm, APTS absorbs only 4% of its absorption maximum at 424 nm, while the APTS-derivatized sugars absorb significantly, about 35% of their absorption maxima at 455 nm. The red shift is expected as a result of alkylation of an aromatic primary amine group.

Fluorescence emission maxima (excitation at 325, 442, or 488 nm) of APTS are at 500–502 nm, while those of the APTS-derivatized sugars are at 511–514 nm as shown in Table 1. At 1.0 μM, the fluorescence intensity of APTS (em λ_{max} = 501 nm) is about half that of APTS-G_6 (em λ_{max} = 512 nm) with excitation at 325 nm (RFU: 53.5 vs 95.9, respectively). The fluorescence intensity of APTS (em λ_{max} = 501 nm) is about 40% that of APTS-G_6 (em λ_{max} = 512 nm) with excitation at 442 nm (RFU: 186.8 vs

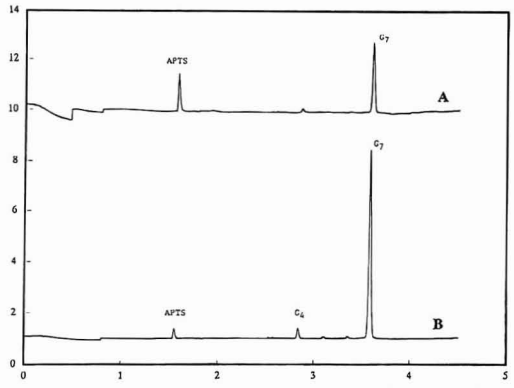

Figure 2. (A) Electropherogram of APTS and APTS-derivatized maltoheptaose at 1.0 μM each. Conditions: untreated fused-silica capillary, 50 μm (i.d.) × 27 cm; light source, 325-nm He/Cd laser; emission filter, 520 ± 20 nm (Oriel, Stratford, CT) and a short pass filter at 380 nm (Barr Associates, Westford, MA); applied potential, 12 kV/46 μA; buffer, 50 mM phosphate, pH 2.2; sample injection, 2 S (3.5 kPa pressure); outlet, anode. (B) Same as that in panel A, except the light source was a 488-nm argon-ion laser.

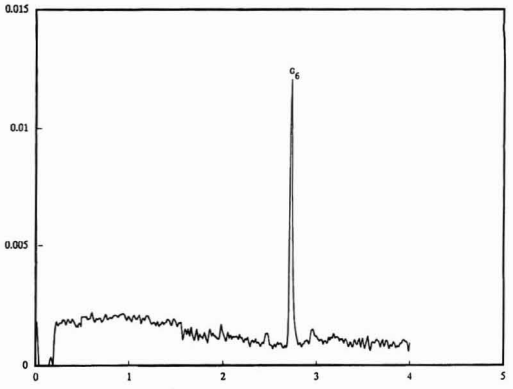

Figure 3. Electropherogram of APTS-derivatized maltohexaose, 0.8 nM. Conditions: untreated fused-silica capillary, 22 μm (i.d.) × 27 cm; light source, 488-nm argon-ion laser; emission filter, 520 ± 20 nm (Oriel, Stratford, CT) and a notch filter at 488 nm (Barr Associates); applied potential, 20 kV/20 μA; buffer, 50 mM phosphate at pH 2.2; sample injection, 40 s, 3.5 kPa pressure; outlet, anode.

486.1, respectively). When APTS-G_6 is excited at 488 nm, its maximum fluorescence intensity is 14 times greater than that of the APTS (RFU: 155.4 vs 11.1 RFU) at their emission maxima (512 and 501 nm, respectively). APTS–rhamnose exhibits similar fluorescence properties as APTS-G_6. Thus, when using an excitation with an argon ion laser at 488 nm coupled with a 520-nm narrow band filter for emission, the fluorescence detection of the APTS sugar adduct is heavily favored. Even though excitation at 442 nm (He/Cd laser line) produces three times the signal for APTS–sugars compared to 488-nm excitation, the partial selective detection of the adduct over the excess reagent is achieved to a greater degree at 488 nm. At 325-nm excitation (He/Cd laser line), ANTS and its sugar derivatives have less than 2% of the fluorescence intensity of the APTS and its sugar derivatives at 488-nm excitation (see Table 1).

Both APTS and APTS-G_7 absorb significantly at 325 nm and can be excited with the He/Cd laser line at 325 nm. Figure 2A shows the electropherogram of a mixture of APTS and APTS-G_7 at 1.0 and 0.83 μM, respectively, showing that the signal of APTS is about half of the APTS-G_7 with 325-nm excitation on equal molar basis. Emission maxima of the APTS and APTS-G_7 are 501 and 512 nm, respectively, and the relative fluorescence intensity favors APTS-G_7 by an almost 2:1 margin, as shown in Table 1. By using a 520-nm narrow band emission filter (±10 nm), the detection system further favors the APTS-G_7 over that of the APTS. Thus, the use of the 488-nm line of the argon-ion laser for LIF detection of APTS and APTS-G_7 in CE produces a partial selectivity in excitation which contributes to the preferential detection of the APTS-G_7 over APTS as shown in Figure 2B. The combination of 488-nm excitation and 520-nm emission filter results in substantially higher fluorescence signal (about 40 times) for the APTS–sugar derivatives than for unreacted APTS. A small peak attributed to APTS-G_4 (confirmed by co-injection of the authentic synthesized sample) can be seen in both Figure 2A and 2B, presumably due to the partial hydrolysis of the APTS-G_7 during storage.

Figure 3 shows the electropherogram of a gel filtration (Sephadex G-10) purified APTS-G_6 diluted to 0.83 nM. The limit of detection for APTS-derivatized sugars with 488-nm argon-ion excitation is estimated to be 0.4 nM (based on a signal/noise ratio of 10). With sample injection of about 2 nL, this amount of sugar detected is equal to 0.8 amol, which compares favorably with the detection limits reported for CBQCA–sugar (240 amol)[12] and ANTS–sugar (a few attomoles),[10] which were also obtained by injection of diluted solutions of sugars derivatized at much higher concentrations.

The lowest amount of sugar analyte that can be derivatized in a reaction and then detected by CE is by far of greater significance in glycobiology research than the lowest dilution of a previously prepared sugar derivative that can be detected by CE. Hence, a quantitative investigation of the APTS adduct formation was performed by derivatizing 10-fold decreasing amounts of saccharides with a constant excess amount of APTS and sodium cyanoborohydride. Derivatization of G_7 and α-Glc-(1→6)-α-Glc-(1→4)-α-Glc-(1→4)-α-Glc-(1→4)-α-Glc (G_4') by APTS and analysis of the diluted unpurified reaction mixture (Figure 4) showed that as little as 2–3 pmol of the reducing sugar could be chemically derivatized and detected by the present CE/LIF using 200 mM borate, pH 10.2, as separation buffer, where the excess APTS does not reach the detector within the analytical time frame of 15 min. The results show that the CE/LIF signal of the APTS–sugar adduct is a linear function of the amount of sugar in the derivatization mixture over 5 orders of magnitude for G_7 (2 pmol–200 nmol) and 4 orders of magnitude for G_4' (3 pmol–30 nmol). Linear correlation between peak area and molar amount of sugar for both G_7 ($r = 0.99953$) and G_4' ($r = 0.99956$) was obtained, indicating that the efficiency of the reductive amination reaction is close to 100% with the present method.

In the analysis of sugar analytes at amounts close to the derivatization detection limits, the fluorescent impurities present in the large excess of APTS appear in the electropherograms (Figure 4), but the impurity peaks have longer migration times than the oligosaccharide-APTS peak. In contrast to some derivatization reagents which produce optimum fluorescence at a certain reagent/sugar ratio, the present method produces a signal that

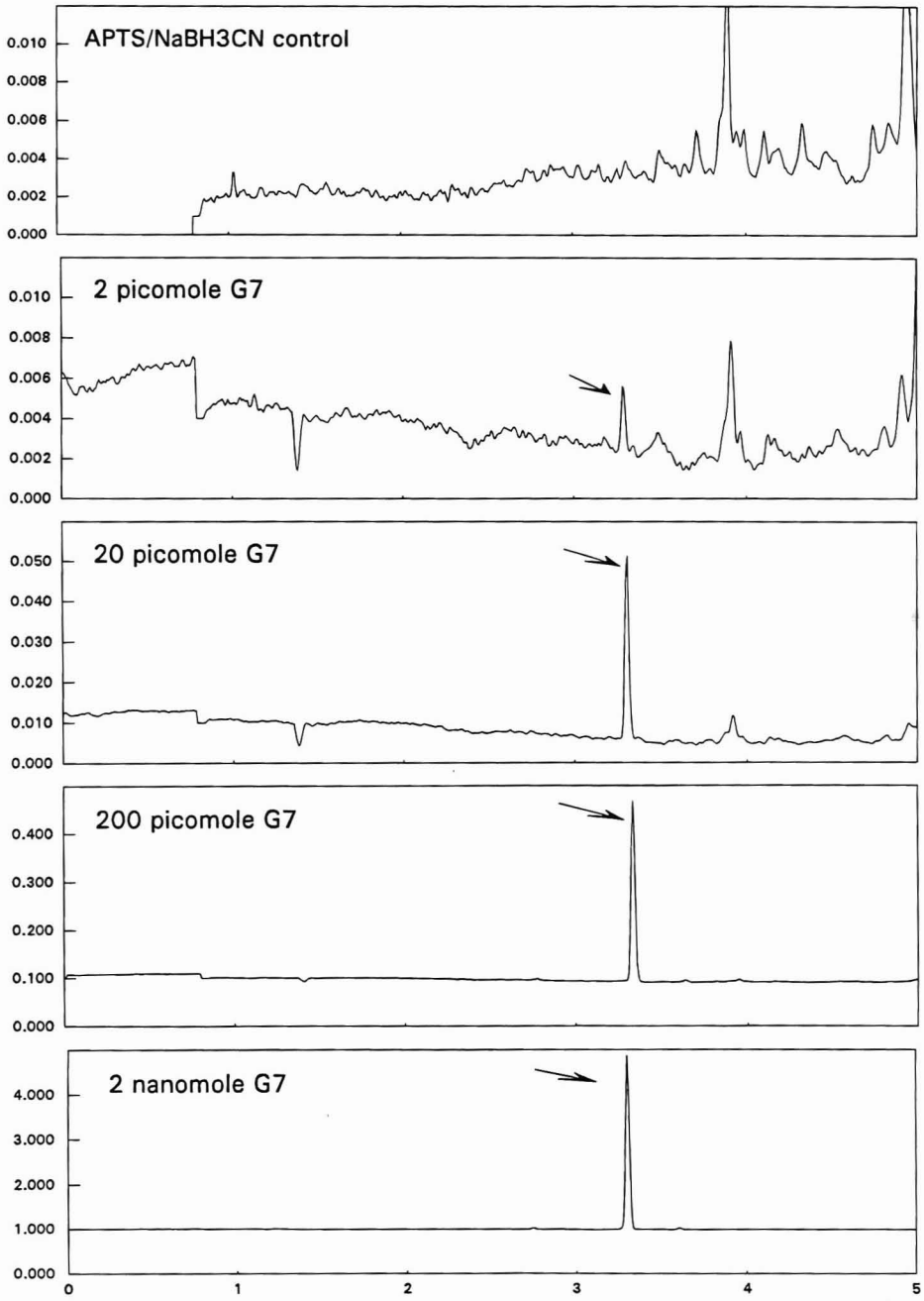

Figure 4. Electropherograms of the 10-fold diluted reaction mixture from derivatization of varying amounts of maltoheptaose (2 pmol–200 mol) with constant amount of APTS and $NaBH_3CN$. Conditions: untreated fused-silica capillary, 20 μm (i.d.) x 27 cm; separation buffer, 200 mM borate, pH 10.2; applied potential, 17 kV/39 μA; sample injection, 30 s (3.5 kPa pressure). Linear regresion analysis of the integrated peak area vs amount of the saccharide produced a linear equation: Peak area = (5.58×10^{10})(mol of sugar) + 18.0; with a correlation coefficient of 0.99953.

is linearly proportional to the amount of sugar regardless of the amount of excess reagent.

The lowest amount of sugar that can be derivatized and analyzed by the present method is substantially lower than those

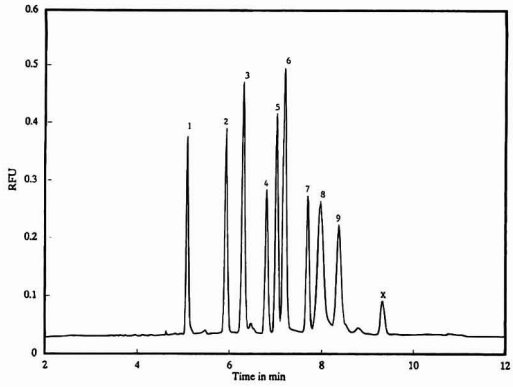

Figure 5. Electropherogram of nine APTS-derivatized monosaccharides at 1.0 μM each. Condition: untreated fused-silica capillary, 20 μm (i.d.) × 27 cm; light source, 488-nm argon-ion laser; emission filter, 520 ± 20 nm (Oriel, Stratford, CT) and a notch filter at 488 nm (Barr Associates); applied potential, 20 kV/19 μA; buffer, 100 mM borate, pH 10.2; sample injection, 20 s, 3.5 kPa pressure; outlet, cathode. Peak identification: (1) *N*-acetylgalactosamine, (2) *N*-acetylglucosamine, (3) rhamnose, (4) mannose, (5) glucose, (6) fructose, (7) xylose, (8) fucose, and (9) galactose. (X) impurity peak derived from APTS. Outlet, cathode.

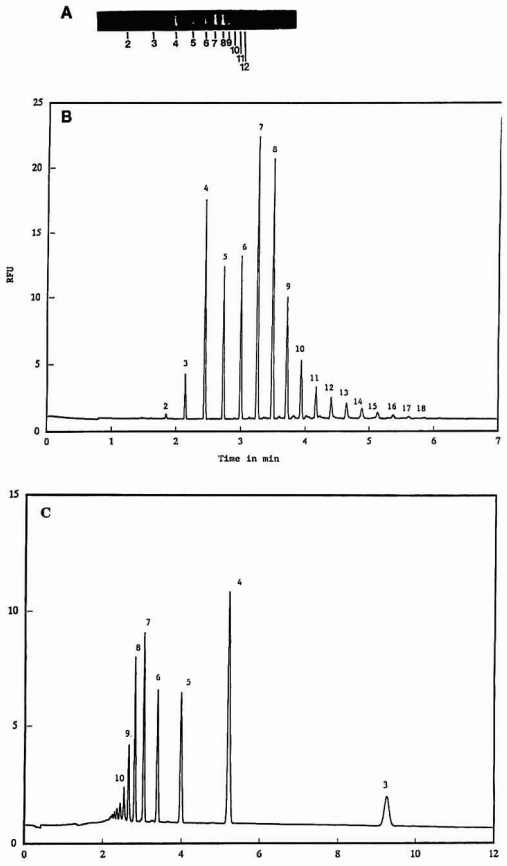

Figure 6. (A) Photograph of the fluorescence image of the gel filtration purified APTS–Dextrin 15, separated by 30% polyacrylamide gel electrophoresis system. Excitation by 366-nm UV lamp. (B) Electropherogram of 1000-fold diluted APTS-derivatized Dextrin 15 (same as that in panel A). Conditions: same as that in Figure 4 except the running buffer was 50 mM sodium phosphate, pH 2.2, and the applied potential was 20 kV/20 μA. Outlet, anode. (C) Electropherogram of 1000-fold diluted APTS-derivatized Dextrin 15 (same as that in panel A) Conditions: same as that in panel B except the running buffer was 200 mM borate, pH 10.2, and the applied potential was 17 kV/36 μA. Outlet, cathode.

used for derivatization with ANTS (10–15 nmol),[18] with AP (0.1–2 mg),[7] with CBQCA (500 μg),[12] with 2-aminoacridone (1 nmol),[19] and with ABN (10 mM sugar in reaction mixture).[13] In terms of concentrations, the 10-μL aqueous saccharide analyte solutions contained 2 × 10^{-7} to 0.02 M G_7 (5 orders of magnitude) before addition of the excess APTS and $NaBH_3CN$. In comparison, derivatization with 4-aminobenzoic acid produced a linear response over a concentration range of only 2 orders of magnitude (0.1–10 mM).[20]

Monosaccharides were derivatized by the standard procedure, and the separation of the mixture of nine APTS-monosaccharides was achieved by CE, shown in Figure 5. Differential complexation of borate with polyhydroxyl moieties of the monosaccharide derivatives appeared to be the primary mechanism of the CE separation.[8,13] Fructose, a ketohexose that has been derivatized with ABN[13] but not with AP and ANTS, was converted to the APTS adduct by the present derivatization procedure with a longer reaction time of 2.5 h at 75 °C (peak 6 in Figure 6). Sorbose, another ketohexose, was derivatized similarly.

A maltooligosaccharide sample (Dextrin 15 from Fluka, Flushing, NY) was derivatized by reductive amination with APTS, and then the mixture was passed through a Sephadex G-10 column. The void volume fraction containing a mixture of oligosaccharides was analyzed by polyacrylamide gel electrophoresis (PAGE, Figure 6A) according to the procedure of Jackson[9] and by CE/LIF (Figure 6B,C) at 1000-fold dilution. Figure 6B shows the electropherogram of the APTS–Dextrin 15 obtained in an untreated fused-silica capillary with 50 mM phosphate buffer, pH 2.2. The APTS-derivatized glucose (G_1) migrated through the detection window first followed by maltose (G_2), maltotriose (G_3), etc, and the individual saccharides were well-resolved and detectable up to APTS-G_{18}. In borate buffer, the electropherogram of the APTS–Dextrin 15 shows that larger oligosaccharide derivatives of APTS migrate faster than the smaller oligosaccharide species, as shown in Figure 6C. At alkaline pH, the electroendoosmotic flow toward cathode is substantially stronger than the electrophoretic mobility of each labeled oligosaccharide toward anode. Thus, all species migrate toward the cathode, and the migration sequence of each species is the reverse of that in Figure 6B. Both analytical systems resolved the oligosaccharide ladders. While the high-resolution PAGE analysis developed for ANTS-labeled saccharides[21] also provided acceptable separation of the APTS-derivatized sugars, CE/LIF, in contrast, produced baseline

(18) Oefner, P.; Chiesa, C.; Bonn, G; Horvath, C. *J. Cap. Elec.* **1994**, *1*, 5–26.
(19) Jackson, P.; Pluskal, M. G.; Skea, W. *Electrophoresis* **1994**, *15*, 896–902.
(20) Grill, E.; Huber, C.; Oefner, P.; Vorndran, A.; Bonn, G. *Electrophoresis* **1994**, *15*, 941–52.
(21) Jackson, P. *Anal. Biochem.* **1994**, *210*, 243–252.

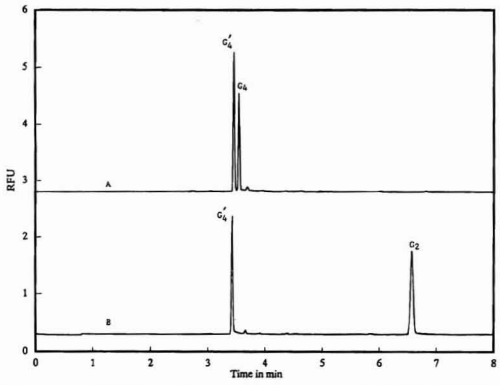

Figure 7. (A) Electropherogram of a mixture of 10^{-5} M APTS-G_4 and APTS-G_4' in borate buffer. Condition: same as in Figure 6 except the running buffer was 150 mM borate, pH 10.2, and the applied potential was 20 kV/21 μA. Sample injection, 20 s, 3.5 kPa pressure. (B) Electropherogram of α-amylase-catalyzed hydrolysis product of APTS-G_4 and APTS-G_4' mixture after 200-min incubation at ambient temperature (20 mM phosphate, pH 7.0) after the addition of 5 μL of α-amylase (100 μg/mL) to the 100 μL in panel A. Outlet, cathode.

resolution even with a 1000-fold diluted sample as shown in Figure 6B,C. The above CE results are consistent with the observation by Chiesa and Horvath[10] using 8-aminonaphthalene-1,3,6-trisulfonic acid (ANTS)-derivatized maltooligosaccharides.

The APTS adducts of maltotetraose, α-Glc(1→4)-α-Glc(1→4)-α-Glc(1→4)-α-Glc (APTS-G_4), and its structural isomer, α-Glc-(1→6)-α-Glc(1→4)-α-Glc(1→4)-α-Glc (APTS-G_4') were prepared, and the electrophoretic separation of these structural isomers was achieved in 150 mM borate buffer with baseline resolution, shown in Figure 7. The electropherogram obtained after incubation with α-amylase (porcine pancreas, EC 3.2.1.1) show that only APTS-G_4 was hydrolyzed to APTS-G_2 as the end product. The APTS-G_4' was resistant to α-amylase-catalyzed hydrolysis due to the presence of the α-(1→6) glucopyranosyl linkage at the nonreducing end of the APTS-G_4'. The use of CE/LIF for the study of a glycosidase-catalyzed reaction using a substrate end-labeled with tetramethylrhodamine has been reported recently.[22]

In conclusion, the use of APTS as a fluorescence reagent for probing sugars was demonstrated using the CE/LIF system. The method has potential application for the analysis of carbohydrate in glycobiology and diagnostic utility for diseases related to sugar metabolism.

ACKNOWLEDGMENT

We thank Dr. James Osborne for his support.

Received for review November 7, 1994. Accepted March 21, 1995.[⊗]

AC9410833

[⊗] Abstract published in *Advance ACS Abstracts,* May 15, 1995.

(22) Zhao, J. Y.; Dovichi, N. J.; Hindsgaul, O.; Gosselin, S.; Palcic, M. M. *Glycobiology* **1994**, *4*, 239–242.

Anal. Chem. **1995,** *67,* 2246–2255

Spatial Discrimination against Background with Different Optical Systems for Collection of Fluorescence in Laser-Excited Atomic Fluorescence Spectrometry with a Graphite Tube Electrothermal Atomizer

Alexander I. Yuzefovsky, Robert F. Lonardo, and Robert G. Michel*

Department of Chemistry, University of Connecticut, 215 Glenbrook Road, Storrs, Connecticut 06269-3060

A single 90° off-axis ellipsoidal mirror fragment was used in a dispersive detection system for electrothermal atomization laser-excited atomic fluorescence spectrometry. The performance of the new optical arrangement was compared with those of optical arrangements that employed a plane mirror in combination with biconvex or planoconvex lenses. All the optical arrangements collected fluorescence in a scheme called front surface illustration. BEAM-4, an optical ray tracing program, was used for calculations of spatial ray distributions and optical collection efficiency for the various optical configurations. Experimentally, the best collection efficiency was obtained by use of the ellipsoidal mirror, in qualitative agreement with simulations done by use of the BEAM-4 software. The best detection limit for cobalt with the new optical arrangement was 20 fg, which was a factor of 5 better than that obtained with conventional optical arrangements with otherwise the same instrumentation. The signal-to-background ratio and the fluorescence collection efficiency were also studied as a function of position of the optical components for the various optical arrangements. For both cobalt and phosphorus, the signal-to-background ratio with the new optical arrangement remained stable within 10–20% during ±8 mm shifts in the position of the detection system from the focal plane of the optics. Overall, the new optical arrangement offered high collection efficiency, excellent sensitivity, and facile optical alignment due to efficient spatial separation between the fluorescence signal and the background radiation. The advantages of the new optical arrangement were particularly important during measurements in the presence of high levels of blackbody radiation.

Electrothermal atomizer laser-excited atomic fluorescence spectrometry (ETA-LEAFS) is characterized by extremely low absolute detection limits at the femtogram level, freedom from background spectral interferences, and 5–7 orders of magnitude in calibration range, as reviewed in several articles.[1-3] Since about 1988, commercially available graphite tube electrothermal atomizers have been reported to be a much better choice for ETA-LEAFS than open graphite atomizers, because a graphite tube atomizer suffers less from diffusion losses and vapor-phase interferences compared to open graphite atomizers.[1,4] As a result, the number of elements studied has been extended,[5-7] the high sensitivity of ETA-LEAFS has been evaluated as a possible means to reach single atom detection for real sample analyses,[8-11] and a wide variety of practical analyses have been demonstrated.[12-15] The focus of the present paper is that the unique geometry of graphite tube atomizers necessitates a re-evaluation of the optical arrangements that have been traditionally used with flames, plasmas, and open graphite electrothermal atomizers. Improved optical arrangements should increase the sensitivity of ETA-LEAFS and further consolidate its position as one of the most sensitive techniques available for ultratrace metal determinations.

There are five main requirements for the development of the optical arrangement for fluorescence detection systems: first, the optical arrangement must have maximum collection efficiency over a wide wavelength range (~196–800); second, it must discriminate between background and analytical signals without significant sacrifice in the latter; third, there must be minimal losses of analytical signal along the optical path due to reflection from different surfaces and apertures; fourth, the optics should not be difficult to align; and fifth, the components should be relatively inexpensive and commercially available. A perusal of the literature

(1) Butcher, D. J.; Dougherty, J. P.; Preli, F. R.; Walton, A. P.; Wei, G.-T.; Irwin, R. L.; Michel, R. G. *J. Anal. At. Spectrom.* **1988**, *3*, 1059–1078.
(2) Sjöström, S. *Spectrochim. Acta Rev.* **1990**, *13*, 407–465.
(3) Sjöström, S.; Mauchien, P. *Spectrochim. Acta Rev.* **1993**, *15*, 153–180.
(4) Bolshov, M. A.; Zybin, A. V.; Smirenkina, I. I. *Spectrochim. Acta* **1981**, *36B*, 1143–1152.
(5) Dougherty, J. P.; Preli, F. R.; McCaffrey, J. T.; Seltzer, M. S.; Michel, R. G. *Anal. Chem.* **1987**, *59*, 1112–1119.
(6) Dougherty, J. P.; Preli, F. R.; Michel, R. G. *J. Anal. At. Spectrom.* **1987**, *2*, 429–434.
(7) Wei, G.-T.; Dougherty, J. P.; Preli, F. R.; Michel, R. G. *J. Anal. At. Spectrom.* **1990**, *5*, 249–259.
(8) Alkemade, C. Th. J. In *Analytical Applications of Lasers*; Piepmeier, E. H., Ed.; Wiley Interscience: New York, 1986; Chapter 4.
(9) Alkemade, C. Th. J. *Appl. Spectrosc.* **1981**, *35*, 1–14.
(10) Omenetto, N.; Smith, B. W.; Winefordner, J. D. *Spectrochim. Acta* **1988**, *43B*, 1111–1118.
(11) Smith, B. W.; Womack, B.; Omenetto, N.; Winefordner, J. D. *Appl. Spectrosc.* **1989**, *43*, 873–876.
(12) Irwin, R. L.; Wei, G.-T.; Butcher, D. J.; Liang, Z.; Su, E. G.; Takahashi, J.; Walton, A. P.; Michel, R. G. *Spectrochim. Acta* **1992**, *47B*, 1497–1515.
(13) Liang, Z.; Lonardo, R. F.; Takahashi, J.; Michel, R. G.; Preli, F. R. *J. Anal. At. Spectrom.* **1992**, 47, 1019–1028.
(14) Dashin, S. A.; Maiorov, I. A.; Bolshov, M. A. *Spectrochim. Acta* **1993**, *48B*, 531–542.
(15) Sjöström, S.; Axner, O.; Norberg, M. *J. Anal. At. Spectrom.* **1993**, *8*, 375–378.

0003-2700/95/0367-2246$9.00/0 © 1995 American Chemical Society

indicates that optical arrangements have not always been optimal, because they were chosen on the basis of minimization of cost rather than maximization of optical performance. This has often led to the use of readily available biconvex lenses, rather than mirrors that have fewer optical aberrations.

For early experiments with flame LEAFS, four different optical arrangements were employed. The most simple and inexpensive consisted of one biconvex lens[16-19] or a plane mirror.[20] Alternative arrangements that consisted of systems of mirrors had much higher collection efficiency and fewer aberrations.[16,21] However, difficulties associated with the optical alignment, together with the absence of inexpensive, standardized, optical components on the market, virtually eliminated the utilization and further development of such arrangements, even though the use of a torroidal mirror[22] or a spherical mirror[23] significantly increased the collection efficiency. A torroidal mirror integrated with biconvex lenses has been used for the enhancement of fluorescence signals by multiple light passes through the atomizer.[24-26] In all of these cases, the optical components were arranged in a manner that allowed for the maximum possible collection efficiency for open type atomizers. Since the solid angle of the fluorescence from an open atomizer is virtually 4π, the collection efficiency depends primarily on the amount of the radiation that is collected by the optics and whether or not the collected radiation can be collected by the solid angle of the detector.

The requirements of the optical arrangements for LEAFS techniques were changed when graphite tube atomizers began to be used, because the solid angle and the direction of the radiation flux are defined by the different shape of the semiclosed graphite tube atomizer. The background radiation in graphite tube atomizers is emitted spatially separated from the fluorescence radiation, because the fluorescence is emitted from within the tube, while the background blackbody radiation is emitted from the tube wall. When imaged onto the detection system, the blackbody emission forms a ring of radiation around the fluorescent volume. This geometry requires that the image of the graphite furnace be transferred with as little distortion as possible, in order to allow spatial filtering to be used to distinguish between the background and the fluorescence. In analytical atomic spectrometry, a comprehensive review of the choice of optical components for spatial discrimination and collection of radiation has been presented by Goldstein and Walters.[27,28] In the context of atomic emission spectrometry, the authors discussed problems associated with different types of aberrations, coma, and astigmatism for a number of optical designs. They also introduced a method for the proper selection and orientation of mirrors in order to achieve high-fidelity image transfer through an optical train. For ETA-LEAFS, a comparative, empirical study of the signal-to-noise ratios and detection limits obtained by the employment of different methods of collection of fluorescence signals has established that the most efficient method is front surface illumination, where the fluorescence is detected at 180° to the direction of the laser beam.[1] Recent improvements in collection efficiency for ETA-LEAFS have almost all involved front surface illumination.[29,30]

The most recent systematic attempt to develop a quantitative model for the collection of fluorescence radiation in ETA-LEAFS was performed by Farnsworth et al.[31] For front surface illumination, the authors compared optical collection efficiencies for biconvex, plano-convex, and achromatic lenses. It was shown that the most aberration-free arrangement consisted of one flat mirror and a pair of achromatic lenses, while a pair of plano-convex lenses provided a useful compromise in cost and efficiency. Their models provided an understanding of the optical phenomena associated with the collection of the radiation flux from graphite tube furnaces and suggested means to improve the optical arrangement. Vera et al.[32] recently described the use of the optical components from a Bomem spectrometer (Bomen/Hartmann & Braun, Quebec, Canada) coupled directly with a photomultiplier tube (PMT) for the collection of atomic fluorescence radiation. This nondispersive approach consisted of an aperture, filters, and a 90° off-axis ellipsoidal mirror. The data indicated that the Bomem system gave fluorescence signals comparable to those collected with conventional optical arrangements, but Vera et al.[32] did not study the spatial discrimination aspects of the arrangement.

The objective of the work described here was to take advantage of the low optical aberrations for image transfer that should accrue from the use of an ellipsoidal mirror. Such low optical aberrations should allow for more efficient spatial discrimination between the fluorescence and blackbody radiation. A single 90° off-axis ellipsoidal mirror fragment was used in a dispersive detection system. The performance of the new optical arrangement was compared with those of conventional optical arrangements that employed a plane mirror in combination with biconvex or plano-convex lenses. All the optical arrangements collected fluorescence by front surface illumination. BEAM-4, an optical ray tracing program, was used to calculate simulations of spatial ray distributions and optical collection efficiency for the various optical configurations. The software was able to take account of the most important types of aberrations in the various optical components that were simulated. The simulations were done for an ideal point source located in various positions in the graphite furnace, because the software did not allow simulation of a real extended source. Qualitatively, the results of the simulations correlated well with the relative experimental performance of the various optical arrangements for the collection of atomic fluorescence radiation. In particular, the experimental results did show that optical systems with fewer optical aberrations led to better detection limits because they allowed better spatial discrimination between blackbody and fluorescence radiation.

(16) Omenetto, N.; Rossi, G. *Anal. Chim. Acta* **1968**, *40*, 195–200.
(17) Omenetto, N. *Anal. Chem.* **1976**, *48*, 75A–82A.
(18) Green, R. B.; Travis, J. C.; Keller, R. A. *Anal. Chem.* **1976**, *48*, 1954–1959.
(19) Epstein, M. S.; Nikdel, S.; Omenetto, N.; Reeves, R.; Bradshaw, J.; Winefordner, J. D. *Anal. Chem.* **1979**, *51*, 2071–2077.
(20) Fraser, L. M.; Winefordner, J. D. *Anal. Chem.* **1971**, *43*, 1693–1696.
(21) Benetti, P.; Omenetto, N.; Rossi, G. *Appl. Spectrosc.* **1971**, *25*, 57–60.
(22) Johnson, D. J.; Plankey, F. W.; Winefordner, J. D. *Anal. Chem.* **1974**, *46*, 1898–1902.
(23) Fowler, W. K.; Winefordner, J. D. *Anal. Chem.* **1977**, *49*, 944–949.
(24) Weeks, S. J.; Haraguchi, H.; Winefordner, J. D. *Anal. Chem.* **1978**, *50*, 360–368.
(25) Epstein, M. S.; Bayer, S.; Bradshaw, J.; Voigtman, E.; Winefordner, J. D. *Spectrochim. Acta* **1980**, *35B*, 233–237.
(26) Kachin, S. V.; Smith, B. W.; Winefordner, J. D. *Appl. Spectrosc.* **1985**, *39*, 587–590.
(27) Goldstein, S. A.; Walters, J. P. *Spectrochim. Acta* **1976**, *31B*, 201–220.
(28) Goldstein, S. A.; Walters, J. P. *Spectrochim. Acta* **1976**, *31B*, 296–316.
(29) Omenetto, N.; Cavalli, P.; Broglia, M.; Qi, P.; Rossi, G. *J. Anal. At. Spectrom.* **1988**, *3*, 231–235.
(30) Liang, Z.; Lonardo, R. F.; Michel, R. G. *Spectrochim. Acta* **1993**, *48B*, 7–23.
(31) Farnsworth, P. B.; Smith, B. W.; Omenetto, N. *Spectrochim. Acta* **1990**, *45B*, 1151–1166.
(32) Vera, J. A.; Leong, M. B.; Omenetto, N.; Smith, B. W.; Womack, B.; Winefordner, J. D. *Spectrochim. Acta* **1989**, *44B*, 939–948.

EXPERIMENTAL SECTION

Computational Procedure. The BEAM-4 optical ray tracing program (Stellar Software, Berkeley, CA) was employed for the calculation and presentation of spatial ray distributions and for the calculation of optical collection efficiency at the monochromator focal plane. Only a brief overview of very basic principles and capabilities is given here, since all the features of this program are thoroughly discussed in its manual. All the computations were done on a personal computer (Gateway 2000, Model 486/25, North Sioux City, SD). BEAM-4 allows different optical elements to be designed with a variety of surfaces such as lenses, mirrors, apertures, and irises. To describe conic sections, ellipses, hyperbolas, etc., the program uses the vertex-Cartesian system. The refraction, reflection, and propagation of light as a function of different media and wavelengths can be taken into account. Initially, all space is uniformly filled with a cone of rays, emanating from the selected point in space, which is forwarded to the first optical surface. BEAM-4 uses a Monte Carlo random ray generator to test each optical system. Each of the generated rays is traced through the optical train until it strikes a stop plane, misses an optical component, or reaches the final plane. The optical collection efficiency is proportional to the fraction of the rays that reach the final plane. Each ray is defined by a point of origin and a direction in which the ray propagates. A ray has no lateral width, no angular extent, and no polarization and is represented by the program as a mathematical abstraction that is a reliable indicator of a light train through an optic, provided that the optic is very much larger than a wavelength of light. BEAM-4 constructs a sequence of ray segments through a succession of optical surfaces, where each change of direction obeys the appropriate law of reflection or refraction at each surface. The program is free from any paraxial, meridional, or saggital simplifications and thus incorporates the effects of lens aberrations and astigmatisms into the efficiency calculations. The optical collection efficiency and spatial ray distribution graphs can be obtained from the software. The spatial ray distribution can be considered similar to a spatial intensity distribution.

The absolute collection efficiency (ϵ_a) from a point source for an individual optical system can be represented as the ratio between the number of rays that reach the final optical plane to the total number of rays, k, that are emitted from the source:[31]

$$\epsilon_a = \left(\sum_{i=1}^{k} n_i p_i / \sum_{i=1}^{k} n_i\right)(\Omega/4\pi) \qquad (1)$$

where n_i is the ith ray, p_i is 0 or 1 for blocked and passed rays, respectively, and Ω is the solid angle of the source cone of rays. Here, rays were generated within the same solid angle as determined by the same graphite furnace for each optical system, in which case eq 1 can be simplified to

$$\epsilon_{a,\Omega} = \sum_{i=1}^{k} n_i p_i / \sum_{i=1}^{k} n_i = N / \sum_{i=1}^{k} n_i \qquad (2)$$

where N is the total number of rays that reach the monochromator focal plane. This number is an indicator of the collection efficiency of different optical systems with the same Σn_i and Ω.

The ideal optical system, which is a system with hypothetical optical components that are free from any aberrations, would image the point source on the entrance slit plane of the monochromator as a dimensionless, abstract point with an intensity N. For a real, low-aberration system, the image of the point source would have real, albeit small, dimensions. The distribution of the collected intensities over the area of the image point would be a Gaussian distribution, due to the assumption that the rays would be generated randomly from the ideal point source.[33] Integration of the distribution over the image area would give the optical collection efficiency (ϵ_Ω),

$$\epsilon_\Omega = N/\int_0^{2\pi}\int_0^{a} e^{-r^2/\sigma^2} r \, dr \, d\theta = \ldots = N/2\pi\sigma^2(1 - e^{-a^2/\sigma^2}) \approx N/2\pi\left(\frac{a^2}{2} - \frac{a^4}{4\sigma^2}\right) \qquad (3)$$

where a is a radius of the image of the point, and r and θ are integration variables in polar coordinates. For a point source and an ideal optical system, it can be said that a would tend to zero, and eq 3 would tend to eq 4, which is a distribution with cylindrical symmetry:

$$\epsilon_\Omega = N/\int_0^{2\pi}\int_0^{a} r \, dr \, d\theta = \ldots = N/\pi a^2 \qquad (4)$$

In view of the observations of eqs 3 and 4, inspection of the shape of optical ray distributions at the image plane would reveal a more spread out Gaussian distribution in the presence of significant optical aberrations, while an optical system with fewer optical aberrations would give a ray distribution that would be less spread out, as it would tend toward cylindrical symmetry. For optical arrangements with approximately equal collection efficiency, visual inspection of the spatial distribution of the rays at the image plane would indicate whether or not there are significant aberrations that might lead to poor spatial resolution between background and fluorescence signals.

BEAM-4 has the capability to present two- and the three-dimensional graphs of the spatial distributions of the collected rays at the focal plane of the image, which can be visually inspected for the presence of aberrations in optical systems. Examples of such graphs are discussed in the following sections.

Model Systems. All of the calculations reported here were based on the experimental arrangements shown in Figure 1. The 45° angled iris (III, Figure 1) represented the angled window at the end of the furnace, as described by Wei et al.,[7] to minimize stray reflections into the detection system. The angled window was designed such that its edges subtended the same solid angle at the center of the furnace as the end of the graphite tube that faced the angled window. This solid angle determined the number of rays that were theoretically available for collection and was constant for all optical arrangements for a point source placed at the center of furnace. For the calculations that involved the point source shifted along the longitudinal axis of the furnace, the number of emitted rays was restricted by the dimensions of the graphite tube or by the iris of the angled window. The number of rays in the calculations varied as a function of the direction of the shift, as shown in Figure 2, where the solid angle filled by the cone of rays emanating from the graphite furnace is shown for each of the three positions in the furnace. BEAM-4 was used

(33) Levi, L. *Applied Optics. A Guide to Optical System Design*; John Wiley & Sons: New York, 1968; Vol. 1.

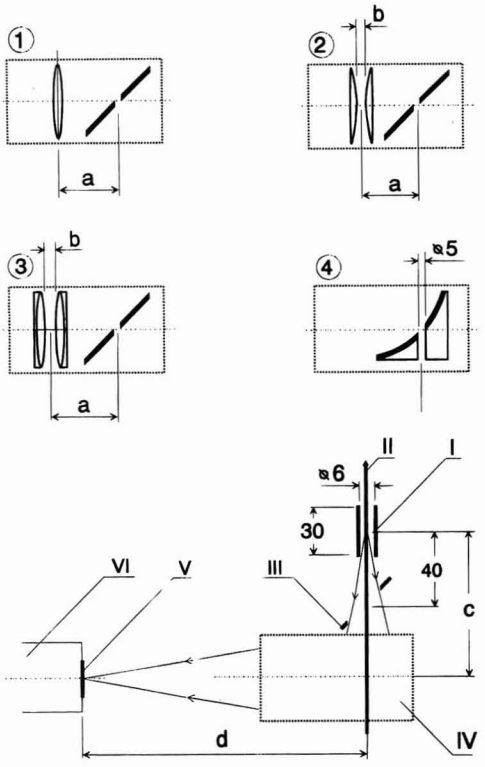

Figure 1. Optical arrangements for the ETA-LEAFS measurements. Lenses and mirrors depicted in the boxes 1–4 were inserted into the optical train depending upon which optical system was to be investigated. Dimensions *a*–*d* (Table 2) were chosen according to the specifications of the optical components (Table 1). I, Graphite tube; II, direction of the laser beam through the furnace; III, 45° angled quatz window; IV, region of the optical setup into which arrangements 1–4 were successively inserted for simulation or experimentation; V, entrance slit; VI, monochromator.

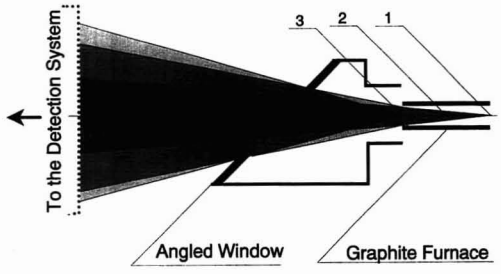

Figure 2. Solid angle filled by the cone of rays emanating from the graphite furnace as a function of the position of the point source within the tube: 1, point source at the end closest to the detection system; 2, point source at the center of the tube; 3, point source located farthest from the detection system.

to model the propagation and detection of the radiation flux at 180° to the direction of the laser beam for all the optical systems. This scheme is called front surface illumination, and it has been discussed in detail elsewhere.[1,34] In place of the dashed box in Figure 1, four different optical arrangements were modeled in BEAM-4, while three of the arrangements were also studied experimentally. The arrangements 1–3 consisted of various combinations of commercially available lenses with a plane mirror pierced centrally by a hole drilled at 45° for passage of the laser beam. The simplest was a single, symmetric, biconvex lens. Two other arrangements included matched pairs of plano-convex and achromatic lenses, respectively. The achromatic lens was modeled for comparison with the theoretical results of Farnsworth et al.,[31] but it was not investigated experimentally. The 90° off-axis ellipsoidal mirror in Figure 1 was designed to allow study of the behavior of an optical system that was nearly free of spherical aberrations, which would allow for maximum spatial discrimination between fluorescence and background signals. In all cases, the optics were arranged to focus the radiation flux on the entrance slit plane of the monochromator, and the optical distances were fixed to place the slit of the monochromator at the paraxial focal point, in order to achieve a 1:1 image. In the case of the off-axis ellipsoidal mirror, the point source and the monochromator slit were placed at opposite foci of the ellipse to gave a 1:1 image. A complete description of the optical components and their spacing is given in Tables 1 and 2. A detailed description of the design of the 90° off-axis ellipsoidal mirror is presented in the instrumentation section and in Figure 3.

The behaviors of the lenses were modeled for the collection of fluorescence at 340.5 nm, which is the wavelength for the determination of cobalt, except for the achromatic lenses, which were modeled at 486.1 nm, because these commercial lens examples did not transmit at wavelengths shorter than 400 nm.

Some simplifications were allowed in the modeling algorithm. The reflectivity of the mirrors and transmittance of the lenses were assumed to both be 1. The reflectivity of the field stops and apertures was assumed to be zero. The monochromator was not included in the ray trace but was assumed to exhibit ideal behavior. The dimensions of the monochromator slit were varied according to the experimental requirements. It was assumed that all rays which arrived at the entrance slit of the monochromator were counted and detected. The calculation for complete ray tracing of 1×10^4 rays from a single point required only several minutes.

Instrumentation and Reagents. The details of the instrumentation for ETA-LEAFS have been discussed elsewhere[5,12] and are summarized here. An excimer laser (EMG 104 MSC, Lambda Physik, Gottingen, Germany), which was operated with xenon chloride (308 nm) at a repetition rate of 500 Hz, was used to pump a tunable dye laser (FL32002E, Lambda Physik). For the determination of cobalt, Rhodamine 610 (*o*-(6-diethylamino-3-diethylimino-3*H*-xanthen-9-yl)benzoic acid; Exiton, Dayton, OH) was employed as the laser dye at concentrations of 0.91 and 0.30 g L^{-1} in absolute methanol for the oscillator and amplifier dye cells, respectively. Cobalt atoms were excited at 304.400 nm, and fluorescence was detected at 340.5 nm. For the determination of phosphorus, stilbene 420 (2,2′-[(1,1′-biphenyl-4,4′-diyl)di-2,1-ethenediyl]bisbenzenesulfonic acid disodium salt; Exiton) was employed as the laser dye at concentrations of 0.65 and 0.22 g L^{-1} in absolute methanol for the oscillator and amplifier dye cells, respectively. Phosphorus atoms were excited at 213.618 nm, and fluorescence was detected simultaneously at 253.4 and 253.6 nm with the monochromator set at 254.5 nm. The frequency-doubled output was passed through the graphite furnace atomizer (HGA-

(34) Goforth, D.; Winefordner, J. D. *Anal. Chem.* **1986**, *58*, 2598–2602.

Table 1. Parameters of the Optical Components

optical component	surface	focal length[a] (mm)	diameter (mm)	curvature[b]	thickness (mm)	model no./manufacturer	material
plane mirror	first		55.0				$AlMgF_2$[e]
biconvex symmetric lens	first	48.45	50.8	0.0202	9.30	39335/Oriel Corp., Stratford, CT	fused silica
	second			−0.0202			
plano-convex lenses	first	95.38	50.8	0.0194	9.70	41765/Oriel Corp., Stratford, CT	fused silica
	second			0			
achromatic lenses	first	100.00	38.1	0.0147	9.20	PAC073/Newport Corp., Fountain Valley, CA	BaFN10[d]
	second			−0.0230	3.20		SF10[d]
	third			−0.0021			
90° off-axis ellipsoidal mirror	first	$F_1 = 140.00$	89.0	0.0110[c]		Aero Research Associates, Inc., Port Washington, NY	$AlMgF_2$[e]
		$F_2 = 260.00$					

[a] Focal length at 486.1 nm for the achromatic lenses; for other optics at 340.5 nm. [b] Curvature = $1/r$, where r is the lens radius. [c] Curvature = $\alpha/\beta^{1/2}$ (Figure 3). [d] BaFN10 and SF10 are glass designations of Scott Glaswerke, Mainz, Germany. [e] Aluminum reflective surface with magnesium fluoride overcoat.

Table 2. Optical Distances for the Different Optical Arrangements

dimension[a]	lens: biconvex	lens: plano-convex	lens: achromatic	90° off-axis ellipsoidal mirror
a	26.9	41.9	47.9	
b		5.0	5.0	
c	70.0	60.0	60.0	140.0
d	129.0	158.5	155.8	260.0
α				200.0
β				134.9
γ				147.7

[a] Dimensions $a-d$ refer to Figure 1; dimensions $\alpha-\gamma$ refer to Figure 3. All dimensions are in mm.

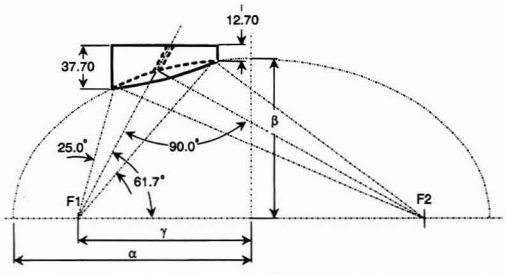

Figure 3. Dimensional diagram for the 90° off-axis ellipsoidal mirror. Solid lines define the body of the mirror fragment. All dimensions and symbols are given in Table 1.

500 with AS-40 autosampler; Perkin-Elmer, Norwalk, CT). Standard graphite furnace temperature programs[35] were used for the determination of cobalt and phosphorus in aqueous solutions. Both windows of the furnace were angled to reduce the stray laser background radiation.[7]

All the optical systems were assembled according to preliminary theoretical calculations. The 90° off-axis ellipsoidal mirror (Figure 3) was designed by use of BEAM-4 in our laboratory and was built by Aero Research Associates Inc. (Port Washington, NY). It was built from brass and the nickel plated. The reflective surface was coated with aluminum, followed by a magnesium fluoride overcoat. The working reflectance range for the mirror was 200−700 nm, with >80% reflectivity through a 1 mm^2 area at F_2 from a point source at F_1.

The detection system consisted of a monochromator (F/3.5, 100 mm focal length, 8 nm mm^{-1} dispersion, Model H-10; Instruments SA, Metuchen, NJ), a photomultiplier tube (9893QB-350; Thorn-EMI, Fairfield, NJ) optimized for pulsed laser operation, a preamplifier (VV 100BTB; LeCroy, Spring Valley, NY) with a gain of 10, and a boxcar integrator (Model 162/165; Princeton Applied Research, Princeton, NJ) with a gate width of 5 ns, a gate time constant of 0.5 μs, and an output time constant of 10 ms. The fluorescence data were collected with a personal computer (PCs Limited 200, Model 80286; DELL Computer Corp., Austin, TX) by use of Asyst software (Rochester, NY). The integrated signal peak area was employed throughout this work.

A commercially available 1000 mg L^{-1} cobalt stock solution was used (J. T. Baker, Phillipsburg, NJ). A 1000 mg L^{-1} phosphorus stock solution was prepared from ammonium dihydrogen phosphate ($NH_3H_2PO_4$) in 0.5% nitric acid (99.999% pure; Aldrich, Milwaukee, WI). The analyte working solutions were prepared daily by dilution of the stock solutions with 0.5% nitric acid. A commercially available 1000 mg L^{-1} nickel solution (J. T. Baker, Phillipsburg, NJ) was employed as a chemical modifier for the determination of phosphorus.[13]

Detection Limits and Calibration Graphs. The standard procedure for the determination of the ETA-LEAFS detection limits has been discussed in detail elsewhere[7,36] and is summarized here. The detection limits were determined by extrapolation of the calibration graph to a signal level equal to 3 times the standard deviation (3σ) of 16 measurements of the blank noise. The measurements of the blank noise were performed either with the laser tuned to the analytical wavelength, which is an "on-line" measurement usually dominated by noise from analyte contamination, or with the laser tuned 0.2 nm away from the analytical wavelength, which is an "off-line" measurements usually dominated by instrumentation noise. Attenuation of the ETA-LEAFS signals was performed by reduction of the PMT voltage and/or by insertion of calibrated neutral density filters in front of the entrance slit of the monochromator.

Signal-to-background ratio measurements were performed experimentally as a function of the position of the optical components relative to the monochromator slit by variation of

(35) Slavin, W. *Graphite Furnace AAS, A Source Book*; The Perkin-Elmer Corp.: Ridgefield, CT, 1984.

(36) Long, G. L.; Winefordner, J. D. *Anal. Chem.* **1983**, *55*, 713A−724A.

distance d in Figure 1. Measurements at each distance d involved duplicate measurements of the analytical signal from a 20 μL aliquot of 1 μg L^{-1} standard solutions and from a blank. For the direct measurement of the mostly blackbody radiation or continuum background signal, the boxcar averager was set to the dc mode. For all other types of measurements, the boxcar averager was set to the ac mode that effectively provided automatic background subtraction from the total signal. The monochromator position was varied along the direction of the propagation of the radiation flux, and the center of the monochromator slit was always positioned in the center of the cross section of the radiation flux.

RESULTS AND DISCUSSION

Two basic types of simulation were done. The first was to obtain spatial ray distribution maps in the image plane. These allowed a pictorial, or qualitative, evaluation of the aberrations that resulted from a particular optical system. Unlike the first, the second simulation restricted the image plane to variable slit sizes typical of those normally used on a monochromator. The ratio between the number of rays that reached the monochromator focal plane through each of the simulated slits to the total number of rays that were emitted from the point source was calculated as a measure of collection efficiency of radiation. Rays aberrated out of the slit opening reduced the predicted collection efficiency. Those distribution maps that indicated that the image had a more spread out distribution were expected to show lower collection efficiencies.

Recent studies[37-41] indicate that, during atomization, atoms practically fill all free space in the atomizer, due to propagation of the analyte cloud along the longitudinal axis of the furnace.[40] Therefore, fluorescence can be expected to be collected simultaneously from almost the full volume of the gaseous phase along the longitudinal axis of the atomizer. BEAM-4 did not allow the simulation of a finite volume volume, but this was circumvented, to some extent, by use of a point source located at one of three positions (Figure 2) at the back, middle, and front of the furnace. The position of the monochromator image plane was fixed during the simulation to focus only the center of the furnace so that the image of the point source became defocused as it was moved to either end of the furnace. This situation attempted to approximate reality, where the monochromator is always in a fixed position. Conversely, during the experimental work, it was assumed that movement of the monochromator would be equivalent to investigation of the collection efficiency from different points within in the furnace.

Simulated spatial ray distributions imaged at the focal plane of the monochromator are shown in Figures 4–7. The details of the scales on these figures were omitted because they were mant to illustrate only the shape of spatial distributions as discussed in connection with eq 4 earlier. A quantitative evaluation of the collection efficiency is discussed later in connection with Figure 8. The example of a biconvex lens in the detection system, Figure

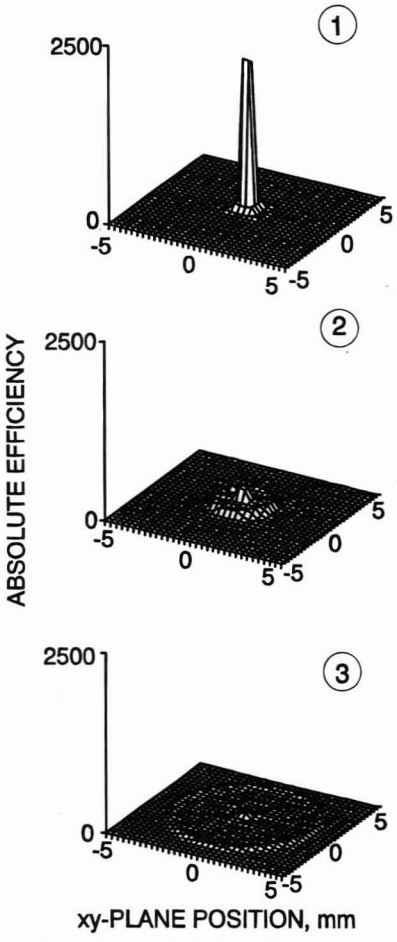

Figure 4. Three-dimensional collection efficiency maps at the focal plane of the monochromator for the biconvex lens. Maps are based on a point source located inside the atomizer in the positions identified as 1, 2, and 3 in Figure 2. For all cases, the optical train dimensions between the optical components were kept constant according to Table 2.

1, arrangement 1, demonstrated the worst case of severe optical aberrations (Figure 4). The rays collected from all three point sources in the furnace gave distributions with significant spreading; moreover, it was surprising to observe that the image of a point source placed at the center of the furnace was spread out more than the image from a point source at the back of the furnace. The presence of strong optical aberrations was confirmed by the worst relative efficiency among all the optical arrangements for all the tested slit widths (Figure 8), which indicated that the aberrations spread out the image so much that most of the light did not pass through the monochromator slit.

The use of plano-convex lenses illustrated improved, less spread ray distribution profiles and a more nearly Gaussian distribution of the image from the central part of the atomizer (Figure 5). This system still had severe aberrations, but it demonstrated a 2-fold improvement in collection efficiency for all

(37) Holcombe, J. A. *Anal. Chem.* **1991**, *63*, 1918–1926.
(38) Gilmutdinov, A. Kh.; Zakharov, Yu. A.; Ivanov, V. P.; Voloshin, A. V. *J. Anal. At. Spectrom.* **1991**, *6*, 505–519.
(39) Gilmutdinov, A. Kh.; Zakharov, Yu. A.; Ivanov, V. P.; Voloshin, A. V.; Dittrich, K. *J. Anal. At. Spectrom.* **1992**, 47, 675–683.
(40) Gilmutdinov, A. Kh.; Zakharov, Yu. A.; Voloshin, A. V. *J. Anal. At. Spectrom.* **1993**, *8*, 387–395.
(41) Gilmutdinov, A. Kh.; Nagulin, K. Yu.; Zakharov, Yu. A. *J. Anal. At. Spectrom.* **1994**, *9*, 643–650.

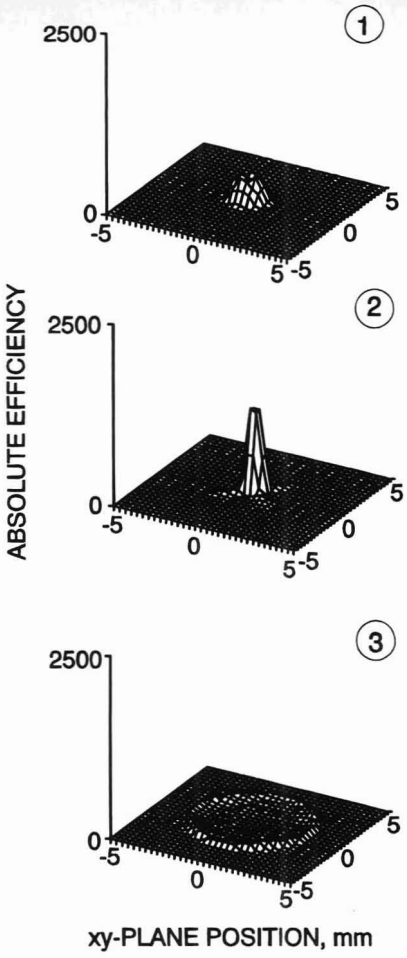

Figure 5. Three-dimensional collection efficiency maps at the focal plane of the monochromator for the plano-convex lenses. Maps are based on a point source located inside the atomizer in the positions identified as 1, 2, and 3 in Figure 2. For all cases, the optical train dimensions between the optical components were kept constant according to Table 2.

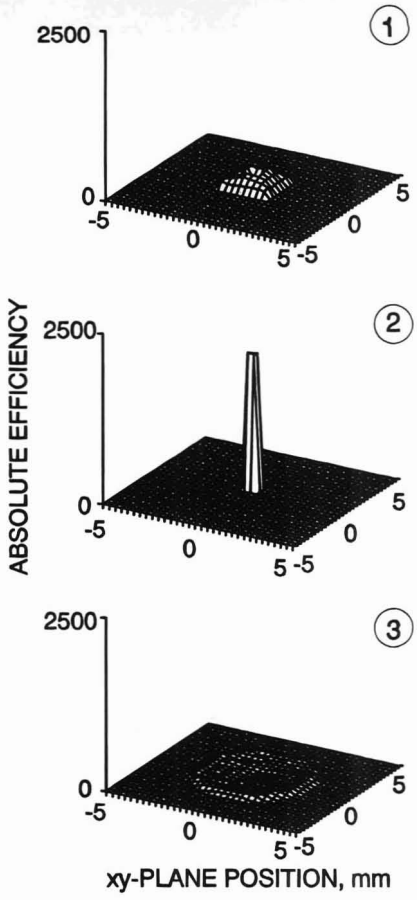

Figure 6. Three-dimensional collection efficiency maps at the focal plane of the monochromator for the achromatic lenses. Maps are based on a point source located inside the atomizer in the positions identified as 1, 2, and 3 in Figure 2. For all cases, the optical train dimensions between the optical components were kept constant according to Table 2.

but the largest slit width over the biconvex lens system (Figure 8). This dramatic change in collection efficiency as a function of slit width has always been a serious problem for the experimental optimization of detection systems of ETA-LEAFS in the presence of blackbody radiation. On the one hand, the slit width must be minimized to spatially block blackbody radiation and thus improve the signal-to-noise ratio. On the other hand, the minimization of the slit width significantly decreases the collection efficiency of the fluorescence radiation due to the optical aberrations, with the most extreme example being for the biconvex lens system quantified in Figure 8.

The last two optical systems were a matched pair of achromatic lenses (Figure 6) and an off-axis ellipsoidal mirror (Figure 7), both of which illustrated the expected very large reductions in spherical aberrations. Both arrangements provided a relatively small image of the focused point source from the center of the furnace and a distribution from the defocused edges of the atomizer that appeared to be closer to Gaussian than the rather distorted distributions seen in Figures 4 and 5. For the mirror, as a result of the absence of many types of optical aberrations in the system, the collection efficiencies from the center of the atomizer were constant and the best ones for all slit widths (Figure 8). From a practical point of view, this indicates that the discrimination against blackbody radiation in the system can be optimized experimentally by changing the slit width on the monochromator, without concomitant compromise in collection efficiency. The collection efficiency as a function of the slit width for the pair of matched achromatic lenses was considerably better than those of the biconvex and plano-convex lenses and almost the same as that of the off-axis mirror at wide slit widths, but not at small slit widths (Figure 8). We did not test the achromatic lenses experimentally.

Effect of the Ellipsoidal MIrror on the Detection Limit. Detection limits were measured for cobalt and phosphorus for the biconvex, plano-convex, and ellipsoidal optical systems to

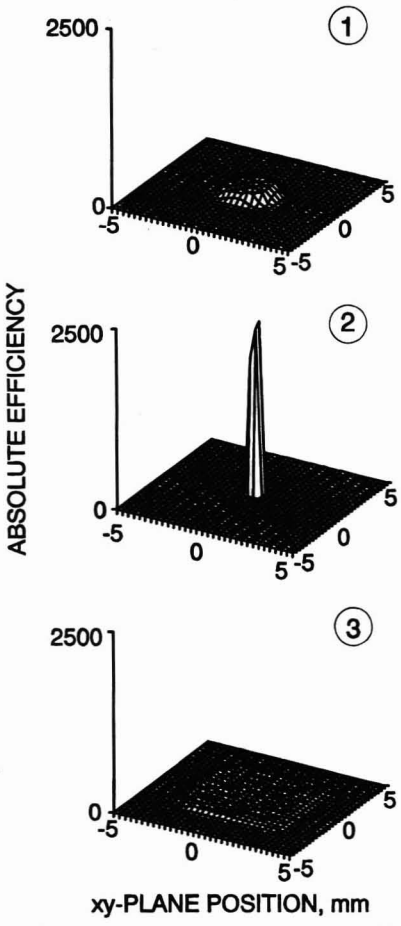

Figure 7. Three-dimensional collection efficiency maps at the focal plane of the monochromator for the ellipsoidal mirror. Maps are based on a point source located inside the atomizer in the positions identified as 1, 2, and 3 in Figure 2. For all cases, the optical train dimensions between the optical components were kept constant according to Table 2.

determine whether or not the mirror was able to provide any improvement through spatial discrimination against blackbody radiation. All the optical arrangements were designed to collect radiation emitted from the same solid angle (0.047π, Figure 2), determined by the physical dimensions of the graphite atomizer, length 28 mm, i.d. 6 mm. As each of the optical arrangements collected radiation from the same solid angle, it was expected that differences in the measured detection limits between different optical arrangements were likely to be due only to variations in the degree of spatial discrimination between blackbody and fluorescence radiation. In order to ensure a rigorous comparison between the three optical systems, the slit widths were optimized prior to measurement of the detection limits.

It is generally accepted[7] that, for dispersive detection systems, the atomic fluorescence signal is proportional to the slit width, while the blackbody radiation signal, which can be considered to be a wavelength continuum, varies in proportion with the square of the slit width, due to a combined increase in both radiant energy collected and spectral band passed by the monochromator. In the case where shot noise on the blackbody radiation is dominant, the signal-to-noise ratio at the detection limit becomes independent of slit width, since the noise is the square root of the total background signal. If flicker noise were to dominate, the noise would be proportional to the background signal, and the signal-to-noise ratio at the detection limit would become degraded with increased monochromator slit width. For cobalt and phosphorus, some simple experiments were done to determine whether or not the ellipsoidal mirror had an effect on the expected relationships. The effect of slit width was done only for the ellipsoidal mirror, as slit width optimizations for lenses have been reported many times before[30] and followed predictable behaviors, albeit they have not been easy to reproduce. For the lens systems, 1 mm slit widths have generally been shown to be optimum with the equipment used here.[30]

Cobalt and phosphorus were of particular interest since they had both been studied extensively in our laboratory in conjunction with lens-based optical systems, and they exhibited two different types of limiting noise. The detection limits were known to be dominated by noise on the blackbody radiation in the case of cobalt and by laser stray radiation in the case of phosphorus. With use of the off-axis mirror, the effect of slit width on the fluorescence signal and background noise of cobalt and phosphorus were measured. The results for cobalt are shown in Figure 9, and the phosphorus data were similar. The background noise was measured in the same way as the noise for all detection limits, i.e., by measurement of the standard deviation (σ) of 16 measurements of the "off-line" acid blank signal. For both elements, the slope of the middle part of the graph of noise vs slit width was 1, as expected for shot noise on a continuum background, while the slope of the signal vs slit width in the middle of the range of slits was different for the two elements. Phosphorus gave a signal slope of 1, as expected, but cobalt gave a slope of 2 (Figure 9), due to the presence of a large number of fluorescent lines at the detection wavelength. There are about half a dozen possible cobalt lines in the region of 340.5 nm. The bandpass of the spectrometer varied from 0.8 nm at 0.1 mm slit width to 32 nm at 4 mm slit width. All these bandpasses included progressively more cobalt lines as the slit width was increased. This would be expected to give a slope of 2 for the same reason that a continuum background signals varies with a slope of 2 during a slit width optimization. The phosphorus fluorescence was detected at two lines 0.2 nm apart which did not appear to behave like a continuum because the two lines were close together and well within the bandpass of the smallest slit width. At the smallest and largest slit widths, the slit width optimization curves bent somewhat, probably due to diffraction effects at small slit widths and a contribution from increased blackbody radiation at large slit widths. The degradations in signal-to-noise ratio at small and large slit widths were no different from past experience with lens-based optical systems. However, the data were much more reproducible for reasons discussed in a following section on optical alignment.

The caption to Figure 9 shows the variation in cobalt detection limit as a function of slit width, calculated from the data in Figure 9. The dominant trend was a degradation in detection limit at small and large slit widths, with the result that the best slit width was in the middle of the range at the 1−2 mm slit widths. This was the same for both cobalt and phosphorus.

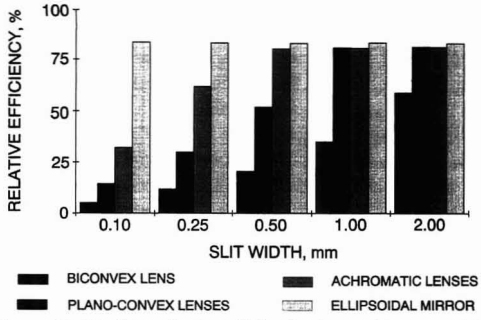

Figure 8. Absolute collection efficiencies for a point source of the center of the furnace (Figure 2) focused on the monochromator slit plane. Computations were done for the different optical arrangements as a function of monochromator slit width. The height for all slits was 5 mm, which corresponded to the slit height of the monochromator in the experimental ETA-LEAFS setup.

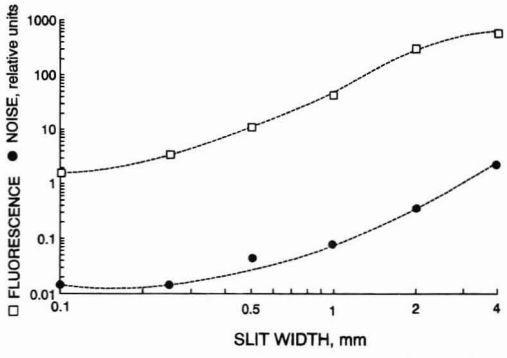

Figure 9. Effect of slit width on the fluorescence signal (□) and "off-line" noise (●) for 20 pg of cobalt. The 90° off-axis ellipsoidal mirror was employed for the collection of radiation flux in the detection system. For cobalt, the corresponding detection limits (fg), at each slit width in parentheses (mm) were 1000 (0.1), 300 (0.25), 80 (0.5), 20 (1.0), 30 (2.0), and 70 (4.0), all rounded to one significant figure.

In a careful substitution experiment, the cobalt detection limit was measured at a slit width of 1 mm with the biconvex lens, the pair of plano-convex lenses, and the ellipsoidal mirror. Detection limits were measured several times for each optical arrangement in order to ensure reproducibility. A detection limit of 200 fg was obtained for the biconvex lens. This value was in agreement with the detection limit reported in previous work[12] on the determination cobalt by ETA-LEAFS at the same slit width and with the same biconvex lens detection system. In the present work, the detection limit was further improved to 100 fg by use of the plano-convex lenses, and a detection limit of 20 fg was obtained by use of the ellipsoidal mirror, under experimental conditions identical to those used in the previous work. The last detection limit was a factor of 5 superior to that obtained with the plano-convex lenses and a factor of 10 superior to that obtained with the bioconvex lens. Visual inspection of the BEAM-4 simulations indicated that the ellipsoidal mirror would have fewer optical aberrations (Figure 7) than the lens systems. This led to predictions of better collection efficiency at all slit widths (Figure 8) because radiation would not aberrate out of the slit area as much as for the lenses. It follows that blackbody radiation would be aberrated into the slit area less for the mirror than the lenses, which should lead to better spatial discrimination between fluorescence and blackbody radiation. This was borne out by the improved detection limits that were observed.

Table 3. Detection Limits of Cobalt by Different Techniques

method	detection limit[a] in fg[b]	detection limit[a] in ng L^{-1}
ETA-LEAFS (present work)	20	1
ETA-LEAFS[12]	100	5
ETV-ICPMS[42]	20	1
ICPMS[43]		7
GF-AAS[44]	1000	50
LEI[c,45]		1000

[a] Rounded to one significant figure. [b] Based on 20 mL sample volumes. [c] Flame laser-enhanced ionization spectrometry.

Some recent detection limits for cobalt, obtained by various alternative spectroscopic techniques, are presented in Table 3 for comparative purposes. The ETA-LEAFS detection limit of 20 fg, reported here, is comparable to the technique of electrothermal vaporization inductively coupled mass spectrometry (ETV-ICPMS). For cobalt, the two techniques are roughly comparable in terms of sensitivity and microsampling capability, and both techniques are single element rather than multielement, as the problems of multielement analysis in ETV-ICPMS are not yet resolved.

For phosphorus, the use of the ellipsoidal mirror again gave no improvement in detection limit over the use of lenses either in the present work or compared to previous ETA-LEAFS phosphorus work;[13] probably because the blackbody radiation was insignificant around 253 nm, and the increased discrimination against blackbody radiation thus became moot. The resultant phosphorus detection limit was 7 pg, which has been compared to other techniques in ref 13.

Effect of the Optical Alignment of the Detection System on the Signal-to-Background Ratio. Experience in the present authors' laboratory has indicated that optical alignment of lens systems is very critical in that the lenses must be in the correct position within about 1 mm. Misalignment of the optical components due to external factors, such as laboratory temperature, vibrationally caused misalignment, or instrument rebuild, affects the reproducibility and the sensitivity of the detection system on both a short-term and a long-term basis. It appears logical that, in order to maintain a more stable collection efficiency in the presence of such factors, the optical arrangement should provide a high degree of discrimination between fluorescence signal and background radiation. It was clear during the experimental work for this paper that the ellipsoidal mirror appeared to be easier to align than lens systems. Hence, experiments were designed to test this.

The normalized signal-to-background ratios for the ellipsoidal mirror and the different lens systems, as a function of the optical alignment, are presented in Figure 10 for cobalt and phosphorus. The zero value on the *x*-axis corresponds to the optimum distances

(42) Tsukahara, R.; Kubota, M. *Spectrochim. Acta* **1990**, *45B*, 779–787.
(43) Akatsuka, K.; McLaren, J. W.; Lam, J. W.; Berman, S. S. *J. Anal. At. Spectrom.* **1992**, *7*, 889–894.
(44) *The Guide To Techniques and Applications of Atomic Spectroscopy*; The Perkin-Elmer Corp.: Norwalk, CT, 1988.
(45) Axner, O.; Rubinsztein-Dunlop, H. *Spectrochim. Acta* **1989**, *44B*, 835–866.

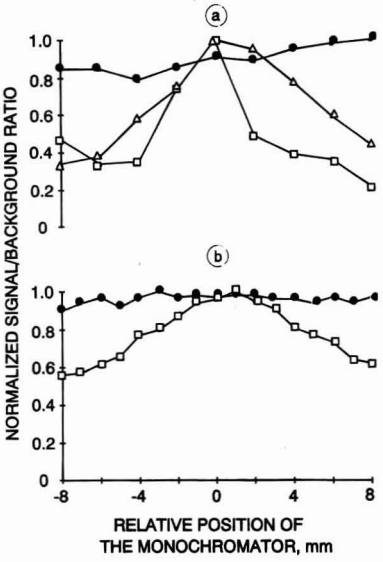

Figure 10. Effect of monochromator-optics position on signal-to-background ratio for cobalt (a) and phosphorus (b). ●, Ellipsoidal mirror; △, plano-convex lenses; and □, biconvex lens. For the optical arrangements, see Figure 1. Each fluorescence signal was calculated as the difference between the analytical signal from a 20 μL aliquot of 1 μg L^{-1} standard solutions and from a blank. The ratios between fluorescence signal and background radiation were calculated for each position of the monochromator. These data were normalized in signal size in order to allow comparisons between different optical arrangements.

d (Table 2) at which the highest signal-to-background ratios were obtained for the each optical arrangement. The signal-to-background ratio for the ellipsoidal mirror remained practically unchanged, with a ±15% average deviation from unity, for all tested positions for both elements. It can be considered that cobalt (Figure 10a) represents cases where blackbody radiation is the dominant noise, while phosphorus (Figure 10b) represents cases where other sources of noise, such as laser-scattered radiation, are dominant. For the lenses and for both elements, the signal-to-background ratio dropped by almost a factor of 2 when the lenses were displaced by 2 mm from the optimal position (Figure 10a). The pair of plano-convex lenses, which was tested only for cobalt, represented an intermediate case that did not seem to display any significant improvement over the biconvex lens from this alignment point of view.

These experimental results were consistent with the collection efficiency calculations and can be interpreted in light of the data obtained for the ray distribution profiles, Figures 4–7, for the different optical arrangements. The almost constant signal-to-background ratio in the case of the ellipsoidal mirror for the all monochromator optics positions indicated that the fluorescence and background signals that were generated from the central and peripheral parts of the atomizer were spatially resolved to a greater degree than for the lenses.

ACKNOWLEDGMENT

This work was supported by an American Chemical Society, Division of Analytical Chemistry, Fellowship sponsored by Perkin-Elmer Co., In. (awarded to A.I.Y.). The material was presented in part at the 45th Pittsburgh Conference on Analytical Chemistry and Applied Spectroscopy, Chicago, IL, February 27–March 4, 1994, paper 528P, and at the XXI Annual Meeting of the Federation of Analytical Chemistry and Spectroscopy Societies (FACSS), St. Louis, MO, October 2–7, 1994, paper 894. The ETA-LEAFS equipment used was purchased with funds from National Institutes of Health Grant GM 32002.

Received for review November 7, 1994. Accepted April 11, 1995.[⊗]

AC941074U

[⊗] Abstract published in *Advance ACS Abstracts*, June 1, 1995.

Anal. Chem. **1995,** *67,* 2256–2263

Detection of ^{14}N and ^{35}Cl in Cocaine Base and Hydrochloride Using NQR, NMR, and SQUID Techniques

James P. Yesinowski,* Michael L. Buess,† and Allen N. Garroway

Chemistry Division, Code 6122, Naval Research Laboratory, Washington, DC 20375-5342

Marcia Ziegeweid and Alexander Pines

Department of Chemistry, University of California, and Materials Sciences Division, Lawrence Berkeley Laboratory, Berkeley, California 94720

Results from ^{14}N pure NQR of cocaine in the free base form (cocaine base) yield a nuclear quadrupole coupling constant (NQCC) e^2Qq/h of 5.0229 (±0.0001) MHz and an asymmetry parameter η of 0.0395 (±0.0001) at 295 K, with corresponding values of 5.0460 (±0.0013) MHz and 0.0353 (±0.0008) at 77 K. The NQR peaks of a sample of cocaine base containing ~1% impurities are a factor of 3 broader than those of a recrystallized sample, but spin–lattice and spin–spin relaxation times are essentially unchanged. Both pure NQR (at 295–77 K) and a superconducting quantum interference device (SQUID) detector (at 4.2 K) were used to measure the very low (<1 MHz) ^{14}N transition frequencies in cocaine hydrochloride; at 295 K the NQCC is 1.1780 (±0.0014) MHz and the asymmetry parameter is 0.2632 (±0.0034). Cocaine hydrochloride exhibits a broad ^{35}Cl pure NQR resonance at 2.53 MHz. The ^{35}Cl NMR spectrum at 7.0 T is that of a central $^1/_2 \rightarrow -^1/_2$ transition greatly broadened by second-order quadrupolar effects. Stepping the carrier frequency enables one to obtain a powder pattern without the severe intensity distortions that otherwise arise from finite pulse power. A powder pattern simulation using an NQCC value of 5.027 MHz and an asymmetry parameter η of 0.2 agrees reasonably well with the experimental stepped-frequency spectrum. The use of pure NQR for providing nondestructive, quantitative, and highly specific detection of crystalline compounds is discussed, as are experimental strategies.

Nuclear quadrupole resonance (NQR) is a radio frequency spectroscopy offering rather special possibilities for the analytical detection of chemical substances in solid form. When carried out in the absence of an external magnetic field, the technique is referred to as "pure NQR". Both continuous-wave (CW) and pulsed versions of pure NQR are feasible. Pure NQR has a number of advantageous characteristics as an analytical technique, since it is (1) highly specific with regard to the chemical and crystalline form of a substance; (2) nondestructive; (3) quantitative; (4) capable of detecting compounds heterogeneously distributed over large volumes; (5) able to yield results quickly (in favorable cases), with no sample preparation; (6) sensitive to the presence of cocrystallized impurities in the sample; (7) not limited by the requirement of an external magnetic field, as is the case with other magnetic resonance techniques; and (8) relatively inexpensive. Some of these same advantages may, in a different context, instead be weaknesses (points 1 and 6 in particular). Also, one serious limitation to the more widespread use of pure NQR as an analytical technique is the general requirement for samples containing many grams or tens of grams of the compound being detected, although schemes mentioned in this paper can offer significant improvements in sensitivity in appropriate cases. Furthermore, it is usually time-consuming, and often impracticable, to use pure NQR to search for unknown NQR transition frequencies. As will be shown in this paper, the use of superconducting quantum interference device (SQUID) techniques to determine unknown NQR frequencies for pulsed NQR detection represents a potentially useful strategy that may enable wider use of NQR as an analytical technique for a greater variety of substances.

Nitrogen is present as a heteroatom in many compounds of pharmacologic and biological interest. The ^{14}N stable isotope of nitrogen has a natural abundance of 99.635%, a nuclear spin $I = 1$ with a corresponding nuclear electric quadrupole moment, and pure NQR transitions at frequencies ranging from 0 to 6 MHz.[1] The frequency of the NQR peaks depends primarily upon the distribution of the electrons in the bonds surrounding the nitrogen atom of interest and, more specifically, upon the electric field gradient (EFG) tensor resulting from this distribution. Knowledge of the latter quantity, obtained from pure NQR measurements, is of some interest from the standpoint of theoretical chemistry. From an analytical chemistry point of view, knowledge of the ^{14}N NQR frequencies and other parameters is important because of the possibility of using ^{14}N NQR as a *compound-selective* technique for the identification of specific crystalline substances in the solid state. The number of reported ^{14}N NQR resonance frequencies taken from a database of ~10 000 compounds[2] (not necessarily containing nitrogen) reaches a maximum of ~600 in the range 2.5–3.0 MHz. For *representative* ^{14}N NQR line widths of <1 kHz, it is apparent that few "NQR interferences" should arise within this set of compounds. Where such interferences do arise, observation of both ν_+ and ν_- transitions in the same sample, as

* Yesinows@nrlfs1.nrl.navy.mil

† SFA, Inc., Landover MD 20875.

(1) Lucken, E. A. C. *Nuclear Quadrupole Coupling Constants;* Academic Press: London, 1969.

(2) Chihara, H. *J. Mol. Struct.* **1982,** *83,* 1–7.

0003-2700/95/0367-2256$9.00/0 © 1995 American Chemical Society

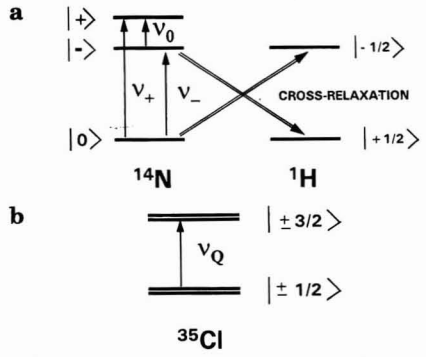

Figure 1. Energy level diagrams of quadrupolar nuclear spins. (a) ^{14}N ($I = 1$) in a weak magnetic field, illustrating the matching of the energy level separations of the nitrogen (ν_- transition) and those of a nearby proton ($I = {}^1/_2$), which results in cross-relaxation. Sweeping the frequency region near the ν_+ transition generates a SQUID signal, as seen in Figure 5. Additional saturation of the third transition ν_0 enhances the signal. For pure ^{14}N NQR, transitions ν_+ and ν_- can be observed directly in zero magnetic field; the ν_0 transition at lower frequency is often much weaker and not observed. (b) ^{35}Cl ($I = {}^3/_2$) in zero magnetic field. The resultant pure NQR spectrum consists of only a single transition between the doubly degenerate states at frequency ν_Q.

discussed below and shown on the left portion of Figure 1a, should provide a unique signature.

Two rather different techniques have been used to obtain ^{14}N NQR data in this paper, pure NQR (using pulsed techniques) and detection using a SQUID. Pulsed pure NQR techniques have proven applicable to the detection of ^{14}N nuclei in large sample volumes of the order of 300 L.[3] Such techniques can also yield reliable information about line widths and the spin–lattice (T_1) and spin–spin (T_2) relaxation times of the ^{14}N nucleus. Pulsed pure NQR techniques are also useful for investigating the effect of impurities in the sample upon these parameters. Only cocrystallized impurities are expected to have an effect, since a simple physical admixture will have parameters characteristic of the individual components. On the other hand, techniques using the SQUID take advantage of its high sensitivity to measure transitions at low frequencies that are more difficult to detect with pulsed pure NQR using Faraday law detectors. The continuous-wave spectrometer used for these SQUID experiments detects the change in magnetic flux proportional to ΔI_z, where I_z is the component of the spin along an externally applied magnetic field. Because of the quenching of the nitrogen magnetic moment in zero and low magnetic fields,[4] the SQUID does not detect the nitrogen transition directly, but rather is employed to probe the effect of the nitrogen transitions on the protons via the nitrogen–proton dipolar interaction. The CW SQUID spectrometer also has the advantage of being able to sweep wide frequency ranges and, therefore, is useful in searching for and identifying transitions.

Nuclei with spin $I = 1$ such as ^{14}N are subject to the electric quadrupole interaction described by the quadrupole Hamiltonian $H_Q = (e^2Qq/4)[3I_z^2 - I^2 + \eta(I_x^2 - I_y^2)]$.[1] The nuclear electric quadrupole moment, eQ, interacts with the electric field gradient, eq, and its associated asymmetry parameter, η, which arise from the local electronic environment surrounding the nucleus. The nuclear quadrupole coupling constant (NQCC) e^2Qq/h and the asymmetry parameter η contain structural information about this environment. In zero magnetic field the quadrupolar eigenstates $|+\rangle = (|1\rangle + |-1\rangle)/(2)^{1/2}$, $|-\rangle = (|1\rangle - |-1\rangle)/(2)^{1/2}$, and $|0\rangle$ (where $|1\rangle$, $|0\rangle$, and $|-1\rangle$ denote states having projections of nuclear spin along the z direction of 1, 0, and -1, respectively) give rise to three transitions at frequencies:

$$\nu_+ = (e^2Qq/h)(3 + \eta)/4$$

$$\nu_- = (e^2Qq/h)(3 - \eta)/4$$

$$\nu_0 = \nu_+ - \nu_- = (e^2Qq/h)(\eta/2)$$

as shown schematically in Figure 1a. Knowledge of two transition frequencies is sufficient to determine the quadrupolar parameters, if the transitions can be assigned to ν_+, ν_-, or ν_0. The transition energies change slightly in the presence of a weak magnetic field;[5] the data in this paper have been corrected for this effect.

Nuclei with $I = {}^3/_2$ such as ^{35}Cl give rise to only a single transition at a frequency of $\nu_Q = (e^2Qq/2h)(1 + \eta^2/3)^{1/2}$, as shown in Figure 1b.[1] Thus, standard pure NQR experiments cannot separate the NQCC from the asymmetry parameter. Observation of the "central" transition between the ${}^1/_2$ and $-{}^1/_2$ states in high-field NMR experiments can provide such information if a second-order quadrupolar-broadened pattern is observed.[6] We note that there are two stable isotopes of chlorine with $I = {}^3/_2$, ^{35}Cl and ^{37}Cl. The ^{35}Cl isotope is more favorable for NQR detection, since it has a higher natural abundance (75.4% vs 24.6% for ^{37}Cl) and a larger nuclear quadrupole moment.[1]

In this paper we report experimental results for ^{14}N NQR signals in samples of cocaine free base ($C_{17}H_{21}NO_4$, CAS 50-36-2) and cocaine hydrochloride ($C_{17}H_{22}NO_4Cl$, CAS 53-21-4), whose crystal structure is depicted in Figure 2. Measuring ^{14}N NQR transition frequencies using the SQUID for detection is shown to represent a useful search strategy in pure NQR studies. We also report both pure ^{35}Cl NQR and high-field stepped-frequency ^{35}Cl NMR results for cocaine hydrochloride; the combined results enable accurate determination of both the NQCC and the asym-

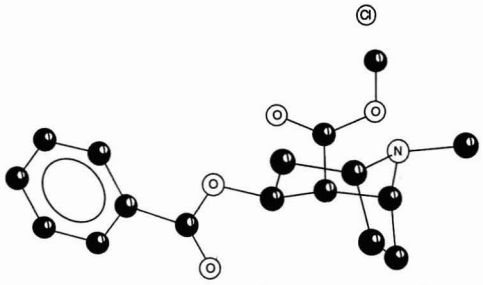

Figure 2. Structure of cocaine hydrochloride, from coordinates of X-ray crystallographic structure given in ref 26. Hydrogen atoms are not shown, including the unlocated acidic hydrogen atom presumed to form a hydrogen bond between the N and Cl atoms.

(3) Buess, M. L.; Garroway, A. N.; Miller, J. B.; Yesinowski, J. P. in *Advances in Analysis and Detection of Explosives*; Yinon, J., Ed.; Kluwer Press: Dordrecht, The Netherlands, 1993; pp 361–368.
(4) Leppelmeier, G. W.; Hahn, E. L. *Phys. Rev.* **1966**, *141*, 724–731.
(5) Muha, G. M. *J. Chem. Phys.* **1980**, *73*, 4139–4140.
(6) (a) Narita, K.; Umeda, J.-I.; Kusumoto, H. *J. Chem. Phys.* **1966**, *44*, 2719–2723. (b) Taylor, P. C.; Baugher, J. F.; Kriz, H. M. *Chem. Rev.* **1975**, *75*, 203–240.

metry parameter. We also discuss a number of different issues related to searching for unknown resonances, identifying NQR transitions, determining impurity effects, measuring parameters that influence the sensitivity of detection, and using different pulse schemes to improve this sensitivity.

EXPERIMENTAL SECTION

Cocaine Base. The sample of cocaine base (nominal purity 99%) was obtained from the U.S. Customs Service, a nontraditional supplier of specialty chemicals. Its identity was confirmed by high-resolution ^{13}C NMR,[7] which revealed some unidentified impurities, and by a measured mp of 92–93 °C (cf. 98 °C for l-cocaine[8]). In order to remove the impurities, a portion of the sample was dissolved in absolute ethanol (USP), heated to the boiling point, filtered, and allowed to crystallize over several days at room temperature. The white powder collected by filtration initially appeared to melt well below the expected melting point of cocaine; however, after drying in open air for over 1 week, the measured melting range was 95.5–97 °C, very close to the reported value. This recrystallized sample (12.9 g) is referred to throughout as "recrystallized". The remainder (150 g) of the original sample is referred to throughout as "as-received."

Cocaine Hydrochloride. A cocaine hydrochloride sample (117.5 g) of 88% purity (mp 186–187 °C) obtained from the U.S. Customs Service was dissolved in 300 mL of hot ethanol (near boiling), filtered, and allowed to cool to room temperature slowly. Filtration yielded a white powder, which after drying on a watch glass in a vacuum dessicator lost 4.5% by weight and yielded 60.0 g of sample with mp 190–192 °C, comparing reasonably with the reported melting point of the hydrochloride of 197 °C.[8]

Pure NQR (Pulsed). All ^{14}N and ^{35}Cl NQR data were obtained with a home-built pulse Fourier transform spectrometer of standard design at the Naval Research Laboratory. We used various combinations of transmitter powers and coil geometries (up to 60 mm diameter) throughout this investigation such that the pulse widths maximizing the free induction decay (FID) signal in powdered samples were typically 10–30 μs. A Faraday shield was used to reduce the electric field component of the radio frequency, since the non-centrosymmetric cocaine hydrochloride structure results in piezoelectric ringing that otherwise would obscure the NQR signal. The shield used for these experiments consisted of strips of copper taped to the bottle in the form of a "hula skirt". However, a thin sheet of copper slightly longer than the sample, wrapped around the sample slightly exceeding its circumference, separated by insulating tape in the region of overlap, and grounded to the chassis appears to work at least as well (a "jelly roll" design). A $90°-\tau-180°$ spin-echo pulse sequence with a pulse interval τ of 335 μs and a repetition period of 200 ms was used to search for the ^{14}N pure NQR lines in both cocaine base samples at room temperature. Two NQR lines were observed in each sample and later confirmed to be ν_+ and ν_-.[9,10] We detected the ^{14}N NQR lines of the as-received cocaine base sample at 77 K by immersing the sample in liquid nitrogen; because of the apparently long ^{14}N T_1, we used a version of the steady-state free-precession (SSFP)[11,12] pulse sequence with a pulse width of 20 μs and a pulse interval of 5 ms.

We measured the ^{14}N and ^{35}Cl spin–lattice relaxation times T_1 with either the inversion–recovery technique[13] or a two-pulse method.[14] We measured spin–spin relaxation times T_2 by the $90°-\tau-180°$ spin-echo method.[13] Relaxation time measurements are estimated to be accurate to within ±10%.

We searched for the companion ^{37}Cl NQR transition in cocaine hydrochloride at a frequency lower by a factor of 0.787 (the ratio of the nuclear quadrupole moments); however, interference from an acoustic ringing signal prevented unambiguous identification of the ^{37}Cl transition.

We assigned the two ^{14}N NQR peaks in each sample to ν_+ and ν_- transitions of a *single* nitrogen nucleus by measuring the NQR signal intensity as a function of an applied Zeeman magnetic field provided by Helmholtz coils. The magnetic field was parallel to the rf coil and ranged from 0 to 5.5 mT. The field strength was measured directly by a Group 3 DTM-141DS digital teslameter equipped with a Hall probe. The maximum reduction in the signal intensity occurs when the Larmor frequency of the protons in the magnetic field is matched to the ^{14}N ν_0 transition frequency.[15]

^{35}Cl NMR. A Bruker MSL-300 NMR spectrometer at the Naval Research Laboratory with a high-power probe containing a 10 mm i.d. solenoidal rf coil was used to obtain ^{35}Cl NMR data at a Larmor frequency of 29.4 MHz. The 90° pulse length determined using NaCl was 8 μs; in the cocaine hydrochloride spectra the corresponding 90° pulse length was half of this, since only the central $^1/_2 \rightarrow -^1/_2$ transition was observed.[16] A $90_x-\tau-180_{x,y}-\tau$ phase-cycled spin-echo sequence described in ref 16a, and analyzed in ref 16b, was used to reduce probe ring-down effects.[16] The rf field strength used was not sufficient to provide accurate spectral intensities over the wide range of frequencies in the powder pattern. To overcome this problem, we stepped the (central) carrier frequency in typically 2 or 4 kHz increments over the entire spectral width, retuning the probe as needed so that the carrier frequency was never more than 30 kHz from the frequency to which the probe was tuned. We processed the spin echo using a line broadening of 5 kHz and measured the absolute intensity of a single point near the center of the Fourier transform spectrum (selected to be 3.9 kHz to high frequency of the carrier, in order to eliminate the influence of zero-frequency artifacts).

SQUID Detection. A SQUID spectrometer at Lawrence Berkeley Laboratory was used to detect the ^{14}N ν_+ and ν_- transitions of cocaine hydrochloride. The direct detection of the nitrogen transitions is difficult since the SQUID detects the changes upon excitation in the expectation values of the magnetic

(7) Avdovich, H. W.; Neville, G. A. *Can. J. Spectrosc.* **1983**, *28*, 1–8.
(8) *Handbook of Chemistry and Physics*, 57th ed.; CRC Press: Cleveland, OH, 1976.
(9) These results have been confirmed by Dr. Julian Shaw of Quantum Magnetics, San Diego, in: Proceedings, Contraband and Cargo Inspection Technology International Symposium, 28–30 October 1992, Washington, DC. Preliminary results have also been reported in: Garroway, A. N.; Buess, M. L.; Yesinowski, J. P.; Miller, J. B. *SPIE Proc.* **1993**, *2092*, (Substance Detection Systems), 1993, 318–327.
(10) Smith, J. A. S. U.S. Patent 4,887,034, 1989, reports cocaine free base ^{14}N NQR signals using indirect detection methods at 4.245 and 4.260 MHz; despite careful searches, we have not observed any signals in this region.
(11) Carr, H. Y. *Phys. Rev.* **1958**, *112*, 1693–1701.
(12) Klainer, S. M.; Hirschfeld, T. B.; Marino, R. A. *Fourier, Hadamard, and Hilbert Transforms in Chemistry*; Plenum Press: New York, 1982; pp 147–182.
(13) Petersen, G.; Bray, P. J. *J. Chem. Phys.* **1976**, *64*, 522–530.
(14) Vega, S. *J. Chem. Phys.* **1974**, *61*, 1093–1100.
(15) (a) Smith, D. H.; Cotts, R. M. *J. Chem. Phys.* **1964**, *41*, 2403–2416. (b) Colligiani, A.; Ambrosetti, R.; Cecchi, P. *J. Chem. Phys.* **1971**, *55*, 4400–4405. (c) Marino, R. A.; Oja, T. *J. Chem. Phys.* **1972**, *56*, 5453–5457.
(16) (a) Kunwar, A. C.; Turner, G. L.; Oldfield, E. *J. Magn. Reson.* **1986**, *69*, 124–127. (b) Haase, J.; Oldfield, E. *J. Magn. Reson. A* **1993**, *104*, 1–9.

Table 1. Variable-Temperature NQR Data for Cocaine Base and Cocaine Hydrochloride

sample	temp (K)	nucleus	transition	frequency (MHz)	line width (Hz)	T_1 (ms)	T_2 (ms)	e^2Qq/h (MHz)	η
cocaine base (as received)	77	^{14}N	ν_-	3.740 ± 0.001	~2300	nd[a]	nd[a]	5.0460 ± 0.0013	0.0353 ± 0.0008
			ν_+	3.829 ± 0.001	~2300	nd[a]	nd[a]		
	295	^{14}N	ν_-	3.7176 ± 0.0001	870	nd[a]	nd[a]	5.0229 ± 0.0001	0.0395 ± 0.0001
			ν_+	3.8168 ± 0.0001	860	210	85		
cocaine base (recrystallized)	295	^{14}N	ν_-	3.7175 ± 0.0001	270	75	75	5.0228_7 ± 0.0001	0.0395_4 ± 0.0001
			ν_+	3.8168 ± 0.0001	260	160	81		
cocaine hydrochloride	4.2 (SQUID)	^{14}N	ν_-	0.815 ± 0.003		nd[a]	nd[a]	1.186_7 ± 0.004	0.258 ± 0.005
			ν_+	0.965 ± 0.003		nd[a]	nd[a]		
	77	^{14}N	ν_-	0.813 ± 0.001	~5000	360	22	1.182_7 ± 0.0015	0.250_3 ± 0.0035
			ν_+	0.961 ± 0.001	~5000	370	25		
	141	^{14}N	ν_-	0.811 ± 0.001	~5000	nd[a]	nd[a]	1.180_7 ± 0.0015	0.252_4 ± 0.0035
			ν_+	0.960 ± 0.001	~5000	820	6		
	295	^{14}N	ν_-	0.806 ± 0.001	~4000[b]	2000	>0.3[c]	1.178 ± 0.0015	0.263_2 ± 0.0035
			ν_+	0.961 ± 0.001	~5000[b]	700	1.5		
	295	^{35}Cl	ν_Q	2.53 ± 0.01	~20000[d]	57	0.15	5.02_7[e] ± 0.02	0.2[e]

[a] Not determined. [b] These transitions were 15%–30% broader in less pure samples (93% and 88% purity). [c] Based on spin–lock spin-echo experiments. [d] The line width increased to ~25 000 Hz for a less pure sample (93% purity). [e] From parameters of a simulation providing a good fit to the experimental ^{35}Cl NMR powder pattern and the ^{35}Cl NQR frequency (see Results section).

moments for nondegenerate quadrupolar eigenstates, and these are zero in the absence of a magnetic field. The application of the low magnetic fields used here does not induce a sufficiently large moment to allow direct detection of the signal. The spectrometer design[17] and experimental technique[18] have been described previously. Briefly, the experiment begins with thermal equilibrium between the proton spin system at the appropriate Zeeman field strength and one of the nitrogen spin subsystems. When rf is swept through a different nitrogen transition frequency, the population of one of the nitrogen eigenstates coupled to the protons changes and causes cross-relaxation to occur until the proton system and nitrogen subsystem equilibrate to a new common spin temperature (Figure 1a). It is the change in proton population, as monitored by the SQUID detector, that provides the indirect measurement of the nitrogen NQR spectrum (in weak magnetic field). Further enhancement can be realized by the additional saturation of the third nitrogen transition. In the limit of complete saturation and fast cross-relaxation times, the full proton signal becomes available to detect the nitrogen transitions. Simultaneous or consecutive excitation of two transitions, used mainly to enhance the signal, can also be used to correlate resonances arising from the same nitrogen site. Additionally, the magnitude, sign, and width of the signals, selective saturation results, and estimates of the quadrupole coupling constant and asymmetry parameter can all support the assignment of the transition frequencies to different nitrogen sites. The SQUID is operated at 4.2 K. Sweeps are usually broken up into 250 kHz scans lasting 100–250 s. Combinations of forward and reverse frequency sweeps are used to remove distortions arising from saturation, relaxation, and instrumental artifacts.

RESULTS

Cocaine Base. The ^{14}N NQR frequencies and line widths for cocaine base at 295 and 77 K are given in Table 1. Only two resonances were observed in each sample (see Figure 3). We assigned these to the ^{14}N ν_- and ν_+ transitions on the basis of room-temperature Zeeman-field experiments discussed in the Experimental Section; results are shown in Figure 4. The nuclear quadrupole coupling constants e^2qQ/h (NQCC) and asymmetry parameters η obtained from these assignments are also given in Table 1.

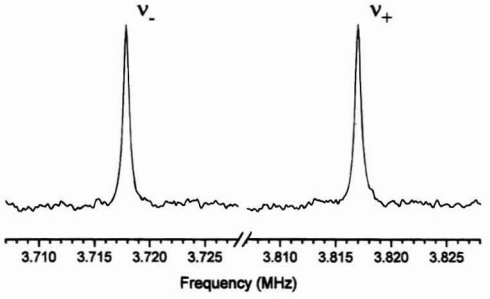

Figure 3. ^{14}N pure NQR composite spectrum of recrystallized cocaine base (12.9 g), obtained in two separate one-pulse experiments: The peak at right, ν_+, was obtained with a spectrometer carrier frequency of 3.816 95 MHz, while the peak at left, ν_-, was obtained with a carrier frequency of 3.717 88 MHz. In both cases the pulse width was 14 μs, the pulse repetition period was 0.5 s, and 200 scans were accumulated. An exponential apodization corresponding to a line broadening of 250 Hz was used prior to Fourier transformation.

The small asymmetry parameter (~4%) of cocaine is typical of nitrogen bonded to three nearly equivalent atoms (of carbon).[19] Although for both samples of differing purity the respective ν_- and ν_+ frequencies are identical, the lines in the as-received sample are over 3 times as broad as those in the recrystallized sample. Such NQR line broadening by impurities has been observed elsewhere and is attributed to a random distribution of electric field gradients in the vicinity of the impurity.[20] The additional line broadening in the as-received cocaine base at 77 K is most likely due to lattice distortions created by rapid cooling when the sample was immersed in liquid nitrogen.[21]

The measured room-temperature ^{14}N relaxation times of cocaine base are also given in Table 1. The T_1 data for the

(17) Connor, C.; Chang, J.; Pines, A. *Rev. Sci. Instrum.* **1990**, *61*, 1059–1063.
(18) Werner, U.; Black, B.; Ziegeweid, M.; Pines, A. *Chem. Phys. Lett.* **1993**, *209*, 17–21.
(19) Hunt, M. J. *J. Magn. Reson.* **1974**, *15*, 113–121.
(20) Woessner, D. E.; Gutowsky, H. S. *J. Chem. Phys.* **1957**, *27*, 1072–1074.
(21) Melnick, S. J.; Whitehead, M. A. *J. Mol. Struct.* **1983**, *111*, 397–413.

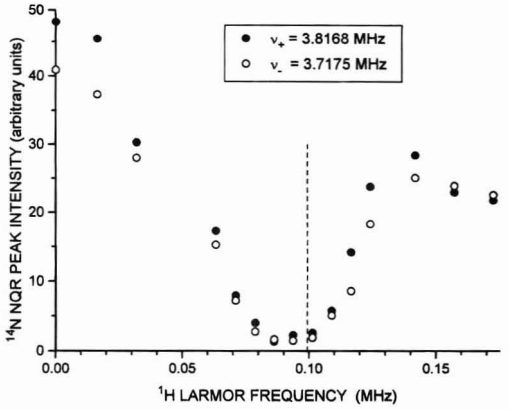

Figure 4. Intensity of ^{14}N ν_+ and ν_- peaks in the as-received cocaine base sample as a function of applied magnetic field, expressed as corresponding proton Larmor frequency. A vertical dashed line indicates the position of the $\nu_+ - \nu_- = \nu_0$ difference frequency; the decrease in peak intensities at this dashed line verifies the assignments of the two peaks (see text).

recrystallized sample for recovery times less than 300 ms (data not shown) were fit to a single exponential; we did not attempt to analyze recovery times longer than 300 ms, which might reveal biexponential behavior characteristic of a three-level system. The measured relaxation times for the ν_- transition in the recrystallized sample are $T_2 = 76$ ms and $T_1 = 74$ ms; since T_2 generally does not exceed T_1, an average value of 75 ms is reported for both. A previous study of the effects of impurities on the ^{35}Cl pure NQR relaxation times in *p*-dichlorobenzene showed T_1 and T_2 to be independent of sample composition.[20] This is also the case within experimental error for T_2 of the ^{14}N ν_+ line of cocaine base. The difference between the T_1 values for the two cocaine base samples lies somewhat outside of experimental error; however, additional data using the same T_1 measurement technique for both samples are required to determine whether or not the difference is real. In any case, T_1 as measured in the as-received sample is only one-third longer than that in the recrystallized sample, whereas there is a factor of 3 difference in line widths. We conclude that the unspecified impurities present in the as-received cocaine base sample have an effect on ^{14}N spin–lattice relaxation that is small or negligible compared with their line broadening effect.

Cocaine Hydrochloride. Figure 5 shows the SQUID ^{14}N NQR results at 4.2 K for the recrystallized cocaine hydrochloride sample. The assignment of the ν_+ and ν_- transitions, whose frequencies are listed in Table 1, was established via field dependence studies. The ν_0 transition, which was expected to be weak, could not be seen.

Using the ^{14}N frequencies that were determined from the SQUID experiments, we were able to finally detect the pure NQR signal, with some difficulty. A composite ^{14}N pure NQR spectrum of cocaine hydrochloride at room temperature showing the ν_+ and ν_- transitions is shown in Figure 6. The assignments to ν_+ and ν_- were made at 77 K by the Zeeman field technique described in the Experimental Section. The 961 kHz signal is observed to vanish at a magnetic field of ~3.5 mT, corresponding to a proton Larmor frequency of 148 kHz, thus confirming the pairing of the 961 and 813 kHz lines (961 − 813 = 148). The spin–lattice relaxation time T_1 of the ν_+ peak was estimated to

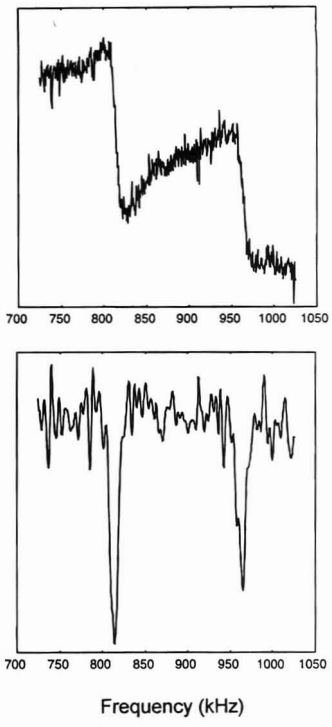

Figure 5. SQUID results at 4.2 K for 144 mg of cocaine hydrochloride. The raw data are shown at top, a derivative mode of presentation emphasizing peak positions at bottom.

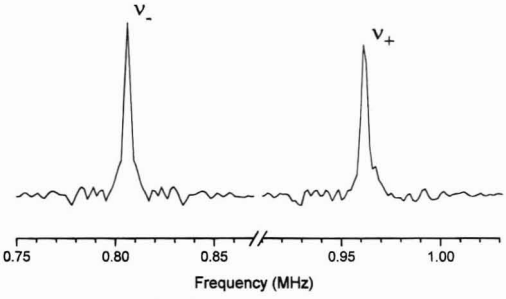

Figure 6. Composite ^{14}N pure NQR spectrum of cocaine hydrochloride (60 g) at 295 K obtained in two separate SLSE experiments (see text). The peaks at right and left (ν_+ and ν_-) were obtained at spectrometer carrier frequencies of 0.961 and 0.806 MHz, respectively. In both experiments the pulse widths were 28 μs, the pulse spacing within the SLSE train was 600 μs, and the first 16 echoes in the train were accumulated and coherently summed. The ν_+ time domain data were obtained with a sequence repetition period of 1 s and a total of 151K scans, while the ν_- data were obtained from 50K scans with a repetition period of 2 s. (The spectral data in the above figure have been normalized to the number of accumulated scans for comparison purposes). An exponential apodization corresponding to a line broadening of 1000 Hz was applied starting at the echo maximum.

be 2 s by comparing the relative peak heights obtained using relaxation delays of 0.2, 1, and 10 s (16%, 42%, and 100%, respectively) with theoretical curves given in ref 22. To improve the sensitivity of detection in order to measure relaxation times, a

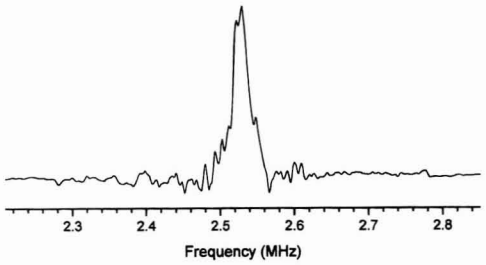

Figure 7. ^{35}Cl pure NQR spectrum of recrystallized cocaine hydrochloride (60 g) obtained using a two-pulse spin-echo sequence with 13 μs pulses separated by 150 μs, a carrier frequency of 2.530 MHz, and 32K acquisitions at 60 ms intervals. Exponential apodization corresponding to a line broadening of 5000 Hz was applied.

pulsed-spin-locking sequence[23] of the form $90_x-\tau-90_y-2\tau-90_y-2\tau-90_y$ ... was used, with a τ delay of 300 μs, and the first eight echoes in the middle of the 2τ periods were added together and processed. Data exhibiting the dependence of the ^{14}N frequencies and relaxation times upon temperature to 77 K are given in Table 1.

A broad ^{35}Cl pure NQR resonance was observed for cocaine hydrochloride at 2.53 MHz (see Figure 7 and Table 1). This frequency is in reasonable agreement with the value of 2.547 MHz reported in ref 10, which also reported the associated ^{37}Cl NQR signal at 1.998 MHz. As discussed above, observation of the single pure NQR peak for an $I = {}^3/_2$ nucleus such as ^{35}Cl does not enable one to disentangle the NQCC from the asymmetry parameter η, but the NMR results described below do so.

The ^{35}Cl NMR spectra obtained using a spin-echo sequence of both the starting 88% purity material (not shown) and the purified cocaine hydrochloride (shown in Figure 8a) are virtually identical, and the spectrum does not change from room temperature to 173 K, the lowest temperature investigated. The spin–lattice relaxation time T_1 was estimated to be several hundred milliseconds at room temperature, and the transverse relaxation time T_2 was measured to be 540 ± 50 μs from peak integration as a function of τ in the echo sequence. The ^{35}Cl NMR spectrum in Figure 8a, which extends over 135 kHz, shows an artifactual decrease in the intensity of the spectrum away from the central carrier frequency arising from the finite excitation power; such an effect is observable under similar conditions in spectra in ref 16a. The resultant distorted powder pattern does not resemble a classical second-order broadened central transition powder pattern for any value of the asymmetry parameter.[6] However, obtaining the ^{35}Cl NMR spectrum by stepping the carrier frequency and measuring the absolute intensity of a particular frequency in the spectrum near the carrier frequency greatly reduces these distortions (solid circles in Figure 8b). This improvement is particularly noticeable in the increased intensity of the two outermost "horns".

Figure 8b shows a comparison of the stepped-frequency ^{35}Cl NMR spectrum with theoretical simulations for three different values of the asymmetry parameter η. A program was written using the mathematical analysis program MATLAB and the expressions for the second-order central-transition frequency given

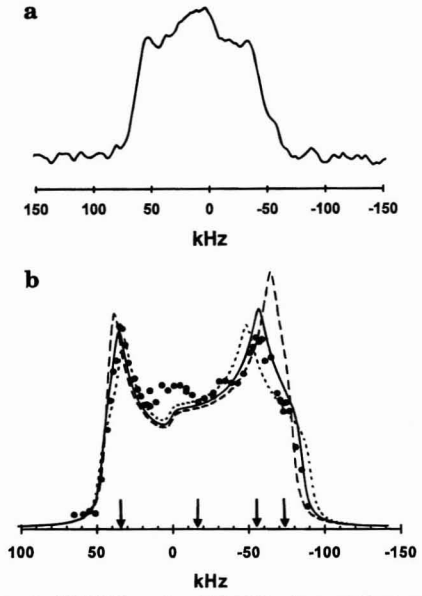

Figure 8. ^{35}Cl NMR spectra at 29.4 MHz of recrystallized cocaine hydrochloride (1.1 g): (a) obtained using a spin-echo sequence (see text) with a τ delay of 200 μs, a relaxation delay of 200 ms, 50K scans, and an exponential apodization corresponding to a line broadening of 5 kHz; zero-frequency corresponds to the carrier frequency, not to the isotropic chemical shift of the powder pattern as in (b); (b) stepped-frequency spectrum (solid circles) obtained from spin-echo sequence with $\tau = 50$ μs as described in the Experimental Section. Each point represents a 1 h accumulation (18K scans). The vertical arrows represent the various frequencies to which the probe was tuned. Theoretical simulations of second-order quadrupolar powder patterns are plotted on an arbitrary intensity scale for three different values of the asymmetry parameter η: 0.1 (dashed), 0.2 (solid), 0.3 (dotted). The NQCC value was constrained as described in the Results section, and an exponential apodization corresponding to a 6 kHz line broadening was used for the simulations. The best agreement is obtained with $\eta = 0.2$.

in ref 6b. The polar coordinates were incremented uniformly by 0.3°, and the calculated (weighted sum) time-domain response was apodized using an exponential function corresponding to a line broadening of 6 kHz. This latter action helps compensate for the exponential apodization corresponding to 5 kHz line broadening that was applied to each stepped-frequency acquisition. A variety of different values of the NQCC, asymmetry parameter, offset frequency, and line broadening were tried, subject to the constraint that the resultant predicted pure NQR frequency (see above) be that actually observed (2.53 MHz). This requirement served to restrict the available parameter space to a region around $\eta = 0.2$, which was deemed to be the best value. The simulation using η=0.2 and an NQCC of 5.0266 MHz is shown as a solid line. The agreement is quite reasonable, except for some apparently larger intensity in the experimental spectrum near zero frequency that could possibly arise from an anisotropy in T_2, impurities, or other artifacts. The fact that the right "horn" of the experimental spectrum is slightly less than the simulation predicts can be plausibly attributed to a slight distribution of NQCC values that broadens this horn more than the other one, which is only half as far from the center frequency.[24] In order to

(22) Buess, M. L.; Garroway, A. N.; Miller, J. B. *J. Magn. Reson.* **1991**, *92*, 348–362.
(23) Marino, R. A.; Klainer, S. M. *J. Chem. Phys.* **1977**, *67*, 3388–3389.

demonstrate that the asymmetry parameter can be determined with reasonable accuracy from our results, simulations for η values of 0.1 and 0.3 are shown as dashed and dotted lines, respectively, in Figure 8b, using the constrained NQCC values of 5.0516 and 4.9858 MHz, respectively. Clearly the fit is not as good, especially in the position of the horns. Therefore, our simulations indicate that the true asymmetry parameter is close to 0.2, with an estimated error of $\sim\pm0.05$.

The ^{35}Cl NMR chemical shift of the powder pattern can best be determined from the frequency offset needed to produce agreement between the frequency-stepped spectrum and the theoretical simulation in Figure 8b. The chemical shift thus determined was equal to that of NaCl (=0 ppm) within experimental error.

DISCUSSION

Cocaine Base. As can be seen from Figure 3, cocaine base represents a favorable sample from the standpoint of ^{14}N NQR detection. The detection sensitivity (see caption for conditions) can be improved further as described below. Since the signal to noise ratio improves as the square root of the number of scans, an improvement in detection sensitivity means that smaller amounts of sample can be detected in a given time, less time can be used for data acquisition, or more accurate quantitation results can be obtained. Both the SSFP pulse sequence[11] (in NQR spectroscopy also called SORC, for strong off-resonant comb[12]) and spin–lock spin-echo (SLSE) sequence[23] are useful sensitivity-enhancement techniques that are most effective for pulse intervals $\tau \ll T_2$, a condition that is easily satisfied for cocaine base. Indeed, both sequences yielded significant improvements in detection sensitivity for cocaine base. We have used numerical simulations to show that the improvement using the SSFP sequence can be accounted for by the Bloch equations, whereas in other compounds in which $T_1 \gg T_2$ additional factors appear responsible.[25] (For ^{14}N, as well as ^{35}Cl, in cocaine hydrochloride, where the direct detection sensitivity is much poorer, the SSFP sequence did not yield a signal even for pulse intervals as short as 340 μs for ^{14}N; the SLSE sequence yielded a rather modest improvement in sensitivity in both cases.)

Cocaine Hydrochloride. The crystal structure of cocaine hydrochloride is orthorhombic with space group $P2_12_12_1$ and $Z = 4$.[26] Low-frequency Raman spectra of this compound have been reported at room temperature and 9 K and assigned; no evidence of any change in the crystalline phase between these temperatures was mentioned.[27] The piperidine ring of the tropane nucleus has the chair form, with the CH_3 group on the N equatorial; the C–N bonds and C–N–C angles are close to normal[26] (see Figure 2). Although the location of the acidic hydrogen atom could not be determined, the short N–Cl bond distance (306.9 pm) suggests the presence of a hydrogen bond between the nitrogen and chlorine, not necessarily a linear one.[26]

It is interesting to note that the ^{14}N spin–lattice relaxation time T_1 of cocaine hydrochloride decreases as the temperature is lowered from room temperature to 77 K. This might be indicative of motions involving the hydrogen-bonded proton that are not yet frozen out at 77 K. In ammonium perchlorate, a very short ^{14}N T_1 value of 63 ms was measured at 1.5 K using a dc SQUID and attributed to fluctuating electric field gradients.[28]

The ^{35}Cl quadrupole coupling constant (NQCC = 5.0266 MHz, $\eta = 0.2$, $\nu_Q = 2.53$ MHz) can be analyzed in terms of a Townes–Dailey approach neglecting the asymmetry parameter to yield an estimated "ionicity" of the chloride ion of 95%. (A free chloride ion with 100% "ionicity" would have an NQR frequency of zero, whereas in the covalent chlorine molecule with 0% ionicity the NQR frequency is 54.5 MHz.[1]) The ν_Q value of 2.53 MHz may be compared to the lower NQR frequencies that have been observed for ^{35}Cl in *n*-decylammonium chloride[29] (1.215 MHz) and trissarcosine calcium chloride[30] (2.16 MHz) and predicted from NMR results for calcium chloroapatite[31] (0.8 MHz). The latter represents a chloride ion having no opportunities for hydrogen bonding, whereas the former two compounds have possibilities for N–H–Cl hydrogen bonding. For cocaine hydrochloride we have shown that the ^{35}Cl asymmetry parameter η is rather small (0.2), consistent with the picture that an axially symmetric, nonzero ^{35}Cl NQCC is created by the hydrogen bond to a proton. It would be worthwhile to further study the relationship between ^{35}Cl NQR coupling constants and asymmetry parameters and the associated hydrogen-bonding geometries in compounds where both are known.

In order to estimate the broadening of the ^{35}Cl NQR spectrum due to dipolar coupling to protons, distances from hydrogen atoms on the same and on neighboring molecules to the chlorine atom were calculated from the X-ray structure coordinates, excluding the non-observed acidic hydrogen.[26] The closest distance was 270 pm, to H(17) on C(16) on the same molecule as the Cl (numbering according to ref 26), corresponding to a dipolar coupling on the order of only 1 kHz; even a H–Cl distance of 150 pm for the acidic hydrogen would yield a dipolar coupling only ~six times as large. The observed 20 kHz line width therefore cannot be attributed predominantly to static dipolar interactions or to the $1/\pi$ T_2 contribution of 2 kHz. Instead, a distribution of field gradients is likely to be responsible, as is also suggested by the ^{35}Cl NMR simulations (see above).

CONCLUSIONS

We have demonstrated that ^{14}N pure NQR offers a means for the quantitative identification of both cocaine base and cocaine hydrochloride and that ^{35}Cl pure NQR can be used to identify cocaine hydrochloride. The specificity of the technique is inherently extremely high. Several general points can be made regarding the extension of this approach to other compounds of interest. First, use of SQUID detection to determine ^{14}N transition frequencies represents a valuable approach, given the difficulty of locating unknown resonances using pulsed pure NQR. Second, high-field stepped-frequency ^{35}Cl NMR of fairly ionic chloride ions can provide values for the ^{35}Cl NQCC and asymmetry parameter that enable one to predict the pure NQR frequency. Third, significant variations in the sensitivity of detection (signal strength

(24) Peterson, G. E.; Kurkjian, C. R.; Carnevale, A. *Phys. Chem. Glasses* **1974**, *15*, 59–64.
(25) Yesinowski, J. P.; Buess, M. L.; Garroway, A. N., to be published.
(26) Gabe, E. J.; Barnes, W. H. *Acta Crystallogr.* **1963**, *16*, 796–801.
(27) (a) Vergoten, G.; Fleury, G.; Gamot, A. P. *J. Raman Spectrosc.* **1983**, *14*, 371–374. (b) Gamot, A. P.; Vergoten, G.; Fleury, G. *Talanta* **1985**, *32*, 363–372.
(28) Hurlimann, M. D.; Pennington, C. H.; Fan, N. Q.; Clarke, J.; Pines, A.; Hahn, E. L. *Phys. Rev. Lett.* **1992**, *69*, 684–687.
(29) Seliger, J.; Žagar, V.; Blinc, R.; Arend, H.; Chapuis, G. *J. Chem. Phys.* **1983**, *78*, 2661–2664.
(30) Blinc, R.; Mali, M.; Osredkar,R.; Seliger, J. *J. Chem. Phys.* **1975**, *63*, 35–37.
(31) Yesinowski, J. P.; Eckert, H., unpublished data, California Institute of Technology, 1985.

per sample mass) are related to relaxation parameters such as T_1 and T_2, as well as to the NQR frequency and line widths. Finally, multipulse techniques such as SSFP and SLSE can provide substantial sensitivity advantages for pure NQR detection, but may require some optimization of both the pulse sequence parameters and the NQR probe characteristics.

ACKNOWLEDGMENT

We are grateful to Dr. Paul Nicholas of the U.S. Customs Service for providing samples and helpful advice concerning purification. J.P.Y. also thanks Dr. Mark Hepp of the Naval Research Laboratory for helpful discussions concerning simulations of second-order quadrupolar patterns. The SQUID work was supported by the Director, Office of Energy Research, Office of Basic Energy Sciences, Materials Sciences Division of the U.S. Department of Energy under Contract DE-AC03-76SF00098. This work is sponsored in part by the Advanced Research Projects Agency. A.N.G. acknowledges the kind hospitality extended by the research group of Professor A. Pines during a visit to Berkeley.

Received for review November 18, 1994. Accepted April 18, 1995.[⊗]

AC941121I

[⊗] Abstract published in *Advance ACS Abstracts,* June 1, 1995.

Anal. Chem. **1995,** *67,* 2264–2268

Linear Response Function for Fluorescence-Based Fiber-Optic CO_2 Sensors

Xiaoying He and Garry A. Rechnitz*

Hawaii Biosensor Laboratory, Department of Chemistry, University of Hawaii, Honolulu, Hawaii 96822

The theoretical basis and experimental evidence for a Stern–Volmer type relationship using the fluorescence ratio (I_{bl}/I) in the absence (I_{bl}) and presence (I) of CO_2 as response function for fluorescence-based fiber-optic CO_2 sensors is explored. By choosing the right indicator, appropriate bicarbonate concentration, and a thin enough sensing layer, a fiber-optic CO_2 sensor with a usable linear range can be easily achieved using I_{bl}/I as the response function. This allows the possibility of one-point calibration, which cannot be accomplished if the measured fluorescence intensity (I) is used directly as the response function.

The carbon dioxide electrode and carbon dioxide optrode, each possessing its own merits and shortcomings, are the two major CO_2 sensors developed to date.[1,2] Among all the CO_2 optrodes explored so far, the fluorescence-based fiber-optic CO_2 optrodes, which were first described by Zhang and Seitz,[3] have the most advantageous features and therefore are preferred in practical usage. Compared to the commercially available CO_2 electrodes, CO_2 optrodes offer advantages for remote sensing and have minimum electrical or magnetic interferences. However, they suffer two major limitations, e.g., the lack of a linear response function, which is a major drawback for biosensor use, and the variation in measured fluorescence intensities due to light source intensity changes or indicator photobleaching. Addressing this latter problem, Zhang and Seitz[4] developed a two-wavelength excitation method which can make the fluorescence-based pH sensor insensitive to the effect of photobleaching, wash out, and light source intensity variations. This method also applies to the fluorescence-based fiber-optic CO_2 optrode, which is based on pH sensing. Since it requires more complicated instrumentation, however, applications using this method are limited. As far as the response function is concerned, either the fluorescence intensities at one wavelength or the ratio of fluorescence intensity at two wavelengths as in the two-wavelength method are commonly adopted as indicators for CO_2 concentration.[3,5,6] In both cases, the calibration curves are not theoretically linear.

In this work, we propose the use of the ratio of fluorescence intensities in the absence (I_{bl}) and the presence (I) of CO_2 as the response function (I_{bl}/I). Using this response function, we demonstrate for the first time that not only can a linear range in the response curve be expected for a CO_2 fiber-optic sensor with a simple sensor tip configuration, but also that without more complicated instrumentation the response curve will be independent of instabilities in light source intensity or the small indicator concentration variations due to photobleaching.

EXPERIMENTAL SECTION

Reagents and Materials. Sodium bicarbonate from Fisher was used to prepare the standard solutions (1 M). Carbon dioxide buffer solution for the CO_2 electrode (Orion Research, Inc.) was used to adjust the standard solution pH to the operating range (4.8–5.2). All the solutions were prepared using distilled, deionized water, and all the reagents were used as received.

The fluorescent indicator employed in our fluorescence-based CO_2 optrode was the trisodium salt of 1-hydroxypyrene-3,6,8-trisulfonate (HPTS) (Molecular Probes, Inc., Eugene, OR). As a fluorescent indicator, HPTS has many attractive features (high quantum yield, high absorbance, and excellent photostability) and has been demonstrated to be a good choice for the fiber-optic CO_2 optrode.[5–8]

Indicator solution was prepared as an aqueous solution containing sodium bicarbonate, HPTS, and sodium chloride. It was kept away from light after preparation and could be used for several days. Sodium chloride was used to balance the osmolarity of the indicator solution and that of the buffer solution across the membrane so that baseline drift could be avoided.[9]

CO_2 porous membranes designed for use with CO_2 electrodes (Orion Research, Inc.) were used as gas-permeable membranes, the O-ring being removed before use.

Optical Components. The radiation source consisted of an Oriel (Model 6333) 100-W QTH lamp plugged in an Oriel (Model 66184) lamp housing which was powered by an Oriel (Model 6393) constant-voltage transformer (12 V). The source radiation was focused by an Oriel (Model 77800) fiber-optic input assembly onto the end of an Oriel (Model 77563) standard grade fused-silica fiber-optic bundle. The fluorescent light at the sensing layer was amplified using an Oriel (Model 77761) photomultiplier tube (PMT) which was powered by an Oriel (Model 7070) photodetection system. The current signal from the PMT was detected by a single-phase lock-in amplifier (Model SR510) from Stanford Research Systems, Inc., and recorded with a Heath Schlumberger strip-chart recorder. The lock-in amplifier was used in conjunction

(1) Turner, A. P. F., Karube, I., Wilson, G. S., Eds. *Biosensors: Fundamentals and Applications*; Oxford University Press: New York, 1987.
(2) Blum, L. J.; Coulet, P. R. *Biosensor Principles and Applications*; Marcel Dekker: New York, 1991.
(3) Zhang, Z.; Seitz, W. R. *Anal. Chim. Acta* **1984**, *160*, 305–309.
(4) Zhang, Z.; Seitz, W. R. *Anal. Chim. Acta* **1984**, *160*, 47–55.
(5) Wolfbeis, O. S.; Weis, L. J.; Leiner, M. J. P.; Ziegler, W. E. *Anal. Chem.* **1988**, *60*, 2028–2030.
(6) Dremel, B. A. A.; Schmid, R. D.; Wolfbeis, O. S. *Anal. Chim. Acta* **1991**, *248*, 351–359.
(7) Wolfbeis, O. S.; Fülinger, E.; Kroneis, H.; Marsoner, H. *Fresenius Z. Anal. Chem.* **1983**, *314*, 119–124.
(8) Offenbacher, H.; Wolfbeis, O. S.; Fürlinger, E. *Sens. Actuators* **1986**, *9*, 73–84.
(9) Rhines, T. D.; Arnold, M. A. *Anal. Chim. Acta* **1989**, *277*, 387–396.

0003-2700/95/0367-2264$9.00/0 © 1995 American Chemical Society

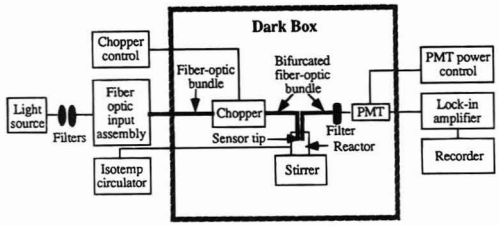

Figure 1. Block diagram of the experimental apparatus showing three sections: the light source apparatus, the sensor enclosed in the dark box, and the data collection equipment.

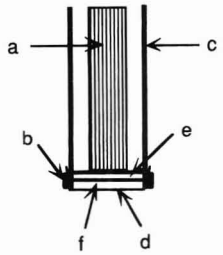

Figure 2. Schematic diagram of the fiber-optic CO_2 sensing probe: (a) common end of the bifurcated fiber; (b) plastic ring; (c) pipet tip; (d) gas-permeable membrane; (e) glass slide; (f) indicator solution.

with an optical chopper (Model SR540) including chopper controller, chopper head, and six-slot blade.

The bifurcated fiber-optic bundle was made of glass fibers from 3M Specialty Optical Fibers (West Haven, CT) with a numerical aperture of 0.40 and a core diameter of 600 μm. The common end of the bifurcated fiber consisted of 14 fibers, 4 in the center and 10 in a symmetrical circle surrounding the central bundle. The 4-fiber bundle in the center was used to carry the incident light, and the surrounding 10 fibers were used to guide signals to the PMT for detection. The fibers were tightly packed with black shrink tubing at both the single ends and the common end and then polished to a flat surface.

All optical fibers, including a 460-nm interference filter with 9-nm bandwidth, a 520-nm filter with 10-nm bandwidth, and a heat-absorbing filter, were obtained from Oriel.

Experimental Setup. The overall experimental setup is shown in Figure 1. Irradiation from the light source was directed onto a heat-absorbing filter and a 460-nm interference filter. It was then focused in the fiber-optic input assembly and sent out as a collimated beam through the fused-silica fiber-optic bundle. Before the excitation light reached the sensor tip through the four-fiber bundle of the bifurcated fiber, it was chopped by a motor-driven chopper to reduce the noise from ambient irradiation. At the sensor tip, fluorescence emitted was returned through the 10-fiber bundle of the bifurcated fiber, passing through a 520-nm interference filter and finally into the PMT. The current signal generated in the PMT was detected by a lock-in amplifier and recorded by a chart recorder. Some components were house in a light-tight box to prevent optical interferences from ambient light.

Sensor Tip Construction. The construction of the sensor tip is shown in Figure 2. A piece of 1-mm-thick round glass slide (e) with a diameter of ~5.5 mm (cut from a microslide) was tightly fitted into the cross section of a 1-mL plastic pipet tip (c). The sharp end of the tip was then cut off so that only a shallow spacer was formed right above the glass slide. The end of the tip could be polished until the desired volume (or thickness) of the spacer was achieved. To mount the sensing layer, the pipet tip was first inverted so that the cavity of the spacer could be filled with the indicator solution (f). The indicator solution was then trapped in the spacer by a CO_2 gas-permeable membrane (d), which was held tightly over the end of the tip by a ring section (b) cut from the pipet tip (3 mm wide). This ring seemed to work better than the conventional O-ring support. The tip was stored in buffer solution with matching osmolarity when not in use.

Procedure. When measurements were to be taken, the sensor tip was mounted on the common end of the bifurcated fiber (a). The polished surface at the common end of the bifurcated fiber was usually wrapped with a thin clear polyester membrane to protect the fiber surface. The fiber bundle (a), which was wrapped by Parafilm, was inserted all the way into the sensor tip until its surface touched the glass slide (e). The Parafilm was used as a space filler to ensure that the fiber bundle was fixed in the center of the tip.

For each measurement, 1 mL of the carbon dioxide buffer solution from Orion was diluted 10 times with water in a 12-mL thermostated cell. The common end of the bifurcated fiber was clamped over the cell so that the sensor tip mounted at its end was at a 20° angle from the vertical while emerged in the constantly stirred buffer solution. This was to avoid trapping air bubbles at the tip of the sensor as in the use of CO_2 electrode. The CO_2 dissolved in the blank buffer solution was neglected since it is quite small (calculated to be ~0.01 mM according to the Henry's law constant at 25 °C)[10] compared to the sample CO_2 concentrations used (0.2–10 mM). To obtain calibration curves, aliquots of freshly prepared standard bicarbonate solutions were added to the blank buffer. For each sample, the concentration of CO_2 generated was estimated to be 95% of its original bicarbonate concentration at pH 5. The ratio of fluorescence intensities (without bicarbonate standard (I_{bl})/with bicarbonate standard (I)), I_{bl}/I, was plotted against the CO_2 concentration. The response times ranged from 1.5 to 3.5 min, depending on the CO_2 concentration measured and the bicarbonate concentration in the indicator solution. The lowest CO_2 concentration measured was 0.2 mM. Detailed studies in regard to both response times and limit of detection will be discussed in future applications of the sensor. An isotemp circulator (Fisher Model 900) in conjunction with the thermostated cell was used to maintain the buffer solution at a constant temperature of 25 °C throughout the experiments.

THEORY

As described above, the sensing layer is a thin layer of indicator solution containing bicarbonate and fluorescent dye (HPTS) entrapped behind a CO_2 gas-permeable membrane. The dissolved CO_2 in the sample buffer solution diffuses through the membrane until an equilibrium is reached between the partial pressure of CO_2 in the sample solution and the CO_2 in the indicator solution. The CO_2 that diffused across the membrane decreases the pH of the sensing layer and inhibits the dissociation of the fluorescent indicator according to the following equilibrium:

(10) Daniels, F.; Alberty, R. A. *Physical Chemistry*, 2nd ed.; Wiley: New York, 1961.

$$HIn \overset{K_{In}}{\rightleftharpoons} In^- + H^+ \quad (1)$$

where HIn and In^- stand for the protonated and deprotonated form of HPTS, respectively. This change can be detected by the fluorescence intensity change of the indicator layer at 520 nm since the deprotonated form of HPTS is the fluorophore with maximum emission at 520 nm and maximum excitation wavelength at 460 nm.[11-13]

In the indicator layer, the concentration of fluorophore $[In^-]$ is related to the total indicator concentration (C_{In}) and the hydrogen ion concentration ($[H^+]$) by the following expression:

$$[In^-] = K_{In}C_{In}/(K_{In} + [H^+]) \quad (2)$$

where K_{In} is the dissociation constant of HIn. If the optical density for the indicator layer is small, the inner filter effect is minimized. The fluorescence intensity (I) measured by the fiber-optic sensor then depends on the intensity of the exciting light (I_0) according to Parker's law:[14,15]

$$I = kI_0\epsilon d\phi_f[In^-] \quad (3)$$

where ϵ is the molecular extinction coefficient, ϕ_f the quantum yield of the base form of the indicator dye (In^-), d the thickness of the indicator layer, and k a geometrical constant that takes into account the different geometries of the optical arrangement. Substitution of eq 2 into eq 3 gives

$$I = \gamma I_0 C_{In}/(K_{In} + [H^+]) \quad (4)$$

where $\gamma = k\epsilon d\phi_f K_{In}$ and is a constant when the optical path and indicator buffer solution are fixed. The $[H^+]$ of the indicator solution is determined by the following equilibrium: $CO_{2(aq)} + H_2O \rightleftarrows H^+ + HCO_3^-$, whose equilibrium constant K is given by $K_1 = [H^+][HCO_3^-]/[CO_{2(aq)}]$. Assuming that the bicarbonate concentration N in the indicator buffer solution is sufficiently large so that its concentration is not altered significantly by the CO_2 entering from the external solution, we may rearrange the previous equation to

$$[H^+] = K_1[CO_{2(aq)}]/N \quad (5)$$

Substituting eq 5 into eq 4 gives

$$I = \gamma I_0 C_{In} N/(K_{In}N + K_1[CO_{2(aq)}]) \quad (6)$$

We can further relate the fluorescence intensity to the carbon dioxide concentration C in the sample solution as follows:

$$I = \gamma I_0 C_{In} N/(K_{In}N + K_1\alpha C) \quad (7)$$

where α is the proportionality constant relating C to $[CO_{2(aq)}]$ after equilibrium has been established on both sides of the membrane. As shown in eq 7, the fluorescent intensity (I) does not have a linear relationship with the CO_2 concentration (C), as confirmed by earlier fiber-optic investigations.[7] However, the reciprocal of the intensity should have a linear relationship as shown by eq 8.

$$1/I = (K_{In}N + K_1\alpha C)/\gamma I_0 C_{In} N \quad (8)$$

The baseline fluorescence intensity (I_{bl}) can be obtained directly from eq 4 by assuming that $[H^+]_{bl}$ is negligible. It is given by

$$I_{bl} = \gamma I_0 C_{In}/K_{In} \quad (9)$$

When eq 8 and eq 9 are combined, the following relationship is obtained:

$$I_{bl}/I = 1 + K_1\alpha C/K_{In}N = 1 + KC \quad (10)$$

where $K = K_1\alpha/K_{In}N$ is a constant once the experimental conditions have been fixed.

There are three points that need to be addressed about the above derivation. First, it is very important to note that inner filter effect was neglected in the derivation of eq 10. The inner filter effect[14-16] comes from the attenuation of the excitation light intensity (I_0) by fluorophores or chromophores in passing through the indicator layer. If this effect become too large, eq 3 will no longer hold and neither will eq 10. Therefore, it is crucial to estimate the magnitude of this effect in the system of interest and make sure that the error caused by neglecting it is tolerable. Fortunately, negligible inner filter effect can be achieved rather easily in the design of fluorescence-based CO_2 fiber-optic sensors. In the design of the CO_2 sensor studied here, the excitation light (460 nm) is mainly absorbed by the deprotonated HPTS (In^-) and there are no serious self-absorption or scattering effects. A low optical density in the sensing layer can be obtained by employing a very thin sensing layer with low indicator concentration. Due to the high sensitivity of the fluorescent indicator used, such an arrangement will not cause serious loss in sensitivity.

Second, eq 10 has the same form as the Stern–Volmer equation, which is often used for oxygen sensors based on the dynamic quenching of indicator fluorescence.[17] This similarity between the fluorescent-based CO_2 optrode and the fluorescence quenching-based O_2 sensor is certainly not a coincidence. In fact, both of them are gas-sensing devices based on the quenching of fluorescence in the sensing layer even though they have different quenching mechanisms. Unlike the O_2 sensor where O_2 quenches the fluorescence of the indicator through collision, in the CO_2 sensor, the H^+ in the indicator layer forms a nonfluorescent compound (HIn) with the fluorophore In^-. As Parker[15] has pointed out, regardless of the quenching mechanism a Stern–Volmer quenching relationship will be observed if the added solute forms a nonfluorescent compound with the fluorescent molecule. As such, a Stern–Volmer quenching relationship with respect to $[H^+]$ is naturally expected for the CO_2 optrode. It needs to be noted though that the proportionality constant in this case is a function of the related equilibrium constant. It is rather different

(11) Förster, T. H. *Z. Elektrochem.* **1950**, *54*, 42–46.
(12) Förster, T. H. *Z. Elektrochem.* **1950**, *54*, 531–535.
(13) Weller, A. *Z. Phys. Chem. (N.F.)* **1958**, *17*, 224–245.
(14) Parker, C. A.; Barnes, W. J. *Analyst (London)* **1957**, *82*, 606–618.
(15) Parker, C. A. *Photoluminescence of Solutions*; Elsevier: London, 1968.
(16) Holland, J. F.; Teets, R. E.; Kelly, P. M.; Timnick, A. *Anal. Chem.* **1977**, *49*, 703–710.
(17) Stern, O.; Volmer, M. *Phys. Z.* **1919**, *20*, 183–188.

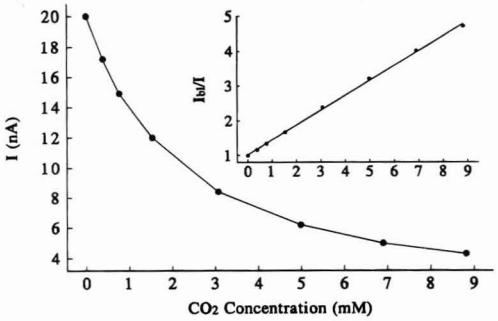

Figure 3. Effect of response function on the appearance of the calibration curve. The graph inside has the same *x*-axis as the outer graph. The sensing layer contains 200 μM HPTS and 10 mM bicarbonate.

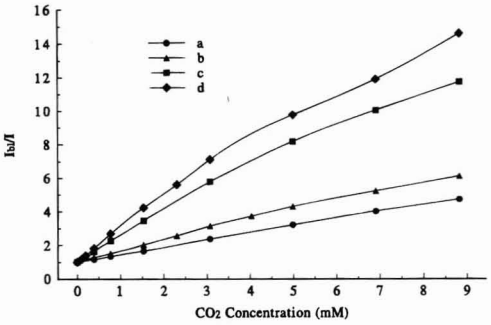

Figure 4. Effect of $NaHCO_3$ concentration on response curves. $NaHCO_3$ concentrations: (a) 10.0, (b) 5, (c) 2.5, and (d) 1.0 mM. Indicator concentration is 200 μM in all cases.

from the Stern–Volmer quenching constant derived from competitive rate considerations as in O_2 quenching. In order to get the same quenching relationship with respect to CO_2 concentration, however, a linear relationship between $[H^+]$ and CO_2 concentration has to hold, which has been demonstrated to be the case in eq 5. Consequently, if I_{bl}/I is employed as a response function in our fluorescence-based fiber-optic CO_2 sensor, a linear calibration curve can be expected as long as the bicarbonate concentration in the indicator solution is sufficiently large. The experimental result of the effect of bicarbonate concentration on calibration curves will be discussed.

Finally, as indicated by eq 10, using I_{bl}/I, instead of I or $1/I$ as a response function, the dependence of calibration curves on light source intensity changes or indicator photobleaching (causing a change in C_{In}) can be avoided. However, in order to take advantage of these features, I_0 and C_{In} must be the same in the blank and sample solutions. In practice, this condition can be met as long as the fluorescence intensity of buffer solution (I_{bl}) is recorded immediately before that of each sample solution (I). Neither the light source intensity changes nor indicator photobleaching is significant during the short period when both I_{bl} and I are measured (several minutes at most). Our results demonstrate that any change of I_0 or C_{In} between measurements of sample points (I_{bl}/I and C) over a long period of time does not affect the calibration curve when I_{bl}/I is used as the response function.

RESULTS AND DISCUSSION

I_{bl}/I and I are plotted against $[CO_2]$ for the same set of experimental data (Figure 3). As expected, I_{bl}/I shows a linear response to the CO_2 concentration over the range tested while I is related to the CO_2 concentration in a nonlinear fashion. Of course, this can be only achieved when all the assumptions made for the derivation of eq 10 are valid. The effects of each of the factors affecting our assumptions will be detailed individually. Note that in Figure 3, as in the rest of the paper, the light intensity (I) has units of nanoamperes. This is because the light signal is measured directly in the form of photocurrent from the PMT, which is proportional to the light intensity.

Effect of Bicarbonate Concentration. Bicarbonate concentration (N) in the indicator layer is an important parameter affecting the sensor's response characteristics. Figure 4 shows response curves of four sensors with varying bicarbonate concentrations (1–10 mM). As expected from eq 10 (slope $\propto 1/N$), the lower the bicarbonate concentration, the more sensitive the response curve becomes. A similar effect was observed when the measured fluorescence intensity (I) was used as the response function.[3] In this case, however, the bicarbonate concentration not only affects the sensor's sensitivity but also seems to affect the linear range of the response curve. Figure 4 clearly shows that the higher the bicarbonate concentration is in the sensing layer, the broader the linear response range will be. In the CO_2 concentration range measured (0.2–10 mM), the bicarbonate concentration in the indicator solution would not be altered significantly enough to make eq 5 invalid, even for the sensor with the lowest bicarbonate concentration (1 mM). Therefore, the invalidation of eq 5 is very unlikely to be the cause for the deviation from linearity of the response curves at higher CO_2 concentrations. A more reasonable explanation for this effect may involve the sensitivity range of the sensors. It is known that when a H^+-sensitive fluorescence indicator is used to measure pH, the sensor is most sensitive when the pH is close to the pK_{In}. In our case, given a sensor with a low bicarbonate concentration, when a sample with a high CO_2 concentration is measured, the pH in the indicator solution could become so low (according to eq 5) that it is no longer within the sensitive range of the sensor. Under these circumstances, the small difference in the measured final intensity (I) between samples becomes comparable to the absolute experimental errors.

Effect of Indicator Concentration. Indicator concentration and the thickness of the indicator layer are crucial parameters that determine the seriousness of the inner filter effect and consequently, the validity of eq 10. In constructing the sensors used in this paper, the indicator solution layer was made as thin as possible (0.1–0.2 mm) so that the optical density was mainly varied through the concentration of the indicator used. Knowing the molar absorption coefficient of HPTS ($\epsilon = 21\,000\ cm^{-1}\ M^{-1}$), the error introduced by neglecting the inner filter effect can be estimated.[15] For a sensor with 200 μM HPTS, the error is ~5%. However, since the thickness of the sensing layer is difficult to estimate exactly, the optimum indicator concentration was determined experimentally. Table 1 shows the effect of indicator concentrations on the fluorometric response. As all the optrodes contain 10 mM bicarbonate in the sensing layer, a linear response is expected within the CO_2 concentration range measured if the

Table 1. Effect of Indicator Concentration[a]

$[CO_2]$ (mM)	I_{bl}/I		
	[HPTS] = 100 μM	[HPTS] = 200 μM	[HPTS] = 400 μM
0.384	1.14	1.16	1.14
0.768	1.34	1.34	1.32
1.53	1.66	1.66	1.63
3.07	2.35	2.35	2.22
4.99	3.17	3.17	2.84

[a] Bicarbonate concentration was 10.0 mM in all cases.

Table 2. Effect of Light Source Intensity[a]

$[CO_2]$ (mM)	I_{bl}/I	
	$I_{bl} = 12.8 \pm 0.2$ nA	$I_{bl} = 20.5 \pm 0.5$ nA
0.384	1.16	1.16
0.768	1.35	1.34
1.53	1.72	1.66
3.07	2.38	2.38
4.99	3.30	3.23

[a] The indicator layer contained 10.0 mM bicarbonate and 200 μM HPTS in all cases.

inner filter effect is negligible. The results show that when HPTS concentration is less than 200 μM, a linear response curve can be obtained under our experimental conditions. Within this range (100 μM was the lowest HPTS concentration tested), however, the response curve seems to be independent of the absolute value of indicator concentrations. In other words, slight photobleaching was not a problem during these measurements. On the other hand, when the concentration of HPTS is too high (such as 400 μM), the response curve begins to deviate from linearity, indicating that the inner filter effect has become too large to be ignored.

The sensing layers presented in this paper were all built on basis of the physical entrapment method. Even though it is usually a simple effective method,[9,18] when the spacer gets too thin, very careful manipulation is required to prevent leakage of the indicator–bicarbonate solution. An attractive alternative to this method is to use a thin film of silicone rubber containing dispersed indicator solution as the sensing layer.[5,6] With this method, a very thin sensing layer can be achieved with better control and improved physical stability.

Effect of Light Source Intensity. As discussed earlier, light source intensity changes have been a problem in the use of CO_2 optrodes when a traditional response curve (I vs $[CO_2]$) is employed. This problem can be avoided if I_{bl}/I is used as response function. To demonstrate this point, two sets of experiments were carried out with varied light source intensity which was adjusted by changing the number of heat absorbing filters in the light path. The results are shown in Table 2, where the light source intensity difference is reflected by the values of baseline current (I_{bl}). As expected, even though the absolute signal (I) changes, the ratio (I_{bl}/I) stays the same within experimental error (2–3%).

CONCLUSIONS

In this paper, a Stern–Volmer type relationship was found for the first time when I_{bl}/I was used to determine carbon dioxide concentration with fluorescence-based fiber-optic CO_2 optrodes. The effects of indicator and bicarbonate concentration in the sensing layer on the linearity and linear range of the calibration curve follow the proposed theory. The measurement of fluorescence intensity at only one wavelength is possible while still ensuring the minimum interference due to light source intensity changes and/or indicator photobleaching. With a linear response and small calibration requirements, we foresee many future applications of this CO_2-sensing technique.

ACKNOWLEDGMENT

We gratefully acknowledge support of National Science Foundation Grant CHE-9216304. We thank W. Cooper for helpful discussions on the design and fabrication of the sensor tip and E. Kawamura for his assistance and advice on the fiber-optic setup. We also thank Dr. D. Coon for insightful discussions.

Received for review February 20, 1995. Accepted April 25, 1995.[⊗]

AC950188I

[⊗] Abstract published in *Advance ACS Abstracts,* June 1, 1995.

(18) Lübbers, D. W.; Opitz, N. *Sens. Actuators* **1983**, *4*, 641–654.

Anal. Chem. **1995,** *67,* 2269–2278

Quantitative Analysis of Bandpass-Filtered Fourier Transform Infrared Interferograms

Mutua J. Mattu and Gary W. Small*

Center for Intelligent Chemical Instrumentation, Department of Chemistry, Clippinger Laboratories, Ohio University, Athens, Ohio 45701-2979

The feasibility of performing quantitative analysis with short segments of bandpass-filtered Fourier transform infrared (FT-IR) interferograms is demonstrated. The protocol developed in this work addresses four limitations that hinder the use of FT-IR spectroscopy in nonlaboratory applications: (1) the need for a rugged, low-cost, and reliable spectrometer, (2) the lack of representative background spectra for use in acquiring absorbance spectra of the target analyte, (3) the presence of overlapping spectral bands that interfere with the analyte determination, and (4) the difficulty in obtaining useful information from data collected near the limit of detection. In this work, spectral information pertaining to a specific analyte band of interest is isolated directly from a short interferogram segment by the application of narrow-bandpass digital filters. When processed in this way, the filtered interferogram segments contain compound-specific information that can be utilized for quantitative analysis. Successful use of a univariate calibration procedure with filtered interferogram data of benzene and nitrobenzene of varying concentrations is demonstrated. Calibrations based on filtered interferogram segment magnitudes vs concentration yield models with values of R^2 in excess of 99%. These results are obtained without the use of a separate background or reference interferogram. This interferogram-based analysis is shown to perform analogously to a conventional spectral-based analysis, with the interferogram method being more efficient in terms of data collection and computational requirements.

Fourier transform infrared (FT-IR) spectroscopy has been used in a variety of dedicated analyses such as the detection of smokestack emissions,[1] air monitoring in the workplace,[2] and in-line monitoring for chemical process control.[3] In addition, feasibility studies have been conducted that may lead to routine applications of FT-IR spectroscopy in monitoring biological processes[4] and for noninvasive determinations of clinically significant analytes such as blood glucose.[5] The practical utility of FT-IR spectroscopy in these nonlaboratory applications is largely determined by the degree to which compact, rugged, reliable, and low-cost spectrometer hardware is available and by the capabilities of the data analysis algorithms used in processing the collected FT-IR data.

The analysis of data arising from these nonlaboratory applications is often complicated by the lack of a representative background or reference spectrum for use in conventional processing of ratioed spectra. For example, in air monitoring applications, interference from water vapor often makes it impossible to collect a representative reference spectrum.[6] Use of poorly matched background and sample spectra can lead to a variety of artifacts in the computed ratioed spectrum, often severely complicating any subsequent data analysis.

Recent work in our laboratory has focused on data analysis algorithms that address both the hardware and data processing requirements associated with nonlaboratory applications of FT-IR spectroscopy.[7-14] We are developing data analysis methodology based on the application of narrow-bandpass digital filters directly to short FT-IR interferograms. Judicious choice of the interferogram segment used in the analysis can eliminate the need for a separate spectral background measurement, while shortening the collected interferogram reduces the length of travel of the moving mirror of the interferometer. This can increase the ruggedness of the spectrometer and also makes possible specialized interferometer designs that are compatible with very short interferograms.

Our previous research has focused on qualitative air monitoring applications in which the collected interferogram data are analyzed for the signature of a target compound. In the course of this work, however, clear evidence of quantitative information has been observed in segments of bandpass-filtered interferograms.[9,11] The focus of the work reported here is to extend this interferogram analysis methodology to quantitative analysis applications. Data from FT-IR transmission studies of benzene and nitrobenzene are used to develop both the theory and the implementation guidelines for a direct quantitative analysis based on short segments of bandpass-filtered interferograms.

(1) Hammaker, R. M.; Fateley, W. G.; Chaffin, C. T.; Marshall, T. L.; Tucker, M. D.; Makepeace, V. D.; Poholarz, J. M. *Appl. Spectrosc.* **1993,** *47,* 1471–1475.
(2) Hongkui, X.; Levine, S. P. *Anal. Chem.* **1993,** *65,* 2262–2269.
(3) Mackison, R.; Brinkworth, S. J.; Belchamber, R. M.; Aries, R. E.; Cutler, D. J.; Deeley, C.; Mould, H. M. *Appl. Spectrosc.* **1992,** *46,* 1020–1024.
(4) Jackson, M.; Mantsch, H. H. *Trends Anal. Chem.* **1992,** *11*(6), 206–210.
(5) Marbach, R.; Koschinsky, Th.; Gries, F. A.; Heise, H. M. *Appl. Spectrosc.* **1993,** *47,* 875–881.
(6) Hanst, P. L. *Spectroscopy* **1993,** *8*(9), 44–49.
(7) Bangalore, A. S.; Small, G. W.; Combs, R. J.; Knapp, R. B.; Kroutil, R. T. *Anal. Chim. Acta* **1994,** *297,* 387–403.
(8) Kroutil, R. T.; Combs, R. J.; Knapp, R. B.; Small, G. W. *Appl. Spectrosc.* **1994,** *48,* 724–732.
(9) Carpenter, S. E.; Small, G. W. *Appl. Spectrosc.* **1992,** *46,* 1790–1798.
(10) Small, G. W.; Carpenter, S. E. *Appl. Spectrosc.* **1992,** *46,* 49–59.
(11) Barber, A. S.; Small, G. W. *Chemom. Intell. Lab. Syst.* **1992,** *15,* 203–217.
(12) Kaltenbach, T. F.; Small, G. W. *Anal. Chem.* **1991,** *63,* 936–944.
(13) Small, G. W.; Carpenter, S. E.; Kaltenbach, T. F.; Kroutil, R. T. *Anal. Chim. Acta* **1991,** *246,* 85–102.
(14) Small, G. W.; Harms, A. C.; Kroutil, R. T.; Ditillo, J. T.; Loerop, W. R. *Anal. Chem.* **1990,** *62,* 1768–1777.

0003-2700/95/0367-2269$9.00/0 © 1995 American Chemical Society

EXPERIMENTAL SECTION

Apparatus. The interferogram data used in this work consisted of transmission measurements of liquid samples of benzene and nitrobenzene in CS_2 at 0.1 mm path length. These data have been used in previous work and have been described in detail there.[10] In order to evaluate the effects of changing infrared signal intensities, a series of neutral density (ND) filters were used during the data collection to vary the total infrared light intensity reaching the detector. Eleven ND filters (19.1, 24.9, 32.5, 39.8, 45.3, 49.6, 55.9, 62.1, 76.4, 83.1, and 88.4% transmittance) were selected for use in the data collection.

The collected interferograms were processed on a Silicon Graphics 4D/460 computer operating under Irix (version 4.0.5, Silicon Graphics, Mountain View, CA). Fourier transform and regression analysis subroutines from the IMSL library (IMSL, Inc., Houston, TX) were used in designing the time domain digital filters. All software used with the Silicon Graphics system was written in FORTRAN 77.

Reagents. Nine standard solutions of benzene (0.020, 0.030, 0.040, 0.050, 0.065, 0.080, 0.090, 0.100, and 0.110 M) were prepared by a one-step direct dilution of a stock solution of benzene in CS_2. A similar procedure was used in preparing nine nitrobenzene standards (0.030, 0.040, 0.050, 0.065, 0.080, 0.090, 0.100, 0.110, and 0.120 M).

Procedures. Single-sided interferograms of 8192 points were collected with a sampling rate of one interferogram point for each zero crossing of the reference laser. The maximum observed spectral frequency for these data was 15 798 cm^{-1}. The point spacing in the transformed spectra was 3.86 cm^{-1}.

For each benzene and nitrobenzene standard, six single-scan interferograms were collected at 20-s time intervals. Signal averaging was not performed in order to obtain a significant noise level in the collected data. Six additional scans were then taken with each of the 11 ND filters in place, yielding a total of 648 interferograms for each analyte. Subsequently, four of the benzene interferograms were found to be anomalous and were removed from further study. This left 644 benzene and 648 nitrobenzene interferograms for use in building calibration models. Also, for each signal intensity, additional interferograms were collected with no sample present and with pure CS_2. These background interferograms were used in computing absorbance spectra.

RESULTS AND DISCUSSION

Quantitative Analysis of Interferogram Domain Data. Two previous studies evaluated the feasibility of interferogram-based quantitative analyses. Sparks et al.[15] developed quantitative calibration models with interferogram data collected during gas chromatography FT-IR spectroscopy (GC/FT-IR) experiments. In their work, reference interferograms were collected at the start of the chromatographic experiment and Gram–Schmidt orthogonalization was used subsequently to subtract the background component from a 100-point segment of each interferogram collected during the chromatographic run. Quantitative calculations were based on the magnitudes of the resulting interferogram segments.

Monfre and Brown[16,17] used classical least squares (K-matrix regression) to implement successful multivariate calibration models from FT-IR interferograms collected with mixture samples of cyclohexanol, decalin, and *m*-xylene. The individual components in the samples reached a maximum of 60% (w/w) and produced absorbance spectra in which the heights of the most intense bands were ~2 absorbance units (AU). The best calibration models were obtained with interferogram segments of ~1400 points in length and displaced 10 points from the interferogram center burst. No background interferograms were used in processing the sample interferograms, although the calculation of the calibration model did contain an average background interferogram as a zero concentration sample.

These previous studies suggest that quantitative information is present in interferogram domain data. However, none of the previous procedures used is ideally suited to nonlaboratory applications of FT-IR spectroscopy. The key requirements for these applications are (1) reduction of the length of the required interferogram, (2) elimination of the need for representative background interferograms, (3) demonstration that spectral overlap can be overcome, and (4) demonstration that the methodology can operate successfully with low analyte concentrations.

The GC/FT-IR work conducted by Sparks et al. employed only a short segment of raw interferogram data, but representative background interferograms were required in the data processing. The issue of spectral overlap was not addressed in this work, as the use of a chemical separation technique (GC) minimized the occurrence of mixture interferograms.

Monfre and Brown demonstrated an ability to overcome spectral overlap, and their approach only employed a background interferogram in the development of the calibration model. However, essentially a full interferogram was required for the analysis and the data employed corresponded to very strong analyte absorbances.

In this paper, we develop the theory for a direct interferogram quantitative analysis which includes spectral selectivity and is based on a short interferogram segment. By application of narrow-bandpass digital filters to the interferogram segment, the signals due to target bands of the analyte can be isolated. The resulting filtered interferogram data can serve as the basis for a quantitative calibration model.

Overview of Methodology. Digital Filtering. The data analysis work described here is based on the application of digital filters directly to FT-IR interferograms collected with a sample in the optical path of the spectrometer. The principal question to be addressed in this work is whether quantitative calibration models can be developed from the filtered interferogram data of low-concentration samples without the use of any background or reference measurement. In this work, digital filters were chosen to coincide with the absorption bands of benzene and nitrobenzene at 1036 and 929.5 cm^{-1}, respectively. The application of these filters has the effect of extracting specific spectral information directly from the interferogram.

Digital filters can be implemented by several approaches.[14,18,19] One of these methods, Fourier filtering, is performed by Fourier transforming the raw interferogram of benzene or nitrobenzene to obtain the corresponding single-beam spectrum. The single-beam spectrum is then multiplied by a desired filter bandpass or frequency response function, which in this work is a Gaussian

(15) Sparks, D. T.; Lam, R.; Isenhour, T. L. *Anal. Chem.* **1982**, *54*, 1922–1926.
(16) Monfre, S. L.; Brown, S. D. *Appl. Spectrosc.* **1992**, *46*, 1699–1710.
(17) Monfre, S. L.; Brown, S. D. *Appl. Spectrosc.* **1992**, *46*, 1711–1718.
(18) Oppenheim, A. V.; Schafer, R. W. *Discrete-Time Signal Processing*; Prentice Hall: Englewood Cliffs, NJ, 1989.
(19) McClellan, J. H.; Parks, T. W. *IEEE Trans. Circuit Theory* **1973**, *CT-20*, 697–701.

curve centered on the benzene or nitrobenzene absorption band. These Gaussian curves are characterized by their centered position and bandpass width at half-height. By multiplying the spectrum by the Gaussian, the target analyte band is isolated. The band is now superimposed on the Gaussian curve, while the remaining spectral features have been suppressed. Hence, the filtered spectrum has now been truncated to the Gaussian function and the superimposed analyte absorption band. Performing an inverse Fourier transform on the filtered spectrum produces a filtered interferogram.

An analogous filtering operation can be performed directly on the interferogram without the use of the Fourier transform. The Fourier transform pair of the Gaussian bandpass function in the interferogram domain is termed the impulse response function. Equivalent operations in the interferogram and frequency domains are defined by the discrete form of the convolution theorem of the Fourier transform.[18] Evaluation of the convolution sum of the interferogram and impulse response is equivalent to the multiplication of the single-beam spectrum and bandpass function, followed by the inverse Fourier transform of the product. Practical implementation of the filters in the time domain requires the calculation of a finite length impulse response that allows the infinite convolution sum to be approximated.[14,18,19]

The work reported here was performed with both Fourier filtering and filters implemented directly in the interferogram domain. For simplicity, initial feasibility studies were conducted with Fourier filtering. Filters were then generated for direct application to the interferogram in order to verify that the entire analysis could be conducted with only short interferogram segments.

Node Phenomenon. As noted above, the filtering operation simplifies the interferograms to contain information about two spectral features: (1) the spectral background truncated to the shape of the filter bandpass and (2) the analyte spectral band. The filtered interferograms are thus characterized by these two features and the interference that occurs as a result of their presence.

Previous work in our laboratory observed the differences in appearance between filtered interferograms of synthetic spectra containing absorption features of different magnitudes centered in the filter bandpass.[11] The presence of a node in the filtered interferogram was attributed to the destructive interference between the positive-going Gaussian filter bandpass function and the negative-going absorption band. The absorption band arises as a negative-going band in the single-beam spectrum because it represents a reduction in detected light intensity due to the absorption transition in the molecule. The occurrence of a node in the filtered interferogram can be understood by considering that a Gaussian function in the spectral domain with a positive maximum can be converted to a corresponding Gaussian with a negative maximum by multiplying by −1. Since the summation of these two functions in the spectral domain is zero, the linearity of the Fourier transform dictates that the summation of their corresponding interferogram domain representations must also be zero. The interferogram domain representation of a Gaussian spectral band is a damping cosine waveform of the form

$$a \exp(-w^2t^2) \cos(2\pi\nu t) \quad (1)$$

where ν is the center frequency of the band, a is proportional to the band intensity, and w is proportional to the bandwidth. In order to add to zero, the two interferogram domain functions referenced here must be out of phase by π radians, thereby causing the $\cos(2\pi\nu t)$ terms to cancel. Thus, the interferogram representation of the absorption band is out of phase with the corresponding representation of the filter bandpass function. This causes the two interferogram functions to undergo destructive interference.

When the two spectral functions are of the same shape, position, and width, complete destructive interference occurs at each interferogram point, resulting in a zero signal. However, when the two spectral functions differ in shape, position, or width, the interferogram representations damp at different rates. In this case, partial destructive interference occurs, giving rise to the observed structure of the filtered interferogram in which the signal damps to a node point and then increases again. The node occurs at the point where complete destructive interference occurs between the interferogram representations of the filter bandpass and spectral absorption band.

This case can be simulated by considering the interaction of the positive-going and negative-going Gaussians centered at frequency ν. Based on eq 1, the interferogram function, $I(t)$, resulting from their interaction is

$$I(t) = [a_1 \exp(-w_1^2t^2) - a_2 \exp(-w_2^2t^2)] \cos(2\pi\nu t) \quad (2)$$

where a_1 and w_1, respectively, describe the intensity and width of the wider positive-going Gaussian and a_2 and w_2 similarly describe the narrower (i.e., $w_2 < w_1$) negative-going Gaussian that models the analyte absorption band. It is assumed here that $0 < a_2 \leq 1$. Equation 2 describes an oscillating function that has a value of zero under two conditions: the regular zero crossings of $\cos(2\pi\nu t)$ and the node point specified by the time at which $a_1 \exp(-w_1^2t^2) - a_2 \exp(-w_2^2t^2) = 0$. By use of the quadratic formula, followed by algebraic simplification, the node point is defined as

$$t = \pm(w_1^2 - w_2^2)^{1/2}(\ln a_1 - \ln a_2)^{1/2}/(w_2^2 - w_1^2) \quad (3)$$

Inspection of eq 3 reveals that, for constant values of a_1 and w_1, the node position moves closer to time zero (i.e., the interferogram center burst) with increasing width (w_2) and intensity (a_2) of the analyte band.

Using synthetic data, two experiments were performed and the movement of the node within the filtered interferograms was noted. First, a synthetic Gaussian filter bandpass of constant width was used to filter three synthetic transmittance spectra of varying intensities (95.3, 94.3, and 91.8%). The transmittance spectra had Gaussian peaks centered at 1036 cm^{-1}, the location of the benzene absorption band serving as the target for the current work. The transmittances selected correspond to experimentally determined values from 0.065, 0.080, and 0.110 M benzene solutions. The Gaussian filter bandpass function was centered at the same spectral feature and had a full width at half-height (fwhh) of 12.6 cm^{-1}.

Filtered interferograms were obtained by multiplying each transmittance spectrum by the Gaussian bandpass function and then performing an inverse Fourier transform. Figure 1 plots points 2900–3800 (relative to the center burst) in these interferograms. Interferograms A–C of Figure 1 correspond to the filtered spectra of peak transmittances 95.3, 94.3, and 91.8%, respectively.

Two features are apparent in the filtered interferograms. First, as indicated by the arrows, nodes are present at different locations in each interferogram. For a given filter width, the node position

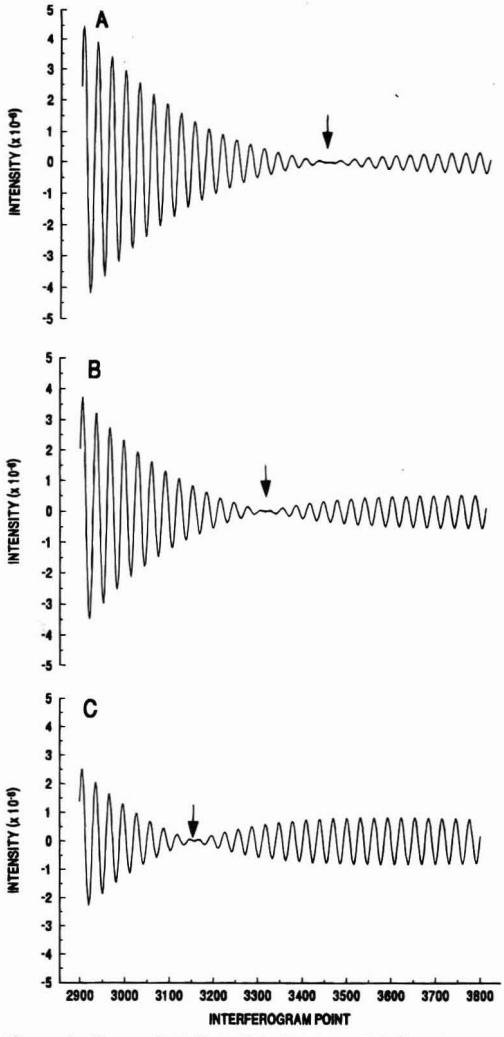

Figure 1. Segments of filtered interferograms. Interferogram segments A–C correspond to the filtered spectra of peak transmittances 95.3, 94.3, and 91.8%, respectively. Arrows denote the node position.

moves toward the center burst as the peak transmittance of the spectral band decreases or equivalently as the magnitude of the absorbance increases. Since the bands are Gaussian-shaped, the bandwidth changes with peak intensity. In the regions on either side of the node, there is an apparent relationship between interferogram magnitude and the magnitude of the spectral band. To the right of the node, interferogram magnitude increases with increasing magnitude (i.e., decreasing transmittance) of the spectral band. To the left of the node, an inverse relationship exists between interferogram and spectral band magnitudes. This suggests that it may be possible to establish a quantitative relationship between the magnitude of the filtered interferogram and sample properties (e.g., concentration) related to the magnitude of the spectral band. However, the presence of the node and its movement with spectral bandwidth and intensity suggest that such a quantitative relationship must take the node into account.

The presence of an interferogram region apparently related to the magnitude of the spectral band can be rationalized by considering the relative widths of the spectral band and filter bandpass function. Since the analyte bands are narrower than the Gaussian bandpass filter, their interferogram signals decay at a slower rate. This can be understood by considering that interferograms are a summation of cosine waveforms of different frequencies that have maximum constructive interference at the center burst. After the center burst, these signals decay at a rate governed by the frequency content of each contributing signal. Hence, the many contributing signals of different frequencies of the wider Gaussian bandpass function interfere destructively after the center burst and thus damp out faster than the fewer contributing frequencies of the narrower analyte band. Around the node position, the signal due to the Gaussian filter bandpass has almost completely decayed. Since the Gaussian is effectively no longer contributing to the signal in this region, the interferogram amplitude, after the node, should arise almost solely from the representation of the analyte spectral band. Parseval's relation for the discrete Fourier transform dictates that the sum of squares of the interferogram signal is directly proportional to the corresponding sum of squares of the spectrum. Since the filtering process allows the region of the interferogram to be isolated that corresponds almost solely to the spectral band, the interferogram magnitude in that region should be proportional to the magnitude of the analyte band.

In the second experiment, a synthetic spectrum of constant transmittance was filtered using three synthetic Gaussian bandpass filters of widths 95, 105, and 110% of the width of the synthetic spectrum. Figure 2 depicts the dependence of the location of the node on the relative widths of the Gaussian filter bandpass and the synthetic analyte band. Only a section (points 2500–3600, relative to the center burst) of the filtered interferogram is shown. Figure 2A plots the interferogram resulting from the use of a Gaussian bandpass filter with a width 95% that of the spectral band. The filter used in generating Figure 2B had a width 105% that of the spectral band, while in Figure 2C the width was 110% that of the same spectral band. It is evident from these plots that an increase in the width of the filter bandpass causes the node to move closer to the center burst of the filtered interferogram. This is due simply to the more rapid damping of the wider filter bandpass. For the cases in Figure 2B and C in which the filter bandpass is wider than the spectral band, the signal after the node increases to approximately the same amplitude. Since the spectral band is the same in both figures, this result supports the contention that the interferogram signal after the node arises almost solely from the targeted spectral band.

Direct Interferogram Analysis. Interferogram Characteristics. The experiments conducted using the synthetic data formed the basis for work on actual laboratory interferogram data derived from solutions of benzene and nitrobenzene in CS_2. Figure 3 displays sections (1090–980 cm^{-1}) of three conventionally processed absorbance spectra corresponding to benzene solutions of concentrations 0.040 (A), 0.080 (B), and 0.110 M (C).

As shown in Figure 4, the raw interferograms corresponding to the above benzene solutions exhibit no discernible differences. The labels in the figure match the spectra in Figure 3 with (D) being the raw interferogram corresponding to pure CS_2. When

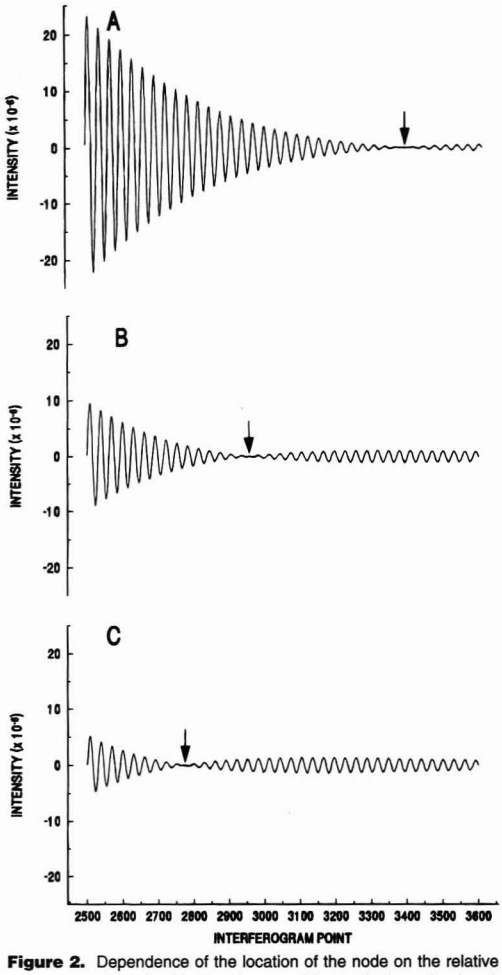

Figure 2. Dependence of the location of the node on the relative widths of the Gaussian filter bandpass and the synthetic analyte band. Interferogram segments A–C result from multiplying a synthetic spectrum by Gaussian bandpass filters whose widths are 95, 105, and 110% that of the synthetic spectral band, respectively.

these interferograms are filtered using a Gaussian filter bandpass centered at 1036 cm^{-1} and with a fwhh value of 25.6 cm^{-1}, however, two characteristic features are uncovered: (1) the node appears in a manner analogous to the synthetic interferograms in Figure 1, and (2) the interferogram amplitude after the node increases with increasing benzene concentration. The filtered interferograms are displayed in Figure 5 in a manner analogous to Figure 4. As in the synthetic data, the node is observed to move closer to the center burst with increasing concentration. However, the node positions in the laboratory data are closer to the center burst than in the synthetic data due to the use of a wider filter bandpass and the shape of the actual absorption band being more Lorentzian than Gaussian. The wider tails of the Lorentzian result in a more rapidly damping interferogram representation, thereby contributing to the movement of the node position closer to the center burst.

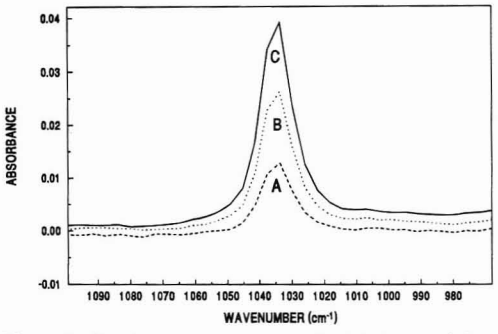

Figure 3. Absorbance spectra corresponding to benzene solutions of concentrations 0.040 (A), 0.080 (B), and 0.110 M (C).

An inspection of the interferogram amplitudes in Figure 5 suggests that a simple estimate of signal power could serve as a dependent variable to be regressed against the actual benzene concentration values in the formation of a univariate calibration model. However, the practical implementation of these concepts requires the derivation of the appropriate mathematical form for a calibration model, the development of an algorithm for finding the node point, and the optimization of experimental variables such as interferogram segment length and filter bandpass width.

Derivation of Calibration Model. Conventional infrared quantitative analysis is based on the familiar Beer–Lambert law in which, under appropriate experimental conditions, the absorbance measured at a fixed spectral wavenumber is linearly related to concentration. Specifically,

$$A(\bar{\nu}) = -\log[B_{sam}(\bar{\nu})/B_{ref}(\bar{\nu})] = \epsilon(\bar{\nu})bC \qquad (4)$$

where A is the absorbance at wavenumber $\bar{\nu}$, $B_{sam}(\bar{\nu})$ is the intensity in the sample single-beam spectrum at that wavenumber, $B_{ref}(\bar{\nu})$ is the corresponding intensity in the single-beam spectrum collected without the sample, $\epsilon(\bar{\nu})$ is the molar absorptivity of the sample molecule at $\bar{\nu}$, b is the sample path length, and C is the sample concentration. The discretely sampled interferogram sequences corresponding to $B_{sam}(\bar{\nu})$ and $B_{ref}(\bar{\nu})$ are $I_{sam}[n]$ and $I_{ref}[n]$, respectively.

Starting with eq 4 and employing the Maclaurin series expansion, $10^{-A(\bar{\nu})} \approx 1 - A(\bar{\nu})$ ln 10, Sparks et al.[15] derived the expression

$$I_{sam}[n] = I_{ref}[n] - CZ[n] \qquad (5)$$

where

$$Z[n] \overset{\mathcal{F}}{\leftrightarrow} \epsilon(\bar{\nu})b(\ln 10)B_{ref}(\bar{\nu}) \qquad (6)$$

The Fourier transform pair of the interferogram domain function, $Z[n]$, is essentially a spectrum of the sample scaled at the absorbing wavenumbers by the intensity of the reference spectrum and the path length. As $\epsilon(\bar{\nu})$ is zero except at wavenumbers where the sample absorbs, the only contribution made by $B_{ref}(\bar{\nu})$ is to scale the absorptivities to account for infrared source intensity, detector sensitivity, and any absorbance due to the sample matrix.

Rearranging eq 5, squaring both sides, and integrating the discrete interferograms over the segment from point n_1 to n_2 yields

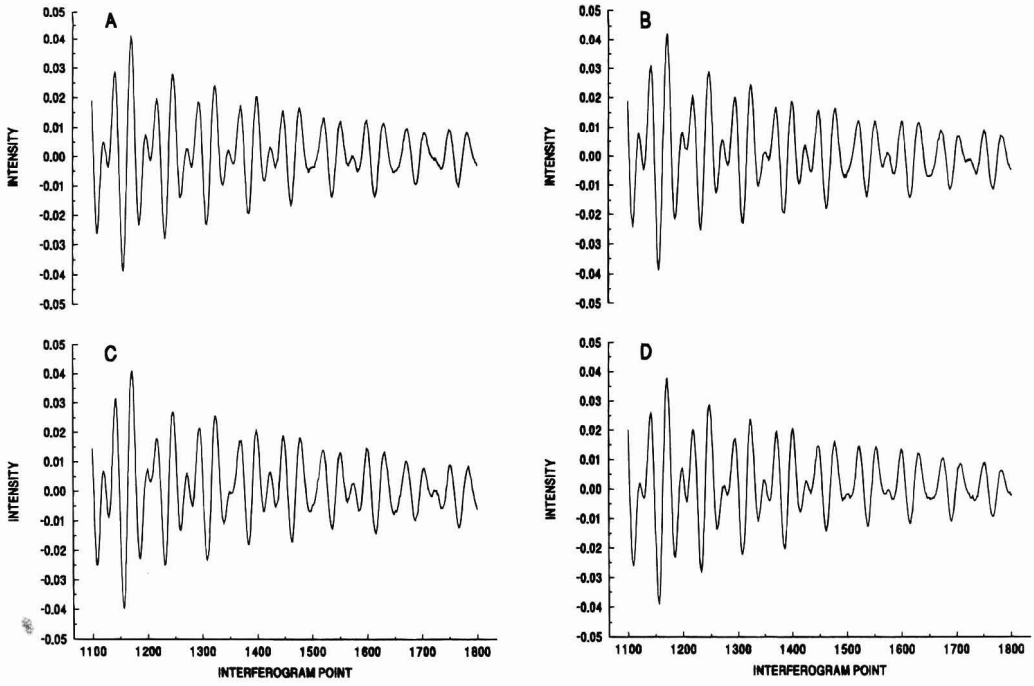

Figure 4. Raw interferograms corresponding to benzene solutions of concentrations 0.040 (A), 0.080 (B), and 0.110 M (C) and pure CS_2 (D). No discernible differences are noted between these interferograms.

$$C^2\sum_{k=n_1}^{n_2} Z[k]^2 = \sum_{k=n_1}^{n_2} (I_{\text{ref}}[k] - I_{\text{sam}}[k])^2 = \sum_{k=n_1}^{n_2} I_{\text{ref}}[k]^2 - 2\sum_{k=n_1}^{n_2} I_{\text{ref}}[k]I_{\text{sam}}[k] + \sum_{k=n_1}^{n_2} I_{\text{sam}}[k]^2 \quad (7)$$

Equation 7 can be simplified if two constraints are placed on $I_{\text{ref}}[n]$ and $I_{\text{sam}}[n]$. First, the two interferograms must be bandpass filtered in the manner described previously. In this case, their frequency content is restricted to the region of the analyte absorption band specified by the filter bandpass. Second, the segment of points n_1 to n_2 must be chosen to begin at the node point or later. Under these constraints, $I_{\text{ref}}[n]$ has little contribution to eq 7, and we obtain

$$C^2\sum_{k=n_1}^{n_2} Z[k]^2 \approx \sum_{k=n_1}^{n_2} I'_{\text{sam}}[k]^2 \quad (8)$$

where I'_{sam} denotes the filtered sample interferogram. Taking the square root of both sides and rearranging yields

$$C \approx NP \quad (9)$$

where P is the magnitude of the filtered interferogram segment computed over the range of points n_1 to n_2 and N is a sensitivity term defined as

$$N = 1/[\sum_{k=n_1}^{n_2} Z[k]^2]^{1/2} \quad (10)$$

The approximate linear relationship between analyte concentration and the magnitude of the filtered interferogram segment beginning after the node is clearly based on several key assumptions. First, the Maclaurin series approximation used in deriving eq 5 only holds for small absorbance values. Sparks et al. estimated that this approximation has less than 5% error if the absorbance value is below 0.12.[15] As displayed in Figure 3, the low benzene concentrations used in this work produce absorbance values that are less than 0.04 AU. The error in the series approximation is estimated to be less than 1% for an absorbance of 0.04 AU.

For a linear calibration model, N in eq 9 must be constant across the calibration samples. As indicated in eq 6, this requires that the sample path length, molar absorptivity, and the intensity of the filtered reference spectrum be constant with respect to concentration. Variation in sample path length is not a problem in the analysis reported here due to the use of a fixed path length sample cell. However, since the entire spectral band is isolated by the bandpass filter instead of a single wavenumber, some change in molar absorptivity is expected across the concentration range. This suggests that the linear relationship in eq 9 will only hold for a limited dynamic range of concentrations.

An assumption of constant intensity of the filtered reference spectrum is also problematical, as some variation in infrared intensity is common in an FT-IR experiment due to changes over time in instrumental characteristics such as interferometer alignment and detector temperature. In fact, even with a cooled detector, Monfre and Brown[16] found variation in interferogram intensity to be a significant source of error in their work with interferogram data. In our work, this issue is even more significant, as the use of 11 ND filters in the data collection produced variation in center burst intensities of a factor of 5 across

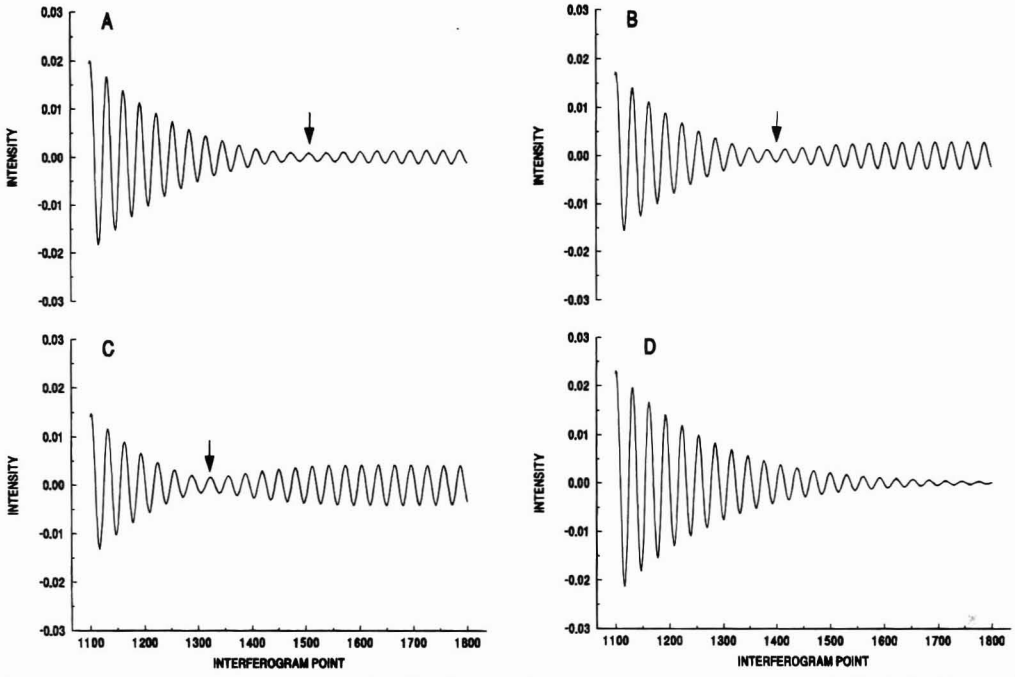

Figure 5. Interferograms from Figure 4 after filtering with a Gaussian filter bandpass centered at 1036 cm^{-1} and with a fwhh of 25.6 cm^{-1}. Note the movement of the location of the node toward the center burst with increasing concentration and the corresponding increase in interferogram amplitude after the node.

the set of collected interferograms. The impact of intensity variation in the interferogram on our analysis will be studied in detail below.

Another assumption inherent in eq 9 is that only a single analyte band has been isolated by the bandpass filter. If other analyte bands or bands from other constituents in the sample matrix fall within the filter bandpass, their interferogram signatures will add to the signature of the targeted analyte band. The filtered interferogram will then possess a more complex structure than that depicted in Figure 5. In the present work, however, this is not an issue as isolated benzene and nitrobenzene bands were used and the CS_2 solvent has no bands within the filter bandpass functions used.

Finally, the equations derived above assume that interferogram phase errors have no impact on the analysis. Examination of phase spectra computed from interferograms collected in this study revealed that, within the frequency ranges passed by the selected bandpass filters (e.g., 1020–1050 cm^{-1}), phase angles varied gradually across a span of ~0.05 radian. This small variation, coupled with the lack of narrow features in the phase spectra, suggests that phase effects will be small and will be concentrated near the center burst region of the interferogram. As indicated in Figure 5, the appropriate interferogram segments for use in a quantitative analysis are significantly displaced from the center burst region.

Node Calculation. Previous work in our laboratory[9] investigated the application of dynamical analysis techniques in the extraction of compound-specific information from FT-IR interferograms. That work detailed the construction of trajectory plots of filtered interferogram segments by plotting the first derivative of intensity (denoted I') vs intensity for each point in the segment. These trajectory plots were then characterized by plotting time (i.e., interferogram point number) as a third dimension for each point on the trajectory. The system modeled by the trajectory was characterized by selecting a plane, termed a surface of section, which intersected the three-dimensional time series graph of the trajectory. The plane selected was that defined by I' and time. A "map" of the system was produced by the points on the surface of section where the trajectory intersected the plane. Stated differently, the map traces the profile of the filtered interferogram in time. This map is termed a surface of section map, or Poincaré map,[20] and forms the basis for the node calculation algorithm used here. Figure 6 is a display of the surface of section map generated from the filtered interferogram in Figure 5C. Comparison of Figures 5C and 6 reveals that the node point coincides with the first minimum in the surface of section map. This point is indicated by the arrow in Figure 6. As the interferogram point spacing is smaller than the point spacing in the surface of section map, some error is introduced by simply taking the minimum point in the surface of section map as the node. However, the effects of this slight imprecision in the node determination on the quantitative analysis appear to be small.

Effect of Variation in Interferogram Intensity. The dependence of N in eq 9 on the intensity of the filtered reference spectrum suggests that variation in interferogram intensity must

(20) Thompson, J. M. T.; Stewart, H. B. *Nonlinear Dynamics and Chaos*; John Wiley & Sons: Chichester, England, 1986.

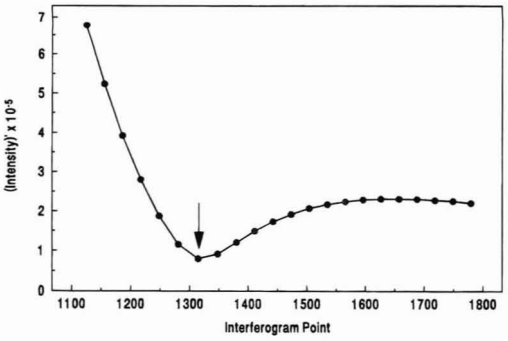

Figure 6. Surface of section map generated from the filtered interferogram in Figure 5C. The arrow points to the location of the node.

be corrected if a linear calibration model is to be obtained. Initial attempts to correlate the magnitude of the filtered interferogram segment with analyte concentration confirmed this hypothesis, thus requiring efforts to normalize the overall infrared intensity. For each interferogram point, i, normalized intensities, $I_{\text{sam},n}[i]$, were computed as

$$I_{\text{sam},n}[i] = I_{\text{sam}}[i]/[\sum_{k=n_a}^{n_b} I_{\text{sam}}[k]^2]^{1/2} \qquad (11)$$

The normalizing constant in the denominator of eq 11 corresponds to the magnitude of a selected segment of the interferogram (i.e., points n_a to n_b) before filtering has been performed. Three experiments were conducted with the benzene interferogram data to assess the impact of the choice of this segment. The segments used in these experiments were (1) the entire interferogram (points 1−8192); (2) segments of length 10, 25, 50, 100, 200, 300, 400, 500, 1000, 1500, 2000, 2500, and 3000 points, beginning at the center burst; and (3) points 1000−2000, relative to the center burst. The latter segment specifies a region of the interferogram displaced from the center burst but which contains the nodes for all benzene concentrations when the interferograms are filtered.

The effects of normalization were studied by use of a Gaussian filter with a fwhh of 25.6 cm^{-1}. The filter was positioned at 1036 cm^{-1}, coinciding with the center of the targeted benzene band. A 400-point segment of the filtered interferogram was used, beginning at the node point. For each experiment, the 644 raw benzene interferograms were normalized and bandpass filtered, the nodes were located, and the magnitudes of the 400-point segments were computed. Regression analysis was then used to obtain a univariate calibration model relating the magnitude of the filtered segment to benzene concentration. Correlation plots were then constructed in which benzene concentration estimated by the calibration model was plotted vs actual concentration.

Figure 7 displays two correlation plots, corresponding to the use of unnormalized data (top) and data normalized by using the entire interferogram (bottom). The normalization significantly reduces the variation within the segment magnitudes corresponding to each concentration. The regression results for the unnormalized data were an R^2 of 47.76% and a t value for the significance of the slope of 24.23. The corresponding values for the normalized data were 99.39% and 323.46. The plots in Figure 7 and the corresponding statistics indicate that an excellent univariate

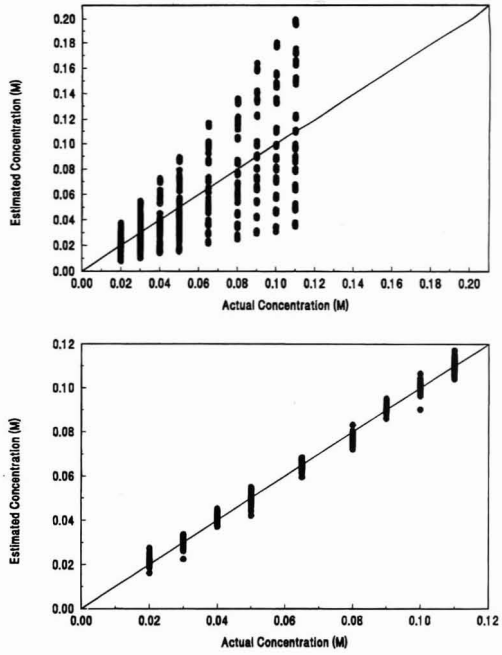

Figure 7. Correlation plots of estimated vs actual benzene concentrations corresponding to the use of unnormalized data (top) and data normalized using the entire interferogram (bottom). Normalization significantly reduces the variation within the segment magnitudes corresponding to each concentration.

calibration model can be obtained with filtered interferogram data, but that normalization is essential to overcome the effects of intensity variation in the interferogram. Although the 5-fold range in interferogram intensity intentionally generated in this experiment is a level of variation that would not be encountered in normal applications, this work suggests that interferogram normalization should still be performed in order to obtain optimal results.

Little difference was noted among the normalization experiments, as long as the segment used in computing the normalizing constant exceeded 50 points. The use of the segment displaced from the center burst also yielded equivalent results. This is significant because it demonstrates that the center burst region is not necessary for normalization purposes. As long as the unfiltered interferogram is used in computing the normalizing constant, it appears that information regarding the overall infrared intensity is still present at segments significantly displaced from the center burst. Given that the various normalizing segments produced equivalent results, the remainder of the work presented here simply used the entire interferogram in computing the normalizing constant.

Optimization of Experimental Variables. The discussion of Figures 1 and 2 demonstrates that the choice of the interferogram segment to be used in computing the power of the filtered interferogram signal depends directly on the width of the filter bandpass. Thus, an optimization of the segment and bandpass width must be performed. Also, the frequency position of the filter bandpass must be considered. Usually, the best filter position will be a location centered on the analyte spectral band

whose interferogram signature is to be extracted by the filter. This location may not be optimal, however, if other species are present in the sample that give rise to interfering spectral bands. In this case, adjustment of the filter position to a location away from the center of the analyte band may produce better results. In the present application, however, no interfering bands were present in the benzene/CS_2 or nitrobenzene/CS_2 spectra. Thus, for both analytes, filters were held at a fixed position, centered on the analyte bands.

An inspection of Figure 5 reveals that, around the node, the signal intensity is very low and thus the contribution to the magnitude calculation is small. It was hypothesized that offsetting the segment magnitude calculation from the node might allow a shortened segment to be used with equivalent or better results. Thus the length of this segment offset defines another experimental variable requiring optimization.

Experiments directed to the optimization of the interferogram segment, filter bandpass, and segment offset were performed first with the benzene data and employed Fourier filtering. Subsequent experiments performed with the nitrobenzene data were found to produce analogous results. The benzene results will be presented in detail first, followed by the nitrobenzene results in summary form. Results from time domain filtering will be presented last to confirm that the entire computation can be performed with a short interferogram segment.

As noted above, all Gaussian functions generated were chosen to coincide with the benzene spectral band at 1036 cm^{-1}. The filter widths studied were 22.8, 24.6, 25.6, 26.5, 28.3, and 30.1 cm^{-1}. The interferogram segments studied were chosen with the node as the starting point and included segment sizes of 100, 200, 300, 400, 500, 600, 700, 800, 900, and 1000 points. A maximum of 1000 points was used as it was anticipated that, beyond this segment size, no further improvement in the calibration results would be observed. The segment offsets studied were 50, 75, 100, 150, and 200 points.

For each filter, the 644 benzene interferograms were filtered, the node in each filtered interferogram was located, and the magnitude of the appropriate segment was computed. As specified by eq 9, univariate linear regression was then performed with the segment magnitudes as the dependent variable and the known benzene concentrations as the independent variable. The t value for the significance of the slope was used as a measure of the goodness of fit of the calibration model. As anticipated, beyond interferogram segment size 400, lengthening the segment produced no additional benefit. The largest t values obtained were in excess of 320, indicating excellent fit. The best results were exhibited by the Gaussian function with fwhh value of 25.6 cm^{-1} (base width 69 cm^{-1}), a segment length of 200 points, and an offset of 100 points. The optimal filter width can be compared to the fwhh of 12 cm^{-1} and the base width of 70 cm^{-1} of the benzene spectral band. The filter thus effectively isolates the entire benzene band. For this optimal model, an excellent fit was obtained, as evidenced by the t value of 328.57 and an R^2 of 99.41%. This result is particularly impressive, given the low signal-to-noise ratios present in the data collected with the least transmissive ND filters. For example, with the 19.1% T filter and the lowest benzene concentration, the signal-to-noise ratio of the benzene band in computed absorbance spectra was only 5.6. This indicates that the interferogram-based methodology is able to extract analyte signals near the limit of detection.

Nitrobenzene Analysis. The studies performed on the benzene data were repeated with the 648 nitrobenzene interferograms. The best results were obtained with a filter with fwhh value of 36.5 cm^{-1} (base width 99 cm^{-1}) centered on the band at 930 cm^{-1}, an interferogram segment length of 200 points, and a segment offset of 100 points. The univariate regression analysis yielded an R^2 of 99.05% and t value of 259.27. The optimal filter width can be compared with the fwhh of 9 cm^{-1} and the base width of 37 cm^{-1} of the nitrobenzene spectral band. For nitrobenzene, the best calibration model employs a filter somewhat wider than the spectral band. However, there are still no other spectral signals within the filter bandpass, and thus the form of the quantitative relationship in eq 9 should still be valid.

Time Domain Filtering. As noted previously, the drawback to the Fourier filtering procedure is that it begins with a single-beam spectrum computed from a full-size interferogram. However, for compatibility with the requirements of an ideal spectrometer for use in nonlaboratory applications, the analysis needs to be implemented with time domain filters able to operate with only the actual interferogram segment required for the calibration model.

To implement time domain filtering in the interferogram analysis, filters must be designed that represent the filter bandpass accurately in the interferogram domain and thus allow the convolution sum to be approximated. The filter design method used here was developed in our laboratory and has been applied successfully in our previous qualitative analysis work with interferogram data.[14] In this work, a dual-stage filtering strategy was used which employed a constant-width wide-bandpass finite impulse response (FIR) filter followed by a narrow-bandpass time-varying FIR filter with separate filter coefficients for use at each interferogram point. The bandpass width of the time-varying filter was varied, and each filter was computed for interferogram points 950–2700, relative to the center burst. This is the region of the interferogram within which all the nodes reside. The effect of offsetting the interferogram segment magnitude calculation from the node point of the time domain filtered interferograms was also studied. The offsets used were 50, 75, 100, 125, and 150 interferogram points from the node.

For benzene, the best calibration model from the studies of time domain filtering was generated with an interferogram segment of 300 points, a segment offset of 75 points, and a filter centered on the benzene band with a fwhh of 62 cm^{-1}. The calibration model produced an R^2 of 99.54% and a t value of 371.63. These values represent a slight improvement to those obtained with Fourier filtering.

The best results for similar studies with the nitrobenzene data used a 500-point segment, a segment offset of 50 points, and a filter with fwhh of 90 cm^{-1}. The values of R^2 and t from the regression analysis were 99.39% and 325.60, respectively. These results are also slightly better than those obtained with Fourier filtering.

The optimal time domain filters are significantly wider than the optimal filters used with the Fourier filtering. This is due to the difficulty in computing accurate time domain filters that have both very narrow widths and good attenuation characteristics for frequencies outside of the filter bandpass. The filters found to be optimal represent the best compromise found between these two properties.

Table 1. Comparison of Spectral- and Interferogram-Based Analyses

	benzene			nitrobenzene		
analysis method	R^2 (%)	s^a (mM)	% error[b]	R^2 (%)	s^a (mM)	% error[b]
spectral	99.63	1.84	2.60	99.51	2.11	2.44
interferogram (Fourier filter)	99.41	2.32	3.42	99.05	2.94	3.28
interferogram (time domain filter)	99.54	2.05	2.98	99.39	2.34	2.49

[a] Standard deviation of the residuals in plot of estimated vs actual concentration. [b] Mean of absolute values of relative errors computed across all observations.

Spectral Domain Analysis. Benzene Analysis. Using the same benzene data set, a conventional quantitative analysis of absorbance spectra was performed in order to compare the results to those obtained above with the interferogram data. Absorbance spectra were computed by use of an air background spectrum collected with no ND filter in place. Both univariate and multivariate calibration models were tested and were found to give equivalent results. The univariate work will be reported here to provide a more direct comparison to the univariate interferogram-based models.

In computing the univariate calibration models, spectral baseline correction was performed by use of spectral regions of 1140–1100 cm^{-1} and 980–940 cm^{-1} to define a second-order polynomial baseline model. The region of the benzene band was 1045–1025 cm^{-1}. Three methods were tested for computing the benzene absorbance: (1) the peak maximum in the band range, (2) the integrated band area, and (3) an automatic area calculation which corrects for band shifts.[21] Calibration models were then computed and compared with those obtained with the interferogram data. Use of the peak maximum gave the best results producing values of R^2 and t of 99.63% and 414.62, respectively.

Nitrobenzene Analysis. A similar experimental procedure was used with the 648 nitrobenzene absorbance spectra. Baseline correction was performed based on the use of the spectral regions from 960 to 950 cm^{-1} and 920 to 910 cm^{-1} to define a linear baseline model. The region of the analyte band was 940–923 cm^{-1}. The same procedures described above for computing absorbance values were used. This study produced a calibration model with an R^2 of 99.51% and a t value of 360.63.

Comparison of Spectral and Interferogram-Based Analyses. Table 1 compares the results obtained with the spectral- and interferogram-based analyses in terms of the R^2 values for the calibration models and the residuals of the correlation plots of estimated vs actual concentrations. For the interferogram work, results are reported for both Fourier filtering and time domain filtering. For both the benzene and nitrobenzene analyses, the standard deviations of the residuals are reported, as well as the mean percent relative error in concentration. The values reported in Table 1 provide further confirmation that the results of the spectral- and interferogram-based analyses are comparable.

(21) Arnold, M. A.; Small, G. W. *Anal. Chem.* **1990**, *62*, 1457–1464.

CONCLUSIONS

The results obtained in this study confirm that a quantitative analysis can be implemented by use of short segments of bandpass-filtered interferograms. This analysis meets the data collection and data processing requirements for the use of FT-IR spectroscopy in nonlaboratory applications. No background interferograms are required at any step of the procedure, and the method incorporates spectral selectivity into the interferogram-based analysis through the use of bandpass digital filters. The interferogram-based analysis performs analogously to spectral-based analyses, even at concentration values that approach the limit of detection. Furthermore, the interferogram-based method is computationally more efficient than the spectral analysis and is compatible with a completely automated implementation. There are no subjective components to the procedure such as the requirement for baseline correction in the spectral analysis.

Current work in our laboratory is focusing on extending the methodology described here to the case in which signals from more than one absorbing species are present within the range of frequencies passed by the digital filter. In this case, one of the key assumptions used in the derivation of eq 9 no longer holds, as the filtering operation itself cannot guarantee complete spectral selectivity. Preliminary results suggest that the use of multivariate calibration techniques in conjunction with digital filtering overcomes this problem while still allowing the analysis to be completed with a short interferogram segment.

ACKNOWLEDGMENT

This research was supported by the National Institutes of Health under Grant 1-R01-DK45126-01A1. The Department of the Army is acknowledged for providing the Silicon Graphics 4D/460 computer system. Portions of this work were presented at the 25th American Chemical Society Central Regional Meeting, Pittsburgh, PA, October 1993.

Received for review December 8, 1994. Accepted April 25, 1995.[⊗]

AC941186L

[⊗] Abstract published in *Advance ACS Abstracts,* June 1, 1995.

Anal. Chem. **1995,** *67,* 2279–2283

Artifacts Related to Sample Introduction in Capillary Gel Electrophoresis Affecting Separation Performance and Quantitation

András Guttman*,† and Herbert E. Schwartz‡

Beckman Instruments, Inc., 2500 Harbor Boulevard, Fullerton, California 92634, and Palomar Analytical Services, 150 Montalvo Road, Redwood City, California 94062

Two injection-related artifacts with capillary gel electrophoresis (CGE) are reported. The first occurs with consecutive injections from the same, low-volume (10–200 μL), aqueous sample: progressively smaller peak heights are obtained with each injection. This phenomenon is explained in qualitative terms by examining the electrochemical processes occurring during the electrokinetic sample introduction. A simple solution to this problem is to perform an intermediate electrokinetic injection from a water vial prior to the sample injection. This two-step injection procedure results not only in dramatically increased precision (important for quantitative studies) but also in increased sample loading. The second artifact observed in CGE is related to the physical shape of the inlet of the gel-filled capillary: employing an oblique edge capillary results in poor performance, peak distortion, and loss in resolution.

In capillary gel electrophoresis (CGE), two types of capillary columns are presently used.[1,2] Those of the first type, involving relatively low-viscosity polymer networks such as those consisting of linear polyacrylamide or alkylcellulose, are often referred to as "replaceable", as the gel can be rinsed in and out of the capillary. In the second type of column, the relatively high-viscosity gel is "fixed" inside the capillary, usually chemically anchored to the capillary wall surface. The first column type is frequently applied to double-stranded (ds) DNA (e.g., PCR product) analysis; the latter capillary column type is typically used for analyzing single-stranded (ss) DNA (primers and probes), including antisense DNA. With replaceable gels, sample introduction can be made by either hydrodynamic (pressure, vacuum) or electrokinetic means. The hydrodynamic injection is generally preferred in quantitative work. Here, the composition of the sample introduced as a plug into the capillary should be exactly that of the original sample. With the electrokinetic injection, mobility differences between sample components cause a sampling bias; high-mobility analytes are preferentially introduced into the capillary over slow-moving ones.[3,4] In addition, effects due to the presence of salt or other substances in the sample must be carefully considered. For example, when electrokinetic injections are made from samples containing different salt concentrations, the amount of analyte detected may vary considerably.[5] This may directly affect quantitation, e.g. in the accuracy of a drug assay,[6] necessitating the use of external and/or internal standards.[6–8] However, with the use of nonreplaceable, fixed gels, electrokinetic sample introduction is the only injection mode feasible, as the high-viscosity gel prevents aqueous sample plugs from entering the capillary.

Clearly, many earlier problems affecting precision and accuracy (e.g., those related to voltage, temperature and electroosmotic flow control) with "manual" capillary electrophoresis (CE) instruments have been overcome by the emergence of automated sample introduction systems[4,9] and commercial CE instrumentation.[10] Butler et al.[8] recently compared the precision feasible with CGE with other methods (slab gel, hybridization, spectrophotometry) for the quantitation of PCR products. Using an internal standard, precision values of ~0.1% and ~3% relative standard deviation (RSD) were reported for migration times and peak areas, respectively. However, as is evident from the recent CE literature, several peculiar effects related to sample introduction and matrix effects are still reported. Grushka and McCormick[11] calculated a "maximum allowable plug length" based on the solute's diffusion coefficient and analysis time. The authors found that the insertion of the capillary into a sample vial may result in an inadvertent injection. A detailed study of this effect, caused by an interfacial pressure difference at the inlet of the capillary, was recently

† Beckman Instruments, Inc.

‡ Palomar Analytical Services.

(1) Guttman, A. In *Handbook of Capillary Electrophoresis*; Landers, J. P., Ed.; CRC Press: Boca Raton, FL, 1994; p 129.

(2) Pariat, Y. F.; Berka, J.; Heiger, D. N.; Schmitt, T.; Cohen, A. S.; Foret, F.; Karger, B. L. *J. Chromatogr. A* **1993**, *652*, 57.

(3) Huang, X.; Gordon, M. J.; Zare, R. N. *Anal. Chem.* **1988**, *60*, 375.

(4) Rose, D. J., Jr.; Jorgenson, J. W. *Anal. Chem.* **1988**, *60*, 642.

(5) Satow, T.; Machida, A.; Funakushi, K.; Palmieri, R. *J. High Resolut. Chromatogr.* **1991**, *14*, 276.

(6) Srivatsa, G. S.; Batt, M.; Schuette, J.; Carlson, R. H.; Fitchett, J.; Lee, C.; Cole, D. L. *J. Chromatogr. A* **1994**, *680*, 469.

(7) Dose, E. V.; Guiochon, G. A. *Anal. Chem.* **1991**, *63*, 1154.

(8) Butler, J. M.; McCord, B. R.; Jung, J. M.; Wilson, M. R.; Budowle, B.; Allen, R. O. *J. Chromatogr. B* **1994**, *658*, 271.

(9) Schwartz, H. E.; Melera, M.; Brownlee, R. G. *J. Chromatogr.* **1989**, *480*, 129.

(10) Warner, M. *Anal. Chem.* **1994**, *66*, 1137A.

(11) Grushka, E.; McCormick, R. M. *J. Chromatogr.* **1989**, *471*, 421.

0003-2700/95/0367-2279$9.00/0 © 1995 American Chemical Society

published by Fishman et al.[12,13] Peak broadening due to penetration of residual analyte from the outside of the capillary was described by Lux et al.[14] By simply dipping the capillary in buffer after sample introduction, the problem can be prevented. Ermakov et al.[15] observed artifactual peak splitting due to interaction of sample and background electrolyte. In the analysis of dsDNA with pressure injection, sample matrix effects were investigated by van der Schans et al.[16] The injection of an additional plug of a low-resistance solution (e.g., 0.1 M Tris–acetate) prior to the sample resulted in improved resolution.

During the course of our work with CGE, we have experienced two injection-related problems which may affect precision and accuracy as well as separation performance. The first problem (chemical artifacts) manifests itself with repetitive electrokinetic injections from the same sample vial. With successive injections, progressively smaller amounts of sample are introduced into the capillary, resulting in decreasing peak heights and areas. This injection problem was especially pronounced when the sample introduction was performed from sample volumes of ~10–200 μL. This phenomenon was briefly mentioned in a paper dealing with PCR product analysis on a replaceable gel matrix[17] and was experienced also with fixed gel capillaries.[18] With capillary zone electrophoresis (CZE), Rose and Jorgenson[4] briefly mentioned the possibility of sample contamination by the formation of electrochemical reaction products resulting from the flow of current through the sample solution. However, no thorough explanation of or solution to the problem has been reported so far. The second injection problem in CGE (physical artifacts) we report involves the physical shape of the capillary end. A nonperpendicular edge (e.g., due to a poor cut during the manufacturing process) at the inlet side of the capillary results in substantial peak distortion, causing serious loss in resolution, whereas a capillary with a straight edge does not. In this technical note, we investigate these effects and propose simple ways to prevent these problems.

EXPERIMENTAL SECTION

In all studies, a P/ACE system 2100 CE apparatus (Beckman Instruments, Inc., Fullerton, CA) was used in reversed polarity mode (cathode on the injection side). The separations were monitored on-column at 254 and 230 nm for the electrokinetic injection (oligonucleotide) and the column edge (naproxen) experiments, respectively. The temperature of the cartridge containing the polymer network-filled capillary column was thermostated at 20 ± 0.1 °C by the liquid cooling system of the P/ACE instrument. The electropherograms were acquired and stored on an IBM 486/66 MHz computer and were evaluated with System Gold software (Beckman Instruments, Inc.).

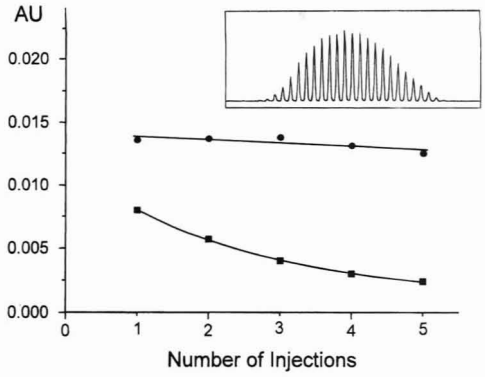

Figure 1. Peak height of the $p(dA)_{50}$ (absorbance units) versus numbers of consecutive injections. Inset: Capillary gel electrophoresis separation of the test mixture of $p(dA)_{40-60}$; time frame, 20–27 min. Conditions: eCAP-ssDNA-100 gel-filled capillary column; E = 300 V/cm; t = 20 °C; sample, 7.4 μg/mL total DNA in water; injection, (■) 1.5 s, 7.5 kV electrokinetic injection from sample vial ("regular injection"), and (●) 1.5 s, 7.5 kV electrokinetic injection from sample vial preceded by a 1.5 s, 7.5 kV electrokinetic injection from water ("water preinjection").

In the oligonucleotide separation experiments the eCAP-ssDNA-100 kit (Beckman Instruments, Inc.) was used with a 100 μm i.d., 30 cm effective length (37 cm total length) coated capillary tubing filled with a high-concentration, non-cross-linked, linear polyacrylamide gel in 100 mM Tris–borate (pH 8.5) buffer. The use of a coated capillary in conjunction with the polymer network results in negligible electroosmotic flow (EOF). A 0.2 OD (7.4 μg/mL total DNA with Na as counterion) solution of poly(deoxyadenylic acid), $p(dA)_{40-60}$, supplied with the kit was dissolved in deionized water to the final concentration of 0.5 μM. During the electrophoresis, an electric field of 300 V/cm was applied to the gel-filled capillary columns in all the experiments. In order to remove impurities from the polyacrylamide gel, the capillary column was pre-electrophoresed with the appropriate running buffer at 100, 200, and 300 V/cm for 10 min each. The samples were injected electrokinetically onto the column by applying a power of 0.124 W (voltage, 7.5 kV; current, 11 μA; injection time, 1.5 s). The tip of the capillary was immersed into deionized water before and after the injections to avoid any buffer and sample carryovers. The pH change of the DNA samples during the different injection procedures was measured with a Beckman ϕ-72 pH meter equipped with a microelectrode.

For the capillary edge evaluation experiments, 25 μm i.d., 375 μm o.d., 20 cm effective length (27 cm total length) untreated fused silica capillary tubing was used. The 25 μm i.d., 375 μm o.d. capillary was selected to investigate the worst possible case (i.e., where the free silica surface to volume ratio is the largest). Ultrapure grade 200 mM 2-(*N*-morpholino)ethanesulfonic acid (MES) was used for the buffer, adjusted to pH 5.0 with tetrabutylammonium hydroxide (TBAH) (ICN, Costa Mesa, CA). The *R,S*-naproxen was used in a 10:1 enantiomeric ratio during the experiments and was a kind gift of Prof. Gyula Vigh, Texas A&M University, College Station, TX. The poly(ethylene oxide) (MW 300 000) was purchased form Sigma (St. Louis, MO) and the hydroxypropyl-β-cyclodextrin (HP-β-CD) was from American Maize (Tucson, AZ). The gel–buffer system contained 200 mM

(12) Fishman, H. A.; Amudi, N. M.; Lee, T. T.; Scheller, R. H.; Zare, R. N. *Anal. Chem.* **1994**, *66*, 2318.
(13) Fishman, H. A.; Scheller, R. H.; Zare, R. N. *J. Chromatogr. A* **1994**, *680*, 99.
(14) Lux, J. A.; Yin, H. F.; Schomburg, G. *Chromatographia* **1990**, *30*, 7.
(15) Ermakov, S. V.; Zhukov, M. Y.; Capelli, L.; Righetti, P. G. *Anal. Chem.* **1994**, *66*, 4034.
(16) van der Schans, M. J.; Allen, J. K.; Wanders, B. J.; Guttman, A. *J. Chromatogr. A* **1994**, *680*, 511.
(17) Schwartz, H. E.; Ulfelder, K.; Sunzeri, F. J.; Busch, M. P.; Brownlee, R. G. *J. Chromatogr.* **1991**, *559*, 267.
(18) Guttman, A.; Ohms, J. I.; Cooke, N. High resolution separations of oligonucleotides using capillary gel electrophoresis; Third International Symposium on High Performance Capillary Electrophoresis, San Diego, CA, 1991; Poster PT-11.

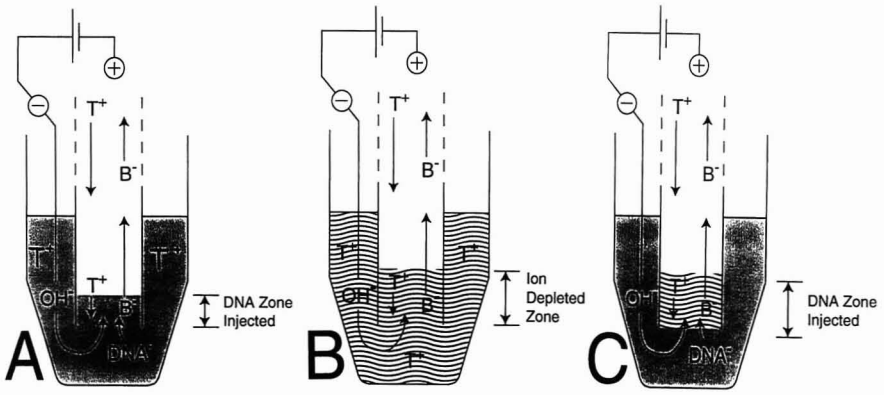

Figure 2. Schematic diagrams illustrating the sample introduction processes. (A) Regular electrokinetic injection. DNA enters the capillary. Hydroxyl ions are generated at the electrode. Tris ions migrate from the capillary into the sample vial. Borate migrates toward the anode. At the end of this injection, a DNA zone has been introduced into the capillary. (B) Electrokinetic injection from water (water preinjection). Tris (T^-) and borate (B^-) migrate to the cathode and anode, respectively. Hydroxyl ions are generated at the cathode. An ion-depleted zone (high resistance, low conductivity) is created at the end of the capillary. (C) Electrokinetic sample injection with prior preinjection of water. The ion-depleted zone at the end of the capillary results in a larger DNA zone to enter the capillary.

MES/TBAH, 10 mM HP-β-CD and 0.4% polymeric additive, pH 5.0. The use of a low-viscosity polymer network permitted replacement of the gel–buffer system in the capillary column by means of the pressure rinse operation mode of the P/ACE apparatus (i.e., replaceable gel). The tip of the oblique edge capillary was rasped to a 45° angle under a microscope using a cutting tool. The polyimide outside coating was removed from the end (5 mm) of the column with a razor blade to avoid any sample or buffer trapping between the fused silica capillary and the coating. The samples were injected by pressure (injection time, 3 s; pressure, 0.5 psi = 3447.4 Pa) into the replaceable gel-filled capillary column. Similar to the DNA experiments, the tip of the capillary was immersed into deionized water before and after the injection to avoid any carryovers.

The samples were either stored at −20 °C or freshly used. All buffer solutions were filtered through a 0.45 μm pore size filter (Schleicher and Schuell, Keene, NH) and carefully vacuum degassed before use.

RESULTS AND DISCUSSION

Chemical Artifacts. In most applications of CE, the injection volumes are small, typically ~1–100 nL. Overloading the capillary, i.e., introducing a sample plug which is too large, results in extra zone broadening,[11] unless stacking conditions with discontinuous buffers prevail.[19] The small volume required for introduction into the capillary can be especially advantageous when sample is available only in limited quantities (low microliter volumes). In this case, however, it is difficult to aliquot the original sample. Therefore, multiple injections (needed to increase the confidence of the analytical results and precision studies) have to be performed from the same sample vial.

The inset in Figure 1 shows the separation of a $p(dA)_{40-60}$ test mixture on a high-viscosity gel-filled capillary column. The sample was electrokinetically (7.5 kV, 1.5 s) injected from a 50 μL, 0.2 OD (~0.5 μM) solution placed in a 400 μL polypropylene minivial ("regular injection"). Consecutive injections from this vial resulted in an observed decrease in peak absorbance and peak area, i.e., a decrease in the amount of sample introduced into the capillary. In Figure 1 (lower trace), this is expressed as an exponential decrease in absorbance of the maximum peak, $p(dA)_{50}$, of the polydeoxyadenylic acid sample over five consecutive runs. Note that injection number 5 had a 70% lower peak height than that of injection number 1. The decrease in absorbance was less pronounced when the sample volume was increased. The same experiment using an 80× larger sample volume (4 mL) did not result in a significant decrease in peak absorbance (results not shown). It should be noted that the same decreasing trend in sample amount was also observed with other types of CGE columns and DNA samples, e.g., with consecutive electrokinetic injections of dsDNA on replaceable polymer network columns.[17,18] For both the replaceable and the fixed gel columns, similar experimental CE conditions apply, such as similar Tris–borate buffer, coated capillary, no EOF, and reversed polarity.

Figure 2A sketches the situation of the first sample injection. Upon applying voltage, negatively charged DNA is drawn into the capillary. OH^- is generated at the cathode according to the electrochemical reaction $2H_2O + 2e \rightharpoonup 2OH^- + H_2$ and is moving into the capillary toward the anode. Tris migrates out of the capillary and into the sample solution. During the injection process, incoming hydoxyl ions will shift the $TH^+ \rightharpoonup T + H^+$ equilibrium to the right, thereby reducing the effective mobility of Tris. Borate migrates toward the anode. The amount of hydroxyl ions generated in the sample vial during the electrolysis can be estimated from Faraday's law and would equal 3.4 μM, corresponding to pH 8.5. With consecutive injections, the hydroxyl and Tris concentrations as well as the pH in the sample vial will continue to increase (electrical resistance decreases). Using a micro-pH meter, the pH in the sample solution was measured. During the series of injections, the pH in the sample solution was found to increase from 7.1 to 8.5 (~20% increase). After the hydroxyl concentration reaches an appreciable number, DNA (sample concentration, 0.5 μM) will compete with hydroxyl for introduction into the capillary. As hydroxyl is more mobile

(19) Chien, R.-L.; Burgi, D. S. *Anal. Chem.* **1992**, *64*, 489A.

than DNA ($\mu_{DNA} = 5 \times 10^{-9}$ m^2 V^{-1} s^{-1}; $\mu_{OH} = 200 \times 10^{-9}$ m^2 V^{-1} s^{-1}), it serves as a more efficient current carrier than the DNA. Consequently, the amount of DNA injected with consecutive injections will decrease, as indeed is seen in Figure 1.

A simple solution to the above problem is to perform an electrokinetic injection from water just prior to the actual sample injection (Figure 2B; the capillary was positioned between two vials containing water; the injection time was the same as that of the sample injection). During this "preinjection", Tris migrates into the water vial, while OH^- is generated at the cathode. An "ion-depleted" zone (i.e., a relatively high-resistance, low-conductivity zone) is created at the end of the capillary. Subsequently, the capillary—with its ion-depleted zone—is positioned into the sample vial for the second (DNA) injection (Figure 2C). pH measurements revealed only a 2% increase in the pH of the sample vial after five injections carried out in this fashion (as opposed to a 20% increase without the preinjection of water, see above).

An important consequence of the introduction of a relatively high-resistance, low-conductivity zone into the capillary is that the local field strength in this zone is relatively high. Hence, more sample is pulled into the capillary than would occur without the intermediate water injection.[19] With the intermediate water injection technique, a substantial increase in UV absorbance (peak height) is observed (2-fold for the first and a 5-fold for the last injection; compare traces in Figure 1). A similar double injection was performed by Ulfelder et al.[20] and Butler et al.[8] with a replaceable gel matrix (alkylcellulose solutions). In these experiments, the water plug was introduced by hydrodynamic means (pressure), with the object to maximize sample detectability for low-copy DNA applications.

The slightly decreasing trend in the upper trace of Figure 1 suggests that the water injection did not completely eliminate the (exponential) decrease in absorbance shown in the lower trace. Perhaps small amounts of Tris—as well as hydroxyl generated at the cathode—still migrate into the sample vial, affecting the sample load with each subsequent injection. However, precision is greatly improved compared to the experiments without the intermediate water injection. The data points of Figure 1 (upper trace) resulted in a RSD peak height of 4.0% (five consecutive injections), typical of the precision achievable with CGE without internal standards.[6] Optimization of the preinjection and sample injection times may further increase precision. In addition, the presence of salt in the sample (common with PCR samples) will affect sample loadability.[17,20,21] Work is in progress in our laboratory to investigate these effects. Encouraging preliminary results have been obtained with the above-described electrokinetic injection technique for nondesalted PCR samples, resulting in excellent DNA peak efficiency.[22]

Physical Artifacts. In recent years, various "physical", injection-related effects, affecting separation performance, have been discussed in the literature. With micellar electrokinetic capillary chromatography (MECC), Lux et al.[14] found that during the injection process, "carryover" liquid at the end of the capillary results in peak asymmetry; the authors suggested an additional rinsing step in the sample introduction procedure. With CZE, Fishman et al.[12,13] studied an "ubiquitous" injection occurring when a capillary just touches a sample solution. The interfacial pressure difference across the curved surface of the droplet at the end of the capillary is causing a small amount of sample to be pulled into the capillary.

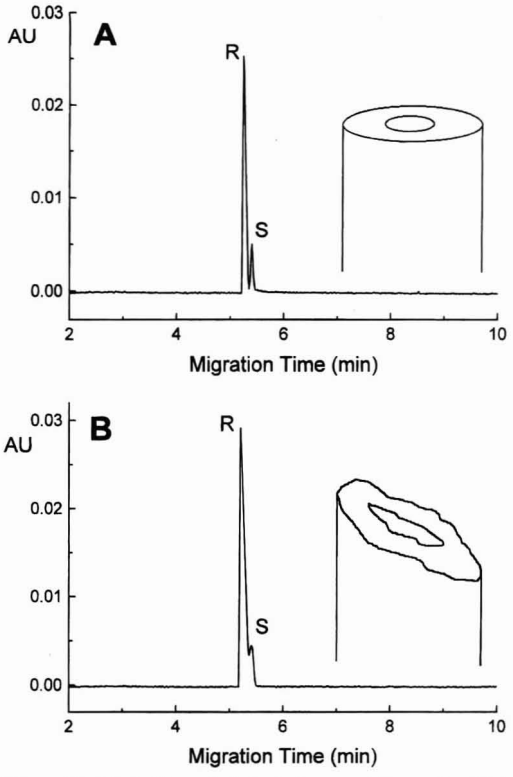

Figure 3. Effect of the actual physical shape of the capillary inlet on the resolution of naproxen enantiomers. Test solute: 0.1 mg/mL (*R*)-naproxen and 0.01 mg/mL (*S*)-naproxen in water. (A) Properly cut (perpendicular to the axis of the capillary) column inlet and (B) oblique (45°) cut column inlet.

In work with CGE, employing non-cross-linked, low-viscosity polymer networks, we found impaired separation performance with capillaries which were improperly cut at the inlet side. Specifically, an oblique inlet side of the capillary yields a separation efficiency (expressed as the theoretical plate number, *N*) significantly lower than that obtainable with a properly cut, straight edge capillary, causing loss in resolution with similar separation selectivities. Recently, a similar phenomenon was independently confirmed by Grushka and co-workers[23] in their work with CZE.

Hence, it appears that the sample plug must be positioned accurately at the inlet in such a way that its boundaries are perpendicular to the axis of the column during the injection process. Assuming otherwise identical injection conditions, in the case of oblique edge capillaries, the injection plug length is slightly increased (relative to the straight edge capillary), resulting in increased extracolumn variance due to the injection plug.[23] Figure 3 shows the chiral separation of naproxen enantiomers, using pressure injection onto a properly (A) and an improperly (B) cut, replaceable gel-filled capillary. Naproxen, one of the most frequently prescribed chiral drugs, was used as a test solute in

(20) Ulfelder, K. J.; Schwartz, H. E.; Hall, J. M.; Sunzeri, F. J. *Anal. Biochem.* **1992**, *200*, 260.

(21) Hjerten, S.; Valtcheva, L.; Li, Y.-M. *J. Cap. Electrophor.* **1994**, *1*, 83.

an enantiomeric ratio of *R/S* 10:1. The chiral selector HP-β-CD was used to attain enantiomeric separation in a low-mobility buffer system (MES/TBAH). In the case of Figure 3B, the inlet-side edge of the capillary was cut with an ~45° angle, as shown in the inset. Note that, under otherwise equivalent injection and separation conditions, with the use of an oblique edge capillary, severe peak distortion occurs, resulting in >60% loss in peak efficiency for both of the enantiomers (41 200 vs 15 500 theoretical plates for the *R*, and 73 500 vs 17 700 theoretical plates for the *S* enantiomers). Likewise, enantiomeric resolution decreased from $R_s = 1.57$ to 0.97.

Thus, careful column edge cutting plays an important role in achieving optimum (Gaussian) peak shape in CGE. In practice, this may not be that important when dealing with well-separated peaks ($R_s > 3$) of similar height. However, the effect may be substantial in trace analysis, e.g., when determining trace impurities in protein preparations with SDS-based replaceable gel columns, for closely related PCR fragments, or especially for chiral compounds with the recent FDA requirement of the analysis of high enantiomeric excess ratios (1000:1).[24] In these instances, employing an oblique injection edge capillary, the trace analyte will not be sufficiently resolved from the main peak in order to perform accurate quantitation.

CONCLUSIONS

In summary, two injection-related artifacts in capillary gel electrophoresis were examined. The first occurs with consecutive electrokinetic injections from small volume aqueous samples and results in progressively smaller analyte peak heights and areas. The problem can simply be prevented by adding an intermediate water injection step in the CGE run sequence. The second problem relates to the capillary inlet shape of the gel-filled column. Here, careful cutting (perpendicular to the axis of the column) and examination of the capillary edge prevents any undesirable peak distortion and consequent resolution loss.

ACKNOWLEDGMENT

The support of this work by Dr. Nelson Cooke is highly appreciated. The authors gratefully acknowledge Professor Eli Grushka and Dr. Bart Wanders for their stimulating discussions.

Received for review December 13, 1994. Accepted April 11, 1995.[⊗]

AC941206J

[⊗] Abstract published in *Advance ACS Abstracts*, June 1, 1995.

(22) Schwartz, H. E.; Ulfelder, K. J.; Guttman, A. Injection Related Artifacts in Capillary Electrophoreseis; Seventh International Symposium on High Performance Capillary Electrophoresis, Würtzburg, Germany, 1995; Poster P428.

(23) Cohen, N.; Grushka, E. *J. Chromatogr. A* **1994**, *684*, 323.

(24) Guttman, A.; Cooke, N. *J. Chromatogr. A* **1994**, *685*, 155.

Anal. Chem. **1995,** *67,* 2284–2287

Manipulation of Sample Fractions on a Capillary Electrophoresis Chip

Carlo S. Effenhauser,* Andreas Manz, and H. Michael Widmer

Corporate Analytical Research, Ciba Ltd., CH-4002 Basel, Switzerland

A microfabricated capillary electrophoresis chip has been used for selective isolation of fraction zones after fast size separation of a synthetic mixture of fluorescent phosphorothioate oligonucleotides. Withdrawal of preselected sample zones is achieved by simple automated switching of the applied potentials to a channel system which has been etched into a glass plate by conventional microfabrication techniques. Both single sample zones and groups of zones can be selectively isolated from unwanted sample components on a time scale of a few minutes. A single sample component, originally injected into a volume of ~90 pL prior to the separation, was still confined within a volume of ~300 pL after the separation and removal procedure; i.e., extensive dilution is avoided. Complex timing protocols allow for the withdrawal of any subset in the sequence of separated fractions. The results demonstrate the high degree of sample control that can be obtained on gel-filled microstructures with samples in the pico- to nanoliter range. They are of particular relevance for future developments of micromanipulation and microanalysis systems for biochemical analysis.

Over the past few years, a number of experimental procedures has been described in the literature for the collection of sample fractions separated by capillary electrophoresis (CE), either for micropreparative purposes or to subject the selected fraction to a subsequent analysis.[1–11] The major difficulty is that the outlet end of the capillary has to be part of a closed electrical circuit to be able to perform the separation, while at the same time it should provide some means for the withdrawal of the separated bands. In the stopped-flow techniques,[2–5] the separation potential has to be interrupted and the end of the separation capillary has to be transferred from the buffer vial into a fraction collection vial. Switching the voltage on again for a brief period of time then drives the sample zone of interest into the collection vial. Although this technique has been successfully applied, it usually leads to considerable dilution of the collected sample zones. In another experimental approach, the capillary is electrically grounded before the outlet orifice,[6–8] e.g., by means of an on-column frit or a specially designed grounding tee assembly in a way similar to the techniqes used for electrochemical detection in CE and for CE–MS coupling. This allows for reduction in the extent of sample dilution, but manufacturing of these devices is not an easy task since dead volumes have to be kept at a sufficiently low level. Recently, elegant fraction collection methods, by means of moving surfaces such as filter paper[6] or membranes,[9,10] have been reported.

In the present article, we describe a novel approach to sample fraction manipulation in CE which is based on the use of microfabricated planar devices. It has been demonstrated in a number of recent publications that column switching operations on planar glass structures can be simply controlled by switching the electric potentials.[12–19] As a consequence of the photolithographic fabrication process, dead volumes at capillary intersections can be kept at a negligibly low level. Micromachined CE devices should therefore be ideally suited for the sample manipulation operations required for fraction collection with samples in the pico- to nanoliter range. We report here on the first sample manipulation experiments carried out on glass chips with gel-filled channel systems, which complement our previously published results on high-speed separations of anti-sense oligonucleotides.[18] In this context, we would like to point out that very recently high-speed separations of DNA fragments on similar devices have been reported.[19]

EXPERIMENTAL SECTION

Most details of the experimental procedure and the detection and data acquisition system were described in two earlier publications.[13,18] Therefore, only some relevant new aspects are described here. The layout of the channel system on the glass chip is identical to the one described previously[13] and is reproduced in Figure 1. The channel system was filled with a non-cross-linked polymerized solution containing 10% polyacrylamide in a 100 mM Tris, 100 mM boric acid, 2 mM EDTA, and 7 M

(1) Hjerten, S.; Zhu, M.-D. *J. Chromatogr.* **1985,** *327,* 157.
(2) Rose, D. J.; Jorgenson, J. W. *J. Chromatogr.* **1988,** *438,* 23.
(3) Cohen, A. S.; Najarian, D. R.; Paulus, A.; Guttman, A.; Smith, J. A.; Karger, B. L. *Proc. Natl. Acad. Sci. U.S.A.* **1988,** *85,* 9660.
(4) Guttman, A.; Cohen, A.; Heiger, D. N.; Karger, B. L. *Anal. Chem.* **1990,** *62,* 137.
(5) Albin, M.; Chen, S.-M.; Louie, A.; Pairaud, C.; Colburn, J.; Wiktorowicz, J. *Anal. Biochem.* **1992,** *206,* 382.
(6) Huang, X.; Zare, R. N. *J. Chromatogr.* **1990,** *516,* 185.
(7) Guzman, N. A.; Trebilcock, M. A.; Advis, J. P. *Anal. Chim. Acta* **1991,** *249,* 247.
(8) Fujimoto, C.; Muramatsu, Y.; Suzuki, M.; Jinno, K. *J. High Resolut. Chromatogr.* **1991,** *14,* 178.
(9) Camilleri, P.; Okafo, G. N.; Southan, C. *Anal. Biochem.* **1991,** *196,* 178.
(10) Cheng, Y.-F.; Fuchs, M.; Andrews, D.; Carson, W. *J. Chromatogr.* **1992,** *608,* 109.
(11) Eriksson, K.-O.; Palm, A.; Hjerten, S. *Anal. Biochem.* **1992,** *201,* 211.
(12) Harrison, D. J.; Fluri, K.; Seiler, K.; Fan, Z.; Effenhauser, C. S.; Manz, A. *Science* **1993,** *261,* 895.
(13) Effenhauser, C. S.; Manz, A.; Widmer, H. M. *Anal. Chem.* **1993,** *65,* 2637.
(14) Seiler, K.; Harrison, D. J.; Manz, A. *Anal. Chem.* **1993,** *65,* 1481.
(15) Seiler, K.; Fan, Z. H.; Fluri, K.; Harrison, D. J. *Anal. Chem.* **1994,** *66,* 3485.
(16) Jacobson, S. C.; Hergenröder, R.; Koutny, L. B.; Ramsey, J. M. *Anal. Chem.* **1994,** *66,* 1114.
(17) Burggraf, N.; Manz, A.; Verpoorte, E.; Effenhauser, C. S.; Widmer, H. M.; de Rooij, N. F. *Sens. Actuators B* **1994,** *20,* 103.
(18) Effenhauser, C. S.; Paulus, A.; Manz, A.; Widmer, H. M. *Anal. Chem.* **1994,** *66,* 2949.
(19) Woolley, A. T.; Mathies, R. A. *Proc. Natl. Acad. Sci. U.S.A.* **1994,** *91,* 11348.

0003-2700/95/0367-2284$9.00/0 © 1995 American Chemical Society

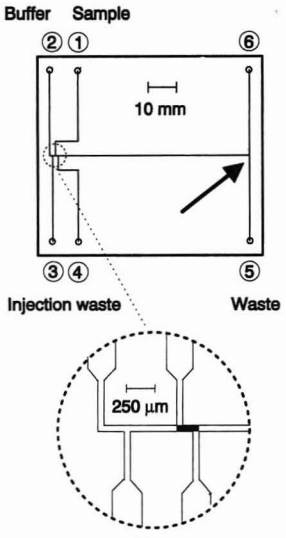

Figure 1. Layout of the glass chip with integrated sample injector. Channel cross sections: 50 × 12 (thin channels) and 250 × 12 μm (broad channels), respectively. After application of a high voltage between reservoirs 1 (sample) and 4 (injection waste), the geometrically defined injection volume (double-"T" injection, shaded area) is filled by electrophoretic migration of the sample ions. After loading is completed, application of a high potential between reservoirs 2 (buffer) and 5 (waste) drives the injected sample plug into the separation channel and causes electrophoretic separation of the sample components. The T-intersection where the selected sample zones are withdrawn is indicated by the arrow.

urea buffer (pH 8.5) according to the method described in ref 18. The injection and separation procedure of the fluorescently labeled mixture of phosphorothioate oligonucleotides PS pd(T)$_{10-25}$ are reported in the same reference. The geometrically defined length of the injected sample plug is 150 μm (corresponding volume, 90 pL). The intersection volume at the junction where the fraction collection takes place is 30 pL.

The maximum voltage applicable to the separation capillary was limited to a potential of 12 kV due to the breakthrough voltage of the high-voltage relays used for potential switching in the experiment. As a result of the chip layout employed in our experiments (maximum usable length of the separation channel, 7 cm), the separation field strength was limited to 1130 V/cm. This figure is a factor of ~2 lower than the field strength used in our earlier experiment.[18] The resulting electropherogram recorded at maximum separation length is shown in Figure 2. In order to allow easy referencing of the individual peaks, the nucleotide length has been tentatively assigned. Due to the lower field strength and the longer separation length, the overall analysis time is increased by a factor of ~4 compared to our earlier results.

The principle of the experiment is schematically shown in Figure 3. Detection was accomplished via laser-induced fluorescence (LIF) with the whole detector unit mounted on a $X-Y$ translational stage,[13] so that any point of the channel system can be used as an on-column detection volume (length of detection volume, 40 μm). Before the first run, the LIF detector was adjusted to a spot on the separation channel very close to the intersection. In this way, the arrival time distribution of the

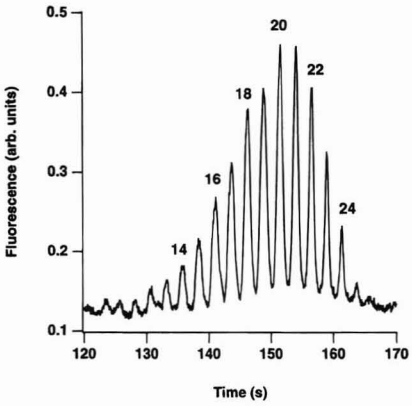

Figure 2. Electropherogram of a fluorescein-labeled phosphorothioate oligonucleotide mixture PS pd(T)$_{10-25}$ mixture recorded at 1130 V/cm in a 10% T non-cross-linked polyacrylamide matrix (buffer: 100 mM Tris, 100 mM boric acid, 2 mM EDTA, 7 M urea, pH 8.5). Separation length, 7.0 cm. The chain length of the oligonucleotides is tentatively assigned.

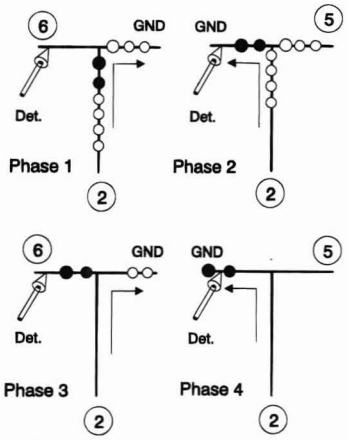

Figure 3. Schematic representation of the various phases of the withdrawal of a preselected sample zone. (phase 1) Application of a negative high potential at reservoir 2 and ground potential at reservoir 5 (reservoir 6, floating) separates the injected sample plug and drives the sample zones toward reservoir 5. When the sample zones of interest (solid circles) have arrived at the intersection, reservoir 6 is grounded for a few seconds and reservoir 5 left floating, thus switching the direction of the electric field toward reservoir 6 (withdrawal phase 2). The remaining sample zones (shaded circles) are removed from the system by switching back to phase 1 until the separation channel has been completely emptied (phase 3). Finally, the extracted fractions are moved past the detector by grounding reservoir 6 again while leaving reservoir 5 floating (phase 4). During the whole sequence, reservoir 2 is kept at a negative high potential. The location of the LIF detector is indicated by the arrows.

separated sample components at the immediate vicinity of the intersection was determined. Subsequently, the detector was aligned to a spot on the channel connecting the junction with reservoir 6, ~2 mm away from the junction (Figure 3).

In the following run, the actual fraction manipulation experiment was carried out by applying the separation field for a predetermined period of time until the sample fraction of interest

had arrived at the junction (phase 1 in Figure 3). Then, the direction of the electric field was switched by application of a brief fraction collection field "pulse" (reservoir 6 was set to ground potential while reservoir 5 was left floating). This pulse was applied for a few seconds with a field strength identical to the separation field (1130 V/cm) in order to drive the sample fraction into the left half of the T-bar channel toward reservoir 6 (phase 2). Switching the potentials back to the arrangement of phase 1 by grounding reservoir 5 then removed the remaining sample zones from the separation channel (phase 3). Finally, reservoir 6 was grounded again, and the selected fractions that were "cut out" from the sequence of sample zones were moved past the detector (phase 4). During the whole procedure, reservoir 2 is constantly kept at a potential of −12 kV.

The timing protocol of the potential switching was controlled with a Labview II program (National Instruments, Austin, TX) running on a Macintosh Quadra 700 personal computer. A National Instruments interface board (NB-MIO-16X) was used for data acquisition at a sampling rate of 100 Hz.

RESULTS AND DISCUSSION

The arrival time distribution of the separated bands at the channel intersection is shown in Figure 2. As has been already mentioned above, due to the lower maximum field strength applied and the longer separation length, the analysis time is a factor of ~4 longer than our previously published results.[18] It is interesting to note that even though the total separation voltage employed is even slightly lower (7.9 vs 8.4 kV in ref 18), the resolution is improved and the bands are almost base-line resolved. We attribute this finding to the fact that the relative band broadening contribution of the sample injection is decreased with increasing separation length (the length of the injected plug (150 μm) is the same in both experiments, whereas the separation length differs by a factor of 2; see discussion of band broadening in ref 18). The separation efficiency obtained amounts to $N = 295\,000$ theoretical plates for the band assigned as $n = 24$ with a corresponding plate height of 0.24 μm (separation length, 70 mm). A plot of the migration time (t) of the individual bands vs the nucleotide length (n) proved to be perfectly linear ($t = 100.1$ s + n2.56 s, correlation coefficient $r =$ 0.999 87).

Figure 4 depicts the results of two fraction withdrawal experiments. Depending on the length of the collection pulse, a group of three sample zones (Figure 4a) or even a single sample zone (Figure 4b) have been selectively "cut out" of the electropherogram. It is important to note that the time scales indicated in this figure do not correspond to the time scale given in Figure 2, but rather represent the total time scale of the experiment including the manipulation procedure after the separation. The time needed to perform the whole operation was dominated by the relatively "long" analysis time of only little less than 3 min, which itself was caused by electric field strength limitations and the rather long separation length as discussed in the Experimental Section. Nevertheless, given the complexitiy of the procedure, the overall operation time of less than 4 min can be considered fast.

The result of the withdrawal of three successive parts of the electropherogram is shown in Figure 5: (a) PS pd(T)$_{16-18}$; (b) PS pd(T)$_{19-21}$; (c) PS pd(T)$_{22-24}$.

After the removal of the sample zones, the compounds are available on the chip in a spatially concentrated form that would

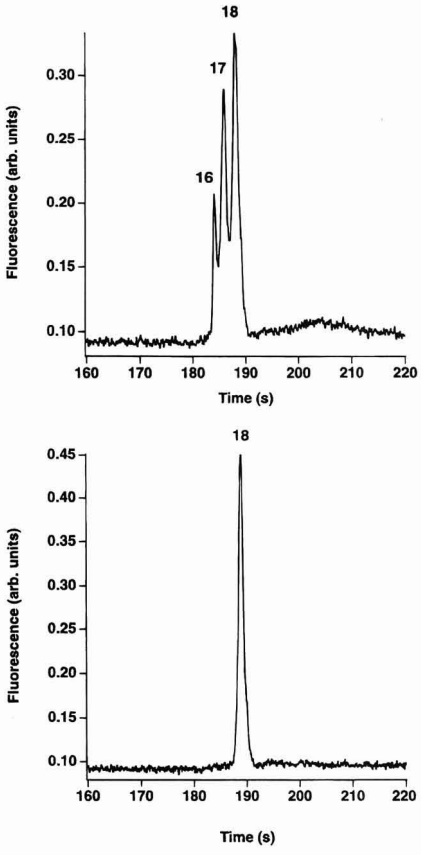

Figure 4. Automated withdrawal of preselected sample zones. (a, top) Fraction collection of PS pd(T)$_{16-18}$: potential switching protocol (phase 1) 140 s, (phase 2) 5 s (fraction withdrawal "pulse"), (phase 3) 40 s, (phase 4) 65 s; total acquisition time, 250 s. (b, bottom) Fraction collection of PS pd(T)$_{18}$: potential switching protocol (phase 1) 143 s, (phase 2) 2 s (fraction withdrawal "pulse"), (phase 3) 40 s, (phase 4) 65 s; total acquisition time, 250 s. Electric field strength, 1130 V/cm.

be suitable for performing further analytical operations. Since dead volume interferences have to be carefully avoided when working with such minute sample volumes, these operations should preferably be carried out on the same device. The full width at half-maximum (fwhm), in time units, of the peak shown in Figure 4b is ~1 s. The migration velocity of this peak at 1130 V/cm was calculated to be 0.48 mm/s from the data depicted in Figure 2; i.e., the corresponding fwhm in length units amounts to ~0.5 mm with a corresponding volume of 300 pL. Compared to the injected sample plug, the average concentration of the zone is reduced by only a factor of 3, with longitudinal diffusion being the dominant (and unavoidable) dispersion mechanism. During the removal of the remaining sample zones (phase 3), the extracted bands are subjected to diffusional band broadening. Furthermore, the intersection itself leads to additional band dispersion as discussed in ref 17 (so-called "corner effects"). For these two reasons, the resolution between individual bands of an extracted group of zones is discernably reduced (see Figure 4a and Figure 5).

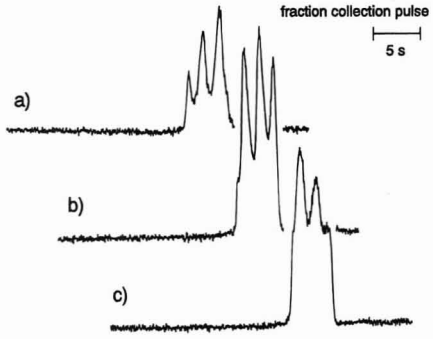

Figure 5. Superposition of three successive portions that have been "cut out" of the electropherogram shown in Figure 2: (a) PS $pd(T)_{16-18}$; (b) PS $pd(T)_{19-21}$; (c) PS $pd(T)_{22-24}$. Fraction collection pulse (phase 2) in each experiment, 5 s.

The whole procedure described above was carried out in a completely automated manner under computer control, and in principle, it can be repeated until a sufficient amount of the compound of interest has been collected within the principal limitations of a microanalytical technique like CE. Since more complex manipulation protocols can be easily applied, one of the major advantages of this method is its versatility; it could be easily extended to collect more than one fraction per run, e.g., all odd- or even-numbered nucleotides. Furthermore, coupled to other analytical techniques (e.g., two-dimensional or "hyphenated" methods like CE–MS or screening procedures based on bioaffinity interactions), it would be a valuable tool to increase selectivity and peak capacity.

In the current experimental setup, determination of the arrival time of the sample zones at the intersection prior to the actual fraction withdrawal is a necessary prerequisite to establish the timing protocol. The degree of control could be improved by installation of a second detector unit at the separation channel, which would allow a computer-controlled prediction of the arrival time of the desired fractions. The quality of the withdrawn zones could then be checked by the second detector unit in the way described above.

In conclusion, we would like to emphasize that the excellent reproducibility of the migration time demonstrated in our earlier work[18] represents an important prerequisite for the experiments presented here. Once the time delay due to the distance between the detector spot and the intersection is known, a single determination of the arrival time distribution is sufficient to determine the proper timing and pulse width of the collection pulses. In repetitive experiments with gel-filled devices, we have carried out several hundred experiments with the same device without a noticable decrease in operation performance. The results underline the high degree of substance transport control that can be obtained on gel-filled microstructures with sample volumes in the pico- to nanoliter range. This capability represents a significant element for the general feasibility of the concept of miniaturized total analysis systems (μ-TAS).[20] Even though the sample volumes are small and the corresponding amount of substance in a sample zone is usually in the range of femtomoles and below, high-sensitivity detection techniques like LIF will allow for adequate monitoring of the analytical operations on the chip. For special applications, micromachined devices can be operated virtually like a molecular "sorting device" and are of relevance to future developments of microreactors as well as for the micromanipulation and microanalysis of biochemical systems.[21]

ACKNOWLEDGMENT

We thank Dr. Lendell L. Cummins (ISIS Pharmaceuticals, Carlsbad, CA) for the synthesis of the oligonucleotide sample. Furthermore, we thank Dr. A. Paulus for assistance with the preparation of the gel-filled devices and Dr. A. E. Bruno and Dr. M. A. Malone (all Ciba) for reading the manuscript.

Received for review January 23, 1995. Accepted April 12, 1995.[⊗]

AC9500693

[⊗] Abstract published in *Advance ACS Abstracts,* June 1, 1995.

(20) Manz, A.; Harrison, D. J.; Verpoorte, E.; Widmer, H. M. *Adv. Chromatogr.* **1993**, *33*, 1.

(21) See, for example, articles in: van den Berg, A., Bergveld, P., Eds. *Micro Total Analysis Systems*; Kluwer Academic Publishers: Dordrecht, The Netherlands, 1995.

Anal. Chem. **1995**, *67*, 2288–2291

Effect of Supercritical Carbon Dioxide Pressurized with Helium on Solute Solubility during Supercritical Fluid Extraction

Jerry W. King,* James H. Johnson, and Fred J. Eller

Food Quality & Safety Research Unit, National Center for Agricultural Utilization Research, Agricultural Research Service/USDA, 1815 North University Street, Peoria, Illinois 61604

Carbon dioxide cylinders, pressurized with a helium headspace, find routine use as a solvent in analytical supercritical fluid extraction (SFE). In this study, the solubilities of soybean oil in neat supercritical carbon dioxide (SC-CO_2) and CO_2 with entrained helium were measured at 70 °C and three different pressures. The oil solubility was found to be substantially diminished when the CO_2/He source was used, presumably by the presence of small amounts of helium dissolved in the extraction fluid. The recorded reductions in solubility (30–50 wt %) should be taken into account in performing and optimizing SFE with helium-pressurized cylinders.

Cylinders containing carbon dioxide pressurized with the aid of a relatively insoluble gas such as helium have been utilized extensively for analytical supercritical fluid extraction (SFE) over the last several years. The rationale for pressurizing the carbon dioxide source by this method is that it permits fluid delivery devices (e.g., syringe or booster pumps) to operate more efficiently by assuring adequate liquification of gas in the pump cylinder or head without the need for external circulating cooling baths. Such gas sources have seen routine use with a variety of commercial instruments and are a item of commerce.

Previous investigators[3,4] have noted the effect of using He-pressurized CO_2 sources on the retention time reproducibility of solutes in supercritical fluid chromatography (SFC). More recently, Raynie and Delaney[5] have reported that He entrained in CO_2 reduces the extraction rate of cholesterol in SFE relative to those values observed with neat CO_2. Raynie and Delaney suggested that this effect is due to a suppression of the cholesterol's solubility in the potential CO_2/He mixture when it is pressurized for use in SFE.

To verify the above hypothesis, we have conducted independent experiments on the solubility of soybean oil in SC-CO_2, with and without He pressurization, in our laboratory. Soybean oil solubility in SC-CO_2 as a function of temperature and pressure has been extensively studied by several researchers,[6–9] and provides a good test case for observing the effect of entrained helium on the solubility of a lipid solute which exhibits a high solubility in SC-CO_2. In addition, soybean oil emulates the behavior of a typical "fat" in SC-CO_2; hence if an appreciable difference does occur in the effective solubility of soybean oil in CO_2 versus a CO_2/He mixture, then the projected time of extraction as well as quantity of CO_2 required for exhaustive delipidation of fat/oil-containing samples would be effected. Such a result is important to the analyst in optimizing the SFE parameters and in this projected high-volume use of analytical SFE.[10]

EXPERIMENTAL SECTION

Our interest in the above phenomena was catalyzed by initial experiments on an Applied Separations (Allentown, PA) Spe-ed supercritical fluid extraction unit. This instrument is based on a earlier extractor design developed in our laboratory[11] and incorporates a Haskel, Inc. (Burbank, CA) liquid booster pump to deliver the extraction fluid, CO_2. Extraction of soya flakes on this unit using a helium-pressurized CO_2 produced a oil solubility (in wt %) that was ~2.5 times less than that previously determined using neat CO_2 at 5000 psi and 70 °C.[12] Oil solubility in the supercritical fluid was calculated from the mass of oil collected per mass of CO_2 passed through the extraction vessel at several intervals in the linear portion of oil extraction curve,[13] and the average of these determinations was used to yield the weight percent of oil in the SC-CO_2.

To more accurately determine the effect of helium entrainment in SC-CO_2 on the solute (oil) solubility in the SC-CO_2, a home-built extraction apparatus was constructed, as shown in Figure 1. In this apparatus, two different Haskel air-driven booster pumps were employed to deliver the CO_2. A Haskel Model AGT 62/152 booster pump was used to deliver gaseous CO_2, while a Haskel liquid pump, Model DSHF-151, was utilized to pump the liquified CO_2. In the latter case, a syphon tube liquid CO_2 source, both with and without helium pressurization, was used to supply the liquid booster pump. As shown in Figure 1, this dual fluid

(1) Cross, R. F.; Ezzell, J. F.; Richter, B. E. *J. Chromatogr. Sci.* **1993**, *31*, 162–169.
(2) Maxwell, R. J.; Fettner, M. J. Abstracts of the 5th International Symposium on Supercritical Fluid Chromatography and Extraction. Supercritical Conferences, Cincinnati, OH, 1994; Abstract E-11.
(3) Porter, N. L.; Richter, B. L.; Bornhop, D. J.; Later, D. W.; Beyerlein. *J. High Resolut. Chromatogr. Chromatogr. Commun.* **1989**, *10*, 477–478.
(4) Rosselli, A. C.; Boyer, D. S.; Houck, R. K. *J. Chromatogr.* **1989**, *465*, 11–15.
(5) Raynie, D. E.; Delaney, T. E. *J. Chromatogr. Sci.* **1994**, *32*, 298–300.
(6) Stahl, E.; Schutz, E.; Mangold, H. K. *J. Agric. Food Chem.* **1980**, *28*, 1153–1157.
(7) Quirin, K. W. *Fette Seifen Anstrichm.* **1982**, *84*, 460–468.
(8) Friedrich, J. P.; Pryde, E. H. *J. Am. Oil Chem. Soc.* **1984**, *61*, 223–228.
(9) del Valle, J. M.; Aguilera, J. M. *Ind. Eng. Chem. Res.* **1988**, *27*, 1553–1555.
(10) King, J. W.; Hopper, M. L. *J. Assoc. Off. Anal. Chem. Int.* **1992**, *75*, 375–378.
(11) King, J. W.; Johnson, J. H.; Friedrich, J. P. *J. Agric. Food Chem.* **1989**, *37*, 951–954.
(12) Friedrich, J. P. U.S. Patent 4,466,923, August 21, 1984.
(13) Favati, F.; King, J. W.; Mazzanti, M. *J. Am. Oil Chem. Soc.* **1991**, *68*, 422–427.

This article not subject to U.S. Copyright. Published 1995 Am. Chem. Soc.

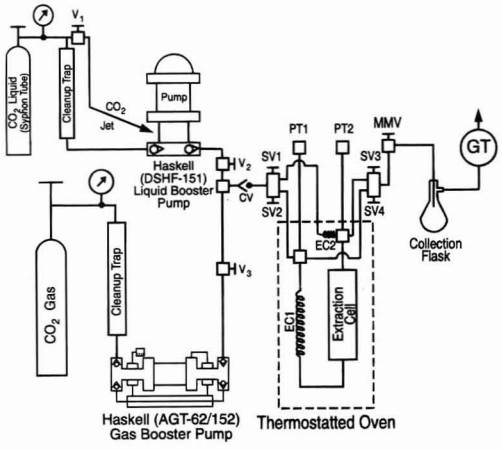

Figure 1. Experimental supercritical fluid extraction unit, permitting the use of two different fluid sources and delivery pumps. Key: V, on/off valves; SV, switching valves; PT, pressure transducer; EC, equilibration coil; MMV, micrometering valve; GT, gas totalizer (dry test meter).

pumping arrangement permitted identical SFEs to be performed on the same extraction apparatus; however, either gaseous, liquid, or liquid CO_2 with entrained helium could be used to perform the SFE.

Welding grade, gaseous and liquified CO_2 obtained from National Welding Supply (Bloomington, IL) were used in our experiments. Helium-pressurized cylinders of liquified CO_2 initially compressed to 1900 psi were also obtained from the above source. The head of the Model DSHF-151 pump was cooled by venting liquified CO_2 onto it to prevent cavitation in the pump head when a liquid CO_2 source without helium pressurization was used.

The details of vegetable oil extraction with this type of apparatus have been described previously.[14,15] Typically, 60 g of soybean flakes, contained in a 10 000 psi-rated extraction cell, 61 cm length × 1.75 cm i.d., was utilized for each SFE run. Extractions were conducted for a time period commensurate with establishing a constant oil solubility in the SC-CO_2. Oil solubilities were calculated from at least three or more consecutive solubility measurements during the same SFE. Recovered oil was measured intermittently by gravimetry, while the CO_2 used in each interval was measured by a dry test meter (Model DTM 200A, American Meter Co., Philadelphia, PA) at ambient conditions.

SFEs were run at 70 °C three different pressures: 5000, 8000 and 10 000 psi. To ensure accurate solubility measurements, triplicate extraction runs were conducted for the three types of fluid delivery systems at each pressure, for a total of 27 individual runs. The resultant solubility data were analyzed with the aid of a Statistix 4.1 software program (Analytical Software, Tallahassee, FL) using multiple regression and analysis of covariance (ANCOVA).

(14) Friedrich, J. P.; List, G. R.; Heakin, A. J. *J. Am. Oil Chem. Soc.* **1982**, *59*, 288–292.

(15) Taylor, S. L.; King, J. W.; List, G. R. *J. Am. Oil Chem. Soc.* **1993**, *70*, 437–439.

Table 1

fluid source	pressure (psi)	wt % oil solubility[a]
CO_2(g)	5000	1.18 ± 0.09*
	8000	4.50 ± 0.27
	10000	7.45 ± 0.23
CO_2(l)	5000	1.06 ± 0.09
	8000	4.66 ± 0.38
	10000	7.57 ± 0.75
CO_2(l)/He(l)	5000	0.61 ± 0.06
	8000	2.80 ± 0.28
	10000	5.53 ± 0.61

[a] Mean ± standard deviation

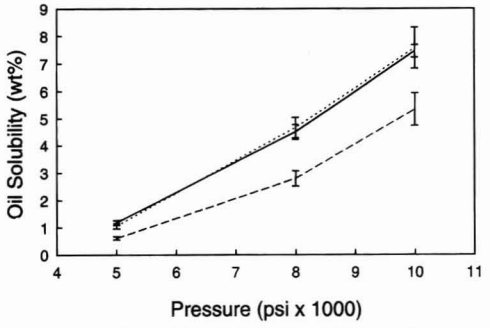

Figure 2. Effect of fluid source on oil solubility as a function of extraction pressure: (—) gaseous CO_2, (···) liquid CO_2, and (- -) liquid CO_2/He.

RESULTS AND DISCUSSION

Results from the measurement of soybean oil solubility in SC-CO_2 and the SC-CO_2/He mixture as a function of pressure at 70 °C are presented in Table 1. The results are tabulated according to the fluid source/pumping system utilized. Fluid from the CO_2-(g) pumping system were delivered to the extractor via a gas booster pump and utilized no helium in the CO_2 cylinder. The data listed under CO_2(l) were obtained with liquid booster pump delivery of the CO_2 sans He. The third group of solubility data were determined on the liquid booster pump system using CO_2 that had been pressurized with helium as noted above.

The results in Table 1 show that solubility of soybean oil in SC-CO_2 increases with pressure at 70 °C.[16] Note that, for the CO_2 sources without helium, the solubility values at each specific pressure are almost identical. When the cylinder containing CO_2 pressurized with He is utilized for the SFE, solubility values are decreased by factors of 0.50, 0.62, and 0.73 at 5000, 8000 and 10 000 psi, respectively. This substantial reduction in oil solubility is outside the limit of experimental error as predicted by the standard deviations associated with the respective means of the multiple solubility determinations for each pressure level and particular fluid source.

The variation of oil solubility with pressure is nearly linear over the pressure interval from 5000 to 10 000 psi as confirmed in Figure 2. The slopes associated with the linear least-squares fits to the experimental data yield r^2 values of 0.86, 0.97, and 0.94 for the CO_2(g), CO_2(l), and CO_2(l)/He(l) source/delivery systems, respectively. It should be noted that this apparent linear relation-

(16) King, J. W. *INFORM* **1993**, *4*, 1089–1098.

ship between weight percent solubility and pressure does not hold for CO_2 over the entire pressure range from ambient to 10 000 psi.[12] Clearly the data show that the utilization of a CO_2/He fluid source results in lowering the oil solubility in the extraction fluid. Figure 2 shows that, within the limits of experimental error, the determined soybean oil solubility values do not vary with pressure when neat CO_2 is used, regardless of the type pump that is used for fluid delivery.

Our experiments also permitted for the statistical evaluation of the effects of parameters such as the source of extraction fluid, pressure, fluid flow rate, and interaction between extraction fluid and pressure on percent oil solubility. The analysis of the covariance verified that there was a significant effect of the fluid source (type) on the oil solubility in the fluid ($F_{2,74} = 81.23$, $P = 0.0000$). Regression analysis confirmed that both CO_2 sources devoid of helium pressurization yielded statistically equivalent oil solubilities $t = 0.30$, $P = 0.7647$, df = 74) (df, degrees of freedom); however, these fluid sources gave statistically higher oil solubilities than the CO_2 source having helium ($t = 2.94$, $P = 0.0043$, df = 74 for gaseous CO_2 and $t = 2.65$, $P = 0.0099$, df = 74 for liquid CO_2). The regression analysis indicated that there was a significant effect of extraction pressure on the resultant oil solubility ($t = 34.13$, $P = 0.0000$, df = 74), and ANCOVA indicated a significant a interaction between the fluid source and extraction pressure ($F_{2,80} = 30.64$, $P = 0.0000$). The slopes of the lines in Figure 2 are equivalent for both CO_2 sources that did not contain helium ($t = 0.11$, $P = 0.9094$, df = 74), however, their slopes were significantly higher than those observed for the helium/CO_2 source ($t = 6.83$, $P = 0.0000$, df = 74 for gaseous CO_2 and $t = 6.73$, $P = 0.0000$, df = 74 for liquid CO_2). The overall regression equation predicting oil solubility was found to be highly significant ($F = 590.75$, $P = 0.0000$), having an R^2 of 0.9795. The regression equations predicting weight percent oil solubility for the three fluid sources are

$$CO_2(g)\ \%\ \text{solubility} = -6.664 + (0.00135)P + (0.240)F \quad (1)$$

$$CO_2(l)\ \%\ \text{solubility} = -6.571 + (0.00134)P + (0.240)F \quad (2)$$

$$CO_2(l)/He(l)\ \%\ \text{solubility} = -5.469 + (0.00100)P + (0.240)F \quad (3)$$

where P is pressure (psi) and F is ambient flow rate (L/min).

It should be noted that eq 3 also predicts that the fluid flow rate can influence the resultant oil solubility ($t = 4.72$, $P = 0.0000$, df = 74), with % oil solubility increasing slightly with pressure.

The influence of dissolved He in liquid CO_2 cylinder sources has also been implicated in a study of flame ionization detector response by Schweighardt and Mathias.[17] These researchers, invoking the vapor/liquid equilibria data of Burfield et al.,[18] suggested that as little as 0.5 wt % (~5 mol %) helium in CO_2 could account for the larger decrease in baseline shift during pressure programming in supercritical fluid chromatography using a FID. This effect, they argued, was due to the differential adiabatic expansion (Joule–Thomson effect) between SC-CO_2 and SC-He as the carrier fluid is expanded through the column outlet restrictor.

Similarly, Gorner et al.[19] observed considerable differences in retention times for solutes in SFC when helium head pressure CO_2 was used in place of neat CO_2 as a mobile phase. They performed rigorous thermodynamic calculations of the density of the CO_2/He mixtures for their experimental conditions and predicted a reduction in the fluid density of up to 20% when neat CO_2 is diluted with small quantities of dissolved He. Such an effect could also be influencing the oil solubility measurements reported in this study since the dissolving power of CO_2 is a function of its density. Unfortunately, there are no experimentally determined densities for He/CO_2 mixtures under the conditions employed in this study. Gahrs[20] noted a reduction in caffeine solubility in SC-CO_2 by the addition of small quantities of N_2 or Ar to the CO_2. This verifies the trends found in our measurements and suggests that further research in this area could lead to a control of extraction selectivity in analytical SFE via compositional changes in the fluid phase.

Schweighardt and Mathias[21] calculated the mole percent of helium dissolved in a liquid CO_2 as a function of pressure for a gas cylinder kept at typical room temperature conditions (21°C). Their calculations predict a decreasing amount of He dissolved in the liquid CO_2 as the pressure decreases. The experiments reported above, which used a liquid CO_2/He cylinder, were started at a tank pressure of 1650 psi, which should contain 4 mol % helium dissolved in the liquid CO_2 (~1 molecule in 20 is helium). Our final extractions (at 8000 and 10 000 psi) were conducted at relative constant tank pressure of 1300 psi, where the amount of helium in the liquid CO_2 is calculated to be 2.36 mol %. Therefore, the effect of decreasing the amount of helium dissolved in liquid CO_2 would be to enhance the solvent power of the fluid mixture from the liquid CO_2/He during the SFE, similar to the density analogy noted above. Whereas this may partially account for the trend noticed at the higher extraction pressures, it cannot explain the considerable differences in the recorded oil solubilities (for example, the next to last extraction conducted with a liquid CO_2/He source at 10 000 psi yielded an oil solubility of 5.47 wt %, and the last extraction at 8000 psi gave a 2.86 wt % oil solubility). It is also worth noting that had all of the extractions been conducted with a liquid CO_2/He source, using all new cylinders pressurized to say 1700 psi, then the recorded solubility differences between neat CO_2 and helium-pressurized cylinders would have been even greater than those reported in this study. Therefore, we feel that the effect noted in this study is valid and should be of importance to analysts using SFE.

The layering or miscibility of binary gas mixtures above and below their respective critical temperatures at high pressures has been studied by several investigators.[22,23] The phenomenon is quite general, as noted by Tsiklis and Rott in an excellent review,[24] and the tendency toward phase separation or mutual miscibility

(17) Schweighardt, F. K.; Mathias, P. M. Abstracts of the 1993 Annual Meeting of the AIChE, American Institute of Chemical Engineers, New York, 1993; Abstract 9a.

(18) Burfield, D. W.; Richardson, H. P.; Guerca, R. A. *AIChE. J.* **1970**, *16*, 97–100.

(19) Gorner, T.; Dellacherie, J.; Perrut, M. *J. Chromatogr.* **1990**, *514*, 309–316.

(20) Gahrs, H. J. *Ber. Bunsenges Phys. Chem.* **1984**, *88*, 894–897.

(21) Schweighardt, F. K., Air Products & Chemicals, Inc., Allentown, PA, personal communication.

(22) Gordon, R. P. *J. Chem Educ.* **1972**, *49*, 249–252.

(23) Maslennikova, V. Y.; Emelyanova, E. A.; Tsiklis, D. S. *Russ. J. Phys. Chem.* **1971**, *45*, 448–450.

(24) Tsiklis, D. S.; Rott, L. A. *Russ. Chem. Rev.* **1967**, *36*, 351–361.

of binary fluid pairs can be qualitatively predicted by a cohesive energy density approach.[25] However, despite the predicted immiscibility of He with CO_2 under the above conditions (which is the basis of using He as a pressurizing medium with liquid CO_2), real experimental measurements show that there is a finite solubility of He in liquid CO_2.[21,26] It is this factor which apparently accounts for the results reported in this study.

CONCLUSIONS

The results presented in this study show that the small amount of helium entrained in liquid carbon dioxide is capable of reducing the dissolution power of supercritical CO_2. The observed reduction in solute solubility resulting from this phenomenon should be appreciated by analysts utilizing SFE, particularly in optimizing extraction conditions and where method validation is required. Small quantities of He in SC-CO_2 can result in an incomplete extraction, particularly if the extraction conditions (time, volume, or mass of fluid used) are based on solute solubilities in pure CO_2. The above trend does not imply that helium-pressurized CO_2 cylinders and their attendant benefits cannot be utilized for analytical SFE. However, analysts should take precautions when utilizing solubility data determined in pure CO_2 with these fluid sources and the booster-type pumps utilized in this study.

(25) Kaplan, R. *AIChE J.* **1967**, *13*, 186–188.
(26) MacKendrick, R. F.; Heck, C. K.; Barrick, P. L. *J. Chem. Eng. Data* **1968**, *13*, 352–353.

ACKNOWLEDGMENT

The authors acknowledge the assistance of Scott Taylor in making some of the solubility measurements reported in this study and Drs. Robert Bartelt, Douglas Raynie (Procter & Gamble), and Frank Schweighardt (Air Products) for helpful discussions. Names are necessary to report factually on available data; however, the USDA neither guarantees nor warrants the standard of the product, and the use of the name by USDA implies no approval of the product to the exclusion of others that may also be suitable.

Received for review February 13, 1995. Accepted April 21, 1995.[⊗]

AC950158F

[⊗] Abstract published in *Advance ACS Abstracts,* June 1, 1995.

Anal. Chem. **1995**, *67*, 2292–2295

Kinetic Analysis and Subambient Temperature Chromatography of an Active Ester

John O. Egekeze, Michael C. Danielski, Nelu Grinberg,* George B. Smith, Daniel R. Sidler, Holly J. Perpall, Gary R. Bicker, and Patricia C. Tway

Merck Research Laboratories, R80Y-115, P.O. Box 2000, Rahway, New Jersey 07065-0914

The inherent instability of active esters provides a chromatographic challenge. A normal phase HPLC gradient was developed using nonprotic solvents and a diol stationary phase to determine the impurity profile of a mesylate which, under protic conditions, undergoes intramolecular ring closure to a cyclic ether. On-column cyclization of the analyte was found to be extensive at room temperature but insignificant at −30 °C. The on-column reaction rate was determined as a function of column temperature, and an Arrhenius activation energy was calculated.

Advances in liquid chromatography, regarding the synthesis of stationary phases with controlled pores and particle sizes along with the development of chemically bonded phases, have led to explosive development in the field of analytical chemistry in the last decade. The speed, high efficiency, and easily manipulated selectivity of modern chromatographic systems continue to make this technique directly applicable in various fields. Production, identification, and impurity profile characterization of new compounds is performed routinely, consistently, and efficiently through the use of these chemically bonded phases.

Chromatography has been applied in the pharmaceutical industry as a powerful analytical method for the determination of impurity profiles. However, when establishing the purity of a drug, care must be taken in interpreting chromatographic zones since not all of them may be due to impurities. Some chromatographic zones may be artifacts of the system due to degradation of the sample during the chromatographic process. We have reported several cases of such artifacts,[1,2] and such phenomena have been extensively documented by others.[3]

There are various sources of multiple zones in chromatography: chemical reactions,[4] impurities present in the sample solution,[5] discontinuities in the stationary[6] and mobile phases,[7] formation of charged species and/or complexes,[8] and equilibrium between species.[9]

It has been long recognized that a chemical reaction occurring during a chromatographic process can give rise to distorted peaks and breakthrough curves.[10] Many such reactions were reviewed recently by Jeng and Langer.[11] Clearly, determining the kinetics of such reactions can help to establish proper chromatographic conditions so that extraneous peaks will be minimized. An undesired reaction may be mitigated by lowering the temperature at which the separation occurs.

The influence of temperature on chromatographic separations has been extensively described in the literature. In general, temperature can have an effect on the mass transfer of the analyte between the mobile and stationary phases, and consequently can lead to improved separations.[12] Sheikh and Touchstone[13] reported improved separation of various steroids at subambient temperature using a nonaqueous mobile phase and a reversed phase column. Jinno et al.[14] investigated the effect of lowering the temperature on the separation mechanism in reversed phase chromatography. The authors concluded that, at subambient temperature and with more than 9.8% water in the mobile phase, the retention mechanism was similar to that of a reversed phase separation at ambient temperature. Below 9.8%, the mechanism was found to be similar to that of a normal phase separation.

Sentell et al.[15] investigated the effect of temperature on the separation of polycyclic aromatic hydrocarbons under reversed phase conditions. The authors observed that the high bonding density of an octadecyl bonded phase afforded better selectivity than a low-density stationary phase. Also, shape selectivity was observed at 25 °C and below for both types of stationary phases. Greater selectivity at lower temperature was observed for the high-density stationary phases. Van't Hoff plots were linear for low-density stationary phases but nonlinear for high-density phases. This was due to a phase transition of the bonded phase from a liquid-like state to a more crystalline state at subambient temperatures.

Henderson and Horvath[16] and Henderson and Mello[17] showed in early reports that lowering the temperature of separation of reversed phase systems retarded the cis–trans isomerization of proline-based peptides. Lowering the temperature of chromatographic separations has served to retard the decomposition of unstable molecules.[18,19]

(1) Grinberg, N.; Bicker, G.; Tway, P.; Baiano, J. A. *J. Liq. Chromatogr.* **1988**, *11* (15), 3138.
(2) Price, K.; Perpall, H.; Bicker, G.; Tway, P.; Grinberg, N. *J. Liq. Chromatogr.* **1990**, *13* (4), 2783.
(3) Keller, R. A.; Giddings, J. C. *J. Chromatogr.* **1960**, *3*, 205.
(4) Zechmeister, L.; Cholnovky, L. *Principles and Practice of Chromatography*; John Wiley & Sons: New York, 1951; p 5.
(5) Strain, H. H. *Ind. Eng. Chem.* **1950**, *42*, 1307.
(6) Moore, S.; Stein, W. H. *Annu. Rev. Biochem.* **1952**, *23*, 521.
(7) Boman, H. G. *Nature* **1949**, *21*, 215.
(8) Landau, A.; Fuerst, R.; Awapar, R. A. *Anal. Chem.* **1951**, *23*, 162.
(9) Partridge, S. M.; Westall, R. G. *Biochem. J.* **1948**, *42*, 238.
(10) Van Swaay, M. In *Advances in Chromatography*; Giddings, J. C., Keller, R. A., Eds.; Marcel Dekker, Inc.: New York, 1969; Vol. 8, p 364.
(11) Jeng, C.-Y.; Langer, S. H. *J. Chromatogr.* **1992**, *589*, 1.
(12) Snyder, L. R. *J. Chromatogr.* **1979**, *179*, 167.
(13) Sheikh, S. U.; Touchstone, J. C. *J. Liq. Chromatogr.* **1987**, *10* (11), 2489.
(14) Jinno, K.; Ohshima, T.; Hirata, Y. *J. High Resolut. Chromatogr., Chromatogr. Commun.* **1982**, *5*, 621.
(15) Sentell, K. B.; Henderson, A. N. *Anal. Chim. Acta* **1991**, *246*, 139.
(16) Henderson, D. E.; Horvath, Cs. *J. Chromatogr.* **1986**, *368*, 203.
(17) Henderson, D. E.; Mello, J. A. *J. Chromatogr.* **1990**, *499*, 79.

0003-2700/95/0367-2292$9.00/0 © 1995 American Chemical Society

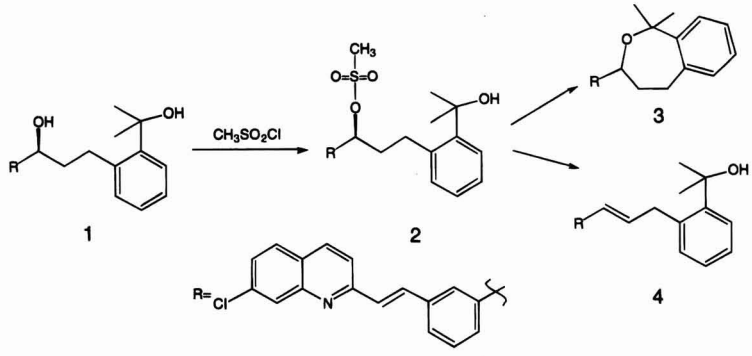

Figure 1. Mesylation of the diol and cyclization of the active mesylate ester.

Active esters are common intermediates in chemical synthesis, and their chromatography may be challenging because of their instability. On the other hand, their accurate quantitation may be essential in optimizing a synthesis.

In this paper, we report the chromatographic separation of an active mesylate, an intermediate in the synthesis of a leukotriene D_4 antagonist, whose tertiary alcohol moiety promotes cyclization to a cyclic ether. In order to quantitate the mesylate and examine its impurity profile, a normal phase gradient was designed using nonprotic solvents and a diol stationary phase column. It was discovered, however, that cyclization occurred on the stationary phase. The rate of on-column degradation was determined at several temperatures, and the chromatography was optimized.

EXPERIMENTAL SECTION

Solvents. Toluene, hexane, and ethyl acetate were purchased from EM Science (Gibbstown, NJ). The solvents were dried over molecular sieves.

Apparatus. Two HPLC systems were utilized for the analyses: a Spectra Physics P4000 ternary pump coupled with a Spectra system AS1000 autosampler (Spectra Physics, San Jose, CA) and a 759A absorbance detector (Applied Biosystems, Foster City, CA). A Beckman System Gold was used with a 126 programmable solvent module, a 167 scanning detector, and a 507 autosampler (Beckman, Fullerton, CA). The column was placed in a column jacket (Aura Industries, Staten Island, NY) containing a thermometer and connected to a constant temperature bath (Neslab Instruments, Newington, NH). Chromatograms were processed using a PE Nelson version 1.8 data acquisition system (Cupertino, CA).

NMR Conditions. ^{1}H NMR spectra were recorded using a Bruker AM 250 instrument. The compounds were collected from the chromatographic system. The solvent was removed and reconstituted in $CDCl_3$. The chemical shifts were reported in parts per million. Cyclization of the mesylate was readily apparent in the ^{1}H NMR spectra due to a chemical shift of the mesylate methine of δ 5.70 (dd, J = 8.0, 5.4 Hz, 1H), while the cyclic ether methine was shifted upfield to δ 4.57 (dd, J = 10.7, 5.6 Hz, 1H). The diol methine had a chemical shift of δ 4.69 (t, J = 6.4 Hz, 1H).

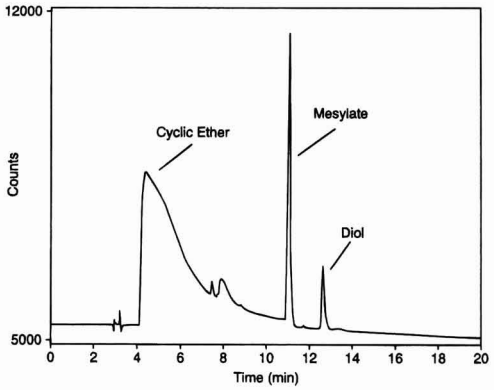

Figure 2. Chromatogram of a mesylate sample. Temperature, 25 °C. For other chromatographic conditions, see the Experimental Section. The diol peak corresponds to unreacted material prior to the chromatography.

Chromatography. A Chromegabond Diol 25- × 0.46-cm i.d. column (ES Industries, Berlin, NJ) was used with a 15-min linear gradient from 15:85 to 5:95 (A:B v/v), followed by a 10-min hold at the final composition [where A consisted of toluene–*n*-hexane (1:3 v/v) and B ethyl acetate]. Analytes were dissolved in ethyl acetate at a concentration of 0.5 mg/mL, and 5 μL was injected into the HPLC system. Compounds were detected by UV at 320 nm, at which all of the compounds of interest exhibited an absorbance maximum, characteristic of the quinoline functionality, with the same molar response.

RESULTS AND DISCUSSION

In the synthesis of leukotriene D_4 antagonist MK-0476, diol **1** was reacted with mesyl chloride to obtain mesylate **2**. Under protic conditions, undesired cyclization to **3** occurred during the chromatography (Figure 1).

A secondary elimination product, **4**, with a double bond in the α position to the R group, formed also, but more slowly. Accurate quantitation of **2** was important. Careful determination of **2** in reaction mixtures established the exact amount of reactants to be used in the next step of the synthesis.

Initially, using reversed phase chromatography, **2** disappeared completely with formation of **3** and **4**. Therefore, a normal phase gradient was developed using a diol stationary phase and a mobile

(18) Henderson, D. E.; O'Connor, D. J. In *Advances in Chromatography*; Giddings, J. C., Grushka, E., Cazes, J., Brown, P. R., Eds.; Marcel Dekker, Inc.: New York, 1984; Vol. 23, p 65.

(19) Henderson, D. E.; O'Connor, D. J.; Kirby, J. F.; Sears, C. P., III. *J. Chromatogr. Sci.* **1985**, *23*, 477.

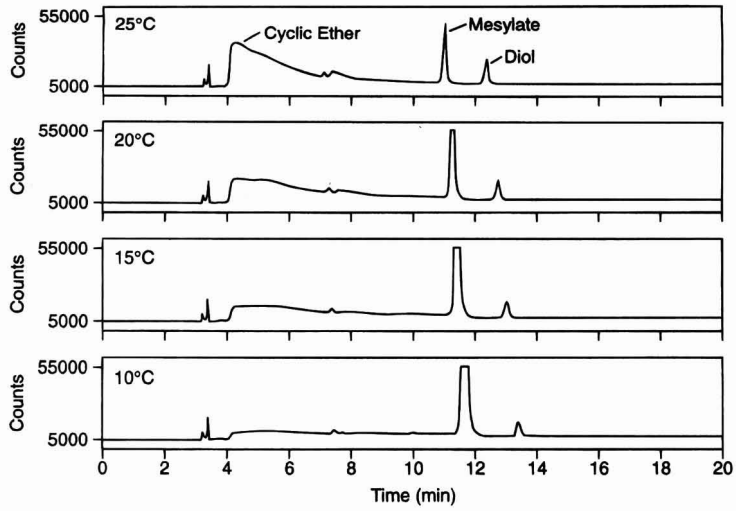

Figure 3. Influence of the temperature on the formation of the cyclic ether. For chromatographic conditions, see the Experimental Section.

phase consisting of the aprotic solvents hexane, toluene, and ethyl acetate. With a column temperature of 25 °C, chromatograms of the mesylate included sharp peaks of **1** and **2** and a broad peak of **3** (Figure 2). When the eluted **3** was collected and reinjected, a sharp peak was observed with the early retention time of 4.5 min, identified as **3** by NMR.

It was assumed that injected **2** remained at or near the top of the column, cyclizing all the while to the rapidly eluting **3**, until the gradient was polar enough to allow the unreacted **2** to elute. Thus the **3** formed from **2** on the column appeared as broad peak. Complete cyclization occurred when the gradient program was delayed for 15 min.

The chromatogram of Figure 2 was examined from 3.8 min to the appearance of the diol peak at ~12 min. To establish the kinetics of cyclization, the mesylate peak was collected and reinjected. A chromatogram like that shown in Figure 2 was obtained again. An estimated baseline was drawn from the beginning of the broad **3** peak to the end of the **2** peak, and perpendiculars (h_i) were drawn at regular intervals. The h_is were assumed to be proportional to the amount of uncyclized **2** on the column at the corresponding retention time, and the retention time and reaction time scales were assumed to be equal.

Plots of ln h_i versus t were linear (r^2 = 0.997) and thus consistent with pseudo-first-order cyclization:

$$\ln\{[\mathbf{2}]/[\mathbf{2}_0]\} = -kt \qquad (1)$$

Upon lowering the column temperature from 25 to 10 °C, the cyclic ether peak decreased significantly, indicating slower cyclization (Figure 3).

Applying a similar mathematical treatment as above, a series of plots were generated in the range of 10–30 °C. The slopes represent the rate constant of cyclization at the respective temperatures (Table 1).

As expected, the slope of the lines decreases as the temperature decreases. A flow rate study showed that the rate constant did not change over a flow rate range of 0.5–2 mL/min.

Table 1. Influence of Temperature on the Rate Constant of Cyclization

T (°C)	k (min^{-1})	SD (min^{-1})[a]
10	0.10	0.011
15	0.13	0.011
20	0.16	0.015
25	0.22	0.014
30	0.32	0.011

[a] Standard deviation.

The relationship between the rate constant k and the temperature is given by the Arrhenius equation:

$$\ln k = -E_a/RT + \text{constant} \qquad (2)$$

where E_a is the activation energy and R is the gas constant. According to eq 2, a plot of ln k vs the reciprocal of the absolute temperature defines a straight line of slope $-E_a/R$. Indeed, a straight line was obtained (r^2 = 0.991), and the activation energy E_a obtained from the slope of the graph was 9.3 kcal/mol, which corresponds approximately to a doubling of the rate with a 10 °C temperature increase.[20]

Figure 4 shows a −30 °C chromatogram of a synthetic mixture of **2** and its known impurities originating in the synthesis.

No cyclization occurred at −30 °C in a 10-min delay of the gradient program, and **2** was recovered quantitatively.

The peak area of all the components of the chromatogram remained unchanged compared to a gradient without isocratic hold. The second elimination product, **4**, observed in the chromatogram was not produced during chromatography but rather originated as a byproduct of the reaction. Since the chromatography under the optimized conditions produced a rugged separation, the next step was to establish the stability of the mesylate in the solvent solution. An ethyl acetate solution of

(20) Adamson, A. W. *A Textbook of Physical Chemistry*; Academic Press: New York, 1973; p 639.

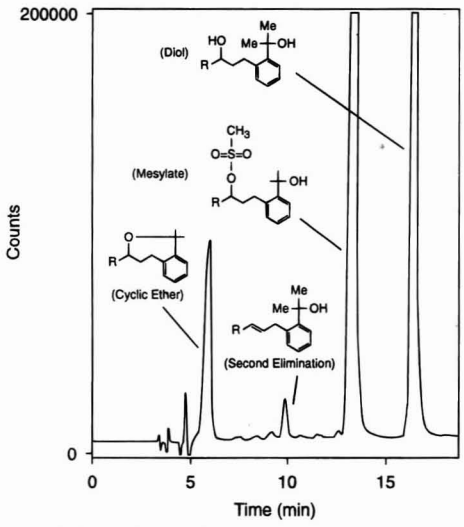

Figure 4. Chromatogram of a synthetic mixture of mesylate and known impurities. For chromatographic conditions, see the Experimental Section.

2 was kept at room temperature and injected repeatedly over a 24-h period. The mesylate peak area counts were recorded, and no changes occurred over the period of time investigated.

Since **2** was stable in aprotic solution at room temperature, the next step was to investigate what factors were responsible for the cyclization of the mesylate in the column. The column used in our experiments consisted of a diol stationary phase. Since the recovery of the compounds from the column was quantitative, the cyclization of the mesylate seemed to be due to residual silanols in the column. To prove this, the same gradient conditions were used, along with a silica gel stationary phase at 25 °C. Compound **3** formed, while **2** disappeared. It was concluded that the on-column reaction of the mesylate was silica-catalyzed cyclization.

Figure 5 shows the separation at −30 °C of an actual reaction mixture from the synthesis of **2**. Under these conditions, the reproducibility of the retention time for the components was 0.36% in day-to-day use of the same column, and 2% variation was observed when different columns were used.

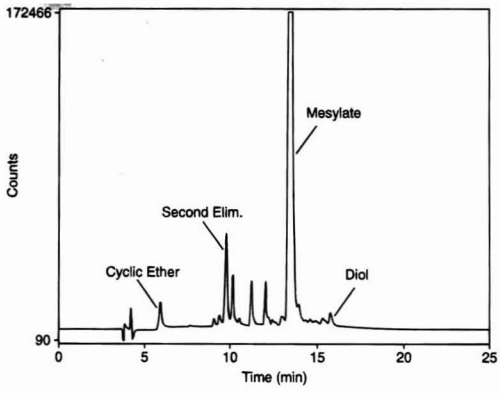

Figure 5. Chromatogram of an actual sample of mesylate originated from the reaction mixture. For chromatographic conditions, see the Experimental Section.

CONCLUSIONS

The chromatographic analysis of an active ester was optimized. Chromatograms at several column temperatures revealed on-column cyclization of the ester. Pseudo-first-order rate constants were obtained, and an Arrhenius energy was calculated. The kinetic analysis justified the low-temperature chromatographic assay, making the on-column cyclization insignificant. The procedure demonstrated that a rate constant can be obtained from a single chromatographic experiment. An accurate chromatographic analysis resulted for samples from the synthesis of the activated ester.

ACKNOWLEDGMENT

The authors would like to thank Prof. Karen Sentell of the Department of Chemistry of The University of Vermont and Dr. B. Feibush of ES Industries for fruitful discussions during the preparation of this work.

Received for review November 28, 1994. Accepted April 17, 1995.[⊗]

AC941134W

[⊗] Abstract published in *Advance ACS Abstracts,* June 1, 1995.

Anal. Chem. **1995,** *67,* 2296–2298

A Vessel for Low-Pressure Acid Dissolutions of Mineral and Inorganic Samples

M. Ravey,*,† B. Farberman,‡ I. Hendel,† S. Epstein,† and R. Shemer‡

IMI Institute for Research and Development, Haifa, Israel

Microwave-assisted acid dissolution of minerals and inorganics is rapid, but difficulties in controlling the temperatures of such systems present potential safety problems. This drawback can be overcome by the use of specifically designed equipment which is, however, expensive. Dissolution under conventional heating, although slower, is inherently safer, temperature control being simple and reliable, as well as inexpensive. For laboratories with high sample loads, the importance of the dissolution time can be reduced significantly simply by heating a large number of samples simultaneously. For such systems, microwave heating holds little or no advantage over conventional heating. Presented here is a vessel designed specifically for this purpose. It is constructed of polyvinylidene difluoride, has a volume of 20 mL, and can be used up to 120 °C at 4 atm. This vessel has two major advantages: the use of conventional heating obviates the need for special (and generally expensive) ancillary equipment and the small size and relatively low cost facilitate heating large numbers of such vessels simultaneously. These vessels have been in routine use in these laboratories for the past 8 years. Forty of them are often heated together in a conventional laboratory oven.

The Analytical Department of the IMI Institute performs a large number of analyses involving minerals and inorganic materials. Most of these are received as heterogeneous solids, and in order to obtain representative samples for analysis, it is necessary to convert them into homogeneous solutions. Two general approaches are generally used: alkaline fusion and acid dissolution. Alkaline fusion introduces high concentrations of cations into the final solution. The presence of these is at best superfluous, but mostly they are undesirable. Therefore, where possible, acid dissolution is the procedure of choice.

Microwave heating has become quite popular for acid dissolutions,[1,2] mainly because of its speed. Under microwave irradiation, dissolutions are achieved in minutes[3,4] compared to the hours generally necessary with conventional heating. However, measuring and controlling the temperature and pressure inside a sealed vessel irradiated by microwave energy is quite difficult, and lack of temperature control can result in serious safety problems.[5] Although equipment with pressure relief devices is available, it is expensive and cumbersome to use.

Most of the minerals and inorganic materials submitted to this laboratory for analysis dissolve in acids below 100 °C. The only potential sources of pressure in these systems are carbonates which may be present.

However, if the sample is acidified (to expel carbonate CO_2) prior to sealing the vessel, the pressure developed on heating will be the vapor pressure of the acid mixture used. At 100 °C, this is relatively low. A vessel resistant to acids at 120 °C and capable of operating up to 2 atm should therefore suffice for this type of work.

Our approach to increasing the sample throughput of the laboratory was based on the development of small, low-pressure vessels, many of which could be heated together, batchwise, in a standard laboratory oven. This was expected to greatly increase the sample throughput, in spite of the relatively slow dissolution rate under conventional heating conditions.

For dissolutions which do not generate pressure, the reliability of modern laboratory ovens makes this approach simpler, safer, and less expensive than microwave heating.

DISCUSSION

The vessel has an internal volume of 20 mL. Design details are given in Figure 1. The parts were turned from poly(vinylidene difluoride) (PVDF) barstock (G. Fischer, Schaffhausen, Switzerland). A poly(tetrafluoroethylene) (PTFE)-sheathed Viton O-ring (2-214 PTFE/Viton, Parker Seal Group, Lexington, KY) was used as the seal. Both PVDF and PTFE are resistant to aqueous HCl, HF, HNO_3, and H_2SO_4 up to 100 °C (manufacturer's information).

In our experience, no deleterious effect was found, either on the vessel or the O-ring, in routine use up to 110 °C. The vessel was designed for operation up to 120 °C at a maximum pressure of 4 atm (test pressure, 10 atm at 120 °C). The O-ring fits into a recess in the plug, where it stays when the vessel is opened. This permits handling of the vessel parts without coming into contact with any of the acid-wetted surfaces.

To test the system, a series of analyses was run on a number of standard materials. The results for two of these standards are given in the Experimental Section. The standards were a phosphate rock and a firebrick. Thirteen samples of the phosphate rock were dissolved simultaneously in 13 vessels, and the resulting solutions were analyzed for silicon. Similarly, 12 samples of the firebrick were dissolved simultaneously in 12 of the vessels, and the resulting solutions were analyzed for aluminum and sodium. In all cases, full recovery of the analyte was achieved.

† Analytical Department.

‡ Technical Services Department.

(1) Kingston, H. M.; Jassie, L. B. *Anal. Chem.* **1986,** *58,* 2534–2541.

(2) Matusiewicz, H.; Sturgeon, R. E. *Prog. Anal. Spectrosc.* **1989,** *12,* 21–39.

(3) Fischer, L. B. *Anal. Chem.* **1986,** *58,* 261–263.

(4) Fernando, L. A.; Heavner, W. D.; Gabrielli, C. C. *Anal. Chem.* **1986,** *58,* 511–512.

(5) Gilman, L.; Grooms, W. *Anal. Chem.* **1988,** *60,* 1624–1625.

0003-2700/95/0367-2296$9.00/0 © 1995 American Chemical Society

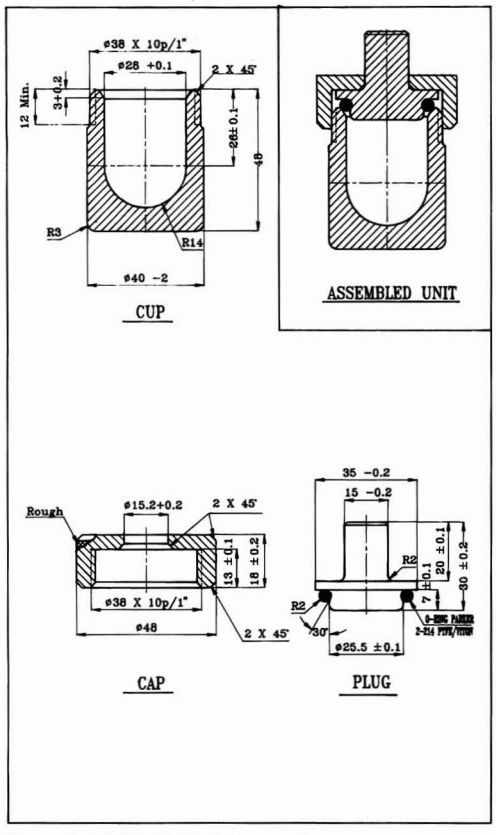

Figure 1. PVDF acid dissolution vessel.

The complete recovery of silicon as its volatile fluoride attests to the integrity of the O-ring seal.

Sealing the vessel requires only slight hand pressure. We have found that hand-tightening the cap slightly past the end of its free-turning point makes a reliable seal. The subjective tendency to "make sure" and overtighten the closure must be resisted, as this will achieve the opposite effect. It will deform the O-ring and result in leaks. Deformation will also reduce the service life of the O-ring.

In Table 1 is a brief list of some of the applications to which we have put these vessels, using 48% HF and prewetting with 35% HCl. These vessels have been in use in these laboratories since we first designed and fabricated them in our workshop in 1987. Since then, we have performed over 20 000 dissolutions in them and have placed up to 40 at a time in the oven. Except for those vessels involved in the temperature overshoot accident discussed below, most of those fabricated in 1987 are still in service today.

Similar vessels have also been fabricated of PTFE (Teflon). Although this material is thermally and chemically more resistant than PVDF, mechanically it is weaker. This results in weaker threads and requires thicker walls, making the vessel bulkier, which reduces the number that can be accommodated in an oven. It also increases heat-up and cool-down time requirements.

Table 1. Applications of the Small, Low-Pressure Vessel Described for Inorganic and Mineral Samples

analytes	substrates
Al, Ca, Fe, K, Mg, Na, Si, Ti	phosphate rock
Al, Fe, K, Na, Si, Ti	clays
Al, Fe, Na, K	sands
Cd, Hg	coal ash
V	boiler ash
Co, Cr, Fe, Mo, Ni	tungsten carbide
SiO_2 (free)	silicon carbide
Al, Na, Si	zeolites
Al, Fe, Mg, Si	limestone[a]

[a] Initial dissolution, to expel CO_2, is in HCl in the open vessel at room temperature. HF is then added, and the vessel is sealed and heated.

Table 2. Average Values for Standard Reference Materials[a]

	NBS Tennessee phosphate rock 56b		Euro CRM firebrick 776-1	
analyte	certified	found	certified	found
SiO_2	10.1	10.28 ± 0.24		
Al			15.50 ± 0.12	15.67 ± 0.13
Na			0.362 ± 0.015	0.360 ± 0.006

[a] Average of 13 determinations for NBS and 12 for CRM. Reported as average (%) ± SD.

SAFETY ASPECTS

This vessel was designed specifically for dissolutions which do *not* generate pressure. It is not suitable for pressure-generating dissolutions, such as, for example, the oxidative destruction of organic matter.

The O-rings are checked visually for signs of deformation or damage after each use. Slightly deformed O-rings usually regain their shape if allowed to "rest". Permanently deformed or damaged O-rings are discarded.

We have been using these vessels on a routine basis for 8 years. In that time, we have had only one accident. This occurred when an old laboratory oven was used which had no temperature overshoot protection. A fault in the thermostat resulted in a temperature overshoot to over 180 °C. Of the 15 vessels in the oven at the time, most were deformed, but only one developed a serious leak. We now use only ovens with double temperature overshoot protection. As an added precaution, we connected the oven vent to a water aspirator, to be turned on if a serious leak does develop.

EXPERIMENTAL SECTION

The standard reference materials used were NBS Tennessee phosphate rock 56b (NIST, Gaithersburg, MD) and Euro CRM firebrick 776-1 (Bureau of Analyzed Samples Ltd., Newham Hall, Middlesborough, U.K.). The procedure was the same for both. Amounts of 100–120 mg were weighed into the PVDF acid dissolution vessels (13 in the case of the NBS and 12 for the CRM). The material in each vessel was wetted down with 10 drops of 35% HCl (to expel CO_2 from the carbonates present), 4 mL of 48% HF was added to each vessel by means of a polypropylene pipet, and the vessels were sealed. All the vessels

in each series were placed together in a laboratory oven set at 105 °C. After 1 h, the vessels were removed from the oven and allowed to cool. The vessel contents were transferred, with the aid of a stream of boric acid solution (35 g of boric acid and 10 mL of 35% HCl in 1 L of water) ejected from a plastic wash bottle, to a 100-mL poly(methylpentene) volumetric flask (Azlon Inc., Brewster, NY). The volume in the flask was made up to the mark with the same boric acid solution. The contents of the volumetric flask were mixed thoroughly. The calcium fluoride dissolved after a few minutes.

The analytes were determined on a Varian Model AA Spectra 40 atomic absorption spectrometer, silicon at 251.6 nm, aluminum at 309.3 nm, and sodium at 589.0 nm. The results are given in Table 2.

Received for review January 3, 1995. Accepted March 17, 1995.[⊗]

AC950015T

[⊗] Abstract published in *Advance ACS Abstracts,* May 1, 1995.

Anal. Chem. **1995**, *67*, 2299–2303

Flow Injection Analysis of Sulfate with a Potentiometry-Based Linear Calibration Graph

Tzyh-Chyang Tang[†] and Hsuan-Jung Huang*[,‡]

Department of Chemistry, National Sun Yat-Sen University, Kaohsiung 80424, Taiwan, and Department of Industrial Safety and Hygiene, Chia-Nan Junior College of Pharmacy, Tainan 71710, Taiwan

Based on the behavior of lead ion selective electrode (Pb ISE) and the interaction between a sulfate-containing solution and solid lead sulfate, equations describing the explicit linear relationships between the measured potential of Pb ISE and the sulfate concentration in sample solutions were derived and applied to the determination of sulfate by the flow injection analysis technique. These proposed procedures improved the sensitivity of the potentiometric method and the reliability of the analytical results. With a mixed solvent system (35 vol % methanol) a detection limit as low as 1.0×10^{-6} M can be obtained optimistically.

Sulfate determination is one of the routine analyses encountered frequently in analytical laboratories. Besides the technique of ion chromatography,[1,2] methods applicable to the analysis of sulfate are indirect. The analytical procedures usually include the precipitation of sulfate ions with barium or lead ions, followed by either turbidimetric, spectrophotometric, or potentiometric determination of the precipitates formed or the remaining barium or lead ions in solution.[3–16] Among these methods, the potentiometric method has attracted continuous attention due to its convenience and ease of operation. Recently, the flow injection technique has been coupled with the lead ion selective electrode and used for the determination of sulfate. Although various procedures have been developed, a nonlinear or semilinear plot is usually obtained and used as the calibration graph, or the equilibrium constant for the reaction of sulfate with lead has to be known or determined in order to linearize the calibration graph.[14–16] This introduces either unpredictable uncertainties or tedious procedures. In order to overcome these drawbacks, equations based on the behavior of the lead ion electrode and the interaction between a sulfate-containing solution and solid lead sulfate have been derived and applied to the potentiometric determination of sulfate in solutions. With the proposed procedures, a linear calibration graph can be obtained from a plot of measured potential-related variables vs the concentration of sulfate in solutions. Similarly, by following the same procedures, a standard addition method can also be applied to the potentiometric determination of sulfate. In order to lower the detection limit, experiments are run with a mixed-solvent system containing 35 vol % methanol. A detection limit as low as 1.0×10^{-6} M which is about 1 order lower than that of the reported potentiometric methods can be obtained optimistically.

PRINCIPLE

The potential of the lead ion electrode in a lead ion-containing solution can be represented by the extended Nikolsky equation

$$E = L + 0.0128 \ln(a_{Pb} + \sum k_{ij} a_j^{Z_i}) \quad (1)$$

where E is the measured potential of the lead ion electrode (with respect to the reference electrode), L is a constant, 0.0128 is the explicit value of RT/nF, a_{Pb} is the activity of lead ion in solution, a_j represents the activity of interfering ions, Z_j is the charge ratio of the lead ion to the interfering ion j, and k_{ij} is the selectivity ratio characteristic of Pb ISE.

A background potential E_b can be obtained when the lead ion electrode is immersed in the blank solution:

$$E_b = L + 0.0128 \ln(\sum k_{ij} a_j^{Z_i}) \quad (2)$$

In a flow system, if the blank solution is allowed to flow through a solid lead sulfate-containing column, the measured potential E_0 will be equal to

$$E_0 = L + 0.0128 \ln(\alpha a_{Pb}^{\circ} + \sum k_{ij} a_j^{Z_j}) \quad (3)$$

where a_{Pb}° is the activity of lead ion that enters the solution from solid lead sulfate under equilibrium conditions, α representing the ratio of lead ion entering the solution from solid lead sulfate under the experimental conditions to those under the equilibrium conditions incorporating the dispersion effect of the flow system and is a constant at a given experimental condition. The potential difference, ΔE_0, caused by the dissolution of lead ion from solid

[†] Chia-Nan Junior College of Pharmacy.
[‡] National Sun Yat-Sen University.

(1) Small, H.; Stevens, T. S.; Bauman, W. C. *Anal. Chem.* **1975**, *47*, 1801.
(2) Mulik, J.; Puckett, D.; Williams, D.; Sawicki, E. *Anal. Lett.* **1976**, *9*, 653.
(3) Greenberg, A. E.; Connors, J. J.; Jenkins, D. *Standard Methods for the Examination of Water and Waste Water*, 15th ed., American Public Health Association: Washington, DC, 1981; pp 439–440.
(4) Appel, B. R.; Kothny, E. L.; Hoffer, E. M.; Buell, G. C.; Wall, S. M.; Wesolowski J. J. Presented at a meeting of the Division of Environmental Chemistry, American Chemical Society, New Orleans, March 20–25, 1977.
(5) Dunk, R.; Mostyn, R. A.; Hoare, H. C. *At. Absorpt. Newsl.* **1969**, *8*, 79.
(6) Forbes, E. A. *Analyst* **1973**, *98*, 506.
(7) Galle, O. K.; Hathaway, L. R. *Appl. Spectrosc.* **1971**, *29*, 518.
(8) Eagner, G. H.; Steele, K. F. *Int. Lab.* **1982**, (Sept. 29), 12.
(9) Levins, R. J. *Anal. Chem.* **1971**, *43*, 1045.
(10) Ross, J. W., Jr.; Frant, M. S. *Anal. Chem.* **1969**, *41*, 967.
(11) *Analytical Methods Guide*, 9th ed.; Orion Research, Cambridge, MA, 1978.
(12) Krug, F. J.; Zagatto, E. A. G.; Reis, B. F.; Bahia, O. F.; Jacintho, A. O.; Jorgensen, S. S. *Anal. Chim. Acta* **1983**, *145*, 179.
(13) Trojanowicz, M. *Anal. Chim. Acta* **1980**, *114*, 293.
(14) Coetzee, J. F.; Gardner, C. W., Jr. *Anal. Chem.* **1986**, *58*, 608.
(15) Hara, H.; Horvai, G.; Pungor, E. *Analyst* **1988**, *113*, 1817.
(16) Hara, H.; Mori, S., *Analyst* **1990**, *115*, 1077.

0003-2700/95/0367-2299$9.00/0 © 1995 American Chemical Society

lead sulfate can be obtained by subtracting eq 2 from eq 3:

$$\Delta E_0 = E_0 - E_b = 0.0128 \ln\left(\frac{\alpha a_{Pb}^\circ + \sum K_{ij} a_j^{Z_j}}{\sum K_{ij} a_j^{Z_j}}\right) \quad (4)$$

With the substitution of $m_{Pb}^\circ \gamma$ for a_{Pb}° in eq 4, the concentration of the dissolved lead ion, αm_{Pb}° can be expressed as

$$\alpha m_{Pb}^\circ = \frac{1}{\gamma} \sum K_{ij} a_j^{Z_j} (\exp(E_0') - 1) \quad (5)$$

where $E'_0 = \Delta E_0/0.0128$ and γ is the activity coefficient of lead ion in solution. When a sulfate-containing solution is allowed to flow through the solid lead sulfate-containing column, an equation similar to eq 5 can be derived for the concentration of lead ion dissolved from solid lead sulfate, αm_{Pb}.

$$\alpha m_{Pb} = \frac{1}{\gamma} \sum K_{ij} a_j^{Z_j} (\exp(E'_n) - 1) \quad (6)$$

where $E'_n = (E_n - E_b)/0.0128$ and E_n is the measured potential for the sulfate-containing solution flowing through the column.

With a flow system, equations describing the relationships between the sulfate-containing solution and the solid lead sulfate can be derived by following the same procedures developed previously.[17] When a sulfate-containing solution is allowed to flow through and react with solid lead sulfate, the dissolved lead and sulfate ions and the originally present sulfate ion will have the following relationship:

$$(\alpha m_{so} + m_{so}')\alpha m_{Pb} = K_{sp}' \quad (7)$$

where αm_{Pb} and αm_{so} are the concentrations of lead and sulfate ions, respectively, that have entered the solution from the solid lead sulfate (assuming that no lead ion was present in the original sample solution), m_{so}' is the concentration of sulfate present in the original sample solution, $\alpha m_{so} + m_{so}'$ is the concentration of sulfate present in solution after flowing through the column, and K_{sp}' is the apparent solubility product of lead sulfate under the experimental conditions. As $\alpha m_{Pb} = \alpha m_{so}$, eq 7 can be expressed as

$$(\alpha m_{Pb} + m_{so}')\alpha m_{Pb} = K_{sp}' \quad (8)$$

If a solution containing no sulfate (blank solution) is allowed to interact with solid lead sulfate, eq 8 becomes

$$\alpha m_{Pb}^\circ \alpha m_{Pb}^\circ = K_{sp}' \quad (9)$$

where αm_{Pb}° represents the concentration of lead or sulfate dissolved from solid lead sulfate. Equating eqs 8 and 9 and putting $m_{Pb}^\circ = P m_{Pb}$, the following equation is obtained:

$$\alpha m_{Pb}^\circ (P - 1/P) = m_{so}' \quad (10)$$

From eq 5 and 6, P can be expressed as

$$P = (\exp(E_0') - 1)/(\exp(E_n') - 1) \quad (11)$$

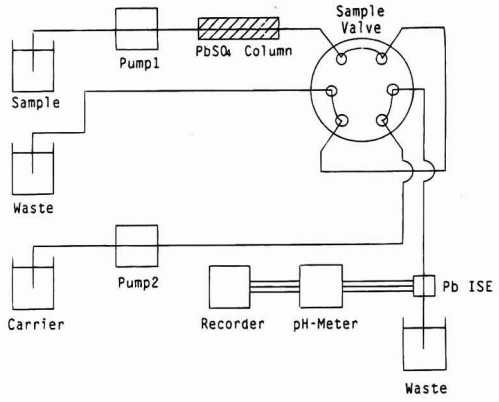

Figure 1. Scheme of the FIA system.

By substituting eq 5 into eq 10, then

$$(P - 1/P) = \frac{\gamma m_{so}'}{\sum K_{ij} a_j^{Z_j} (\exp(E_0') - 1)} \quad (12)$$

or

$$(P - 1/P) = K' m_{so}' \quad (13)$$

where $K' = \gamma/(\sum k_{ij} a_j^{Z_j})(\exp(E_0') - 1)$ is constant at the given experimental conditions. A straight line with an intercept at the origin and a slope equal to K' could be obtained when values of $(P - 1/P)$ were plotted against m'_{so}.

If an unknown concentration of sulfate present originally in the sample solution, a standard addition method can be derived (following the same procedures as described above) to find the unknown concentration m_x in solution. With the addition of standard sulfate solution (with a concentration of m_{so}'') to the sample solution, the sulfate concentration in the sample solution will become $m_x + m_{so}''$. After interaction with solid lead sulfate, a relationship similar to that in eq 8 can be obtained:

$$(m_x + \alpha m_{Pb} + m_{so}'')\ \alpha m_{Pb} = K_{sp}' \quad (14)$$

Following the same treatment as above for eqs 14 and 9, a new equation similar to eq 13 can be obtained:

$$(P - 1/P) = K'(m_x + m_{so}'') \quad (15)$$

From eq 15 it can be seen that a plot of $(P - 1/P)$ vs m''_{so} should yield a straight line with a slope equal to K' that intercepts the abscissa at $-m_x$. Hence the unknown concentration of sulfate in solution can be obtained.

EXPERIMENTAL SECTION

Flow Injection System. The flow system consists of two peristaltic pumps, one solid lead sulfate reaction column, and one injection valve (Rheodyne 5020) with a sample loop of 0.10 mL (Figure 1). Pump 1 was used for the delivery of sample or

(17) Tang, T. C.; Huang, H-J, *Anal. Chim. Acta* **1990**, *238*, 431.

standard solutions to the lead sulfate column. Pump 2 was used for the delivery of sample solution from the sample loop to the potentiometric detector. The lead sulfate column was prepared by packing lead sulfate powder (particle size 80–120 mesh) into a piece of PTFE tubing (300 mm × 3 mm i.d.). A 0.45 μm pore-size filter was placed at the outlet of column to prevent the flow-through of solid lead sulfate into the detection system. The potentiometric detector was made from a piece of PTFE block which contained a commercial Pb ISE (Orion, Model 94-82), and a homemade reference electrode (Ag/AgCl in 3 M NaCl). A PVDF spacer of 0.015 cm in thickness with a 0.1 cm wide slot defining the flow path between the inlet and outlet ports was used. The potential of the Pb ISE was measured with a Corning pH meter-140. The output of the pH meter was recorded with a Yokogawa 3025 recorder. All of the sample and standard solutions were analyzed in triplicate. The optimum flow rate for the delivery of sample or standard solutions and the reacted solution (by carrier) was 0.3 and 0.9 mL/min, respectively. In order to improve the sensitivity of the studied method, 35 vol % methanol was added to all the sample or standard sulfate solutions.

In order to minimize the possible contamination resulting from the residue of the previous sample, 4 min was allowed for the blank solution to flush and clean the solid lead sulfate column before new sample solution was introduced. It took about 3 min for each sample to go through the injection and detection processes. The ionic strength of the sample and carrier solutions was adjusted to 0.10 by the addition of 0.10 M $NaClO_4$ to the solutions.

Ion Chromatographic Analysis. A Dionex series 4500i ion chromatograph with a conductivity detector was used for the direct analysis of SO_4^{2-} content in rainwater sample. An IonPac AG4A (P/N 37042) column and an Anion Micro Membrane Suppressor (AMMS, P/N 037072) were equipped for the IC, and 0.1 M NaOAc/0.06 M HOAc solution was used as the buffer solution.

Reagents. All chemicals used were of GR grade (Merck) or better. Standard sulfate solutions were prepared from the dilution of Merck Titrisol solution. All the solutions were prepared from the deionized/distilled water.

RESULTS AND DISCUSSION

Effect of Flow Rate on the Sulfate Determination. This method is based upon the steady state interaction that existed between the sulfate ion in the sample solutions flowing through solid lead sulfate and the amount of lead ion dissolved; thus, the sensitivity of the Pb ISE determination is affected by the steady state obtained. The flow rate of the sample solution will thus affect the sensitivity of this method. With a higher flow rate, sample solution takes a shorter time to pass through the column and introduces less lead ions into the sample solution. A smaller α value in eq 7 will result. Conversely, if a lower flow rate is used, a larger amount of lead ions will dissolve and a larger α value will result to give a better sensitivity, although it takes a longer analysis time. The responses of potential difference ΔE_n at various flow rates are studied by the injection of 6.0×10^{-5} M sulfate solution into the system. It is found that the measured potential difference decreases as the flow rate increases. A compromise value of 0.3 mL/min is chosen as the optimal flow rate of sample solution for the following studies.

Calibration Graphs for Sulfate Determination. Figure 2a shows the conventional calibration graph of a plot of ΔE_n vs m_{so}'. The concentration of standard sulfate solution, m_{so}', is varied in the range 4.0×10^{-6}–1.2×10^{-4} M. the curve in Figure 2a is nonlinear in character. The same data are plotted according to eq 13 and shown in Figure 2b. A straight line with an intercept of $(0.05 \pm 0.01) \times 10^{-6}$ (at the 90% confidence level) and a linear correlation coefficient of 0.9997 is obtained. In another experiment, a known concentration of sulfate (6.0×10^{-6} M) is added to the standard sulfate solutions. The obtained data are plotted according to eq 15 and shown in Figure 2c. A straight line with a linear correlation coefficient of 0.9998 and an intercept of -(6.14 ± 0.20) × 10^{-6} (at the 90% confidence level) at the abscissa is obtained. The determined sulfate concentration agrees with the known value very well.

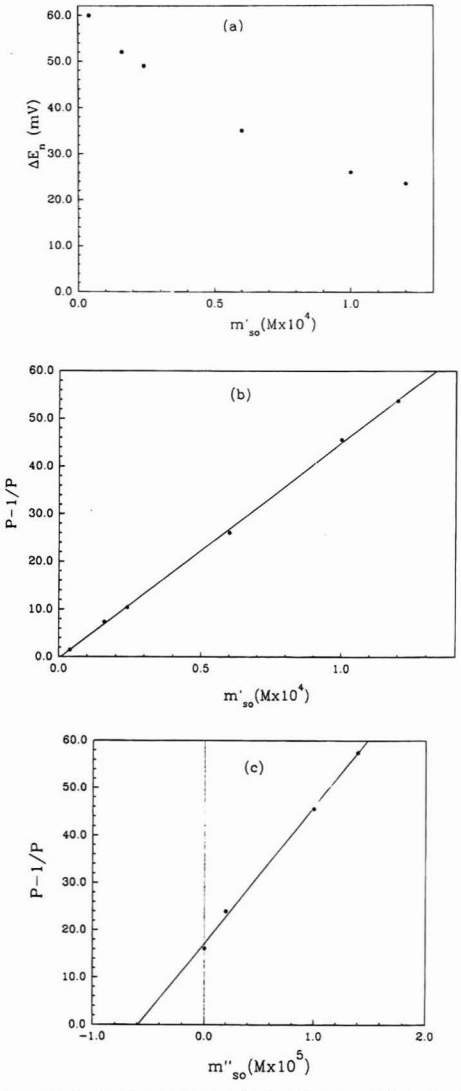

Figure 2. Calibration graphs obtained (a) from the plot of potential difference ΔE_n vs sulfate concentration in solution (b) according to eq 13 and (c) according to eq 15.

Effect of Methanol on the Detection Limit of Sulfate Determination. As the solubility of lead sulfate decreases with the decrement of the dielectric in solution, the K_{sp}' value of lead sulfate and therefore the detection limit of sulfate can be lowered by using a methanol-containing solution in the system. Calibration graphs for solutions contained 25 and 35 vol % of methanol were constructed. Straight lines with linear correlation coefficients better than 0.999 are obtained for these two plots. The slopes of the linear calibration graph obtained are 5.2 ± 0.1 and 45.2 ± 1.0, respectively. The variation of slope is due to the change in the exp (E_0') value in the studied system. The value of exp(E_0') for solutions containing a higher concentration of methanol is smaller than that with a lower concentration of methanol. From eq 12, the slope of the linear plot obtained from solutions containing 35% methanol is thus larger than that obtained from solutions with 25% methanol.

The much larger slope obtained from solutions contained 35% methanol may be attributed to the passivation effect of the lead ion electrode. For a passivated Pb ISE, its sensitivity is supposed to decrease; i.e., the value of E_0' *and* E_n' obtained should be smaller than those from a nonpassivated electrode. From eq 11, P is an exponential function of E_0' and E_n', and a small variation of E_0' and E_n' may result in a larger change of P value and thus a significant change of the slope. The passivation effect of Pb ISE causes the slopes obtained from experiments to deviate from the theoretical value predicted by eq 13 or 15. Different from the conventional calibration plot for an ion selective electrode, the slope obtained from a plot of eq 13 or 15 has a unit of M^{-1} and is a function of the activity coefficient γ, dissolution characteristic of solid lead sulfate and exponential of E_0'. The slope so obtained has nothing to do with the Nernstian of non-Nernstian response of an ion electrode. Therefore, eqs 13 and 15 should apply equally well to the measurement obtained from either a Nernstian or a non-Nernstian electrode. As the reproducibility of the measured potential deteriorates when the methanol in solution was higher than 35%, solutions containing 35% methanol are used throughout the whole experiment. The detection limit of sulfate for the proposed potentiometric method is estimated to be 1.0×10^{-6} M under the optimized experimental conditions.

Interferences. Two types of interference are found in the studied system. The first type of interference comes from the dissolution process of lead sulfate. Ions (such as oxalate, chromate, and phosphate) that form more insoluble compounds with the dissolved lead ion than sulfate does cause positive errors in sulfate determination (induce an upward shift of the calibration graph) at lower sulfate concentrations. Figure 3 shows the calibration graph obtained with the addition of 1.0×10^{-6} M oxalate to the standard sulfate solutions. Adequate linearity can be obtained for solutions with a sulfate concentration higher than 6.0×10^{-5} M, but deviation occurs at lower sulfate concentrations. In the presence of oxalate, part of the dissolved lead ions will be reprecipitated as insoluble lead oxalate (when the sulfate content in solution is low) and disturb the existing steady state between lead and sulfate ions, which will trigger further dissolution of solid lead sulfate. The overdissolved sulfate ions in solution thus induce a positive error in the calibration graph. But when the sulfate concentration in solution is high, the concentration of lead ion dissolved from solid lead sulfate is low, and no interactions between oxalate and lead ions will occur. A linear relationship is thus reinstated for solutions of higher sulfate concentration. The

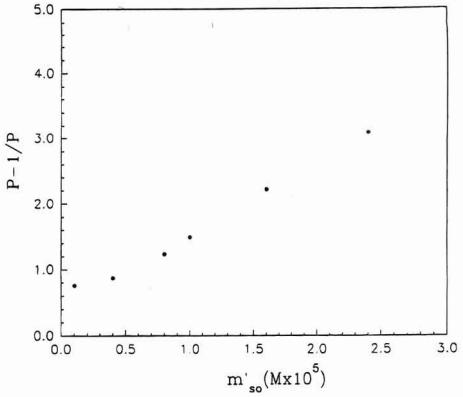

Figure 3. Calibration graphs obtained from standard sulfate solutions in the presence of 1.0×10^{-6} M oxalate.

curvature found in Figure 3 thus shows the influence of the oxalate (at a concentration of 1.0×10^{-6} M) on the calibration graph. The calibration graph shown in Figure 3 is useful for diagnosing whether any interferent is present in the sample solutions or not. From the curvature obtained and the level of interferent present, the effect of interferent on the calibration graph can be understood. It assures the reliability of the analytical results obtained.

Different from anions mentioned above, cations which form more insoluble compounds with sulfate ion than lead ion do induce an overdissolution of lead ions from solid lead sulfate and introduce negative errors (cause a downward shift of the calibration graph) at higher sulfate concentrations. Barium ion is a typical example showing this type of interference.

The second type of interference comes from the interference inherent with the Pb ISE. From the literature, cations such as Cd^{2+} Cu^{2+}, Hg^{2+}, and Ag^{+} interfere with the lead ion determination. The presence of these ions causes an enhancement of potentiometric response which introduces a constant additive error. The effect of this constant error can be calculated by taking the differential of m_{so}' or ($m_x + m_{so}''$) with respect to m_{Pb} in eq 13 or 15.

$$dm_{so}'/dm_{Pb} = -(P^2 + 1) \qquad (16)$$

From eq 16, if dm_{Pb} is the constant additive error introduced by the presence of Cd^{2+}, Cu^{2+}, Ag^{2+}, and Cd^{2+} in sample solutions, dm_{so}' will be the resulting deviation in the determination of m_{so}' and dm_{so}' is equal to $-(P^2 + 1)\, dm_{Pb}$. At low sulfate concentrations, P^2 approaches 1 so $dm_{so}' \simeq -2\, dm_{Pb}$. The effect of the constant error on sulfate determination is insignificant if dm_{Pb} is small compared with m_{Pb}. However, at high sulfate concentrations, P^2 becomes much larger than 1 so that a small error in dm_{Pb} will result a significant error in dm_{so}'.

Besides the heavy metal ions mentioned, chloride, nitrate, and bicarbonate when present in 100-fold excess over the concentration of SO_4^{2-} might seriously interfer with the lead ion determination.[16] The possible interference of Cl^- is studied as it is the most common anion existing in various sample solutions. With the addition of 2.0×10^{-4} M Cl^- to the standard sulfate solutions, a calibration graph similar to that of Figure 3 was obtained.

Adequate linearity is found for solutions with sulfate concentration higher than 7.5×10^{-5} M. The upward shift of the calibration graph occurred when the sulfate concentration was lower than 4.0×10^{-5} M. The deviation may be due to the complexing effect of Cl^- with the dissolved lead ion.

To test the validity of this method, a rainwater sample collected at Kaohsiung was measured by the proposed standard addition procedures. The sulfate content in the collected rainwater sample was found to be $(1.36 \pm 0.10) \times 10^{-4}$ M. Another portion of the rainwater sample was analyzed by the ion chromatography method and a result of $(1.46 \pm 0.06) \times 10^{-4}$ M was obtained. Comparing these two results, the discrepancy is less than 10% and is thought to be tolerable from the viewpoint of potentiometric analysis.

CONCLUSIONS

With the proposed method, linear calibration graphs are obtainable for the potentiometric determination of sulfate. The precision and sensitivity of the proposed method are improved compared with the potentiometric methods reported by Coetzee and by Pungor[14-16] as the calibration graphs used by them were obtained by a series of tedious procedures and deviations occurred at a low SO_4^{2-} concentration range. In this experiment, a parameter such as K_{sp} is eliminated during the process of equation derivation; the error possibly inherent with the determination of K_{sp} is thus eliminated. The other superior point of this method isthat whenever interferences are present in the determination system, a curvature of the linear calibration graph will be found. This warning curvature will assure the reliability of the determined results. With the proposed flow injection method, as the solid lead sulfate inside the column dissolves gradually as the sample or carrier solution flows through the column continuously, the degree of partial equilibrium between the sulfate ions in the sample solution and the lead sulfate in the column may change gradually and thus induce errors. This type of error can be minimized by using a column of larger capacity or by decreasing the volume of sample solutions flowing through the lead sulfate column. Due to the passivation of the lead ion electrode, the sensitivity of a Pb ISE may be lowered and thus the slope of the linear plots may by varied, but the linearity of the plots will not be affected as long as the experiment is run for the same continuous period of time. The same procedures should be applicable to the other indirect potentiometric determination systems that are based on precipitation or complex formation processes, e.g., the determination of nitrate,[18] perchlorate,[19] and various phosphates.[14,20]

ACKNOWLEDGMENT

The authors thank the National Science Council of R.O.C. for financial support.

Received for review November 28, 1994. Accepted March 21, 1995.[⊗]

AC941155Q

[⊗] Abstract published in *Advance ACS Abstracts,* May 15, 1995.

(18) Kumamaru, T., Tao, E., Okamoto, N.,; Yamamoto, Y. *Bull. Chem. Soc. Jpn.* **1966**, *38*, 2204.

(19) Collinson, W. J., Boltz, D. F. *Anal Chem.* **1968**, *40*, 1896.

(20) Hara, H.; Kuzu, S. *Anal. Chim. Acta* **1992**, *26*, 411.

Anal. Chem. **1995,** *67,* 2304–2307

UV-Polymerizable Screen-Printed Enzyme Pastes

Ingrid Rohm,* Wolfgang Künnecke, and Ursula Bilitewski

Department of Enzymology, GBF-Gesellschaft für Biotechnologische Forschung mbH, Mascheroder Weg 1, 38124 Braunschweig, Germany

A new technique for immobilization of enzymes on amperometric thick-film electrodes was developed with the aim to generate stable enzyme layers suitable for use as the analyte-specific part of biosensors with sufficient mechanical stability to withstand the continuous use in wall-jet cells of flow injection analysis (FIA) systems. To demonstrate the successful production of defined enzyme layers, the oxidoreductase glucose oxidase (GOx) was used as a model protein for immobilization. The enzyme was mixed with a UV-polymerizable screen-printable paste, and the influence of various additives on viscosity and sensor sensitivity was tested. The enzyme layer was formed by screen printing of this mixture and UV polymerization for 3–5 s. Scanning electron microscopy visualized the surface properties of different enzyme layers. Amperometric measurements were performed in a FIA device with respect to operational stability, sensitivity, linear range, influence of pH, and influence of ascorbic acid used as a model for an interfering compound. These parameters were compared to those obtained with sensors based on glutardialdehyde cross-linked GOx. The sensors showed an improved stability but a reduced sensitivity compared to those with glutardialdehyde immobilization. Within a series of 10 measurements, the standard deviation was <1%, and between sensors produced in one batch it was <10%.

In recent years, thick-film technology has developed into a suitable tool for mass production of electrochemical sensors for measurements in gaseous[1,2] or aqueous media.[3] Due to a widespread establishment of screen-printing processes in the microelectronics industry, devices and various basic materials are commercially available that allow automated production of electrochemical transducers.[4] These sensors have been used for the quantification of clinical and biotechnological parameters as well as different analytes in food. The required specificity was achieved by immobilizing biological compounds such as whole cells or isolated enzymes.[5–7] The majority of applications, to date, are in the field of batch analysis using so-called "one-shot" biosensors. Their operational stability is of minor importance, whereas for process analysis, sensors with improved operational lifetime are of utmost importance.

In general, there are mainly three ways to immobilize enzymes onto an electrode surface:

(i) Adsorption onto a graphite surface.[8] These sensors showed rapidly decreasing signals caused by the washing out of the enzyme with continuous use.

(ii) Covalent binding of enzymes to the activated surface of the electrode by bifunctional reagents such as glutardialdehyde.[9]

(iii) Entrapment in a matrix. Enzymes were fixed within gels or polymers, such as poly(vinyl alcohol),[10] carbon paste,[11,12] gelatin, polyurethanes, or polypyrrole.[13] With drying and polymerization, these materials form an enzyme layer with a specific diffusion resistance depending on the content of polymers within the film.

Up to now, automated immobilization of enzymes onto the surface of thick-film electrodes has been achieved by ink jet printing[14] and screen printing[12,15,16] of carbon-containing inks or pastes. The latter is a particularly favorable application for the generation of amperometric enzyme electrodes because only one technique is required for the production of complete sensors. Moreover, the industrial application of this technology for the production of glucose sensors for blood analysis by companies such as Medisense Inc. (Cambridge, MA) demonstrates the high relevance of this immobilization technique. However, these sensors were developed for one-shot measurements, thus their application in process monitors and flow injection systems is impossible due to decomposition of the active layer within the liquid flow.

UV photopolymerization, another principle for immobilization of cells or enzymes within a suitable matrix, was applied successfully to the production of biosensors.[17,18]

It was the aim of this work to combine the mass production capacities of screen printing with the formation of durable enzyme layers by UV polymerizable materials.

EXPERIMENTAL SECTION

Thick-film electrodes were printed on conventional Al_2O_3 ceramics using commercially available metal and insulating pastes as described elsewhere.[19]

(1) Ikegami, A.; Arima, H.; Iwanaga, S.; Kaneyasu, M. *Proceedings of the 4th European Hybrid Microelectronics Conference,* Copenhagen, May 18–20, 1983; International Society for Hybrid Microelectronics: 1983.
(2) Chu, W. F.; Fischer, D.; Erdmann, H.; Ilgenstein, M.; Köppen, H.; Leonhard, V. *Solid State Ionics* **1992**, *53–56*, 80–84.
(3) Wang, J.; Tian, B. *Anal. Chim. Acta* **1993**, *274*, 1–6.
(4) Alvarez-Icaza, M.; Bilitewski, U. *Anal. Chem.* **1993**, *65*, 525A–533A.
(5) Karube, I. *Methods Enzymol.* **1988**, *137*, 131–138.
(6) Scholze, J.; Hampp, N.; Bräuchle, C. *Sens. Actuators* **1991**, *B4*, 211–215.
(7) Schmidt, A.; Rohm, I.; Rüger, P.; Weise, W.; Bilitewski, U. *Fresenius J. Anal. Chem.* **1994**, *349*, 607–612.
(8) Palleschi, G.; Rathore, H. S. *Anal. Chim. Acta* **1988**, *209*, 223.
(9) Husain, Q.; Saleemuddin, M. *Enzyme Microb. Technol.* **1986**, *8*, 686–690.
(10) Mascini, M.; Mateescu, M. A.; Pilloton, R. *Bioelectrochem. Bioeng.* **1986**, *16*, 149–157.
(11) Wang, J.; Wu, L.-H.; Lu, Z.; Li, R.; Sanchez, J. *Anal. Chim. Acta* **1990**, *228*, 251–257.
(12) Bilitewski, U.; Chemnitius, G. C.; Rüger, P.; Schmid, R. D. *Sens. Actuators* **1992**, *B7*, 351–355.
(13) Foulds, N. C.; Lowe, C. R. *J. Chem. Soc. Faraday Trans.* **1986**, *82*, 1259–1264.
(14) Newman, J. D.; Turner, A. P. F.; Marrazza, G. *Anal. Chim. Acta* **1992**, *262*, 13–17.
(15) Cardosi, M. F.; Birch, S. W. *Anal. Chim. Acta* **1993**, *276*, 69–74.
(16) Marcinkeviciene, J.; Kulys, J. *Biosens. Bioelectron.* **1993**, *8*, 209–212.
(17) Heineman, W. R. *Appl. Biochem. Biotechnol.* **1993**, *41*, 87.
(18) Marty, J.-L.; Mionetto, N.; Rouillon, R. *Anal. Lett.* **1992**, *25*, 1389–1398.

0003-2700/95/0367-2304$9.00/0 © 1995 American Chemical Society

Immobilization. (i) UV Enzyme Paste. A mixture of water-soluble UV-polymerizable matrix with different amounts of porous SiO_2 material (diameter, 4 μm; Syloid ED 40, Grace, Bad Homburg, Germany), graphite (fine powder, pure quality; Merck, Darmstadt, Germany), and glucose oxidase (GOx) (EC 1.1.3.4., 200 units/mg; Boehringer Mannheim, Mannheim, Germany) solution (30 mg/mL) in 0.1 M potassium phosphate buffer (pH 7.5) was screen-printed to a thickness of 50–100 μm onto the surfaces of the platinum working electrodes. The polymerization was done by UV irradiation with a mercury vapor lamp (100 W; Osram, Hannover, Germany) for 3–5 s at a distance of 10–15 cm. The UV enzyme electrodes were stored under dry conditions at 4 °C.

Using rotating disk viscosimetry (Rotovisco RV 20, Haake, Karlsruhe, Germany), the viscous behavior of the nonpolymerized pastes during increasing and following decreasing rotation velocity was measured. A UV-polymerizable screen printing ink was used as a reference (UVLM-N1, Marabu, Thamm, Germany).

(ii) Cross-Linking with Glutardialdehyde. The electrodes were silanized by immersion in 10% (3-aminopropyl)triethoxysilane (APTES) (Sigma, Deisenhofen, Germany) solution in 0.1 M potassium phosphate buffer (pH 7.5) for 15 min. After being washed with distilled water and dried in air, 100 μL of GOx solution (1 mg/mL) containing bovine serum albumin (BSA, 30 mg/mL; Sigma) in 0.1 M potassium phosphate buffer (pH 7.5) was mixed with 16 μL of a 2.5% glutardialdehyde (GA, for microscopy; Merck) solution in 0.1 M potassium phosphate buffer (pH 7.5), and 2 μL of this mixture was pipetted onto the working electrode surface. After being left to dry for 30 min at room temperature, the sensors were stored in 0.1 M potassium phosphate buffer at 4 °C.

(iii) FIA Manifold. The flow injection analysis (FIA) system used consisted of two peristaltic pumps (Meredos, Nörten Hardenberg, Germany), one injection valve (V 100, Perstorp, Rodgau, Germany), and a wall-jet cell with a volume of ~50 μL (GBF, Braunschweig, Germany), in which the thick-film sensor was integrated. The amperometric measurements were done by using a potentiostat (VA 641, Metrohm, Herisau, Switzerland) and applying a constant potential of +600 mV in a three-electrode configuration. A hypodermic needle was inserted as an inlet to the flow-through device and used simultaneously as the counter electrode. The tubing was made of PTFE (Omnifit, Cambridge, England) and had an inner diameter of 0.5 mm, and the carrier buffer (see below) was pumped at 0.75 mL/min. A sample volume of 30 μL was injected. The program FIA-FOX 2.0[20] (GBF) controlled the FIA system via PC and enabled the recording and processing of data by calculating standard curves and resulting sample concentrations.

The following were utilized as carrier buffers to determine the pH optimum of the sensors: 0.1 M potassium phosphate buffers from pH 6 to 8; 0.05 M Hepes [4-(2-hydroxyethyl)-1-piperazineethanesulfonic acid]–NaOH buffers of pH 7 and 8, and Clark & Lubs solutions (0.05 M with respect to both KCl and H_3BO_3 and an appropriate amount of NaOH) from pH 7.5 to 9. All chemicals of analytical grade were obtained from Merck.

(19) Günther, A.; Bilitewski, U. *Anal. Chim. Acta* **1995**, *300*, 117–125.
(20) Stiene, M.; Bilitewski, U. *Proceedings of the 7th European Congress on Biotechnology*, Abstracts Book; Nice, France, Feb 19-23, 1995; Societé frauçaise de Microbiologie: Paris, 1995; Vol. 3, MEP 174.

RESULTS AND DISCUSSION

Modification of Viscosity. Rotating disk viscosimetry was used to investigate the properties of the UV paste (UVP) viscosity by supplementation with different amounts of solid particles (0–30% w/w). As expected, SiO_2 and graphite particles increased the viscosity of the paste. By adding aqueous enzyme solutions, the viscosity could be decreased. A mixture of the basis paste material with solid particles (15% SiO_2 w/w) and the enzyme solution (10% v/w) possessed a viscous behavior comparable to that which was measured for a commercially available screen-printable paste.

Visual Appearance of the Electrode Surface. Enlargement of printed and polymerized enzyme layers by scanning electron microscopy showed the topography of the working electrodes. The UVP without additional solid compounds showed a relatively dense constitution, presenting a regular pattern caused by the events during the photopolymerization (Figure 1a). A more porous enzyme layer was obtained upon the addition of SiO_2 particles (Figure 1b). This membrane surface showed pores of 5–10 μm diameter spread regularly over the whole printed area, ~100 μm apart. A GOx–BSA layer cross-linked with glutardialdehyde (Figure 1c) showed more similarities to the SiO_2-containing enzyme layer. Graphite as a UVP supplement yielded an image comparable to that obtained upon SiO_2 (syloid) addition to the paste.

Sensitivity to H_2O_2. Amperometric detections of 1 mM H_2O_2 indicated the influence of graphite and syloid addition to the UVP on the sensitivity of the sensor. Decreased signals of 26 nA were obtained in the presence of graphite (25%). The addition of syloids with the graphite improved sensitivity (64 nA; 15% graphite, 10% syloids), but the signals were smaller than those obtained for a paste containing only syloids (20%) and no graphite (3450 nA). Probably, diffusion of H_2O_2 to the electrode is hindered by the UVP, which is improved by the syloids, whereas the graphite does not form an electrical conducting layer.

Due to these results, graphite was not used as an enzyme paste ingredient in subsequent experiments.

Amperometric Detection of Glucose by Screen-Printed Enzyme Electrodes. The addition of GOx (10% enzyme solution v/w) to the UVP enabled the quantitative analysis of glucose standards. Corresponding to the measurements of peroxide described above, the signal intensity was improved by increasing the amount of porous SiO_2 material within the UVP from 8.2 to 123 nA. Unfortunately, it was not possible to add more than 20% SiO_2 (w/w) to the paste due to the weak adhesion of the enzyme layer to the platinum surface, which led to the removal of the membrane by the carrier stream in the FIA device. The linear range from 0 to 10 mM glucose (Figure 2) of this kind of detection system was comparable with that obtained by using GOx–BSA–GA thick-film electrodes in previous work.

Figure 3 presents the results of a long-term stability test executed with both UVP–GOx and GOx–BSA–GA thick-film electrodes. In contrast to the latter, which showed a reduction of response to below 50% within the first 12 h, the signal intensity of the UVP–GOx electrode was relatively stable over the whole testing period. In comparison to stability explorations using a glutardialdehyde-based sensor, the absence of temperature control led to increased sensitivity to changes in room temperature when the UV sensor was tested. After a short disconnection of the power supply (after 42 h), the signals increased significantly up

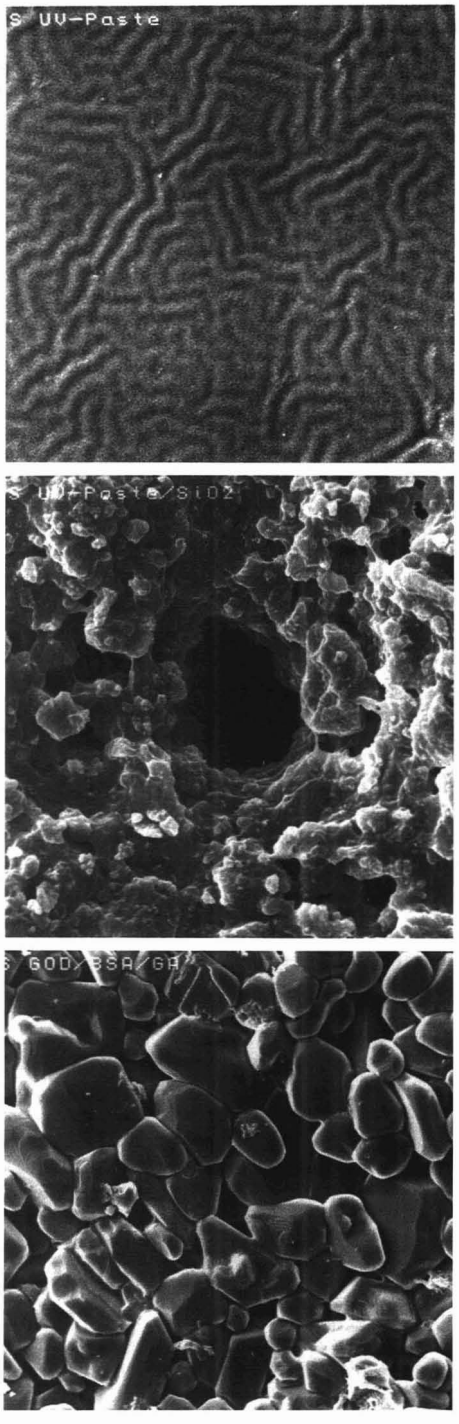

Figure 1. Surface of the enzyme electrode, enlarged (3000×) by scanning electron microscopy. (a, top) UVP containing 10% enzyme solution (v/w). (b, middle) UVP enriched with 10% enzyme solution (v/w) and 15% SiO_2 particles (w/w). (c, bottom) GOx–GA immobilization. The original photographs have been reduced 85% for publication.

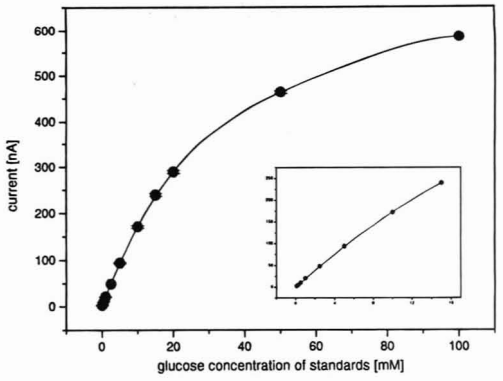

Figure 2. Glucose standard curve obtained by amperometric detection utilizing UV-polymerized screen-printed enzyme layers (10% SiO_2 w/w) at the surface of platinum working electrodes.

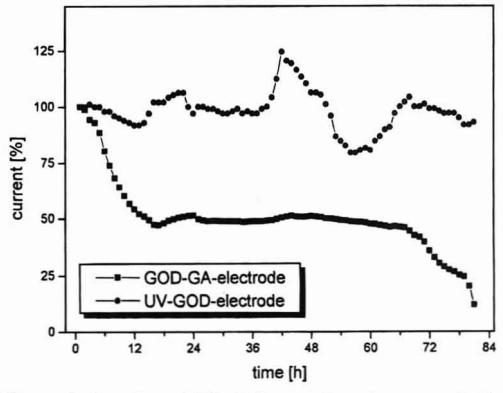

Figure 3. Long-term stability test comparing values generated by a UVP–GOx electrode (●) (10% syloids w/w) and an amperometric sensor pretreated by covalent immobilization (■).

to 125% but decreased within the next 6 h to the normal level. After 80 h, with more than 2880 detections done by each sensor, the GOx–BSA–GA sensor retained <10 % of its residual activity, whereas the UVP–GOx electrode produced signals >95% of the original size. A possible explanation for this effect could be the immobilization technique itself, supported by the amount of enzyme immobilized on each electrode, which was approximately 3–6 times higher in the enzyme paste than in the GOx–BSA–GA membrane. The standard deviation for both sensors was <1% in a series of 10 measurements during this experiment.

No significant difference in pH dependence between both types of sensors could be detected, as Figure 4 demonstrates. The best detection range was between pH 8 and 9, with maximum values at pH 8.5 based on the maximum of the hydrogen peroxide oxidation in basic pH medium, whereas the optimum of the homogeneous enzyme reaction is in the range of neutral pH. Only a small tendency to an increased tolerance with respect to relatively high or low pH values was measurable in the case of UV electrodes. The utilization of Hepes as carrier buffer (data not shown) as compared to potassium phosphate and Clark & Lubs buffers indicated that the pH value had a much higher effect than the buffer composition.

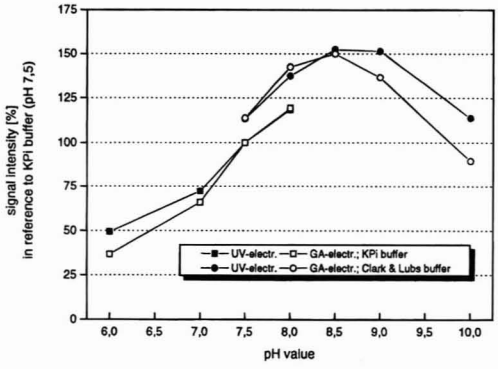

Figure 4. pH optima of amperometric glucose measurements by UVP–GOx (closed symbols) (10% syloids w/w) and GOx–GA electrodes (open symbols).

Table 1. Comparison of Data Obtained by Measurements Using Different Types of Thick-Film Electrodes Based on the Transducer Described[19]

	type of electrode[a]		
sample injected	blank[b]	GA–GOx[c]	UVP–GOx[d]
1 mM H_2O_2	10	5.419	4.025
1 mM ascorbic acid	9.992	2.588	2.086
10 mM glucose	0.070	7.084	0.9096

[a] Responses are in units of μA. [b] Standard deviation between different electrodes, 2–5%. [c] Standard deviation between different electrodes, 25%. [d] Standard deviation between different electrodes, 10%.

A comparison of characteristic parameters obtained with different types of electrodes is presented in Table 1. The data produced by the injection of peroxide decreased in the cases of both enzyme-modified electrodes to 50%. Possible interfering effects caused by direct oxidation of substances occurring in real samples were tested with ascorbic acid as a model, which is present in different matrices, e.g., blood and fruit juices. Compared to results obtained with a blank thick-film electrode, the GOx–BSA–GA membrane reduced the unspecific signals by 74%, whereas the UVP membrane eliminated ~80% of the unspecific signals. The specific sensitivity to glucose was different for both immobilization methods: the GOx–BSA–GA electrode produced signals higher than 7 μA/10 mM glucose, whereas the sensitivity of the UVP electrode reached only 13% of this value. However, recent investigations demonstrated that the sensitivity could be further improved by optimizing type and quantity of paste ingredients.

CONCLUSION

Compared to time-consuming immobilization procedures done manually on the surfaces of conventional platinum electrodes like wires or rods by covalent binding or adsorption described previously, the complete immobilization procedure described herein consisted only of the mixing of an enzyme paste, the screen printing process, and the subsequent polymerization by UV irradiation. Each step takes only a few moments and can be performed automatically. Moreover, the aim of our work was to develop an enzyme electrode which not only could be produced in at least medium scale but which also shows a high mechanical stability and a high stability when in permanent use. This was also achieved by this immobilization procedure, and therefore, we could extend the applicability of enzyme electrodes, fabricated totally by screen printing, to use as detectors in automated instruments.

Other enzymes will be tested as catalytic materials fixed by UV polymerization to expand the applications of this new immobilization technique.

ACKNOWLEDGMENT

The authors would like to thank Dr. Manfred Rohde (Department of Microbiology, GBF, Braunschweig, Germany) for performing the scanning electron microscopy, Dr. Wolfgang Schäfer (Marabu, Thamm, Germany) for demonstrating the production of UV-polymerizable screen printing inks, and the Bundesministerium für Forschung und Technologie for their financial support through Trace (Braunschweig, Germany, BEO-0317351A).

Received for review November 15, 1994. Accepted March 17, 1995.[⊗]

AC941115M

[⊗] Abstract published in *Advance ACS Abstracts,* May 15, 1995.

Anal. Chem. **1995,** *67,* 2308–2313

UV Photometer Based on Radioluminescence with Applications in HPLC and Process Control

Günter Rinke* and Christian Hartig

Forschungszentrum Karlsruhe, Postfach 3640, D-76021 Karlsruhe, Germany

A new UV photometer based on radioluminescence was developed. The light source consists of a luminous crystal which is irradiated by a radioactive element. This UV source has a lifetime of more than 10 years. A special absorption cell with high light throughput together with a fiber rod was used. Although radioluminescence has a rather weak intensity, it was possible to use an inexpensive and robust silicon photodiode. This photometer is especially suited for process control applications, explosive environments, and HPLC because there are no movable parts and because of its good stability. The minimum detectable absorbance, limited by noise, amounts to 1.2×10^{-5} AU, and the peak form of our special HPLC cell is comparable with or better than those obtained with conventional HPLC cells.

The aim of this work was to develop a new UV photometer with a UV light source having a lifetime of several years. Such instruments are used, for example, as pure photometers or UV detectors in high-performance liquid-chromatography (HPLC). Because of the long lifetime of the radiation source, the instrument described in this paper is especially suited for process control applications.

Common UV photometers always use deuterium, mercury, or high-pressure xenon lamps as UV radiation sources, which have two major disadvantages. First, the lifetime of these lamps varies between 3 months (D_2 and Xe lamp) and 1 year (Hg lamp). This is too short for process control applications, where the lamp is running all day long. Furthermore, all these lamps show a limited short- and long-time stability, which requires two-beam optics for compensation.

Even if the lamp with the longest lifetime is used (Hg), the application fields are small because only one emission line (254 nm) has a high intensity. Phosphor-coated Hg lamps are not an alternative, firstly because the emission wavelength is longer than 270 nm and secondly because the degradation is by far stronger compared with that of pure Hg lamps.

These disadvantages can be avoided if the radioluminescence of special crystals is used: a closed radioactive element emits electrons, which are absorbed in a crystal, creating electron–hole pairs. This recombination leads to a luminescence in the ultraviolet spectral region. The lifetime of this "light source" is determined by the radioactive decay time and can amount to some years or more.

The process of radioluminescence is not new. It was used, for example, in the first part of this century in watches containing phosphors and radioactive elements. Furthermore, all glass dosimeters are based on this principle. Some similarity also exists in television systems containing a phosphor-coated tube, which in this case is activated by an electron gun.

The first realization of radioluminescence in analytical instruments was done by K. Jones and D. J. Malcome-Lawes.[1-3] Because of the low UV luminescence intensity, they had to employ a photomultiplier tube as optical detector.

By using a completely different optical design, we were able to get a robust analytical instrument for process control without using a fragile photomultiplier tube and with good stability. This is very important here, because this detector should be used as part of a process HPLC system.[4]

BACKGROUND

Radiation Source and Luminescent Crystals. The radiation source should ideally emit only electrons but no γ-rays to simplify the radiation shielding. In order to get a high UV intensity, the activity must be as high as possible, and the electron energy spectrum should have a lot of high-energy particles. On the other hand, the maximum electron energy should be below a few megaelectronvolts in order to keep the bremsstrahlung low. The decay-time should be between 5 and 30 years to get a long lifetime and a high specific activity. Last, but not least, the possible nuclides should have a low price and should be easily available. These conditions can be fulfilled by only a few elements, for example, nickel-63, tritium, and strontium-90. Because nickel-63 and tritium have low β-energies, we decided to use strontium-90, which has a high β-energy, no γ-rays, and a satisfactorily long decay time.[5]

The specifications for good luminescent crystals are (a) high UV intensity by electron activation, (b) low UV absorption, and (c) long-term stability. The geometry of the crystal is, in general, less important. However, for crystals that show some UV absorption, there exists an optimum thickness, because total absorption of the electrons requires a large thickness, whereas UV absorption requires a low thickness in order to get a good optical transmission.

Optical Design. The design of the flow cell is the most important part of this new photometer for applications in HPLC. Usually, a HPLC cell has an optical length of 10 mm and an inner diameter of 1 mm, so that the cell volume amounts to 10 μL. In HPLC, the volume of the cell has to be low in order to get sharp peaks. The disadvantage of such a HPLC cell lies in its flow

(1) Jones, K.; Malcolme-Lawes, D. J. *J. Chromatogr.* **1985,** *329,* 25–32.
(2) Jones, K.; Malcolme-Lawes, D. J. *J. Chem. Soc., Faraday Trans. 2* **1986,** *82,* 665–677.
(3) Jones, K.; Malcolme-Lawes, D. J. *J. Chromatogr.* **1988,** *441,* 387–393.
(4) Steinmüller, D. *Instrumentalized Analytical Chemistry and Computer Technology (InCom)*; GIT-Verlag: Darmstadt, 1990; pp 214–224.
(5) Horen, D. J.; Ewbank, W. B. *Nuclear Level Schemes A = 45 through A = 257 from Nuclear Data Sheets*; Academic Press: New York, 1973.

0003-2700/95/0367-2308$9.00/0 © 1995 American Chemical Society

sensitivity by refractive index changes[6,7] and its low light transmission because of its low solid angle to accept light. A simple consideration shows a possible way to improve such a cell to get a better throughput. The well-known Lambert–Beer law may be written in the form

$$c_{min} = A_{min}/(ab)$$

where a is the absorptivity, c_{min} the minimum detectable concentration (limit of detection), b the optical length of the cell, and A_{min} the minimum detectable absorbance. In order to get a low limit of detection (c_{min}), the length b should be as large as possible, if A_{min} is assumed to be independent of b. This is the usual way to design absorption cells.

On the other hand, the limit of detection is also determined by the noise, which determines A_{min}. If this noise is limited by photon shot noise,[8] which may be reached by good UV detectors,[9,10] A_{min} is inversely proportional to the square root of the photon flux on the detector; the electrical signal current, I, of the photodiode is proportional to the photon flux S, and the noise, δI, of this current is proportional to the square root of the flux S. This means that the signal-to-noise ratio is proportional to the square root of the flux S. Because the absorbance, A, is defined as the logarithm of the transmittance T ($A = -\log T$), any variation in T, and therefore in I, leads to a minimum detectable absorbance,

$$A_{min} = 0.43\delta I/I = kS^{-1/2}$$

where k is a proportionality constant. The light flux S on the detector is proportional to the solid angle Ω ($S = m\Omega$; m = constant) the cell can transmit. In the simplest optical arrangement without any lenses,

$$\Omega \approx A/b^2 = V/b^3$$

where A is the cross section of the HPLC cell, which is assumed here to be smaller than the constant area of the detector, and V is its volume. For the following approximation, it is important that the cell volume is assumed to be constant (typically 10 μL) in order to get small peaks in HPLC, but A may be varied to get an optimum light throughput. Returning now to the equation for the limit of detection and expressing S by Ω, c_{min} becomes

$$c_{min} = (ab)^{-1}k(mVb^{-3})^{-1/2} = db^{1/2}, \quad d = \text{constant}$$

This simple estimation shows two important things: the limit of detection is proportional to b^{-1}, as usual, and it is proportional to $b^{+3/2}$ because of the length-dependent minimum detectable absorbance. Therefore, the limit of detection c_{min} decreases with $b^{1/2}$.

(6) White, P. C. *Analyst* **1984**, *109*, 677–697.
(7) Stevenson, R. L. *Liquid Chromatography Detectors*; Marcel Dekker: New York, 1983.
(8) Grum, F.; Becherer, R. J. *Optical Radiation Measurements, Vol. 1*; Academic Press: New York, 1979
(9) Wiese, A.; Teitz, K.; Brombacher, V.; Höschele, G.; Kuderer, H. *Hewlett-Packard J.* **1990**, *April*, 36–43.
(10) Yeung, E. S. *Detectors for Liquid Chromatography*; John Wiley & Sons: New York, 1986; Chapter 2.

Table 1. Luminescent Properties of Some Crystals

crystal	intensity	wavelength region (nm)
CaF_2	high (35 nA)	230–330
SrF_2	high (35 nA)	240–340
Al_2O_3	high (20 nA)	370–450
BaF_2	high (15 nA)	210–350
$MgAl_2O_4$	high (12 nA)	220–270
$CaWO_4$	medium (8 nA)	350–450
$CdWO_4$	medium (8 nA)	350–450
$LiYF_4$	medium (4 nA)	300–450
$ZnWO_4$	medium (4 nA)	350–450
diamond	medium (3 nA)	350–450
LiF_2	low (1 nA)	200–350
MgF_2	low (1 nA)	200–300
SiO_2	low (1 nA)	200–300
BaB_2O_4	no emission	200–450
$CaCO_3$	no emission	200–450
KBr	no emission	200–450
KCl	no emission	200–450
MgO	no emission	200–450
NaCl	no emission	200–450
ZrO_2	no emission	200–450

Of course, this is a very crude calculation with many approximations, but it shows the way to design a cell which is better suited for low-level applications: the optical length b of this cell should be short and the diameter large. However, the length b has to be larger than a minimum value, which depends of other noise terms, such as electronic noise. This length-independent noise leads to an optimum cell length, which can only be calculated by a better theory, but this goes beyond the scope of this work.

Besides electronic noise and photon shot noise, in photometers further noise arises from fluctuations of lamp intensity[10,11] and small changes of the refractive index in the cell.[6,7] However, these noise sources do not cause a disturbance in the case described herein, because this light source is quite stable due to the radioactive decay. Furthermore, our cell is insensitive to changes in flow speed and has only to be thermostated in order to eliminate noise caused by remaining refractive index changes. However, these temperature effects are considerably lower than those in conventional photometers using hot discharge lamps.

EXPERIMENTAL SECTION

Samples. In order to build a UV lamp based on luminescence with a high intensity and a large spectral emission bandwidth, we examined a lot of crystals, as shown in Table 1. In many cases, we bought crystals of the same type by different manufacturers, because we expected differences depending on impurities.

Absorption and Emission Measurement Setup. We measured the absorption spectra with a commercial dual-beam spectrophotometer (Perkin Elmer, Lambda 9). Because some crystals had a small diameter (diamond (C), for example, was only 4 mm), both measurement beam and reference beam included the same optical aperture. Before a measurement was started, a background correction with both stops was done. In addition to these measurements, all crystals were irradiated for 24 h with the strontium-90 source. Immediately after this excitation, the absorption spectrum was recorded again.

In order to measure the luminescence spectra of our crystals, we used a modified HPLC detector (Shimadzu SPD6A). This

(11) Christian, G. D.; Callis, J. B. *Trace Analysis*; John Wiley & Sons: New York, 1986.

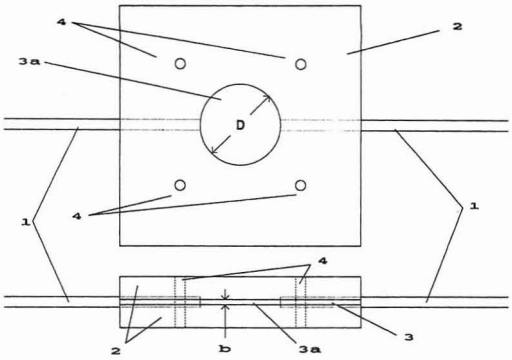

Figure 1. Design of the HPLC cell, top and side view. 1, Inlet and outlet; 2, quartz plates 20 mm × 20 mm; 3, quartz spacer with opening 3a; 4, drillings; b, optical path length; *D*, optical diameter of the cell.

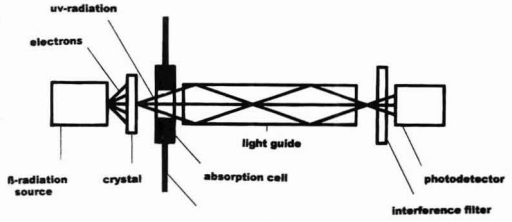

Figure 2. Optical layout of the UV photometer.

instrument is a variable wavelength spectrometer consisting of an entrance slit, a concave collimating mirror, and a diffraction grating. Its absorption cell was replaced by an extra exit slit, the photodiode by a photomultiplier tube (Hamamatsu R 1527), and the original deuterium lamp by a combination of a strontium-90 point source (SIF 33, Amersham, 370 MBq = 10 mCi) and changeable crystals.

The output signal of the first amplifier of this instrument was connected to an external analog–digital converter, which was situated in a personal computer. This PC also created some digital signals to control the wavelength scanning via the back-side interface. The instrument spectral response was measured with the help of a deuterium lamp and a calibrated high-pressure mercury lamp, and all luminescent spectra were corrected for this response. The measured wavelength region was 200–450 nm.

Chromatographic Equipment. We used naphthalene in methanol as a test substance, injected by a Rheodyne injection valve (7520) and a 0.5 μL loop. The HPLC pump (Gynkotek 300 C) was used with a flow rate of 0.8 mL/min at a pressure of 48 bar. The column was a 5 μm C_{18} type, and the eluent was a methanol–water mixture (9:1).

Construction of the Prototype. The strontium-90 source was bought from Amersham (SIF 1177). It has an activity of 3.7 GBq (100 mCi) and an active diameter of 5 mm. This source is completely closed and allows temperatures up to 1000 K. Other experiments were done with a 1 Ci tritium source, but the results were worse compared with those with strontium-90. The reason is the low β-energy of tritium, which could not be compensated by its much higher activity.

The final design of our flow cell is shown in Figure 1. It consists of two fused quartz plates, each 2 mm thick and with a 20 mm base length, melted together with a special opaque quartz

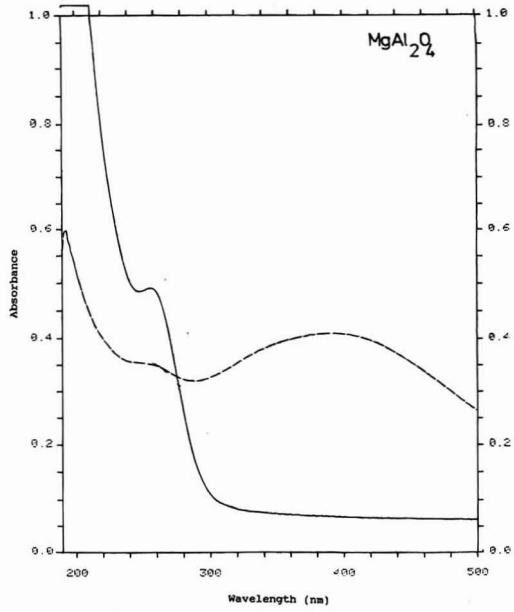

Figure 3. Absorption spectra of spinel 1 with (broken line) and without (solid line) preceding electron excitation.

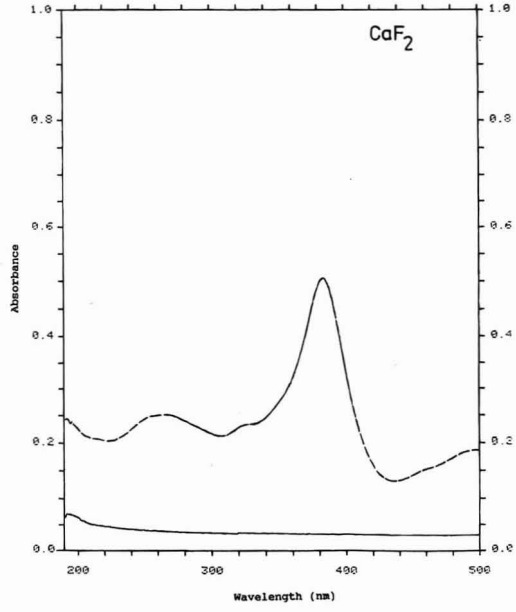

Figure 4. Absorption spectra of calcium fluoride with (broken line) and without (solid line) electron excitation.

plate used as a spacer. This spacer determines the optical path length *b* by its thickmess. We tested different cells with nearly the same internal volume of 10 μL but with spacers varying between 0.2 and 2 mm thickness, corresponding to an optical diameter between 8 and 2.5 mm. The in- and outlets are small stainless steel tubes. This design not only gives a high optical throughput, but it also has no dead volume and the liquid flows

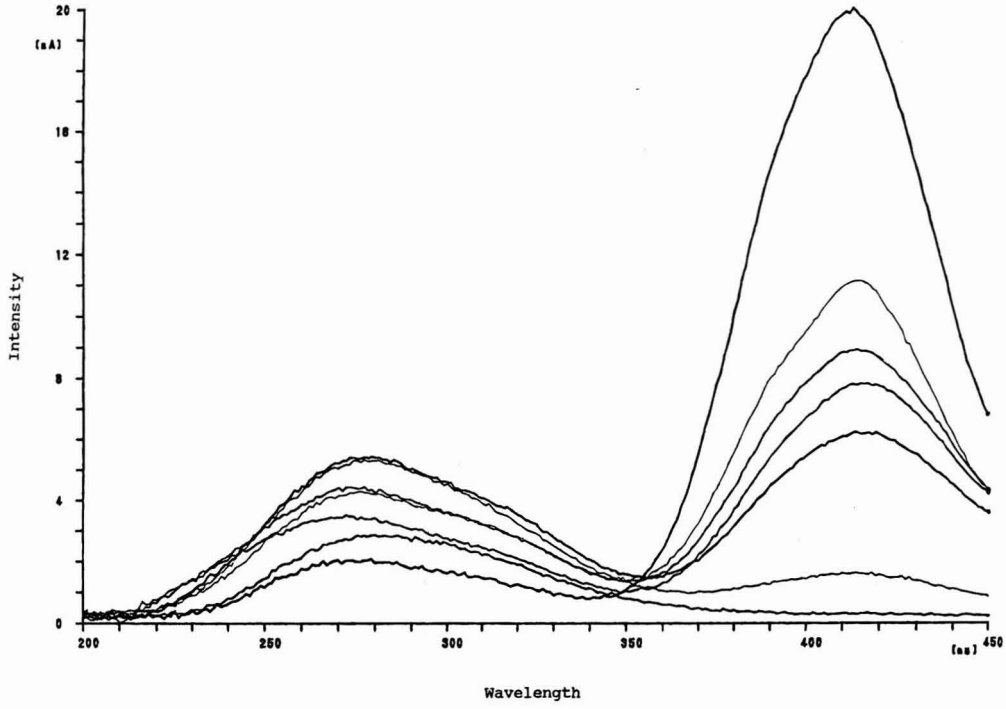

Figure 5. Luminescence spectra of seven different sapphires.

rectangular to the optical axis. As we will show later, this will give excellent peak forms because of the optimized flow profile.

During our investigations we noticed an increased noise when we reduced the distance between the β-source and the detector, dependent on the type of detector. As a result, the final solution utilized a fiber-optic rod of 8 mm diameter to guide the light and to increase the distance.

Figure 2 shows the complete design. All optical elements are arranged as close together as possible. In the middle part, where the light guide is located, a metal plate serves to divide regions which are located in an explosive environment from nonexplosive regions. This often is necessary in process control.

As photodetector, we used a silicon photodiode with an active area of 100 mm^2. The signal current of this photodiode is large compared to the cathode current of the photomultiplier tube used by Malcolme-Lawes and Jones.[1] However, it is still small compared to typical signal currents of UV photometers using an electric discharge lamp. Therefore, the preamplifier has to be able to handle currents in the picoampere range without drift and noise. We used two different circuits. One was the first part of a Shimadzu SPD6A HPLC detector, which utilizes the OPA 111BM integrated circuit from Burr Brown. The other version was a modified FID amplifier from a Siemens gas chromatograph. Both circuits work as current-to-voltage converters with a typical feedback resistor of 10 GΩ and a parallel capacitance of 15 pF to reduce the noise.

All optical parts are surrounded by iron and lead to reduce the bremsstrahlung which is created inside the radiation source. The construction also completely eliminates any high-energy electrons. It must be emphasized that this detector may not be used without this shielding.

RESULTS AND DISCUSSION

Absorption Measurements. All crystals have a sufficient UV transmission down to 200 nm except ZrO_2, diamond, $CaWO_4$, $CdWO_4$, and $ZnWO_4$.

Figure 3 shows the absorption spectra of one spinel (spinel 1) with and without excitation with strontium-90. The absorption bands at 260 and 195 nm are produced by impurities, especially by iron ions. Another spinel (spinel 2) shows a similar absorption spectrum, but without the peak at 260 nm and with only a little change after β-excitation. The increased transmission below 280 nm after β-irradiation of spinel 1 can be understood by reduction of Fe^{3+} to Fe^{2+}.[12,13] The low Fe impurity content is essential for a good conversion.

The absorption spectra of seven different sapphires were measured. All show slight differences at the absorption band at 205 nm, which is produced by an F center which varies with the manufacturing process.

All the tested BaF_2 crystals show not significantly different absorption spectra, and these spectra did not change, even with β-irradiation.

Figure 4 shows the absorption spectra of calcium fluoride with and without electron excitation. Two specimens show increased

(12) White, G. S.; Lee, K. H.; Crawford, J. H. *Phys. Stat. Solidi* **1977**, *A42*, K139–K141.

(13) White, G. S.; Jones, R. V.; Crawford, J. H. *J. Appl. Phys.* **1982**, *53*, 265–270.

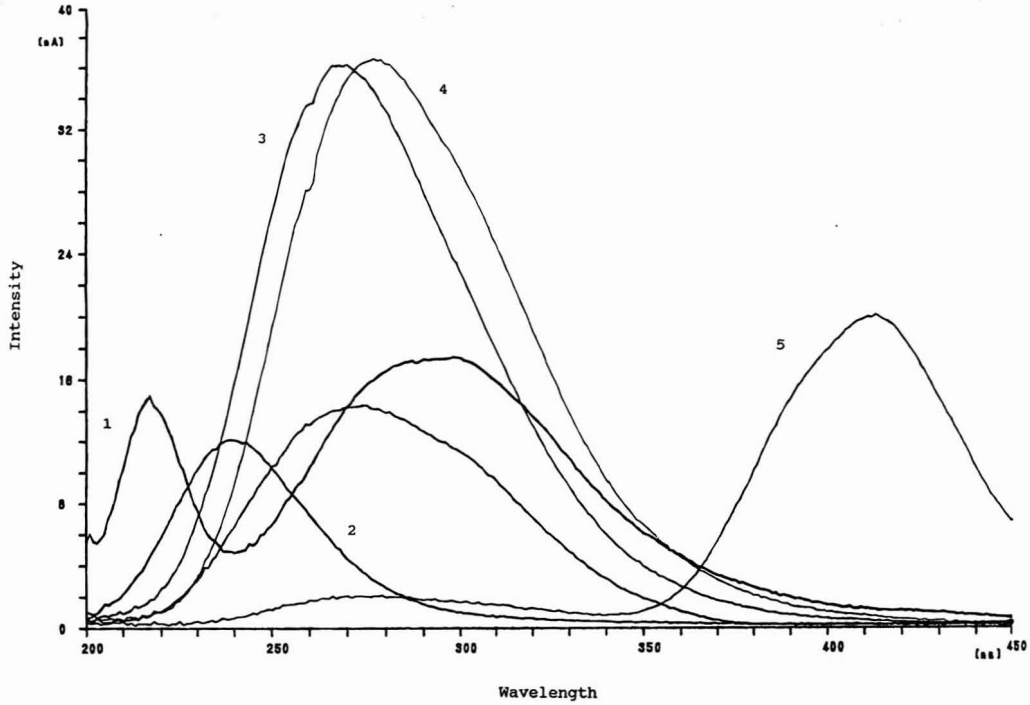

Figure 6. Luminescence spectra of the most interesting crystals: 1, BaF_2; 2, $MgAl_2O_4$; 3, CaF_2; 4, SrF_2; 5, Al_2O_3.

absorption at 200 and 250 nm after β-irradiation, which was also found by other workers[14] and which is not well understood. Furthermore, the α-absorption band at 370 nm is created. In contrast to these types, we also found one which did not change the normal UV absorption spectrum.

Emission Measurements. Figure 5 shows the emission spectra of seven different sapphires. The differences in the luminescent bands at 275 and 410 nm between the various crystals can be explained by different impurity contents, leading to different amounts of quenching and lattice distortion.

Figure 6 show the emission spectra of the most interesting crystals. The luminescent performance of all spinels is different. The chemical analysis of these crystals shows a correlation between luminescent intensity and iron content, which is the dominant impurity. The luminescent spectrum of barium fluoride consists of two bands at 215 and 310 nm. Luminescence at 215 nm is the result of a cross-over transition ($2p\ F^- - 5p\ Ba^{2+}$), and the emission at 310 nm is produced by excitons.[15] The height and form of these spectra are influenced little by the choice of the manufacturer. All tested calcium fluoride crystals show nearly the same luminescent spectrum. However, only one crystal has a good long-term stability; the other crystals degraded within 1 day. This can be explained by the production technique, which leads to different impurity levels.

Other crystals not shown in Figures 5 and 6 show that no or little luminescence or emission takes place in the visible spectral region. Table 1 summarizes all results and gives the photomultiplier anode current in parentheses.

Measurements with the Prototype. To test the long-term stability of the whole instrument, the best crystals of BaF_2, CaF_2, and spinel were irradiated by direct contact with the β-source (3.7 GBq = 100 mCi) between 1500 and 2400 h. BaF_2 showed no degradation, CaF_2 displayed some gray color without influencing luminescence intensity, and spinel developed a brown color after 500 h and gave a higher (!) intensity.

A further investigation should reveal the influence of temperature. Heating of the silicon photodiode alone without the β-source showed an exponential increase of the dark current, in agreement with the physics of photodiodes. However, this effect has a minor influence, because this drift is not the dominating one. The dominating effect comes from the crystal itself, because the luminescent intensity is a strong function of temperature, which is well known, too. This drift leads to a change in absorbance of 2.4×10^{-3} AU/K. Therefore, this UV photometer has to be thermostated. This is not a problem here, because it should work within a process HPLC system, which is already thermostated. The interference filter showed no measurable effect on temperature.

Chromatographic Tests. We investigated linearity, reproducibility, and peak form of this new UV photometer used as HPLC detector. Linearity measurements were done at 215 nm with a 0.5 mm cell for up to 100 ng of naphthalene. The result is a straight line, and the limit of detection (3σ) amounts to 0.9 ng. The reproducibility was measured by repeating an injection 10 times with the same concentration. Figure 7 shows the results.

(14) Heath, D. F.; Sacher, P. A. *Appl. Opt.* **1966**, *5*, 937–943.

(15) Schotanus, P.; van Eijk, C.; Blasse, G.; den Hartog, H. *Phys. Stat. Solidi* **1988**, *B148*, K77–K81.

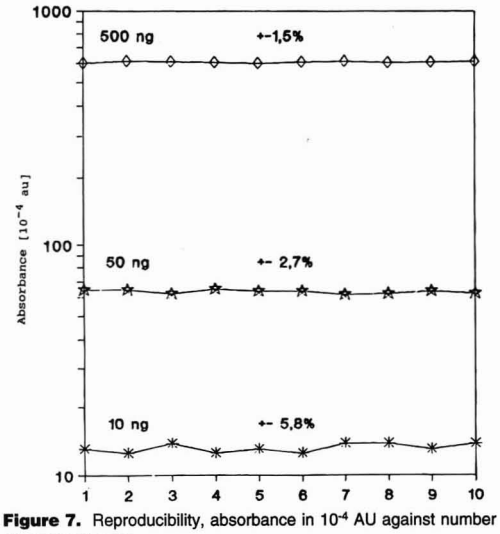

Figure 7. Reproducibility, absorbance in 10^{-4} AU against number of measurements.

Especially important is the measurement of the peak form, because an unconventional cell type was used. Our measurements show that there is no evidence for tailing or fronting up to a cell length of 1 mm.

UV Intensity and Noise. It is very interesting to analyze the signal currents and minimun detectable absorbance of this detector, firstly to compare it with conventional HPLC detectors and secondly for further improvements. This experiment was done under the following conditions: β-source, ^{90}Sr, 3.7 GBq (100 mCi); crystal, CaF_2; filter, 260 nm, fwhm 34 nm, $T = 31\%$; detector, silicon photodiode, 100 mm^2, 0.12 A/W (260 nm); distance, 50 mm (crystal photodiode). Under these conditions, a signal current of 330 pA was measured, and the minimum detectable absorbance amounts to 9×10^{-5} AU at 2 Hz bandwidth. If shot noise as the physical limiting noise were the dominating term, the resulting minimum detectable absorbance would be 4×10^{-5} AU.

Further experiments were done to measure the noise as a function of the cell length b. Cells with a relatively long length of 2 mm have a small optical diameter of 2.5 mm, and therefore the transmitted intensity was low and the noise high. Short cells (0.2 mm) with 8 mm optical diameter, on the other hand, showed the highest intensity, but there was an additional constant electronic noise, which degraded the limit of detection. As the final result, a path length between 0.5 and 1 mm was the optimum.

For most of the experiments, we used BaF_2 and a wavelength of 215 nm. In this case, the minimum detectable absorbance was 5×10^{-5} AU. To compare this value with that of commercial HPLC detectors, we first have to calculate the rms values from our peak-to-peak values. This gives a minimum detectable absorbance of $\sim 1.25 \times 10^{-5}$ AU. Second, we have to take into consideration that the limit of detection is also determined by the path length. If the peak form were the same for both types of detectors, the upper path length would be 1 mm. So, a typical, commercial HPLC detector (10 mm cell) must have a minimum detectable absorbance of 1.25×10^{-4} AU to show the same limit of detection. This minimum detectable absorbance is higher than that of actual HPLC detectors but indeed much lower than one would expect from the low luminescence intensity.

ACKNOWLEDGMENT

We thank Dr. N. Zeug and the Siemens Co. for supporting this development.

Received for review October 5, 1994. Accepted March 20, 1995.[⊗]

AC940982O

[⊗] Abstract published in *Advance ACS Abstracts,* May 1, 1995.

Author Index

Abraham, M. H., 2162
Agüí, M. L., 2195
Aguilar, M.-I., 2145
Aizawa, M., 2212
Anigbogu, V. C., 2037
Appelhans, A. D., 1987
Armstrong, D. W., 2088

Barnabas, I. J., 2064
Beckert, W. F., 2020, 2096
Beeson, M. D., 1981
Benedicto, J., 2096
Berg, R. W., 2129
Bicker, G. R., 2292
Bilitewski, U., 2304
Bjerrum, N. J., 2129
Bletsos, I. V., 1955
Bordel García, N., 2216
Bright, F. V., 1935
Brown, R. S., 1998
Brumfield, J. C., 2201
Buess, M. L., 2256

Cai, J., 2054
Centonze, D., 2207
Chen, F.-T. A., 2239
Christensen, E., 2129
Claessens, H. A., 2103
Clemons, P. S., 1929
Collins, G. E., 2224
Copper, C. L., 2037
Cotter, R. J., 2180
Cramers, C. A., 2103
Crescenzi, C., 1968

Dadoo, R., 2026
Danielski, M. C., 2292
Dasgupta, P. K., 2042, 2110
Davidson, F., 1955
Dean, J. R., 2064
de Dios, C., 2231
Delmore, J. E., 1987
Di Corcia, A., 1968
Diehl, J. W., 2015
DiSanzo, F. P., 2015
Dolguine, A. I., 1963
Doroshenko, V. M., 2180

Effenhauser, C. S., 2284
Egekeze, J. O., 2292
Eller, F. J., 2288
Epstein, S., 2296
Evangelista, R. A., 2239

Farberman, B., 2296
Felinger, A., 2078
Fernández de la Campa, M. R., 2216
Finkbeiner, J. W., 2015
Fujimoto, C., 2050
Fung, E. N., 1913

García-Martínez, A. A., 2231
Garroway, A. N., 2256
Gómez-Carneros, A. M., 2231
Goss, C. A., 2201
Grate, J. W., 2162
Grinberg, N., 2292
Groenewold, G. S., 1987
Guttman, A., 2279

Hall, E. A. H., 1940
Hartig, C., 2308
Haruyama, T., 2212
Hathcock, K. W., 2201
He, X., 2264
Hearn, M. T. W., 2145
Hendel, I., 2296
Henion, J. D., 2054
Ho, P., 2096
Houk, R. S., 1929
Huang, H.-J., 2299

Ingram, J. C., 1987
Irene, E. A., 2201

Jacobson, S. C., 2059
Johnson, J. H., 2288
Jurkiewicz, A., 2188

Kerridge, D. H., 2129
Khodorkovski, M. A., 1963
Kim, R., 2096
King, J. W., 2288
Kobatake, E., 2212
Kriz, D., 2142
Krutchinsky, A. N., 1963
Künnecke, W., 2304

Laven, J., 2103
Lee, H.-B., 1976
Lennon, J. J., 1998
Li, L., 1950
Liu, M.-S., 2239
Liu, S., 2042
Liu, Y., 2020
Lonardo, R. F., 2246
Lopez-Avila, V., 2020, 2096

Maciel, G. E., 2188
Majcen, N., 2154
Malitesta, C., 2207
Manz, A., 2284
Marchese, S., 1968
Martin, C. R., 1920
Másson, M., 2212
Mattu, M. J., 2269
Menon, V. P., 1920
Michel, R. G., 2246
Minnich, M. G., 1929
Moore, A. W., 2059
Moore, W. N., 2030
Moreno-Bondi, M. C., 2231
Mosbach, K., 2142
Murray, K. K., 1981
Murray, R. W., 2201

Narang, U., 1935
Novič, M., 2154

Ong, S., 2119
Orellana, G., 2231
Owen, S. P., 2064

Palmisano, F., 2207
Patrash, S. J., 2162
Pawliszyn, J., 2010
Peart, T. E., 1976
Perpall, H. J., 2292
Pesic, B., 1987
Pidgeon, C., 2119
Pines, A., 2256
Pingarrón, J. M., 2195
Prasad, P. N., 1935
Preuss, M., 1940
Prosser, S. J., 1992

Rahman, M. H., 1935
Rajer-Kanduč, K., 2154
Rakestraw, D. J., 2026
Ramsey, J. M., 2059
Ramström, O., 2142
Ravey, M., 2296
Rechnitz, G. A., 2264
Reviejo, A. J., 2195
Rinke, G., 2308
Rohm, I., 2304
Rose-Pehrsson, S. L., 2224
Rundlett, K. L., 2088
Russell, D. H., 1981
Ruyken, M. M. A., 2170

Samperi, R., 1968
Sanz-Medel, A., 2216
Schwartz, H. E., 2279
Scrimgeour, C. M., 1992
Sepaniak, M. J., 2037
Shemer, R., 2296
Sheppard, R. L., 2054
Shirey, S. B., 2136
Sidler, D. R., 2292
Simpson, N., 1955
Sjögren, A., 2110
Slinn, D., 1955
Small, G. W., 2269
Smilde, A. K., 2170
Smith, G. B., 2292
Svensson, A., 2142

Tang, T.-C., 2299
Taylor, L. T., 2030
Thormann, W., 2070
Tomlinson, W. R., 2064
Tong, X., 2054
Tuminello, W. H., 1955
Tway, P. C., 2292

Valdés-Hevia y Temprano, M. C., 2216
van Breemen, R. B., 2004
Visser, J. A., 2170
Vissers, J. P. C., 2103
von Barner, J. H., 2129
von Heeren, F., 2070

Walker, R. J., 2136
Wang, J. H., 1935
Weigert, F. J., 1955
Whitaker, K. W., 2037
Whittal, R. M., 1950
Widmer, H. M., 2284
Wiederin, D. R., 2020
Wu, J., 2010

Yan, C., 2026
Yáñez-Sedeño, P., 2195
Yarovsky, I., 2145
Yesinowski, J. P., 2256
Yeung, E. S., 1913
Young, R., 2096
Yun, K., 2212
Yuzefovsky, A. I., 2246

Zambonin, P. G., 2207
Zare, R. N., 2026
Zhang, C.-X., 2070
Zhao, H., 2026
Zhu, J. J., 2020
Ziegeweid, M., 2256
Zupan, J., 2154

Focus
Insight
Depth

The New Dimension to ***Environmental Science & Technology***

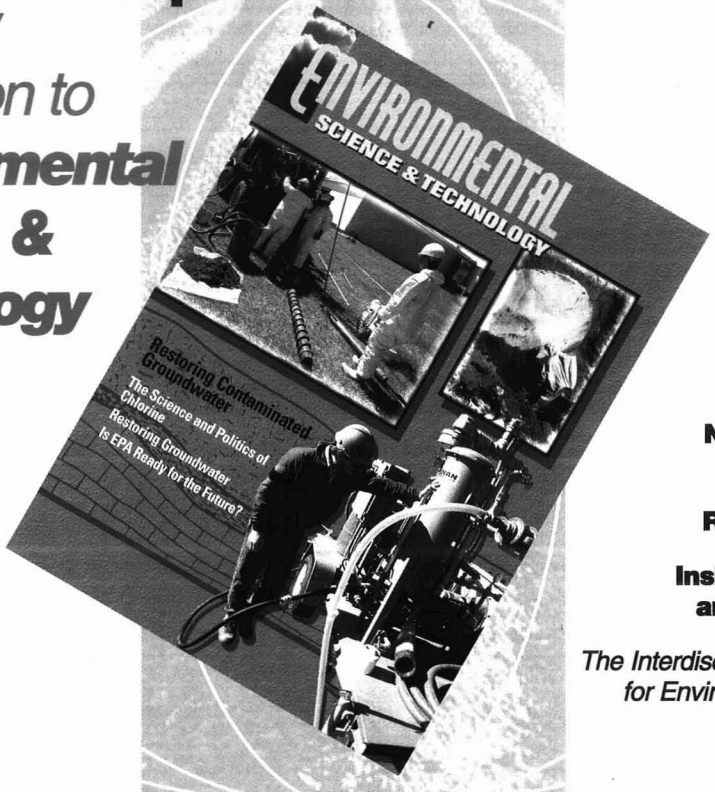

New Editorial Mix

Expanded News

Research Articles

Insights into Trends and Controversies

The Interdisciplinary Publication for Environmental Scientists and Professionals

Our expanded editorial coverage provides a balance of focus, insight, and depth in topics ranging from remediation and air quality to regulations and public policy. Two new departments, "Research Watch" and "EPA Watch," highlight current activities emerging at these two ends of the spectrum.

Critical analysis of policy, worldwide news, innovations in measurement, research articles by well-known authorities — all of these features offer you a broader base of knowledge than ever before. And, our new cover and interior design spotlight information so you'll know exactly where to look for new developments in areas that are beginning to affect your work.

In addition to the cutting-edge research for which this publication is highly acclaimed, the new editorial mix includes in-depth feature articles covering the areas that drive the environmental field: Science, technology, government, and society.

While many other environmental publications are devoted to one discipline or another, no other journal completely integrates all disciplines of the environmental field.

Experience the new *Environmental Science & Technology*. Subscribe today!

To order your one-year subscription right away call toll-free, 1-800-333-9511 (U.S. only). Outside the U.S. call 614-447-3776. Fax to 614-447-3671.

Editor

William H. Glaze
University of North Carolina, Chapel Hill

Associate Editors

Walter Giger
EAWAG, Switzerland

Ronald A. Hites
Indiana University at Bloomington

Cass T. Miller
University of North Carolina, Chapel Hill

Jerald L. Schnoor
University of Iowa

John Seinfeld
California Institute of Technology

Joseph M. Suflita
University of Oklahoma

1995 Subscription Rates

	U.S.	Canada & Mexico	Europe*	All Other Countries*
Member	$44	$68	$96	$113
Nonmember Personal	$90	$114	$142	$159
Nonmember Institutional	$585	$609	$637	$654

**Includes air service.*

ACS PUBLICATIONS
Essential Resources for the Chemical Sciences

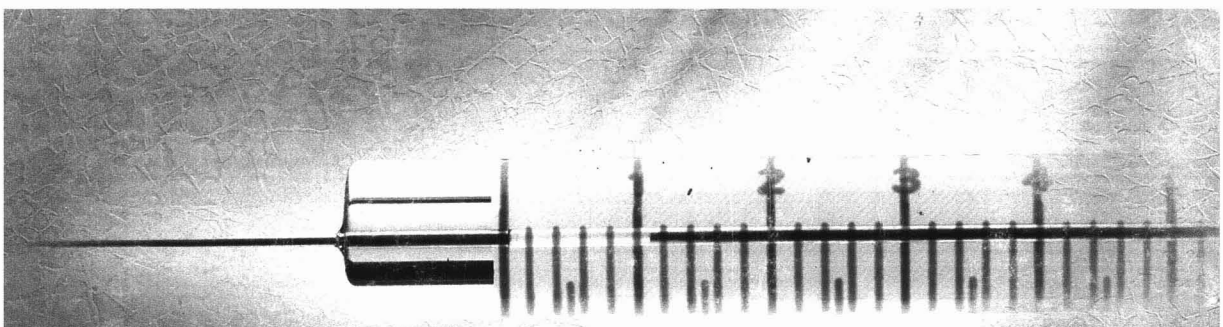

For Those Who Can't Always Read Between The Lines.

We Have Your Syringe.

• Accuracy and precision, depending on syringe series, is better than ±0.5%

• Plunger Drag easily adjusts to your preference

• Large Digital Display allows easy-to-read selection of syringe volumes

• Fine Adjustment Thumbwheel provides ease in setting syringe volumes

• Digital Syringes come with their own Certificate of Calibration based on N.I.S.T. traceable methods

• Plunger Stop can be set for repetitive, precise injections

The New Digital Syringe℠

HAMILTON

The Measure Of Excellence℠

Hamilton Company, 4970 Energy Way, Reno, Nevada 89502-4178 U.S.A.
Tel: (800) 648-5950, +1-702-858-3000 Fax: +1-702-856-7259

CIRCLE 4 ON READER SERVICE CARD